Muon Neutrino Charged Current Single Pion Production on Various Targets in the MINERvA Detector

by

Aaron Bercellie

Submitted in Partial Fulfillment of the

Requirements for the Degree

Doctor of Philosophy in Physics

Supervised by Professor Kevin McFarland

Department of Physics and Astronomy

Arts, Sciences and Engineering

School of Arts and Sciences

University of Rochester

Rochester, New York

2022

Table of Contents

Biographical Sketch ix
Acknowledgements x
Abstract xii
Contributors and Funding Sources xiii

List of Tables **xiv**

List of Figures **xxxiv**

1 Theory **1**

1.1 The Standard Model 1
1.1.1 Elementary fermions 2
1.1.2 Fundamental forces 3
1.2 Neutrino Oscillations 9
1.2.1 History of neutrino oscillations 9
1.2.2 Neutrino oscillation formalism 10
1.2.3 Cross sections on pion production 16
1.3 Charged Current Neutrino Interactions 18
1.3.1 Charged current quasielastic scattering (CCQE) 22
1.3.2 Resonant pion production 23

1.3.3 Deep inelastic scattering (DIS) . . . 27
1.3.4 Coherent pion production . . . 29
1.4 The Nuclear Medium . . . 33
1.4.1 Nucleons in the Nuclear Potential . . . 33
1.4.2 Multinucleon correlations . . . 34
1.4.3 Final State Interactions (FSI) . . . 36
1.5 Discussion of previous measurements of charged current single pion production . . . 38

2 The NuMI Beamline and the Neutrino Flux 43
2.1 Creating the Neutrino Beam . . . 44
2.1.1 Accelerating protons at the Main Injector . . . 44
2.1.2 The NuMI beam . . . 46
2.2 Characterizing the neutrino flux . . . 52
2.2.1 G4NuMI and Hadron Production . . . 53
2.2.2 In Situ Constraints . . . 55
2.2.3 Spatial Dependence of the Flux . . . 60

3 The MINERvA Detector 65
3.1 The Minerva Subdetectors . . . 66
3.1.1 Active tracking planes . . . 67
3.1.2 Scintillator Strips . . . 69
3.2 Data Acquisition . . . 70
3.2.1 Cross Talk . . . 73
3.2.2 Nuclear Target Region . . . 74
3.3 MINOS Near Detector . . . 76
3.4 Calibrations . . . 77

3.4.1 Energy Calibration 77
3.4.2 Timing Calibration 82
3.4.3 Plane alignment 83
3.4.4 Nuclear Target Positions 84

4 Simulation **87**

4.1 GENIE Neutrino Interaction Simulation 88
4.1.1 Quasielastic scattering 88
4.1.2 Resonant Pion Production 89
4.1.3 Deep Inelastic Scattering 91
4.1.4 Coherent Pion Production 92
4.2 The Nuclear Medium and Final State Interactions 93
4.2.1 Simulating the nucleus 93
4.2.2 Final State Interactions (FSI) 94
4.3 Detector Simulation 94
4.3.1 Particle Propagation 94
4.3.2 Data Overlay 96
4.3.3 Readout Simulation 96
4.4 Michel Simulation 98
4.4.1 Uncertainties in the Michel Electron Reconstruction Efficiency 104
4.5 Event Weights 109
4.5.1 Flux 109
4.5.2 MINOS Track Matching Efficiency 109
4.5.3 Particle Propagation 111
4.5.4 The MINERvA Tune and Additional Reweights 115

5 Reconstruction 126

5.1 Time Slicing . . . 126

5.2 Clustering . . . 127

5.3 Track Reconstruction . . . 131

5.3.1 The Long Tracker . . . 133

5.3.2 Short Trackers . . . 135

5.4 Vertex Reconstruction . . . 138

5.5 Muon Reconstruction . . . 140

5.5.1 MINOS Track Matching . . . 140

5.5.2 Charge and Momentum Reconstruction . . . 142

5.6 Michel Electron Reconstruction . . . 146

5.6.1 Selecting Michel Electron Candidates . . . 146

5.6.2 Michel Views . . . 148

5.6.3 Estimating the Michel endpoints using linear fits . . . 149

5.7 Pion Reconstruction . . . 153

5.7.1 Hadron Energy Reconstruction . . . 153

5.7.2 Charged Pion Selection . . . 154

5.7.3 Michel Match to the Track Endpoint . . . 155

5.7.4 Log Likelihood Ratio Particle Identification (PID) Score . . . 161

5.7.5 Track End Node Energy . . . 163

5.8 Hadron Calorimetry . . . 170

5.8.1 Passive Material Correction . . . 170

5.8.2 Calorimetric Spline Correction . . . 171

5.8.3 Calorimetric Additive Correction . . . 173

5.8.4 Hadron Calorimetry Used in this Analysis . . . 176

6 Analysis **177**

6.1 Signal Definition . . . 177

6.2 Differential Cross Section Overview . . . 179

6.2.1 Analysis Variables . . . 180

6.3 Event Selection . . . 182

6.3.1 Interaction Vertex Selection . . . 183

6.3.2 Muon Selection . . . 184

6.3.3 Charged Pion Selection . . . 186

6.3.4 Invariant Hadronic Mass W_{exp} Selection . . . 188

6.3.5 Isolated Prong Selection . . . 189

6.3.6 Event Selection Results . . . 192

6.4 Analysis Backgrounds . . . 201

6.4.1 Background constraints . . . 202

6.4.2 High W_{exp} Sideband Fit in the Tracker . . . 204

6.4.3 Plastic Signal Model Fit in the Tracker . . . 207

6.4.4 Plastic Contamination Sideband Fit in the Nuclear Targets . . . 209

6.4.5 High W_{exp} Sideband Fits in the Nuclear Targets . . . 212

6.5 Background Subtraction . . . 221

6.6 Unfolding . . . 230

6.6.1 Migration Matrices . . . 231

6.6.2 Iterative "Bayesian" Unfolding . . . 240

6.6.3 Unfolding Warping Study . . . 241

6.6.4 Unfolded Distributions . . . 251

6.7 Efficiency Correction . . . 261

6.8 Cross Section Normalizations . . . 271

6.9 Differential Cross Sections . . . 272

6.9.1 Differential Cross Sections 272
6.9.2 Differential Cross Sections Compared to Predictions of Different Neutrino Interaction Types 281
6.9.3 Area Normalized Cross Sections 290
6.9.4 Ratios of Differential Cross Sections on Passive Materials to Scintillator 299
6.9.5 Integrated Cross Sections 308
6.10 Systematic Uncertainties 310
6.10.1 Cross section models 322
6.10.2 FSI (Final State Interactions) Models 327
6.10.3 Flux 331
6.10.4 Muon Reconstruction 334
6.10.5 Pion Reconstruction 337
6.10.6 Sideband Fit Errors 340
6.10.7 Other Uncertainties 344

7 Conclusions **348**

Bibliography **361**

Appendices **377**

Appendix A The MINERvA Collaboration **378**

Appendix B Purity Efficiency Tables **381**

Appendix C Tables of measured cross sections, uncertainties, and covariance matrices **385**

Appendix D Tables of measured cross section ratios, uncertainties, and covariance matrices **451**

Appendix E Cross Section Error Plots **504**

Appendix F Cross Section Ratio Error Plots **625**

Appendix G Cross Section Correlation Matrices **746**

Appendix H Cross Section Ratio Correlation Matrices **771**

Biographical Sketch

The author was born in Seoul, South Korea, and grew up in Littleton, Colorado. He attended the University of Colorado at Boulder, graduating in 2012 with a Bachelor of Arts degree in physics, with a minor in mathematics. After graduation, he started at the University of Rochester as a Ph.D. student. Initially working with the T2K collaboration in 2013, he joined the MINERvA collaboration in 2014 under the supervision of Kevin McFarland and Steve Manly.

As a member of the MINERvA collaboration, the author contributed to detector operations, the second MINERvA testbeam detector, software development, and data analysis. This culminated with the physics results described in this thesis.

Acknowledgments

This thesis would not have been completed without the help of all the people that have supported me throughout my years as a physics student. Physics is one of my true passions, but without the physics communities at the University of Colorado at Boulder, the University of Rochester, the MINERvA collaboration, and Fermilab, I would not have been able to get this far. I'm grateful for everyone that I've met during my physics journey.

First, let me thank all my physics professors at the University of Colorado, with a special thank you to Dr. Zimmerman, Dr. Marino, and Dr. Becker. I wouldn't have started down the path of neutrino physics and would never have understood quantum mechanics well enough to get into graduate school without all of you. I'd also like to thank my friends Scott, Lance, Jeff, Pat, Cristina, Mariah, Ed, David, and Mike for supporting me through my undergraduate studies.

I'd also like to acknowledge everyone I met in my first few years at the University of Rochester. The support we provided each other and the fun times we had were the only things that kept me sane for those long, sleep-deprived times. Thank you to Alan, Lucien, Dev, Yi-ting, Levi, Andrew, and Marissa.

To Kevin and Steve, thank you for advising and mentoring me. Thank you to Phil and Dan for being very patient mentors, and answering all my incessant questions throughout the years. And thanks to the rest of the Rochester neutrino group: Arie, Chris, Jeremy, Aaron M, Ko, Tejin, Gonzalo, Mehreen, Clarence, Ryan, and Sarah. And a special thanks to Connie, Laura B, and Linda for all the administrative support at the University of Rochester.

For all my fellow MINERvA collaborators, I am extremely honored to be counted among all of you. You have all nurtured and guided me throughout this entire analysis.

Thanks to Tammy W for providing me the analysis tool I've used throughout these years. To Trung, Anne, and Laura F, I cannot thank you all enough for the time you've taken to teach me and listen to me as I've struggled through my research. To Andrew, Ben, Rob, and Jeffrey, I would not have gotten as far as I did without being able to collaborate and discuss things with you.

Finally, thank you to all of my family and friends. Mom and Angie, you have always been there to encourage and support me, and listen to me as I go off on tangents about physics. Dad, thank you for instilling my love of math and physics, and understanding those physics tangents. Thank you to my friends Phyllis, Patrick, Dan A, and Krista for your unwavering support. And a huge thanks to Kelly and Luna for your patience and love through this entire process.

Abstract

Measurements of neutrino oscillation parameters at accelerator-based experiments require precise knowledge of neutrino interaction cross sections. A significant fraction of neutrino interactions observed in these experiments produce single charged pions. While single charged pion production has been measured on hydrocarbon and water, few precise measurements exist for heavier targets, and there are no high statistics measurements that directly compare pion production on different targets.

This thesis measures differential cross sections of muon neutrino charged current single charged pion production with no other mesons in the final state in a neutrino beam with a mean energy of $\approx$ 6 GeV. The pion production is studied on targets of scintillator, carbon, water, iron, and lead at MINERvA, a neutrino cross section experiment located in the NuMI beamline at Fermilab. These measured cross sections are differential in μ^- and π^+ kinematics.

A strong suppression of low Q^2 and an enhancement of low T_π are observed relative to commonly used neutrino interaction models in both the light and heavy nuclear targets. Incorporation of these observed effects in future neutrino oscillation experiments will improve their ability to measure energy of neutrino interactions, and therefore measure the parameters governing neutrino oscillations.

Contributors and Funding Sources

This work was supervised by a committee consisting of Advisor Kevin McFarland (Department of Physics), Professor Steve Manly (Department of Physics), Professor Steven Teitel (Department of Physics), Professor Andrew Berger (Department of Optics), and chaired by Professor Dustin Trail (Department of Earth & Environmental Sciences).

This thesis documents work performed by the author as a member of the MINERvA collaboration. Chapter 6 describes the analysis performed by the author using software and methods developed by the collaboration. The author was one of the primary developers of the unfolding tool described in section 6.6.3. Section 2.2 describes the development of the neutrino flux prediction by the collaboration. Chapter 3 describes work done by the collaboration involving the MINERvA detector. Chapter 4 describes work done by the collaboration involving the MINERvA simulation. The author was closely involved with the development of the particle propagation weights described in section 4.5.3. The author was responsible for the developing the weighting scheme for resonant pion production in section 4.5.4.2, the diffractive pion production weights in section 4.5.4.4, and the low Q^2 suppression described in 4.5.4.6. The collaboration developed the reconstruction techniques described in Chapter 5. The author was one of the primary developers of the Michel electron reconstruction (section 5.6), the pion identification (section 5.7), and the calorimetric additive correction (section 5.8). As a member of the collaboration, the author contributed to the maintenance of the detector and supported the overall operation of the experiment. The author has also developed common software used support other MINERvA analyses. A list of collaborators is found in Appendix A. This work was supported by Department of Energy grant DE-SC0008475.

List of Tables

1.1 Three neutrino mixing best fit oscillation parameters 17

1.2 Summary of relevant neutrino interaction processes 20

1.3 Llewellyn-Smith Model Parameters 22

1.4 Rein-Seghal Resonant Pion Production Model Parameters 26

1.5 Deep Inelastic Scattering Parameters 28

1.6 Primary FSI modes for charged pions 37

2.1 Explanation of variables involved in the calculation of a flux integrated differential cross section 52

2.2 $\sigma(\nu_\mu e^- \rightarrow \nu_\mu e^-)$ Parameters 56

2.3 Daisy Petal Variables 62

3.1 Calibration Parameters 78

3.2 Best longitudinal shifts for the nuclear targets 85

4.1 GENIE Pion Angle Model Parameters 91

4.2 Birk's Law Parameters 97

4.3 GEANT4 Michel Electron Energy Parameters 100

4.4 Critical energies of the passive materials in the nuclear targets . . . 104

4.5 Michel Electron Reconstruction Efficiencies for FHC and RHC beam configurations . . . 107
4.6 Michel Electron Reconstruction Efficiencies for μ^+ and μ^- . . . 108
4.7 Nominal and fitted GENIE single pion production model parameters 118
4.8 Fit parameters of the ME $1\pi^+$ low Q^2 suppression function. . . . 124

5.1 Cluster types and descriptions . . . 129
5.2 Measurement of muon momentum by curvature parameters . . . 143
5.3 Michel Linear Fit Parameters . . . 150
5.4 Maximum distance cut for Michel match (cm) . . . 156
5.5 Node energy cut values for each target (MeV) . . . 163

6.1 Definitions of the variables measured in this analysis . . . 179
6.2 Definitions of the variables measured in this analysis . . . 180
6.3 Z ranges of the nuclear target fiducial volume . . . 184
6.4 Increase in signal purity and cut efficiency (%) of events having ≥ 1 Michel matched hadron tracks . . . 186
6.5 Increase in signal purity and cut efficiency (%) of events having ≥ 1 Michel matched hadron track with LLR Score > 0 . . . 187
6.6 Increase in signal purity and cut efficiency (%) of events having 1 charged pion track with good energy reconstruction . . . 188
6.7 Increase in signal purity and cut efficiency (%) of the reconstructed $W_{exp} < 1.4$ GeV/c^2 cut . . . 190
6.8 Increase in signal purity and cut efficiency (%) of the number of isolated prongs < 2 cut . . . 190
6.9 Purity and Efficiency of Final Event Selection . . . 192

6.10 Tracker W_{exp} sideband scales found from the fit in the high $W > 1.4$ GeV sideband for all tracker events 207
6.11 Upstream and downstream plastic contamination scales 212
6.12 Nuclear target W_{exp} sideband scales found from the fit in the high $W > 1.4$ GeV sideband 215
6.13 List of warp models used in the unfolding study 242
6.14 Number of unfolding iterations used by each analysis variable 243
6.15 Cross section normalization factors 271
6.16 Definitions of the neutrino interaction categories 281
6.17 Integrated Carbon Cross Section (cm^2/nucleon) 308
6.18 Integrated Water Cross Section (cm^2/nucleon) 308
6.19 Integrated Iron Cross Section (cm^2/nucleon) 309
6.20 Integrated Lead Cross Section (cm^2/nucleon) 309
6.21 Integrated Tracker Cross Section (cm^2/nucleon) 309
6.22 Systematic uncertainty covariance matrix variables 311
6.23 Systematic Uncertainty Groups 313
6.24 GENIE charged current quasielastic (CCQE) model uncertainties . . 322
6.25 GENIE resonant pion production model uncertainties 323
6.26 GENIE Nonresonant pion production model uncertainties 323
6.27 GENIE coherent and diffractive pion production model uncertainties 324
6.28 GENIE FSI uncertainties 330
6.29 Sideband fit uncertainties 343
6.30 Target mass uncertainties 344
6.31 Particle response uncertainties 344

B.1 Purity, Efficiency, and Cut Efficiency of Signal Events on Carbon . . 382

B.2 Purity, Efficiency, and Cut Efficiency of Signal Events on Water . . . 382

B.3 Purity, Efficiency, and Cut Efficiency of Signal Events on Iron 383

B.4 Purity, Efficiency, and Cut Efficiency of Signal Events on Lead . . . 383

B.5 Purity, Efficiency, and Cut Efficiency of Signal Events on Tracker . . 384

C.1 Measured cross section in p_μ on scintillator, in units of 10^{-42} cm^2/GeV/c/nucleon, and the absolute and fractional cross section uncertainties 386

C.2 Statistical covariance matrix of measured cross section in p_μ on scintillator, in units of 10^{-84} (cm^2/GeV/c/nucleon)^2 386

C.3 Systematic covariance matrix of measured cross section in p_μ on scintillator, in units of 10^{-84} (cm^2/GeV/c/nucleon)^2 386

C.4 Measured cross section in θ_μ on scintillator, in units of 10^{-42} cm^2/degree/nucleon, and the absolute and fractional cross section uncertainties 387

C.5 Statistical covariance matrix of measured cross section in θ_μ on scintillator, in units of 10^{-84} (cm^2/degree/nucleon)^2 387

C.6 Systematic covariance matrix of measured cross section in θ_μ on scintillator, in units of 10^{-84} (cm^2/degree/nucleon)^2 387

C.7 Measured cross section in $p_{\mu,||}$ on scintillator, in units of 10^{-42} cm^2/GeV/c/nucleon, and the absolute and fractional cross section uncertainties 388

C.8 Statistical covariance matrix of measured cross section in $p_{\mu,||}$ on scintillator, in units of 10^{-84} (cm^2/GeV/c/nucleon)^2 388

C.9 Systematic covariance matrix of measured cross section in $p_{\mu,||}$ on scintillator, in units of 10^{-84} (cm^2/GeV/c/nucleon)^2 388

C.10 Measured cross section in $p_{\mu,T}$ on scintillator, in units of 10^{-42} cm^2/GeV/c/nucleon, and the absolute and fractional cross section uncertainties 389

C.11 Statistical covariance matrix of measured cross section in $p_{\mu,T}$ on scintillator, in units of 10^{-84} (cm^2/GeV/c/nucleon)^2 390
C.12 Systematic covariance matrix of measured cross section in $p_{\mu,T}$ on scintillator, in units of 10^{-84} (cm^2/GeV/c/nucleon)^2 391
C.13 Measured cross section in Q^2 on scintillator, in units of 10^{-42} cm^2/GeV^2/nucleon, and the absolute and fractional cross section uncertainties 392
C.14 Statistical covariance matrix of measured cross section in Q^2 on scintillator, in units of 10^{-84} (cm^2/GeV^2/nucleon)^2 393
C.15 Systematic covariance matrix of measured cross section in Q^2 on scintillator, in units of 10^{-84} (cm^2/GeV^2/nucleon)^2 394
C.16 Measured cross section in W_{exp} on scintillator, in units of 10^{-42} cm^2/GeV/c^2/nucleon, and the absolute and fractional cross section uncertainties 395
C.17 Statistical covariance matrix of measured cross section in W_{exp} on scintillator, in units of 10^{-84} (cm^2/GeV/c^2/nucleon)^2 395
C.18 Systematic covariance matrix of measured cross section in W_{exp} on scintillator, in units of 10^{-84} (cm^2/GeV/c^2/nucleon)^2 395
C.19 Measured cross section in T_π on scintillator, in units of 10^{-42} cm^2/GeV/nucleon, and the absolute and fractional cross section uncertainties 395
C.20 Statistical covariance matrix of measured cross section in T_π on scintillator, in units of 10^{-84} (cm^2/GeV/nucleon)^2 396
C.21 Systematic covariance matrix of measured cross section in T_π on scintillator, in units of 10^{-84} (cm^2/GeV/nucleon)^2 396
C.22 Measured cross section in θ_π on scintillator, in units of 10^{-42} cm^2/degree/nucleon, and the absolute and fractional cross section uncertainties 396
C.23 Statistical covariance matrix of measured cross section in θ_π on scintillator, in units of 10^{-84} (cm^2/degree/nucleon)^2 397

C.24 Systematic covariance matrix of measured cross section in θ_π on scintillator, in units of 10^{-84} (cm^2/degree/nucleon)^2 398
C.25 Measured cross section in p_μ on carbon, in units of 10^{-42} cm^2/GeV/c/nucleon, and the absolute and fractional cross section uncertainties 399
C.26 Statistical covariance matrix of measured cross section in p_μ on carbon, in units of 10^{-84} (cm^2/GeV/c/nucleon)^2 399
C.27 Systematic covariance matrix of measured cross section in p_μ on carbon, in units of 10^{-84} (cm^2/GeV/c/nucleon)^2 399
C.28 Measured cross section in θ_μ on carbon, in units of 10^{-42} cm^2/degree/nucleon, and the absolute and fractional cross section uncertainties 400
C.29 Statistical covariance matrix of measured cross section in θ_μ on carbon, in units of 10^{-84} (cm^2/degree/nucleon)^2 400
C.30 Systematic covariance matrix of measured cross section in θ_μ on carbon, in units of 10^{-84} (cm^2/degree/nucleon)^2 400
C.31 Measured cross section in $p_{\mu,||}$ on carbon, in units of 10^{-42} cm^2/GeV/c/nucleon, and the absolute and fractional cross section uncertainties 401
C.32 Statistical covariance matrix of measured cross section in $p_{\mu,||}$ on carbon, in units of 10^{-84} (cm^2/GeV/c/nucleon)^2 401
C.33 Systematic covariance matrix of measured cross section in $p_{\mu,||}$ on carbon, in units of 10^{-84} (cm^2/GeV/c/nucleon)^2 401
C.34 Measured cross section in $p_{\mu,T}$ on carbon, in units of 10^{-42} cm^2/GeV/c/nucleon, and the absolute and fractional cross section uncertainties 402
C.35 Statistical covariance matrix of measured cross section in $p_{\mu,T}$ on carbon, in units of 10^{-84} (cm^2/GeV/c/nucleon)^2 403
C.36 Systematic covariance matrix of measured cross section in $p_{\mu,T}$ on carbon, in units of 10^{-84} (cm^2/GeV/c/nucleon)^2 404

C.37 Measured cross section in Q^2 on carbon, in units of 10^{-42} cm^2/GeV^2/nucleon, and the absolute and fractional cross section uncertainties 405
C.38 Statistical covariance matrix of measured cross section in Q^2 on carbon, in units of 10^{-84} (cm^2/GeV^2/nucleon)^2 406
C.39 Systematic covariance matrix of measured cross section in Q^2 on carbon, in units of 10^{-84} (cm^2/GeV^2/nucleon)^2 407
C.40 Measured cross section in W_{exp} on carbon, in units of 10^{-42} cm^2/GeV/c^2/nucleon, and the absolute and fractional cross section uncertainties 408
C.41 Statistical covariance matrix of measured cross section in W_{exp} on carbon, in units of 10^{-84} (cm^2/GeV/c^2/nucleon)^2 408
C.42 Systematic covariance matrix of measured cross section in W_{exp} on carbon, in units of 10^{-84} (cm^2/GeV/c^2/nucleon)^2 408
C.43 Measured cross section in T_π on carbon, in units of 10^{-42} cm^2/GeV/nucleon, and the absolute and fractional cross section uncertainties 408
C.44 Statistical covariance matrix of measured cross section in T_π on carbon, in units of 10^{-84} (cm^2/GeV/nucleon)^2 409
C.45 Systematic covariance matrix of measured cross section in T_π on carbon, in units of 10^{-84} (cm^2/GeV/nucleon)^2 409
C.46 Measured cross section in θ_π on carbon, in units of 10^{-42} cm^2/degree/nucleon, and the absolute and fractional cross section uncertainties 409
C.47 Statistical covariance matrix of measured cross section in θ_π on carbon, in units of 10^{-84} (cm^2/degree/nucleon)^2 410
C.48 Systematic covariance matrix of measured cross section in θ_π on carbon, in units of 10^{-84} (cm^2/degree/nucleon)^2 411
C.49 Measured cross section in p_μ on water, in units of 10^{-42} cm^2/GeV/c/nucleon, and the absolute and fractional cross section uncertainties 412

C.50 Statistical covariance matrix of measured cross section in p_μ on water, in units of 10^{-84} (cm^2/GeV/c/nucleon)^2 412
C.51 Systematic covariance matrix of measured cross section in p_μ on water, in units of 10^{-84} (cm^2/GeV/c/nucleon)^2 412
C.52 Measured cross section in θ_μ on water, in units of 10^{-42} cm^2/degree/nucleon, and the absolute and fractional cross section uncertainties 413
C.53 Statistical covariance matrix of measured cross section in θ_μ on water, in units of 10^{-84} (cm^2/degree/nucleon)^2 413
C.54 Systematic covariance matrix of measured cross section in θ_μ on water, in units of 10^{-84} (cm^2/degree/nucleon)^2 413
C.55 Measured cross section in $p_{\mu,||}$ on water, in units of 10^{-42} cm^2/GeV/c/nucleon, and the absolute and fractional cross section uncertainties 414
C.56 Statistical covariance matrix of measured cross section in $p_{\mu,||}$ on water, in units of 10^{-84} (cm^2/GeV/c/nucleon)^2 414
C.57 Systematic covariance matrix of measured cross section in $p_{\mu,||}$ on water, in units of 10^{-84} (cm^2/GeV/c/nucleon)^2 414
C.58 Measured cross section in $p_{\mu,T}$ on water, in units of 10^{-42} cm^2/GeV/c/nucleon, and the absolute and fractional cross section uncertainties 415
C.59 Statistical covariance matrix of measured cross section in $p_{\mu,T}$ on water, in units of 10^{-84} (cm^2/GeV/c/nucleon)^2 416
C.60 Systematic covariance matrix of measured cross section in $p_{\mu,T}$ on water, in units of 10^{-84} (cm^2/GeV/c/nucleon)^2 417
C.61 Measured cross section in Q^2 on water, in units of 10^{-42} cm^2/GeV^2/nucleon, and the absolute and fractional cross section uncertainties 418
C.62 Statistical covariance matrix of measured cross section in Q^2 on water, in units of 10^{-84} (cm^2/GeV^2/nucleon)^2 419

C.63 Systematic covariance matrix of measured cross section in Q^2 on water, in units of 10^{-84} $(\mathrm{cm}^2/\mathrm{GeV}^2/\mathrm{nucleon})^2$ 420
C.64 Measured cross section in W_{exp} on water, in units of 10^{-42} $\mathrm{cm}^2/\mathrm{GeV}/\mathrm{c}^2/\mathrm{nucleon}$, and the absolute and fractional cross section uncertainties 421
C.65 Statistical covariance matrix of measured cross section in W_{exp} on water, in units of 10^{-84} $(\mathrm{cm}^2/\mathrm{GeV}/\mathrm{c}^2/\mathrm{nucleon})^2$ 421
C.66 Systematic covariance matrix of measured cross section in W_{exp} on water, in units of 10^{-84} $(\mathrm{cm}^2/\mathrm{GeV}/\mathrm{c}^2/\mathrm{nucleon})^2$ 421
C.67 Measured cross section in T_π on water, in units of 10^{-42} $\mathrm{cm}^2/\mathrm{GeV}/\mathrm{nucleon}$, and the absolute and fractional cross section uncertainties 421
C.68 Statistical covariance matrix of measured cross section in T_π on water, in units of 10^{-84} $(\mathrm{cm}^2/\mathrm{GeV}/\mathrm{nucleon})^2$ 422
C.69 Systematic covariance matrix of measured cross section in T_π on water, in units of 10^{-84} $(\mathrm{cm}^2/\mathrm{GeV}/\mathrm{nucleon})^2$ 422
C.70 Measured cross section in θ_π on water, in units of 10^{-42} $\mathrm{cm}^2/\mathrm{degree}/\mathrm{nucleon}$, and the absolute and fractional cross section uncertainties 422
C.71 Statistical covariance matrix of measured cross section in θ_π on water, in units of 10^{-84} $(\mathrm{cm}^2/\mathrm{degree}/\mathrm{nucleon})^2$ 423
C.72 Systematic covariance matrix of measured cross section in θ_π on water, in units of 10^{-84} $(\mathrm{cm}^2/\mathrm{degree}/\mathrm{nucleon})^2$ 424
C.73 Measured cross section in p_μ on iron, in units of 10^{-42} $\mathrm{cm}^2/\mathrm{GeV}/\mathrm{c}/\mathrm{nucleon}$, and the absolute and fractional cross section uncertainties 425
C.74 Statistical covariance matrix of measured cross section in p_μ on iron, in units of 10^{-84} $(\mathrm{cm}^2/\mathrm{GeV}/\mathrm{c}/\mathrm{nucleon})^2$ 425
C.75 Systematic covariance matrix of measured cross section in p_μ on iron, in units of 10^{-84} $(\mathrm{cm}^2/\mathrm{GeV}/\mathrm{c}/\mathrm{nucleon})^2$ 425

C.76 Measured cross section in θ_μ on iron, in units of 10^{-42} cm^2/degree/nucleon, and the absolute and fractional cross section uncertainties 426
C.77 Statistical covariance matrix of measured cross section in θ_μ on iron, in units of 10^{-84} (cm^2/degree/nucleon)^2 426
C.78 Systematic covariance matrix of measured cross section in θ_μ on iron, in units of 10^{-84} (cm^2/degree/nucleon)^2 426
C.79 Measured cross section in $p_{\mu,||}$ on iron, in units of 10^{-42} cm^2/GeV/c/nucleon, and the absolute and fractional cross section uncertainties 427
C.80 Statistical covariance matrix of measured cross section in $p_{\mu,||}$ on iron, in units of 10^{-84} (cm^2/GeV/c/nucleon)^2 427
C.81 Systematic covariance matrix of measured cross section in $p_{\mu,||}$ on iron, in units of 10^{-84} (cm^2/GeV/c/nucleon)^2 427
C.82 Measured cross section in $p_{\mu,T}$ on iron, in units of 10^{-42} cm^2/GeV/c/nucleon, and the absolute and fractional cross section uncertainties 428
C.83 Statistical covariance matrix of measured cross section in $p_{\mu,T}$ on iron, in units of 10^{-84} (cm^2/GeV/c/nucleon)^2 429
C.84 Systematic covariance matrix of measured cross section in $p_{\mu,T}$ on iron, in units of 10^{-84} (cm^2/GeV/c/nucleon)^2 430
C.85 Measured cross section in Q^2 on iron, in units of 10^{-42} cm^2/GeV^2/nucleon, and the absolute and fractional cross section uncertainties 431
C.86 Statistical covariance matrix of measured cross section in Q^2 on iron, in units of 10^{-84} (cm^2/GeV^2/nucleon)^2 432
C.87 Systematic covariance matrix of measured cross section in Q^2 on iron, in units of 10^{-84} (cm^2/GeV^2/nucleon)^2 433
C.88 Measured cross section in W_{exp} on iron, in units of 10^{-42} cm^2/GeV/c^2/nucleon, and the absolute and fractional cross section uncertainties 434

C.89 Statistical covariance matrix of measured cross section in W_{exp} on iron, in units of 10^{-84} $(\mathrm{cm}^2/\mathrm{GeV}/\mathrm{c}^2/\mathrm{nucleon})^2$ 434
C.90 Systematic covariance matrix of measured cross section in W_{exp} on iron, in units of 10^{-84} $(\mathrm{cm}^2/\mathrm{GeV}/\mathrm{c}^2/\mathrm{nucleon})^2$ 434
C.91 Measured cross section in T_π on iron, in units of 10^{-42} $\mathrm{cm}^2/\mathrm{GeV}/\mathrm{nucleon}$, and the absolute and fractional cross section uncertainties 434
C.92 Statistical covariance matrix of measured cross section in T_π on iron, in units of 10^{-84} $(\mathrm{cm}^2/\mathrm{GeV}/\mathrm{nucleon})^2$ 435
C.93 Systematic covariance matrix of measured cross section in T_π on iron, in units of 10^{-84} $(\mathrm{cm}^2/\mathrm{GeV}/\mathrm{nucleon})^2$ 435
C.94 Measured cross section in θ_π on iron, in units of 10^{-42} $\mathrm{cm}^2/\mathrm{degree}/\mathrm{nucleon}$, and the absolute and fractional cross section uncertainties 435
C.95 Statistical covariance matrix of measured cross section in θ_π on iron, in units of 10^{-84} $(\mathrm{cm}^2/\mathrm{degree}/\mathrm{nucleon})^2$ 436
C.96 Systematic covariance matrix of measured cross section in θ_π on iron, in units of 10^{-84} $(\mathrm{cm}^2/\mathrm{degree}/\mathrm{nucleon})^2$ 437
C.97 Measured cross section in p_μ on lead, in units of 10^{-42} $\mathrm{cm}^2/\mathrm{GeV}/\mathrm{c}/\mathrm{nucleon}$, and the absolute and fractional cross section uncertainties 438
C.98 Statistical covariance matrix of measured cross section in p_μ on lead, in units of 10^{-84} $(\mathrm{cm}^2/\mathrm{GeV}/\mathrm{c}/\mathrm{nucleon})^2$ 438
C.99 Systematic covariance matrix of measured cross section in p_μ on lead, in units of 10^{-84} $(\mathrm{cm}^2/\mathrm{GeV}/\mathrm{c}/\mathrm{nucleon})^2$ 438
C.100 Measured cross section in θ_μ on lead, in units of 10^{-42} $\mathrm{cm}^2/\mathrm{degree}/\mathrm{nucleon}$, and the absolute and fractional cross section uncertainties 439
C.101 Statistical covariance matrix of measured cross section in θ_μ on lead, in units of 10^{-84} $(\mathrm{cm}^2/\mathrm{degree}/\mathrm{nucleon})^2$ 439

C.102 Systematic covariance matrix of measured cross section in θ_μ on lead, in units of 10^{-84} (cm^2/degree/nucleon)^2 439
C.103 Measured cross section in $p_{\mu,||}$ on lead, in units of 10^{-42} cm^2/GeV/c/nucleon, and the absolute and fractional cross section uncertainties 440
C.104 Statistical covariance matrix of measured cross section in $p_{\mu,||}$ on lead, in units of 10^{-84} (cm^2/GeV/c/nucleon)^2 440
C.105 Systematic covariance matrix of measured cross section in $p_{\mu,||}$ on lead, in units of 10^{-84} (cm^2/GeV/c/nucleon)^2 440
C.106 Measured cross section in $p_{\mu,T}$ on lead, in units of 10^{-42} cm^2/GeV/c/nucleon, and the absolute and fractional cross section uncertainties 441
C.107 Statistical covariance matrix of measured cross section in $p_{\mu,T}$ on lead, in units of 10^{-84} (cm^2/GeV/c/nucleon)^2 442
C.108 Systematic covariance matrix of measured cross section in $p_{\mu,T}$ on lead, in units of 10^{-84} (cm^2/GeV/c/nucleon)^2 443
C.109 Measured cross section in Q^2 on lead, in units of 10^{-42} cm^2/GeV^2/nucleon, and the absolute and fractional cross section uncertainties 444
C.110 Statistical covariance matrix of measured cross section in Q^2 on lead, in units of 10^{-84} (cm^2/GeV^2/nucleon)^2 445
C.111 Systematic covariance matrix of measured cross section in Q^2 on lead, in units of 10^{-84} (cm^2/GeV^2/nucleon)^2 446
C.112 Measured cross section in W_{exp} on lead, in units of 10^{-42} cm^2/GeV/c^2/nucleon, and the absolute and fractional cross section uncertainties 447
C.113 Statistical covariance matrix of measured cross section in W_{exp} on lead, in units of 10^{-84} (cm^2/GeV/c^2/nucleon)^2 447
C.114 Systematic covariance matrix of measured cross section in W_{exp} on lead, in units of 10^{-84} (cm^2/GeV/c^2/nucleon)^2 447

C.115 Measured cross section in T_π on lead, in units of 10^{-42} cm^2/GeV/nucleon, and the absolute and fractional cross section uncertainties 447

C.116 Statistical covariance matrix of measured cross section in T_π on lead, in units of 10^{-84} (cm^2/GeV/nucleon)^2 448

C.117 Systematic covariance matrix of measured cross section in T_π on lead, in units of 10^{-84} (cm^2/GeV/nucleon)^2 448

C.118 Measured cross section in θ_π on lead, in units of 10^{-42} cm^2/degree/nucleon, and the absolute and fractional cross section uncertainties 448

C.119 Statistical covariance matrix of measured cross section in θ_π on lead, in units of 10^{-84} (cm^2/degree/nucleon)^2 449

C.120 Systematic covariance matrix of measured cross section in θ_π on lead, in units of 10^{-84} (cm^2/degree/nucleon)^2 450

D.1 Measured cross section ratio of carbon over scintillator in p_μ, and the absolute and fractional cross section ratio uncertainties 452

D.2 Statistical covariance matrix of measured cross section ratio of carbon over scintillator in p_μ 452

D.3 Systematic covariance matrix of measured cross section ratio of carbon over scintillator in p_μ 452

D.4 Measured cross section ratio of carbon over scintillator in θ_μ, and the absolute and fractional cross section ratio uncertainties 453

D.5 Statistical covariance matrix of measured cross section ratio of carbon over scintillator in θ_μ 453

D.6 Systematic covariance matrix of measured cross section ratio of carbon over scintillator in θ_μ 453

D.7 Measured cross section ratio of carbon over scintillator in $p_{\mu,||}$, and the absolute and fractional cross section ratio uncertainties 454
D.8 Statistical covariance matrix of measured cross section ratio of carbon over scintillator in $p_{\mu,||}$ 454
D.9 Systematic covariance matrix of measured cross section ratio of carbon over scintillator in $p_{\mu,||}$ 454
D.10 Measured cross section ratio of carbon over scintillator in $p_{\mu,T}$, and the absolute and fractional cross section ratio uncertainties 455
D.11 Statistical covariance matrix of measured cross section ratio of carbon over scintillator in $p_{\mu,T}$ 456
D.12 Systematic covariance matrix of measured cross section ratio of carbon over scintillator in $p_{\mu,T}$ 457
D.13 Measured cross section ratio of carbon over scintillator in Q^2, and the absolute and fractional cross section ratio uncertainties 458
D.14 Statistical covariance matrix of measured cross section ratio of carbon over scintillator in Q^2 459
D.15 Systematic covariance matrix of measured cross section ratio of carbon over scintillator in Q^2 460
D.16 Measured cross section ratio of carbon over scintillator in W_{exp}, and the absolute and fractional cross section ratio uncertainties 461
D.17 Statistical covariance matrix of measured cross section ratio of carbon over scintillator in W_{exp} 461
D.18 Systematic covariance matrix of measured cross section ratio of carbon over scintillator in W_{exp} 461
D.19 Measured cross section ratio of carbon over scintillator in T_π, and the absolute and fractional cross section ratio uncertainties 461

D.20 Statistical covariance matrix of measured cross section ratio of carbon over scintillator in T_π 462
D.21 Systematic covariance matrix of measured cross section ratio of carbon over scintillator in T_π 462
D.22 Measured cross section ratio of carbon over scintillator in θ_π, and the absolute and fractional cross section ratio uncertainties 462
D.23 Statistical covariance matrix of measured cross section ratio of carbon over scintillator in θ_π 463
D.24 Systematic covariance matrix of measured cross section ratio of carbon over scintillator in θ_π 464
D.25 Measured cross section ratio of water over scintillator in p_μ, and the absolute and fractional cross section ratio uncertainties 465
D.26 Statistical covariance matrix of measured cross section ratio of water over scintillator in p_μ 465
D.27 Systematic covariance matrix of measured cross section ratio of water over scintillator in p_μ 465
D.28 Measured cross section ratio of water over scintillator in θ_μ, and the absolute and fractional cross section ratio uncertainties 466
D.29 Statistical covariance matrix of measured cross section ratio of water over scintillator in θ_μ 466
D.30 Systematic covariance matrix of measured cross section ratio of water over scintillator in θ_μ 466
D.31 Measured cross section ratio of water over scintillator in $p_{\mu,||}$, and the absolute and fractional cross section ratio uncertainties 467
D.32 Statistical covariance matrix of measured cross section ratio of water over scintillator in $p_{\mu,||}$ 467

D.33 Systematic covariance matrix of measured cross section ratio of water over scintillator in $p_{\mu,||}$ 467
D.34 Measured cross section ratio of water over scintillator in $p_{\mu,T}$, and the absolute and fractional cross section ratio uncertainties 468
D.35 Statistical covariance matrix of measured cross section ratio of water over scintillator in $p_{\mu,T}$ 469
D.36 Systematic covariance matrix of measured cross section ratio of water over scintillator in $p_{\mu,T}$ 470
D.37 Measured cross section ratio of water over scintillator in Q^2, and the absolute and fractional cross section ratio uncertainties 471
D.38 Statistical covariance matrix of measured cross section ratio of water over scintillator in Q^2 472
D.39 Systematic covariance matrix of measured cross section ratio of water over scintillator in Q^2 473
D.40 Measured cross section ratio of water over scintillator in W_{exp}, and the absolute and fractional cross section ratio uncertainties 474
D.41 Statistical covariance matrix of measured cross section ratio of water over scintillator in W_{exp} 474
D.42 Systematic covariance matrix of measured cross section ratio of water over scintillator in W_{exp} 474
D.43 Measured cross section ratio of water over scintillator in T_π, and the absolute and fractional cross section ratio uncertainties 474
D.44 Statistical covariance matrix of measured cross section ratio of water over scintillator in T_π 475
D.45 Systematic covariance matrix of measured cross section ratio of water over scintillator in T_π 475

D.46 Measured cross section ratio of water over scintillator in θ_π, and the absolute and fractional cross section ratio uncertainties 475
D.47 Statistical covariance matrix of measured cross section ratio of water over scintillator in θ_π 476
D.48 Systematic covariance matrix of measured cross section ratio of water over scintillator in θ_π 477
D.49 Measured cross section ratio of iron over scintillator in p_μ, and the absolute and fractional cross section ratio uncertainties 478
D.50 Statistical covariance matrix of measured cross section ratio of iron over scintillator in p_μ 478
D.51 Systematic covariance matrix of measured cross section ratio of iron over scintillator in p_μ 478
D.52 Measured cross section ratio of iron over scintillator in θ_μ, and the absolute and fractional cross section ratio uncertainties 479
D.53 Statistical covariance matrix of measured cross section ratio of iron over scintillator in θ_μ 479
D.54 Systematic covariance matrix of measured cross section ratio of iron over scintillator in θ_μ 479
D.55 Measured cross section ratio of iron over scintillator in $p_{\mu,||}$, and the absolute and fractional cross section ratio uncertainties 480
D.56 Statistical covariance matrix of measured cross section ratio of iron over scintillator in $p_{\mu,||}$ 480
D.57 Systematic covariance matrix of measured cross section ratio of iron over scintillator in $p_{\mu,||}$ 480
D.58 Measured cross section ratio of iron over scintillator in $p_{\mu,T}$, and the absolute and fractional cross section ratio uncertainties 481

D.59 Statistical covariance matrix of measured cross section ratio of iron over scintillator in $p_{\mu,T}$ 482
D.60 Systematic covariance matrix of measured cross section ratio of iron over scintillator in $p_{\mu,T}$ 483
D.61 Measured cross section ratio of iron over scintillator in Q^2, and the absolute and fractional cross section ratio uncertainties 484
D.62 Statistical covariance matrix of measured cross section ratio of iron over scintillator in Q^2 485
D.63 Systematic covariance matrix of measured cross section ratio of iron over scintillator in Q^2 486
D.64 Measured cross section ratio of iron over scintillator in W_{exp}, and the absolute and fractional cross section ratio uncertainties 487
D.65 Statistical covariance matrix of measured cross section ratio of iron over scintillator in W_{exp} 487
D.66 Systematic covariance matrix of measured cross section ratio of iron over scintillator in W_{exp} 487
D.67 Measured cross section ratio of iron over scintillator in T_π, and the absolute and fractional cross section ratio uncertainties 487
D.68 Statistical covariance matrix of measured cross section ratio of iron over scintillator in T_π 488
D.69 Systematic covariance matrix of measured cross section ratio of iron over scintillator in T_π 488
D.70 Measured cross section ratio of iron over scintillator in θ_π, and the absolute and fractional cross section ratio uncertainties 488
D.71 Statistical covariance matrix of measured cross section ratio of iron over scintillator in θ_π 489

D.72 Systematic covariance matrix of measured cross section ratio of iron over scintillator in θ_π 490
D.73 Measured cross section ratio of lead over scintillator in p_μ, and the absolute and fractional cross section ratio uncertainties 491
D.74 Statistical covariance matrix of measured cross section ratio of lead over scintillator in p_μ 491
D.75 Systematic covariance matrix of measured cross section ratio of lead over scintillator in p_μ 491
D.76 Measured cross section ratio of lead over scintillator in θ_μ, and the absolute and fractional cross section ratio uncertainties 492
D.77 Statistical covariance matrix of measured cross section ratio of lead over scintillator in θ_μ 492
D.78 Systematic covariance matrix of measured cross section ratio of lead over scintillator in θ_μ 492
D.79 Measured cross section ratio of lead over scintillator in $p_{\mu,||}$, and the absolute and fractional cross section ratio uncertainties 493
D.80 Statistical covariance matrix of measured cross section ratio of lead over scintillator in $p_{\mu,||}$ 493
D.81 Systematic covariance matrix of measured cross section ratio of lead over scintillator in $p_{\mu,||}$ 493
D.82 Measured cross section ratio of lead over scintillator in $p_{\mu,T}$, and the absolute and fractional cross section ratio uncertainties 494
D.83 Statistical covariance matrix of measured cross section ratio of lead over scintillator in $p_{\mu,T}$ 495
D.84 Systematic covariance matrix of measured cross section ratio of lead over scintillator in $p_{\mu,T}$ 496

D.85 Measured cross section ratio of lead over scintillator in Q^2, and the absolute and fractional cross section ratio uncertainties 497
D.86 Statistical covariance matrix of measured cross section ratio of lead over scintillator in Q^2 498
D.87 Systematic covariance matrix of measured cross section ratio of lead over scintillator in Q^2 499
D.88 Measured cross section ratio of lead over scintillator in W_{exp}, and the absolute and fractional cross section ratio uncertainties 500
D.89 Statistical covariance matrix of measured cross section ratio of lead over scintillator in W_{exp} 500
D.90 Systematic covariance matrix of measured cross section ratio of lead over scintillator in W_{exp} 500
D.91 Measured cross section ratio of lead over scintillator in T_π, and the absolute and fractional cross section ratio uncertainties 500
D.92 Statistical covariance matrix of measured cross section ratio of lead over scintillator in T_π 501
D.93 Systematic covariance matrix of measured cross section ratio of lead over scintillator in T_π 501
D.94 Measured cross section ratio of lead over scintillator in θ_π, and the absolute and fractional cross section ratio uncertainties 501
D.95 Statistical covariance matrix of measured cross section ratio of lead over scintillator in θ_π 502
D.96 Systematic covariance matrix of measured cross section ratio of lead over scintillator in θ_π 503

List of Figures

1-1 Particle content of the Standard Model 1

1-2 Feynman diagrams of electromagnetic interactions 4

1-3 Feynman diagrams of strong nuclear force interactions 5

1-4 Feynman diagrams of weak nuclear force interactions 6

1-5 The mass splittings of the normal and inverted neutrino hierarchies. Figure from [13] 16

1-6 A generic charged current neutrino-nucleon interaction Feynman diagram with labelled momenta. 19

1-7 Overview of the charged current neutrino-nucleon interaction processes 21

1-8 Muon neutrino charged current resonant pion production from a proton through the Δ^{++} resonance 24

1-9 Feynman diagrams of charged current muon neutrino coherent (left) and diffractive (right) charged pion production 30

1-10 Measured cross sections $\frac{d\sigma}{dE_\pi}$ and $\frac{d\sigma}{d\theta_\pi}$ for ν_μ CC coherent π^+ production at MINERvA 31

1-11 Feynman diagrams of Np-Nh processes 35

1-12 Diagram of possible final state interactions on charged pions 36

1-13 MINERvA pion production absolute differential cross sections as a function of Q^2 40
1-14 MINERvA pion production absolute differential cross sections as a function of T_π 41
1-15 MINERvA $\nu_\mu CC1\pi^0$ absolute differential cross section as a function of invariant hadronic mass 42

2-1 Simulation of the MINERvA flux in the low energy (LE) and medium energy (ME) configuration 44
2-2 Overhead diagram of the Fermilab accelerator complex 45
2-3 Schematic of the components of the NuMI beam 47
2-4 Diagram of particle trajectories through a magnetic horn 49
2-5 Diagram of particle trajectories through both NuMI magnetic horns 50
2-6 Arachne event display of a rock muon passing through the MINERvA detector. The rock muon is the top track 51
2-7 The PPFX weighted simulated LE and ME fluxes and the ratios to the baseline flux 55
2-8 The unconstrained and $\nu - e$ constrained simulated LE and ME ν_μ fluxes 57
2-9 The unconstrained and $\nu - e$ constrained fractional uncertainties of the ME ν_μ flux 57
2-10 The ratio of the constrained IMD flux over the unconstrained flux and the uncertainties on the flux before and after the constraint 58
2-11 Comparison of the FHC flux in different materials in MINERvA . . 61
2-12 Diagram of the "daisy" petal bins 62
2-13 The daisy petal reweights for each passive material 63

3-1 Diagram of the side view of the MINERvA detector 66
3-2 Front view of the MINERvA tracking plane 68
3-3 Examples of trajectories of particles passing through strips in the same plane 68
3-4 Orientation of X, U, and V planes 69
3-5 Pictures of scintillator strips used in the MINERvA inner detector . 69
3-6 A single optical readout channel 71
3-7 Disassembled photomultiplier box. The photomultiplier tube is the black box 72
3-8 The mapping of the input from the face plate to the photomultiplier 73
3-9 Diagram of the nuclear target region in MINERvA 74
3-10 Diagrams of MINOS Near Detector 76
3-11 Measurement of a pedestal distribution for one channel, including an outlier at ~ 550 ADC counts 79
3-12 The high, medium, and low gain response for a typical TriP-t 80
3-13 Peak energy per unit length and MEU factor versus time 82
3-14 Alignment fits for two separate planes 85
3-15 The longitudinal position of the reconstructed POCA for nuclear targets 3 and 5 in both data and simulation before and after the longitudinal shift 86

4-1 Feynman diagram of μ^+ resulting in the creation of a Michel e^+ . . . 99
4-2 Michel electron calorimetric energy in data and simulation 101
4-3 Calorimetric energy of Michel electrons matched to a hadron track . 102
4-4 Muon decay time in data and simulation 102
4-5 Percentage of different types of Michel candidates 103

4-6 Simulated μ^+ and μ^- reconstruction efficiency in active tracker region 105
4-7 MINOS stopped μ^+ and μ^- populations and contamination fractions for FHC neutrino playlists ME1A and RHC antineutrino playlist ME6A as a function of muon momentum 107
4-8 An example of corrections to the MINOS track matching efficiency for given muon momentum 110
4-9 Neutron path lengths before the first interaction. The red and blue lines represent the neutron cross section shift by +10% and -10%, respectively. Figure from [98]. 113
4-10 Examples of normalization factors for a given particle and target/material that the neutrino interaction occurred on. 116
4-11 Data/MC cross section ratios in θ_π without any reweight and E_π after applying the θ_π reweight 120
4-12 Hydrogen and coherent pion production subtracted differential cross section in Q^2 for the active tracking region 123
4-13 Hydrogen and Coherent Pion Production Subtracted Data/Simulation Cross Section Ratio and the ME $1\pi^+$ suppression function 123

5-1 Time profile of hits within a 16 μs beam gate 127
5-2 Cluster formation from hits in an ID plane 128
5-3 Examples of cluster topologies 130
5-4 Diagram of tracks built from the interaction vertex in a muon neutrino analysis 131
5-5 Illustration of the long tracking procedure 134
5-6 Illustration of the MINERvA planes (XUXV) and 3D points along the track produced by the long tracker and short tracker 136

5-7 Charged pion tracking efficiency in the active tracker region as a function of momentum and angle with respect to the z-axis 137
5-8 MINOS Near Detector event display of a MINOS track matched to a MINERvA track in U and V plane orientations 140
5-9 Diagram of a muon track exiting MINERvA and entering the MINOS Near Detector 141
5-10 The low-ν "wiggle" discrepancy 144
5-11 Percentage of different types of Michel candidates 148
5-12 Illustration of a Michel electron with a linear fit 150
5-13 Reconstructed - true endpoint position of Michel electrons in X and Y 152
5-14 $\frac{dE}{dX}$ profiles for reconstructed tracks 154
5-15 Arachne readout display of a simulated pion track with a Michel electron at later time slice 155
5-16 Illustration of Michel matching to hadron endpoints 157
5-17 Distance from simulated track endpoint to Michel endpoint (cm) versus T_π resolution for fitted Michels and 2,3 view Michels with no fits 158
5-18 T_π Resolution for all simulated hadron tracks and simulated Michel matched tracks 159
5-19 Log Likelihood Ratio PID Score for all Michel Matched hadron tracks 165
5-20 Illustration of the nodes of a track. The vertex is upstream of the track. Figure from X. Lu. 166
5-21 Node 0+1 energy versus T_π resolution 166
5-22 Node 0+1 energy for Michel Matched hadron tracks that have an LLR Score > 0 167
5-23 T_π resolution for hadron tracks before the node energy cuts and tracks which passed the cuts 168

5-24 The final T_π resolution for hadron tracks which passed all charged pion selection cuts . . . 169
5-25 The energy resolution of events in given energy range of E_{had}^{pmc} 172
5-26 Distributions of true $E_{had,no\ \pi}$ - reconstructed $E_{had,no\ \pi}^{pmc}$ 174
5-27 The additive corrections β as a function of energy and target 175

6-1 Diagram of the nuclear target region with the transverse shapes of the targets . . . 183
6-2 Reconstructed p_μ distribution including events with $p_\mu < 1.5$ GeV/c and $p_\mu > 20$ GeV/c with signal and background 185
6-3 Number of hadron tracks matched to a Michel electron per event by signal and background . . . 187
6-4 Reconstructed W_{exp} distribution of events which have 1 charged pion track with good energy reconstruction with signal and background . 189
6-5 Number of isolated prongs per event by signal and background . . . 191
6-6 p_μ Event Selection . . . 193
6-7 $p_{\mu,||}$ Event Selection . . . 194
6-8 $p_{\mu,T}$ Event Selection . . . 195
6-9 θ_μ Event Selection . . . 196
6-10 Q^2 Event Selection . . . 197
6-11 W_{exp} Event Selection . . . 198
6-12 T_π Event Selection . . . 199
6-13 θ_π Event Selection . . . 200
6-14 Percentage of selected events by signal and background type . . . 201
6-15 W_{exp} No Sideband Fits. The region to the right of the arrow shows the high W_{exp} sideband region . . . 205

6-16 $W_{exp} > 1.5$ GeV/c^2 No Sideband Fits 206
6-17 Plastic High W_{exp} Sideband Fit in full W_{exp} (top) and $W_{exp} > 1.5$ GeV/c^2 (bottom) distributions 208
6-18 Plastic Signal T_π vs θ_π Reweight. Reweight only applied to $\theta_\pi > 90°$ or $T_\pi < 0.1$ GeV 209
6-19 Effects of Signal Reweight on T_π and θ_π in Signal Region 210
6-20 Interaction Vertex z Distributions With True Interaction Vertex Categories Before Plastic Contamination Sideband Fits 211
6-21 Vertex Z Distributions With True Interaction Vertex Categories After Plastic Contamination Fits 213
6-22 $W_{exp} > 1.4$ Sideband After Plastic Contamination Fits 214
6-23 $W_{exp} > 1.5$ GeV/c^2 Sideband After High W_{exp} Sideband Fits in the Nuclear Targets 217
6-24 W_{exp} After High W_{exp} Sideband Fits in the Nuclear Targets 218
6-25 $p_{\mu,T}$ in $W_{exp} > 1.5$ GeV/c^2 Sideband After High W_{exp} Sideband Fits in the Nuclear Targets 219
6-26 T_π in $W_{exp} > 1.5$ GeV/c^2 Sideband After High W_{exp} Sideband Fits in the Nuclear Targets 220
6-27 p_μ Background Subtracted 222
6-28 $p_{\mu,||}$ Background Subtracted 223
6-29 $p_{\mu,T}$ Background Subtracted 224
6-30 θ_μ Background Subtracted 225
6-31 Q^2 Background Subtracted 226
6-32 W_{exp} Background Subtracted 227
6-33 T_π Background Subtracted 228
6-34 θ_π Background Subtracted 229

6-35 p_μ Row Normalized Migration Matrix (N Bins = 10) 232
6-36 $p_{\mu,||}$ Row Normalized Migration Matrix (N Bins = 9) 233
6-37 $p_{\mu,T}$ Row Normalized Migration Matrix (N Bins = 8) 234
6-38 θ_μ Row Normalized Migration Matrix (N Bins = 8) 235
6-39 Q^2 Row Normalized Migration Matrix (N Bins = 12) 236
6-40 W_{exp} Row Normalized Migration Matrix (N Bins = 4) 237
6-41 T_π Row Normalized Migration Matrix (N Bins = 4) 238
6-42 θ_π Row Normalized Migration Matrix (N Bins = 11) 239
6-43 Carbon $p_{\mu,T}$ Median χ^2 vs Unfolding Iterations 243
6-44 Iron $p_{\mu,T}$ Median χ^2 vs Unfolding Iterations 244
6-45 Lead $p_{\mu,T}$ Median χ^2 vs Unfolding Iterations 245
6-46 Tracker $p_{\mu,T}$ Median χ^2 vs Unfolding Iterations 246
6-47 Carbon W_{exp} Median χ^2 vs Unfolding Iterations 247
6-48 Iron W_{exp} Median χ^2 vs Unfolding Iterations 248
6-49 Lead W_{exp} Median χ^2 vs Unfolding Iterations 249
6-50 Tracker W_{exp} Median χ^2 vs Unfolding Iterations 250
6-51 $p_{\mu,T}$ statistical covariance matrices after two unfolding iterations . . 252
6-52 p_μ Unfolded Iteration 1 253
6-53 $p_{\mu,||}$ Unfolded Iteration 1 254
6-54 $p_{\mu,T}$ Unfolded Iteration 2 255
6-55 θ_μ Unfolded Iteration 2 256
6-56 Q^2 Unfolded Iteration 2 257
6-57 W_{exp} Unfolded Iteration 10 258
6-58 T_π Unfolded Iteration 2 259
6-59 θ_π Unfolded Iteration 2 260
6-60 p_μ Efficiency 263

6-61 $p_{\mu,||}$ Efficiency . . . 264
6-62 $p_{\mu,T}$ Efficiency . . . 265
6-63 θ_μ Efficiency . . . 266
6-64 Q^2 Efficiency . . . 267
6-65 W_{exp} Efficiency . . . 268
6-66 T_π Efficiency . . . 269
6-67 θ_π Efficiency . . . 270
6-68 p_μ Cross Section . . . 273
6-69 $p_{\mu,||}$ Cross Section . . . 274
6-70 $p_{\mu,T}$ Cross Section . . . 275
6-71 θ_μ Cross Section . . . 276
6-72 Q^2 Cross Section . . . 277
6-73 W_{exp} Cross Section . . . 278
6-74 T_π Cross Section . . . 279
6-75 θ_π Cross Section . . . 280
6-76 p_μ Cross Section: Neutrino Interactions . . . 282
6-77 $p_{\mu,||}$ Cross Section: Neutrino Interactions . . . 283
6-78 $p_{\mu,T}$ Cross Section: Neutrino Interactions . . . 284
6-79 θ_μ Cross Section: Neutrino Interactions . . . 285
6-80 Q^2 Cross Section: Neutrino Interactions . . . 286
6-81 W_{exp} Cross Section: Neutrino Interactions . . . 287
6-82 T_π Cross Section: Neutrino Interactions . . . 288
6-83 θ_π Cross Section: Neutrino Interactions . . . 289
6-84 p_μ Cross Section Area Normalized . . . 291
6-85 $p_{\mu,||}$ Cross Section Area Normalized . . . 292
6-86 $p_{\mu,T}$ Cross Section Area Normalized . . . 293

6-87 θ_μ Cross Section Area Normalized 294
6-88 Q^2 Cross Section Area Normalized 295
6-89 W_{exp} Cross Section Area Normalized 296
6-90 T_π Cross Section Area Normalized 297
6-91 θ_π Cross Section Area Normalized 298
6-92 p_μ Target Cross Section Ratio to Scintillator 300
6-93 $p_{\mu,||}$ Target Cross Section Ratio to Scintillator 301
6-94 $p_{\mu,T}$ Target Cross Section Ratio to Scintillator 302
6-95 θ_μ Target Cross Section Ratio to Scintillator 303
6-96 Q^2 Target Cross Section Ratio to Scintillator 304
6-97 W_{exp} Target Cross Section Ratio to Scintillator 305
6-98 T_π Target Cross Section Ratio to Scintillator 306
6-99 θ_π Target Cross Section Ratio to Scintillator 307
6-100 p_μ Cross Section Error Summary 314
6-101 $p_{\mu,||}$ Cross Section Error Summary 315
6-102 $p_{\mu,T}$ Cross Section Error Summary 316
6-103 θ_μ Cross Section Error Summary 317
6-104 Q^2 Cross Section Error Summary 318
6-105 W_{exp} Cross Section Error Summary 319
6-106 T_π Cross Section Error Summary 320
6-107 θ_π Cross Section Error Summary 321
6-108 $p_{\mu,T}$ Cross Section Model Errors 325
6-109 T_π Cross Section Model Errors 326
6-110 $p_{\mu,T}$ FSI Errors 328
6-111 T_π FSI Errors 329
6-112 $p_{\mu,T}$ Flux Error 332

6-113 T_π Flux Error . . . 333
6-114 $p_{\mu,T}$ Muon Reconstruction Errors . . . 335
6-115 T_π Muon Reconstruction Errors . . . 336
6-116 $p_{\mu,T}$ Pion Reconstruction Errors . . . 338
6-117 T_π Pion Reconstruction Errors . . . 339
6-118 $p_{\mu,T}$ Sideband Fit Errors . . . 341
6-119 T_π Sideband Fit Errors . . . 342
6-120 $p_{\mu,T}$ Other Systematic Errors . . . 346
6-121 T_π Other Systematic Errors . . . 347

7-1 $p_{\mu,T}$ differential cross sections on iron, lead, and scintillator . . . 350
7-2 T_π differential cross sections on iron,lead and scintillator . . . 351
7-3 p_μ differential cross sections on carbon, iron, lead, and scintillator . . 352
7-4 Q^2 differential cross sections on iron, lead, and scintillator . . . 353
7-5 Area normalized $p_{\mu,||}$ differential cross sections on carbon, iron, lead, and scintillator . . . 354
7-6 Area normalized W_{exp} differential cross sections on carbon, iron, lead, and scintillator . . . 355
7-7 W_{exp} differential cross sections on scintillator, carbon, and lead . . . 356
7-8 T_π and θ_π differential cross sections on iron and scintillator . . . 357
7-9 Q^2 cross section ratios . . . 358
7-10 T_π cross section ratios . . . 359
7-11 θ_π cross section ratios . . . 360

E-1 p_μ Error Summary . . . 505
E-2 $p_{\mu,||}$ Error Summary . . . 506
E-3 $p_{\mu,T}$ Error Summary . . . 507

E-4 θ_μ Error Summary . . . 508
E-5 Q^2 Error Summary . . . 509
E-6 W_{exp} Error Summary . . . 510
E-7 T_π Error Summary . . . 511
E-8 θ_π Error Summary . . . 512
E-9 p_μ All Cross Section Model Errors . . . 513
E-10 $p_{\mu,||}$ All Cross Section Model Errors . . . 514
E-11 $p_{\mu,T}$ All Cross Section Model Errors . . . 515
E-12 θ_μ All Cross Section Model Errors . . . 516
E-13 Q^2 All Cross Section Model Errors . . . 517
E-14 W_{exp} All Cross Section Model Errors . . . 518
E-15 T_π All Cross Section Model Errors . . . 519
E-16 θ_π All Cross Section Model Errors . . . 520
E-17 p_μ CCQE Model Errors . . . 521
E-18 $p_{\mu,||}$ CCQE Model Errors . . . 522
E-19 $p_{\mu,T}$ CCQE Model Errors . . . 523
E-20 θ_μ CCQE Model Errors . . . 524
E-21 Q^2 CCQE Model Errors . . . 525
E-22 W_{exp} CCQE Model Errors . . . 526
E-23 T_π CCQE Model Errors . . . 527
E-24 θ_π CCQE Model Errors . . . 528
E-25 p_μ Coherent/Diffractive π Model Errors . . . 529
E-26 $p_{\mu,||}$ Coherent/Diffractive π Model Errors . . . 530
E-27 $p_{\mu,T}$ Coherent/Diffractive π Model Errors . . . 531
E-28 θ_μ Coherent/Diffractive π Model Errors . . . 532
E-29 Q^2 Coherent/Diffractive π Model Errors . . . 533

E-30 W_{exp} Coherent/Diffractive π Model Errors 534
E-31 T_π Coherent/Diffractive π Model Errors 535
E-32 θ_π Coherent/Diffractive π Model Errors 536
E-33 p_μ DIS/Hadronization Model Errors 537
E-34 $p_{\mu,||}$ DIS/Hadronization Model Errors 538
E-35 $p_{\mu,T}$ DIS/Hadronization Model Errors 539
E-36 θ_μ DIS/Hadronization Model Errors 540
E-37 Q^2 DIS/Hadronization Model Errors 541
E-38 W_{exp} DIS/Hadronization Model Errors 542
E-39 T_π DIS/Hadronization Model Errors 543
E-40 θ_π DIS/Hadronization Model Errors 544
E-41 p_μ Elastic Scattering Model Errors 545
E-42 $p_{\mu,||}$ Elastic Scattering Model Errors 546
E-43 $p_{\mu,T}$ Elastic Scattering Model Errors 547
E-44 θ_μ Elastic Scattering Model Errors 548
E-45 Q^2 Elastic Scattering Model Errors 549
E-46 W_{exp} Elastic Scattering Model Errors 550
E-47 T_π Elastic Scattering Model Errors 551
E-48 θ_π Elastic Scattering Model Errors 552
E-49 p_μ MnvTune Model Errors 553
E-50 $p_{\mu,||}$ MnvTune Model Errors 554
E-51 $p_{\mu,T}$ MnvTune Model Errors 555
E-52 θ_μ MnvTune Model Errors 556
E-53 Q^2 MnvTune Model Errors 557
E-54 W_{exp} MnvTune Model Errors 558
E-55 T_π MnvTune Model Errors 559

E-56 θ_π MnvTune Model Errors . . . 560
E-57 p_μ Nonresonant π Model Errors . . . 561
E-58 $p_{\mu,||}$ Nonresonant π Model Errors . . . 562
E-59 $p_{\mu,T}$ Nonresonant π Model Errors . . . 563
E-60 θ_μ Nonresonant π Model Errors . . . 564
E-61 Q^2 Nonresonant π Model Errors . . . 565
E-62 W_{exp} Nonresonant π Model Errors . . . 566
E-63 T_π Nonresonant π Model Errors . . . 567
E-64 θ_π Nonresonant π Model Errors . . . 568
E-65 p_μ Resonant π Model Errors . . . 569
E-66 $p_{\mu,||}$ Resonant π Model Errors . . . 570
E-67 $p_{\mu,T}$ Resonant π Model Errors . . . 571
E-68 θ_μ Resonant π Model Errors . . . 572
E-69 Q^2 Resonant π Model Errors . . . 573
E-70 W_{exp} Resonant π Model Errors . . . 574
E-71 T_π Resonant π Model Errors . . . 575
E-72 θ_π Resonant π Model Errors . . . 576
E-73 p_μ FSI Errors . . . 577
E-74 $p_{\mu,||}$ FSI Errors . . . 578
E-75 $p_{\mu,T}$ FSI Errors . . . 579
E-76 θ_μ FSI Errors . . . 580
E-77 Q^2 FSI Errors . . . 581
E-78 W_{exp} FSI Errors . . . 582
E-79 T_π FSI Errors . . . 583
E-80 θ_π FSI Errors . . . 584
E-81 p_μ Flux Error . . . 585

E-82 $p_{\mu,||}$ Flux Error . . . 586
E-83 $p_{\mu,T}$ Flux Error . . . 587
E-84 θ_μ Flux Error . . . 588
E-85 Q^2 Flux Error . . . 589
E-86 W_{exp} Flux Error . . . 590
E-87 T_π Flux Error . . . 591
E-88 θ_π Flux Error . . . 592
E-89 p_μ Muon Reconstruction Errors . . . 593
E-90 $p_{\mu,||}$ Muon Reconstruction Errors . . . 594
E-91 $p_{\mu,T}$ Muon Reconstruction Errors . . . 595
E-92 θ_μ Muon Reconstruction Errors . . . 596
E-93 Q^2 Muon Reconstruction Errors . . . 597
E-94 W_{exp} Muon Reconstruction Errors . . . 598
E-95 T_π Muon Reconstruction Errors . . . 599
E-96 θ_π Muon Reconstruction Errors . . . 600
E-97 p_μ Pion Reconstruction Errors . . . 601
E-98 $p_{\mu,||}$ Pion Reconstruction Errors . . . 602
E-99 $p_{\mu,T}$ Pion Reconstruction Errors . . . 603
E-100 θ_μ Pion Reconstruction Errors . . . 604
E-101 Q^2 Pion Reconstruction Errors . . . 605
E-102 W_{exp} Pion Reconstruction Errors . . . 606
E-103 T_π Pion Reconstruction Errors . . . 607
E-104 θ_π Pion Reconstruction Errors . . . 608
E-105 p_μ Sideband Fit Errors . . . 609
E-106 $p_{\mu,||}$ Sideband Fit Errors . . . 610
E-107 $p_{\mu,T}$ Sideband Fit Errors . . . 611

E-108 θ_μ Sideband Fit Errors . . . 612
E-109 Q^2 Sideband Fit Errors . . . 613
E-110 W_{exp} Sideband Fit Errors . . . 614
E-111 T_π Sideband Fit Errors . . . 615
E-112 θ_π Sideband Fit Errors . . . 616
E-113 p_μ Other Systematic Errors . . . 617
E-114 $p_{\mu,||}$ Other Systematic Errors . . . 618
E-115 $p_{\mu,T}$ Other Systematic Errors . . . 619
E-116 θ_μ Other Systematic Errors . . . 620
E-117 Q^2 Other Systematic Errors . . . 621
E-118 W_{exp} Other Systematic Errors . . . 622
E-119 T_π Other Systematic Errors . . . 623
E-120 θ_π Other Systematic Errors . . . 624

F-1 p_μ Error Summary . . . 626
F-2 $p_{\mu,||}$ Error Summary . . . 627
F-3 $p_{\mu,T}$ Error Summary . . . 628
F-4 θ_μ Error Summary . . . 629
F-5 Q^2 Error Summary . . . 630
F-6 W_{exp} Error Summary . . . 631
F-7 T_π Error Summary . . . 632
F-8 θ_π Error Summary . . . 633
F-9 p_μ All Cross Section Model Errors . . . 634
F-10 $p_{\mu,||}$ All Cross Section Model Errors . . . 635
F-11 $p_{\mu,T}$ All Cross Section Model Errors . . . 636
F-12 θ_μ All Cross Section Model Errors . . . 637

F-13 Q^2 All Cross Section Model Errors 638
F-14 W_{exp} All Cross Section Model Errors 639
F-15 T_π All Cross Section Model Errors 640
F-16 θ_π All Cross Section Model Errors 641
F-17 p_μ CCQE Model Errors 642
F-18 $p_{\mu,||}$ CCQE Model Errors 643
F-19 $p_{\mu,T}$ CCQE Model Errors 644
F-20 θ_μ CCQE Model Errors 645
F-21 Q^2 CCQE Model Errors 646
F-22 W_{exp} CCQE Model Errors 647
F-23 T_π CCQE Model Errors 648
F-24 θ_π CCQE Model Errors 649
F-25 p_μ Coherent/Diffractive π Model Errors 650
F-26 $p_{\mu,||}$ Coherent/Diffractive π Model Errors 651
F-27 $p_{\mu,T}$ Coherent/Diffractive π Model Errors 652
F-28 θ_μ Coherent/Diffractive π Model Errors 653
F-29 Q^2 Coherent/Diffractive π Model Errors 654
F-30 W_{exp} Coherent/Diffractive π Model Errors 655
F-31 T_π Coherent/Diffractive π Model Errors 656
F-32 θ_π Coherent/Diffractive π Model Errors 657
F-33 p_μ DIS/Hadronization Model Errors 658
F-34 $p_{\mu,||}$ DIS/Hadronization Model Errors 659
F-35 $p_{\mu,T}$ DIS/Hadronization Model Errors 660
F-36 θ_μ DIS/Hadronization Model Errors 661
F-37 Q^2 DIS/Hadronization Model Errors 662
F-38 W_{exp} DIS/Hadronization Model Errors 663

F-39 T_π DIS/Hadronization Model Errors 664
F-40 θ_π DIS/Hadronization Model Errors 665
F-41 p_μ Elastic Scattering Model Errors 666
F-42 $p_{\mu,||}$ Elastic Scattering Model Errors 667
F-43 $p_{\mu,T}$ Elastic Scattering Model Errors 668
F-44 θ_μ Elastic Scattering Model Errors 669
F-45 Q^2 Elastic Scattering Model Errors 670
F-46 W_{exp} Elastic Scattering Model Errors 671
F-47 T_π Elastic Scattering Model Errors 672
F-48 θ_π Elastic Scattering Model Errors 673
F-49 p_μ MnvTune Model Errors 674
F-50 $p_{\mu,||}$ MnvTune Model Errors 675
F-51 $p_{\mu,T}$ MnvTune Model Errors 676
F-52 θ_μ MnvTune Model Errors 677
F-53 Q^2 MnvTune Model Errors 678
F-54 W_{exp} MnvTune Model Errors 679
F-55 T_π MnvTune Model Errors 680
F-56 θ_π MnvTune Model Errors 681
F-57 p_μ Nonresonant π Model Errors 682
F-58 $p_{\mu,||}$ Nonresonant π Model Errors 683
F-59 $p_{\mu,T}$ Nonresonant π Model Errors 684
F-60 θ_μ Nonresonant π Model Errors 685
F-61 Q^2 Nonresonant π Model Errors 686
F-62 W_{exp} Nonresonant π Model Errors 687
F-63 T_π Nonresonant π Model Errors 688
F-64 θ_π Nonresonant π Model Errors 689

F-65 p_μ Resonant π Model Errors . . . 690
F-66 $p_{\mu,||}$ Resonant π Model Errors . . . 691
F-67 $p_{\mu,T}$ Resonant π Model Errors . . . 692
F-68 θ_μ Resonant π Model Errors . . . 693
F-69 Q^2 Resonant π Model Errors . . . 694
F-70 W_{exp} Resonant π Model Errors . . . 695
F-71 T_π Resonant π Model Errors . . . 696
F-72 θ_π Resonant π Model Errors . . . 697
F-73 p_μ FSI Errors . . . 698
F-74 $p_{\mu,||}$ FSI Errors . . . 699
F-75 $p_{\mu,T}$ FSI Errors . . . 700
F-76 θ_μ FSI Errors . . . 701
F-77 Q^2 FSI Errors . . . 702
F-78 W_{exp} FSI Errors . . . 703
F-79 T_π FSI Errors . . . 704
F-80 θ_π FSI Errors . . . 705
F-81 p_μ Flux Error . . . 706
F-82 $p_{\mu,||}$ Flux Error . . . 707
F-83 $p_{\mu,T}$ Flux Error . . . 708
F-84 θ_μ Flux Error . . . 709
F-85 Q^2 Flux Error . . . 710
F-86 W_{exp} Flux Error . . . 711
F-87 T_π Flux Error . . . 712
F-88 θ_π Flux Error . . . 713
F-89 p_μ Muon Reconstruction Errors . . . 714
F-90 $p_{\mu,||}$ Muon Reconstruction Errors . . . 715

F-91 $p_{\mu,T}$ Muon Reconstruction Errors 716
F-92 θ_μ Muon Reconstruction Errors 717
F-93 Q^2 Muon Reconstruction Errors 718
F-94 W_{exp} Muon Reconstruction Errors 719
F-95 T_π Muon Reconstruction Errors 720
F-96 θ_π Muon Reconstruction Errors 721
F-97 p_μ Pion Reconstruction Errors 722
F-98 $p_{\mu,||}$ Pion Reconstruction Errors 723
F-99 $p_{\mu,T}$ Pion Reconstruction Errors 724
F-100 θ_μ Pion Reconstruction Errors 725
F-101 Q^2 Pion Reconstruction Errors 726
F-102 W_{exp} Pion Reconstruction Errors 727
F-103 T_π Pion Reconstruction Errors 728
F-104 θ_π Pion Reconstruction Errors 729
F-105 p_μ Sideband Fit Errors 730
F-106 $p_{\mu,||}$ Sideband Fit Errors 731
F-107 $p_{\mu,T}$ Sideband Fit Errors 732
F-108 θ_μ Sideband Fit Errors 733
F-109 Q^2 Sideband Fit Errors 734
F-110 W_{exp} Sideband Fit Errors 735
F-111 T_π Sideband Fit Errors 736
F-112 θ_π Sideband Fit Errors 737
F-113 p_μ Other Systematic Errors 738
F-114 $p_{\mu,||}$ Other Systematic Errors 739
F-115 $p_{\mu,T}$ Other Systematic Errors 740
F-116 θ_μ Other Systematic Errors 741

F-117 Q^2 Other Systematic Errors 742
F-118 W_{exp} Other Systematic Errors 743
F-119 T_π Other Systematic Errors 744
F-120 θ_π Other Systematic Errors 745

G-1 p_μ Total Cross Section Correlation Matrix 747
G-2 $p_{\mu,||}$ Total Cross Section Correlation Matrix 748
G-3 $p_{\mu,T}$ Total Cross Section Correlation Matrix 749
G-4 θ_μ Total Cross Section Correlation Matrix 750
G-5 Q^2 Total Cross Section Correlation Matrix 751
G-6 W_{exp} Total Cross Section Correlation Matrix 752
G-7 T_π Total Cross Section Correlation Matrix 753
G-8 θ_π Total Cross Section Correlation Matrix 754
G-9 p_μ Statistical Cross Section Uncertainty Correlation Matrix 755
G-10 $p_{\mu,||}$ Statistical Cross Section Uncertainty Correlation Matrix 756
G-11 $p_{\mu,T}$ Statistical Cross Section Uncertainty Correlation Matrix 757
G-12 θ_μ Statistical Cross Section Uncertainty Correlation Matrix 758
G-13 Q^2 Statistical Cross Section Uncertainty Correlation Matrix 759
G-14 W_{exp} Statistical Cross Section Uncertainty Correlation Matrix 760
G-15 T_π Statistical Cross Section Uncertainty Correlation Matrix 761
G-16 θ_π Statistical Cross Section Uncertainty Correlation Matrix 762
G-17 p_μ Systematic Cross Section Uncertainty Correlation Matrix 763
G-18 $p_{\mu,||}$ Systematic Cross Section Uncertainty Correlation Matrix 764
G-19 $p_{\mu,T}$ Systematic Cross Section Uncertainty Correlation Matrix 765
G-20 θ_μ Systematic Cross Section Uncertainty Correlation Matrix 766
G-21 Q^2 Systematic Cross Section Uncertainty Correlation Matrix 767

G-22 W_{exp} Systematic Cross Section Uncertainty Correlation Matrix . . . 768
G-23 T_π Systematic Cross Section Uncertainty Correlation Matrix 769
G-24 θ_π Systematic Cross Section Uncertainty Correlation Matrix 770

H-1 p_μ Total Cross Section Ratio Correlation Matrix 772
H-2 $p_{\mu,||}$ Total Cross Section Ratio Correlation Matrix 773
H-3 $p_{\mu,T}$ Total Cross Section Ratio Correlation Matrix 774
H-4 θ_μ Total Cross Section Ratio Correlation Matrix 775
H-5 Q^2 Total Cross Section Ratio Correlation Matrix 776
H-6 W_{exp} Total Cross Section Ratio Correlation Matrix 777
H-7 T_π Total Cross Section Ratio Correlation Matrix 778
H-8 θ_π Total Cross Section Ratio Correlation Matrix 779
H-9 p_μ Statistical Cross Section Ratio Uncertainty Correlation Matrix . . 780
H-10 $p_{\mu,||}$ Statistical Cross Section Ratio Uncertainty Correlation Matrix . 781
H-11 $p_{\mu,T}$ Statistical Cross Section Ratio Uncertainty Correlation Matrix . 782
H-12 θ_μ Statistical Cross Section Ratio Uncertainty Correlation Matrix . . 783
H-13 Q^2 Statistical Cross Section Ratio Uncertainty Correlation Matrix . 784
H-14 W_{exp} Statistical Cross Section Ratio Uncertainty Correlation Matrix 785
H-15 T_π Statistical Cross Section Ratio Uncertainty Correlation Matrix . . 786
H-16 θ_π Statistical Cross Section Ratio Uncertainty Correlation Matrix . . 787
H-17 p_μ Systematic Cross Section Ratio Uncertainty Correlation Matrix . 788
H-18 $p_{\mu,||}$ Systematic Cross Section Ratio Uncertainty Correlation Matrix 789
H-19 $p_{\mu,T}$ Systematic Cross Section Ratio Uncertainty Correlation Matrix 790
H-20 θ_μ Systematic Cross Section Ratio Uncertainty Correlation Matrix . 791
H-21 Q^2 Systematic Cross Section Ratio Uncertainty Correlation Matrix . 792
H-22 W_{exp} Systematic Cross Section Ratio Uncertainty Correlation Matrix 793

H-23 T_π Systematic Cross Section Ratio Uncertainty Correlation Matrix . 794
H-24 θ_π Systematic Cross Section Ratio Uncertainty Correlation Matrix . 795

Chapter 1

Theory

1.1 The Standard Model

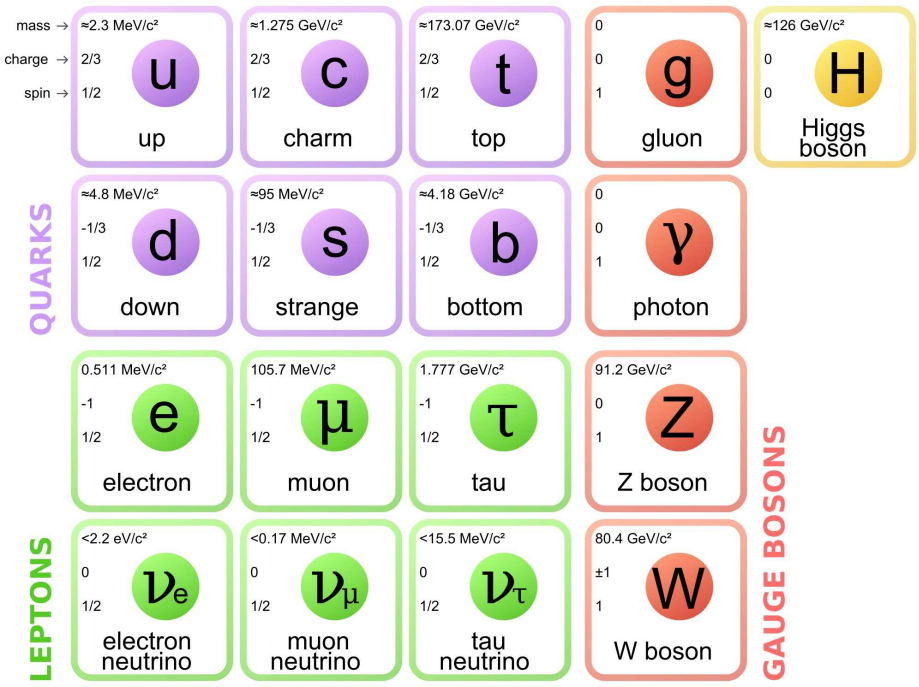


Figure 1-1: Particle content of the Standard Model. Figure from [1]

The Standard Model (SM) of particle physics consists of seventeen elementary particles and their corresponding antiparticles. Using the framework of quantum field theory, the model describes three of the four known fundamental forces of nature and their interactions with the elementary particles. Almost all predictions from Standard Model have agreed with experimental results within the precision of the measurements. When describing these predictions in equations, particle physics typically uses the natural units, where $\hbar = c = 1$. The equations in this thesis are written in these natural units.

1.1.1 Elementary fermions

Elementary particles can be divided into two groups defined by their spin: fermions and bosons. For fundamental particles, spin is the intrinsic angular momentum. Fermions have a half integer spin, while bosons have an integer spin. All elementary fermions have a spin of $\frac{1}{2}$.

The elementary fermions can further be divided into two groups: quarks and leptons. Quarks cannot be observed in isolation, rather only groups of quarks called hadrons can be observed. Hadrons typically come in two varieties: mesons, which consist of a quark and an antiquark, and baryons, which include three quarks or three antiquarks [2]. There have been claims of observations of hadrons with four or five quarks. The up (u), charm (c), and top (t) quarks have a charge of $+\frac{2}{3}e$, while the down (d), strange (s), and bottom (b) quarks have charge of $-\frac{1}{3}e$. There are two types of leptons: neutral and charged. Charged leptons include the electron (e), muon (μ), and tau (τ). The neutral leptons are called neutrinos (ν), and each charged lepton has a corresponding neutrino (ν_e, ν_μ, ν_τ).

Both groups of fermions can also be classified into three generations. Each gener-

ation has a particle corresponding to a member of the first generation, which includes an up quark, a bottom quark, an electron and an electron neutrino. The sole difference between corresponding particles in different generations is the mass.

1.1.2 Fundamental forces

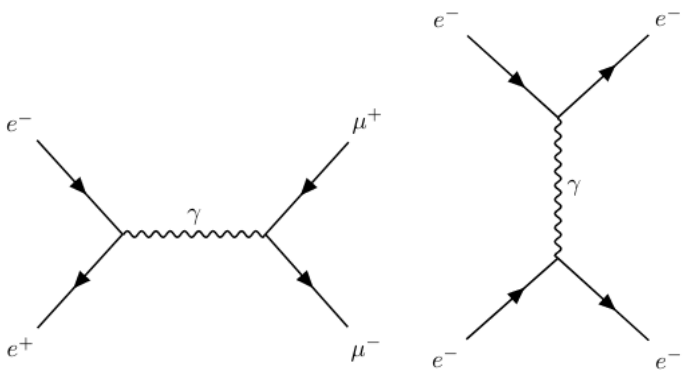
The three fundamental forces in the Standard Model use bosons, the other group of elementary particles in the Standard Model, to mediate the interactions between elementary particles. The exception to this is the scalar H boson, where the strength of a particle's interaction with the H boson determines the particle's mass. The remaining gauge bosons include photons γ, $W\pm/Z$ bosons, and gluons g. Hypothetical particles known as gravitons, which are currently not part of the Standard Model, would mediate gravitational interactions.

1.1.2.1 Electromagnetic force

The prototypical interaction involves the electromagnetic force, where photons couple solely with particles with electric charge. The electromagnetic interaction conserves electric charge. Figure 1-2 shows examples of electromagnetic interactions.

1.1.2.2 Strong nuclear force

Analogous to photons in electromagnetism, gluons mediate strong nuclear force interactions, coupling to an intrinsic property called color charge. There exist three types of color charge which are labelled red, blue, and green. These charges can either be positive or negative, where the negative charges are called antired, antiblue, and antigreen. Both quarks and gluons carry color charge, while leptons do not. Thus, leptons will not be affected by the strong force. Quarks carry one color charge while



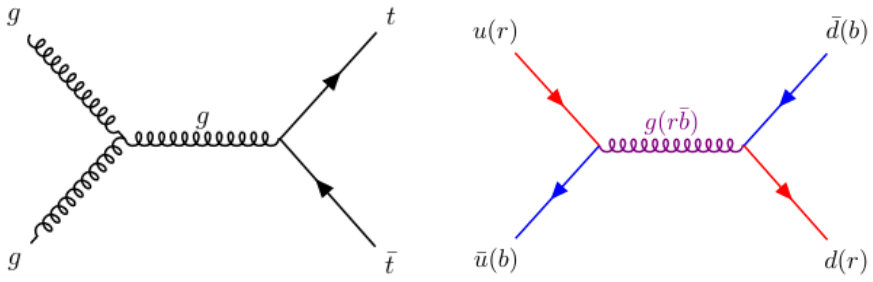
(a) Pair production

(b) Møller (e^- e^-) scattering

Figure 1-2: Feynman diagrams of electromagnetic interactions

gluons have two. Since gluons have color charge, gluons can interact with each other. This property is known as self coupling. Combinations of color charge are considered to be colorless if there is an anticolor for every color in the combination or if there are complete sets of colors, such as a red-blue-green trio. A fundamental property called color confinement requires that color charge cannot directly be observed in nature, which explains why quarks cannot be observed in isolation. Thus, all hadrons must be colorless.

The strength of the strong force increases as the distance between quarks increases. Gluon self coupling causes energetic gluons to create more gluons, which further increases the strength of the strong force in the interaction. This property enforces color confinement. If enough energy is applied to a bound quark, the mediating gluon will have enough energy to produce quark-antiquark pair from the vacuum to create a hadron in a process called hadronization. Figure 1-3 shows examples of strong interactions.



(a) Gluon fusion to $t\bar{t}$ production

(b) Pair production
Shows exchange of color charge red (r)
and blue (b) between two quarks

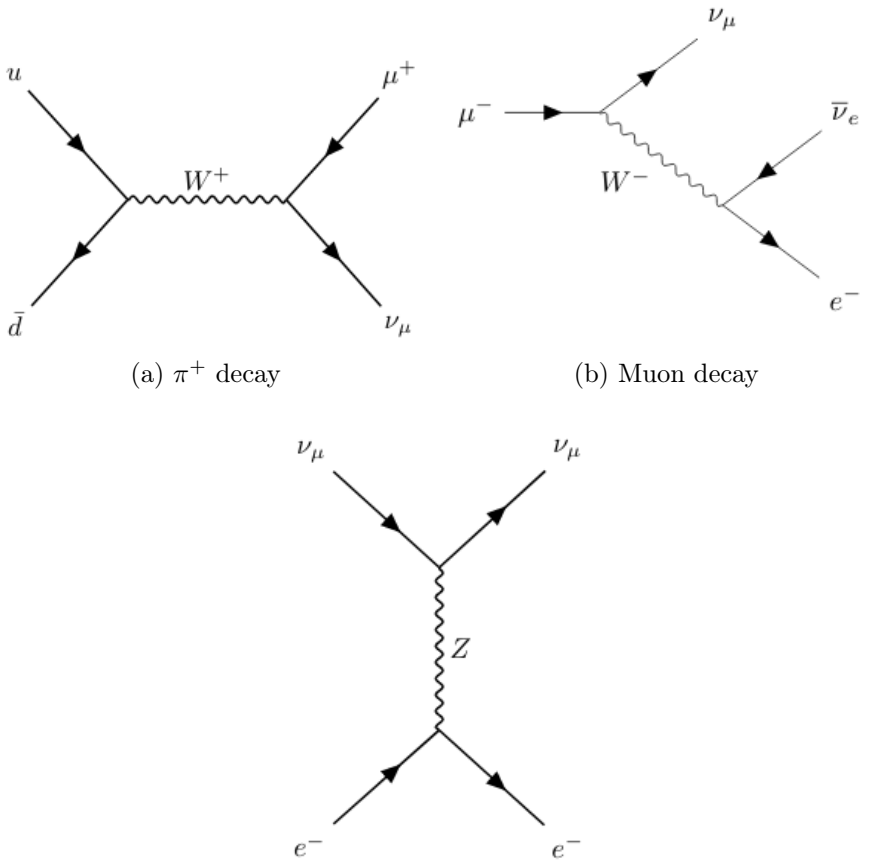
Figure 1-3: Feynman diagrams of strong nuclear force interactions

1.1.2.3 Weak nuclear force

The $W^{\pm}/Z$ bosons mediate the weak nuclear interaction with the ability to couple with all elementary fermions. The weak force couples with the quantum property called flavor, which is effectively the species of each elementary particle. Due to its charge, photons can also interact with $W^{\pm}$ bosons. Figure 1-4 shows examples of weak interactions.

Weak interactions mediated by the Z boson do not change the flavor of the particles. These are very similar to electromagnetic interactions, differing only in strength as well as the fact that Z boson has mass. As the Z boson does not carry an electric charge, these are interactions are called neutral current (NC). An example of a neutral current interaction is neutrino-electron scattering, $\nu_{\mu}e^{-} \rightarrow \nu_{\mu}e^{-}$.

Interactions mediated by the $W^{\pm}$ bosons change the flavor of the particle to the weak isospin doublet partner. Weak isospin is a quantum property which places pairs of quarks or pairs of leptons from the same generation into groups called a doublet. For the first generation, the quark doublet would contain both the up



(a) π^+ decay

(b) Muon decay

(c) Neutrino-electron scattering

Figure 1-4: Feynman diagrams of weak nuclear force interactions

and down quark, while the lepton doublet would contain the electron and electron neutrino. The difference in electric charge between the doublet pair is carried by the $W^{\pm}$ boson, thus this is called a charged current (CC) interaction. Weak charged current interactions can change the generation of the doublet due to the fact that the flavor eigenstates are not equivalent to the mass eigenstates. As the mass eigenstates control the propagation of the particle through space, the particle will consist of a

superposition of the flavor eigenstates. The $W^{\pm}$ boson can interact with any flavor eigenstate in the superposition. The Cabbibo-Kobayashi-Maskawa (CKM) matrix describes the mixing of the quark flavor and mass eigenstates. The Pontecorvo-Maki-Nakagawa-Sakata (PMNS) matrix, further explained in section 1.2.2.1, quantifies the mixing of neutrino mass and flavor eigenstates.

Parity and Charge Symmetry Violation A key aspect of the weak nuclear force involves parity and charge symmetry. Often referred to a mirror or reflection transform, a parity transformation flips the sign of one or all spatial coordinates. It should be noted that angular momentum, including spin, is invariant under a transform in parity. Likewise, charge conjugation transforms all particles involved in their event into their antiparticles, or vice versa. It is expected that the physics involved in particle interactions should be the same under either a parity transformation or a charge conjugation, as the choice of coordinates and sign of the charge is arbitrary. These invariant interaction properties are called parity and charge symmetry.

In 1956, theoretical physicists Tsung-Dao Lee and Chen-Ning Yang first proposed that the weak force could cause parity violation in charged kaon decays [3]. To further investigate parity violation in the weak force, Chien Shiung Wu developed an experiment to directly probe the conservation of parity [4]. Using cobalt-60, which is a unstable isotope of cobalt which has spin, the Wu experiment measured the direction of the decay products from the nuclear β-decay, ${}^{60}_{27}\mathrm{Co} \rightarrow {}^{60}_{28}\mathrm{Ni} + e^{-} + \bar{\nu}_e + 2\gamma$. The electron and electron neutrino are products of the β-decay of a neutron, which involves the weak force. As a parity transform would reverse the direction of the particle while leaving the spin of the cobalt unchanged, any preference in direction in relation to the spin would violate parity. The two photons are from the deexcitation of the nickel nuclei via an electromagnetic process, which is known to conserve parity.

This served as a calibration to determine the direction of the spin of the cobalt nuclei. The experiment found that the electron is preferentially emitted anti-parallel to the spin of the nuclei, which definitively proved parity violation as a property of the weak force.

To conserve momentum, the electron antineutrino would be emitted in the direction parallel to the atomic spin. The experiment shows that the weak force predominantly prefers antineutrinos with a right-handed helicity. Helicity is the projection of the spin angular momentum on the linear momentum, and right-handed helicity means the spin direction is in the same direction as the momentum. Further experiments showed that charged weak force violates parity maximally[5], which means that only right-handed antineutrinos are produced in weak interactions. As the weak force is the only force besides gravity that would operate on neutrinos, there are only right-handed antineutrinos in nature. Consequently, all neutrinos must be left-handed. The maximal parity violation is established as the vector-axial current (V-A) in the Standard Model.

As a result of parity violation, weak interactions do not have charge symmetry. For instance, charge conjugation transforms positively charged pion decay $\pi^+ \to \mu^+ + \nu_\mu$ into negatively charged pion decay $\pi^- \to \mu^- + \bar{\nu}_\mu$. However, charge conjugation does not affect the helicity of the particles in the event. Since the weak interaction only produces left-handed neutrinos, the conjugation from positively to negatively charged pion decay should transform a left-handed neutrino into a left-handed antineutrino. However, as noted beforehand, there are no left-handed antineutrinos, thus the weak interaction also violates charge symmetry.

One possible symmetry for weak interactions combines both the parity and charge transform into the charge parity transform (CP) where the particle becomes the antiparticle and the parity is flipped. Here, a left-handed neutrino transforms into

a right-handed antineutrino. This symmetry was shown not to hold in kaon decay experiments [6], which showed a small violation of CP symmetry for the weak force in the quark sector. The question of whether the neutrino sector also violates the CP symmetry is a current research topic for neutrino experiments.

1.2 Neutrino Oscillations

Neutrino oscillations describe the non-zero probability of a neutrino of a given flavor being observed as a different flavor after propagating through space. This phenomenon is beyond the Standard Model, and has changed the concept of neutrinos as massless, static particles to a dynamic sector of particle physics.

1.2.1 History of neutrino oscillations

As explained in section 1.1.2.3, parity violation in the weak force solely produces left-handed neutrinos and right-handed antineutrinos. As helicity is not Lorentz invariant, it was posited that neutrinos must travel at the speed of light to preserve helicity. While it was already known that neutrinos could have a very light mass, this property required that the neutrinos were massless.

The first hint of neutrino oscillations were seen at the Homestake experiment. A team led by Raymond Davis, Jr. placed a 380 m^3 tank full of perchloroethylene, which contains chlorine, into a gold mine. The experiment looked for electron neutrinos from the sun by counting the number of radioactive argon nuclei decays resulting from the reaction $\nu_e + {}^{37}\mathrm{Cl} \rightarrow {}^{37}\mathrm{Ar}^{+} + e^{-}$. Compared to the theoretical calculations provided by John N. Bachall, the experiment only found a third of the expected electron neutrino events [7]. One possible explanation for the reduced number of events was neutrino oscillations, as electron neutrinos would oscillate to other flavors

as they travel from the sun to the Earth. Later experiments confirmed that the cause of the reduced number of interactions was neutrino oscillations. For instance, the Sudbury Neutrino Observatory (SNO) experiment measured the event rate of both solar electron neutrinos and all solar neutrinos. The fraction of solar electron neutrinos to all solar neutrinos was found to be 34%, agreeing with predictions made with neutrino oscillations [8]. Another study of atmospheric neutrinos by Super-Kamiokande observed half the rate of muon neutrinos coming up through the Earth in a comparison those coming from down above. This can be accounted by neutrino oscillating as they propagate through the Earth [9].

Neutrino oscillations require that neutrinos travel slower than the speed of light in order for the flavor of neutrino to change. This requirement means that neutrinos can have mass. Bruno Portecorvo first suggested that neutrinos could have mass and thus oscillate[10]. The mechanism which gives mass to neutrinos and related those masses to the neutrino flavors was developed by Ziro Maki, Masami Nakagawa, and Shoichi Sakata in the Pontecorvo-Maki-Nakagawa-Sakata (PMNS) matrix[11].

1.2.2 Neutrino oscillation formalism

1.2.2.1 Pontecorvo-Maki-Nakagawa-Sakata (PMNS) Matrix

Neutrinos are created in a flavor eigenstate, however, the mass eigenstates are the only solutions to the vacuum Hamiltonian. Thus, the mass eigenstates will determine time evolution of the particle. The Pontecorvo-Maki-Nakagawa-Sakata (PMNS) 3×3 unitary matrix connects the flavor eigenstates, ν_α, $\alpha = e, \mu, \tau$ to the mass eigenstates, ν_j, $j = 1, 2, 3$ as shown in equation 1.1. Each mass eigenstate has a corresponding

mass m_1, m_2, and m_3.

$$|\nu_\alpha\rangle = \sum_j U_{\alpha j} |\nu_j\rangle \tag{1.1}$$

$$\begin{pmatrix} \nu_e \\ \nu_\mu \\ \nu_\tau \end{pmatrix} = \begin{pmatrix} U_{e1} & U_{e2} & U_{e3} \\ U_{\mu 1} & U_{\mu 2} & U_{\mu 3} \\ U_{\tau 1} & U_{\tau 2} & U_{\tau 3} \end{pmatrix} \begin{pmatrix} \nu_1 \\ \nu_2 \\ \nu_3 \end{pmatrix}$$

For Dirac neutrinos, where fermions are not their antiparticles, the PMNS matrix can be expressed using only four free parameters, as five of the original nine elements are related to the lepton phases which can be absorbed into the other parameters. Three parameters are mixing angles, θ_{12}, θ_{13}, and θ_{23}, which describe the rotation of the mass eigenstates into the flavor eigenstates. The remaining parameter is δ_{CP}, which is the Dirac CP-violating phase factor which describes the strength of the CP violation. Equation 1.2 shows the matrix written out in with these four parameters, with $s_{ij} \equiv \sin\theta_{ij}$ and $c_{ij} \equiv \cos\theta_{ij}$.

$$\begin{pmatrix} 1 & 0 & 0 \\ 0 & c_{23} & s_{23} \\ 0 & -s_{23} & c_{23} \end{pmatrix} \begin{pmatrix} c_{13} & 0 & s_{13}e^{-i\delta_{CP}} \\ 0 & 1 & 0 \\ -s_{13}e^{i\delta_{CP}} & 0 & c_{13} \end{pmatrix} \begin{pmatrix} c_{12} & s_{12} & 0 \\ -s_{12} & c_{12} & 0 \\ 0 & 0 & 1 \end{pmatrix} \tag{1.2}$$

$$= \begin{pmatrix} c_{13}c_{23} & s_{12}c_{13} & s_{13}e^{-i\delta_{CP}} \\ -s_{12}c_{23} - c_{12}s_{23}s_{13}e^{i\delta_{CP}} & c_{12}c_{23} - s_{12}s_{23}s_{13}e^{i\delta_{CP}} & s_{23}c_{13} \\ s_{12}s_{23} - c_{12}c_{23}s_{13}e^{i\delta_{CP}} & -c_{12}s_{23} - s_{12}c_{23}s_{13}e^{i\delta_{CP}} & c_{23}c_{13} \end{pmatrix}$$

For sake of completeness, if neutrinos are Majorana particles, then neutrinos would be equivalent to antineutrinos. Due to this additional constraint, the PMNS matrix would have two additional free parameters in the form of complex phases.

1.2.2.2 Neutrino Propagation

The equation for the free propagation of the neutrino flavor eigenstate α is a superposition of the neutrino mass eigenstates j propagators.

$$\begin{aligned} |\nu_\alpha(t)\rangle &= \sum_j U_{\alpha j} |\nu_j(t)\rangle \\ &= \sum_j U_{\alpha j} e^{-i(p_j \cdot x_j)} |\nu_j(0)\rangle \end{aligned}$$

Here, p_j is the momentum four-vector, x_j is the position four-vector, and $p_j \cdot x_j$ is the Minkowski inner product of the two vectors.

For accelerator neutrinos, the neutrino propagator should be approximated as a wave packet, however, using a plane wave equation with a few assumptions will have a negligible differences with the wave packet treatment[12]. It can be assumed that the neutrino components are aligned in the same direction (z) and that the neutrinos are ultrarelativistic ($t \sim z$). Thus, the phase, $p_j \cdot x_j$ on each of the neutrino mass eigenstates becomes

$$\begin{aligned} p_j \cdot x_j &= E_j t - \vec{p}_j \cdot \vec{x}_j \\ &\approx (E_j - p_j) z \\ &= \frac{E_j^2 - p_j^2}{E_j + p_j} z \\ &\approx \frac{m_j^2}{2E} z \end{aligned} \tag{1.3}$$

$\vec{p}_j$ and $\vec{x}_j$ are the momentum and position three-vectors, respectively, and $\vec{p}_j \cdot \vec{x}_j$ is the Euclidean inner product of the two vectors.

The last step uses the relativistic dispersion relation, $E_j^2 = \vec{p}_j^2 + m_j^2$. As the

neutrino masses are small, they can be neglected in the denominator, where $E_j \sim |\vec{p}_j|$. Also, since the masses are small, the mass eigenstates will approximate have the same energy, $E = E_j$. Thus, the propagator for the neutrino flavor eigenstate α over distance L is

$$\begin{aligned} |\nu_\alpha(L)\rangle &= \sum_j U_{\alpha j} e^{-im_j^2(L/2E)} |\nu_j\rangle \\ &= \sum_\beta \left(\sum_j U^*_{\beta j} U_{\alpha j} e^{-im_j^2(L/2E)} \right) |\nu_\beta\rangle \end{aligned} \tag{1.4}$$

The latter equation is rewritten in the flavor basis β. The probability that a neutrino created in flavor state α will be observed in as flavor β after travelling distance L can be expressed as

$$P_{\nu_\alpha \to \nu_\beta}(L) = |\langle \nu_\beta | \nu_\alpha(L) \rangle|^2 \tag{1.5}$$

$$= \sum_j \sum_k U_{\beta j} U^*_{\alpha j} U^*_{\beta k} U_{\alpha k} e^{-i(m_k^2 - m_j^2)L/2E} \tag{1.6}$$

The difference between the squares of the masses, $m_k^2 - m_j^2$, are often written as Δm^2_{kj}. The expression for the probability is commonly rewritten as

$$\begin{aligned} P_{\nu_\alpha \to \nu_\beta}(L) &= \sum_j \sum_k U_{\beta j} U^*_{\alpha j} U^*_{\beta k} U_{\alpha k} \left[1 - 2\sin^2\left(\frac{\Delta m^2_{kj} L}{4E}\right) - i \sin\left(\frac{\Delta m^2_{kj} L}{2E}\right) \right] \\ &= \sum_j \sum_k U_{\beta j} U^*_{\alpha j} U^*_{\beta k} U_{\alpha k} \\ &\quad - \sum_{j \neq k} U_{\beta j} U^*_{\alpha j} U^*_{\beta k} U_{\alpha k} \left[2\sin^2\left(\frac{\Delta m^2_{kj} L}{4E}\right) + i \sin\left(\frac{\Delta m^2_{kj} L}{2E}\right) \right] \end{aligned} \tag{1.7}$$

This can be further simplified using the properties of sines to produce

$$P_{\nu_\alpha \to \nu_\beta}(L) = \delta_{\alpha\beta} - 4 \sum_{j>k} \mathrm{Re}(U_{\beta j} U^*_{\alpha j} U^*_{\beta k} U_{\alpha k}) \sin^2 \left(\frac{\Delta m^2_{kj} L}{4E} \right) \mp 2 \sum_{j>k} \mathrm{Im}(U_{\beta j} U^*_{\alpha j} U^*_{\beta k} U_{\alpha k}) \sin \left(\frac{\Delta m^2_{kj} L}{2E} \right) \quad (1.8)$$

The sign in front of the imaginary term is negative when looking at the probability of neutrino oscillation, and it will be positive for the probability of antineutrino oscillation. The imaginary term will be zero if $\delta_{CP} = 0$ or π.

1.2.2.3 Oscillation parameters

The neutrino oscillation probability calculation needs the parameters present in the PMNS matrix, including the three mixing angles as well as the CP-violating phase. However, equation 1.8 shows five additional parameters, the energy of the neutrino E, the length between the creation and observation of the neutrino L and the three differences between the squared masses of the mass eigenstates called the mass splittings, Δm^2_{kj}. E and L are external factors that can be tuned by an experiment in order to increase the measurement sensitivity of the intrinsic neutrino properties. Also, only two of the mass splittings need to be measured, as $\Delta m^2_{21} + \Delta m^2_{32} = \Delta m^2_{31}$. Overall, there are six independent parameters that govern neutrino oscillations, $\theta_{12}, \theta_{23}, \theta_{13}, \delta_{\mathrm{CP}}, \Delta m^2_{21}$, and Δm^2_{32}.

It should be noted that the probability of neutrino oscillations is independent of the absolute masses of the neutrinos. Oscillations are only sensitive to the mass splitting Δm^2_{kj}. Current estimates from cosmological studies places an upper bound on the sum of all the neutrino masses as $\sum_i m_i < 0.15$ eV[2], but it is very difficult to measure the neutrino masses directly. Experiments have found that the difference

between m_1^2 and m_2^2 is small, but the difference with m_3^2 is much larger.

$$\Delta m_{21}^2 \ll |\Delta m_{32}^2| \sim |\Delta m_{31}^2| \tag{1.9}$$

As the mass splittings only appear as an argument to $\sin^2$, the signs of the mass splittings cannot be found by oscillations of neutrinos propagating in vacuum. However, neutrinos that propagate through matter will interact with electrons in matter differently than antineutrinos. This ultimately can enhance or suppress the electron neutrino appearance relative to the electron antineutrino appearance, depending on the sign of Δm_{21}^2. Thus, the sign of Δm_{21}^2 has been found through matter effects.

Still, the sign of Δm_{32}^2, and thus Δm_{31}^2, is unknown. Knowledge of the sign, and thus the ordering of the neutrino masses, is known as the neutrino mass hierarchy problem. There are two possible configurations. Normal hierarchy refers to the case where $\Delta m_{32}^2 > 0$, and thus $m_1 < m_2 < m_3$. Inverted hierarchy refers to the opposite case, where $\Delta m_{32}^2 < 0$ and $m_3 < m_1 < m_2$. This is illustrated in figure 1.2.2.3.

Different neutrino experiments will be more sensitive to certain parameters given E, L, and the flavor of neutrino studied. Solar and reactor neutrino experiments have provided the values for θ_{12} and Δm_{12}^2, while θ_{23} and $|\Delta m_{32}^2|$ have been measured by atmospheric and accelerator neutrino experiments. Data from both reactor neutrino and accelerator neutrino experiments led to the measurement of θ_{13}. As previously noted, the difference between the oscillation probability for neutrino and antineutrinos is the sign in front of the imaginary term. This is the only term to depend on δ_{CP}, thus the measurment of this parameter will require comparisons between neutrinos and antineutrinos, primarily from accelerator experiments. Measurements from one experiment lead to constraints on different parameters, and the current values are the result of the best fit from multiple experiments. Table 1.1 gives the best fit oscillation

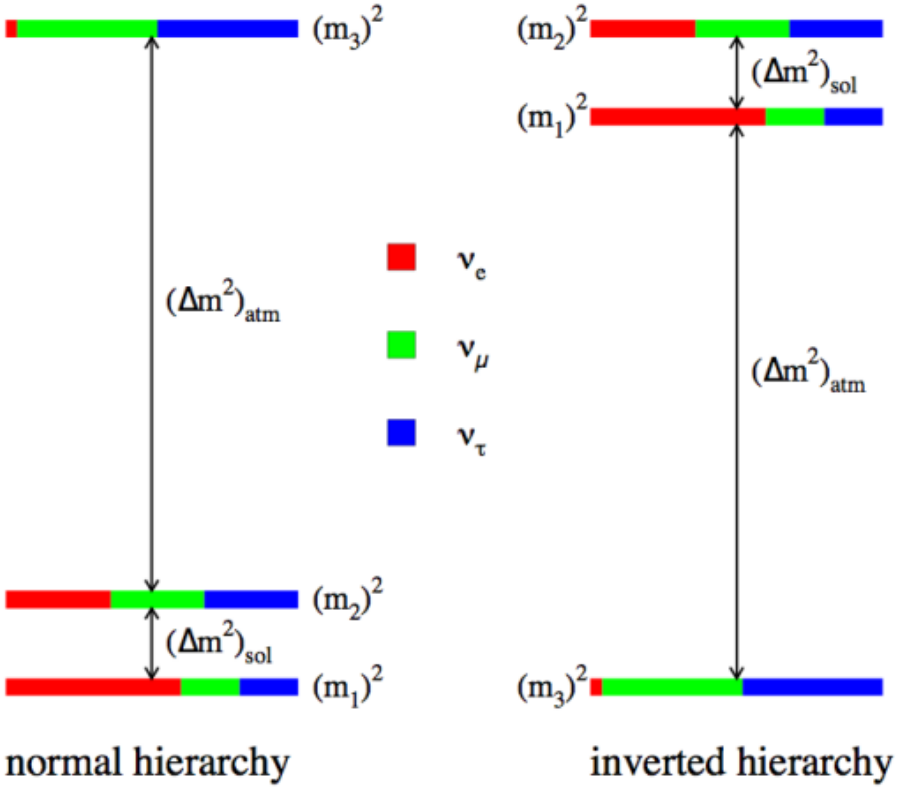


Figure 1-5: The mass splittings of the normal and inverted neutrino hierarchies. Figure from [13]

values.

1.2.3 Cross sections on pion production

Ultimately, in order to measure the neutrino oscillation parameters experiments compare the detected event rate of neutrinos of a given flavor and energy to the probability that an initial set of neutrinos will oscillate into that flavor. These experiments primarily look for charged current interactions, as the flavor of the neutrino can be determined by the charged lepton produced in the event. The energy of the neutrino

Parameter	best fit value $^{+1\sigma}_{-1\sigma}$
$\sin^2\theta_{12}$	$0.307^{+0.013}_{-0.012}$
$\sin^2\theta_{13}$	$2.18^{+0.07}_{-0.07} \times 10^{-2}$
$\sin^2\theta_{23}$ (NH)	$0.545^{+0.021}_{-0.021}$
$\sin^2\theta_{23}$ (IH)	$0.547^{+0.021}_{-0.021}$
Δm^2_{21}	$7.53^{+0.18}_{-0.18} \times 10^{-5}$ eV^2
Δm^2_{32} (NH)	$2.453^{+0.034}_{-0.034} \times 10^{-3}$ eV^2
Δm^2_{32} (IH)	$-2.546^{+0.034}_{-0.040} \times 10^{-3}$ eV^2
δ_{CP}	$1.36^{+0.17}_{-0.17}$ π rad

Table 1.1: Three neutrino mixing best fit oscillation parameters assuming normal (NH) or inverted (IH) mass hierarchy[2].

can be reconstructed by measuring the energy of the product particles of the neutrino interaction. Different processes in the experiments will affect the accuracy of the reconstruction.

One process of particular interest is pion production. Each detector will have a different energy response to pions which will affect the reconstruction of the neutrino energy. Also, pions can affect the flavor reconstruction as charged pions can mimic the behavior of muons and neutral pions can mimic behavior of electrons. To account for these effects, experiments need to calculate the probability that pions will be produced in a neutrino interaction as well as the kinematics of the products.

Experiments can use cross section measurements of pion production to estimate these quantities, however, these cross sections come with uncertainties which translate to uncertainties on the oscillation parameters. For instance, two oscillation experiments looking at accelerator neutrinos, T2K and NOvA, have reported 2-8%[14] and 3-5%[15] cross section uncertainties. T2K uses water (H_2O) as the detector medium

while NOvA uses scintillator (CH). A future oscillation experiment, called DUNE, is based on liquid argon and has set a goal of 2% cross section uncertainties[16]. Note that these detectors are built with materials with varied sized nuclei. Pion production has been previously measured on lighter nuclei, such as oxygen in water and carbon. However, there have been few measurements on heavier nuclei, and future neutrino experiments will use heavier nuclei in their detectors. This analysis aims to provide cross sections of charged current single pion production on heavy nuclei while providing comparisons with measurements of pion production on scintillator.

1.3 Charged Current Neutrino Interactions

Using first principles to extract neutrino-nucleus scattering cross sections requires knowledge of the structure of both nucleons and the nucleus. Currently, there are not enough measurements to fully construct a function that accounts for all of the structure. Thus, neutrino interactions on nuclei are broken into three separate processes: the fundamental neutrino interaction which primarily occur on nucleons, modifications of the initial state of the nuclear medium, and the final state interactions on the resultant particles from the fundamental interaction. The fundamental neutrino interaction is typically subdivided into separate interaction models, each which produces a different particle topology.

There are two variables are often used to characterize the neutrino interaction: the space-like four momentum transfer of the event, Q^2, which is equivalent to the

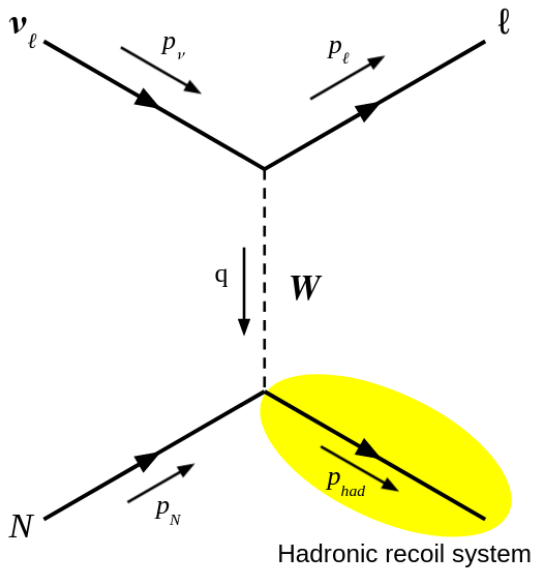


Figure 1-6: A generic charged current neutrino-nucleon interaction Feynman diagram with labelled momenta.

negative Mandelstram variable t, and the invariant hadronic mass of the event W.

$$Q^2 = -q^2 = -t = -(p_\nu - p_l)^2 \tag{1.10}$$

$$\begin{aligned} W^2 = p_{had}^2 &= (p_\nu + p_N - p_l)^2 \\ &= 2qp_N - Q^2 + m_N^2 \end{aligned} \tag{1.11}$$

Several of the relevant interaction models and their kinematic regions are explained in table 1.2.

The contributions of first three interaction models to the calculation of total charged current interaction cross section and their respective Feynman diagram are shown in figure 1-7. Coherent pion production is a subdominant process, only producing $\sim 1\%$ of the total CC event rate.

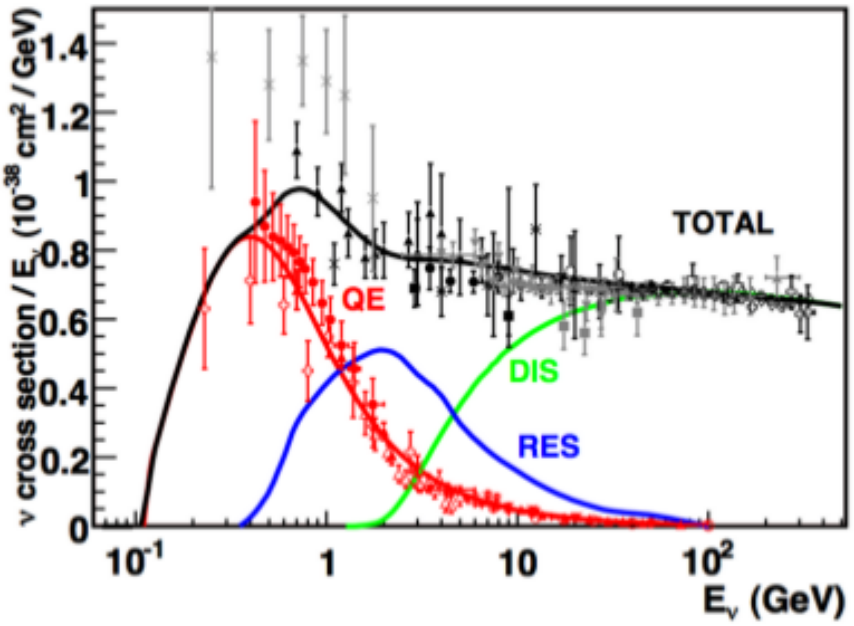
At lower W, the QE and resonant pion production models have the neutrino

Models	W Range	Description
Quasielastic (QE) $\nu_l + N \to l + N^{'}$	$W \approx m_N \sim 1$ GeV	Target nucleon N changes to isospin partner N', no other particles produced in initial interaction
Resonant Pion Production $\nu_l + N \to l + N^{'} + \pi$	$m_\Delta \sim 1.2 \lesssim W \lesssim 1.8$ GeV	The interaction excites the target nucleon into a baryon resonance, which decays into a nucleon and pion
Deep Inelastic Scattering (DIS) $\nu_l + N \to l + N^{'}$	$W \gtrsim 2$ GeV	The neutrino interacts with a constituent quark in a nucleon, producing multiple hadrons. Nonresonant pion production is governed by DIS
Coherent Pion Production $\nu_l + A \to l + A + \pi$		The neutrino interacts with the entire nucleus with a small momentum transfer, producing a charged pion and leaving an unmodified nucleus

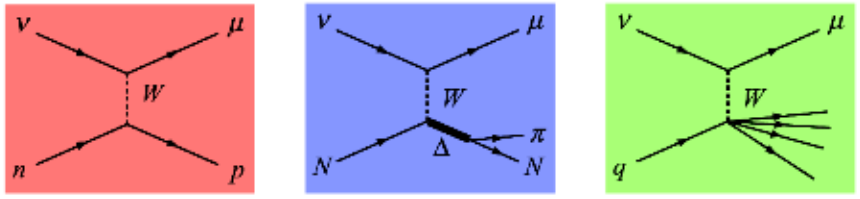
Table 1.2: Summary of relevant neutrino-nucleon and nucleus interaction processes

interacting with the entire nucleon. At higher W, the DIS model has the neutrino interacting with individual quarks. These models work the best in their kinematic regions, and these models are treated as exclusive processes, where the model does not provide a prediction outside of its kinematic region. However, quark-hadron duality has shown that the neutrino cross section on the individual quarks is an average of the cross sections of nucleon resonances [17]. This shows that these processes contain the same physics, and each model uses a different picture of the interaction. A complete model would be able to provide a prediction equally well in each kinematic range. This is particularly important in the region where the dominant model changes from

resonant to DIS, $1 < E_\nu < 10$ GeV, as both models should transition into one another when producing events with a single pion.



(a) Total neutrino charged current cross section per nucleon on an isoscalar nucleus. Data comes from several neutrino experiments, and the predictions come from the NUANCE generator, with the total cross section subdivided into separate models. Plot from [18]



(b) Diagrams of CCQE (left), resonant (middle), and DIS (right).

Figure 1-7: Overview of the charged current neutrino-nucleon interaction processes

1.3.1 Charged current quasielastic scattering (CCQE)

The Llewellyn-Smith model [19] provides a differential cross section in Q^2 for CCQE. The model uses form factors based in the nucleon rest frame in order to describe the structure of the struck nucleon. Table 1.3 explains the model parameters.

$$\frac{d\sigma}{dQ^2} = \frac{m_N^4 G_F^2 |V_{ud}|^2}{8\pi(p_\nu \cdot p_N)^2}\left(A(Q^2) \pm B(Q^2)\frac{s-u}{m_N^2} + C(Q^2)\frac{(s-u)^2}{m_N^4}\right) \tag{1.12}$$

Parameter	Description
m_N	Mass of nucleon
G_F	Reduced Fermi constant (1.166×10^{-5} GeV^{-2})
V_{ud}	CKM matrix element describing transition probability between u and d quarks
$s = (p_\nu + p_N)^2$	Mandelstam variable
$u = (p_l - p_N)^2$	Mandelstam variable

Table 1.3: Llewellyn-Smith Model Parameters

The $\pm$ sign in front of B will flip to be positive for neutrino scattering, negative for antineutrino. A, B, and C are functions of several form factors: the two vector form factors $F_1^V(Q^2)$ and $F_2^V(Q^2)$, the axial form factor $F_A(Q^2)$, and the pseudoscalar form factor $F_P(Q^2)$. The two vector form factors can be related to the nucleon electromagnetic form factors found from electron-nucleon scattering due to the conservation of vector current (CVC) hypothesis, which states the strong force conserves both electromagnetic and weak vector currents.

Electron scattering data at low Q^2 supports using a dipole approximation for describing the distributions of electric charge and magnetic moment inside nucleons.

$$F_A(Q^2) = \frac{g_A}{(1 + Q^2/M_{A,CCQE}^2)^2} \tag{1.13}$$

g_A is the axial coupling constant which can be measured using the lifetime of a neutron. It is equivalent to the difference between the up and down quark's spin spin contributions in the nucleon, $g_A = \Delta u - \Delta d = -1.267$[20]. $M_{A,CCQE}$ is the axial mass which is extracted from neutrino and antineutrino quasielastic cross sections, which currently has a measured value of 1.014 ± 0.014 GeV/c^2 [21][22]. However, measurements of scattering event with high Q^2 have shown deviations from the dipole approximation [23].

The pseudoscalar factor F_P can be related to $F_A(Q^2)$ due to the partial conservation of axial current (PCAC) [24], which says that axial current is conserved when the mass of the pion goes to 0. However, the factor is scaled by $\sim m_l^2/m_N^2$ and it only appears in the function A, thus its effect on the cross section is small for both electron and muon neutrino scattering, but this approximation does not hold for tau neutrinos.

Charged-current quasielastic scattering does not produce any pions in the neutrino interaction, thus these events will only show up in pion measurements if there were final state interactions in the nucleus or reinteractions of the final state particles in the detector. The former process can be included in the signal of an analysis due to the inability to distinguish between an event with a pion produced in the neutrino interaction versus FSI, while the latter is exclusively considered to be a background process.

1.3.2 Resonant pion production

For resonant pion production, the neutrino interaction excites the nucleon into a baryon resonance, which quickly decays back into a nucleon while emitting a pion. Figure 1-8 shows the Feynman diagram for resonant pion production via $\nu_\mu + p \rightarrow$

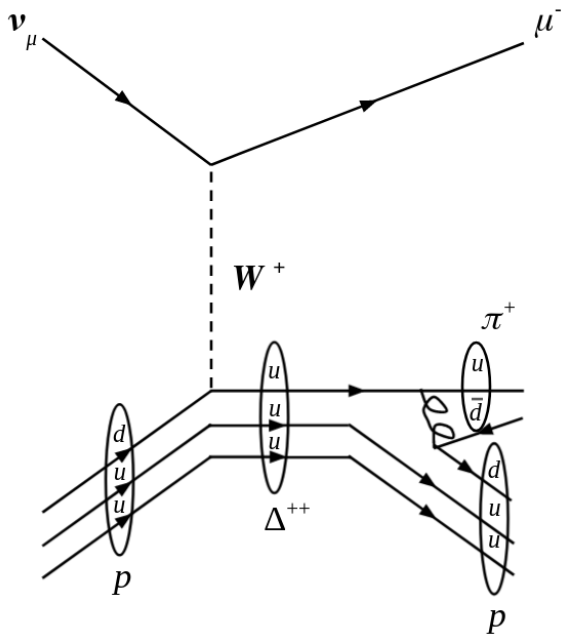


Figure 1-8: Muon neutrino charged current resonant pion production from a proton through the Δ^{++} resonance. Similar processes can occur with neutrons ($\nu_\mu + n \rightarrow \mu^- + \Delta^+ \rightarrow \mu^- + p + \pi^0$ and $\nu_\mu + n \rightarrow \mu^- + \Delta^+ \rightarrow \mu^- + n + \pi^+$)

$\mu^- + p + \pi^+$ process. Typically, only the smaller baryon resonances of N^* with isospin $1/2$ and Δ with isospin $3/2$ are accessible at the energy range of neutrino oscillation experiments.

Baryon resonances have short lifetimes, and they have larger masses than the baryons in the ground state. The resonances will often be made of quarks from the same generation. For instance, both Δ^+ and the $N^+(1440)$ baryon have the same valence quarks of the proton, *uud*. However, the proton has a rest mass of 938 MeV/c^2 with spin and isospin of $1/2$, while $N^+(1440)$ has a rest mass of 1440 MeV/c^2 with spin and isopin of $1/2$ and Δ^+ has a rest mass of 1232 MeV/c^2 as well as spin and isospin of $3/2$. The mean lifetime of the Δ and $N^*(1440)$ baryons are $O(10^{-24})$ s[2].

Scattering cross sections for resonance production are proportional to the Briet-

Wigner factor:

$$\sigma_{\text{res}} \propto \frac{\Gamma}{(W - M_{\text{res}})^2 + \Gamma^2/4} \tag{1.14}$$

where M_{res} is the mass of the baryon resonance and W is the invariant mass of the baryonic system. Γ is the resonance width, which is the energy range where the factor is more than half the maximum. It should be noted that the cross section will peak when W is equal to the baryon resonance mass. The resonance width is related to the mean lifetime of the particle τ through

$$\Gamma = \hbar/\tau \tag{1.15}$$

Most neutrino experiments uses the Rein-Seghal model to predict resonant pion production [25]. The model treats the excited baryon state as a superposition of 18 possible baryon resonances whose invariant masses $W < 2.0GeV$. Interference is only considered between resonances with identical spin and orbital angular momenta. Quarks are treated as harmonic oscillators outlined by the Feynman, Kislinger, and Ravndal (FKR) relativistic quark model [26]. By first assuming that the resonance distribution is sharply peaked, implying an infinitesimal resonance width, the differential cross section is

$$\frac{d^2\sigma}{dQ^2 dE_{had}} = -\frac{G_F^2}{4\pi^2}\frac{Q^2}{|\vec{p}_W|^2}\kappa\left(u^2\sigma_L^{\nu,\bar{\nu}} + v^2\sigma_R^{\nu,\bar{\nu}} \mp 2uv\sigma_0^{\nu,\bar{\nu}}\right)\delta(W - M_{res}) \tag{1.16}$$

Parameter	Description
$\lvert\vec{p}_W\rvert$	Magnitude of three-momentum of the virtual $W^{\pm}$ boson
$\sigma_L^{\nu,\bar{\nu}}/\sigma_R^{\nu,\bar{\nu}}/\sigma_0^{\nu,\bar{\nu}}$	Partial cross sections for the absorption of a virtual $W^{\pm}$ boson of left/right/zero handed helicity

Table 1.4: Rein-Seghal Resonant Pion Production Model Parameters

The terms u, v, and κ are abbreviations for

$$\begin{aligned} u &= \frac{E_\nu + E_l + |\vec{p}|}{2E_\nu} \\ v &= \frac{E_\nu + E_l - |\vec{p}|}{2E_\nu} \\ \kappa &= \frac{M_{\text{res}}^2 - m_N^2}{2m_N} \end{aligned} \tag{1.17}$$

The partial cross sections and the $\mp$ sign on the third term will change for neutrinos (negative) and antineutrinos (positive). The FKR quark model provides the helicity amplitudes $f_\mp$ and f_0 of the production process, which can be used to derive the partial cross sections:

$$\begin{aligned} \sigma_{L/R}(Q^2) &= \frac{\pi M_{\text{res}}}{2m_N\kappa} \sum_{\text{spins}} |f_\mp|^2 \\ \sigma_0(Q^2) &= \frac{\pi m_N}{2M_{\text{res}}\kappa} \left(\frac{|\vec{p}_W|^2}{Q^2}\right) \sum_{\text{spins}} |f_0|^2 \end{aligned}$$

The helicity amplitudes are proportional to vector and axial transition form factors $G^V(Q^2)$ and $G^A(Q^2)$, which are modeled as dipoles:

$$G^{V,A}(Q^2) \propto \left(\frac{1}{1 + Q^2/M_{V/A,res}^2}\right) \tag{1.18}$$

Neutrino-nucleus scattering cross sections provide the best fit values for the vector and axial resonant mass [27]:

$$M_V^{RES} = 0.84 \text{ GeV} \tag{1.19}$$

$$M_A^{RES} = 1.12 \text{ GeV} \tag{1.20}$$

Relaxing the assumption that the distribution is sharply peaked, the δ-function becomes the Breit-Wigner factor:

$$\delta(W - M_{\text{res}}) = \frac{1}{2\pi} \frac{\Gamma}{(W - M_{\text{res}})^2 + \Gamma^2/4} \tag{1.21}$$

It should be noted that nonresonant pion production, which is ascribed here to the deep inelastic scattering model, can interfere with resonant pion production. This interference can shift apparent energy of the resonance peak. However, the nonresonant pion processes are treated separately in most models in order to improve agreement with data. For $W < 2$ GeV, DIS hadronization models do not perform well. Thus, in order to simulate nonresonant pion production, Rein-Seghal adds the contributions from a nonresonant process with isospin $\frac{1}{2}$ incoherently to the resonant model. Care must be taken to not double count nonresonant pion events created by both the Rein-Seghal and DIS models. Recently, extensions to Rein-Seghal by Kabirnezhad have tried to account for the interference [28].

1.3.3 Deep inelastic scattering (DIS)

As deep inelastic scattering occurs when the neutrino interacts with a constituent quark, the DIS cross section can be parameterized by the momentum of the quark as well as the amount of energy transferred to the hadronic system. Neglecting terms

proportional to the mass of the lepton squared, the following equation is the DIS neutrino-nucleon cross section [29][30]. Table 1.5 explains the parameters in the cross section.

$$\begin{aligned}\frac{d^2\sigma}{dxdy} =& \frac{G_F^2 m_N E_\nu}{\pi}\left(1+\frac{Q^2}{m_W^2}\right)^{-2} \\ &\times\left[xy^2F_1^{W^\pm N}+\left(1-y-\frac{xym_N}{2E_\nu}\right)F_2^{W^\pm N}\pm xy\left(1-\frac{y}{2}\right)F_3^{W^\pm N}\right] \end{aligned} \tag{1.22}$$

Parameter	Description
$E_{had}=E_\nu-E_l$	Energy of the hadronic system
$x=\frac{Q^2}{2m_N E_{had}}$	Bjorken-x: fraction of nucleon momentum carried by the struck quark
$y=\frac{E_{had}}{E_\nu}$	Inelasticity: fraction of neutrino energy transferred to hadronic system
m_W	Mass of W boson

Table 1.5: Deep Inelastic Scattering Parameters

The $\pm$ sign on the third term will be positive for neutrino scattering, negative for antineutrino scattering. The nucleon structure functions, $F_i^{W^\pm N}$, represent the interaction of $W^\pm$ boson with nucleons. All of the structure functions are dependent on both Q^2 and x. The structure functions rely on the parton distribution functions, which describe the distributions of quark momenta $p_q = xp_N$. Both sets of functions must be found empirically from many different experiments including lepton-nucleon scattering [12].

After the initial neutrino interaction, hadronization and the resultant hadronic showers can be described by the several models such as the phenomenological Lund string model, which works well for events where $W \geq 2$ GeV.

The reconstruction of exclusive hadron kinematics can be onerous, as it can be

difficult to separate hadrons in deep inelastic scattering events with high multiplicity. Most deep inelastic scattering events are characterized with event kinematics such as Q^2 or the momentum of the final state lepton. Due to the difficulty of measuring the hadron kinematics in high multiplicity events, single pion analyses try to restrict the contributions from DIS events, which can be removed by requiring that $W < 1.8$ GeV.

1.3.4 Coherent pion production

In charged current coherent pion production, the neutrino interacts with the entire nucleus, producing both a lepton and pion while leaving the nucleus in its original state. For coherent pion production, $|t|$ refers to the square of the four momentum transferred to the nucleus.

$$|t| = (p_\nu - p_l - p_\pi)^2 \tag{1.23}$$

To preserve the state of the nucleus, the four-momentum transferred to the nucleus must be small, $|t| \lesssim 1/R^2$, where R is the radius of the nucleus. There are many different pictures that describe how $|t|$ is transferred to the nucleus. In the PCAC picture of coherent pion production, the intermediate weak boson fluctuates to a virtual pion that scatters elastically off the nucleus.

Adler uses the partially conserved axial current theorem to relate pion-nucleus scattering to coherent pion cross sections at the limit where the neutrino transfers no momentum to the target nucleus ($Q^2 = 0$) [31]. Rein-Seghal provides a model that extends the Adler cross section to $Q^2 > 0$ by introducing a multiplicative axial-vector dipole form factor [32][33]. The model also relates the differential pion-nucleus $\pi^\pm A$ elastic scattering cross section to a pion-nucleon $\pi^\pm N$ elastic scattering cross

section. This allows for predictions off of any nuclei using $\pi^{\pm}A$ or $\pi^{\pm}N$ scattering data. Overall, the Rein-Seghal model predicts that the coherent cross sections will scale as a function of $A^{1/3}$, with A being the number of nucleons, due to $|t|$-dependence, pion absorption, and nuclear coherence. [34]

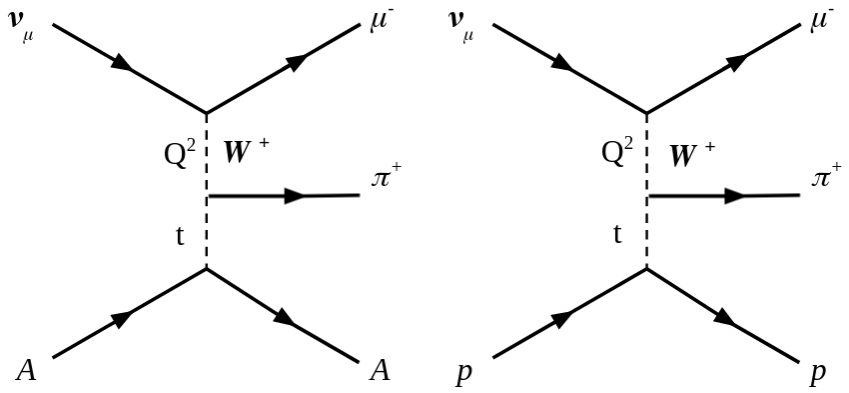


Figure 1-9: Feynman diagrams of charged current muon neutrino coherent (left) and diffractive (right) charged pion production. A in the left diagram is any nucleus, while p is a proton in hydrogen

Overall, coherent pion production is a subdominant process. For neutrino interactions on carbon nuclei where $E_\nu = 1.0$ GeV, the event generator GENIE predicts the rate of coherent pion production to be $\sim 1\%$ of the total CC interaction rate. GENIE also predicts that coherent pion production will be $\sim 10\%$ of all π^+ production on carbon. While coherent pion production cross section will increase with heavier nuclei, the fraction of pions produced coherently will decrease. This process on scintillator has been well measured by the MINERvA using data collected during its low energy ν_μ and $\bar{\nu}_\mu$ beam configurations [35]. Figure 1-10 show these measurements by MINERvA, and these beam configurations are further explained in section 2.

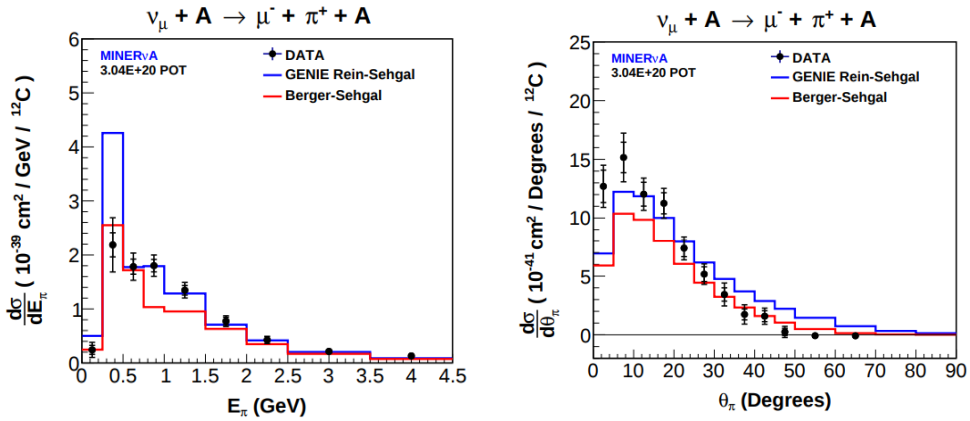


Figure 1-10: Measured cross sections $\frac{d\sigma}{dE_\pi}$ (left) and $\frac{d\sigma}{d\theta_\pi}$ (right) for ν_μ CC coherent π^+ production at MINERvA. The red line is the Rein-Seghal model implemented in GENIE described above. The blue line is the Berger-Seghal model which replaces the $\pi^\pm A$ scattering parameterization in the R-S model with a fit to π^C scattering data. Figures from [35].

1.3.4.1 Diffractive pion production

Previous MINERvA results have shown discrepancies consistent with diffractive pion production [36], which is not currently modelled in the GENIE event generator. Similar to coherent pion production, the diffractive process, shown in figure 1-9, replaces the nucleus with a proton. The neutrino interaction will leave the proton intact, however the proton may absorb some kinetic energy and become visible in a detector. Still, the kinetic energy of the proton will be small at low $|t|$, thus diffractive pion production will be indistinguishable from coherent pion production in low $|t|$ kinematic region. In MINERvA, this process will only occur on targets with hydrogen, which limits diffractive events to both scintillator (CH) and water (H_2O). It should be noted that predicting diffractive pion production may be difficult due to interference from both resonant and nonresonant processes.

Assuming the interference from other pion processes are negligible, diffractive pion

production can be predicted by the Rein-Sehgal model for coherent scattering. As the overall normalization of the cross section scales with $A^{1/3}$, the diffractive process can be simulated by scaling up coherent pion production. For instance, coherent pion production on carbon in scintillator can be scaled up by a factor of

$$\frac{A^{1/3}_{\text{hydrogen}}}{A^{1/3}_{\text{carbon}}} = \frac{1^{1/3}}{12^{1/3}} = 0.437 \tag{1.24}$$

Comparing with other π^+ processes, this scaling suggests that diffractive pion production is $\sim 33\%$ of the total π^+ production.

However, this naive scaling is imperfect substitution for diffractive events due to $|t|$ dependence in the coherent cross section. The coherent cross sections are derived from the $\pi^{\pm}A$ elastic scattering cross sections, which are proportional to $\exp(-b|t|)$, in the Rein-Seghal model. The exponential slope b is given as

$$b = \frac{1}{3}R_0^2 A^{2/3} \tag{1.25}$$

where R_0 is the nuclear length scale. The slope for carbon will be ~ 40 $(\text{GeV/c})^2$ versus ~ 8 $(\text{GeV/c})^2$ for hydrogen, which means that the cross section for diffractive scattering will fall slower than the coherent cross section on carbon. Also, diffractive interactions with larger $|t|$ will impart more kinetic energy onto the proton, which cannot be replicated by scaling the coherent pion production. Further discussion of diffractive pion production in MINERvA can be found at [35].

1.4 The Nuclear Medium

The nucleus consists of nucleons held together through the residual strong force, where mesons are exchanged between nucleons. Due to these dynamics, it is clear that the nuclear medium is a complex environment, and previous results from other neutrino experiments have shown the need to accurately model the nucleus. For instance, a measurement of the CCQE cross section on scintillator, published by the MiniBooNE experiment, showed an excess in data in comparison to simulation in the low Q^2 region[37]. By applying nuclear effects that were found from electron scattering results[38] to their base model, the disagreement between data and simulation decreased. There are multiple effects to account for, including the global behavior of the nucleons in the nucleus as well as the correlations between nucleons.

1.4.1 Nucleons in the Nuclear Potential

In the GENIE event generator, the base model for the nucleus is the relativistic Fermi gas (RFG) by Smith and Moniz[39]. Here, nucleons are confined to a potential well with walls at the nuclear radius. Starting from the lowest energy, the nucleons will fill each quantum state. All nucleons are considered to be separate non-interacting fermions whose binding energy lowers the effective nucleon mass. The average binding energy is approximately 30 MeV. As nucleons are fermions, they must obey the Pauli exclusion principle, which limits the occupancy of each quantum state to one nucleon. The Fermi momentum is derived from the energy of the highest filled quantum state, which is $p_F \sim 250$ MeV/c relative to the nucleus rest frame. In the RFG model, the nucleon momentum distribution is flat from 0 to p_F, and the nucleus has a uniform density. The Pauli exclusion principle also leads to Pauli blocking, which requires that any nucleon ejected from the nucleus must have a momentum greater than p_F.

This suppresses interactions with low Q^2.

Unfortunately, the RFG model does not account for interactions between nucleons, which can lead to nucleons with momentum greater than p_F. Bodek and Ritchie provided a prescription that adds a high momentum tail to the RFG momentum distribution in order to model these interactions [40]. The tail is derived from comparing DIS structure functions on nuclear targets to free proton/neutron structure functions.

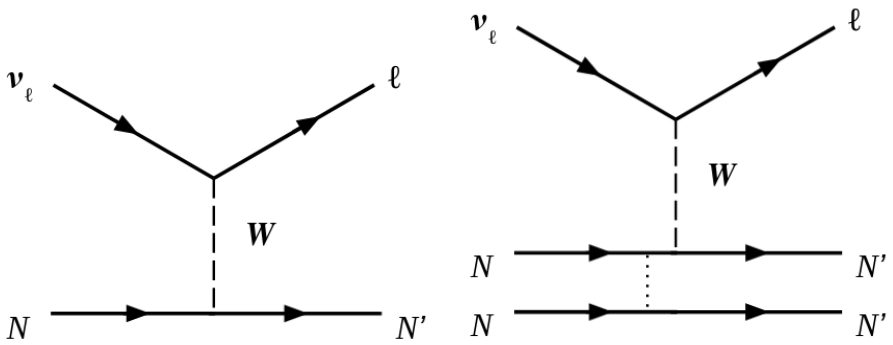
Other alternative models of the nucleus relax the assumptions that the nucleus has uniform density and the nucleons have a flat momentum distribution. For instance, the local Fermi gas (LFG) model varies the particle density as a function of the position inside the nucleus[41], where different densities of nucleons produce different Fermi momentum distributions. Ultimately, this correlates momentum and binding energy to position, as nucleons that are closer to the center of the nucleus will have larger binding energies.

Another alternate model tries to use spectral functions, which provides distributions of momentum and binding energy for the individual nucleons [42][43].

1.4.2 Multinucleon correlations

Beyond the nuclear potential, consideration must be made for correlations between nucleons, both in the short and long range. For the short range, two nucleons that are close to one another can act like a correlated pair. For a carbon nucleus, about 20% of the nucleons are in a correlated pair [44]. Dominated by np pairs [45], neutrinos will often interact with these correlated nucleons. The nucleons share the transferred momentum from the interaction and they may be ejected from the nucleus, leaving two holes. As this involves two particles, interactions like this are referred to as two particle-two hole, or 2p2h. These can be a large background for measurements

looking at CCQE interactions on uncorrelated nucleons, and overall the 2p2h events are a significant portion of the MINERvA dataset [46]. This type of event primarily occurs in the neutrino energy range between the CCQE cross section peak and the first resonant pion production peak. Correlations with three or more particles do exist, but these correlations are less common.



(a) 1p1h (CCQE) (b) 2p2h

Figure 1-11: Feynman diagrams of Np-Nh processes

Meson exchange current (MEC) is a model that describes the interactions that occur in nucleon-nucleon correlations. Here, the nucleon pair interacts with each other via a virtual pion exchange [47]. The MEC model increases the neutrino interaction rate at low Q^2 [48][49]. This affects the total neutrino cross sections by enhancing the transverse components in a manner consistent with electron nucleon scattering data [50]. It should be noted that there are currently no models which account for interactions on correlated nucleon pairs that also produce a pion (2p2h1π).

Long distance nucleon correlations are modelled using the random phase approximation (RPA) [51]. Often described as the weak force analogue to charge screening, the intermediate vector boson will polarize the nuclear medium, modifying the electroweak coupling. This effect tends to suppress the interaction rate at low Q^2, and

the effect disappears at higher Q^2.

1.4.3 Final State Interactions (FSI)

Final state interactions can occur on the resultant particles from the neutrino interactions as they traverse the nucleus. These interactions can alter the kinematics as well as the population of particles which exit the nucleus. Since pions are the lightest meson, they are a useful probe for studying FSI, as any scattering interaction can easily change the magnitude and direction of the pion momentum. Pions can undergo several different final state interactions. Table 1.6 describes the most important channels.

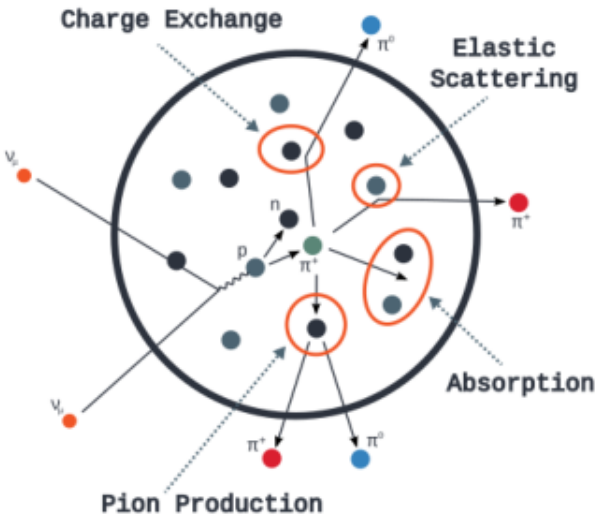


Figure 1-12: Diagram of possible final state interactions on charged pions. Figure from [52].

It is difficult to model final state interactions from first principles, as the nucleus

Elastic Scattering ($\pi N \to \pi N$)	The kinetic energy of the pion and the nucleon are unchanged, but the direction of the pion may change
Inelastic Scattering ($\pi N \to \pi N X$)	The pion loses kinetic energy and can change direction. Can transfer energy to the nucleon N or can create a hadronic shower X.
Charge Exchange (ex. $\pi^+ n \to \pi^0 p$)	The charge of the pion changes, possibly affecting all particles in the final state.
Absorption $\pi^+ np \to pp$	No pion in the final state. This often occurs with interactions with pairs of nucleons.

Table 1.6: Primary FSI modes for charged pions

has many bodies subject to the strong force. Thus, there are two primary methods for developing a FSI model: rely on external data or simulate the propagation of particles through the nucleus.

External cross sections of πA or pA scattering are used to estimate the interactions of particles moving through the nucleus. Isospin symmetry allows for predictions on n as well as π^0 and π^-. However, this method is imperfect as nuclear scattering processes occur near the surface of the nucleus, while neutrino interactions occur uniformly across the nuclear volume. This method also fails to account for particles with no scattering data, and it requires further external data to set the four momenta of the particles that exit the nucleus. Typically, if there is insufficient data, the available phase space can be uniformly sampled to estimate the outgoing kinematics of the particles.

The other primary method for developing a FSI model uses a hadronic cascade simulation to step particles through the nucleus using Monte Carlo methods. At each step, the simulation uses free nucleon scattering cross sections to randomly decides whether the particle interacts. If the particle interacts, the interaction process and the four momenta of the resultant particles will be randomly determined using the branching ratio from the cross sections. Any particles which are produced by FSI are

also subject to further interactions within the nuclear medium. There are limitations to the simulation due to the availability of both cross section data and predictions for the nucleon scattering processes. There are also concerns regarding the validity of applying free nucleon cross sections to interactions with bound nucleons.

Finally, there also exists another method using the classical Boltzmann-Uehling-Uhlenback equation [53], which evolves each particle through time using a function based on its phase space density.

It should be noted that, while FSI primarily focuses on hadron interactions due to the strong force, there still exists some effects on the final state leptons. These include multiple Coulomb scattering and the binding energy of the nuclear potential affecting the energy of the outgoing lepton.

1.5 Discussion of previous measurements of charged current single pion production

Two bubble chamber experiments at Argonne [54] and Brookhaven [55] National Lab studied single pion production from ν_μ scattering on hydrogen and deuterium targets. Studying pion production on hydrogen isotopes helps limits the effects of final state interactions, thus constraining the single pion production model at the neutrino interaction vertex. However, low statistics and poor modeling of the flux gave these datasets large uncertainties. There were initially discrepancies between these two studies in regards to the normalization of the measured cross sections, however, a reanalysis of the experimental data led to agreement between the results [56].

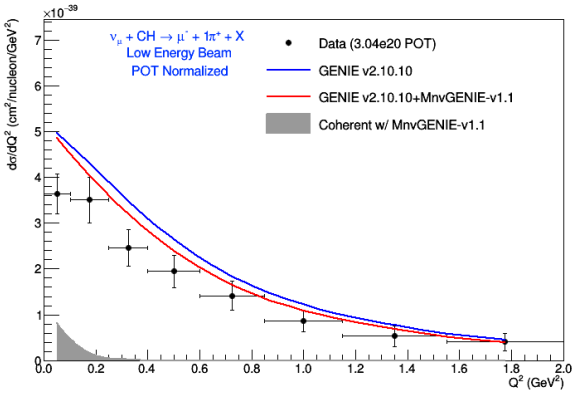
Several experiments within the last decade have released absolute cross sections of $\nu_\mu CC1\pi^+$ production on moderately sized nuclei. These include T2K on water

[57] and scintillator (CH) [58], MiniBooNE on mineral oil (CH_2) [59], and MINERvA on scintillator [60]. These measurements have smaller statistical uncertainties and better flux modelling than the deuterium cross sections, however, these measurements disagree with each other in shape and normalization. A summary of the disagreement between MINERvA and MiniBooNE can be seen in [61].

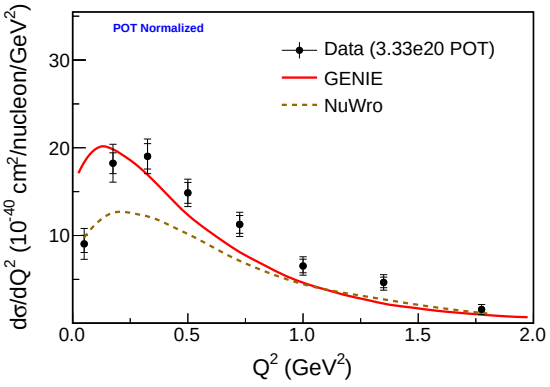
Furthermore, MINERvA has also released cross sections on related pion production channels, $\nu_\mu CCN\pi^+$ [62], $\nu_\mu CC1\pi^0$ [63], and $\bar{\nu}_\mu CC1\pi^0$ [64]. A recent study used the NUISANCE framework [65] to tune the pion production parameters within the GENIE event generator in order to improve the agreement between simulation and the pion datasets from ANL, BNL, and MINERvA. While the study did significantly reduce the disagreements between model and data, tensions still remain between the datasets [66].

One of these tensions exist at low Q^2, where models overpredict the pion production differential cross section in Q^2 compared to data. Three experiments, MiniBooNE [59], which uses the NUANCE model [67], MINOS [68], which uses NeuGen [69], and MINERvA, which uses GENIE [70], see the need for a suppression of the pion production prediction at low Q^2. For MINERvA, the two neutral pion channels at MINERvA shows evidence for a larger suppression at low Q^2, however, the data from the $\nu_\mu CC1\pi^+$ channel prefers a smaller suppression. This implies there is a process that creates charged pion events at low Q^2 that is missing for the neutral pion channels, like diffractive pion production. Figure 1-13 shows the previous MINERvA results. It should be noted that the NUISANCE study that fitted the GENIE pion production parameters [66] found an empirical suppression function using MINERvA pion data, and the study found that the suppression was stronger for the π^0 channels than for the π^+ channels.

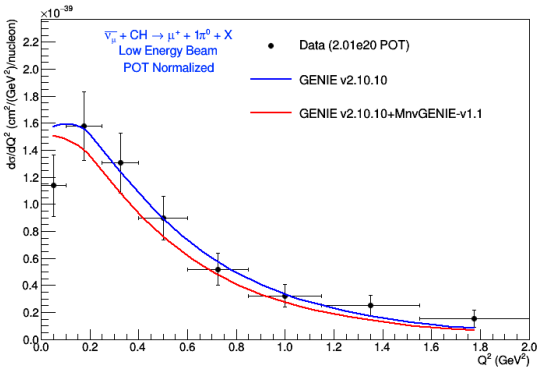
Another tension is the apparent shifts in the measured differential cross sections in



(a) $\nu_\mu CC1\pi^+$



(b) $\nu_\mu CC1\pi^0$

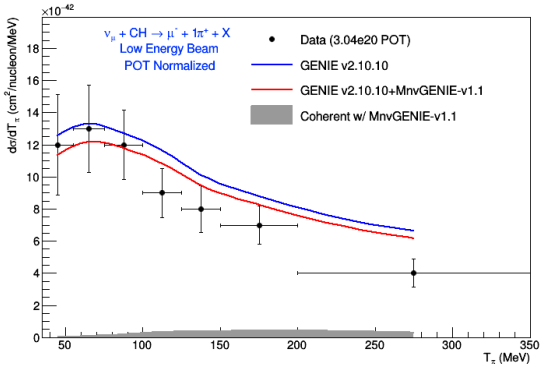


(c) $\bar{\nu}_\mu CC1\pi^0$

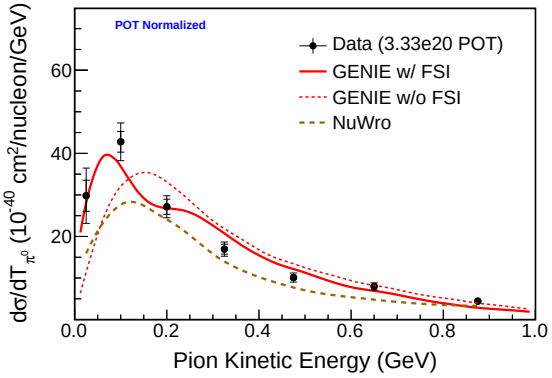
Figure 1-13: MINERvA pion production absolute differential cross sections as a function of Q^2. The primary simulation follows the red curve in each plot. Note the turnover in data for the π^0 channels versus a lack of a turnover for the $\nu_\mu CC1\pi^+$. Plots from [63] and [71]

both the invariant hadronic mass W and the kinetic energy in the pions T_π. GENIE underpredicts pion production at low T_π and overpredicts at high T_π, suggesting that interactions at higher T_π should be shifted to lower T_π. MINERvA only measured a W differential cross section for $\nu_\mu CC1\pi^0$ production, but it shows that the simulation is lower than the data at low W. The shift in W primarily occurs in the region of

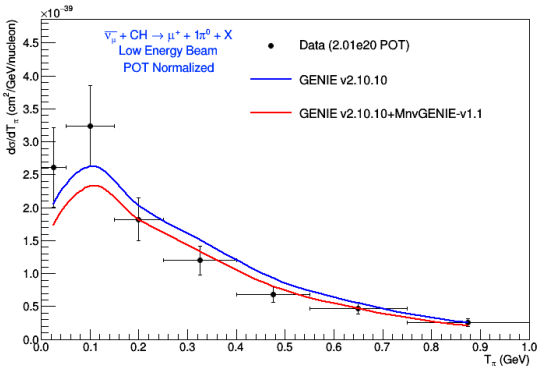
the Δ mass at 1232 MeV/c^2. These shifts could possibly be attributed to interference between resonant and nonresonant pion production not currently present within the models. Figures 1-14 and 1-15 show the differential cross sections for T_π and W.



(a) $\nu_\mu CC1\pi^+$

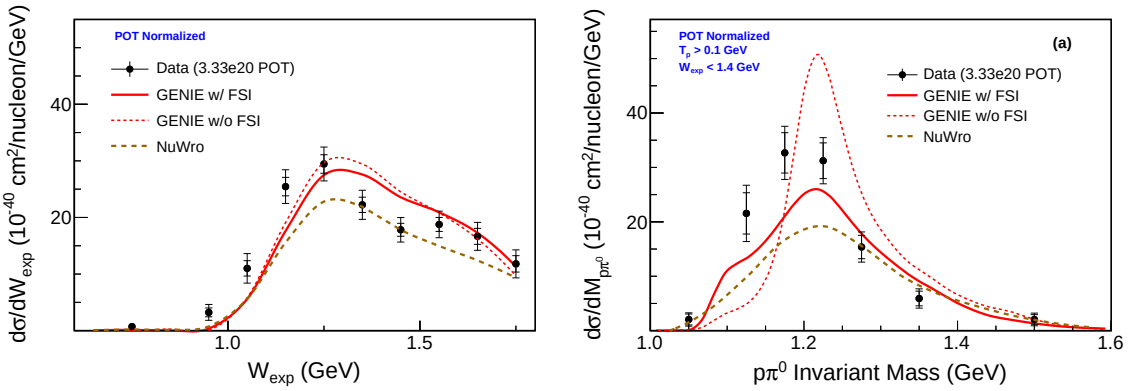


(b) $\nu_\mu CC1\pi^0$



(c) $\bar{\nu}_\mu CC1\pi^0$

Figure 1-14: MINERvA pion production absolute differential cross sections as a function of T_π. The data favors lower T_π compared to simulation. The primary simulation follows the red curve in each plot. Plots from [63] and [71]



(a) W (b) $M_{p\pi^0}$

Figure 1-15: MINERvA $\nu_\mu CC1\pi^0$ absolute differential cross section as a function of invariant hadronic mass. The plot on the left uses the entire $\nu_\mu CC1\pi^0$ sample, while the plot on the right tries to select a $\Delta(1232)$ enriched sample by requiring that the reconstructed $W < 1.4$ GeV. Also, the plot on the right uses $M_{p\pi^0}$, which is the invariant hadronic mass using solely kinematics of a proton and π^0. The primary simulation follows the red curve in each plot. Plots from [63]

Chapter 2

The NuMI Beamline and the Neutrino Flux

The MINERvA experiment uses the neutrinos supplied by the NuMI (Neutrinos at the Main Injector) beamline [72]. Located in Batavia, IL at the Fermi National Accelerator Laboratory, also known as Fermilab, the beam provides ν_μ and $\bar{\nu}_\mu$ to several experiments including MINERvA, MINOS, and NOvA. Fermilab creates the neutrino beam using the decay products of focused pions and kaons resulting from the collision of a proton beam on a graphite target.

For MINERvA, the intensity and the energy spectrum of the neutrino beam has varied throughout the time the experiment collected data. There were two eras of the neutrino beam: between 2005 to 2013, the beam was set in the low energy (LE) configuration where the beam peaked at 3.5 GeV, and from 2013 to the end of data taking, the beam was in the medium energy (ME) configuration, where the beam peaked near 7 GeV. Figure 2-1 shows the comparison between the fluxes in the LE and ME eras.

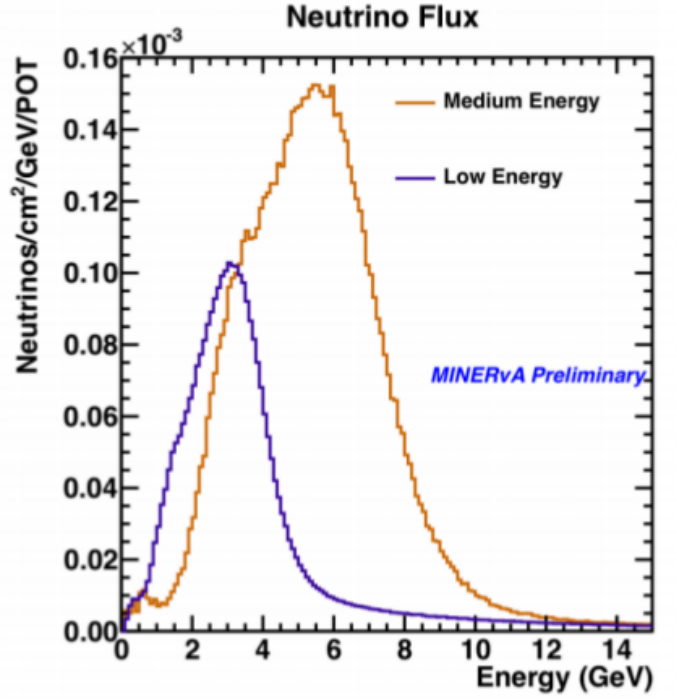


Figure 2-1: Simulation of the MINERvA flux in the low energy (LE) and medium energy (ME) configuration

2.1 Creating the Neutrino Beam

2.1.1 Accelerating protons at the Main Injector

The proton beam starts off as hydrogen gas which is ionized in a magnetized sputtering chamber. These 18 keV H^- ions are then accelerated to 750 keV by an RF quadrupole, then fed to a series of linear accelerators (Linac), which are composed of multiple resonant RF cavities concatenated together. Using an RF frequency of 201.2 MHz, the Linac accelerates the ions up to 400 MeV. During this time, the ions are placed into bunches synchronized to an RF phase frequency.

As the beam moves to the Booster synchotron, the hydrogen ions pass through

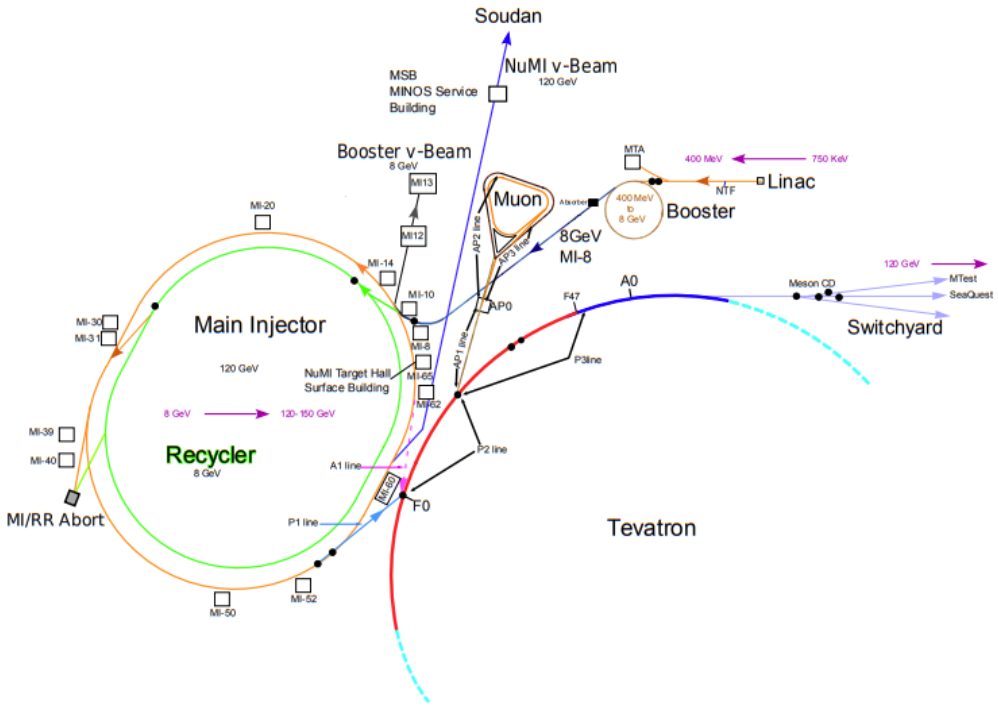


Figure 2-2: Overhead diagram of the Fermilab accelerator complex. To create the NuMI beamline, protons from the Linac on the right are fed into the Booster, where there they are directed towards the Main Injector. Protons are then extracted and sent towards the graphite target. Figure from [73]

a thin carbon foil to strip them of electrons, creating a proton beam. The Booster synchotron accelerates the protons to 8 GeV while debunching, or combining, bunches into a batch. The Booster can hold one 1.6 μs wide batch of 8 GeV protons.

A kicker quadrapole magnet steers the beam out of the Booster into the Recycler ring, where the batches are set up to be placed into the Main Injector. Initially, only six batches were injected into the Main Injector, however, a technique known as slip-stacking was developed in order to increase the intensity of the beam. The Main Injector decelerates the six initial proton batches slightly, while the Recycler provides another set of batches at the original momentum. The difference in the revolution

frequency of the two sets of batches allows them to slip, or occupy, the same spatial area. The RF frequency is then adjusted to combine both sets into one batch with double the intensity [74]. The protons in the double intensity batch are accelerated to the final beam energy of 120 GeV. Further dicussion of the Fermilab accelerator complex can be found in [75].

It should be noted that slip stacking began during MINERvA's data run, where the number of batches in the second set was increased from two to four to finally six. Ultimately, this leads to varying neutrino beam intensities across the MINERvA dataset. The MINERvA data is separated into playlists that roughly correspond to these different periods of intensity.

2.1.2 The NuMI beam

Another set of kicker magnets extracts the protons from the Main Injector, sending a set of proton batches, called a spill, downwards at an angle of 58 milliradians, or 3.3°. These protons will enter the underground Target Hall, which contains the NuMI graphite target and the magnetic focusing horns [73]. Before impacting on the graphite target, the beam passes through a graphite/aluminum baffle with a 13 mm beam aperture. This collimates the beam, which protects the downstream equipment from stray bunches.

As it is difficult to measure the intensity of the neutrino beam, the number of protons that impact onto the target, abbreviated as protons on target (POT), is a useful metric for determining the number of neutrinos created. For the sake of reference, downstream refers to the direction of the proton beam. Figure 2-3 shows the NuMI components which are downstream of the Main Injector.

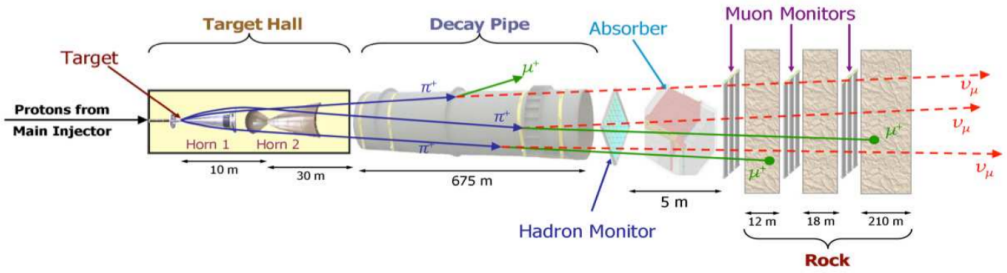


Figure 2-3: Schematic of the components of the NuMI beam. Figure from [73].

2.1.2.1 Graphite Target

For the ME era, the graphite target has a length of 1.2 m, or roughly 2.5 nuclear interaction lengths. The target consists of 48 rectangular graphite fins, each 24 mm long, mounted on stainless steel pipes which circulate water in order cool the target. Lengthening the graphite target maximizes the number of protons interactions, which increases the intensity of the neutrino beam.

However, lengthening the target also increases the number of hadron reinteractions which are difficult to simulate as well as increasing the heat retained by the target. Thus, the fins have a small cross section of $7.4 \times 63\text{mm}^2$, allowing for more hadrons to escape out the side of the target. Still, a substantial portion of these hadrons will reinteract which can lead to large systematic uncertainties. All the graphite fins, as well as the water cooling pipes, are enclosed in a aluminum cylinder filled with helium gas.

The final state particles which escape the target will spray out at many different angles and energies, and the majority of the charged mesons will eventually decay into neutrinos. Beamline neutrino experiments require the best approximation of a monochromatic and monochiral neutrino beam, which requires a filter to select and focus the mesons of a given energy and charge.

2.1.2.2 Magnetic Horns

A system of magnetic horns focuses the charged particles emerging from the target. For the NuMI beamline, the system consists of two parabolic focusing horns made of aluminum, where the horns are rotationally symmetric around their longitudinal axis. The horns are treated similarly to a coaxial cable, where the current pulses over the outer surface in longitudinal direction and then returns over the inner surface. This setup helps confine the magnetic field to the inside of the horns. Each pulse of current peaks at 200 kA, and the direction of the current determines the direction of the magnetic field. This ultimately determines whether horns focus or deflect positive or negative charged particles.

Figure 2-4 shows trajectory of particles through a single magnetic in the forward horn current (FHC) configuration, which deflects negatively charged particles and focuses positively charged particles. The positively charged mesons, π^+ and K^+, will primarily decay into ν_μ. This horn configuration is often called "neutrino" mode. The reverse horn current (RHC) configuration will focus negatively charged mesons and thus will produce a beam of antineutrinos, which leads to the configuration called "antineutrino" mode.

Particles coming from the first horn will have a variety of trajectories, most of which will not be in the downstream direction. This requires a second horn to correct the trajectory those particles which were under or overfocused, as well as focusing particles which may not have entered the first horn. Figure 2-5 shows the possible trajectories through both horns.

The energy spectrum of the neutrino flux depends on the momenta of the parent mesons. Mesons with an initial momentum primarily downstream tend to have higher energies, while those with more transverse momentum will tend to have lower energies.

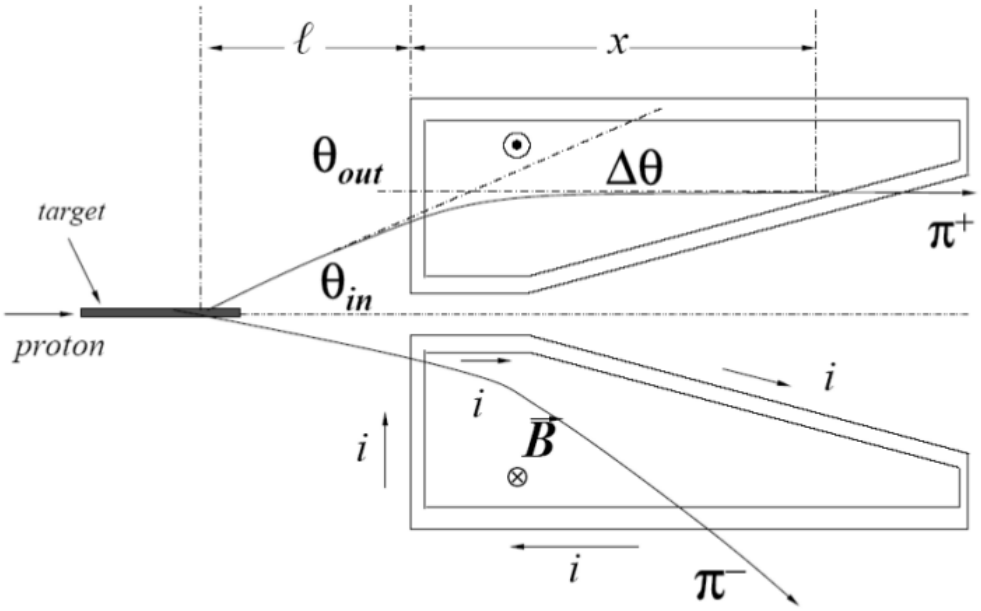


Figure 2-4: Diagram of particle trajectories through a magnetic horn. For this configuration of the horn current, π^+ are focused downstream while π^- are deflected away. Figure from [76].

The distance between the target and the first horn, the distance between the two horns, and the direction and strength of the current will determine which mesons are focused. In order to switch from the LE to the ME flux, the graphite target was placed further upstream of the first horn, while the second horn was placed further downstream. This allowed for the increased selection of more forward mesons which creates a neutrino flux with a higher energy peak. The peak in the flux is often called the focusing peak.

It should be noted that regardless of the horn configuration, there will be a narrow range of particles heading downstream that do not enter either horn. There is no way to select for the charge of these particles, and as they are highly forward moving, the neutrinos from these decays will typically have high energy, dominating the flux

above the focusing peak.

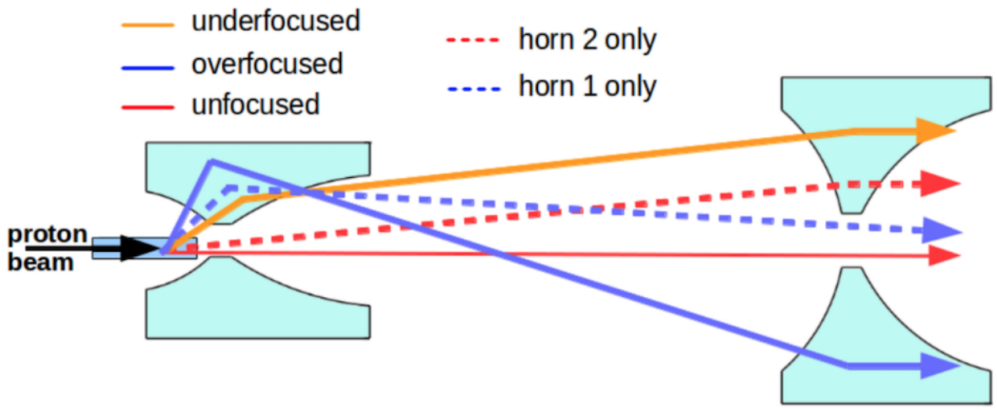


Figure 2-5: Diagram of particle trajectories through both NuMI magnetic horns. Figure from [77].

2.1.2.3 Decay Pipe

The focused hadron beam enters the decay pipe, a 675 m-long tunnel with a 1.8 m diameter. Helium gas at an absolute pressure of 13.2 PSI, or 0.9 atmospheres, makes up most of the atmosphere inside the decay pipe in order to limit the number of interactions with the hadron beam. Assuming that NuMI is running in the FHC configuration, most of the mesons in the beam will be π^+, with another significant population being K^+. As the mesons traverse the decay pipe, the mesons will primarily decay into muon neutrinos, as $\pi^+ \to \mu^+\nu_\mu$ with a branching ratio over 99% and $K^+ \to \mu^+\nu_\mu$ with a branching ratio of 63.5%. However, there will be contamination of ν_e, $\bar{\nu}_e$ and $\bar{\nu}_\mu$ in the beam due to other meson decay modes, such as $K^+ \to e^+\nu_e\pi^0$, and decays of muons from pion decays, $\pi^+ \to \mu^+\nu_\mu \to e^+\nu_e\bar{\nu}_\mu\nu_\mu$. Any antineutrinos are called wrong sign contamination. Besides the processes mentioned above, wrong sign contamination can also be the result of the unfocused negatively charged mesons

which did not pass through the horns, such as $\pi^- \rightarrow \mu^- \bar{\nu}_\mu$.

2.1.2.4 Monitors, Absorbers, and Downstream Rock

A hadron monitor has been placed at the end of the decay pipe to detect any remaining hadrons or undecayed mesons. These will then be absorbed in downstream concrete hadron absorbers. The remaining particles in the beam, muons and neutrinos, will pass through 240 m of dolomite rock before entering the MINOS hall where the MINERvA detector is located. The rock has several muon monitoring stations which can measure the location, intensity, and energy of the muons in the beam. This can provide some constraint on the neutrino flux [78]. The thickness of the rock will stop the muons created within the decay pipe, however, muon neutrinos can interact in the rock and create muons which can travel downstream to the MINERvA detector. These muons are often referred to as rock muons. Due to the number of neutrino interactions that occur in the rock, the number of rock muons that pass through the MINERvA detector will outnumber the neutrino interaction in the detector.

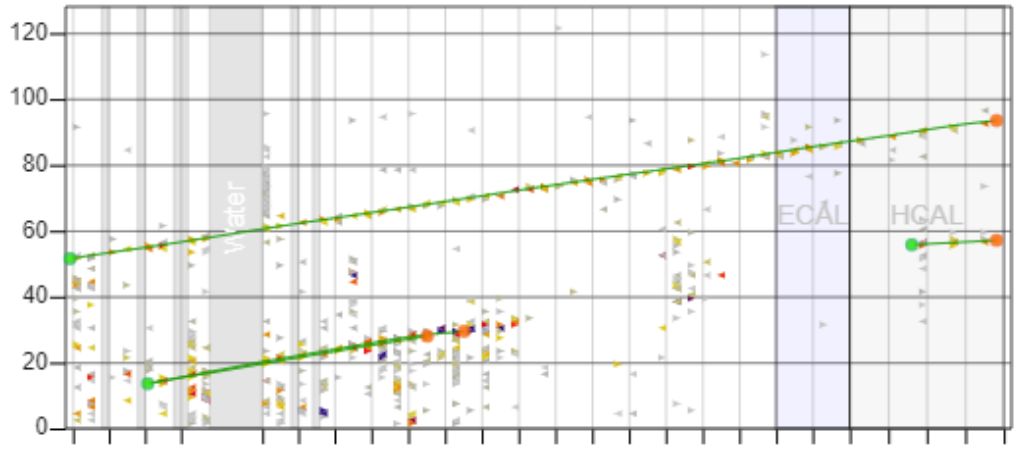


Figure 2-6: Arachne event display of a rock muon passing through the MINERvA detector. The rock muon is the top track. Arachne is a program used to show activity in the MINERvA detector. The neutrino beam is incident to the left.

2.2 Characterizing the neutrino flux

Neutrino interaction cross sections and oscillation measurements both need an accurate prediction of the neutrino flux. It is instructive here to present a simplified flux integrated differential cross section shown in equation 2.1. Differential cross sections are typically binned, meaning that the cross section is measured in separate ranges, or bins, of variable X.

$$\frac{d\sigma}{dX_i} = \frac{N_{\text{events,i}}}{\epsilon_i (T\Phi)\Delta X_i} \tag{2.1}$$

$N_{\text{events,i}}$	Number of events observed within the range of bin i
ϵ_i	Efficiency of selecting events in bin i
T	Number of targets available for neutrino interactions
Φ	Neutrino flux integrated over neutrino energy
ΔX_i	Width of bin i

Table 2.1: Explanation of variables involved in the calculation of a flux integrated differential cross section

The neutrino flux enters the flux integrated differential cross section in two ways. Clearly, the integral of the neutrino flux needs the neutrino flux as an input. But the neutrino flux is also used to seed the simulation of the neutrino interactions in the MINERvA detector, as will be discussed in 4. Changing the neutrino flux will alter the efficiency ϵ_i as well as the $N_{\text{events,i}}$.

It is difficult to measure either the energy or number of neutrinos due to their small interaction rate and neutral charge. This makes any direct measurement of the neutrino flux difficult. The simulation of the flux has also proven arduous, as the creation of the neutrino beam has multiple components that require the simulation

of complex interactions, especially those in the target assembly.

Fortunately, several methods exist to help model the neutrino flux. An *a priori* flux can be constructed using external hadron production data, and several techniques have been developed that use *in situ* MINERvA data to constrain the simulated flux. Unfortunately, it is computationally expensive to create new simulations with the improved fluxes found by these methods. Thus, each method supplies a set of reweights to apply to the simulation after its production. This often occurs at the stage where analyses select neutrino events. These reweights are the ratio between the improved and baseline flux, and they are applied according to the simulated neutrino energy.

2.2.1 G4NuMI and Hadron Production

G4NuMI, which uses the GEANT4 (GEometry ANd Tracking) toolkit to model the passage of particles through matter using Monte Carlo methods, simulates the geometry and the physics interactions in the NuMI beamline. G4NuMI simulates the entire creation of the NuMI neutrino beam, including the impact of the 120 GeV protons onto the graphite target, the propagation of the resulting secondary particles from the target assembly all the way to the decay pipe, and finally the decay of the charged mesons into neutrinos. The decay points of the mesons and the momentum spectrum of the neutrinos are used to produce the neutrino flux, which will be passed onto neutrino event generators.

The beam simulation relies heavily on the modelling of hadron production, which is composed of the proton-carbon interactions as well as the reinteractions of secondary particles within the graphite target. The base simulation uses FTFP_BERT FRITIOF precompound [79] [80] with Bertini cascade models [81] [82] implemented

in GEANT4 to model hadron production, but these models have shown to have significant disagreements with external data.

In order to reduce these disagreements, the hadron production models are tuned to data from the NA49 experiment at CERN [83], which in part studied proton-carbon interactions using a 158 GeV proton beam. The FLUKA simulation [84] translates a 158 GeV proton interaction to a 120 GeV proton interaction, which is used in the NuMI beamline. The dataset primarily focused on mesons produced from a single interactions on the target. Thus, the simulated neutrinos are reweighted so that the identity and kinematics of their decay parent mesons agree with data. Additional data from NA49 can also provide reweights for neutrinos that were the result of multiple interactions within the target or interactions on other beamline components.

MINERvA created the Package to Predict the FluX (PPFX) [85] to generate the NuMI flux predictions using the constraints from hadron production data. The package also propagates the uncertainties from the external data to the uncertainties on the flux. In order to propagate the correlation between these uncertainties, many different fluxes are produced using randomly thrown flux parameters in PPFX. Each parameter is limited to be within 1σ of its uncertainty. The spread of these fluxes gives the overall flux uncertainty.

The effects of applying the PPFX hadron production tune on the neutrino flux can be seen on the bottom plots in figure 2-7. Note the large uncertainties at higher energies, which are primarily due to unfocused pions and kaons. Further information on the tuning of hadron production models can be found in [85].

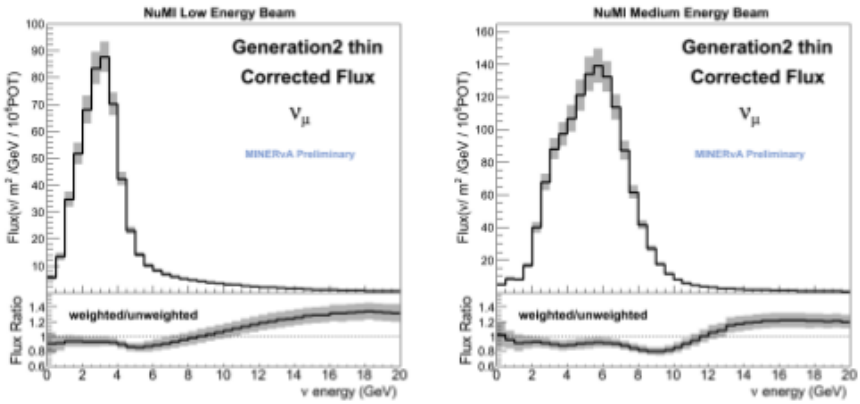


Figure 2-7: The PPFX weighted simulated LE (left) and ME (right) fluxes and the ratios to the baseline flux. Figure from [77].

2.2.2 In Situ Constraints

There are several neutrino interactions that occur in the MINERvA detector that have well known cross sections, due to a combination of being theoretically calculable and having distinct topologies which reduces the number of background interactions. Using known cross sections, the neutrino flux can be extracted to act as a constraint on the simulated flux. MINERvA has developed three techniques which will be explored below.

2.2.2.1 Neutrino Electron Scattering Flux Constraint

Calculating the cross section of the neutrino nucleon scattering requires knowledge of the structure of the quarks in nucleon. Also, as nucleons are often in nuclei, the calculation needs to account for nuclear effects. Often, these are not fully theoretically calculable. However, electroweak scattering theory does allow for a first principles calculation of a high precision cross section of neutrinos scattering off of atomic electrons [86]. The tree level cross section for $\nu_\mu e^- \rightarrow \nu_\mu e^-$, shown in equation 2.2, does

not require any form factors, and every parameter is well measured.

$$\sigma(\nu_\mu e^- \to \nu_\mu e^-) = \frac{G_F^2 s}{\pi}\left(\frac{1}{4} - \sin^2\theta_W + \frac{4}{3}\sin^4\theta_W\right) \tag{2.2}$$

Parameter	Description
G_F	Reduced Fermi constant (1.166×10^{-5} GeV^{-2})
$s = (p_\nu + p_e)^2$	Mandelstam variable
θ_W	Weak mixing angle

Table 2.2: $\sigma(\nu_\mu e^- \to \nu_\mu e^-)$ Parameters

While these events are extremely rare, roughly $\frac{1}{1000}$ times less likely than a neutrino interaction on a nucleus, they can be selected with few backgrounds due to their distinct topology of a single forward-going electron with no other particles. The energy of the electron is only weakly correlated to the incoming neutrino energy, in that $E_e < E_\nu + m_e$. The shape of the neutrino flux can be determined using this weak correlation, however, this requires a large number of neutrino electron scattering interactions. There are not enough of these interactions in the MINERvA data in order to determine the shape of the flux. Therefore, the $\nu - e$ cross section can only provide a constraint on the normalization of the flux.

MINERvA has released cross sections of $\nu - e$ scattering in both the LE [88] and ME [87] era. The ν_μ flux with and without $\nu - e$ constraint can be seen in figure 2-8. The constraint extracted from the ME cross sections was applied to the simulated flux as well as the parameter thrown fluxes in PPFX described in the previous section. This has the effect of reducing the overall normalization uncertainty of the integrated flux between 2 and 20 GeV from 7.8% to 3.9% [87]. This is currently the strongest technique in constraining the uncertainties on the flux. The effects on the fractional

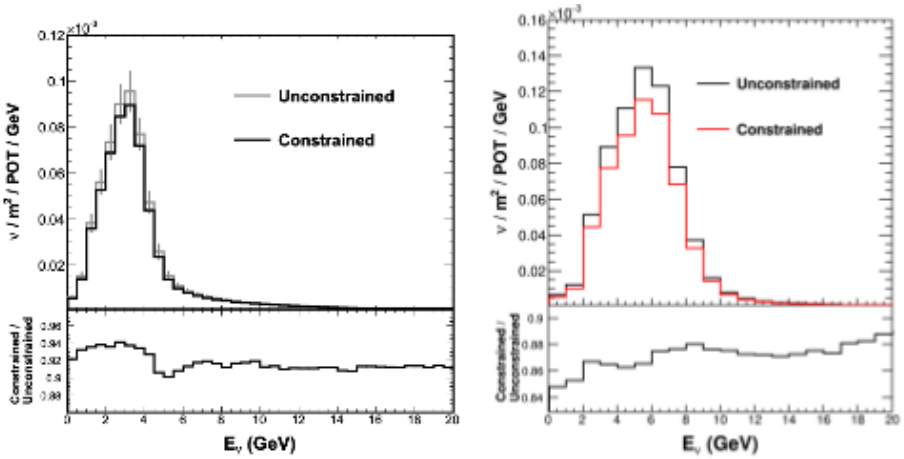


Figure 2-8: The unconstrained and $\nu - e$ constrained simulated LE (left) and ME (right) ν_μ fluxes. Figure from [87].

uncertainties of the ME ν_μ flux are shown in figure 2-9.

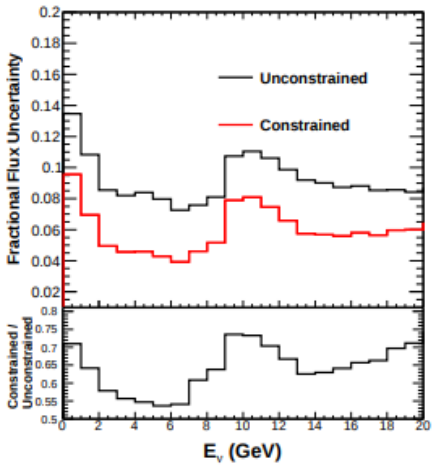


Figure 2-9: The unconstrained and $\nu - e$ constrained fractional uncertainties of the ME ν_μ flux. Figure from [87].

2.2.2.2 Inverse Muon Decay Constraint

The flux constraint from $\nu - e$ mostly constrains the integral distribution and therefore the peak of the flux. However, the highest energy neutrinos in the beam are produced by high energy $\pi^{\pm}$ and $K^{\pm}$, different from the mesons that produce most of the neutrinos, and therefore are not well constrained by this technique. Inverse muon decay (IMD), $\nu_{\mu} e^{-} \rightarrow \mu^{-} \nu_{e}$, can provide a probe into high energy tail of the flux, which is primarily populated by neutrinos produced from the decay of unfocused and underfocused mesons. Here, the muon neutrino scatters with an atomic electron using a W boson, producing a muon and an electron neutrino. Similar to neutrino electron scattering, electroweak scattering theory predicts the IMD cross section with small uncertainties. Inverse muon decay only occurs at higher neutrino energies, with a low energy reaction threshold of ≈ 11 GeV. Due to its distinct topology, which has a forward-going high energy muon with no other particles, these events can be selected with few backgrounds. This process has been measured on MINERvA [89], and figure 2-10 shows the effect of the IMD constraint on the NuMI flux.

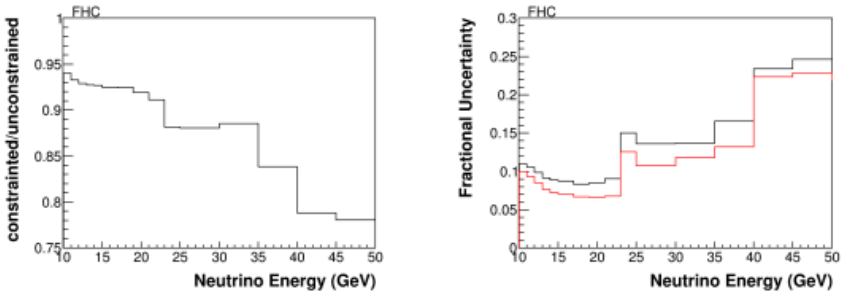


Figure 2-10: The ratio of the constrained IMD flux over the unconstrained flux (left) and the uncertainties on the flux (right) before (black) and after (red) the constraint. For these plots, the NuMI beamline was configured in neutrino mode (FHC). Figure from [89]

2.2.2.3 Low-ν and High-ν Constraint

An *in situ* method that constrains the shape of the flux needs an interaction process where the energy of the neutrino can be measured. The low-ν technique uses the inclusive sample of charged current neutrino interactions, where outgoing charged lepton allows for the measurement of neutrino energy. It is known that the inclusive charged current scattering cross section for neutrinos can be expanded in terms of $\frac{\nu}{E_\nu}$, where $\nu \equiv E_\nu - E_\mu$ is the recoil. At low recoil (low-ν) energy, where $\nu \ll E_\nu$, the higher terms become vanishingly small, and thus the inclusive cross section becomes constant as a function of neutrino energy. Therefore, by selecting for low-ν events at different ranges of neutrino energy, the shape of the neutrino flux can be derived using the constant low-ν cross section. The normalization on the flux is set using the NOMAD CC total inclusive cross section measurement [90].

The low-ν technique has been used by several neutrino experiments, including MINERvA which derived the low energy flux using the LE dataset [91] [92]. However, using the low-ν constrained flux presents a challenge for cross section measurements which have a significant number of neutrino events with low recoil, such as the charged current quasielastic cross section. For these cases, there would be an unmeasured statistical correlation between the two samples, as there is a significant overlap in the number of observed events in the cross section and the events used to create the constrained flux. This correlation could alter the flux uncertainty on the cross section. The high-ν technique was developed in order to address this issue for ME era MINERvA analyses with a large number of low-ν events, such as measurement of quasielastic scattering.

Instead of using low-ν interactions, the high-ν technique uses all events that do not have low recoil, hence the high-ν. This technique relies on the LE low-ν measurements

to provide a low-ν cross section. This can be subsequently used with the total charged current inclusive cross section to derive a high-ν cross section. These cross sections should be independent of the neutrino flux, thus the high-ν cross section can be used with high-ν events in the ME era to measure the medium energy flux.

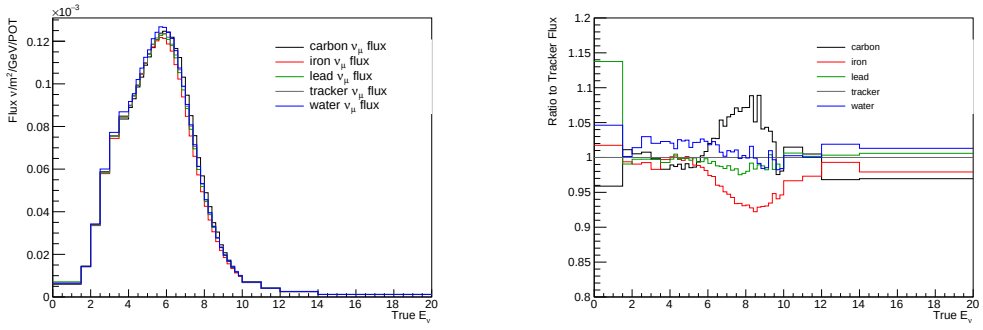
This constraint is currently used to calculate the ME charged current quasielastic cross sections on MINERvA. Further discussion on the low-ν and high-ν techniques can be found here [76].

2.2.3 Spatial Dependence of the Flux

The neutrino flux has a spatial dependence, where the distribution of neutrino energy varies across the transverse position of the NuMI beam. MINERvA uses PPFX to insert the spatial dependence of the flux into the simulation, and this sufficiently models the flux for analyses across the detector. However, analyses must account for this spatial dependence when comparing cross section measurements taken from different areas of the detector. For instance, it will be shown in section 3.2.2 that the passive targets in MINERvA have different transverse shapes than that of the active tracker region. Therefore, any comparisons between the two regions must limit the differences between the fluxes due to the spatial dependence. Figure 2-11 shows the fluxes in each passive target material as well as the flux in the active tracker region.

2.2.3.1 Daisy Bin Flux Reweight

To compare the cross sections measured on a passive nuclear target material to those measured on the active tracker region, MINERvA developed a method which supplies spatial reweights to the neutrino interactions in the active tracker region [93]. First, the method divides the face of MINERvA plane, explained further in section 3.1.1,



(a) Fluxes in different materials

(b) Ratios of the fluxes to the active tracker flux

Figure 2-11: Comparison of the FHC flux in different materials in MINERvA ($\nu^2/cm^2/POT$)

into 12 separate "petals", as shown in figure 2-12.

For this method, the neutrino flux $\Phi(E_\nu)$ needs to be calculated for each petal. In principle, the NuMI beamline simulation can provide the petal fluxes, however, rerunning the simulation in order to find these fluxes is expensive computationally. In order to extract the petal flux, the method counts the number of events in the inclusive sample of simulated ν_μ charged current (CC) interactions in each petal. Using this number with equation 2.3 will provide the petal fluxes. The average cross section of ν_μ CC interactions used the flux calculation is supplied as a spline from the GENIE event generator.

$$\Phi(E_\nu) = \frac{\text{Total } \nu_\mu \text{ CC events}(E_\nu)}{\sigma_{\text{avg}}(E_\nu) N_{\text{atoms}} \text{POT}} \tag{2.3}$$

There should be a set of spatial reweights which reduce the difference between the sum of reweighted petal fluxes and the flux in the passive nuclear target material.

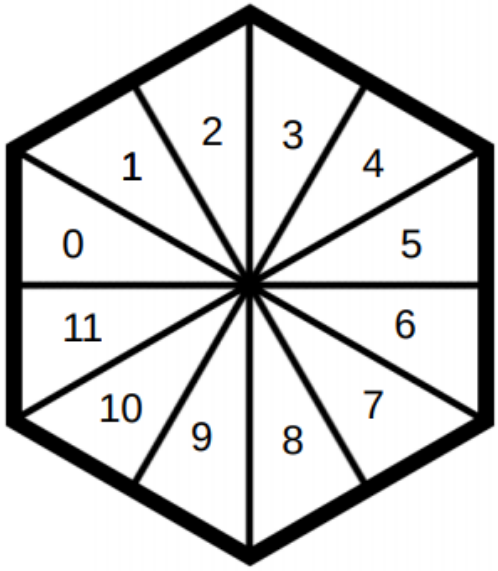


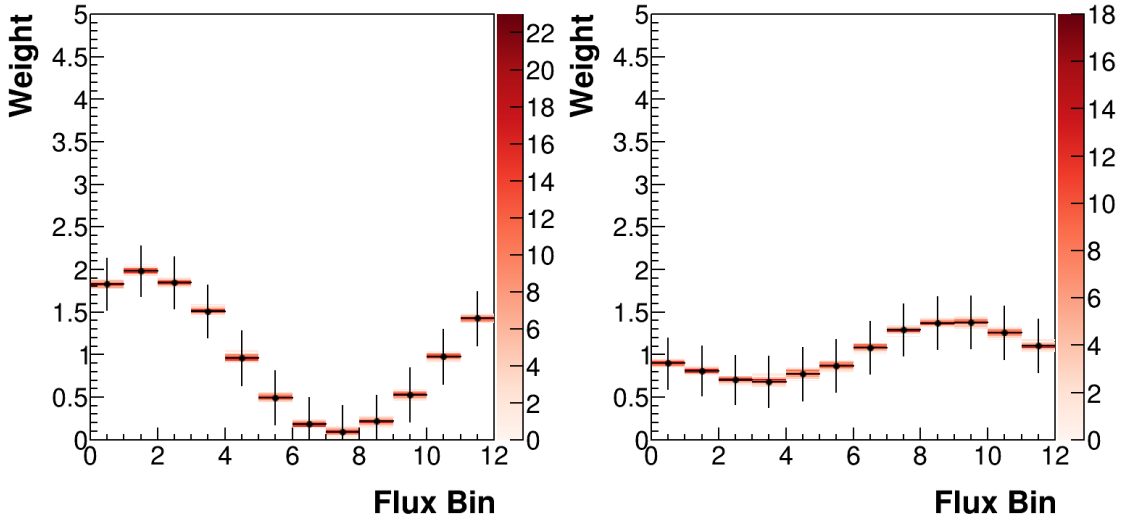
Figure 2-12: Diagram of the "daisy" petal bins

$\sigma_{\text{avg}}(E_\nu)$	average ν_μ CC cross section at neutrino energy E_ν
N_{atoms}	number of atoms per cm^2 in the target
POT	Number of protons impacted on the graphite target

Table 2.3: Explanation of variables used to calculate the neutrino flux in a daisy petal

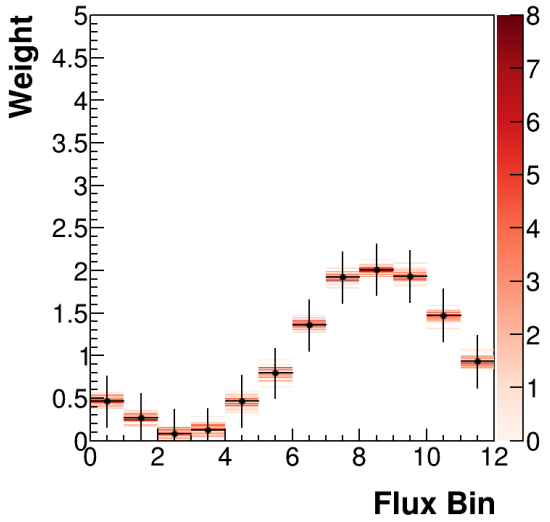
The reweights for each petal are found by fitting a weighted sum of the daisy petal fluxes to the simulated flux in the passive targets using a regularized χ^2 fitter. Figure 2-13 shows the daisy petal reweights for each passive material in the nuclear targets, using the petal numbering scheme shown in figure 2-12.

As shown in equation 2.1, the flux enters differential cross section calculation in two ways: the integrated neutrino flux normalization and the flux used to seed the neutrino events. To make the comparison with the cross section on the passive material, the active material cross section calculation replaces the original flux normalization with the integrated flux for the passive target. In order to account for the

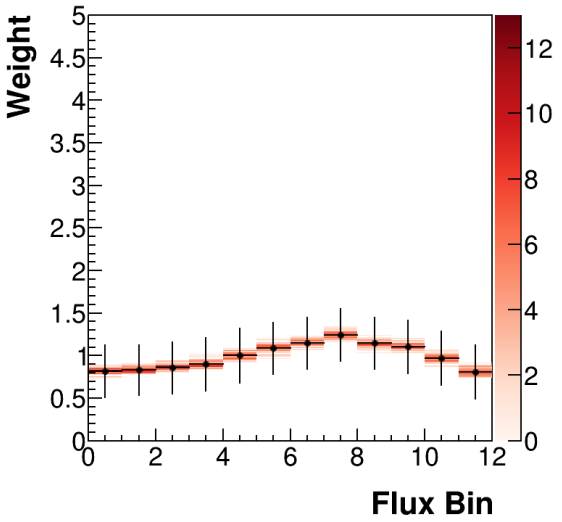


(a) Carbon

(b) Water



(c) Iron



(d) Lead

Figure 2-13: The daisy petal reweights for each passive material in the nuclear targets

flux used to seed the generated neutrino events, the weights found by the daisy petal flux fit are applied to simulated neutrino interactions that occur in a given petal.

Chapter 3

The MINERvA Detector

The Main Injector Experiment for ν-A (MINERvA) studies neutrino interactions on various nuclei, and measures neutrino scattering cross sections on these nuclei over a wide range of energies. These measurements help improve theoretical interaction models, which are essential component of the neutrino oscillation program. Proposed by a collaboration of nuclear and particle physicists in the early 2000s, the detector finished construction in 2013 at the MINOS Hall, which is located at Fermilab in Batavia, IL. Using the neutrino beam provided by the NuMI beamline, MINERvA collected neutrino data until the end of its data taking run in 2019. Overall, the experiment recorded interactions from a ν_μ beam made from 16.1e20 Protons on Target (POT) and an $\bar{\nu}_\mu$ beam made from 14.1e20 POT. (For comparison, that is the number of protons in 6 mg of ordinary matter, and has a charge of 1/4 kiloCoulomb.) The MINERvA dataset continues to be analyzed, and many measurements are still yet to come.

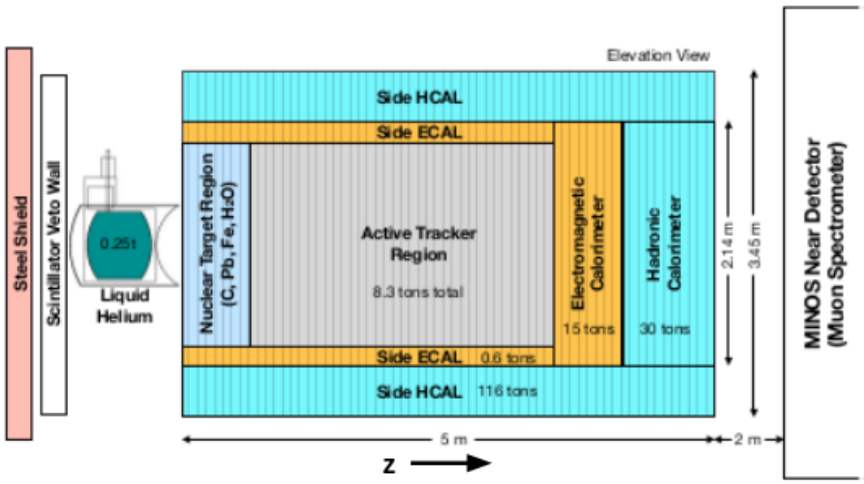


Figure 3-1: Diagram of the side view of the MINERvA detector. The NuMI beam is incident from the left. The detector coordinate system sets the longitudinal axis of the detector as the z axis. Figure from [94]

3.1 The Minerva Subdetectors

The MINERvA detector is divided into subdetectors, which are arranged to contain and categorize particles produced from neutrino interactions. Figure 3-1 shows the arrangement of the MINERvA detector. The center of the detector contains an active tracking region primarily made of finely segmented plastic scintillator surrounded by sampling calorimeters. This $\sim$ 2.5 m long subdetector is primarily known as the tracker. In order to contain and reconstruct the energy of particles exiting the sides of the detector, the tracker region was surrounded by both an electromagnetic calorimeter (ECAL) and a hadronic calorimeter (HCAL). Labelled as the side ECAL and HCAL above, the lead based ECAL can capture the energy from electrons and photons, and the HCAL uses steel and scintillator to capture the energy from hadrons like pions and protons. The tracker and the ECAL are collectively known as the inner detector (ID), while the HCAL is called the outer detector (OD).

The nuclear target region lies upstream of the active tracking region. The region has several layers of different passive materials that are used to study neutrino interactions on heavier nuclei. "Passive material" here means that no energy deposited in the material can be collected and studied. Both a veto wall and a cryogenic container of liquid helium are upstream of the face of the detector.

Downstream of the active tracking region are the two additional electromagnetic (DSECAL) and hadronic (DSHCAL) calorimeters. The DSECAL and DSHCAL are made of planes of scintillator interleaved with planes of lead and iron, respectively. These calorimeters capture the energy of particles exiting by the back of detector. Further downstream of the MINERVA detector is the MINOS Near Detector, which will be discussed further in section 3.3.

3.1.1 Active tracking planes

The MINERvA detector is composed of a stack of 208 hexagonal planes. The planes either have a core of passive material, such as those used in the nuclear target region, or active tracking material. The core of the planes used for tracking consists of 127 scintillator strips interleaved into a hexagon and held together with epoxy. A charged particle traversing a tracking plane will deposit energy in two adjacent strips, as seen in figure 3-3. By comparing the energy deposition between the two strips, the reconstruction can achieve a 3 mm resolution in position.

Each plane is framed by a steel hexagon, which is used as the HCAL. Tracking planes will have a width of 1.7 cm, and the scintillator hexagon has an apothem of 90 cm. The scintillator core is framed by a lead hexagon which is used as the ECAL.

Tracking planes come in three orientations, which are called views. The X view has the the strips are aligned vertically, while the U and V views have the strips rotated

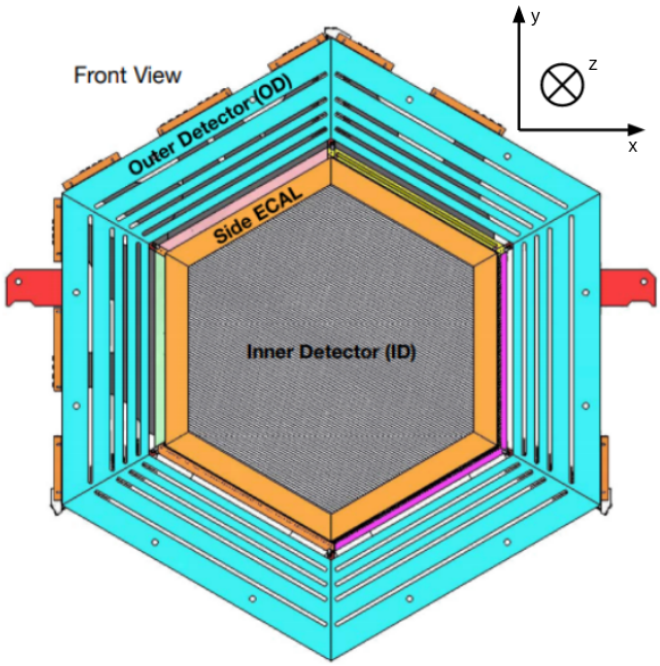


Figure 3-2: Front view of the MINERvA tracking plane. The x, y, and z axes of the detector coordinate system are drawn. It should be the noted that the neutrino beam is pointed 3.3° downwards with respect to the detector's longitudinal (z) axis. Figure from [94].

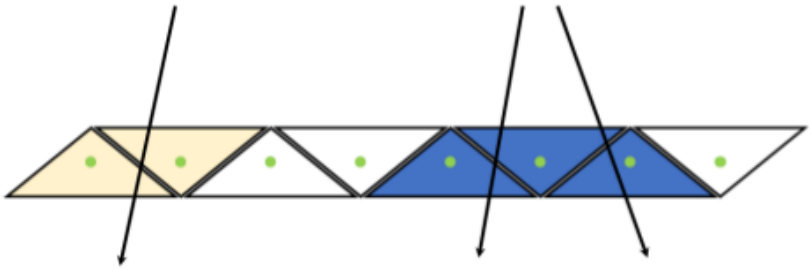


Figure 3-3: Examples of trajectories of particles passing through strips in the same plane. Figure from [95]

60° clockwise and counterclockwise, respectively. Figure 3-4 shows the orientation of plane views. Planes are grouped into modules, which contain two planes. For the

active tracking region, the modules will always have two planes with different views, either XU or XV. These modules are stacked such that the views will follow a pattern of XUXV. Two views can provide tracking in three dimensions, however, three views can remove ambiguities when two particles pass through the same planes.

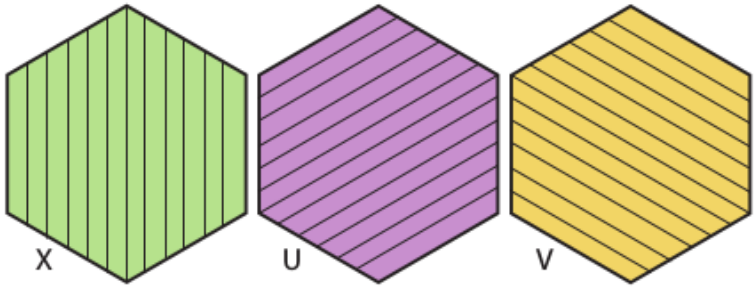
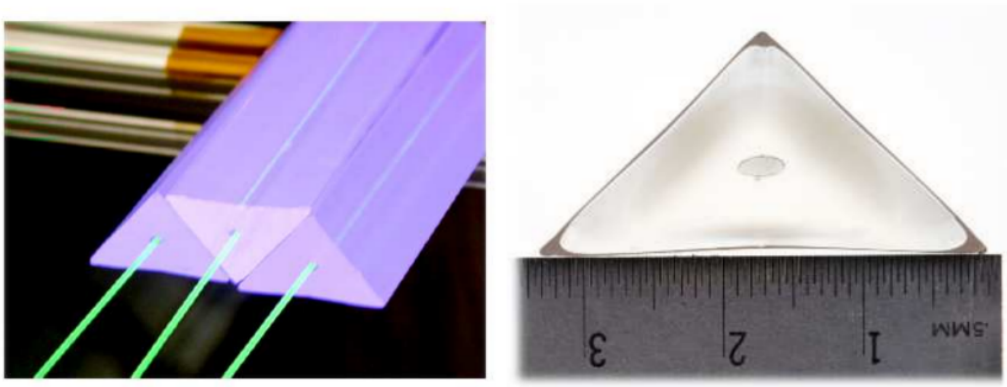


Figure 3-4: Orientation of X, U, and V planes. Figure from [96]

3.1.2 Scintillator Strips



(a) Interleaved stack of strips (b) Scintillator strip cross section

Figure 3-5: Pictures of scintillator strips used in the MINERvA inner detector

The MINERvA detector primarily uses triangular strips of scintillator to detect

charged particles travelling through the detector. The strips have a base width of 3.3 cm and a height of 1.7 cm. Primarily composed of polystyrene, the strips are doped with two wavelength shifting organic scintillators, 2,5-diphenyloxazole (PPO) and 1,4-bis(5-phenyloxazol-2-yl) benzene (POPOP). These two scintillators comprise less than 2% of the strip by weight. These three materials form a scintillator chain, where initially the polystyrene scintillates far UV light, the PPO shifts the light from far to near UV, and finally the POPOP shifts the near UV to visible blue.

In order to collect the scintillated blue light, a wavelength-shifting optical fiber was placed inside of a hole drilled in the center of the strip. The fiber absorbs blue light, then re-emits the light as green. The re-emission serves two purposes: one, re-emission is method in which light is captured in the fiber, and two, green light transmits more efficiently through the PMT glass windows. One end of the fiber is mirrored, which reflects light so that the photons are only collected on one side of the strip. The other side of the wavelength-shifting fiber connects to a clear fiber optical cable which leads to the rest of the readout chain. To prevent light escaping, the strips are covered by a reflective coating consisting of titanium dioxide and polystyrene.

3.2 Data Acquisition

The readout chain continues as the clear fiber cable transports the photons to a Hamamatsu 64-anode photomultiplier tube (PMT). The shell of a photomultiplier tube is made of steel in order shield the photomultiplier from light and magnetic interference from the MINOS Near Detector.

The photomultiplier tube can accept the inputted light from 64 separate scintillator strips. The readout chain of each strip is often referred to as a channel. Each channel has its own set of 12 amplification dynodes. Here, the initial set of photons

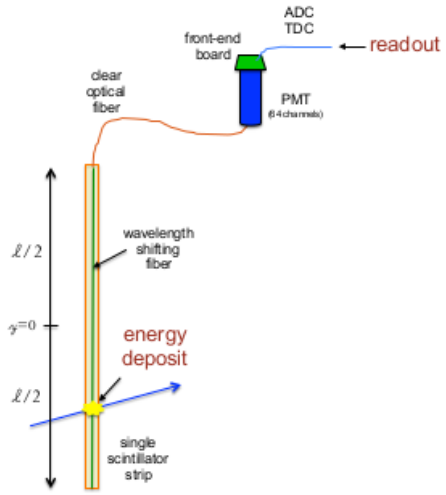


Figure 3-6: A single optical readout channel. Figure from [94]

excite photoelectrons, which proceed to move from dynode to dynode producing more electrons through secondary emissions. A typical dynode chain will amplify a single photoelectron by a factor of 5e5. For a minimum ionizing particle, which typically produces 1-10 photoelectrons, the amplified output for a channel would be 200-500 fC.

A front end board (FEB) uses six TriP-t chips to read out the charge from the PMT. The 64 channels are divided into two groups, where 32 channels are read out by a group of three TriP-t chips. In this group, each TriP-t collects charge with a different level of gain, which includes low, medium, and high. Each chip digitizes and stores the charge using an analog to digital converter (ADC).

FEBs will only store charge if there is enough activity in a strip. When the charge from the PMT exceeds a discriminator threshold, the FEB creates a timestamp and starts integrating charge for 151 ns. The grouping of the accumulated charge from a strip and the timestamp is called a hit. The hit timestamp has a resolution of 2.35

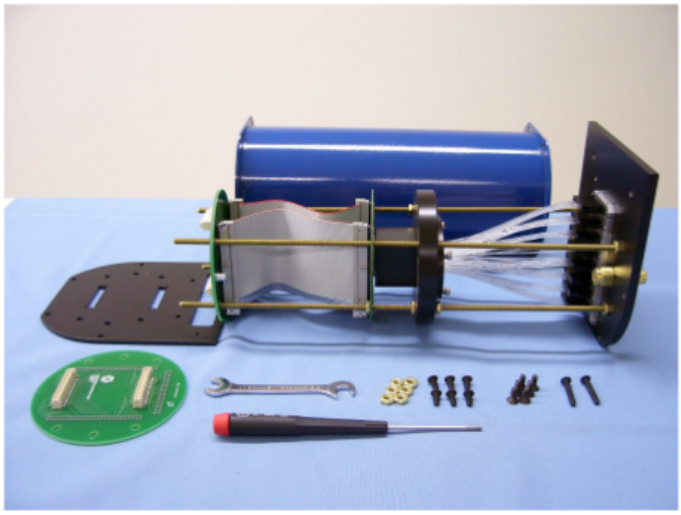


Figure 3-7: Disassembled photomultiplier box. The photomultiplier tube is the black box. Figure from [94]

ns.

After the hit accumulates charge for 151 ns, the FEB must reset the integrated charge to zero. The reset takes 188 ns, and during this time, no charge can be collected. This phenomenon is known as deadtime, and this can lead to missing activity. For instance, deadtime could cause the FEB to not record hits from Michel electrons which come from muons decays during the 188 ns window.

A set of FEBs are connected together into chains, which are read out by a Chain ReadOut Controller (CROC). Chains can have 3 to 11 boards, but a typical chain would have 10 boards. The CROC can connect up to 4 chains. The CROC syncs all the clocks on the FEBs, and it accounts for the time offset due to the data readout. The number of channels on the detector requires 15 CROCs for readout, and these CROCs were placed into VME crates. These crates use CROC Interface Modules (CRIM) to provide timing and trigger information to the CROCs. When the CRIMs receive a signal from the NuMI control center that a spill of neutrinos are coming

down the beamline, they open a readout gate, allowing the FEBs to record hits. A readout gate lasts for 16 μs, starting 500 ns before the spill and ending 5.5 μs after the end of the spill. At the end of a gate, the CROCs read out all the recorded hits from the FEBs to data acquisition computers, which stores the gate information. Further information about MINERvA's data acquisition can be found in [97].

3.2.1 Cross Talk

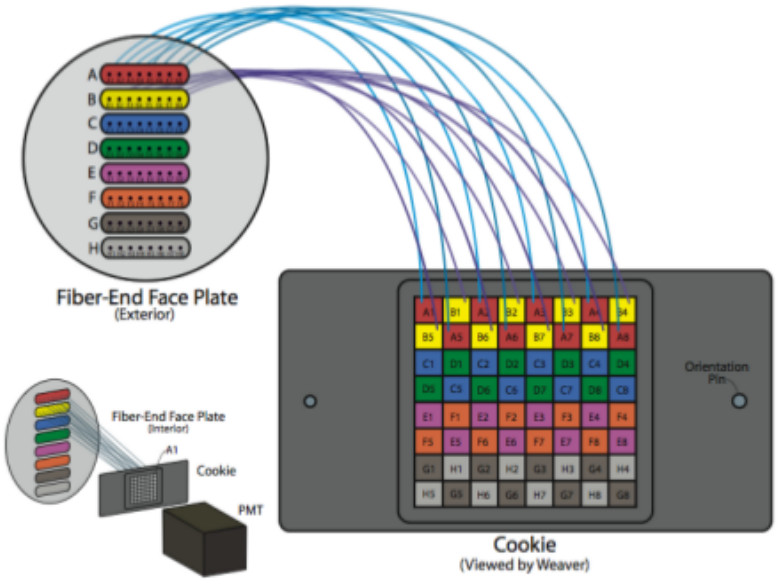


Figure 3-8: The mapping of the input from the face plate to the photomultiplier. The clear optical fibers are weaved to produce to pattern on the right. Figure from [97]

The photomultiplier tubes can have signal leakage between channels due to the close proximity of channels to each other. This signal leakage is called cross talk, and MINERvA has dealt with this problem by altering the channel inputs to the photomultiplier. The clear optical fibers from adjacent strips are bundled together into groups of 8. The face plate of photomultiplier tube can accept 8 of these fiber

groups, creating an 8×8 grid. Clear optical fibers take the input from the faceplate to the photomultiplier. These cables are weaved in such a way that fibers from adjacent strips are not adjacent to each other, which can be seen in figure 3-8. Cross talk can be seen when there is coincident activity between two strips that are not spatially near each other. MINERvA has simulated this effect and estimates the amount of cross talk in each strip. This activity is subtracted from the data during reconstruction.

3.2.2 Nuclear Target Region

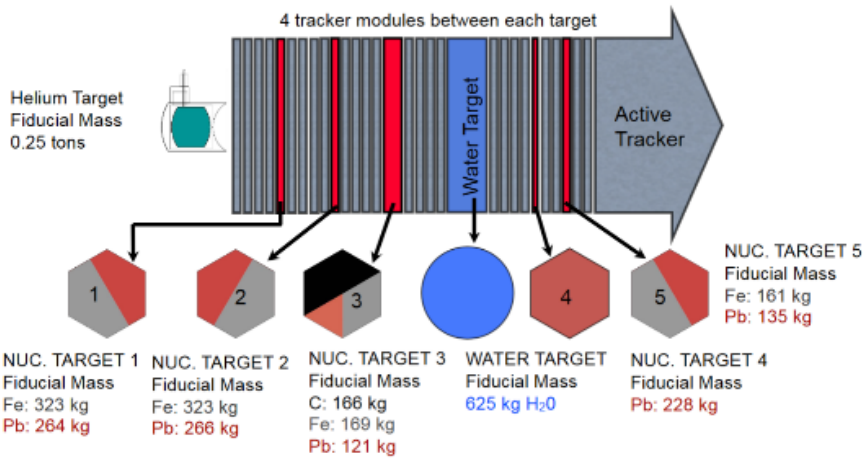


Figure 3-9: Diagram of the nuclear target region in MINERvA. The beam enters from the left. Figure from [98]

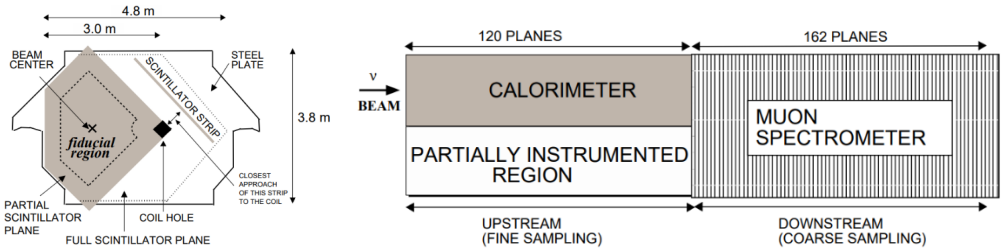
The nuclear target region contains five passive materials: helium, water, carbon, iron, and lead. In five planes, carbon, iron, and lead replace the scintillator core. These planes are called the nuclear targets. Figure 3-9 shows the layout of the nuclear target region and the layout of the passive material planes, as well as the mass of the material in each target. The patterns of the nuclear targets were chosen so that neutrinos which do not interact in the nuclear targets will pass through the same

amount of material. The uncertainties on the density of the targets are less than 1%. The nuclear targets are interspersed between active tracking regions. With the exception between targets 4 and 5, each active tracking region contains 4 active scintillator modules, or 8 active scintillator planes. Targets 4 and 5 are separated by 2 scintillator modules.

In front of the nuclear target region is the veto wall and the helium target. The veto wall consists of layers of steel and scintillator, and it was built to shield the front of the detector from low energy hadrons as well as tagging rock muons before they enter the detector. The helium target, which is a 2300 liter aluminum cryostat, was placed between the veto wall and the detector. Currently, cross sections on helium are being measured, but this has not been done for this analysis.

The water target contains liquid water in a circular neoprene balloon, where the shape of the target is held in place by a circular steel ring and a thin kevlar sheet. The radius of the circular steel ring is $\sim$ 120 cm, which is larger than the apothem of scintillator hexagon (85 cm) in a tracking plane. When the water target is full, the mass of the balloon and kevlar are less than 1% the mass of the water. After MINERvA stopped taking data, lasers were used to take the measurements of the water target volume. These measurements were used to build a model that related fill meter readings with the mass of the contained water. The model found that the average mass over the ME data taking era was 636.5 kg. Since the water target extends farther than the scintillator hexagon, neutrino interactions beyond the 85 cm hexagonal apothem rarely create particles that enter the tracking region, which prevents them from being reconstructed. Thus, analyses typically only consider neutrino interactions inside that 85 cm apothem. The model above measures the mass of the water within the 85 cm apothem was 454.1 kg with an uncertainty less than 1%.

3.3 MINOS Near Detector



(a) Front view of a plane in the fine sampling region

(b) Side view

Figure 3-10: Diagrams of MINOS Near Detector

As muon neutrinos comprise the majority of the NuMI beam, it is critical to reconstruct the muon momentum accurately for charged current interactions. Most muons produced in MINERvA have enough forward going momentum to escape out the back of the detector. While the momentum of exiting muons can be reconstructed using multiple scattering deflection [98], this method has poor resolution and it cannot determine the charge of the muon. Thus, the MINERvA detector was built two meters in front of the MINOS Near Detector (ND) in order to reconstruct the muons which exit the back of the detector.

The MINOS neutrino oscillation experiment built their near detector as a magnetized tracking iron calorimeter [99]. The MINOS ND was built as a stack of steel and scintillator planes. The steel planes are 2.54 cm thick, while the 1 cm thick scintillator planes consist of 4.1 cm wide rectangular scintillator strips stacked together. Similar to the tracking planes on MINERvA, the scintillator planes have two orientations, U and V, which are rotated by $\pm 45°$ from vertical. These planes allow for tracking of charged particles travelling through the detector. The detector had two sections which tracked particles with different sampling intervals. The fine sampling region

had a scintillator plane after every steel plane, while the coarse sampling region had a scintillator plane after every 5 steel planes. Figure 3-10 shows the layout of the MINOS ND.

Building the detector with steel planes allowed for the MINOS Near Detector to be magnetized. To accomplish this, the MINOS ND has an insulated coil that runs through the center of the detector. If a current runs through the coil, it produces a toroidal magnetic field with an average strength of 1.3 T. With the magnetic field, muon momentum can be reconstructed either by range, for muons that stop in the detector, or by curvature, for muons which escape the back of the MINOS ND.

Given the NuMI horn current configuration, the beam will consist primarily of muon neutrinos or antineutrinos. To account for this, the polarity of the magnetic field is adjusted to focus either μ^- (FHC) or μ^+ (RHC) towards the coil in order to maximize track length. Section 5.5.2 has further discussion of muon reconstruction in the MINOS Near Detector.

3.4 Calibrations

The primary goal of calibrations is to convert raw hit information into quantities useful for reconstruction. This involves converting the digitized integrated charge, or raw ADC counts, back into the energy deposited in the strip, as well as accounting various effects which may skew the conversion. Calibrations must also adjust the timestamp of the hit to account for timing offsets from various detector components.

3.4.1 Energy Calibration

In order to find the energy E deposited in strip s, the calibration procedure goes through two steps. First, for each strip s, the raw hit $ADC(s,t)$ counts are converted

back into PMT photoelectrons. This involves subtracting background noise (pedestal) and deamplifying the ADC signal using the gain of the PMT. Second, the PMT photoelectrons are converted into the energy deposited in the hit. As the conversion from charge to energy uses a single energy scale applied across the detector, physical effects that may cause signal degradation in the strip or differences in the responses between strips must be accounted for. Equation 3.1 shows the various components required for the energy calibration, and the calibration process is further discussed in [94].

$$E(s,t) = \left([ADC(s,t) - P(s,t)] \frac{Q(s,ADC)}{G(s,t)} \right) (n_{att}(s) S(s,t) C(t)) \tag{3.1}$$

Parameter	Description
$P(s,t)$	Pedestals
$Q(s,ADC)$	ADC-to-charge conversion
$G(s,t)$	PMT Gain
$n_{att}(s)$	Strip Attenuation
$S(s,t)$	Strip-to-strip corrections
$C(t)$	Absolute detector energy scale

Table 3.1: Calibration Parameters

3.4.1.1 Pedestals $P(s,t)$

The readout electronics and PMTs have inherent background noise levels which need to be subtracted from the raw ADC counts. During the MINERvA data taking, gates were dedicated to measure detector activity without neutrino beam. Figure 3-11 shows the distribution of background detector activity, which is called a pedestal. Most activity coalesces around a main peak, however cosmic rays or radioactivity

could create outlying activity which is removed using Peirce's criterion [100].

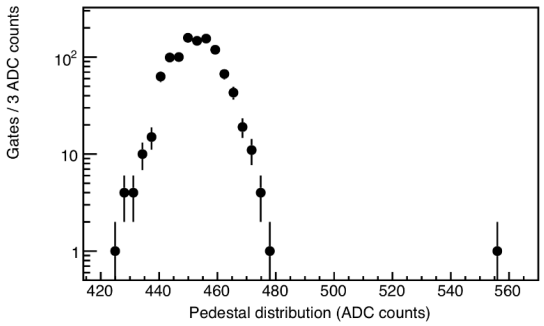


Figure 3-11: Measurement of a pedestal distribution for one channel, including an outlier at $\sim$ 550 ADC counts. Figure from [94].

The calibration applies the pedestal correction by subtracting the mean of the pedestal's main peak from the raw ADC count. Also, the pedestal correction applies a "suppression" to each channel by removing any hits less than three standard deviations above the pedestal average. This removes 99.8% of noise, but it also leads to a lower energy threshold in which the detector will not register hits. This threshold is at $\sim$ 0.4 PE, or 5 MeV.

3.4.1.2 ADC-to-charge conversion $Q(s, ADC)$

After pedestal subtraction and suppression, the calibration converts the ADC counts to charge using an analog-to-digital response curve. The response curve varies depending on the type of gain amplification, and these curves are different for each TriP-t chip. These gain curves were measured before the construction of MINERvA by inputting a known charge and measuring the corresponding ADC counts. Figure 3-12 shows the gain curves for a single TriP-t. Note that the gains will saturate around 2900 ADC counts.

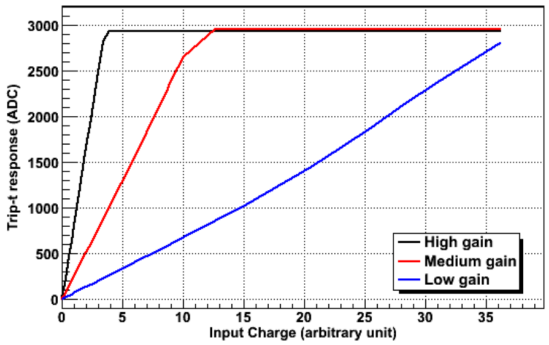


Figure 3-12: The high, medium, and low gain response for a typical TriP-t. Figure from [94].

3.4.1.3 PMT Gain $G(s,t)$

The gain represents the charge amplification for each PMT. This requires an *in-situ* measurement as the gain may drift on the timescale of weeks. Periodically, a set of optical fibers injects light into the PMT in between beam spills. The light comes from a flashing LED with a known intensity. The resulting ADC counts are then fit to a function based on the inner workings of a PMT. The parameters of the fit are used to find the gain [94].

3.4.1.4 Strip Attentuation $n_{att}(s)$

In order to reconstruct the hit energy, the calibration needs to account for the light attenuation between the hit location and the PMT. Light attenuation occurs in the two clear optical fibers between the strip and the PMT as well as the WLS fiber within the scintillator strip. Before construction, MINERvA measured the light attenuation in all of these components using a radioactive ^{137}Cs source to scan the length of the strip. The two clear optical fibers will have the same attenuation due to their fixed lengths, but the attenuation in the WLS fiber will depend on the location

of the hit along the strip. If reconstruction can determine the hit position in three dimensions, the attenuation will be calculated using the distance to the hit; otherwise, the reconstruction will assume that the hit occurred at the center length of the strip.

3.4.1.5 Strip-to-strip corrections $S(s,t)$

Each strip can have a different energy response for a myriad reasons, ranging from manufacturing inconsistencies to time dependent effects including aging scintillator and the buildup of radiation damage. In order to apply a single energy scale across the detector, the strips need to have the same energy response. This is done by looking for tracks created by rock muons, whose creation is explained in section 2.1.2.4.

Rock muons are nearly minimum ionizing particles, which means that they will deposit a known amount of ionization energy per unit length along their path through the detector [2]. Using the sample of rock muon tracks, the correction looks at each strip and calculates a truncated mean of the deposited energy per unit path length in that strip. The average of the truncated means is also calculated. The correction applies a calibration constant to the hit energy in a strip so that the strip's truncated mean is the same as the average truncated mean.

3.4.1.6 Absolute detector energy scale $C(t)$

The final step in the energy calibration converts the correct number of photoelectrons into energy using a detector wide scale known as the muon equivalent, or energy, unit (MEU). This conversion factor can be found in simulation, however, differences between data and simulation must be accounted for.

Estimates of the MEU use rock muons that have passed through the MINERvA detector and have entered the MINOS ND, where the momentum of the muon can be measured. Rock muon simulation then uses the positions and the momenta of the

rock muons in data to seed their events. Thus, each measured rock muon track in data will have an equivalent muon track in simulation. The calibration then finds the peak energy per unit length for each track in data and simulation. The MEU is the product of the conversion factor found in simulation and the ratio of the two peak energies, $\frac{E_{\text{data}}}{E_{\text{simulation}}}$.

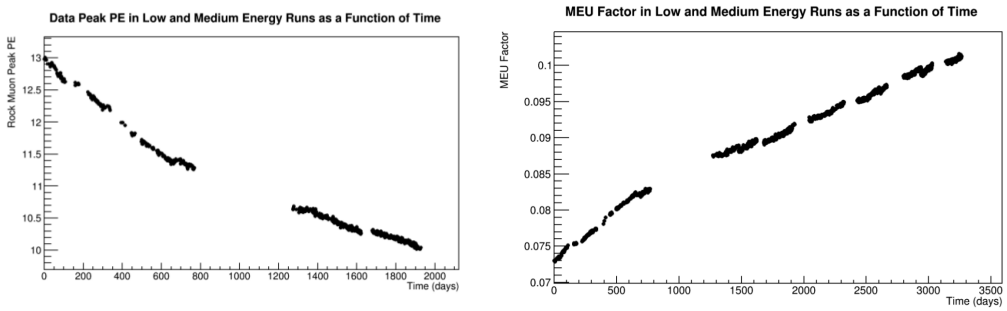


Figure 3-13: Peak energy per unit length (left) and MEU factor (right) versus time

Figure 3-13 shows the peak energy per unit length and the MEU factor over time. It should be noted that MEU factor increases with time in order to compensate for aging in the scintillator and WLS fiber, which reduces the light yield from the scintillator.

3.4.2 Timing Calibration

A FEB creates a hit timestamp as soon as the charge from the PMT passes a discriminator threshold, however, there are still several effects that need to be corrected in order to find the true timing of the hit. There are three primary time corrections that need to be considered. The first correction accounts for the travel time of the photon through the optical fibers, which depends of the position of the hit in the strip. Another correction is the electronic timing offsets, which are unique to each

FEB. Finally, there is the "time-slewing" correction, which depends on the amount of energy deposited in the hit.

The probability that the scintillator emits a photon at a given time after the hit energy is deposited follows an exponential curve. For a given hit, it is more likely that the time until the first photon is emitted will be small if there are large number of photons are produced. Thus, on average, it will take longer for the first photon to be emitted in low energy events. The timing calibration needs to estimate this timing offset and its energy dependence.

There's an additional effect which also depends on the number of photon emitted. Photons in the WLS fiber could either go towards the PMT or towards the mirrored where they are reflected back. If there are more photons in the hit, it's more likely that at least one photon will initially head in the direction of the PMT, reducing the average timing offset. The time-slewing correction will also account for this.

The timing calibration relies on a through-going rock muon sample. An average time for the muon track can be determined, and from that the reference time of each hit can be calculated using the muon momentum and path length. The offsets are determined by the difference between the hit time and the reference time. Hits with a large number of photoelectrons will have a small time-slewing correction, thus any offsets should be due to the offsets. After applying the electronic timing offsets, further differences are assigned to the time slewing offsets.

3.4.3 Plane alignment

Plane alignment on MINERvA relies the triangle cross section of the scintillator strips. Figure 3-5 shows that, if the plane was perpendicular to a particle's trajectory, the maximum energy deposited in the strip should occur when the particle passes through

the middle of the strip. Using a sample of through-going rock muons, the average energy deposited by the muons in each strip in a given plane is found as function of the triangular base position. This distribution is fitted to the shape of the strip. If the triangular point of the fit does not align with the zero base position, there is a translational misalignment of the plane. This measurement is repeated six different regions along the longitudinal length of the strip. If positions of triangular points differ, there is a rotational misalignment. An alignment correction for each plane is applied during calibrations. On average, the correction is within 0.3 mm and 0.5 millradians. Figure 3-14 shows an example of the alignment fits.

3.4.4 Nuclear Target Positions

A survey originally determined the positions of the nuclear target planes by measuring their location at the outer edge of detector. However, these positions may be inaccurate for the center of the nuclear targets. In order to study the accuracy of the longitudinal position of the nuclear targets, the point of closest approach (POCA) was calculated for events with two or more reconstructed tracks in data and simulation. The study selected events whose POCA was within a nuclear target.

Figure 3-15 shows the longitudinal position of the POCA in both data and simulation. In order to reduce the disagreements between data and simulation, the longitudinal POCA position was shifted in simulation. The best shift value for each target was found by looking for shift that resulted in the minimum χ^2/ndf, where

$$\chi^2 = \sum_{i}^{\#\text{ of bins}} \frac{(N_i^{data} - N_i^{MC})}{N_i^{data}}$$

The shifts for each nuclear target are shown in 3.2. Further discussion of this can be

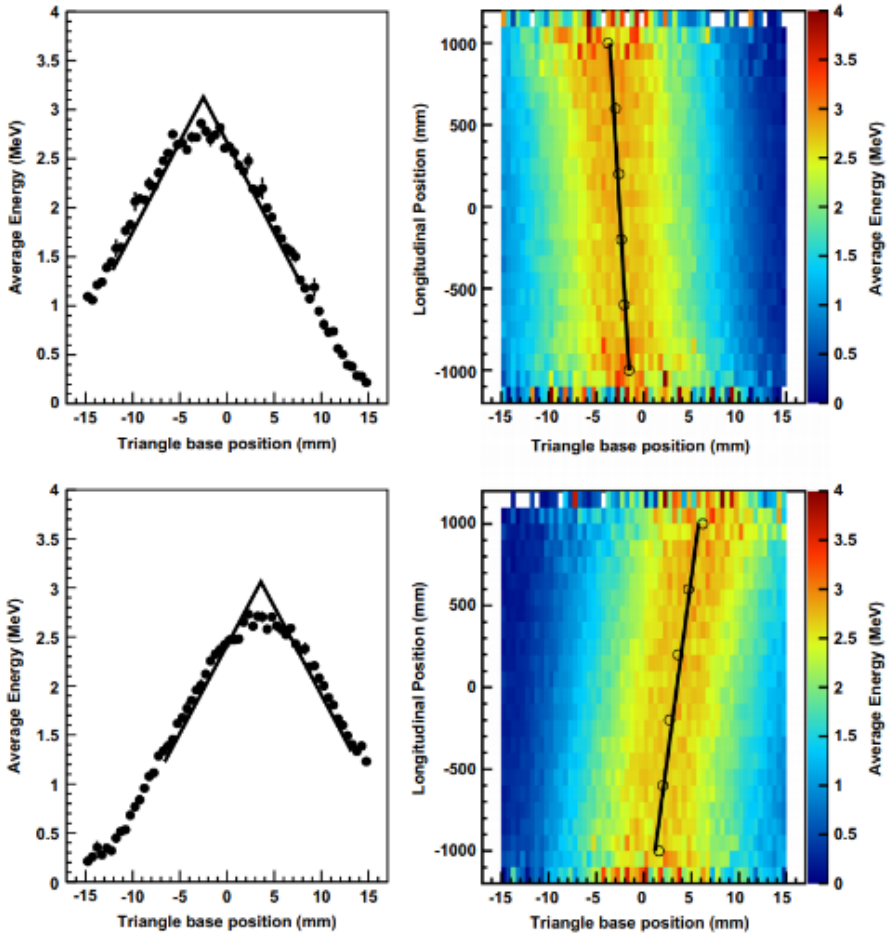


Figure 3-14: Alignment fits for two separate planes (top and bottom). Plots on the left show the translational misalignment, and the plots on the right show the rotational misalignment. Figure from [94]

found in [98].

Nuclear Target	1	2	3	4	5
Shift (mm)	-4.3	-3.5	-5.1	0	-2.4
χ^2/ndf	36/6	4.3/5	18/9	7.8/6	3.7/5

Table 3.2: Best longitudinal shifts for the nuclear targets based on the minimum χ^2/ndf. Table from [98]

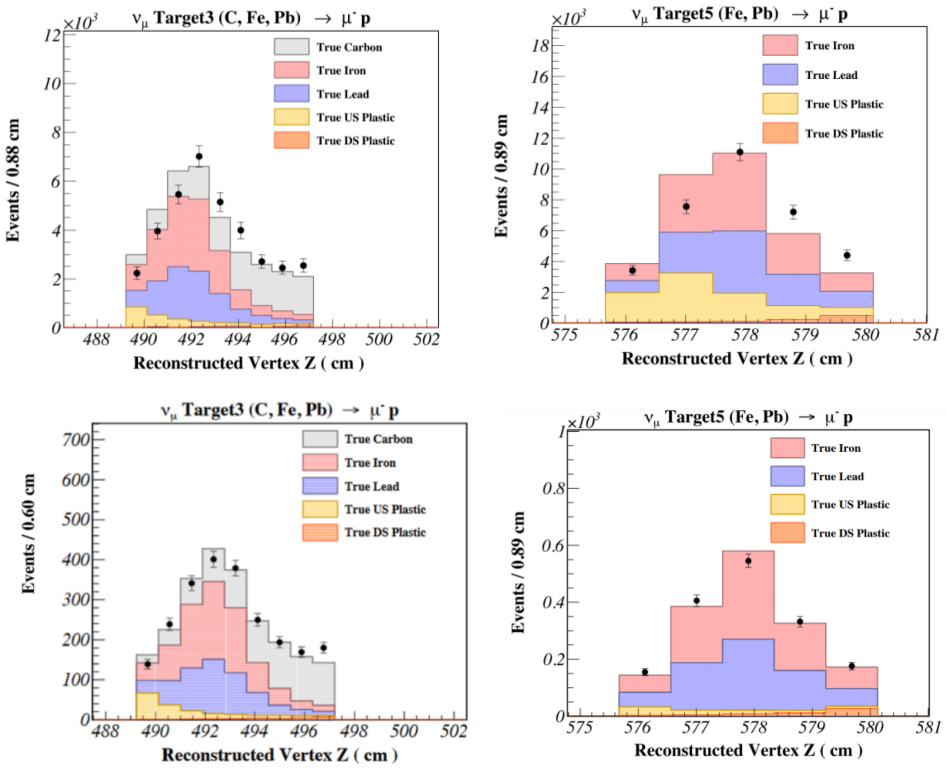


Figure 3-15: The longitudinal position of the reconstructed POCA for nuclear targets 3 and 5 in both data and simulation before (top) and after (bottom) the longitudinal shift. The simulated neutrino interaction occurred on the passive material listed in the legend of the plots. Figure from [98].

Chapter 4

Simulation

The MINERvA experiment requires simulation for a variety of purposes including the estimation of backgrounds, studying the inefficiencies of the detector and reconstruction, and producing distributions for model comparisons. The following sections describe the steps to produce the MINERvA simulation.

The simulation begins with the neutrino flux simulation described in Section 2.2. The desired POT dictates how many neutrino events are created. To create an event, the simulation randomly chooses a neutrino from the flux and notes the position where its parent particle decayed. The identity and kinematics of the parent particle are also recorded. Next, a point in the MINERvA detector geometry is randomly chosen as the direction for the neutrino trajectory from the upstream decay point. Each point has an associated weight reflecting the probability of a neutrino having that particular trajectory. The simulation refers the total neutrino interaction cross section ($\sigma(E_\nu)$) of each material the neutrino traverses in order to determine whether an interaction occurs along the neutrino's trajectory. The total neutrino cross section has been tuned to external data. If an interaction occurs, the simulation randomly chooses an interaction point and target material. Any interactions within the downstream ECAL

or HCAL are not simulated because studies have shown that such events neither enter as signal nor background in this analysis. This information about the interaction is then passed to the GENIE event generator.

4.1 GENIE Neutrino Interaction Simulation

The GENIE event generator simulates neutrino events in the nucleus, starting from the initial neutrino interaction to the exit of the final state particles from the nucleus. Using version 2.12.6 [70], GENIE provides a record of the interaction as well as the identity and kinematics of each final state particle. GENIE generates events through several exclusive interaction processes, including rare process like charged current charm production, $\nu - e$ elastic scattering, as well as inverse muon decay $\nu_\mu e^- \rightarrow \nu_e \mu^-$. The simulation randomly chooses the interaction type for the neutrino event. The probability that exclusive interaction process A occurs is the ratio of the cross section of the exclusive process to the total cross section, $\frac{\sigma_A}{\sigma_{total}}$. The cross section models of each type of interaction provides the kinematics of the particles produced in the interaction.

The relevant interaction models for this charged current ν_μ analysis include quasielastic scattering, resonant pion production, deep inelastic scattering (DIS) and coherent pion production. The following sections describe these models in further detail.

4.1.1 Quasielastic scattering

Quasielastic scattering is defined by two channels: $\nu_\mu n \rightarrow \mu^- p$ and $\bar{\nu}_\mu p \rightarrow \mu^+ n$. The former channel is a background for this analysis, as the final state proton can be misreconstructed as a charged pion. A small number of quasielastic scattering events will produce a charged pion due to a nucleon reinteraction in the nucleus.

This analysis will consider these events as signal if the pion was created within the nucleus.

GENIE uses the Llewellyn-Smith formalism [19] to model quasielastic scattering, explained in section 1.3.1. Instead of using a dynamical quark model, Llewellyn-Smith uses general Lorentz-invariant form factors to parameterize the hadronic current. The form factors used in GENIE are found from experimental results.

The conserved vector current hypothesis relates the electromagnetic form factors found from electron scattering experiments to the two vector form factors in quasielastic model. GENIE uses the BBA2005 parameterization of the electromagnetic form factors [101].

The axial form factor $F_A(Q^2)$ is related to the pseudo-scalar form factors by the partially conserved axial current hypothesis [24]. Using a dipole approximation for the axial form factor, GENIE uses a default axial mass $M_{A,CCQE} = 0.99\text{GeV}/c^2$.

It should be noted that a new model of quasielastic scattering relaxes the assumption that $F_A(Q^2)$ has a form of a dipole; instead, $F_A(Q^2)$ is treated as an expansion of a variable named z [23]. The coefficients of the z-expansion were determined by a fit to quasielastic scattering data on deuterium. Generally, the systematic uncertainties associated with z-expansion are smaller than those associated with the dipole approximation. However, this model was not used in this analysis as the contribution of quasielastic scattering events to the sample is small.

4.1.2 Resonant Pion Production

Resonant pion production focuses on neutrino-nucleon interactions which excite the nucleon into a Δ or N^* resonance. The baryon resonance decays into a neutral or charged pion, and this analysis focuses on the positively charged pions which escape

the nucleus.

Both charged and neutral current resonant pion production are simulated by the Rein-Seghal model[25], described in section 1.3.2, with some modifications. Two of the sixteen resonances in the original Rein-Seghal model are omitted in GENIE because the Particle Data Group considers evidence for their existence to be ambiguous [2]. Also, no interference is allowed between neighboring resonances. Finally, the lepton mass terms are not included into the differential cross section calculations, however they are considered when calculating the kinematic phase space of the produced particles.

The Rein-Seghal model relies on vector and axial dipole form factors, similar to those used in quasielastic scattering. By default, the resonant vector mass M_V^{RES} is 0.84 GeV with an uncertainty of 10%, while the resonant axial mass M_A^{RES} is 1.12GeV/c^2 with an uncertainty of 20% [102]. However, a recent analysis that fit the GENIE prediction to pion production cross sections measured in ANL/BNL deuterium bubble chamber has constrained the M_A^{RES} parameter in GENIE to 0.94 GeV/c^2 [103][1]. The GENIE simulation of events was produced with the default parameters above; therefore, the events had to be reweighted to reflect the updated value for the axial mass. These weights are discussed later in section 4.5.4.2.

The simulation relies on the equation 4.1 to produce the pion angular distribution ($W_\pi(\cos\theta)$) from Δ decays. Table 4.1 explains the equation parameters

$$W_\pi(\cos\theta) = 1 - p_{\frac{3}{2}} P_2(\cos\theta) + p_{\frac{1}{2}} P_2(\cos\theta) \tag{4.1}$$

By default, GENIE simulates an anisotropic pion angular distribution from the

[1]This bubble chamber data was discussed in section 1.5

Parameter	Description
θ	Pion angle with respect to the Δ angular momentum quantization axis in the Δ rest frame
P_2	Second order Legendre polynomial
$p_{\frac{3}{2}}, p_{\frac{1}{2}}$	coefficients for $\frac{3}{2}$ and $\frac{1}{2}$ angular momentum states

Table 4.1: GENIE Pion Angle Model Parameters

decay, where $p_{\frac{3}{2}} = 0.75$ and $p_{\frac{1}{2}} = 0.25$ [70].

In order to predict nonresonant pion production, the Rein-Seghal model includes contributions from nonresonant processes with isospin $\frac{1}{2}$. As this does not account for all nonresonant pion production, the DIS model also provides a prediction of the nonresonant pion production. Care must be taken to not double count nonresonant pion events predicted by both models.

4.1.3 Deep Inelastic Scattering

In our model for deep inelastic scattering (DIS), the neutrino interacts with a single quark which proceeds to hadronize, resulting in multiple hadrons in the event. This analysis selects some of these events where the hadronization produces a single charged pion which escapes the nucleus with no other mesons. Therefore, this model simulates some pions that are not produced by the decays of baryon resonances described above.

All nonresonant inelastic interactions use the Bodek-Yang model [104], previously described in 1.3.3, which extends DIS interactions to low Q^2 and E_ν. Caution must be taken when using both the Rein-Seghal and Bodek-Yang models, as Bodek-Yang will produce interactions that are also predicted by Rein-Seghal. To prevent this, GENIE stops using the Rein-Seghal model for events with an invariant hadronic mass $W > 1.7$ GeV/c^2. For events with $W < 1.7$ GeV/c^2, the Bodek-Yang model is modified to make the prediction of 1π production, 2π production, and total cross

section agrees with external measurements. The fit of the GENIE prediction to pion production cross sections measured in ANL/BNL deuterium bubble chamber (section 1.5) has suggested a 43% suppression of nonresonant pion production. This suppression will be discussed further in section 4.5.4.2.

The AGKY model [105] simulates hadronization using KNO scaling [106] for events with $W < 2.3$ GeV/c^2. KNO scaling generates a nucleon and any number of kinematically available low-mass mesons. The average charged hadron multiplicity is calculated using the an empirical expression tuned to data. After the particle generation, the invariant hadronic mass is divided among the outgoing hadrons. This hadronization is used for the DIS events that are part of the signal for this analysis.

For events with $W > 3$ GeV/c^2, PYTHIA/ JETSET [107] is used. PYTHIA/ JETSET is a standard program for high-energy collisions, simulating the initial and final parton showers as well as other high energy processes. This program uses a variety of models, but models' contributions are negligible until $E_\nu > 3$ GeV.

In order to create a transition region between $W = 2.3$ GeV/c^2 and 3.0 GeV/c^2, GENIE scales each model linearly, decreasing the contributions from KNO while simultaneously increasing the contributions from PYTHIA/JETSET.

4.1.4 Coherent Pion Production

Coherent pion production occurs when the neutrino interacts with the entire nucleus and creates a pion, leaving the nucleus unchanged. This analysis is primarily concerned with CC charged coherent pion production. GENIE simulates coherent pion production using the coherent pion Rein-Seghal model [108], described further in section 1.3.4, with modified lepton mass terms [32]. Similarly to resonant pion production, the model assumes the axial form factor $F_A(Q^2)$ is a dipole with an axial

mass of 1 GeV/c^2. External cross sections of pion nucleus scattering on protons and deuterium constrain the normalization value of $F_A(Q^2 = 0)$. These events are tuned later in the analysis to match coherent pion production data from the MINERvA experiment. Section 4.5.4.3 explains this tune.

4.2 The Nuclear Medium and Final State Interactions

A neutrino interaction that occurs inside of a nucleus is subject to a complex environment. This environment can alter the kinematics involved in the initial neutrino interaction, as well as interact with the particles produced in the interaction. The nuclear model is discussed in section 1.4, and this section explains how GENIE simulates the nucleus.

4.2.1 Simulating the nucleus

GENIE models the nucleus as a relativistic Fermi gas (RFG) [39] using the implementation from Martini *et. al.* [109]. This implementation adds the Bodek-Ritchie high momentum tail to the RFG momentum distribution [40], but the implementation does not include two-particle knockout. GENIE models the Pauli blocking suppression as a function of the atomic mass. Because resonant pion production produces a final state excited baryon, rather than a final state nucleon directly, resonant pion production is not subject to Pauli blocking. Further details of the nuclear initial state model were discussed in Section 1.4.1.

4.2.2 Final State Interactions (FSI)

GENIE uses the two primary methods for estimating final state interactions: simulate the effect using external data measuring hadron scattering on nuclei, or use a hadronic cascade simulation to propagate particles in multiple steps through the nucleus. These two methods are further explained in section 1.4.3.

For the external data, GENIE uses nuclear scattering cross sections of π^+ and p on ^{56}Fe [70], where the cross sections can be scaled by $A^{2/3}$ to make predictions on other nuclei. For the simulation of the hadronic cascade, GENIE uses the hA effective cascade model implemented by INTRANUKE[70]. This data constrained model simulates a full cascade from a single interaction. It is easy to produce weights that vary the FSI processes in the hA model. Thus, MINERvA only uses the hA model to predict FSI in the simulation.

GENIE does not apply FSI on final state muons; therefore only the hadronic products of the interaction are affected by FSI.

4.3 Detector Simulation

After the final state particles leave the nucleus, the MINERvA simulation needs to model the propagation of the particles through a simulated MINERvA detector. This includes simulating the interactions of the final state particles in the detector as well as simulating any possible secondary particles produced from these interactions.

4.3.1 Particle Propagation

The final state particles and their kinematics are passed to a program based on the Geant4 toolkit [110], which simulates the trajectory of particles through a simulated

version of the MINERvA detector geometry. The particles are propagated in segments according to their four momenta. These segments, often called steps, will vary in length, but the typical length will be small compared to the size of a scintillator strip small compared to the average distance a particle travels before an inelastic interaction. For each step, the Geant4-based program will use Monte Carlo to determine if the particle interacts. The particle can decay, interact elastically or inelastically. As the thickness of the MINERvA plane (1.7 cm) is larger than a step, there can be several interactions and several energy depositions in a single strip. The program will record the timing and the amount of energy deposited in each active detector strip. This is passed to the readout simulation, which is explained in section 4.3.3.

The program uses interaction cross sections in order to determine whether a particle interacts in a step. Different types of interactions are simulated using different physics models, which are implemented in different modules in Geant4.

Strong inelastic interactions between hadrons and detector nuclei use the QGSP_BERT physics list. Interactions due to particles with momentum below 10 GeV/c are governed by the Bertini cascade model (BERT)[81][82]. The Geant4 simulation uses the quark gluon string precompound (QGSP) [111] to simulate interactions of hadrons with momenta larger than 10 GeV/c, which are rare in the MINERvA detector. Geant4 tunes the implementation of QGSP_BERT to hadron-nucleus scattering data. Elastic hadron interactions use the Hadron_Elastic module, which relies on the Glauber model [112].

The EmStandard module handles electromagnetic interactions. For charged particles, this includes ionization, multiple Coulomb scattering, and bremsstrahlung. For photons, this includes e^+e^- pair production, Compton scattering from atomic electrons, and photoelectric interactions. The DecayPhysics module deals with particle decays.

4.3.2 Data Overlay

The detector simulation has primarily focused on the particles created from neutrino interactions; however, data taken from the physical MINERvA detector will contain additional activity that may not be associated with the neutrino. This incidental activity is known as pileup, and it may affect several reconstruction techniques like tracking. To account for this incidental activity, random gates from the data are overlaid onto Monte Carlo events in order to simulate pileup.

4.3.3 Readout Simulation

In order to reconstruct the Monte Carlo with the same methods used on data, the simulated neutrino interactions need to be decalibrated from the true deposits of energy provided by the Geant4-based program to raw ADC counts and digital hit times. This decalibrated simulation can then be passed through the same reconstruction as the data, including the calibration. Both the energy and the timing need to be decalibrated in order to mirror uncertainties in the calibration process.

The readout simulation grabs information from the data overlay to estimate the absolute detector energy scale (MEU), which is explained further in section 3.4.1.6. This accounts for the increase in the MEU scale over time due to reduced light yield in the MINERvA scinitillator.

If the data overlay gate contains a dead channel, that channel is excluded from the readout, even if the simulation has activity in that channel. This accounts for the effects of dead time and dead channels. A more detailed explanation of the dead time simulation can be found here [113].

To decalibrate the energy, the readout simulation moves backwards through the calibration process, fully explained in section 3.4.1. First, the energy deposited by the

Geant4 program needs to be converted into the number of photoelectrons incident on the PMT. The readout simulation first uses Birk's law [114], shown in equation 4.2, which relates the energy loss $\frac{dE}{dX}$ of particle over a path length to scintillated light intensity. Table 4.2 explains the parameters in Birk's law. Birk's law accounts for saturation of light emission with increasing density of ionization.

$$\frac{dL}{dx} = S\frac{\frac{dE}{dx}}{1 + \kappa_B \frac{dE}{dx}} \tag{4.2}$$

Parameter	Description
L	Light yield
S	scintillation efficiency
κ_B	Birk's constant

Table 4.2: Birk's Law Parameters

Birk's law uses the true path length of the particle through the strip to convert the true deposited energy into an estimated amount of scintillation light. The MINERvA testbeam detector, which provided energy calibrations for the main detector, measured the Birk's constant κ_B at 0.0905 ± 0.014 mm/MeV [115] for MINERvA's scintillator.

Next, the readout simulation continues the decalibration by dividing out the absolute energy scale correction (MEU) to determine the number of photoelectrons. The strip-to-strip and plane-to-plane relative response corrections are then removed and effect of attenuation of light in the fibers is added. To account for uncertainties in the calibration process, the simulation smears the number of photoelectrons by multiplying the photoelectrons with a random number sampled from a Gaussian distribution centered on 1. The width of this Gaussian distribution is an estimate on the calibra-

tion's fractional uncertainty. Finally, using the smeared number of photoelectrons as the mean of a Poisson distribution, the simulation sets the number of photoelectrons incident on the PMT as a random throw of that Poisson distribution.

These photoelectrons then translated into raw ADC counts. The readout amplifies the photoelectron signal using the gain of the PMT. The value of the gain comes from the data overlay. The simulation then adds electronic noise and cross talk to the signal. Using the known analog-to-digital response curves, the charge is converted to ADC counts.

To decalibrate the timing, the hit time is first rounded to the nearest 2.35 ns, which is the resolution of the FEB clock time. Next, the known timing offsets of each FEB and the travel time of photons to the PMT given the location of the hit along the scinitillator strip are added to the hit time. To account for "time-slewing" effect, which is explained in section 3.4.2, the hit time is smeared by randomly sampling the measured time-slewing distribution for a given number of photoelectrons. The time-slewing distribution is measured while calibrating the detector. After this, the simulated hits are given back to the calibration algorithm, which will treat the hits from data and simulation the same.

4.4 Michel Simulation

All muon decays result in the creation of a Michel electron and a corresponding electron neutrino. Michel electrons are used to identify π^+ because 99.9% of π^+ decays follow the decay chain $\pi^+ \rightarrow \mu^+\bar{\nu}_\mu \rightarrow e^+\nu_e\bar{\nu_\mu}$, which will be described in greater detail in section 5.7.

Any difference in the behavior of Michel electrons between data and simulation needs to be understood. If simulation models Michel electrons incorrectly, then the

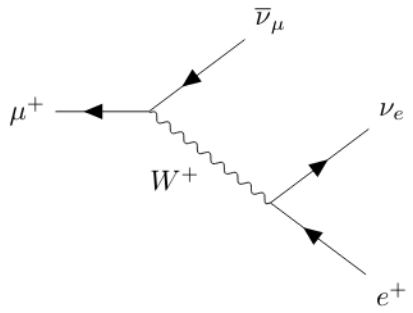


Figure 4-1: Feynman diagram of μ^+ resulting in the creation of a Michel e^+

fraction of Michel electrons that are reconstructed, called the reconstruction efficiency, will differ between data and simulation. Because of the complex geometry and non-uniformity of the detector, the final determination of reconstruction efficiency must come from the simulation. Therefore, it is important that simulation accurately models the behavior of Michel electrons in the detector, and that the model is verified with data wherever possible.

MINERvA uses GEANT4 to simulate Michel electrons in the MINERvA detector and key properties of the Michel electron simulation have been studied in the active tracking region. One of these key properties is the Michel energy spectrum, which can be theoretically calculated using $V - A$ theory. Since μ^+ will not enter into a bound state with a nucleus, the μ^+ decay can be modelled assuming a free muon. GEANT4 samples equation 4.3 in order to determine the energy of the Michel electron from a muon decay in the muon rest frame [116]. Table 4.3 explains the parameters in equation 4.3. When using this equation, GEANT4 neglects small effects from the neutrino and electron masses and another small effect from radiative corrections.

Parameter	Description
Γ	Muon decay rate
G_F	Reduced Fermi constant
m_μ	Mass of muon
ϵ	E_e/E_{max}
E_e	Electron energy
E_{max}	Maximum electron energy $= m_\mu c^2/2$

Table 4.3: GEANT4 Michel Electron Energy Parameters

Also, GEANT4 does not consider the polarization of the muon.

$$\frac{d\Gamma}{d\epsilon} = \frac{G_F^2 m_\mu^5}{192\pi^3}\left[2\epsilon^2(3-2\epsilon)\right] \tag{4.3}$$

Note that the maximum Michel electron energy is set at $m_\mu c^2/2 = 52.8$ MeV, however the detected Michel energy spectrum will have a higher cutoff due to the energy resolution of the detector. Therefore, for Michel electrons that are used to identify π^+, the higher cutoff will be larger than E_{max} by ~ 20 MeV.

The Michel interaction model determines how simulated Michel electrons deposit energy into the scinitillator. If the interactions are mismodelled, then the reconstructed Michel energy spectrum from simulation will differ from the measured Michel energy spectrum from data. The Michel reconstruction uses this energy to select for Michel electrons; thus the reconstruction efficiency is affected by the Michel electron energy. The critical energy[2] for polystyrene is ~ 90 MeV [2]. As the energy of Michel electrons that are used to identify π^+ are below the critical energy, Michel electrons travelling through the scintillator will primarily lose energy through ionization. The

[2]For electrons, the critical energy of a material is the energy where the energy loss due to bremsstrahlung equals the energy loss due to collisions, which is primarily ionization

ionization process for electrons is well modelled in GEANT4 as this model has been verified by many external experiments.

MINERvA has shown a small disagreement between data and simulation in the distribution of reconstructed calorimetric energy of Michel electrons in the active tracking region, which is shown in figure 4-2. Figure 4-3 shows that this disagreement is also seen in Michel electrons used to select for charged pion tracks in this analysis. The calorimetric energy corrects for any passive material, like epoxy, in the active tracking region. The data measures slightly higher calorimetric energies, and a $\sim 2\%$ shift towards higher energies in the simulation would resolve the disagreement. This disagreement in the calorimetric energy reconstruction have been quantified as an uncertainty in electromagnetic response, which is further discussed in section 6.10.7.

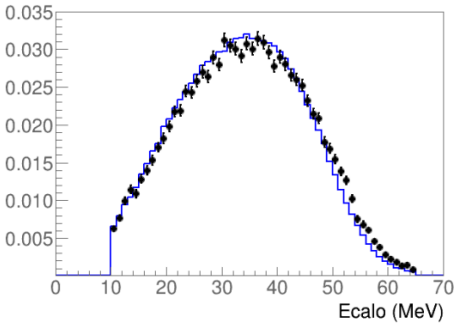


Figure 4-2: Michel electron calorimetric energy in data and simulation. The Michel electrons were the result of the decay of rock muons that stop in the MINERvA detector. The cutoff at 10 MeV is a requirement from Michel reconstruction, further explained in section 5.6. The plot is area normalized. Plot from [117]

Another key property is the timing distribution of the appearance of the Michel electrons. Studies looking at muon decay time in simulation and data show agreement with each other. Section 5.6 explains how the reconstruction searches for Michel electrons after the neutrino interaction.

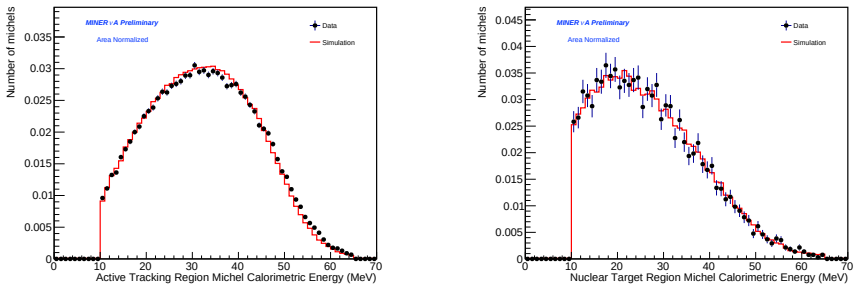


Figure 4-3: Calorimetric energy of Michel electrons matched to a hadron track, which is explained further in section 5.7.3. Michel electrons were reconstructed in either the tracker (left) or the nuclear target region (right). Plots are area normalized.

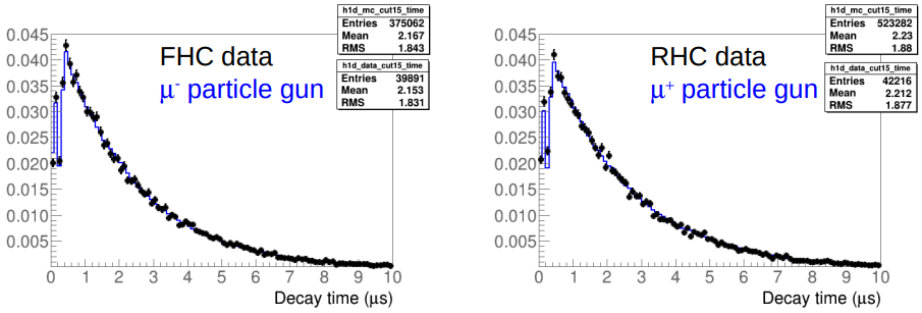


Figure 4-4: Muon decay time in data and simulation. The data comes from rock muons that stopped in the MINERvA detector. The FHC (ν_μ) beam configuration will primarily produce rock μ^-, and the RHC ($\bar{\nu}_\mu$) beam configuration will primarily produce rock μ^+. Plots are area normalized. Plots from [117]

One possible reason for a difference between data and simulation could be the mismodelling of the directions of Michel electrons with respect to the detector orientation. This might result from the assumption that the μ^+ is not polarized at the time of the decay. This assumption is likely correct because the muon scatters significantly as it comes to rest before decaying and may further depolarize in the fields of nearby nuclei, but this assumption is not independently tested in our detector. The number of clusters created and the number of planes traversed by a Michel electron

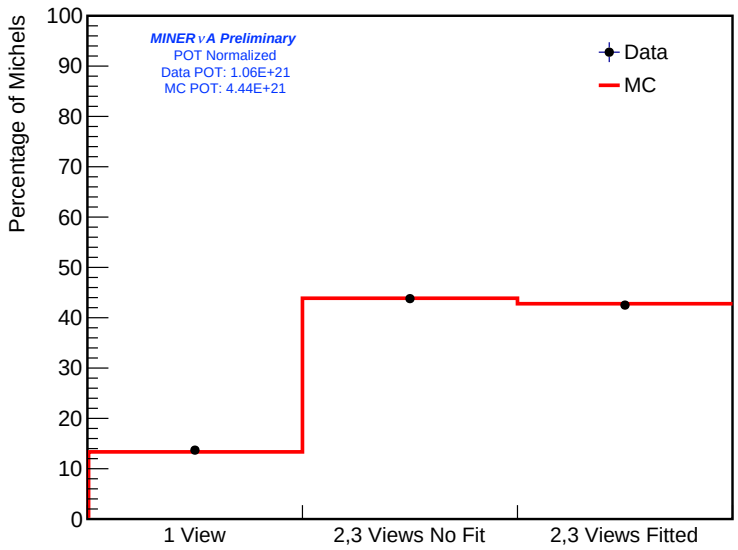


Figure 4-5: Percentage of different types of Michel candidates

will depend on the angle of its trajectory. These quantities are used during the reconstruction of the Michel electron, explained further in section 5.6, and therefore the Michel angle will impact the overall reconstruction efficiency. The number of planes traversed by the Michels impacts how many "views" it is reconstructed in and if its direction can be fit as part of reconstruction, as described in Section 5.6. As can be seen in figure 4-5, the number of Michels of a given type agree between data and simulation, so no flaw in the Michel angle modelling is evident.

One aspect of Michel reconstruction efficiency which relies heavily on the simulation is the effect of the passive materials in the nuclear targets. Michel electrons that traverse the passive material in the nuclear targets will deposit energy that cannot be read out by the detector. This effect increases the difficulty in reconstructing Michel electrons. Furthermore, while the critical energies of carbon and water are large

Material	Critical Energy (MeV)
Carbon (Graphite)	79.51
Water	76.24
Iron	21.00
Lead	7.16

Table 4.4: Critical energies of the passive materials in the nuclear targets. These values were derived for e^+ traversing the material [2].

enough that Michel electrons in these materials will lose energy through ionization, the critical energies of iron and lead are low enough that other process dominate over ionization. Table 4.4 shows the critical energies of the passive materials in the nuclear targets. The dominant interaction processes for Michel electrons in iron and lead include bremsstrahlung and pair production from photons created by bremsstrahlung or Compton scattering. These processes are well modelled in GEANT4, and the simulation should accurately model the behavior of Michel electrons produced in a nuclear target as well as Michel electrons which enter a target from the scinitillator.

While this section suggests that the simulated Michel electrons will have the same reconstruction efficiency as Michels in data, this must be confirmed by looking at the reconstruction efficiency in data. The following section, 4.4.1, will look for any differences between the reconstruction efficiencies in data and simulation, and quantify these differences as an uncertainty on Michel reconstruction.

4.4.1 Uncertainties in the Michel Electron Reconstruction Efficiency

The Michel reconstruction efficiency is measured in simulation using particle cannon Monte Carlo that simulates a pure sample of μ^+ or μ^- that stops in the MINERvA detector. Studying Michels that come from stopped rock muons in MINERvA provide

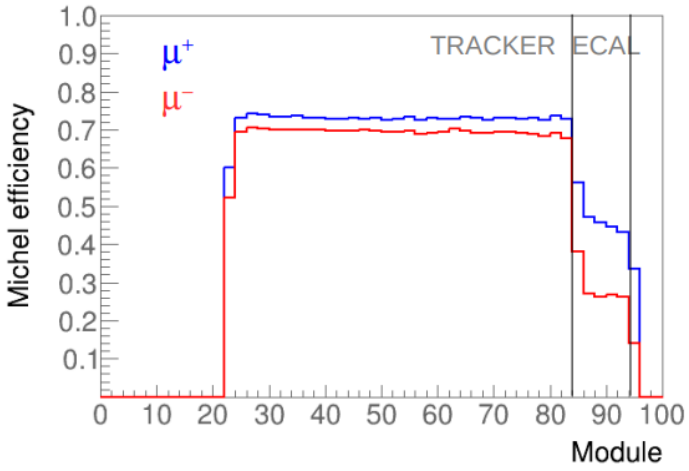


Figure 4-6: Simulated μ^+ and μ^- reconstruction efficiency in active tracker region. This study primarily used the Michel in between modules 46 and 80. Plot from [118].

the efficiency in data. These stopped rock muons are selected using tracks which enter the front and stop within the detector. To ensure the purity of the muon sample, the tracks must also pass a log-likelihood ratio score cut. The log-likelihood ratio score (LLR) is explained further in section 5.7.4. Since charged pions and muons have similar masses, the LLR score which selects for pions will also select for muons. Contrary to the rest of the analysis, the LLR score used to select for muons associated the positive scores with protons. Thus, a negative LLR score shows the track is more pion/muon-like. Tracks that are in the stopped rock muon sample have a proton positive LLR score < -10 [118]. This is more stringent than the cut used to select for charged pions in this analysis. This cut is also applied to the tracks in the simulation so both data and simulation have muons with similar properties.

The efficiencies from data and simulation cannot be directly compared because the rock muons have wrong-sign contamination due to wrong-signed neutrinos in the flux. μ^+ and μ^- have $\sim 10\%$ a difference in reconstruction efficiency on carbon. Stopped μ^+ will decay within the nominal muon lifetime, but stopped μ^- tend to occupy s-

wave orbits, where their wavefunctions overlap with the nucleus. μ^- will occupy these orbits until being captured through $\mu^- + p \rightarrow \nu_\mu + n$. Thus, a comparison between simulation and data needs to account for the fraction of wrong-signed muons in the sample [119]. The efficiencies of a pure particle cannon $\mu^\pm$ sample can be converted to the efficiencies of the rock muon samples using the equations 4.4. ϵ is the efficiency of Michel reconstruction for $\mu^\pm$ and $f_{\mu^\pm}$ is the fraction of $\mu^\pm$ in the sample, $\frac{\mu^\pm}{\text{Total } \mu}$.

$$\epsilon_{\nu \text{ beam}} = f_{\mu^+}\epsilon_{\mu^+} + (1 - f_{\mu^+})\epsilon_{\mu^-} \tag{4.4}$$

$$\epsilon_{\bar{\nu} \text{ beam}} = f_{\mu^-}\epsilon_{\mu^-} + (1 - f_{\mu^-})\epsilon_{\mu^+} \tag{4.5}$$

Originally, data from the MINOS Near Detector provided the ratio $\mu^+/\mu^- = 0.09 \pm 0.04$ with the magnetic horns on and $\mu^+/\mu^- = 0.44$ without magnetic horn focusing [119]. These values were determined using the curvature of stopped rock muons in the MINOS ND, as the momentum of these muons will be in the range of stopped muons in the MINERvA detector. However, these measurements were taken with a different neutrino beam before the MINERvA detector was placed in front of the MINOS Near Detector. Therefore, a similar study was repeated in the ME era for both FHC (ν_μ) and RHC ($\bar{\nu}_\mu$) beam configurations.

Integrating over the wrong-sign sample, the FHC ν_μ beam has 10% contamination and the RHC $\bar{\nu}_\mu$ beam has 15% contamination. However, these are the contaminations of muons that stop in the MINOS Near Detector; the muons which stop in MINERvA detector will have lower momentum than the muons which stopped in the MINOS ND . The magnetic horns tend to focus lower momentum particles better, selecting for particles with the correct charge. Thus, low momentum rock muons which come low energy neutrinos will have less contamination. Thus, the wrong-side contamination in MINOS is the upper bound for the contamination in MINERvA. The estimates for

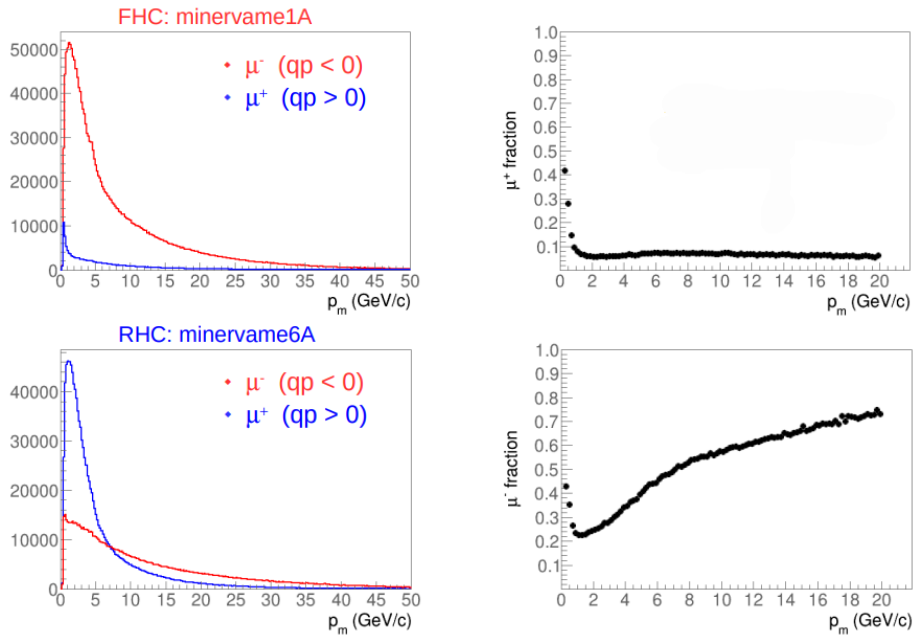


Figure 4-7: MINOS stopped μ^+ and μ^- populations (left) and contamination fractions (right) for FHC neutrino playlists ME1A (top) and RHC antineutrino playlist ME6A (bottom) as a function of muon momentum (p_m). The wrong signed muon is μ^+ for FHC and μ^- for RHC. This analysis look at events where $1.5 < p_m < 20$ GeV/c. Plots from [117]

MINERvA assumes half the value of the MINOS values, and sets the error to cover from the lower bound of 0% to the upper bound set by MINOS. Thus, the FHC ν_μ contamination is $f_{\mu^+} = 0.05 \pm .05$ and RHC $\bar{\nu}_\mu$ contamination has $f_{\mu^-} = 0.15 \pm 0.15$.

The Michel reconstruction efficiencies for FHC and RHC were calculated using the fractions of wrong-sign muon contamination. Table 4.5 shows these efficiencies.

Horn Configuration	Playlist	Data ϵ	Simulation ϵ	Ratio
FHC (ν_μ beam)	ME1A	0.645 ± 0.003 (stat)	0.693 ± 0.002 (sys)	0.929
RHC ($\bar{\nu}_\mu$ beam)	ME6A	0.709 ± 0.003 (stat)	0.728 ± 0.005 (sys)	0.974

Table 4.5: Michel Electron Reconstruction Efficiencies for FHC and RHC beam configurations. Values from [118].

Michel electrons are primarily used to identify charged pions, thus the reconstruction efficiencies for each beam configuration need to be converted to the Michel reconstruction efficiencies for μ^+ and μ^-. Rewriting equation 4.4, the efficiencies for $\mu^\pm$ are expressed in equation 4.6.

$$\begin{aligned} \epsilon_{\mu^+} &= \frac{(1 - f_{\mu^+})\epsilon_{\bar{\nu}_\mu} - f_{\mu^-}\epsilon_{\nu_\mu}}{1 - f_{\mu^-} - f_{\mu^+}} \\ \epsilon_{\mu^-} &= \frac{(1 - f_{\mu^-})\epsilon_{\nu_\mu} + f_{\mu^+}\epsilon_{\bar{\nu}_\mu}}{1 - f_{\mu^-} - f_{\mu^+}} \end{aligned} \tag{4.6}$$

Table 4.6 shows the calculated Michel reconstructed efficiencies by muon type. The differences between the μ^+ and μ^- ratios in data and simulation can possibly be attributed to mismodelling of μ^- capture on the nucleus. Michel electrons are primarily used to tag π^+, so the focus of this study is on ϵ_{μ^+}.

Any additional uncertainties beyond the statistical uncertainties associated with data and the uncertainties on the wrong sign contamination are estimated as the full size of the discrepancies between the data and simulation ϵ_{μ^+}. Combining these uncertainties, the overall uncertainty on the Michel electron reconstruction is determined to be 2.5% [118].

Particle	Data ϵ	Simulation ϵ	Ratio
μ^+	0.721	0.735	0.982
μ^-	0.641	0.691	0.928

Table 4.6: Michel Electron Reconstruction Efficiencies for μ^+ and μ^-

The systematic uncertainty for the Michel electron reconstruction was found in the active tracker region of MINERvA. As noted previously, the Michel electrons in the passive targets are equally well modelled as those in the active tracker region, therefore, this systematic uncertainty can be extended to the nuclear target region.

4.5 Event Weights

Physics models used to create the simulation can change over the lifetime of an experiment, due to fits to new experimental data or updates to theoretical models. Recreating the simulation with the new models can be computationally expensive. Instead of rerunning the simulation, a weight can be applied to each event that effectively scales the probability that the event would occur under the new models. This analysis contains several reweights which are described below.

4.5.1 Flux

Section 2.2 explains how MINERvA simulates the NuMI neutrino flux. This section also explains the improvements and constraints placed on the flux modelling, including PPFX, $\nu - e^-$ elastic scattering, and inverse muon decay. MINERvA analyses apply these improvements as event weights. These weights are the ratio between the improved and baseline flux, and they are applied as a function of neutrino energy in the simulated interaction.

Flux weights are also used to account for measured time variations in the physical NuMI beamline over the course of run. Over the ME era, the transverse cross section of the proton beam increased as the beam increased in intensity [120]. A set of MINERvA data taken under similar conditions, including similar intensities, is called a playlist. As different playlists tend to reflect different beam intensities, the flux weights are different for each playlist.

4.5.2 MINOS Track Matching Efficiency

Section 5.5.1 explains how MINERvA tracks exiting the back of the detector are matched with tracks in the MINOS ND. The efficiency of the track matching has been

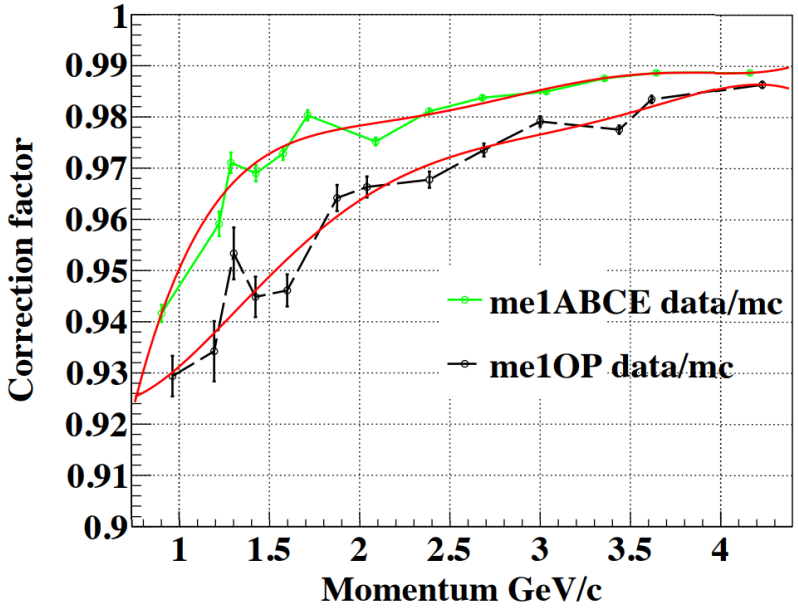


Figure 4-8: An example of corrections to the MINOS track matching efficiency for given muon momentum. As different playlists reflect different intensities, the corrections vary between playlists. Figure from [121]

measured using rock muons in both data and simulation. The efficiency is dependent on the momentum of the muon, and the efficiencies found in data and simulation do not agree with each other. Mismodelling in the MINOS data overlay simulation may have led to an overestimated efficiency for the MINOS tracking. It was also found that increasing beam intensity over the ME era created larger differences between data and simulation. Therefore, every simulated event with a MINOS matched track receives a correction weight dependent on the muon momentum and NuMI batch intensity, where the weights were designed to remove the disagreement between the efficiencies in data and simulation.

4.5.3 Particle Propagation

Section 4.3.1 details how the simulation uses the Geant4 toolkit to step simulated particles through the detector. At each step, the simulation randomly determines whether the particle interacts elastically or inelastically using interaction cross sections. Each cross section has an uncertainty, either due to uncertainty in the underlying data, or due to disagreements between the Geant4 model and one or more underlying datasets. Some of these datasets were not used to tune the Geant4 model. For some inelastic interactions, these disagreement between simulation and data can be as large as 10% in scintillator and 25% in lead and iron.

MINERvA has developed several improvements to the Geant4 model that were not present at the time the data was simulated. Instead of rerunning the Geant4 simulation, a reweighting scheme was developed to reflect the improvements to the cross sections as well as propagate the interaction cross section uncertainties to the simulation. These reweights are applied to adjust the interaction cross sections of neutrons, protons, and charged pions.

The reweighting scheme effectively alters the probability that a particle of a given species will interact elastically or inelastically along its trajectory. For instance, increasing the interaction cross section will increase the probability that the particle will interact, shortening the trajectories of that particle. By weighting up events with the given particle which has shorter tracks and weighing down events with the given particle with lower tracks, the increase in the interaction cross section is applied to the sample. Reversing the direction of the reweight will simulate a decrease in the interaction cross section.

The probability that a particle will not interact over length L is given by

$$P_{no\ interaction}(L, \rho) = e^{-\rho L \sigma_{total}} \tag{4.7}$$

where ρ is the areal density of the material and $\sigma_{total} = \sigma_{elastic} + \sigma_{inelastic}$ is the total interaction cross section, which is dependent on the energy of the particle. Thus, the probability that a particle will interact elastically or inelastically over a distance L is

$$\begin{aligned} P_{elastic}(L, \rho) &= \left(1 - e^{-\rho L \sigma_{total}}\right) \frac{\sigma_{elastic}}{\sigma_{total}} \\ P_{inelastic}(L, \rho) &= \left(1 - e^{-\rho L \sigma_{total}}\right) \frac{\sigma_{inelastic}}{\sigma_{total}} \end{aligned} \tag{4.8}$$

The reweight replaces the probability of a particle interaction based on the old cross section with the probability with the updated cross section. Thus, the weights are

the ratio of the new and old probabilities.

$$
\begin{aligned}
W_{no\ interaction}(L,\rho) &= \frac{P^{new}_{no\ interaction}(L,\rho)}{P^{old}_{no\ interaction}(L,\rho)} = e^{-\rho L\left(\sigma^{new}_{total}-\sigma^{old}_{total}\right)} \\
W_{elastic}(L,\rho) &= \frac{P^{new}_{elastic}(L,\rho)}{P^{old}_{elastic}(L,\rho)} = \frac{\left(1-e^{-\rho L\sigma^{new}_{total}}\right)\frac{\sigma^{new}_{elastic}}{\sigma^{new}_{total}}}{\left(1-e^{-\rho L\sigma^{old}_{total}}\right)\frac{\sigma^{old}_{elastic}}{\sigma^{old}_{total}}} \\
W_{inelastic}(L,\rho) &= \frac{P^{new}_{inelastic}(L,\rho)}{P^{old}_{inelastic}(L,\rho)} = \frac{\left(1-e^{-\rho L\sigma^{new}_{total}}\right)\frac{\sigma^{new}_{inelastic}}{\sigma^{new}_{total}}}{\left(1-e^{-\rho L\sigma^{old}_{total}}\right)\frac{\sigma^{old}_{inelastic}}{\sigma^{old}_{total}}}
\end{aligned}
\tag{4.9}
$$

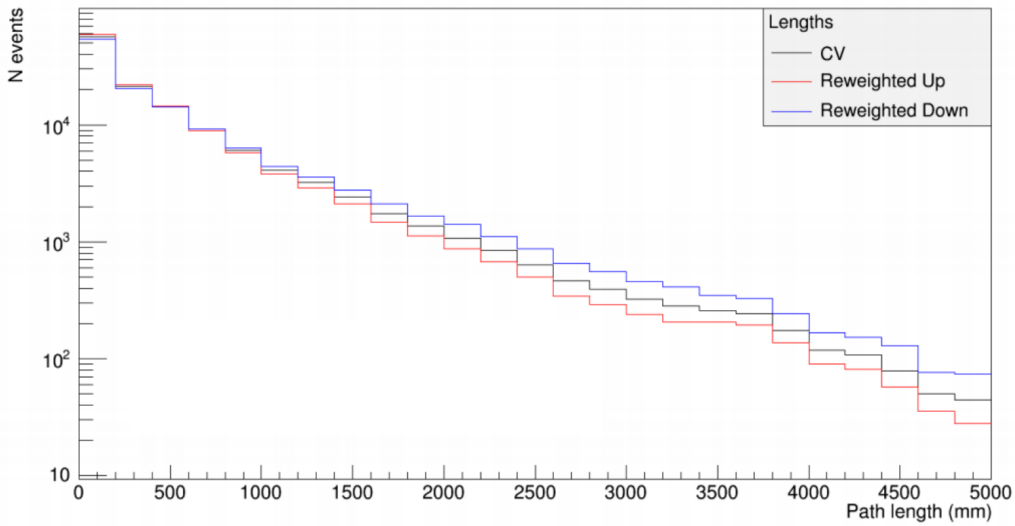


Figure 4-9: Neutron path lengths before the first interaction. The red and blue lines represent the neutron cross section shift by +10% and -10%, respectively. Figure from [98].

Over the trajectory, the particle loses energy and may traverse several different materials, each of which has different cross section uncertainties and areal densities. Therefore, the reweight breaks the particle's track into small segments and determines the weight for each segment. The type of weight function used is determined by whether there was no interaction, an elastic interaction, or an inelastic interaction

in the segment. The overall weight function associated with a particle track is the product of all the weight functions. The overall weight used for the event comes from the product of all of the weight functions.

$$W_{event} = \prod_{j}^{\text{all trajectories}} \left(\prod_{i}^{\text{all segments of trajectory } j} W_j(L_i, \rho_i) \right) \tag{4.10}$$

The reweighting scheme affects only the interaction probabilities of particles propagating through the detector, and therefore should not affect the neutrino interaction cross sections. This is true both for the overall cross section as well as for the cross section of an exclusive neutrino interaction process with particular kinematics.

If the length of each segment $L \to 0$, the weights would have no effect on the neutrino cross sections. However, having infinitesimal segments was deemed too computationally expensive. The resulting mistake from using finite length segments appears as small changes to the underlying neutrino interaction probabilities in the sample, which in turn changes the number of neutrino events simulated with a given interaction and kinematics.

Applying a single scaling factor would preserve the total number of neutrino interactions. However, this is not sufficient to preserve the event rate of all exclusive neutrino interaction processes. To preserve these event rates, small corrections had to be determined as a function of important kinematic properties of the neutrino interactions.

For each shift in the a given particle's interaction cross section in the detector, a scale factor is calculated by summing all the weights in bins of momentum and angle for the leading, i.e. highest energy, final state particle of that particular type. When applying the weight to the event, the weight is normalized by dividing by the

sum of the weights in the bin of momentum and angle of the leading particle of that particular type.

$$N(p,\theta)_{particle} = \frac{\sum^{\text{events in bin}(p,\theta)} W_{event,particle}}{N_{events}}$$
$$W^{normalized}_{event,particle} = N(p,\theta)_{particle} W_{event,particle} \tag{4.11}$$

These normalizations are classified by particle type, the direction of the shift of the cross section, and the target and material on which the neutrino interaction occurred. Figure 4-10 shows examples of normalization factors binned in momentum and angle.

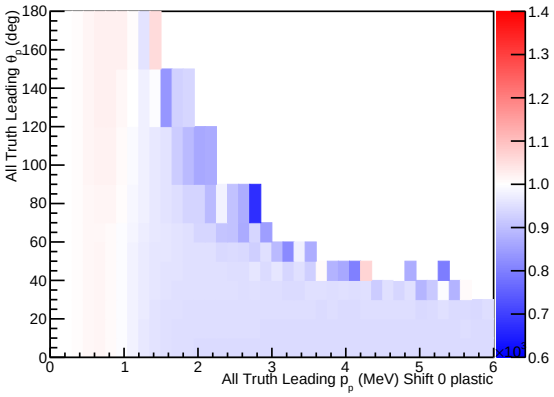
The simulation of neutron interactions is particularly poorly simulated in the QGSP_Bert model, in part because the underlying data is so uncertain. Here, the reweighting was tuned to MINERvA data itself in order to more closely match distributions of neutron candidates in the detector [122].

4.5.4 The MINERvA Tune and Additional Reweights

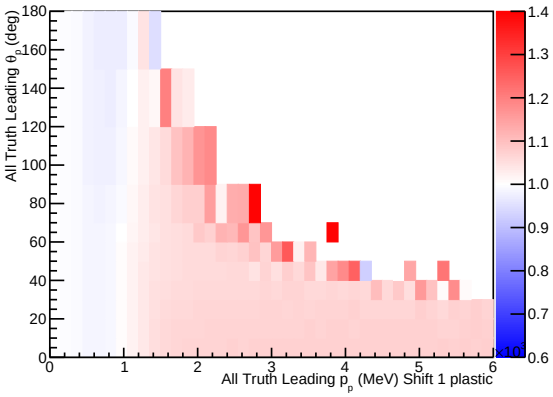
The MINERvA tune (MnvTune) refers to several standard sets of weights which modify various different models in the default GENIE simulation, version 2.12.6, in order to improve agreement to both internal and external datasets. Different versions of the MINERvA tune implement different sets of weights. This analysis uses the standard MnvTune version 1.2.1 with an additional set of weights that are currently not part of a MINERvA tune.

4.5.4.1 RPA and 2p2h Reweights

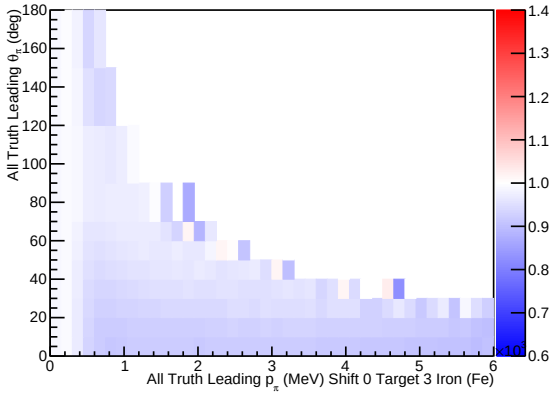
There exists a tension between quasielastic events in data and simulation in GENIE at low Q^2. This tension shows the suppression of data in the low Q^2 region, and the



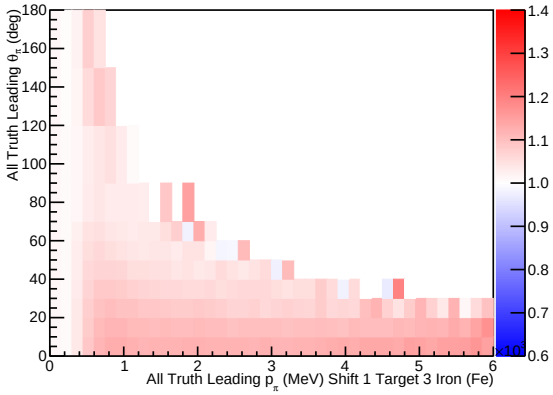
(a) Tracker Proton
σ_{total} Increased



(b) Tracker Proton
σ_{total} Decreased



(c) Target 3 Iron Pion
σ_{total} Increased



(d) Target 3 Iron Pion
σ_{total} Decreased

Figure 4-10: Examples of normalization factors for a given particle and target/material that the neutrino interaction occurred on.

primary cause is thought to be due to long range correlations in the nucleus. The simulation can be improved by using a calculation that includes the random phase approximation (RPA) [51], explained in section 1.4.2. MINERvA applies this model using reweights as a function of the energy and momentum transferred in the event [123].

In the MINERvA low hadronic recoil neutrino scattering sample, a discrepancy between the simulation and data can be attributed to an underestimation of a multi-nucleon 2p2h process, described in section 1.4.2. A reweight that enhances the 2p2h component was found using an 2D Gaussian empirical fit of the simulation to MINERvA data [49][48]. The 2p2h model was fitted in energy and momentum transfer phase space [46].

Overall, quasielastic and 2p2h events only make up a very small part ($< 1\%$) of the signal sample in this analysis that requires a final state charged pion. Therefore, these reweights have a negligible effect on this analysis. MnvTune v1.2.1 uses both of these reweights.

4.5.4.2 Single Pion Production on Deuterium

Using the two datasets of single pion production on deuterium targets from Argonne National Lab and Brookhaven National Lab, which were referenced in section 1.5, a fit extracted three parameters involved in single pion production: the resonant pion production axial mass M_A^{RES} and the normalization factors for resonant and non-resonant pion production [103]. The nominal and fitted parameters in GENIE 2.8[3] are listed in table 4.7.

The normalization factors scale the number of events produced by their respective

[3]Which are identical to the parameters in the version of GENIE, 2.12, used as the basis for the reference model in this analysis.

Parameter	Nominal GENIE value	Fitted GENIE value
Resonant axial mass (M_A^{RES})	1.12 ± 0.22 GeV [102]	0.94 ± 0.05 GeV
Resonant Normalization	100 ± 20%	115 ± 7 %
Nonresonant Normalization	100 ± 50%	43 ± 4 %

Table 4.7: The nominal and fitted GENIE single pion production model parameters [70][103]. MnvTune v1.2.1 only uses the nonresonant normalization.

pion production processes. Changing M_A^{RES} changes both how events are distributed in Q^2 and also the total number of resonant pion events. Section 1.3.2 has further discussion of M_A^{RES} in the Rein-Seghal model.

Weights were developed in order to propagate these fitted values to simulation that was already produced. Resonant and nonresonant pion events were scaled by their respective fitted normalization factors. A more complex weighting scheme was required to reflect a shift in M_A^{RES}. The difference between the nominal value and the fitted value of M_A^{RES} is -0.18 GeV, which is a shift in the parameter of $-0.818\sigma_{nominal}$. MINERvA has produced simulation where the nominal value of M_A^{RES} was shifted up and down by $1\sigma_{nominal}$. For each event, weights were extracted which, if applied to the simulation produced with the nominal value of M_A^{RES}, will produce the simulation with a $\pm1\sigma$ shifted value of M_A^{RES}. To extract the weights that reflect a $-0.818\sigma_{nominal}$ shift from weights that reflect a -1σ shift, the effect is assumed to be linear in M_A^{RES}. Accordingly,

$$\text{weight}_{-0.818\sigma} = \text{weight}_{nominal} - 0.818(\text{weight}_{nominal} - \text{weight}_{-1\sigma})$$

Here, the $\text{weight}_{-1\sigma}$ is the weight that reflects a $-1\sigma_{nominal}$ shift, and $\text{weight}_{nominal}$ is the weight used to produce the simulation with the nominal M_A^{RES}. The nominal

weight is 1, so the previous expression can be rewritten as

$$\text{weight}_{-0.818\sigma} = 1 - 0.818(1 - \text{weight}_{-1\sigma})$$

Reweighting every resonant pion event with $\text{weight}_{-0.818\sigma}$ will produce simulation with the fitted value of M_A^{RES}. This reweight tends to favor events with low Q^2. It should be noted that this method can be used to derive the weights for any shift in $\sigma_{nominal}$. This method was used to provide the weights which reflect the uncertainty on the fitted M_A^{RES} value.

New electro-nucleus scattering data which provide measurements of helicity amplitudes in resonant pion production agree with the value of resonant vector mass M_V^{RES} used in GENIE. Our analysis of the possible variations allowed by this data in M_V^{RES} allows for a 3% uncertainty in this parameters, which is smaller than the GENIE default 10% uncertainty [124]. The weights that quantify this uncertainty are found in a similar manner as the weights found for the uncertainty of M_A^{RES}.

4.5.4.3 ME Coherent Pion Reweight

A recent MINERvA analysis focused on charged current coherent pion production on scintillator in the ME era has shown disagreements between the data and the simulation. Coherent pion production is explained in section 1.3.4. The disagreement is most apparent in the pion angle (θ_π), where the data has far fewer pions produced at large angles relative to the incoming neutrino.

In order to correct the simulation, the coherent pion sample on scintillator was reweighted using the ratio of data to simulation so that the simulation matched the data in $d\sigma/d\theta_\pi$. This reweight improved, but did not completely fix another discrepancy observed in the pion energy. Therefore, a smaller reweight was applied

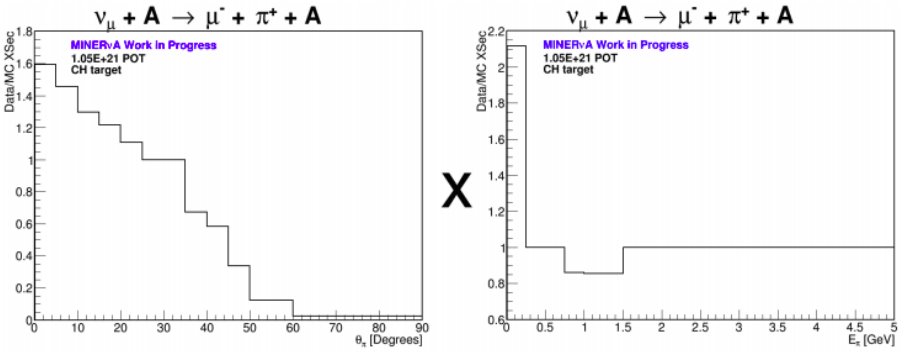


Figure 4-11: Data/MC cross section ratios in θ_π without any reweight (left) and E_π after applying the θ_π reweight (right). The ME coherent pion reweight is the product of the ratios of both cross sections. MnvTune v1.2.1 uses this reweight. Figure from [125].

after this to cover the remaining discrepancies in $d\sigma/dE_\pi$.

The combined reweight was given an uncertainty of 20% for this analysis, to reflect the uncertainty of the measured cross section in the energy range of the selected pions in this analysis, $E_\pi < 500$ MeV [125].

This reweight, while developed for scintillator, is also applied to events on the passive nuclear targets, as it is the best estimate of the coherent cross section. An increased uncertainty of 40% is applied to the reweight in the passive targets to account for both increased statistical uncertainties on the measured coherent pion cross sections in the nuclear targets as well as any additional discrepancies. Recall from the earlier discussion of coherent scattering that for heavier nuclei, i.e. iron and lead, coherent events are a much smaller fraction of pion production, and therefore this correction is much less important for those materials.

4.5.4.4 Diffractive Reweight

GENIE does not currently model diffractive pion production, the analog of coherent pion production on hydrogen nuclei. For the purposes of this analysis, diffractive and coherent pion events look largely the same, with a single energetic, pion carrying away the bulk of the hadronic energy at a small angle relative to the neutrino direction. Therefore, diffractive events are accounted for by increasing the weight of coherent events in hydrogen containing materials in the detector, scintillator and water.

Coherent pion production on scintillator (CH) and on water (H_2O) are increased by 43.68%. This origin of this scaling factor, and well as the process of diffractive pion production, are explained in section 1.3.4.1. Given the lack of experimental constraint to verify this effect, a fractional uncertainty of 50% was applied to this reweight.

4.5.4.5 FSI Reweight

There is a known error in the FSI simulation in GENIE 2.12 which affects hadron-nucleus scattering, single nucleon knockout reactions, and pion absorption that leads to the ejection of two nucleons. The error improperly mixed kinematic quantities from the center of mass and the lab frame, and led to nucleons with unphysical momenta in the lab frame. Using the Monte Carlo record of final state particle interactions, the fix to the error reweights events according to the FSI of each particle in the nucleus [126]. This reweight is part of MnvTune v1.2.1, and it is only applied to the events on scintillator, as parameters for the reweights on larger nuclei are not available.

4.5.4.6 Low Q^2 Suppression

As noted in section 1.5, there exists a disagreement between model and data for pion production on scintillator at low Q^2, where the model overpredicts the cross

section measured in data. This was seen in all four MINERvA LE pion results: $\nu_\mu CC1\pi^+$[60], $\nu_\mu CCN\pi^+$ [62], $\nu_\mu CC1\pi^0$ [63], and $\bar{\nu}_\mu CC1\pi^0$ [64]. Multiple low Q^2 suppression functions were extracted from fits to MINERvA data using NUISANCE [66]. Separate suppressions were found for π^+ production and π^0 production channels, as well as a joint suppression based on all of the MINERvA pion datasets.

An early version of this analysis used the suppression function developed for the π^+ production channel ("NU1PI"), which was only applied to resonant pion production in the active tracking region. However, this suppression was insufficient as the suppressed model did not agree with the measured cross section on scintillator. Accurate simulation of pion production on scintillator is needed in the nuclear target region, as this process is a background for pion production in the nuclear targets. Therefore, a new low Q^2 suppression function was developed in order improve agreement between simulation and data for pion production on scintillator.

The new low Q^2 suppression, labelled as the ME $1\pi^+$ low Q^2 suppression, assumes that the cause of the low Q^2 is due to interactions in the nucleus. Thus, the suppression function should only account for pion production on nucleons in non-hydrogen nuclei. Using the signal defined in section 6.1, which is designed to look for $\nu_\mu CC1\pi^+$ interactions, the differential cross sections in Q^2 were extracted for the active tracking region. Simulated contributions from both hydrogen and coherent pion production were subtracted from model and data. Figure 4-12 shows the differential cross sections in Q^2 for the active tracking region without contributions from hydrogen or coherent pion production.

The ME $1\pi^+$ low Q^2 suppression function was designed to capture the discrepancies between data and simulation across all ranges of Q^2. Figure 4-13 shows that the ratio of data to simulation monotonically increases at Q^2 increases, however the slope of the ratio decreases as Q^2 increases. This change in slope occurs logarithmically.

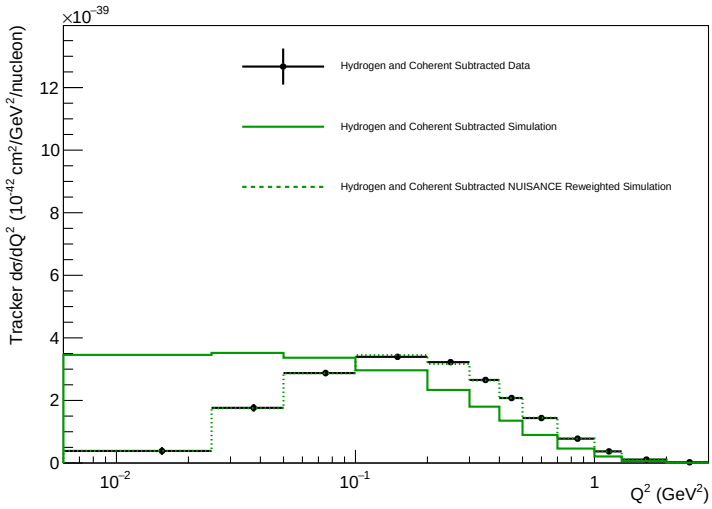


Figure 4-12: Hydrogen and coherent pion production subtracted differential cross section in Q^2 for the active tracking region. The solid line has no low Q^2 suppression applied, while the dotted line has ME $1\pi^+$ low Q^2 suppression

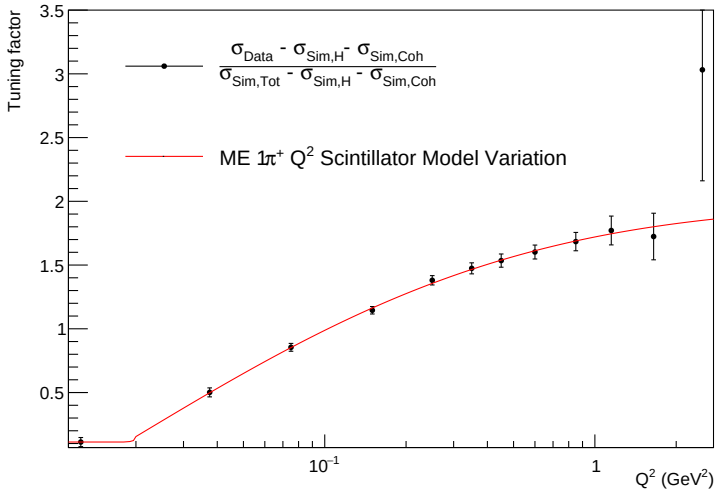


Figure 4-13: Hydrogen and Coherent Pion Production Subtracted Data/Simulation Cross Section Ratio and the ME $1\pi^+$ suppression function

The behavior of ratio can be described using a Gauss error function (Erf), however, the lowest data point does not fit well with the error function. Thus, suppression function was designed to switch from a flat suppression at the lowest Q^2 to a suppression dependent on the Gauss error function. Equation 4.12 shows the ME $1\pi^+$ low Q^2 suppression function $w(Q^2)$.

$$w(Q^2) = a + b \times \text{Max}\left[0, \text{Erf}\left[x_3 \ln\left(\frac{Q^2}{x_1}\right)\right]\right] \tag{4.12}$$

The Max function will be zero when the Gauss error function is negative. In the suppression function, a is the value of the flat suppression at low Q^2, b is the normalization factor of the Gauss error function, x_1 is the value of Q^2 where the suppression switches from a flat suppression to the error function, and x_3 adjusts the change in the slope of the error function.

The ME $1\pi^+$ low Q^2 suppression function was fitted to the ratio of the data and simulation hydrogen subtracted differential cross sections in Q^2. Table 4.8 shows the results of the fit and the red line in figure 4-13 shows the ME $1\pi^+$ suppression function compared to the ratio of the data and simulation cross sections.

Parameter	Fitted Value
a	0.112 ± 0.036
b	1.866 ± 0.165
x_1	0.019 ± 0.002
x_3	0.263 ± 0.042
χ^2/ndf	1.15/9.0

Table 4.8: Fit parameters of the ME $1\pi^+$ low Q^2 suppression function.

The ME $1\pi^+$ low Q^2 suppression is applied to events on all targets in order to keep the model consistent across all nuclei. As the cause of the low Q^2 suppression

is assumed to be due to interactions in the nucleus, the suppression is not applied to interactions that occur on hydrogen, nor is it applied coherent pion production events. The suppression function was also limited to interactions which produced a pion in the initial neutrino interaction. This includes resonant pion production, including all baryon resonances, and nonresonant pion production.

Chapter 5

Reconstruction

The MINERvA reconstruction turns calibrated hits into objects used to reconstruct neutrino events. The following chapter details the reconstruction required for this analysis.

5.1 Time Slicing

The high intensity of the neutrino beam means that multiple events can occur during the 16 μs beam gate. The first step of reconstruction is grouping hits within a gate into a smaller window of time called a time slice. These smaller windows are designed to isolate all activity related to a single physics event, whether that be a single neutrino interaction or the decay of a muon into a Michel electron.

The slicer algorithm orders the hits in the gate by hit time. The slicer will then sum the energy of hits that are contiguous in time. If the summed energy reaches a threshold of 10 photoelectrons, a window of time is placed around the hits. Any hits within the window are grouped together into a time slice.

The slicer algorithm places a lower limit on the size of a time slice due to timing

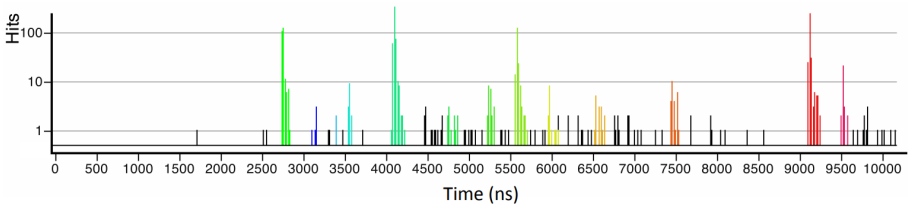


Figure 5-1: Time profile of hits within a 16 μs beam gate. Time slices are colored, while black groups are hits below the threshold for forming a time slice. Reprinted from [94]

uncertainties. For example, the timing resolution on the MINERvA electronics is 2.35 ns, the WLS fiber emission time is $\sim$ 10 ns, and low energy hits will have longer time delay due to time slewing, as explained in section 3.4.2. However, the intensity of neutrino beam in the ME era is high enough that pile up, which is the accidental grouping of two or separate events into a time slice, has a significant effect on the reconstruction efficiency of neutrino events. Therefore, the time slicer in the ME era has reduced the minimum time window to 24 ns from 80 ns in the LE era.

Once the initial window of the time slice has been set, the time slicer looks for further hits that are outside of the window. If there is a hit that is within 9 ns of the edge of the window, the width of the time slice will increase to add the hit to the time slice. This continues until there are no hits less than 9 ns away from the edge of the slice. The time slice is considered to be the fundamental grouping of hits required to reconstruct an event, so all further reconstruction steps are performed in a time slice.

5.2 Clustering

Once hits have been collated into time slices, contiguous hits within a plane are spatially grouped into objects called clusters. A cluster primarily takes on the aggregate properties of its constituent hits; the total cluster energy is the sum of the energy of

the hits, the transverse position is the energy-weighted average transverse position, and the cluster time is the time of the highest energy hit. The longitudinal position of the cluster is the z-center position of the plane in the detector.

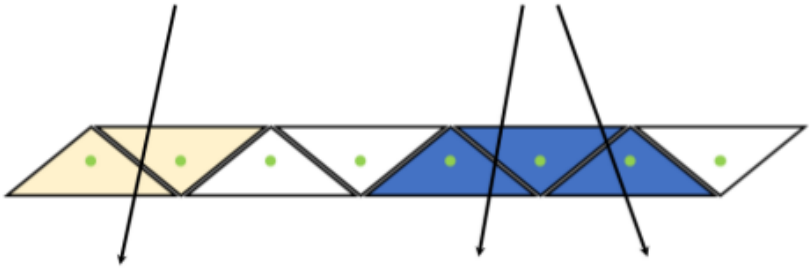


Figure 5-2: Cluster formation from hits in an ID plane. The arrows represent the trajectory of particles. [95]

A minimum ionizing particle (MIP) transversing the detector will most likely deposit energy into a cluster with hits in two adjacent strips. However, the energy loss profile of a particle will vary according to its mass and initial momentum, thus different particles will create clusters with different topologies and energy densities. Different cluster topologies can also arise from overlapping particles in the event. For instance, an electromagnetic shower or multiple hadrons near the interaction vertex can create wide clusters. Figure 5-2 shows examples of clusters created by different particle trajectories. Clusters can be classified using the quantity, energy and position of the hits. These are described in table 5.1 with graphical examples shown in figure 5-3.

Cluster type	Description
Cross-talk	Identified by correlating hits that are directly adjacent in electronics space on the PMT input face. These are typically low energy and isolated physically from other hits. Cross talk clusters are not used in later reconstruction steps.
Low activity	Visible $E_{\text{total}} \leq 1$ MeV. Low activity clusters are not used when building tracks, but can be used with calorimetry to measure recoil energy.
Trackable	Composed of 1-4 hits with visible E_{total} between 1-12 MeV. There must be at least one hit with energy between 0.5-12.0 MeV. If two of the hits have energies between 0.5-12.0 MeV, the hits must be on adjacent strips. These are indicative of minimum ionizing particles.
Heavy ionizing	Composed of 1-4 hits with visible $E_{\text{total}} \geq 12.0$ MeV. 1-3 hits must have energies greater than 0.5 MeV. Two or more of the hits with $E_{\text{hit}} > 0.5$ MeV must be sequential. These can be seen with neutron interactions or at the endpoints of hadron tracks. with Bragg peak energy deposits
Supercluster	Does not satisfy the conditions of the previously described cluster. Must have at least 1 MeV of energy. These are typically very wide with large energy deposition, which is associated with multiple particles.

Table 5.1: Cluster types and descriptions

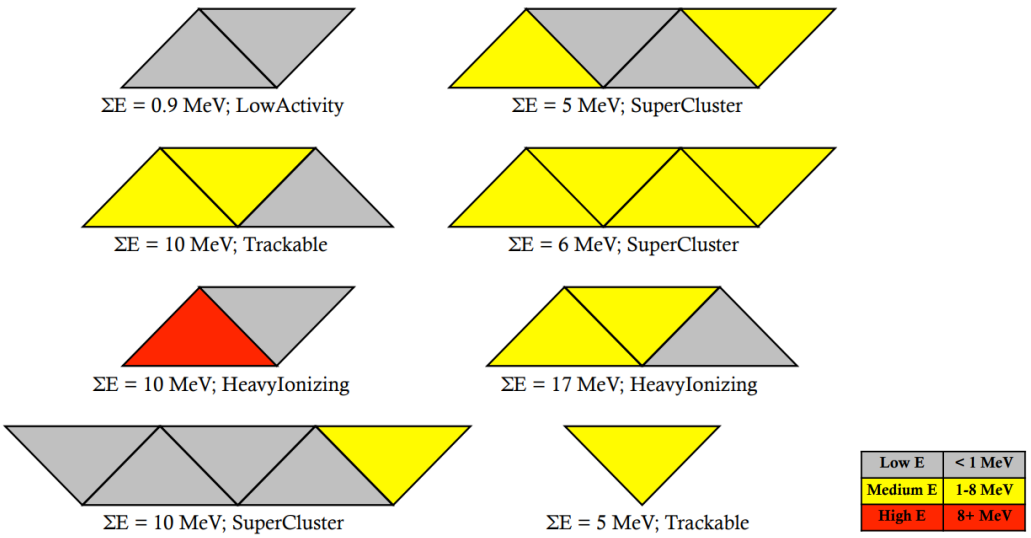


Figure 5-3: Examples of cluster topologies. Figure from G. Perdue [127]

5.3 Track Reconstruction

After grouping hits into 2D clusters, the clusters can be assembled into a track, which is the reconstructed 3D trajectory of a particle propagating in the MINERvA detector. Due to elastic or inelastic scattering, a particle may need multiple tracks in order to estimate its trajectory. The minimum length requirements of different tracking algorithms, also called trackers, necessitate the use of multiple algorithms during reconstruction. There are two types of trackers, based on the length of the track: the long tracker, which were primarily developed to reconstruct muon tracks, and short trackers.

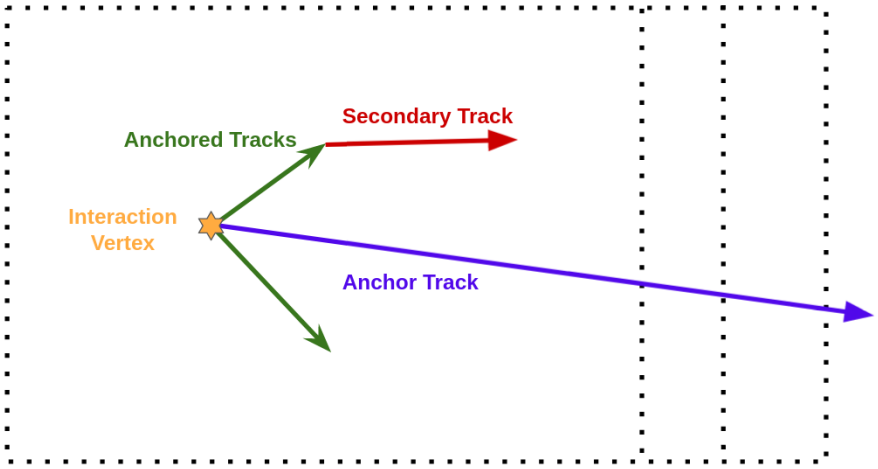


Figure 5-4: Diagram of tracks built from the interaction vertex in a muon neutrino analysis

Track-based event creation starts during the common reconstruction, where the long tracker is run. It proceeds through the steps outlined in the following paragraphs until no other long tracks can be added to the event. The short trackers are run afterwards during the analysis-specific reconstruction. Starting from the second step

below, any tracks created by the short trackers are added to the event.

The first step of track-based event creation selects an anchor track. During the common reconstruction, the long tracker creates tracks from trackable and heavy ionizing clusters. The longest of these tracks, typically a muon, is used as an anchor track. This anchor track must span at least 25 planes, and it assumed the particle is travelling downstream, toward the MINOS near detector. The interaction vertex is set as the most upstream cluster of the track.

Next, anchored tracks are made. Anchored tracks are made using clusters unused by the anchor track. Both the long and short trackers can create these tracks. The trackers make sure the anchored track is consistent with the interaction vertex set by the anchor track. A track is considered consistent with a vertex if the origin of the track is within 250 mm of the vertex and the projection of the track towards the vertex is less than 100 mm away at its closest approach. Anchored tracks are created continuously until no other tracks with consistent vertices can be created. The upstream vertices of the anchor track and all of the anchored tracks are fitted simultaneously to form a common vertex. This vertex becomes the new interaction vertex.

Finally, the algorithm searches for secondary tracks. Scattering within the detector can change the direction of the particle or create multiple particles. To account for this, the trackers search for additional secondary tracks using the endpoints of anchored tracks. The reconstruction checks the consistency between the anchored track endpoint and the upstream vertex of the secondary tracks, using the criteria previously outlined and rejects secondary tracks that are not consistent. These vertices are fitted together to create a common vertex. Further information on track based event formation can be found here [95].

5.3.1 The Long Tracker

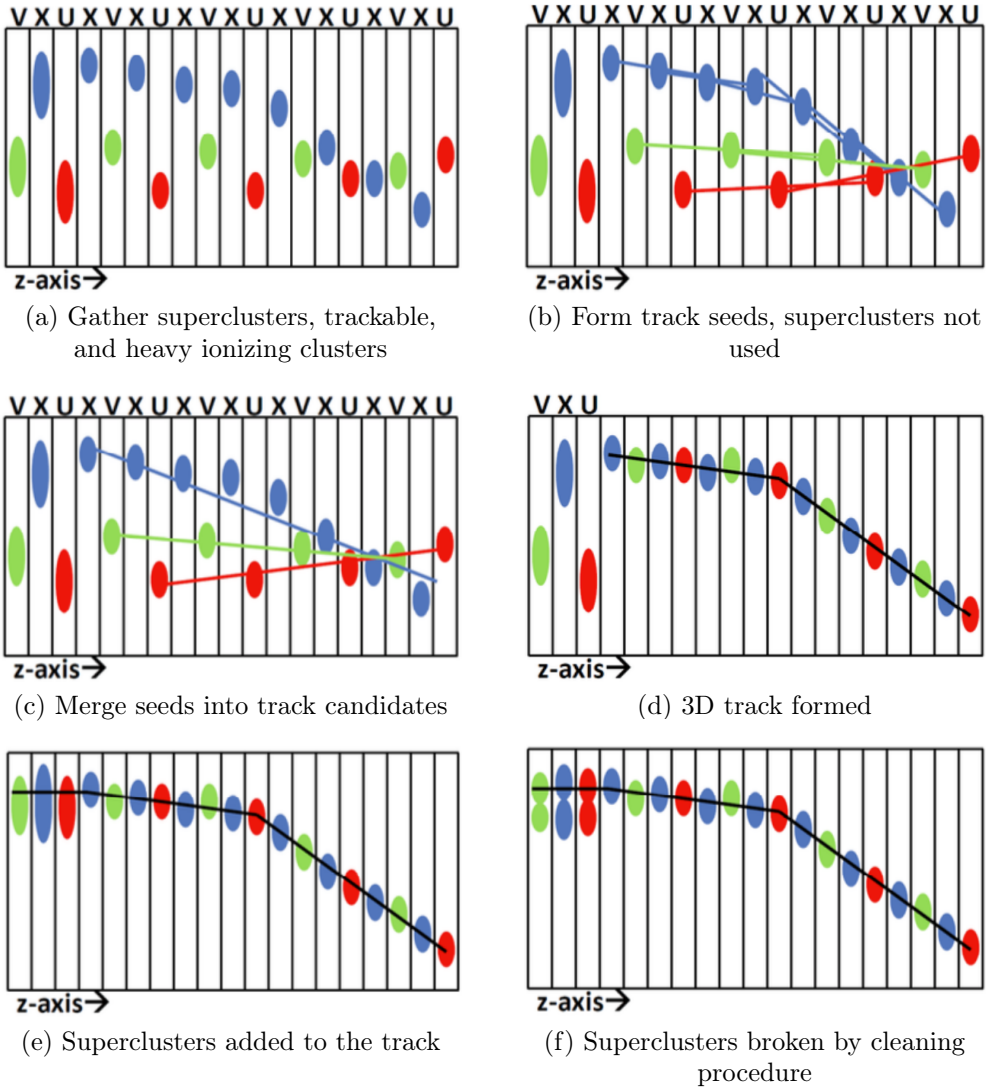
The long tracker is run during the common reconstruction phase. Trackable or heavy ionizing clusters in the same plane view (X,U,V) are grouped into track seeds. Each seed consists of three consecutive clusters in the same view. A cluster can be part of multiple seeds. Each seed needs to pass a least squares χ^2 fit to a 2D line, which determines the quality of the seed. The geometry of the MINERvA detector prevents the creation of seeds with angles greater than 60° with respect to the longitudinal detector axis.

Track seeds in the same view can be merged into track candidates if the seeds share at least one cluster, none of the clusters are in the same plane, and the slopes of the seeds are consistent with one another. Seed merging begins with the downstream track seeds and moves upstream in order to limit the influence of heavy activity near the interaction vertex on the creation of track candidates. After all track candidates have been created, compatible track candidates may be merged into a new track candidate afterwards, even if there is a missing cluster in a scintillator plane between the two candidates.

The final step which creates a three-dimensional track uses two separate algorithms: the 3D routine and the 2D routine. The 3D routine looks for all possible combinations of candidates in X, U, and V orientations. If a combination of candidates overlap along the longitudinal axis and are compatible with the same line, the 3D routine creates a track. This requires a minimum of 11 planes.

After the 3D routine has tested all track candidate combinations, the 2D routine searches and compares pairs of remaining track candidates. If the track candidates are compatible, they are merged into tracks. This helps in the cases where track candidates in one view are obscured by activity in the detector or there is a plane

with missing clusters .



(a) Gather superclusters, trackable, and heavy ionizing clusters

(b) Form track seeds, superclusters not used

(c) Merge seeds into track candidates

(d) 3D track formed

(e) Superclusters added to the track

(f) Superclusters broken by cleaning procedure

Figure 5-5: Illustration of the long tracking procedure. Figures from [97].

Newly created tracks are fitted by a Kalman filter, a local χ^2 minimizer that minimizes the sum of the distances between the cluster position and the estimated track parameters, which includes the track angle and position at that point. Accounting

for these parameters locally allows the predicted track to deviate from a straight line hypothesis [128]. To allow for multiple Coulomb scattering along the track in the fit, additional contributions are added to the covariance matrix of track parameters as the track steps through the material of the detector. Further information on the use of Kalman filter in MINERvA can be found here [129].

Long tracks are then run through a "track cleaning" algorithm, which removes additional energy from the track by breaking up large clusters or high energy clusters that are part of the track. Track cleaning seeks to remove energy that does not come from the particle that created the track, like activity from another particle that overlaps the track in one view. In the analysis, a muon track near the interaction vertex will often overlap with low energy protons created with the reconstructed π^+. Anchor tracks are assumed to be primarily created by muons; thus if the deposited energy per unit length, $\frac{dE}{dX}$, is inconsistent with a minimum ionizing muon, the extra energy is removed in order make the profile consistent. Track cleaning only breaks up superclusters for anchored tracks, as they are most likely to be hadrons. The track cleaning will not break up superclusters at the end of the anchored tracks, as low energy hadrons deposit significant energy near the end of their path and often have a visible Bragg peak.

5.3.2 Short Trackers

The long tracker can only resolve tracks that are at least nine planes long and have angles less than 60°. The short trackers can create tracks which only span five planes, as well as create tracks with angles between $60° - 80°$ and $100° - 180°$. Five clusters from five different planes are need to give the degrees of freedom required by a fit. Starting from the center of first plane, the distance to the center of the fifth plane is

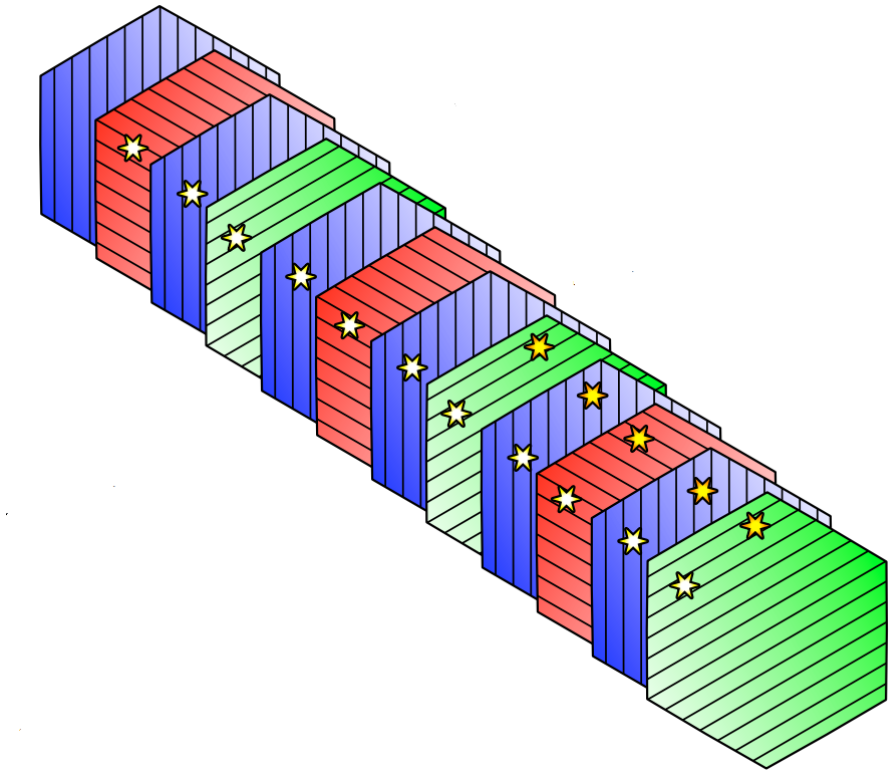


Figure 5-6: Illustration of the MINERvA planes (XUXV) and 3D points along the track produced by the long tracker (left) and short tracker (right). Figure from G. Perdue[127].

6.8 cm. This distance corresponds to a charged pion with at least 35 MeV of kinetic energy, which is the lower tracking threshold for pions. The tracking efficiency for charged pions are shown in figure 5-7.

Short trackers are less rigorous than the long tracker, and care must be taken when applying the short trackers to events with heavy energy activity. In this analysis, tracks created by the short trackers are not cleaned. Also, the tracks are not fitted by the Kalman filter, as the tracks are short enough that multiple Coulomb scattering is a small effect. Therefore, it is acceptable to assume that track is a straight line. This analysis uses two short trackers that are dependent on having an anchor track as a

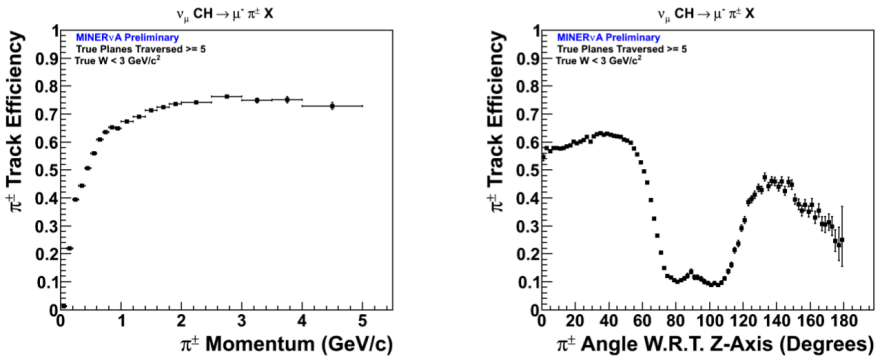


Figure 5-7: Charged pion tracking efficiency in the active tracker region as a function of momentum and angle with respect to the z-axis. Pion interactions are the primary cause of the inefficiencies. Figure from [97]

starting point for the track.

The anchored short tracker creates 3D track seeds with at least four consecutive clusters with two X planes, one U plane and one V plane. Note that these seeds are different than the 2D track seeds used by the long tracker. The track requires at least two seeds with contiguous clusters to meet the requirement of five planes. These track seeds are merged in a similar manner as used in the long tracker. The track is only accepted if the start position of the short track and the vertex of the anchor track are within a reasonable distance.

The Vertex Energy Short Tracker (VEST) groups cluster together using a Hough transform as an angle scan between the anchor track and possible short track clusters [130]. Clusters near the interaction vertex are not initially used, as they can influence the transform. The remaining clusters are separated by plane view and grouped according to their angle to the anchor track. Track candidates are created from all possible combinations of groups of clusters from the different plane views. These candidates are then merged similarly to the track candidates in the long tracker.

Clusters that were excluded for being near the interaction vertex are added to the track only if the cluster and track candidate are in adjacent planes. Tracks are accepted if they pass through the anchor vertex and if they contain a cluster near the vertex.

5.4 Vertex Reconstruction

This analysis requires the accurate reconstruction of the position of the interaction vertex, and this reconstruction finds the common interaction vertex using the track vertices.

Track-based vertex reconstruction begins by calculating an initial approximation of the vertex position. For each pair of tracks, the reconstruction computes a crossing point, which is the algebraic mean of the two points of closest approach (POCA) of the two tracks. This is effectively the midpoint between tracks at their closest points. Each crossing point receives a weight:

$$w = (d_{min} + d)^n \tag{5.1}$$

where d is the distance of the closest approach (DOCA) between the two tracks, d_{min} = 0.01 mm, and n=-0.5. This gives a larger weight to pairs of tracks with shorter DOCAs. The initial approximation of the vertex position is taken as the weighted average of all the crossing points.

This vertex is then refitted using an adaptive Kalman filter minimization technique [131]. Using the initial approximation of the vertex position and the slope of each of track, the technique predicts each track's nearest position and slope to the vertex. The residual between the prediction and the actual position and slope is used to

update the fit, which then is used to update the vertex position.

To lessen the influence of outlying tracks on the fit, the adaptive vertex fitter assigns weights to each track according to how well the fit predicts the track's position and slope. Poorly predicted tracks receive smaller weights compared to tracks with good predictions. These weights may change as the vertex position is updated by the fitter. Further details on the adaptive vertex fitting procedure in MINERvA can be found here [129].

5.5 Muon Reconstruction

This analysis needs accurate reconstruction of the muon momentum in order to study pion production from charged current (CC) neutrino interactions. Furthermore, this analysis looks specifically for CC ν_μ interactions, which produce μ^-. Also, in order to combat wrong sign ($\bar{\nu}_\mu$) contamination in the beam, the analysis must be able to reconstruct the charge of the muon.

This analysis looks for events that have low hadronic recoil energy, which means there is low transverse momentum transfer in the neutrino interaction. Thus, the resulting muon will typically be energetic and moving in the forward direction. The muon will often leave the MINERvA detector and enter the MINOS Near Detector, described further in section 3.3, where the magnetic field and steel calorimeter can be used to measure the charge and momentum.

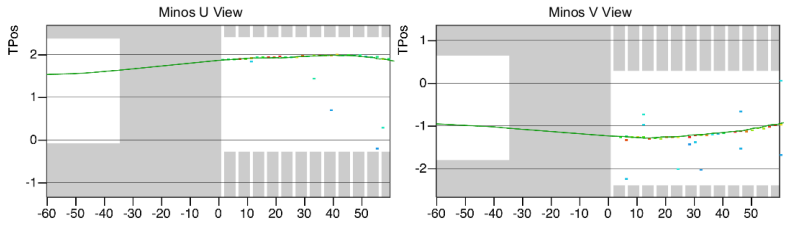


Figure 5-8: MINOS Near Detector event display of a MINOS track matched to a MINERvA track in U (left) and V (right) plane orientations. Figure from [132].

5.5.1 MINOS Track Matching

As described in the previous section 5.3 on track reconstruction, the reconstruction sets the longest track as the anchor track. If the longest track exits the back of the MINERvA detector, the track is considered a muon, as the downstream electromagnetic and hadron calorimeters limit the number of electrons, photons, and strongly

interacting particles escaping downstream.

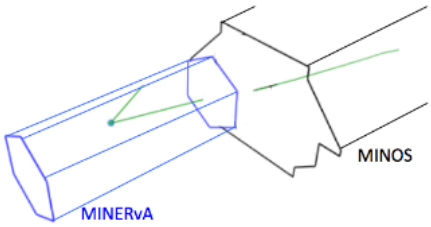


Figure 5-9: Diagram of a muon track exiting MINERvA and entering the MINOS Near Detector. Figure from [96]

MINERvA tracks which leave from the back of the detector can be matched to tracks in the MINOS Near Detector. The track matching algorithm requires that the MINERvA track has at least one cluster in the last five modules of the detector and that the MINOS track has at least one hit in the first four instrumented planes. The former requirement effectively excludes MINERvA tracks that leave the side of the detector. MINOS matching also requires that the tracks must be within a 200 ns window of each other.

The matching algorithm checks the consistency of the match. The MINERvA track is projected forward into the MINOS Near Detector, where the residual between the projection and the start of the MINOS track is calculated. Likewise, the MINOS track is projected back into the MINERvA detector, and the residual between the projection and the end of the MINERvA track is calculated. Both projections use Kalman filters, so any scattering in the material is taken into account. If the residuals are both under 40 cm, the two tracks are matched. If there are multiple MINOS tracks that can be matched, the one with the lowest projection residual is used.

If the previous algorithm does not find a match between the tracks, the matching algorithm tries see if the tracks are compatible at the point of closest approach

between projections of the MINERvA and MINOS tracks. This is useful when the muon scatters off passive material between the two detectors.

After the tracks are matched, no refitting is done to combine the two tracks into a joint track with shared properties. The MINOS Near Detector has more passive material than the MINERvA detector, thus the muon direction is much more precisely measured in MINERvA alone. The only information taken from the MINOS track is the charge and momentum, which cannot be measured in MINERvA alone.

Requiring that the muon track matches to a MINOS track restricts the kinematic space of the reconstructed muons. The matching requirement places a lower threshold on the muon momentum, as the muon must have enough momentum to escape the back of the MINERvA detector and enter MINOS ND. This requirement also restricts the muon angle. In the active tracking region of the detector, muons will typically only enter the MINOS ND if the muon angle $\theta_\mu < 20°$. These limits will depend on the longitudinal position of the interaction. Muons created in the nuclear target region of the detector, which is farther away from the MINOS ND, will have a smaller angle of acceptance ($\theta_\mu < 13°$), and they will need larger momenta in order to reach MINOS. As will be seen in section 6.10.7, the analysis only considers events with muons that have angles $\theta_\mu < 13°$ and momentum $p_\mu > 1.5$ GeV/c in both the nuclear target and active tracking regions. These restrictions were placed on both regions so that comparisons between the regions will be over the same kinematic space.

5.5.2 Charge and Momentum Reconstruction

The MINOS Near Detector's magnetic field deflects muons according to their charge. When studying ν_μ, the magnetic field is set to bend μ^- towards the magnetic coil. This allows the analysis to select μ^- and reject μ^+. This also has the added benefit

of providing the maximum range for the muon track.

Being a steel calorimeter, the MINOS Near Detector can reconstruct the momentum of the muon using the range of muons that stop in the detector. Range reconstruction uses the Bethe-Bloch equation to calculate the energy lost over a given distance by a charged particle traversing through material [2]. Muon momentum found by range has a 0.98% uncertainty. The range uncertainty also accounts for the uncertainty in the muon energy scale in MINOS.

However, the range method only works for muons with lower angles and lower energies (< 10 GeV). Muon tracks with with high angles can leave the side of the detector, and muons with greater than 10 GeV can exit out the back of the detector. In these cases, the muon momentum can be reconstructed using the curvature of the muon. Equation 5.2 is used to calculate the muon momentum.

$$\frac{1}{R} = \frac{0.3Bq_\mu}{p_\mu} \tag{5.2}$$

Parameter	Description
R	Radius of the curvature
B	Magnetic field strength
q_μ	Muon charge
p_μ	Muon momentum

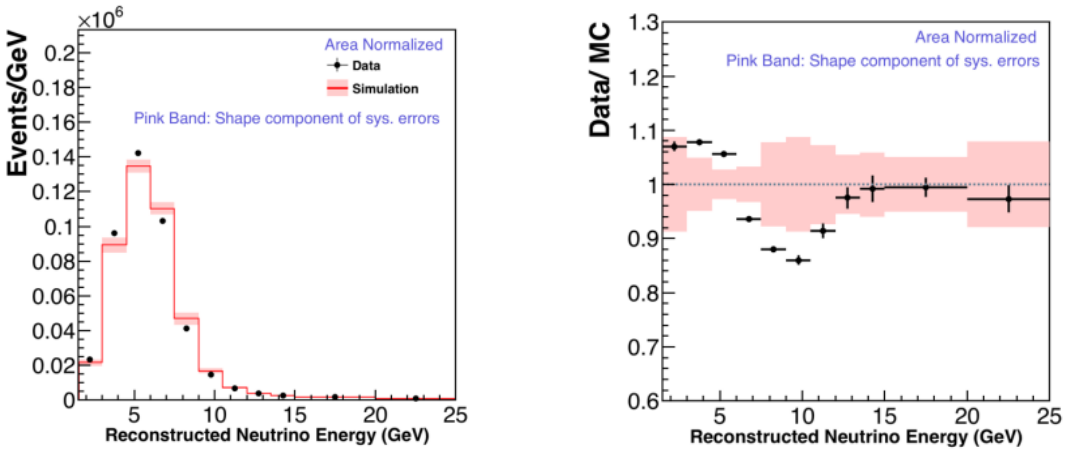
Table 5.2: Measurement of muon momentum by curvature parameters

Curvature momentum reconstruction has an uncertainty of 2.5% for muons with less than 1 GeV/c of momentum and 0.6% for muons with momentum greater than 1 GeV/c. The uncertainty on curvature is added in quadrature to the range uncertainty, as the range uncertainty contains the uncertainty of the MINOS ND muon energy scale.

The momentum reconstruction also needs to account for the energy lost while the muon traversed through the MINERvA. This energy is calculated using the Bethe-Bloch equation and added to the reconstructed energy of the muon in MINOS.

The reconstructed energy loss in Minerva has two sources of uncertainty. The first source is the parameters of the Bethe Bloch equation, which varies the energy by 30 MeV for tracks that start in the active tracker region and 40 MeV for tracks that start in the nuclear target region. The second source is the material assay, which can vary the energy by 11 MeV for tracks that start in the active tracker region and 17 MeV for tracks that start in the nuclear target region.

5.5.2.1 MINOS Near Detector Muon Energy Scale



(a) Area normalized low-ν event rate in data and simulation

(b) Ratio of the area normalized data and simulation

Figure 5-10: The low-ν "wiggle" discrepancy. The errors on the simulation represent the shape component of the systematic uncertainties. Plots from [133].

The ME era low-ν analysis probed the muon energy scale in the MINOS Near Detector. While measuring the number of low-ν events in order to extract the low-ν

flux, explained further in section 2.2.2.3, the analysis discovered a significant discrepancy in the shape of the event rate between data and simulation, shown in figure 5-10. Several studies looked for the cause of this "wiggle" in the shape of the event rate. Initially, studies concentrated on the possible mismodelling of the neutrino flux, as the low-ν flux provides excellent constraints on the shape of the total flux. However, a fit of simulation to data showed that varying the parameters involved in the magnetic horn focusing system produced very modest effects on the distribution of neutrino energy. The focusing parameters would need to be shifted far beyond their measured tolerances in order to get agreement between data and simulation.

Another possible source of this discrepancy could be misreconstruction of the muon momentum. As muon momentum reconstruction primarily occurs in the MINOS Near Detector, variation in the muon energy scale of the MINOS ND was added as a parameter to these fits. This joint fit found that the "wiggle" discrepancy was best resolved by a 1.75 σ shift in the MINOS muon energy scale plus variations of the focusing parameters within 1 σ of their measured tolerances. No obvious explanation for the miscalibration of the MINOS muon energy scale has been found.

It is more likely that the discrepancy was caused by the misreconstruction of the muon momentum of less than two standard deviations of the estimated uncertainty, as opposed to many standard deviation uncertainties in parameters that affect the neutrino flux shape in the region of the "wiggle". Thus, MINERvA attributed the muon energy scale as the cause of the discrepancy, and the muon energy scale in the MINOS ND was shifted by 3.6% for muon reconstruction in data. By using the shifted energy scale, the joint fit also reduced the uncertainty in the MINOS muon energy scale from 2% to 0.98%, which is used in this analysis. A summary of studies into the "wiggle" discrepancy and their conclusions can be found in [133].

5.6 Michel Electron Reconstruction

Charged pions that stop without interacting in the MINERvA detector decay 99.9% of the time into a muon and its corresponding neutrino [2]. This muon will eventually itself decay into a Michel electron and a corresponding electron neutrino. Matching Michel electrons to hadron tracks is an important method to identify π^+ tracks. This method is effective because π^+ and μ^+ are electrostatically repelled away from nuclei, and therefore, they are not captured by nuclei in the detector and are able to decay.

Michel electron reconstruction effectively looks for groups of deposited energy in the detector after the neutrino interaction. The following reconstruction steps try to identify which of the groups of energy are Michel electrons while limiting the number of misreconstructed particles which can produce similar energy depositions.

5.6.1 Selecting Michel Electron Candidates

Starting from the first time slice after the neutrino interaction, the Michel reconstruction selects time slices whose visible energy is less than 100 MeV. The upper threshold on visible energy, which is simply the calibrated energy deposited in the scintillator strips, helps remove slices with neutrino interactions or rock muons. The reconstruction uses all of the inner detector clusters which are not low activity or cross-talk in each of the time slices.

The reconstruction searches the time slices after the interaction because the mean lifetime of the muon ($\tau = 2.2$ μs) delays the appearance of the Michel electron. The mean lifetime of a π^+ ($\tau = 26$ ns) causes negligible delay. Thus, the muon is not seen in the same time slice as the Michel electron. Before its decay, the muon will only deposit a ~ 4 MeV of visible energy in the detector. Deadtime[1] can prevent the

[1]Explained in section 3.2, hits in the MINERvA detector are only recorded for 151 ns after the

readout of this energy, which prevents the muon from being placed in its own time slice, and it will most likely appear in the same time slice as the neutrino interaction. Therefore, low visible energy and a lack of a time slice prevents the muon from being used as a signature of pion decay.

For each of these slices, the reconstruction finds the energy weighted average time and longitude position of the inner detector clusters. To remove unrelated background activity that's synchronous with the Michel electron, any clusters 25 ns before or after the energy weighted time average, as well as any cluster that is more than 35 cm away from the energy weighted longitudinal position, are removed. Finally, the passive material corrected energy of the remaining clusters must be between 10 and 65 MeV. Passive material corrected energy accounts for the "invisible" energy deposited in materials that do not produce photons. The lower cut removes neutrons with low kinetic energy (< 10 MeV). These "slow" neutrons will have a time delay similar to the decay time of Michel electrons before they interact, primarily knocking out protons from carbon or elastically scattering on protons in hydrogen. The upper cut removes cosmic rays and any neutrino interactions. Clusters which pass this selection are then considered to be a Michel electron candidate.

Each Michel electron candidate has several basic reconstructed quantities, including the energy weighted average time of the Michel candidate and its longitudinal position, as well as the visible and passive material corrected (calorimetric) energy of the candidate.

initial activity. The FEB board must then reset for 188 ns, in which no hits can be recorded. This period of time is known as deadtime.

5.6.2 Michel Views

The Michel electron candidates can be reconstructed with clusters with 1, 2 or all 3 plane orientations (views) in MINERvA, which can be seen in figure 3-4. Michels with 1 view only have access to 2D information on the position. These Michel candidates will only have the energy weighted average transverse position for that view. Because this analysis needs to associate Michels with the endpoint of a pion candidate, 1 view Michels are not used in this analysis.

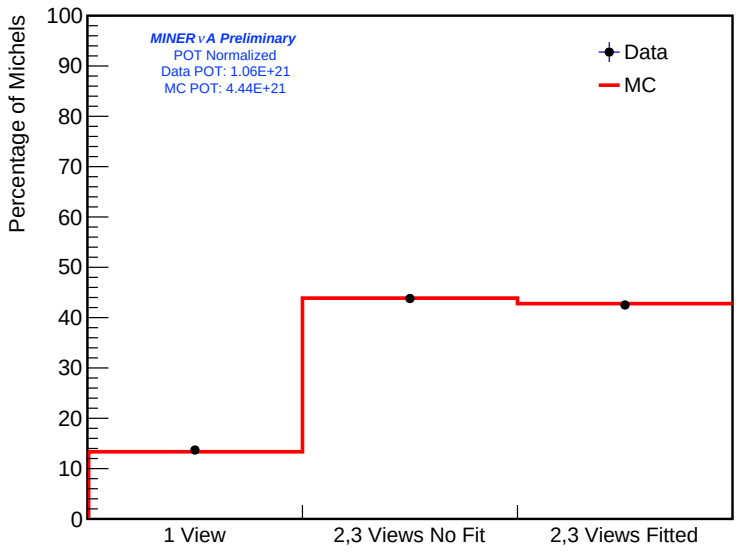


Figure 5-11: Percentage of different types of Michel candidates

For Michel candidates with 2 or 3 views, the transverse position of the Michel in 3D space can be reconstructed. The energy weighted average transverse position is found for each view that the Michel candidate has a cluster in. Using the average transverse position in the X, U, and V views, the candidate can reconstruct the average X and Y position.

5.6.3 Estimating the Michel endpoints using linear fits

Clusters only have 2D information about their positions, thus finding the 3D positions of the endpoints of the Michel candidate requires additional steps. The transverse position of the endpoints can be found by fitting a line through the clusters of a Michel candidate and then estimating the endpoints using the longitudinal positions of the most upstream and downstream clusters of the Michel candidate. The linear relationship between the transverse and the longitudinal position of clusters in the X, U, and V views respectively can be estimated with the equation 5.3, while equation 5.4 shows the equation for the fitted line. Table 5.3 explains the parameters involved with the fit.

$$\begin{pmatrix} w_x & 0 & w_x z_x & 0 \\ 0 & w_u & 0 & w_u z_u \\ w_v & -w_v & w_v z_v & -w_v z_v \end{pmatrix} \begin{pmatrix} x_0 \\ u_0 \\ dx \\ du \end{pmatrix} = \begin{pmatrix} w_x x_{cluster} \\ w_u u_{cluster} \\ w_v v_{cluster} \end{pmatrix} \tag{5.3}$$

$$\begin{aligned} x_{fit} &= x_0 + z dx \\ u_{fit} &= u_0 + z du \end{aligned} \tag{5.4}$$

The fitted values are translated from an XU coordinate system to an XY coordinate system using equation 5.5.

$$y = \frac{1}{\sqrt{3}}(x - 2u) \tag{5.5}$$

The best fit values for the line are found by using singular value decomposition

Parameter	Description
$x, u, v_{cluster}$	Transverse position of X/U/V cluster
$z_{x,u,v}$	Longitudinal position of X/U/V cluster
$w_{x,u,v}$	Cluster's fraction of total energy of Michel candidate
x_0, u_0	Fitted line intercepts at $z = 0$
dx, du	Fitted slopes in X and U views

Table 5.3: Michel Linear Fit Parameters

(SVD) to invert the matrix in equation 5.3. The SVD is the solution to a "least norm" fit, which can be considered as the generalization of a least squares fit to multiple views [134].

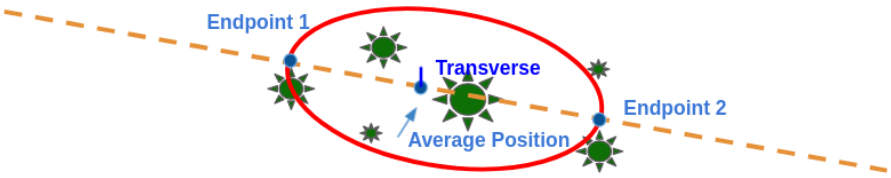
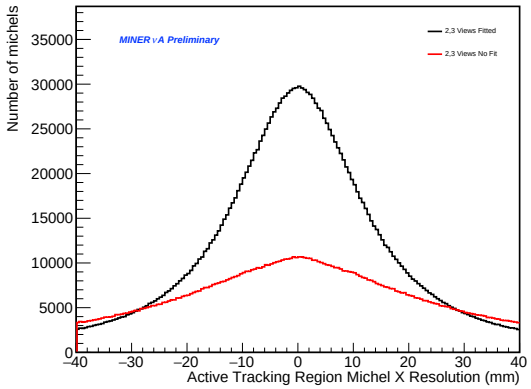


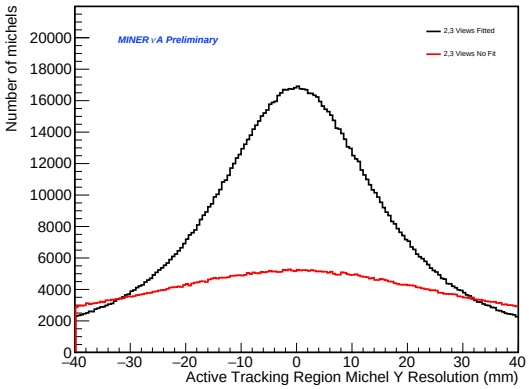
Figure 5-12: Illustration of a Michel electron with a linear fit. The endpoints have the z-position of the most upstream/downstream cluster, but the transverse position given by the fit.

The Michel candidate needs to meet some additional requirements in order to get a unique solution from the singular value decomposition. There needs to be at least 4 clusters in at least two different views. Also, there must be at least two clusters and at least two planes outside the view with the most clusters. The last requirement removes the degeneracy of a fit with two clusters with the same longitudinal position. If a 2 or 3 view Michel candidate cannot be fit, primarily because the candidate fails one of the conditions required by the SVD, then the reconstruction assumes that the slope of the fit is 0. Here, the Michel endpoints will have the same transverse

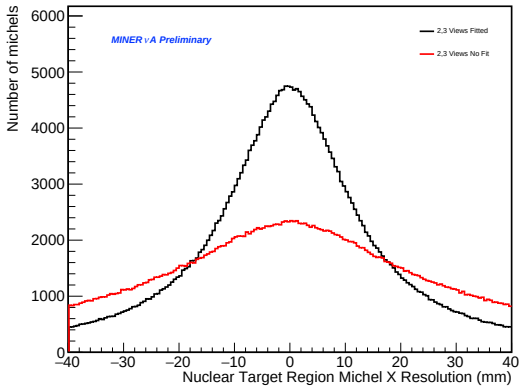
position as the average transverse position of the candidate. Figure 5-13 shows the performance of the Michel electron endpoint reconstruction in the transverse position of the endpoints.



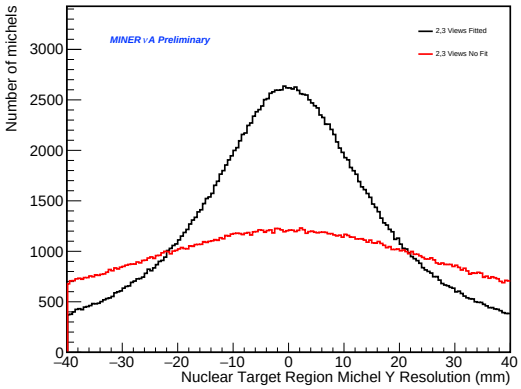
(a) Tracker, X position



(b) Tracker, Y position



(c) Nuclear Targets, X position



(d) Nuclear Targets, Y position

Figure 5-13: Reconstructed - true endpoint position of Michel electrons in X and Y. The units are in millimeters. This was measured using simulated Michel electrons in the active tracking region (tracker, top) and the nuclear target region (bottom). The black lines are 2,3 view Michel candidates with a linear fit, while the red lines are 2,3 view Michel candidates without a fit

5.7 Pion Reconstruction

After determining the muon track in the event, every remaining track is considered to be a hadron track. The kinematics of each hadron track are reconstructed under a charged pion and a proton hypothesis, meaning that two sets of kinematics are calculated. The analysis then tries to identify charged pions with good kinetic energy reconstruction from the hadron tracks.

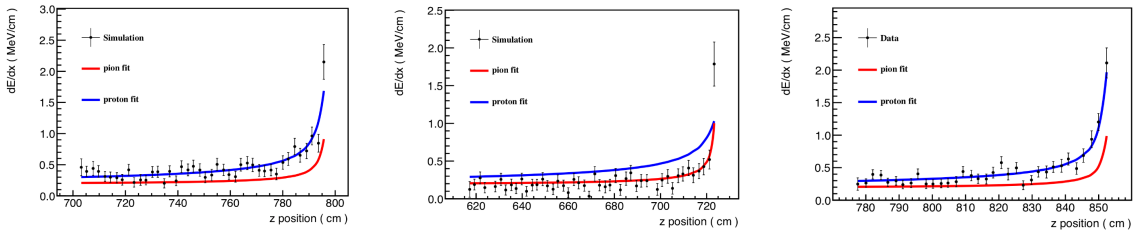
5.7.1 Hadron Energy Reconstruction

First, the hadron reconstruction calculates two estimates of the momentum using the track length. These estimates correspond to either a proton or charged pion hypothesis. The estimates are then refined by looking at the $\frac{dE}{dX}$ profile of the track. An iterative process compares the measured $\frac{dE}{dX}$ profile of the track to a range of calculated $\frac{dE}{dx}$ profiles. Each calculated profile was created using a different momentum. The iterative procedure searches for the best fitted momentum for each particle hypothesis by minimizing the χ^2 between the measured and calculated profiles.

This procedure cannot account for particles which overlap the track near the interaction vertex, or soft nuclear interactions which do not change the direction of the hadron but leave behind deposited energy consistent with low energy particles. To remove these sources of possible misconstruction, the χ^2 minimization is run again with outlier removal techniques. Outlier removal excludes clusters from the $\frac{dE}{dx}$ χ^2 calculation if the energy loss profile for those clusters is inconsistent with a single particle. The two χ^2/ndf calculated with and without the outlier removal are compared. The technique that produces the smaller of the two χ^2/ndf gives the reconstructed momentum for the track.

Finally, if there were any clusters close to the track's end position, then the passive

material corrected energy of the clusters is added to the reconstructed energy of the track. Passive material corrected energy accounts for the "invisible" energy deposited in materials that do not produce scintillation photons.



(a) Simulated Proton (b) Simulated Pion (c) Proton candidate in data

Figure 5-14: $\frac{dE}{dX}$ profiles for reconstructed tracks compared to best fitted Bethe curves. Figures from [94]

5.7.2 Charged Pion Selection

The kinetic energy resolution of a charged pion quantifies how accurately the kinetic energy is reconstructed, assuming the particle is a charged pion. It is defined as:

$$\text{Resolution} = \frac{\text{reconstructed } T_\pi - \text{true } T}{\text{true } T} \tag{5.6}$$

where reconstructed T_π = reconstructed $E_\pi - m_\pi$, and true T is the true kinetic energy of the particle regardless of its identity. For example, true T_p = true $E_p - m_p$.

The kinetic energy resolution in the nuclear targets is poor, primarily due to proton contamination in the sample as well as interacting charged pions. These interacting pions are often misreconstructed due to having a smaller track length than a stopped charged pion, which lose all their energy through ionization and atomic excitation. To improve the accuracy of the reconstructed T_π, selection cuts were developed in

order to identify charged pions with good kinetic energy reconstruction.

In order for a hadron track to be considered a charged pion with good reconstruction, the track must be matched to a Michel electron at the track endpoint. Then, the track must pass a particle identification (PID) score cut based off of a log likelihood ratio (LLR). Finally, the energy of the end nodes of the track must fall within a certain range in order to remove interacting pions and protons. The following sections detail how these selection cuts work, as well as how the values of the cuts were developed.

5.7.3 Michel Match to the Track Endpoint

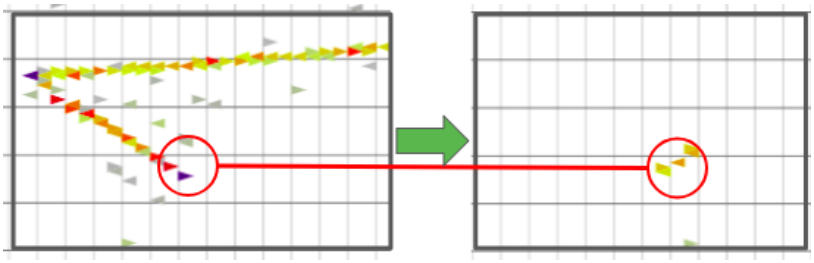


Figure 5-15: Arachne readout display of a simulated pion track (left) with a Michel electron (right) at later time slice. The triangles are hits on strips in the detector. Figure from [71]

Matching Michel electron candidates to hadron tracks relies on the distance between the endpoint of the hadron track and the endpoints of the Michel electron. Further discussion of the Michel electron reconstruction can be found in section 5.6. For each hadron track, the reconstruction calculates the 3D distance between the endpoint of the track and the closest endpoint of each Michel candidate. Since a 3D distance cannot be calculated from 2D information from one view, the matching algorithm excludes 1 view Michel electrons. The matching algorithm will match a

Target	Fitted Michel	2,3 View No Fit Michel
Target 1	11.00	14.50
Target 2	14.00	17.75
Target 3	13.25	18.50
Water Target	13.25	21.50
Target 4	10.25	21.50
Target 5	8.00	14.00
Tracker	9.25	16.25

Table 5.4: Maximum distance cut for Michel match (cm)

Michel electron to a track endpoint if the distance is less than a maximum value. These maximum matching distances are shown in table 5.4.

Initially, multiple hadron tracks may be matched to the same Michel electron. To make sure that there is at most one match per Michel, the hadron track whose endpoint has the shortest distance to the Michel electron will be considered matched. Any other tracks who were originally matched to that Michel electron will be unmatched. Figure 5-16 illustrates the Michel matching process.

The maximum distance at which the Michel is considered matched was determined by studies which compared the T_π resolution of each hadron track to the distance between the Michel and hadron endpoints. Plots in figure 5-17 are row normalized in order to look at where the peak of the resolution is at a particular distance. Originally, the maximum distance was determined by looking for the distance where the T_π resolution no longer peaks at 0. However, this cut was deemed to be too restrictive, as these distance cuts removed too many pions with good reconstruction. Thus, the distance cuts were expanded to include more hadron tracks with good T_π resolution at the cost of including tracks with poor resolution. The effects of the Michel match on T_π resolution can be seen in figure 5-18.

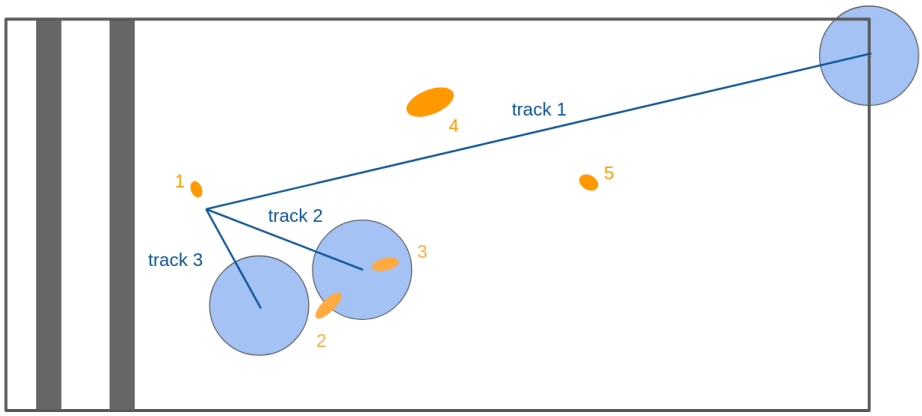
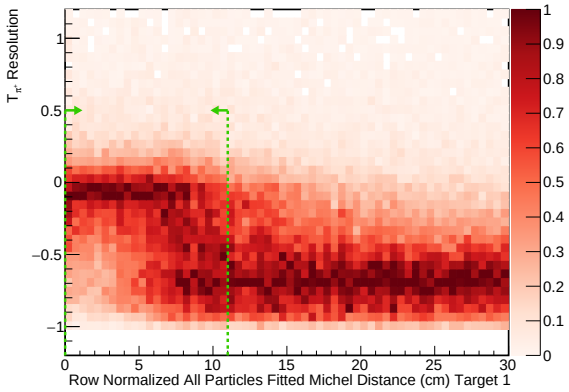


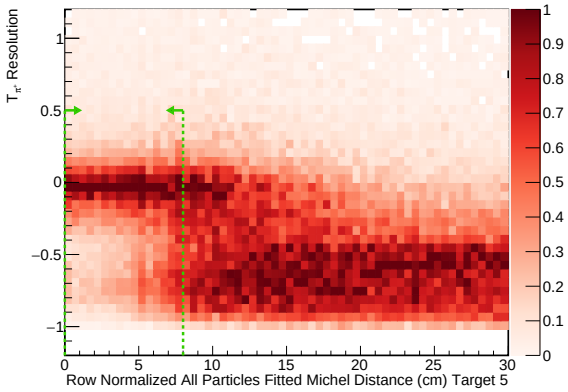
Figure 5-16: Illustration of Michel matching to hadron endpoints. The orange ellipses are Michel candidates. Michel candidates 1,4,5 are not matched to any endpoints, while Michel candidate 2 is not matched to track 2 as candidate 3 is closer. Michel candidate 2 is also not matched to track 3, as it does not fall within the maximum distance cut.

The majority of the selected tracks with poor resolution are made by interacting pions and interacting protons. The interacting pions may have elastically scattered near the end of the track while still decaying into a Michel electron, while interacting protons typically produce a low energy pion near the end of the track that decays into a Michel.

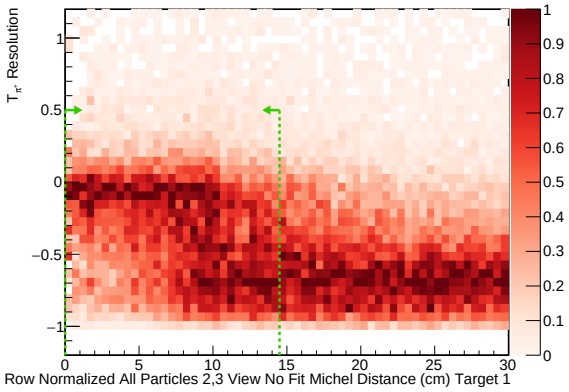
The maximum distance cut depends on the Michel type as well as the nuclear target that the interaction occurred on. Fitted Michels have a smaller distance cut compared to Michel without a fit, as the linear fit provides a more accurate reconstruction on the transverse position of the Michel endpoint. Thus, resolution of estimated distance from the track endpoint to a fitted Michel endpoint is sharper, allowing for a smaller maximum distance. Section 5.6.3 explains the method that finds the Michel endpoint. Also, the maximum distance cuts are larger in the nuclear target region than the tracker. This can be attributed to passive material in a nuclear target obscuring the true endpoint for the Michel electron from the reconstruction. The



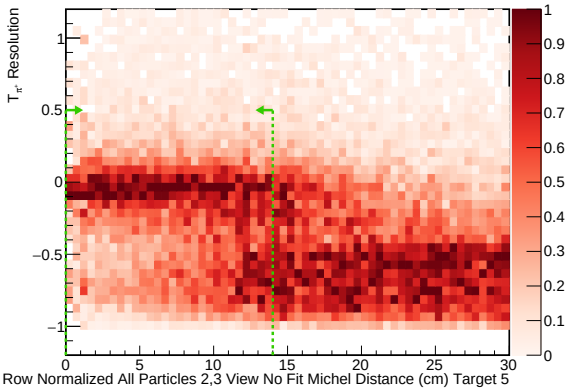
(a) Fitted Michel Target 1



(b) Fitted Michel Target 5

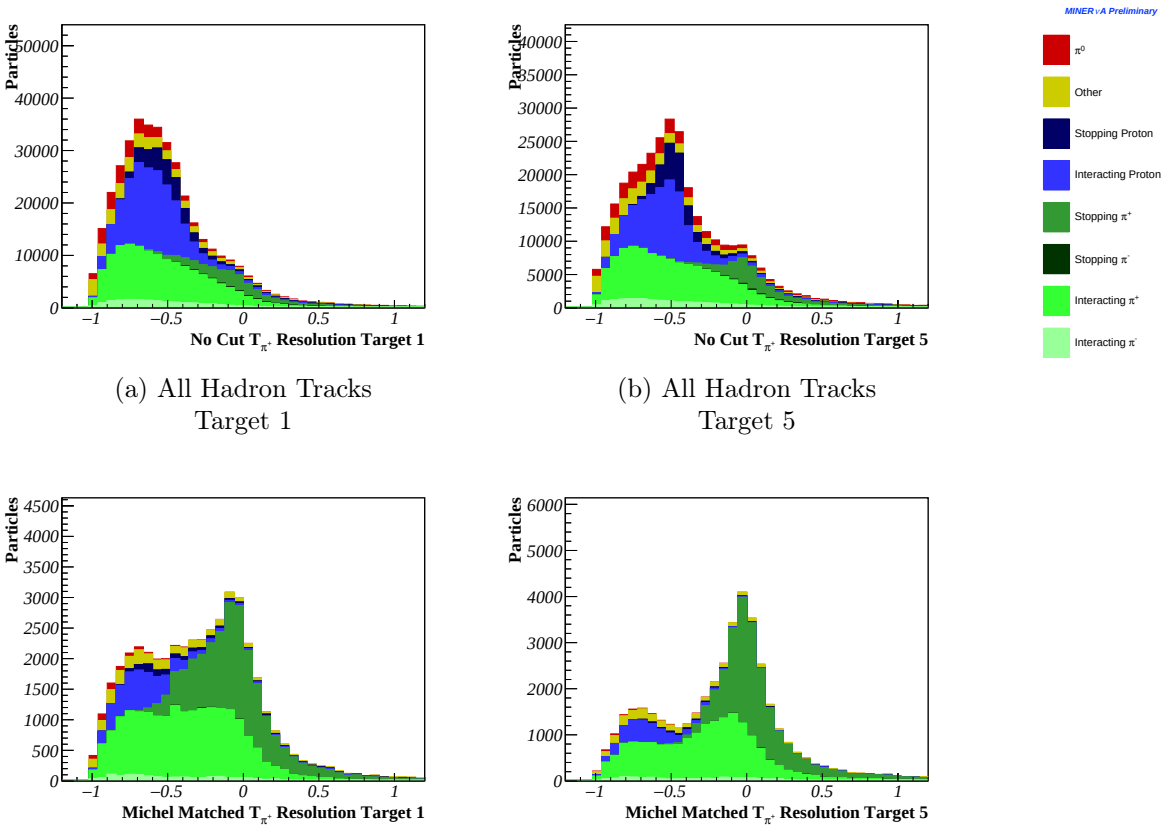


(c) 2,3 View No Fit Michel Target 1



(d) 2,3 View No Fit Michel Target 5

Figure 5-17: Distance from simulated track endpoint to Michel endpoint (cm) versus T_π resolution for fitted Michels (top) and 2,3 view Michels with no fits (bottom). For each bin of distance, the bins in T_π resolution are row normalized so that the maximum resolution bin has a content of 1. Rows are parallel to the y-axis. The green arrows represent the distance cuts used for the Michel match



(a) All Hadron Tracks Target 1

(b) All Hadron Tracks Target 5

(c) Michel Matched Tracks Target 1

(d) Michel Matched Tracks Target 5

Figure 5-18: T_π Resolution for all simulated hadron tracks (top) and simulated Michel matched tracks (bottom). Stopped $\pi^\pm$ are defined as having less than 25 MeV at end of the track, while stopped protons will have less than 100 MeV. The stopped particles do not interact before stopping. Interacting $\pi^\pm$ and protons do not meet the previous definition for stopped pions and protons.

maximum distance cuts are determined by nuclear target due to the geometry of the detector causing the variation between cuts.

5.7.4 Log Likelihood Ratio Particle Identification (PID) Score

The Bethe-Bloch formula for energy loss of charged particles through matter shows that charged pions and protons will have their own characteristic energy loss ($\frac{dE}{dX}$) profiles in the detector [135]. The $\frac{dE}{dX}$ profiles for simulated pions and protons in the MINERvA detector compared to the Bethe curves are shown in 5-14. Based on this difference in energy loss, the reconstruction assigns a particle identification (PID) score to each hadron track. The PID score quantifies whether the track is pion-like or proton-like.

A large number of pion and proton tracks of varying angles and energies were simulated using particle gun Monte Carlo. These tracks serve as a likelihood template for the PID score. When calculating a PID score for a given track, the reconstruction compares each node[2] on the track with the likelihood template. For each node, the likelihood template uses the position of the node along the track and the energy of the node to assign a probability that a proton or pion created the track. The likelihood template calculates the probability by determining the fraction of pion or proton tracks that have a node of the same energy in the same position along the track. The product of all the probabilities forms the likelihood function $\mathcal{L}$.

$$\mathcal{L}(\text{particle}|\text{track}) = \prod_{\text{nodes}} P(E_{\text{node}}|\text{particle}) \tag{5.7}$$

Pion or proton interactions in the detector can shorten the track. Thus, the final track node of an interacting particle may be offset by n nodes from a final node of a stopped particle. To account for these interactions, the likelihoods of all possible offsets are calculated, and the maximum likelihood is used.

Overlapping tracks near the interaction vertex can obscure node energies, which

[2] A track node represents the clusters associated with the track at a given plane.

was found to bias the likelihood function. To limit this effect, the reconstruction searched the first 10 nodes of the track for a drop in energy that is more than 1.94 MeV between two consecutive nodes. The node with the higher energy of the pair is then removed from the calculation.

Finally, the PID score is created by taking the log ratio of the pion and proton likelihood functions. Neyman-Pearson lemma states that the log ratio of the likelihoods is the most power statistical test [136].

$$\begin{aligned}\text{PID Score}_{\text{track}} &= \log\left(\frac{\mathcal{L}(\pi|\text{track})}{\mathcal{L}(p|\text{track})}\right) = \log\left(\frac{\prod_{\text{nodes}} P(E_{\text{node}}|\pi)}{\prod_{\text{nodes}} P(E_{\text{node}}|p)}\right) \\ &= \sum_{\text{nodes}} \log P(E_{\text{node}}|\pi) - \log P(E_{\text{node}}|p) \end{aligned} \tag{5.8}$$

A track with a PID score that is greater than 0 is considered to be pion-like, and it is considered proton-like with a score less than 0. The PID score cut removes protons which may have erroneously matched to a Michel electron. Figure 5-19 shows the distribution of the log likelihood ratio (LLR) scores for Michel matched hadron tracks. A track that has passed the PID score cut and has been matched to a Michel electron will continue to the node energy cuts. A track that only passes the PID score cut is still considered a possible charged pion, but the track will not undergo further selection cuts.

Note that the orientation of the likelihoods in the ratio is arbitrary. The proton likelihood could have been in the numerator instead of the pion likelihood. In that case, a PID score greater than 0 is proton-like. This analysis focuses on pions, thus the ratio shown in equation 5.8 is used.

Node	Target 1	Target 2	Target 3	Water Tar	Target 4	Target 5	Tracker
Node 0+1	4-33	5-27	6-27	6-28	8-28	10-28	6-32
Node 2	1-14	3-13	0-17	0-17	0-10	1-11	2-22
Node 3	0-24	1-21	0-22	0-22	3-9	0-17	0-19
Node 4	2-17	0-20	0-28	0-28	0-10	2-28	0-31
Node 5	2-28	1-32	0-35	0-35	1-18	0-60	0-60

Table 5.5: Node energy cut values for each target (MeV). Node 0 is the last node of the track, node number increases moving towards the interaction vertex

5.7.5 Track End Node Energy

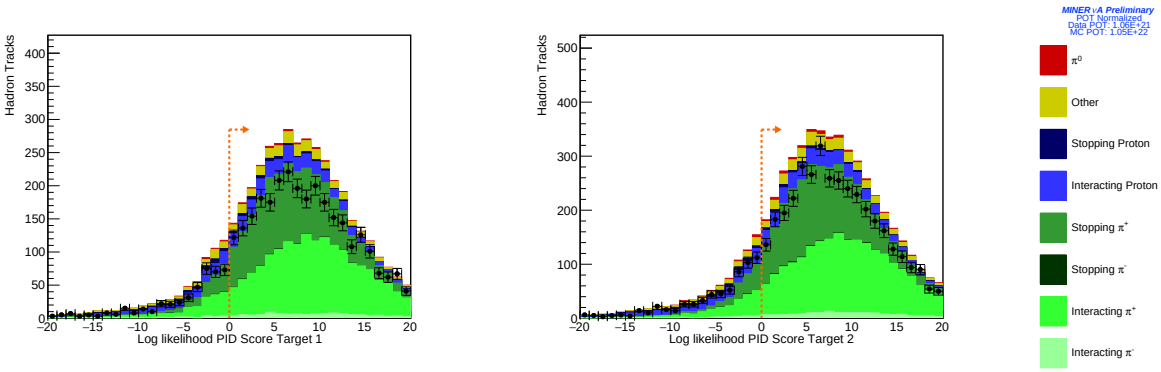
The track end node energy cut uses the energies of the last six nodes of a hadron track. The nodes are numbered starting at 0 at the end of the track, and the node number increases when moving towards the interaction vertex. This method relies on the Bragg peak, which is the sharp increase in the $\frac{dE}{dX}$ profile at the end of a stopped charged particle's track. The lack of a Bragg peak signals that the particle interacted inelastically in the detector. Thus, a minimum node energy cut can remove interacting pions from the sample. Also, the sharpness of the Bragg peak differs between proton and pions, seen in figure 5-14. A maximum node energy cut will continue to remove misreconstructed protons from the sample.

It can be difficult to determine where the particle deposited energy when the particle stopped. It is possible that most of the Bragg peak occurred in the second-to-last node, as the particle just came to a stop in the last node. Thus, the energies of the final two nodes are combined together when making the node energy cuts to make the best determination of the Bragg peak. This combined node is labelled as node 0+1. The energy cut values for each of the nodes are listed in table 5.5

The node energy cuts were determined similarly to the distance cuts of the Michel match. The energy of the given node was plotted against the resolution, and the

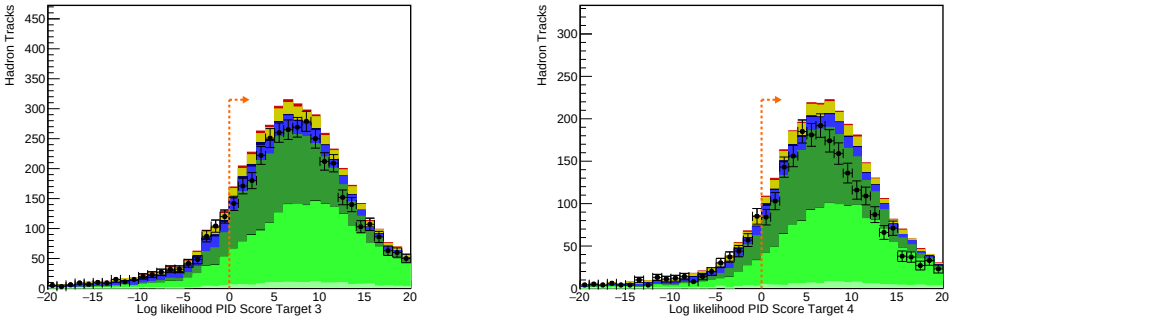
node energy cuts were placed so the maximum of the resolution distribution for each node energy was close to 0. These cuts were estimated conservatively to include more hadron tracks. Figure 5-21 shows the node energy vs row normalized T_π resolution for node 0+1.

If a track has passed all the preceding cuts, it is considered to be a charged pion with good energy reconstruction. Figure 5-23 shows the effect of the node energy cuts on T_π resolution. Figure 5-24 shows the final T_π resolution for all targets.



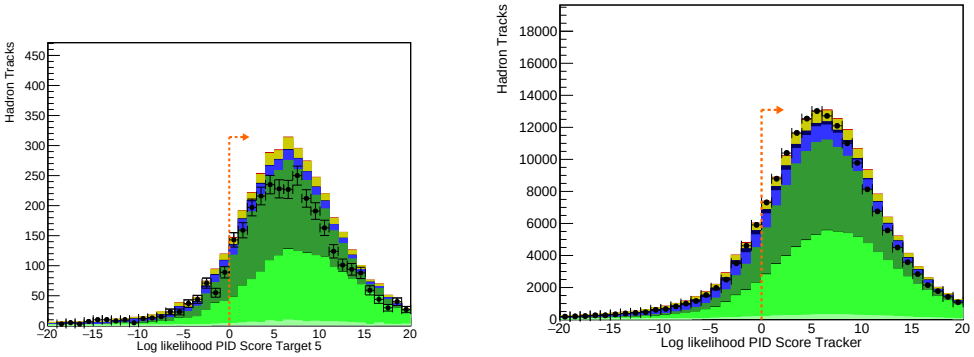
(a) Target 1

(b) Target 2



(c) Target 3

(d) Target 4



(e) Target 5

(f) Tracker

Figure 5-19: Log Likelihood Ratio PID Score for all Michel Matched hadron tracks. Orange arrow is the cut on the LLR Score. Explanation for the categories of particles in figure 5-18.

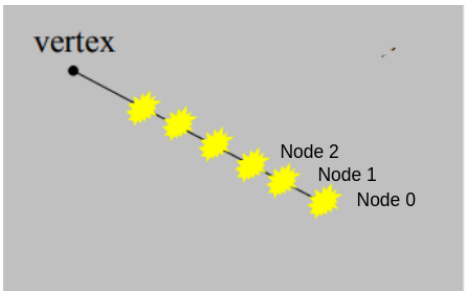
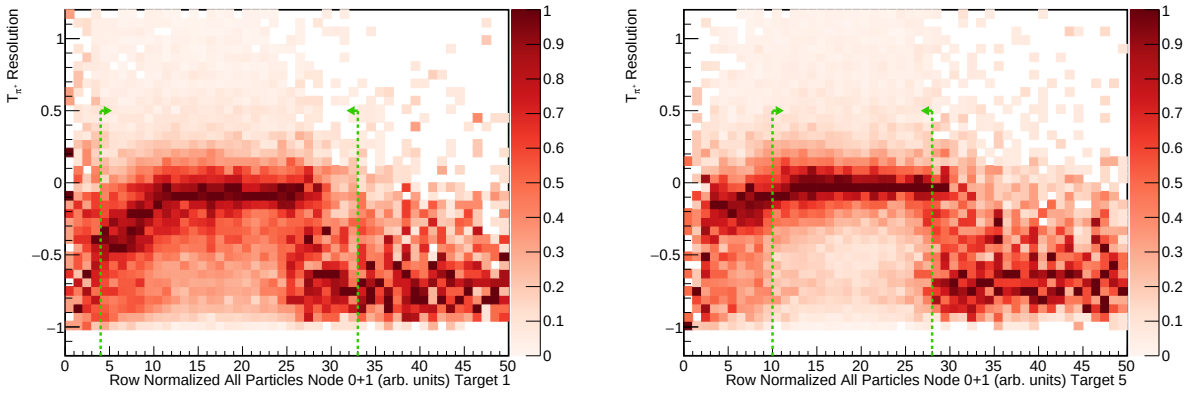


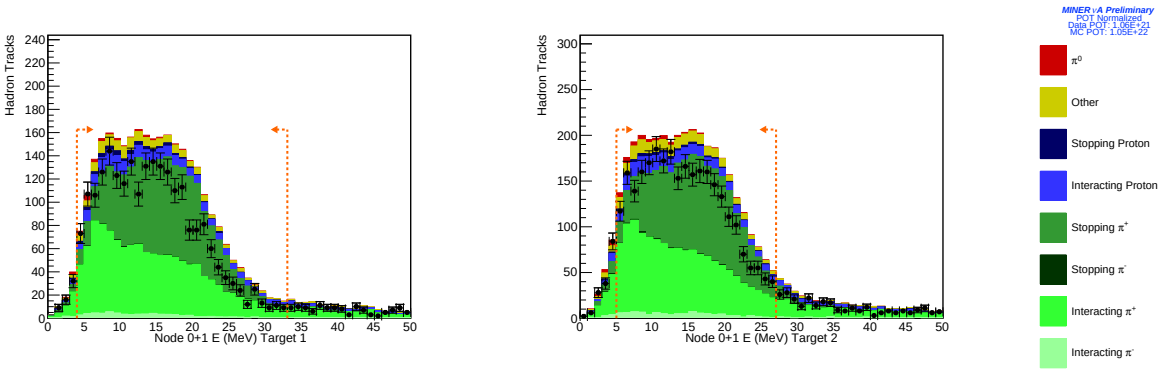
Figure 5-20: Illustration of the nodes of a track. The vertex is upstream of the track. Figure from X. Lu.



(a) Node 0+1 Target 1

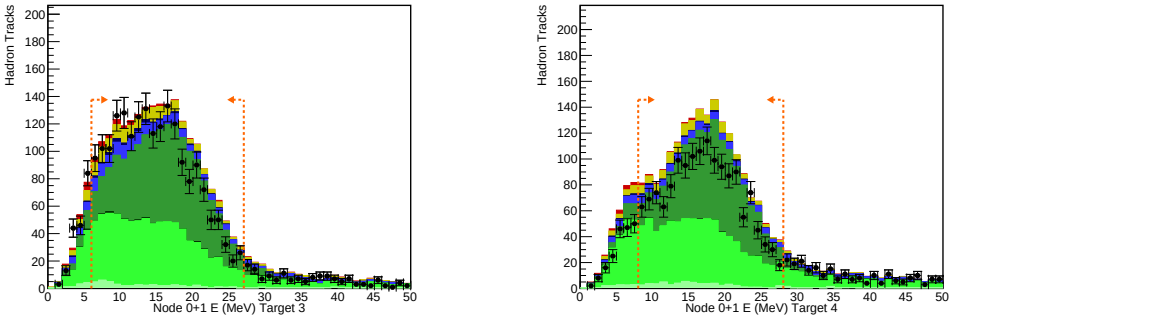
(b) Node 0+1 Target 5

Figure 5-21: Node 0+1 energy versus T_π resolution. For each bin of distance, the bins in T_π resolution are row normalized so that the maximum resolution bin has a content of 1. Rows are parallel to the y-axis. The green arrows represent the node energy cuts



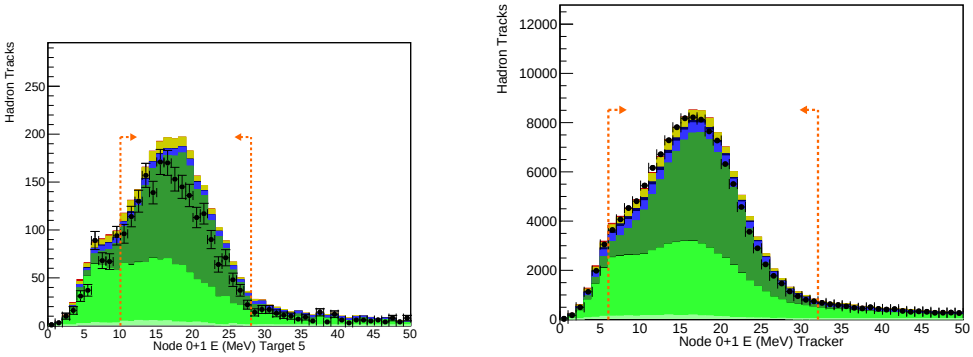
(a) Target 1

(b) Target 2



(c) Target 3

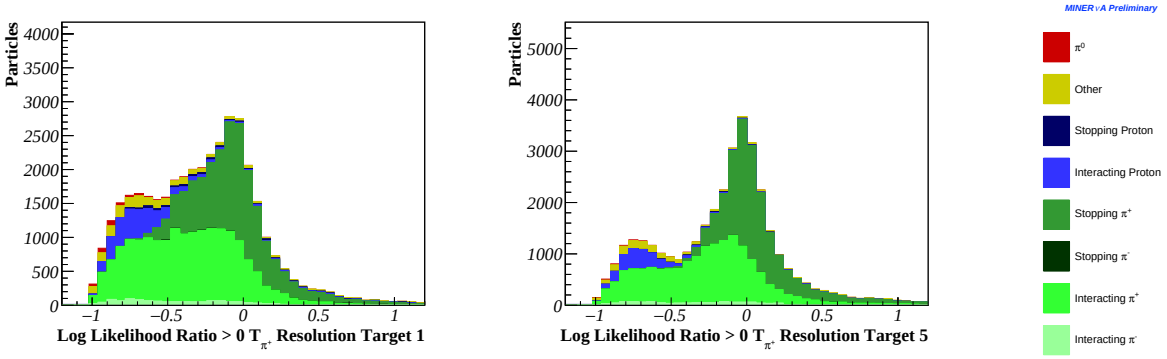
(d) Target 4



(e) Target 5

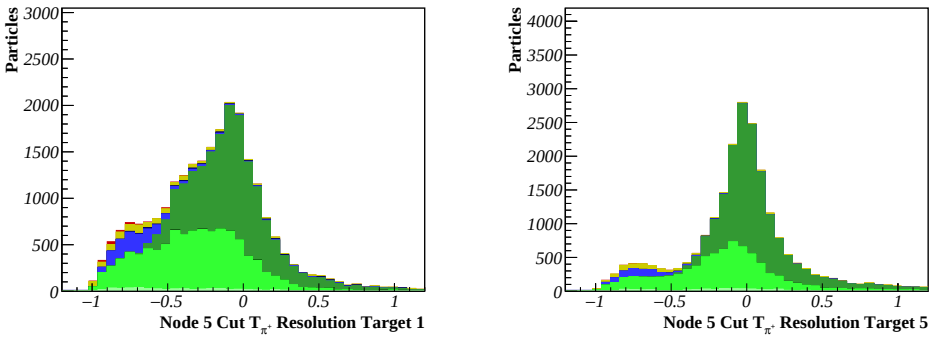
(f) Tracker

Figure 5-22: Node 0+1 energy for Michel Matched hadron tracks that have an LLR Score > 0. Orange arrow are the cuts on the node energy. Explanation for the categories of particles in figure 5-18



(a) Hadron Tracks with No Node Energy Cuts Target 1

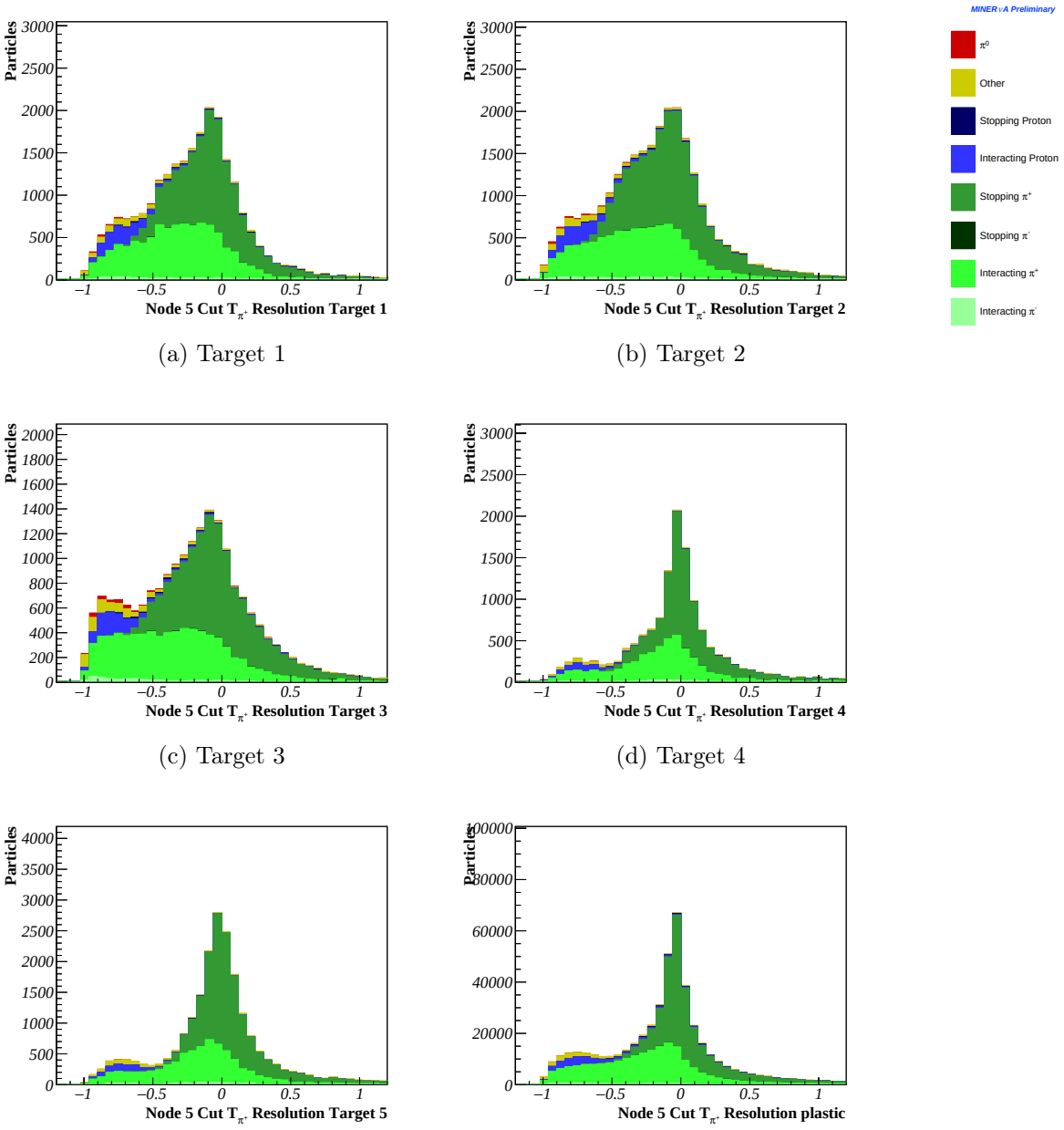
(b) Hadron Tracks with No Node Energy Cuts Target 5



(c) Hadron Tracks Passed All Node Energy Cuts Target 1

(d) Hadron Tracks Passed All Node Energy Cuts Target 5

Figure 5-23: T_π resolution for hadron tracks before the node energy cuts (top) and tracks which passed the cuts (bottom). Both sets of plots refer to Michel matched tracks that passed the log likelihood ratio PID score cut. Explanation for the categories of particles in figure 5-18.



(a) Target 1

(b) Target 2

(c) Target 3

(d) Target 4

(e) Target 5

(f) Tracker

Figure 5-24: The final T_π resolution for hadron tracks which passed all charged pion selection cuts. Explanation for the categories of particles in figure 5-18.

5.8 Hadron Calorimetry

The hadronic recoil energy[3], E_{had}, is the total energy of the final state hadrons in a neutrino interaction. As the name suggests, this is meant to include energy that is not present in the initial state, but rather added to the hadronic system by the neutrino interactions. Therefore, the rest energy of the recoil nucleus and any ejected nucleons from the nucleus are not included in this definition. The rest energy of these stable particles is generally not deposited in the detector, but rather only their kinetic energy that is lost as they travel and scatter through the detector can be detected.

Hadronic recoil energy reconstruction needs to account for hadron energy that is not deposited in the active materials in the detector. This "missing" energy has multiple causes including the passive materials in the detector, particles that escape out the side of the detector, charged particles with energy below the detection threshold, and final state neutral particles that do not produce scintillation light. Hadron calorimetry uses multiple techniques to produce an accurate and precise correction that accounts for the missing energy.

5.8.1 Passive Material Correction

For this analysis, any cluster that is not part of the muon track is considered to be a hadron cluster. This includes the clusters on hadron tracks. Hadron calorimetry starts with the visible energy of every hadron cluster in the event. The visible energy of a cluster represents the ionization energy in each strip of the cluster. The visible energy does not include energy deposited in passive materials. These passive materials include the nuclear targets, the iron and steel in ECAL and HCAL, and the materials in the scintillator planes that do not scintillate light, such as epoxy.

[3]Also referred to as recoil energy E_{recoil}

To correct for the energy deposited in the passive materials, the calorimetry applies a multiplicative constant, c_i, to the visible energy of each cluster based on the MINERvA subdetector i that the cluster is in. These constants also account for the percentage of passive material in a scintillator plane. Summing all of the passive material corrected energy of each non-muon cluster produces the passive material corrected E_{had}, which is labelled as E_{had}^{pmc}.

$$E_{had}^{pmc} = \sum_{i}^{\text{subdetector}} c_i E_{vis,i} \tag{5.9}$$

It should be noted that the passive material correction in the nuclear target region tries to account for the location of the clusters with respect to the nuclear targets. For instance, if hadron clusters are located around the nuclear target 5 but not nuclear target 1, the calorimetry will only apply a correction derived for nuclear target 5 to these clusters. Also, if the hadron clusters were only on one side of target 5, only half of the correction would be applied. Further details on the passive material correction can be found in [137].

5.8.2 Calorimetric Spline Correction

Most neutrino interactions still require an additional correction to the passive material corrected E_{had}. This additional correction needs to account for any missing kinetic energy of stable hadrons or total energy of unstable hadrons. The sources of missing energy described above include particles which exit out the side of the detector, most notably final state neutral particles which do not lose energy due to ionization. This latter effect is important for this analysis, as pion production can produce final state neutrons whose kinetic energy cannot be reconstructed. Also, this additional

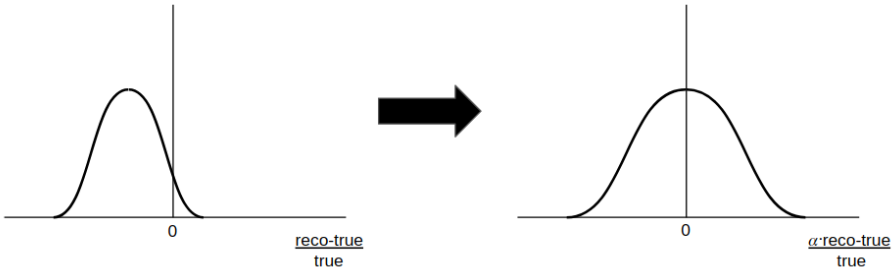


Figure 5-25: The energy resolution of events in given energy range of E_{had}^{pmc} are fitted to a Gaussian distribution (left). When applying the multiplicative factor α to the E_{had}^{pmc}, the energy resolution will center at zero (right).

correction needs to be energy dependent, as higher energy processes can produce more neutral particles in the final state or create higher energy particles which leave the detector. There are two different calorimetric corrections developed to account for the missing energy: calorimetric splice correction and calorimetric additive correction.

The calorimetric spline correction applies a multiplicative factor α to the reconstructed E_{had}^{pmc}. This multiplicative factor is dependent on the reconstructed E_{had}^{pmc}. To determine this factor, the correction finds the energy resolution $(\frac{reco-true}{true})$ of simulated events within a range of E_{had}^{pmc}. The distribution of the energy resolution is then fitted to a Gaussian distribution. The multiplicative factor α for this energy range is the factor that, when applied to the reconstructed E_{had}^{pmc} in this energy range, will center the resolution at zero. Figure 5-25 shows the effect of the multiplicative factor. This process is repeated in multiple energy ranges of E_{had}^{pmc} to extract the multiplicative factors for different values of E_{had}^{pmc}. Thus, the calorimetric spline corrected E_{had} is defined as

$$\text{Calorimetric Spline Corrected } E_{had} = \alpha\,(E_{had}^{pmc})\,E_{had}^{pmc} \tag{5.10}$$

Any group of events can be used to create a calorimetric spline, thus splines can be tailored for different analyses. A calorimetric spline was developed for this analysis, using events which passed all selection cuts except for $W_{exp} < 1.4$ GeV/c^2 cut, as the calculation of W_{exp} requires E_{had}. Section 6.2.1 gives the definition of W_{exp} and section 6.3 explains the $W_{exp} < 1.4$ GeV/c^2 cut. This analysis specific calorimetric spline was given the label "NukeCCPion".

There are some drawbacks to the calorimetric spline correction. For one, the calorimetric spline correction is fully dependent on the models in the GENIE event generator, as the correction fully relies on simulation to predict the number and energy of neutral particles in the final state. Also, each energy range requires enough events in order to fit a Gaussian distribution on the energy resolution, which can be difficult in bins of lower energy. Finally, applying a multiplicative factor to E_{had}^{pmc} increases the width of the energy resolution, which reduces the precision of the E_{had} reconstruction.

5.8.3 Calorimetric Additive Correction

The calorimetric spline correction only considers the passive material corrected energy of all hadron clusters in the event when making a correction; it does not use the energy estimated by other methods, like the energy of the pion found by the $\frac{dE}{dX}$ method, as explained in section 5.7.1. But if the pion has good energy reconstruction, then the pion energy resolution has a small width and it is centered at zero. For events with one charged pion track with good energy reconstruction, this part of the hadronic recoil energy reconstruction is more accurate then the reconstruction by calorimetry alone. Thus, for these events, only the hadronic recoil energy without energy from the pion track, $E_{had,no\ \pi}$, needs a correction.

The passive material corrected $E_{had,no\ \pi}$ subtracts the passive material corrected

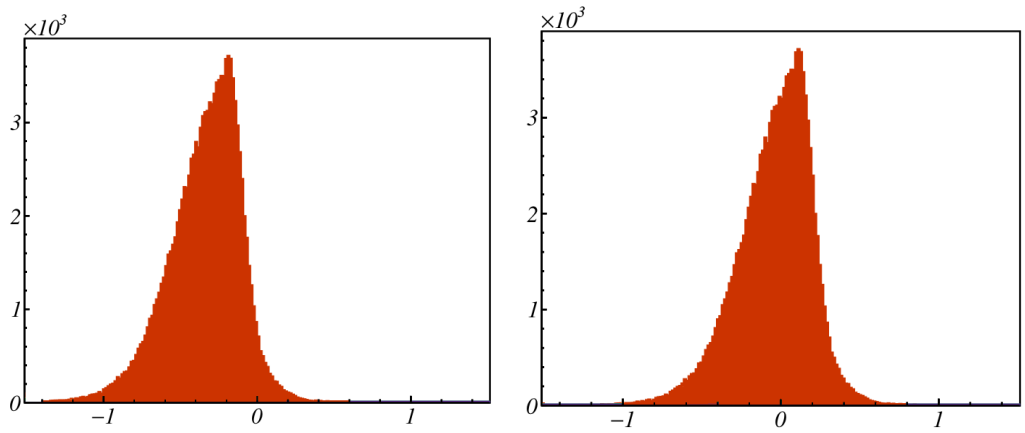


Figure 5-26: Distributions of true $E_{had,no\ \pi}$ - reconstructed $E^{pmc}_{had,no\ \pi}$ (GeV) for scintillator events with reconstructed $E^{pmc}_{had,no\ \pi} \in [0.5, 0.7]$ GeV. The plots on the left is before the additive correction, while the plot on the right is after the correction.

energy of the clusters associated with the charged pion track with good energy reconstruction from the total passive material corrected E_{had}. Equation 5.11 defines the passive material corrected $E_{had,no\ \pi}$.

$$E^{pmc}_{had,no\ \pi} = E^{pmc}_{had} - E^{pmc}_{had,\pi} \tag{5.11}$$

Instead of multiplying by an energy dependent factor to correct $E^{pmc}_{had,no\ \pi}$, the calorimetric additive correction adds an energy dependent correction β to $E^{pmc}_{had,no\ \pi}$. To develop this additive correction, the difference between true $E_{had,no\ \pi}$ and the reconstructed $E^{pmc}_{had,no\ \pi}$ was calculated for simulated events in a given range of reconstructed $E^{pmc}_{had,no\ \pi}$. The offset of the peak of the distribution of the differences from zero is the additive correction β to $E^{pmc}_{had,no\ \pi}$ for events within the $E^{pmc}_{had,no\ \pi}$ range. Figure 5-26 shows an example of the additive correction, while figure 5-27 show the corrections for different ranges in energy. The additive corrections were calculated by target and material, and it was found that the corrections were more dependent on the target.

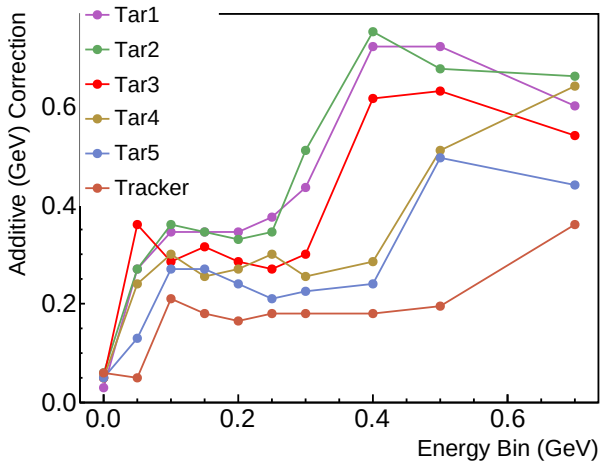


Figure 5-27: The additive corrections β as a function of energy and target. The additive corrections are binned in $E^{pmc}_{had,no\ \pi} = [0.0, 0.05, 0.1, 0.15, 0.2, 0.25, 0.3, 0.4, 0.5, 0.7, 1.0]$ GeV. Note that the lines in the plot are only to guide the eye.

The corrections were then averaged by target to help remove stochastic behavior.

One feature of these corrections are the "shelves" between 0-0.1 GeV and 0.1-0.25 GeV. These shelves represent hadronic recoil energy ranges where it is more likely to produce higher energy pions than it is to excite nucleons out of the nucleus.

It should be noted that the calorimetric additive correction has the benefit that it will not increase the width of the energy resolution, and it doesn't require high statistics in each bin for a Gaussian fit. However, the calorimetric additive correction is still dependent on the model prediction of neutral particles in the final state.

After the additive correction β is applied to $E^{pmc}_{had,no\ \pi}$, this is added to the total pion energy reconstructed by the $\frac{dE}{dX}$ method to estimate the total hadronic recoil energy, as shown in equation 5.12. It should be noted that the calorimetric additive correction should not be applied to coherent pion production, described fully in section

1.3.4, as there should be no final state hadrons in the event besides the final state pion. To limit the correction to incoherent pion production, any event with $|t| = (p_\nu - p_\mu - p_\pi)^2 < 0.125$ GeV^2 will not receive an additive correction.

$$E_{had} = T_\pi + m_\pi + E^{pmc}_{had,no\ \pi} + \beta\left(E^{pmc}_{had,no\ \pi}\right) \tag{5.12}$$

5.8.4 Hadron Calorimetry Used in this Analysis

For this analysis, the calorimetric additive correction is only applied for events with reconstructed $E^{pmc}_{had,no\ \pi}$ between 0 and 1 GeV. Beyond 1 GeV, there are additional modes of production that prevent an accurate description of the hadronic recoil energy using the additive correction method. Thus, for events with $E^{pmc}_{had,no\ \pi} > 1$ GeV, the total hadronic recoil energy is found using the calorimetric spline method with the "NukeCCPion" spline.

Chapter 6

Analysis

6.1 Signal Definition

This analysis focuses on muon neutrino charged current single charged pion production on various target materials in the MINERvA detector. These materials include carbon, iron, lead, water, and scintillator.

This analysis has multiple signal definitions, each of which is defined by the material that neutrino interacts with. For instance, the carbon signal definition requires that the neutrino interacts with carbon in a nuclear target, while the scintillator signal requires that the neutrino interacts with scintillator in the tracker region. The material that the neutrino is required to interact with is labelled as the "signal target".

All signal definitions require that a muon neutrino interacts via charged current in a signal target. This interaction must produce one muon and one positively charged pion, and it can knock out any number of nucleons from the nucleus, however, no other mesons may be present in the final state. The GENIE event generator simulates nuclear deexcitation of oxygen nuclei. The deexcitation produces photons whose

energy $E_\gamma < 10$ MeV. Therefore, the signal definition allows for final state photons in the event with energy < 10 MeV, but no other photons. The invariant hadronic mass W_{exp} of the interaction, defined later in section 6.2.1, must not exceed 1.4 GeV/c^2. As mentioned in section 1.3.2, both the resonant pion production model and DIS model predict the same nonresonant pion events at higher W; therefore limiting the $W_{exp} < 1.4$ GeV/c^2 reduces the number of double counted nonresonant pion events. In events with W_{exp} below this cut, decays of the $\Delta(1232)$ baryon resonance are expected to produce the majority of pions.

The geometry and resolution of the MINERvA and MINOS detectors limit the kinematic phase space that can be measured by this analysis. For muon reconstruction, this analysis requires that the muon exits the back of the MINERvA detector and enters the MINOS Near Detector. This restricts the angle of the muon, $\theta_\mu < 13^\circ$ from the beam axis, as muons created in the nuclear target region at higher θ_μ are too unlikely to be reconstructed in MINOS to permit a reliable measurement. Also, muon momentum must be between $1.5 < p_\mu < 20$ GeV/c. Muons created in the nuclear target region with $p_\mu < 1.5$ GeV/c do not have enough momentum to reach the MINOS Near Detector. The upper limit of p_μ at 20 GeV/c is set because the flux simulation at neutrino energies above 20 GeV is poorly constrained compared to the lower energy neutrinos that make up most of the flux. Finally, the kinetic energy of the charged pion must be between $35 < T_\pi < 350$ MeV. The lower limit of T_π at 35 MeV is the kinetic energy threshold for pions to pass through five planes, which is required by the short trackers described in section 5.3.2. Pions with a kinetic energy above 350 MeV will exit the back of the MINERvA detector if they do not interact inelastically. Therefore, these pions will not be identified by a Michel electron from the decay at the end of its path, or that decay will happen after an inelastic interaction which will cause the pion energy to be badly underestimated. In either case, events

with pions with kinetic energy above 350 MeV cannot be reliably characterized.

6.2 Differential Cross Section Overview

The flux integrated differential cross section is expressed in Equation 6.1, and the input variables in this equation are explained in Table 6.1. Most of these input variables are measured in different steps of the cross section extraction process. The following sections in this chapter described the steps of the cross section extraction in detail.

$$\frac{d\sigma}{dX_i} = \frac{\sum_j U_{ij}(N_j^{observed} - N_j^{background})}{\epsilon_i (T\Phi)\Delta X_i} \tag{6.1}$$

Variable	Definition
X_i	True bin i of variable X
ΔX_i	Width of true bin i of variable X
$N_i^{observed}$	Number of selected events observed in reconstructed bin j. Section 6.3 discusses the event selection process.
$N_i^{background}$	Number of simulated background events in reconstructed bin j. Section 6.4 describes the backgrounds to this analysis and their constraints. Section 6.5 details the background subtraction.
U_{ij}	Simulated unfolding matrix which maps reconstructed bin j onto true bin i. Section 6.6 describes the unfolding process.
ϵ_i	Simulated efficiency of selecting signal events in true bin i, as well as the acceptance of detecting signal events in true bin i. Section 6.7 describes the efficiency correction.
T	Number of targets within the fiducial volume
Φ	Integrated neutrino flux. Section 2.2 discusses the prediction of the neutrino flux.

Table 6.1: Definitions of the variables measured in this analysis

6.2.1 Analysis Variables

This analysis has measured differential cross sections in eight kinematic variables, which are listed in table 6.2.

Variable	Definition
p_μ	Magnitude of the three-vector muon momentum
θ_μ	Muon polar angle with respect to the direction of the neutrino beam
$p_{\mu,\|\|} = p_\mu \cos\theta_\mu$	Longitudinal muon momentum with respect to the direction of the neutrino beam
$p_{\mu,T} = p_\mu \sin\theta_\mu$	Transverse muon momentum with respect to the direction of the neutrino beam
Q^2	Four momentum transfer from the neutrino. Further discussion below
W_{exp}	Experimental invariant hadronic mass calculated using the final state kinematics. Further dicussion below
T_π	Pion kinetic energy
θ_π	Pion polar angle with respect to the direction of the neutrino beam

Table 6.2: Definitions of the variables measured in this analysis

6.2.1.1 Comments on reconstructed Q^2 and W_{exp}

The kinematic variable Q^2 is the negative of the four momentum transfer squared, and the variable W is the invariant mass of the hadronic system produced in the recoil of the neutrino interaction. As seen in figure 1.3, conservation of energy and momentum allows both quantities to be derived from the four-vector q carried by the W boson in the event. In turn, that q can be derived either from measurements of the lepton side or the hadron side of the interaction. However, because the incoming neutrino energy is unknown and because some details of the hadronic recoil are difficult or

impossible to measure in the detector, the measurements we make use elements of both the lepton and the recoil. This analysis defines Q^2 using the kinematics of lepton system, as shown in equation 6.2.

$$Q^2 = 2E_\nu(E_\mu - p_\mu \cos\theta_\mu) \tag{6.2}$$

However, the neutrino energy E_ν cannot be directly measured. Instead, it is estimated by summing the energy of the muon E_μ and the hadronic recoil energy E_{had}, which is discussed further in section 5.8.

$$E_\nu = E_\mu + E_{had} \tag{6.3}$$

The invariant hadronic mass W is defined as

$$W^2 = (p_\nu + p_N - p_\mu)^2 \tag{6.4}$$

p_ν, p_N, and p_μ are the four momenta of the neutrino, nucleon, and muon, respectively. This definition is used in the GENIE event generator when determining the kinematics of the initial neutrino interaction, before Final State Interactions (FSI). However, this W cannot be measured as the four momentum of the nucleon p_N cannot be measured. The presence of FSI also prevents the measurement of W. The experimental invariant hadronic mass W_{exp} is calculated using the leptonic variables and assumes that the nucleon is at rest in the laboratory frame. Therefore, the four momentum of the

nucleon $p_N = m_N$, and equation 6.4 reduces to:

$$\begin{aligned} W_{exp}^2 &= 2m_N(E_\nu - E_\mu) - Q^2 + m_N^2 \\ &= 2m_N E_{had} - Q^2 + m_N^2 \end{aligned} \tag{6.5}$$

W_{exp} allows for comparisons between different experiments as it is directly observable. When discussing about the true value of W_{exp}, the true kinematics of the final state particles are used to calculate true W_{exp}.

6.3 Event Selection

A series of cuts select a sample of neutrino events which match the signal definition based on their reconstructed properties. These cuts have been developed using multiple criteria. One of these criteria is the need to select signal events while removing events which are not signal, which are known as background. The selection cuts should maximize the signal purity, or the fraction of signal events in the sample, while maximizing the signal selection efficiency. The selection cuts also have the goal of selecting events whose kinematics can be reconstructed, and minimizing systematic uncertainties due to the detector reconstruction or modeling of the signal.

Events which pass all of the selection cuts are placed into histograms, each of which is binned in an analysis variable, or a quantity in which a differential cross-section will be measured. A simulated event receives a weight as described in section 4.5, and it is determined whether this simulated event is signal or background. These histograms are passed along to the next step of the cross section extraction process. Figure 6-6 shows an example of these histograms.

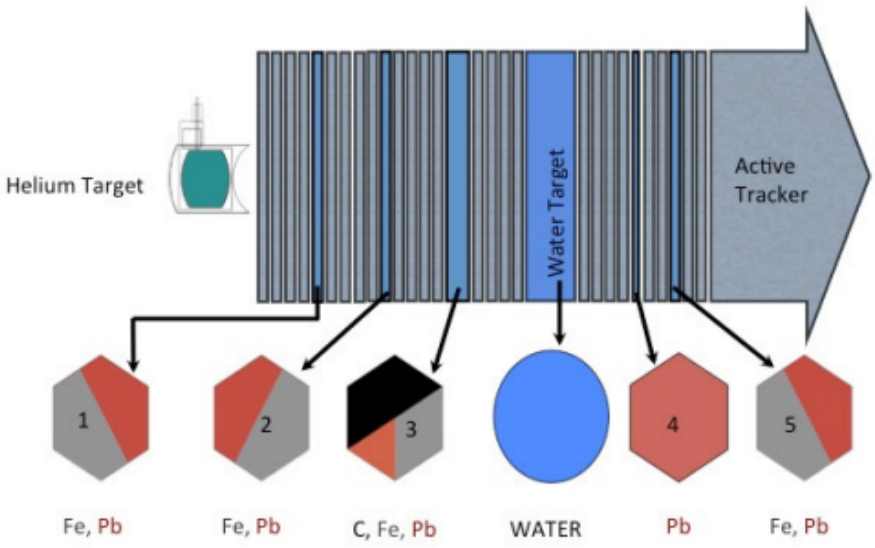


Figure 6-1: Diagram of the nuclear target region with the transverse shapes of the targets

6.3.1 Interaction Vertex Selection

For a given signal target, the position of the interaction vertex of the event must be within the specified fiducial volume that contains that signal target. Section 5.4 explains the reconstruction of the position of the interaction vertex. The fiducial volumes of the nuclear targets lie within different z ranges, which are listed in table 6.3. The transverse positions of the nuclear target materials and the layout of the nuclear target regions can be seen in figure 6-1. The fiducial volume of each nuclear targets has an apothem of 850 mm. Requiring that the interaction vertex is within the 850 mm apothem limits events which occurred outside of the inner detector from entering the sample. The nuclear target region is further explained in section 3.2.2. The bounds of the z range of the active tracking region, or tracker, limit events which occurred on nuclear target 5 or the downstream ECAL.

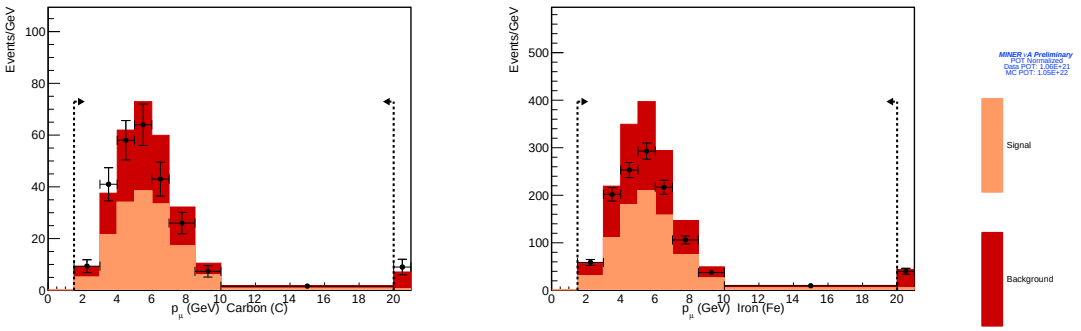
Target	Event Selection Cuts (mm)	True Target Range (mm)
Target 1 (Pb/Fe)	4467.19-4510.09	4469.441-4495.191
Target 2 (Pb/Fe)	4688.26-4731.16	4689.449-4715.199
Target 3 C	4892.41-4972.00	4907.77-4984.07
Target 3 (Pb/Fe)	4892.41-4972.00	4907.82-4933.57
Water Target	5200.00-5420.00	5200.00-5420.00
Target 4 Pb	5630.80-5664.80	5637.68-5645.68
Target 5 (Pb/Fe)	5756.71-5801.24	5769.82-5782.82
Tracker	5991.29-8400.91	5991.29 - 8408.91

Table 6.3: Z ranges of the nuclear target fiducial volume. The z coordinate is defined as the longitudinal axis of the MINERvA detector, further explained in section 3.1. Interaction vertices which fall in the event selection range are considered to have occurred on that nuclear target. True target ranges are the true position of the nuclear targets, and are used to define signal.

6.3.2 Muon Selection

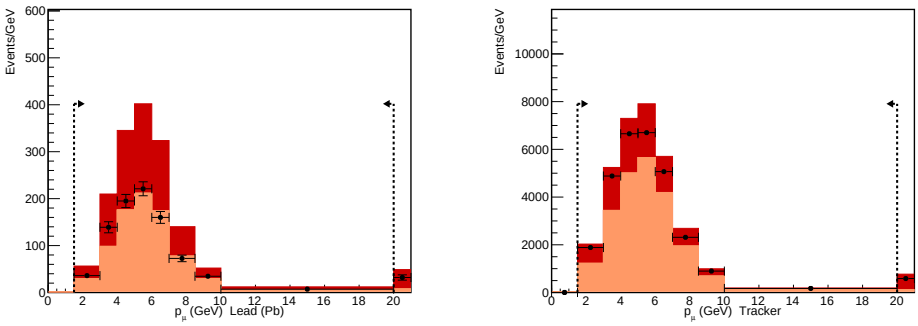
If the interaction vertex occurs on the correct target, the analysis then looks for a reconstructed muon track which can be matched to a track in MINOS. Reconstruction considers the longest track coming from the interaction vertex to be the muon track, and section 5.5 details how muon charge and momentum are reconstructed. To ensure that ν_μ CC events are selected, the muon track in the MINOS Near Detector must have curvature in the magnetic field of MINOS that is consistent with a negative electric charge.

Due to the restrictions placed on the kinematic phase space by the MINERvA detector, which further explained in the signal definition in section 6.1, the reconstructed muon momentum must be between $1.5 \leq p_\mu \leq 20$ GeV/c, and the reconstructed muon angle with respect to the neutrino beam must be $\theta_\mu < 13°$. Figure 6-2 shows the distribution of events that have passed all selection cuts in reconstructed p_μ.



(a) Carbon

(b) Iron



(c) Lead

(d) Scintillator

Figure 6-2: Reconstructed p_μ distribution including events with $p_\mu < 1.5$ GeV/c and $p_\mu > 20$ GeV/c with signal (orange) and background (red). These events have passed all of the selection cuts.

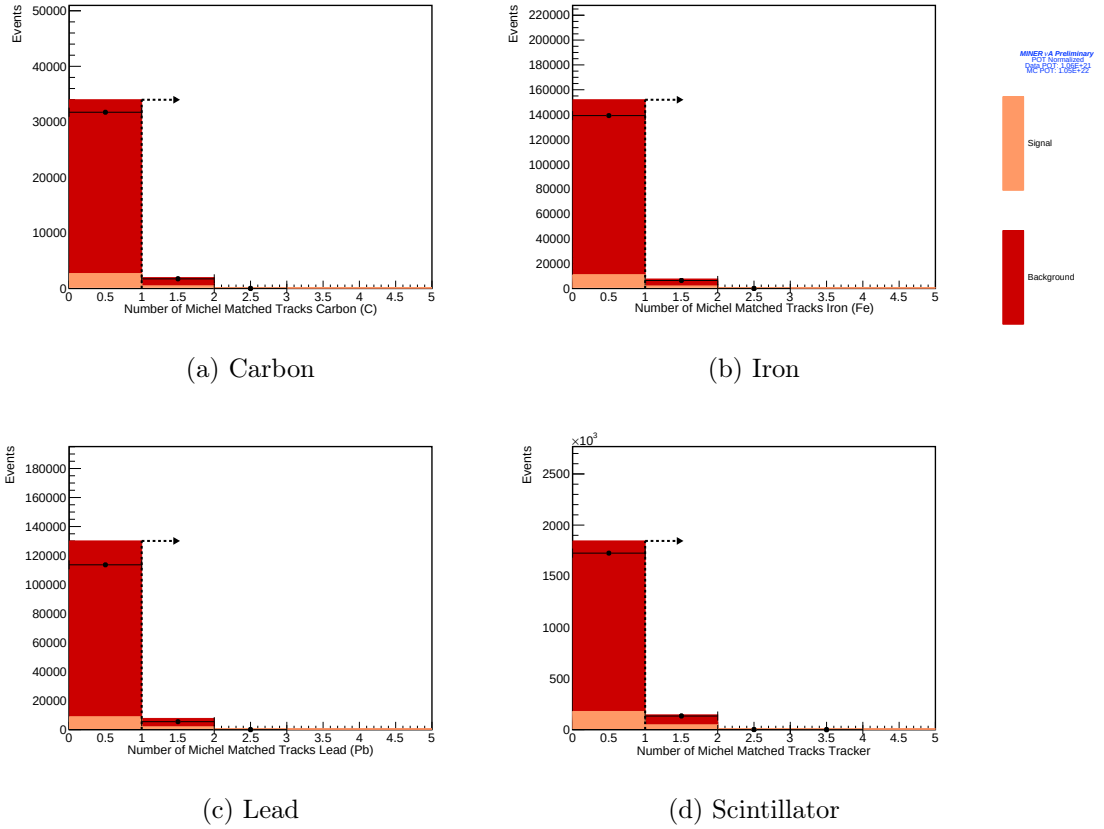
Target	Δ Purity	Cut Efficiency
Carbon (C)	10.05	13.20
Water (H_2O)	7.43	14.79
Iron (Fe)	12.59	13.66
Lead (Pb)	12.4	16.27
Tracker	14.63	20.12

Table 6.4: Increase in signal purity and cut efficiency (%) of events having ≥ 1 Michel matched hadron tracks

6.3.3 Charged Pion Selection

After identifying a MINOS matched muon track, the analysis searches the remaining tracks, which it considers to be hadron tracks, to identify charged pions with good energy reconstruction. To be considered to be a charged pion with good energy reconstruct, the endpoint of the hadron track must first be matched with Michel electron. Section 5.7.3 explains the method that matches a Michel electron to the endpoint of a hadron track. Figure 6-3 shows the number of hadron tracks matched to Michel electrons per event. Table 6.4 shows the increase in signal purity and cut efficiency on each material for having ≥ 1 hadron tracks matched to a Michel electron. Cut efficiency is the number of signal events present after the selection cut over the number of signal events before the selection cut.

Next, the log likelihood ratio (LLR) score is calculated for every hadron track. For hadron tracks with a Michel match, the analysis selects tracks which have a LLR score greater than 0. An LLR score means that the track behaves more like a pion than a proton. The log likelihood ratio score is explained in section 5.7.4. Figure 5-19 shows the LLR score distributions for all hadron tracks with a Michel match. Table 6.3.3 shows the increase in purity and cut efficiency on each material for having ≥ 1 Michel matched hadron tracks with a LLR score > 0. For each Michel matched hadron track



(a) Carbon

(b) Iron

(c) Lead

(d) Scintillator

Figure 6-3: Number of hadron tracks matched to a Michel electron per event by signal (orange) and background (red). These events have passed the interaction vertex and muon selection cuts.

Target	Δ Purity	Cut Efficiency
Carbon (C)	1.11	88.36
Water (H_2O)	1.4	91.95
Iron (Fe)	1.51	89.98
Lead (Pb)	1.5	89.97
Tracker	1.89	88.03

Table 6.5: Increase in signal purity and cut efficiency (%) of events having ≥ 1 Michel matched hadron track with LLR Score > 0

Target	Δ Purity	Cut Efficiency
Carbon (C)	9.75	69.47
Water (H_2O)	4.6	88.29
Iron (Fe)	7.6	79.21
Lead (Pb)	7.52	77.48
Tracker	5.13	87.71

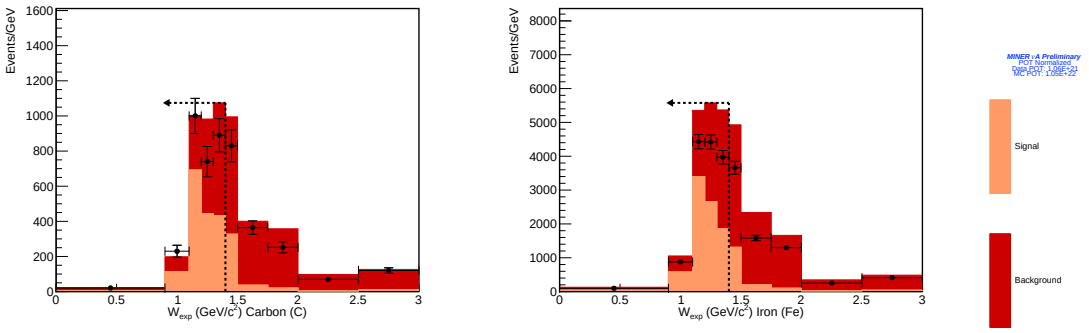
Table 6.6: Increase in signal purity and cut efficiency (%) of events having 1 charged pion track with good energy reconstruction

with LLR score > 0, the analysis sees if the hadron track passes the track end node energy cuts, which is covered thoroughly in section 5.7.5. If a hadron track passes these cuts, it is labelled a charged pion track with good energy reconstruction.

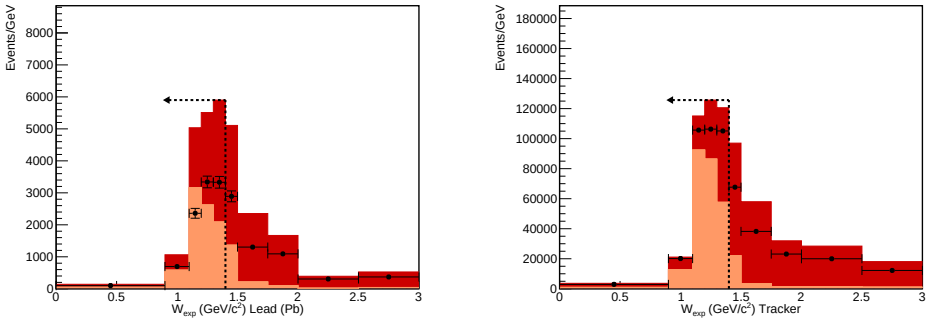
The event must have only one charged pion track with good energy reconstruction. The cut efficiency and increase in purity for each material shown in table 6.6 refer to events with only one track that passed all the selection cuts looking for a charged pion with good energy reconstruction. Finally, the reconstructed T_π of the selected charged pion track must be between $35 < T_\pi < 350$ MeV. Every hadron track whose log likelihood ratio which favors the pion hypothesis is labelled as a possible charged pion track. Only one track is allowed to have a LLR score > 0. This track must be the charged pion track with good energy reconstruction in the event.

6.3.4 Invariant Hadronic Mass W_{exp} Selection

The invariant hadronic mass W_{exp}, as defined in section 6.2.1, is reconstructed using the Q^2 derived from the lepton kinematics as well as the E_{had} estimated using an additive correction, further explained in section 5.8. The invariant hadronic mass must be less than 1.4 GeV/c^2. This helps remove events with an undetected pion in addition to the reconstructed pion candidate. Figure 6-4 shows the reconstructed



(a) Carbon (b) Iron



(c) Lead (d) Scintillator

Figure 6-4: Reconstructed W_{exp} distribution of events which have 1 charged pion track with good energy reconstruction with signal (orange) and background (red)

W_{exp} distribution before the cut. Table 6.7 shows the increase in signal purity and cut efficiency of the reconstructed $W_{exp} < 1.4$ GeV/c^2 cut.

6.3.5 Isolated Prong Selection

An isolated prong is a collection of clusters in the same time slice as the interaction which is not associated with the interaction vertex and its related tracks. These isolated prongs are a signature of neutral pions in MINERvA, as neutral pions decay

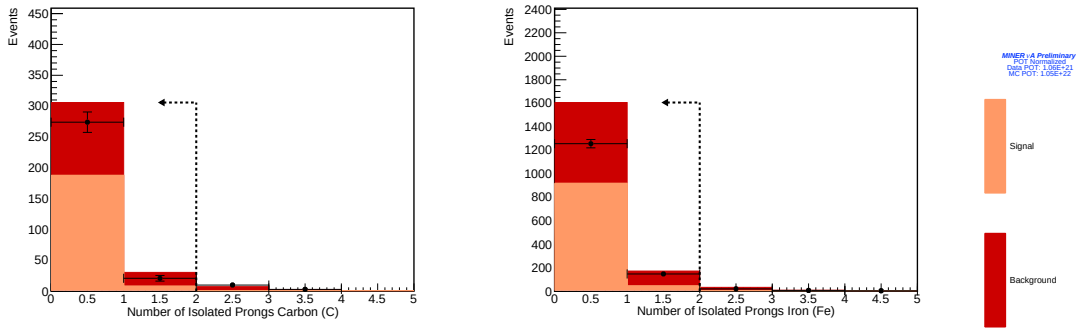
Target	Δ Purity	Cut Efficiency
Carbon (C)	22.55	74.98
Water (H_2O)	16.27	76.07
Iron (Fe)	20.08	76.97
Lead (Pb)	19.53	76.50
Tracker	32.13	83.35

Table 6.7: Increase in signal purity and cut efficiency (%) of the reconstructed $W_{exp} < 1.4$ GeV/c^2 cut

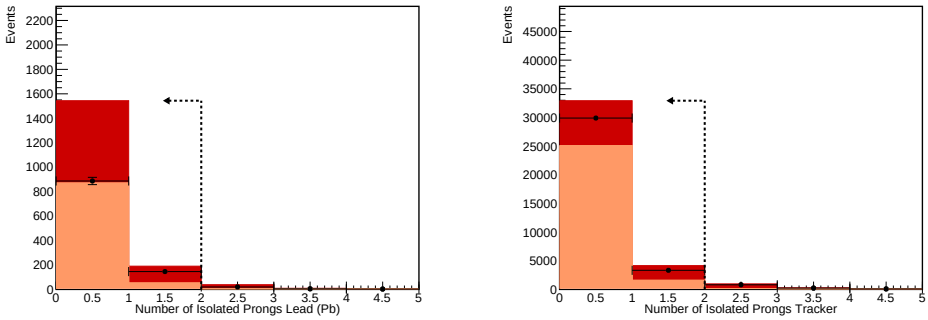
Target	Δ Purity	Cut Efficiency
Carbon (C)	1.51	99.53
Water (H_2O)	1.67	98.73
Iron (Fe)	1.23	99.57
Lead (Pb)	1.36	99.39
Tracker	2.74	99.25

Table 6.8: Increase in signal purity and cut efficiency (%) of the number of isolated prongs < 2 cut

into two photons which create two isolated electromagnetic showers. Cutting events with ≥ 2 isolated prongs removes many events with neutral pions in the final state. This cut also removes other background events with true $W_{exp} > 1.4$ GeV/c^2, as higher W_{exp} is correlated with additional hadronic energy in the event. Figure 6-5 shows the number of isolated prongs per event. Table 6.8 shows the increase in signal purity and the cut efficiency of the number of isolated prongs < 2 cut.



(a) Carbon (b) Iron



(c) Lead (d) Scintillator

Figure 6-5: Number of isolated prongs per event by signal (orange) and background (red). These events have passed all previous selection cuts except for the isolated prong selection cut

Target	Data Events	MC Events	Signal Events	Purity (%)	Efficiency (%)
Carbon (C)	295	335.85	178.85	53.25	1.18
Water (H_2O)	291	317.24	113.78	35.86	1.52
Iron (Fe)	1403	1804.13	926.56	51.36	1.31
Lead (Pb)	1033	1849.55	930.27	50.30	1.40
Tracker	33231	37849.70	25628.45	67.71	5.10

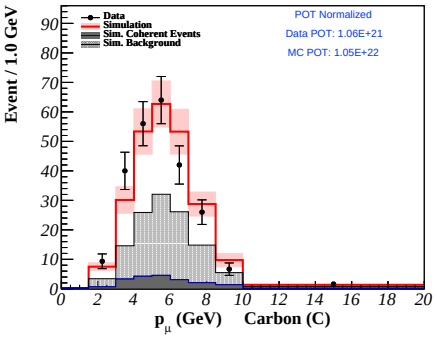
Table 6.9: Purity and Efficiency of Final Event Selection. MC and Signal Events are normalized to data POT

6.3.6 Event Selection Results

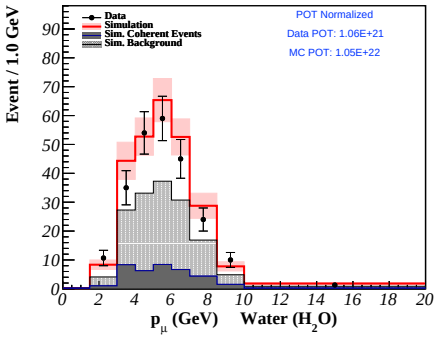
Table 6.9 shows the number of data, total MC (simulated) and simulated signal events which remain in the sample after passing all the selection cuts. The number of MC and signal events have been normalized to data POT. The signal purity and the signal efficiency are also displayed.

Figures 6-6 through 6-13 shows the distributions of events remaining in the sample after passing the analysis selection cuts. These event distributions are binned in the eight reconstructed analysis variables. The errors on the data are purely statistical, while the errors on the simulation include systematic uncertainties, which will be discussed further in section 6.10. These figures also show the distributions of simulated background and simulated coherent pion production events. Events in the coherent pion production distributions meet the signal definition.

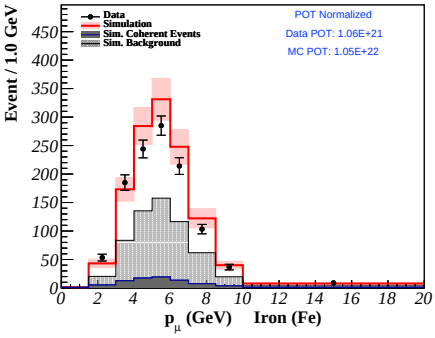
Note that, unlike in many plots in this thesis, the histograms of the background and signals in Figures 6-6 through 6-13 are not displayed as cumulative contributions; in other words, the simulated background in these plots is displayed as a number of events, and not a number of events *above* the coherent pion signal contribution also displayed on the plot. The jargon for this is that the two histograms are not "stacked".



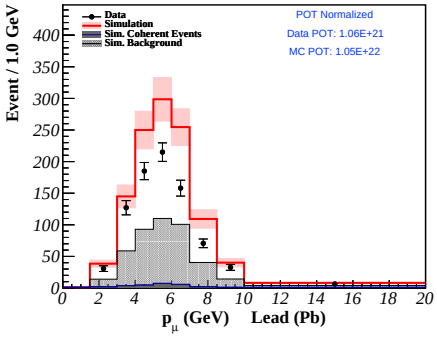
(a) Carbon



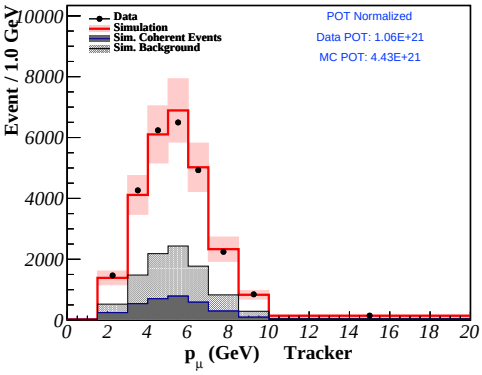
(b) Water



(c) Iron

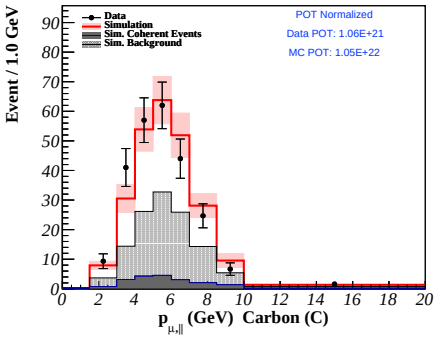


(d) Lead

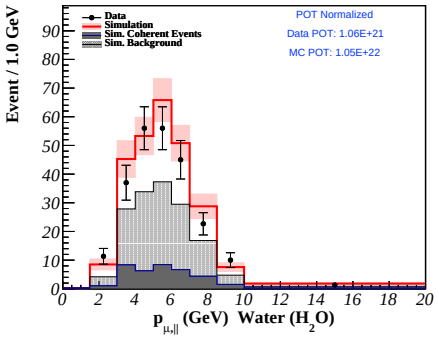


(e) Scintillator

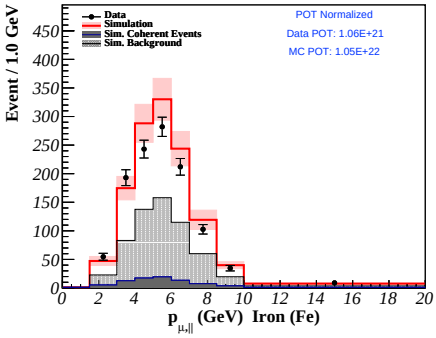
Figure 6-6: p_μ Event Selection. Note that the coherent and background histograms are not "stacked"; see discussion in the text.



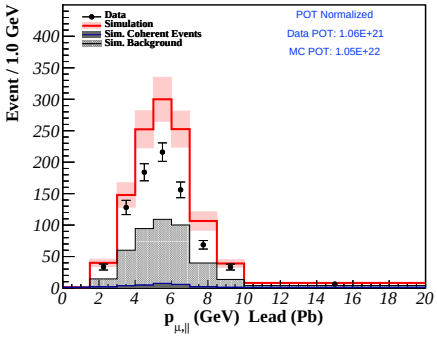
(a) Carbon



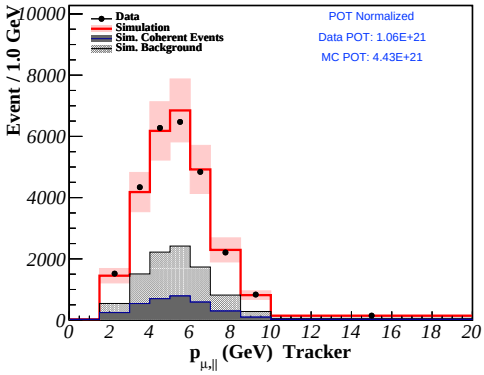
(b) Water



(c) Iron

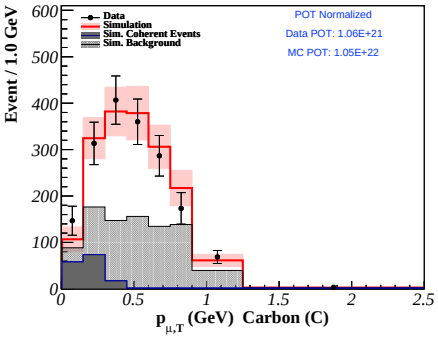


(d) Lead

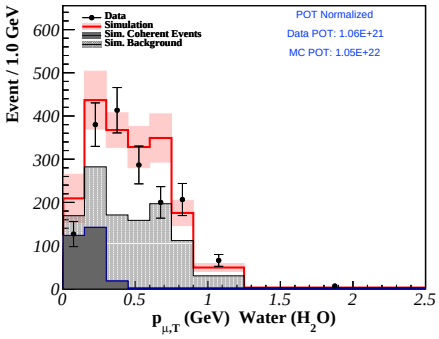


(e) Scintillator

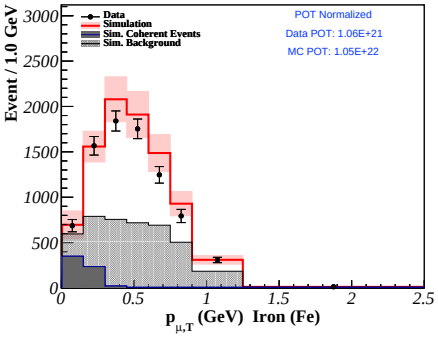
Figure 6-7: $p_{\mu,||}$ Event Selection. Note that the coherent and background histograms are not "stacked"; see discussion in the text.



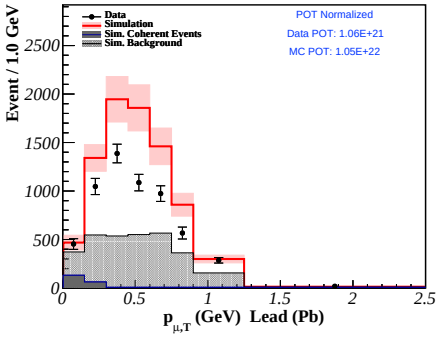
(a) Carbon



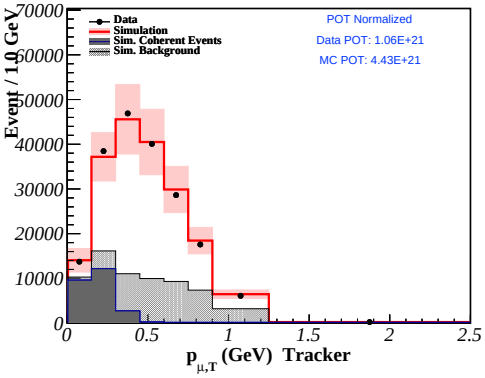
(b) Water



(c) Iron

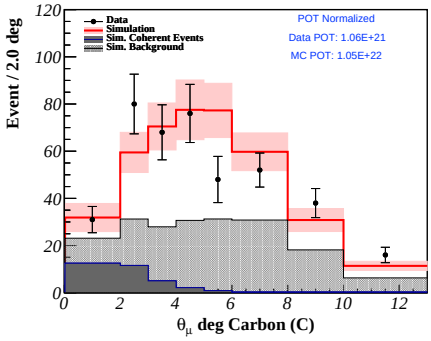


(d) Lead

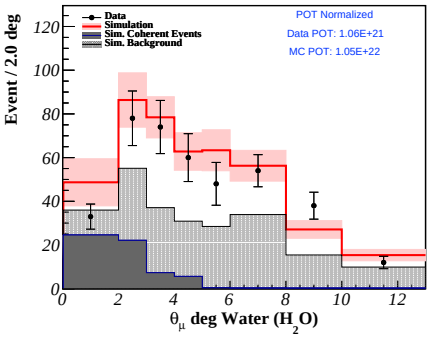


(e) Scintillator

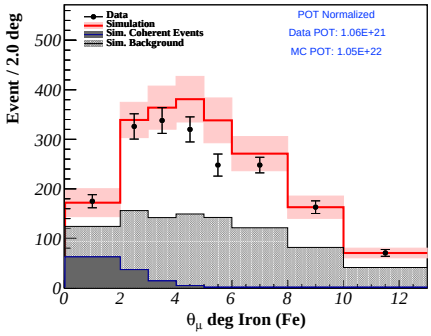
Figure 6-8: $p_{\mu,T}$ Event Selection. Note that the coherent and background histograms are not "stacked"; see discussion in the text.



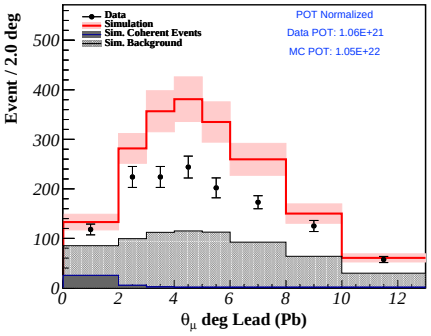
(a) Carbon



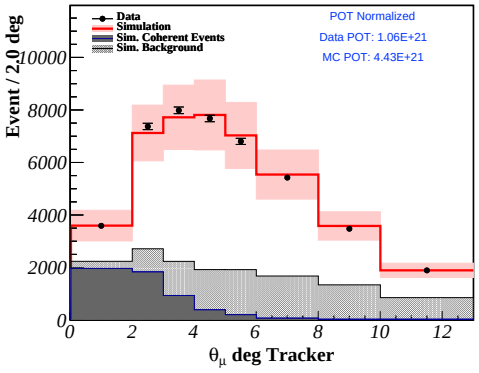
(b) Water



(c) Iron

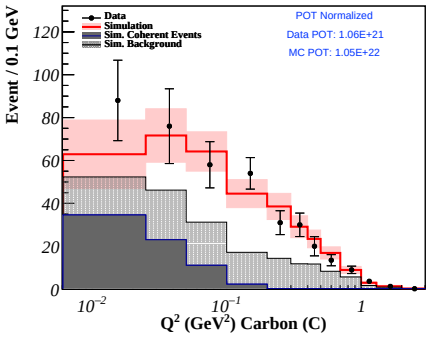


(d) Lead

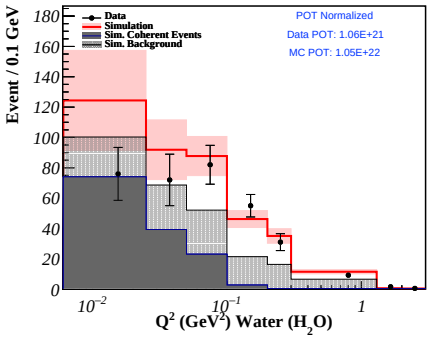


(e) Scintillator

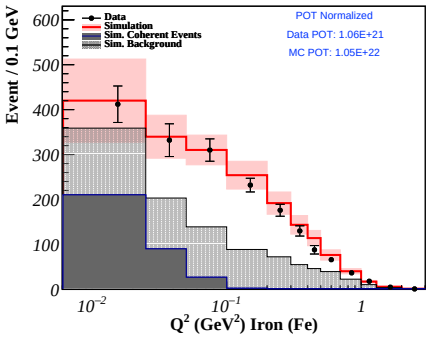
Figure 6-9: θ_μ Event Selection. Note that the coherent and background histograms are not "stacked"; see discussion in the text.



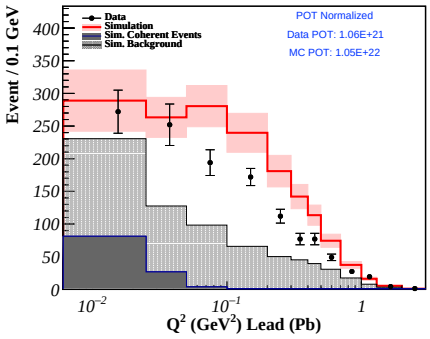
(a) Carbon



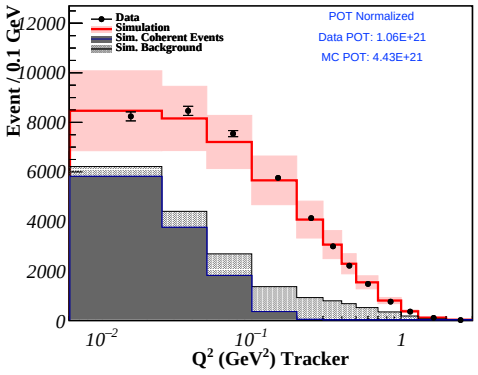
(b) Water



(c) Iron

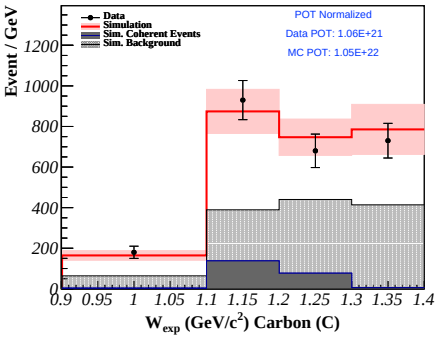


(d) Lead

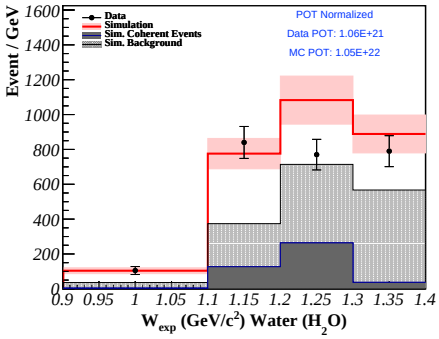


(e) Scintillator

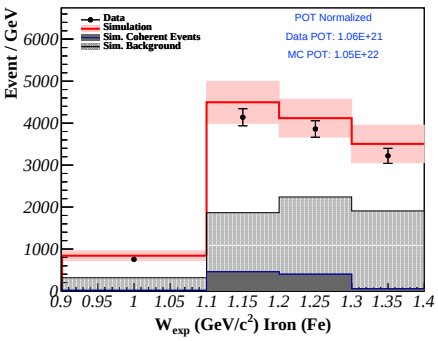
Figure 6-10: Q^2 Event Selection. Note that the coherent and background histograms are not "stacked"; see discussion in the text.



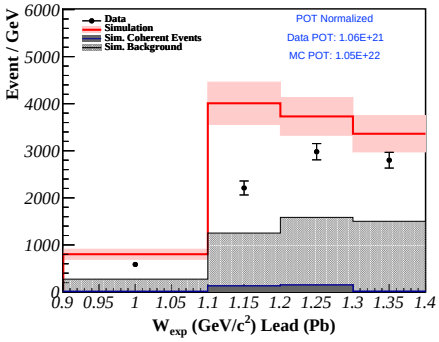
(a) Carbon



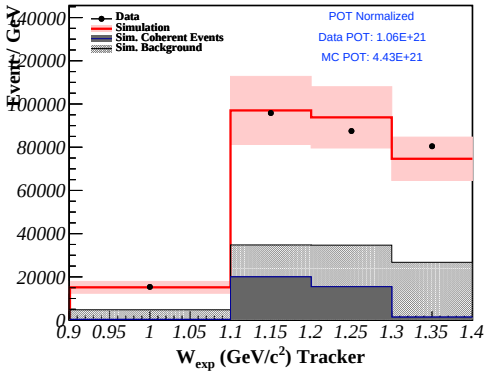
(b) Water



(c) Iron

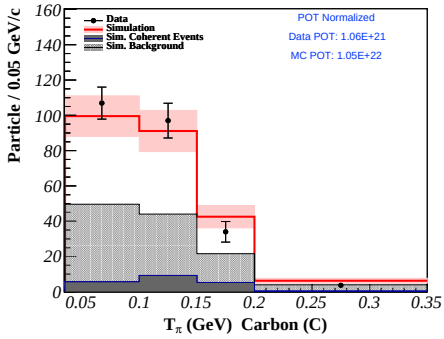


(d) Lead

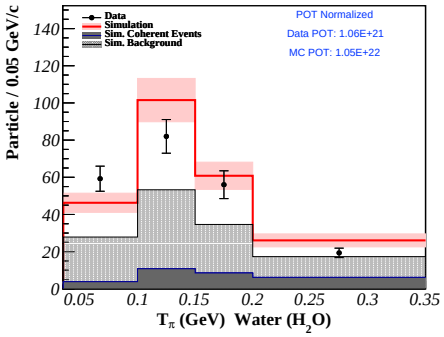


(e) Scintillator

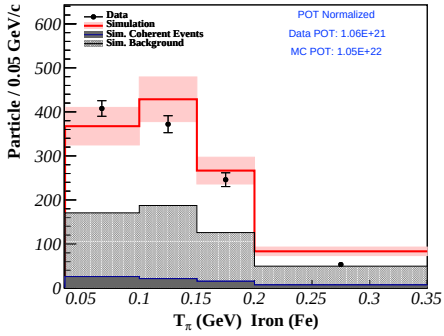
Figure 6-11: W_{exp} Event Selection. Note that the coherent and background histograms are not "stacked"; see discussion in the text.



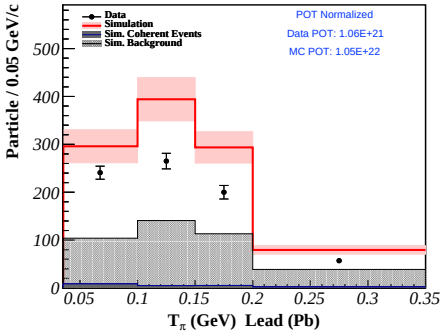
(a) Carbon



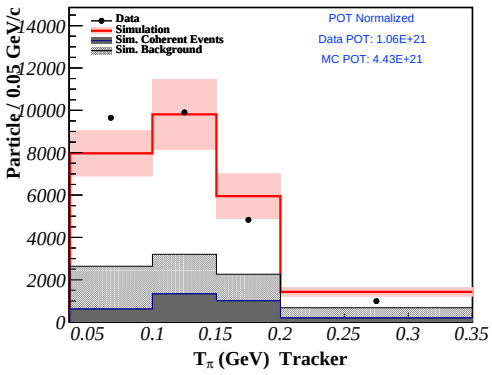
(b) Water



(c) Iron

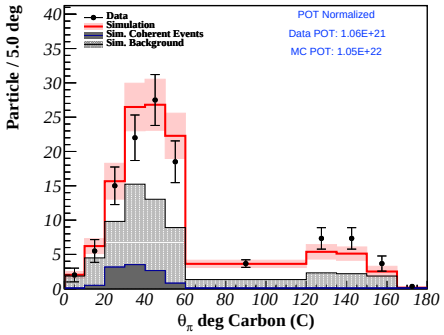


(d) Lead

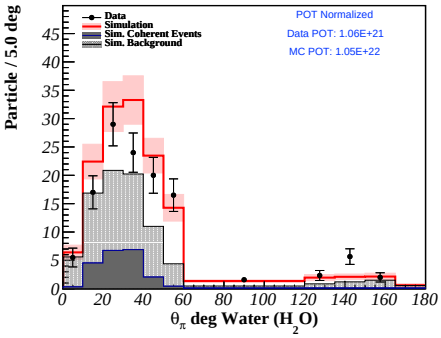


(e) Scintillator

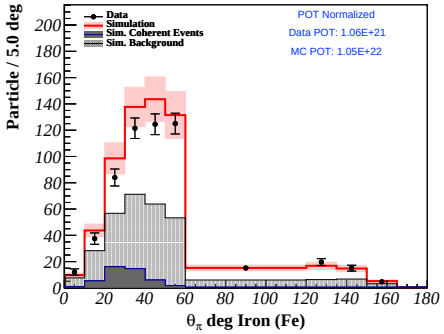
Figure 6-12: T_π Event Selection. Note that the coherent and background histograms are not "stacked"; see discussion in the text.



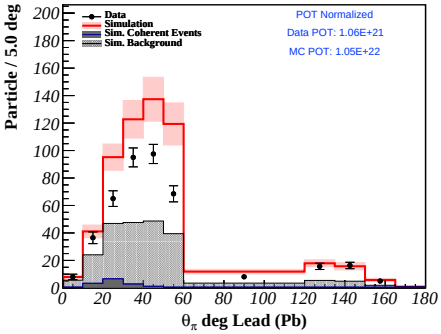
(a) Carbon



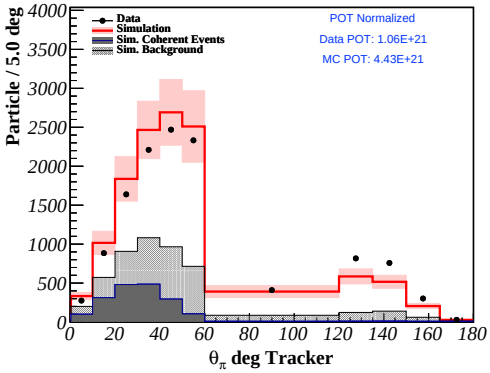
(b) Water



(c) Iron



(d) Lead



(e) Scintillator

Figure 6-13: θ_π Event Selection. Note that the coherent and background histograms are not "stacked"; see discussion in the text.

6.4 Analysis Backgrounds

Simulation predicts the background events that remain in the event samples after passing selection cuts. For this analysis, the two largest types of background are the high W_{exp} background and plastic contamination.

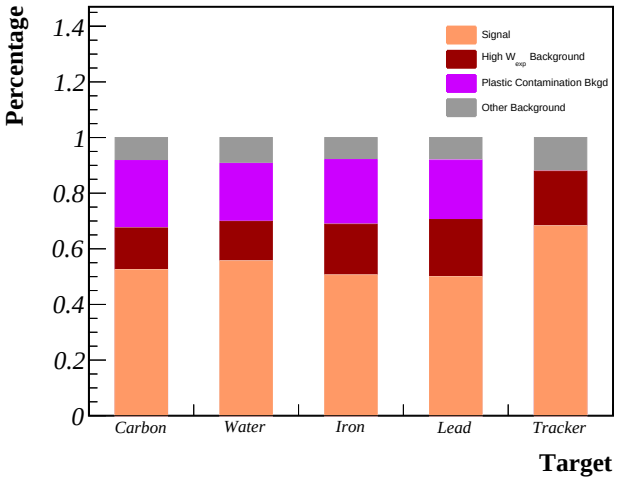


Figure 6-14: Percentage of selected events by signal and background type. Events in the other background category fail to meet the signal definition for various reasons, including having T_π outside of the [35,350] MeV range, or having additional mesons in the event

The high W_{exp} background consists of events with true $W_{exp} > 1.4$ GeV/c^2. These background events have a reconstructed $W_{exp} < 1.4$ GeV/c^2 primarily due to the misreconstruction of the hadron recoil energy E_{had}, which is further explained in section 5.8. This background is present in all samples, regardless of the signal target.

For samples whose signal targets are the passive materials, the plastic contamination background consists of events which are reconstructed on passive material in the nuclear target, but truly occurred on scintillator. These background events are present within the sample due to inaccuracies in the reconstruction of the interaction

vertex. This background is only present for samples of candidate events with the neutrino interaction in the passive materials in the nuclear targets.

6.4.1 Background constraints

Before the analysis removes the background events from the selected sample, the backgrounds and their associated uncertainties are tuned to agree with *in situ* experimental data. This tuning reduces the model dependence in the prediction of the central value, or nominal, of the background events and their systematic uncertainties. The backgrounds are tuned to data in sidebands, which are samples of events which pass all but one of the selection cuts. The sideband for the high W_{exp} background contains events with reconstructed $W_{exp} > 1.5$ GeV/c^2, while the sideband for the plastic contamination background contains events whose reconstructed interaction vertices are outside the fiducial volumes of the nuclear targets.

It should be noted that a sideband is designed to primarily consist of background events, as this limits the background tune's dependence on the signal model. Also, a sideband is typically only good at constraining one type of background. When tuning backgrounds in a sideband, the backgrounds that are not associated with the sideband are held fixed. For instance, the plastic contamination background would not be well constrained by a tune in the high W_{exp} sideband.

Tuning high W_{exp} background in the passive materials requires an accurate estimation of plastic contamination background, as this tune should only account for the physics of the high W_{exp} background in the passive targets. However, the plastic contamination sideband contains events that would be considered signal if the signal target was scintillator. Therefore, an accurate prediction of the plastic contamination background requires an accurate plastic signal model. This plastic signal model

can be obtained by tuning the signal model in tracker sample to data; however, this requires that the high W_{exp} background in the tracker has been tuned as well.

In order to handle these multiple dependencies, the background tune follows the several steps. First, the high W_{exp} background in the tracker is tuned, followed by the plastic signal model in the tracker. Then, the plastic background in the passive materials is tuned. The events in the plastic background have a tuned plastic high W_{exp} background and a tuned plastic signal model. Finally the high W_{exp} background in the passive materials is tuned.

When tuning the high W_{exp} background or the plastic background in sidebands, the distributions of both the central value background prediction and the systematic uncertainties are fit to data. To prevent overfitting, the fit is only allowed to scale the normalization of the background events. The fit was done using an iterative χ^2 minimization technique, where the χ^2 is defined in equation 6.6.

$$\chi^2 = \sum_{i}^{\text{N bins}} \frac{\left(N_{\text{simulation},i} - N_{\text{Data},i}\right)^2}{\sigma^2_{\text{Data},i}} \tag{6.6}$$

The simulated events, $N_{\text{simulation}}$, are broken up into signal and background events. Background events can also be broken up into different categories. Equation 6.7 relates the simulated events to the signal and background events.

$$N_{\text{simulation},i} = N_{\text{signal},i} + \sum_{j}^{\text{categories}} N_{\text{background } j,i} \tag{6.7}$$

For a given sideband, the scale of some of these background categories will be allowed to float in the fit, while the rest of the categories will be held fixed. For those categories that are allowed to float, the uncertainties on the scales fitted to the central value are added as additional systematic uncertainties, further explained in section 6.10.6.

These systematic uncertainties are representative of the statistical uncertainty in the sideband.

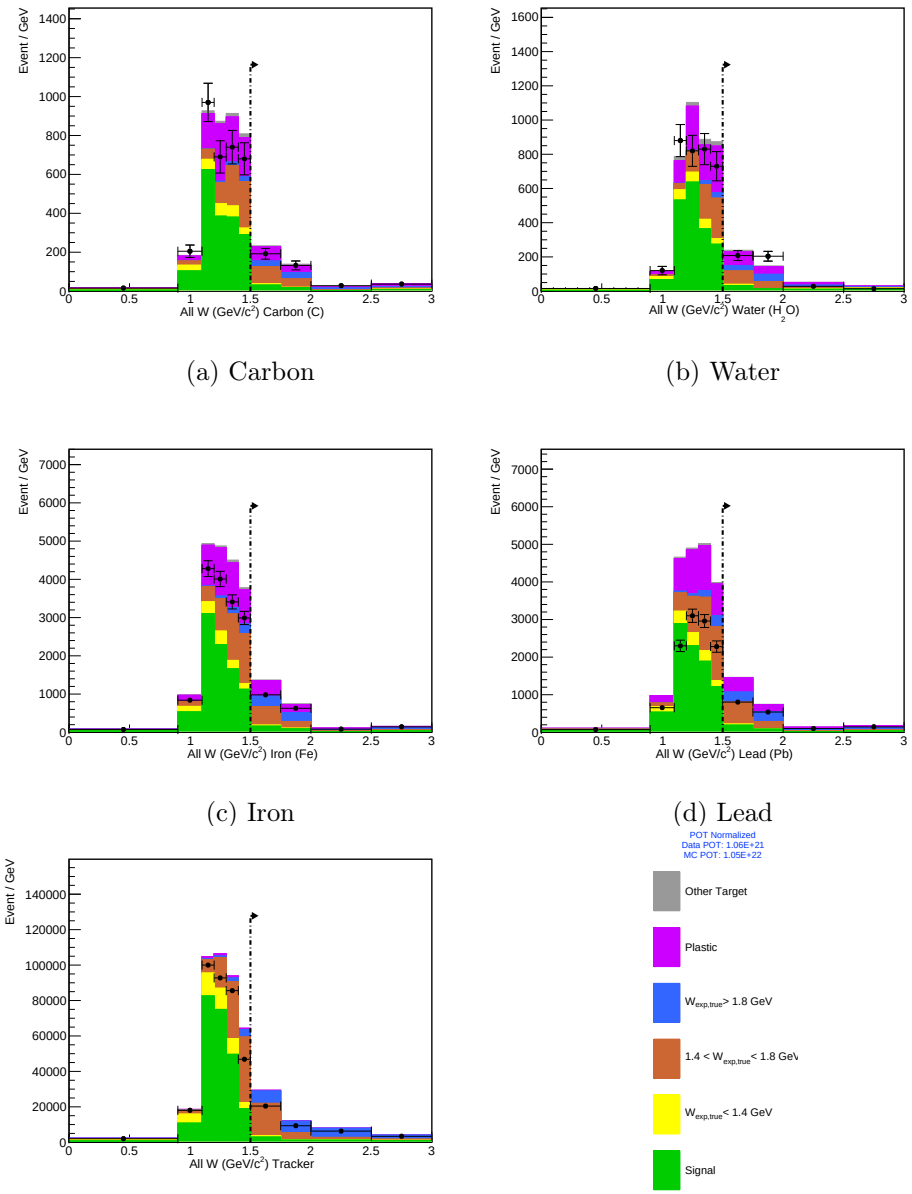
When tuning the signal model, only the central value of the signal model is fitted to data. This fit is applied equally to all systematic uncertainties such that the fractional systematic uncertainties are the same before and after the fit. This is similar to the method used in the low Q^2 suppression fit discussed in section 4.5.4.6.

6.4.2 High W_{exp} Sideband Fit in the Tracker

The high W_{exp} sideband contains events which meet the requirements of the event selection except that the reconstructed $W_{exp} > 1.5$ GeV/c^2. Requiring that the reconstructed W_{exp} is greater than 1.5 GeV/c^2 helps reduce signal in the sideband. Figure 6-15 shows the full W_{exp} distributions for all targets before background tuning while figure 6-16 shows the high W_{exp} sideband for all targets before background tuning.

For the tracker high W_{exp} sideband, the categories consist of signal and the three background categories: $W_{exp,true} < 1.4$ GeV/c^2, $1.4 < W_{exp,true} < 1.8$ GeV/c^2, and $W_{exp,true} > 1.8$ GeV/c^2. Background events in the $W_{exp,true} < 1.4$ GeV/c^2 category fulfill the true W_{exp} requirement in the signal definition, but fail to meet another signal requirement. The value of $W_{exp,true} = 1.8$ GeV/c^2 was chosen as the location where the generator model in GENIE switches from a resonance+hadronization model, which uses KNO and PYTHIA, to a pure hadronization model, which uses PYTHIA alone [70]. Only $1.4 < W_{exp,true} < 1.8$ GeV/c^2 and $W_{exp,true} > 1.8$ GeV/c^2 are allowed to be float in the fit, as $W_{exp,true} < 1.4$ GeV/c^2 background was determined to be poorly constrained in this fit.

Table 6.10 shows the results of the fit, which suppresses all high W_{exp} background. Figure 6-17 shows the high W_{exp} sideband before and after the fit. The χ^2 is calculated



(a) Carbon

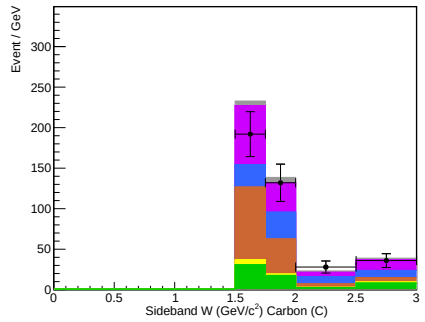
(b) Water

(c) Iron

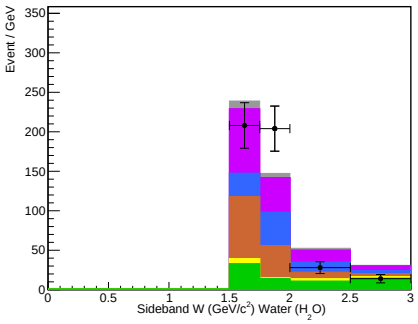
(d) Lead

(e) Scintillator

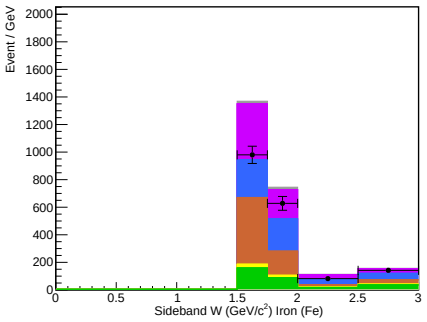
Figure 6-15: W_{exp} No Sideband Fits. The region to the right of the arrow shows the high W_{exp} sideband region



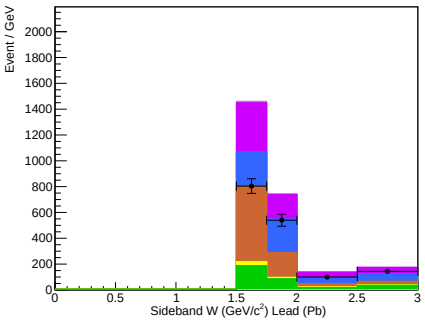
(a) Carbon



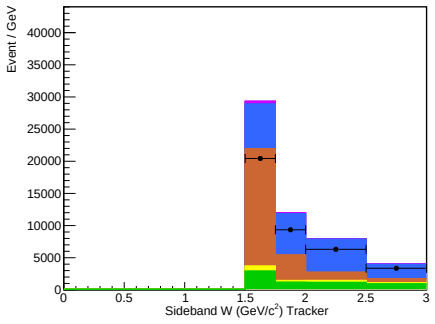
(b) Water



(c) Iron



(d) Lead



(e) Scintillator

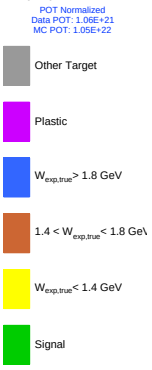


Figure 6-16: $W_{exp} > 1.5$ GeV/c^2 No Sideband Fits

$1.4 < W_{exp,true} < 1.8$ GeV/c^2	$1.8 < W_{exp,true}$ GeV/c^2	χ^2/ndf
0.593 ± 0.019	0.799 ± 0.019	3.039/4

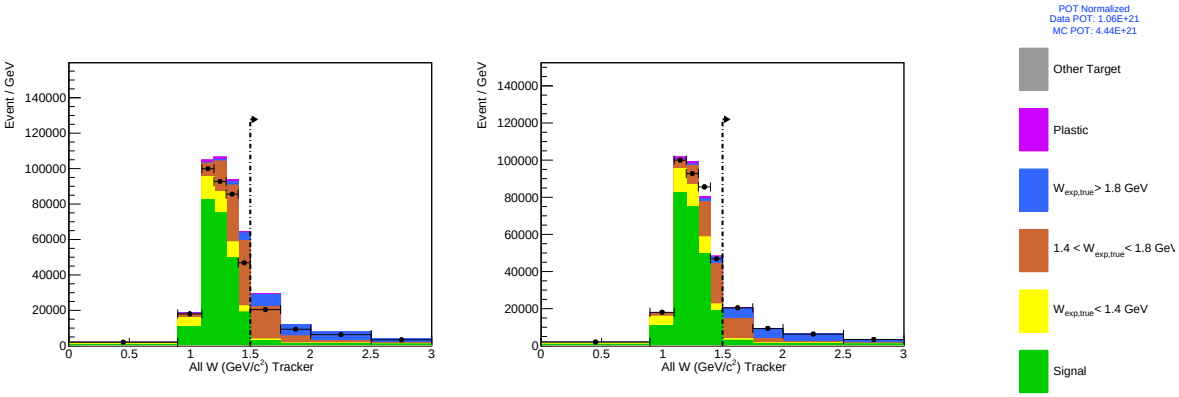
Table 6.10: Tracker W_{exp} sideband scales found from the fit in the high $W > 1.4$ GeV sideband for all tracker events. The fit holds the scales of both signal and $W_{exp,true} < 1.4$ GeV/c^2 as fixed. The calculation of χ^2 uses statistical uncertainties only.

using only the statistical error on the data. While the χ^2/ndf is greater than 1, an examination of the W_{exp} sideband in figure 6-17 shows good enough agreement between simulation and data to estimate the background in the reconstructed $W_{exp} <$ 1.4 GeV/c^2 region.

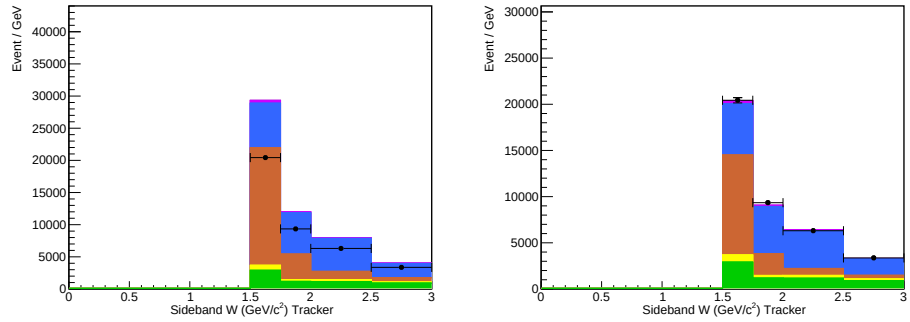
6.4.3 Plastic Signal Model Fit in the Tracker

After applying the plastic high W sideband fit to background events in the tracker, the central value of the plastic signal model is reweighted so that the simulation matches the data for events in the tracker with reconstructed $W_{exp} < 1.4$ GeV/c^2. Similar to the low Q^2 suppression, the uncertainties are tuned using the same set of reweights used on the central value signal model.

The signal model is only reweighted where the largest disagreement between simulation and data occurs: at low pion energy ($T_\pi < 0.1$ GeV) and at angles where the pion is going backwards ($\theta_\pi > 90°$). Figure 6-18 shows the plastic signal reweight in T_π and θ_π, while figure 6-19 shows the effects of applying the reweight to the signal events with reconstructed $W_{exp} < 1.4$ GeV/c^2 in the tracker. This reweight was required so that the plastic contamination background in the nuclear targets had an accurate estimation of the plastic signal model. Thus, the plastic signal model reweight is only applied to events which occurred on scintillator in the nuclear targets, and not to any signal events in the tracker.



(a) Prefit (b) Postfit



(c) Prefit (d) Postfit

Figure 6-17: Plastic High W_{exp} Sideband Fit in full W_{exp} (top) and $W_{exp} > 1.5$ GeV/c^2 (bottom) distributions

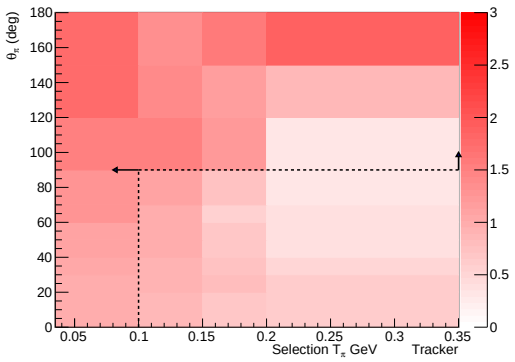
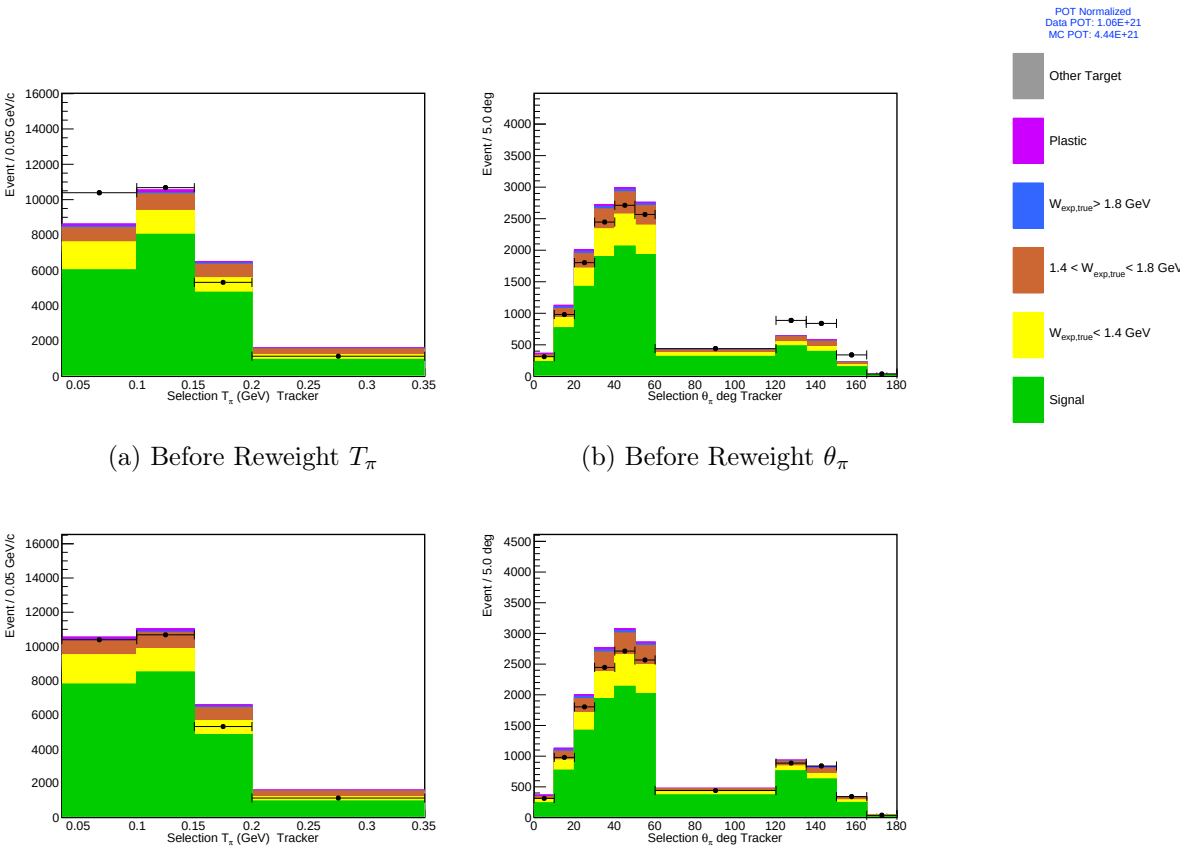


Figure 6-18: Plastic Signal T_π vs θ_π Reweight. Reweight only applied to $\theta_\pi > 90°$ or $T_\pi < 0.1$ GeV

6.4.4 Plastic Contamination Sideband Fit in the Nuclear Targets

For each nuclear target, there are two sidebands based on the longitudinal (z) position of the interaction vertex, one upstream and one downstream of the fiducial volume of the target module. Figure 6-20 shows the longitudinal position of the sidebands with respect to the nuclear targets, as well as the distributions of the z position of the interaction vertex before the plastic contamination sideband fit. These sidebands are selected to remove events from both the target and the sideband on the other side of the target.

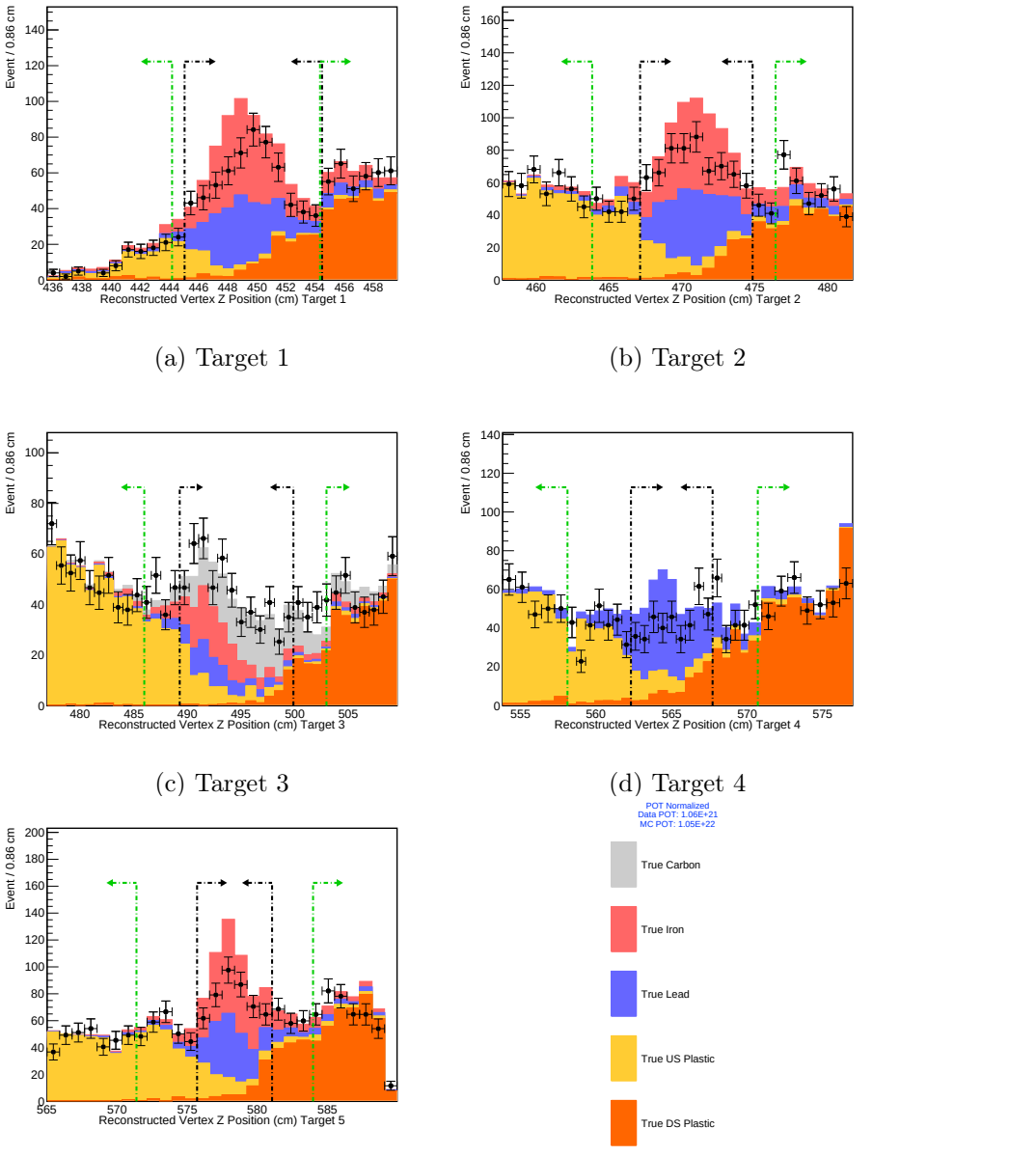
When the downstream sideband of one target and the upstream sideband of a subsequent target overlap, the two scales from both regions are averaged and applied to both regions. The exception to this is the water target, which did not have a separate fit applied to upstream and downstream scintillator because it completely overlapped with sidebands from other targets, and the analysis relied on values found from the fit downstream target 3 and upstream target 4.



(a) Before Reweight T_π (b) Before Reweight θ_π

(c) After Reweight T_π (d) After Reweight θ_π

Figure 6-19: Effects of Signal Reweight on T_π and θ_π in Signal Region



(a) Target 1

(b) Target 2

(c) Target 3

(d) Target 4

(e) Target 5

Figure 6-20: Interaction Vertex z Distributions With True Interaction Vertex Categories Before Plastic Contamination Sideband Fits. Green arrows represent the sideband regions while the black arrows represent the target fiducial volume

Target	Upstream Scale	χ^2/ndf	Downstream Scale	χ^2/ndf
Target 1	0.694 ± 0.123	1.452/6	0.936 ± 0.068	2.514/6
Target 2	0.988 ± 0.054	4.154/7	0.878 ± 0.071	11.965/6
Target 3	0.915 ± 0.043	7.516/10	0.881 ± 0.063	3.751/7
Target 4	0.918 ± 0.062	4.796/5	0.842 ± 0.047	11.818/7
Target 5	0.925 ± 0.054	9.207/7	0.858 ± 0.051	11.498/7

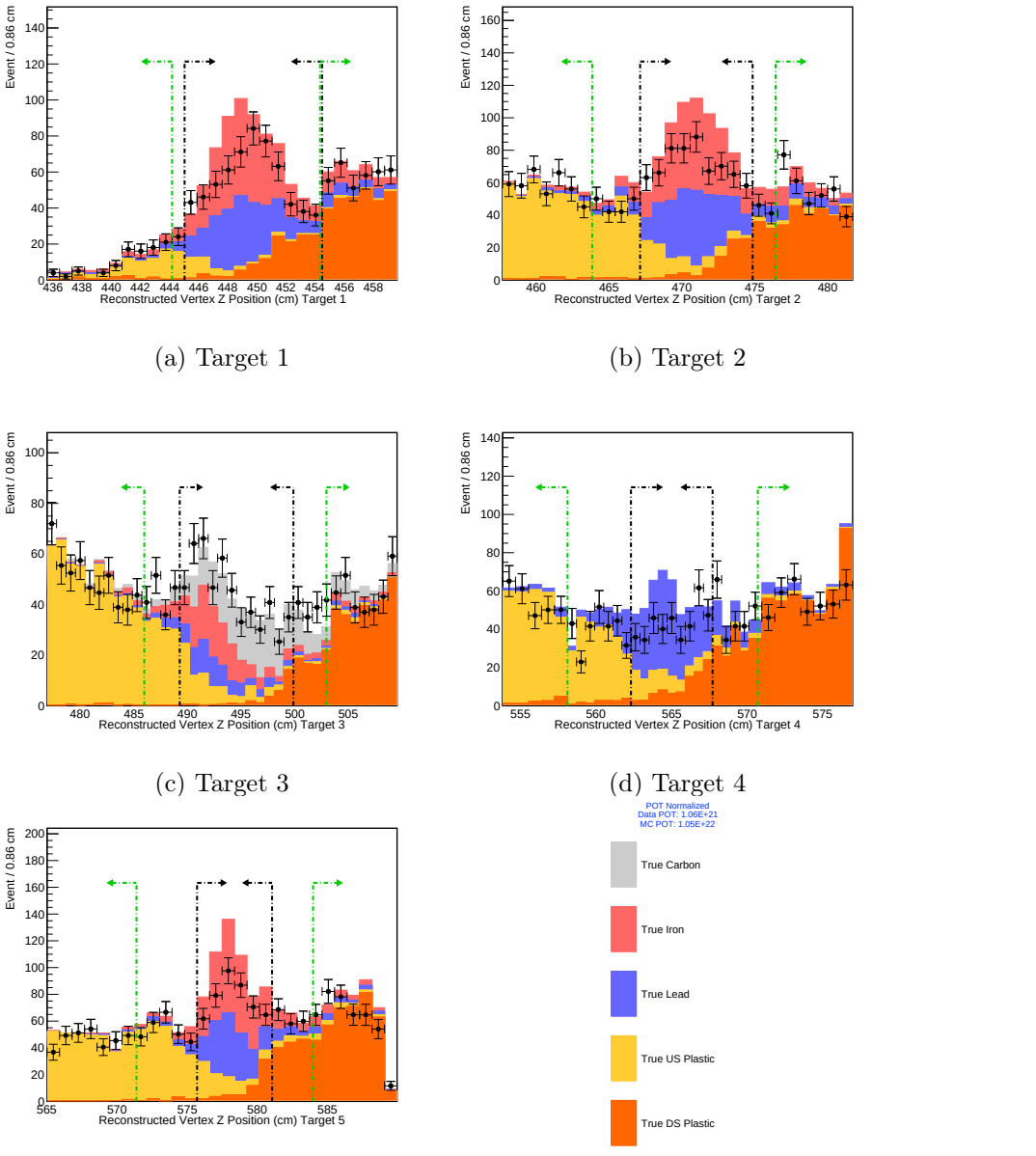
Table 6.11: Upstream and downstream plastic contamination scales found from the sideband fit in z-coordinate of the interaction vertex. The fit holds the target categories fixed

In all targets, the sideband fits decrease the amount of predicted plastic events in the nuclear target region. Table 6.11 shows the results of the plastic contamination sideband fits. Figure 6-21 shows the distributions of the z position of the interaction vertex after the plastic contamination sideband fit, while figure 6-22 shows the high W_{exp} sidebands for all targets after applying the plastic contamination sideband fit scales.

6.4.5 High W_{exp} Sideband Fits in the Nuclear Targets

The high W_{exp} sideband fit in the nuclear targets is similar to the fit done in the tracker region. These fits are based on the nuclei of the passive material, as there are not enough statistics in this analysis to fit target and material separately. There are two additional categories which are held fixed during the fit: plastic, which is an event that occurred on scintillator, and "other" target, which describes any event not on scintillator or the signal target. The other target contribution is negligible.

Table 6.12 shows the result of the high W_{exp} sideband fit in the targets. For iron and lead, the fit suppresses both categories of high W_{exp} background. In carbon, the simulation overpredicts the data in the lowest bin and matches the data in every other bin. As the $1.4 < W_{exp,true} < 1.8$ GeV/c^2 background dominates in the lowest



(a) Target 1

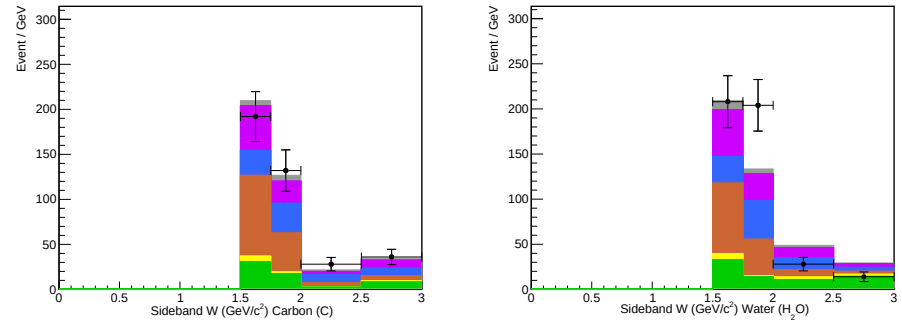
(b) Target 2

(c) Target 3

(d) Target 4

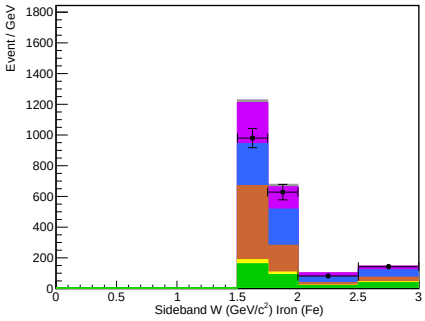
(e) Target 5

Figure 6-21: Vertex Z Distributions With True Interaction Vertex Categories After Plastic Contamination Fits. Green arrows represent the sideband regions while the black arrows represent the target fiducial volume

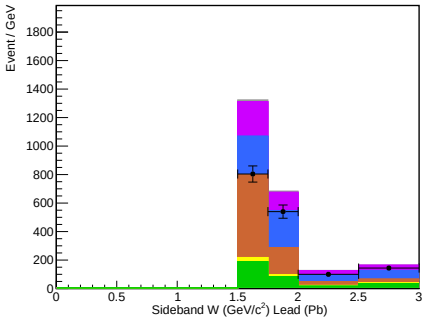


(a) Carbon

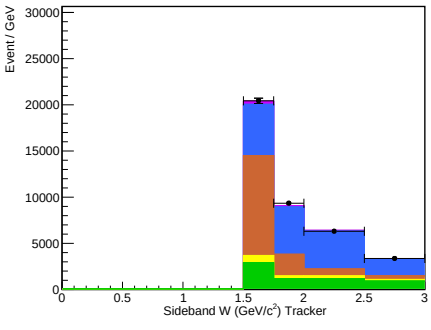
(b) Water

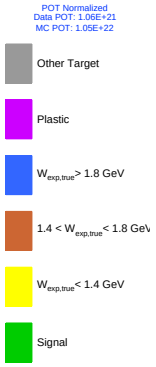


(c) Iron



(d) Lead





(e) Scintillator

Figure 6-22: $W_{exp} > 1.4$ Sideband After Plastic Contamination Fits

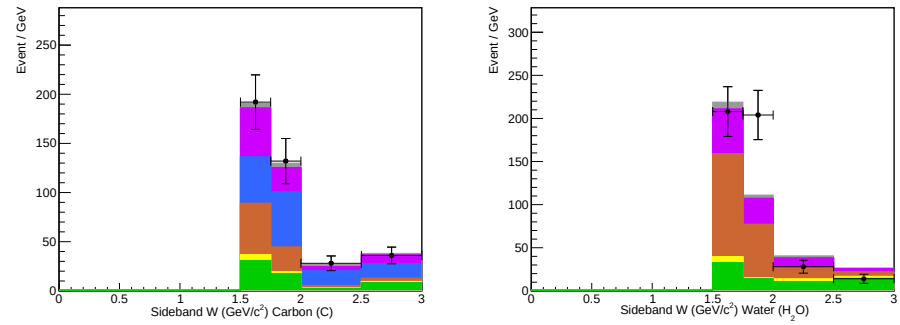
Target	$1.4 < W_{exp,true} < 1.8$ GeV/c^2	$1.8 < W_{exp,true}$ GeV/c^2	χ^2/ndf
Carbon	0.581 ± 0.436	1.708 ± 0.711	0.147/4
Iron	0.479 ± 0.248	1.052 ± 0.288	1.705/4
Lead	0.085 ± 0.159	1.058 ± 0.204	0.324/4
Water	1.530 ± 0.301	0.000 ± 0.903	18.956/4

Table 6.12: Nuclear target W_{exp} sideband scales found from the fit in the high $W > 1.4$ GeV sideband. The fit holds the plastic, other target and $W_{exp,bkgd} < 1.4$ categories as fixed. The χ^2 calculation uses statistical errors only. $\chi^2/ndf < 1$ for most targets due to low statistics in the sideband.

bin, the fit suppresses the $1.4 < W_{exp,true} < 1.8$ GeV/c^2 category while increasing the $1.8 < W_{exp,true}$ GeV/c^2 category. The fit on the water target completely suppresses the $1.8 < W_{exp,true}$ GeV/c^2 category, as the simulation overpredicts the data in the 2-3 GeV/c^2 bins and the $1.8 < W_{exp,true}$ GeV/c^2 contributes the most in these bins. Figure 6-23 and figure 6-24 show the W_{exp} sidebands after the high W_{exp} sideband fits in the passive targets.

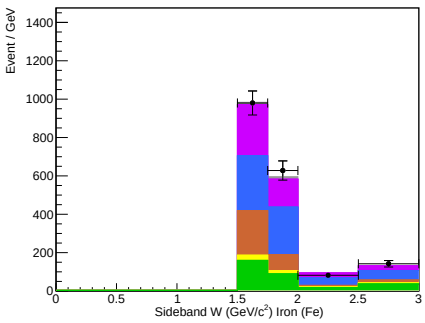
After scaling the high W_{exp} background by the normalization factors found in the sideband fit, there should be good agreement in the sideband between data and simulation for each analysis variable. Agreement between data and simulation would show that the tuned background is well modelled, which gives confidence in the tuned background prediction in selected event sample. Any disagreement may require further constraints on the background model. Figures 6-25 and 6-26 show the $p_{\mu,T}$ and T_π distributions of $W_{exp} > 1.5$ GeV sideband events after the high W_{exp} sideband fit. Both sets of distributions show some disagreement in shape. The simulated distribution in carbon and iron is shifted towards smaller $p_{\mu,T}$, however the simulated distribution is shifted towards larger $p_{\mu,T}$ in the tracker. Also, the simulation tends to underpredict at lower T_π and overpredict for high T_π in all targets. Most of these disagreements in simulation are within the statistical uncertainty of the data. In

addition, the model has systematic uncertainties in pion production which are not included in the uncertainties in these comparisons.

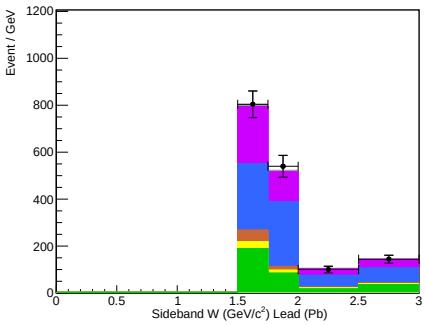


(a) Carbon

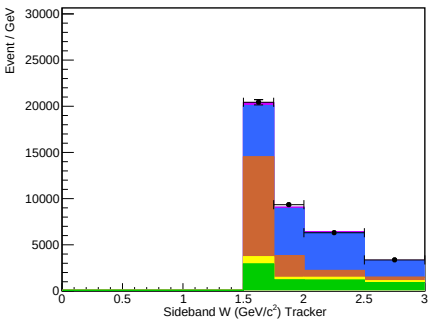
(b) Water

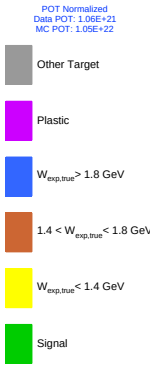


(c) Iron



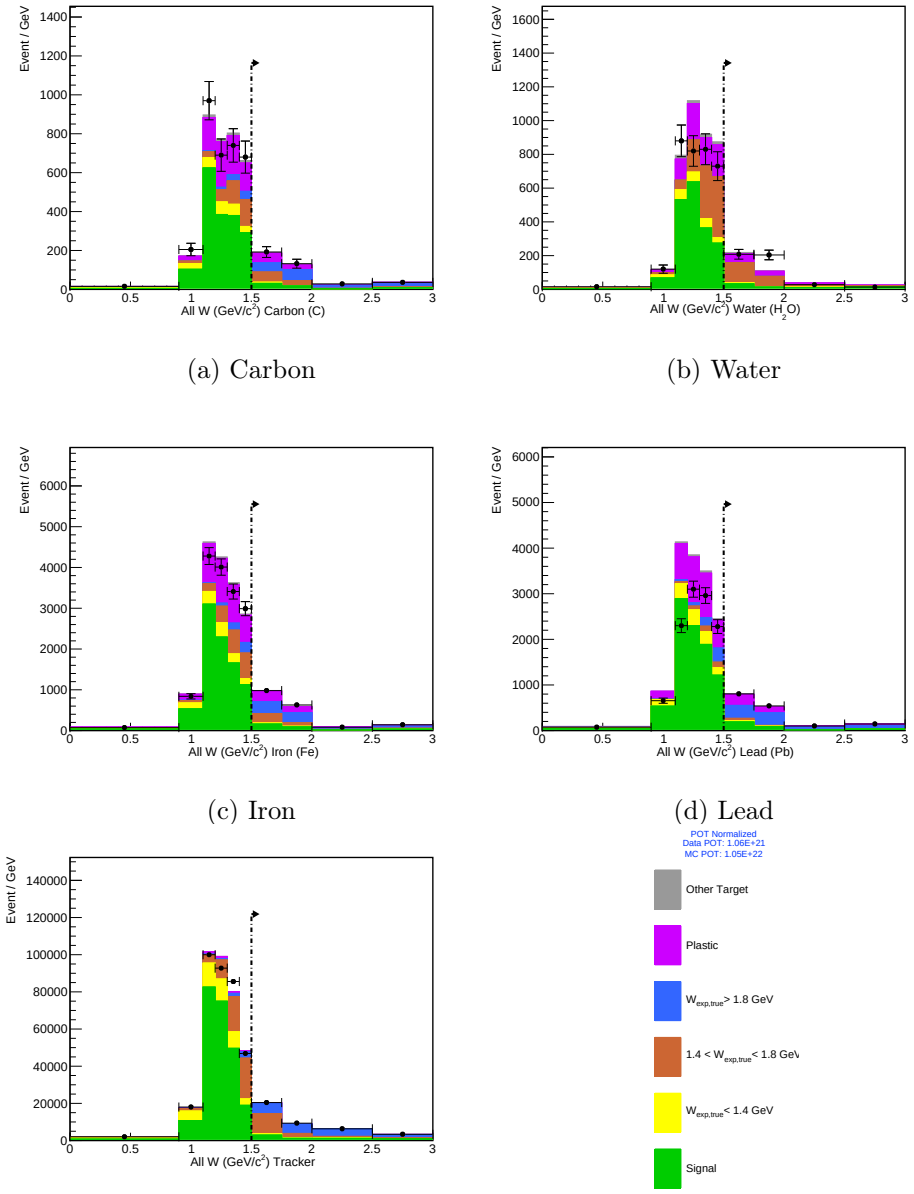
(d) Lead





(e) Scintillator

Figure 6-23: $W_{exp} > 1.5$ GeV/c^2 Sideband After High W_{exp} Sideband Fits in the Nuclear Targets



(a) Carbon

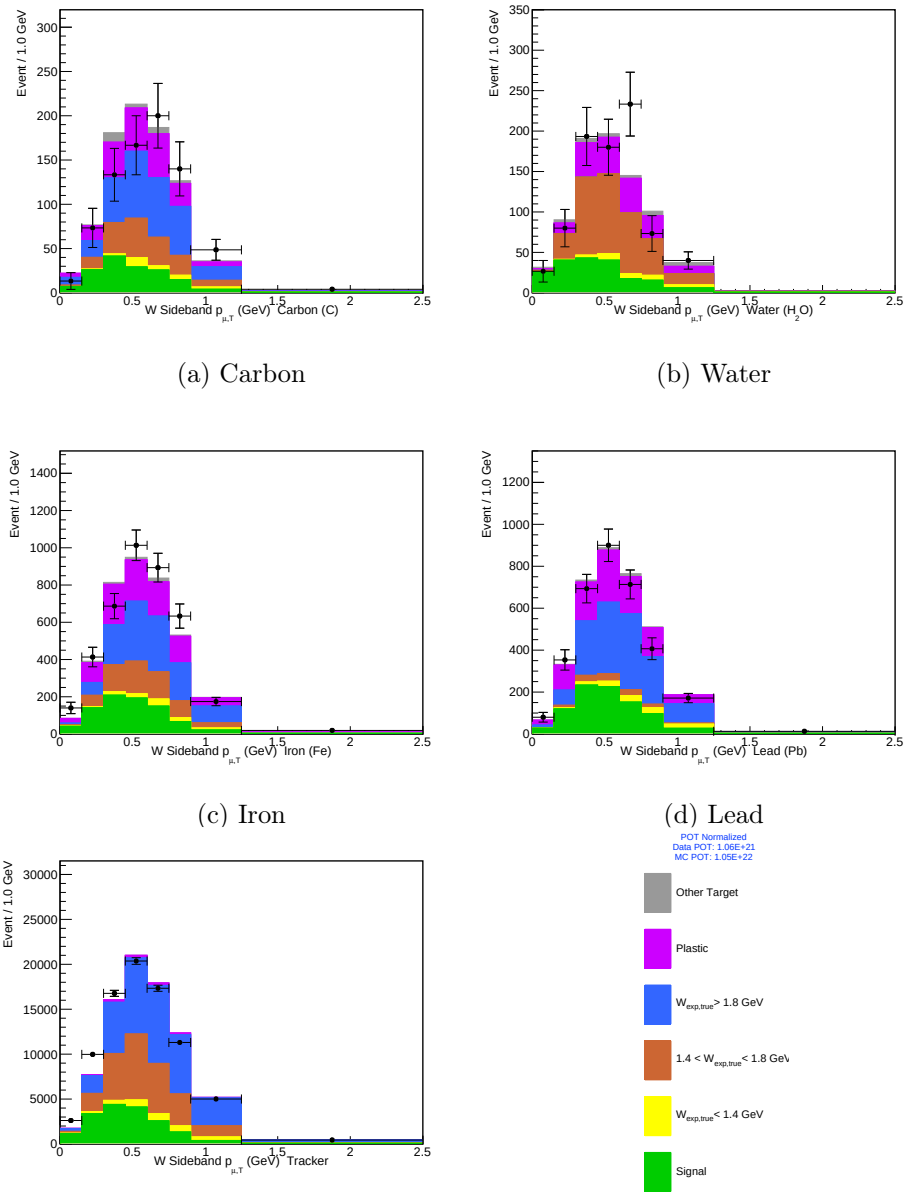
(b) Water

(c) Iron

(d) Lead

(e) Scintillator

Figure 6-24: W_{exp} After High W_{exp} Sideband Fits in the Nuclear Targets



(a) Carbon

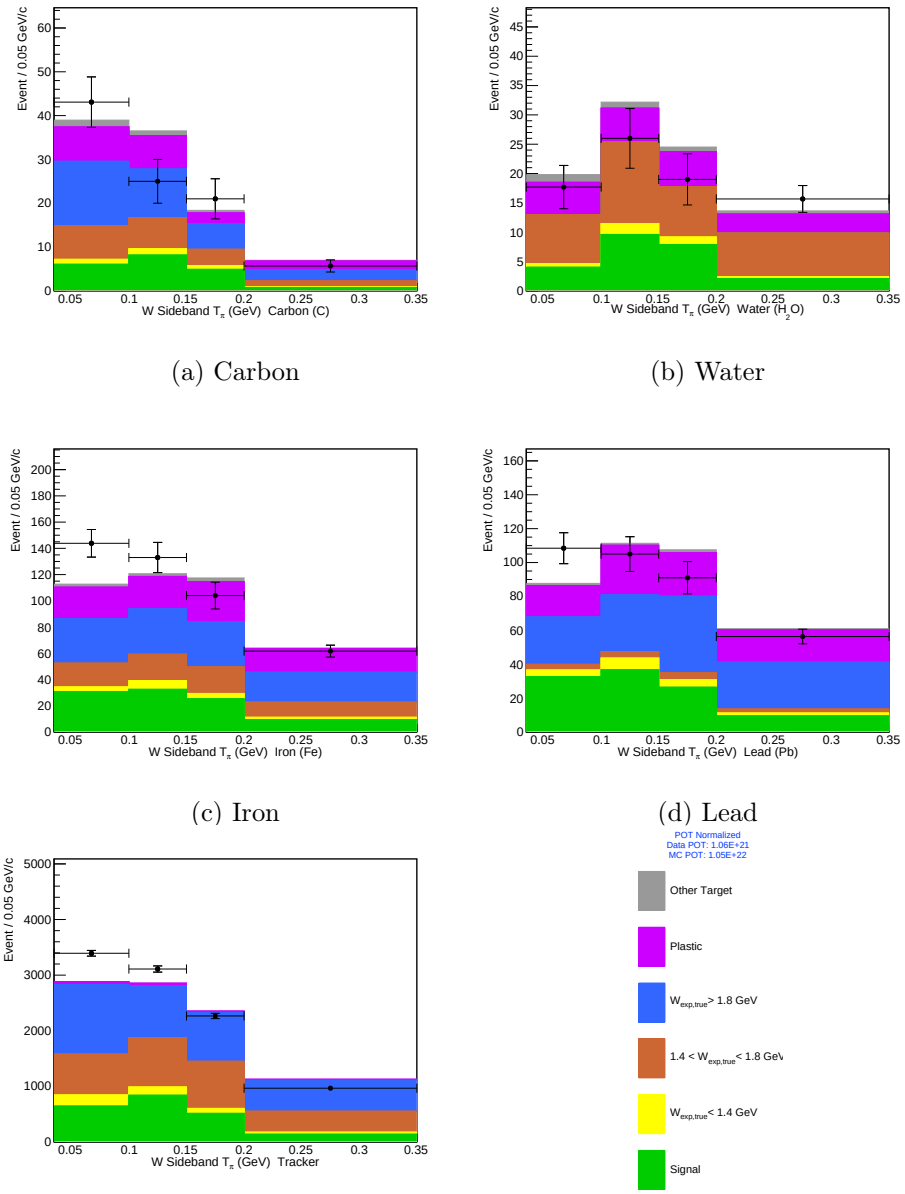
(b) Water

(c) Iron

(d) Lead

(e) Scintillator

Figure 6-25: $p_{\mu,T}$ in $W_{exp} > 1.5$ GeV/c^2 Sideband After High W_{exp} Sideband Fits in the Nuclear Targets



(a) Carbon

(b) Water

(c) Iron

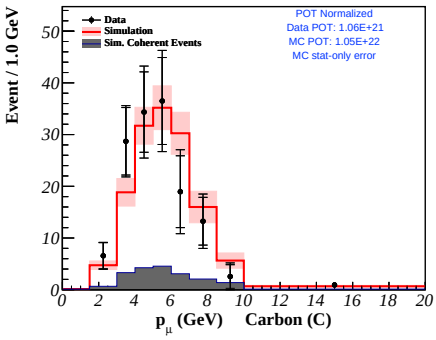
(d) Lead

(e) Scintillator

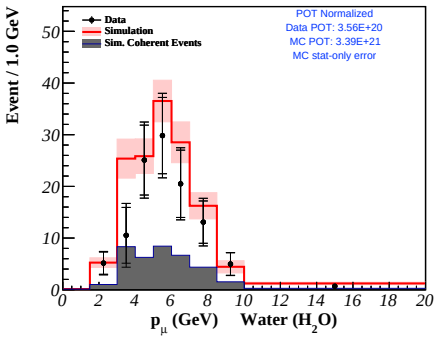
Figure 6-26: T_π in $W_{exp} > 1.5$ GeV/c^2 Sideband After High W_{exp} Sideband Fits in the Nuclear Targets

6.5 Background Subtraction

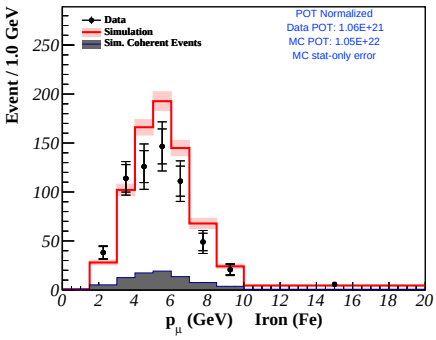
After the prediction of background events have been constrained by the sideband fits, the constrained background is subtracted bin-by-bin from data and simulation. Systematic uncertainties from the background prediction are included when subtracting the constrained background from the data. Therefore, the error bars on the background subtracted data contain both systematic and statistical uncertainties. The background subtracted simulation contains only signal events, and the error bars of the signal simulation contain only statistical uncertainties. Figures 6-27 through 6-34 show background subtracted distributions.



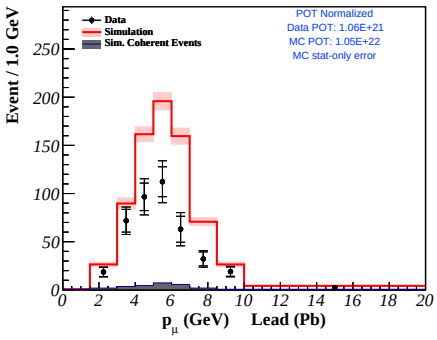
(a) Carbon



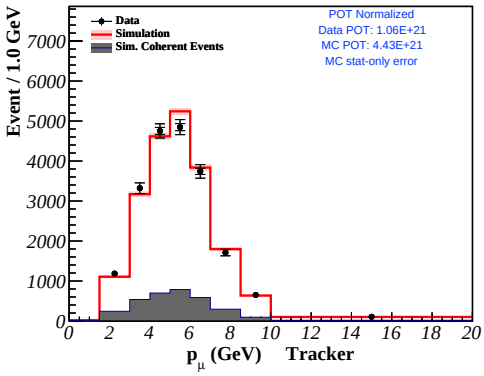
(b) Water



(c) Iron

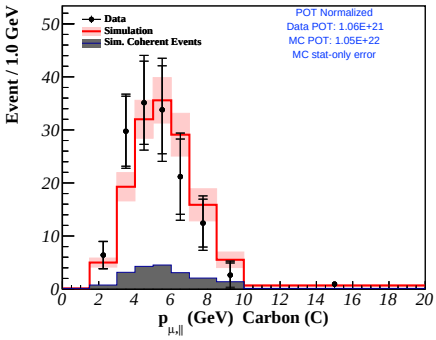


(d) Lead

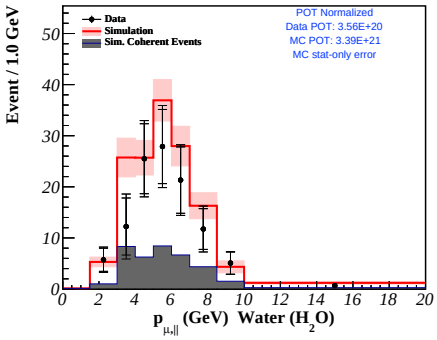


(e) Scintillator

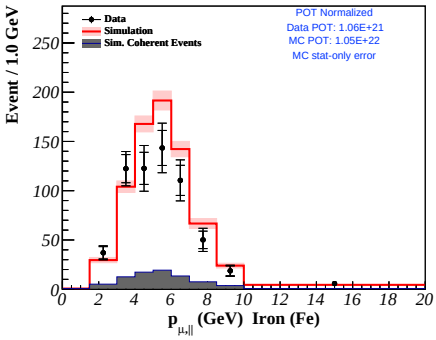
Figure 6-27: p_μ Background Subtracted



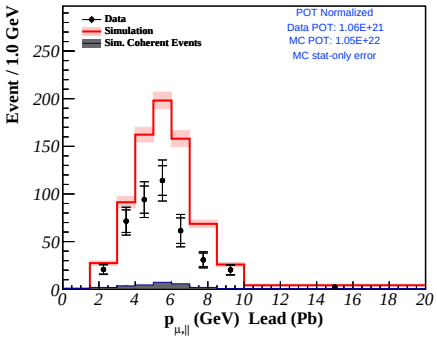
(a) Carbon



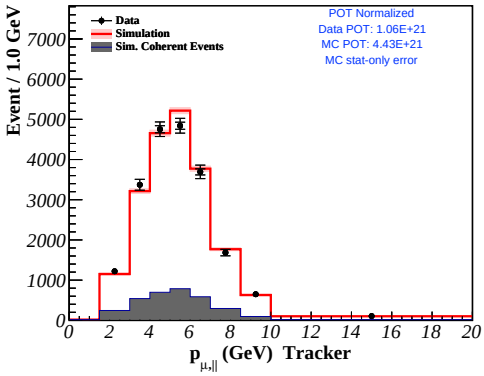
(b) Water



(c) Iron

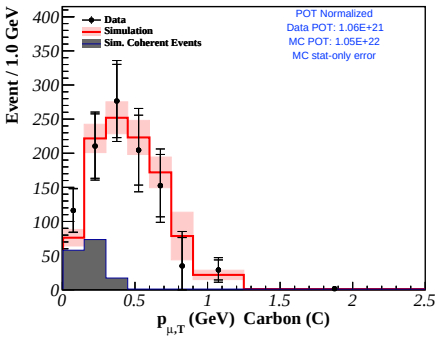


(d) Lead

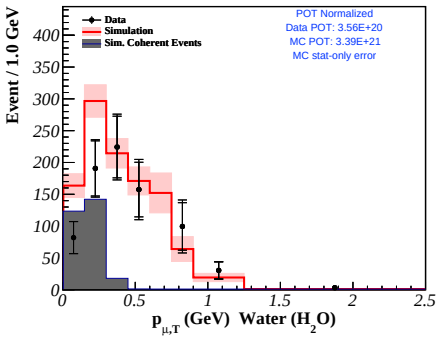


(e) Scintillator

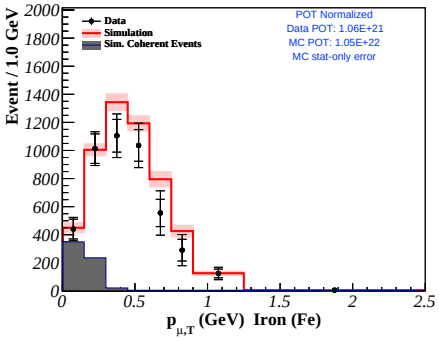
Figure 6-28: $p_{\mu,||}$ Background Subtracted



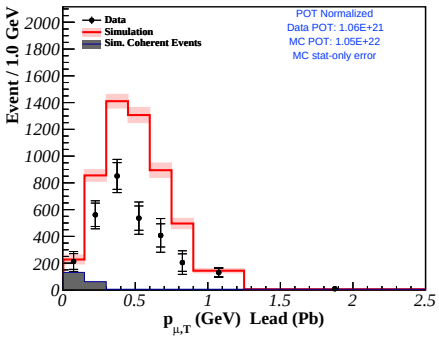
(a) Carbon



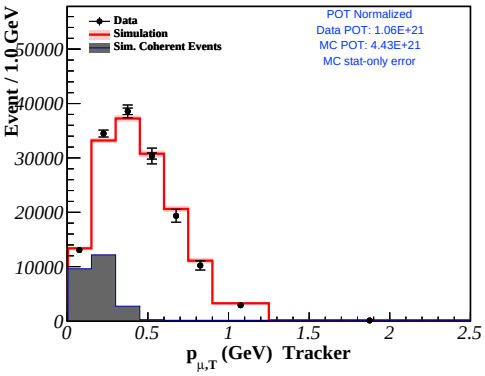
(b) Water



(c) Iron

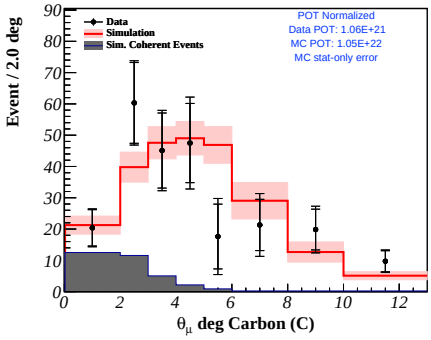


(d) Lead

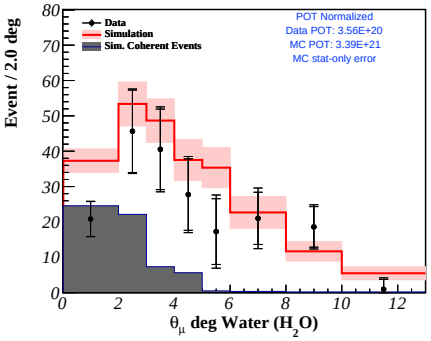


(e) Scintillator

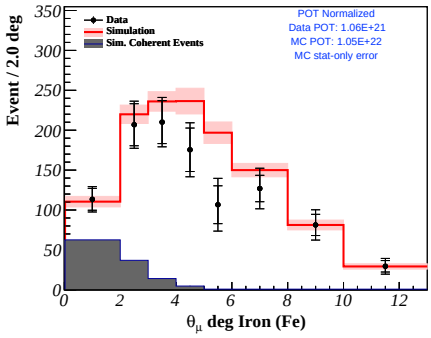
Figure 6-29: $p_{\mu,T}$ Background Subtracted



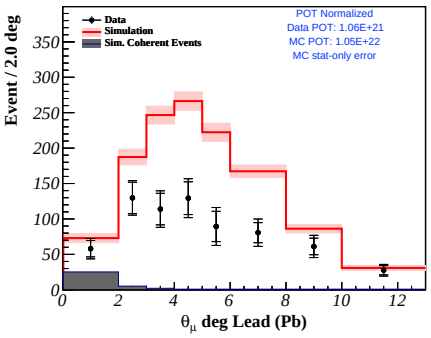
(a) Carbon



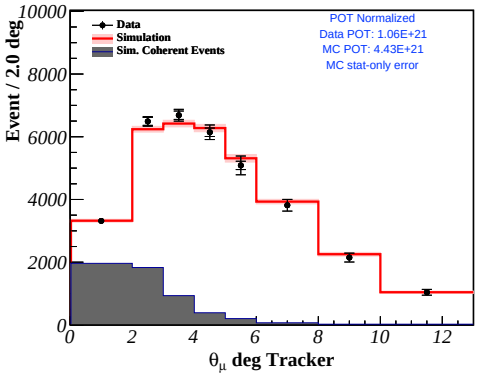
(b) Water



(c) Iron

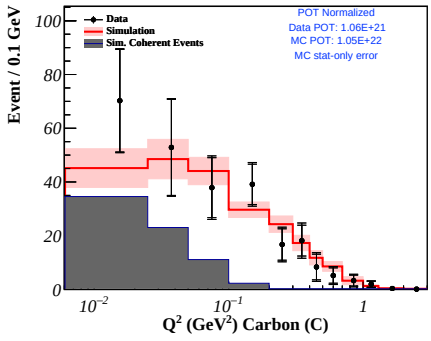


(d) Lead

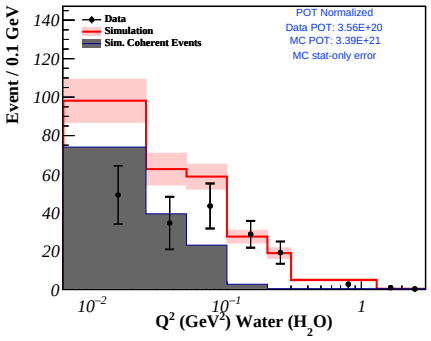


(e) Scintillator

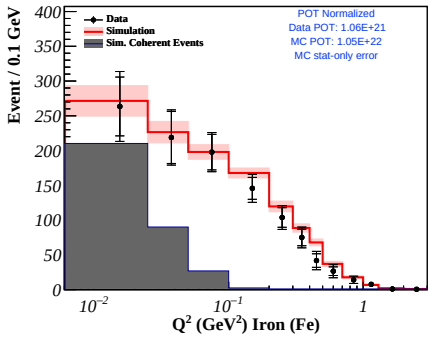
Figure 6-30: θ_μ Background Subtracted



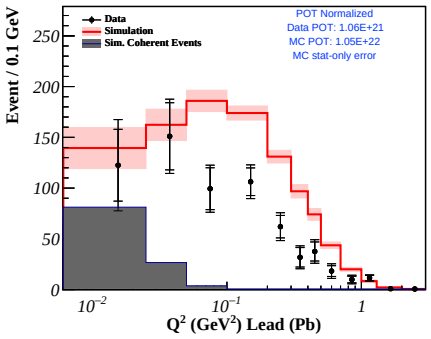
(a) Carbon



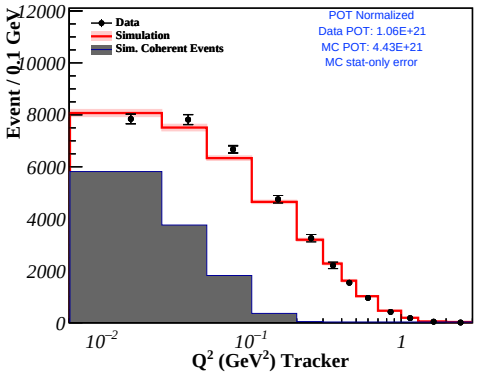
(b) Water



(c) Iron

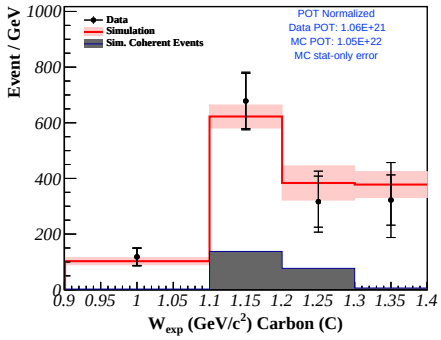


(d) Lead

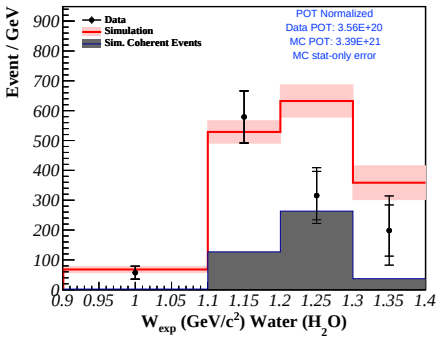


(e) Scintillator

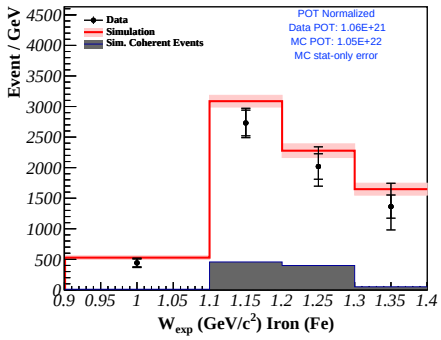
Figure 6-31: Q^2 Background Subtracted



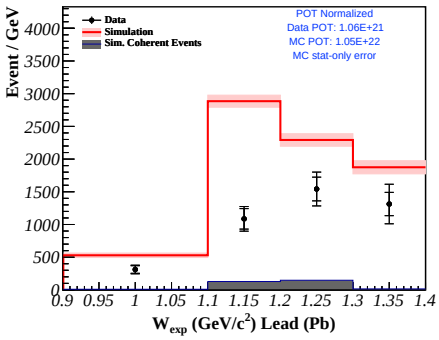
(a) Carbon



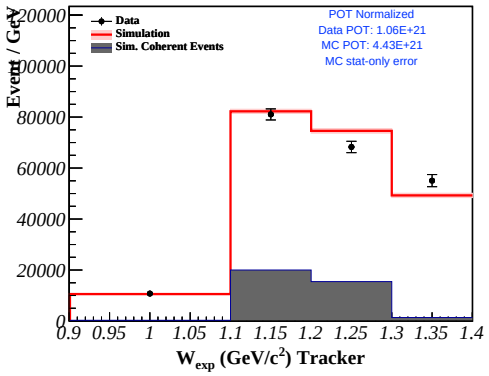
(b) Water



(c) Iron

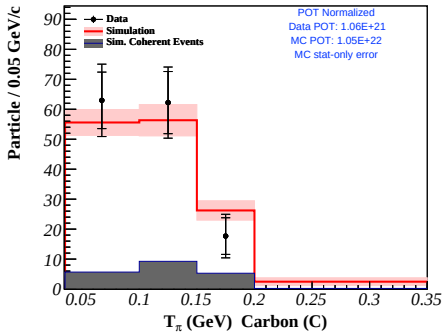


(d) Lead

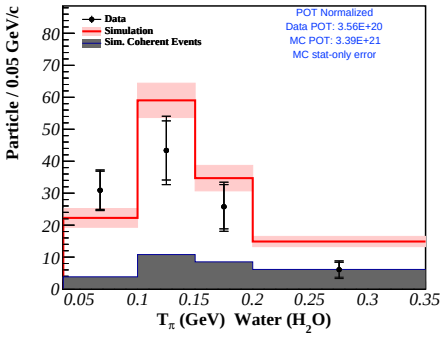


(e) Scintillator

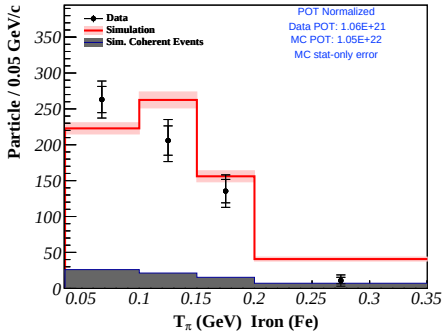
Figure 6-32: W_{exp} Background Subtracted



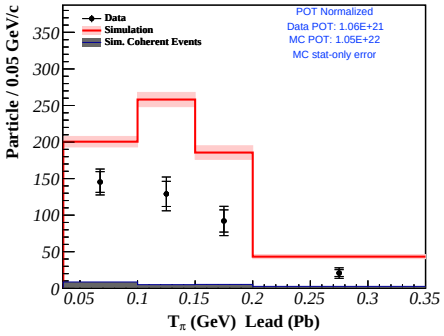
(a) Carbon



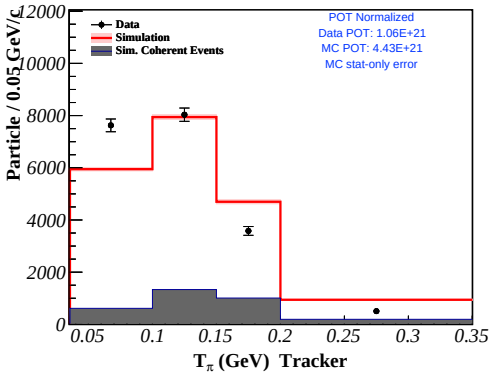
(b) Water



(c) Iron

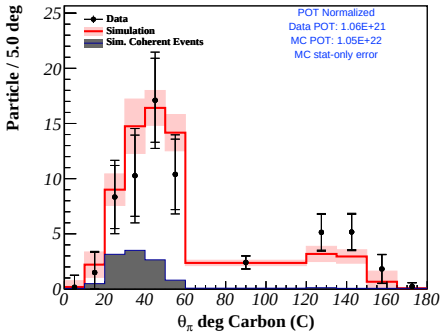


(d) Lead

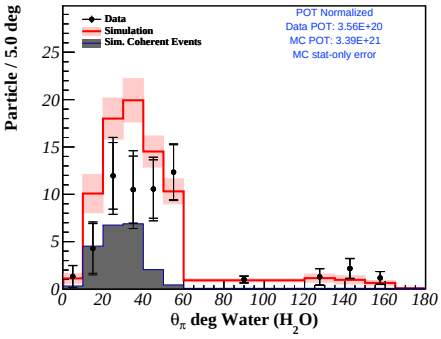


(e) Scintillator

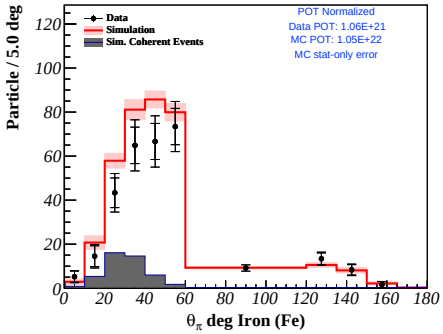
Figure 6-33: T_π Background Subtracted



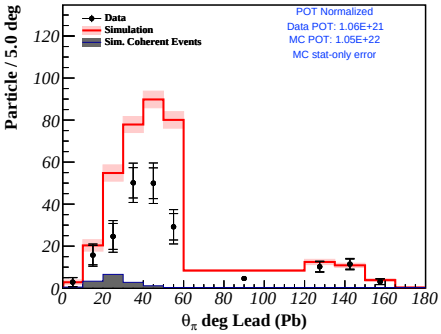
(a) Carbon



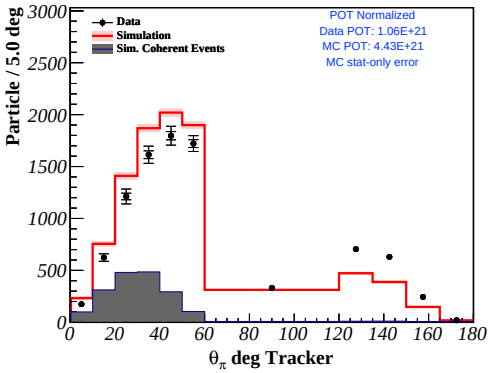
(b) Water



(c) Iron



(d) Lead



(e) Scintillator

Figure 6-34: θ_π Background Subtracted

6.6 Unfolding

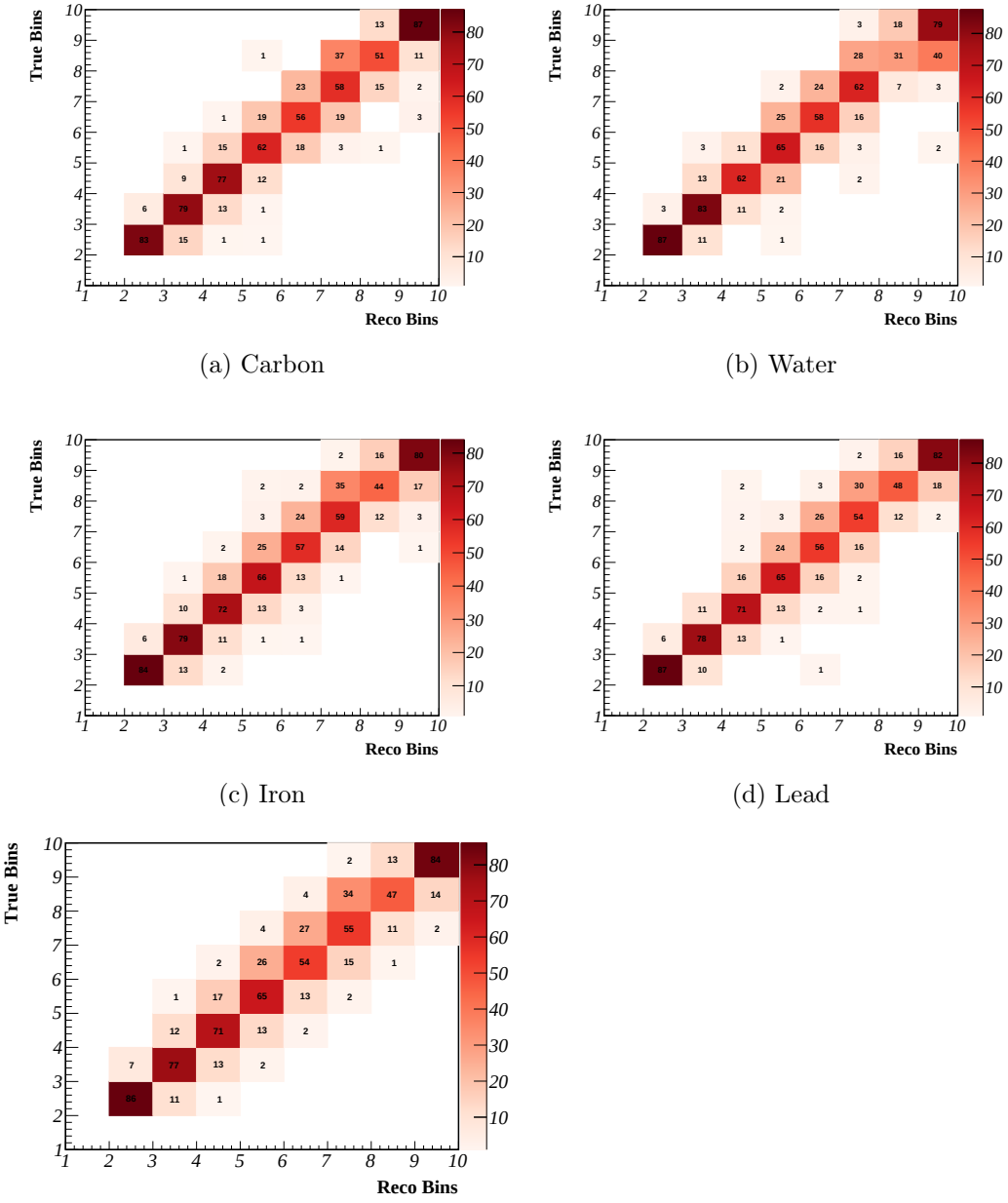
Reconstructed kinematic quantities can differ from true kinematic quantities due to limitations in detector resolution and inaccuracies in reconstruction. Processes that cause events to migrate from a truth bin i to a reconstruction bin j, where $i \neq j$, are called smearing. An example of a limitation in detector resolution is the size of the scintillator strips, which may smear the length of particle tracks, which smears the reconstruction of the particle momentum. An example of an inaccuracy in reconstruction is the calorimetric correction used to estimate neutron energy in the hadronic recoil energy reconstruction. This correction could under- or over-predict the energy contribution from neutrons, smearing the hadronic recoil energy. The smearing process can be expressed in the equation 6.8, where y_j is the number of events in reconstructed bin j and λ_i is the number of events in truth bin i.

$$y_j = \sum_{i}^{\text{truth bins}} U_{ij}\lambda_i \tag{6.8}$$

U_{ij} is called the migration matrix, and each element is the fraction of events in truth bin i reconstructed in reconstruction bin j. At this step of the cross section extraction, the only events in the background subtracted sample are signal events, therefore the migration matrix here quantifies the smearing of the kinematics of signal events. The migration matrix is constructed from simulated signal events which pass the selection cuts. These events are placed into a 2D histogram binned with the reconstructed kinematic on the x-axis and true kinematics on the y-axis. The reconstructed and true kinematics have the same binning.

6.6.1 Migration Matrices

Figures 6-35 to 6-42 show the row normalized migration matrices for each analysis variable in each target. Each row has been normalized such that the sum of each row is 100. The numbers in each cell of the matrix shows the percentage of events in truth bin i smeared into reconstructed bin j. The migration bin may include underflow and overflow bins that are not shown here. These bins include events which are truly within the studied range of some quantity, but not reconstructed within that range, or vice versa.



(a) Carbon

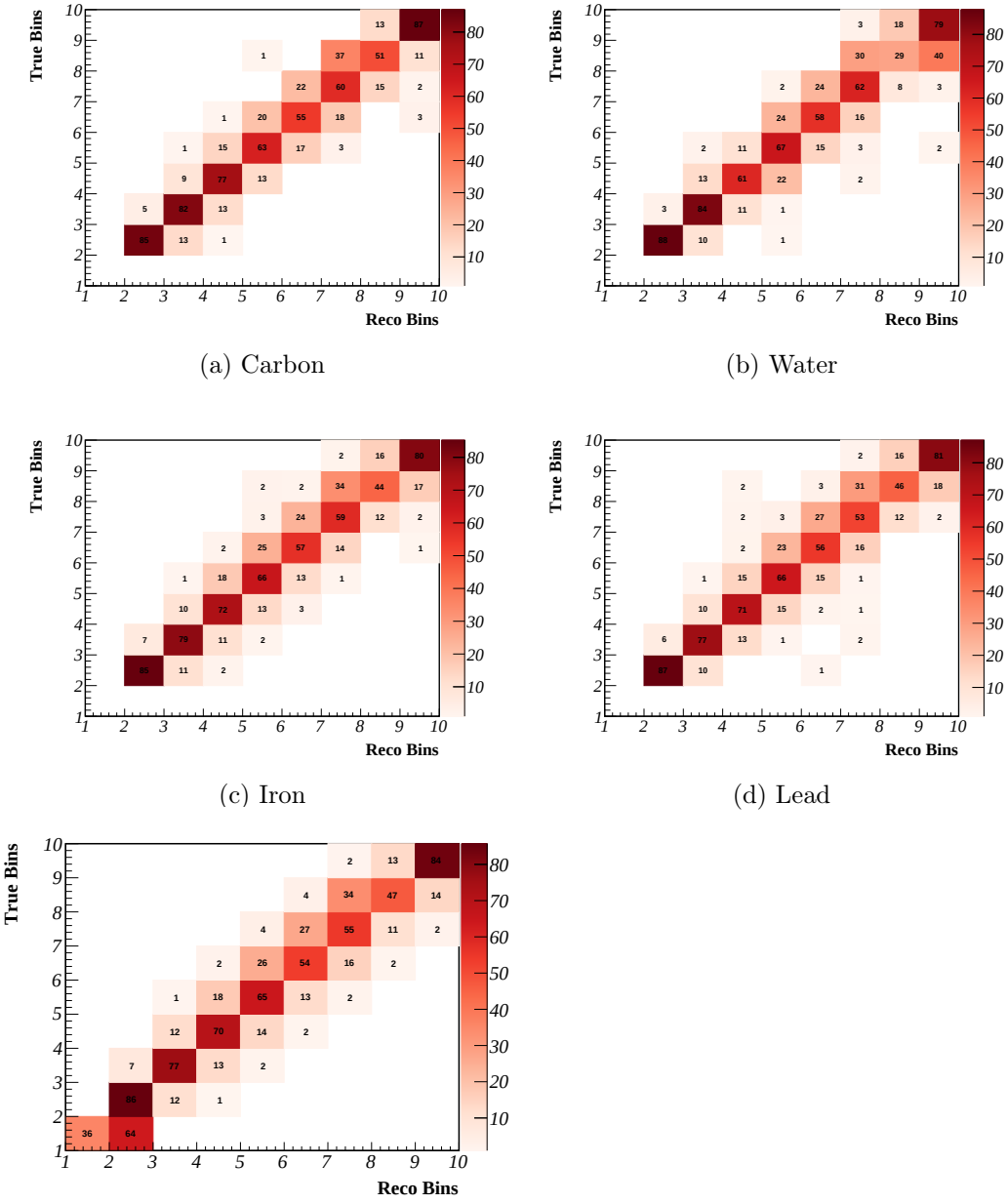
(b) Water

(c) Iron

(d) Lead

(e) Scintillator

Figure 6-35: p_μ Row Normalized Migration Matrix (N Bins = 10)
Bins [0.0, 1.5, 3.0, 4.0, 5.0, 6.0, 7.0, 8.5, 10.0, 20.0] GeV



(a) Carbon

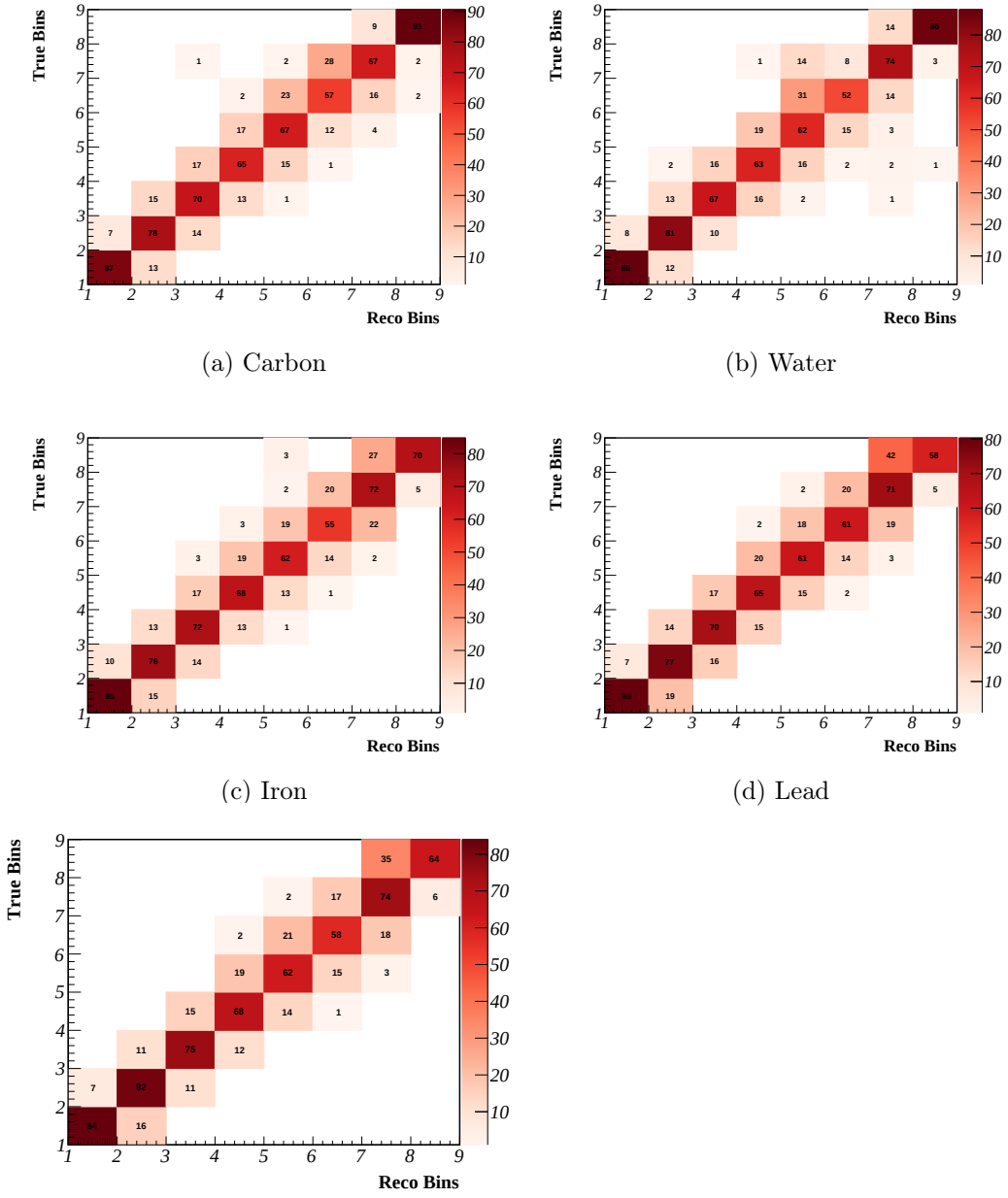
(b) Water

(c) Iron

(d) Lead

(e) Scintillator

Figure 6-36: $p_{\mu,||}$ Row Normalized Migration Matrix (N Bins = 9)
Bins [0.0, 1.5, 3.0, 4.0, 5.0, 6.0, 7.0, 8.5, 10.0, 20.0] GeV



(a) Carbon

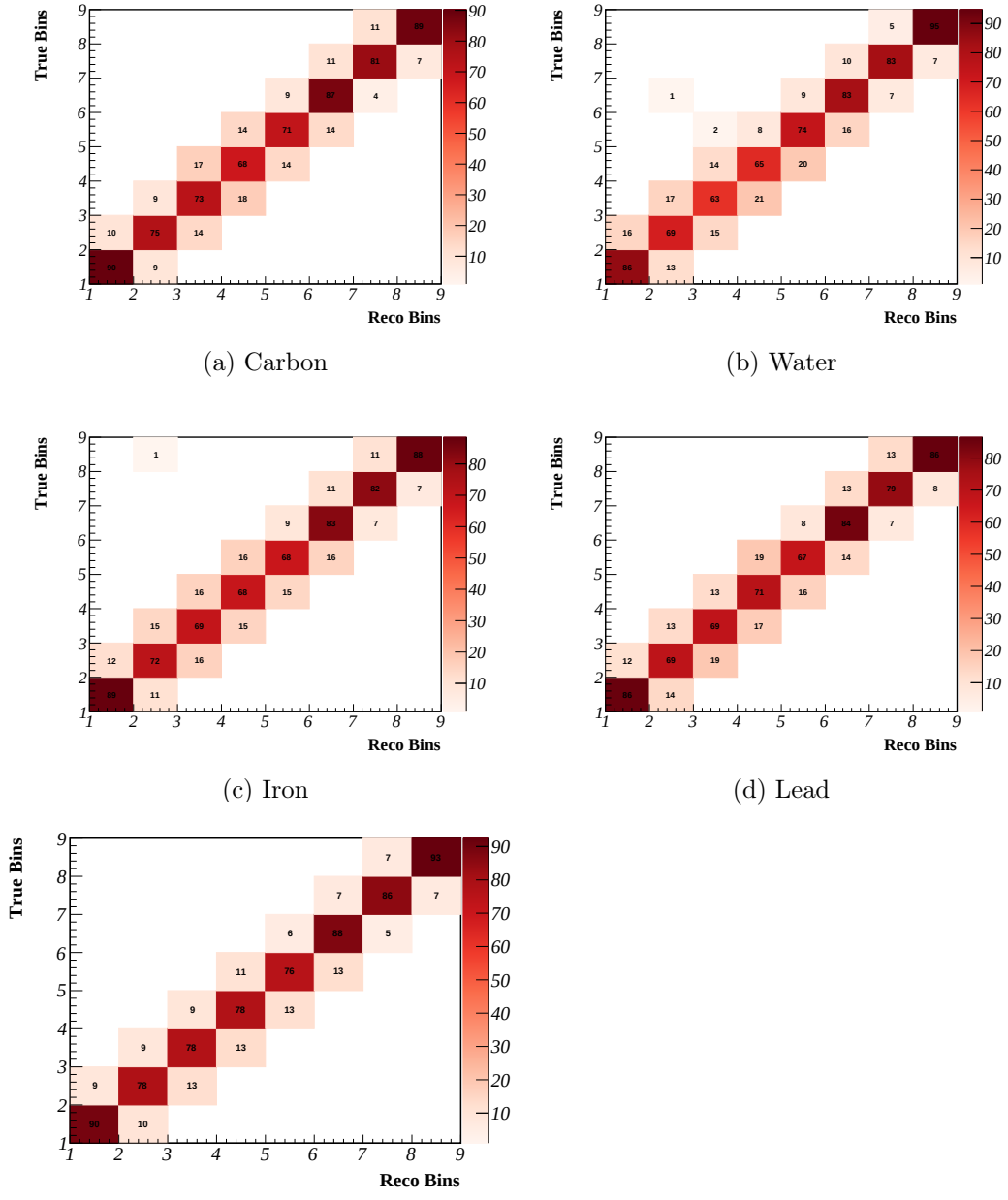
(b) Water

(c) Iron

(d) Lead

(e) Scintillator

Figure 6-37: $p_{\mu,T}$ Row Normalized Migration Matrix (N Bins = 8) Bins [0.0, 0.15, 0.3, 0.45, 0.6, 0.75, 0.90, 1.25, 2.5] GeV



(a) Carbon

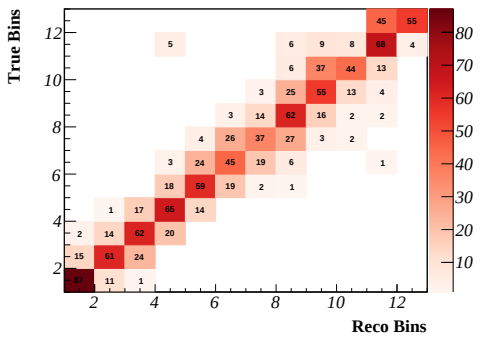
(b) Water

(c) Iron

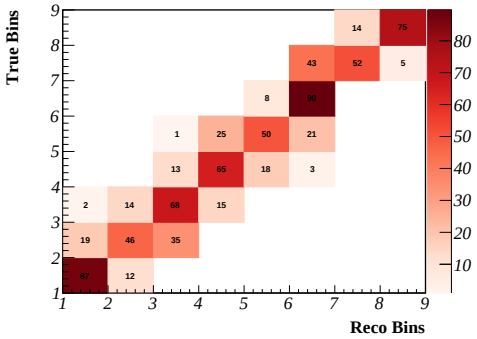
(d) Lead

(e) Scintillator

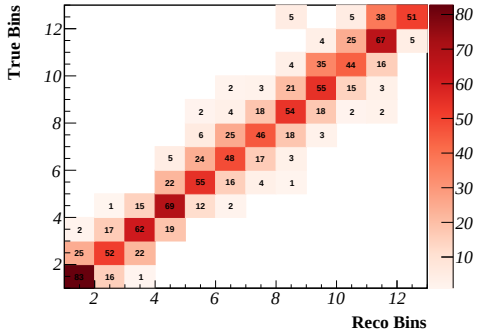
Figure 6-38: θ_μ Row Normalized Migration Matrix (N Bins = 8)
Bins [0.0, 2.0, 3.0, 4.0, 5.0, 6.0, 8.0, 10.0, 13.0] degrees



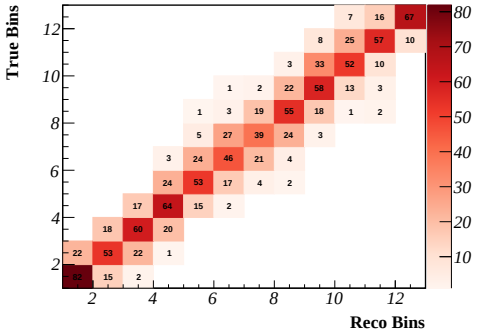
(a) Carbon



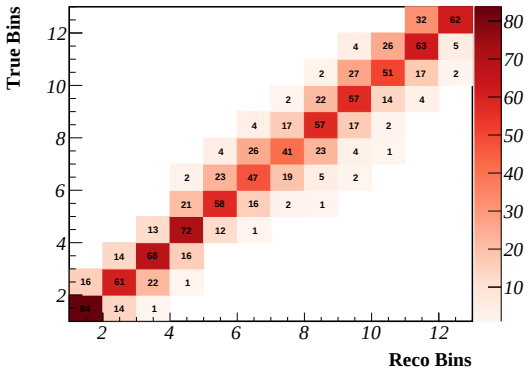
(b) Water



(c) Iron

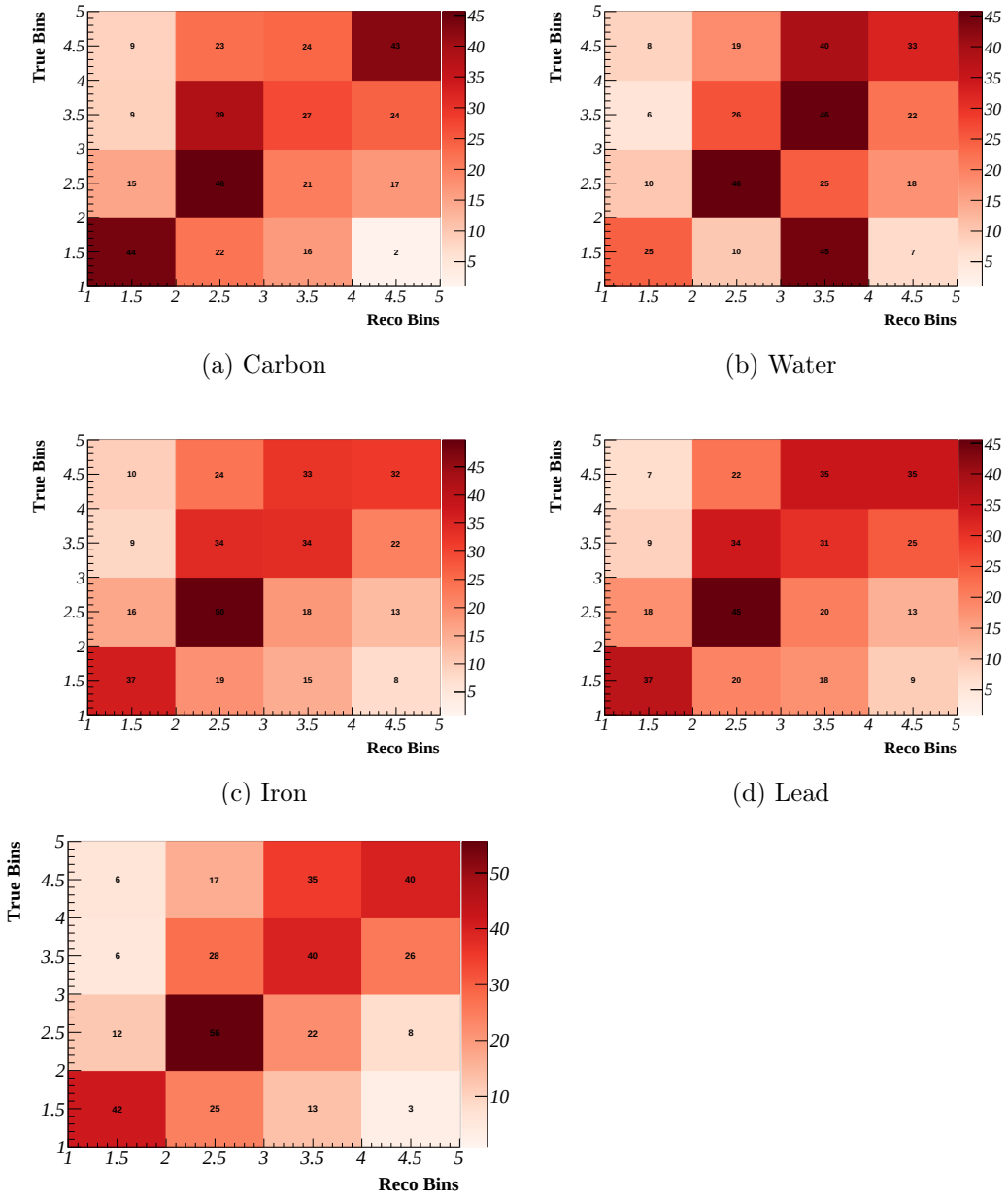


(d) Lead



(e) Scintillator

Figure 6-39: Q^2 Row Normalized Migration Matrix (N Bins = 12)
Bins [0.0, 0.025, 0.050, 0.1, 0.2, 0.3, 0.4, 0.5, 0.7, 1.0, 1.3, 2.0, 3.0] GeV^2
Water Target Bins [0.0, 0.025, 0.050, 0.1, 0.2, 0.3, 1.3, 2.0, 3.0] GeV^2



(a) Carbon

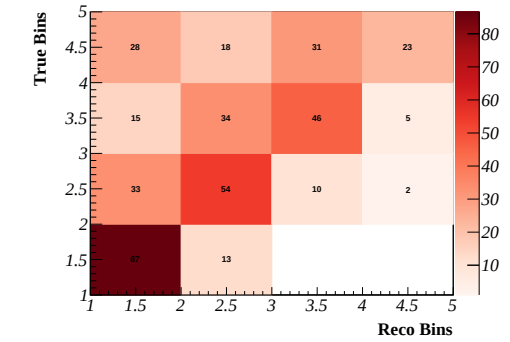
(b) Water

(c) Iron

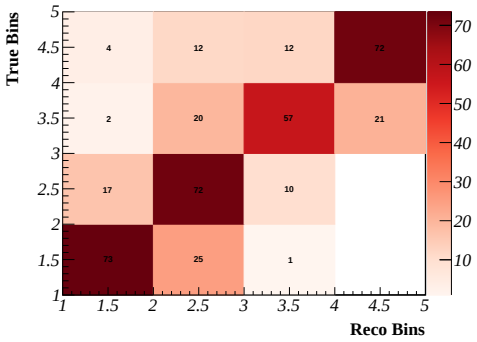
(d) Lead

(e) Scintillator

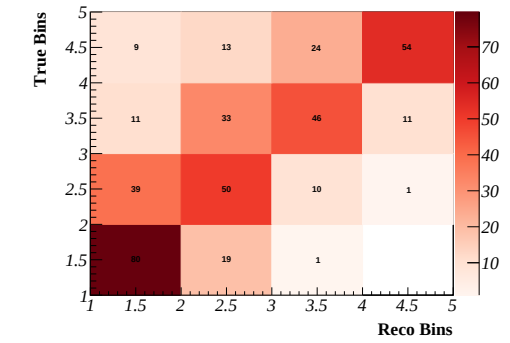
Figure 6-40: W_{exp} Row Normalized Migration Matrix (N Bins = 4) Bins [0.9, 1.1, 1.2, 1.3, 1.4] GeV/c^2



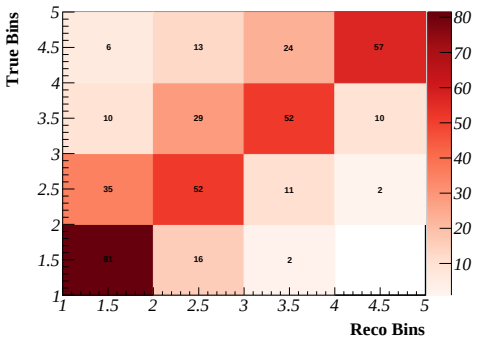
(a) Carbon



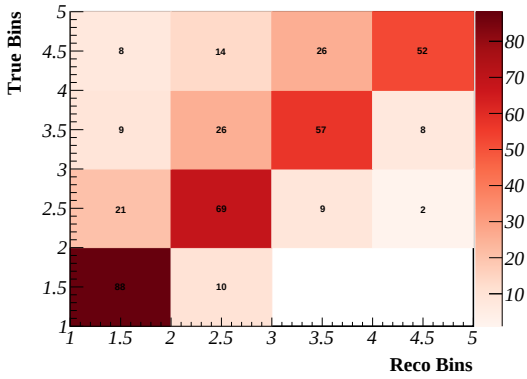
(b) Water



(c) Iron

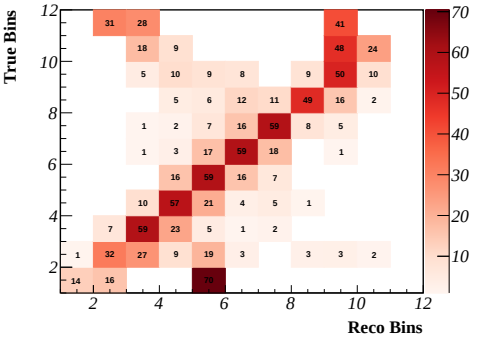


(d) Lead

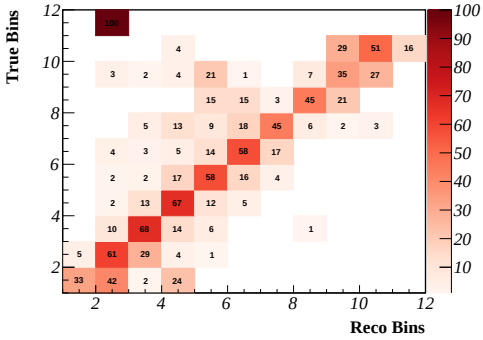


(e) Scintillator

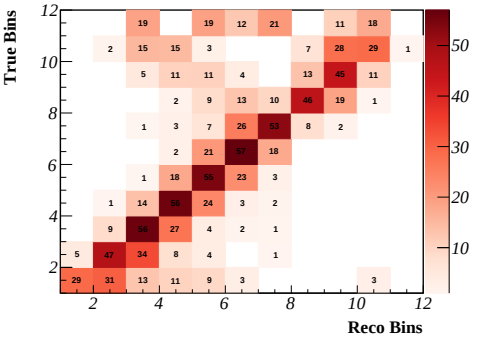
Figure 6-41: T_π Row Normalized Migration Matrix (N Bins = 4)
Bins [0.035, 0.1, 0.15, 0.20, 0.35] GeV



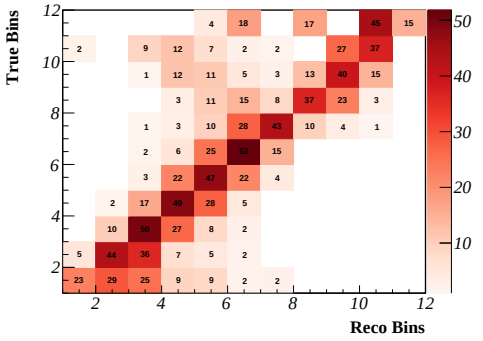
(a) Carbon



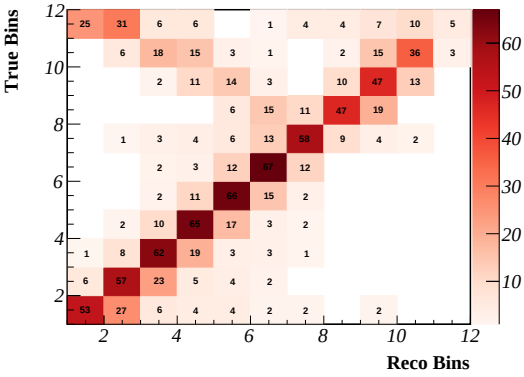
(b) Water



(c) Iron



(d) Lead



(e) Scintillator

Figure 6-42: θ_π Row Normalized Migration Matrix (N Bins = 11)
Bins [0.0, 10.0, 20.0, 30.0, 40.0, 50.0, 60.0, 120.0, 135.0, 150.0, 165.0, 180.0] degrees

6.6.2 Iterative "Bayesian" Unfolding

In order to undo the effects of smearing, MINERvA analyses migrate events from reconstruction bin j back to truth bin i in a process called unfolding. Inverting the migration matrix can unsmear the reconstructed kinematics into truth bins, as shown in equation 6.9.

$$\lambda_i = \sum_{j}^{\text{reconstruction bins}} U_{ij}^{-1} y_j \tag{6.9}$$

The migration matrix is inverted numerically using the D'Agostini or iterative "Bayesian" procedure [138][139]. This procedure reduces the variance of the unfolded quantity compared to the true quantity at the cost of increasing bias. Regularization is implemented by truncating the number of iterations used by the procedure. This truncation occurs when the cost of increasing bias outweighs the reduction in variance. By unfolding simulations where the distribution of the true kinematics λ are known, the number of iterations can be determined by finding the least number of iterations required for the χ^2 measure in equation 6.10 to stabilize near a minimum.

$$\chi^2 = \sum_{\alpha,\beta} \left(\hat{\lambda}^{(k)} - \lambda\right)_\beta V^{-1}_{\beta\alpha} \left(\hat{\lambda}^{(k)} - \lambda\right)_\alpha . \tag{6.10}$$

Here, $\hat{\lambda}^{(k)}$ is the unfolded kinematic after k iterations, α and β are the bin indices of the unfolded distribution, and V is the unfolding covariance matrix. The following section details how the number of iterations were determined.

6.6.3 Unfolding Warping Study

If the migration matrix accurately represents the smearing of true kinematics to reconstructed kinematics, the D'Agostini unfolding procedure will perfectly unfold the simulation in one iteration. However, if the signal model is not in agreement with the measurement in the data, signal events in the data may have a different migration matrix than simulation, therefore the unfolding procedure requires additional iterations to unfold data distributions correctly. The required number of iterations must stable regardless of the smearing model. Therefore, the unfolding procedure must be tested with alternative models in order to determine the required number of unfolding iterations.

To test the unfolding procedure, the reconstructed and corresponding true kinematic distributions were reweighted, or "warped", in order to reflect alternative models. These alternative models are built by exaggerating a feature of the model. This is done to determine the sensitivity of the unfolding to that feature. The warped reconstructed distributions are then unfolded using the unwarped migration matrix, and the χ^2 expressed in equation 6.10 is calculated for each unfolding iteration. In order to account for statistical fluctuations, the warped reconstructed distribution is unfolded multiple times. Each time it is unfolded, the content of each bin in the distribution is randomly determined by a Poisson distribution. The number of iterations used for unfolding the unwarped distribution is the iteration with lowest median χ^2. As the Trekkie/Trekker that I am, I named the tool that does this study for the MINERvA collaboration as the "TransWarpExtraction Tool". All instances are named after starships.

This test must be run for each kinematic distribution as each distribution has a different migration matrix. For this analysis, four alternative warped models are used

Warped Model	Description
Resonant M_A^{RES} Warp	Resonant axial mass M_A^{RES} in the Rein Seghal model, described in sections 1.3.2 and 4.5.4.2, is shifted by $+2\sigma_{M_A}$.
Low Q^2 Warp	The low Q^2 reweight, described in section 4.5.4.6, is applied in the unwarped simulation. This warp removes the reweight.
Nonresonant Pion Warp	The nonresonant pion production weight determined in the deuterium bubble chamber fits, described in section 4.5.4.2, is shifted by $+2\sigma$.
Anisotropic Δ Warp	Changes the angular distribution of pion from Δ decay from anisotropic to isotropic. This is explained in sections 6.10.1 and 4.1.2.

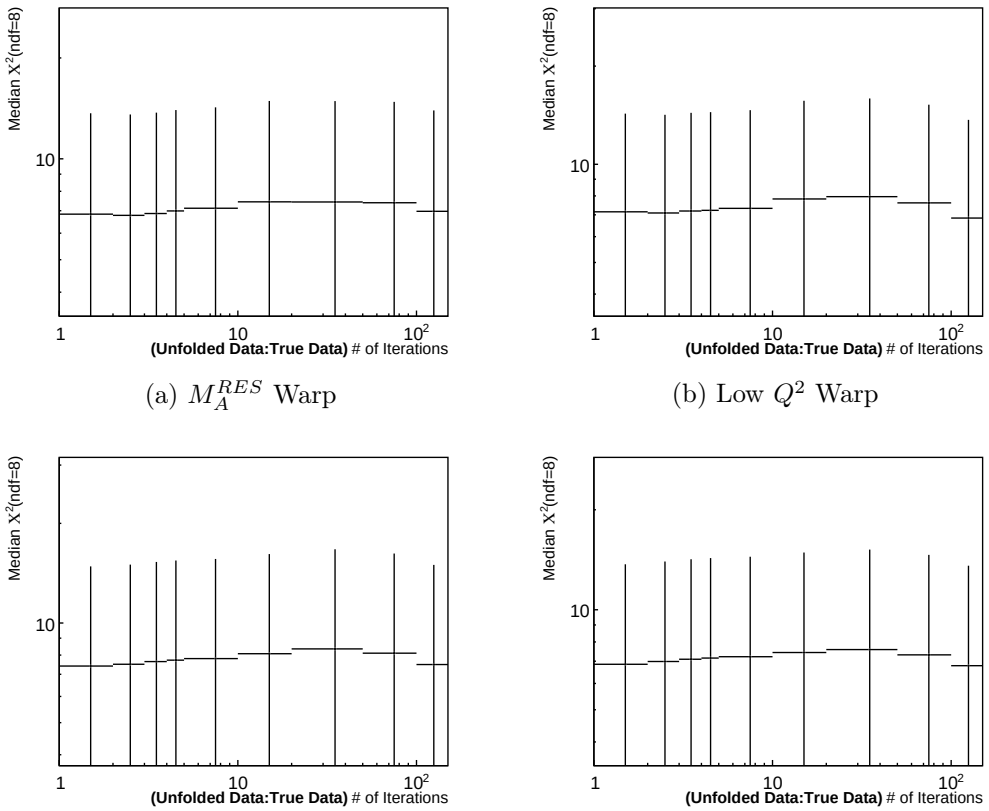
Table 6.13: List of warp models used in the unfolding study

to find the number of iterations. These models are explained in table 6.13.

Figures 6-43 to 6-46 show median χ^2 versus unfolding iterations distributions for $p_{\mu,T}$. When there is a similar distribution in the kinematic variable being studied between the reference and warped model, only one or two iterations are required for unfolding. A feature that is commonly seen is that the median in some distributions with sparsely populated bins increases at high numbers of iterations, past the location of the desired minimum. This happens when the thrown statistical fluctuations put the event rate near zero in a given test, and the unfolding procedure lands on zero content for that bin. This failure does not occur in the data unfolding. Occasionally, a model variation is extreme in a measured kinematic variable, such as for W_{exp}, where the M_A^{RES} warp model required 10 iterations. The warp studies for W_{exp} are shownn in figures 6-47 through 6-50. Table 6.14 shows the number of iterations used for each analysis variable.

Variable	Number of iterations
p_μ	1
$p_{\mu,\|\|}$	1
$p_{\mu,T}$	2
θ_μ	2
Q^2	2
W_{exp}	10
T_π	2
θ_π	2

Table 6.14: Number of unfolding iterations used by each analysis variable



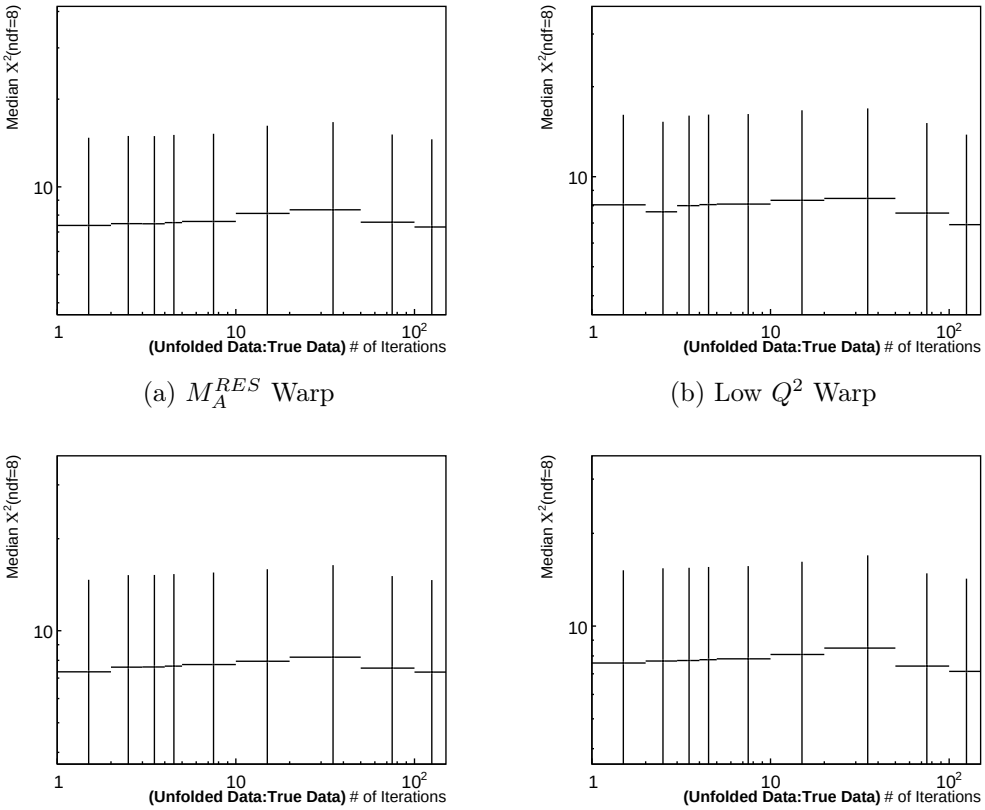
(a) M_A^{RES} Warp

(b) Low Q^2 Warp

(c) Nonresonant π Warp

(d) Anisotropic Δ Warp

Figure 6-43: Carbon $p_{\mu,T}$ Median χ^2 vs Unfolding Iterations



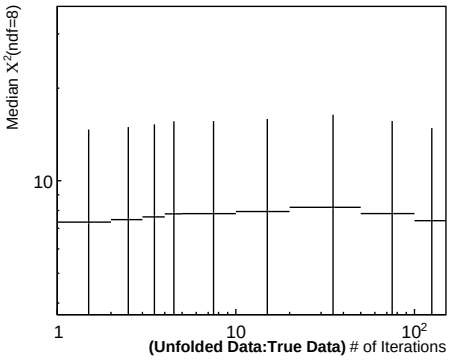
(a) M_A^{RES} Warp

(b) Low Q^2 Warp

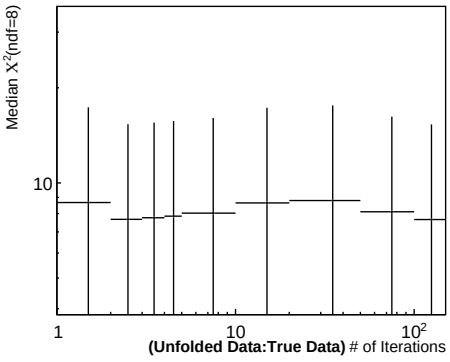
(c) Nonresonant π Warp

(d) Anisotropic Δ Warp

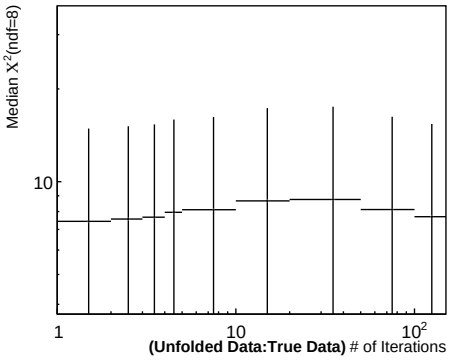
Figure 6-44: Iron $p_{\mu,T}$ Median χ^2 vs Unfolding Iterations



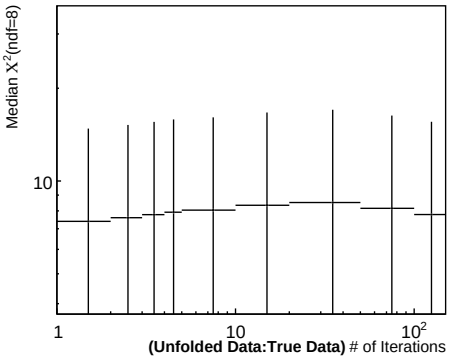
(a) M_A^{RES} Warp



(b) Low Q^2 Warp

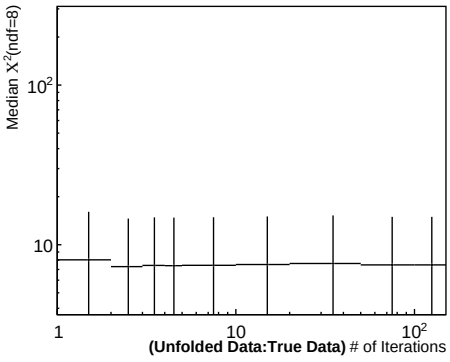


(c) Nonresonant π Warp

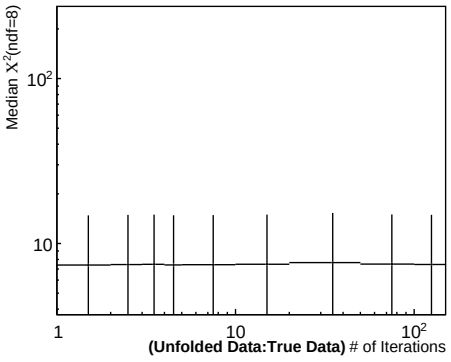


(d) Anisotropic Δ Warp

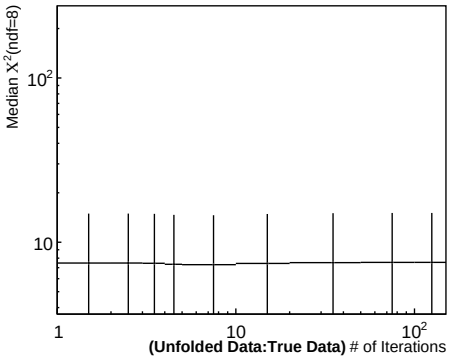
Figure 6-45: Lead $p_{\mu,T}$ Median χ^2 vs Unfolding Iterations



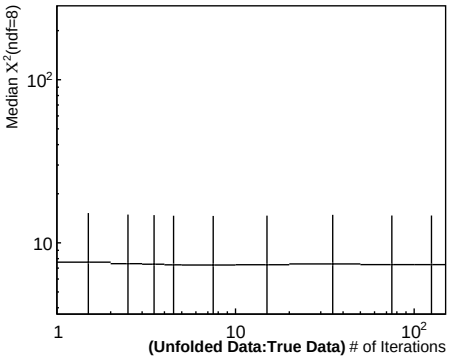
(a) M_A^{RES} Warp



(b) Low Q^2 Warp

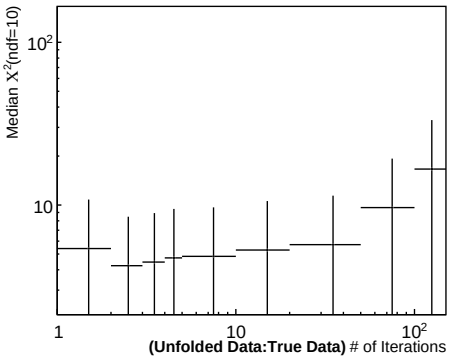


(c) Nonresonant π Warp

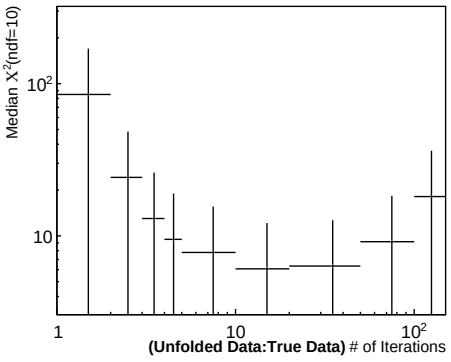


(d) Anisotropic Δ Warp

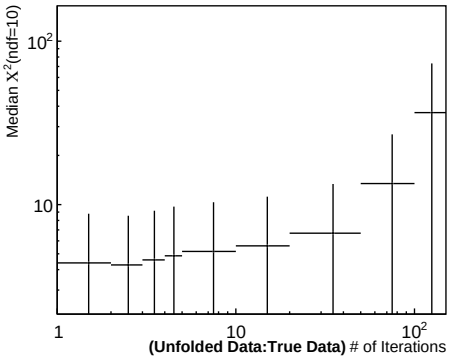
Figure 6-46: Tracker $p_{\mu,T}$ Median χ^2 vs Unfolding Iterations



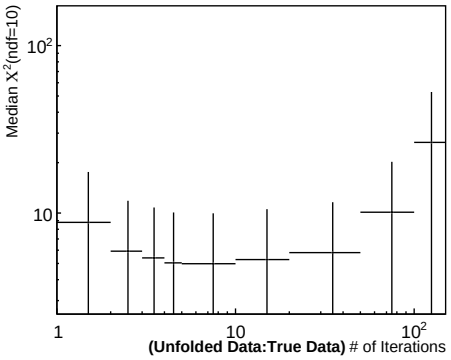
(a) M_A^{RES} Warp



(b) Low Q^2 Warp

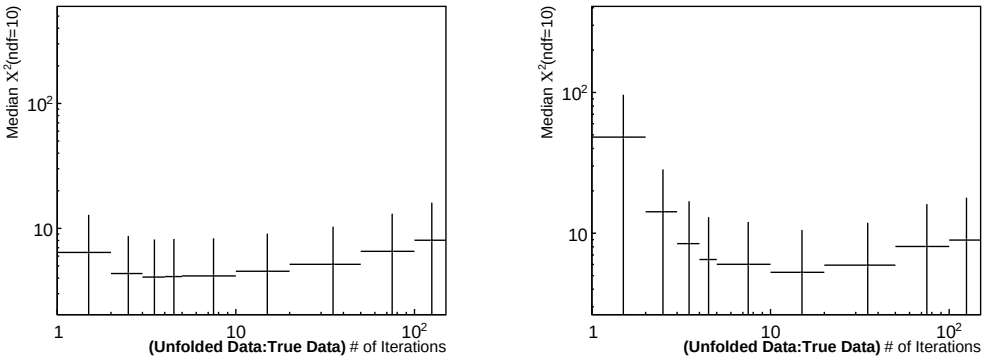


(c) Nonresonant π Warp



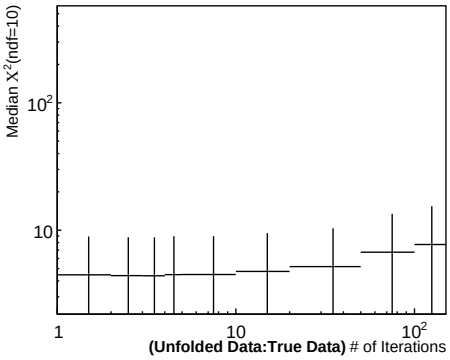
(d) Anisotropic Δ Warp

Figure 6-47: Carbon W_{exp} Median χ^2 vs Unfolding Iterations

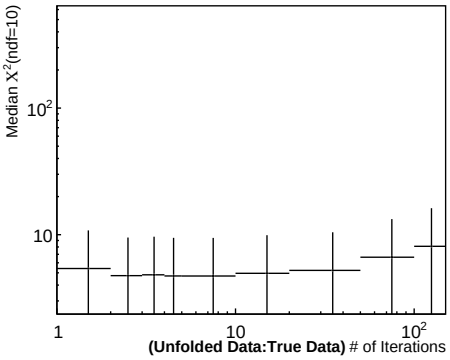


(a) M_A^{RES} Warp

(b) Low Q^2 Warp

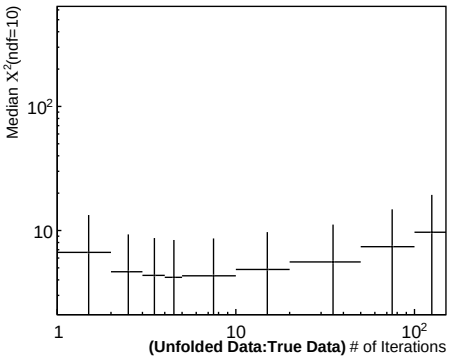


(c) Nonresonant π Warp

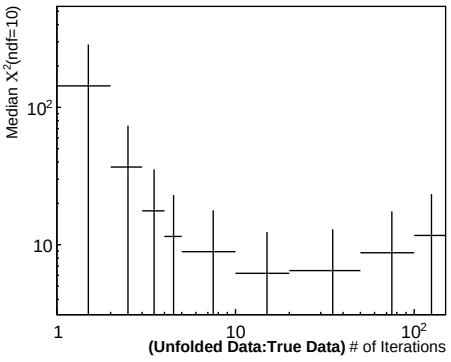


(d) Anisotropic Δ Warp

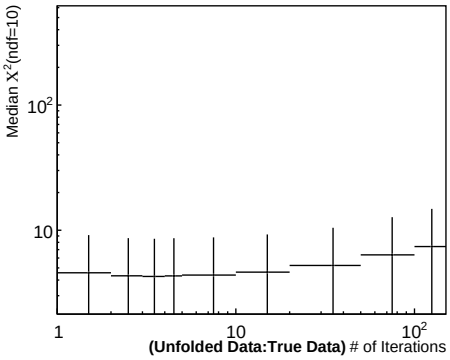
Figure 6-48: Iron W_{exp} Median χ^2 vs Unfolding Iterations



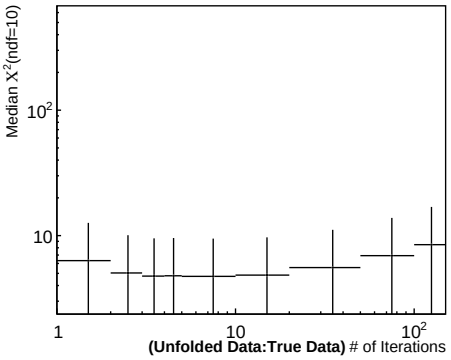
(a) M_A^{RES} Warp



(b) Low Q^2 Warp

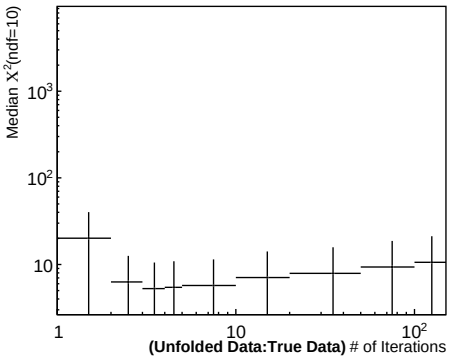


(c) Nonresonant π Warp

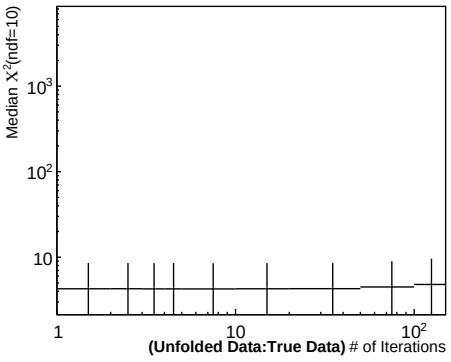


(d) Anisotropic Δ Warp

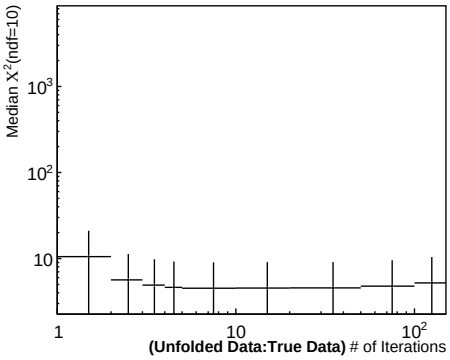
Figure 6-49: Lead W_{exp} Median χ^2 vs Unfolding Iterations



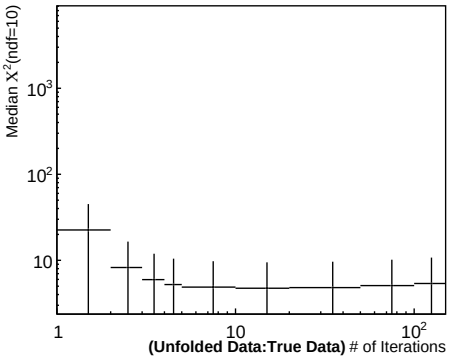
(a) M_A^{RES} Warp



(b) Low Q^2 Warp



(c) Nonresonant π Warp



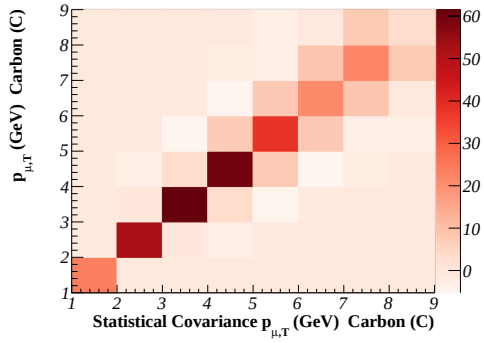
(d) Anisotropic Δ Warp

Figure 6-50: Tracker W_{exp} Median χ^2 vs Unfolding Iterations

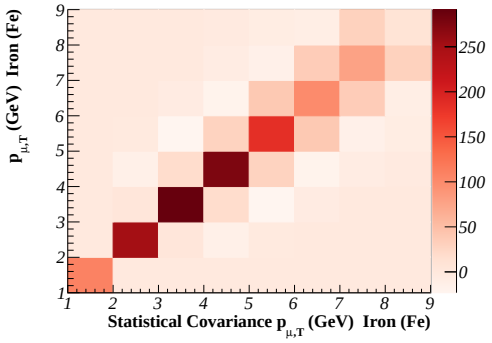
6.6.4 Unfolded Distributions

Figures 6-52 to 6-59 show the unfolded background subtracted distributions in each analysis variable in all the targets. It should be noted that the unfolding procedure also unfolds all systematic uncertainties, which are present in the error bars of the data distributions. Each systematic uncertainty has its own migration matrix.

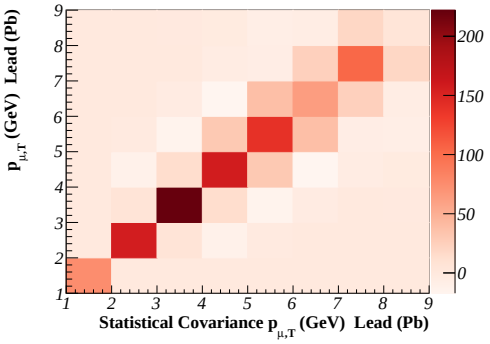
As the unfolding procedure causes migration of events between bins, the statistical uncertainty will be correlated between bins, and the statistical covariance matrix therefore will have off-diagonal terms that must be considered when comparing the result to a model. These correlations typically increase with the number of iterations. This correlated statistical covariance matrix is propagated through the rest of the cross section extraction. Figure 6-51 shows examples of statistical covariance matrices.



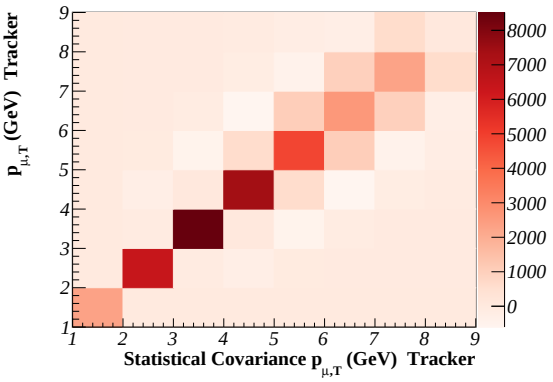
(a) Carbon



(b) Iron

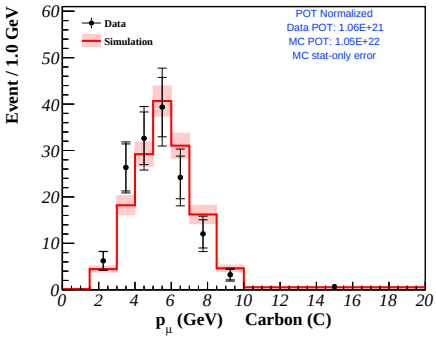


(c) Lead

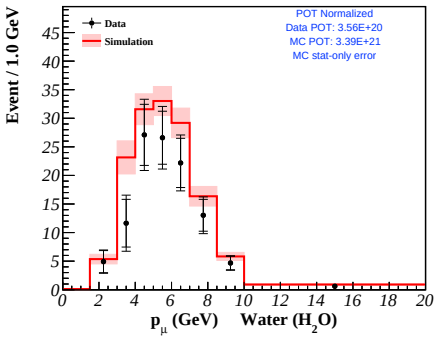


(d) Scintillator

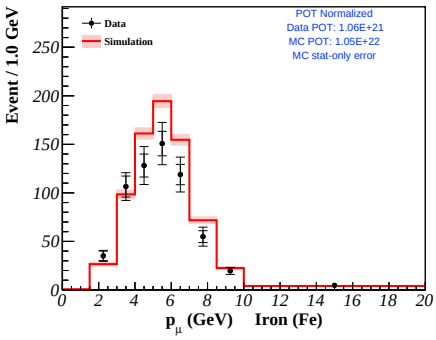
Figure 6-51: $p_{\mu,T}$ statistical covariance matrices after two unfolding iterations



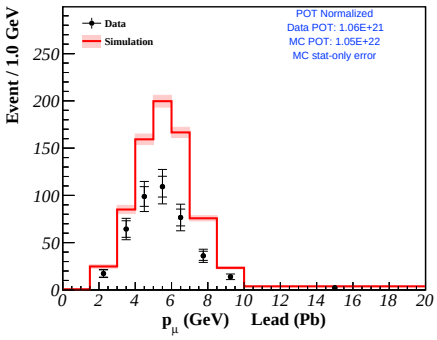
(a) Carbon



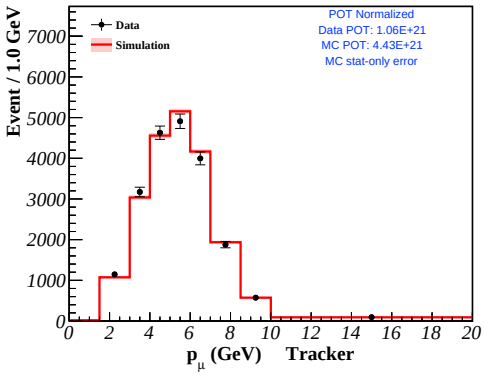
(b) Water



(c) Iron

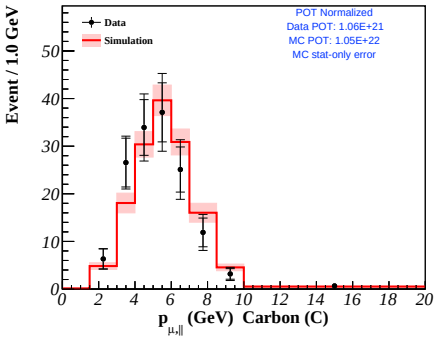


(d) Lead

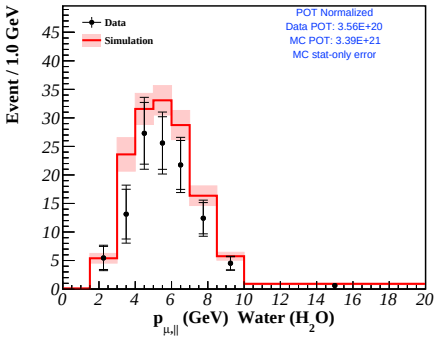


(e) Scintillator

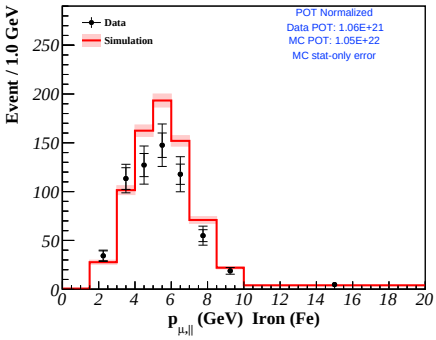
Figure 6-52: p_μ Unfolded Iteration 1



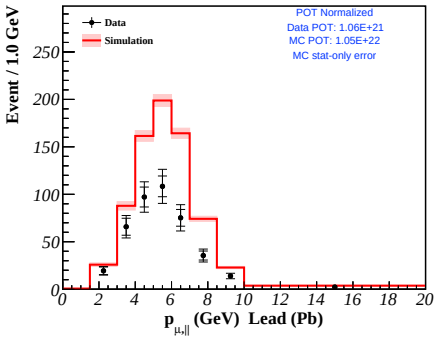
(a) Carbon



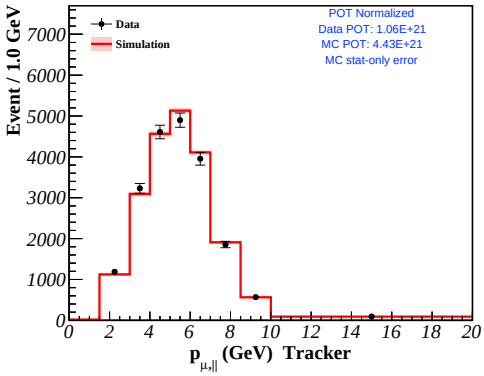
(b) Water



(c) Iron

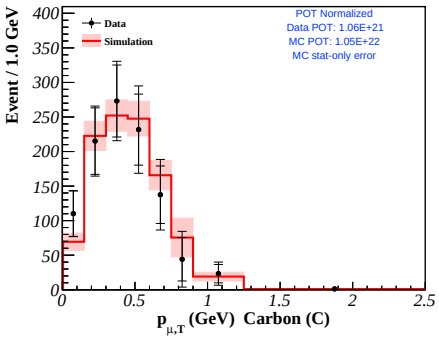


(d) Lead

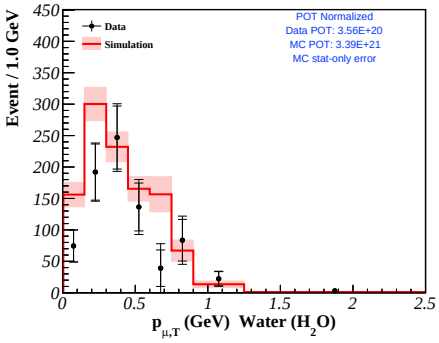


(e) Scintillator

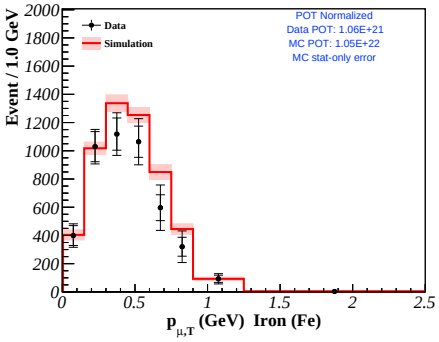
Figure 6-53: $p_{\mu,||}$ Unfolded Iteration 1



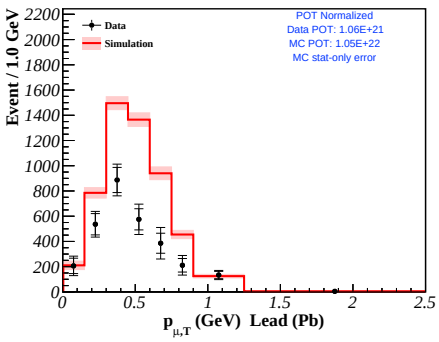
(a) Carbon



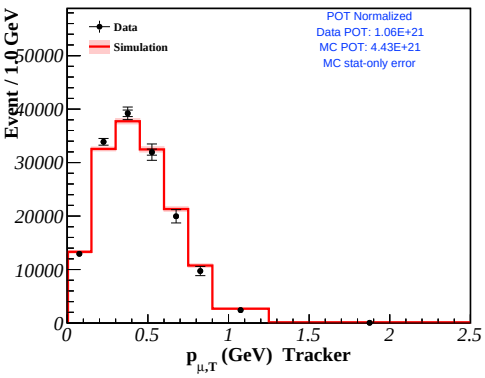
(b) Water



(c) Iron

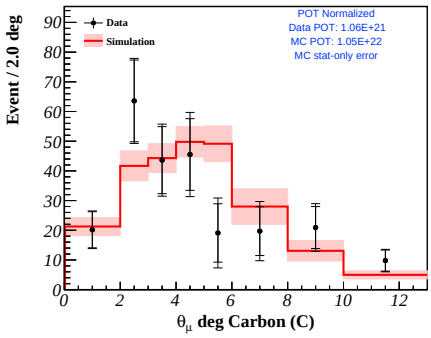


(d) Lead

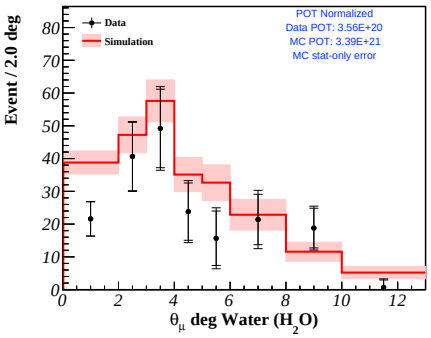


(e) Scintillator

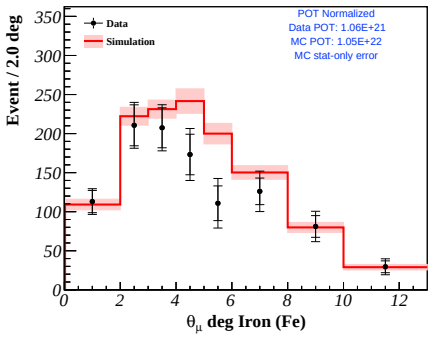
Figure 6-54: $p_{\mu,T}$ Unfolded Iteration 2



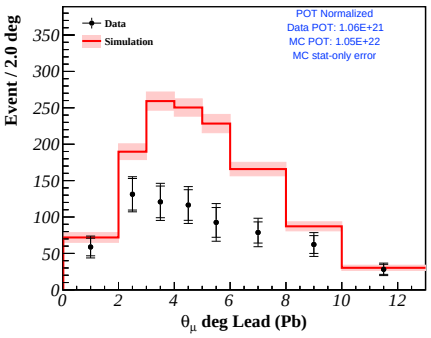
(a) Carbon



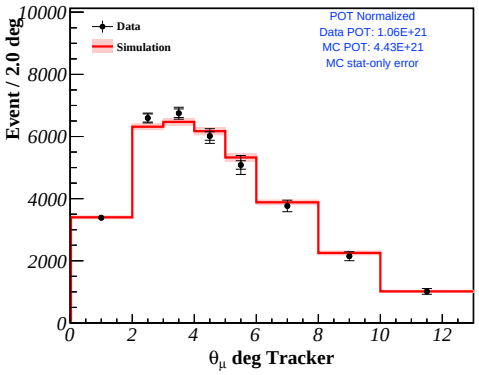
(b) Water



(c) Iron

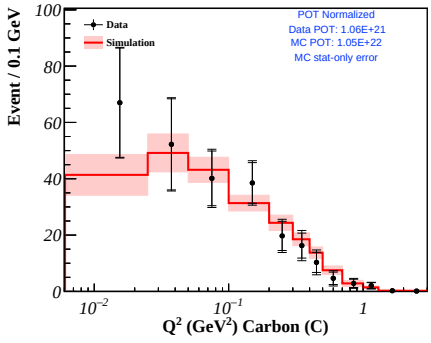


(d) Lead

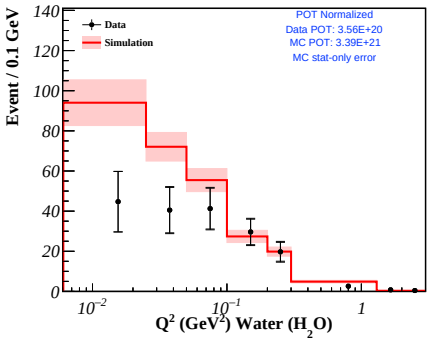


(e) Scintillator

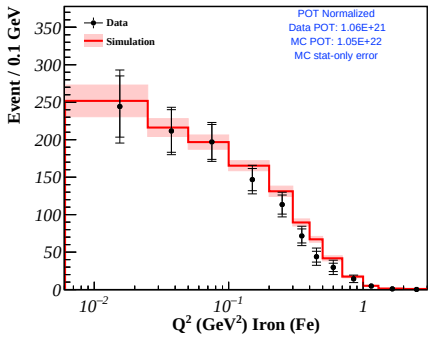
Figure 6-55: θ_μ Unfolded Iteration 2



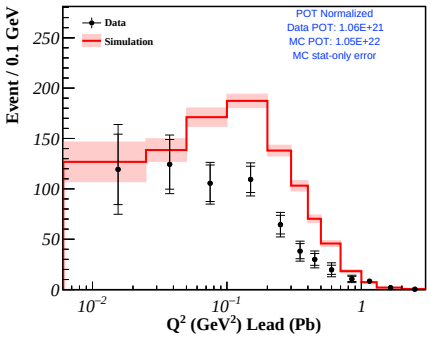
(a) Carbon



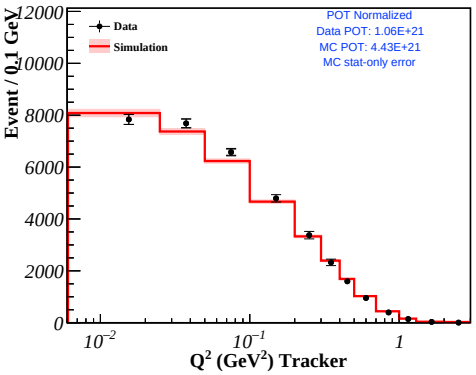
(b) Water



(c) Iron

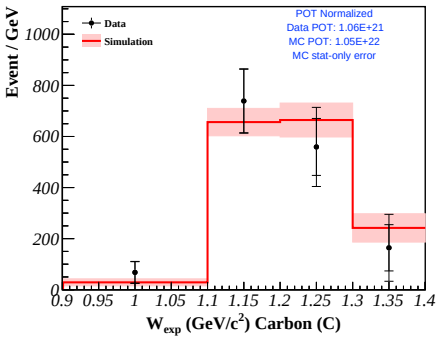


(d) Lead

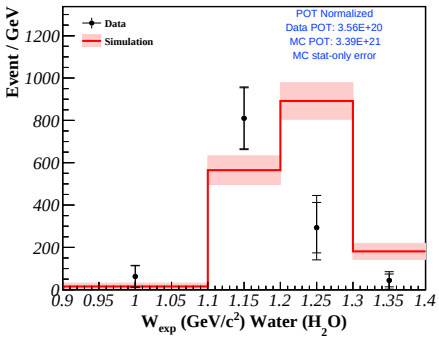


(e) Scintillator

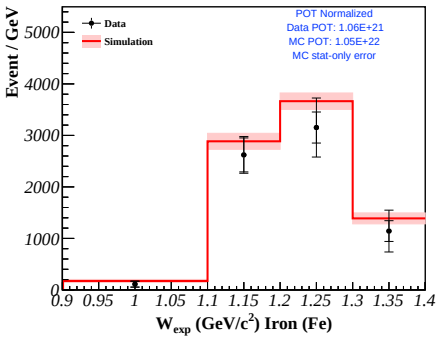
Figure 6-56: Q^2 Unfolded Iteration 2



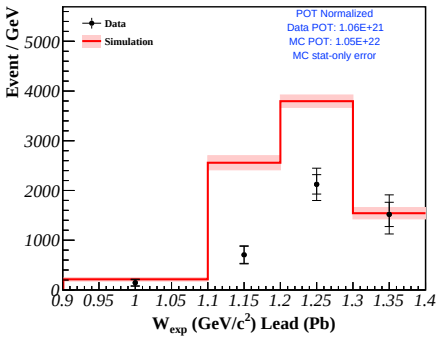
(a) Carbon



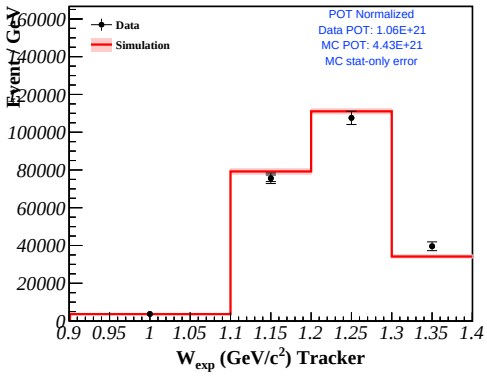
(b) Water



(c) Iron

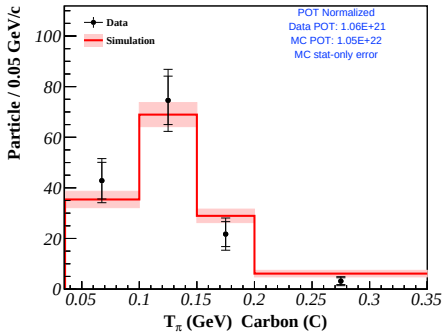


(d) Lead

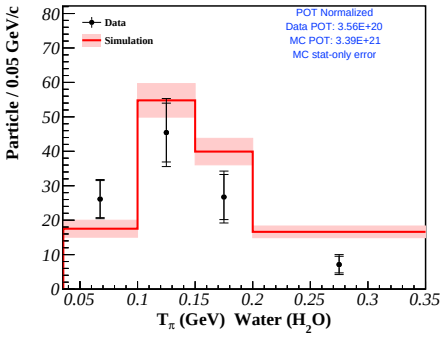


(e) Scintillator

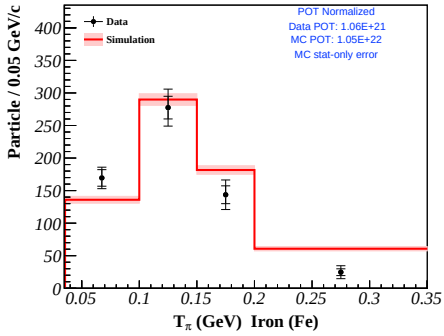
Figure 6-57: W_{exp} Unfolded Iteration 10



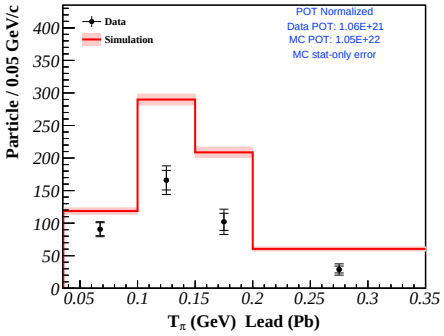
(a) Carbon



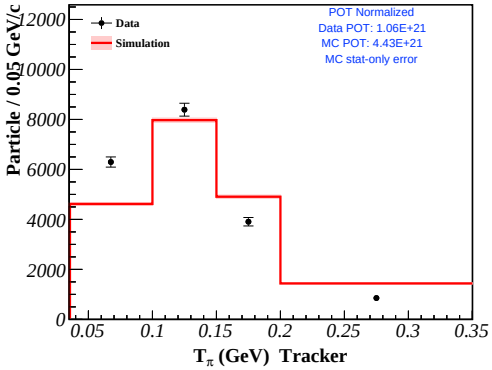
(b) Water



(c) Iron

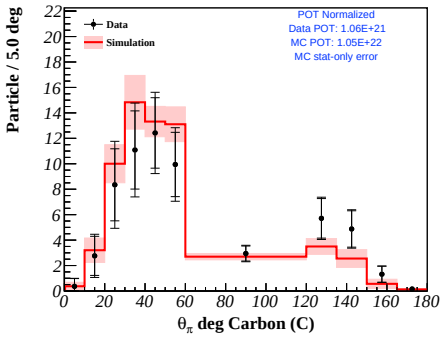


(d) Lead

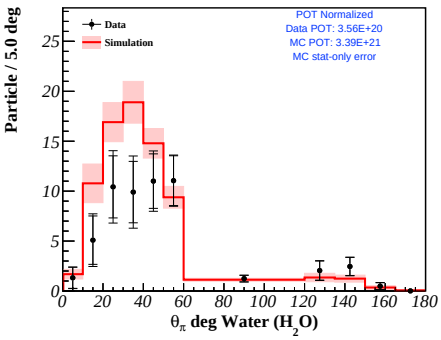


(e) Scintillator

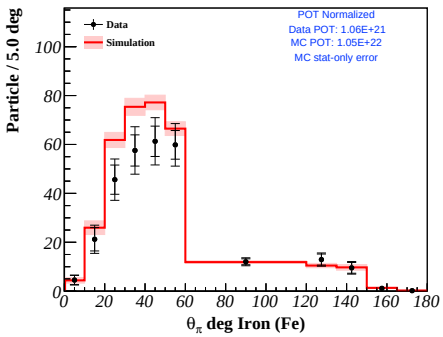
Figure 6-58: T_π Unfolded Iteration 2



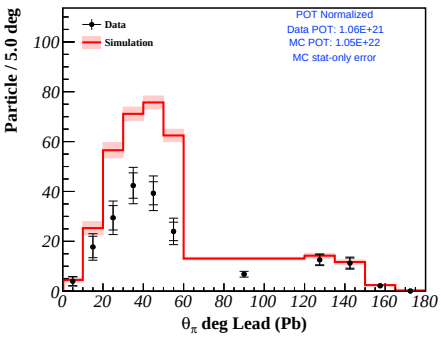
(a) Carbon



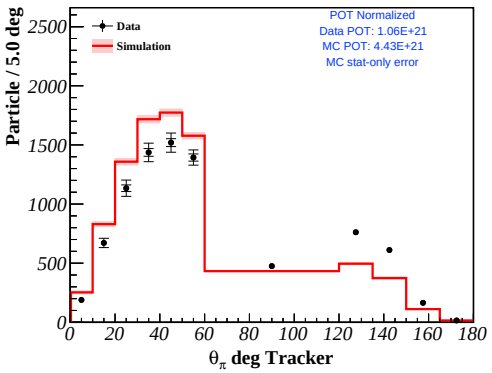
(b) Water



(c) Iron



(d) Lead



(e) Scintillator

Figure 6-59: θ_π Unfolded Iteration 2

6.7 Efficiency Correction

Signal events may not be selected due to inefficiencies in the selection cuts or they may not be detected due to the limitations of the MINERvA and MINOS detectors. An example of the former case would be a misreconstruction of hadronic recoil energy leading to a misreconstructed W_{exp} above 1.4 GeV/c^2[1]. An example of the latter case would be events with a muon that does not enter the MINOS detector. The efficiency correction accounts for these missing signal events by dividing the number of observed events by the selection efficiency.

The selection efficiency ϵ, or simply efficiency, is the fraction of simulated signal events that were detected and selected by the analysis selection cuts. Table 6.9 shows the efficiency for each signal target. For the tracker, the efficiency is 5.1%, while the passive materials have efficiencies $\sim 1.3\%$.

$$\epsilon = \frac{\text{Number of selected signal events}}{\text{Total number of signal events}} \tag{6.11}$$

For the efficiency correction, the efficiency is found for each truth bin of an analysis variable, as the efficiency is dependent on event kinematics. To correct truth bin i of an unfolded distribution, the number of unfolded events in the bin are divided by the efficiency of truth bin i, ϵ_i.

$$\text{Total number of signal events in bin } i = \frac{\text{Number of unfolded events in bin } i}{\epsilon_i} \tag{6.12}$$

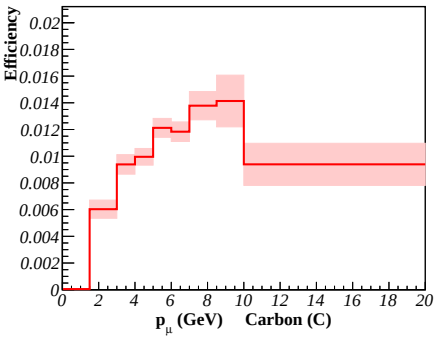
For a given analysis variable, the efficiency is constructed using two histograms

[1]Actually, this example holds only when measuring differential distributions in variables *other than* W_{exp}. For W_{exp} this correction is made in the unfolding process that was described previously.

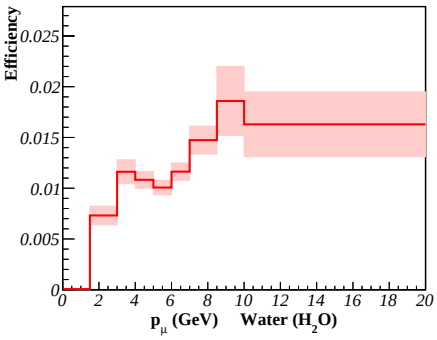
as the numerator and denominator. Both are filled using the true kinematics of the events. The efficiency numerator is filled with selected signal events[2]. As the selection cuts depend on reconstructed quantities, the efficiency numerator has all the systematic uncertainties associated with the signal events. The efficiency denominator contains all the signal events produced by GENIE.

The signal events in the denominator are generated before being passed to the detector simulation, therefore the true kinematic distribution of the signal events is independent of the event reconstruction. Thus, the efficiency denominator does not contain any reconstruction systematic uncertainties. Only systematic uncertainties associated with the generation of neutrino events are included. These uncertainties come from the neutrino interaction models, final state interaction (FSI) models, flux simulation, and target mass. Further description of the systematic uncertainties in this analysis will be discussed in section 6.10. Figures 6-60 to 6-67 show the efficiency distributions in each analysis variable in all the targets.

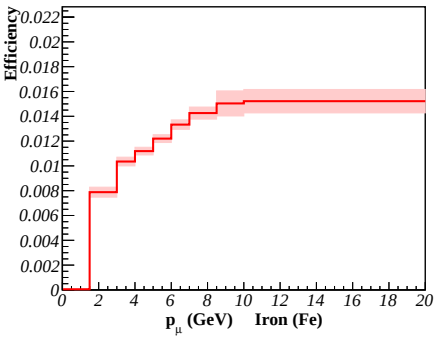
[2]The true interaction vertices of these signal events must be within the true fiducial volume of the nuclear target. If the interaction vertex falls outside of the fiducial volume, then the event is removed during background subtraction.



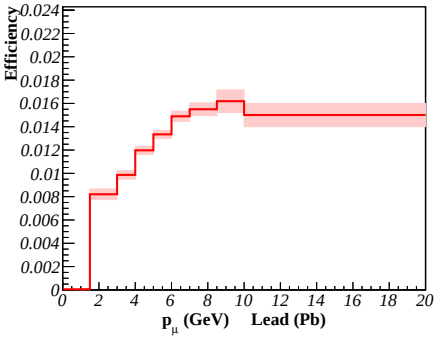
(a) Carbon



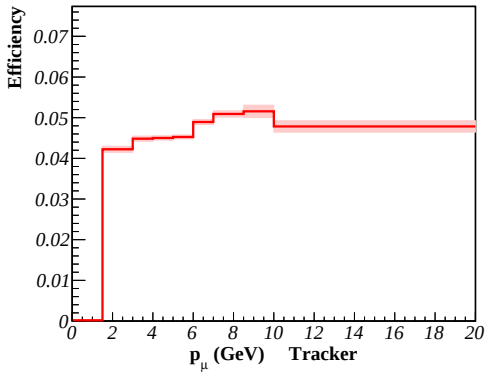
(b) Water



(c) Iron

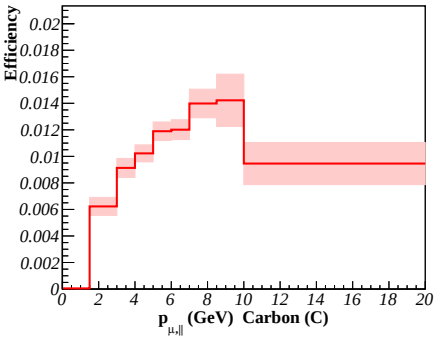


(d) Lead

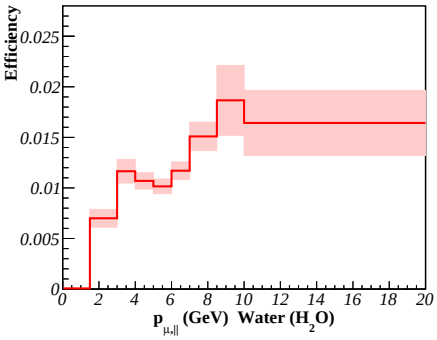


(e) Scintillator

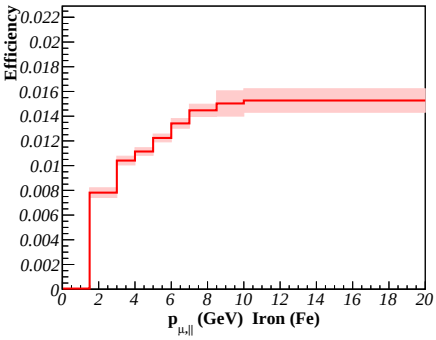
Figure 6-60: p_μ Efficiency



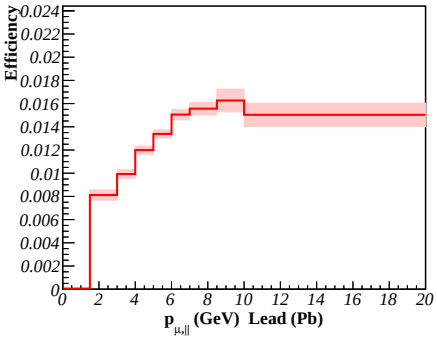
(a) Carbon



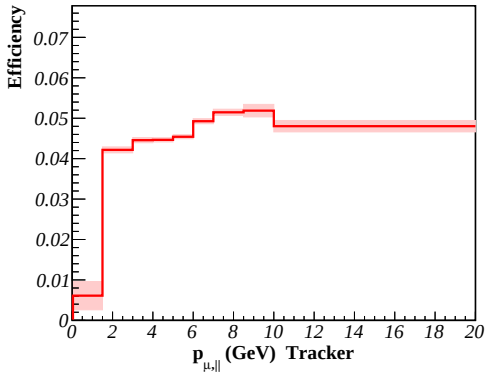
(b) Water



(c) Iron

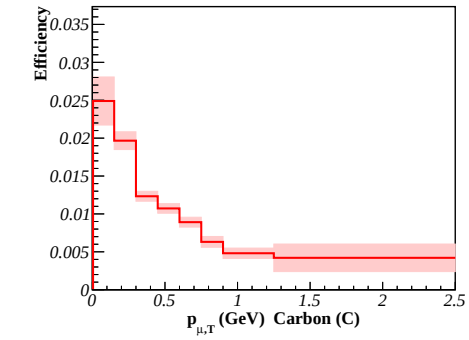


(d) Lead

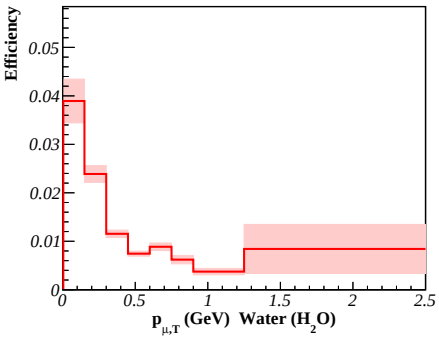


(e) Scintillator

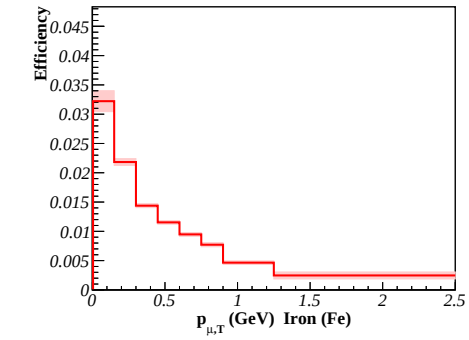
Figure 6-61: $p_{\mu,||}$ Efficiency



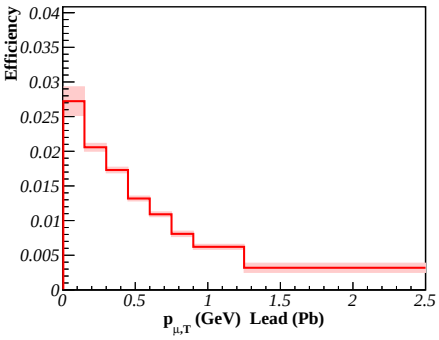
(a) Carbon



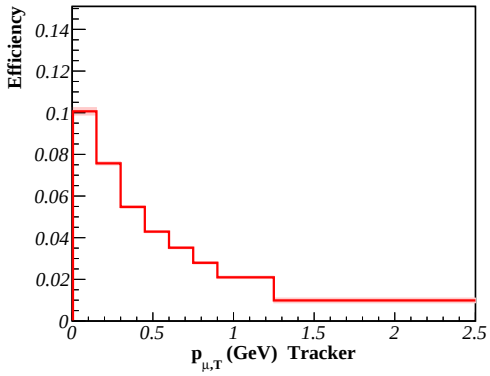
(b) Water



(c) Iron

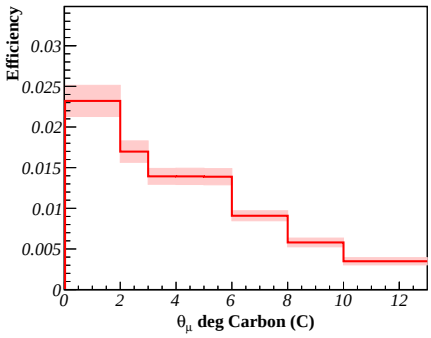


(d) Lead

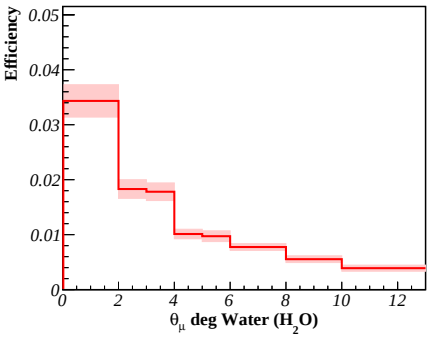


(e) Scintillator

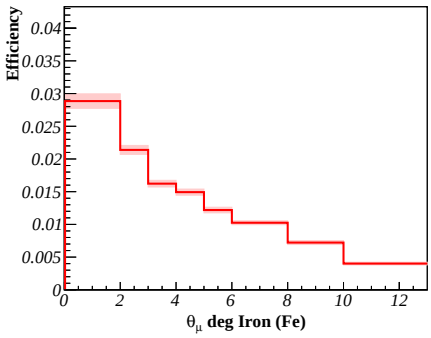
Figure 6-62: $p_{\mu,T}$ Efficiency



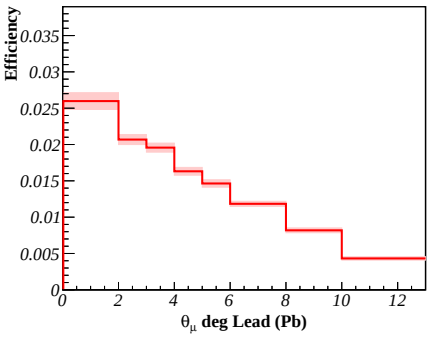
(a) Carbon



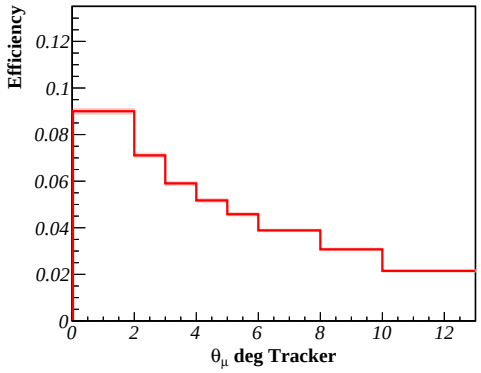
(b) Water



(c) Iron

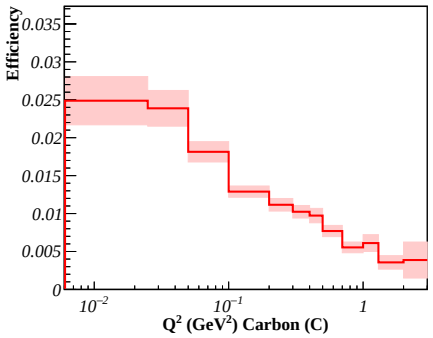


(d) Lead

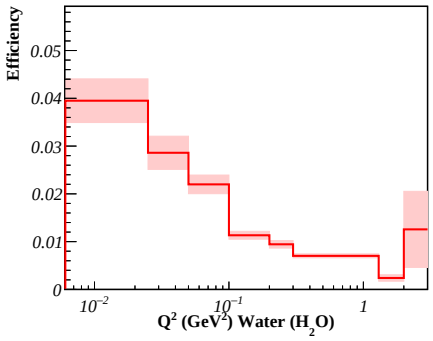


(e) Scintillator

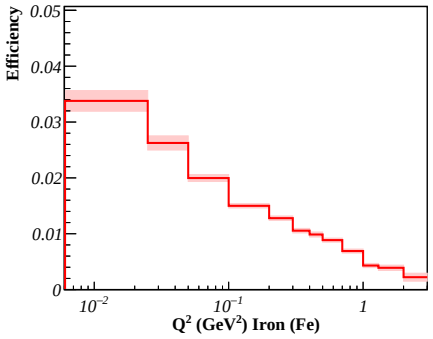
Figure 6-63: θ_μ Efficiency



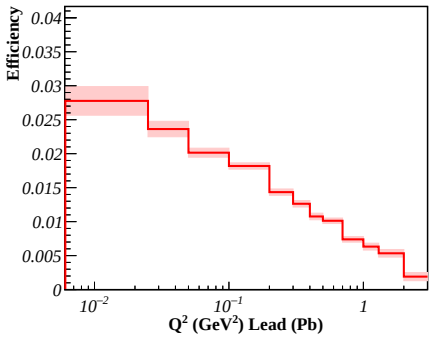
(a) Carbon



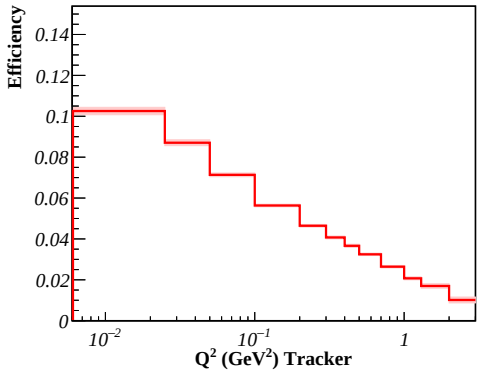
(b) Water



(c) Iron

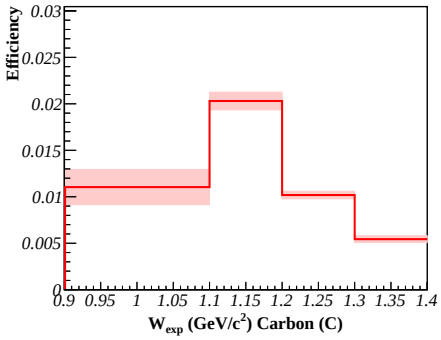


(d) Lead

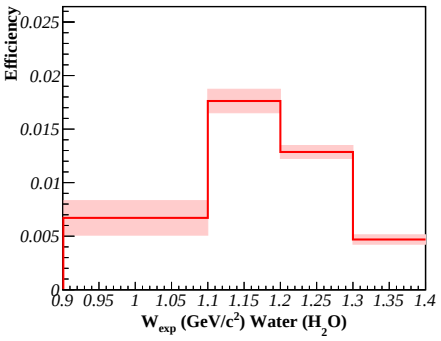


(e) Scintillator

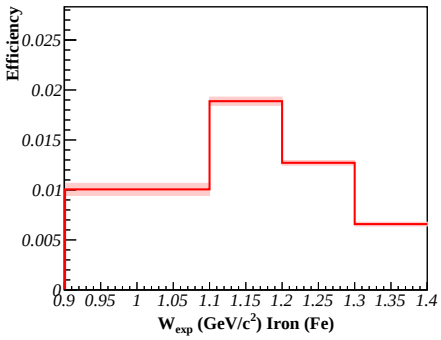
Figure 6-64: Q^2 Efficiency



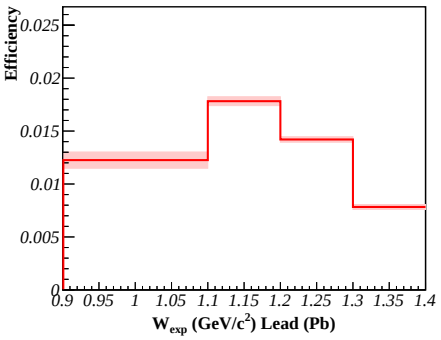
(a) Carbon



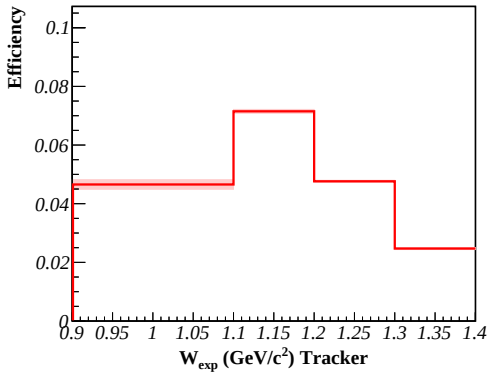
(b) Water



(c) Iron

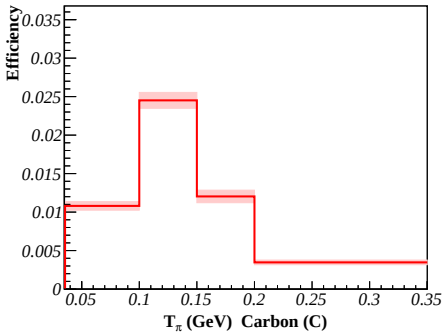


(d) Lead

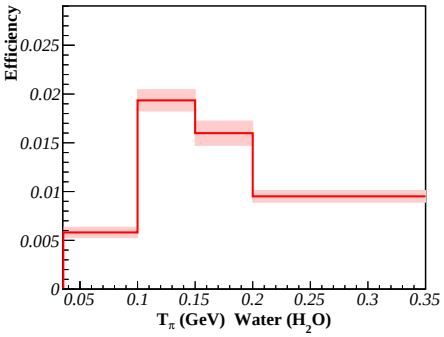


(e) Scintillator

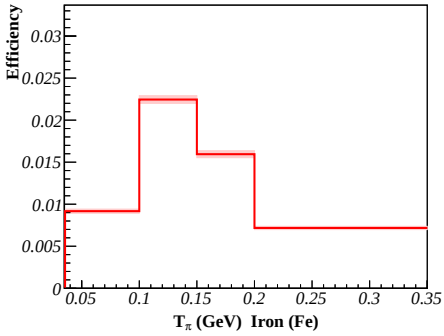
Figure 6-65: W_{exp} Efficiency



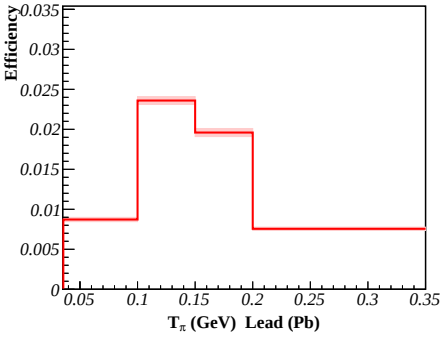
(a) Carbon



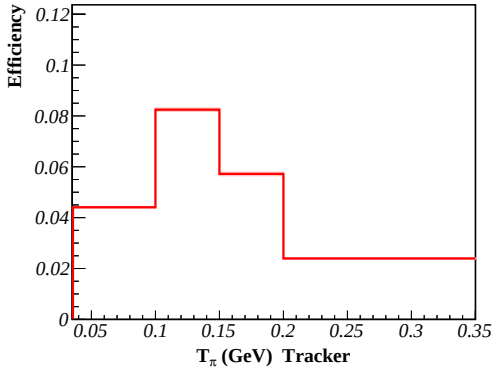
(b) Water



(c) Iron

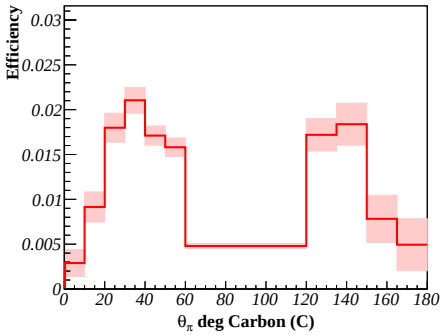


(d) Lead

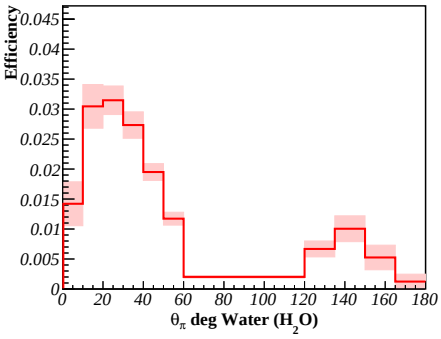


(e) Scintillator

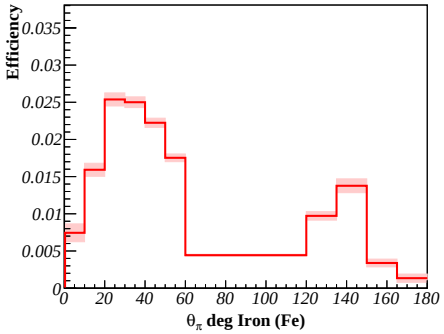
Figure 6-66: T_π Efficiency



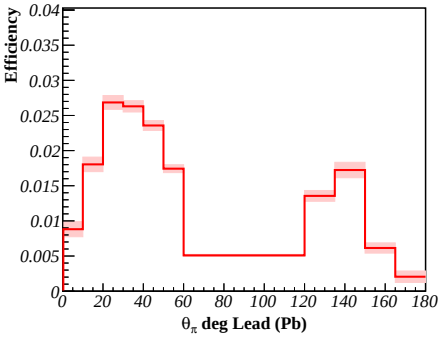
(a) Carbon



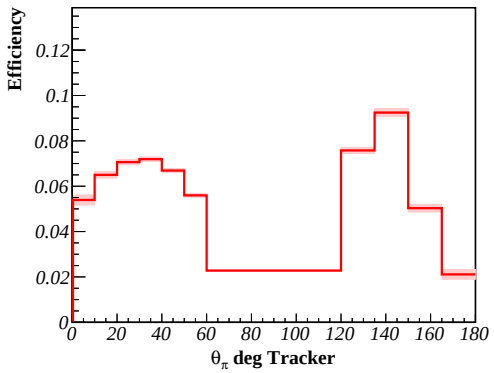
(b) Water



(c) Iron



(d) Lead



(e) Scintillator

Figure 6-67: θ_π Efficiency

Target	Number of Nucleons	Integrated Flux ($\nu_\mu/cm^2/POT$)	POT (Data)	POT (Simulation)
Carbon	9.986×10^{28}	6.401×10^{-8}	1.06×10^{21}	1.053×10^{22}
Water	2.591×10^{29}	6.193×10^{-8}	3.56×10^{20}	3.417×10^{21}
Iron	5.858×10^{29}	6.154×10^{-8}	1.06×10^{21}	1.053×10^{22}
Lead	6.055×10^{29}	6.282×10^{-8}	1.06×10^{21}	1.053×10^{22}
Tracker	3.205×10^{30}	6.322×10^{-8}	1.06×10^{21}	4.448×10^{21}

Table 6.15: Cross section normalization factors on the passive materials and tracker

6.8 Cross Section Normalizations

The final step of the calculation of a flux integrated differential cross section normalizes the efficiency corrected distribution by three factors: the widths of the bins, the number of targets, and the integrated flux prediction. For the first factor, the content of each bin in the efficiency corrected distribution is divided by the width of the bin. The bin width normalization makes the cross section differential.

The targets for neutrino interactions in this analysis are the nucleons within the fiducial volume. Therefore, the differential cross sections are normalized to be per nucleon. The number of nucleons in the fiducial volume are listed in table 6.15. The target normalization propagates the uncertainties on the number of nucleons within the fiducial volume to the differential cross section. These uncertainties comes from the uncertainties on the masses of the targets, which are listed in table 6.30.

Finally, the integrated flux normalization divides the efficiency corrected distribution by the integrated flux prediction scaled by the number of protons on target (POT) in the data. The bounds of flux integral are $E_\nu = 0$ to 100 GeV. The flux normalization propagates the uncertainties associated with the flux, further explained in sections 2.2.1 and 6.10.3. Also, the flux normalization is constrained by the $\nu - e$ and IMD constraints, explained in sections 2.2.2.1 and 2.2.2.2.

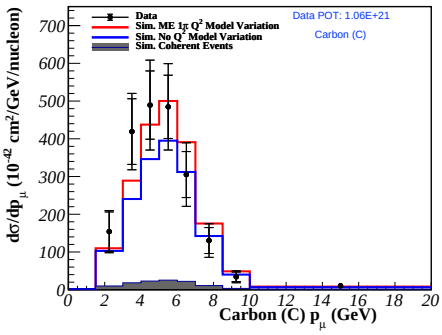
6.9 Differential Cross Sections

The following section contains the final results of this analysis. These results include the flux integrated differential cross sections, area normalized differential cross sections, the ratios of passive material cross sections to the cross sections found on scintillator, and the integrated cross sections. These results are compared to two sets of predicted cross sections, one with the low Q^2 suppression described in section 4.5.4.6, and one without the suppression. The predicted cross sections are provided by the reweighted GENIE v2.12.6 event generator, where the reweights are described in section 4.5.4. The systematic uncertainties on the measured cross sections are discussed in section 6.10. The discussion on the final results and their physics interpretation is in chapter 7.

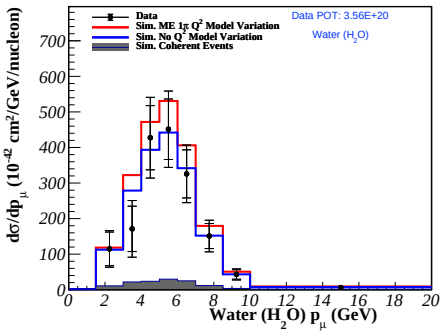
The water differential cross section in Q^2 has two large data points which are unreasonably large. This is due to low statistics in the sample and errors in unfolding. Future work, either reducing the number of unfolding iterations or combining adjacent bins, will fix this issue before publication of the result.

6.9.1 Differential Cross Sections

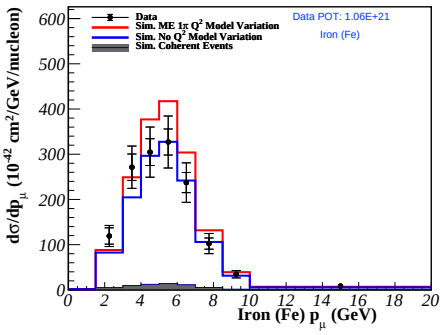
The following plots compare the measured differential cross sections to the predicted differential cross sections, with and without the low Q^2 suppression. The error bars on the measured cross section contain both systematic and statistical uncertainties. The inner set of error bars represents the statistical uncertainty, while the outer set represents the total uncertainty. Each plot also shows the contribution of coherent pion production to the predicted cross section.



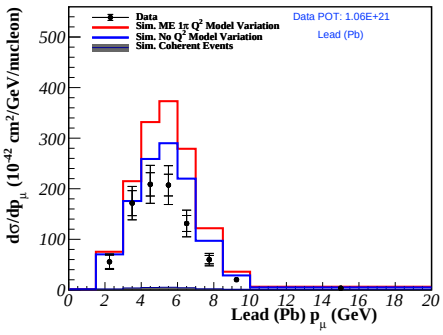
(a) Carbon



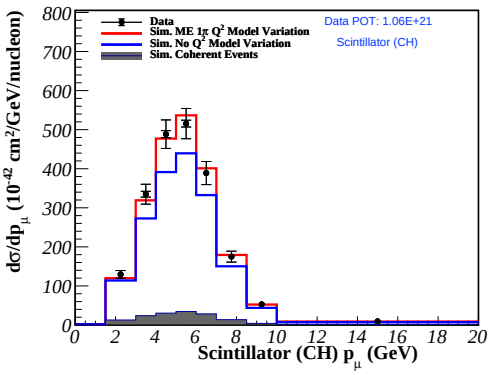
(b) Water



(c) Iron

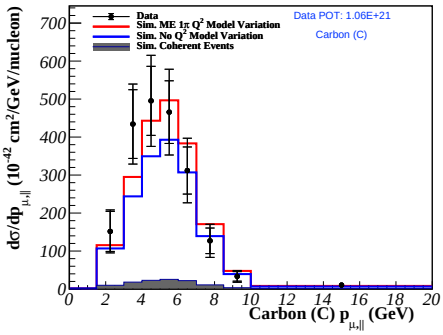


(d) Lead

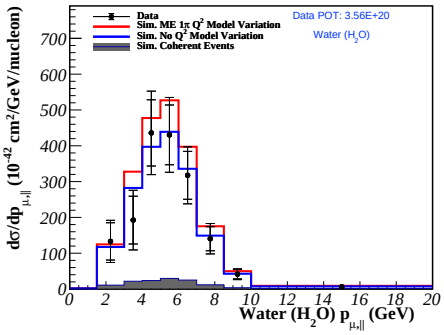


(e) Scintillator

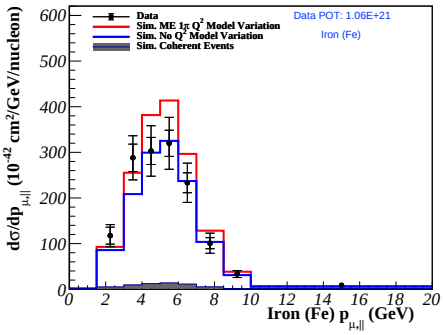
Figure 6-68: p_μ Cross Section



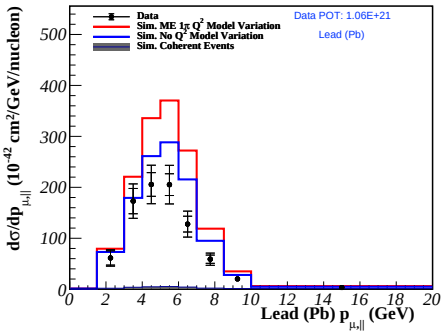
(a) Carbon



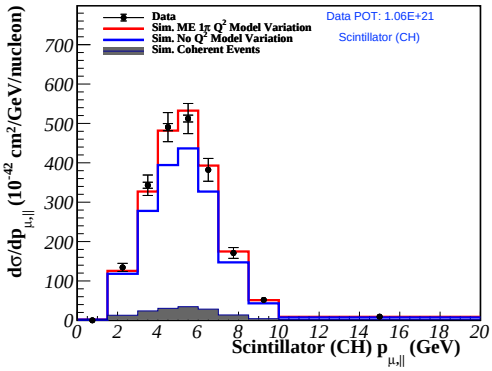
(b) Water



(c) Iron

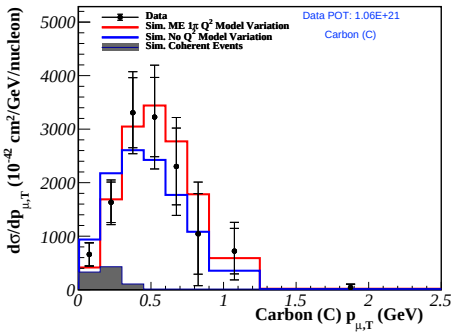


(d) Lead

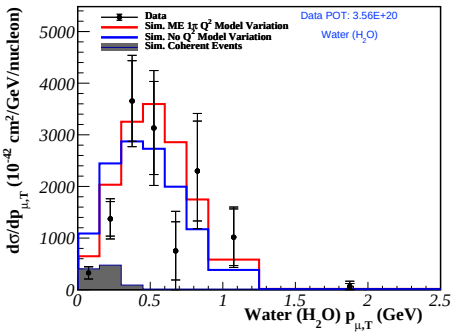


(e) Scintillator

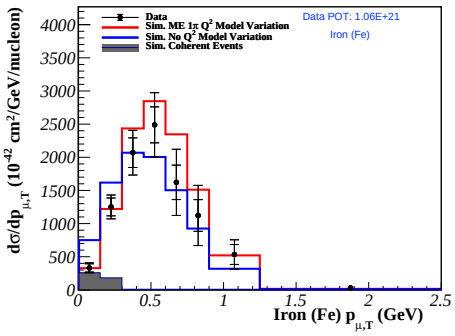
Figure 6-69: $p_{\mu,||}$ Cross Section



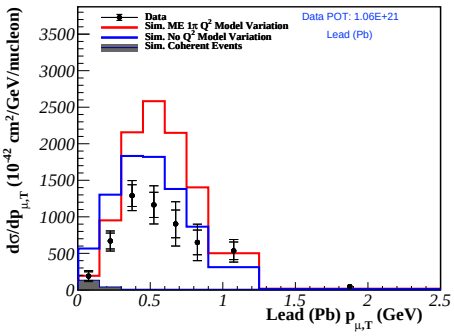
(a) Carbon



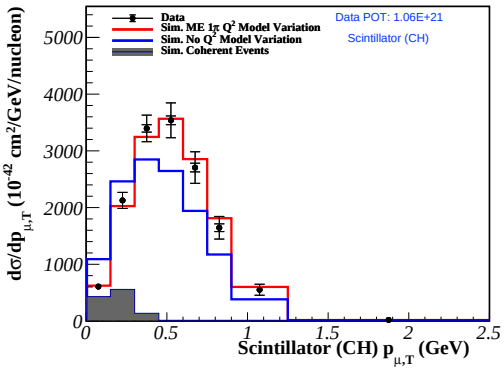
(b) Water



(c) Iron

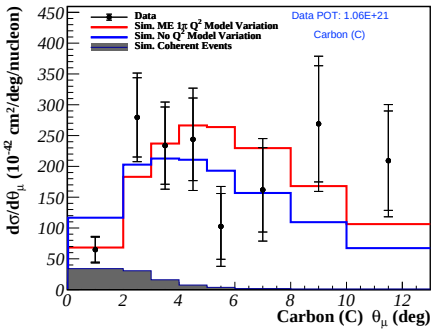


(d) Lead

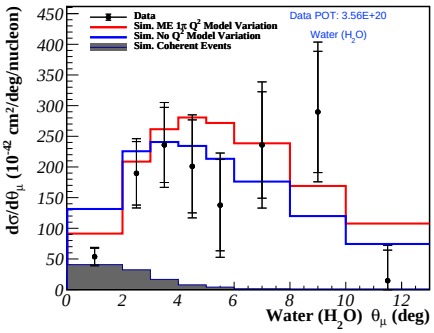


(e) Scintillator

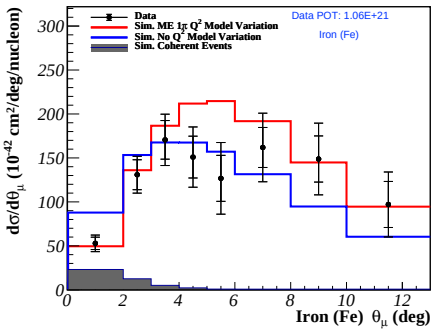
Figure 6-70: $p_{\mu,T}$ Cross Section



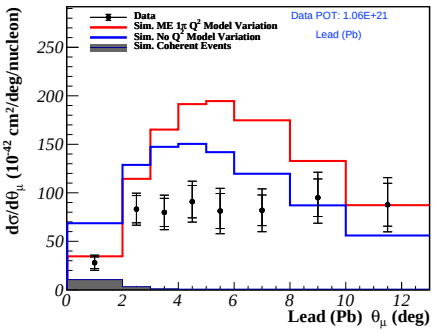
(a) Carbon



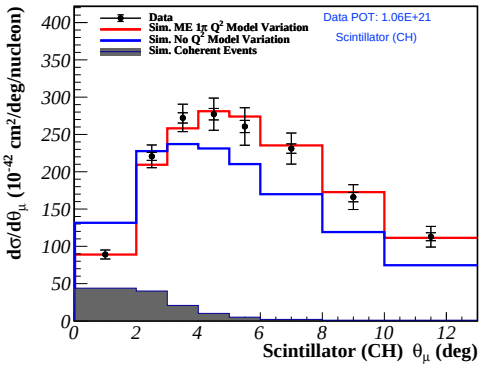
(b) Water



(c) Iron

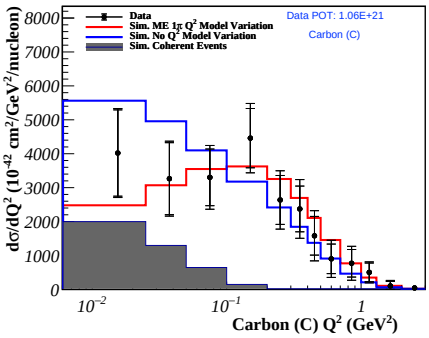


(d) Lead

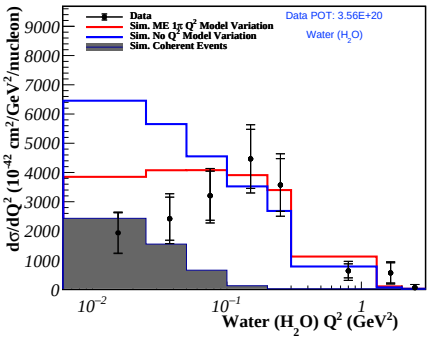


(e) Scintillator

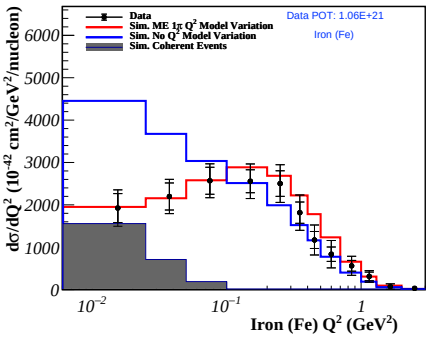
Figure 6-71: θ_μ Cross Section



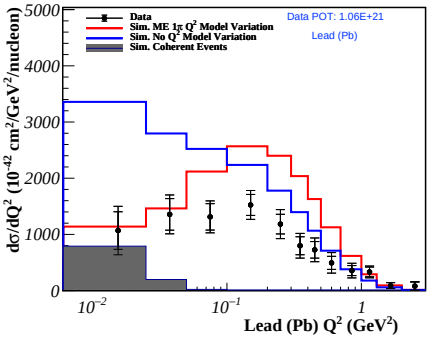
(a) Carbon



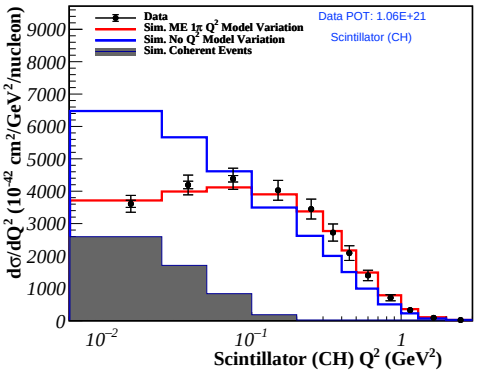
(b) Water



(c) Iron

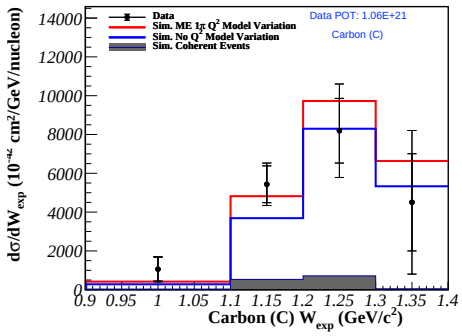


(d) Lead

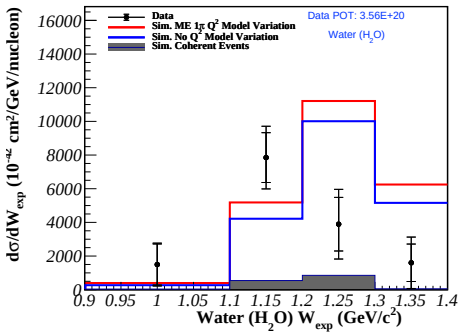


(e) Scintillator

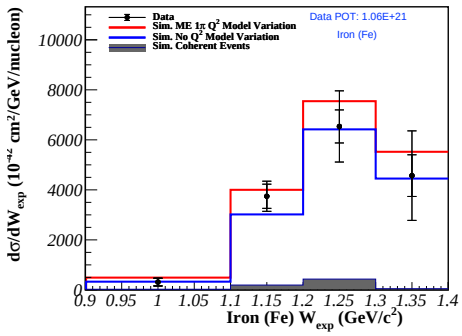
Figure 6-72: Q^2 Cross Section



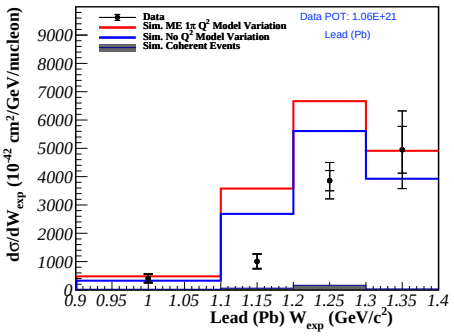
(a) Carbon



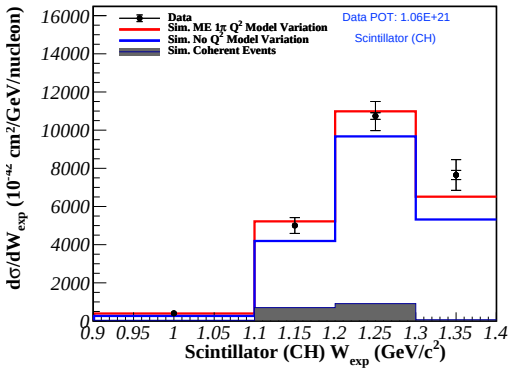
(b) Water



(c) Iron

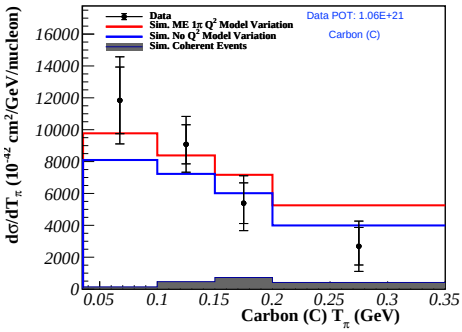


(d) Lead

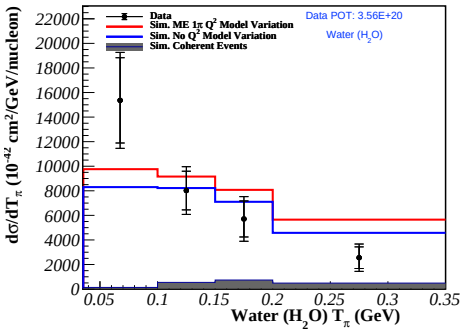


(e) Scintillator

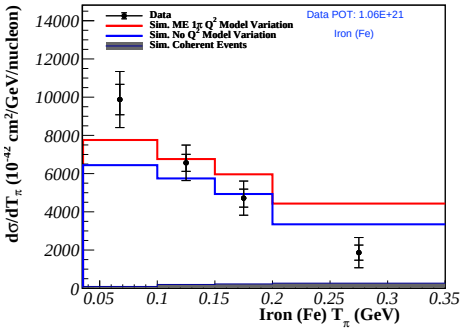
Figure 6-73: W_{exp} Cross Section



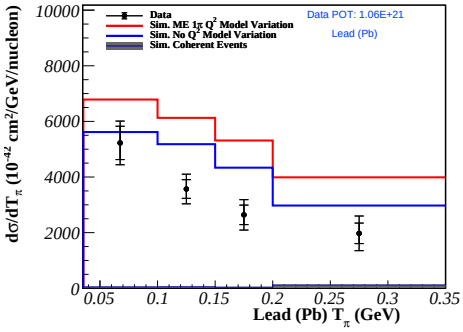
(a) Carbon



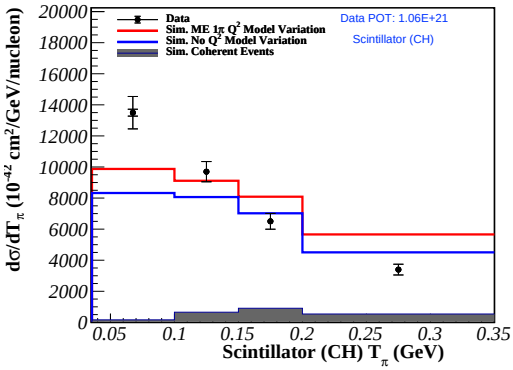
(b) Water



(c) Iron

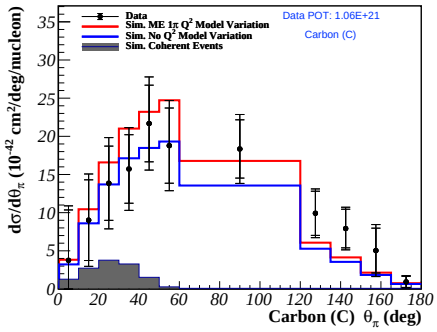


(d) Lead

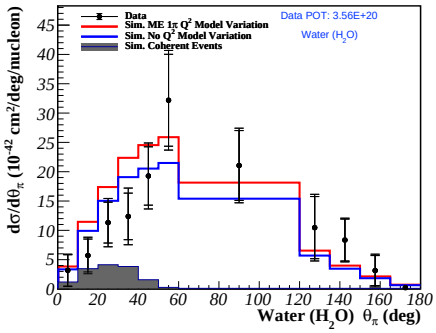


(e) Scintillator

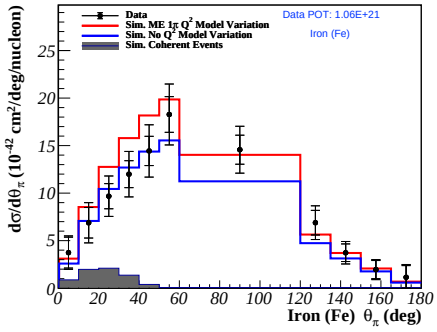
Figure 6-74: T_π Cross Section



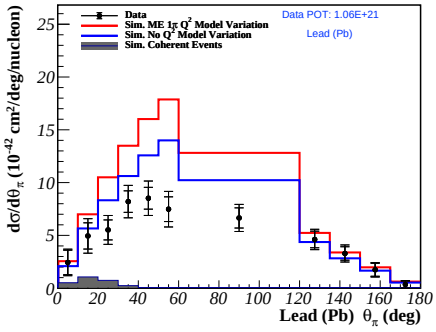
(a) Carbon



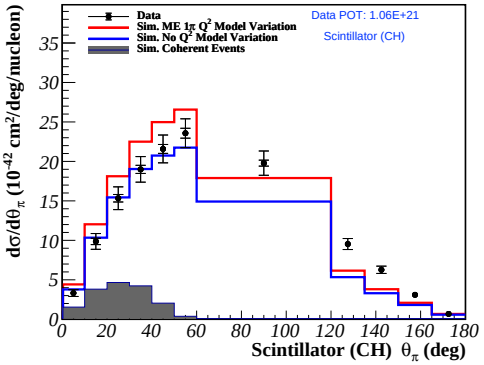
(b) Water



(c) Iron



(d) Lead



(e) Scintillator

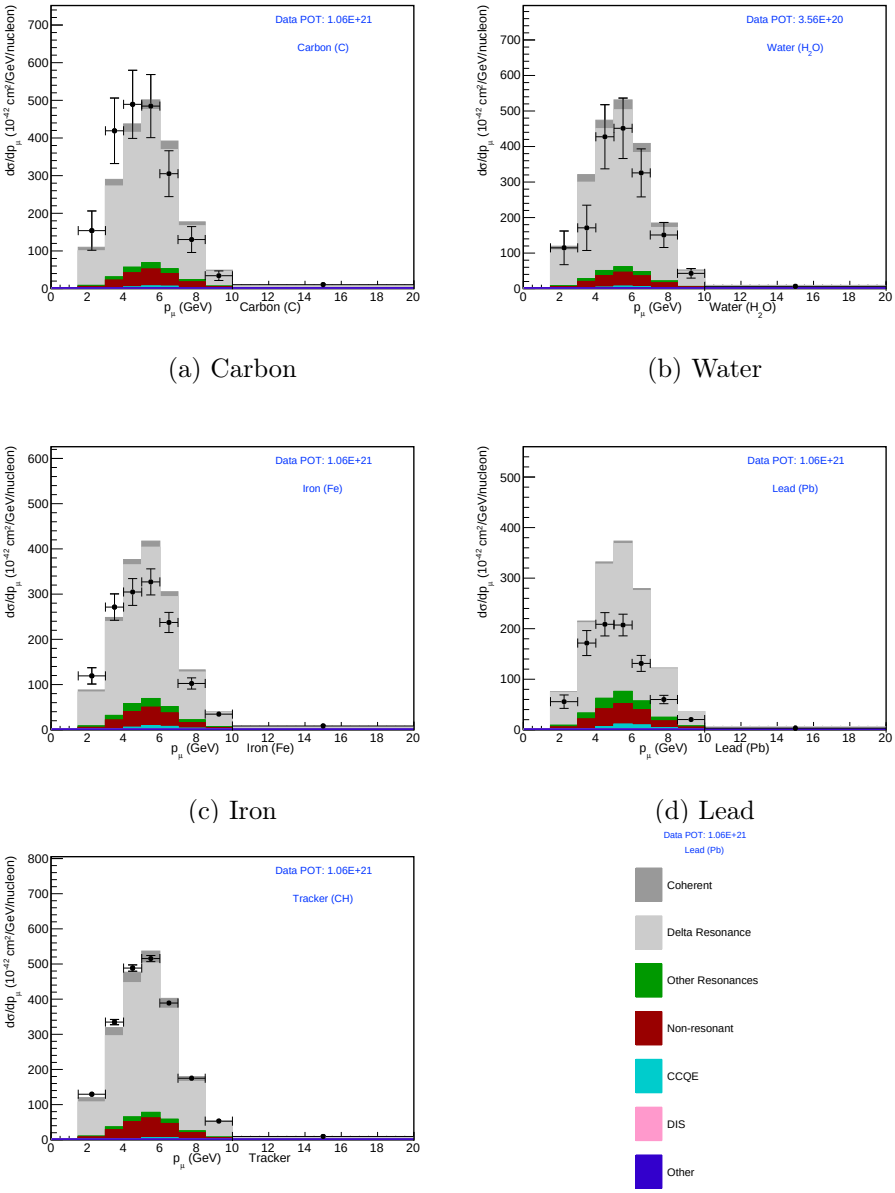
Figure 6-75: θ_π Cross Section

6.9.2 Differential Cross Sections Compared to Predictions of Different Neutrino Interaction Types

The following plots compare the measured cross sections to the predicted cross sections with the low Q^2 suppression. The error bars on the measured cross sections only contain statistical uncertainties. The predicted cross section is broken down into different categories of neutrino interactions. These neutrino interactions categories are determined by GENIE, and the interactions occur before any FSI. These categories are briefly described in table 6.16. DIS and "other" neutrino interactions contribute little to the predicted cross section.

Label	Definition
Coherent	CC coherent and diffractive pion production (Sections 1.3.4, 1.3.4.1)
Delta Resonance	CC resonant pion production from Δ decay (Section 1.3.2)
Other Resonance	CC resonant pion production from other baryon resonance decay (Section 1.3.2)
Non-resonant	CC nonresonant pion production (Sections 1.3.2,1.3.3)
CCQE	Charged current quasielastic scattering (Section 1.3.1)
DIS	Deep inelastic scattering (Section 1.3.3)
Other	Any other neutrino interaction not previously listed

Table 6.16: Definitions of the neutrino interaction categories



(a) Carbon

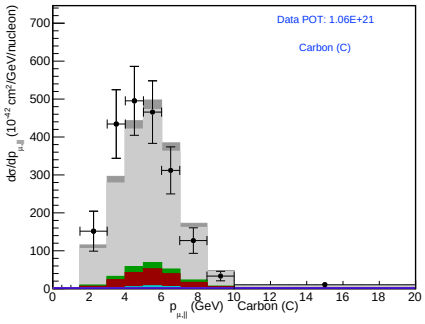
(b) Water

(c) Iron

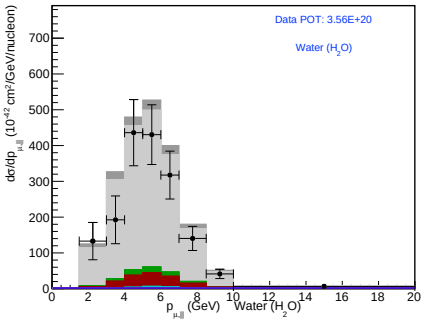
(d) Lead

(e) Scintillator

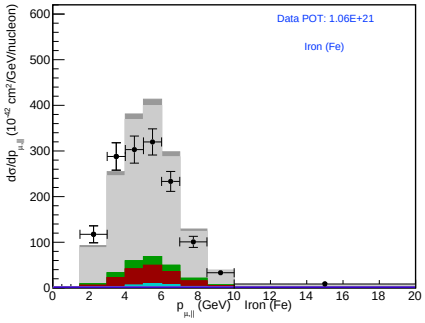
Figure 6-76: p_μ Cross Section: Neutrino Interactions



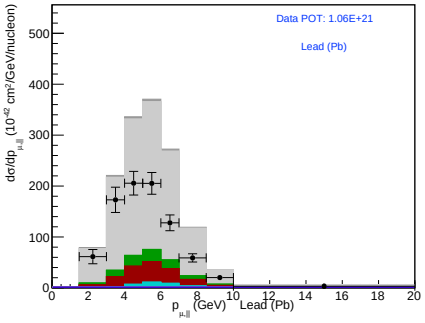
(a) Carbon



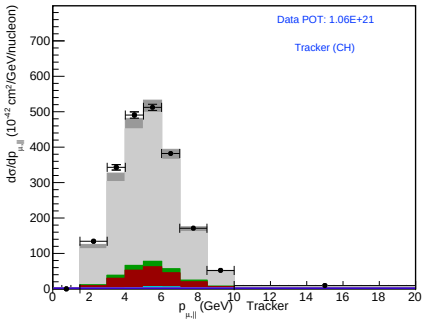
(b) Water



(c) Iron



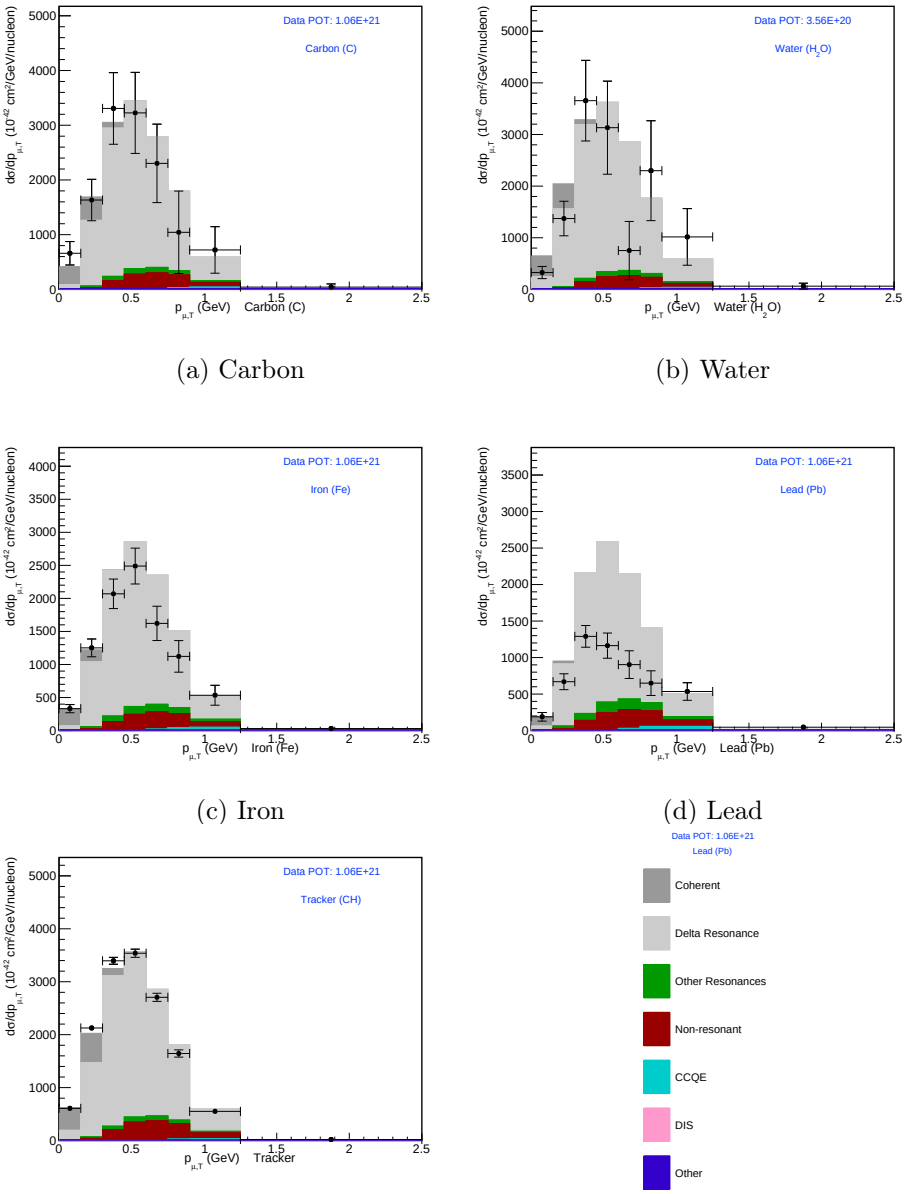
(d) Lead



(e) Scintillator



Figure 6-77: $p_{\mu,||}$ Cross Section: Neutrino Interactions



(a) Carbon

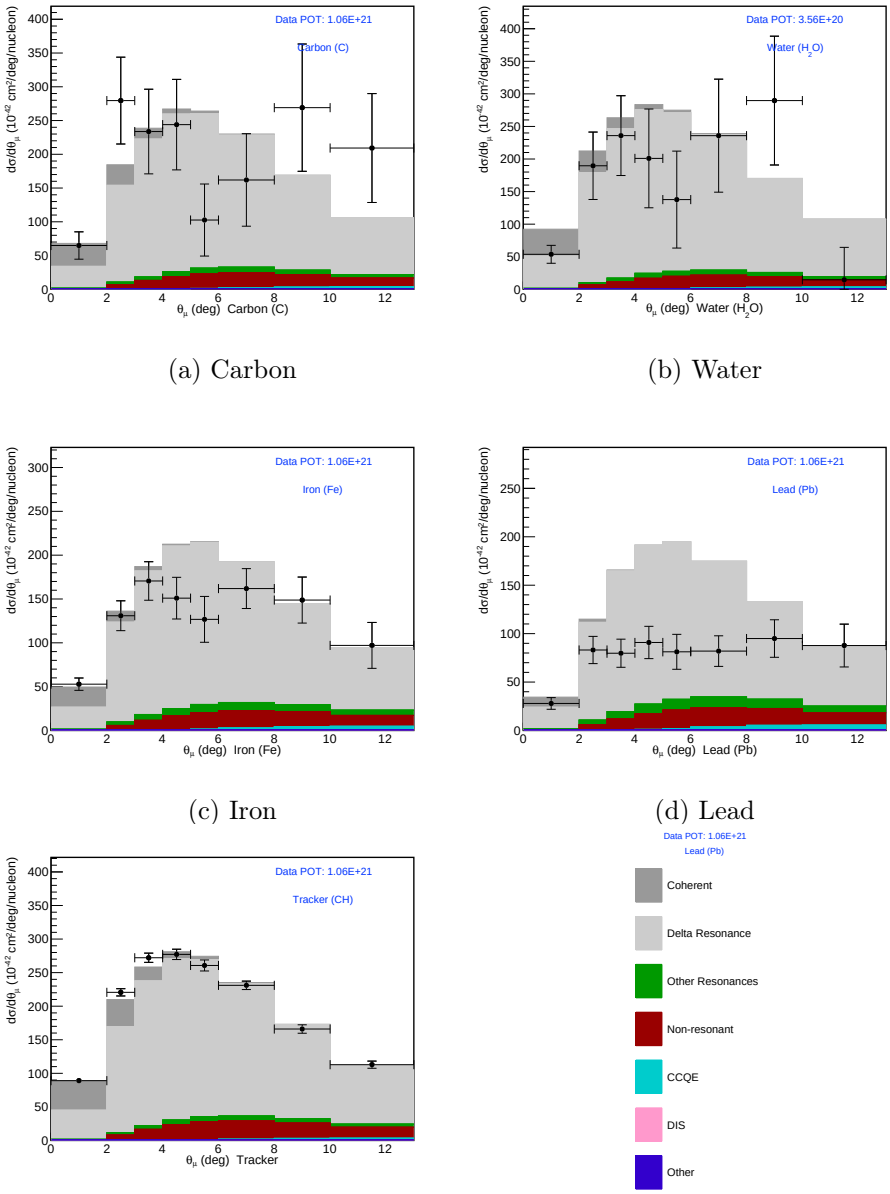
(b) Water

(c) Iron

(d) Lead

(e) Scintillator

Figure 6-78: $p_{\mu,T}$ Cross Section: Neutrino Interactions



(a) Carbon

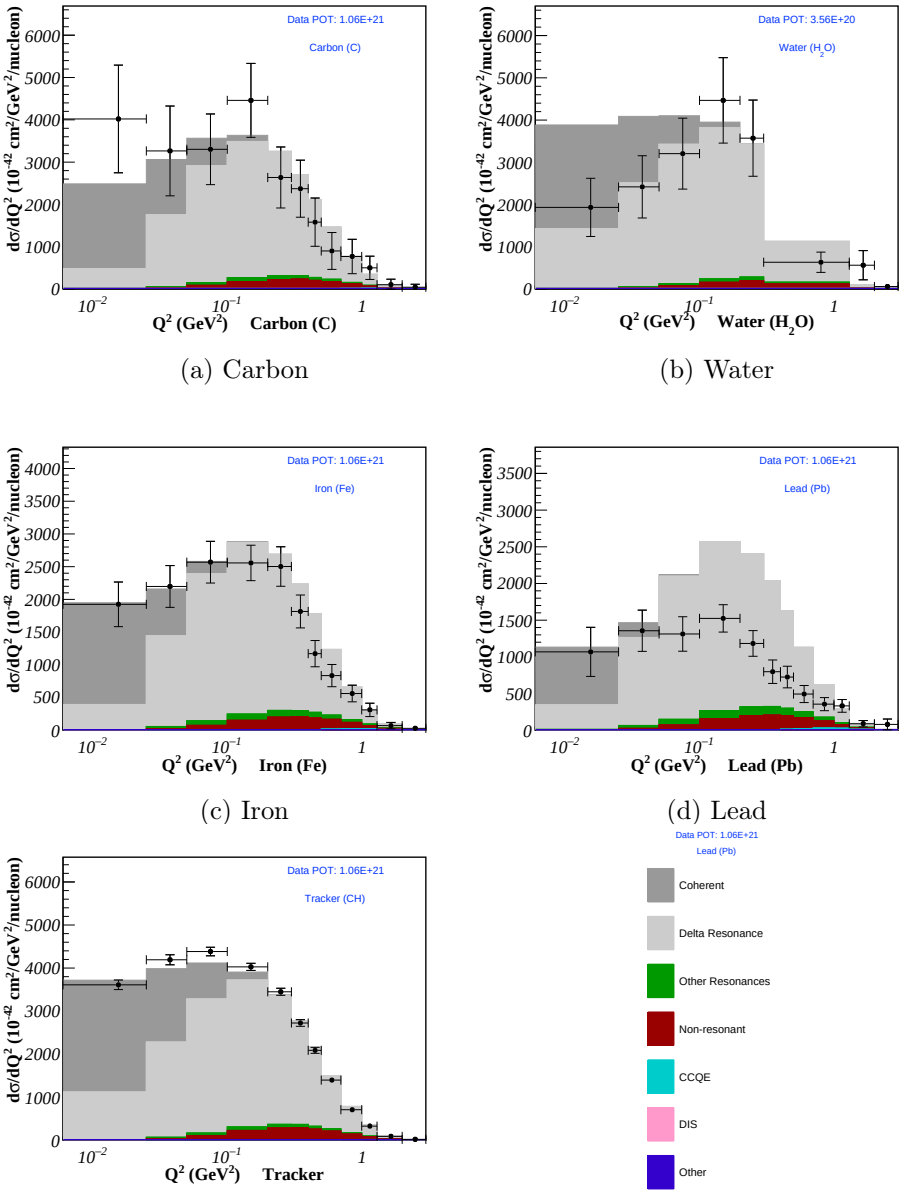
(b) Water

(c) Iron

(d) Lead

(e) Scintillator

Figure 6-79: θ_μ Cross Section: Neutrino Interactions



(a) Carbon

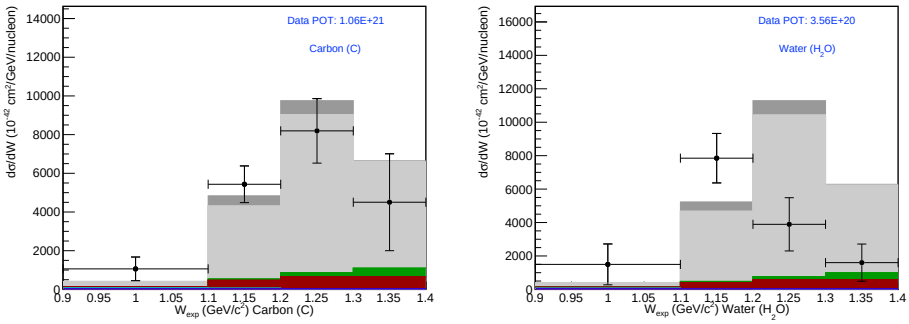
(b) Water

(c) Iron

(d) Lead

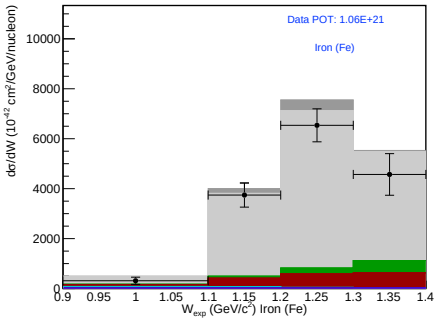
(e) Scintillator

Figure 6-80: Q^2 Cross Section: Neutrino Interactions

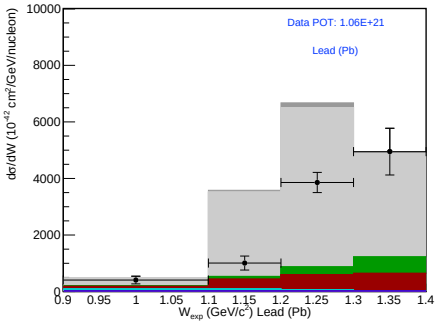


(a) Carbon

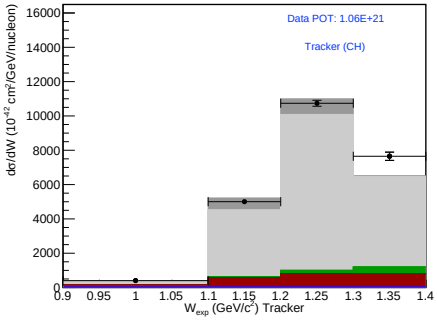
(b) Water



(c) Iron



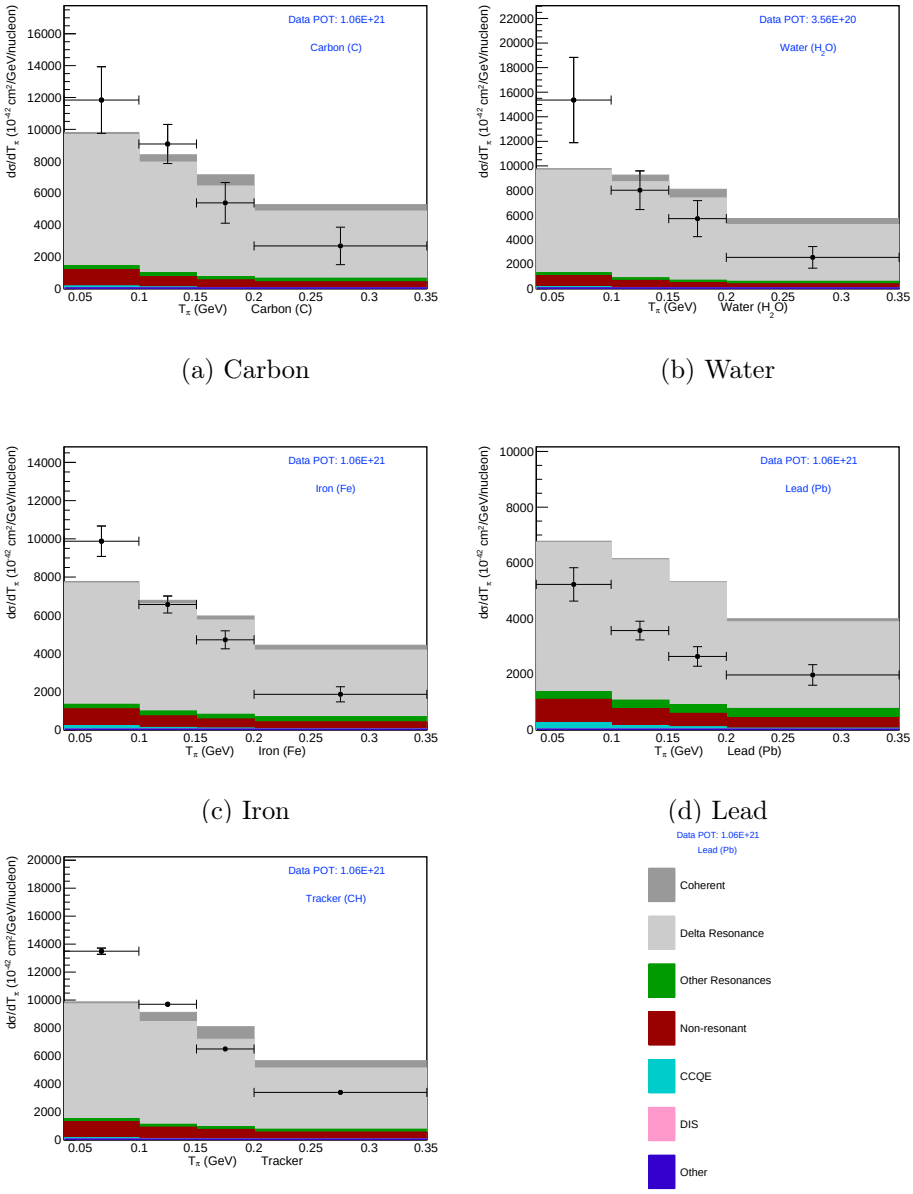
(d) Lead



(e) Scintillator



Figure 6-81: W_{exp} Cross Section: Neutrino Interactions



(a) Carbon

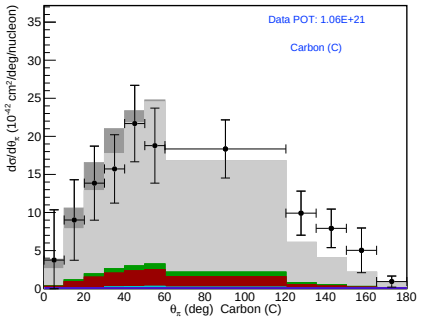
(b) Water

(c) Iron

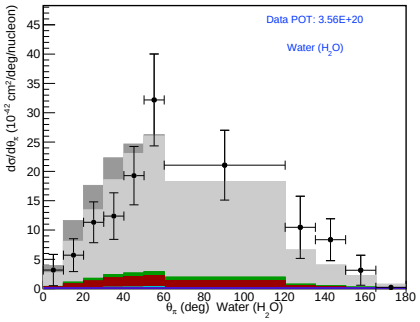
(d) Lead

(e) Scintillator

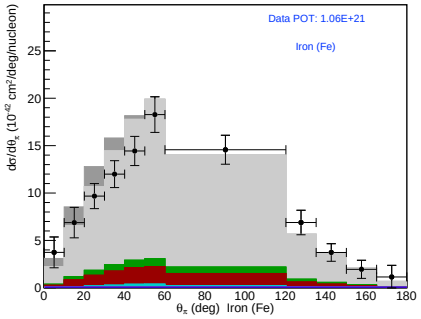
Figure 6-82: T_π Cross Section: Neutrino Interactions



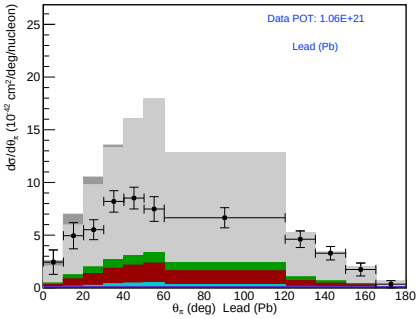
(a) Carbon



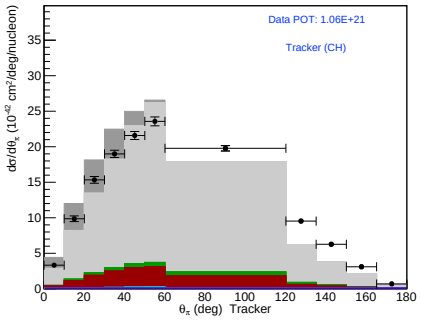
(b) Water



(c) Iron



(d) Lead



(e) Scintillator

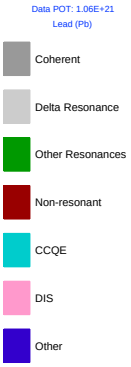
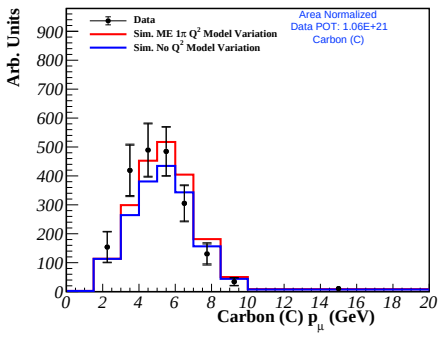


Figure 6-83: θ_π Cross Section: Neutrino Interactions

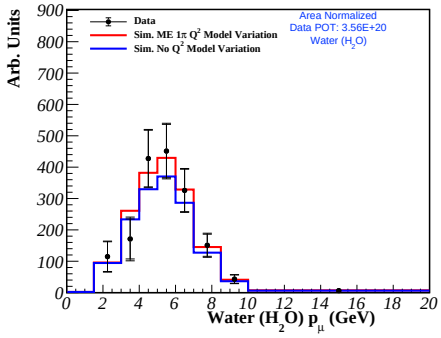
6.9.3 Area Normalized Cross Sections

Area normalization[3] scales the predicted cross sections so that the integral of the measured and predicted cross sections are equal. The following plots compare the measured cross sections to the area normalized predicted cross sections, with and without the low Q^2 suppression. This normalization reduces the contribution from some systematic uncertainties.

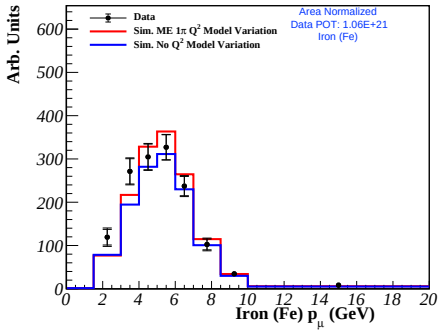
[3]Also referred to as shape normalization



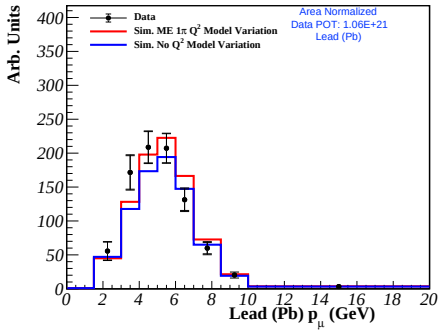
(a) Carbon



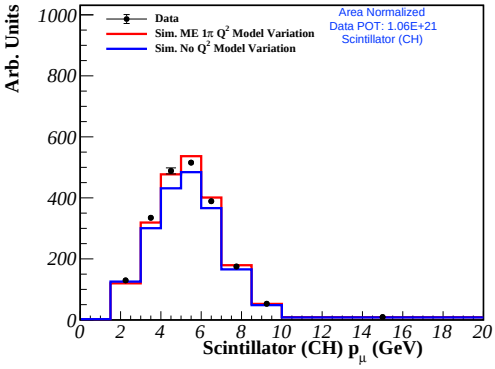
(b) Water



(c) Iron

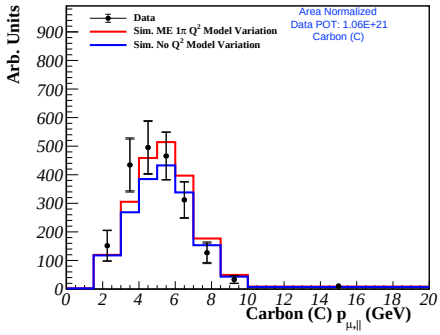


(d) Lead

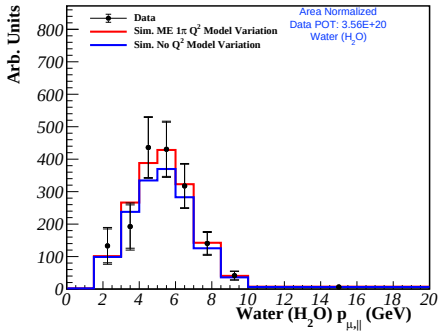


(e) Scintillator

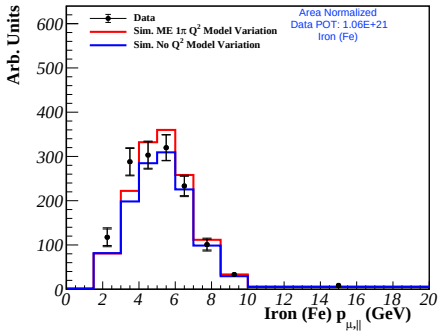
Figure 6-84: p_μ Cross Section Area Normalized



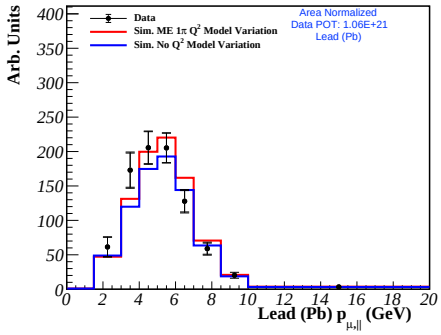
(a) Carbon



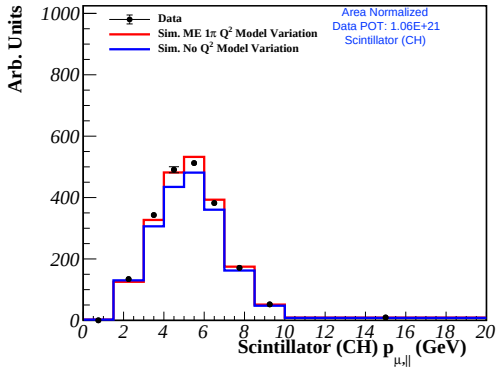
(b) Water



(c) Iron

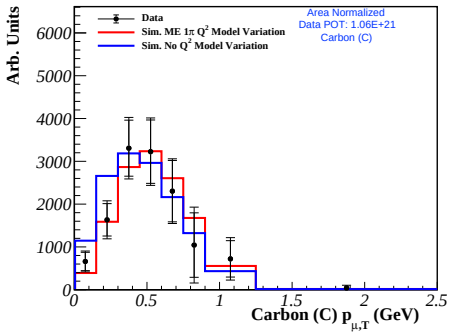


(d) Lead

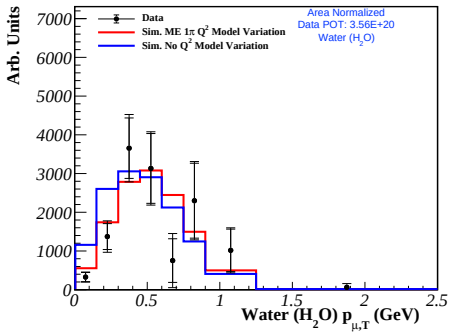


(e) Scintillator

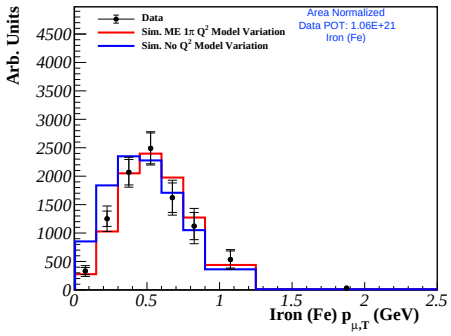
Figure 6-85: $p_{\mu,||}$ Cross Section Area Normalized



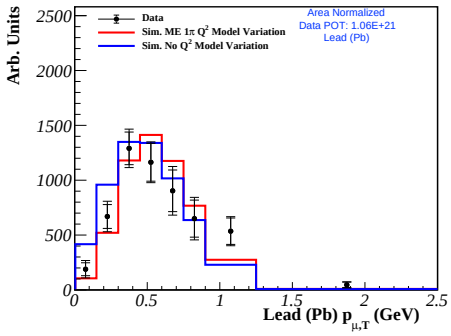
(a) Carbon



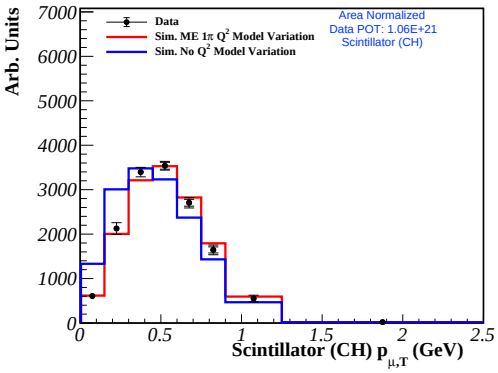
(b) Water



(c) Iron

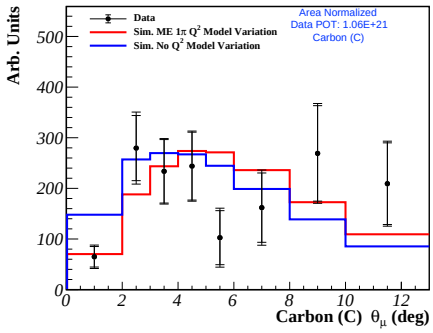


(d) Lead

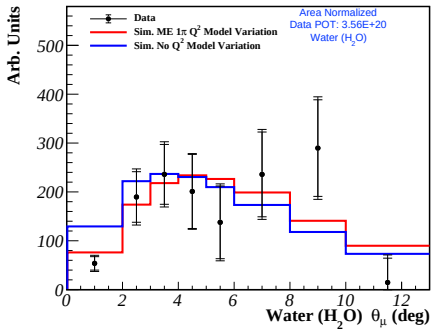


(e) Scintillator

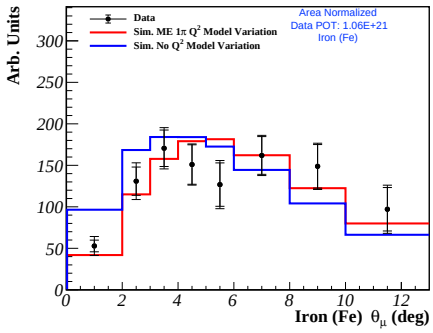
Figure 6-86: $p_{\mu,T}$ Cross Section Area Normalized



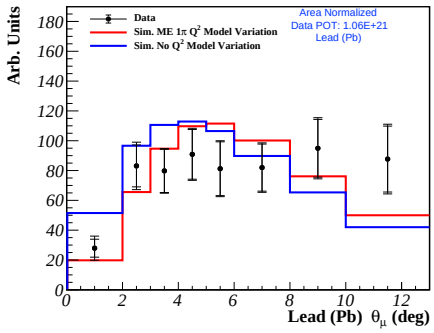
(a) Carbon



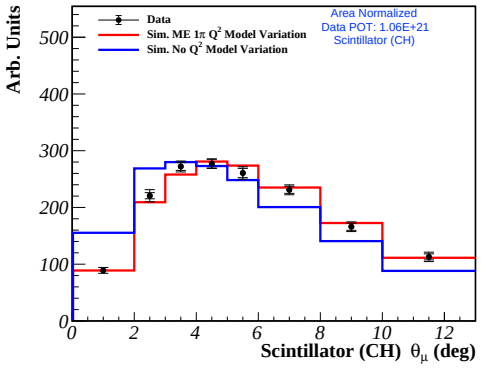
(b) Water



(c) Iron

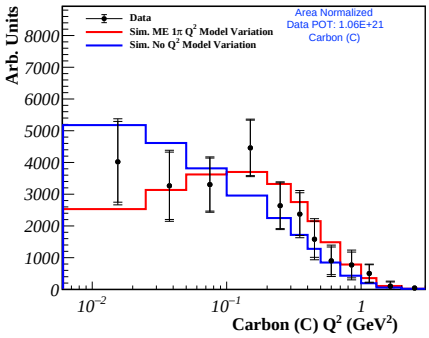


(d) Lead

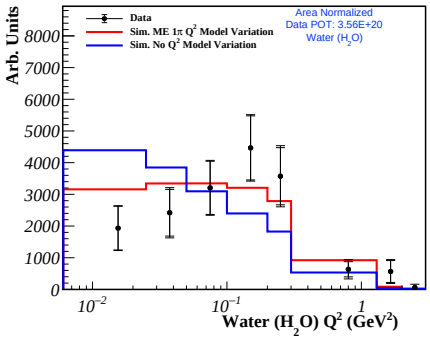


(e) Scintillator

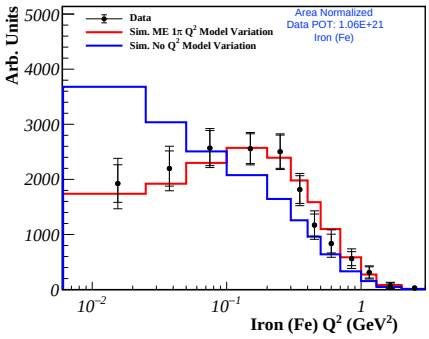
Figure 6-87: θ_μ Cross Section Area Normalized



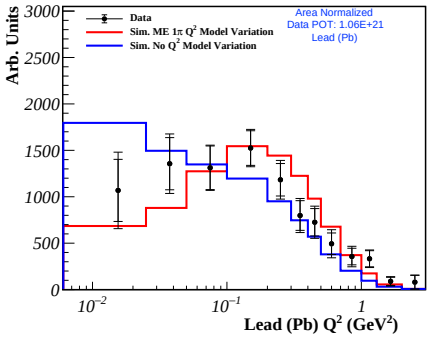
(a) Carbon



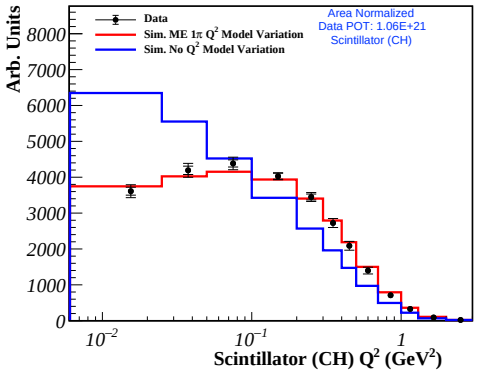
(b) Water



(c) Iron

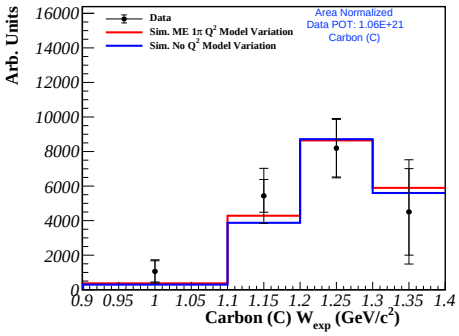


(d) Lead

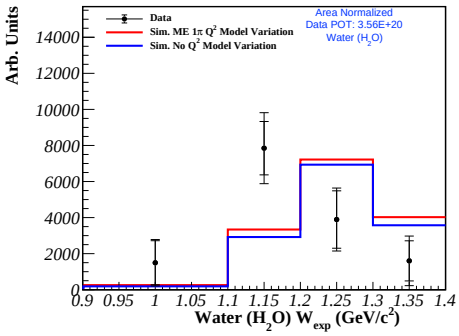


(e) Scintillator

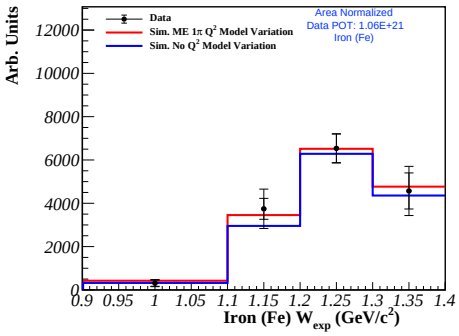
Figure 6-88: Q^2 Cross Section Area Normalized



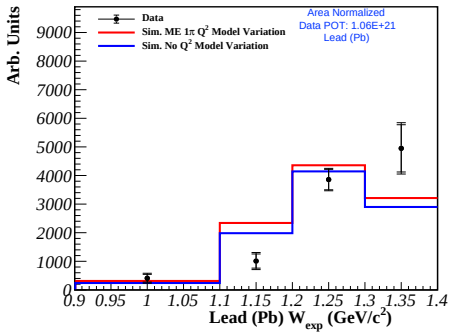
(a) Carbon



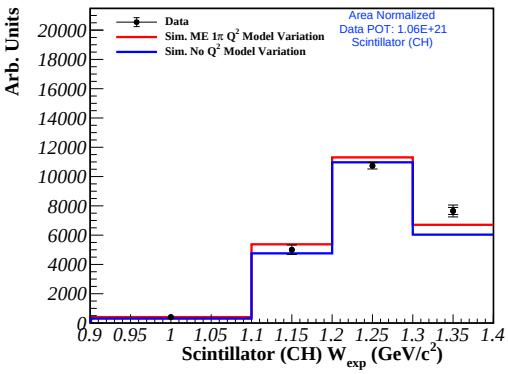
(b) Water



(c) Iron

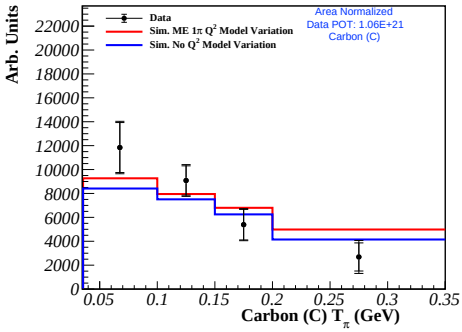


(d) Lead

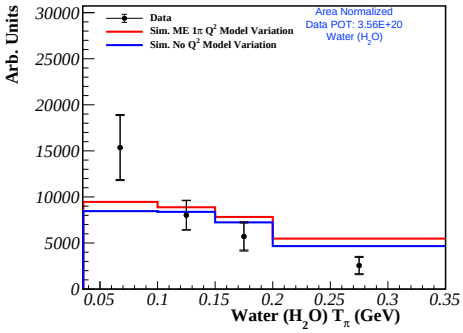


(e) Scintillator

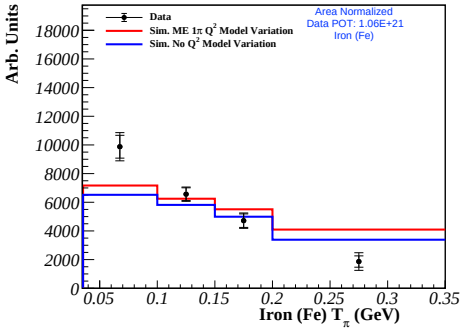
Figure 6-89: W_{exp} Cross Section Area Normalized



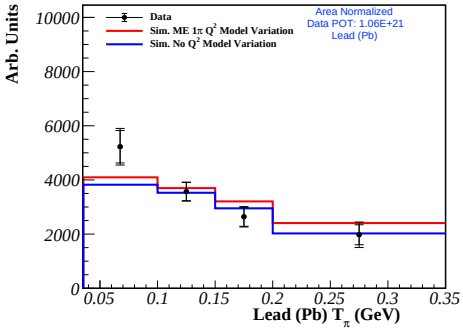
(a) Carbon



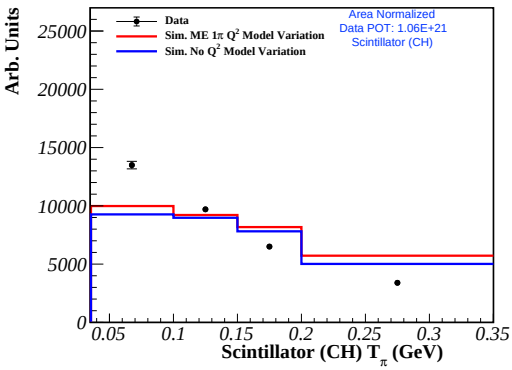
(b) Water



(c) Iron

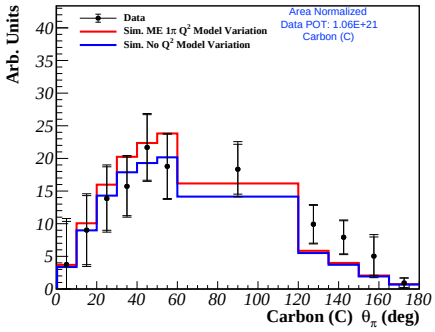


(d) Lead

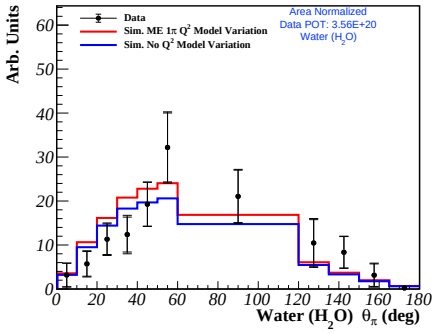


(e) Scintillator

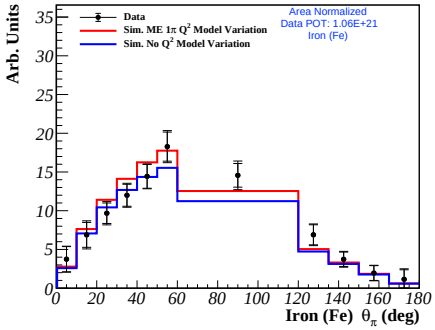
Figure 6-90: T_π Cross Section Area Normalized



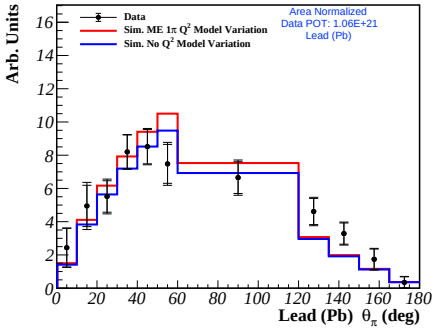
(a) Carbon



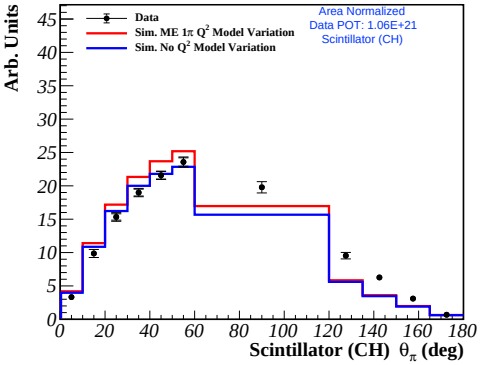
(b) Water



(c) Iron



(d) Lead

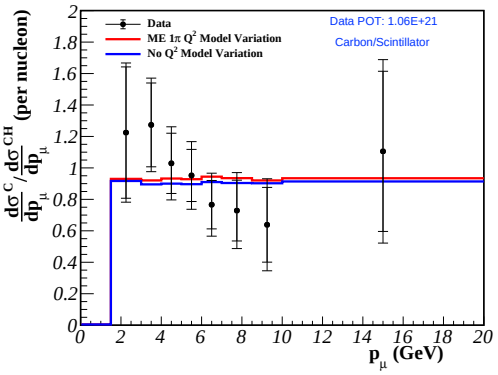


(e) Scintillator

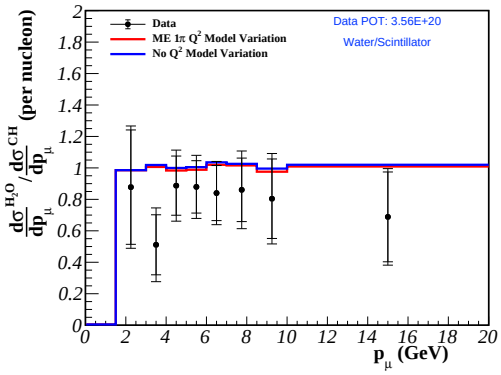
Figure 6-91: θ_π Cross Section Area Normalized

6.9.4 Ratios of Differential Cross Sections on Passive Materials to Scintillator

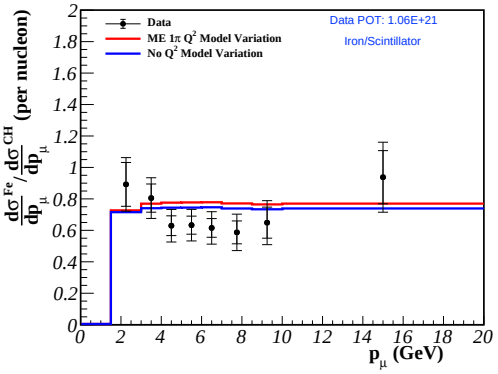
When calculating the ratios of cross sections on passive material to cross sections on scintillator, the calculation must account for the differences between the fluxes due to the transverse position of the nuclear targets. The following ratios use the method outlined in section 2.2.3.1 to reweight the cross section on scintillator so that the neutrino flux in the active tracker matches the flux in the passive material.



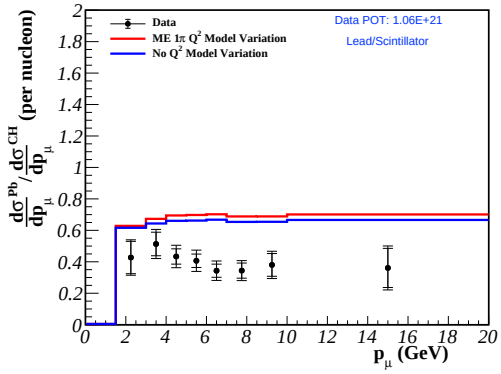
(a) Carbon



(b) Water

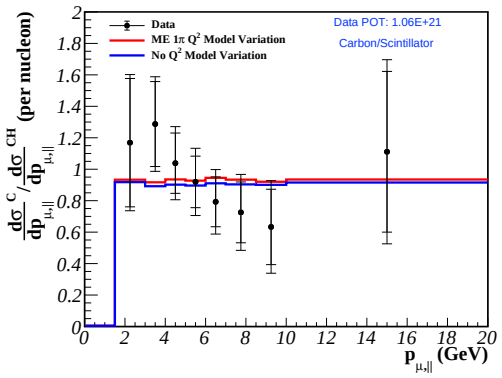


(c) Iron

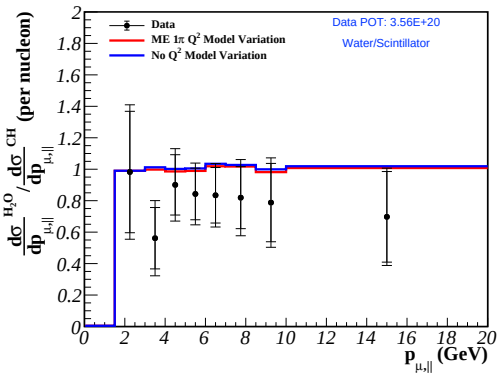


(d) Lead

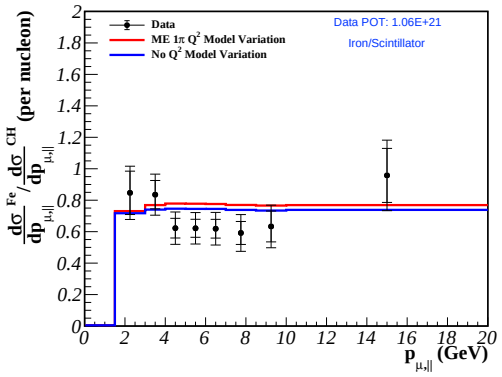
Figure 6-92: p_μ Target Cross Section Ratio to Scintillator



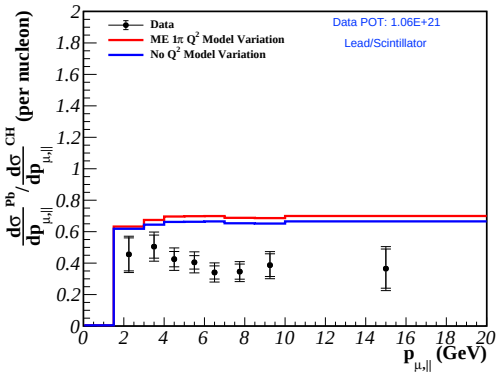
(a) Carbon



(b) Water

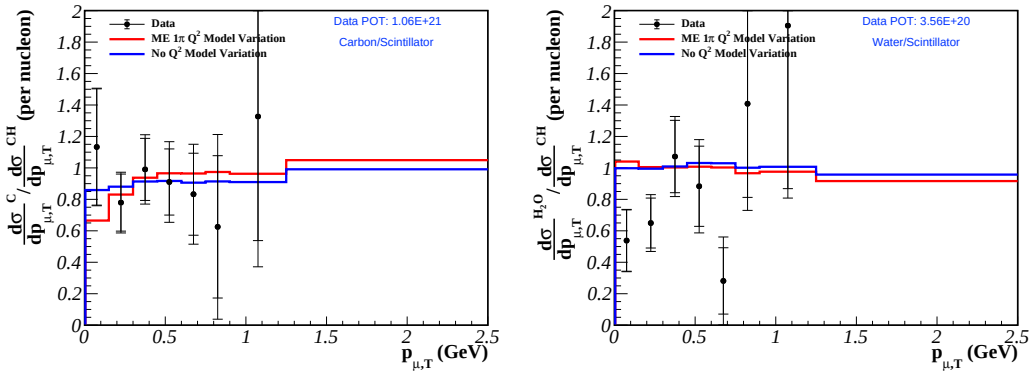


(c) Iron



(d) Lead

Figure 6-93: $p_{\mu,||}$ Target Cross Section Ratio to Scintillator



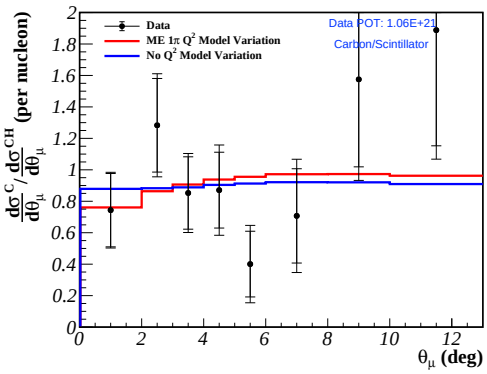
(a) Carbon

(b) Water

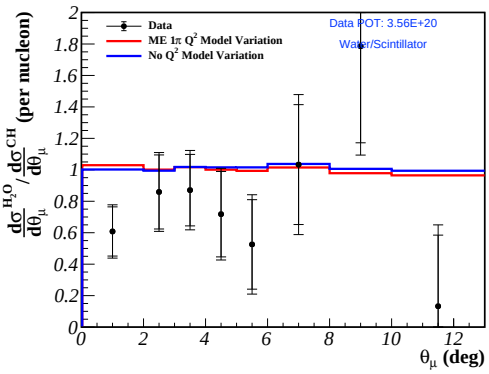
(c) Iron

(d) Lead

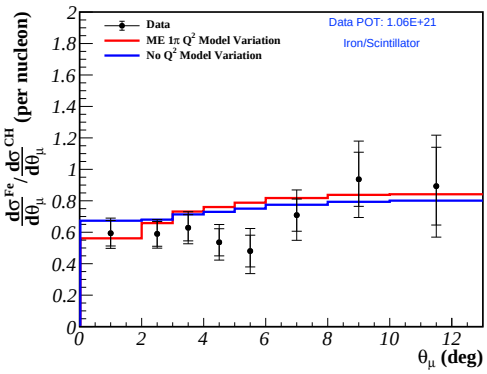
Figure 6-94: $p_{\mu,T}$ Target Cross Section Ratio to Scintillator



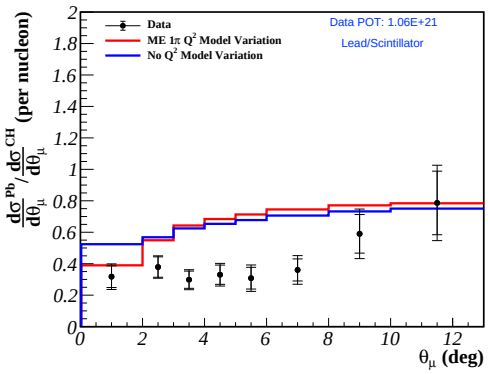
(a) Carbon



(b) Water

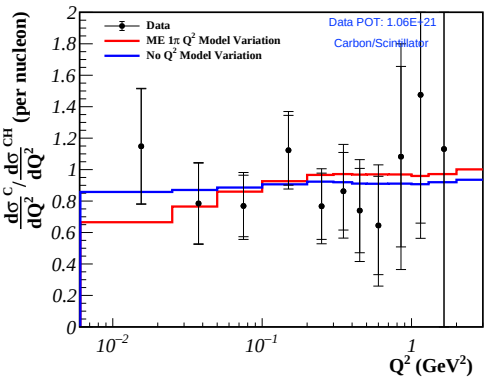


(c) Iron

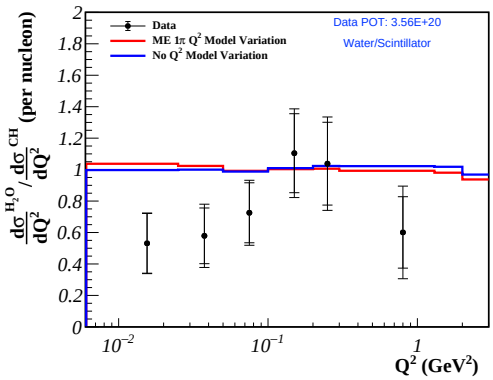


(d) Lead

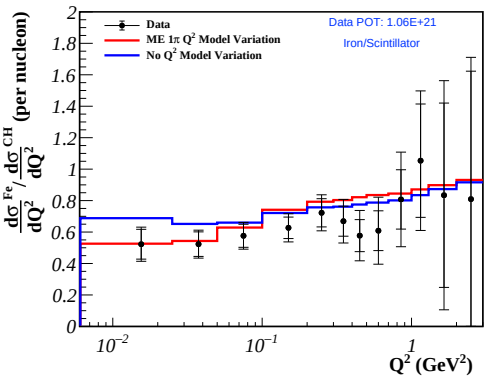
Figure 6-95: θ_μ Target Cross Section Ratio to Scintillator



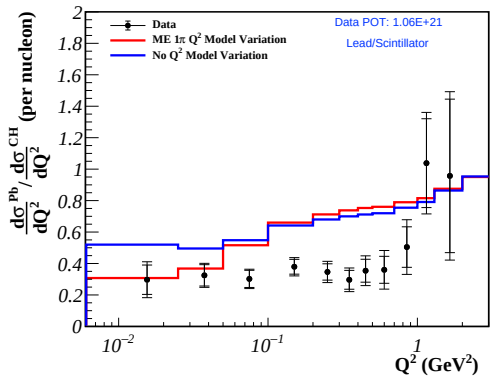
(a) Carbon



(b) Water

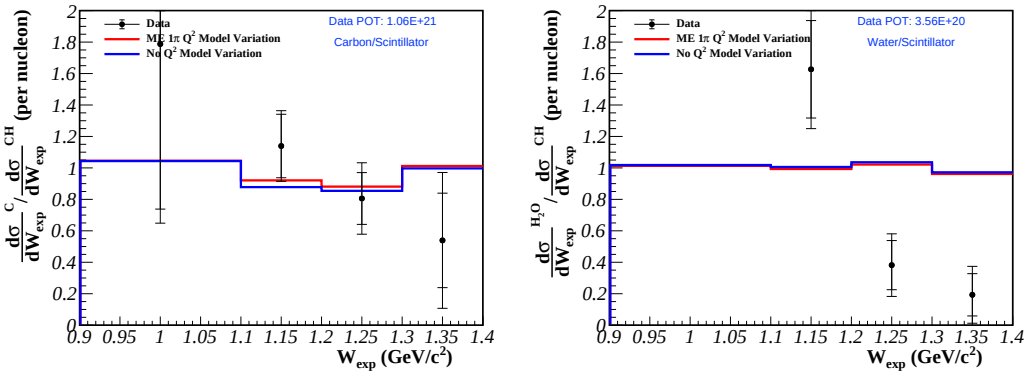


(c) Iron



(d) Lead

Figure 6-96: Q^2 Target Cross Section Ratio to Scintillator



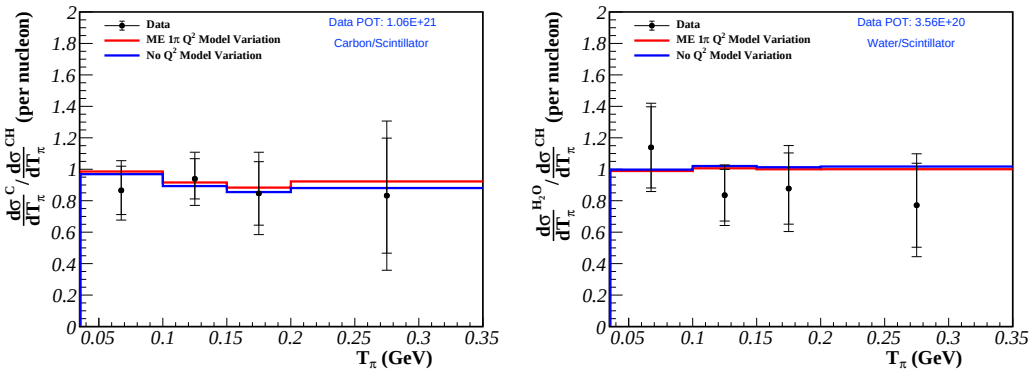
(a) Carbon

(b) Water

(c) Iron

(d) Lead

Figure 6-97: W_{exp} Target Cross Section Ratio to Scintillator



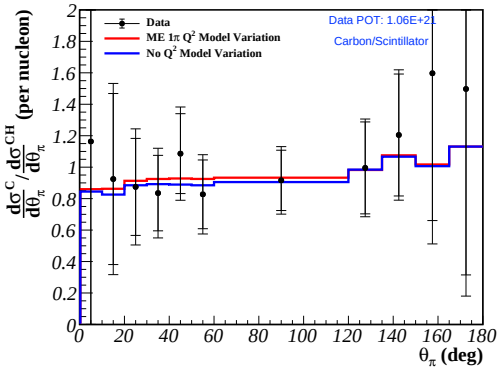
(a) Carbon

(b) Water

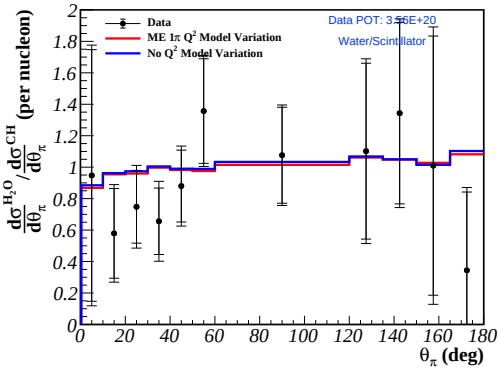
(c) Iron

(d) Lead

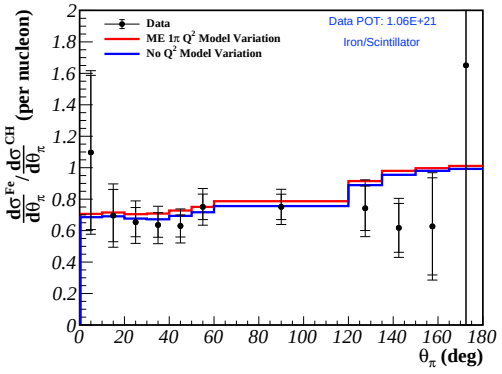
Figure 6-98: T_π Target Cross Section Ratio to Scintillator



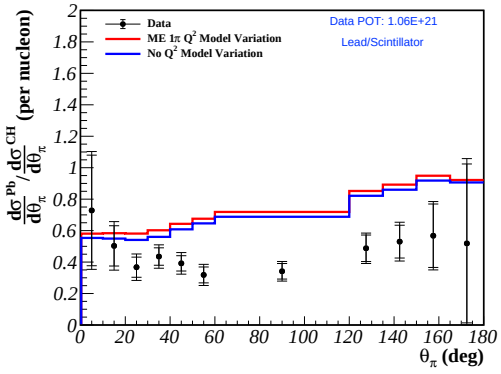
(a) Carbon



(b) Water



(c) Iron



(d) Lead

Figure 6-99: θ_π Target Cross Section Ratio to Scintillator

6.9.5 Integrated Cross Sections

Integrated cross sections are calculated by integrating over the efficiency corrected signal events in each distribution, and then normalizing by the integrated flux prediction scaled by the data POT exposure and the number of nucleons. Tables 6.17 through 6.21 list the integrated cross sections in each analysis variable for each target.

	Data	MC
p_μ	2.2807e-39	2.2013e-39
θ_μ	2.4793e-39	2.2013e-39
$p_{\mu,\|\|}$	2.2791e-39	2.2013e-39
$p_{\mu,T}$	2.1303e-39	2.2013e-39
Q^2	2.1310e-39	2.2013e-39
W_{exp}	2.0419e-39	2.2013e-39
T_π	1.8964e-39	2.2013e-39
θ_π	2.2858e-39	2.2013e-39

Table 6.17: Integrated Carbon Cross Section (cm^2/nucleon)

	Data	MC
p_μ	1.9017e-39	2.3439e-39
θ_μ	1.9665e-39	2.3439e-39
$p_{\mu,\|\|}$	1.9121e-39	2.3439e-39
$p_{\mu,T}$	2.1642e-39	2.3439e-39
Q^2	2.1646e-39	2.3439e-39
W_{exp}	1.6558e-39	2.3439e-39
T_π	2.0681e-39	2.3439e-39
θ_π	2.4366e-39	2.3439e-39

Table 6.18: Integrated Water Cross Section (cm^2/nucleon)

	Data	MC
p_μ	1.6088e-39	1.8052e-39
θ_μ	1.5974e-39	1.8052e-39
$p_{\mu,\|\|}$	1.6068e-39	1.8052e-39
$p_{\mu,T}$	1.5585e-39	1.8052e-39
Q^2	1.5469e-39	1.8052e-39
W_{exp}	1.5479e-39	1.8052e-39
T_π	1.4855e-39	1.8052e-39
θ_π	1.7298e-39	1.8052e-39

Table 6.19: Integrated Iron Cross Section (cm^2/nucleon)

	Data	MC
p_μ	9.5551e-40	1.6114e-39
θ_μ	1.0077e-39	1.6114e-39
$p_{\mu,\|\|}$	9.5567e-40	1.6114e-39
$p_{\mu,T}$	9.7428e-40	1.6114e-39
Q^2	1.0130e-39	1.6114e-39
W_{exp}	1.0750e-39	1.6114e-39
T_π	9.4625e-40	1.6114e-39
θ_π	9.1979e-40	1.6114e-39

Table 6.20: Integrated Lead Cross Section (cm^2/nucleon)

	Data	MC
p_μ	2.3572e-39	2.3507e-39
θ_μ	2.3415e-39	2.3507e-39
$p_{\mu,\|\|}$	2.3569e-39	2.3507e-39
$p_{\mu,T}$	2.3202e-39	2.3507e-39
Q^2	2.3177e-39	2.3507e-39
W_{exp}	2.4200e-39	2.3507e-39
T_π	2.1967e-39	2.3507e-39
θ_π	2.4072e-39	2.3507e-39

Table 6.21: Integrated Tracker Cross Section (cm^2/nucleon)

6.10 Systematic Uncertainties

MINERvA estimates systematic uncertainties, often called "systematics", using the "many-universe" method, which relies on predictions provided by simulation. A universe is a simulated sample of events where a parameter associated with a source of uncertainty is shifted away from the parameter's central, or measured, value. Each universe undergoes the same cross section extraction process as the simulation with no parameter shifts, which is called the central universe.

For a given uncertainty, the parameter is typically shifted by $\pm 1\sigma$, where σ is the parameter's uncertainty. Each $\pm 1\sigma$ shift requires its own universe, therefore most uncertainties will only require two universes each. The exception is the uncertainty on the flux simulation, which uses 100 universes in order to capture the correlations between the parameters in the flux model, which is further explained in section 2.2.

These shifted samples are created by either reweighting events, which alters the probability that certain processes occur, or shifting the reconstructed event kinematics. An example of a $\pm 1\sigma$ reweight can be seen with the diffractive pion production event weight, further explained in section 4.5.4.4. Recall that diffractive pion production is accounted for in the simulation by weighting up coherent pion production by 43.68%. This weight has an uncertainty of 50%, therefore a $\pm 1\sigma$ shift will adjust the weight by $\pm 21.84\%$. For a -1σ shift, coherent pion production events will be weighted up by only 21.84%, and for a $+1\sigma$ shift, the events will be weighted up by 65.52%. An example of a shift in the event kinematics is the uncertainty in the muon momentum reconstruction due to the Bethe Bloch equation, explained further in section 5.5.2. For muons in the active tracking region of MINERvA, this uncertainty is accounted for by shifting the reconstructed muon momentum by ± 30 MeV. This shift will appear in the distribution of the reconstructed muon momentum. Also, as

the shifted kinematics are propagated through the selection cuts of the analysis, an event with this shift in muon momentum may fail one of the selection cuts. This event would not be selected, and thus would not appear in any distributions whose events have been shifted in muon momentum.

The impact of an individual systematic uncertainty is described by a covariance matrix C, shown in equation 6.13.

$$C_{ij} = \frac{1}{N}\sum_{n=1}^{N}(x_{n,i} - \overline{x}_i)(x_{n,j} - \overline{x}_j) \tag{6.13}$$

Variable	Definition
C_{ij}	i, j element of covariance matrix C
N	Number of universes
$x_{n,i}$	Bin content of bin i of universe n
$\overline{x}_i$	Average bin content of all shifted universes in bin i

Table 6.22: Systematic uncertainty covariance matrix variables

The diagonal element C_{ii} is the uncertainty squared for bin i, while the correlations between bins i and j are expressed in the off-diagonals, $C_{ij}, i \neq j$. MINERvA assumes there are no correlations between systematic uncertainties, therefore the total covariance matrix is the sum of the covariance matrices of individual systematic uncertainties.

Different systematic uncertainties of the measured data cross section enter at different steps of the cross section extraction. During the event selection, the data has no systematic uncertainties. Uncertainties related to background processes enter during background subtraction (section 6.5), as there may be systematic variations from the default background prediction which is subtracted from the data. Uncertainties

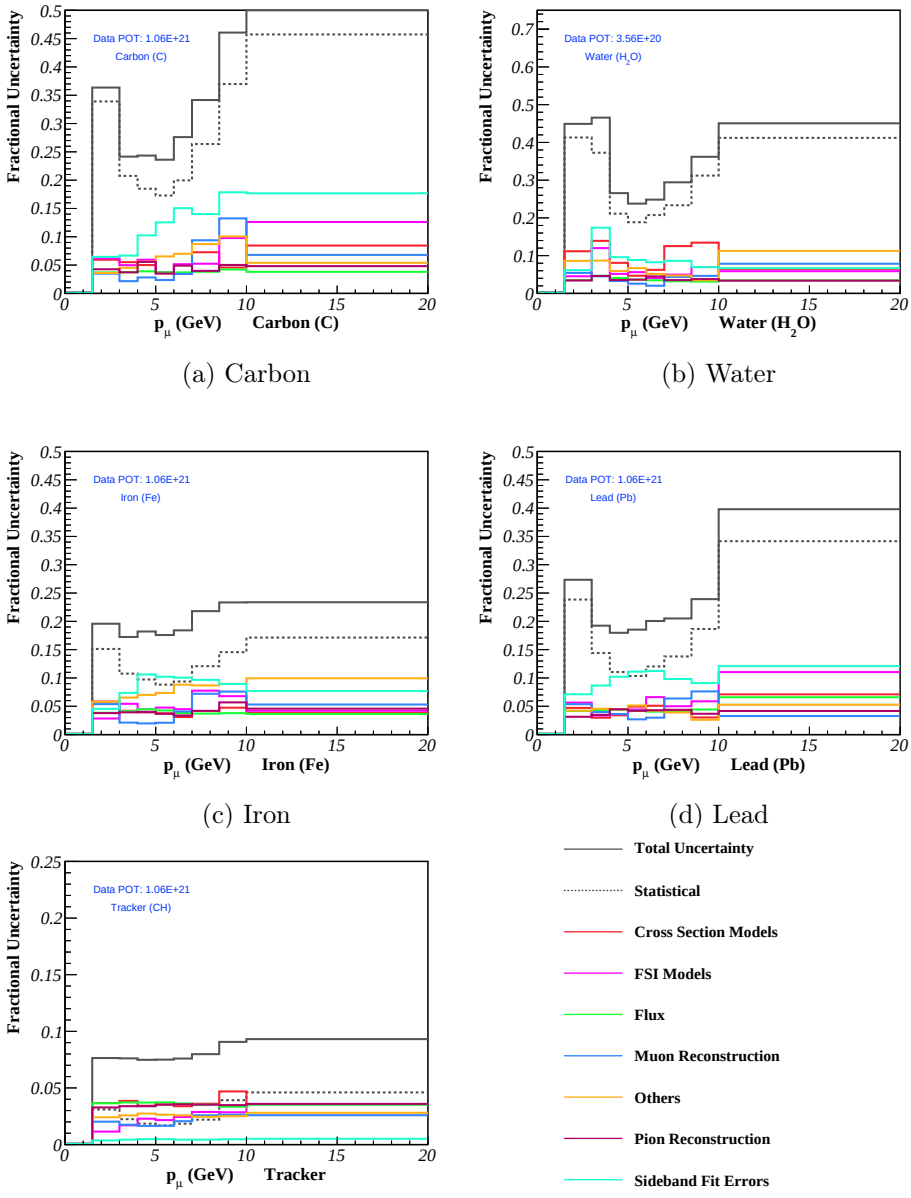
on the detector response primarily enter during the unfolding step (section 6.6). For example, universes with shifted kinematics due to energy scale uncertainties will have migration matrices with more off diagonal elements, which impacts the unfolding procedure. Finally, uncertainties on models related to signal events enter during the efficiency correction (section 6.7), as only the efficiency contains model uncertainties related to the signal.

Figures 6-100 to 6-107 shows the measured differential cross section error summaries for every target nucleus in each analysis variable. The summaries show the statistical uncertainty of cross sections, and groups of related systematic uncertainties. The systematic uncertainties shown in the error summaries are the square root of the diagonals of their respective covariance matrices. The full covariance matrix is reported in the analysis result. The groups of systematics are explained in table 6.23. The following sections describe the groups of systematic uncertainties in this analysis, focusing on the systematics in the transverse muon momentum $p_{\mu,T}$ and pion kinetic energy T_π distributions.

It should be noted that the systematic uncertainties for the water differential cross sections can become very large in some distributions, mostly those related to the angle of the muon. This can be attributed to the small number of events in the water sample.

Group Name	**Description of the sources of uncertainties**
Cross Section Models	GENIE neutrino interaction models, ME coherent pion production reweight, diffractive pion production reweight, MINERvA 2p2h and RPA tunes
FSI Models	GENIE final state interaction models
Flux	MINERvA flux simulation
Muon Reconstruction	Muon momentum and angle reconstruction, MINOS track matching efficiency
Pion Reconstruction	Pion momentum reconstruction, Michel electron matching efficiency, end node cut efficiency
Sideband Fit Errors	High W_{exp} background sideband fit, plastic contamination sideband fit
Other Uncertainties	GEANT4 hadron interaction cross sections, target mass, energy response

Table 6.23: Systematic Uncertainty Groups



(a) Carbon

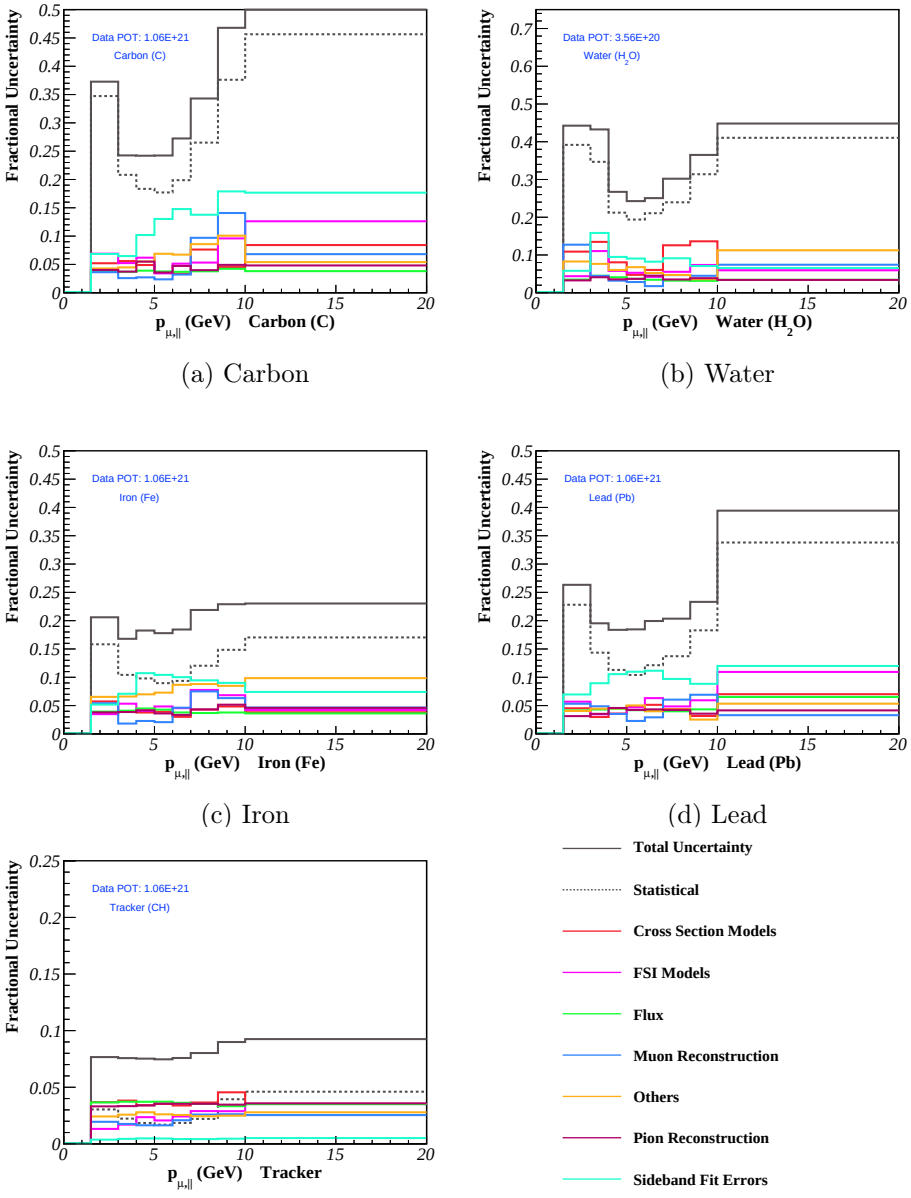
(b) Water

(c) Iron

(d) Lead

(e) Scintillator

Figure 6-100: p_μ Cross Section Error Summary



(a) Carbon

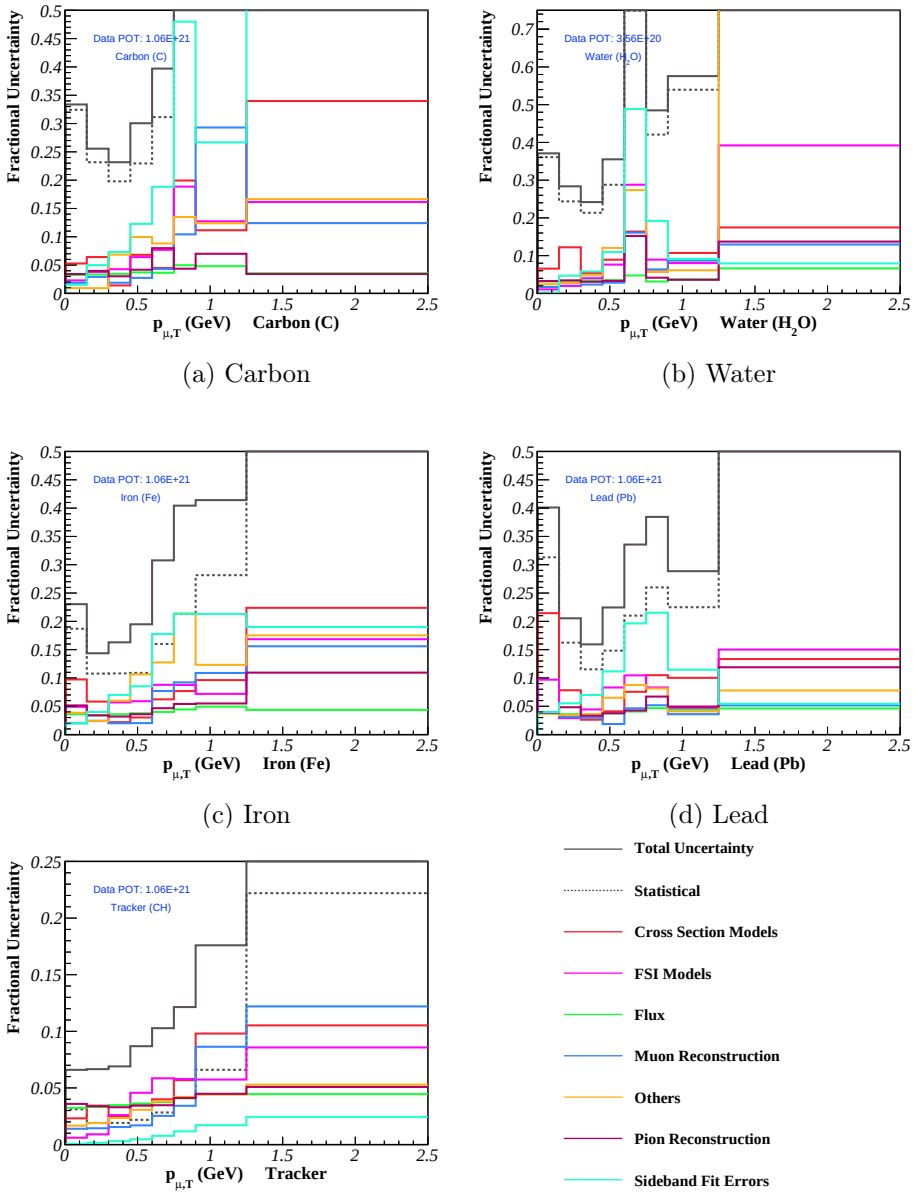
(b) Water

(c) Iron

(d) Lead

(e) Scintillator

Figure 6-101: $p_{\mu,||}$ Cross Section Error Summary



(a) Carbon

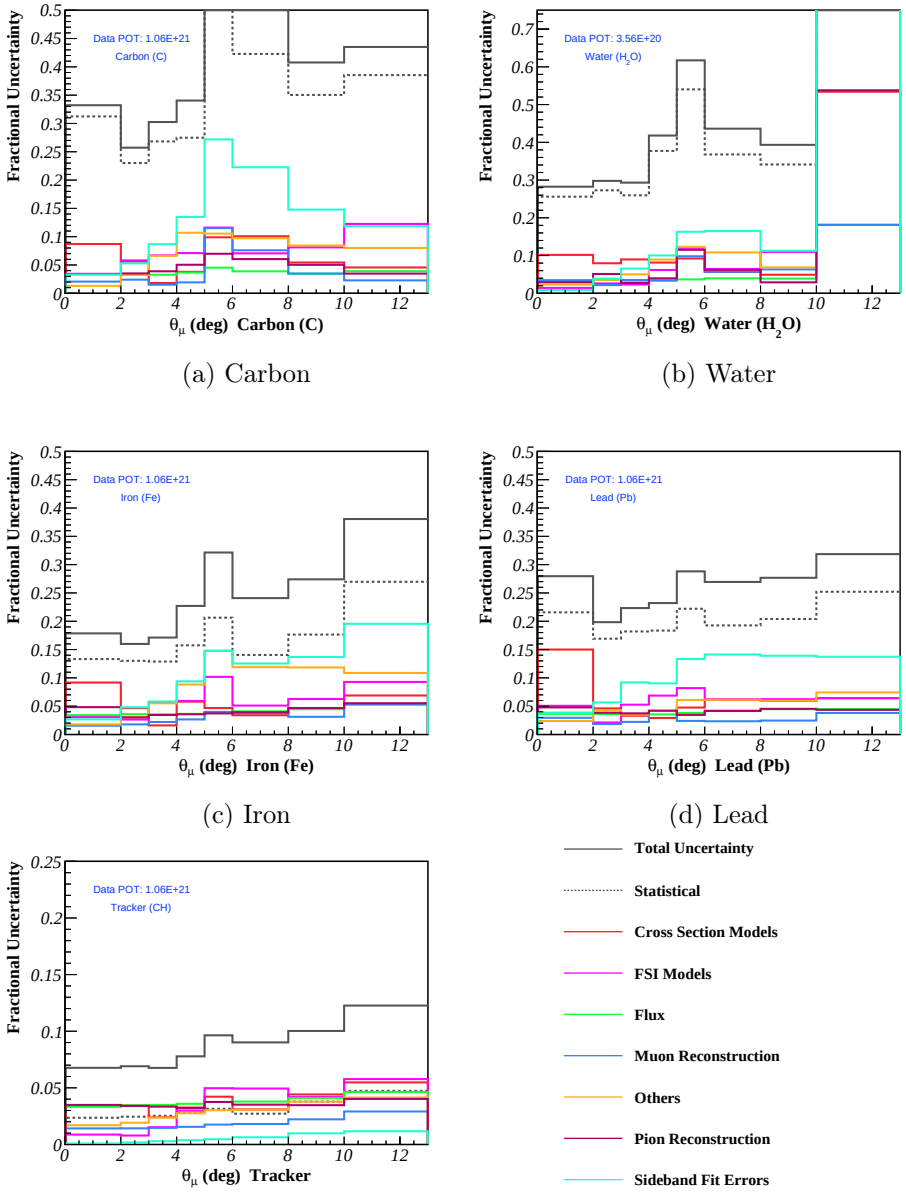
(b) Water

(c) Iron

(d) Lead

(e) Scintillator

Figure 6-102: $p_{\mu,T}$ Cross Section Error Summary



(a) Carbon

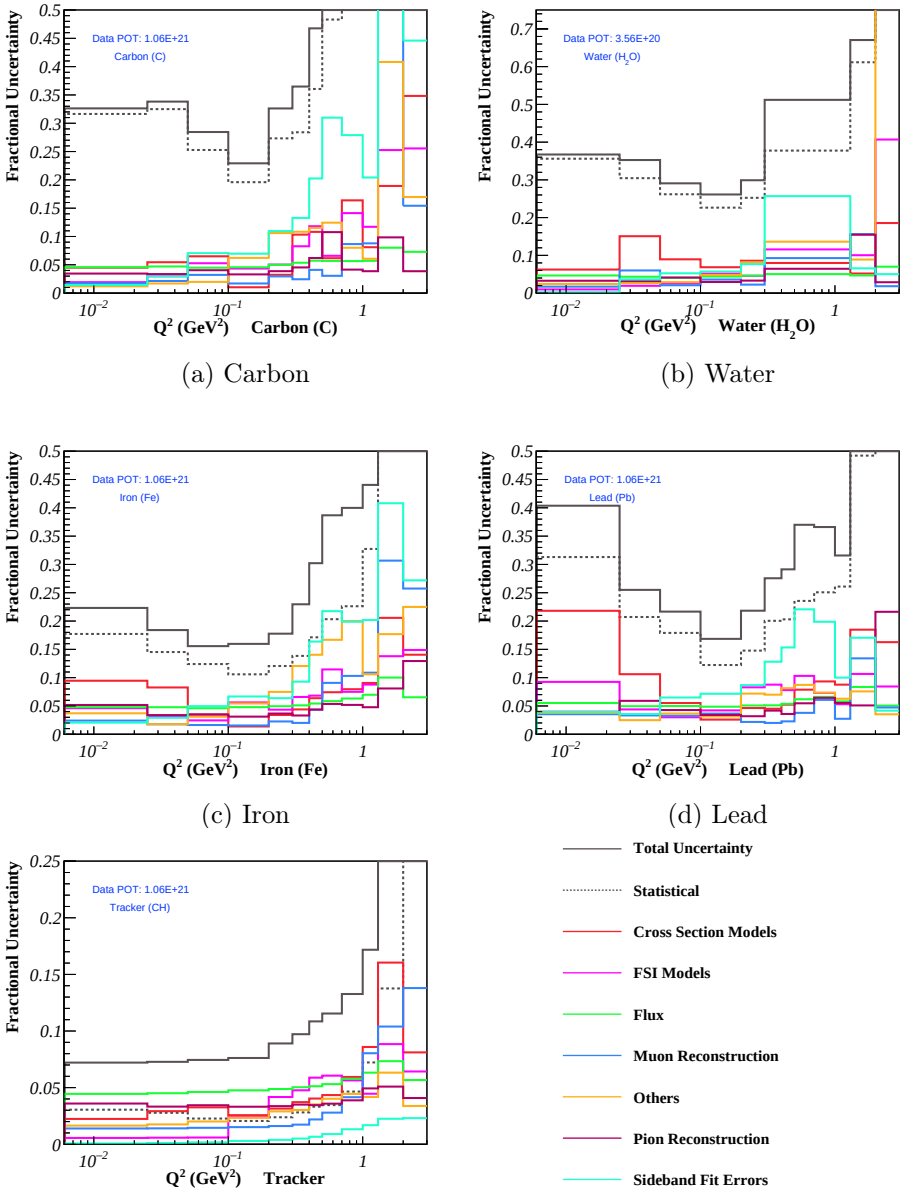
(b) Water

(c) Iron

(d) Lead

(e) Scintillator

Figure 6-103: θ_μ Cross Section Error Summary



(a) Carbon

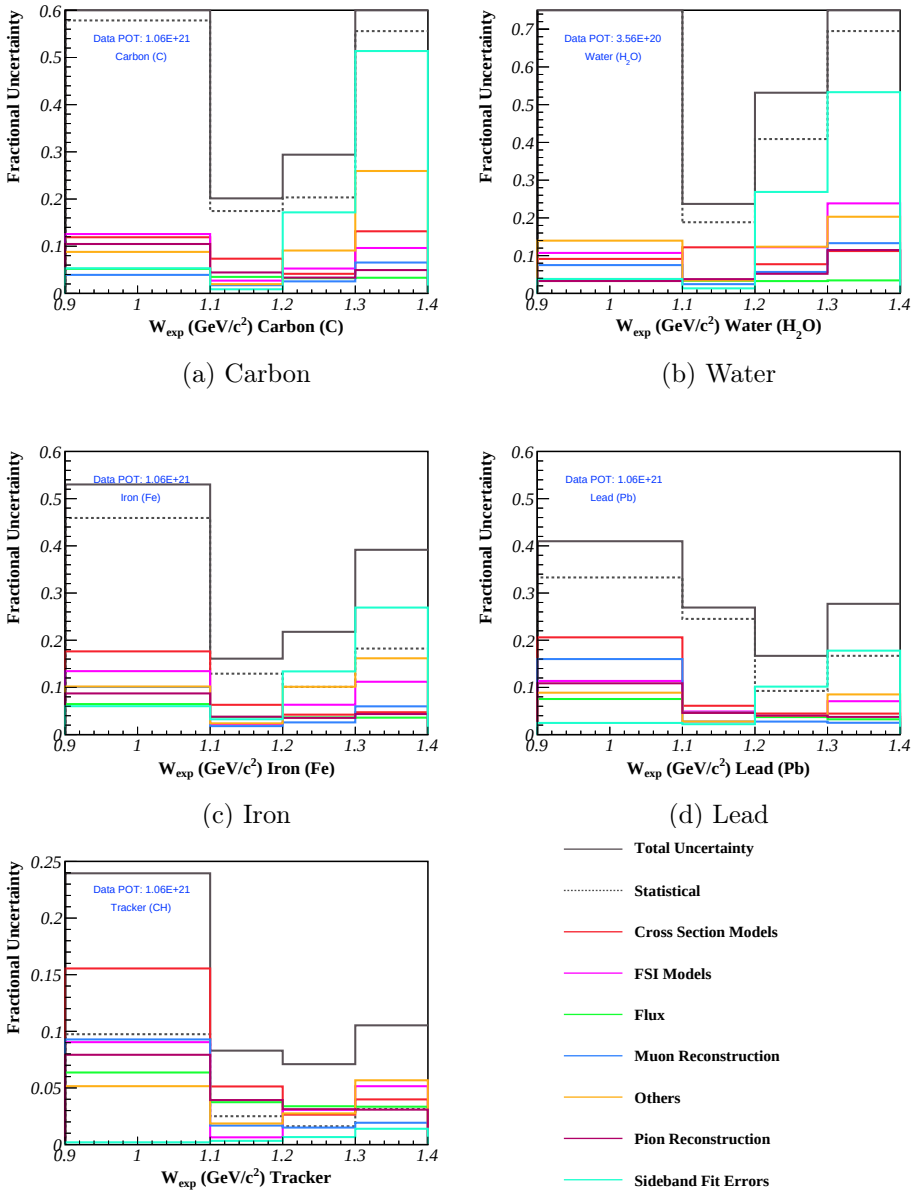
(b) Water

(c) Iron

(d) Lead

(e) Scintillator

Figure 6-104: Q^2 Cross Section Error Summary



(a) Carbon

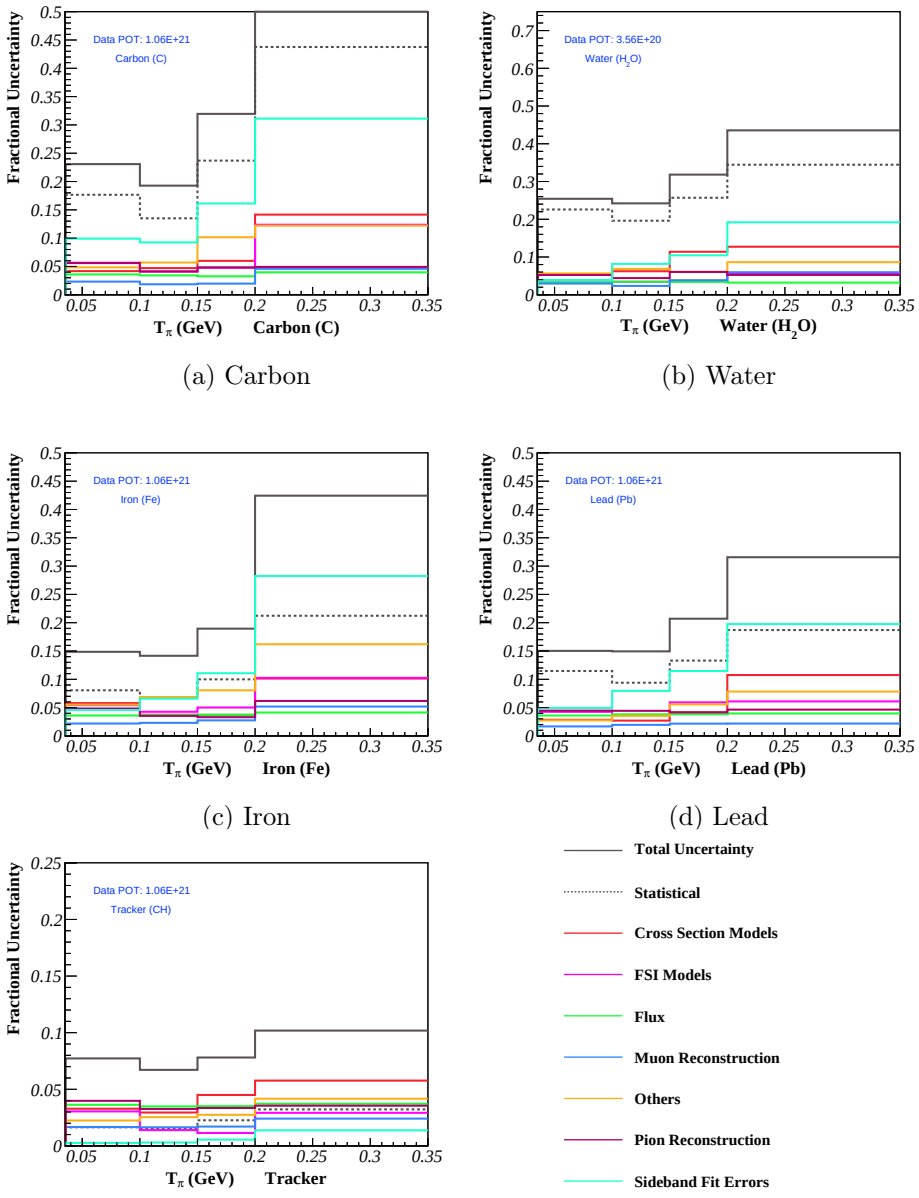
(b) Water

(c) Iron

(d) Lead

(e) Scintillator

Figure 6-105: W_{exp} Cross Section Error Summary



(a) Carbon

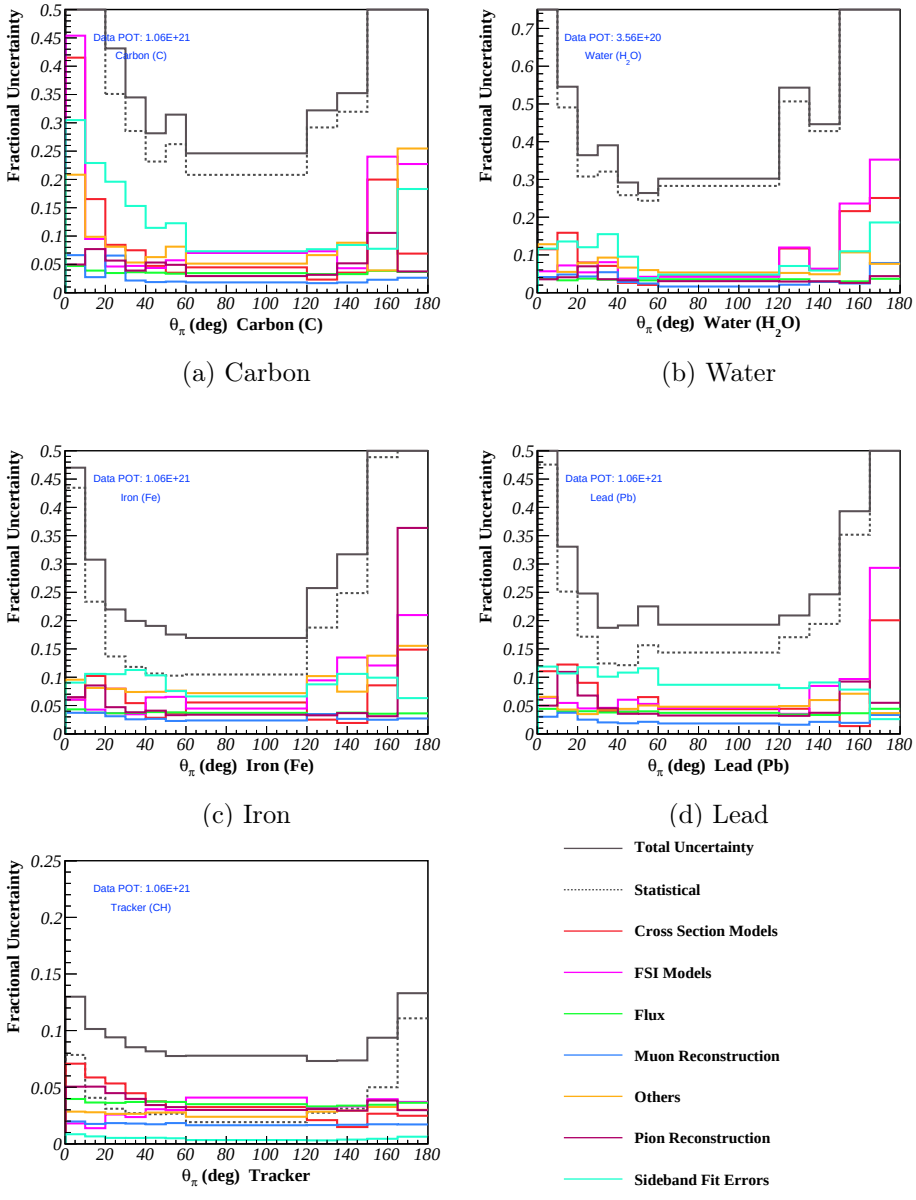
(b) Water

(c) Iron

(d) Lead

(e) Scintillator

Figure 6-106: T_π Cross Section Error Summary



(a) Carbon

(b) Water

(c) Iron

(d) Lead

(e) Scintillator

Figure 6-107: θ_π Cross Section Error Summary

6.10.1 Cross section models

The GENIE neutrino interaction models have several parameters which adjust the probability of an interaction process occurring. The largest sources of systematic uncertainty for these models come from charged current quasielastic scattering, the pion angular distribution in Δ decay, and nonresonant pion production. The uncertainties on resonant, coherent and diffractive pion production will be discussed further in this section.

The primary source of the uncertainty in the charged current quasielastic (CCQE) scattering model, which is discussed further in sections 1.3.1 and 4.1.1, is the axial mass $M_{A,CCQE}$. The fractional uncertainty of the modeled cross-section due to the axial mass increases with $p_{\mu,T}$, becoming as large as $10 - 15\%$ at high $p_{\mu,T}$. The uncertainties from the other parameters in the CCQE model are small ($< 5\%$). Table 6.24 shows the CCQE model parameters.

Parameter	Shift in Parameter
Axial mass $M_{A,CCQE}$	$^{+25\%}_{-15\%}$
Pauli suppression of CCQE at low Q^2	$\pm 30\%$
Vector form factor model	BBBA $\rightarrow$ Dipole

Table 6.24: GENIE charged current quasielastic (CCQE) model uncertainties

Section 4.1.2 shows the equation used by GENIE to produce the angular distribution of pions in Δ decay. By default, GENIE assumes that the angular distribution is anisotropic, and varying the parameter would make the angular distribution more or less isotropic. Due to a bug in the weight calculation, the shifts in the parameter do not have a physical interpretation, however these shifts most likely overestimate the uncertainty. This bug will be fixed in future work. The angular distribution of pions is the largest contributor to uncertainty in resonant pion production. Fits to

Parameter	Shift in Parameter
NC Normalization	±20%
CC Normalization	±7%
Axial mass M_A^{RES}	±0.05 GeV
Vector Mass M_V^{RES}	±3%
Pion angular distribution in $\Delta \to N\pi$	Anisotropy → isotropy

Table 6.25: GENIE resonant pion production model uncertainties

the data from neutrino deuterium bubble chamber experiments, discussed in sections 1.5, 4.1.2, and 4.5.4.2, extracted the values of two parameters involved in resonant pion production: the axial mass M_A^{RES} and the normalization of charged current pion production. These fits have also limited the uncertainty of the parameter, which are listed in table 6.25. Electro-nucleus scattering data constraint the vector mass M_V^{RES} to 3% uncertainty.

The bubble chamber fits also found the normalization of nonresonant 1π production, which is governed by a tuned Bodek-Yang model, explained further in section 4.1.3. This also limited the uncertainty of the normalization of nonresonant 1π production, however, the fits had weaker constraints on the normalization of nonresonant 2π production, thus the uncertainty is at 50%. The nonresonant 2π production can occur due to neutrino interactions on a proton ($\nu + p$) or a neutron ($\nu + n$). The $\nu + p$ production channel contributes more to the uncertainty. The nonresonant 2π production uncertainty increases with T_π, with a fractional uncertainty of the modelled cross section of $\sim 5\%$. Table 6.26 shows the nonresonant pion production uncertainties.

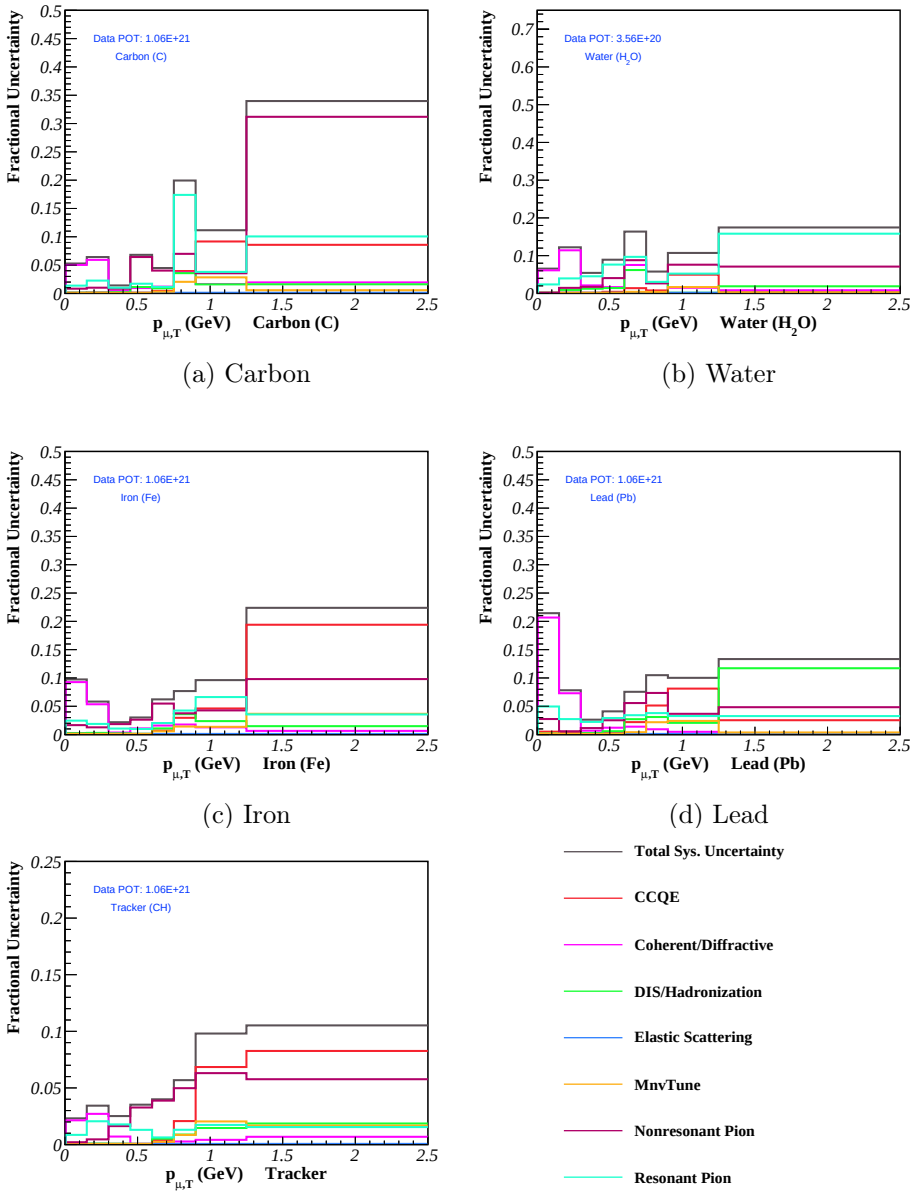
Parameter	Shift in Parameter
Normalization of 1π production	±4%
Normalization of 2π production	±50%

Table 6.26: GENIE Nonresonant pion production model uncertainties

Parameter	Shift in Parameter
Norm of coherent pion production in scintillator	±20%
Norm of coherent pion production in passive materials	±40%
Norm of diffractive pion production	±50%

Table 6.27: GENIE coherent and diffractive pion production model uncertainties

Sections 4.5.4.3 and 4.5.4.4 describe the reweights that account for coherent and diffractive pion production. Table 6.27 shows the uncertainties on these two production processes. These are the dominant uncertainties at low $p_{\mu,T}$.



(a) Carbon

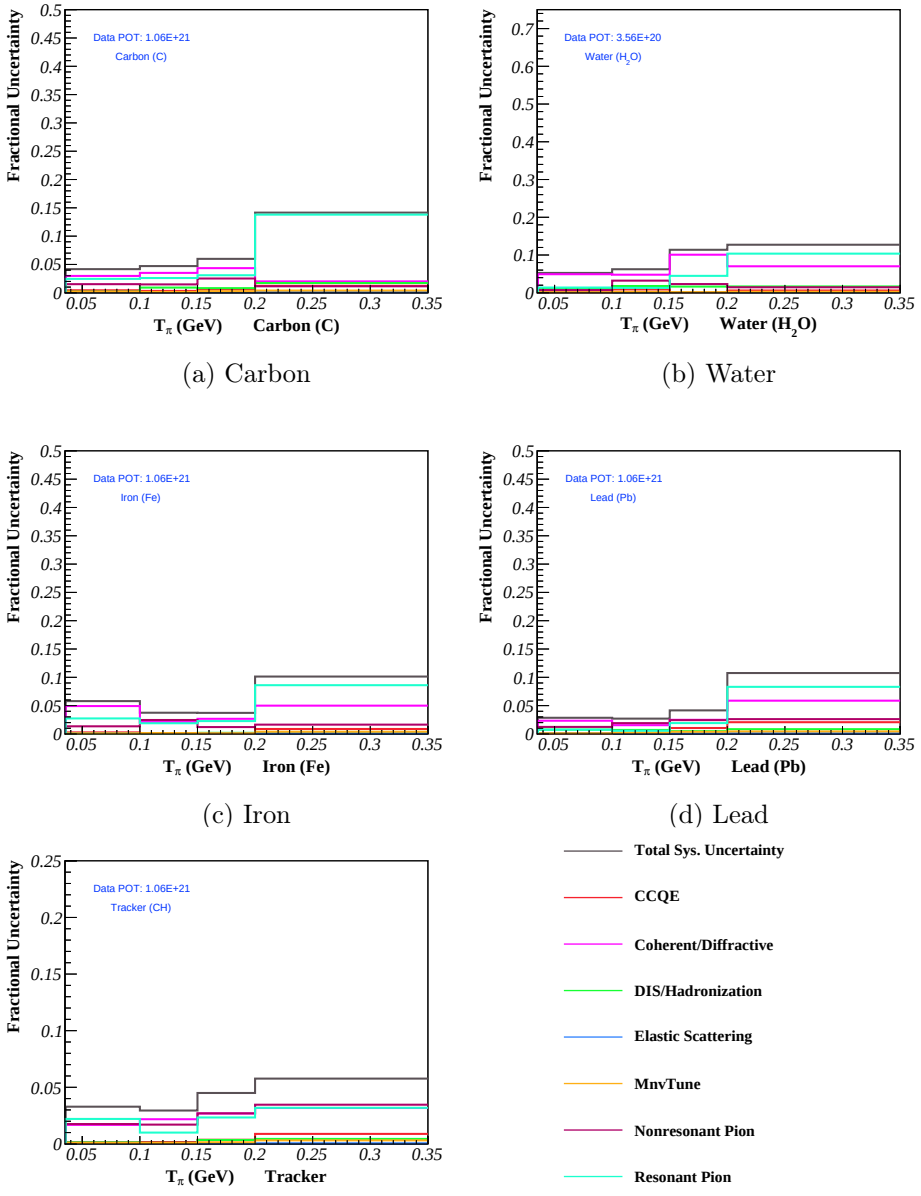
(b) Water

(c) Iron

(d) Lead

(e) Scintillator

Figure 6-108: $p_{\mu,T}$ Cross Section Model Errors



(a) Carbon

(b) Water

(c) Iron

(d) Lead

(e) Scintillator

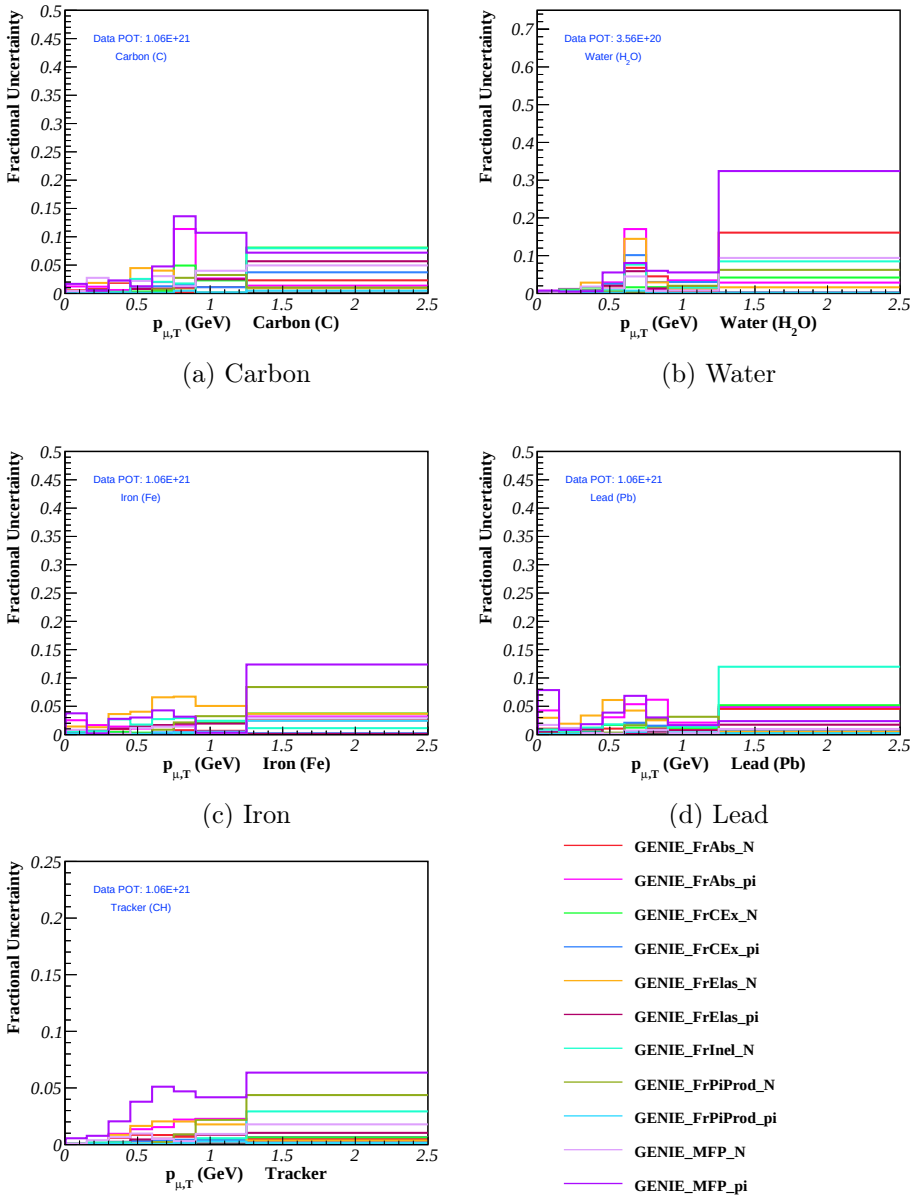
Figure 6-109: T_π Cross Section Model Errors

6.10.2 FSI (Final State Interactions) Models

Final state interaction uncertainties depend on the parameters in GENIE that alter the probabilities that different final state interaction (FSI) processes occur. These FSI processes include absorption, charge exchange, elastic scattering, and inelastic scattering, which are further explained in table 1.6. GENIE includes final state pion production as an additional FSI process. Another parameter, the mean free path, adjusts the overall FSI probability by changing the distance a particle propagates inside a nucleus before interacting. Each FSI process and the mean free path has a separate parameter for nucleons and pions. The one exception is pion inelastic scattering, whose parameters is excluded due to large anticorrelations with the other FSI parameters.

The sources of the largest FSI uncertainties are the mean free path of the pion, nucleon pion production, and nucleon elastic scattering. The signal definition of this analysis requires one charged pion in the final state, and the first two sources directly affect the number of pions in the final state. Varying the nucleon elastic scattering parameter affects the reconstructed hadronic energy, which changes the events selected by the reconstructed $W_{exp} < 1.4$ GeV/c^2 cut.

The fractional uncertainty of the modelled cross section due to the mean free path of the pion is $\sim 5-15\%$ in the targets and $< 5\%$ in the tracker, and it tends to increase with T_π. Varying nucleon pion production provides a fractional uncertainty of $\sim 5\%$, which increases with $p_{\mu,T}$. Nucleon elastic scattering has a fractional uncertainty of $\sim 5\%$, which has small variation in $p_{\mu,T}$ and T_π. Table 6.28 lists the GENIE FSI parameters.



(a) Carbon

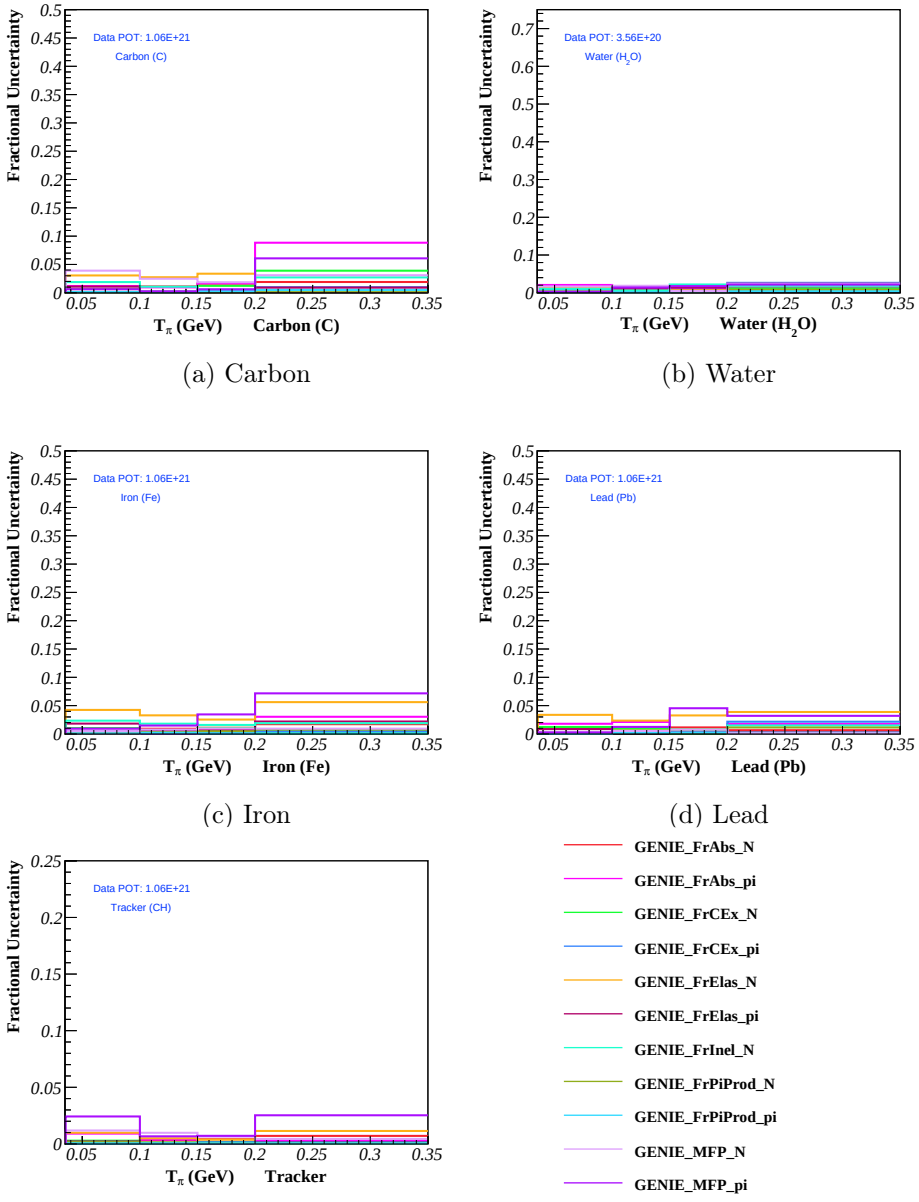
(b) Water

(c) Iron

(d) Lead

(e) Scintillator

Figure 6-110: $p_{\mu,T}$ FSI Errors



(a) Carbon

(b) Water

(c) Iron

(d) Lead

(e) Scintillator

Figure 6-111: T_π FSI Errors

FSI Uncertainty	Parameter Name	Shift in Parameter
Nucleon FSI Parameters		
Mean free path	MFP_N	±20%
Absorption probability	FrAbs_N	±20%
Charge exchange probability	FrCEx_N	±50%
Elastic scattering probability	FrElas_N	±30%
Inelastic scattering probability	FrInel_N	±40%
FS pion production probability	FrPiProd_N	±20%
Pion FSI Parameters		
Mean free path	MFP_pi	±20%
Absorption probability	FrAbs_pi	±30%
Charge exchange probability	FrCEx_pi	±50%
Elastic scattering probability	FrElas_pi	±10%
FS pion production probability	FrPiProd_pi	±20%

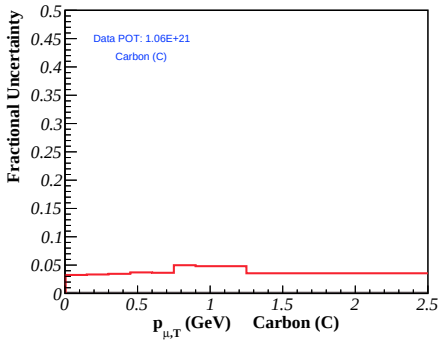
Table 6.28: GENIE FSI uncertainties

6.10.3 Flux

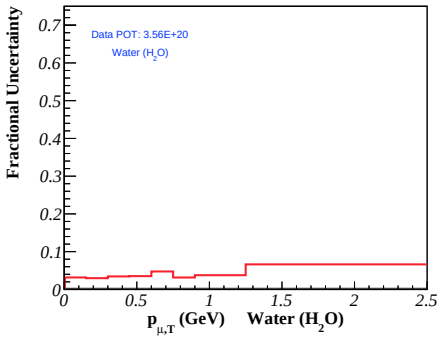
The flux simulation, which has been explained in section 2.2, has many free parameters and thus many sources of uncertainty. There are two main types of uncertainty: focusing uncertainties, which are the uncertainties associated with the components of the NuMI beamline, and the hadron production uncertainties, which are the uncertainties of hadron production in the graphite target due to the incident proton beam. These uncertainties have a large number of correlations between them, thus it is difficult to treat each free parameter separately by shifting by $\pm 1\sigma$.

Recall that MINERvA uses Package to Predict the FluX (PPFX) [85] to propagate the uncertainties from the external data to the uncertainties on the flux. In order to capture the correlations between the uncertainties, many different simulated fluxes are produced using randomly thrown flux parameters. Each parameter is limited to be within 1σ of its central value, and each simulated flux is called a flux universe. By comparing a flux universe to the central value flux, an event weight can be found which adjusts the likelihood of an event occurring with the given true neutrino energy and flavor. The flux systematic uncertainty is estimated by using the spread of the weighted distributions.

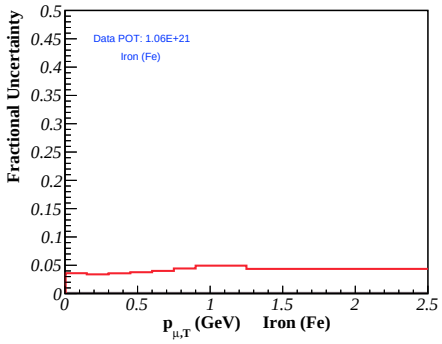
When the $\nu - e$ and IMD flux constraints, explained in sections 2.2.2.1 and 2.2.2.2, are applied to the flux universes, the total flux uncertainty is reduced. This can be seen in figures 2-8 and 2-10. While MINERvA has generated 1000 different flux universes, it was determined that only 200 flux universes were needed to estimate the flux uncertainty with the constraints. Due to the constraints, the flux uncertainty is $\sim 5\%$.



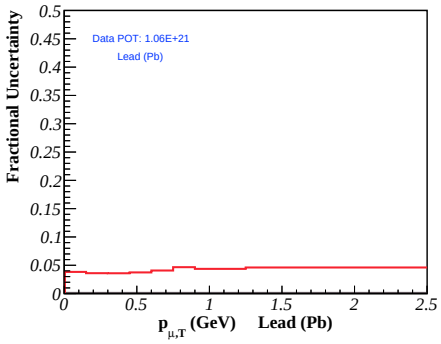
(a) Carbon



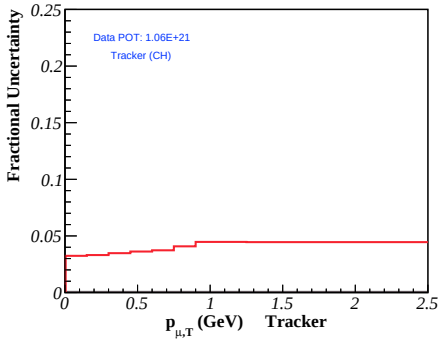
(b) Water



(c) Iron

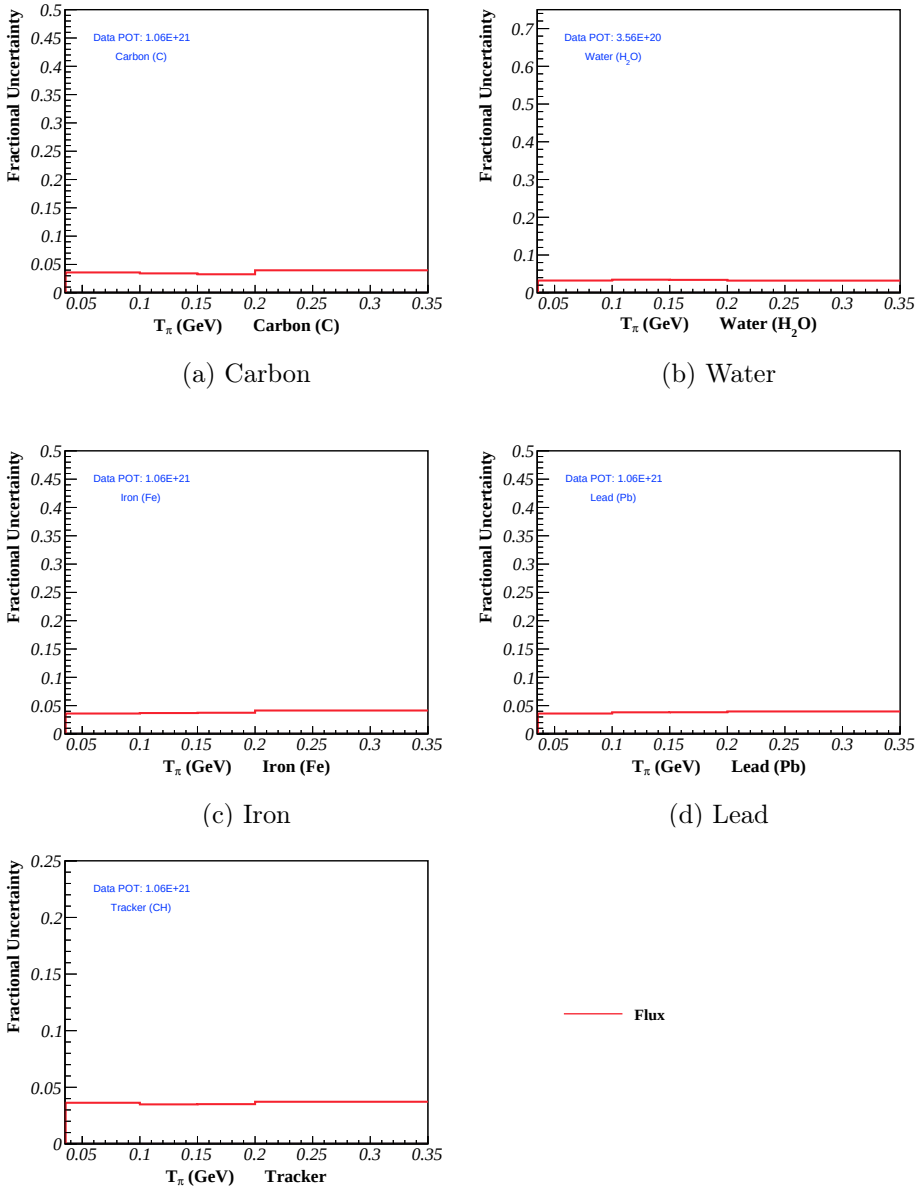


(d) Lead



(e) Scintillator

Figure 6-112: $p_{\mu,T}$ Flux Error



(a) Carbon

(b) Water

(c) Iron

(d) Lead

(e) Scintillator

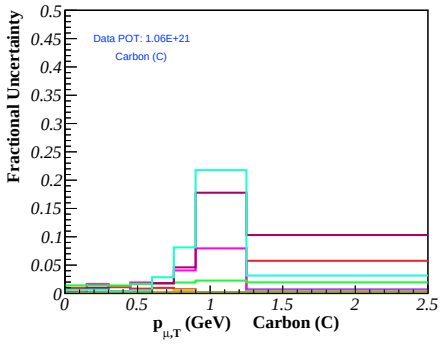
Figure 6-113: T_π Flux Error

6.10.4 Muon Reconstruction

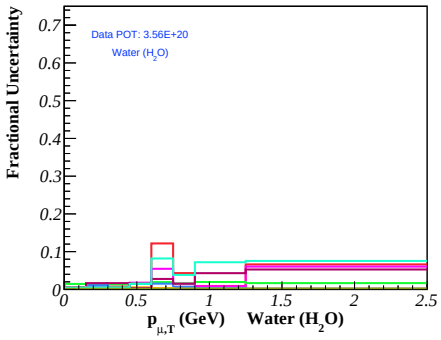
The systematic uncertainties of muon reconstruction can be divided into muon energy, muon angle and MINOS track matching efficiency. The systematics of muon energy reconstruction are the largest contributor to muon reconstruction systematics. These have been outlined in section 5.5.2. The muon energy resolution systematic uncertainty quantifies the difference in the resolution of muon energy, $\frac{\text{reco}-\text{true}}{true}$, between data and simulation, which has been measured at 0.4%.

The muon angle reconstruction systematics include the uncertainties in the angle of the neutrino beam and the difference in muon angle resolution between data and simulation. These uncertainties are small in this analysis.

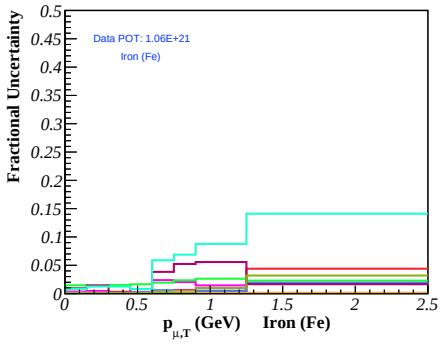
Section 4.5.2 explains the MINOS track matching efficiency weights, which corrects the difference in matching efficiencies between data and simulation. The uncertainty is the statistical errors on the measurement of the efficiencies, and it is dependent on muon energy and beam intensity.



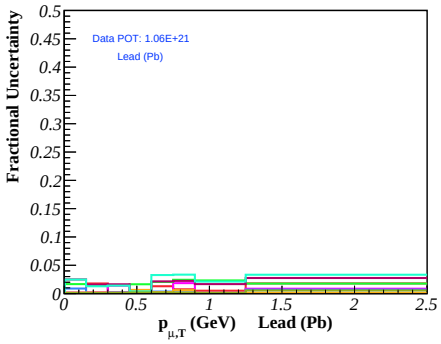
(a) Carbon



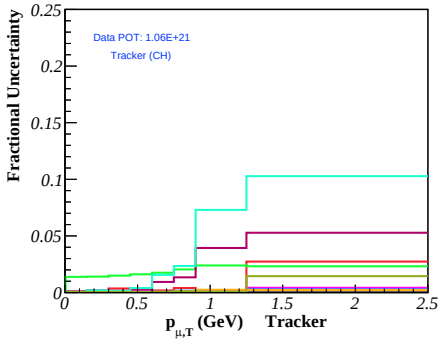
(b) Water

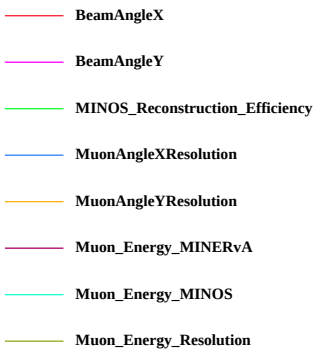


(c) Iron



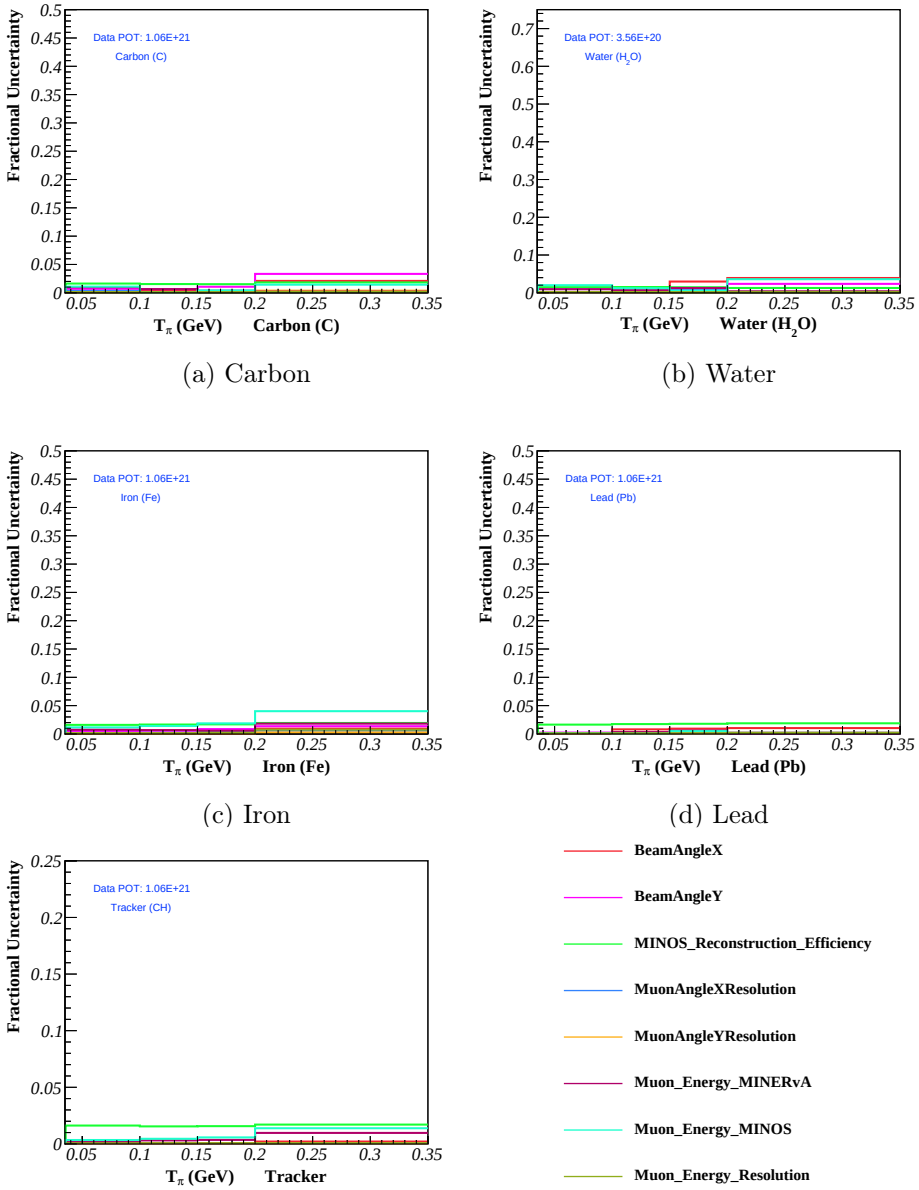
(d) Lead





(e) Scintillator

Figure 6-114: $p_{\mu,T}$ Muon Reconstruction Errors



(a) Carbon

(b) Water

(c) Iron

(d) Lead

(e) Scintillator

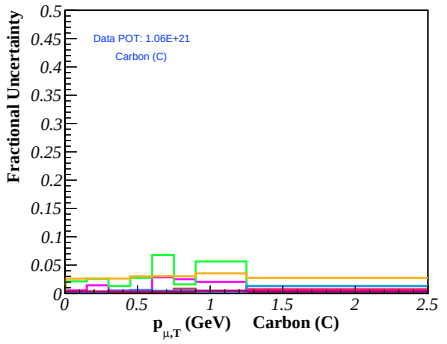
Figure 6-115: T_π Muon Reconstruction Errors

6.10.5 Pion Reconstruction

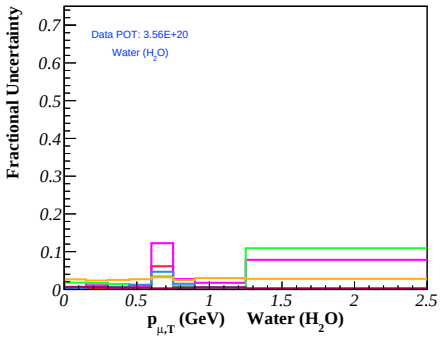
Most of the systematic uncertainties of pion reconstruction are related to the reconstruction of pion kinetic energy, outlined in section 5.7.1. The reconstruction relies on $\frac{dE}{dX}$ profile curves. The shapes of the curves can vary due to uncertainties on several parameters. These include the uncertainties in the Bethe Bloch equation, uncertainties on the measured Birks constant in the MINERvA detector, which is explained further in section 4.3.3, the uncertainties on the energy scale of the detector (MEU), which is explained in section 3.4.1.6, and uncertainties on the mass of the detector.

The systematic uncertainty of Michel electron tagging efficiency is one of the dominant systematics in the pion reconstruction. The evaluation of this uncertainty, which is 2.5%, is discussed in section 4.4.1.

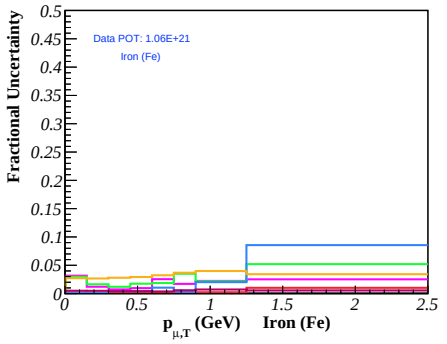
A systematic uncertainty must also be placed on the track end node energy cut, discussed in section 5.7.5, to account for the difference of the deposition of the energy at the end of hadron tracks between data and simulation. Studies showed that any difference would be covered by an uncertainty of 0.15% for events with a reconstructed charged pion with $T_\pi < 0.15$ GeV and an uncertainty of 1% for events with $T_\pi > 0.15$ GeV.



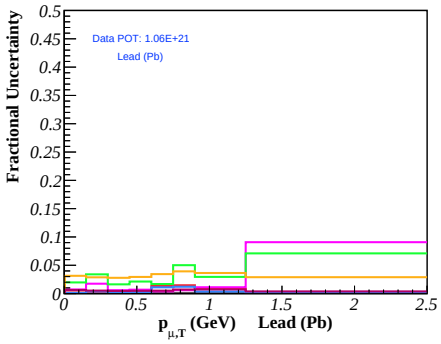
(a) Carbon



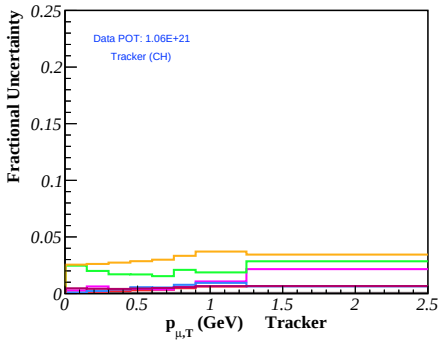
(b) Water

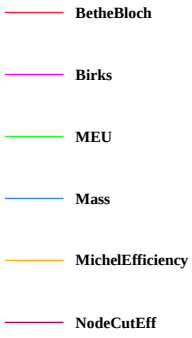


(c) Iron



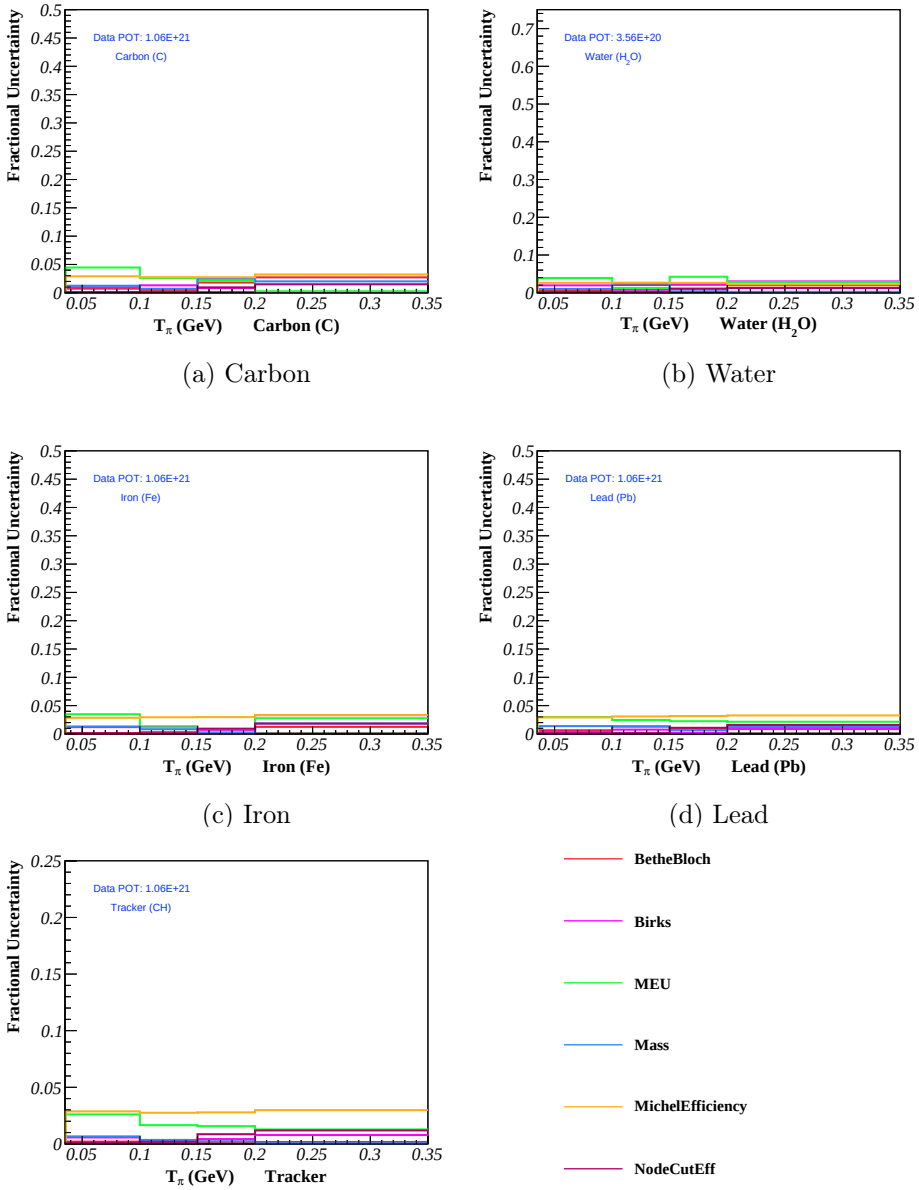
(d) Lead





(e) Scintillator

Figure 6-116: $p_{\mu,T}$ Pion Reconstruction Errors



(a) Carbon

(b) Water

(c) Iron

(d) Lead

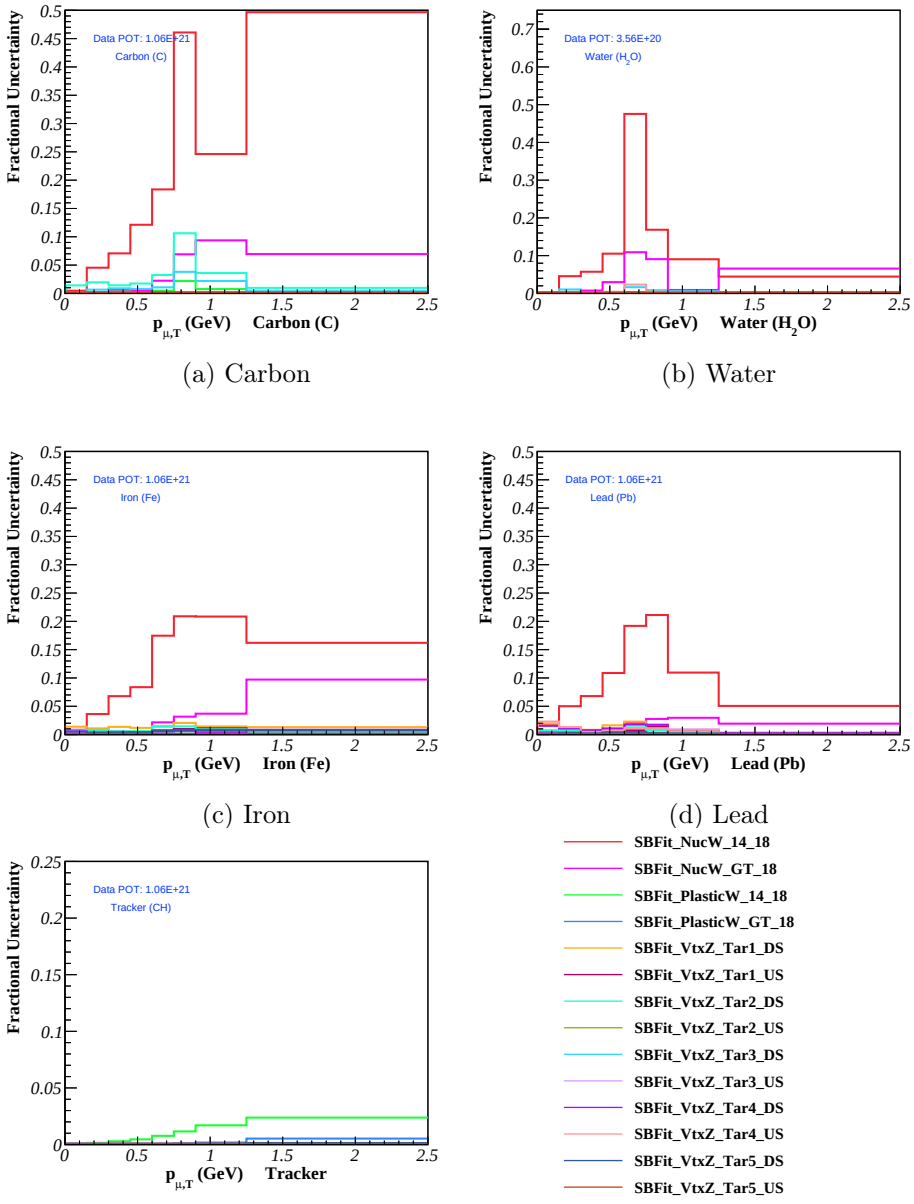
(e) Scintillator

Figure 6-117: T_π Pion Reconstruction Errors

6.10.6 Sideband Fit Errors

Section 6.4 describes the normalization fits on background events in the sidebands. The uncertainty on these fits are added as systematic uncertainties. These systematic uncertainties are representative of the statistical uncertainty in the sidebands. Table 6.29 lists the uncertainties on the sideband fits.

The largest systematics come from the uncertainties on the $1.4 < W_{exp,true} < 1.8$ GeV/c^2 fit in the nuclear targets. This is due to both small number of events from data in the sideband and the large number of background events with $1.4 < W_{exp,true} < 1.8$ GeV/c^2 in the selected event sample. The fractional uncertainties on the $1.8 < W_{exp,true}$ GeV/c^2 contributions are also large; however there are few background events with $1.8 < W_{exp,true}$ GeV/c^2 in the selected event sample.



(a) Carbon

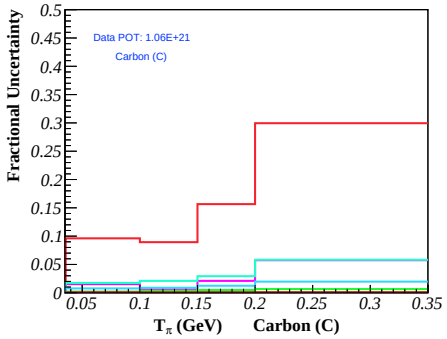
(b) Water

(c) Iron

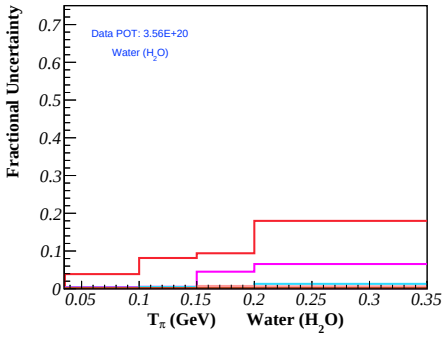
(d) Lead

(e) Scintillator

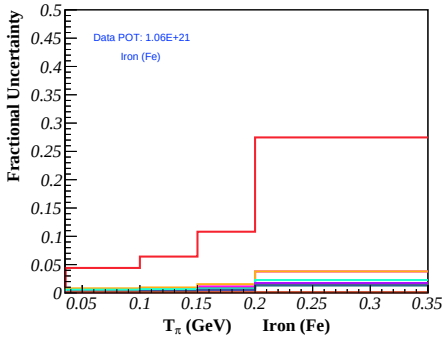
Figure 6-118: $p_{\mu,T}$ Sideband Fit Errors



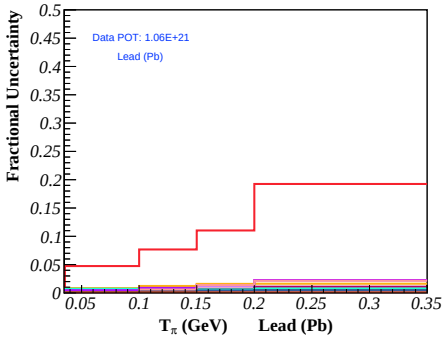
(a) Carbon



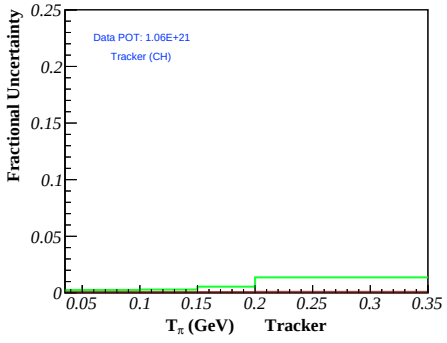
(b) Water



(c) Iron



(d) Lead



(e) Scintillator

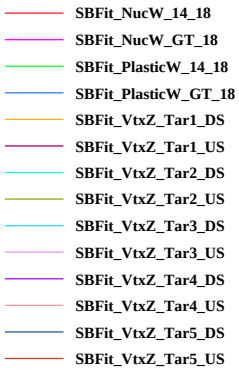


Figure 6-119: T_π Sideband Fit Errors

Background Category	Label	Shift in Normalization
High W_{exp} sideband fit in the tracker		
$1.4 < W_{exp,true} < 1.8$ GeV/c^2	PlasticW_14_18	± 0.018
$1.8 < W_{exp,true}$ GeV/c^2	PlasticW_GT_18	± 0.015
High W_{exp} sideband fit in the carbon		
$1.4 < W_{exp,true} < 1.8$ GeV/c^2	NucW_14_18	0.705 ± 0.404
$1.8 < W_{exp,true}$ GeV/c^2	NucW_GT_18	1.185 ± 0.527
High W_{exp} sideband fit in the water		
$1.4 < W_{exp,true} < 1.8$ GeV/c^2	NucW_14_18	1.508 ± 0.304
$1.8 < W_{exp,true}$ GeV/c^2	NucW_GT_18	0.000 ± 0.347
High W_{exp} sideband fit in the iron		
$1.4 < W_{exp,true} < 1.8$ GeV/c^2	NucW_14_18	0.540 ± 0.222
$1.8 < W_{exp,true}$ GeV/c^2	NucW_GT_18	0.769 ± 0.212
High W_{exp} sideband fit in the lead		
$1.4 < W_{exp,true} < 1.8$ GeV/c^2	NucW_14_18	0.130 ± 0.148
$1.8 < W_{exp,true}$ GeV/c^2	NucW_GT_18	0.812 ± 0.156
Plastic contamination sideband fit in the nuclear targets		
Target 1 Upstream Plastic	VtxZ_Tar1_US	± 0.173
Target 1 Downstream Plastic	VtxZ_Tar1_DS	± 0.068
Target 2 Upstream Plastic	VtxZ_Tar2_US	± 0.054
Target 2 Downstream Plastic	VtxZ_Tar2_DS	± 0.072
Target 3 Upstream Plastic	VtxZ_Tar3_US	± 0.043
Target 3 Downstream Plastic	VtxZ_Tar3_DS	± 0.063
Target 4 Upstream Plastic	VtxZ_Tar4_US	± 0.060
Target 4 Downstream Plastic	VtxZ_Tar4_DS	± 0.045
Target 5 Upstream Plastic	VtxZ_Tar5_US	± 0.051
Target 5 Downstream Plastic	VtxZ_Tar5_DS	± 0.050

Table 6.29: Sideband fit uncertainties

6.10.7 Other Uncertainties

The target mass systematics represent the uncertainties in the measurement of the density of both the passive and active targets. Table 6.30 shows the uncertainties in the target mass. The response systematics quantify the uncertainty of the calorimetric

Target	Label	Shift
Scintillator	Target_Mass_CH	±1.4%
Carbon	Target_Mass_C	±0.5%
Water	Target_Mass_H20	±2.0%
Iron	Target_Mass_Fe	±1.0%
Lead	Target_Mass_Pb	±0.5%

Table 6.30: Target mass uncertainties

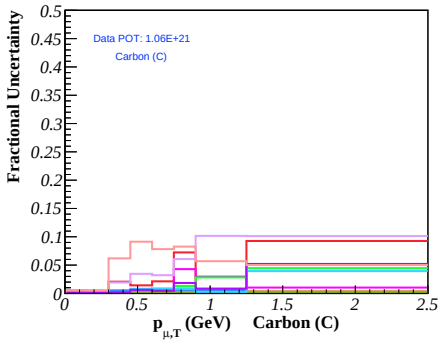
energy response of the detector. These uncertainties were measured at the MINERvA testbeam detector, a smaller version of the MINERvA detector which received proton, pion, and electron beams of known energy [140] [141]. The energy response of neutrons was not measured at the testbeam detector. The response systematics are only applied to the hadronic recoil energy reconstructed with calorimetry. These uncertainties do not affect the pion energy reconstruction, which relies on $\frac{dE}{dX}$ profiles of tracks. The largest systematic uncertainty comes from the proton response. Table 6.31 lists the particle response uncertainties.

Particle	Label	Shift
Proton	response_proton	±3.5%
e/γ	response_em	±3.0%
Meson	response_meson	±5.0%
Other	response_other	±20.0%

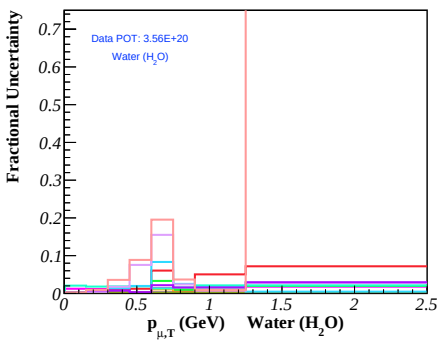
Table 6.31: Particle response uncertainties

The "GEANT" systematics account for the uncertainties on the interaction cross

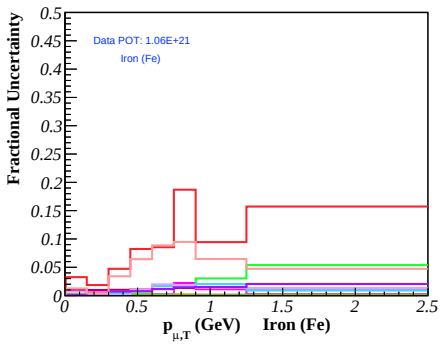
sections used by GEANT to simulate particles traversing through the MINERvA detector. Section 4.5.3 explains the reweighting scheme that propagates these uncertainties to the event sample. The uncertainties on pion angle reconstruction are captured by the GEANT systematics because the reconstructed pion angle is highly dependent on pion scattering in the detector. Also, the GEANT systematics account for the uncertainty of the neutron energy response, as the neutron energy deposition is dependent on the neutron interaction cross sections.



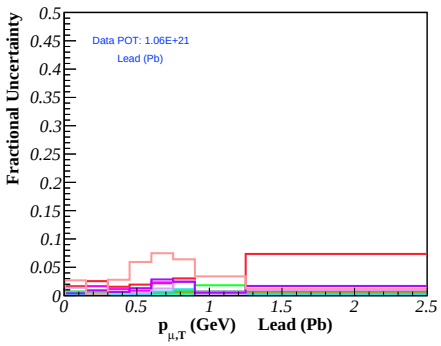
(a) Carbon



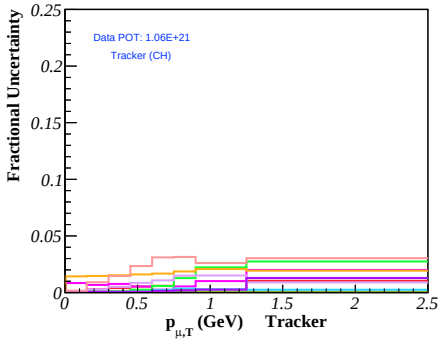
(b) Water



(c) Iron



(d) Lead



(e) Scintillator

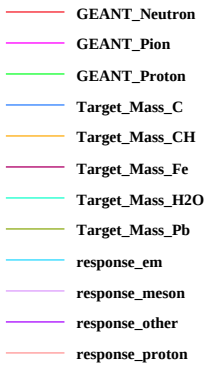
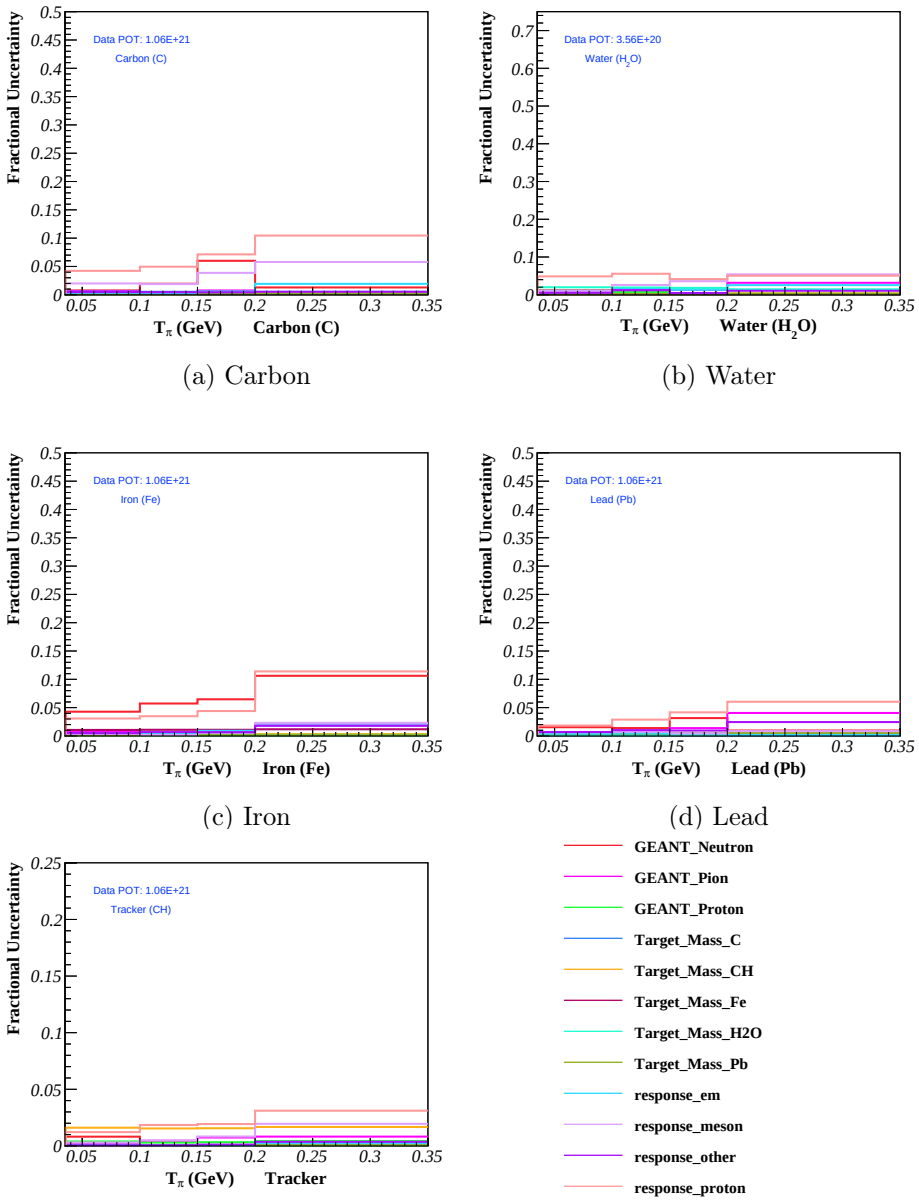


Figure 6-120: $p_{\mu,T}$ Other Systematic Errors



(a) Carbon

(b) Water

(c) Iron

(d) Lead

(e) Scintillator

Figure 6-121: T_π Other Systematic Errors

Chapter 7

Conclusions

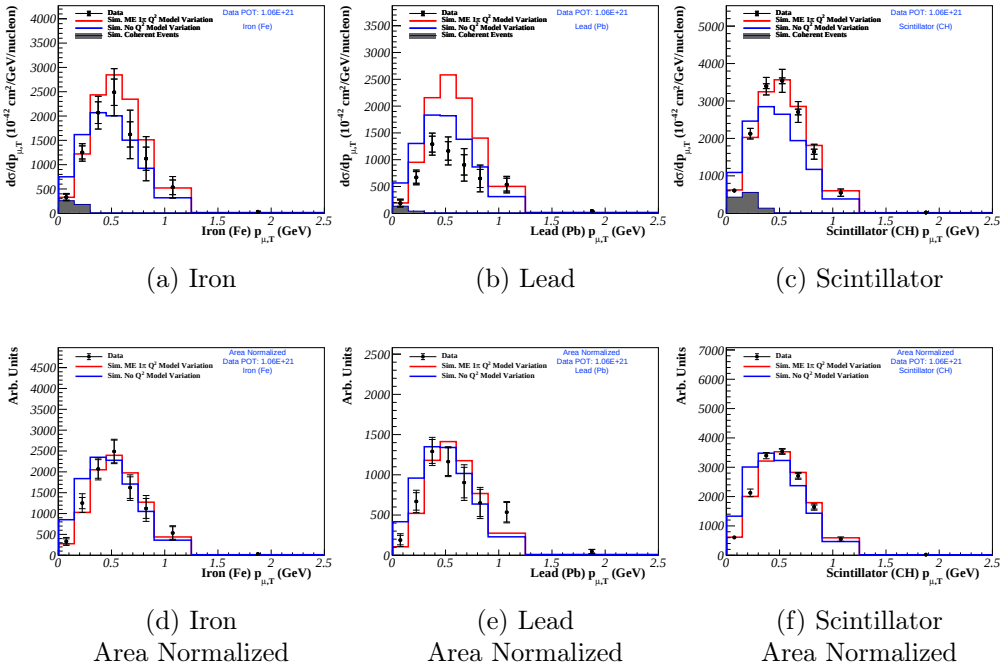
This analysis measured the differential cross sections of muon neutrino charged current single pion production on five separate targets in the MINERvA detector. The differential cross sections were measured in eight kinematic variables, including muon momentum and angle, transverse and longitudinal muon momentum, four-momentum transferred squared, invariant hadronic mass, and pion angle and kinetic energy. The final cross section results of this analysis are presented in section 6.9.

Comparisons between the two predictions show that the most significant differences in shape occur in θ_μ, Q^2 and $p_{\mu,T}$, which are all correlated variables. Figure 7-1 shows that there is a dramatic suppression of events at the lowest $p_{\mu,T}$, below 0.3 GeV/c, and an enhancement at the highest $p_{\mu,T}$, above 0.5 GeV/c. This disagreement is so dramatic that the impact of this distribution shows up in nearly every other variable, even those mostly uncorrelated with $p_{\mu,T}$, at least as a dramatic change in normalization. Therefore, for ease of comparison, the plots show each prediction with and without the "low Q^2 suppression" model described in Section 4.5.4.6. Generally, the comparison is more meaningful taking account this low Q^2 suppression which was tuned on the scintillator sample, but applied on all nuclei, except hydrogen,

independent of nucleus.

Variables mostly uncorrelated with Q^2 see an enhancement – which emphasizes the point that the "low Q^2 suppression" name refers to a relative suppression on top of an overall enhancement relative to model predictions – which is largely a normalization factor. A good illustration of this is shown in figure 7-2, where the differential cross-sections see a large difference from the suppression model, but the area normalization cross-section is almost unaffected.

Predictions of other models than the MINERvA tuned GENIE model could be insightful, although most other predictions share a common theoretical basis with this one. As part of publication of the work, comparisons to other neutrino interaction generators, including GENIE3, NuWro, NEUT, and GiBUU, will be added.

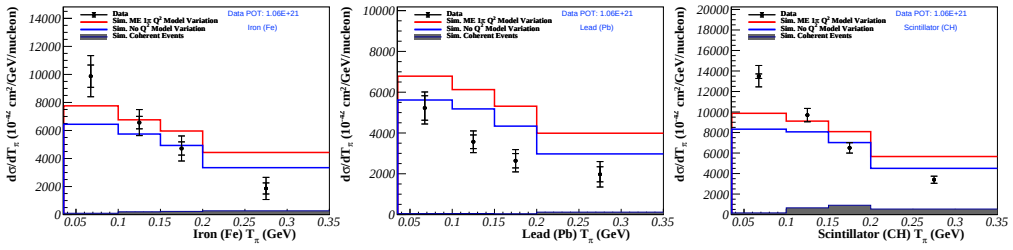


(a) Iron (b) Lead (c) Scintillator

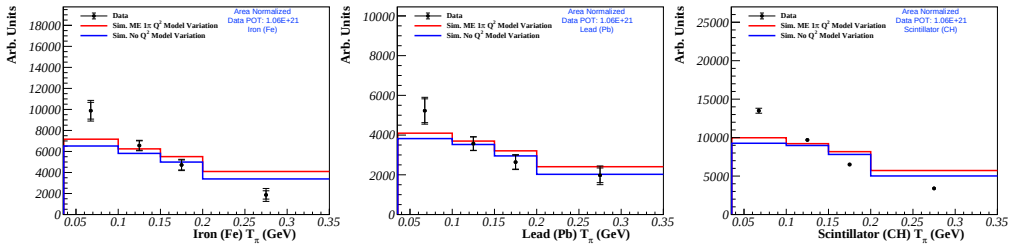
(d) Iron Area Normalized (e) Lead Area Normalized (f) Scintillator Area Normalized

Figure 7-1: $p_{\mu,T}$ differential cross sections on iron, lead, and scintillator. The bottom plots show the shape difference between the predictions with and without the low Q^2 suppression

Neither the default prediction, nor the "low Q^2 suppression", accurately models the nuclear dependence of the normalization of pion production, as shown in figure 7-3. However, the low Q^2 suppression is needed to explain the shape of the measured Q^2 differential cross section in all nuclei, as can be seen in figure 7-4. By construction, scintillator is mostly well modeled with the low Q^2 suppression, and carbon appears to be as well. But in the heavier nuclei, iron is overpredicted by the low Q^2 suppression, but the prediction without suppression matches the measured iron cross section well, except at low Q^2. Lead is well below both predictions, and shows almost a complete elimination of the cross-section at the very lowest Q^2. These predictions include both the primary neutrino interactions and FSI effects, which makes it difficult to



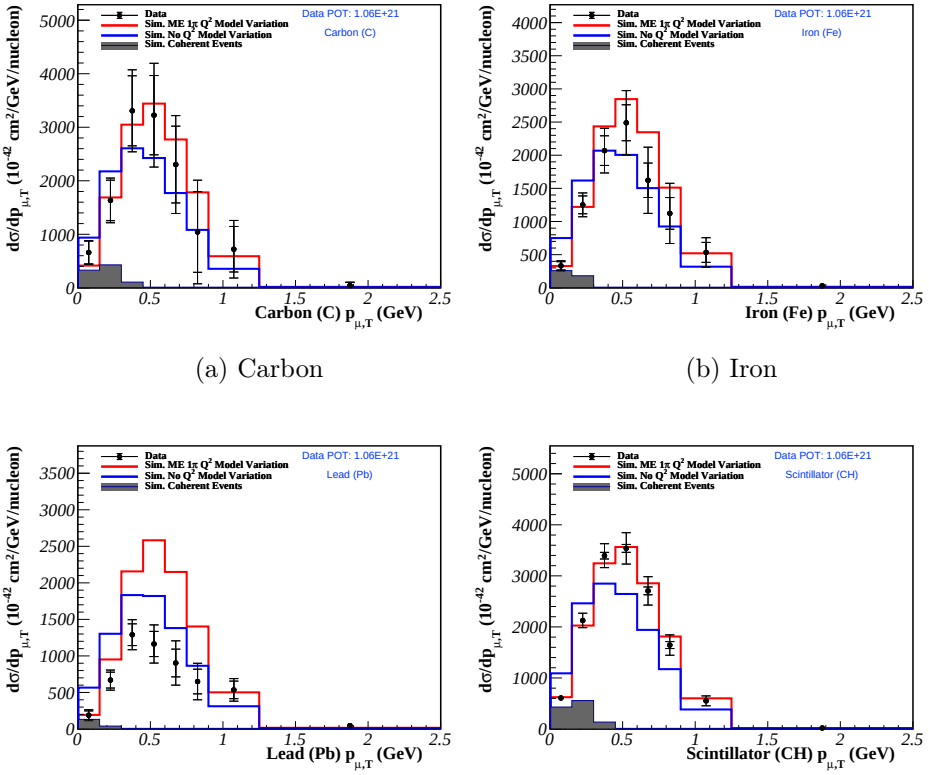
(a) Iron (b) Lead (c) Scintillator



(d) Iron Area Normalized (e) Lead Area Normalized (f) Scintillator Area Normalized

Figure 7-2: T_π differential cross sections on iron,lead and scintillator. The top plots show the difference in the normalization, while the bottom plots show little difference in shape difference between the predictions with and without the low Q^2 suppression

unambiguously ascribe the suppression or enhancement to a single deficiency in the model. However, since the FSI depends strongly on pion energies which themselves are not a strong function of Q^2, it is likely that the primary production is a major source of this disagreement.

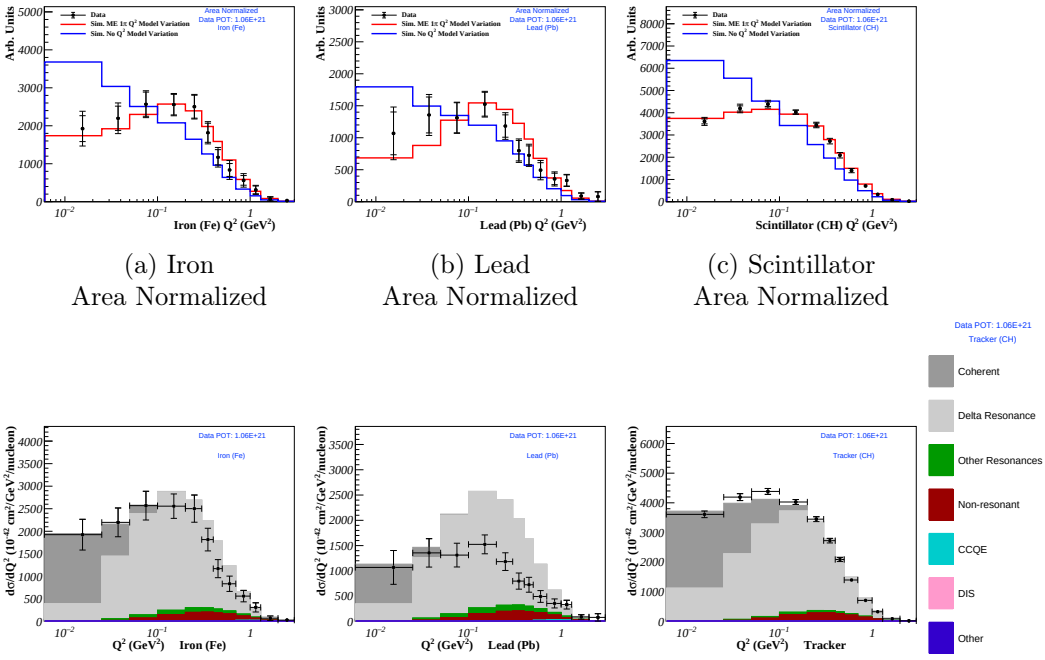


(a) Carbon (b) Iron

(c) Lead (d) Scintillator

Figure 7-3: p_μ differential cross sections on carbon, iron, lead, and scintillator

The neutrino energy E_ν and the longitudinal muon momentum $p_{\mu,||}$ are closely related quantities. Using $p_{\mu,||}$ as a stand in for E_ν, the shape of the measured cross section in $p_{\mu,||}$, shown in figure 7-5, seems to underpredict neutrino interactions with lower E_ν in the heavier targets. This could be indicating that the threshold for pion



(a) Iron Area Normalized

(b) Lead Area Normalized

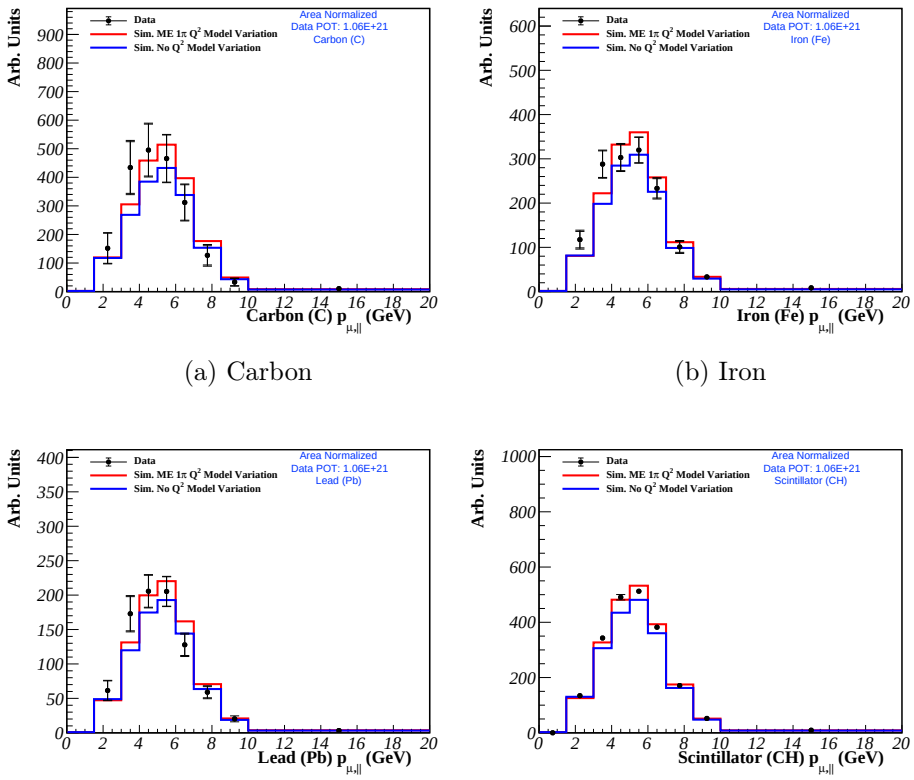
(c) Scintillator Area Normalized

(d) Iron

(e) Lead

(f) Scintillator

Figure 7-4: Q^2 differential cross sections on iron, lead, and scintillator



(a) Carbon

(b) Iron

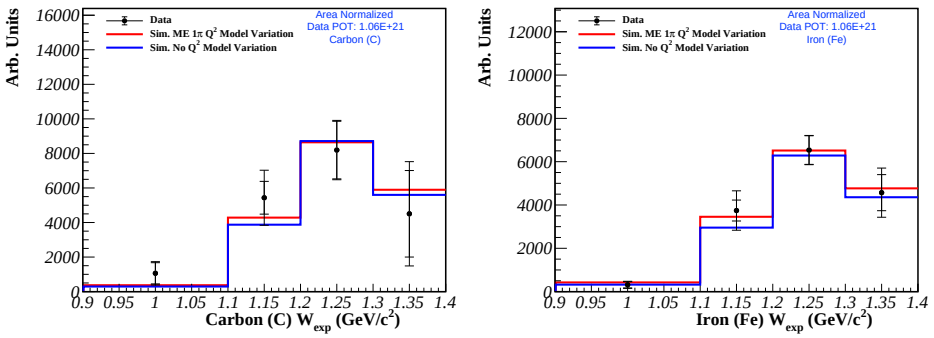
(c) Lead

(d) Scintillator

Figure 7-5: Area normalized $p_{\mu,||}$ differential cross sections on carbon, iron, lead, and scintillator

production has some nuclear effect not included in the model.

The differential cross sections in W_{exp} are shown in figure 7-7 and 7-6. The high statistics scintillator shows a slightly less peaked distribution in the region of the Δ resonance than the model, which could be due to deficiencies in modeling the resonant-nonresonant interference. In lead, however, there is a strong suppression observed at low W_{exp} not seen in the other nuclei. This again could be a threshold effect not present in the nuclear modeling.

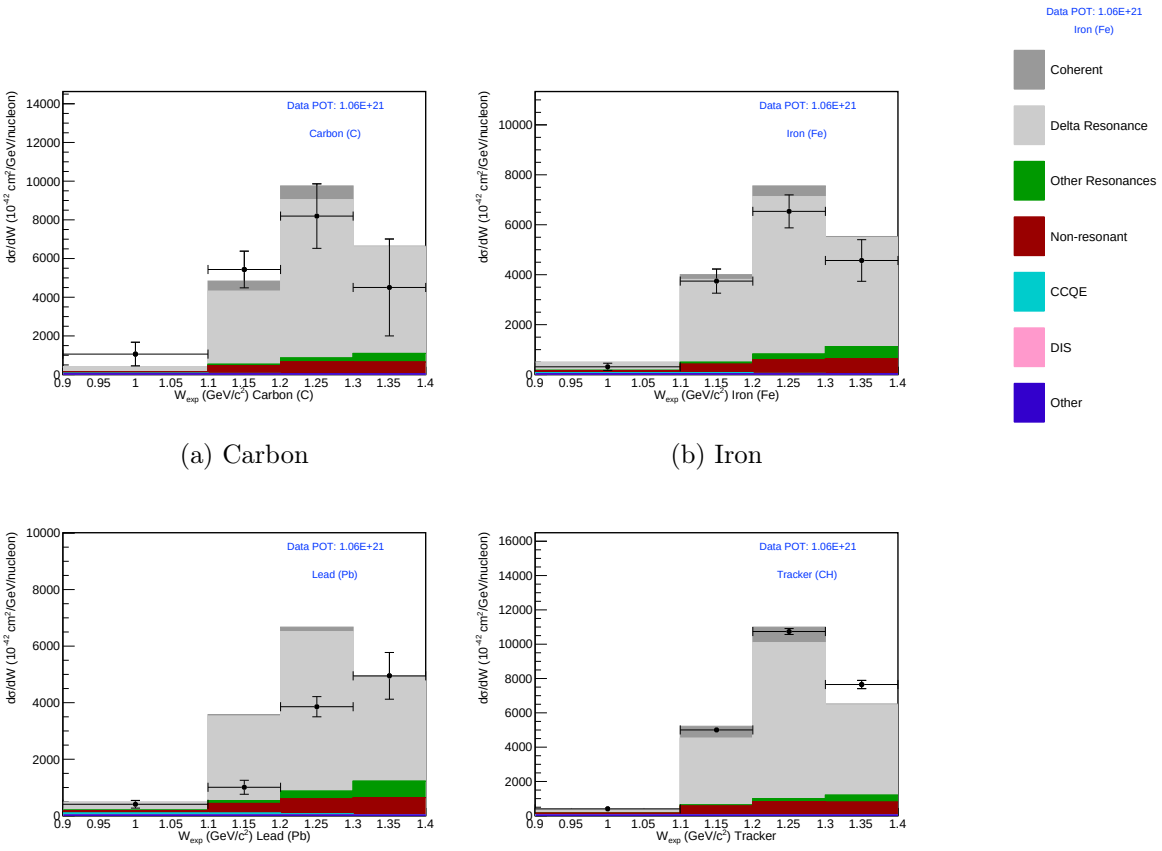


(a) Carbon (b) Iron

(c) Lead (d) Plastic

Figure 7-6: Area normalized W_{exp} differential cross sections on carbon, iron, lead, and scintillator

There is disagreement between the measured and predicted differential cross sections in the pion energy and angle. Figure 7-8 shows the area normalized cross section in T_π and θ_π. In all targets, the shape of the measured cross section prefers pions with lower kinetic energy compared to both predictions. This has been seen in prior measurements [60]. Backward going pions ($\theta_\pi > 120°$) agree with both predictions in iron and lead, while carbon and scintillator are underpredicted by both models. Pion energy and angle are likely strongly affected by FSI, as noted above, and the model



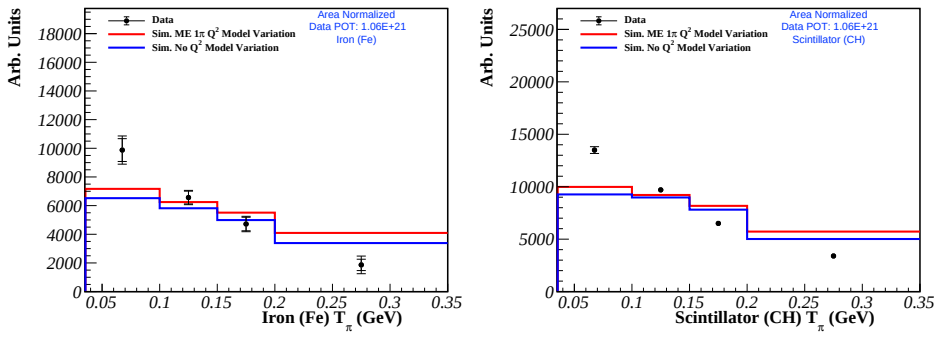
(a) Carbon (b) Iron

(c) Lead (d) Plastic

Figure 7-7: W_{exp} differential cross sections on scintillator, carbon, and lead

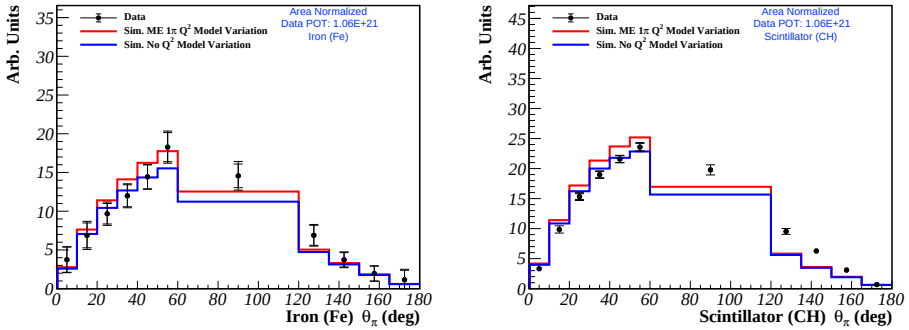
deficiencies seen here might have FSI as a least a part of their source.

Cross section ratios between lead and scintillator show large disagreements that are not present in the ratio to carbon or iron. Figure 7-9 shows that the Q^2 differential cross section in lead plateaus compared to the differential cross section in scintillator in between $Q^2 = 10^{-1}$ GeV^2 and 1 GeV^2. This phenomenon is not seen in the other targets. Also, the measured cross section ratio of lead to scintillator is smaller than either predicted cross section ratios. Figure 7-10 shows that lead has fewer low T_π



(a) Iron T_π
Area Normalized

(b) Scintillator T_π
Area Normalized



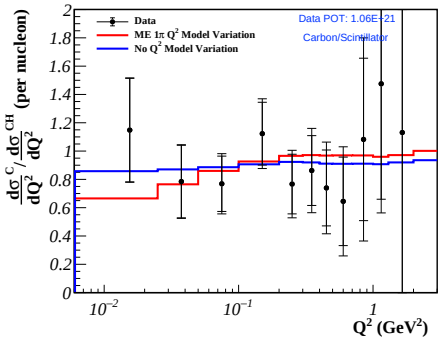
(c) Iron θ_π
Area Normalized

(d) Scintillator θ_π
Area Normalized

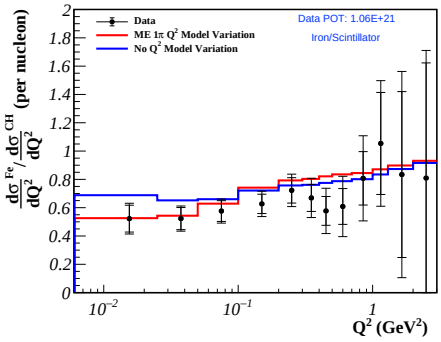
Figure 7-8: T_π and θ_π differential cross sections on iron and scintillator

pions compared to scintillator, and figure 7-11 shows that lead has fewer sideways and backwards going pions.

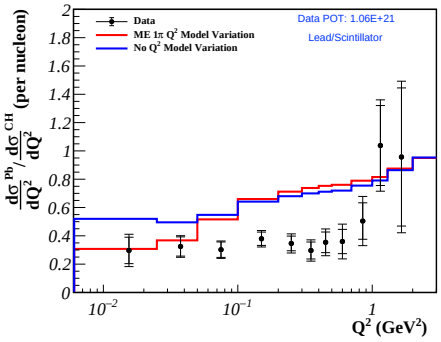
In summary, the predicted cross section favors the low Q^2 suppression model in all targets in θ_μ, $p_{\mu,T}$, and Q^2. Lead seems to be unique among the studied nuclei requiring large additional nuclear modifications to reproduce the data. The pion kinematics are not well predicted with or without the low Q^2 suppression and generally favor an enhancement of low energy pions and pions produced at large



(a) Carbon to scintillator



(b) Iron to scintillator

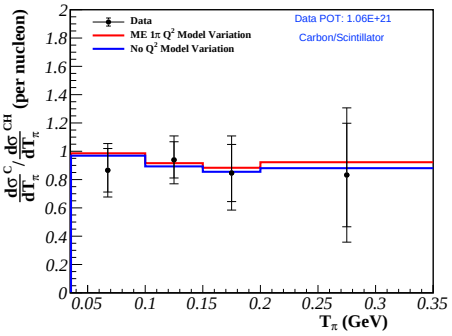


(c) Lead to scintillator

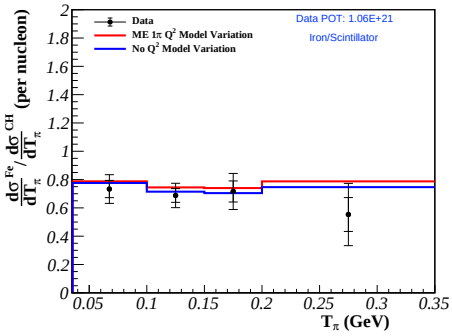
Figure 7-9: Q^2 cross section ratios

angles with respect to the neutrino beam.

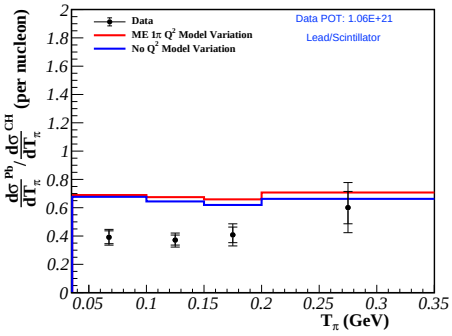
These measured cross sections provide guidance for modifications of simulations in order to produce more accurate predictions for production of π^+ on a wide range of nuclei. Incorporation of this data in future modelling will improve the ability of oscillation experiments to predict their neutrino energy resolution and biases. This also improves the modelling of rare processes where pions provide backgrounds to the leptons used to identify neutrino flavor.



(a) Carbon to scintillator

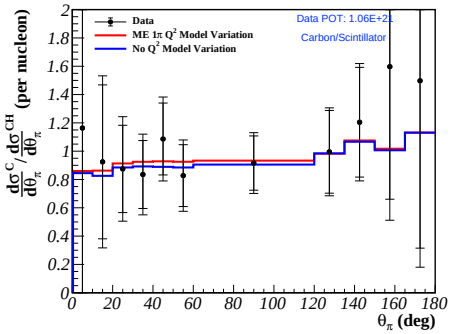


(b) Iron to scintillator

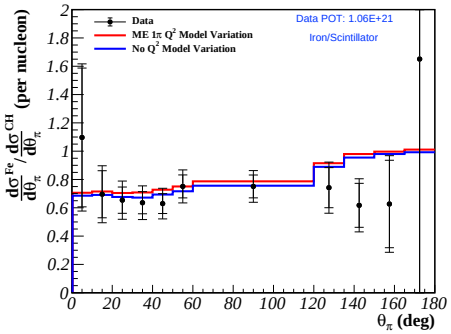


(c) Lead to scintillator

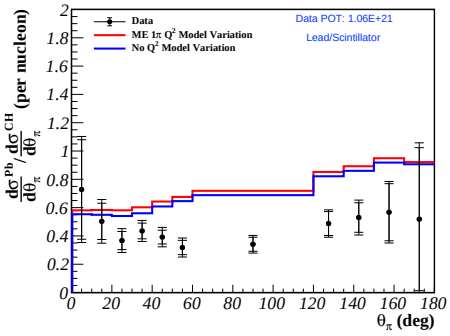
Figure 7-10: T_π cross section ratios



(a) Carbon to scintillator



(b) Iron to scintillator



(c) Lead to scintillator

Figure 7-11: θ_π cross section ratios

Bibliography

1. MissMJ & Cush. *Particle content of the standard model* https://en.wikipedia.org/wiki/File:Standard_Model_of_Elementary_Particles.svg (2021).
2. Group, P. D. *et al.* Review of Particle Physics. *Progress of Theoretical and Experimental Physics* **2020.** 083C01. ISSN: 2050-3911. eprint: https://academic.oup.com/ptep/article-pdf/2020/8/083C01/34673722/ptaa104.pdf. https://doi.org/10.1093/ptep/ptaa104 (Aug. 2020).
3. Lee, T. D. & Yang, C. N. Question of Parity Conservation in Weak Interactions. *Phys. Rev.* **104,** 254–258. https://link.aps.org/doi/10.1103/PhysRev.104.254 (1 Oct. 1956).
4. Wu, C. S. *et al.* Experimental Test of Parity Conservation in Beta Decay. *Phys. Rev.* **105,** 1413–1415. https://link.aps.org/doi/10.1103/PhysRev.105.1413 (4 Feb. 1957).
5. Ziino, G. New Electroweak Formulation Fundamentally Accounting for the Effect Known as "Maximal Parity-Violation". *International Journal of Theoretical Physics* **45,** 1993–2050 (Nov. 2006).
6. Christenson, J. H. *et al.* Evidence for the 2π Decay of the K_2^0 Meson. *Phys. Rev. Lett.* **13,** 138–140. https://link.aps.org/doi/10.1103/PhysRevLett.13.138 (4 July 1964).

7. Cleveland, B. T. *et al.* Measurement of the Solar Electron Neutrino Flux with the Homestake Chlorine Detector. *The Astrophysical Journal* **496,** 505–526. https://doi.org/10.1086/305343 (Mar. 1998).

8. Bellerive, A. *et al.* The Sudbury Neutrino Observatory. *Nucl. Phys. B* **908,** 30–51. arXiv: 1602.02469 [nucl-ex] (2016).

9. Fukuda, Y. *et al.* Evidence for oscillation of atmospheric neutrinos. *Phys. Rev. Lett.* **81,** 1562–1567. arXiv: hep-ex/9807003 (1998).

10. Pontecorvo, B. INVERSE β PROCESSES AND NONCONSERVATION OF LEPTON CHARGE. *Zhur. Eksptl'. i Teoret. Fiz.* **34.** https://www.osti.gov/biblio/4349231 (Jan. 1958).

11. Maki, Z. *et al.* Remarks on the Unified Model of Elementary Particles. *Progress of Theoretical Physics* **28,** 870–880. ISSN: 0033-068X. eprint: https://academic.oup.com/ptp/article-pdf/28/5/870/5258750/28-5-870.pdf. https://doi.org/10.1143/PTP.28.870 (Nov. 1962).

12. Giunti, C. & Kim, C. W. *Fundamentals of Neutrino Physics and Astrophysics* ISBN: 978-0-19-850871-7 (2007).

13. Cahn, R. N. *et al. White Paper: Measuring the Neutrino Mass Hierarchy* in *Community Summer Study 2013: Snowmass on the Mississippi* (July 2013). arXiv: 1307.5487 [hep-ex].

14. Abe, K. *et al.* Search for CP Violation in Neutrino and Antineutrino Oscillations by the T2K Experiment with 2.2×10^{21} Protons on Target. *Phys. Rev. Lett.* **121,** 171802. https://link.aps.org/doi/10.1103/PhysRevLett.121.171802 (17 Oct. 2018).

15. Acero, M. A. *et al.* First measurement of neutrino oscillation parameters using neutrinos and antineutrinos by NOvA. *Phys. Rev. Lett.* **123,** 151803. https://link.aps.org/doi/10.1103/PhysRevLett.123.151803 (15 Oct. 2019).

16. Acciarri, R. *et al.* Long-Baseline Neutrino Facility (LBNF) and Deep Underground Neutrino Experiment (DUNE): Conceptual Design Report, Volume 2: The Physics Program for DUNE at LBNF. arXiv: 1512.06148 [physics.ins-det] (Dec. 2015).

17. Bloom, E. D. & Gilman, F. J. Scaling, Duality, and the Behavior of Resonances in Inelastic electron-Proton Scattering. *Phys. Rev. Lett.* **25,** 1140 (1970).

18. Formaggio, J. A. & Zeller, G. P. From eV to EeV: Neutrino Cross Sections Across Energy Scales. *Rev. Mod. Phys.* **84,** 1307–1341. arXiv: 1305.7513 [hep-ex] (2012).

19. Llewellyn Smith, C. Neutrino reactions at accelerator energies. *Physics Reports* **3,** 261–379. ISSN: 0370-1573. https://www.sciencedirect.com/science/article/pii/0370157372900105 (1972).

20. Katori, T. *A Measurement of the Muon Neutrino Charged Current QuasiElastic A Test of the Lorentz Violation with the MiniBooNE Experiment* PhD thesis (Indiana University, Dec. 2008).

21. Bodek, A. *et al.* Vector and Axial Nucleon Form Factors:A Duality Constrained Parameterization. *Eur. Phys. J. C* **53,** 349–354. arXiv: 0708.1946 [hep-ex] (2008).

22. Kuzmin, K. S. *et al.* Quasielastic axial-vector mass from experiments on neutrino-nucleus scattering. *Eur. Phys. J.* **C54,** 517–538 (2008).

23. Meyer, A. S. *et al.* Deuterium target data for precision neutrino-nucleus cross sections. *Phys. Rev. D* **93,** 113015. arXiv: 1603.03048 [hep-ph] (2016).

24. Adler, S. Tests of the Conserved Vector Current and Paritally Conserved Axial-Vector Current Hypotheses in High-Energy Neutrino Reactions. *Phys. Rev.* **135(4B):B963** (1964).

25. Rein, D. & Sehgal, L. Neutrino-Excitation of Baryon Resonances and Single Pion Production. *Annals of Physics* **133(1),** 79–153 (1981).

26. Feynman, R. P. *et al.* Current Matrix Elements from a Relativistic Quark Model. *Phys. Rev. D* **3,** 2706–2732. https://link.aps.org/doi/10.1103/PhysRevD.3.2706 (11 June 1971).

27. Kuzmin, K. S. *et al.* Fine-tuning parameters to describe the total charged-current neutrino-nucleon cross section. *Phys. Atom. Nucl.* **69,** 1857–1871 (2006).

28. Kabirnezhad, M. Single pion production in neutrino-nucleon interactions. *Phys. Rev. D* **97,** 013002. https://link.aps.org/doi/10.1103/PhysRevD.97.013002 (1 Jan. 2018).

29. McFarland, K. S. *Neutrino Interactions* in *61st Scottish Universities Summer School in Physics: Neutrinos in Particle Physics, Astrophysics and Cosmology (SUSSP61)* (Apr. 2008), 65–90. arXiv: 0804.3899 [hep-ex].

30. Kretzer, S. & Reno, M. H. Tau neutrino deep inelastic charged current interactions. *Phys. Rev. D* **66,** 113007. arXiv: hep-ph/0208187 (2002).

31. Adler, S. L. Photoproduction, electroproduction and weak single pion production in the (3,3) resonance region. *Annals Phys.* **50,** 189–311 (1968).

32. Rein, D. & Sehgal, L. M. PCAC and the deficit of forward muons in π^+ production by neutrinos. *Physics Letters B* **657,** 207–209 (2007).

33. Rein, D. & Sehgal, L. M. Coherent π^0 Production in Neutrino Reactions. *Nucl. Phys. B* **223,** 29–44 (1983).

34. Martins, P. *Charged Current Coherent Pion Production in Neutrino Scattering* in *Prospects in Neutrino Physics* (Apr. 2016). arXiv: 1605.00095 [hep-ex].

35. Mislivec, A. *et al.* Measurement of total and differential cross sections of neutrino and antineutrino coherent $\pi^{\pm}$ production on carbon. *Phys. Rev. D* **97,** 032014. https://link.aps.org/doi/10.1103/PhysRevD.97.032014 (3 Feb. 2018).

36. Wolcott, J. *et al.* Evidence for Neutral-Current Diffractive π^0 Production from Hydrogen in Neutrino Interactions on Hydrocarbon. *Phys. Rev. Lett.* **117,** 111801. arXiv: 1604.01728 [hep-ex] (2016).

37. Aguilar-Arevalo, A. A. *et al.* First measurement of the muon neutrino charged current quasielastic double differential cross section. *Phys. Rev. D* **81,** 092005. https://link.aps.org/doi/10.1103/PhysRevD.81.092005 (9 May 2010).

38. Gil, A. *et al.* Many body approach to the inclusive (e, e-prime) reaction from the quasielastic to the Delta excitation region. *Nucl. Phys. A* **627,** 543–598. arXiv: nucl-th/9711009 (1997).

39. Smith, R. & Moniz, E. Neutrino Reactions on Nuclear Targets. *Nuclear Physics B* **43,** 605–622 (1972). Erratum: Nucl. Phys.B101,547(1975).

40. Bodek, A. & Ritchie, J. Fermi-Motion Effects in Deep-Inelastic Lepton Scattering from Nuclear Targets. *Phys. Rev. D* **23(5),** 1070 (1981).

41. Sobczyk, J. E. Intercomparison of lepton-nucleus scattering models in the quasielastic region. *Phys. Rev. C* **96,** 045501. https://link.aps.org/doi/10.1103/PhysRevC.96.045501 (4 Oct. 2017).

42. Bodek, A. *et al.* Effective Spectral Function for Quasielastic Scattering on Nuclei. *Eur. Phys. J. C* **74,** 3091. arXiv: 1405.0583 [hep-ph] (2014).

43. Benhar, O. *et al.* The Nucleon Spectral Function in Nuclear Matter. *Nucl. Phys. A* **505(2),** 267–299 (1989).

44. Egiyan, K. S. *et al.* Measurement of Two- and Three-Nucleon Short-Range Correlation Probabilities in Nuclei. *Phys. Rev. Lett.* **96,** 082501. https://link.aps.org/doi/10.1103/PhysRevLett.96.082501 (8 Mar. 2006).

45. Subedi, R. *et al.* Probing Cold Dense Nuclear Matter. *Science* **320,** 1476–1478. arXiv: 0908.1514 [nucl-ex] (2008).

46. Rodrigues, P. *et al.* Identification of nuclear effects in neutrino-carbon interactions at low three-momentum transfer. *Phys. Rev. Lett.* **116:071802.** Addendum: Phys. Rev. Lett.121,no.20,209902(2018) (2016).

47. Orden, J. W. V. & Donnelly, T. W. Mesonic processes in deep inelastic electron scattering from nuclei. *Annals Phys.* **131,** 451–493 (1981).

48. Gran, R. *et al.* Neutrino-nucleus quasi-elastic and 2p2h interactions up to 10 GeV. *Phys. Rev. D* **88(11):113007** (2013).

49. Nieves, J. *et al.* Inclusive charged-current neutrino-nucleus reactions. *Phys. Rev. C* **83:045501** (Apr. 2011).

50. Bodek, A. *et al.* Neutrino Quasielastic Scattering on Nuclear Targets. *The European Physical Journal C* **71(9),** 1–18 (2011).

51. Nieves, J. *et al.* Inclusive quasi-elastic neutrino reactions. *Phys. Rev. C* **70:055503.** Erratum: Phys. Rev.C72,019902(2005) (2004).

52. Alvarez-Ruso, L. *et al.* NuSTEC White Paper: Status and challenges of neutrino–nucleus scattering. *Progress in Particle and Nuclear Physics* **100,** 1–68. ISSN: 0146-6410. https://www.sciencedirect.com/science/article/pii/S0146641018300061 (2018).

53. Uehling, E. & Uhlenbeck, G. Transport Phenomena in Einstein-Bose and Fermi-Dirac Gases. *I. Phys. Rev.* **43,** 552–561 (1933).

54. Radecky, G. M. *et al.* Study of single-pion production by weak charged currents in low-energy νd interactions. *Phys. Rev. D* **25,** 1161–1173. https://link.aps.org/doi/10.1103/PhysRevD.25.1161 (5 Mar. 1982). Erratum: Phys. Rev.D26,3297(1982).

55. Kitagaki, T. *et al.* Charged-current exclusive pion production in neutrino-deuterium interactions. *Phys. Rev. D* **34,** 2554–2565. https://link.aps.org/doi/10.1103/PhysRevD.34.2554 (9 Nov. 1986).

56. Wilkinson, C. *et al.* Reanalysis of bubble chamber measurements of muon-neutrino induced single pion production. *Phys. Rev. D* **90,** 112017. https://link.aps.org/doi/10.1103/PhysRevD.90.112017 (11 Dec. 2014).

57. Abe, K. *et al.* First measurement of the muon neutrino charged current single pion production cross section on water with the T2K near detector. *Phys. Rev. D* **95,** 012010. https://link.aps.org/doi/10.1103/PhysRevD.95.012010 (1 Jan. 2017).

58. Abe, K. *et al.* Measurement of the muon neutrino charged-current single π^+ production on hydrocarbon using the T2K off-axis near detector ND280. *Phys. Rev. D* **101,** 012007. https://link.aps.org/doi/10.1103/PhysRevD.101.012007 (1 Jan. 2020).

59. Aguilar-Arevalo, A. A. *et al.* Measurement of Neutrino-Induced Charged-Current Charged Pion Production Cross Sections on Mineral Oil at $E_\nu \sim 1$ GeV. *Phys. Rev. D* **83,** 052007. arXiv: 1011.3572 [hep-ex] (2011).

60. Eberly, B. *et al.* Charged Pion Production in ν_μ Interactions on Hydrocarbon at E_ν= 4.0 GeV. *Phys. Rev. D* **92,** 092008. arXiv: 1406.6415 [hep-ex] (2015).

61. Sobczyk, J. T. & Żmuda, J. Investigation of recent weak single-pion production data. *Phys. Rev. C* **91,** 045501. arXiv: 1410.7788 [nucl-th] (2015).

62. McGivern, C. L. *et al.* Cross sections for ν_μ and $\overline{\nu}_\mu$ induced pion production on hydrocarbon in the few-GeV region using MINERvA. *Phys. Rev. D* **94,** 052005. https://link.aps.org/doi/10.1103/PhysRevD.94.052005 (5 Sept. 2016).

63. Altinok, O. *et al.* Measurement of ν_μ charged-current single π^0 production on hydrocarbon in the few-GeV region using MINERvA. *Phys. Rev. D* **96,** 072003. https://link.aps.org/doi/10.1103/PhysRevD.96.072003 (7 Oct. 2017).

64. Le, T. *et al.* Single Neutral Pion Production by Charged-Current $\bar{\nu}_\mu$ Interactions on Hydrocarbon at E_ν =3.6 GeV. *Phys. Lett. B* **749,** 130–136. arXiv: 1503.02107 [hep-ex] (2015).

65. Stowell, P. *et al.* NUISANCE: a neutrino cross-section generator tuning and comparison framework. *JINST* **12,** P01016. arXiv: 1612.07393 [hep-ex] (2017).

66. Stowell, P. *et al.* Tuning the genie pion production model with MINERvA data. *Physical Review D* **100** (Oct. 2019).

67. Casper, D. The Nuance neutrino physics simulation, and the future. *Nucl. Phys. B Proc. Suppl.* **112** (eds Morfin, J. G. *et al.*) 161–170. arXiv: hep-ph/0208030 (2002).

68. Adamson, P. *et al.* Study of quasielastic scattering using charged-current ν_μ-iron interactions in the MINOS near detector. *Phys. Rev. D* **91,** 012005. https://link.aps.org/doi/10.1103/PhysRevD.91.012005 (1 Jan. 2015).

69. Gallagher, H. The NEUGEN neutrino event generator. *Nucl. Phys. B Proc. Suppl.* **112** (eds Morfin, J. G. *et al.*) 188–194 (2002).

70. Andreopoulos, C. *et al. The GENIE Neutrino Monte Carlo Generator: Physics and User Manual* 2015.

71. Bercellie, A. *How Well are MINERvA* 1π *Results Modeled?* Presented at NuINT 2018 on Behalf of the MINERvA Collaboration, Gran Sasso Science Institute, Italy. Oct. 2018.

72. Crane, D. A. *et al.* Status Report: Technical Design of Neutrino Beams for the Main Injector (NuMI) (July 1995).

73. Adamson, P. *et al.* The NuMI Neutrino Beam. *Nucl. Instrum. Meth. A* **806,** 279–306. arXiv: 1507.06690 [physics.acc-ph] (2016).

74. Ainsworth, R. *et al.* High intensity operation using proton stacking in the Fermilab Recycler to deliver 700 kW of 120 GeV proton beam. *Phys. Rev. Accel. Beams* **23,** 121002. https://link.aps.org/doi/10.1103/PhysRevAccelBeams.23.121002 (12 Dec. 2020).

75. Convery, M. *et al.* Fermilab Accelerator Complex: Status and Improvement Plans. https://www.osti.gov/biblio/1556948 (Dec. 2018).

76. Finer, R. *Measurement of Medium Energy NuMI Flux Using the Low-ν and High-ν Methods at MINERvA* PhD thesis (U. Rochester, 2020).

77. Soplin, L. A. *Neutrino Flux Prediction for the NuMI Beamline* PhD thesis (William and Mary, 2016).

78. Loiacono, L. *Measurement of the Muon Neutrino Inclusive Charged Current Cross Section on Iron Using the MINOS Detector* PhD thesis (University of Texas at Austin, 2011).

79. Andersson, B. *et al.* A model for low-pT hadronic reactions with generalizations to hadron-nucleus and nucleus-nucleus collisions. *Nuclear Physics B* **281,** 289–309. ISSN: 0550-3213. https://www.sciencedirect.com/science/article/pii/0550321387902574 (1987).

80. Nilsson-Almqvist, B. & Stenlund, E. Interactions between hadrons and nuclei: The Lund Monte Carlo - FRITIOF version 1.6 -. *Computer Physics Communications* **43,** 387–397. ISSN: 0010-4655. https://www.sciencedirect.com/science/article/pii/0010465587900567 (1987).

81. Meth., N. I. Calculation of the capture of negative pions in light elements and comparison with experiments pertaining to cancer radiotherapy. **66,** 29–36 (1968).

82. Bertini, H. W. & Guthrie, M. P. News item results from medium-energy intranuclear-cascade calculation. *Nucl. Phys. A* **169,** 670–672 (1971).

83. Alt, C. *et al.* Inclusive production of charged pions in p+C collisions at 158-GeV/c beam momentum. *Eur. Phys. J. C* **49,** 897–917. arXiv: hep-ex/0606028 (2007).

84. Birattari, C. *et al.* Measurements and characterization of high energy neutron fields. *Nuclear Instruments and Methods in Physics Research Section A: Accelerators, Spectrometers, Detectors and Associated Equipment* **338,** 534–543. ISSN: 0168-9002. https://www.sciencedirect.com/science/article/pii/0168900294913382 (1994).

85. Aliaga, L. *et al.* Neutrino flux predictions for the NuMI beam. *Phys. Rev. D* **94,** 092005. https://link.aps.org/doi/10.1103/PhysRevD.94.092005 (9 Nov. 2016).

86. Tomalak, O. & Hill, R. J. Theory of elastic neutrino-electron scattering. *Phys. Rev. D* **101,** 033006. https://link.aps.org/doi/10.1103/PhysRevD.101.033006 (3 Feb. 2020).

87. Valencia, E. *et al.* Constraint of the MINERvA medium energy neutrino flux using neutrino-electron elastic scattering. *Phys. Rev. D* **100,** 092001. https://link.aps.org/doi/10.1103/PhysRevD.100.092001 (9 Nov. 2019).

88. Park, J. *et al.* Measurement of neutrino flux from neutrino-electron elastic scattering. *Phys. Rev. D* **93,** 112007. https://link.aps.org/doi/10.1103/PhysRevD.93.112007 (11 June 2016).

89. Ruterbories, D. *et al.* Constraining the NuMI neutrino flux using inverse muon decay reactions in MINERvA. *Phys. Rev. D* **104,** 092010. arXiv: 2107.01059 [hep-ex] (2021).

90. Wu, Q. *et al.* A precise measurement of the muon neutrino–nucleon inclusive charged current cross section off an isoscalar target in the energy range $2.5 < E_\nu < 40$ GeV by NOMAD. *Physics Letters B* **660,** 19–25. ISSN: 0370-2693. https://www.sciencedirect.com/science/article/pii/S0370269307015390 (2008).

91. Devan, J. *et al.* Measurements of the inclusive neutrino and antineutrino charged current cross sections in MINERvA using the low-ν flux method. *Phys. Rev. D* **94,** 112007. https://link.aps.org/doi/10.1103/PhysRevD.94.112007 (11 Dec. 2016).

92. Ren, L. *et al.* Measurement of the antineutrino to neutrino charged-current interaction cross section ratio in MINERvA. *Phys. Rev. D* **95,** 072009. https://link.aps.org/doi/10.1103/PhysRevD.95.072009 (7 Apr. 2017).

93. Kleykamp, J. *Flux Daisy Corrections* MINERvA Internal Document 29577-v2 (Aug. 2021).

94. Aliaga, L. *et al.* Design, Calibration, and Performance of the MINERvA Detector. *Nucl. Instrum. Meth. A* **743,** 130–159. arXiv: 1305.5199 [physics.ins-det] (2014).

95. Walton, T. *A Measurment of the Muon Neutrino Charged Current Quasielastic-like Cross Section on a Hydrocarbon Target and Final State Interaction Effects* PhD thesis (Hampton University, May 2014).

96. Messerly, B. *Single Charged Pion Production by Muon Neutrinos in the MINERvA Detector using the NuMI Beam* PhD thesis (University of Pittsburgh, 2019).

97. Eberly, B. M. *Characterization of Final State Interaction Strength in Plastic Scintillator by Muon-Neutrino Charged Current Charged Pion Production* PhD thesis (Pittsburgh U., 2014).

98. Kleykamp, J. *A-Scaling of CCQE-like Cross Sections at MINERvA* PhD thesis (University of Rochester, 2021).

99. Michael, D. G. *et al.* The Magnetized steel and scintillator calorimeters of the MINOS experiment. *Nucl. Instrum. Meth. A* **596,** 190–228. arXiv: 0805.3170 [physics.ins-det] (2008).

100. Ross, S. Peirce's criterion for the elimination of suspect experimental data. *J. Eng. Technol.* **20** (Sept. 2003).

101. Bradford, R. *et al.* A new parameterization of the nucleon elastic form factors. *Nuclear Physics B-Proceedings Supplements* **159,** 127–132 (2006).

102. Kuzmin, K. S. *et al.* Axial masses in quasielastic neutrino scattering and single-pion neutrinoproduction on nucleons and nuclei. *Acta Phys. Polon. B* **37** (eds Graczyk, K. M. & Sobczyk, J. T.) 2337–2348. arXiv: `hep-ph/0606184` (2006).

103. Rodrigues, P. *et al.* Constraining the GENIE model of neutrino-induced single pion production using reanalyzed bubble chamber data. *Eur. Phys. J.* **C76(8),** 474 (2016).

104. Bodek, A. & Yang, U. Higher Twist, ϵ_ω Scaling, and effective LO PDFs for Lepton Scattering in the Few GeV Region. *J. Phys. G* **29,** 1899–1906 (2003).

105. Yang, T. *et al.* A Hadronization Model for Few-GeV Neutrino Interactions. *The European Physical Journal C* **63(1),** 1–10 (2009).

106. Koba, Z. *et al.* Scaling of Multiplicity Distributions in High-Energy Hadron Collisions. *Nucl. Phys. B* **40,** 317–334 (1972).

107. Sjöstrand, T. *et al.* High-Energy-Physics Event Generation with PYTHIA 6.1. *Computer Physics Communications* **135(2),** 238–259 (2001).

108. D.Rein & L.M.Sehgal. Coherent π^0 Production in Neutrino Reactions. *Nucl.Phys. B* **223** (1983).

109. M.Martini *et al.* A Unified approach for nucleon knock-out, coherent and incoherent pion production in neutrino interactions with nuclei. *Phys. Rev. C* **80:065501** (2009).

110. Agostinelli, S. *et al.* GEANT4: A Simulation toolkit. *Nucl. Instrum. Meth. A* **506,** 250–303 (2003).

111. Kaidalov, A. B. The Quark-Gluon Structure of the Pomeron and the Rise of Inclusive Spectra at High-Energies. *Phys. Lett.* **116B,** 459–463 (1982).

112. Glauber, R. *High Energy Physics and Nuclear Structure* (Plenum Press, 1970).

113. Marshall, C. *Measurement of charged kaon production by neutrinos at MINERvA* PhD thesis (U. Rochester, 2016).

114. Birks, J. Scintillations from Organic Crystals: Specific Fluorescence and Relative Response to Different Radiations. *Proc. Phys. Soc.* **A64,** 874–877 (1951).

115. Gran, R. *Birks law parameter from minerva testbeam data* MINERvA Technical Note No. 037 (Fermilab, Nov. 2014).

116. *GEANT4: Physics Reference Manual* 11.0. Geant4 Collaboration (Dec. 2021).

117. Le, T. *Michel efficiency data/mc comparison* MINERvA Internal Document 25880-v1 (Feb. 2020).

118. Le, T. *Michel efficiency data/mc comparison* MINERvA Internal Document 27916-v1 (Sept. 2020).

119. Le, T. *New Michel systematics discussion* MINERvA Internal Document 25491-v1 (Jan. 2020).

120. Hylen, J. *Numi horn 1 mis-alignment* NuMI-X Internal Document 131-v1 (Nov. 2016).

121. Ghosh, A. *Minos matched muons tracking efficiency at medium energy: End game* MINERvA Internal Document 20760-v1 (Oct. 2018).

122. Elkins, M. *et al.* Neutron measurements from antineutrino hydrocarbon reactions. *Phys. Rev. D* **100** (Sept. 2019).

123. Gran, R. *Model Uncertainties for Valencia RPA Effect for MINERvA* 2017.

124. Tiator, L. *et al.* Electroproduction of nucleon resonances. *Eur. Phys. J. A* **19,** 55–60 (2004).

125. Ramirez, A. *ME Coherent Weight And Work Ahead* MINERvA Internal Document 27746-v2 (Aug. 2020).

126. Harewood, L. A. & Gran, R. *Elastic hadron-nucleus scattering in neutrino-nucleus reactions and transverse kinematics measurements* 2019. arXiv: 1906.10576 [hep-ex].

127. Perdue, G. *Minerva Reconstruction from 1,000 Feet* MINERvA Internal Document 10017-v2 (Oct. 2015).

128. Frühwirth, R. Application of Kalman filtering to track and vertex fitting. *Nucl.Instrum.Meth. A* **262,** 444–450 (1987).

129. Tice, B. *Measurement of Nuclear Dependence in Inclusive Charged Current Neutrino Scattering* PhD thesis (Rutgers, The State University of New Jersey, 2014).

130. Belkov, A. Implementation of the hough transform for 3d track reconstruction in drift chambers, arxiv:0201071[physic.comp–ph] (2002).

131. Früwirth, R. *et al. Adaptive vertex reconstruction* Technical Report CMS-NOTE-2008-033 (CERN, Geneva, 2008).

132. Mislivec, A. *Measurement of Charged Current Coherent Pion Production by Neutrinos on Carbon at MINERνA* PhD thesis (University of Rochester, 2017).

133. Bashyal, A. *et al.* Use of Neutrino Scattering Events with Low Hadronic Recoil to Inform Neutrino Flux and Detector Energy Scale. arXiv: 2104.05769 [hep-ex] (Apr. 2021).

134. Blum, A. *et al. Foundations of data science* https://www.cs.cornell.edu/jeh/book.pdf. 2015.

135. Tanabashi, M. *et al.* Review of particle physics. *Phys. Rev. D* **93:030001** (Aug. 2018).

136. Neyman, J. & Pearson, E. S. On the problem of the most efficient tests of statistical hypotheses. *Philosophical Transactions of the Royal Society of London. Series A, Containing Papers of a Mathematical or Physical Character* **231,** 289–337 (1933).

137. Norrick, A. *Calorimetry in MINERvA* MINERvA Technical Note (Dec. 2017).

138. D'Agostini, G. A multidimensional unfolding method based on Bayes' theorem. *Nuclear Instruments and Methods in Physics Research Section A: Accelerators, Spectrometers, Detectors and Associated Equipment* **362,** 487–498. ISSN: 0168-9002. https://www.sciencedirect.com/science/article/pii/016890029500274X (1995).

139. D'Agostini, G. *Improved iterative Bayesian unfolding* 2010. arXiv: 1010.0632 [physics.data-an].

140. Gran, R. *Pion calorimetry from MINERvA testbeam data* MINERvA Technical Note No. 045 (Feb. 2015).

141. Devan, J. *Test beam proton calorimetry note* MINERvA Technical Note No. 051 (July 2014).

Appendices

Appendix A

The MINERvA Collaboration

Active members of the MINERvA collaboration as of Janaury 2022.

Faiza Akbar, Mohammad Sajjad Athar, Huma Haider, Vaniya Ansari, Prameet Gaur, Sayeed Akhter
Aligarh Muslim University, Aligarh, India

Gian Caceres, Helio da Motta, Adrian Lozano, Gilson Silva
Centro Brasileiro de Pesquisas Físicas, Rio de Janeiro, Brazil

Omar Miranda, Luis Montano, Marco Torres
Centro de Investigación y de Estudios Avanzados del Instituto Politécnico Nacional, Mexico City, Mexico

Jennica LeClerc, Christian Nguyen, Heather Ray
University of Florida, Gainsville, Florida

Leo Bellantoni, Minerba Betancourt, Robert Hatcher, Deepika Jena, Jorge Morfin, Gabe Perdue *Fermilab, Batavia, Illinois*

Eric Christy
Hampton University, Hampton, Virginia

Alessandro Bravar
University of Geneva, Geneva, Switzerland

Diego Andrade, Jose Luis Bonilla, Julian Felix
Universidad de Guanajuato, Guanajuato, Mexico

Anežka Klustová, Abbey Waldron
Imperial College London, London, UK

Nishat Fiza, Satyajit Jena
Indian Institute of Science Education and Research, Mohali, India

Emily Maher
Massachusetts College of Liberal Arts, North Adams, Massachusetts

Laura Fields
University of Notre Dame, Notre Dame, IN
Amit Bashyal, Mateus Carneiro, Sean Gilligan, Maggie Greenwood, Heidi Schellman, Noah Vaughan
Oregon State University, Corvallis, Oregon

Nathaniel Tagg
Otterbein College, Westerville, Ohio

Komninos-John Plows, David Wark *University of Oxford, Oxford, United Kingdom*

Steve Dytman, Ben Messerly, Donna Naples, Vittorio Paolone, Hang Su
University of Pittsburgh, Pittsburgh, Pennsylvania

Marvin Ascencio Sosa, Alberto Gago
Pontificia Universidad Catolica del Peru, Lima, Peru

Arie Bodek, Howard Budd, Tejin Cai, Gonzalo Diaz, Rob Fine, Sarah Henry, Jeffrey Kleykamp, Steve Manly, Kevin McFarland, Aaron McGowan, Miriam Moore, Andrew Olivier, Daniel Ruterbories, Mehreen Sultana, Clarence Wret
University of Rochester, Rochester, New York

Ronald Ransome
Rutgers University, New Brunswick, New Jersey

Hugh Gallagher, Trung Le, Tony Mann, Vladyslav Syrotenko
Tufts University, Medford, Massachusetts

Rik Gran, Emily Haase, Kyle Jacobsen, Ishmam Mahbub, Brandon Reed, Asit Srivastava
University of Minnesota at Duluth, Duluth, Minnesota

Ivancovish Julian Huancco Mamani, Carlos Solano Salinas
Universidad Nacional de Ingeniería, Lima, Peru

Jorge Chaves, Keith Kroma-Wiley, David Last, Christopher Mauger, Alejandro Ramirez Delgado
University of Pennsylvania, Philadelphia, Pennsylvania

William Brooks, Anushree Ghosh, Jonathan Miller, Barbara Yaeggy
Universidad Técnica Federico Santa María, Valparaiso, Chile

Steve Boyd, Xianguo Lu
University of Warwick

Jan Sobczyk
University of Wroclaw

Zubair Ahmad Dar, Amy Filkins, Michael Kordosky, Oscar E Moreno, Jeffrey Nelson, Edgar Valencia, Luis Zazueta
College of William and Mary, Williamsburg, Virginia

Deborah Harris, Maria Mehmood
University of York, Toronto, Ontario, Canada

Appendix B

Purity Efficiency Tables

Carbon (C) Signal Purity and Efficiency, Playlists ME1A-P

Cuts	Data Events	MC Events	Signal	Purity	Efficiency	Cut Efficiency
All Events	637137720	5717521.81	150079.89	100.00	100.00	2.62
Has Int Vertex	586389	6565468.31	125470.73	1.91	83.60	83.60
In Fiducial Volume	586389	6565468.31	125470.73	1.91	83.60	100.00
N Hadron Tracks > 0	344066	4289007.43	76007.09	1.77	50.64	60.58
Refit In Fid Vol	346201	4286778.05	72107.15	1.68	48.05	94.87
Has 1 Muon Track	161673	2047807.55	63680.48	3.11	42.43	88.31
Has > 0 Hadron Track	135161	1680835.90	59089.82	3.52	39.37	92.79
Correct Target	77786	962101.24	49883.70	5.18	33.24	84.42
Broken Muon Cut	73837	953297.45	49811.66	5.23	33.19	99.86
Minos Matched Muon	46290	613261.07	40902.10	6.67	27.25	82.11
Hadron Tracks Contained	33473	436815.23	30210.42	6.92	20.13	73.86
≥ 1 Track w/ Michel Match	1741	23495.66	3987.75	16.97	2.66	13.20
≥ 1 Track w/ LLR Score> 0	1455	19487.81	3523.64	18.08	2.35	88.36
1 Track w/ End Node Energy Cut	739	8796.16	2447.96	27.83	1.63	69.47
Reco $W_{exp} < 1.4$ GeV	327	3643.34	1835.36	50.38	1.22	74.98
Only 1 Track w/ LLR>0	308	3438.74	1779.26	51.74	1.19	96.94
N Isolated Prongs < 2	295	3325.48	1770.95	53.25	1.18	99.53

Table B.1: Purity, Efficiency, and Cut Efficiency of Signal Events on Carbon

Water (H_2O) Signal Purity and Efficiency, Playlists ME1A-P

Cuts	Data Events	MC Events	Signal	Purity	Efficiency	Cut Efficiency
All Events	637137720	4619960.48	74145.32	100.00	100.00	1.60
Has Int Vertex	180602	1766918.54	24624.11	1.39	33.21	33.21
In Fiducial Volume	180602	1766918.54	24624.11	1.39	33.21	100.00
N Hadron Tracks > 0	180602	1766918.54	24624.11	1.39	33.21	100.00
Refit In Fid Vol	180602	1766918.54	24624.11	1.39	33.21	100.00
Has 1 Muon Track	84841	876805.96	21267.87	2.43	28.68	86.37
Has > 0 Hadron Track	72121	746594.28	20097.11	2.69	27.11	94.50
Correct Target	72121	746594.28	20097.11	2.69	27.11	100.00
Broken Muon Cut	65235	727967.52	19796.27	2.72	26.70	98.50
Minos Matched Muon	40092	463790.86	16200.12	3.49	21.85	81.83
Hadron Tracks Contained	31043	356625.79	12816.94	3.59	17.29	79.12
≥ 1 Track w/ Michel Match	1444	17201.64	1896.15	11.02	2.56	14.79
≥ 1 Track w/ LLR Score> 0	1215	14041.52	1743.56	12.42	2.35	91.95
1 Track w/ End Node Energy Cut	810	9046.21	1539.46	17.02	2.08	88.29
Reco $W_{exp} < 1.4$ GeV	336	3517.07	1170.99	33.29	1.58	76.07
Only 1 Track w/ LLR>0	306	3337.00	1141.04	34.19	1.54	97.44
N Isolated Prongs < 2	291	3141.24	1126.57	35.86	1.52	98.73

Table B.2: Purity, Efficiency, and Cut Efficiency of Signal Events on Water

Iron (Fe) Signal Purity and Efficiency, Playlists ME1A-P

Cuts	Data Events	MC Events	Signal	Purity	Efficiency	Cut Efficiency
All Events	637137720	32477227.98	702457.34	100.00	100.00	2.16
Has Int Vertex	3151708	31514155.42	607856.92	1.93	86.53	86.53
In Fiducial Volume	3151708	31514155.42	607856.92	1.93	86.53	100.00
N Hadron Tracks > 0	1794835	20504651.91	337418.61	1.65	48.03	55.51
Refit In Fid Vol	1703193	19596362.55	314102.01	1.60	44.71	93.09
Has 1 Muon Track	710704	8305281.03	244295.32	2.94	34.78	77.78
Has > 0 Hadron Track	597493	6795197.50	229676.29	3.38	32.70	94.02
Correct Target	384625	4369308.18	203929.55	4.67	29.03	88.79
Broken Muon Cut	335258	4191349.43	201898.61	4.82	28.74	99.00
Minos Matched Muon	197171	2581874.72	159125.44	6.16	22.65	78.81
Hadron Tracks Contained	145644	1888989.29	126738.47	6.71	18.04	79.65
≥ 1 Track w/ Michel Match	6458	89695.94	17309.91	19.30	2.46	13.66
≥ 1 Track w/ LLR Score> 0	5475	74832.74	15574.94	20.81	2.22	89.98
1 Track w/ End Node Energy Cut	3367	43417.96	12337.05	28.41	1.76	79.21
Reco $W_{exp} < 1.4$ GeV	1543	19582.69	9495.67	48.49	1.35	76.97
Only 1 Track w/ LLR>0	1435	18381.68	9214.02	50.13	1.31	97.03
N Isolated Prongs < 2	1403	17863.93	9174.56	51.36	1.31	99.57

Table B.3: Purity, Efficiency, and Cut Efficiency of Signal Events on Iron

Lead (Pb) Signal Purity and Efficiency, Playlists ME1A-P

Cuts	Data Events	MC Events	Signal	Purity	Efficiency	Cut Efficiency
All Events	637137720	35020084.86	659854.06	100.00	100.00	1.88
Has Int Vertex	3049651	33595014.96	607957.78	1.81	92.14	92.14
In Fiducial Volume	3049651	33595014.96	607957.78	1.81	92.14	100.00
N Hadron Tracks > 0	1636949	20472182.02	310859.31	1.52	47.11	51.13
Refit In Fid Vol	1563626	19198005.20	287288.66	1.50	43.54	92.42
Has 1 Muon Track	670044	8636193.56	235681.04	2.73	35.72	82.04
Has > 0 Hadron Track	554949	6913497.26	219236.62	3.17	33.23	93.02
Correct Target	322192	4035999.42	185368.79	4.59	28.09	84.55
Broken Muon Cut	290546	3900864.06	183564.84	4.71	27.82	99.03
Minos Matched Muon	169722	2417686.85	144873.58	5.99	21.96	78.92
Hadron Tracks Contained	119152	1663219.52	109126.73	6.56	16.54	75.33
≥ 1 Track w/ Michel Match	5534	93610.08	17753.04	18.96	2.69	16.27
≥ 1 Track w/ LLR Score> 0	4644	78058.04	15972.27	20.46	2.42	89.97
1 Track w/ End Node Energy Cut	2648	44234.55	12374.77	27.98	1.88	77.48
Reco $W_{exp} < 1.4$ GeV	1130	19924.71	9466.94	47.51	1.43	76.50
Only 1 Track w/ LLR>0	1064	18935.45	9267.81	48.94	1.40	97.90
N Isolated Prongs < 2	1033	18313.71	9211.25	50.30	1.40	99.39

Table B.4: Purity, Efficiency, and Cut Efficiency of Signal Events on Lead

Tracker Signal Purity and Efficiency, Playlists ME1A-P

Cuts	Data Events	MC Events	Signal	Purity	Efficiency	Cut Efficiency
All Events	637137720	82513177.16	2095472.68	100.00	100.00	2.54
Has Int Vertex	15726438	79239080.43	1916295.60	2.42	91.45	91.45
In Fiducial Volume	15726438	79239080.43	1916295.60	2.42	91.45	100.00
N Hadron Tracks > 0	10372996	60029407.06	1463984.54	2.44	69.86	76.40
Refit In Fid Vol	10386422	60038617.27	1461054.25	2.43	69.72	99.80
Has 1 Muon Track	6017162	35020414.23	1377894.37	3.93	65.76	94.31
Has > 0 Hadron Track	5016774	28556277.36	1289927.05	4.52	61.56	93.62
Correct Target	3975515	23337036.42	1268409.09	5.44	60.53	98.33
Broken Muon Cut	3873464	22850755.86	1251718.93	5.48	59.73	98.68
Minos Matched Muon	2536714	15024866.67	1102743.97	7.34	52.63	88.10
Hadron Tracks Contained	1859922	10953993.36	879017.65	8.02	41.95	79.71
≥ 1 Track w/ Michel Match	134068	780677.58	176845.32	22.65	8.44	20.12
≥ 1 Track w/ LLR Score> 0	111760	634488.30	155671.96	24.54	7.43	88.03
1 Track w/ End Node Energy Cut	83750	460254.02	136537.87	29.67	6.52	87.71
Reco $W_{exp} < 1.4$ GeV	38355	184137.99	113802.13	61.80	5.43	83.35
Only 1 Track w/ LLR>0	34420	165648.84	107625.30	64.97	5.14	94.57
N Isolated Prongs < 2	33231	157757.18	106819.13	67.71	5.10	99.25

Table B.5: Purity, Efficiency, and Cut Efficiency of Signal Events on Tracker

Appendix C

Tables of measured cross sections, uncertainties, and covariance matrices

Table C.1: Measured cross section in p_μ on scintillator, in units of 10^{-42} cm^2/GeV/c/nucleon, and the absolute and fractional cross section uncertainties

Bin edges (GeV/c)	σ	Abs. Unc.	Frac. Stat. Unc.	Frac. Sys. Unc.	Frac. Flux Unc.
1.5-3.0	194.28	14.85	0.031	0.070	0.036
3.0-4.0	334.78	25.48	0.022	0.073	0.037
4.0-5.0	488.44	36.55	0.018	0.073	0.037
5.0-6.0	515.50	38.66	0.017	0.073	0.037
6.0-7.0	388.97	29.54	0.018	0.074	0.036
7.0-8.5	262.49	20.95	0.022	0.077	0.035
8.5-10.0	79.43	7.20	0.039	0.082	0.033
10.0-20.0	93.29	8.69	0.046	0.081	0.035

Table C.2: Statistical covariance matrix of measured cross section in p_μ on scintillator, in units of 10^{-84} (cm^2/GeV/c/nucleon)^2

Bin edges (GeV/c)	1.5-3.0	3.0-4.0	4.0-5.0	5.0-6.0	6.0-7.0	7.0-8.5	8.5-10.0	10.0-20.0
1.5-3.0	36.174	5.847	1.318	0.468	0.236	0.102	0.042	0.037
3.0-4.0	5.847	56.212	12.544	2.983	0.886	0.331	0.060	0.049
4.0-5.0	1.318	12.544	81.578	18.498	4.131	1.067	0.204	0.162
5.0-6.0	0.468	2.983	18.498	76.057	17.407	4.330	0.584	0.442
6.0-7.0	0.236	0.886	4.131	17.407	51.305	12.409	1.648	0.610
7.0-8.5	0.102	0.331	1.067	4.330	12.409	33.280	4.272	1.513
8.5-10.0	0.042	0.060	0.204	0.584	1.648	4.272	9.677	2.202
10.0-20.0	0.037	0.049	0.162	0.442	0.610	1.513	2.202	18.444

Table C.3: Systematic covariance matrix of measured cross section in p_μ on scintillator, in units of 10^{-84} (cm^2/GeV/c/nucleon)^2

Bin edges (GeV/c)	1.5-3.0	3.0-4.0	4.0-5.0	5.0-6.0	6.0-7.0	7.0-8.5	8.5-10.0	10.0-20.0
1.5-3.0	184.203	321.090	455.217	478.278	345.440	230.226	71.922	79.382
3.0-4.0	321.090	593.107	844.605	895.130	650.317	434.789	140.316	152.458
4.0-5.0	455.217	844.605	1254.177	1322.195	981.469	661.024	209.541	235.365
5.0-6.0	478.278	895.130	1322.195	1418.526	1059.633	720.436	226.630	254.347
6.0-7.0	345.440	650.317	981.469	1059.633	821.546	564.137	175.994	199.692
7.0-8.5	230.226	434.789	661.024	720.436	564.137	405.715	124.007	145.036
8.5-10.0	71.922	140.316	209.541	226.630	175.994	124.007	42.167	45.676
10.0-20.0	79.382	152.458	235.365	254.347	199.692	145.036	45.676	57.033

Table C.4: Measured cross section in θ_μ on scintillator, in units of 10^{-42} cm^2/degree/nucleon, and the absolute and fractional cross section uncertainties

Bin edges (degree)	σ	Abs. Unc.	Frac. Stat. Unc.	Frac. Sys. Unc.	Frac. Flux Unc.
0-2	178.11	12.06	0.024	0.063	0.033
2-3	220.64	15.24	0.024	0.065	0.035
3-4	272.17	18.40	0.025	0.063	0.035
4-5	277.18	21.57	0.028	0.073	0.036
5-6	260.67	25.13	0.031	0.091	0.038
6-8	462.13	41.65	0.027	0.086	0.038
8-10	332.00	33.28	0.038	0.093	0.041
10-13	338.61	41.53	0.047	0.113	0.046

Table C.5: Statistical covariance matrix of measured cross section in θ_μ on scintillator, in units of 10^{-84} (cm^2/degree/nucleon)^2

Bin edges (degree)	0-2	2-3	3-4	4-5	5-6	6-8	8-10	10-13
0-2	17.648	-0.525	-0.912	-0.067	-0.002	-0.008	-0.009	-0.009
2-3	-0.525	29.215	0.472	-1.545	-0.168	-0.028	-0.030	-0.038
3-4	-0.912	0.472	47.298	1.130	-2.453	-0.253	0.004	-0.010
4-5	-0.067	-1.545	1.130	59.250	2.482	-3.397	-0.122	0.024
5-6	-0.002	-0.168	-2.453	2.482	67.370	-0.289	-2.147	-0.063
6-8	-0.008	-0.028	-0.253	-3.397	-0.289	157.558	-3.483	-3.597
8-10	-0.009	-0.030	0.004	-0.122	-2.147	-3.483	158.129	-7.152
10-13	-0.009	-0.038	-0.010	0.024	-0.063	-3.597	-7.152	256.892

Table C.6: Systematic covariance matrix of measured cross section in θ_μ on scintillator, in units of 10^{-84} (cm^2/degree/nucleon)^2

Bin edges (degree)	0-2	2-3	3-4	4-5	5-6	6-8	8-10	10-13
0-2	127.679	155.256	167.110	156.980	151.471	235.702	174.167	189.058
2-3	155.256	203.031	229.242	235.090	237.767	366.550	270.846	305.258
3-4	167.110	229.242	291.104	324.105	347.087	564.083	423.542	490.527
4-5	156.980	235.090	324.105	406.106	460.384	743.319	562.420	661.942
5-6	151.471	237.767	347.087	460.384	563.960	898.878	672.924	811.321
6-8	235.702	366.550	564.083	743.319	898.878	1576.906	1181.336	1443.950
8-10	174.167	270.846	423.542	562.420	672.924	1181.336	949.142	1151.078
10-13	189.058	305.258	490.527	661.942	811.321	1443.950	1151.078	1467.905

Table C.7: Measured cross section in $p_{\mu,||}$ on scintillator, in units of 10^{-42} cm^2/GeV/c/nucleon, and the absolute and fractional cross section uncertainties

Bin edges (GeV/c)	σ	Abs. Unc.	Frac. Stat. Unc.	Frac. Sys. Unc.	Frac. Flux Unc.
1.5-3.0	201.56	15.45	0.030	0.070	0.037
3.0-4.0	343.03	25.98	0.022	0.072	0.037
4.0-5.0	490.59	36.93	0.018	0.073	0.037
5.0-6.0	512.38	38.26	0.017	0.073	0.037
6.0-7.0	382.11	28.98	0.018	0.074	0.036
7.0-8.5	256.60	20.58	0.022	0.077	0.035
8.5-10.0	77.99	7.01	0.039	0.081	0.033
10.0-20.0	92.61	8.57	0.046	0.080	0.035

Table C.8: Statistical covariance matrix of measured cross section in $p_{\mu,||}$ on scintillator, in units of 10^{-84} (cm^2/GeV/c/nucleon)^2

Bin edges (GeV/c)	1.5-3.0	3.0-4.0	4.0-5.0	5.0-6.0	6.0-7.0	7.0-8.5	8.5-10.0	10.0-20.0
1.5-3.0	37.526	6.178	1.390	0.537	0.243	0.097	0.038	0.037
3.0-4.0	6.178	58.473	12.938	3.099	0.863	0.331	0.059	0.049
4.0-5.0	1.390	12.938	81.888	18.964	4.043	1.036	0.198	0.164
5.0-6.0	0.537	3.099	18.964	75.405	16.899	4.204	0.562	0.439
6.0-7.0	0.243	0.863	4.043	16.899	49.835	12.138	1.634	0.614
7.0-8.5	0.097	0.331	1.036	4.204	12.138	32.023	4.093	1.474
8.5-10.0	0.038	0.059	0.198	0.562	1.634	4.093	9.448	2.118
10.0-20.0	0.037	0.049	0.164	0.439	0.614	1.474	2.118	18.205

Table C.9: Systematic covariance matrix of measured cross section in $p_{\mu,||}$ on scintillator, in units of 10^{-84} (cm^2/GeV/c/nucleon)^2

Bin edges (GeV/c)	1.5-3.0	3.0-4.0	4.0-5.0	5.0-6.0	6.0-7.0	7.0-8.5	8.5-10.0	10.0-20.0
1.5-3.0	201.090	343.236	487.458	504.026	360.387	242.692	75.028	84.415
3.0-4.0	343.236	616.436	866.572	900.451	646.544	432.400	138.393	152.136
4.0-5.0	487.458	866.572	1282.231	1322.556	973.163	659.200	206.277	235.984
5.0-6.0	504.026	900.451	1322.556	1388.462	1025.014	699.085	217.549	247.276
6.0-7.0	360.387	646.544	973.163	1025.014	789.865	544.359	168.289	193.340
7.0-8.5	242.692	432.400	659.200	699.085	544.359	391.657	119.012	140.220
8.5-10.0	75.028	138.393	206.277	217.549	168.289	119.012	39.756	43.791
10.0-20.0	84.415	152.136	235.984	247.276	193.340	140.220	43.791	55.228

Table C.10: Measured cross section in $p_{\mu,T}$ on scintillator, in units of 10^{-42} cm^2/GeV/c/nucleon, and the absolute and fractional cross section uncertainties

Bin edges (GeV/c)	σ	Abs. Unc.	Frac. Stat. Unc.	Frac. Sys. Unc.	Frac. Flux Unc.
0.00-0.15	91.09	6.01	0.031	0.058	0.032
0.15-0.30	318.98	21.24	0.019	0.064	0.033
0.30-0.45	509.33	35.15	0.019	0.066	0.035
0.45-0.60	530.77	46.10	0.022	0.084	0.036
0.60-0.75	405.86	41.71	0.028	0.099	0.037
0.75-0.90	246.68	29.95	0.042	0.114	0.041
0.90-1.25	192.97	33.96	0.066	0.163	0.045
1.25-2.50	24.56	7.39	0.222	0.203	0.045

Table C.11: Statistical covariance matrix of measured cross section in $p_{\mu,T}$ on scintillator, in units of 10^{-84} $(\mathrm{cm}^2/\mathrm{GeV/c/nucleon})^2$

Bin edges (GeV/c)	0.00-0.15	0.15-0.30	0.30-0.45	0.45-0.60	0.60-0.75	0.75-0.90	0.90-1.25	1.25-2.50
0.00-0.15	8.039	-0.106	-0.956	-0.162	-0.010	-0.017	-0.020	-0.005
0.15-0.30	-0.106	37.091	0.617	-3.299	-0.842	-0.195	-0.102	-0.010
0.30-0.45	-0.956	0.617	94.729	5.907	-6.954	-2.068	-0.938	-0.170
0.45-0.60	-0.162	-3.299	5.907	133.985	15.869	-7.738	-4.143	-0.509
0.60-0.75	-0.010	-0.842	-6.954	15.869	132.030	23.024	-7.597	-0.527
0.75-0.90	-0.017	-0.195	-2.068	-7.738	23.024	104.962	24.620	-1.705
0.90-1.25	-0.020	-0.102	-0.938	-4.143	-7.597	24.620	162.258	15.147
1.25-2.50	-0.005	-0.010	-0.170	-0.509	-0.527	-1.705	15.147	29.735

Table C.12: Systematic covariance matrix of measured cross section in $p_{\mu,T}$ on scintillator, in units of 10^{-84} $(\mathrm{cm}^2/\mathrm{GeV/c/nucleon})^2$

Bin edges (GeV/c)	0.00-0.15	0.15-0.30	0.30-0.45	0.45-0.60	0.60-0.75	0.75-0.90	0.90-1.25	1.25-2.50
0.00-0.15	28.073	103.041	135.903	129.856	93.514	62.009	49.829	6.494
0.15-0.30	103.041	414.163	547.218	531.675	372.228	237.963	185.421	23.489
0.30-0.45	135.903	547.218	1141.014	1417.912	1156.131	735.973	579.222	76.851
0.45-0.60	129.856	531.675	1417.912	1991.179	1732.826	1133.406	945.320	126.055
0.60-0.75	93.514	372.228	1156.131	1732.826	1607.628	1081.678	975.935	133.775
0.75-0.90	62.009	237.963	735.973	1133.406	1081.678	792.081	787.712	109.140
0.90-1.25	49.829	185.421	579.222	945.320	975.935	787.712	990.769	147.438
1.25-2.50	6.494	23.489	76.851	126.055	133.775	109.140	147.438	24.907

Table C.13: Measured cross section in Q^2 on scintillator, in units of 10^{-42} cm^2/GeV^2/nucleon, and the absolute and fractional cross section uncertainties

Bin edges (GeV^2)	σ	Abs. Unc.	Frac. Stat. Unc.	Frac. Sys. Unc.	Frac. Flux Unc.
0.000-0.025	90.26	5.90	0.031	0.058	0.032
0.025-0.050	104.81	6.90	0.028	0.060	0.033
0.050-0.100	219.20	14.79	0.023	0.064	0.034
0.100-0.200	402.76	27.74	0.021	0.066	0.035
0.200-0.300	344.86	28.47	0.024	0.079	0.036
0.300-0.400	272.35	24.73	0.028	0.086	0.036
0.400-0.500	208.85	21.43	0.033	0.097	0.037
0.500-0.700	279.50	30.61	0.035	0.104	0.038
0.700-1.000	212.70	26.87	0.047	0.117	0.041
1.000-1.300	98.25	16.28	0.072	0.149	0.044
1.300-2.000	62.76	16.95	0.138	0.232	0.051
2.000-3.000	20.81	6.99	0.280	0.186	0.039

Table C.14: Statistical covariance matrix of measured cross section in Q^2 on scintillator, in units of 10^{-84} $(\mathrm{cm}^2/\mathrm{GeV}^2/\mathrm{nucleon})^2$

Bin edges (GeV^2)	0.000-0.025	0.025-0.050	0.050-0.100	0.100-0.200	0.200-0.300	0.300-0.400	0.400-0.500	0.500-0.700	0.700-1.000	1.000-1.300	1.300-2.000	2.000-3.000
0.000-0.025	7.587	0.517	-0.877	-0.395	-0.035	-0.008	-0.004	-0.002	-0.014	-0.006	-0.009	-0.004
0.025-0.050	0.517	8.480	2.167	-1.361	-0.493	-0.083	-0.022	-0.025	-0.032	-0.013	-0.007	-0.001
0.050-0.100	-0.877	2.167	24.723	3.149	-2.391	-0.907	-0.309	-0.162	-0.022	-0.043	-0.046	-0.006
0.100-0.200	-0.395	-1.361	3.149	68.658	7.957	-3.727	-2.455	-1.517	-0.592	-0.178	-0.165	-0.048
0.200-0.300	-0.035	-0.493	-2.391	7.957	67.563	14.197	-1.338	-4.313	-1.698	-0.576	-0.199	-0.168
0.300-0.400	-0.008	-0.083	-0.907	-3.727	14.197	58.628	17.441	-0.490	-3.872	-1.378	-0.501	-0.248
0.400-0.500	-0.004	-0.022	-0.309	-2.455	-1.338	17.441	48.039	17.862	-2.302	-1.672	-0.806	0.047
0.500-0.700	-0.002	-0.025	-0.162	-1.517	-4.313	-0.490	17.862	93.375	21.329	-2.968	-2.906	-0.390
0.700-1.000	-0.014	-0.032	-0.022	-0.592	-1.698	-3.872	-2.302	21.329	97.891	21.646	0.710	-1.355
1.000-1.300	-0.006	-0.013	-0.043	-0.178	-0.576	-1.378	-1.672	-2.968	21.646	50.389	19.209	0.918
1.300-2.000	-0.009	-0.007	-0.046	-0.165	-0.199	-0.501	-0.806	-2.906	0.710	19.209	74.572	7.665
2.000-3.000	-0.004	-0.001	-0.006	-0.048	-0.168	-0.248	0.047	-0.390	-1.355	0.918	7.665	33.876

Table C.15: Systematic covariance matrix of measured cross section in Q^2 on scintillator, in units of 10^{-84} $(\mathrm{cm}^2/\mathrm{GeV}^2/\mathrm{nucleon})^2$

Bin edges (GeV^2)	0.000-0.025	0.025-0.050	0.050-0.100	0.100-0.200	0.200-0.300	0.300-0.400	0.400-0.500	0.500-0.700	0.700-1.000	1.000-1.300	1.300-2.000	2.000-3.000
0.000-0.025	27.204	31.957	68.100	106.721	84.028	65.562	49.357	65.802	50.486	29.048	16.112	4.964
0.025-0.050	31.957	39.107	84.876	133.928	106.476	82.658	64.030	83.240	61.522	33.482	20.426	5.525
0.050-0.100	68.100	84.876	193.919	321.433	264.798	206.048	161.678	210.364	151.732	81.615	50.830	13.131
0.100-0.200	106.721	133.928	321.433	700.641	684.659	564.395	468.415	629.259	465.205	204.591	177.673	37.231
0.200-0.300	84.028	106.476	264.798	684.659	742.901	630.838	537.980	740.159	566.405	236.378	238.472	45.450
0.300-0.400	65.562	82.658	206.048	564.395	630.838	552.774	468.766	660.613	513.076	215.554	225.538	44.719
0.400-0.500	49.357	64.030	161.678	468.415	537.980	468.766	410.994	576.418	454.288	193.268	204.915	40.987
0.500-0.700	65.802	83.240	210.364	629.259	740.159	660.613	576.418	843.358	689.768	313.029	320.996	66.639
0.700-1.000	50.486	61.522	151.732	465.205	566.405	513.076	454.288	689.768	624.011	320.520	319.078	67.524
1.000-1.300	29.048	33.482	81.615	204.591	236.378	215.554	193.268	313.029	320.520	214.691	190.548	45.833
1.300-2.000	16.112	20.426	50.830	177.673	238.472	225.538	204.915	320.996	319.078	190.548	212.849	42.806
2.000-3.000	4.964	5.525	13.131	37.231	45.450	44.719	40.987	66.639	67.524	45.833	42.806	14.980

Table C.16: Measured cross section in W_{exp} on scintillator, in units of 10^{-42} $cm^2/GeV/c^2$/nucleon, and the absolute and fractional cross section uncertainties

Bin edges (GeV/c^2)	σ	Abs. Unc.	Frac. Stat. Unc.	Frac. Sys. Unc.	Frac. Flux Unc.
0.9-1.1	75.72	17.93	0.100	0.214	0.059
1.1-1.2	500.34	41.49	0.025	0.079	0.037
1.2-1.3	1073.88	76.24	0.016	0.069	0.034
1.3-1.4	765.05	80.54	0.031	0.100	0.033

Table C.17: Statistical covariance matrix of measured cross section in W_{exp} on scintillator, in units of 10^{-84} $(cm^2/GeV/c^2/nucleon)^2$

Bin edges (GeV/c^2)	0.9-1.1	1.1-1.2	1.2-1.3	1.3-1.4
0.9-1.1	57.750	3.055	-36.676	-0.076
1.1-1.2	3.055	156.700	-68.785	-157.891
1.2-1.3	-36.676	-68.785	300.339	171.462
1.3-1.4	-0.076	-157.891	171.462	576.435

Table C.18: Systematic covariance matrix of measured cross section in W_{exp} on scintillator, in units of 10^{-84} $(cm^2/GeV/c^2/nucleon)^2$

Bin edges (GeV/c^2)	0.9-1.1	1.1-1.2	1.2-1.3	1.3-1.4
0.9-1.1	263.562	269.034	697.218	760.399
1.1-1.2	269.034	1565.131	2029.215	1172.973
1.2-1.3	697.218	2029.215	5512.155	5097.243
1.3-1.4	760.399	1172.973	5097.243	5910.151

Table C.19: Measured cross section in T_π on scintillator, in units of 10^{-42} $cm^2/GeV/$nucleon, and the absolute and fractional cross section uncertainties

Bin edges (GeV)	σ	Abs. Unc.	Frac. Stat. Unc.	Frac. Sys. Unc.	Frac. Flux Unc.
0.035-0.100	877.16	67.77	0.016	0.075	0.036
0.100-0.150	484.93	32.57	0.015	0.065	0.035
0.150-0.200	325.15	25.38	0.023	0.075	0.035
0.200-0.350	509.43	51.88	0.032	0.097	0.037

Table C.20: Statistical covariance matrix of measured cross section in T_π on scintillator, in units of 10^{-84} $(\text{cm}^2/\text{GeV}/\text{nucleon})^2$

Bin edges (GeV)	0.035-0.100	0.100-0.150	0.150-0.200	0.200-0.350
0.035-0.100	207.638	2.555	-6.545	-10.961
0.100-0.150	2.555	56.238	5.787	-2.987
0.150-0.200	-6.545	5.787	54.139	22.728
0.200-0.350	-10.961	-2.987	22.728	269.680

Table C.21: Systematic covariance matrix of measured cross section in T_π on scintillator, in units of 10^{-84} $(\text{cm}^2/\text{GeV}/\text{nucleon})^2$

Bin edges (GeV)	0.035-0.100	0.100-0.150	0.150-0.200	0.200-0.350
0.035-0.100	4384.602	1933.361	1446.173	2770.460
0.100-0.150	1933.361	1004.270	731.145	1350.185
0.150-0.200	1446.173	731.145	590.148	1129.798
0.200-0.350	2770.460	1350.185	1129.798	2421.754

Table C.22: Measured cross section in θ_π on scintillator, in units of 10^{-42} $\text{cm}^2/\text{degree}/\text{nucleon}$, and the absolute and fractional cross section uncertainties

Bin edges (degree)	σ	Abs. Unc.	Frac. Stat. Unc.	Frac. Sys. Unc.	Frac. Flux Unc.
0-10	33.23	4.32	0.079	0.104	0.040
10-20	98.63	10.00	0.041	0.093	0.036
20-30	153.35	14.42	0.031	0.089	0.036
30-40	189.91	16.20	0.027	0.081	0.037
40-50	215.81	17.63	0.026	0.077	0.037
50-60	235.70	18.28	0.027	0.073	0.037
60-120	1186.84	92.35	0.019	0.075	0.035
120-135	143.00	10.46	0.027	0.068	0.033
135-150	94.03	6.93	0.031	0.067	0.034
150-165	46.50	4.36	0.050	0.079	0.034
165-180	10.20	1.36	0.111	0.074	0.036

Table C.23: Statistical covariance matrix of measured cross section in θ_π on scintillator, in units of 10^{-84} $(\mathrm{cm}^2/\mathrm{degree}/\mathrm{nucleon})^2$

Bin edges (degree)	0-10	10-20	20-30	30-40	40-50	50-60	60-120	120-135	135-150	150-165	165-180
0-10	6.806	1.861	-0.137	-0.227	-0.097	-0.140	-0.270	-0.107	-0.049	-0.037	0.634
10-20	1.861	16.053	2.698	-0.534	-0.385	-0.325	-1.604	-0.212	-0.294	0.176	0.509
20-30	-0.137	2.698	22.565	3.271	-0.873	-0.500	-1.841	-0.561	-0.399	0.624	-0.029
30-40	-0.227	-0.534	3.271	26.410	3.923	-1.068	-2.940	-0.952	0.217	0.278	-0.034
40-50	-0.097	-0.385	-0.873	3.923	31.852	4.379	-3.448	-0.557	0.335	-0.448	-0.121
50-60	-0.140	-0.325	-0.500	-1.068	4.379	39.289	12.113	0.222	-0.873	-0.264	-0.054
60-120	-0.270	-1.604	-1.841	-2.940	-3.448	12.113	516.078	7.115	-1.781	0.299	0.231
120-135	-0.107	-0.212	-0.561	-0.952	-0.557	0.222	7.115	15.417	2.153	-0.189	0.023
135-150	-0.049	-0.294	-0.399	0.217	0.335	-0.873	-1.781	2.153	8.562	1.790	0.132
150-165	-0.037	0.176	0.624	0.278	-0.448	-0.264	0.299	-0.189	1.790	5.395	0.212
165-180	0.634	0.509	-0.029	-0.034	-0.121	-0.054	0.231	0.023	0.132	0.212	1.278

Table C.24: Systematic covariance matrix of measured cross section in θ_π on scintillator, in units of 10^{-84} $(\mathrm{cm}^2/\mathrm{degree}/\mathrm{nucleon})^2$

Bin edges (degree)	0-10	10-20	20-30	30-40	40-50	50-60	60-120	120-135	135-150	150-165	165-180
0-10	11.831	30.629	44.591	49.403	49.114	45.545	166.266	19.417	12.506	7.141	1.643
10-20	30.629	83.967	119.039	132.126	129.767	119.103	463.782	56.473	35.661	20.721	4.363
20-30	44.591	119.039	185.356	206.894	214.536	204.453	896.087	89.045	57.502	33.949	6.852
30-40	49.403	132.126	206.894	235.944	248.833	239.674	1069.617	106.328	69.555	40.394	8.526
40-50	49.114	129.767	214.536	248.833	278.836	278.214	1273.972	125.514	82.834	44.633	9.409
50-60	45.545	119.103	204.453	239.674	278.214	294.704	1351.335	137.044	92.045	49.387	9.866
60-120	166.266	463.782	896.087	1069.617	1273.972	1351.335	8011.679	622.390	426.688	263.518	45.957
120-135	19.417	56.473	89.045	106.328	125.514	137.044	622.390	93.989	59.348	25.696	4.712
135-150	12.506	35.661	57.502	69.555	82.834	92.045	426.688	59.348	39.400	18.536	3.514
150-165	7.141	20.721	33.949	40.394	44.633	49.387	263.518	25.696	18.536	13.588	2.387
165-180	1.643	4.363	6.852	8.526	9.409	9.866	45.957	4.712	3.514	2.387	0.564

Table C.25: Measured cross section in p_μ on carbon, in units of 10^{-42} cm^2/GeV/c/nucleon, and the absolute and fractional cross section uncertainties

Bin edges (GeV/c)	σ	Abs. Unc.	Frac. Stat. Unc.	Frac. Sys. Unc.	Frac. Flux Unc.
1.5-3.0	230.97	83.98	0.339	0.131	0.037
3.0-4.0	419.12	101.24	0.208	0.124	0.037
4.0-5.0	489.36	119.13	0.185	0.158	0.039
5.0-6.0	484.70	114.44	0.173	0.161	0.037
6.0-7.0	305.19	84.25	0.200	0.191	0.037
7.0-8.5	195.47	66.76	0.264	0.217	0.038
8.5-10.0	51.37	23.66	0.370	0.275	0.042
10.0-20.0	104.52	54.80	0.457	0.256	0.038

Table C.26: Statistical covariance matrix of measured cross section in p_μ on carbon, in units of 10^{-84} (cm^2/GeV/c/nucleon)^2

Bin edges (GeV/c)	1.5-3.0	3.0-4.0	4.0-5.0	5.0-6.0	6.0-7.0	7.0-8.5	8.5-10.0	10.0-20.0
1.5-3.0	6132.835	1313.702	206.484	124.812	118.991	48.493	0.932	7.411
3.0-4.0	1313.702	7567.510	1928.715	436.937	100.752	12.352	0.249	0.000
4.0-5.0	206.484	1928.715	8185.356	2524.531	368.806	77.674	10.370	0.000
5.0-6.0	124.812	436.937	2524.531	7023.169	2452.218	530.146	85.630	41.569
6.0-7.0	118.991	100.752	368.806	2452.218	3711.402	1718.045	223.842	308.796
7.0-8.5	48.493	12.352	77.674	530.146	1718.045	2659.591	599.005	199.496
8.5-10.0	0.932	0.249	10.370	85.630	223.842	599.005	360.832	283.322
10.0-20.0	7.411	0.000	0.000	41.569	308.796	199.496	283.322	2285.470

Table C.27: Systematic covariance matrix of measured cross section in p_μ on carbon, in units of 10^{-84} (cm^2/GeV/c/nucleon)^2

Bin edges (GeV/c)	1.5-3.0	3.0-4.0	4.0-5.0	5.0-6.0	6.0-7.0	7.0-8.5	8.5-10.0	10.0-20.0
1.5-3.0	919.027	1248.851	1700.944	1661.237	1211.345	459.019	182.113	556.611
3.0-4.0	1248.851	2681.743	3331.972	3491.932	2449.752	1334.104	429.728	1074.937
4.0-5.0	1700.944	3331.972	6005.496	5570.616	3970.502	2215.695	578.611	1433.112
5.0-6.0	1661.237	3491.932	5570.616	6074.163	4245.971	2409.949	682.978	1591.893
6.0-7.0	1211.345	2449.752	3970.502	4245.971	3386.353	2026.419	619.400	1209.951
7.0-8.5	459.019	1334.104	2215.695	2409.949	2026.419	1797.524	535.686	695.932
8.5-10.0	182.113	429.728	578.611	682.978	619.400	535.686	199.180	264.702
10.0-20.0	556.611	1074.937	1433.112	1591.893	1209.951	695.932	264.702	717.129

Table C.28: Measured cross section in θ_μ on carbon, in units of 10^{-42} cm^2/degree/nucleon, and the absolute and fractional cross section uncertainties

Bin edges (degree)	σ	Abs. Unc.	Frac. Stat. Unc.	Frac. Sys. Unc.	Frac. Flux Unc.
0-2	129.73	43.10	0.312	0.113	0.034
2-3	279.55	71.91	0.230	0.115	0.033
3-4	233.69	70.70	0.268	0.140	0.033
4-5	243.92	83.04	0.275	0.201	0.037
5-6	102.61	64.81	0.520	0.358	0.045
6-8	323.87	166.36	0.423	0.292	0.039
8-10	538.15	219.41	0.350	0.209	0.035
10-13	627.78	273.17	0.385	0.202	0.039

Table C.29: Statistical covariance matrix of measured cross section in θ_μ on carbon, in units of 10^{-84} (cm^2/degree/nucleon)^2

Bin edges (degree)	0-2	2-3	3-4	4-5	5-6	6-8	8-10	10-13
0-2	1643.003	-85.934	-108.779	-19.048	0.446	0.708	-8.441	-11.908
2-3	-85.934	4136.631	180.508	-331.032	-50.560	-1.002	-37.691	-12.607
3-4	-108.779	180.508	3929.241	562.719	-273.916	-113.747	-8.750	-20.774
4-5	-19.048	-331.032	562.719	4493.411	600.864	-642.696	-74.843	10.652
5-6	0.446	-50.560	-273.916	600.864	2847.940	631.020	-362.996	-25.008
6-8	0.708	-1.002	-113.747	-642.696	631.020	18750.792	-500.317	-868.157
8-10	-8.441	-37.691	-8.750	-74.843	-362.996	-500.317	35550.692	-2090.695
10-13	-11.908	-12.607	-20.774	10.652	-25.008	-868.157	-2090.695	58544.885

Table C.30: Systematic covariance matrix of measured cross section in θ_μ on carbon, in units of 10^{-84} (cm^2/degree/nucleon)^2

Bin edges (degree)	0-2	2-3	3-4	4-5	5-6	6-8	8-10	10-13
0-2	214.485	255.754	94.006	128.127	42.846	273.768	461.313	115.038
2-3	255.754	1033.703	665.497	1056.901	644.297	1651.375	1965.802	2601.327
3-4	94.006	665.497	1069.368	1445.651	997.848	2112.905	2575.292	3255.228
4-5	128.127	1056.901	1445.651	2402.945	1500.850	3399.238	4215.134	4773.122
5-6	42.846	644.297	997.848	1500.850	1352.648	2446.059	2965.789	3290.603
6-8	273.768	1651.375	2112.905	3399.238	2446.059	8925.832	7454.234	7083.876
8-10	461.313	1965.802	2575.292	4215.134	2965.789	7454.234	12590.175	8345.326
10-13	115.038	2601.327	3255.228	4773.122	3290.603	7083.876	8345.326	16077.709

Table C.31: Measured cross section in $p_{\mu,||}$ on carbon, in units of 10^{-42} cm^2/GeV/c/nucleon, and the absolute and fractional cross section uncertainties

Bin edges (GeV/c)	σ	Abs. Unc.	Frac. Stat. Unc.	Frac. Sys. Unc.	Frac. Flux Unc.
1.5-3.0	227.51	84.81	0.347	0.135	0.038
3.0-4.0	434.23	105.31	0.208	0.124	0.037
4.0-5.0	495.35	119.87	0.183	0.158	0.039
5.0-6.0	465.67	112.86	0.177	0.165	0.038
6.0-7.0	311.95	85.00	0.199	0.186	0.037
7.0-8.5	190.37	65.31	0.265	0.218	0.038
8.5-10.0	49.96	23.37	0.376	0.278	0.042
10.0-20.0	104.04	54.46	0.457	0.256	0.038

Table C.32: Statistical covariance matrix of measured cross section in $p_{\mu,||}$ on carbon, in units of 10^{-84} (cm^2/GeV/c/nucleon)^2

Bin edges (GeV/c)	1.5-3.0	3.0-4.0	4.0-5.0	5.0-6.0	6.0-7.0	7.0-8.5	8.5-10.0	10.0-20.0
1.5-3.0	6244.649	1166.627	193.234	120.985	113.063	46.135	0.892	7.128
3.0-4.0	1166.627	8173.392	1927.489	394.431	87.133	10.584	0.075	0.000
4.0-5.0	193.234	1927.489	8254.745	2535.001	383.115	74.845	9.909	0.000
5.0-6.0	120.985	394.431	2535.001	6800.439	2476.093	525.067	81.290	40.620
6.0-7.0	113.063	87.133	383.115	2476.093	3844.505	1630.408	203.660	302.355
7.0-8.5	46.135	10.584	74.845	525.067	1630.408	2547.445	575.971	197.434
8.5-10.0	0.892	0.075	9.909	81.290	203.660	575.971	353.094	281.156
10.0-20.0	7.128	0.000	0.000	40.620	302.355	197.434	281.156	2255.768

Table C.33: Systematic covariance matrix of measured cross section in $p_{\mu,||}$ on carbon, in units of 10^{-84} (cm^2/GeV/c/nucleon)^2

Bin edges (GeV/c)	1.5-3.0	3.0-4.0	4.0-5.0	5.0-6.0	6.0-7.0	7.0-8.5	8.5-10.0	10.0-20.0
1.5-3.0	948.413	1259.569	1755.414	1707.784	1259.809	460.718	175.502	576.940
3.0-4.0	1259.569	2917.439	3411.642	3542.203	2493.912	1276.700	408.965	1073.737
4.0-5.0	1755.414	3411.642	6113.551	5507.709	4018.040	2153.075	560.741	1415.968
5.0-6.0	1707.784	3542.203	5507.709	5937.682	4229.854	2303.521	669.132	1575.591
6.0-7.0	1259.809	2493.912	4018.040	4229.854	3380.197	1928.376	602.230	1221.390
7.0-8.5	460.718	1276.700	2153.075	2303.521	1928.376	1717.980	515.431	666.188
8.5-10.0	175.502	408.965	560.741	669.132	602.230	515.431	193.256	256.342
10.0-20.0	576.940	1073.737	1415.968	1575.591	1221.390	666.188	256.342	709.683

Table C.34: Measured cross section in $p_{\mu,T}$ on carbon, in units of 10^{-42} cm^2/GeV/c/nucleon, and the absolute and fractional cross section uncertainties

Bin edges (GeV/c)	σ	Abs. Unc.	Frac. Stat. Unc.	Frac. Sys. Unc.	Frac. Flux Unc.
0.00-0.15	99.00	33.04	0.324	0.079	0.033
0.15-0.30	244.98	62.62	0.232	0.108	0.033
0.30-0.45	496.04	114.93	0.198	0.120	0.035
0.45-0.60	483.82	145.41	0.230	0.194	0.037
0.60-0.75	345.45	137.16	0.311	0.246	0.036
0.75-0.90	156.48	145.16	0.722	0.582	0.050
0.90-1.25	252.37	188.18	0.590	0.456	0.048
1.25-2.50	52.15	80.47	1.394	0.662	0.036

Table C.35: Statistical covariance matrix of measured cross section in $p_{\mu,T}$ on carbon, in units of 10^{-84} $(\mathrm{cm}^2/\mathrm{GeV/c/nucleon})^2$

Bin edges (GeV/c)	0.00-0.15	0.15-0.30	0.30-0.45	0.45-0.60	0.60-0.75	0.75-0.90	0.90-1.25	1.25-2.50
0.00-0.15	1030.615	0.111	-199.416	-25.471	-0.928	4.769	-5.173	0.027
0.15-0.30	0.111	3220.563	421.632	-561.749	-108.194	-53.468	-20.845	-4.775
0.30-0.45	-199.416	421.632	9640.239	1311.186	-1043.630	-413.349	-166.396	-96.620
0.45-0.60	-25.471	-561.749	1311.186	12336.677	1863.697	-854.187	-1187.566	103.324
0.60-0.75	-0.928	-108.194	-1043.630	1863.697	11568.307	3685.863	-177.400	-412.400
0.75-0.90	4.769	-53.468	-413.349	-854.187	3685.863	12767.580	6164.734	-95.716
0.90-1.25	-5.173	-20.845	-166.396	-1187.566	-177.400	6164.734	22145.036	-136.078
1.25-2.50	0.027	-4.775	-96.620	103.324	-412.400	-95.716	-136.078	5283.197

Table C.36: Systematic covariance matrix of measured cross section in $p_{\mu,T}$ on carbon, in units of 10^{-84} $(\mathrm{cm}^2/\mathrm{GeV/c/nucleon})^2$

Bin edges (GeV/c)	0.00-0.15	0.15-0.30	0.30-0.45	0.45-0.60	0.60-0.75	0.75-0.90	0.90-1.25	1.25-2.50
0.00-0.15	60.820	164.157	87.136	80.511	98.094	96.726	100.842	22.107
0.15-0.30	164.157	700.303	878.922	1105.634	1201.415	1024.191	917.583	292.551
0.30-0.45	87.136	878.922	3567.985	5026.216	4449.160	3049.770	2830.071	1088.935
0.45-0.60	80.511	1105.634	5026.216	8806.367	7215.905	4722.860	4741.798	1694.203
0.60-0.75	98.094	1201.415	4449.160	7215.905	7245.813	5062.351	4237.793	1744.737
0.75-0.90	96.726	1024.191	3049.770	4722.860	5062.351	8304.216	7997.688	2298.146
0.90-1.25	100.842	917.583	2830.071	4741.798	4237.793	7997.688	13266.409	2490.226
1.25-2.50	22.107	292.551	1088.935	1694.203	1744.737	2298.146	2490.226	1192.807

Table C.37: Measured cross section in Q^2 on carbon, in units of 10^{-42} $\mathrm{cm}^2/\mathrm{GeV}^2/\mathrm{nucleon}$, and the absolute and fractional cross section uncertainties

Bin edges (GeV^2)	σ	Abs. Unc.	Frac. Stat. Unc.	Frac. Sys. Unc.	Frac. Flux Unc.
0.000-0.025	100.52	32.64	0.316	0.073	0.033
0.025-0.050	81.63	27.49	0.325	0.089	0.035
0.050-0.100	165.17	46.71	0.253	0.127	0.032
0.100-0.200	445.96	101.34	0.196	0.115	0.034
0.200-0.300	263.76	85.53	0.273	0.174	0.035
0.300-0.400	237.25	86.12	0.284	0.226	0.039
0.400-0.500	158.16	73.69	0.361	0.295	0.041
0.500-0.700	180.28	109.24	0.483	0.366	0.040
0.700-1.000	231.12	149.76	0.527	0.377	0.039
1.000-1.300	150.85	92.36	0.546	0.276	0.039
1.300-2.000	72.40	113.34	1.262	0.926	0.059
2.000-3.000	43.89	76.37	1.608	0.665	0.049

Table C.38: Statistical covariance matrix of measured cross section in Q^2 on carbon, in units of 10^{-84} $(\mathrm{cm}^2/\mathrm{GeV}^2/\mathrm{nucleon})^2$

Bin edges (GeV^2)	0.000-0.025	0.025-0.050	0.050-0.100	0.100-0.200	0.200-0.300	0.300-0.400	0.400-0.500	0.500-0.700	0.700-1.000	1.000-1.300	1.300-2.000	2.000-3.000
0.000-0.025	1011.574	48.628	-96.749	-99.671	-2.744	-0.298	0.044	-1.689	2.636	-0.416	-0.942	-0.075
0.025-0.050	48.628	703.550	323.214	-222.443	-69.588	-10.515	-4.085	-5.962	-9.875	-2.008	-3.724	0.254
0.050-0.100	-96.749	323.214	1743.493	771.226	-287.345	-115.833	-39.214	-17.429	-3.315	-8.825	-19.675	-3.822
0.100-0.200	-99.671	-222.443	771.226	7633.958	1115.904	-549.191	-371.569	-96.672	-104.736	-82.562	-33.791	-31.700
0.200-0.300	-2.744	-69.588	-287.345	1115.904	5196.740	1946.123	-102.155	-522.096	-286.702	-139.234	-171.403	-22.930
0.300-0.400	-0.298	-10.515	-115.833	-549.191	1946.123	4541.983	2276.448	26.725	-770.983	-314.715	173.766	-9.728
0.400-0.500	0.044	-4.085	-39.214	-371.569	-102.155	2276.448	3251.411	2320.197	-68.016	-294.089	-112.768	-51.800
0.500-0.700	-1.689	-5.962	-17.429	-96.672	-522.096	26.725	2320.197	7587.926	3947.869	-133.797	-32.228	-134.666
0.700-1.000	2.636	-9.875	-3.315	-104.736	-286.702	-770.983	-68.016	3947.869	14853.308	4675.749	112.475	-364.952
1.000-1.300	-0.416	-2.008	-8.825	-82.562	-139.234	-314.715	-294.089	-133.797	4675.749	6791.844	1800.244	-205.642
1.300-2.000	-0.942	-3.724	-19.675	-33.791	-171.403	173.766	-112.768	-32.228	112.475	1800.244	8346.961	1477.751
2.000-3.000	-0.075	0.254	-3.822	-31.700	-22.930	-9.728	-51.800	-134.666	-364.952	-205.642	1477.751	4981.142

Table C.39: Systematic covariance matrix of measured cross section in Q^2 on carbon, in units of 10^{-84} $(\mathrm{cm}^2/\mathrm{GeV}^2/\mathrm{nucleon})^2$

Bin edges (GeV^2)	0.000-0.025	0.025-0.050	0.050-0.100	0.100-0.200	0.200-0.300	0.300-0.400	0.400-0.500	0.500-0.700	0.700-1.000	1.000-1.300	1.300-2.000	2.000-3.000
0.000-0.025	53.609	42.389	103.754	81.879	51.403	46.141	29.115	62.897	106.616	63.615	44.975	31.348
0.025-0.050	42.389	52.240	101.682	159.379	79.705	69.784	70.444	156.840	178.294	92.527	63.111	53.431
0.050-0.100	103.754	101.682	438.238	690.599	577.178	631.881	557.528	832.980	931.231	418.440	402.035	214.513
0.100-0.200	81.879	159.379	690.599	2636.407	2124.807	2161.214	1935.758	2775.467	2236.814	1084.290	1255.787	597.165
0.200-0.300	51.403	79.705	577.178	2124.807	2118.097	2234.047	1923.859	2367.665	1914.062	967.589	1147.362	452.127
0.300-0.400	46.141	69.784	631.881	2161.214	2234.047	2873.985	2290.715	2631.178	2156.800	1012.384	1512.464	537.751
0.400-0.500	29.115	70.444	557.528	1935.758	1923.859	2290.715	2179.379	2473.816	1925.684	958.782	1350.235	527.442
0.500-0.700	62.897	156.840	832.980	2775.467	2367.665	2631.178	2473.816	4346.350	4409.334	2062.935	2495.838	1187.339
0.700-1.000	106.616	178.294	931.231	2236.814	1914.062	2156.800	1925.684	4409.334	7574.963	3106.652	3705.723	1778.106
1.000-1.300	63.615	92.527	418.440	1084.290	967.589	1012.384	958.782	2062.935	3106.652	1738.855	2144.827	911.978
1.300-2.000	44.975	63.111	402.035	1255.787	1147.362	1512.464	1350.235	2495.838	3705.723	2144.827	4499.072	1230.996
2.000-3.000	31.348	53.431	214.513	597.165	452.127	537.751	527.442	1187.339	1778.106	911.978	1230.996	851.560

Table C.40: Measured cross section in W_{exp} on carbon, in units of 10^{-42} $cm^2/GeV/c^2$/nucleon, and the absolute and fractional cross section uncertainties

Bin edges (GeV/c^2)	σ	Abs. Unc.	Frac. Stat. Unc.	Frac. Sys. Unc.	Frac. Flux Unc.
0.9-1.1	183.35	123.04	0.642	0.195	0.044
1.1-1.2	543.34	109.43	0.175	0.100	0.035
1.2-1.3	819.40	240.92	0.203	0.212	0.032
1.3-1.4	450.52	370.04	0.556	0.605	0.033

Table C.41: Statistical covariance matrix of measured cross section in W_{exp} on carbon, in units of 10^{-84} $(cm^2/GeV/c^2/nucleon)^2$

Bin edges (GeV/c^2)	0.9-1.1	1.1-1.2	1.2-1.3	1.3-1.4
0.9-1.1	13864.694	-594.193	-8802.136	-6344.277
1.1-1.2	-594.193	8994.107	1466.611	-11091.101
1.2-1.3	-8802.136	1466.611	27785.187	20182.710
1.3-1.4	-6344.277	-11091.101	20182.710	62726.884

Table C.42: Systematic covariance matrix of measured cross section in W_{exp} on carbon, in units of 10^{-84} $(cm^2/GeV/c^2/nucleon)^2$

Bin edges (GeV/c^2)	0.9-1.1	1.1-1.2	1.2-1.3	1.3-1.4
0.9-1.1	1273.719	733.269	705.107	923.055
1.1-1.2	733.269	2980.610	1696.554	900.804
1.2-1.3	705.107	1696.554	30257.826	44841.241
1.3-1.4	923.055	900.804	44841.241	74205.905

Table C.43: Measured cross section in T_π on carbon, in units of 10^{-42} $cm^2/GeV/nucleon$, and the absolute and fractional cross section uncertainties

Bin edges (GeV)	σ	Abs. Unc.	Frac. Stat. Unc.	Frac. Sys. Unc.	Frac. Flux Unc.
0.035-0.100	769.68	177.61	0.177	0.149	0.036
0.100-0.150	454.17	87.53	0.135	0.138	0.034
0.150-0.200	269.42	86.08	0.237	0.214	0.033
0.200-0.350	403.09	236.65	0.438	0.391	0.040

Table C.44: Statistical covariance matrix of measured cross section in T_π on carbon, in units of 10^{-84} $(\text{cm}^2/\text{GeV}/\text{nucleon})^2$

Bin edges (GeV)	0.035-0.100	0.100-0.150	0.150-0.200	0.200-0.350
0.035-0.100	18470.163	1416.599	-1257.920	49.564
0.100-0.150	1416.599	3760.620	1405.837	1794.339
0.150-0.200	-1257.920	1405.837	4074.259	6059.867
0.200-0.350	49.564	1794.339	6059.867	31119.900

Table C.45: Systematic covariance matrix of measured cross section in T_π on carbon, in units of 10^{-84} $(\text{cm}^2/\text{GeV}/\text{nucleon})^2$

Bin edges (GeV)	0.035-0.100	0.100-0.150	0.150-0.200	0.200-0.350
0.035-0.100	13073.613	6383.641	5389.178	12304.482
0.100-0.150	6383.641	3900.307	3241.973	6560.703
0.150-0.200	5389.178	3241.973	3335.085	7422.032
0.200-0.350	12304.482	6560.703	7422.032	24881.666

Table C.46: Measured cross section in θ_π on carbon, in units of 10^{-42} $\text{cm}^2/\text{degree}/\text{nucleon}$, and the absolute and fractional cross section uncertainties

Bin edges (degree)	σ	Abs. Unc.	Frac. Stat. Unc.	Frac. Sys. Unc.	Frac. Flux Unc.
0-10	37.51	71.40	1.760	0.724	0.047
10-20	90.16	60.51	0.586	0.327	0.039
20-30	138.55	59.77	0.351	0.251	0.035
30-40	157.23	54.22	0.286	0.193	0.036
40-50	216.80	61.03	0.232	0.160	0.035
50-60	187.83	59.06	0.262	0.173	0.033
60-120	1100.75	270.89	0.208	0.131	0.035
120-135	148.73	47.89	0.292	0.136	0.033
135-150	118.79	41.86	0.320	0.149	0.033
150-165	75.48	51.12	0.583	0.344	0.038
165-180	13.96	12.23	0.781	0.398	0.037

Table C.47: Statistical covariance matrix of measured cross section in θ_π on carbon, in units of 10^{-84} $(\mathrm{cm}^2/\mathrm{degree}/\mathrm{nucleon})^2$

Bin edges (degree)	0-10	10-20	20-30	30-40	40-50	50-60	60-120	120-135	135-150	150-165	165-180
0-10	4360.800	1218.856	675.088	-163.955	224.795	-69.726	-448.373	-59.130	-73.467	-88.841	17.722
10-20	1218.856	2793.595	1029.189	-17.311	20.435	-102.757	-294.454	29.607	-10.671	45.667	279.350
20-30	675.088	1029.189	2364.471	465.750	-224.215	-138.651	-520.805	-115.102	-85.977	60.404	103.705
30-40	-163.955	-17.311	465.750	2015.286	728.137	-65.504	-533.880	-50.671	8.105	-40.487	-28.459
40-50	224.795	20.435	-224.215	728.137	2521.062	661.268	-191.757	-106.226	-92.746	-184.735	-46.719
50-60	-69.726	-102.757	-138.651	-65.504	661.268	2427.601	2640.003	-74.805	-51.058	-92.265	-25.361
60-120	-448.373	-294.454	-520.805	-533.880	-191.757	2640.003	52456.077	1247.128	-133.926	-98.176	-19.332
120-135	-59.130	29.607	-115.102	-50.671	-106.226	-74.805	1247.128	1883.995	303.661	33.863	10.971
135-150	-73.467	-10.671	-85.977	8.105	-92.746	-51.058	-133.926	303.661	1441.009	1023.212	84.997
150-165	-88.841	45.667	60.404	-40.487	-184.735	-92.265	-98.176	33.863	1023.212	1939.037	23.754
165-180	17.722	279.350	103.705	-28.459	-46.719	-25.361	-19.332	10.971	84.997	23.754	118.773

Table C.48: Systematic covariance matrix of measured cross section in θ_π on carbon, in units of 10^{-84} $(\text{cm}^2/\text{degree}/\text{nucleon})^2$

Bin edges (degree)	0-10	10-20	20-30	30-40	40-50	50-60	60-120	120-135	135-150	150-165	165-180
0-10	736.946	185.606	318.951	258.298	209.084	240.508	1025.324	209.047	198.366	276.741	12.166
10-20	185.606	867.273	922.057	707.486	830.518	742.214	2380.160	366.502	301.533	232.634	89.445
20-30	318.951	922.057	1208.495	948.939	988.960	873.244	2948.546	429.014	380.186	260.884	87.138
30-40	258.298	707.486	948.939	924.950	820.516	737.871	2589.254	369.795	338.673	280.877	75.968
40-50	209.084	830.518	988.960	820.516	1203.575	1081.528	4029.047	563.562	448.829	230.245	92.356
50-60	240.508	742.214	873.244	737.871	1081.528	1060.784	3990.557	579.191	430.930	273.246	97.731
60-120	1025.324	2380.160	2948.546	2589.254	4029.047	3990.557	20926.337	2425.741	1623.709	990.315	470.998
120-135	209.047	366.502	429.014	369.795	563.562	579.191	2425.741	409.658	278.197	292.558	65.717
135-150	198.366	301.533	380.186	338.673	448.829	430.930	1623.709	278.197	311.344	181.440	39.858
150-165	276.741	232.634	260.884	280.877	230.245	273.246	990.315	292.558	181.440	674.076	59.417
165-180	12.166	89.445	87.138	75.968	92.356	97.731	470.998	65.717	39.858	59.417	30.807

Table C.49: Measured cross section in p_μ on water, in units of 10^{-42} cm^2/GeV/c/nucleon, and the absolute and fractional cross section uncertainties

Bin edges (GeV/c)	σ	Abs. Unc.	Frac. Stat. Unc.	Frac. Sys. Unc.	Frac. Flux Unc.
1.5-3.0	172.13	77.31	0.413	0.176	0.035
3.0-4.0	171.09	79.67	0.373	0.279	0.047
4.0-5.0	427.45	113.56	0.211	0.161	0.041
5.0-6.0	451.30	107.34	0.189	0.145	0.037
6.0-7.0	325.77	80.94	0.208	0.137	0.035
7.0-8.5	226.44	66.65	0.234	0.179	0.032
8.5-10.0	64.40	23.31	0.312	0.183	0.031
10.0-20.0	63.09	28.43	0.412	0.183	0.034

Table C.50: Statistical covariance matrix of measured cross section in p_μ on water, in units of 10^{-84} (cm^2/GeV/c/nucleon)^2

Bin edges (GeV/c)	1.5-3.0	3.0-4.0	4.0-5.0	5.0-6.0	6.0-7.0	7.0-8.5	8.5-10.0	10.0-20.0
1.5-3.0	5055.096	551.954	69.433	45.040	38.465	18.886	18.142	0.258
3.0-4.0	551.954	4065.158	1668.811	433.218	45.035	37.590	4.617	8.382
4.0-5.0	69.433	1668.811	8153.681	2985.054	613.491	170.510	35.751	26.288
5.0-6.0	45.040	433.218	2985.054	7241.755	2818.484	622.392	67.021	70.020
6.0-7.0	38.465	45.035	613.491	2818.484	4571.381	1709.811	109.348	18.146
7.0-8.5	18.886	37.590	170.510	622.392	1709.811	2796.166	406.360	174.908
8.5-10.0	18.142	4.617	35.751	67.021	109.348	406.360	403.996	300.852
10.0-20.0	0.258	8.382	26.288	70.020	18.146	174.908	300.852	675.713

Table C.51: Systematic covariance matrix of measured cross section in p_μ on water, in units of 10^{-84} (cm^2/GeV/c/nucleon)^2

Bin edges (GeV/c)	1.5-3.0	3.0-4.0	4.0-5.0	5.0-6.0	6.0-7.0	7.0-8.5	8.5-10.0	10.0-20.0
1.5-3.0	921.052	808.411	1299.079	1126.191	961.736	896.021	250.222	154.532
3.0-4.0	808.411	2281.803	2675.288	2488.409	1514.644	1277.443	346.055	279.926
4.0-5.0	1299.079	2675.288	4741.085	3940.068	2613.890	2060.127	504.277	493.528
5.0-6.0	1126.191	2488.409	3940.068	4280.443	2474.818	1684.590	469.290	517.678
6.0-7.0	961.736	1514.644	2613.890	2474.818	1979.170	1455.533	369.401	361.277
7.0-8.5	896.021	1277.443	2060.127	1684.590	1455.533	1645.510	429.792	305.551
8.5-10.0	250.222	346.055	504.277	469.290	369.401	429.792	139.182	75.488
10.0-20.0	154.532	279.926	493.528	517.678	361.277	305.551	75.488	132.643

Table C.52: Measured cross section in θ_μ on water, in units of 10^{-42} cm^2/degree/nucleon, and the absolute and fractional cross section uncertainties

Bin edges (degree)	σ	Abs. Unc.	Frac. Stat. Unc.	Frac. Sys. Unc.	Frac. Flux Unc.
0-2	107.43	30.34	0.256	0.119	0.031
2-3	189.63	56.47	0.273	0.119	0.036
3-4	235.91	69.17	0.260	0.136	0.034
4-5	200.95	83.99	0.377	0.180	0.034
5-6	137.72	85.00	0.540	0.298	0.037
6-8	471.67	205.75	0.368	0.234	0.040
8-10	579.39	227.87	0.341	0.195	0.039
10-13	43.80	172.07	3.410	1.951	0.182

Table C.53: Statistical covariance matrix of measured cross section in θ_μ on water, in units of 10^{-84} (cm^2/degree/nucleon)^2

Bin edges (degree)	0-2	2-3	3-4	4-5	5-6	6-8	8-10	10-13
0-2	756.487	66.380	-148.546	-28.112	-0.299	-13.842	-1.272	0.051
2-3	66.380	2677.585	405.849	-459.017	-65.175	-23.534	-18.894	0.357
3-4	-148.546	405.849	3752.049	905.910	-383.572	-205.129	10.297	0.409
4-5	-28.112	-459.017	905.910	5747.238	1167.333	-880.775	-74.550	2.556
5-6	-0.299	-65.175	-383.572	1167.333	5536.834	1174.713	-688.517	-8.265
6-8	-13.842	-23.534	-205.129	-880.775	1174.713	30100.990	-1607.264	-430.902
8-10	-1.272	-18.894	10.297	-74.550	-688.517	-1607.264	39100.566	3503.381
10-13	0.051	0.357	0.409	2.556	-8.265	-430.902	3503.381	22309.790

Table C.54: Systematic covariance matrix of measured cross section in θ_μ on water, in units of 10^{-84} (cm^2/degree/nucleon)^2

Bin edges (degree)	0-2	2-3	3-4	4-5	5-6	6-8	8-10	10-13
0-2	164.019	220.556	311.350	126.568	36.207	72.003	104.907	-66.199
2-3	220.556	511.739	579.807	470.506	461.639	852.758	533.810	590.128
3-4	311.350	579.807	1032.856	718.802	576.648	1902.686	1613.136	1058.896
4-5	126.568	470.506	718.802	1306.954	1262.036	2778.796	2442.642	2112.055
5-6	36.207	461.639	576.648	1262.036	1687.987	2676.651	2566.107	2676.283
6-8	72.003	852.758	1902.686	2778.796	2676.651	12232.359	7767.974	7103.935
8-10	104.907	533.810	1613.136	2442.642	2566.107	7767.974	12825.606	6248.427
10-13	-66.199	590.128	1058.896	2112.055	2676.283	7103.935	6248.427	7299.421

Table C.55: Measured cross section in $p_{\mu,||}$ on water, in units of 10^{-42} cm^2/GeV/c/nucleon, and the absolute and fractional cross section uncertainties

Bin edges (GeV/c)	σ	Abs. Unc.	Frac. Stat. Unc.	Frac. Sys. Unc.	Frac. Flux Unc.
1.5-3.0	199.50	88.30	0.392	0.206	0.035
3.0-4.0	192.47	83.27	0.347	0.259	0.045
4.0-5.0	435.98	116.51	0.212	0.163	0.041
5.0-6.0	430.44	104.47	0.194	0.146	0.037
6.0-7.0	317.48	79.57	0.211	0.136	0.034
7.0-8.5	210.74	63.65	0.240	0.184	0.032
8.5-10.0	62.02	22.64	0.314	0.186	0.031
10.0-20.0	63.46	28.45	0.410	0.180	0.034

Table C.56: Statistical covariance matrix of measured cross section in $p_{\mu,||}$ on water, in units of 10^{-84} (cm^2/GeV/c/nucleon)^2

Bin edges (GeV/c)	1.5-3.0	3.0-4.0	4.0-5.0	5.0-6.0	6.0-7.0	7.0-8.5	8.5-10.0	10.0-20.0
1.5-3.0	6106.567	619.865	73.779	44.523	40.746	18.388	20.244	0.252
3.0-4.0	619.865	4455.167	1766.544	406.867	39.493	38.287	4.740	8.415
4.0-5.0	73.779	1766.544	8552.511	2961.101	585.092	163.510	35.137	26.950
5.0-6.0	44.523	406.867	2961.101	6962.055	2640.309	578.823	65.162	69.989
6.0-7.0	40.746	39.493	585.092	2640.309	4472.734	1614.780	104.041	17.143
7.0-8.5	18.388	38.287	163.510	578.823	1614.780	2547.800	389.062	169.522
8.5-10.0	20.244	4.740	35.137	65.162	104.041	389.062	379.008	295.578
10.0-20.0	0.252	8.415	26.950	69.989	17.143	169.522	295.578	678.379

Table C.57: Systematic covariance matrix of measured cross section in $p_{\mu,||}$ on water, in units of 10^{-84} (cm^2/GeV/c/nucleon)^2

Bin edges (GeV/c)	1.5-3.0	3.0-4.0	4.0-5.0	5.0-6.0	6.0-7.0	7.0-8.5	8.5-10.0	10.0-20.0
1.5-3.0	1689.715	754.413	1499.543	1136.390	952.848	999.085	269.808	162.522
3.0-4.0	754.413	2478.208	2858.454	2524.935	1556.781	1320.454	371.737	300.130
4.0-5.0	1499.543	2858.454	5022.287	3965.595	2603.550	1964.189	504.051	510.942
5.0-6.0	1136.390	2524.935	3965.595	3952.459	2340.934	1549.603	447.632	490.863
6.0-7.0	952.848	1556.781	2603.550	2340.934	1859.156	1330.404	345.026	348.368
7.0-8.5	999.085	1320.454	1964.189	1549.603	1330.404	1503.141	394.986	289.904
8.5-10.0	269.808	371.737	504.051	447.632	345.026	394.986	133.533	72.156
10.0-20.0	162.522	300.130	510.942	490.863	348.368	289.904	72.156	130.838

Table C.58: Measured cross section in $p_{\mu,T}$ on water, in units of 10^{-42} cm^2/GeV/c/nucleon, and the absolute and fractional cross section uncertainties

Bin edges (GeV/c)	σ	Abs. Unc.	Frac. Stat. Unc.	Frac. Sys. Unc.	Frac. Flux Unc.
0.00-0.15	48.95	18.16	0.361	0.086	0.032
0.15-0.30	205.88	58.40	0.244	0.145	0.030
0.30-0.45	548.23	132.66	0.214	0.114	0.034
0.45-0.60	469.78	166.89	0.288	0.208	0.035
0.60-0.75	112.85	114.84	0.749	0.689	0.047
0.75-0.90	344.82	167.22	0.421	0.241	0.032
0.90-1.25	355.74	204.80	0.540	0.201	0.038
1.25-2.50	77.95	128.18	0.923	1.361	0.066

Table C.59: Statistical covariance matrix of measured cross section in $p_{\mu,T}$ on water, in units of 10^{-84} $(\mathrm{cm}^2/\mathrm{GeV/c/nucleon})^2$

Bin edges (GeV/c)	0.00-0.15	0.15-0.30	0.30-0.45	0.45-0.60	0.60-0.75	0.75-0.90	0.90-1.25	1.25-2.50
0.00-0.15	312.129	-7.872	-108.336	-16.451	-1.155	-1.404	0.165	0.221
0.15-0.30	-7.872	2517.246	146.375	-529.829	-113.687	-39.753	-123.597	-4.540
0.30-0.45	-108.336	146.375	13710.133	1947.909	-482.937	-858.259	-222.186	-201.092
0.45-0.60	-16.451	-529.829	1947.909	18276.357	3899.333	-981.154	-380.750	147.044
0.60-0.75	-1.155	-113.687	-482.937	3899.333	7144.261	5443.676	254.066	-239.731
0.75-0.90	-1.404	-39.753	-858.259	-981.154	5443.676	21050.961	1864.215	-283.797
0.90-1.25	0.165	-123.597	-222.186	-380.750	254.066	1864.215	36844.542	42.499
1.25-2.50	0.221	-4.540	-201.092	147.044	-239.731	-283.797	42.499	5173.235

Table C.60: Systematic covariance matrix of measured cross section in $p_{\mu,T}$ on water, in units of 10^{-84} $(\mathrm{cm}^2/\mathrm{GeV/c/nucleon})^2$

Bin edges (GeV/c)	0.00-0.15	0.15-0.30	0.30-0.45	0.45-0.60	0.60-0.75	0.75-0.90	0.90-1.25	1.25-2.50
0.00-0.15	17.659	104.856	115.257	57.747	-31.438	2.225	31.415	-15.773
0.15-0.30	104.856	893.876	1045.216	892.996	395.450	476.841	244.443	183.517
0.30-0.45	115.257	1045.216	3887.651	4374.788	2394.688	2524.122	1364.305	1881.899
0.45-0.60	57.747	892.996	4374.788	9574.998	5762.236	5627.477	1718.442	4799.821
0.60-0.75	-31.438	395.450	2394.688	5762.236	6045.001	5532.386	2413.121	3021.764
0.75-0.90	2.225	476.841	2524.122	5627.477	5532.386	6910.335	2523.603	2770.742
0.90-1.25	31.415	244.443	1364.305	1718.442	2413.121	2523.603	5097.378	389.213
1.25-2.50	-15.773	183.517	1881.899	4799.821	3021.764	2770.742	389.213	11257.217

Table C.61: Measured cross section in Q^2 on water, in units of 10^{-42} cm^2/GeV^2/nucleon, and the absolute and fractional cross section uncertainties

Bin edges (GeV^2)	σ	Abs. Unc.	Frac. Stat. Unc.	Frac. Sys. Unc.	Frac. Flux Unc.
0.000-0.025	48.35	17.68	0.356	0.083	0.032
0.025-0.050	60.49	21.26	0.305	0.175	0.033
0.050-0.100	160.28	46.38	0.262	0.123	0.028
0.100-0.200	446.61	116.04	0.226	0.127	0.034
0.200-0.300	357.19	106.22	0.252	0.157	0.034
0.300-1.300	635.34	324.63	0.378	0.344	0.038
1.300-2.000	395.61	264.96	0.612	0.273	0.035
2.000-3.000	60.70	108.30	0.883	1.550	0.072

Table C.62: Statistical covariance matrix of measured cross section in Q^2 on water, in units of 10^{-84} $(\mathrm{cm}^2/\mathrm{GeV}^2/\mathrm{nucleon})^2$

Bin edges (GeV^2)	0.000-0.025	0.025-0.050	0.050-0.100	0.100-0.200	0.200-0.300	0.300-1.300	1.300-2.000	2.000-3.000
0.000-0.025	296.215	38.938	-81.271	-48.320	-3.344	-5.685	0.066	-0.026
0.025-0.050	38.938	339.223	328.996	-197.005	-95.901	-20.153	-6.184	-0.057
0.050-0.100	-81.271	328.996	1761.229	504.354	-345.436	-293.228	-80.146	-3.608
0.100-0.200	-48.320	-197.005	504.354	10222.934	2945.256	-2445.436	-487.594	-67.465
0.200-0.300	-3.344	-95.901	-345.436	2945.256	8130.221	2534.670	-912.240	17.422
0.300-1.300	-5.685	-20.153	-293.228	-2445.436	2534.670	57535.247	1154.238	-345.996
1.300-2.000	0.066	-6.184	-80.146	-487.594	-912.240	1154.238	58540.595	53.230
2.000-3.000	-0.026	-0.057	-3.608	-67.465	17.422	-345.996	53.230	2871.574

Table C.63: Systematic covariance matrix of measured cross section in Q^2 on water, in units of 10^{-84} $(\mathrm{cm}^2/\mathrm{GeV}^2/\mathrm{nucleon})^2$

Bin edges (GeV^2)	0.000-0.025	0.025-0.050	0.050-0.100	0.100-0.200	0.200-0.300	0.300-1.300	1.300-2.000	2.000-3.000
0.000-0.025	16.254	34.463	61.964	114.183	53.783	-32.863	101.599	-15.720
0.025-0.050	34.463	112.568	180.464	328.816	147.127	136.801	18.625	-7.496
0.050-0.100	61.964	180.464	389.928	658.814	484.678	1408.940	544.107	191.809
0.100-0.200	114.183	328.816	658.814	3242.332	2285.134	5299.681	581.860	1360.068
0.200-0.300	53.783	147.127	484.678	2285.134	3153.346	8432.598	1066.234	1902.064
0.300-1.300	-32.863	136.801	1408.940	5299.681	8432.598	47850.795	10451.427	7501.581
1.300-2.000	101.599	18.625	544.107	581.860	1066.234	10451.427	11661.316	2274.081
2.000-3.000	-15.720	-7.496	191.809	1360.068	1902.064	7501.581	2274.081	8857.906

Table C.64: Measured cross section in W_{exp} on water, in units of 10^{-42} $cm^2/GeV/c^2$/nucleon, and the absolute and fractional cross section uncertainties

Bin edges (GeV/c^2)	σ	Abs. Unc.	Frac. Stat. Unc.	Frac. Sys. Unc.	Frac. Flux Unc.
0.9-1.1	318.89	278.68	0.840	0.241	0.037
1.1-1.2	784.92	186.08	0.189	0.144	0.033
1.2-1.3	389.25	206.96	0.409	0.340	0.033
1.3-1.4	160.05	152.68	0.695	0.653	0.034

Table C.65: Statistical covariance matrix of measured cross section in W_{exp} on water, in units of 10^{-84} $(cm^2/GeV/c^2/nucleon)^2$

Bin edges (GeV/c^2)	0.9-1.1	1.1-1.2	1.2-1.3	1.3-1.4
0.9-1.1	71772.455	-12968.164	-7780.373	-4307.838
1.1-1.2	-12968.164	21893.058	-6125.301	-2823.400
1.2-1.3	-7780.373	-6125.301	25336.473	13179.072
1.3-1.4	-4307.838	-2823.400	13179.072	12373.717

Table C.66: Systematic covariance matrix of measured cross section in W_{exp} on water, in units of 10^{-84} $(cm^2/GeV/c^2/nucleon)^2$

Bin edges (GeV/c^2)	0.9-1.1	1.1-1.2	1.2-1.3	1.3-1.4
0.9-1.1	5892.332	1142.665	1096.031	865.616
1.1-1.2	1142.665	12731.895	3398.008	500.749
1.2-1.3	1096.031	3398.008	17494.322	12887.881
1.3-1.4	865.616	500.749	12887.881	10937.902

Table C.67: Measured cross section in T_π on water, in units of 10^{-42} cm^2/GeV/nucleon, and the absolute and fractional cross section uncertainties

Bin edges (GeV)	σ	Abs. Unc.	Frac. Stat. Unc.	Frac. Sys. Unc.	Frac. Flux Unc.
0.035-0.100	998.50	253.86	0.226	0.117	0.032
0.100-0.150	401.01	97.10	0.196	0.142	0.035
0.150-0.200	285.41	90.84	0.257	0.188	0.034
0.200-0.350	383.17	166.90	0.345	0.266	0.032

Table C.68: Statistical covariance matrix of measured cross section in T_π on water, in units of 10^{-84} (cm^2/GeV/nucleon)^2

Bin edges (GeV)	0.035-0.100	0.100-0.150	0.150-0.200	0.200-0.350
0.035-0.100	50889.183	2492.142	-2001.282	-1455.416
0.100-0.150	2492.142	6188.155	605.237	-648.221
0.150-0.200	-2001.282	605.237	5379.231	1934.857
0.200-0.350	-1455.416	-648.221	1934.857	17429.099

Table C.69: Systematic covariance matrix of measured cross section in T_π on water, in units of 10^{-84} (cm^2/GeV/nucleon)^2

Bin edges (GeV)	0.035-0.100	0.100-0.150	0.150-0.200	0.200-0.350
0.035-0.100	13554.055	5364.056	3386.945	6147.677
0.100-0.150	5364.056	3239.447	2197.745	4098.671
0.150-0.200	3386.945	2197.745	2872.537	4540.256
0.200-0.350	6147.677	4098.671	4540.256	10426.692

Table C.70: Measured cross section in θ_π on water, in units of 10^{-42} cm^2/degree/nucleon, and the absolute and fractional cross section uncertainties

Bin edges (degree)	σ	Abs. Unc.	Frac. Stat. Unc.	Frac. Sys. Unc.	Frac. Flux Unc.
0-10	31.74	27.61	0.840	0.225	0.036
10-20	57.11	31.16	0.491	0.238	0.033
20-30	113.18	41.22	0.308	0.195	0.037
30-40	123.76	48.32	0.321	0.223	0.034
40-50	192.72	56.25	0.258	0.136	0.032
50-60	321.83	84.96	0.244	0.102	0.033
60-120	1263.54	381.70	0.283	0.106	0.036
120-135	156.93	85.24	0.507	0.196	0.036
135-150	125.23	55.90	0.428	0.127	0.029
150-165	47.12	41.91	0.814	0.358	0.030
165-180	3.47	5.28	1.442	0.487	0.037

Table C.71: Statistical covariance matrix of measured cross section in θ_π on water, in units of 10^{-84} $(\mathrm{cm}^2/\mathrm{degree}/\mathrm{nucleon})^2$

Bin edges (degree)	0-10	10-20	20-30	30-40	40-50	50-60	60-120	120-135	135-150	150-165	165-180
0-10	710.990	240.240	-91.078	44.777	-28.440	-37.948	-163.468	-22.083	-15.061	-4.319	9.438
10-20	240.240	785.602	212.521	-64.280	-60.620	29.693	-548.950	-49.008	21.448	-8.333	89.580
20-30	-91.078	212.521	1212.693	196.813	-59.658	-190.257	-131.936	-16.639	-50.540	-28.652	-5.580
30-40	44.777	-64.280	196.813	1575.884	376.253	-160.859	381.320	-140.665	-60.963	-21.035	-9.280
40-50	-28.440	-60.620	-59.658	376.253	2476.834	714.837	-10.514	-56.480	70.660	-127.461	-2.219
50-60	-37.948	29.693	-190.257	-160.859	714.837	6143.359	7778.428	-198.701	-378.338	-162.988	11.165
60-120	-163.468	-548.950	-131.936	381.320	-10.514	7778.428	127675.901	2713.492	1.350	372.377	-56.336
120-135	-22.083	-49.008	-16.639	-140.665	-56.480	-198.701	2713.492	6323.068	1056.822	-27.058	-4.630
135-150	-15.061	21.448	-50.540	-60.963	70.660	-378.338	1.350	1056.822	2872.917	1238.282	1.410
150-165	-4.319	-8.333	-28.652	-21.035	-127.461	-162.988	372.377	-27.058	1238.282	1472.308	-1.611
165-180	9.438	89.580	-5.580	-9.280	-2.219	11.165	-56.336	-4.630	1.410	-1.611	24.980

Table C.72: Systematic covariance matrix of measured cross section in θ_π on water, in units of 10^{-84} $(\text{cm}^2/\text{degree/nucleon})^2$

Bin edges (degree)	0-10	10-20	20-30	30-40	40-50	50-60	60-120	120-135	135-150	150-165	165-180
0-10	51.168	38.890	72.761	131.382	94.028	70.575	219.850	98.928	28.782	-7.920	3.757
10-20	38.890	185.379	242.318	211.546	207.981	182.264	942.317	138.725	68.641	64.160	10.644
20-30	72.761	242.318	486.616	432.882	453.888	460.605	1805.569	279.699	167.639	145.667	15.552
30-40	131.382	211.546	432.882	759.385	580.306	454.946	2022.227	210.377	221.326	102.552	9.782
40-50	94.028	207.981	453.888	580.306	687.111	636.174	2632.201	386.036	277.077	216.356	16.387
50-60	70.575	182.264	460.605	454.946	636.174	1075.071	3136.165	540.830	294.155	313.441	10.874
60-120	219.850	942.317	1805.569	2022.227	2632.201	3136.165	18015.439	1114.554	1502.135	1134.133	23.366
120-135	98.928	138.725	279.699	210.377	386.036	540.830	1114.554	943.544	133.547	140.841	19.456
135-150	28.782	68.641	167.639	221.326	277.077	294.155	1502.135	133.547	251.401	189.375	-6.543
150-165	-7.920	64.160	145.667	102.552	216.356	313.441	1134.133	140.841	189.375	284.189	-2.876
165-180	3.757	10.644	15.552	9.782	16.387	10.874	23.366	19.456	-6.543	-2.876	2.846

Table C.73: Measured cross section in p_μ on iron, in units of 10^{-42} cm^2/GeV/c/nucleon, and the absolute and fractional cross section uncertainties

Bin edges (GeV/c)	σ	Abs. Unc.	Frac. Stat. Unc.	Frac. Sys. Unc.	Frac. Flux Unc.
1.5-3.0	178.82	35.01	0.151	0.124	0.038
3.0-4.0	271.32	46.77	0.108	0.135	0.041
4.0-5.0	304.70	55.48	0.097	0.154	0.045
5.0-6.0	327.04	57.51	0.088	0.152	0.043
6.0-7.0	237.31	43.69	0.094	0.158	0.038
7.0-8.5	153.66	33.50	0.121	0.181	0.037
8.5-10.0	51.88	12.11	0.146	0.182	0.038
10.0-20.0	84.11	19.66	0.171	0.159	0.036

Table C.74: Statistical covariance matrix of measured cross section in p_μ on iron, in units of 10^{-84} (cm^2/GeV/c/nucleon)^2

Bin edges (GeV/c)	1.5-3.0	3.0-4.0	4.0-5.0	5.0-6.0	6.0-7.0	7.0-8.5	8.5-10.0	10.0-20.0
1.5-3.0	731.335	160.569	33.875	23.652	4.140	0.562	2.937	4.256
3.0-4.0	160.569	853.063	227.111	55.160	12.204	9.665	2.333	4.848
4.0-5.0	33.875	227.111	878.339	342.357	70.811	14.402	2.824	5.530
5.0-6.0	23.652	55.160	342.357	831.824	300.742	52.759	8.713	10.300
6.0-7.0	4.140	12.204	70.811	300.742	495.501	190.623	23.997	15.134
7.0-8.5	0.562	9.665	14.402	52.759	190.623	344.530	76.920	32.015
8.5-10.0	2.937	2.333	2.824	8.713	23.997	76.920	57.076	42.701
10.0-20.0	4.256	4.848	5.530	10.300	15.134	32.015	42.701	207.710

Table C.75: Systematic covariance matrix of measured cross section in p_μ on iron, in units of 10^{-84} (cm^2/GeV/c/nucleon)^2

Bin edges (GeV/c)	1.5-3.0	3.0-4.0	4.0-5.0	5.0-6.0	6.0-7.0	7.0-8.5	8.5-10.0	10.0-20.0
1.5-3.0	494.056	637.405	790.600	785.662	514.255	319.535	112.998	179.248
3.0-4.0	637.405	1334.621	1613.332	1703.558	1207.028	823.511	282.300	396.039
4.0-5.0	790.600	1613.332	2199.492	2268.663	1629.427	1097.583	359.968	508.189
5.0-6.0	785.662	1703.558	2268.663	2475.367	1805.414	1251.663	409.881	574.686
6.0-7.0	514.255	1207.028	1629.427	1805.414	1413.053	996.684	323.303	459.789
7.0-8.5	319.535	823.511	1097.583	1251.663	996.684	777.682	254.201	340.619
8.5-10.0	112.998	282.300	359.968	409.881	323.303	254.201	89.626	114.613
10.0-20.0	179.248	396.039	508.189	574.686	459.789	340.619	114.613	178.767

Table C.76: Measured cross section in θ_μ on iron, in units of 10^{-42} cm^2/degree/nucleon, and the absolute and fractional cross section uncertainties

Bin edges (degree)	σ	Abs. Unc.	Frac. Stat. Unc.	Frac. Sys. Unc.	Frac. Flux Unc.
0-2	105.67	18.87	0.133	0.119	0.034
2-3	130.90	20.93	0.130	0.093	0.036
3-4	170.56	29.20	0.129	0.113	0.035
4-5	150.96	34.28	0.157	0.164	0.036
5-6	126.77	40.75	0.206	0.246	0.039
6-8	323.78	78.00	0.141	0.196	0.041
8-10	297.56	81.55	0.176	0.210	0.045
10-13	291.19	110.82	0.270	0.268	0.053

Table C.77: Statistical covariance matrix of measured cross section in θ_μ on iron, in units of 10^{-84} (cm^2/degree/nucleon)^2

Bin edges (degree)	0-2	2-3	3-4	4-5	5-6	6-8	8-10	10-13
0-2	198.175	1.323	-23.266	-3.817	0.162	0.063	-0.022	-2.846
2-3	1.323	289.992	45.006	-35.711	-9.301	-0.598	-1.335	-3.151
3-4	-23.266	45.006	482.767	76.057	-48.084	-16.675	-0.112	-5.459
4-5	-3.817	-35.711	76.057	565.253	116.673	-69.989	-11.075	-0.014
5-6	0.162	-9.301	-48.084	116.673	684.132	75.300	-62.334	-4.683
6-8	0.063	-0.598	-16.675	-69.989	75.300	2069.660	-33.563	-129.864
8-10	-0.022	-1.335	-0.112	-11.075	-62.334	-33.563	2756.851	-94.372
10-13	-2.846	-3.151	-5.459	-0.014	-4.683	-129.864	-94.372	6168.079

Table C.78: Systematic covariance matrix of measured cross section in θ_μ on iron, in units of 10^{-84} (cm^2/degree/nucleon)^2

Bin edges (degree)	0-2	2-3	3-4	4-5	5-6	6-8	8-10	10-13
0-2	157.941	111.188	84.943	53.891	42.981	135.197	131.539	171.574
2-3	111.188	148.249	179.495	208.618	255.481	514.445	507.232	584.754
3-4	84.943	179.495	369.818	419.997	520.260	1078.660	1046.368	1293.961
4-5	53.891	208.618	419.997	609.643	727.569	1458.362	1406.096	1662.435
5-6	42.981	255.481	520.260	727.569	976.505	1848.929	1817.774	2130.901
6-8	135.197	514.445	1078.660	1458.362	1848.929	4014.154	3805.154	4550.917
8-10	131.539	507.232	1046.368	1406.096	1817.774	3805.154	3893.551	4588.952
10-13	171.574	584.754	1293.961	1662.435	2130.901	4550.917	4588.952	6112.221

Table C.79: Measured cross section in $p_{\mu,||}$ on iron, in units of 10^{-42} cm^2/GeV/c/nucleon, and the absolute and fractional cross section uncertainties

Bin edges (GeV/c)	σ	Abs. Unc.	Frac. Stat. Unc.	Frac. Sys. Unc.	Frac. Flux Unc.
1.5-3.0	176.11	36.27	0.158	0.132	0.039
3.0-4.0	287.97	48.36	0.104	0.132	0.041
4.0-5.0	303.02	55.32	0.098	0.154	0.045
5.0-6.0	319.80	56.90	0.090	0.154	0.043
6.0-7.0	233.31	43.02	0.094	0.159	0.038
7.0-8.5	151.26	33.11	0.120	0.183	0.037
8.5-10.0	49.83	11.41	0.148	0.174	0.038
10.0-20.0	85.51	19.70	0.170	0.155	0.036

Table C.80: Statistical covariance matrix of measured cross section in $p_{\mu,||}$ on iron, in units of 10^{-84} (cm^2/GeV/c/nucleon)^2

Bin edges (GeV/c)	1.5-3.0	3.0-4.0	4.0-5.0	5.0-6.0	6.0-7.0	7.0-8.5	8.5-10.0	10.0-20.0
1.5-3.0	776.642	160.678	32.071	25.183	3.833	0.470	3.004	5.369
3.0-4.0	160.678	901.287	231.843	56.044	11.053	8.762	2.264	5.025
4.0-5.0	32.071	231.843	880.983	341.136	72.194	13.887	2.590	4.803
5.0-6.0	25.183	56.044	341.136	821.752	292.880	53.170	9.406	10.316
6.0-7.0	3.833	11.053	72.194	292.880	476.755	186.471	23.615	15.683
7.0-8.5	0.470	8.762	13.887	53.170	186.471	331.538	71.884	28.643
8.5-10.0	3.004	2.264	2.590	9.406	23.615	71.884	54.742	41.701
10.0-20.0	5.369	5.025	4.803	10.316	15.683	28.643	41.701	212.245

Table C.81: Systematic covariance matrix of measured cross section in $p_{\mu,||}$ on iron, in units of 10^{-84} (cm^2/GeV/c/nucleon)^2

Bin edges (GeV/c)	1.5-3.0	3.0-4.0	4.0-5.0	5.0-6.0	6.0-7.0	7.0-8.5	8.5-10.0	10.0-20.0
1.5-3.0	539.204	699.599	868.838	852.609	545.284	356.291	122.069	197.857
3.0-4.0	699.599	1437.412	1667.502	1757.637	1257.137	876.808	285.846	426.751
4.0-5.0	868.838	1667.502	2179.852	2208.264	1551.124	1030.425	329.533	498.879
5.0-6.0	852.609	1757.637	2208.264	2416.090	1742.075	1205.954	379.483	559.562
6.0-7.0	545.284	1257.137	1551.124	1742.075	1373.564	976.403	298.843	449.973
7.0-8.5	356.291	876.808	1030.425	1205.954	976.403	764.834	231.459	332.484
8.5-10.0	122.069	285.846	329.533	379.483	298.843	231.459	75.498	102.355
10.0-20.0	197.857	426.751	498.879	559.562	449.973	332.484	102.355	175.661

Table C.82: Measured cross section in $p_{\mu,T}$ on iron, in units of 10^{-42} cm^2/GeV/c/nucleon, and the absolute and fractional cross section uncertainties

Bin edges (GeV/c)	σ	Abs. Unc.	Frac. Stat. Unc.	Frac. Sys. Unc.	Frac. Flux Unc.
0.00-0.15	49.74	11.46	0.187	0.135	0.036
0.15-0.30	187.70	26.95	0.108	0.095	0.034
0.30-0.45	310.40	50.57	0.108	0.122	0.036
0.45-0.60	373.39	72.74	0.109	0.162	0.038
0.60-0.75	243.28	74.86	0.160	0.263	0.040
0.75-0.90	168.37	68.09	0.213	0.344	0.044
0.90-1.25	187.02	77.45	0.282	0.304	0.049
1.25-2.50	38.62	36.97	0.856	0.428	0.044

Table C.83: Statistical covariance matrix of measured cross section in $p_{\mu,T}$ on iron, in units of 10^{-84} $(\mathrm{cm}^2/\mathrm{GeV/c/nucleon})^2$

Bin edges (GeV/c)	0.00-0.15	0.15-0.30	0.30-0.45	0.45-0.60	0.60-0.75	0.75-0.90	0.90-1.25	1.25-2.50
0.00-0.15	86.472	4.561	-21.536	-2.985	-0.241	-0.359	-0.162	-0.013
0.15-0.30	4.561	408.301	47.622	-67.450	-17.240	-2.998	-3.947	-3.141
0.30-0.45	-21.536	47.622	1123.473	128.266	-94.084	-41.591	-30.462	-2.188
0.45-0.60	-2.985	-67.450	128.266	1654.214	253.521	-111.529	-99.662	-6.717
0.60-0.75	-0.241	-17.240	-94.084	253.521	1516.244	367.032	-159.357	-6.414
0.75-0.90	-0.359	-2.998	-41.591	-111.529	367.032	1283.942	662.348	-85.713
0.90-1.25	-0.162	-3.947	-30.462	-99.662	-159.357	662.348	2772.521	272.072
1.25-2.50	-0.013	-3.141	-2.188	-6.717	-6.414	-85.713	272.072	1092.779

Table C.84: Systematic covariance matrix of measured cross section in $p_{\mu,T}$ on iron, in units of 10^{-84} $(\mathrm{cm}^2/\mathrm{GeV/c/nucleon})^2$

Bin edges (GeV/c)	0.00-0.15	0.15-0.30	0.30-0.45	0.45-0.60	0.60-0.75	0.75-0.90	0.90-1.25	1.25-2.50
0.00-0.15	44.834	79.353	-13.767	-55.619	-57.123	-67.518	-32.360	6.438
0.15-0.30	79.353	318.224	378.982	529.494	458.043	397.218	353.668	84.401
0.30-0.45	-13.767	378.982	1434.340	2171.579	2202.389	1901.588	1687.703	283.392
0.45-0.60	-55.619	529.494	2171.579	3636.624	3567.464	3200.224	2747.111	464.009
0.60-0.75	-57.123	458.043	2202.389	3567.464	4087.606	3508.142	3331.081	578.142
0.75-0.90	-67.518	397.218	1901.588	3200.224	3508.142	3351.908	3071.410	616.706
0.90-1.25	-32.360	353.668	1687.703	2747.111	3331.081	3071.410	3226.707	684.790
1.25-2.50	6.438	84.401	283.392	464.009	578.142	616.706	684.790	273.709

Table C.85: Measured cross section in Q^2 on iron, in units of 10^{-42} cm^2/GeV^2/nucleon, and the absolute and fractional cross section uncertainties

Bin edges (GeV^2)	σ	Abs. Unc.	Frac. Stat. Unc.	Frac. Sys. Unc.	Frac. Flux Unc.
0.000-0.025	48.11	10.63	0.177	0.132	0.036
0.025-0.050	54.94	9.95	0.145	0.108	0.035
0.050-0.100	128.42	19.58	0.124	0.089	0.034
0.100-0.200	255.70	39.98	0.106	0.115	0.035
0.200-0.300	250.23	43.70	0.121	0.126	0.037
0.300-0.400	181.56	41.21	0.138	0.180	0.038
0.400-0.500	117.09	35.12	0.171	0.246	0.040
0.500-0.700	167.10	64.27	0.203	0.327	0.042
0.700-1.000	168.48	66.94	0.226	0.327	0.044
1.000-1.300	93.42	40.88	0.327	0.290	0.048
1.300-2.000	49.85	45.44	0.683	0.604	0.074
2.000-3.000	29.40	30.91	0.924	0.502	0.047

Table C.86: Statistical covariance matrix of measured cross section in Q^2 on iron, in units of 10^{-84} $(\mathrm{cm}^2/\mathrm{GeV}^2/\mathrm{nucleon})^2$

Bin edges (GeV^2)	0.000-0.025	0.025-0.050	0.050-0.100	0.100-0.200	0.200-0.300	0.300-0.400	0.400-0.500	0.500-0.700	0.700-1.000	1.000-1.300	1.300-2.000	2.000-3.000
0.000-0.025	72.675	16.918	-14.220	-10.281	-1.038	-0.498	-0.018	-0.036	-0.244	-0.046	-0.002	0.011
0.025-0.050	16.918	63.692	39.140	-17.905	-8.718	-1.171	-0.556	-0.462	-0.537	-0.328	-0.453	-0.228
0.050-0.100	-14.220	39.140	253.688	80.986	-47.078	-19.554	-5.622	-2.877	-0.518	-0.596	-3.510	-2.777
0.100-0.200	-10.281	-17.905	80.986	733.191	162.340	-44.312	-41.317	-26.186	-17.415	-15.673	3.035	3.581
0.200-0.300	-1.038	-8.718	-47.078	162.340	910.213	246.812	2.645	-69.784	-40.578	-20.760	-23.377	-25.259
0.300-0.400	-0.498	-1.171	-19.554	-44.312	246.812	631.724	229.577	-26.921	-65.768	-19.456	-4.548	25.755
0.400-0.500	-0.018	-0.556	-5.622	-41.317	2.645	229.577	402.074	277.443	-33.721	-57.056	-10.895	10.731
0.500-0.700	-0.036	-0.462	-2.877	-26.186	-69.784	-26.921	277.443	1153.723	402.704	-36.101	-25.495	-20.652
0.700-1.000	-0.244	-0.537	-0.518	-17.415	-40.578	-65.768	-33.721	402.704	1451.741	561.009	21.086	-12.963
1.000-1.300	-0.046	-0.328	-0.596	-15.673	-20.760	-19.456	-57.056	-36.101	561.009	935.281	408.561	-4.537
1.300-2.000	-0.002	-0.453	-3.510	3.035	-23.377	-4.548	-10.895	-25.495	21.086	408.561	1157.615	335.174
2.000-3.000	0.011	-0.228	-2.777	3.581	-25.259	25.755	10.731	-20.652	-12.963	-4.537	335.174	737.971

Table C.87: Systematic covariance matrix of measured cross section in Q^2 on iron, in units of 10^{-84} $(\mathrm{cm}^2/\mathrm{GeV}^2/\mathrm{nucleon})^2$

Bin edges (GeV^2)	0.000-0.025	0.025-0.050	0.050-0.100	0.100-0.200	0.200-0.300	0.300-0.400	0.400-0.500	0.500-0.700	0.700-1.000	1.000-1.300	1.300-2.000	2.000-3.000
0.000-0.025	40.318	30.933	35.513	-0.417	-13.320	-27.417	-19.552	-55.707	-59.598	-14.609	-14.592	-9.305
0.025-0.050	30.933	35.341	51.306	57.918	45.038	42.417	35.228	59.230	54.316	29.692	24.580	12.681
0.050-0.100	35.513	51.306	129.679	275.273	257.978	255.705	219.912	399.526	386.053	179.912	148.515	71.877
0.100-0.200	-0.417	57.918	275.273	865.106	845.923	865.701	749.443	1394.038	1313.254	596.124	501.273	236.602
0.200-0.300	-13.320	45.038	257.978	845.923	999.096	976.302	851.434	1569.002	1508.836	659.545	559.546	282.307
0.300-0.400	-27.417	42.417	255.705	865.701	976.302	1066.531	893.346	1605.074	1571.897	663.419	564.513	304.473
0.400-0.500	-19.552	35.228	219.912	749.443	851.434	893.346	831.397	1511.381	1461.475	666.140	633.271	307.044
0.500-0.700	-55.707	59.230	399.526	1394.038	1569.002	1605.074	1511.381	2977.187	2880.506	1348.064	1298.297	601.462
0.700-1.000	-59.598	54.316	386.053	1313.254	1508.836	1571.897	1461.475	2880.506	3029.232	1367.674	1316.805	654.264
1.000-1.300	-14.609	29.692	179.912	596.124	659.545	663.419	666.140	1348.064	1367.674	735.596	750.647	325.042
1.300-2.000	-14.592	24.580	148.515	501.273	559.546	564.513	633.271	1298.297	1316.805	750.647	907.551	392.367
2.000-3.000	-9.305	12.681	71.877	236.602	282.307	304.473	307.044	601.462	654.264	325.042	392.367	217.435

Table C.88: Measured cross section in W_{exp} on iron, in units of 10^{-42} cm^2/GeV/c^2/nucleon, and the absolute and fractional cross section uncertainties

Bin edges (GeV/c^2)	σ	Abs. Unc.	Frac. Stat. Unc.	Frac. Sys. Unc.	Frac. Flux Unc.
0.9-1.1	56.83	31.36	0.489	0.256	0.058
1.1-1.2	374.43	60.25	0.129	0.096	0.037
1.2-1.3	653.64	142.35	0.101	0.193	0.036
1.3-1.4	456.94	178.96	0.182	0.347	0.036

Table C.89: Statistical covariance matrix of measured cross section in W_{exp} on iron, in units of 10^{-84} (cm^2/GeV/c^2/nucleon)^2

Bin edges (GeV/c^2)	0.9-1.1	1.1-1.2	1.2-1.3	1.3-1.4
0.9-1.1	771.007	155.990	-595.784	-194.049
1.1-1.2	155.990	2335.609	-1329.885	-2346.439
1.2-1.3	-595.784	-1329.885	4363.889	3110.752
1.3-1.4	-194.049	-2346.439	3110.752	6939.849

Table C.90: Systematic covariance matrix of measured cross section in W_{exp} on iron, in units of 10^{-84} (cm^2/GeV/c^2/nucleon)^2

Bin edges (GeV/c^2)	0.9-1.1	1.1-1.2	1.2-1.3	1.3-1.4
0.9-1.1	212.350	126.076	637.509	812.405
1.1-1.2	126.076	1294.491	111.547	-1026.185
1.2-1.3	637.509	111.547	15901.003	19252.277
1.3-1.4	812.405	-1026.185	19252.277	25085.504

Table C.91: Measured cross section in T_π on iron, in units of 10^{-42} cm^2/GeV/nucleon, and the absolute and fractional cross section uncertainties

Bin edges (GeV)	σ	Abs. Unc.	Frac. Stat. Unc.	Frac. Sys. Unc.	Frac. Flux Unc.
0.035-0.100	641.92	95.37	0.081	0.125	0.036
0.100-0.150	328.17	46.46	0.068	0.124	0.037
0.150-0.200	235.80	44.68	0.100	0.161	0.037
0.200-0.350	279.60	118.65	0.212	0.367	0.041

Table C.92: Statistical covariance matrix of measured cross section in T_π on iron, in units of 10^{-84} (cm^2/GeV/nucleon)^2

Bin edges (GeV)	0.035-0.100	0.100-0.150	0.150-0.200	0.200-0.350
0.035-0.100	2676.859	485.433	-175.626	-279.299
0.100-0.150	485.433	495.283	155.601	-67.292
0.150-0.200	-175.626	155.601	555.393	462.136
0.200-0.350	-279.299	-67.292	462.136	3521.984

Table C.93: Systematic covariance matrix of measured cross section in T_π on iron, in units of 10^{-84} (cm^2/GeV/nucleon)^2

Bin edges (GeV)	0.035-0.100	0.100-0.150	0.150-0.200	0.200-0.350
0.035-0.100	6419.091	2901.122	2200.381	5122.192
0.100-0.150	2901.122	1663.160	1401.706	3328.267
0.150-0.200	2200.381	1401.706	1440.898	3735.106
0.200-0.350	5122.192	3328.267	3735.106	10556.714

Table C.94: Measured cross section in θ_π on iron, in units of 10^{-42} cm^2/degree/nucleon, and the absolute and fractional cross section uncertainties

Bin edges (degree)	σ	Abs. Unc.	Frac. Stat. Unc.	Frac. Sys. Unc.	Frac. Flux Unc.
0-10	37.40	17.58	0.435	0.179	0.043
10-20	68.81	21.17	0.233	0.200	0.037
20-30	96.76	21.26	0.137	0.172	0.036
30-40	119.94	23.92	0.118	0.161	0.037
40-50	144.37	27.52	0.107	0.158	0.038
50-60	182.74	32.05	0.103	0.142	0.038
60-120	874.00	147.99	0.105	0.133	0.037
120-135	103.37	26.61	0.188	0.176	0.034
135-150	55.93	17.74	0.249	0.197	0.037
150-165	29.29	15.84	0.489	0.232	0.035
165-180	17.21	20.16	1.069	0.478	0.036

Table C.95: Statistical covariance matrix of measured cross section in θ_π on iron, in units of 10^{-84} $(\mathrm{cm}^2/\mathrm{degree}/\mathrm{nucleon})^2$

Bin edges (degree)	0-10	10-20	20-30	30-40	40-50	50-60	60-120	120-135	135-150	150-165	165-180
0-10	264.269	90.286	-6.507	-2.031	1.291	-5.366	-24.237	-4.946	6.746	8.514	-0.304
10-20	90.286	257.977	66.095	-11.236	-17.312	-9.906	-28.174	-6.536	-4.134	-2.822	-1.231
20-30	-6.507	66.095	174.915	61.591	-13.671	-18.336	-47.886	-9.772	-0.564	1.707	-1.897
30-40	-2.031	-11.236	61.591	201.081	88.310	-19.189	-104.289	-13.094	2.559	2.408	-3.765
40-50	1.291	-17.312	-13.671	88.310	236.784	115.641	-81.062	-9.301	-0.558	-4.798	-3.949
50-60	-5.366	-9.906	-18.336	-19.189	115.641	352.616	585.621	-22.902	-19.300	-12.218	-0.404
60-120	-24.237	-28.174	-47.886	-104.289	-81.062	585.621	8391.807	292.473	-31.049	-6.656	49.937
120-135	-4.946	-6.536	-9.772	-13.094	-9.301	-22.902	292.473	376.337	99.013	8.456	-30.039
135-150	6.746	-4.134	-0.564	2.559	-0.558	-19.300	-31.049	99.013	193.349	95.392	27.506
150-165	8.514	-2.822	1.707	2.408	-4.798	-12.218	-6.656	8.456	95.392	204.929	151.074
165-180	-0.304	-1.231	-1.897	-3.765	-3.949	-0.404	49.937	-30.039	27.506	151.074	338.547

Table C.96: Systematic covariance matrix of measured cross section in θ_π on iron, in units of 10^{-84} $(\mathrm{cm}^2/\mathrm{degree}/\mathrm{nucleon})^2$

Bin edges (degree)	0-10	10-20	20-30	30-40	40-50	50-60	60-120	120-135	135-150	150-165	165-180
0-10	44.927	73.140	84.962	93.871	111.180	114.052	477.869	93.827	48.997	28.482	-20.462
10-20	73.140	190.133	207.509	224.581	238.188	207.659	736.547	162.780	80.740	55.858	-34.464
20-30	84.962	207.509	277.140	303.847	328.881	313.701	1210.485	230.917	128.231	78.792	-26.309
30-40	93.871	224.581	303.847	371.160	412.805	415.782	1671.006	265.489	145.040	87.590	-13.705
40-50	111.180	238.188	328.881	412.805	520.737	559.230	2246.993	359.752	197.705	107.217	-14.968
50-60	114.052	207.659	313.701	415.782	559.230	674.829	2859.786	405.175	216.838	108.668	-0.790
60-120	477.869	736.547	1210.485	1671.006	2246.993	2859.786	13510.024	1576.145	796.295	376.405	90.966
120-135	93.827	162.780	230.917	265.489	359.752	405.175	1576.145	331.973	181.790	103.399	-26.985
135-150	48.997	80.740	128.231	145.040	197.705	216.838	796.295	181.790	121.278	62.691	-15.939
150-165	28.482	55.858	78.792	87.590	107.217	108.668	376.405	103.399	62.691	46.040	-5.401
165-180	-20.462	-34.464	-26.309	-13.705	-14.968	-0.790	90.966	-26.985	-15.939	-5.401	67.685

Table C.97: Measured cross section in p_μ on lead, in units of 10^{-42} cm^2/GeV/c/nucleon, and the absolute and fractional cross section uncertainties

Bin edges (GeV/c)	σ	Abs. Unc.	Frac. Stat. Unc.	Frac. Sys. Unc.	Frac. Flux Unc.
1.5-3.0	83.42	22.81	0.239	0.134	0.042
3.0-4.0	171.55	33.00	0.144	0.128	0.043
4.0-5.0	208.69	37.51	0.111	0.142	0.044
5.0-6.0	207.23	38.41	0.103	0.154	0.042
6.0-7.0	131.30	26.34	0.120	0.160	0.040
7.0-8.5	89.81	18.42	0.138	0.152	0.040
8.5-10.0	30.39	7.27	0.187	0.150	0.044
10.0-20.0	33.11	13.18	0.342	0.204	0.066

Table C.98: Statistical covariance matrix of measured cross section in p_μ on lead, in units of 10^{-84} (cm^2/GeV/c/nucleon)^2

Bin edges (GeV/c)	1.5-3.0	3.0-4.0	4.0-5.0	5.0-6.0	6.0-7.0	7.0-8.5	8.5-10.0	10.0-20.0
1.5-3.0	395.873	86.970	19.263	3.219	9.210	1.407	0.204	0.133
3.0-4.0	86.970	610.446	173.769	29.891	8.550	4.649	1.157	0.686
4.0-5.0	19.263	173.769	531.835	186.597	41.435	18.098	4.991	1.934
5.0-6.0	3.219	29.891	186.597	459.518	180.682	41.897	5.315	5.537
6.0-7.0	9.210	8.550	41.435	180.682	249.579	108.689	11.964	5.843
7.0-8.5	1.407	4.649	18.098	41.897	108.689	153.578	37.453	18.639
8.5-10.0	0.204	1.157	4.991	5.315	11.964	37.453	32.123	31.154
10.0-20.0	0.133	0.686	1.934	5.537	5.843	18.639	31.154	127.874

Table C.99: Systematic covariance matrix of measured cross section in p_μ on lead, in units of 10^{-84} (cm^2/GeV/c/nucleon)^2

Bin edges (GeV/c)	1.5-3.0	3.0-4.0	4.0-5.0	5.0-6.0	6.0-7.0	7.0-8.5	8.5-10.0	10.0-20.0
1.5-3.0	124.348	211.976	270.367	286.192	161.159	75.758	21.095	41.473
3.0-4.0	211.976	478.475	601.588	629.755	363.979	191.658	51.357	93.024
4.0-5.0	270.367	601.588	875.472	908.163	533.176	299.467	73.970	132.438
5.0-6.0	286.192	629.755	908.163	1015.697	626.884	352.634	94.571	153.974
6.0-7.0	161.159	363.979	533.176	626.884	444.070	263.186	78.779	110.257
7.0-8.5	75.758	191.658	299.467	352.634	263.186	185.732	55.598	67.734
8.5-10.0	21.095	51.357	73.970	94.571	78.779	55.598	20.721	22.934
10.0-20.0	41.473	93.024	132.438	153.974	110.257	67.734	22.934	45.838

Table C.100: Measured cross section in θ_μ on lead, in units of 10^{-42} cm^2/degree/nucleon, and the absolute and fractional cross section uncertainties

Bin edges (degree)	σ	Abs. Unc.	Frac. Stat. Unc.	Frac. Sys. Unc.	Frac. Flux Unc.
0-2	55.83	15.61	0.216	0.178	0.036
2-3	83.11	16.49	0.169	0.104	0.036
3-4	79.77	17.81	0.182	0.129	0.036
4-5	90.87	21.09	0.184	0.142	0.035
5-6	81.23	23.40	0.222	0.184	0.038
6-8	163.94	44.17	0.193	0.188	0.042
8-10	189.88	52.55	0.204	0.187	0.045
10-13	263.09	83.82	0.252	0.195	0.045

Table C.101: Statistical covariance matrix of measured cross section in θ_μ on lead, in units of 10^{-84} (cm^2/degree/nucleon)^2

Bin edges (degree)	0-2	2-3	3-4	4-5	5-6	6-8	8-10	10-13
0-2	145.136	2.480	-14.662	-2.026	0.128	-0.045	-0.221	-1.302
2-3	2.480	197.696	29.780	-22.236	-7.005	-0.102	-0.248	-1.402
3-4	-14.662	29.780	210.630	34.474	-21.731	-7.973	-0.212	-2.000
4-5	-2.026	-22.236	34.474	278.115	59.543	-35.517	-5.699	1.029
5-6	0.128	-7.005	-21.731	59.543	325.531	30.016	-31.542	-3.668
6-8	-0.045	-0.102	-7.973	-35.517	30.016	997.586	-4.747	-86.749
8-10	-0.221	-0.248	-0.212	-5.699	-31.542	-4.747	1500.726	-56.051
10-13	-1.302	-1.402	-2.000	1.029	-3.668	-86.749	-56.051	4398.989

Table C.102: Systematic covariance matrix of measured cross section in θ_μ on lead, in units of 10^{-84} (cm^2/degree/nucleon)^2

Bin edges (degree)	0-2	2-3	3-4	4-5	5-6	6-8	8-10	10-13
0-2	98.560	53.536	39.246	34.628	19.802	36.872	39.620	65.995
2-3	53.536	74.215	76.444	76.913	91.315	178.689	201.216	248.860
3-4	39.246	76.444	106.607	118.372	139.111	284.455	301.228	424.739
4-5	34.628	76.913	118.372	166.791	171.277	339.026	378.707	525.577
5-6	19.802	91.315	139.111	171.277	222.176	434.646	458.295	634.728
6-8	36.872	178.689	284.455	339.026	434.646	953.204	1024.559	1402.579
8-10	39.620	201.216	301.228	378.707	458.295	1024.559	1260.853	1604.782
10-13	65.995	248.860	424.739	525.577	634.728	1402.579	1604.782	2626.499

Table C.103: Measured cross section in $p_{\mu,||}$ on lead, in units of 10^{-42} cm^2/GeV/c/nucleon, and the absolute and fractional cross section uncertainties

Bin edges (GeV/c)	σ	Abs. Unc.	Frac. Stat. Unc.	Frac. Sys. Unc.	Frac. Flux Unc.
1.5-3.0	92.09	24.25	0.228	0.132	0.041
3.0-4.0	172.94	33.78	0.143	0.133	0.043
4.0-5.0	205.59	37.78	0.113	0.145	0.044
5.0-6.0	205.27	37.90	0.104	0.153	0.042
6.0-7.0	127.79	25.48	0.121	0.158	0.040
7.0-8.5	88.37	17.99	0.137	0.150	0.040
8.5-10.0	30.38	7.08	0.183	0.145	0.043
10.0-20.0	33.24	13.11	0.338	0.203	0.065

Table C.104: Statistical covariance matrix of measured cross section in $p_{\mu,||}$ on lead, in units of 10^{-84} $(cm^2/GeV/c/nucleon)^2$

Bin edges (GeV/c)	1.5-3.0	3.0-4.0	4.0-5.0	5.0-6.0	6.0-7.0	7.0-8.5	8.5-10.0	10.0-20.0
1.5-3.0	441.252	86.372	18.733	3.841	9.559	1.431	0.203	0.143
3.0-4.0	86.372	615.777	159.197	34.567	9.389	6.835	1.530	0.709
4.0-5.0	18.733	159.197	539.275	188.186	42.037	17.093	4.933	1.951
5.0-6.0	3.841	34.567	188.186	456.046	169.288	39.769	5.143	5.359
6.0-7.0	9.559	9.389	42.037	169.288	240.333	108.560	12.578	5.489
7.0-8.5	1.431	6.835	17.093	39.769	108.560	147.062	37.190	19.727
8.5-10.0	0.203	1.530	4.933	5.143	12.578	37.190	30.870	31.152
10.0-20.0	0.143	0.709	1.951	5.359	5.489	19.727	31.152	126.219

Table C.105: Systematic covariance matrix of measured cross section in $p_{\mu,||}$ on lead, in units of 10^{-84} $(cm^2/GeV/c/nucleon)^2$

Bin edges (GeV/c)	1.5-3.0	3.0-4.0	4.0-5.0	5.0-6.0	6.0-7.0	7.0-8.5	8.5-10.0	10.0-20.0
1.5-3.0	146.756	243.169	292.404	304.490	168.948	82.979	23.965	44.247
3.0-4.0	243.169	525.397	629.090	639.398	358.007	188.128	50.084	93.998
4.0-5.0	292.404	629.090	888.356	896.973	521.636	302.125	75.114	132.259
5.0-6.0	304.490	639.398	896.973	980.032	598.811	348.431	94.010	151.975
6.0-7.0	168.948	358.007	521.636	598.811	408.827	247.576	73.708	106.231
7.0-8.5	82.979	188.128	302.125	348.431	247.576	176.433	51.458	67.856
8.5-10.0	23.965	50.084	75.114	94.010	73.708	51.458	19.305	22.751
10.0-20.0	44.247	93.998	132.259	151.975	106.231	67.856	22.751	45.522

Table C.106: Measured cross section in $p_{\mu,T}$ on lead, in units of 10^{-42} cm^2/GeV/c/nucleon, and the absolute and fractional cross section uncertainties

Bin edges (GeV/c)	σ	Abs. Unc.	Frac. Stat. Unc.	Frac. Sys. Unc.	Frac. Flux Unc.
0.00-0.15	28.25	11.33	0.313	0.251	0.038
0.15-0.30	100.37	20.62	0.162	0.126	0.036
0.30-0.45	193.54	30.85	0.115	0.110	0.036
0.45-0.60	174.52	39.18	0.148	0.169	0.037
0.60-0.75	135.49	45.48	0.210	0.262	0.041
0.75-0.90	97.46	37.47	0.260	0.283	0.047
0.90-1.25	187.28	54.04	0.225	0.181	0.044
1.25-2.50	57.36	34.81	0.548	0.261	0.046

Table C.107: Statistical covariance matrix of measured cross section in $p_{\mu,T}$ on lead, in units of 10^{-84} $(\mathrm{cm}^2/\mathrm{GeV/c/nucleon})^2$

Bin edges (GeV/c)	0.00-0.15	0.15-0.30	0.30-0.45	0.45-0.60	0.60-0.75	0.75-0.90	0.90-1.25	1.25-2.50
0.00-0.15	78.226	8.376	-15.749	-2.951	0.086	-0.462	0.034	-0.783
0.15-0.30	8.376	265.752	29.746	-39.966	-10.652	-1.362	-2.182	-0.969
0.30-0.45	-15.749	29.746	497.413	91.150	-64.082	-21.133	-11.724	-1.469
0.45-0.60	-2.951	-39.966	91.150	669.263	174.478	-39.419	-57.519	-8.476
0.60-0.75	0.086	-10.652	-64.082	174.478	810.430	176.346	-51.327	-18.976
0.75-0.90	-0.462	-1.362	-21.133	-39.419	176.346	641.687	278.820	-71.844
0.90-1.25	0.034	-2.182	-11.724	-57.519	-51.327	278.820	1774.439	194.275
1.25-2.50	-0.783	-0.969	-1.469	-8.476	-18.976	-71.844	194.275	987.339

Table C.108: Systematic covariance matrix of measured cross section in $p_{\mu,T}$ on lead, in units of 10^{-84} $(\mathrm{cm}^2/\mathrm{GeV/c/nucleon})^2$

Bin edges (GeV/c)	0.00-0.15	0.15-0.30	0.30-0.45	0.45-0.60	0.60-0.75	0.75-0.90	0.90-1.25	1.25-2.50
0.00-0.15	50.131	66.524	17.876	-26.987	-37.558	-11.133	-5.338	3.353
0.15-0.30	66.524	159.270	180.541	169.244	157.542	143.217	144.817	37.686
0.30-0.45	17.876	180.541	454.067	574.035	583.386	440.191	429.987	86.150
0.45-0.60	-26.987	169.244	574.035	866.052	925.737	677.326	647.210	118.247
0.60-0.75	-37.558	157.542	583.386	925.737	1257.789	909.915	951.307	149.634
0.75-0.90	-11.133	143.217	440.191	677.326	909.915	762.157	835.347	135.866
0.90-1.25	-5.338	144.817	429.987	647.210	951.307	835.347	1146.337	140.097
1.25-2.50	3.353	37.686	86.150	118.247	149.634	135.866	140.097	224.597

Table C.109: Measured cross section in Q^2 on lead, in units of 10^{-42} $\mathrm{cm}^2/\mathrm{GeV}^2/\mathrm{nucleon}$, and the absolute and fractional cross section uncertainties

Bin edges (GeV^2)	σ	Abs. Unc.	Frac. Stat. Unc.	Frac. Sys. Unc.	Frac. Flux Unc.
0.000-0.025	26.71	10.73	0.313	0.252	0.038
0.025-0.050	33.90	8.57	0.207	0.145	0.036
0.050-0.100	65.61	14.04	0.179	0.117	0.036
0.100-0.200	152.45	25.20	0.122	0.111	0.036
0.200-0.300	118.30	25.50	0.148	0.157	0.038
0.300-0.400	79.80	21.81	0.200	0.186	0.037
0.400-0.500	72.54	20.95	0.203	0.205	0.038
0.500-0.700	98.75	36.26	0.236	0.282	0.042
0.700-1.000	106.82	38.76	0.251	0.262	0.045
1.000-1.300	99.69	31.19	0.261	0.173	0.039
1.300-2.000	62.18	36.60	0.492	0.323	0.058
2.000-3.000	80.01	76.98	0.915	0.296	0.045

Table C.110: Statistical covariance matrix of measured cross section in Q^2 on lead, in units of 10^{-84} $(\mathrm{cm}^2/\mathrm{GeV}^2/\mathrm{nucleon})^2$

Bin edges (GeV^2)	0.000-0.025	0.025-0.050	0.050-0.100	0.100-0.200	0.200-0.300	0.300-0.400	0.400-0.500	0.500-0.700	0.700-1.000	1.000-1.300	1.300-2.000	2.000-3.000
0.000-0.025	69.901	14.660	-10.631	-7.152	-0.350	-0.582	-0.304	0.362	-0.651	0.422	-0.375	-0.691
0.025-0.050	14.660	49.322	28.920	-12.059	-6.635	-1.286	-0.372	-0.226	-0.336	-0.179	-0.173	-0.155
0.050-0.100	-10.631	28.920	137.984	47.220	-25.387	-7.854	-3.696	-1.579	-0.611	-1.178	-0.957	0.112
0.100-0.200	-7.152	-12.059	47.220	347.744	83.634	-21.517	-25.960	-15.202	-7.459	-4.421	-0.541	-1.920
0.200-0.300	-0.350	-6.635	-25.387	83.634	305.607	123.571	9.254	-29.071	-12.340	-0.852	-2.832	-2.012
0.300-0.400	-0.582	-1.286	-7.854	-21.517	123.571	255.726	144.910	0.600	-32.766	-17.752	-16.409	-1.055
0.400-0.500	-0.304	-0.372	-3.696	-25.960	9.254	144.910	216.851	163.408	-10.406	-26.937	-11.704	-7.109
0.500-0.700	0.362	-0.226	-1.579	-15.202	-29.071	0.600	163.408	541.015	229.389	-36.389	-2.314	-21.975
0.700-1.000	-0.651	-0.336	-0.611	-7.459	-12.340	-32.766	-10.406	229.389	717.470	241.129	-13.823	-97.343
1.000-1.300	0.422	-0.179	-1.178	-4.421	-0.852	-17.752	-26.937	-36.389	241.129	676.546	123.136	-68.843
1.300-2.000	-0.375	-0.173	-0.957	-0.541	-2.832	-16.409	-11.704	-2.314	-13.823	123.136	936.756	212.755
2.000-3.000	-0.691	-0.155	0.112	-1.920	-2.012	-1.055	-7.109	-21.975	-97.343	-68.843	212.755	5364.548

Table C.111: Systematic covariance matrix of measured cross section in Q^2 on lead, in units of 10^{-84} $(\mathrm{cm}^2/\mathrm{GeV}^2/\mathrm{nucleon})^2$

Bin edges (GeV^2)	0.000-0.025	0.025-0.050	0.050-0.100	0.100-0.200	0.200-0.300	0.300-0.400	0.400-0.500	0.500-0.700	0.700-1.000	1.000-1.300	1.300-2.000	2.000-3.000
0.000-0.025	45.255	29.002	29.204	20.088	-15.498	-14.302	-13.223	-20.338	-6.395	0.350	-14.773	21.319
0.025-0.050	29.002	24.090	29.477	37.183	13.045	7.914	8.043	19.909	25.884	20.656	-1.458	37.405
0.050-0.100	29.204	29.477	59.016	112.392	91.044	66.081	66.993	117.589	113.747	76.107	23.131	56.779
0.100-0.200	20.088	37.183	112.392	287.443	259.434	210.786	210.902	360.393	324.419	193.778	101.119	119.133
0.200-0.300	-15.498	13.045	91.044	259.434	344.758	239.312	235.690	409.382	381.602	216.285	148.075	92.133
0.300-0.400	-14.302	7.914	66.081	210.786	239.312	219.824	211.083	373.751	328.701	178.135	151.191	67.913
0.400-0.500	-13.223	8.043	66.993	210.902	235.690	211.083	221.978	393.954	351.285	194.192	166.449	53.684
0.500-0.700	-20.338	19.909	117.589	360.393	409.382	373.751	393.954	774.130	726.558	368.401	378.893	112.666
0.700-1.000	-6.395	25.884	113.747	324.419	381.602	328.701	351.285	726.558	785.250	409.779	430.315	157.211
1.000-1.300	0.350	20.656	76.107	193.778	216.285	178.135	194.192	368.401	409.779	296.344	226.977	63.143
1.300-2.000	-14.773	-1.458	23.131	101.119	148.075	151.191	166.449	378.893	430.315	226.977	403.117	5.956
2.000-3.000	21.319	37.405	56.779	119.133	92.133	67.913	53.684	112.666	157.211	63.143	5.956	561.179

Table C.112: Measured cross section in W_{exp} on lead, in units of 10^{-42} $cm^2/GeV/c^2$/nucleon, and the absolute and fractional cross section uncertainties

Bin edges (GeV/c^2)	σ	Abs. Unc.	Frac. Stat. Unc.	Frac. Sys. Unc.	Frac. Flux Unc.
0.9-1.1	59.51	29.83	0.430	0.258	0.055
1.1-1.2	100.86	27.16	0.245	0.111	0.046
1.2-1.3	385.75	64.36	0.092	0.139	0.037
1.3-1.4	494.90	137.15	0.167	0.221	0.032

Table C.113: Statistical covariance matrix of measured cross section in W_{exp} on lead, in units of 10^{-84} $(cm^2/GeV/c^2/nucleon)^2$

Bin edges (GeV/c^2)	0.9-1.1	1.1-1.2	1.2-1.3	1.3-1.4
0.9-1.1	654.646	208.411	-342.372	-548.264
1.1-1.2	208.411	611.465	232.477	-1333.169
1.2-1.3	-342.372	232.477	1273.201	741.110
1.3-1.4	-548.264	-1333.169	741.110	6823.774

Table C.114: Systematic covariance matrix of measured cross section in W_{exp} on lead, in units of 10^{-84} $(cm^2/GeV/c^2/nucleon)^2$

Bin edges (GeV/c^2)	0.9-1.1	1.1-1.2	1.2-1.3	1.3-1.4
0.9-1.1	235.223	95.958	1.797	87.468
1.1-1.2	95.958	126.030	210.858	148.766
1.2-1.3	1.797	210.858	2868.984	5430.435
1.3-1.4	87.468	148.766	5430.435	11986.374

Table C.115: Measured cross section in T_π on lead, in units of 10^{-42} cm^2/GeV/nucleon, and the absolute and fractional cross section uncertainties

Bin edges (GeV)	σ	Abs. Unc.	Frac. Stat. Unc.	Frac. Sys. Unc.	Frac. Flux Unc.
0.035-0.100	339.69	51.03	0.115	0.097	0.036
0.100-0.150	178.43	26.65	0.094	0.116	0.038
0.150-0.200	131.95	27.32	0.133	0.159	0.038
0.200-0.350	296.19	93.50	0.187	0.254	0.040

Table C.116: Statistical covariance matrix of measured cross section in T_π on lead, in units of 10^{-84} (cm^2/GeV/nucleon)^2

Bin edges (GeV)	0.035-0.100	0.100-0.150	0.150-0.200	0.200-0.350
0.035-0.100	1518.440	244.154	-82.221	-234.898
0.100-0.150	244.154	281.144	75.846	-64.480
0.150-0.200	-82.221	75.846	308.231	229.833
0.200-0.350	-234.898	-64.480	229.833	3067.420

Table C.117: Systematic covariance matrix of measured cross section in T_π on lead, in units of 10^{-84} (cm^2/GeV/nucleon)^2

Bin edges (GeV)	0.035-0.100	0.100-0.150	0.150-0.200	0.200-0.350
0.035-0.100	1085.605	618.309	528.783	1616.771
0.100-0.150	618.309	429.183	398.313	1283.558
0.150-0.200	528.783	398.313	438.204	1423.444
0.200-0.350	1616.771	1283.558	1423.444	5674.185

Table C.118: Measured cross section in θ_π on lead, in units of 10^{-42} cm^2/degree/nucleon, and the absolute and fractional cross section uncertainties

Bin edges (degree)	σ	Abs. Unc.	Frac. Stat. Unc.	Frac. Sys. Unc.	Frac. Flux Unc.
0-10	24.37	12.57	0.476	0.200	0.044
10-20	49.46	16.35	0.251	0.215	0.040
20-30	55.17	13.67	0.172	0.179	0.040
30-40	82.00	15.36	0.124	0.140	0.038
40-50	85.17	16.30	0.121	0.148	0.039
50-60	74.80	16.84	0.157	0.162	0.040
60-120	399.07	76.95	0.144	0.129	0.037
120-135	69.18	14.47	0.171	0.121	0.034
135-150	49.27	12.14	0.194	0.152	0.033
150-165	26.10	10.26	0.352	0.176	0.036
165-180	5.20	5.38	0.967	0.366	0.044

Table C.119: Statistical covariance matrix of measured cross section in θ_π on lead, in units of 10^{-84} $(\text{cm}^2/\text{degree}/\text{nucleon})^2$

Bin edges (degree)	0-10	10-20	20-30	30-40	40-50	50-60	60-120	120-135	135-150	150-165	165-180
0-10	134.280	53.404	4.529	-1.514	-3.589	-4.087	-17.625	-2.600	-2.199	4.847	-0.483
10-20	53.404	154.461	49.827	-2.469	-11.876	-9.049	-27.375	-5.633	-4.649	-0.134	-0.686
20-30	4.529	49.827	89.582	43.559	-1.088	-10.263	-30.342	-4.726	-1.705	1.691	0.535
30-40	-1.514	-2.469	43.559	103.869	55.233	4.050	-62.648	-8.988	0.248	-0.008	-1.916
40-50	-3.589	-11.876	-1.088	55.233	106.711	67.200	53.861	-2.853	-3.692	-2.061	-2.483
50-60	-4.087	-9.049	-10.263	4.050	67.200	137.057	291.218	-0.761	-11.818	-4.276	-2.505
60-120	-17.625	-27.375	-30.342	-62.648	53.861	291.218	3283.581	152.210	6.814	-5.687	27.648
120-135	-2.600	-5.633	-4.726	-8.988	-2.853	-0.761	152.210	139.432	56.744	1.010	14.638
135-150	-2.199	-4.649	-1.705	0.248	-3.692	-11.818	6.814	56.744	91.520	42.832	3.450
150-165	4.847	-0.134	1.691	-0.008	-2.061	-4.276	-5.687	1.010	42.832	84.295	-0.975
165-180	-0.483	-0.686	0.535	-1.916	-2.483	-2.505	27.648	14.638	3.450	-0.975	25.321

Table C.120: Systematic covariance matrix of measured cross section in θ_π on lead, in units of 10^{-84} $(\text{cm}^2/\text{degree/nucleon})^2$

Bin edges (degree)	0-10	10-20	20-30	30-40	40-50	50-60	60-120	120-135	135-150	150-165	165-180
0-10	23.763	38.627	39.288	44.959	46.046	37.907	161.131	31.474	27.635	12.359	-0.402
10-20	38.627	112.878	94.809	89.930	80.107	61.233	239.268	53.310	45.253	21.097	-2.828
20-30	39.288	94.809	97.403	102.018	96.959	77.996	297.893	64.011	51.503	23.746	-0.890
30-40	44.959	89.930	102.018	132.014	136.991	123.425	489.115	76.820	66.079	29.893	3.065
40-50	46.046	80.107	96.959	136.991	159.085	143.463	583.242	83.653	74.149	34.623	0.889
50-60	37.907	61.233	77.996	123.425	143.463	146.525	584.904	64.250	58.723	26.698	5.717
60-120	161.131	239.268	297.893	489.115	583.242	584.904	2636.955	271.119	272.099	114.719	17.994
120-135	31.474	53.310	64.011	76.820	83.653	64.250	271.119	69.824	55.537	26.621	-0.603
135-150	27.635	45.253	51.503	66.079	74.149	58.723	272.099	55.537	55.870	27.861	-1.506
150-165	12.359	21.097	23.746	29.893	34.623	26.698	114.719	26.621	27.861	21.068	-0.746
165-180	-0.402	-2.828	-0.890	3.065	0.889	5.717	17.994	-0.603	-1.506	-0.746	3.634

Appendix D

Tables of measured cross section ratios, uncertainties, and covariance matrices

Table D.1: Measured cross section ratio of carbon over scintillator in p_μ, and the absolute and fractional cross section ratio uncertainties

Bin edges (GeV/c)	Ratio	Abs. Unc.	Frac. Stat. Unc.	Frac. Sys. Unc.	Frac. Flux Unc.
1.5-3.0	1.22	0.443	0.341	0.120	0.004
3.0-4.0	1.27	0.297	0.209	0.104	0.003
4.0-5.0	1.03	0.232	0.186	0.128	0.005
5.0-6.0	0.95	0.215	0.174	0.144	0.003
6.0-7.0	0.77	0.200	0.201	0.167	0.008
7.0-8.5	0.73	0.242	0.265	0.199	0.021
8.5-10.0	0.64	0.293	0.372	0.267	0.028
10.0-20.0	1.11	0.583	0.461	0.257	0.015

Table D.2: Statistical covariance matrix of measured cross section ratio of carbon over scintillator in p_μ

Bin edges (GeV/c)	1.5-3.0	3.0-4.0	4.0-5.0	5.0-6.0	6.0-7.0	7.0-8.5	8.5-10.0	10.0-20.0
1.5-3.0	0.1744	0.0212	0.0023	0.0013	0.0016	0.0010	0.0001	0.0004
3.0-4.0	0.0212	0.0710	0.0123	0.0026	0.0008	0.0001	0.0000	0.0000
4.0-5.0	0.0023	0.0123	0.0367	0.0104	0.0019	0.0006	0.0003	0.0000
5.0-6.0	0.0013	0.0026	0.0104	0.0275	0.0121	0.0039	0.0021	0.0009
6.0-7.0	0.0016	0.0008	0.0019	0.0121	0.0237	0.0161	0.0070	0.0082
7.0-8.5	0.0010	0.0001	0.0006	0.0039	0.0161	0.0373	0.0277	0.0079
8.5-10.0	0.0001	0.0000	0.0003	0.0021	0.0070	0.0277	0.0565	0.0372
10.0-20.0	0.0004	0.0000	0.0000	0.0009	0.0082	0.0079	0.0372	0.2593

Table D.3: Systematic covariance matrix of measured cross section ratio of carbon over scintillator in p_μ

Bin edges (GeV/c)	1.5-3.0	3.0-4.0	4.0-5.0	5.0-6.0	6.0-7.0	7.0-8.5	8.5-10.0	10.0-20.0
1.5-3.0	0.022	0.015	0.012	0.013	0.012	0.008	0.013	0.030
3.0-4.0	0.015	0.017	0.013	0.015	0.013	0.011	0.014	0.031
4.0-5.0	0.012	0.013	0.017	0.016	0.015	0.013	0.013	0.027
5.0-6.0	0.013	0.015	0.016	0.019	0.016	0.015	0.015	0.031
6.0-7.0	0.012	0.013	0.015	0.016	0.016	0.015	0.017	0.028
7.0-8.5	0.008	0.011	0.013	0.015	0.015	0.021	0.022	0.025
8.5-10.0	0.013	0.014	0.013	0.015	0.017	0.022	0.029	0.035
10.0-20.0	0.030	0.031	0.027	0.031	0.028	0.025	0.035	0.081

Table D.4: Measured cross section ratio of carbon over scintillator in θ_μ, and the absolute and fractional cross section ratio uncertainties

Bin edges (degree)	Ratio	Abs. Unc.	Frac. Stat. Unc.	Frac. Sys. Unc.	Frac. Flux Unc.
0-2	0.74	0.241	0.314	0.080	0.003
2-3	1.28	0.328	0.232	0.107	0.004
3-4	0.85	0.251	0.270	0.118	0.005
4-5	0.87	0.287	0.277	0.179	0.002
5-6	0.40	0.246	0.521	0.325	0.011
6-8	0.71	0.360	0.424	0.282	0.011
8-10	1.57	0.642	0.353	0.204	0.009
10-13	1.89	0.820	0.390	0.193	0.010

Table D.5: Statistical covariance matrix of measured cross section ratio of carbon over scintillator in θ_μ

Bin edges (degree)	0-2	2-3	3-4	4-5	5-6	6-8	8-10	10-13
0-2	0.0544	-0.0023	-0.0023	-0.0004	0.0000	0.0000	-0.0001	-0.0002
2-3	-0.0023	0.0886	0.0030	-0.0054	-0.0009	-0.0000	-0.0005	-0.0002
3-4	-0.0023	0.0030	0.0529	0.0073	-0.0039	-0.0009	-0.0001	-0.0002
4-5	-0.0004	-0.0054	0.0073	0.0581	0.0084	-0.0050	-0.0008	0.0001
5-6	0.0000	-0.0009	-0.0039	0.0084	0.0436	0.0054	-0.0041	-0.0003
6-8	0.0000	-0.0000	-0.0009	-0.0050	0.0054	0.0899	-0.0032	-0.0057
8-10	-0.0001	-0.0005	-0.0001	-0.0008	-0.0041	-0.0032	0.3092	-0.0184
10-13	-0.0002	-0.0002	-0.0002	0.0001	-0.0003	-0.0057	-0.0184	0.5409

Table D.6: Systematic covariance matrix of measured cross section ratio of carbon over scintillator in θ_μ

Bin edges (degree)	0-2	2-3	3-4	4-5	5-6	6-8	8-10	10-13
0-2	0.004	0.003	0.001	0.001	0.000	0.002	0.007	0.002
2-3	0.003	0.019	0.008	0.014	0.010	0.013	0.021	0.031
3-4	0.001	0.008	0.010	0.013	0.010	0.011	0.018	0.023
4-5	0.001	0.014	0.013	0.024	0.016	0.020	0.036	0.038
5-6	0.000	0.010	0.010	0.016	0.017	0.016	0.027	0.026
6-8	0.002	0.013	0.011	0.020	0.016	0.040	0.043	0.040
8-10	0.007	0.021	0.018	0.036	0.027	0.043	0.103	0.064
10-13	0.002	0.031	0.023	0.038	0.026	0.040	0.064	0.132

Table D.7: Measured cross section ratio of carbon over scintillator in $p_{\mu,||}$, and the absolute and fractional cross section ratio uncertainties

Bin edges (GeV/c)	Ratio	Abs. Unc.	Frac. Stat. Unc.	Frac. Sys. Unc.	Frac. Flux Unc.
1.5-3.0	1.17	0.433	0.349	0.124	0.004
3.0-4.0	1.29	0.301	0.210	0.103	0.003
4.0-5.0	1.04	0.232	0.185	0.127	0.005
5.0-6.0	0.92	0.214	0.178	0.149	0.002
6.0-7.0	0.79	0.205	0.200	0.164	0.007
7.0-8.5	0.73	0.241	0.266	0.199	0.021
8.5-10.0	0.63	0.294	0.379	0.270	0.028
10.0-20.0	1.11	0.585	0.460	0.257	0.015

Table D.8: Statistical covariance matrix of measured cross section ratio of carbon over scintillator in $p_{\mu,||}$

Bin edges (GeV/c)	1.5-3.0	3.0-4.0	4.0-5.0	5.0-6.0	6.0-7.0	7.0-8.5	8.5-10.0	10.0-20.0
1.5-3.0	0.1666	0.0178	0.0021	0.0012	0.0015	0.0009	0.0001	0.0004
3.0-4.0	0.0178	0.0730	0.0120	0.0023	0.0007	0.0001	0.0000	0.0000
4.0-5.0	0.0021	0.0120	0.0368	0.0105	0.0020	0.0006	0.0003	0.0000
5.0-6.0	0.0012	0.0023	0.0105	0.0268	0.0124	0.0040	0.0020	0.0009
6.0-7.0	0.0015	0.0007	0.0020	0.0124	0.0251	0.0158	0.0066	0.0082
7.0-8.5	0.0009	0.0001	0.0006	0.0040	0.0158	0.0374	0.0278	0.0080
8.5-10.0	0.0001	0.0000	0.0003	0.0020	0.0066	0.0278	0.0574	0.0380
10.0-20.0	0.0004	0.0000	0.0000	0.0009	0.0082	0.0080	0.0380	0.2611

Table D.9: Systematic covariance matrix of measured cross section ratio of carbon over scintillator in $p_{\mu,||}$

Bin edges (GeV/c)	1.5-3.0	3.0-4.0	4.0-5.0	5.0-6.0	6.0-7.0	7.0-8.5	8.5-10.0	10.0-20.0
1.5-3.0	0.021	0.014	0.013	0.013	0.013	0.008	0.012	0.032
3.0-4.0	0.014	0.017	0.013	0.015	0.013	0.011	0.014	0.030
4.0-5.0	0.013	0.013	0.017	0.016	0.015	0.013	0.012	0.027
5.0-6.0	0.013	0.015	0.016	0.019	0.017	0.014	0.015	0.031
6.0-7.0	0.013	0.013	0.015	0.017	0.017	0.015	0.017	0.030
7.0-8.5	0.008	0.011	0.013	0.014	0.015	0.021	0.022	0.025
8.5-10.0	0.012	0.014	0.012	0.015	0.017	0.022	0.029	0.034
10.0-20.0	0.032	0.030	0.027	0.031	0.030	0.025	0.034	0.082

Table D.10: Measured cross section ratio of carbon over scintillator in $p_{\mu,T}$, and the absolute and fractional cross section ratio uncertainties

Bin edges (GeV/c)	Ratio	Abs. Unc.	Frac. Stat. Unc.	Frac. Sys. Unc.	Frac. Flux Unc.
0.00-0.15	1.13	0.374	0.326	0.049	0.002
0.15-0.30	0.78	0.193	0.233	0.085	0.002
0.30-0.45	0.99	0.221	0.199	0.099	0.003
0.45-0.60	0.91	0.256	0.231	0.161	0.004
0.60-0.75	0.83	0.318	0.313	0.218	0.008
0.75-0.90	0.63	0.587	0.724	0.599	0.042
0.90-1.25	1.33	0.956	0.595	0.406	0.021
1.25-2.50	2.02	3.180	1.419	0.678	0.020

Table D.11: Statistical covariance matrix of measured cross section ratio of carbon over scintillator in $p_{\mu,T}$

Bin edges (GeV/c)	0.00-0.15	0.15-0.30	0.30-0.45	0.45-0.60	0.60-0.75	0.75-0.90	0.90-1.25	1.25-2.50
0.00-0.15	0.1367	0.0000	-0.0046	-0.0005	-0.0000	0.0002	-0.0003	0.0000
0.15-0.30	0.0000	0.0329	0.0027	-0.0034	-0.0008	-0.0007	-0.0003	-0.0006
0.30-0.45	-0.0046	0.0027	0.0390	0.0049	-0.0050	-0.0033	-0.0017	-0.0075
0.45-0.60	-0.0005	-0.0034	0.0049	0.0442	0.0085	-0.0064	-0.0117	0.0075
0.60-0.75	-0.0000	-0.0008	-0.0050	0.0085	0.0680	0.0355	-0.0022	-0.0385
0.75-0.90	0.0002	-0.0007	-0.0033	-0.0064	0.0355	0.2048	0.1295	-0.0148
0.90-1.25	-0.0003	-0.0003	-0.0017	-0.0117	-0.0022	0.1295	0.6226	-0.0277
1.25-2.50	0.0000	-0.0006	-0.0075	0.0075	-0.0385	-0.0148	-0.0277	8.2292

Table D.12: Systematic covariance matrix of measured cross section ratio of carbon over scintillator in $p_{\mu,T}$

Bin edges (GeV/c)	0.00-0.15	0.15-0.30	0.30-0.45	0.45-0.60	0.60-0.75	0.75-0.90	0.90-1.25	1.25-2.50
0.00-0.15	0.003	0.002	0.001	0.001	0.001	0.003	0.004	0.011
0.15-0.30	0.002	0.004	0.003	0.004	0.007	0.011	0.014	0.036
0.30-0.45	0.001	0.003	0.010	0.012	0.014	0.024	0.029	0.092
0.45-0.60	0.001	0.004	0.012	0.022	0.023	0.035	0.044	0.132
0.60-0.75	0.001	0.007	0.014	0.023	0.033	0.049	0.050	0.168
0.75-0.90	0.003	0.011	0.024	0.035	0.049	0.140	0.167	0.359
0.90-1.25	0.004	0.014	0.029	0.044	0.050	0.167	0.291	0.465
1.25-2.50	0.011	0.036	0.092	0.132	0.168	0.359	0.465	1.880

Table D.13: Measured cross section ratio of carbon over scintillator in Q^2, and the absolute and fractional cross section ratio uncertainties

Bin edges (GeV^2)	Ratio	Abs. Unc.	Frac. Stat. Unc.	Frac. Sys. Unc.	Frac. Flux Unc.
0.000-0.025	1.15	0.369	0.318	0.042	0.002
0.025-0.050	0.78	0.260	0.327	0.058	0.002
0.050-0.100	0.77	0.213	0.254	0.109	0.004
0.100-0.200	1.12	0.246	0.197	0.095	0.003
0.200-0.300	0.77	0.239	0.275	0.146	0.004
0.300-0.400	0.86	0.298	0.286	0.194	0.003
0.400-0.500	0.74	0.324	0.363	0.246	0.005
0.500-0.700	0.64	0.385	0.485	0.350	0.019
0.700-1.000	1.08	0.718	0.530	0.398	0.030
1.000-1.300	1.48	0.912	0.553	0.277	0.022
1.300-2.000	1.13	1.748	1.271	0.880	0.022
2.000-3.000	2.52	4.799	1.689	0.885	0.035

Table D.14: Statistical covariance matrix of measured cross section ratio of carbon over scintillator in Q^2

Bin edges (GeV^2)	0.000-0.025	0.025-0.050	0.050-0.100	0.100-0.200	0.200-0.300	0.300-0.400	0.400-0.500	0.500-0.700	0.700-1.000	1.000-1.300	1.300-2.000	2.000-3.000
0.000-0.025	0.1337	0.0053	-0.0051	-0.0029	-0.0001	-0.0000	0.0000	-0.0001	0.0001	-0.0000	-0.0002	-0.0000
0.025-0.050	0.0053	0.0657	0.0145	-0.0054	-0.0019	-0.0004	-0.0002	-0.0002	-0.0004	-0.0002	-0.0006	0.0001
0.050-0.100	-0.0051	0.0145	0.0382	0.0090	-0.0039	-0.0020	-0.0009	-0.0003	-0.0001	-0.0004	-0.0014	-0.0010
0.100-0.200	-0.0029	-0.0054	0.0090	0.0492	0.0082	-0.0050	-0.0044	-0.0009	-0.0012	-0.0020	-0.0013	-0.0046
0.200-0.300	-0.0001	-0.0019	-0.0039	0.0082	0.0444	0.0206	-0.0014	-0.0054	-0.0039	-0.0040	-0.0078	-0.0038
0.300-0.400	-0.0000	-0.0004	-0.0020	-0.0050	0.0206	0.0608	0.0387	0.0003	-0.0131	-0.0112	0.0099	-0.0020
0.400-0.500	0.0000	-0.0002	-0.0009	-0.0044	-0.0014	0.0387	0.0719	0.0388	-0.0015	-0.0134	-0.0082	-0.0139
0.500-0.700	-0.0001	-0.0002	-0.0003	-0.0009	-0.0054	0.0003	0.0388	0.0977	0.0661	-0.0047	-0.0018	-0.0276
0.700-1.000	0.0001	-0.0004	-0.0001	-0.0012	-0.0039	-0.0131	-0.0015	0.0661	0.3292	0.2141	0.0082	-0.0980
1.000-1.300	-0.0000	-0.0002	-0.0004	-0.0020	-0.0040	-0.0112	-0.0134	-0.0047	0.2141	0.6653	0.2750	-0.1153
1.300-2.000	-0.0002	-0.0006	-0.0014	-0.0013	-0.0078	0.0099	-0.0082	-0.0018	0.0082	0.2750	2.0659	1.3239
2.000-3.000	-0.0000	0.0001	-0.0010	-0.0046	-0.0038	-0.0020	-0.0139	-0.0276	-0.0980	-0.1153	1.3239	18.0723

Table D.15: Systematic covariance matrix of measured cross section ratio of carbon over scintillator in Q^2

Bin edges (GeV^2)	0.000-0.025	0.025-0.050	0.050-0.100	0.100-0.200	0.200-0.300	0.300-0.400	0.400-0.500	0.500-0.700	0.700-1.000	1.000-1.300	1.300-2.000	2.000-3.000
0.000-0.025	0.002	0.001	0.003	0.001	0.001	0.001	0.001	0.001	0.003	0.005	0.004	0.018
0.025-0.050	0.001	0.002	0.002	0.002	0.001	0.001	0.001	0.003	0.006	0.008	0.008	0.033
0.050-0.100	0.003	0.002	0.007	0.006	0.006	0.008	0.009	0.012	0.017	0.019	0.030	0.066
0.100-0.200	0.001	0.002	0.006	0.011	0.010	0.013	0.014	0.019	0.023	0.026	0.051	0.119
0.200-0.300	0.001	0.001	0.006	0.010	0.013	0.016	0.017	0.020	0.026	0.029	0.056	0.106
0.300-0.400	0.001	0.001	0.008	0.013	0.016	0.028	0.027	0.027	0.035	0.035	0.088	0.141
0.400-0.500	0.001	0.001	0.009	0.014	0.017	0.027	0.033	0.032	0.037	0.037	0.084	0.148
0.500-0.700	0.001	0.003	0.012	0.019	0.020	0.027	0.032	0.051	0.075	0.069	0.132	0.251
0.700-1.000	0.003	0.006	0.017	0.023	0.026	0.035	0.037	0.075	0.186	0.151	0.264	0.483
1.000-1.300	0.005	0.008	0.019	0.026	0.029	0.035	0.037	0.069	0.151	0.167	0.274	0.526
1.300-2.000	0.004	0.008	0.030	0.051	0.056	0.088	0.084	0.132	0.264	0.274	0.991	0.591
2.000-3.000	0.018	0.033	0.066	0.119	0.106	0.141	0.148	0.251	0.483	0.526	0.591	4.959

Table D.16: Measured cross section ratio of carbon over scintillator in W_{exp}, and the absolute and fractional cross section ratio uncertainties

Bin edges (GeV/c^2)	Ratio	Abs. Unc.	Frac. Stat. Unc.	Frac. Sys. Unc.	Frac. Flux Unc.
0.9-1.1	1.66	1.151	0.651	0.238	0.019
1.1-1.2	1.14	0.225	0.177	0.087	0.003
1.2-1.3	0.81	0.227	0.204	0.194	0.006
1.3-1.4	0.54	0.432	0.557	0.576	0.008

Table D.17: Statistical covariance matrix of measured cross section ratio of carbon over scintillator in W_{exp}

Bin edges (GeV/c^2)	0.9-1.1	1.1-1.2	1.2-1.3	1.3-1.4
0.9-1.1	1.1690	-0.0113	-0.0784	-0.0688
1.1-1.2	-0.0113	0.0407	0.0030	-0.0278
1.2-1.3	-0.0784	0.0030	0.0271	0.0237
1.3-1.4	-0.0688	-0.0278	0.0237	0.0902

Table D.18: Systematic covariance matrix of measured cross section ratio of carbon over scintillator in W_{exp}

Bin edges (GeV/c^2)	0.9-1.1	1.1-1.2	1.2-1.3	1.3-1.4
0.9-1.1	0.156	0.006	0.005	0.003
1.1-1.2	0.006	0.010	0.000	-0.000
1.2-1.3	0.005	0.000	0.024	0.046
1.3-1.4	0.003	-0.000	0.046	0.096

Table D.19: Measured cross section ratio of carbon over scintillator in T_π, and the absolute and fractional cross section ratio uncertainties

Bin edges (GeV)	Ratio	Abs. Unc.	Frac. Stat. Unc.	Frac. Sys. Unc.	Frac. Flux Unc.
0.035-0.100	0.87	0.189	0.178	0.127	0.003
0.100-0.150	0.94	0.169	0.136	0.118	0.003
0.150-0.200	0.85	0.262	0.239	0.197	0.009
0.200-0.350	0.83	0.474	0.439	0.363	0.022

Table D.20: Statistical covariance matrix of measured cross section ratio of carbon over scintillator in T_π

Bin edges (GeV)	0.035-0.100	0.100-0.150	0.150-0.200	0.200-0.350
0.035-0.100	0.0236	0.0033	-0.0044	0.0001
0.100-0.150	0.0033	0.0164	0.0091	0.0077
0.150-0.200	-0.0044	0.0091	0.0408	0.0393
0.200-0.350	0.0001	0.0077	0.0393	0.1338

Table D.21: Systematic covariance matrix of measured cross section ratio of carbon over scintillator in T_π

Bin edges (GeV)	0.035-0.100	0.100-0.150	0.150-0.200	0.200-0.350
0.035-0.100	0.012	0.011	0.015	0.023
0.100-0.150	0.011	0.012	0.017	0.023
0.150-0.200	0.015	0.017	0.028	0.041
0.200-0.350	0.023	0.023	0.041	0.091

Table D.22: Measured cross section ratio of carbon over scintillator in θ_π, and the absolute and fractional cross section ratio uncertainties

Bin edges (degree)	Ratio	Abs. Unc.	Frac. Stat. Unc.	Frac. Sys. Unc.	Frac. Flux Unc.
0-10	1.16	2.206	1.763	0.699	0.015
10-20	0.92	0.608	0.588	0.294	0.008
20-30	0.87	0.369	0.353	0.232	0.004
30-40	0.84	0.285	0.287	0.184	0.010
40-50	1.09	0.297	0.234	0.141	0.007
50-60	0.83	0.252	0.264	0.152	0.007
60-120	0.92	0.215	0.209	0.105	0.003
120-135	1.00	0.311	0.294	0.106	0.003
135-150	1.20	0.414	0.322	0.122	0.009
150-165	1.60	1.085	0.586	0.343	0.008
165-180	1.50	1.317	0.790	0.388	0.016

Table D.23: Statistical covariance matrix of measured cross section ratio of carbon over scintillator in θ_π

Bin edges (degree)	0-10	10-20	20-30	30-40	40-50	50-60	60-120	120-135	135-150	150-165	165-180
0-10	4.2059	0.3876	0.1321	-0.0270	0.0349	-0.0095	-0.0116	-0.0123	-0.0231	-0.0583	0.0590
10-20	0.3876	0.2957	0.0666	-0.0009	0.0010	-0.0046	-0.0025	0.0020	-0.0011	0.0099	0.3073
20-30	0.1321	0.0666	0.0951	0.0156	-0.0071	-0.0039	-0.0027	-0.0049	-0.0055	0.0081	0.0702
30-40	-0.0270	-0.0009	0.0156	0.0576	0.0194	-0.0015	-0.0024	-0.0018	0.0004	-0.0046	-0.0162
40-50	0.0349	0.0010	-0.0071	0.0194	0.0645	0.0146	-0.0008	-0.0036	-0.0047	-0.0196	-0.0251
50-60	-0.0095	-0.0046	-0.0039	-0.0015	0.0146	0.0478	0.0097	-0.0022	-0.0023	-0.0086	-0.0120
60-120	-0.0116	-0.0025	-0.0027	-0.0024	-0.0008	0.0097	0.0368	0.0069	-0.0011	-0.0017	-0.0017
120-135	-0.0123	0.0020	-0.0049	-0.0018	-0.0036	-0.0022	0.0069	0.0854	0.0206	0.0048	0.0079
135-150	-0.0231	-0.0011	-0.0055	0.0004	-0.0047	-0.0023	-0.0011	0.0206	0.1503	0.2196	0.0925
150-165	-0.0583	0.0099	0.0081	-0.0046	-0.0196	-0.0086	-0.0017	0.0048	0.2196	0.8771	0.0539
165-180	0.0590	0.3073	0.0702	-0.0162	-0.0251	-0.0120	-0.0017	0.0079	0.0925	0.0539	1.3979

Table D.24: Systematic covariance matrix of measured cross section ratio of carbon over scintillator in θ_π

Bin edges (degree)	0-10	10-20	20-30	30-40	40-50	50-60	60-120	120-135	135-150	150-165	165-180
0-10	0.660	0.052	0.058	0.038	0.028	0.029	0.030	0.027	0.042	0.174	0.027
10-20	0.052	0.074	0.049	0.033	0.036	0.029	0.018	0.021	0.026	0.038	0.090
20-30	0.058	0.049	0.041	0.028	0.025	0.020	0.013	0.014	0.021	0.030	0.051
30-40	0.038	0.033	0.028	0.024	0.017	0.014	0.010	0.010	0.015	0.032	0.040
40-50	0.028	0.036	0.025	0.017	0.023	0.018	0.011	0.014	0.016	0.018	0.046
50-60	0.029	0.029	0.020	0.014	0.018	0.016	0.010	0.012	0.013	0.019	0.037
60-120	0.030	0.018	0.013	0.010	0.011	0.010	0.009	0.009	0.008	0.018	0.039
120-135	0.027	0.021	0.014	0.010	0.014	0.012	0.009	0.011	0.010	0.023	0.039
135-150	0.042	0.026	0.021	0.015	0.016	0.013	0.008	0.010	0.022	0.015	0.028
150-165	0.174	0.038	0.030	0.032	0.018	0.019	0.018	0.023	0.015	0.300	0.100
165-180	0.027	0.090	0.051	0.040	0.046	0.037	0.039	0.039	0.028	0.100	0.337

Table D.25: Measured cross section ratio of water over scintillator in p_μ, and the absolute and fractional cross section ratio uncertainties

Bin edges (GeV/c)	Ratio	Abs. Unc.	Frac. Stat. Unc.	Frac. Sys. Unc.	Frac. Flux Unc.
1.5-3.0	0.88	0.389	0.414	0.157	0.005
3.0-4.0	0.51	0.235	0.373	0.267	0.021
4.0-5.0	0.89	0.226	0.212	0.141	0.008
5.0-6.0	0.88	0.201	0.189	0.127	0.004
6.0-7.0	0.84	0.201	0.208	0.118	0.006
7.0-8.5	0.86	0.247	0.235	0.165	0.008
8.5-10.0	0.80	0.287	0.314	0.170	0.006
10.0-20.0	0.69	0.307	0.415	0.164	0.012

Table D.26: Statistical covariance matrix of measured cross section ratio of water over scintillator in p_μ

Bin edges (GeV/c)	1.5-3.0	3.0-4.0	4.0-5.0	5.0-6.0	6.0-7.0	7.0-8.5	8.5-10.0	10.0-20.0
1.5-3.0	0.1322	0.0084	0.0007	0.0004	0.0005	0.0004	0.0012	0.0000
3.0-4.0	0.0084	0.0364	0.0103	0.0025	0.0003	0.0004	0.0002	0.0003
4.0-5.0	0.0007	0.0103	0.0354	0.0121	0.0033	0.0013	0.0009	0.0006
5.0-6.0	0.0004	0.0025	0.0121	0.0277	0.0142	0.0046	0.0016	0.0015
6.0-7.0	0.0005	0.0003	0.0033	0.0142	0.0307	0.0168	0.0035	0.0005
7.0-8.5	0.0004	0.0004	0.0013	0.0046	0.0168	0.0408	0.0193	0.0073
8.5-10.0	0.0012	0.0002	0.0009	0.0016	0.0035	0.0193	0.0639	0.0410
10.0-20.0	0.0000	0.0003	0.0006	0.0015	0.0005	0.0073	0.0410	0.0815

Table D.27: Systematic covariance matrix of measured cross section ratio of water over scintillator in p_μ

Bin edges (GeV/c)	1.5-3.0	3.0-4.0	4.0-5.0	5.0-6.0	6.0-7.0	7.0-8.5	8.5-10.0	10.0-20.0
1.5-3.0	0.019	0.009	0.009	0.007	0.009	0.014	0.013	0.006
3.0-4.0	0.009	0.019	0.014	0.012	0.009	0.012	0.011	0.007
4.0-5.0	0.009	0.014	0.016	0.012	0.010	0.012	0.011	0.008
5.0-6.0	0.007	0.012	0.012	0.013	0.009	0.009	0.009	0.008
6.0-7.0	0.009	0.009	0.010	0.009	0.010	0.011	0.010	0.007
7.0-8.5	0.014	0.012	0.012	0.009	0.011	0.020	0.017	0.009
8.5-10.0	0.013	0.011	0.011	0.009	0.010	0.017	0.019	0.008
10.0-20.0	0.006	0.007	0.008	0.008	0.007	0.009	0.008	0.013

Table D.28: Measured cross section ratio of water over scintillator in θ_μ, and the absolute and fractional cross section ratio uncertainties

Bin edges (degree)	Ratio	Abs. Unc.	Frac. Stat. Unc.	Frac. Sys. Unc.	Frac. Flux Unc.
0-2	0.61	0.169	0.257	0.107	0.008
2-3	0.86	0.251	0.274	0.100	0.008
3-4	0.87	0.252	0.261	0.126	0.005
4-5	0.72	0.291	0.378	0.147	0.004
5-6	0.53	0.316	0.541	0.261	0.014
6-8	1.03	0.445	0.369	0.223	0.008
8-10	1.79	0.692	0.344	0.179	0.007
10-13	0.13	0.517	3.411	1.896	0.151

Table D.29: Statistical covariance matrix of measured cross section ratio of water over scintillator in θ_μ

Bin edges (degree)	0-2	2-3	3-4	4-5	5-6	6-8	8-10	10-13
0-2	0.0245	0.0017	-0.0031	-0.0006	-0.0000	-0.0002	-0.0000	0.0000
2-3	0.0017	0.0554	0.0068	-0.0074	-0.0011	-0.0002	-0.0003	0.0000
3-4	-0.0031	0.0068	0.0516	0.0119	-0.0054	-0.0017	0.0001	0.0000
4-5	-0.0006	-0.0074	0.0119	0.0738	0.0159	-0.0069	-0.0008	0.0000
5-6	-0.0000	-0.0011	-0.0054	0.0159	0.0809	0.0098	-0.0081	-0.0001
6-8	-0.0002	-0.0002	-0.0017	-0.0069	0.0098	0.1453	-0.0109	-0.0029
8-10	-0.0000	-0.0003	0.0001	-0.0008	-0.0081	-0.0109	0.3768	0.0327
10-13	0.0000	0.0000	0.0000	0.0000	-0.0001	-0.0029	0.0327	0.2044

Table D.30: Systematic covariance matrix of measured cross section ratio of water over scintillator in θ_μ

Bin edges (degree)	0-2	2-3	3-4	4-5	5-6	6-8	8-10	10-13
0-2	0.004	0.004	0.005	0.001	-0.000	0.000	0.001	-0.002
2-3	0.004	0.007	0.007	0.004	0.005	0.005	0.002	0.006
3-4	0.005	0.007	0.012	0.006	0.005	0.013	0.016	0.008
4-5	0.001	0.004	0.006	0.011	0.012	0.015	0.015	0.017
5-6	-0.000	0.005	0.005	0.012	0.019	0.016	0.017	0.025
6-8	0.000	0.005	0.013	0.015	0.016	0.053	0.040	0.036
8-10	0.001	0.002	0.016	0.015	0.017	0.040	0.102	0.038
10-13	-0.002	0.006	0.008	0.017	0.025	0.036	0.038	0.063

Table D.31: Measured cross section ratio of water over scintillator in $p_{\mu,||}$, and the absolute and fractional cross section ratio uncertainties

Bin edges (GeV/c)	Ratio	Abs. Unc.	Frac. Stat. Unc.	Frac. Sys. Unc.	Frac. Flux Unc.
1.5-3.0	0.98	0.427	0.393	0.187	0.005
3.0-4.0	0.56	0.239	0.348	0.246	0.019
4.0-5.0	0.90	0.230	0.213	0.142	0.008
5.0-6.0	0.84	0.196	0.195	0.128	0.005
6.0-7.0	0.83	0.202	0.212	0.117	0.006
7.0-8.5	0.82	0.242	0.241	0.172	0.009
8.5-10.0	0.79	0.284	0.316	0.174	0.006
10.0-20.0	0.70	0.309	0.413	0.162	0.012

Table D.32: Statistical covariance matrix of measured cross section ratio of water over scintillator in $p_{\mu,||}$

Bin edges (GeV/c)	1.5-3.0	3.0-4.0	4.0-5.0	5.0-6.0	6.0-7.0	7.0-8.5	8.5-10.0	10.0-20.0
1.5-3.0	0.1490	0.0089	0.0008	0.0004	0.0005	0.0004	0.0013	0.0000
3.0-4.0	0.0089	0.0381	0.0106	0.0023	0.0003	0.0004	0.0002	0.0003
4.0-5.0	0.0008	0.0106	0.0368	0.0120	0.0032	0.0013	0.0009	0.0006
5.0-6.0	0.0004	0.0023	0.0120	0.0269	0.0136	0.0044	0.0016	0.0015
6.0-7.0	0.0005	0.0003	0.0032	0.0136	0.0311	0.0165	0.0035	0.0005
7.0-8.5	0.0004	0.0004	0.0013	0.0044	0.0165	0.0388	0.0192	0.0072
8.5-10.0	0.0013	0.0002	0.0009	0.0016	0.0035	0.0192	0.0620	0.0413
10.0-20.0	0.0000	0.0003	0.0006	0.0015	0.0005	0.0072	0.0413	0.0830

Table D.33: Systematic covariance matrix of measured cross section ratio of water over scintillator in $p_{\mu,||}$

Bin edges (GeV/c)	1.5-3.0	3.0-4.0	4.0-5.0	5.0-6.0	6.0-7.0	7.0-8.5	8.5-10.0	10.0-20.0
1.5-3.0	0.034	0.007	0.010	0.007	0.010	0.017	0.015	0.007
3.0-4.0	0.007	0.019	0.014	0.012	0.009	0.012	0.011	0.007
4.0-5.0	0.010	0.014	0.016	0.012	0.010	0.012	0.011	0.008
5.0-6.0	0.007	0.012	0.012	0.012	0.009	0.009	0.009	0.007
6.0-7.0	0.010	0.009	0.010	0.009	0.010	0.011	0.010	0.007
7.0-8.5	0.017	0.012	0.012	0.009	0.011	0.020	0.017	0.009
8.5-10.0	0.015	0.011	0.011	0.009	0.010	0.017	0.019	0.008
10.0-20.0	0.007	0.007	0.008	0.007	0.007	0.009	0.008	0.013

Table D.34: Measured cross section ratio of water over scintillator in $p_{\mu,T}$, and the absolute and fractional cross section ratio uncertainties

Bin edges (GeV/c)	Ratio	Abs. Unc.	Frac. Stat. Unc.	Frac. Sys. Unc.	Frac. Flux Unc.
0.00-0.15	0.54	0.198	0.362	0.065	0.008
0.15-0.30	0.65	0.181	0.245	0.133	0.005
0.30-0.45	1.07	0.255	0.215	0.102	0.004
0.45-0.60	0.88	0.297	0.289	0.171	0.004
0.60-0.75	0.28	0.279	0.750	0.651	0.016
0.75-0.90	1.41	0.678	0.423	0.230	0.011
0.90-1.25	1.90	1.097	0.544	0.188	0.014
1.25-2.50	2.99	4.786	0.956	1.281	0.055

Table D.35: Statistical covariance matrix of measured cross section ratio of water over scintillator in $p_{\mu,T}$

Bin edges (GeV/c)	0.00-0.15	0.15-0.30	0.30-0.45	0.45-0.60	0.60-0.75	0.75-0.90	0.90-1.25	1.25-2.50
0.00-0.15	0.0380	-0.0003	-0.0023	-0.0003	-0.0000	-0.0001	0.0000	0.0001
0.15-0.30	-0.0003	0.0252	0.0009	-0.0031	-0.0009	-0.0005	-0.0021	-0.0006
0.30-0.45	-0.0023	0.0009	0.0529	0.0072	-0.0024	-0.0069	-0.0023	-0.0151
0.45-0.60	-0.0003	-0.0031	0.0072	0.0650	0.0183	-0.0075	-0.0038	0.0106
0.60-0.75	-0.0000	-0.0009	-0.0024	0.0183	0.0445	0.0554	0.0034	-0.0230
0.75-0.90	-0.0001	-0.0005	-0.0069	-0.0075	0.0554	0.3547	0.0408	-0.0445
0.90-1.25	0.0000	-0.0021	-0.0023	-0.0038	0.0034	0.0408	1.0747	0.0087
1.25-2.50	0.0001	-0.0006	-0.0151	0.0106	-0.0230	-0.0445	0.0087	8.2036

Table D.36: Systematic covariance matrix of measured cross section ratio of water over scintillator in $p_{\mu,T}$

Bin edges (GeV/c)	0.00-0.15	0.15-0.30	0.30-0.45	0.45-0.60	0.60-0.75	0.75-0.90	0.90-1.25	1.25-2.50
0.00-0.15	0.001	0.003	0.001	0.000	-0.001	-0.001	0.000	-0.014
0.15-0.30	0.003	0.007	0.004	0.003	0.002	0.005	0.005	0.002
0.30-0.45	0.001	0.004	0.012	0.010	0.008	0.018	0.020	0.058
0.45-0.60	0.000	0.003	0.010	0.023	0.020	0.030	0.008	0.211
0.60-0.75	-0.001	0.002	0.008	0.020	0.034	0.044	0.014	0.210
0.75-0.90	-0.001	0.005	0.018	0.030	0.044	0.105	0.052	0.194
0.90-1.25	0.000	0.005	0.020	0.008	0.014	0.052	0.128	-0.235
1.25-2.50	-0.014	0.002	0.058	0.211	0.210	0.194	-0.235	14.705

Table D.37: Measured cross section ratio of water over scintillator in Q^2, and the absolute and fractional cross section ratio uncertainties

Bin edges (GeV^2)	Ratio	Abs. Unc.	Frac. Stat. Unc.	Frac. Sys. Unc.	Frac. Flux Unc.
0.000-0.025	0.53	0.193	0.357	0.062	0.007
0.025-0.050	0.58	0.201	0.306	0.165	0.005
0.050-0.100	0.73	0.207	0.263	0.110	0.009
0.100-0.200	1.10	0.282	0.227	0.116	0.005
0.200-0.300	1.04	0.297	0.254	0.132	0.003
0.300-1.300	0.60	0.294	0.378	0.312	0.007
1.300-2.000	6.32	4.281	0.627	0.256	0.028
2.000-3.000	2.15	3.883	0.967	1.524	0.078

Table D.38: Statistical covariance matrix of measured cross section ratio of water over scintillator in Q^2

Bin edges (GeV^2)	0.000-0.025	0.025-0.050	0.050-0.100	0.100-0.200	0.200-0.300	0.300-1.300	1.300-2.000	2.000-3.000
0.000-0.025	0.0361	0.0041	-0.0040	-0.0013	-0.0001	-0.0001	0.0000	-0.0000
0.025-0.050	0.0041	0.0314	0.0143	-0.0047	-0.0027	-0.0002	-0.0009	-0.0000
0.050-0.100	-0.0040	0.0143	0.0364	0.0056	-0.0045	-0.0013	-0.0058	-0.0006
0.100-0.200	-0.0013	-0.0047	0.0056	0.0631	0.0212	-0.0057	-0.0193	-0.0059
0.200-0.300	-0.0001	-0.0027	-0.0045	0.0212	0.0693	0.0070	-0.0423	0.0018
0.300-1.300	-0.0001	-0.0002	-0.0013	-0.0057	0.0070	0.0516	0.0174	-0.0116
1.300-2.000	0.0000	-0.0009	-0.0058	-0.0193	-0.0423	0.0174	15.7039	0.0301
2.000-3.000	-0.0000	-0.0000	-0.0006	-0.0059	0.0018	-0.0116	0.0301	4.3266

Table D.39: Systematic covariance matrix of measured cross section ratio of water over scintillator in Q^2

Bin edges (GeV^2)	0.000-0.025	0.025-0.050	0.050-0.100	0.100-0.200	0.200-0.300	0.300-1.300	1.300-2.000	2.000-3.000
0.000-0.025	0.001	0.003	0.002	0.002	0.001	-0.001	0.002	-0.010
0.025-0.050	0.003	0.009	0.006	0.006	0.003	0.001	0.009	0.000
0.050-0.100	0.002	0.006	0.006	0.004	0.003	0.004	0.020	0.009
0.100-0.200	0.002	0.006	0.004	0.016	0.012	0.010	0.031	0.056
0.200-0.300	0.001	0.003	0.003	0.012	0.019	0.016	0.019	0.083
0.300-1.300	-0.001	0.001	0.004	0.010	0.016	0.035	0.076	0.150
1.300-2.000	0.002	0.009	0.020	0.031	0.019	0.076	2.624	0.320
2.000-3.000	-0.010	0.000	0.009	0.056	0.083	0.150	0.320	10.750

Table D.40: Measured cross section ratio of water over scintillator in W_{exp}, and the absolute and fractional cross section ratio uncertainties

Bin edges (GeV/c^2)	Ratio	Abs. Unc.	Frac. Stat. Unc.	Frac. Sys. Unc.	Frac. Flux Unc.
0.9-1.1	2.92	2.573	0.845	0.249	0.023
1.1-1.2	1.63	0.377	0.190	0.132	0.007
1.2-1.3	0.38	0.199	0.409	0.323	0.008
1.3-1.4	0.19	0.181	0.696	0.627	0.015

Table D.41: Statistical covariance matrix of measured cross section ratio of water over scintillator in W_{exp}

Bin edges (GeV/c^2)	0.9-1.1	1.1-1.2	1.2-1.3	1.3-1.4
0.9-1.1	6.0941	-0.2462	-0.0699	-0.0476
1.1-1.2	-0.2462	0.0960	-0.0125	-0.0071
1.2-1.3	-0.0699	-0.0125	0.0244	0.0156
1.3-1.4	-0.0476	-0.0071	0.0156	0.0181

Table D.42: Systematic covariance matrix of measured cross section ratio of water over scintillator in W_{exp}

Bin edges (GeV/c^2)	0.9-1.1	1.1-1.2	1.2-1.3	1.3-1.4
0.9-1.1	0.528	0.013	0.007	0.002
1.1-1.2	0.013	0.046	0.005	0.000
1.2-1.3	0.007	0.005	0.015	0.014
1.3-1.4	0.002	0.000	0.014	0.015

Table D.43: Measured cross section ratio of water over scintillator in T_π, and the absolute and fractional cross section ratio uncertainties

Bin edges (GeV)	Ratio	Abs. Unc.	Frac. Stat. Unc.	Frac. Sys. Unc.	Frac. Flux Unc.
0.035-0.100	1.14	0.281	0.227	0.097	0.007
0.100-0.150	0.83	0.193	0.197	0.120	0.002
0.150-0.200	0.88	0.273	0.258	0.175	0.003
0.200-0.350	0.77	0.327	0.346	0.245	0.010

Table D.44: Statistical covariance matrix of measured cross section ratio of water over scintillator in T_π

Bin edges (GeV)	0.035-0.100	0.100-0.150	0.150-0.200	0.200-0.350
0.035-0.100	0.0666	0.0059	-0.0070	-0.0033
0.100-0.150	0.0059	0.0270	0.0039	-0.0027
0.150-0.200	-0.0070	0.0039	0.0513	0.0120
0.200-0.350	-0.0033	-0.0027	0.0120	0.0713

Table D.45: Systematic covariance matrix of measured cross section ratio of water over scintillator in T_π

Bin edges (GeV)	0.035-0.100	0.100-0.150	0.150-0.200	0.200-0.350
0.035-0.100	0.012	0.008	0.009	0.010
0.100-0.150	0.008	0.010	0.011	0.014
0.150-0.200	0.009	0.011	0.023	0.023
0.200-0.350	0.010	0.014	0.023	0.036

Table D.46: Measured cross section ratio of water over scintillator in θ_π, and the absolute and fractional cross section ratio uncertainties

Bin edges (degree)	Ratio	Abs. Unc.	Frac. Stat. Unc.	Frac. Sys. Unc.	Frac. Flux Unc.
0-10	0.95	0.829	0.845	0.229	0.009
10-20	0.58	0.310	0.493	0.210	0.012
20-30	0.75	0.263	0.309	0.167	0.007
30-40	0.66	0.254	0.322	0.215	0.005
40-50	0.88	0.254	0.260	0.127	0.007
50-60	1.36	0.353	0.245	0.087	0.006
60-120	1.08	0.320	0.283	0.089	0.003
120-135	1.10	0.587	0.508	0.163	0.008
135-150	1.34	0.600	0.429	0.124	0.011
150-165	1.01	0.882	0.816	0.311	0.007
165-180	0.34	0.526	1.448	0.497	0.014

Table D.47: Statistical covariance matrix of measured cross section ratio of water over scintillator in θ_π

Bin edges (degree)	0-10	10-20	20-30	30-40	40-50	50-60	60-120	120-135	135-150	150-165	165-180
0-10	0.6400	0.0727	-0.0180	0.0071	-0.0039	-0.0048	-0.0042	-0.0046	-0.0048	-0.0028	0.0280
10-20	0.0727	0.0813	0.0142	-0.0035	-0.0028	0.0013	-0.0047	-0.0035	0.0023	-0.0018	0.0901
20-30	-0.0180	0.0142	0.0536	0.0069	-0.0018	-0.0053	-0.0007	-0.0008	-0.0036	-0.0041	-0.0037
30-40	0.0071	-0.0035	0.0069	0.0446	0.0091	-0.0036	0.0017	-0.0052	-0.0035	-0.0024	-0.0049
40-50	-0.0039	-0.0028	-0.0018	0.0091	0.0522	0.0138	-0.0000	-0.0018	0.0035	-0.0125	-0.0010
50-60	-0.0048	0.0013	-0.0053	-0.0036	0.0138	0.1106	0.0279	-0.0059	-0.0171	-0.0147	0.0047
60-120	-0.0042	-0.0047	-0.0007	0.0017	-0.0000	0.0279	0.0930	0.0162	0.0000	0.0068	-0.0048
120-135	-0.0046	-0.0035	-0.0008	-0.0052	-0.0018	-0.0059	0.0162	0.3127	0.0796	-0.0041	-0.0032
135-150	-0.0048	0.0023	-0.0036	-0.0035	0.0035	-0.0171	0.0000	0.0796	0.3324	0.2846	0.0015
150-165	-0.0028	-0.0018	-0.0041	-0.0024	-0.0125	-0.0147	0.0068	-0.0041	0.2846	0.6790	-0.0034
165-180	0.0280	0.0901	-0.0037	-0.0049	-0.0010	0.0047	-0.0048	-0.0032	0.0015	-0.0034	0.2480

Table D.48: Systematic covariance matrix of measured cross section ratio of water over scintillator in θ_π

Bin edges (degree)	0-10	10-20	20-30	30-40	40-50	50-60	60-120	120-135	135-150	150-165	165-180
0-10	0.047	0.007	0.011	0.020	0.013	0.009	0.005	0.016	0.007	-0.005	0.009
10-20	0.007	0.015	0.012	0.008	0.007	0.004	0.005	0.008	0.005	0.012	0.009
20-30	0.011	0.012	0.016	0.012	0.010	0.008	0.006	0.009	0.007	0.013	0.007
30-40	0.020	0.008	0.012	0.020	0.013	0.009	0.007	0.006	0.011	0.007	0.004
40-50	0.013	0.007	0.010	0.013	0.013	0.009	0.007	0.009	0.011	0.013	0.004
50-60	0.009	0.004	0.008	0.009	0.009	0.014	0.007	0.010	0.009	0.014	-0.001
60-120	0.005	0.005	0.006	0.007	0.007	0.007	0.009	0.005	0.009	0.004	0.000
120-135	0.016	0.008	0.009	0.006	0.009	0.010	0.005	0.032	0.001	0.014	0.011
135-150	0.007	0.005	0.007	0.011	0.011	0.009	0.009	0.001	0.028	0.030	-0.009
150-165	-0.005	0.012	0.013	0.007	0.013	0.014	0.004	0.014	0.030	0.099	-0.007
165-180	0.009	0.009	0.007	0.004	0.004	-0.001	0.000	0.011	-0.009	-0.007	0.029

Table D.49: Measured cross section ratio of iron over scintillator in p_μ, and the absolute and fractional cross section ratio uncertainties

Bin edges (GeV/c)	Ratio	Abs. Unc.	Frac. Stat. Unc.	Frac. Sys. Unc.	Frac. Flux Unc.
1.5-3.0	0.89	0.170	0.156	0.110	0.004
3.0-4.0	0.81	0.129	0.111	0.116	0.007
4.0-5.0	0.63	0.104	0.100	0.131	0.009
5.0-6.0	0.63	0.100	0.091	0.130	0.006
6.0-7.0	0.62	0.103	0.097	0.137	0.005
7.0-8.5	0.59	0.116	0.124	0.154	0.017
8.5-10.0	0.65	0.140	0.152	0.153	0.014
10.0-20.0	0.94	0.223	0.180	0.154	0.005

Table D.50: Statistical covariance matrix of measured cross section ratio of iron over scintillator in p_μ

Bin edges (GeV/c)	1.5-3.0	3.0-4.0	4.0-5.0	5.0-6.0	6.0-7.0	7.0-8.5	8.5-10.0	10.0-20.0
1.5-3.0	0.0194	0.0024	0.0003	0.0002	0.0001	0.0000	0.0002	0.0002
3.0-4.0	0.0024	0.0080	0.0014	0.0003	0.0001	0.0001	0.0001	0.0002
4.0-5.0	0.0003	0.0014	0.0040	0.0014	0.0004	0.0001	0.0001	0.0001
5.0-6.0	0.0002	0.0003	0.0014	0.0033	0.0015	0.0004	0.0002	0.0002
6.0-7.0	0.0001	0.0001	0.0004	0.0015	0.0035	0.0019	0.0008	0.0004
7.0-8.5	0.0000	0.0001	0.0001	0.0004	0.0019	0.0053	0.0037	0.0014
8.5-10.0	0.0002	0.0001	0.0001	0.0002	0.0008	0.0037	0.0097	0.0060
10.0-20.0	0.0002	0.0002	0.0001	0.0002	0.0004	0.0014	0.0060	0.0286

Table D.51: Systematic covariance matrix of measured cross section ratio of iron over scintillator in p_μ

Bin edges (GeV/c)	1.5-3.0	3.0-4.0	4.0-5.0	5.0-6.0	6.0-7.0	7.0-8.5	8.5-10.0	10.0-20.0
1.5-3.0	0.010	0.006	0.006	0.005	0.005	0.005	0.006	0.009
3.0-4.0	0.006	0.009	0.007	0.007	0.007	0.007	0.008	0.012
4.0-5.0	0.006	0.007	0.007	0.007	0.006	0.006	0.007	0.009
5.0-6.0	0.005	0.007	0.007	0.007	0.007	0.007	0.007	0.010
6.0-7.0	0.005	0.007	0.006	0.007	0.007	0.007	0.007	0.011
7.0-8.5	0.005	0.007	0.006	0.007	0.007	0.008	0.009	0.011
8.5-10.0	0.006	0.008	0.007	0.007	0.007	0.009	0.010	0.012
10.0-20.0	0.009	0.012	0.009	0.010	0.011	0.011	0.012	0.021

Table D.52: Measured cross section ratio of iron over scintillator in θ_μ, and the absolute and fractional cross section ratio uncertainties

Bin edges (degree)	Ratio	Abs. Unc.	Frac. Stat. Unc.	Frac. Sys. Unc.	Frac. Flux Unc.
0-2	0.59	0.096	0.136	0.087	0.002
2-3	0.59	0.091	0.134	0.076	0.002
3-4	0.63	0.102	0.133	0.093	0.001
4-5	0.54	0.113	0.161	0.137	0.005
5-6	0.48	0.143	0.210	0.212	0.003
6-8	0.71	0.160	0.145	0.174	0.002
8-10	0.94	0.243	0.184	0.183	0.003
10-13	0.89	0.324	0.277	0.235	0.006

Table D.53: Statistical covariance matrix of measured cross section ratio of iron over scintillator in θ_μ

Bin edges (degree)	0-2	2-3	3-4	4-5	5-6	6-8	8-10	10-13
0-2	0.0066	0.0000	-0.0005	-0.0001	0.0000	0.0000	-0.0000	-0.0000
2-3	0.0000	0.0062	0.0007	-0.0006	-0.0002	-0.0000	-0.0000	-0.0000
3-4	-0.0005	0.0007	0.0069	0.0010	-0.0007	-0.0001	-0.0000	-0.0001
4-5	-0.0001	-0.0006	0.0010	0.0074	0.0016	-0.0005	-0.0001	-0.0000
5-6	0.0000	-0.0002	-0.0007	0.0016	0.0102	0.0006	-0.0007	-0.0001
6-8	0.0000	-0.0000	-0.0001	-0.0005	0.0006	0.0105	-0.0002	-0.0009
8-10	-0.0000	-0.0000	-0.0000	-0.0001	-0.0007	-0.0002	0.0296	-0.0009
10-13	-0.0000	-0.0000	-0.0001	-0.0000	-0.0001	-0.0009	-0.0009	0.0611

Table D.54: Systematic covariance matrix of measured cross section ratio of iron over scintillator in θ_μ

Bin edges (degree)	0-2	2-3	3-4	4-5	5-6	6-8	8-10	10-13
0-2	0.003	0.001	0.001	0.001	0.001	0.001	0.002	0.003
2-3	0.001	0.002	0.002	0.002	0.003	0.003	0.006	0.006
3-4	0.001	0.002	0.003	0.004	0.005	0.006	0.008	0.010
4-5	0.001	0.002	0.004	0.005	0.007	0.008	0.011	0.013
5-6	0.001	0.003	0.005	0.007	0.010	0.011	0.016	0.018
6-8	0.001	0.003	0.006	0.008	0.011	0.015	0.019	0.023
8-10	0.002	0.006	0.008	0.011	0.016	0.019	0.029	0.032
10-13	0.003	0.006	0.010	0.013	0.018	0.023	0.032	0.044

Table D.55: Measured cross section ratio of iron over scintillator in $p_{\mu,||}$, and the absolute and fractional cross section ratio uncertainties

Bin edges (GeV/c)	Ratio	Abs. Unc.	Frac. Stat. Unc.	Frac. Sys. Unc.	Frac. Flux Unc.
1.5-3.0	0.85	0.169	0.163	0.116	0.005
3.0-4.0	0.84	0.131	0.108	0.113	0.006
4.0-5.0	0.62	0.103	0.101	0.131	0.009
5.0-6.0	0.62	0.100	0.092	0.132	0.006
6.0-7.0	0.62	0.104	0.096	0.137	0.005
7.0-8.5	0.59	0.117	0.123	0.154	0.017
8.5-10.0	0.63	0.135	0.155	0.147	0.014
10.0-20.0	0.96	0.224	0.179	0.150	0.004

Table D.56: Statistical covariance matrix of measured cross section ratio of iron over scintillator in $p_{\mu,||}$

Bin edges (GeV/c)	1.5-3.0	3.0-4.0	4.0-5.0	5.0-6.0	6.0-7.0	7.0-8.5	8.5-10.0	10.0-20.0
1.5-3.0	0.0190	0.0022	0.0003	0.0002	0.0000	0.0000	0.0002	0.0003
3.0-4.0	0.0022	0.0081	0.0014	0.0003	0.0001	0.0001	0.0001	0.0002
4.0-5.0	0.0003	0.0014	0.0039	0.0014	0.0004	0.0001	0.0001	0.0001
5.0-6.0	0.0002	0.0003	0.0014	0.0033	0.0015	0.0004	0.0002	0.0002
6.0-7.0	0.0000	0.0001	0.0004	0.0015	0.0036	0.0019	0.0008	0.0005
7.0-8.5	0.0000	0.0001	0.0001	0.0004	0.0019	0.0053	0.0036	0.0013
8.5-10.0	0.0002	0.0001	0.0001	0.0002	0.0008	0.0036	0.0096	0.0059
10.0-20.0	0.0003	0.0002	0.0001	0.0002	0.0005	0.0013	0.0059	0.0295

Table D.57: Systematic covariance matrix of measured cross section ratio of iron over scintillator in $p_{\mu,||}$

Bin edges (GeV/c)	1.5-3.0	3.0-4.0	4.0-5.0	5.0-6.0	6.0-7.0	7.0-8.5	8.5-10.0	10.0-20.0
1.5-3.0	0.010	0.007	0.006	0.006	0.005	0.005	0.006	0.010
3.0-4.0	0.007	0.009	0.007	0.007	0.007	0.008	0.008	0.012
4.0-5.0	0.006	0.007	0.007	0.006	0.006	0.006	0.006	0.009
5.0-6.0	0.006	0.007	0.006	0.007	0.007	0.007	0.007	0.010
6.0-7.0	0.005	0.007	0.006	0.007	0.007	0.007	0.007	0.011
7.0-8.5	0.005	0.008	0.006	0.007	0.007	0.008	0.008	0.011
8.5-10.0	0.006	0.008	0.006	0.007	0.007	0.008	0.009	0.011
10.0-20.0	0.010	0.012	0.009	0.010	0.011	0.011	0.011	0.021

Table D.58: Measured cross section ratio of iron over scintillator in $p_{\mu,T}$, and the absolute and fractional cross section ratio uncertainties

Bin edges (GeV/c)	Ratio	Abs. Unc.	Frac. Stat. Unc.	Frac. Sys. Unc.	Frac. Flux Unc.
0.00-0.15	0.54	0.117	0.191	0.104	0.003
0.15-0.30	0.59	0.079	0.110	0.076	0.001
0.30-0.45	0.60	0.088	0.111	0.098	0.001
0.45-0.60	0.70	0.121	0.112	0.132	0.001
0.60-0.75	0.61	0.169	0.164	0.222	0.003
0.75-0.90	0.70	0.265	0.219	0.310	0.009
0.90-1.25	1.01	0.399	0.295	0.261	0.008
1.25-2.50	1.51	1.493	0.910	0.389	0.014

Table D.59: Statistical covariance matrix of measured cross section ratio of iron over scintillator in $p_{\mu,T}$

Bin edges (GeV/c)	0.00-0.15	0.15-0.30	0.30-0.45	0.45-0.60	0.60-0.75	0.75-0.90	0.90-1.25	1.25-2.50
0.00-0.15	0.0105	0.0002	-0.0004	-0.0001	-0.0000	-0.0000	-0.0000	-0.0000
0.15-0.30	0.0002	0.0042	0.0003	-0.0004	-0.0001	-0.0000	-0.0001	-0.0004
0.30-0.45	-0.0004	0.0003	0.0044	0.0005	-0.0005	-0.0003	-0.0003	-0.0002
0.45-0.60	-0.0001	-0.0004	0.0005	0.0062	0.0012	-0.0009	-0.0010	-0.0005
0.60-0.75	-0.0000	-0.0001	-0.0005	0.0012	0.0102	0.0038	-0.0022	-0.0006
0.75-0.90	-0.0000	-0.0000	-0.0003	-0.0009	0.0038	0.0234	0.0149	-0.0139
0.90-1.25	-0.0000	-0.0001	-0.0003	-0.0010	-0.0022	0.0149	0.0895	0.0576
1.25-2.50	-0.0000	-0.0004	-0.0002	-0.0005	-0.0006	-0.0139	0.0576	1.8862

Table D.60: Systematic covariance matrix of measured cross section ratio of iron over scintillator in $p_{\mu,T}$

Bin edges (GeV/c)	0.00-0.15	0.15-0.30	0.30-0.45	0.45-0.60	0.60-0.75	0.75-0.90	0.90-1.25	1.25-2.50
0.00-0.15	0.003	0.001	-0.001	-0.001	-0.001	-0.002	0.000	0.002
0.15-0.30	0.001	0.002	0.002	0.002	0.003	0.005	0.007	0.011
0.30-0.45	-0.001	0.002	0.003	0.005	0.007	0.011	0.013	0.018
0.45-0.60	-0.001	0.002	0.005	0.009	0.011	0.019	0.021	0.032
0.60-0.75	-0.001	0.003	0.007	0.011	0.018	0.028	0.032	0.042
0.75-0.90	-0.002	0.005	0.011	0.019	0.028	0.047	0.052	0.078
0.90-1.25	0.000	0.007	0.013	0.021	0.032	0.052	0.070	0.101
1.25-2.50	0.002	0.011	0.018	0.032	0.042	0.078	0.101	0.344

Table D.61: Measured cross section ratio of iron over scintillator in Q^2, and the absolute and fractional cross section ratio uncertainties

Bin edges (GeV^2)	Ratio	Abs. Unc.	Frac. Stat. Unc.	Frac. Sys. Unc.	Frac. Flux Unc.
0.000-0.025	0.52	0.109	0.181	0.101	0.004
0.025-0.050	0.52	0.089	0.149	0.081	0.002
0.050-0.100	0.58	0.085	0.127	0.075	0.002
0.100-0.200	0.63	0.090	0.109	0.093	0.001
0.200-0.300	0.72	0.115	0.124	0.099	0.002
0.300-0.400	0.67	0.139	0.143	0.150	0.002
0.400-0.500	0.58	0.160	0.176	0.214	0.002
0.500-0.700	0.61	0.213	0.208	0.282	0.005
0.700-1.000	0.81	0.301	0.234	0.290	0.007
1.000-1.300	1.05	0.444	0.342	0.246	0.006
1.300-2.000	0.83	0.728	0.703	0.519	0.032
2.000-3.000	0.81	0.902	1.005	0.480	0.020

Table D.62: Statistical covariance matrix of measured cross section ratio of iron over scintillator in Q^2

Bin edges (GeV^2)	0.000-0.025	0.025-0.050	0.050-0.100	0.100-0.200	0.200-0.300	0.300-0.400	0.400-0.500	0.500-0.700	0.700-1.000	1.000-1.300	1.300-2.000	2.000-3.000
0.000-0.025	0.0090	0.0017	-0.0007	-0.0003	-0.0000	-0.0000	-0.0000	-0.0000	-0.0000	-0.0000	-0.0000	0.0000
0.025-0.050	0.0017	0.0061	0.0017	-0.0004	-0.0002	-0.0000	-0.0000	-0.0000	-0.0000	-0.0000	-0.0001	-0.0001
0.050-0.100	-0.0007	0.0017	0.0054	0.0009	-0.0006	-0.0003	-0.0001	-0.0000	-0.0000	-0.0000	-0.0003	-0.0003
0.100-0.200	-0.0003	-0.0004	0.0009	0.0047	0.0011	-0.0004	-0.0005	-0.0002	-0.0002	-0.0004	0.0001	0.0002
0.200-0.300	-0.0000	-0.0002	-0.0006	0.0011	0.0080	0.0026	0.0000	-0.0007	-0.0006	-0.0007	-0.0011	-0.0020
0.300-0.400	-0.0000	-0.0000	-0.0003	-0.0004	0.0026	0.0091	0.0042	-0.0004	-0.0012	-0.0008	-0.0003	0.0026
0.400-0.500	-0.0000	-0.0000	-0.0001	-0.0005	0.0000	0.0042	0.0104	0.0050	-0.0008	-0.0032	-0.0009	0.0015
0.500-0.700	-0.0000	-0.0000	-0.0000	-0.0002	-0.0007	-0.0004	0.0050	0.0160	0.0070	-0.0015	-0.0016	-0.0021
0.700-1.000	-0.0000	-0.0000	-0.0000	-0.0002	-0.0006	-0.0012	-0.0008	0.0070	0.0356	0.0303	0.0017	-0.0017
1.000-1.300	-0.0000	-0.0000	-0.0000	-0.0004	-0.0007	-0.0008	-0.0032	-0.0015	0.0303	0.1299	0.0771	-0.0014
1.300-2.000	-0.0000	-0.0001	-0.0003	0.0001	-0.0011	-0.0003	-0.0009	-0.0016	0.0017	0.0771	0.3435	0.1544
2.000-3.000	0.0000	-0.0001	-0.0003	0.0002	-0.0020	0.0026	0.0015	-0.0021	-0.0017	-0.0014	0.1544	0.6619

Table D.63: Systematic covariance matrix of measured cross section ratio of iron over scintillator in Q^2

Bin edges (GeV^2)	0.000-0.025	0.025-0.050	0.050-0.100	0.100-0.200	0.200-0.300	0.300-0.400	0.400-0.500	0.500-0.700	0.700-1.000	1.000-1.300	1.300-2.000	2.000-3.000
0.000-0.025	0.003	0.002	0.000	-0.000	-0.000	-0.001	-0.001	-0.002	-0.002	-0.000	-0.000	-0.004
0.025-0.050	0.002	0.002	0.001	0.001	0.001	0.001	0.001	0.002	0.002	0.003	0.005	0.002
0.050-0.100	0.000	0.001	0.002	0.002	0.002	0.003	0.004	0.005	0.007	0.009	0.011	0.009
0.100-0.200	-0.000	0.001	0.002	0.003	0.003	0.005	0.006	0.009	0.011	0.013	0.018	0.015
0.200-0.300	-0.000	0.001	0.002	0.003	0.005	0.007	0.008	0.011	0.015	0.015	0.021	0.020
0.300-0.400	-0.001	0.001	0.003	0.005	0.007	0.010	0.011	0.015	0.021	0.021	0.028	0.030
0.400-0.500	-0.001	0.001	0.004	0.006	0.008	0.011	0.015	0.020	0.026	0.027	0.043	0.037
0.500-0.700	-0.002	0.002	0.005	0.009	0.011	0.015	0.020	0.029	0.038	0.039	0.061	0.048
0.700-1.000	-0.002	0.002	0.007	0.011	0.015	0.021	0.026	0.038	0.055	0.052	0.078	0.069
1.000-1.300	-0.000	0.003	0.009	0.013	0.015	0.021	0.027	0.039	0.052	0.067	0.092	0.065
1.300-2.000	-0.000	0.005	0.011	0.018	0.021	0.028	0.043	0.061	0.078	0.092	0.187	0.122
2.000-3.000	-0.004	0.002	0.009	0.015	0.020	0.030	0.037	0.048	0.069	0.065	0.122	0.151

Table D.64: Measured cross section ratio of iron over scintillator in W_{exp}, and the absolute and fractional cross section ratio uncertainties

Bin edges (GeV/c^2)	Ratio	Abs. Unc.	Frac. Stat. Unc.	Frac. Sys. Unc.	Frac. Flux Unc.
0.9-1.1	0.53	0.279	0.502	0.176	0.013
1.1-1.2	0.76	0.123	0.133	0.091	0.001
1.2-1.3	0.64	0.127	0.103	0.170	0.002
1.3-1.4	0.56	0.203	0.187	0.314	0.003

Table D.65: Statistical covariance matrix of measured cross section ratio of iron over scintillator in W_{exp}

Bin edges (GeV/c^2)	0.9-1.1	1.1-1.2	1.2-1.3	1.3-1.4
0.9-1.1	0.0694	0.0029	-0.0054	-0.0022
1.1-1.2	0.0029	0.0104	-0.0027	-0.0058
1.2-1.3	-0.0054	-0.0027	0.0044	0.0037
1.3-1.4	-0.0022	-0.0058	0.0037	0.0108

Table D.66: Systematic covariance matrix of measured cross section ratio of iron over scintillator in W_{exp}

Bin edges (GeV/c^2)	0.9-1.1	1.1-1.2	1.2-1.3	1.3-1.4
0.9-1.1	0.008	0.003	0.004	0.005
1.1-1.2	0.003	0.005	-0.001	-0.004
1.2-1.3	0.004	-0.001	0.012	0.018
1.3-1.4	0.005	-0.004	0.018	0.031

Table D.67: Measured cross section ratio of iron over scintillator in T_π, and the absolute and fractional cross section ratio uncertainties

Bin edges (GeV)	Ratio	Abs. Unc.	Frac. Stat. Unc.	Frac. Sys. Unc.	Frac. Flux Unc.
0.035-0.100	0.73	0.101	0.083	0.110	0.001
0.100-0.150	0.69	0.086	0.070	0.104	0.002
0.150-0.200	0.72	0.127	0.104	0.144	0.001
0.200-0.350	0.55	0.220	0.216	0.334	0.003

Table D.68: Statistical covariance matrix of measured cross section ratio of iron over scintillator in T_π

Bin edges (GeV)	0.035-0.100	0.100-0.150	0.150-0.200	0.200-0.350
0.035-0.100	0.0037	0.0012	-0.0006	-0.0006
0.100-0.150	0.0012	0.0023	0.0010	-0.0003
0.150-0.200	-0.0006	0.0010	0.0055	0.0028
0.200-0.350	-0.0006	-0.0003	0.0028	0.0143

Table D.69: Systematic covariance matrix of measured cross section ratio of iron over scintillator in T_π

Bin edges (GeV)	0.035-0.100	0.100-0.150	0.150-0.200	0.200-0.350
0.035-0.100	0.007	0.005	0.005	0.008
0.100-0.150	0.005	0.005	0.007	0.011
0.150-0.200	0.005	0.007	0.011	0.018
0.200-0.350	0.008	0.011	0.018	0.034

Table D.70: Measured cross section ratio of iron over scintillator in θ_π, and the absolute and fractional cross section ratio uncertainties

Bin edges (degree)	Ratio	Abs. Unc.	Frac. Stat. Unc.	Frac. Sys. Unc.	Frac. Flux Unc.
0-10	1.10	0.520	0.447	0.158	0.002
10-20	0.70	0.201	0.239	0.163	0.005
20-30	0.65	0.135	0.142	0.150	0.001
30-40	0.64	0.119	0.123	0.141	0.002
40-50	0.63	0.108	0.111	0.131	0.003
50-60	0.75	0.117	0.108	0.112	0.001
60-120	0.75	0.112	0.107	0.103	0.002
120-135	0.74	0.181	0.191	0.151	0.003
135-150	0.62	0.188	0.252	0.171	0.005
150-165	0.63	0.341	0.493	0.232	0.006
165-180	1.65	1.961	1.081	0.492	0.016

Table D.71: Statistical covariance matrix of measured cross section ratio of iron over scintillator in θ_π

Bin edges (degree)	0-10	10-20	20-30	30-40	40-50	50-60	60-120	120-135	135-150	150-165	165-180
0-10	0.2404	0.0268	-0.0013	-0.0003	0.0002	-0.0006	-0.0006	-0.0010	0.0022	0.0053	-0.0009
10-20	0.0268	0.0277	0.0045	-0.0006	-0.0008	-0.0004	-0.0002	-0.0005	-0.0005	-0.0006	-0.0012
20-30	-0.0013	0.0045	0.0086	0.0022	-0.0004	-0.0005	-0.0003	-0.0005	-0.0000	0.0002	-0.0012
30-40	-0.0003	-0.0006	0.0022	0.0061	0.0020	-0.0004	-0.0005	-0.0005	0.0001	0.0003	-0.0019
40-50	0.0002	-0.0008	-0.0004	0.0020	0.0049	0.0021	-0.0003	-0.0003	-0.0000	-0.0004	-0.0017
50-60	-0.0006	-0.0004	-0.0005	-0.0004	0.0021	0.0066	0.0021	-0.0007	-0.0009	-0.0011	-0.0002
60-120	-0.0006	-0.0002	-0.0003	-0.0005	-0.0003	0.0021	0.0065	0.0018	-0.0003	-0.0001	0.0041
120-135	-0.0010	-0.0005	-0.0005	-0.0005	-0.0003	-0.0007	0.0018	0.0200	0.0078	0.0013	-0.0207
135-150	0.0022	-0.0005	-0.0000	0.0001	-0.0000	-0.0009	-0.0003	0.0078	0.0241	0.0225	0.0291
150-165	0.0053	-0.0006	0.0002	0.0003	-0.0004	-0.0011	-0.0001	0.0013	0.0225	0.0954	0.3102
165-180	-0.0009	-0.0012	-0.0012	-0.0019	-0.0017	-0.0002	0.0041	-0.0207	0.0291	0.3102	3.1858

Table D.72: Systematic covariance matrix of measured cross section ratio of iron over scintillator in θ_π

Bin edges (degree)	0-10	10-20	20-30	30-40	40-50	50-60	60-120	120-135	135-150	150-165	165-180
0-10	0.030	0.014	0.012	0.011	0.011	0.011	0.011	0.015	0.011	0.013	-0.041
10-20	0.014	0.013	0.010	0.009	0.008	0.006	0.006	0.009	0.007	0.010	-0.018
20-30	0.012	0.010	0.010	0.008	0.007	0.006	0.006	0.009	0.007	0.010	-0.006
30-40	0.011	0.009	0.008	0.008	0.007	0.006	0.006	0.008	0.006	0.009	0.001
40-50	0.011	0.008	0.007	0.007	0.007	0.006	0.006	0.008	0.007	0.007	-0.003
50-60	0.011	0.006	0.006	0.006	0.006	0.007	0.006	0.008	0.006	0.006	0.001
60-120	0.011	0.006	0.006	0.006	0.006	0.006	0.006	0.007	0.005	0.006	0.005
120-135	0.015	0.009	0.009	0.008	0.008	0.008	0.007	0.013	0.010	0.011	-0.010
135-150	0.011	0.007	0.007	0.006	0.007	0.006	0.005	0.010	0.011	0.011	-0.012
150-165	0.013	0.010	0.010	0.009	0.007	0.006	0.006	0.011	0.011	0.021	-0.001
165-180	-0.041	-0.018	-0.006	0.001	-0.003	0.001	0.005	-0.010	-0.012	-0.001	0.659

Table D.73: Measured cross section ratio of lead over scintillator in p_μ, and the absolute and fractional cross section ratio uncertainties

Bin edges (GeV/c)	Ratio	Abs. Unc.	Frac. Stat. Unc.	Frac. Sys. Unc.	Frac. Flux Unc.
1.5-3.0	0.43	0.113	0.241	0.108	0.010
3.0-4.0	0.51	0.093	0.146	0.106	0.009
4.0-5.0	0.43	0.071	0.112	0.121	0.009
5.0-6.0	0.41	0.068	0.105	0.129	0.005
6.0-7.0	0.34	0.062	0.122	0.133	0.007
7.0-8.5	0.34	0.064	0.140	0.121	0.019
8.5-10.0	0.38	0.087	0.190	0.126	0.026
10.0-20.0	0.36	0.140	0.345	0.177	0.044

Table D.74: Statistical covariance matrix of measured cross section ratio of lead over scintillator in p_μ

Bin edges (GeV/c)	1.5-3.0	3.0-4.0	4.0-5.0	5.0-6.0	6.0-7.0	7.0-8.5	8.5-10.0	10.0-20.0
1.5-3.0	0.0106	0.0013	0.0002	0.0000	0.0001	0.0000	0.0000	0.0000
3.0-4.0	0.0013	0.0056	0.0011	0.0002	0.0001	0.0001	0.0000	0.0000
4.0-5.0	0.0002	0.0011	0.0024	0.0008	0.0002	0.0001	0.0001	0.0000
5.0-6.0	0.0000	0.0002	0.0008	0.0018	0.0009	0.0003	0.0001	0.0001
6.0-7.0	0.0001	0.0001	0.0002	0.0009	0.0017	0.0011	0.0004	0.0002
7.0-8.5	0.0000	0.0001	0.0001	0.0003	0.0011	0.0023	0.0018	0.0008
8.5-10.0	0.0000	0.0000	0.0001	0.0001	0.0004	0.0018	0.0052	0.0043
10.0-20.0	0.0000	0.0000	0.0000	0.0001	0.0002	0.0008	0.0043	0.0155

Table D.75: Systematic covariance matrix of measured cross section ratio of lead over scintillator in p_μ

Bin edges (GeV/c)	1.5-3.0	3.0-4.0	4.0-5.0	5.0-6.0	6.0-7.0	7.0-8.5	8.5-10.0	10.0-20.0
1.5-3.0	0.002	0.002	0.002	0.002	0.002	0.001	0.001	0.002
3.0-4.0	0.002	0.003	0.003	0.002	0.002	0.002	0.002	0.002
4.0-5.0	0.002	0.003	0.003	0.003	0.002	0.002	0.001	0.002
5.0-6.0	0.002	0.002	0.003	0.003	0.002	0.002	0.002	0.002
6.0-7.0	0.002	0.002	0.002	0.002	0.002	0.002	0.002	0.002
7.0-8.5	0.001	0.002	0.002	0.002	0.002	0.002	0.002	0.002
8.5-10.0	0.001	0.002	0.001	0.002	0.002	0.002	0.002	0.002
10.0-20.0	0.002	0.002	0.002	0.002	0.002	0.002	0.002	0.004

Table D.76: Measured cross section ratio of lead over scintillator in θ_μ, and the absolute and fractional cross section ratio uncertainties

Bin edges (degree)	Ratio	Abs. Unc.	Frac. Stat. Unc.	Frac. Sys. Unc.	Frac. Flux Unc.
0-2	0.32	0.081	0.217	0.136	0.010
2-3	0.38	0.071	0.171	0.078	0.003
3-4	0.30	0.064	0.184	0.108	0.003
4-5	0.33	0.072	0.186	0.115	0.006
5-6	0.31	0.084	0.224	0.155	0.006
6-8	0.36	0.091	0.195	0.161	0.003
8-10	0.59	0.158	0.208	0.168	0.002
10-13	0.79	0.240	0.257	0.164	0.005

Table D.77: Statistical covariance matrix of measured cross section ratio of lead over scintillator in θ_μ

Bin edges (degree)	0-2	2-3	3-4	4-5	5-6	6-8	8-10	10-13
0-2	0.0048	0.0001	-0.0003	-0.0000	0.0000	-0.0000	-0.0000	-0.0000
2-3	0.0001	0.0042	0.0005	-0.0004	-0.0001	-0.0000	-0.0000	-0.0000
3-4	-0.0003	0.0005	0.0030	0.0005	-0.0003	-0.0001	-0.0000	-0.0000
4-5	-0.0000	-0.0004	0.0005	0.0038	0.0008	-0.0003	-0.0001	0.0000
5-6	0.0000	-0.0001	-0.0003	0.0008	0.0048	0.0003	-0.0004	-0.0000
6-8	-0.0000	-0.0000	-0.0001	-0.0003	0.0003	0.0049	-0.0000	-0.0006
8-10	-0.0000	-0.0000	-0.0000	-0.0001	-0.0004	-0.0000	0.0150	-0.0005
10-13	-0.0000	-0.0000	-0.0000	0.0000	-0.0000	-0.0006	-0.0005	0.0409

Table D.78: Systematic covariance matrix of measured cross section ratio of lead over scintillator in θ_μ

Bin edges (degree)	0-2	2-3	3-4	4-5	5-6	6-8	8-10	10-13
0-2	0.002	0.001	0.000	0.000	0.000	0.000	0.001	0.001
2-3	0.001	0.001	0.001	0.001	0.001	0.001	0.002	0.002
3-4	0.000	0.001	0.001	0.001	0.001	0.002	0.002	0.003
4-5	0.000	0.001	0.001	0.001	0.002	0.002	0.003	0.004
5-6	0.000	0.001	0.001	0.002	0.002	0.003	0.004	0.005
6-8	0.000	0.001	0.002	0.002	0.003	0.003	0.005	0.006
8-10	0.001	0.002	0.002	0.003	0.004	0.005	0.010	0.011
10-13	0.001	0.002	0.003	0.004	0.005	0.006	0.011	0.017

Table D.79: Measured cross section ratio of lead over scintillator in $p_{\mu,||}$, and the absolute and fractional cross section ratio uncertainties

Bin edges (GeV/c)	Ratio	Abs. Unc.	Frac. Stat. Unc.	Frac. Sys. Unc.	Frac. Flux Unc.
1.5-3.0	0.46	0.115	0.230	0.106	0.009
3.0-4.0	0.50	0.093	0.145	0.112	0.009
4.0-5.0	0.43	0.071	0.114	0.123	0.009
5.0-6.0	0.40	0.067	0.105	0.127	0.005
6.0-7.0	0.34	0.061	0.123	0.130	0.007
7.0-8.5	0.35	0.064	0.139	0.120	0.019
8.5-10.0	0.39	0.086	0.187	0.121	0.025
10.0-20.0	0.37	0.140	0.341	0.174	0.043

Table D.80: Statistical covariance matrix of measured cross section ratio of lead over scintillator in $p_{\mu,||}$

Bin edges (GeV/c)	1.5-3.0	3.0-4.0	4.0-5.0	5.0-6.0	6.0-7.0	7.0-8.5	8.5-10.0	10.0-20.0
1.5-3.0	0.0110	0.0012	0.0002	0.0000	0.0001	0.0000	0.0000	0.0000
3.0-4.0	0.0012	0.0054	0.0010	0.0002	0.0001	0.0001	0.0001	0.0000
4.0-5.0	0.0002	0.0010	0.0024	0.0008	0.0002	0.0001	0.0001	0.0000
5.0-6.0	0.0000	0.0002	0.0008	0.0018	0.0009	0.0003	0.0001	0.0001
6.0-7.0	0.0001	0.0001	0.0002	0.0009	0.0017	0.0011	0.0004	0.0002
7.0-8.5	0.0000	0.0001	0.0001	0.0003	0.0011	0.0023	0.0019	0.0008
8.5-10.0	0.0000	0.0001	0.0001	0.0001	0.0004	0.0019	0.0052	0.0044
10.0-20.0	0.0000	0.0000	0.0000	0.0001	0.0002	0.0008	0.0044	0.0155

Table D.81: Systematic covariance matrix of measured cross section ratio of lead over scintillator in $p_{\mu,||}$

Bin edges (GeV/c)	1.5-3.0	3.0-4.0	4.0-5.0	5.0-6.0	6.0-7.0	7.0-8.5	8.5-10.0	10.0-20.0
1.5-3.0	0.002	0.002	0.002	0.002	0.002	0.001	0.001	0.002
3.0-4.0	0.002	0.003	0.003	0.003	0.002	0.002	0.002	0.002
4.0-5.0	0.002	0.003	0.003	0.003	0.002	0.002	0.001	0.002
5.0-6.0	0.002	0.003	0.003	0.003	0.002	0.002	0.002	0.002
6.0-7.0	0.002	0.002	0.002	0.002	0.002	0.002	0.002	0.002
7.0-8.5	0.001	0.002	0.002	0.002	0.002	0.002	0.002	0.002
8.5-10.0	0.001	0.002	0.001	0.002	0.002	0.002	0.002	0.002
10.0-20.0	0.002	0.002	0.002	0.002	0.002	0.002	0.002	0.004

Table D.82: Measured cross section ratio of lead over scintillator in $p_{\mu,T}$, and the absolute and fractional cross section ratio uncertainties

Bin edges (GeV/c)	Ratio	Abs. Unc.	Frac. Stat. Unc.	Frac. Sys. Unc.	Frac. Flux Unc.
0.00-0.15	0.31	0.119	0.315	0.219	0.008
0.15-0.30	0.32	0.060	0.164	0.094	0.002
0.30-0.45	0.38	0.056	0.117	0.088	0.001
0.45-0.60	0.33	0.067	0.150	0.136	0.002
0.60-0.75	0.34	0.104	0.212	0.222	0.010
0.75-0.90	0.40	0.143	0.263	0.245	0.009
0.90-1.25	0.99	0.278	0.235	0.153	0.006
1.25-2.50	2.14	1.442	0.601	0.307	0.030

Table D.83: Statistical covariance matrix of measured cross section ratio of lead over scintillator in $p_{\mu,T}$

Bin edges (GeV/c)	0.00-0.15	0.15-0.30	0.30-0.45	0.45-0.60	0.60-0.75	0.75-0.90	0.90-1.25	1.25-2.50
0.00-0.15	0.0096	0.0003	-0.0003	-0.0001	0.0000	-0.0000	0.0000	-0.0003
0.15-0.30	0.0003	0.0027	0.0002	-0.0002	-0.0001	-0.0000	-0.0000	-0.0001
0.30-0.45	-0.0003	0.0002	0.0020	0.0003	-0.0003	-0.0002	-0.0001	-0.0001
0.45-0.60	-0.0001	-0.0002	0.0003	0.0025	0.0008	-0.0003	-0.0006	-0.0006
0.60-0.75	0.0000	-0.0001	-0.0003	0.0008	0.0052	0.0018	-0.0007	-0.0018
0.75-0.90	-0.0000	-0.0000	-0.0002	-0.0003	0.0018	0.0110	0.0060	-0.0109
0.90-1.25	0.0000	-0.0000	-0.0001	-0.0006	-0.0007	0.0060	0.0544	0.0383
1.25-2.50	-0.0003	-0.0001	-0.0001	-0.0006	-0.0018	-0.0109	0.0383	1.6498

Table D.84: Systematic covariance matrix of measured cross section ratio of lead over scintillator in $p_{\mu,T}$

Bin edges (GeV/c)	0.00-0.15	0.15-0.30	0.30-0.45	0.45-0.60	0.60-0.75	0.75-0.90	0.90-1.25	1.25-2.50
0.00-0.15	0.005	0.001	0.000	-0.000	-0.000	0.000	0.003	0.005
0.15-0.30	0.001	0.001	0.001	0.001	0.001	0.002	0.003	0.003
0.30-0.45	0.000	0.001	0.001	0.001	0.002	0.003	0.004	0.005
0.45-0.60	-0.000	0.001	0.001	0.002	0.003	0.004	0.005	0.006
0.60-0.75	-0.000	0.001	0.002	0.003	0.006	0.007	0.007	0.004
0.75-0.90	0.000	0.002	0.003	0.004	0.007	0.009	0.011	0.007
0.90-1.25	0.003	0.003	0.004	0.005	0.007	0.011	0.023	0.030
1.25-2.50	0.005	0.003	0.005	0.006	0.004	0.007	0.030	0.431

Table D.85: Measured cross section ratio of lead over scintillator in Q^2, and the absolute and fractional cross section ratio uncertainties

Bin edges (GeV^2)	Ratio	Abs. Unc.	Frac. Stat. Unc.	Frac. Sys. Unc.	Frac. Flux Unc.
0.000-0.025	0.30	0.114	0.315	0.221	0.008
0.025-0.050	0.32	0.076	0.209	0.108	0.002
0.050-0.100	0.30	0.062	0.181	0.094	0.002
0.100-0.200	0.38	0.058	0.124	0.090	0.002
0.200-0.300	0.35	0.068	0.150	0.125	0.002
0.300-0.400	0.30	0.075	0.202	0.153	0.003
0.400-0.500	0.35	0.095	0.206	0.171	0.005
0.500-0.700	0.36	0.123	0.238	0.244	0.010
0.700-1.000	0.50	0.174	0.255	0.231	0.007
1.000-1.300	1.04	0.323	0.272	0.150	0.009
1.300-2.000	0.96	0.535	0.510	0.230	0.016
2.000-3.000	3.07	3.290	0.988	0.418	0.051

Table D.86: Statistical covariance matrix of measured cross section ratio of lead over scintillator in Q^2

Bin edges (GeV^2)	0.000-0.025	0.025-0.050	0.050-0.100	0.100-0.200	0.200-0.300	0.300-0.400	0.400-0.500	0.500-0.700	0.700-1.000	1.000-1.300	1.300-2.000	2.000-3.000
0.000-0.025	0.0087	0.0016	-0.0005	-0.0002	-0.0000	-0.0000	-0.0000	0.0000	-0.0000	0.0000	-0.0001	-0.0003
0.025-0.050	0.0016	0.0046	0.0013	-0.0003	-0.0002	-0.0000	-0.0000	-0.0000	-0.0000	-0.0000	-0.0000	-0.0001
0.050-0.100	-0.0005	0.0013	0.0030	0.0005	-0.0003	-0.0001	-0.0001	-0.0000	-0.0000	-0.0001	-0.0001	0.0000
0.100-0.200	-0.0002	-0.0003	0.0005	0.0022	0.0006	-0.0002	-0.0003	-0.0001	-0.0001	-0.0001	-0.0000	-0.0002
0.200-0.300	-0.0000	-0.0002	-0.0003	0.0006	0.0027	0.0013	0.0001	-0.0003	-0.0002	-0.0000	-0.0001	-0.0002
0.300-0.400	-0.0000	-0.0000	-0.0001	-0.0002	0.0013	0.0036	0.0026	0.0000	-0.0006	-0.0007	-0.0009	-0.0002
0.400-0.500	-0.0000	-0.0000	-0.0001	-0.0003	0.0001	0.0026	0.0053	0.0029	-0.0002	-0.0014	-0.0009	-0.0013
0.500-0.700	0.0000	-0.0000	-0.0000	-0.0001	-0.0003	0.0000	0.0029	0.0073	0.0039	-0.0014	-0.0001	-0.0031
0.700-1.000	-0.0000	-0.0000	-0.0000	-0.0001	-0.0002	-0.0006	-0.0002	0.0039	0.0166	0.0119	-0.0010	-0.0176
1.000-1.300	0.0000	-0.0000	-0.0001	-0.0001	-0.0000	-0.0007	-0.0014	-0.0014	0.0119	0.0798	0.0197	-0.0275
1.300-2.000	-0.0001	-0.0000	-0.0001	-0.0000	-0.0001	-0.0009	-0.0009	-0.0001	-0.0010	0.0197	0.2382	0.1255
2.000-3.000	-0.0003	-0.0001	0.0000	-0.0002	-0.0002	-0.0002	-0.0013	-0.0031	-0.0176	-0.0275	0.1255	9.1773

Table D.87: Systematic covariance matrix of measured cross section ratio of lead over scintillator in Q^2

Bin edges (GeV^2)	0.000-0.025	0.025-0.050	0.050-0.100	0.100-0.200	0.200-0.300	0.300-0.400	0.400-0.500	0.500-0.700	0.700-1.000	1.000-1.300	1.300-2.000	2.000-3.000
0.000-0.025	0.004	0.002	0.001	0.000	-0.000	-0.000	-0.000	-0.000	0.001	0.002	0.001	0.012
0.025-0.050	0.002	0.001	0.001	0.001	0.000	0.000	0.000	0.001	0.001	0.002	0.001	0.008
0.050-0.100	0.001	0.001	0.001	0.001	0.001	0.001	0.001	0.002	0.002	0.004	0.002	0.006
0.100-0.200	0.000	0.001	0.001	0.001	0.001	0.001	0.002	0.002	0.003	0.005	0.004	0.013
0.200-0.300	-0.000	0.000	0.001	0.001	0.002	0.002	0.002	0.003	0.004	0.004	0.004	0.002
0.300-0.400	-0.000	0.000	0.001	0.001	0.002	0.002	0.003	0.004	0.004	0.005	0.006	0.008
0.400-0.500	-0.000	0.000	0.001	0.002	0.002	0.003	0.004	0.005	0.006	0.007	0.009	0.012
0.500-0.700	-0.000	0.001	0.002	0.002	0.003	0.004	0.005	0.008	0.010	0.009	0.014	0.005
0.700-1.000	0.001	0.001	0.002	0.003	0.004	0.004	0.006	0.010	0.014	0.012	0.019	0.011
1.000-1.300	0.002	0.002	0.004	0.005	0.004	0.005	0.007	0.009	0.012	0.024	0.013	0.066
1.300-2.000	0.001	0.001	0.002	0.004	0.004	0.006	0.009	0.014	0.019	0.013	0.048	0.001
2.000-3.000	0.012	0.008	0.006	0.013	0.002	0.008	0.012	0.005	0.011	0.066	0.001	1.645

Table D.88: Measured cross section ratio of lead over scintillator in W_{exp}, and the absolute and fractional cross section ratio uncertainties

Bin edges (GeV/c^2)	Ratio	Abs. Unc.	Frac. Stat. Unc.	Frac. Sys. Unc.	Frac. Flux Unc.
0.9-1.1	0.55	0.255	0.440	0.157	0.013
1.1-1.2	0.21	0.056	0.247	0.088	0.011
1.2-1.3	0.38	0.058	0.094	0.119	0.003
1.3-1.4	0.60	0.158	0.170	0.204	0.004

Table D.89: Statistical covariance matrix of measured cross section ratio of lead over scintillator in W_{exp}

Bin edges (GeV/c^2)	0.9-1.1	1.1-1.2	1.2-1.3	1.3-1.4
0.9-1.1	0.0577	0.0040	-0.0031	-0.0061
1.1-1.2	0.0040	0.0027	0.0005	-0.0034
1.2-1.3	-0.0031	0.0005	0.0013	0.0009
1.3-1.4	-0.0061	-0.0034	0.0009	0.0103

Table D.90: Systematic covariance matrix of measured cross section ratio of lead over scintillator in W_{exp}

Bin edges (GeV/c^2)	0.9-1.1	1.1-1.2	1.2-1.3	1.3-1.4
0.9-1.1	0.007	0.001	-0.001	-0.001
1.1-1.2	0.001	0.000	-0.000	-0.001
1.2-1.3	-0.001	-0.000	0.002	0.005
1.3-1.4	-0.001	-0.001	0.005	0.015

Table D.91: Measured cross section ratio of lead over scintillator in T_π, and the absolute and fractional cross section ratio uncertainties

Bin edges (GeV)	Ratio	Abs. Unc.	Frac. Stat. Unc.	Frac. Sys. Unc.	Frac. Flux Unc.
0.035-0.100	0.39	0.056	0.116	0.082	0.003
0.100-0.150	0.37	0.050	0.095	0.094	0.004
0.150-0.200	0.41	0.078	0.135	0.136	0.005
0.200-0.350	0.60	0.177	0.190	0.225	0.003

Table D.92: Statistical covariance matrix of measured cross section ratio of lead over scintillator in T_π

Bin edges (GeV)	0.035-0.100	0.100-0.150	0.150-0.200	0.200-0.350
0.035-0.100	0.0021	0.0006	-0.0003	-0.0005
0.100-0.150	0.0006	0.0013	0.0005	-0.0003
0.150-0.200	-0.0003	0.0005	0.0030	0.0014
0.200-0.350	-0.0005	-0.0003	0.0014	0.0130

Table D.93: Systematic covariance matrix of measured cross section ratio of lead over scintillator in T_π

Bin edges (GeV)	0.035-0.100	0.100-0.150	0.150-0.200	0.200-0.350
0.035-0.100	0.001	0.001	0.001	0.002
0.100-0.150	0.001	0.001	0.002	0.004
0.150-0.200	0.001	0.002	0.003	0.006
0.200-0.350	0.002	0.004	0.006	0.018

Table D.94: Measured cross section ratio of lead over scintillator in θ_π, and the absolute and fractional cross section ratio uncertainties

Bin edges (degree)	Ratio	Abs. Unc.	Frac. Stat. Unc.	Frac. Sys. Unc.	Frac. Flux Unc.
0-10	0.73	0.375	0.483	0.177	0.005
10-20	0.50	0.154	0.255	0.171	0.002
20-30	0.37	0.084	0.174	0.148	0.002
30-40	0.44	0.074	0.127	0.114	0.004
40-50	0.39	0.069	0.124	0.124	0.004
50-60	0.32	0.067	0.159	0.139	0.006
60-120	0.34	0.062	0.145	0.111	0.005
120-135	0.49	0.097	0.173	0.097	0.001
135-150	0.53	0.123	0.197	0.124	0.003
150-165	0.57	0.217	0.355	0.143	0.003
165-180	0.52	0.539	0.974	0.364	0.026

Table D.95: Statistical covariance matrix of measured cross section ratio of lead over scintillator in θ_π

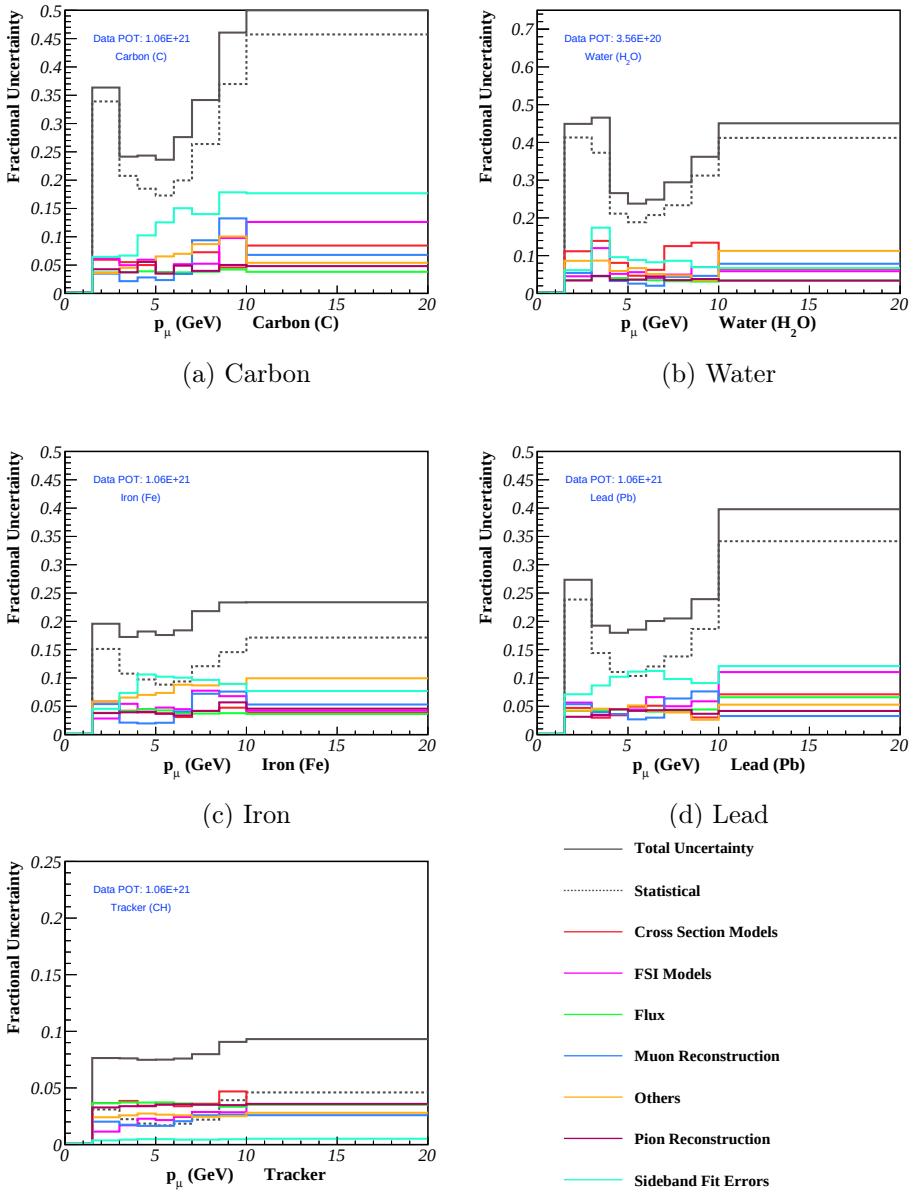
Bin edges (degree)	0-10	10-20	20-30	30-40	40-50	50-60	60-120	120-135	135-150	150-165	165-180
0-10	0.1236	0.0162	0.0009	-0.0002	-0.0005	-0.0005	-0.0005	-0.0005	-0.0007	0.0031	-0.0014
10-20	0.0162	0.0164	0.0034	-0.0001	-0.0006	-0.0004	-0.0002	-0.0004	-0.0005	-0.0000	-0.0007
20-30	0.0009	0.0034	0.0041	0.0015	-0.0000	-0.0003	-0.0002	-0.0002	-0.0001	0.0002	0.0004
30-40	-0.0002	-0.0001	0.0015	0.0031	0.0013	0.0001	-0.0003	-0.0003	0.0000	-0.0000	-0.0010
40-50	-0.0005	-0.0006	-0.0000	0.0013	0.0024	0.0013	0.0002	-0.0001	-0.0002	-0.0002	-0.0011
50-60	-0.0005	-0.0004	-0.0003	0.0001	0.0013	0.0026	0.0011	-0.0000	-0.0005	-0.0004	-0.0011
60-120	-0.0005	-0.0002	-0.0002	-0.0003	0.0002	0.0011	0.0024	0.0009	0.0001	-0.0001	0.0024
120-135	-0.0005	-0.0004	-0.0002	-0.0003	-0.0001	-0.0000	0.0009	0.0071	0.0043	0.0002	0.0103
135-150	-0.0007	-0.0005	-0.0001	0.0000	-0.0002	-0.0005	0.0001	0.0043	0.0109	0.0100	0.0037
150-165	0.0031	-0.0000	0.0002	-0.0000	-0.0002	-0.0004	-0.0001	0.0002	0.0100	0.0407	-0.0021
165-180	-0.0014	-0.0007	0.0004	-0.0010	-0.0011	-0.0011	0.0024	0.0103	0.0037	-0.0021	0.2553

Table D.96: Systematic covariance matrix of measured cross section ratio of lead over scintillator in θ_π

Bin edges (degree)	0-10	10-20	20-30	30-40	40-50	50-60	60-120	120-135	135-150	150-165	165-180
0-10	0.017	0.008	0.005	0.005	0.005	0.004	0.003	0.004	0.006	0.005	-0.002
10-20	0.008	0.007	0.004	0.003	0.002	0.002	0.002	0.002	0.003	0.003	-0.004
20-30	0.005	0.004	0.003	0.002	0.002	0.002	0.001	0.002	0.003	0.002	-0.001
30-40	0.005	0.003	0.002	0.002	0.002	0.002	0.002	0.002	0.003	0.002	0.000
40-50	0.005	0.002	0.002	0.002	0.002	0.002	0.002	0.002	0.003	0.002	-0.001
50-60	0.004	0.002	0.002	0.002	0.002	0.002	0.001	0.001	0.002	0.001	0.002
60-120	0.003	0.002	0.001	0.002	0.002	0.001	0.001	0.001	0.002	0.001	-0.001
120-135	0.004	0.002	0.002	0.002	0.002	0.001	0.001	0.002	0.003	0.003	-0.000
135-150	0.006	0.003	0.003	0.003	0.003	0.002	0.002	0.003	0.004	0.004	-0.002
150-165	0.005	0.003	0.002	0.002	0.002	0.001	0.001	0.003	0.004	0.007	-0.005
165-180	-0.002	-0.004	-0.001	0.000	-0.001	0.002	-0.001	-0.000	-0.002	-0.005	0.036

Appendix E

Cross Section Error Plots



(a) Carbon

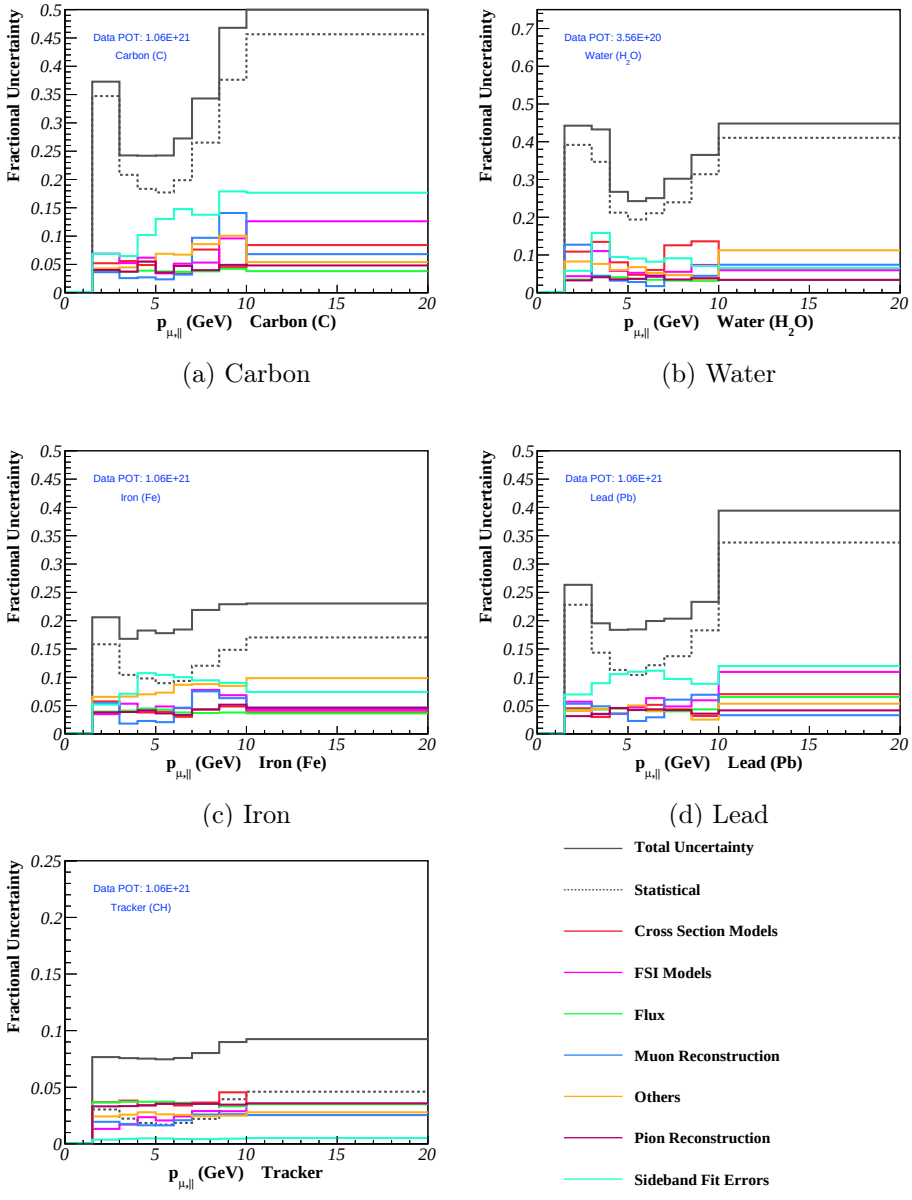
(b) Water

(c) Iron

(d) Lead

(e) Scintillator

Figure E-1: p_μ Error Summary



(a) Carbon

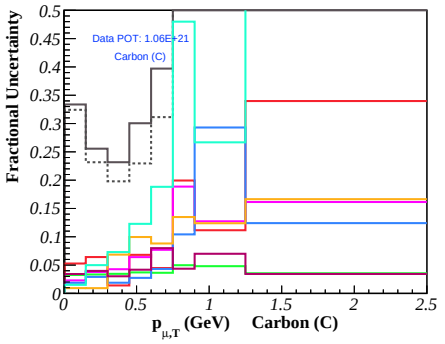
(b) Water

(c) Iron

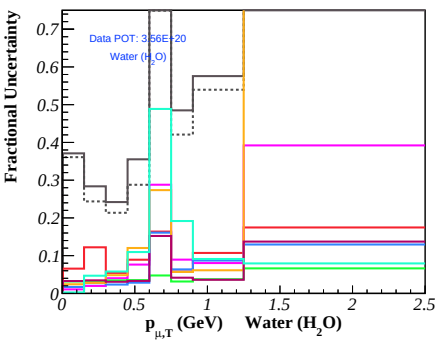
(d) Lead

(e) Scintillator

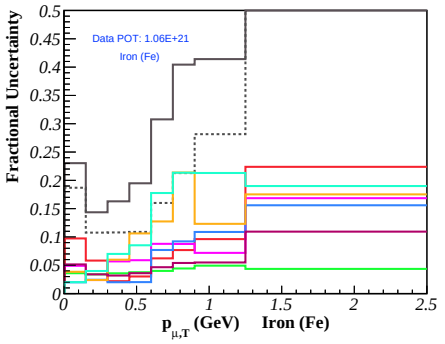
Figure E-2: $p_{\mu,||}$ Error Summary



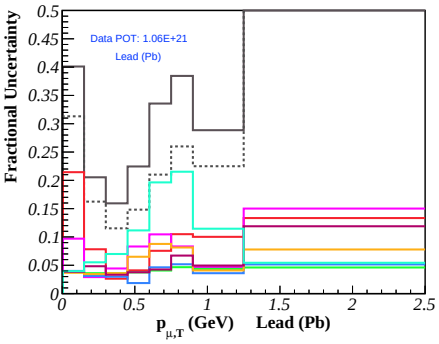
(a) Carbon



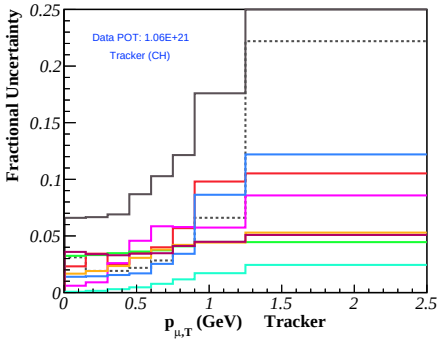
(b) Water



(c) Iron



(d) Lead



(e) Scintillator

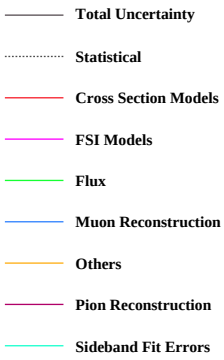
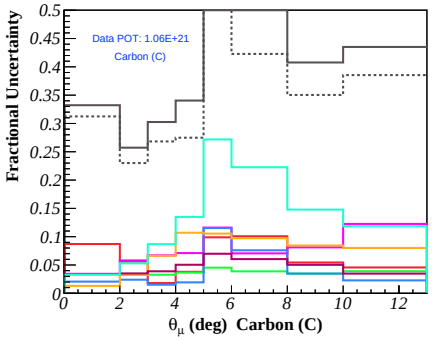
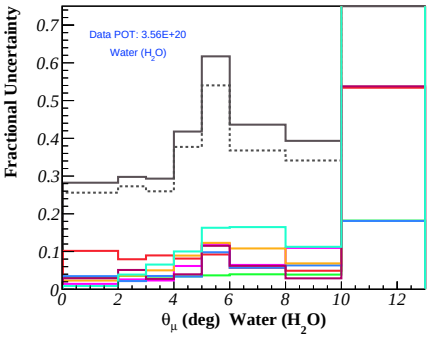


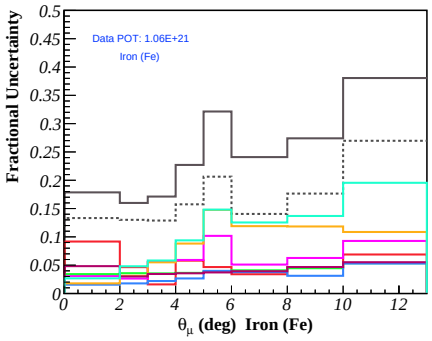
Figure E-3: $p_{\mu,T}$ Error Summary



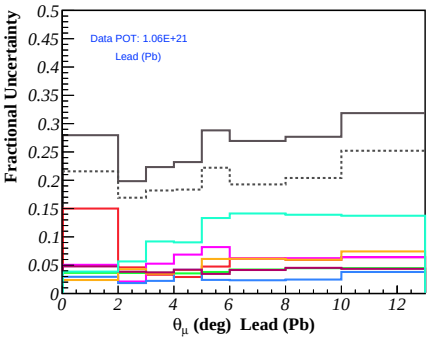
(a) Carbon



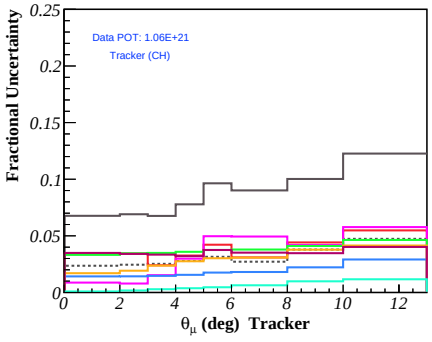
(b) Water

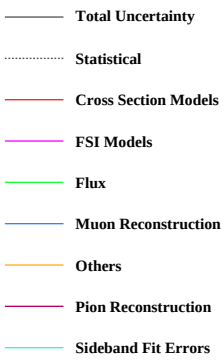


(c) Iron



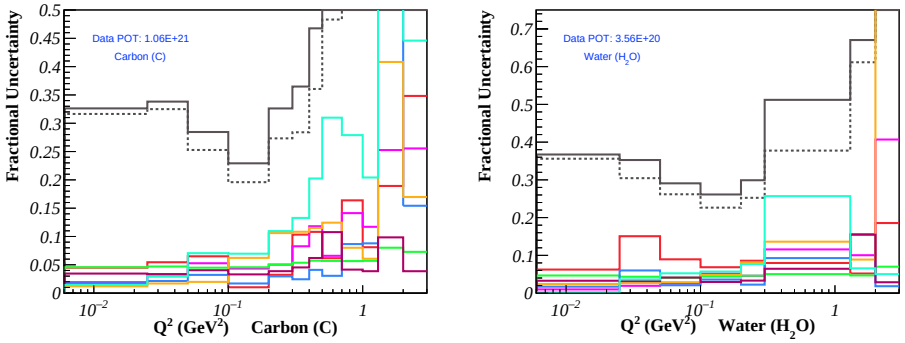
(d) Lead





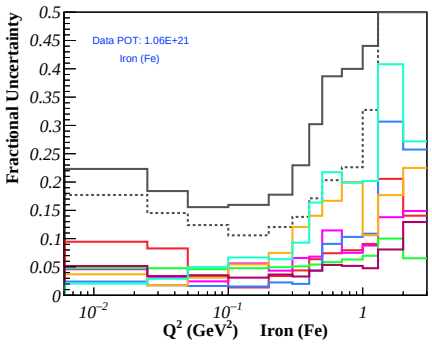
(e) Scintillator

Figure E-4: θ_μ Error Summary

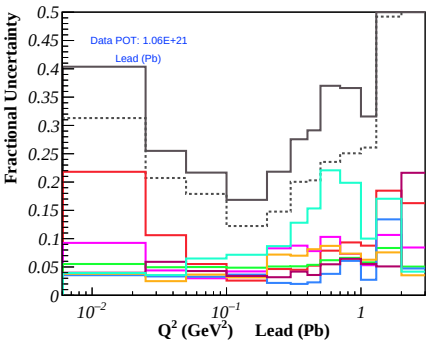


(a) Carbon

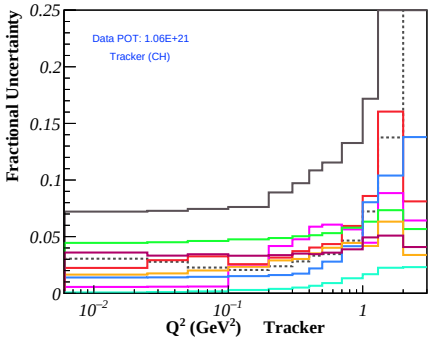
(b) Water



(c) Iron



(d) Lead



(e) Scintillator

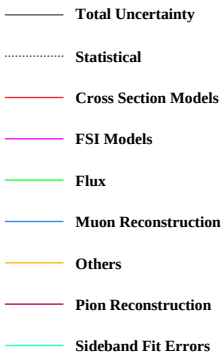
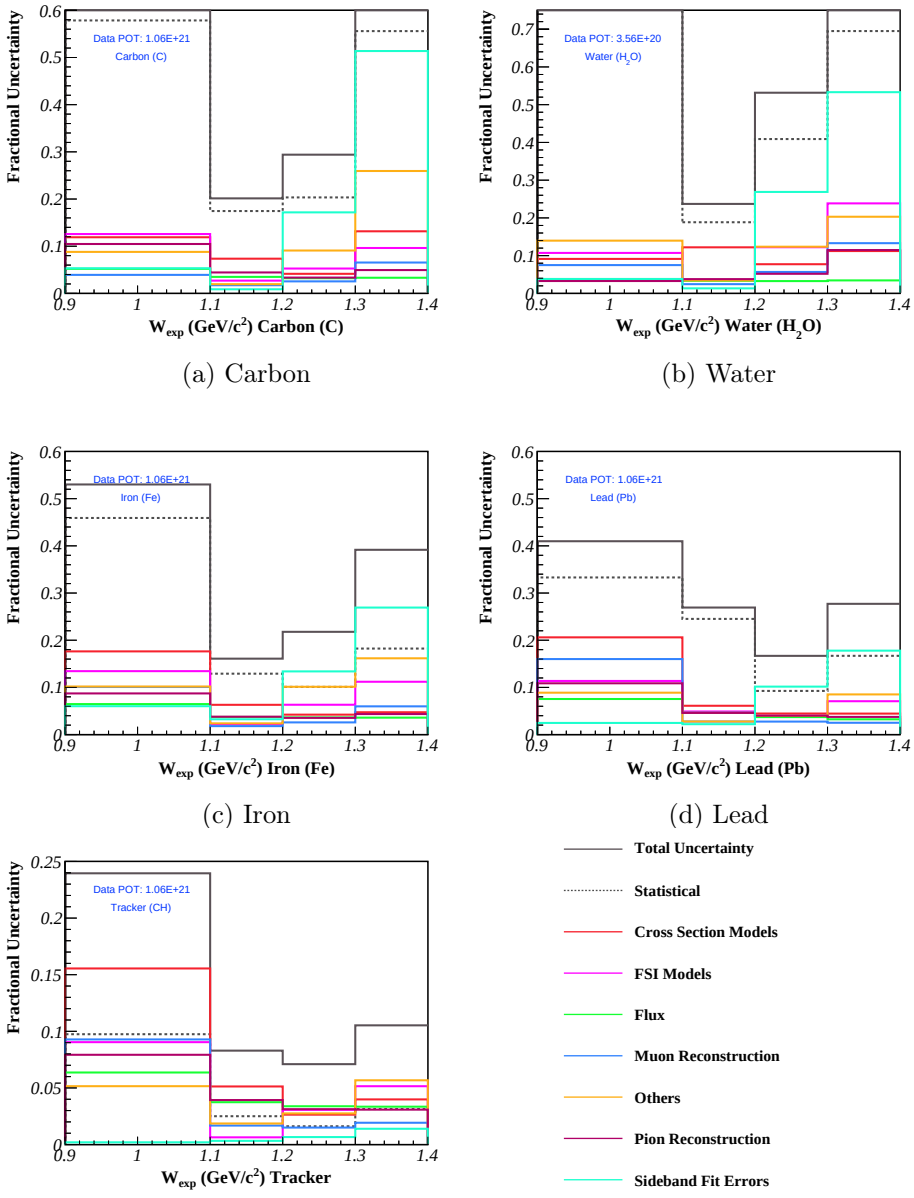


Figure E-5: Q^2 Error Summary



(a) Carbon

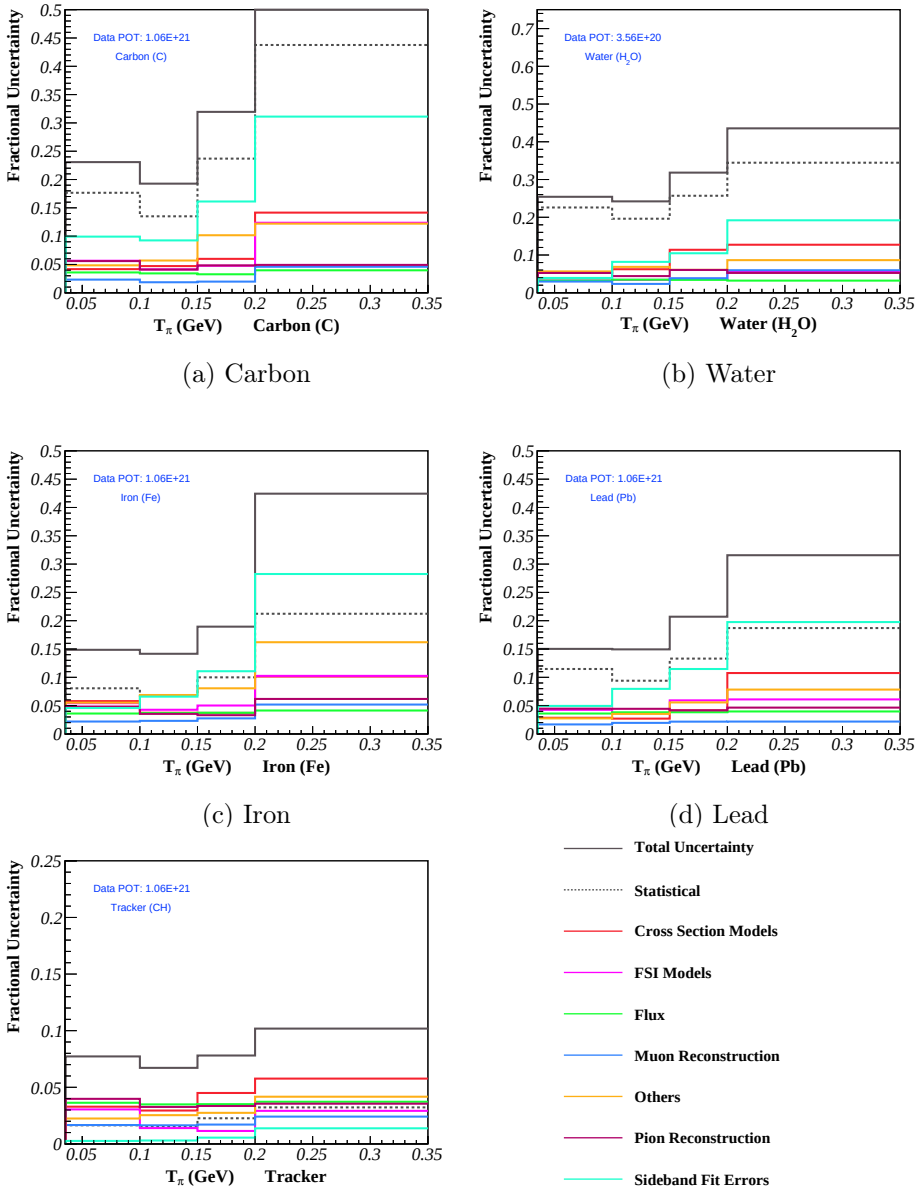
(b) Water

(c) Iron

(d) Lead

(e) Scintillator

Figure E-6: W_{exp} Error Summary



(a) Carbon

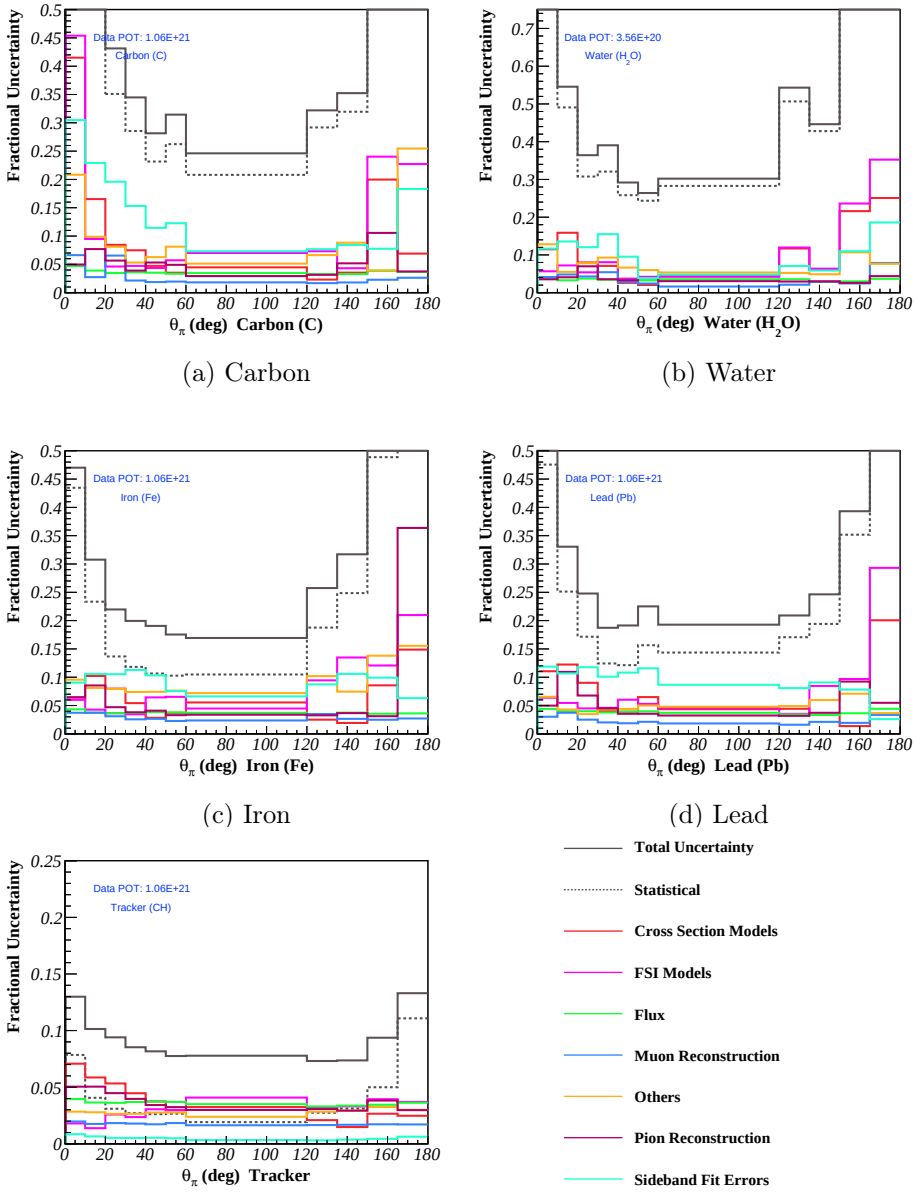
(b) Water

(c) Iron

(d) Lead

(e) Scintillator

Figure E-7: T_π Error Summary



(a) Carbon

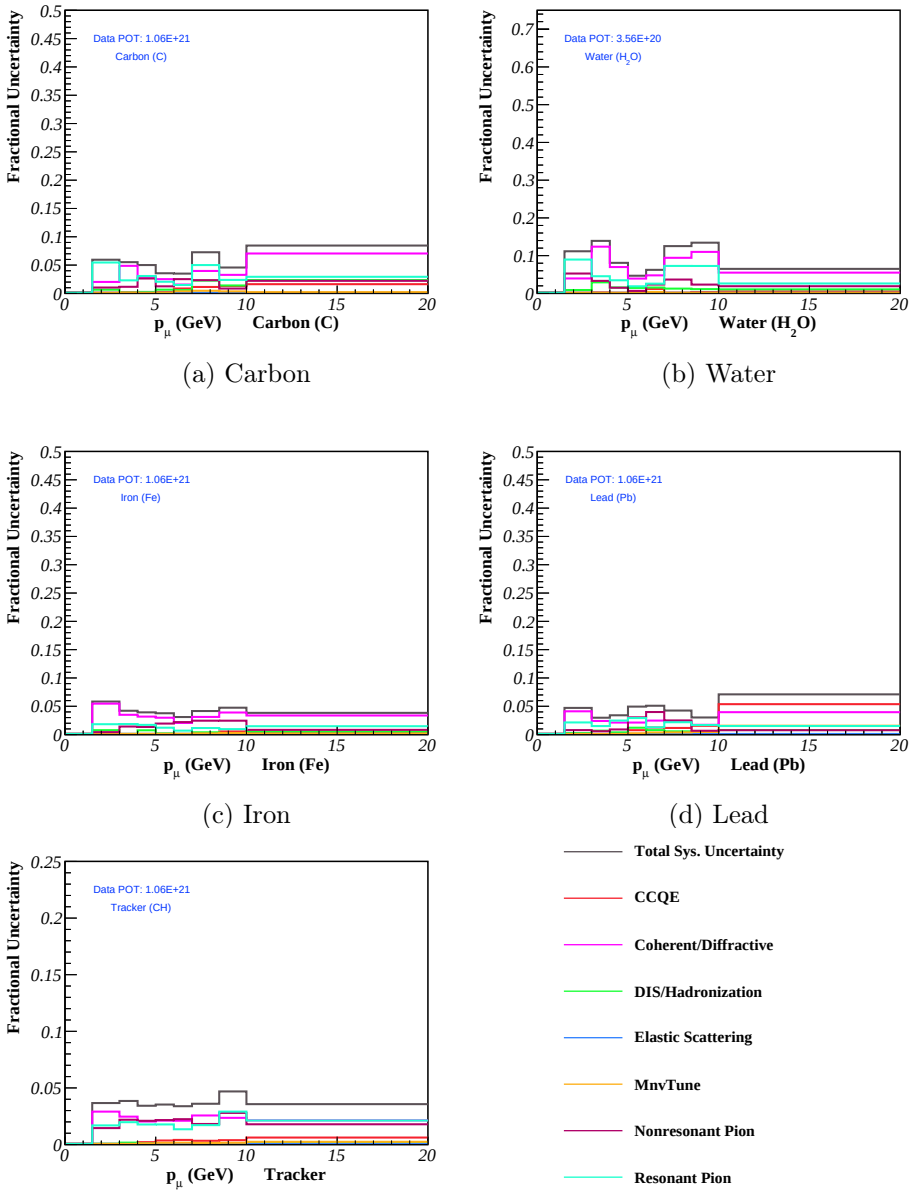
(b) Water

(c) Iron

(d) Lead

(e) Scintillator

Figure E-8: θ_π Error Summary



(a) Carbon

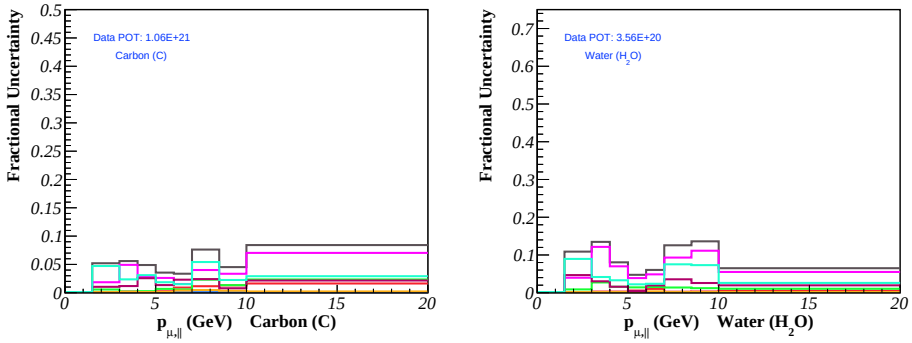
(b) Water

(c) Iron

(d) Lead

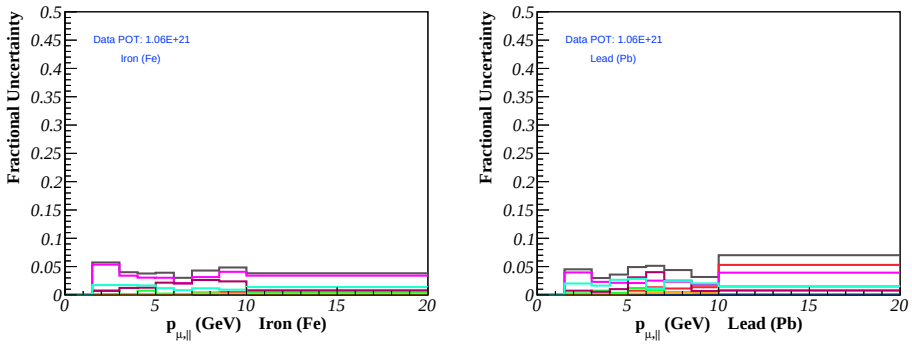
(e) Scintillator

Figure E-9: p_μ All Cross Section Model Errors



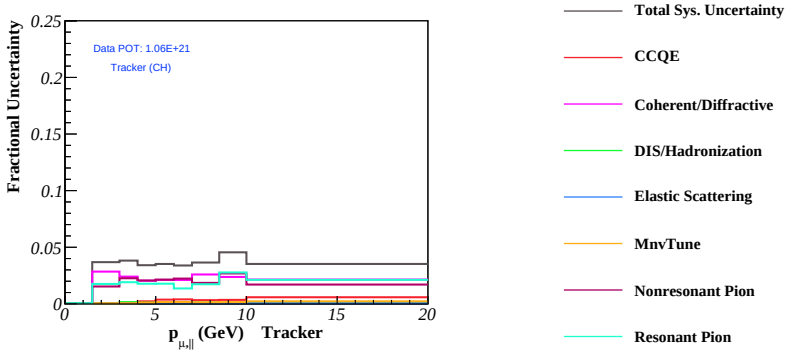
(a) Carbon

(b) Water



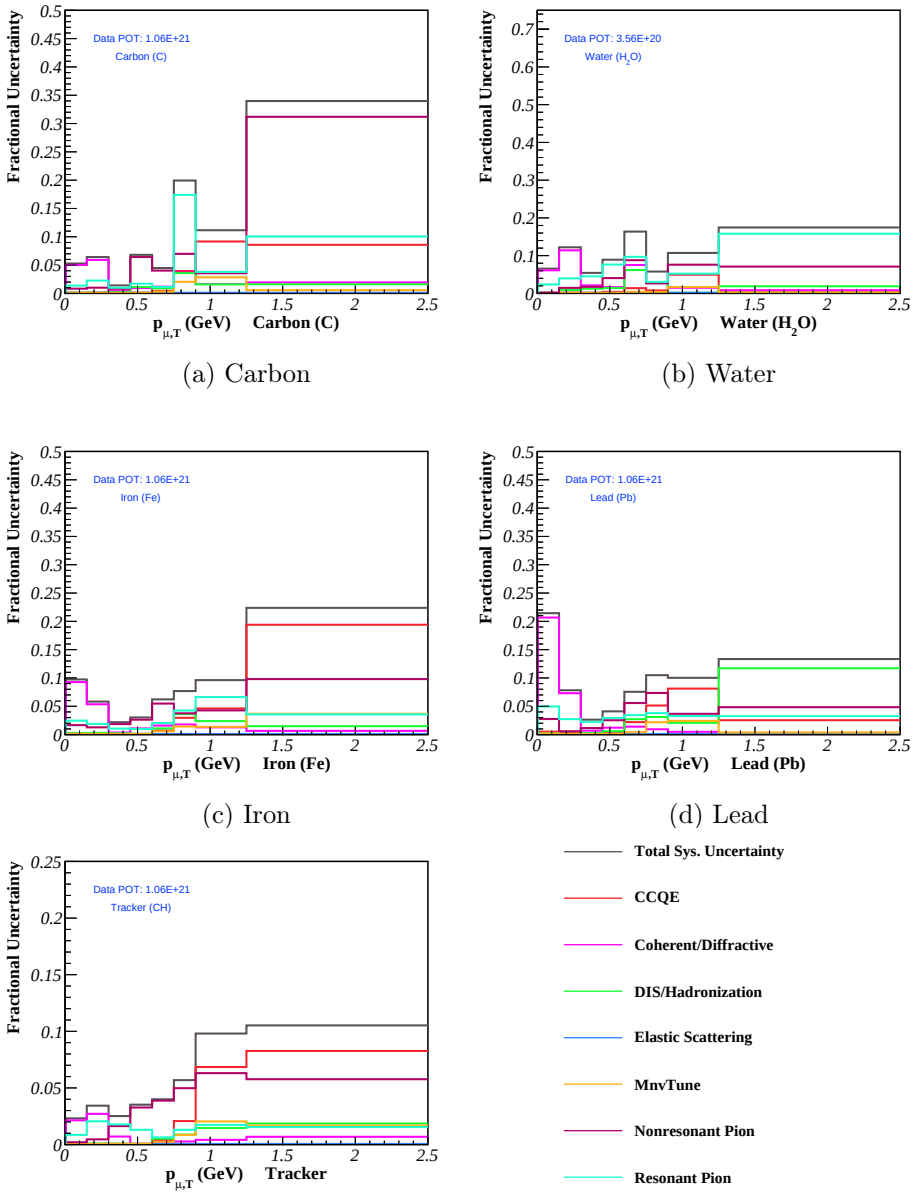
(c) Iron

(d) Lead



(e) Scintillator

Figure E-10: $p_{\mu,||}$ All Cross Section Model Errors



(a) Carbon

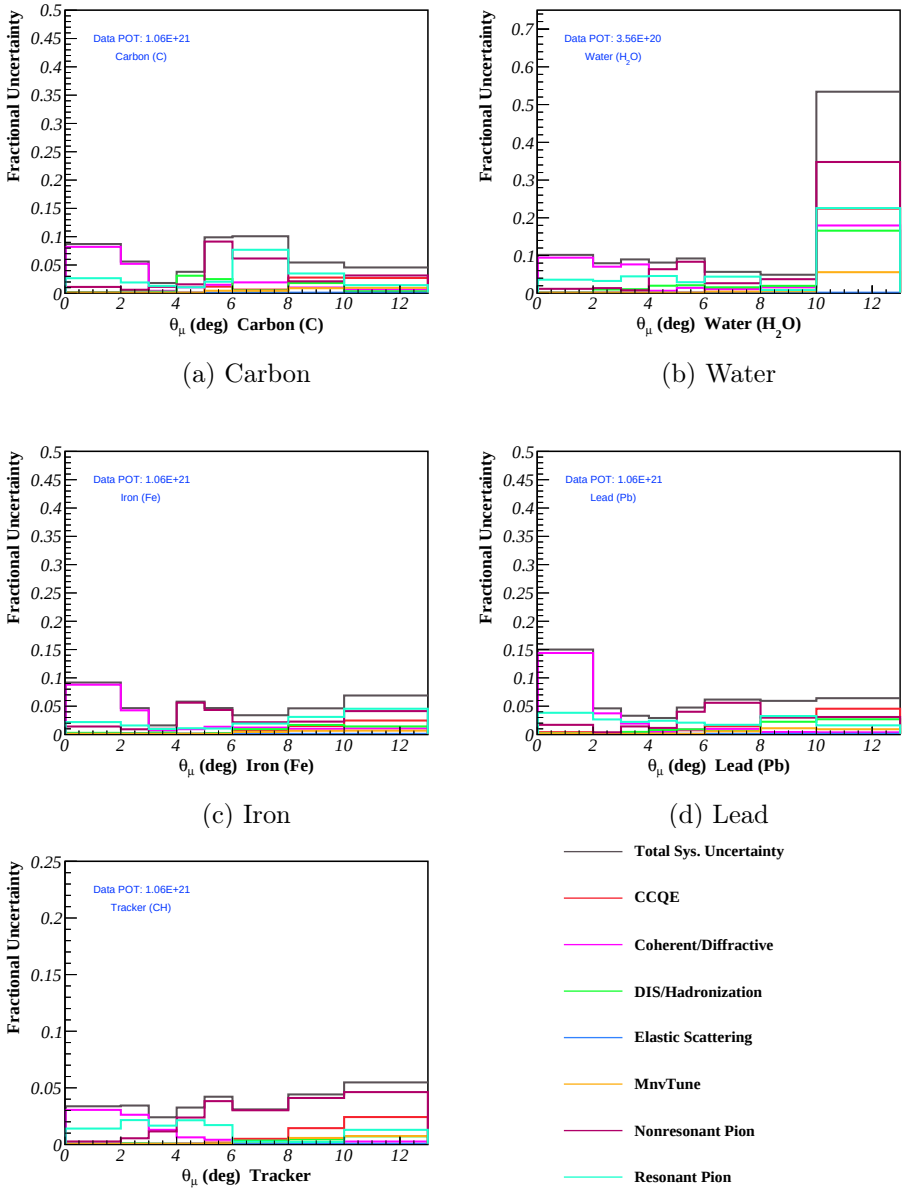
(b) Water

(c) Iron

(d) Lead

(e) Scintillator

Figure E-11: $p_{\mu,T}$ All Cross Section Model Errors



(a) Carbon

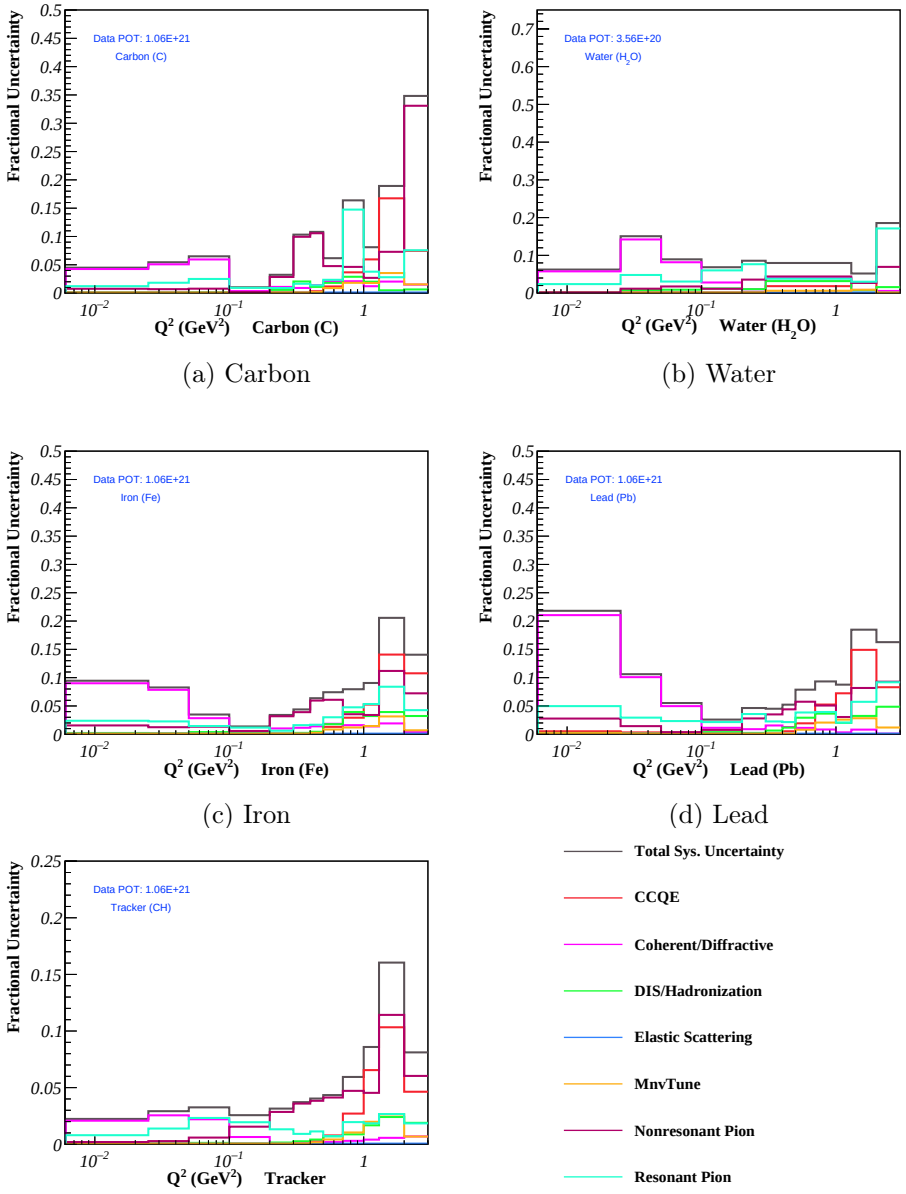
(b) Water

(c) Iron

(d) Lead

(e) Scintillator

Figure E-12: θ_μ All Cross Section Model Errors



(a) Carbon

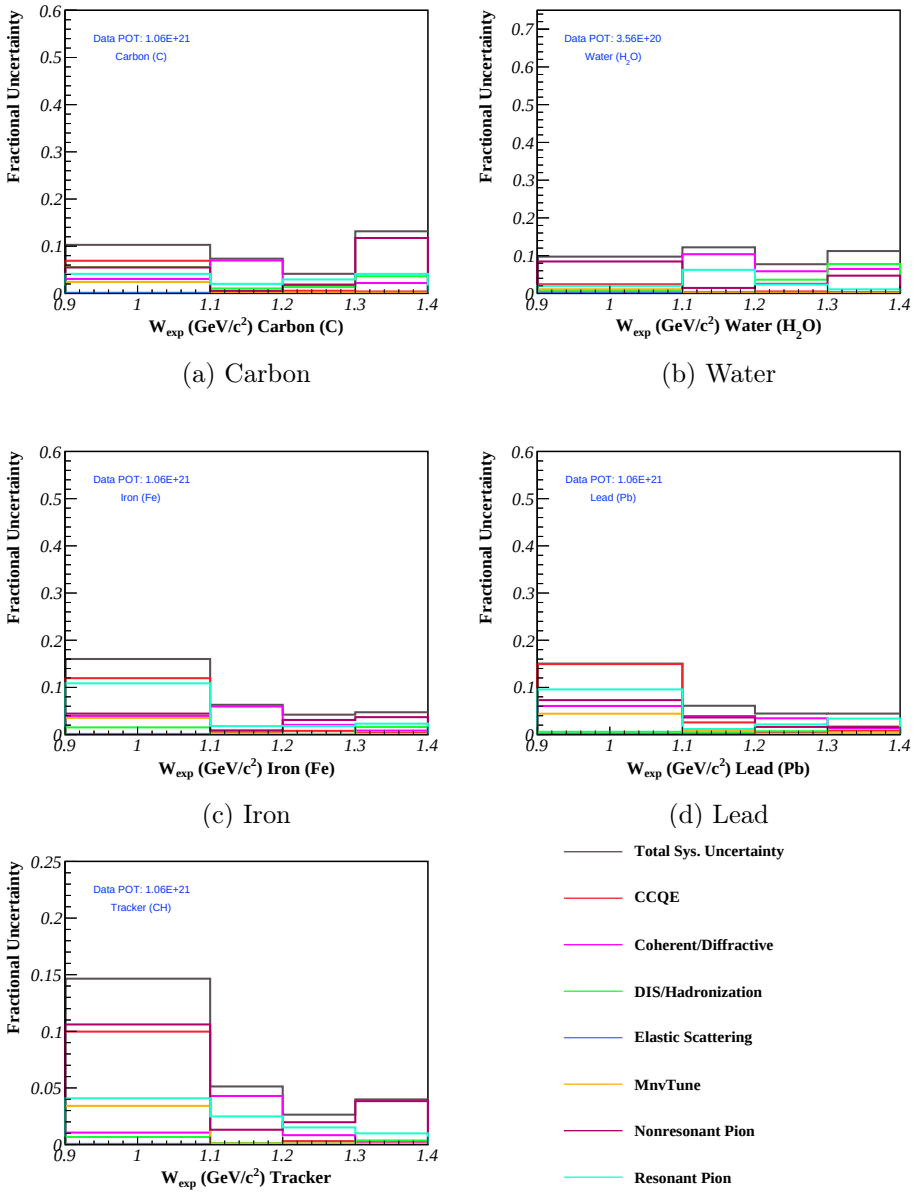
(b) Water

(c) Iron

(d) Lead

(e) Scintillator

Figure E-13: Q^2 All Cross Section Model Errors



(a) Carbon

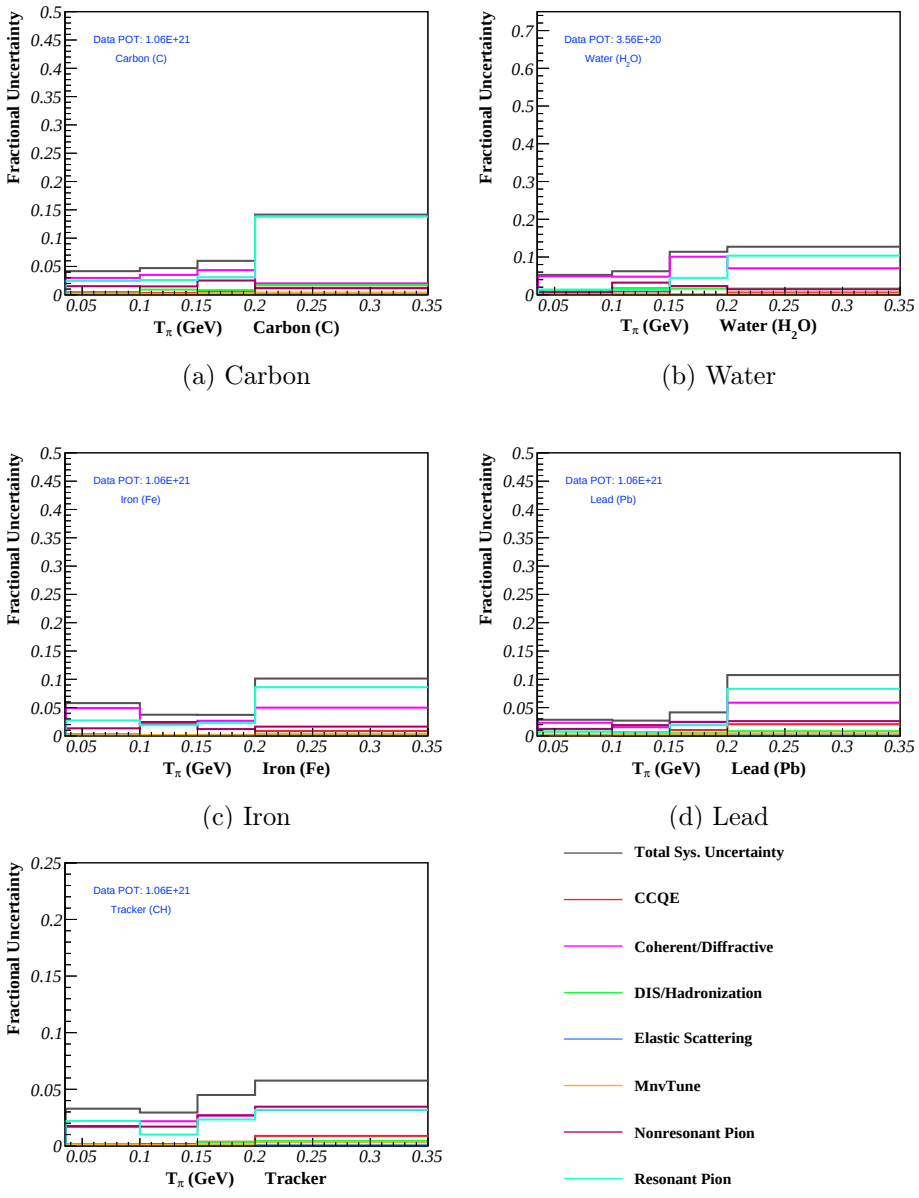
(b) Water

(c) Iron

(d) Lead

(e) Scintillator

Figure E-14: W_{exp} All Cross Section Model Errors



(a) Carbon

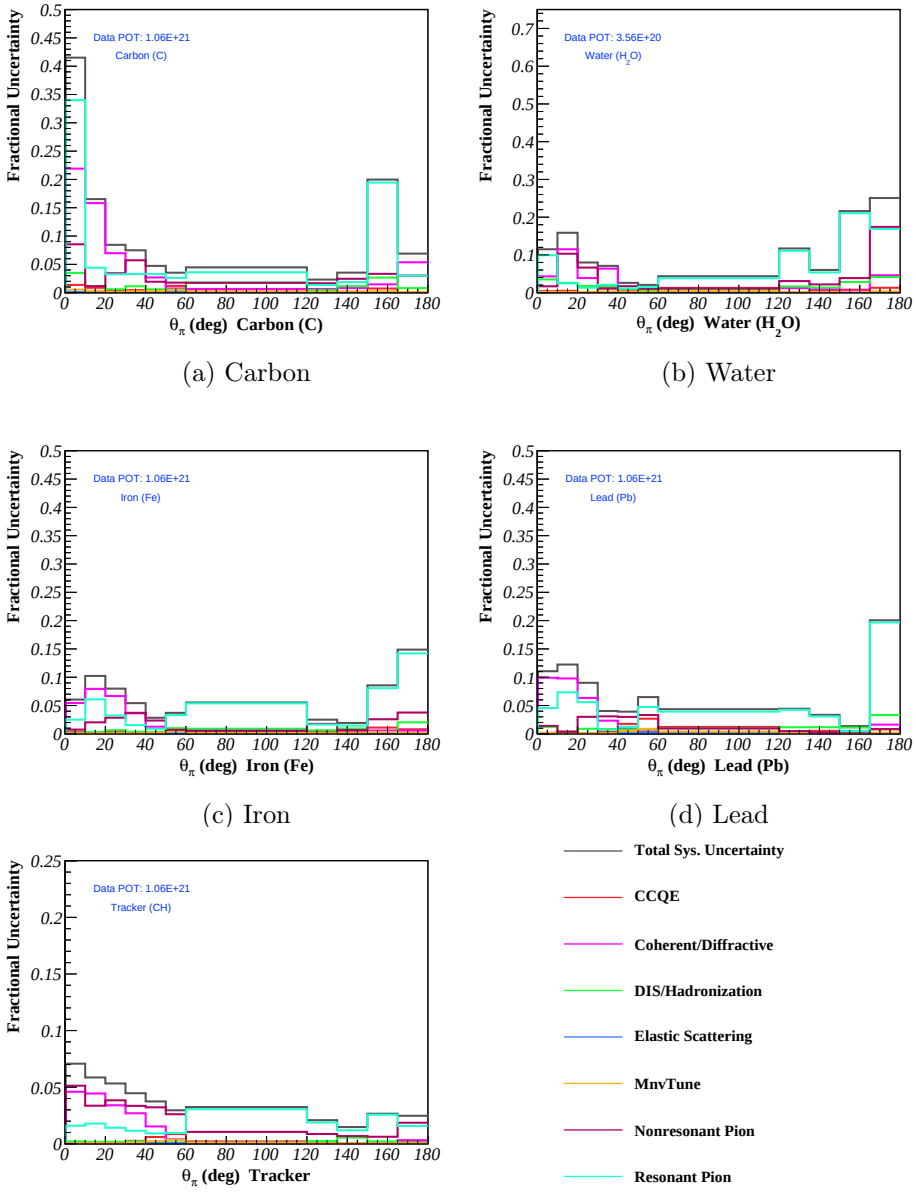
(b) Water

(c) Iron

(d) Lead

(e) Scintillator

Figure E-15: T_π All Cross Section Model Errors



(a) Carbon

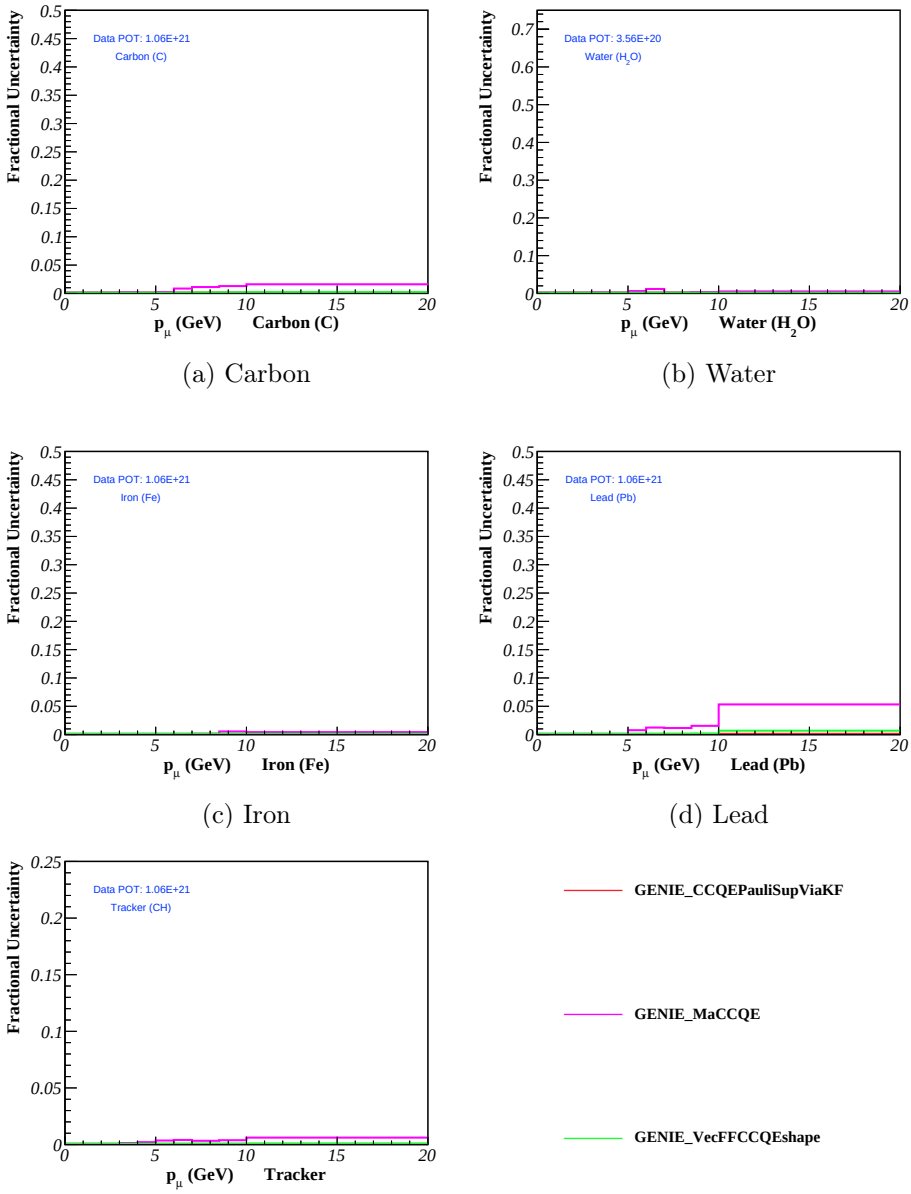
(b) Water

(c) Iron

(d) Lead

(e) Scintillator

Figure E-16: θ_π All Cross Section Model Errors



(a) Carbon

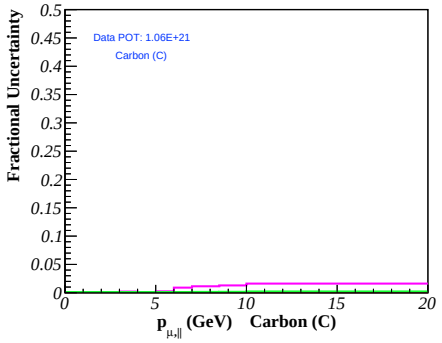
(b) Water

(c) Iron

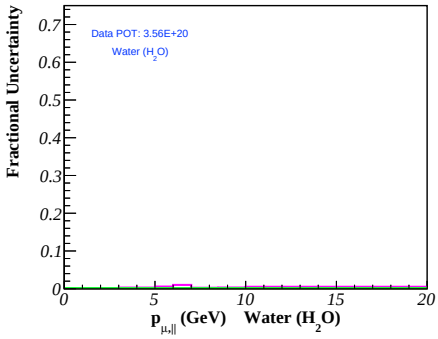
(d) Lead

(e) Scintillator

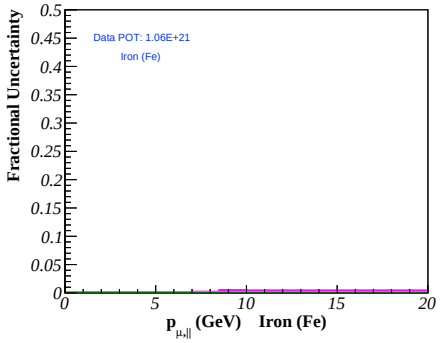
Figure E-17: p_μ CCQE Model Errors



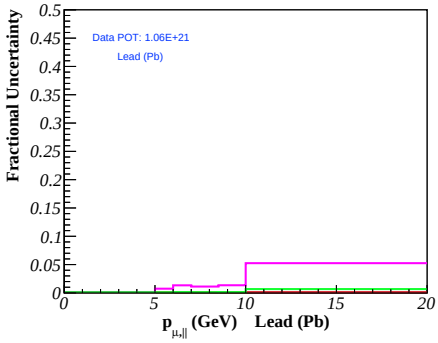
(a) Carbon



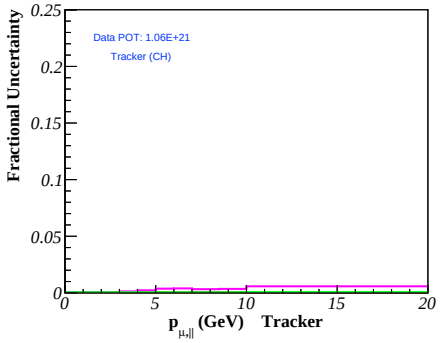
(b) Water

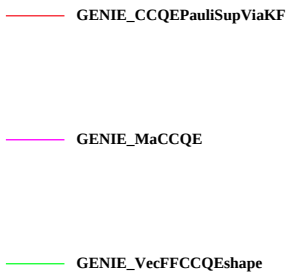


(c) Iron



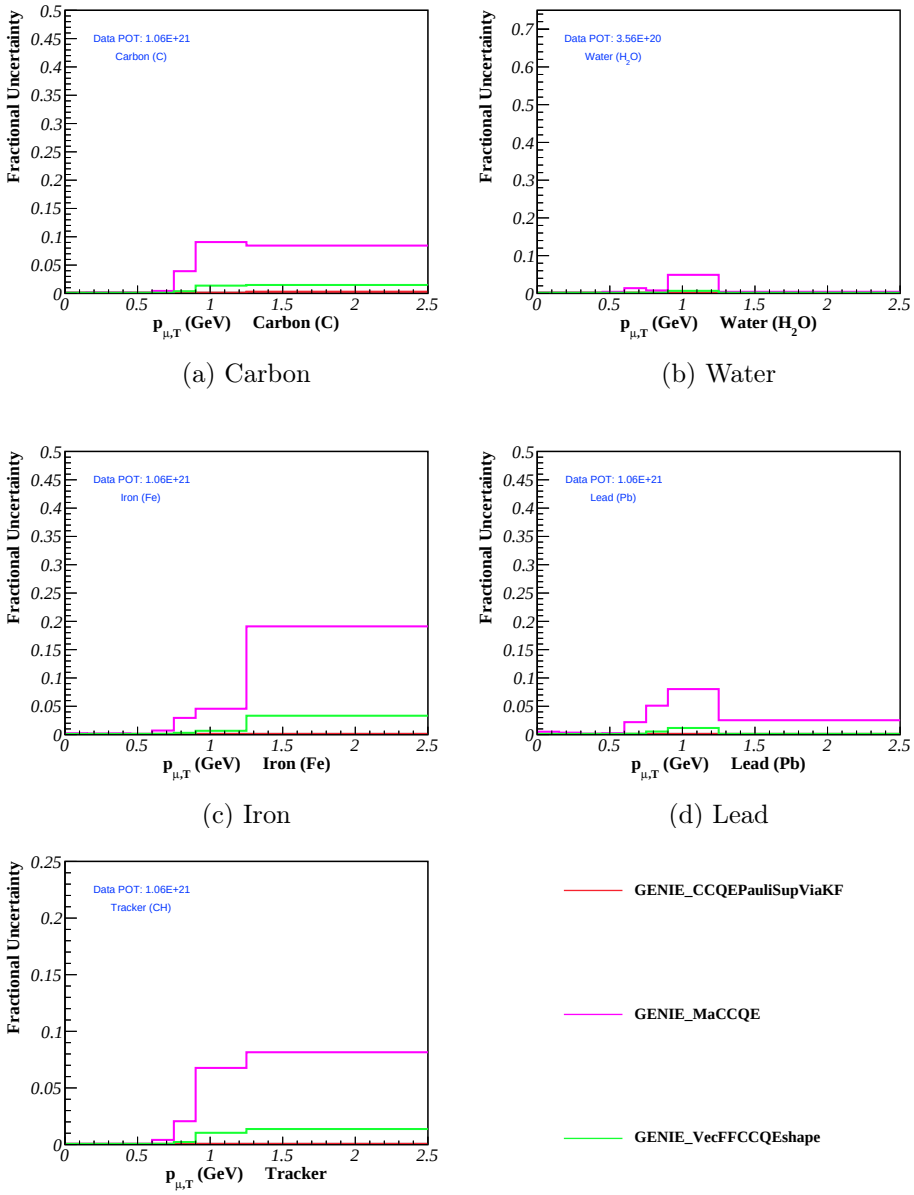
(d) Lead





(e) Scintillator

Figure E-18: $p_{\mu,||}$ CCQE Model Errors



(a) Carbon

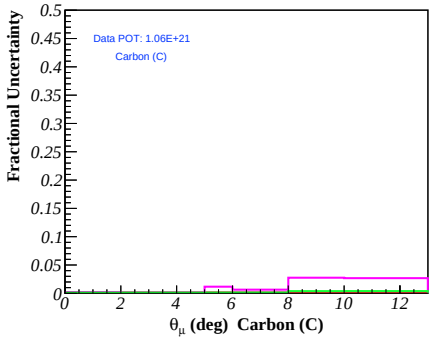
(b) Water

(c) Iron

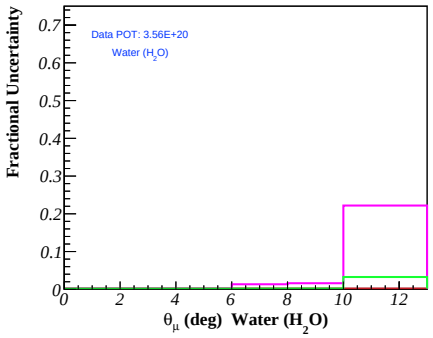
(d) Lead

(e) Scintillator

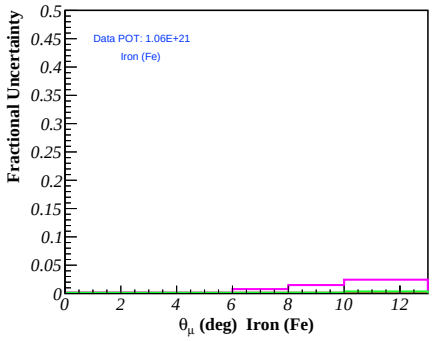
Figure E-19: $p_{\mu,T}$ CCQE Model Errors



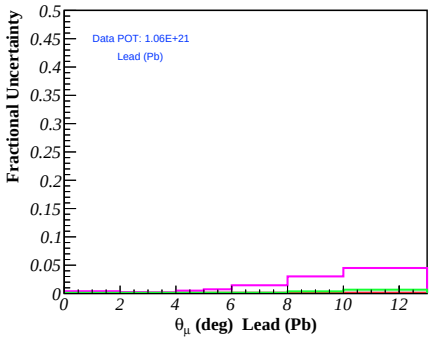
(a) Carbon



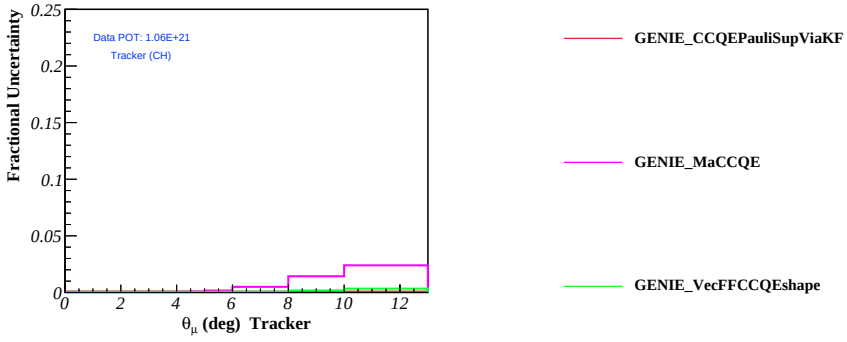
(b) Water



(c) Iron

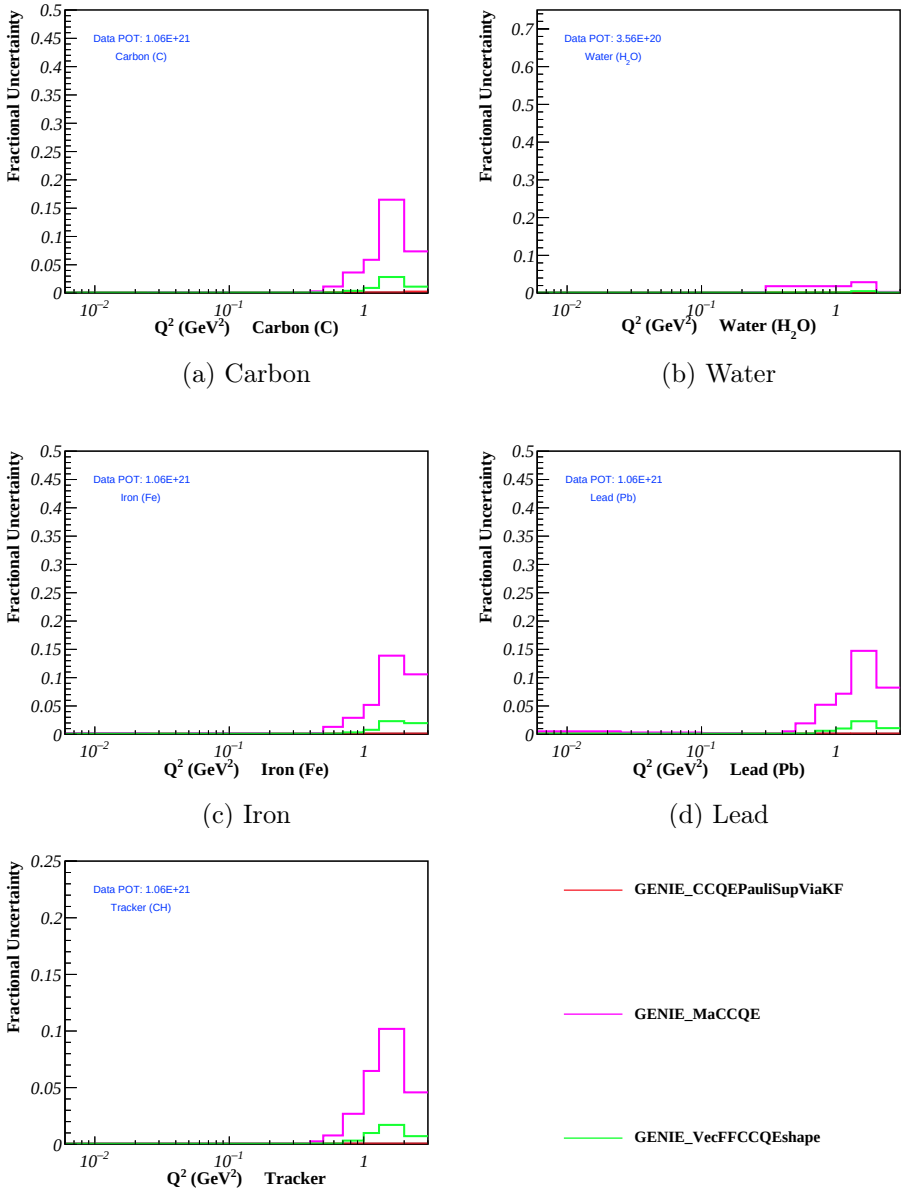


(d) Lead



(e) Scintillator

Figure E-20: θ_μ CCQE Model Errors



(a) Carbon

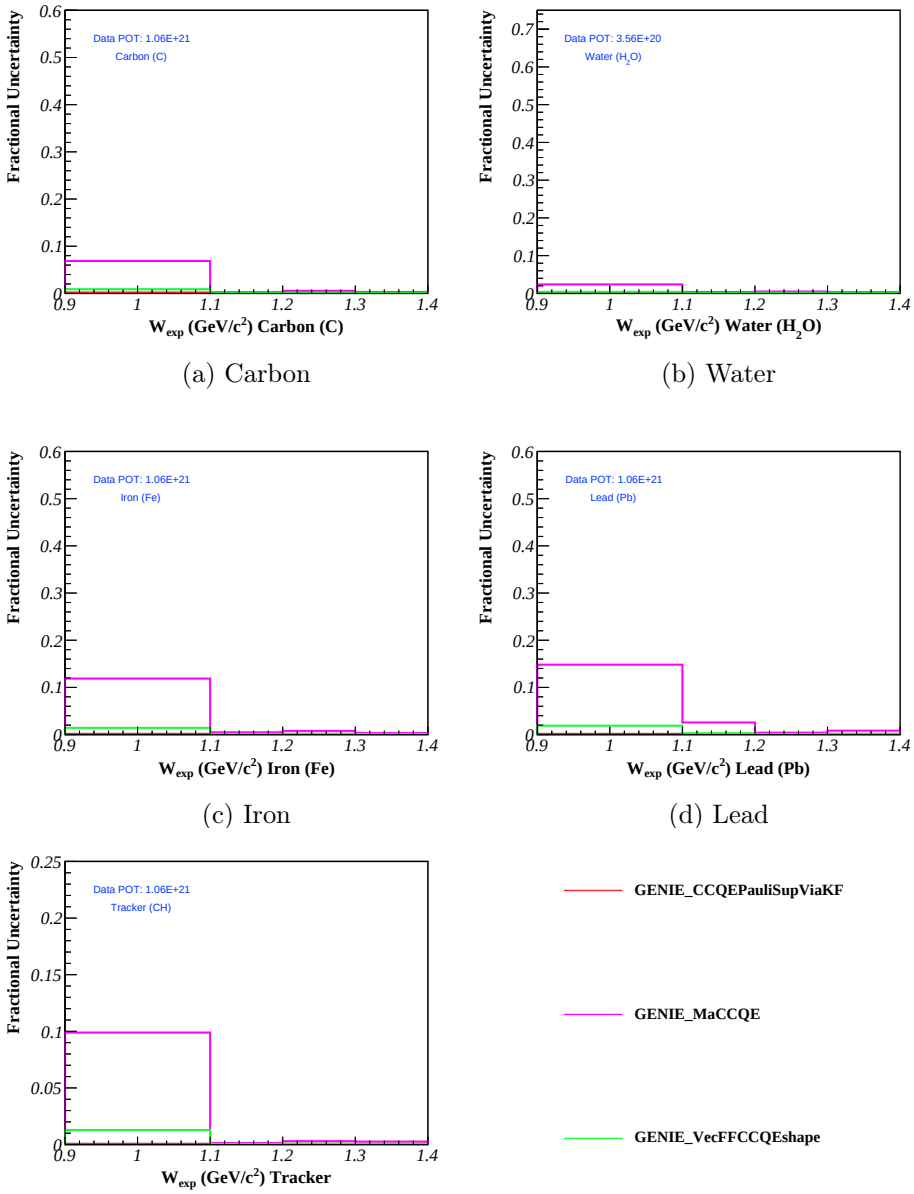
(b) Water

(c) Iron

(d) Lead

(e) Scintillator

Figure E-21: Q^2 CCQE Model Errors



(a) Carbon

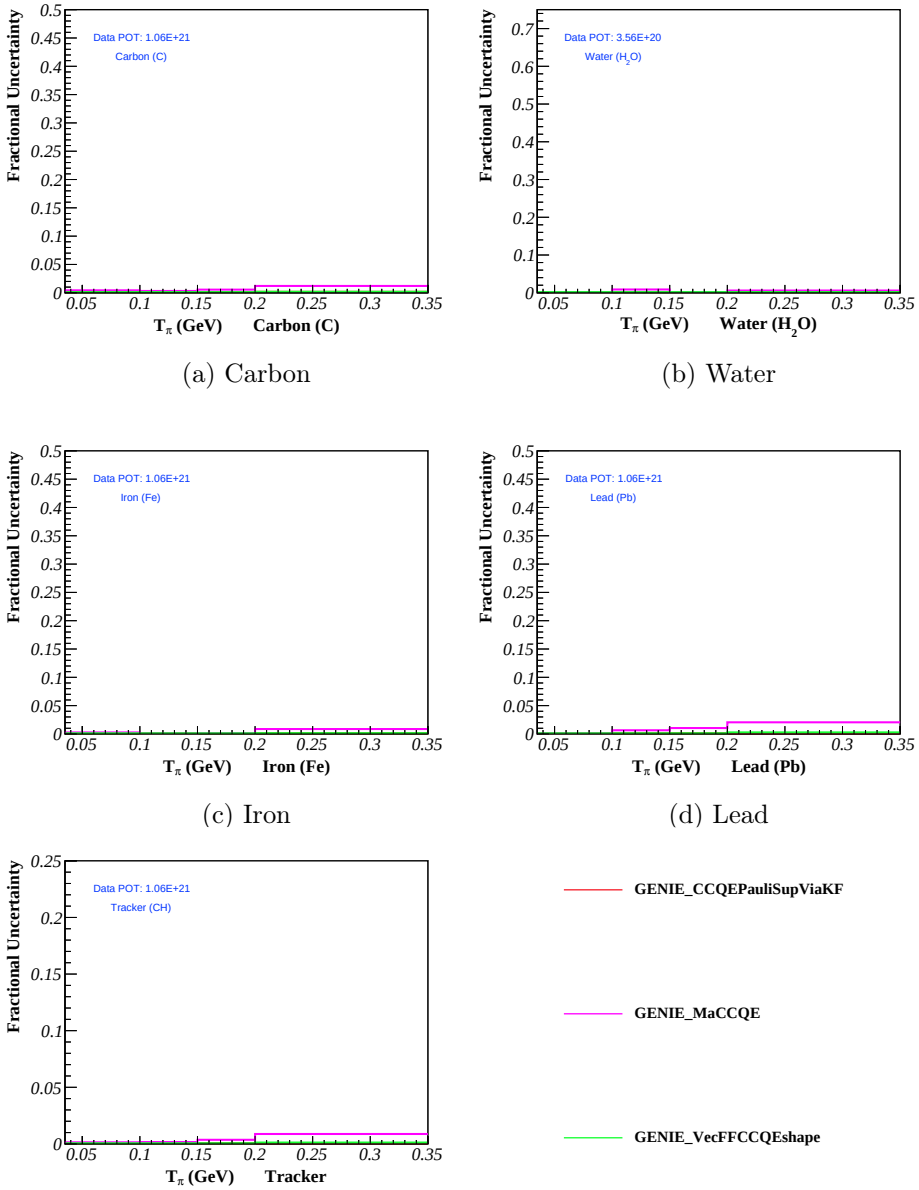
(b) Water

(c) Iron

(d) Lead

(e) Scintillator

Figure E-22: W_{exp} CCQE Model Errors



(a) Carbon

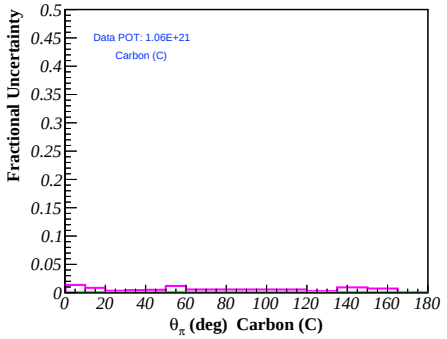
(b) Water

(c) Iron

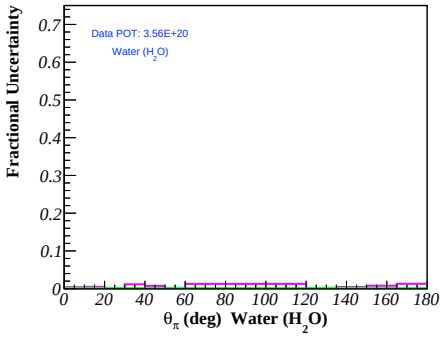
(d) Lead

(e) Scintillator

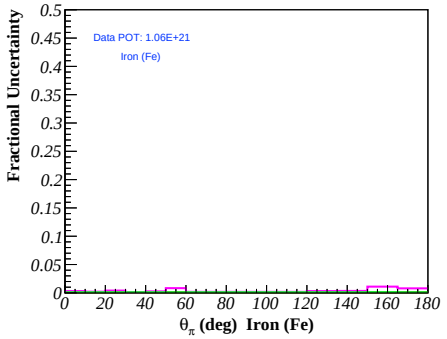
Figure E-23: T_π CCQE Model Errors



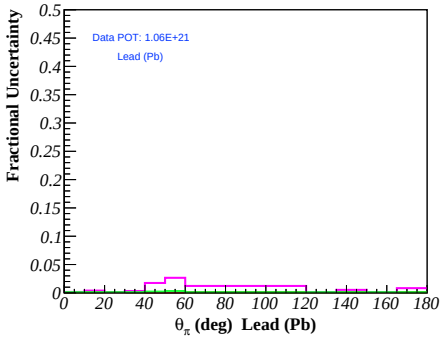
(a) Carbon



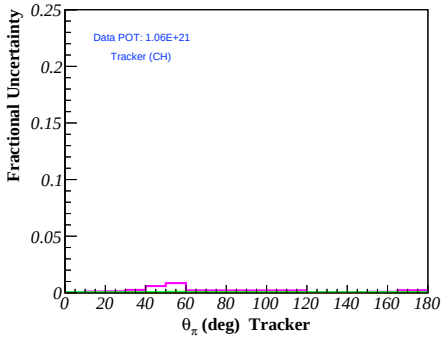
(b) Water

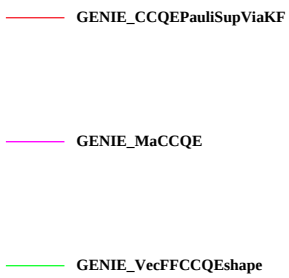


(c) Iron



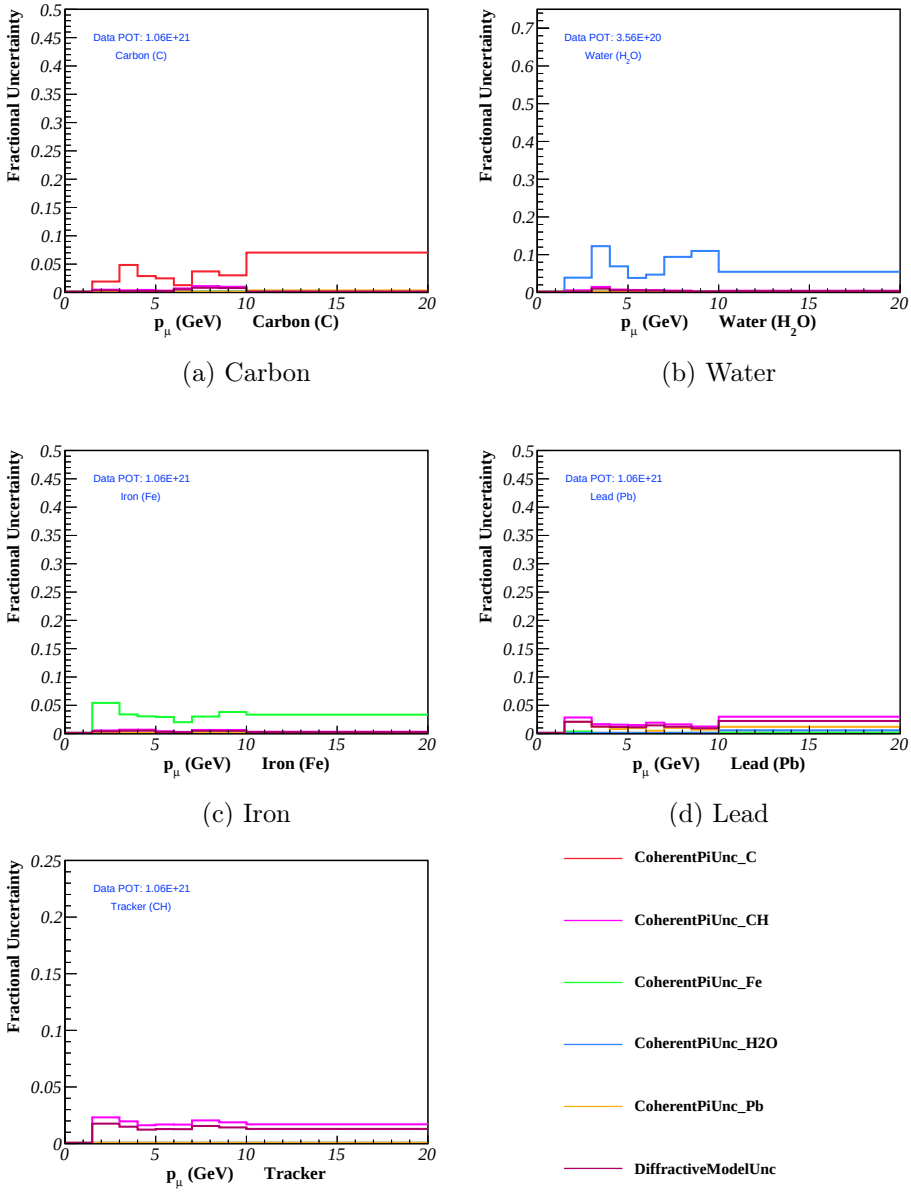
(d) Lead





(e) Scintillator

Figure E-24: θ_π CCQE Model Errors



(a) Carbon

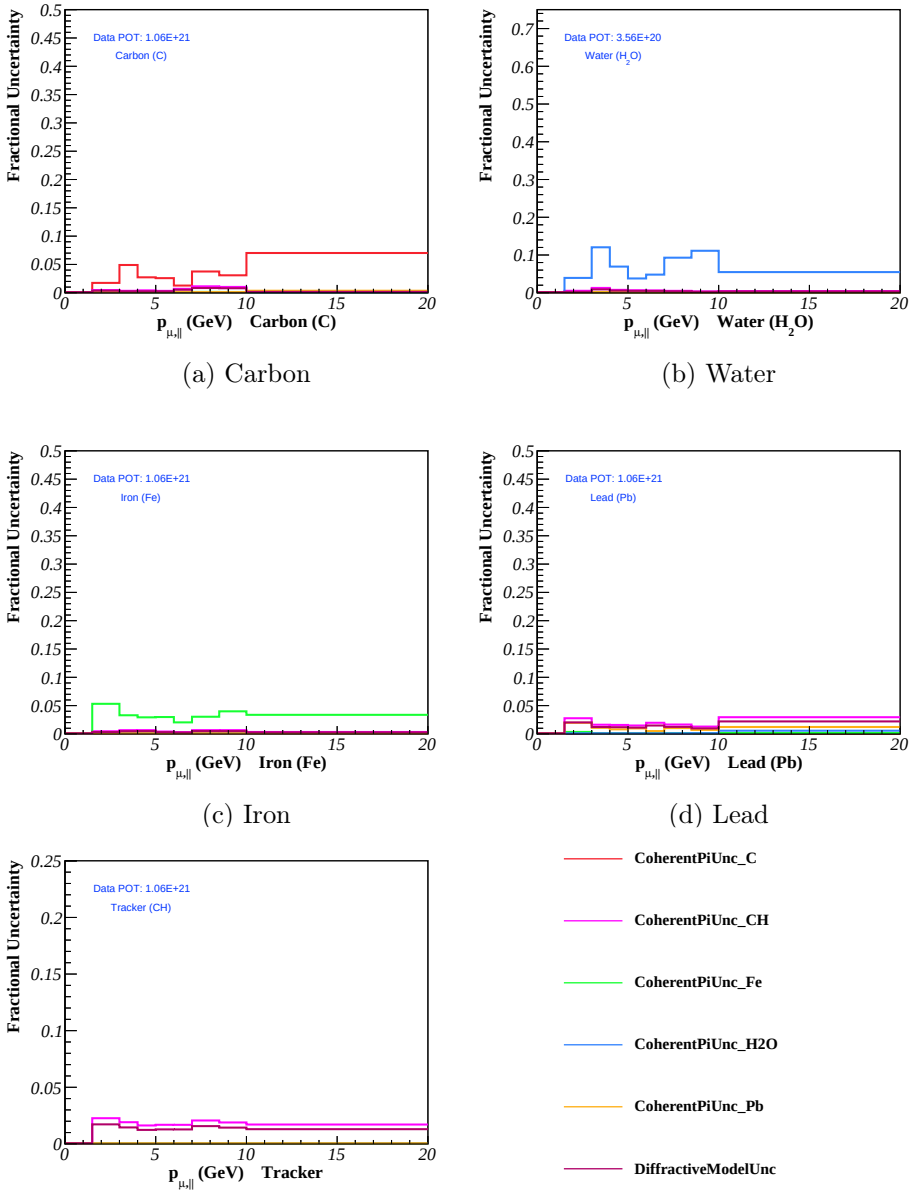
(b) Water

(c) Iron

(d) Lead

(e) Scintillator

Figure E-25: p_μ Coherent/Diffractive π Model Errors



(a) Carbon

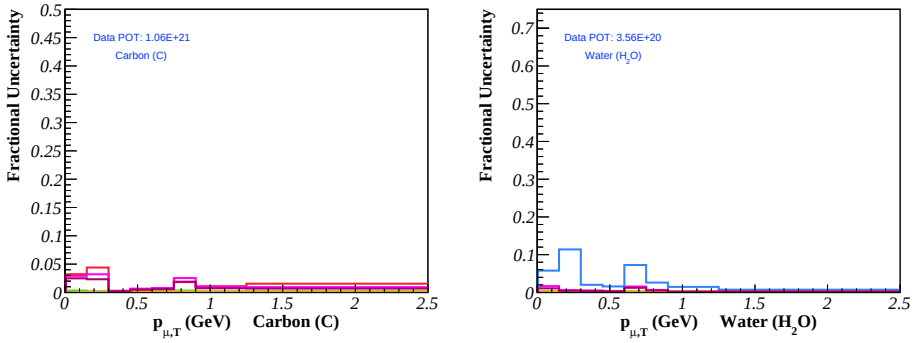
(b) Water

(c) Iron

(d) Lead

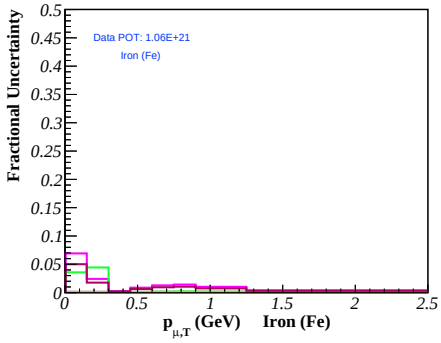
(e) Scintillator

Figure E-26: $p_{\mu,||}$ Coherent/Diffractive π Model Errors

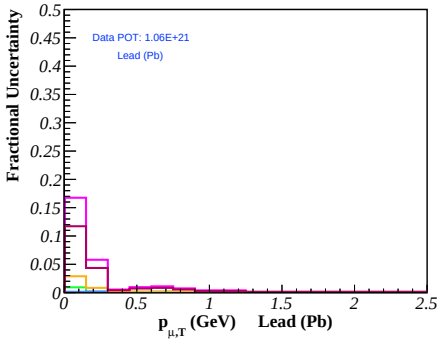


(a) Carbon

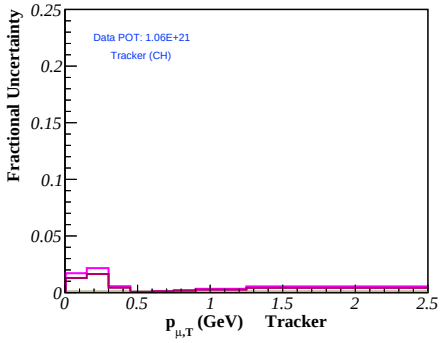
(b) Water

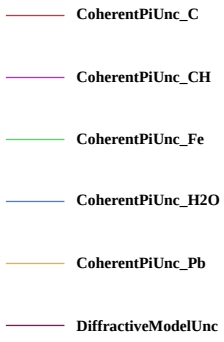


(c) Iron



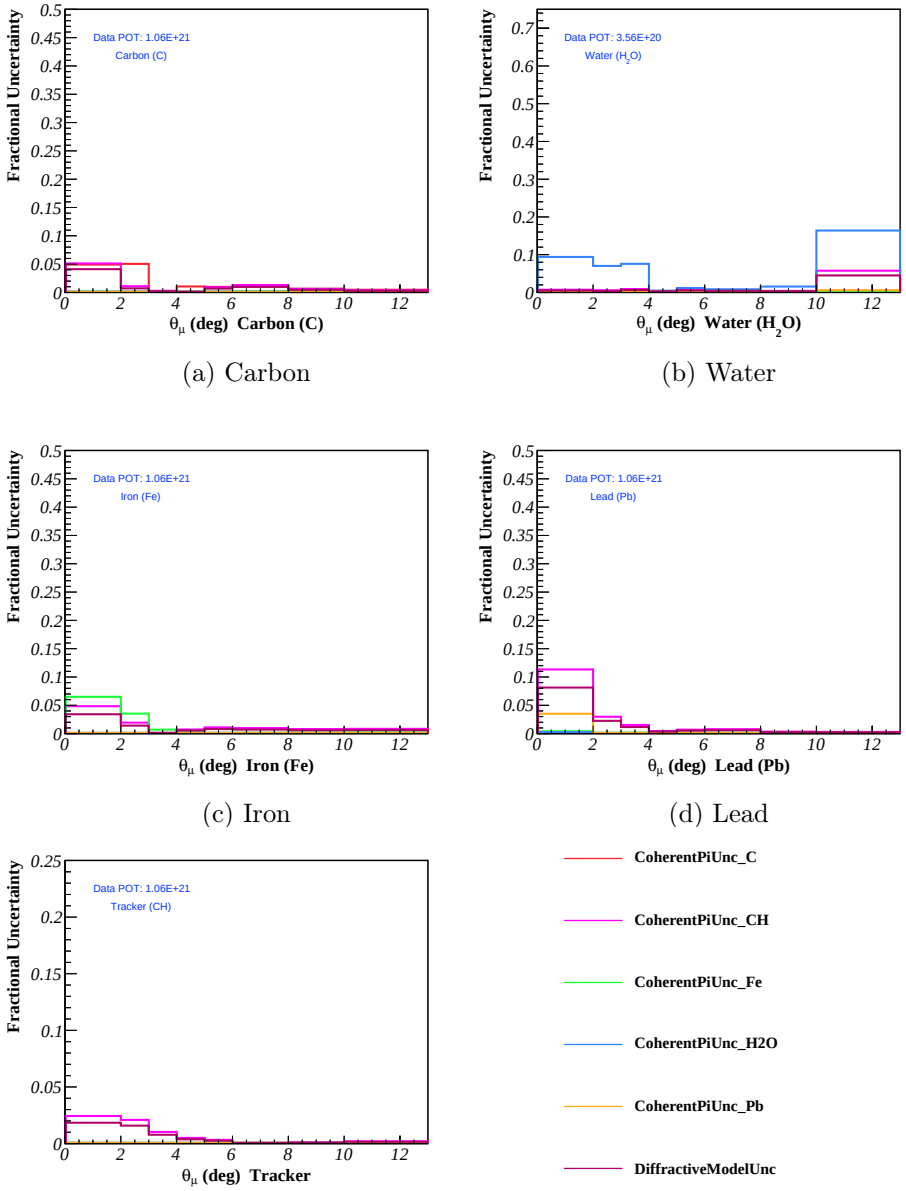
(d) Lead





(e) Scintillator

Figure E-27: $p_{\mu,T}$ Coherent/Diffractive π Model Errors



(a) Carbon

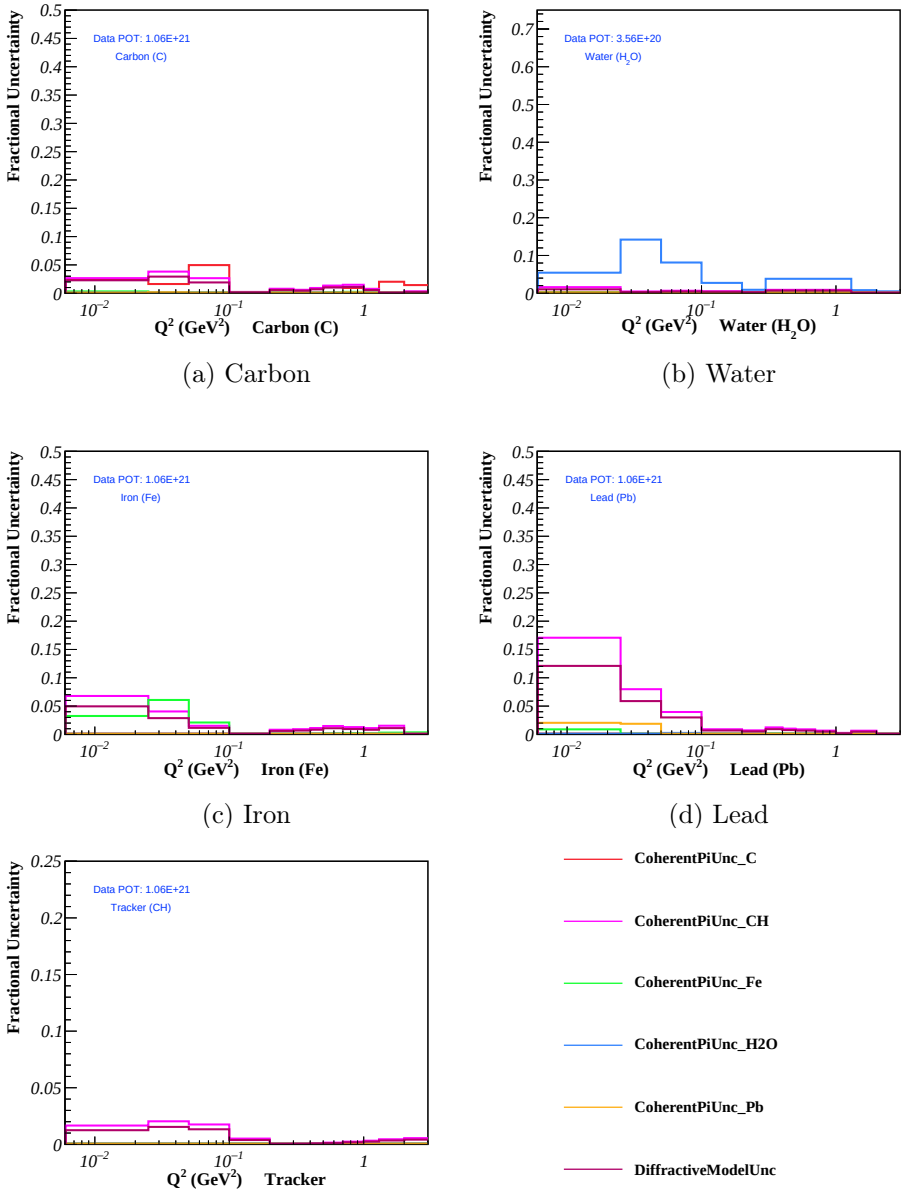
(b) Water

(c) Iron

(d) Lead

(e) Scintillator

Figure E-28: θ_μ Coherent/Diffractive π Model Errors



(a) Carbon

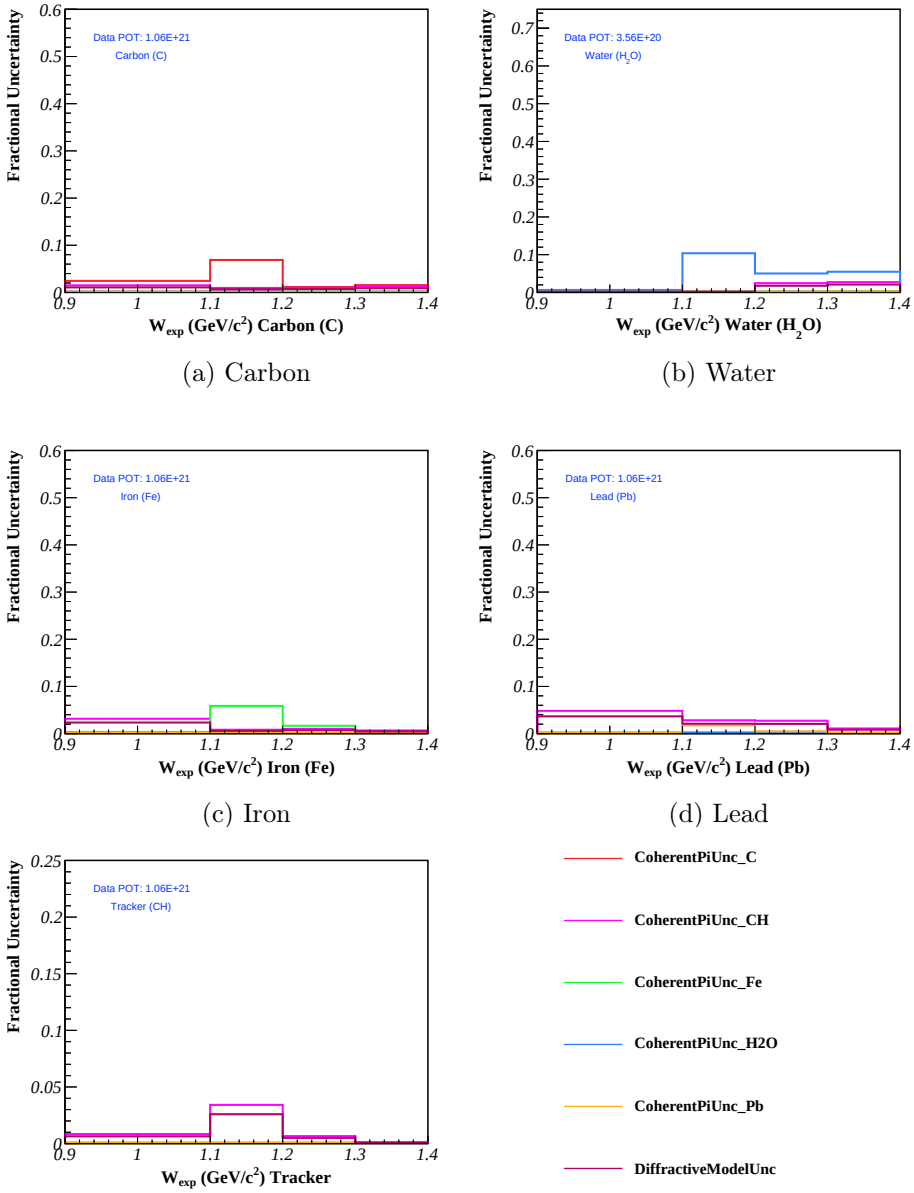
(b) Water

(c) Iron

(d) Lead

(e) Scintillator

Figure E-29: Q^2 Coherent/Diffractive π Model Errors



(a) Carbon

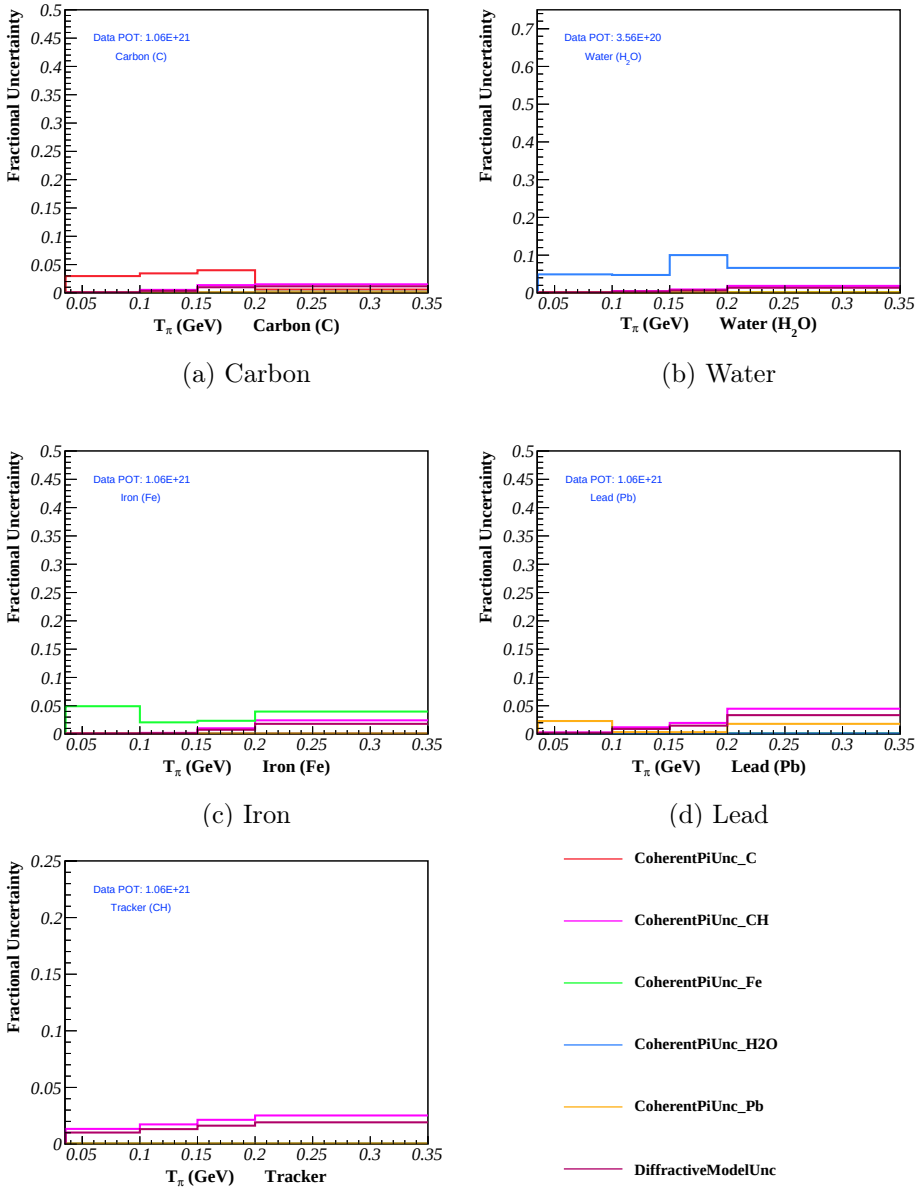
(b) Water

(c) Iron

(d) Lead

(e) Scintillator

Figure E-30: W_{exp} Coherent/Diffractive π Model Errors



(a) Carbon

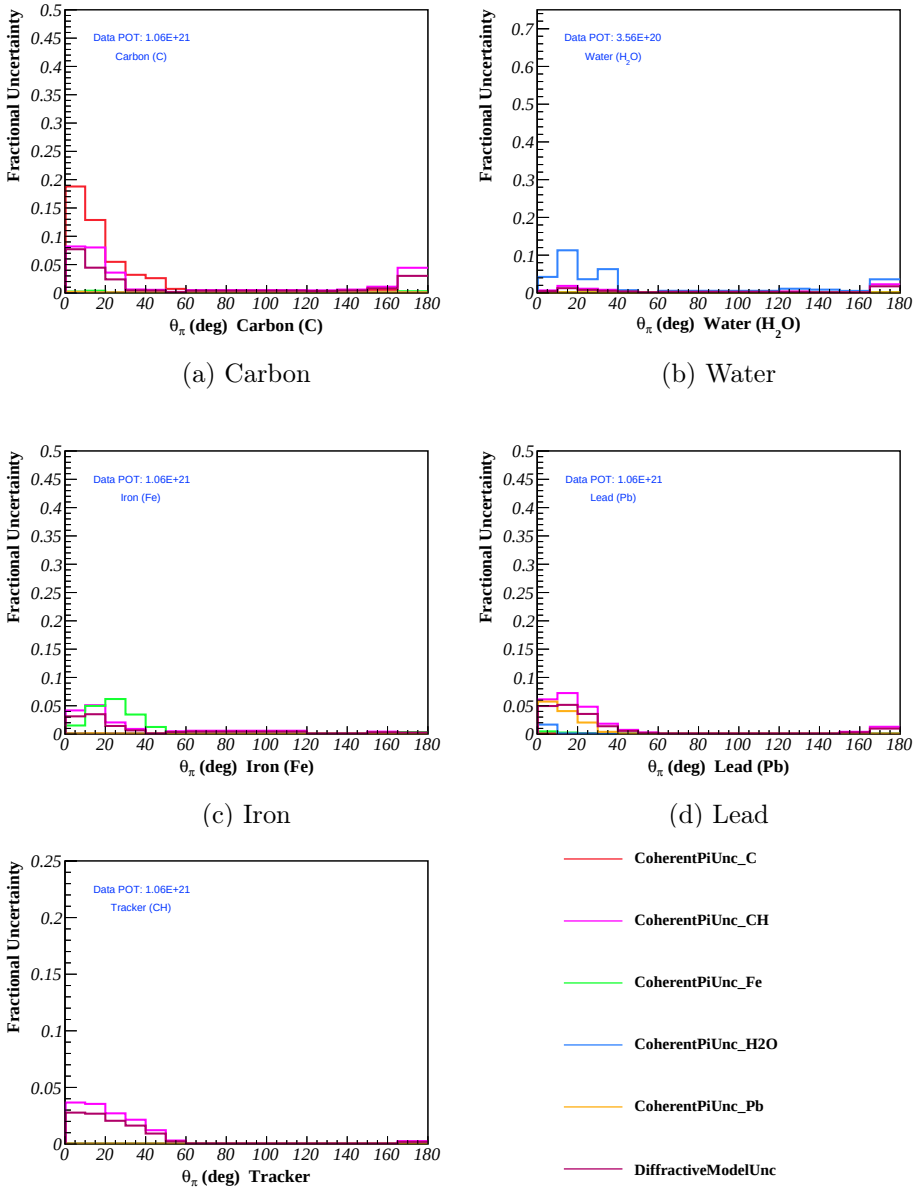
(b) Water

(c) Iron

(d) Lead

(e) Scintillator

Figure E-31: T_π Coherent/Diffractive π Model Errors



(a) Carbon

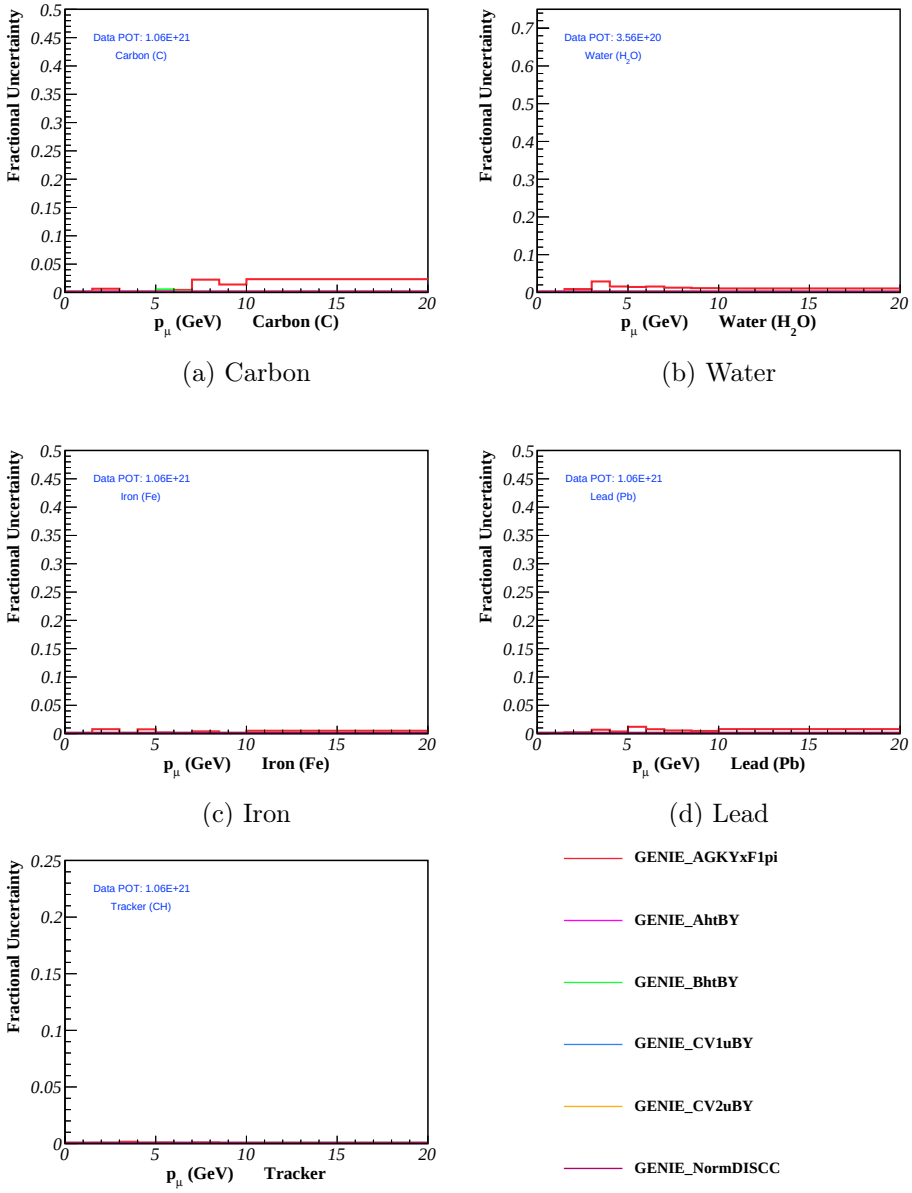
(b) Water

(c) Iron

(d) Lead

(e) Scintillator

Figure E-32: θ_π Coherent/Diffractive π Model Errors



(a) Carbon

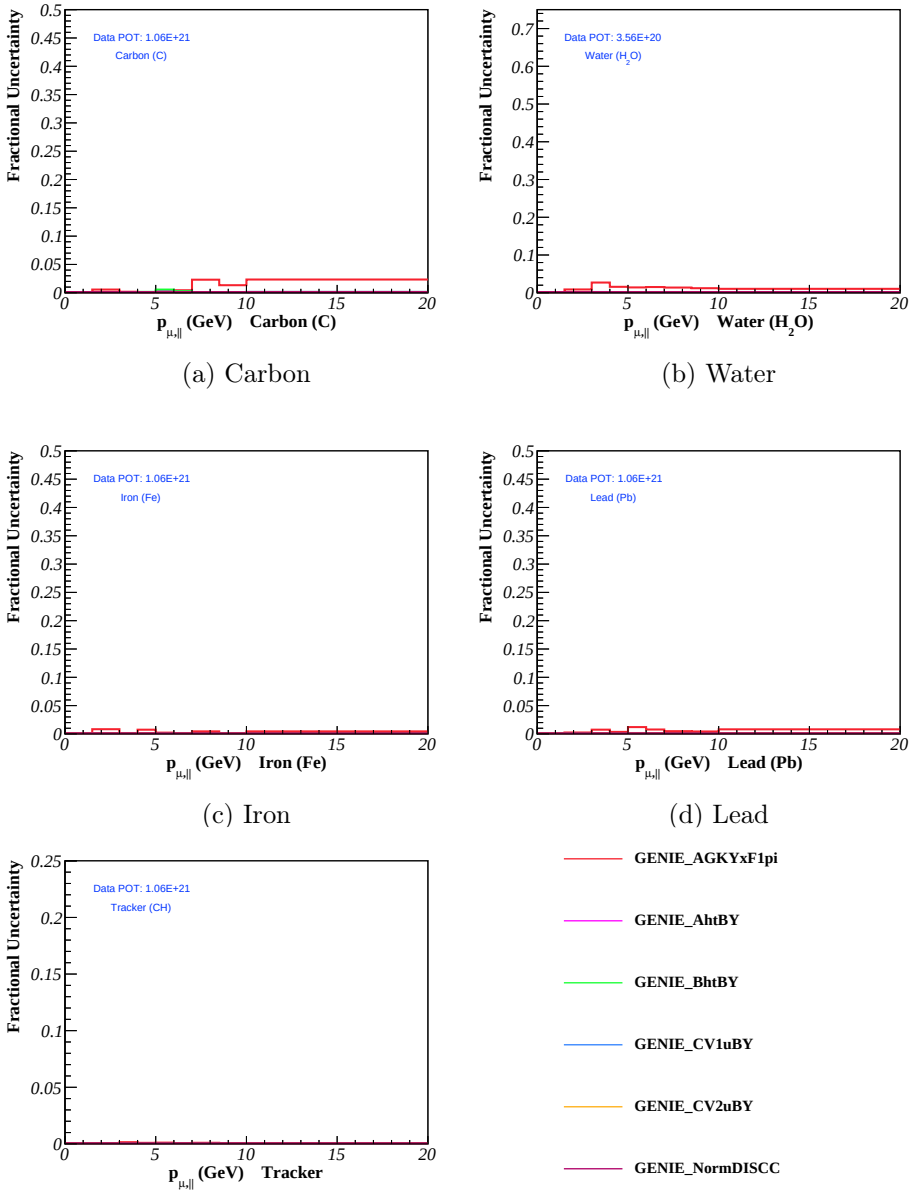
(b) Water

(c) Iron

(d) Lead

(e) Scintillator

Figure E-33: p_μ DIS/Hadronization Model Errors



(a) Carbon

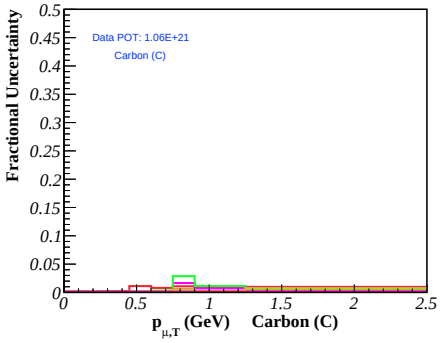
(b) Water

(c) Iron

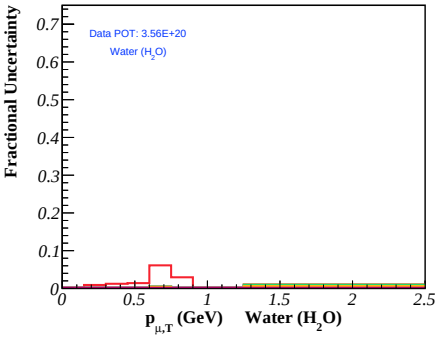
(d) Lead

(e) Scintillator

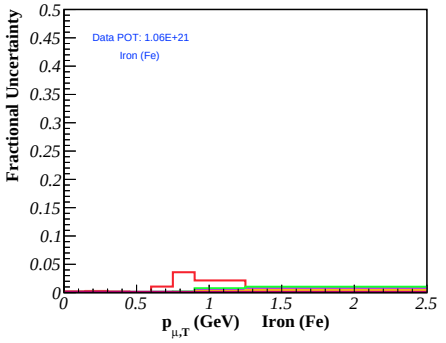
Figure E-34: $p_{\mu,||}$ DIS/Hadronization Model Errors



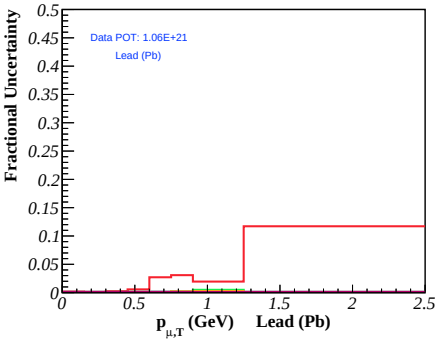
(a) Carbon



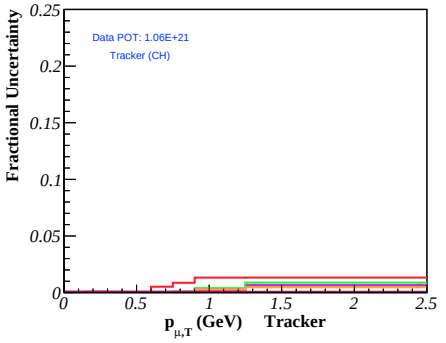
(b) Water

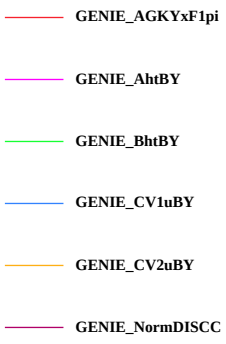


(c) Iron



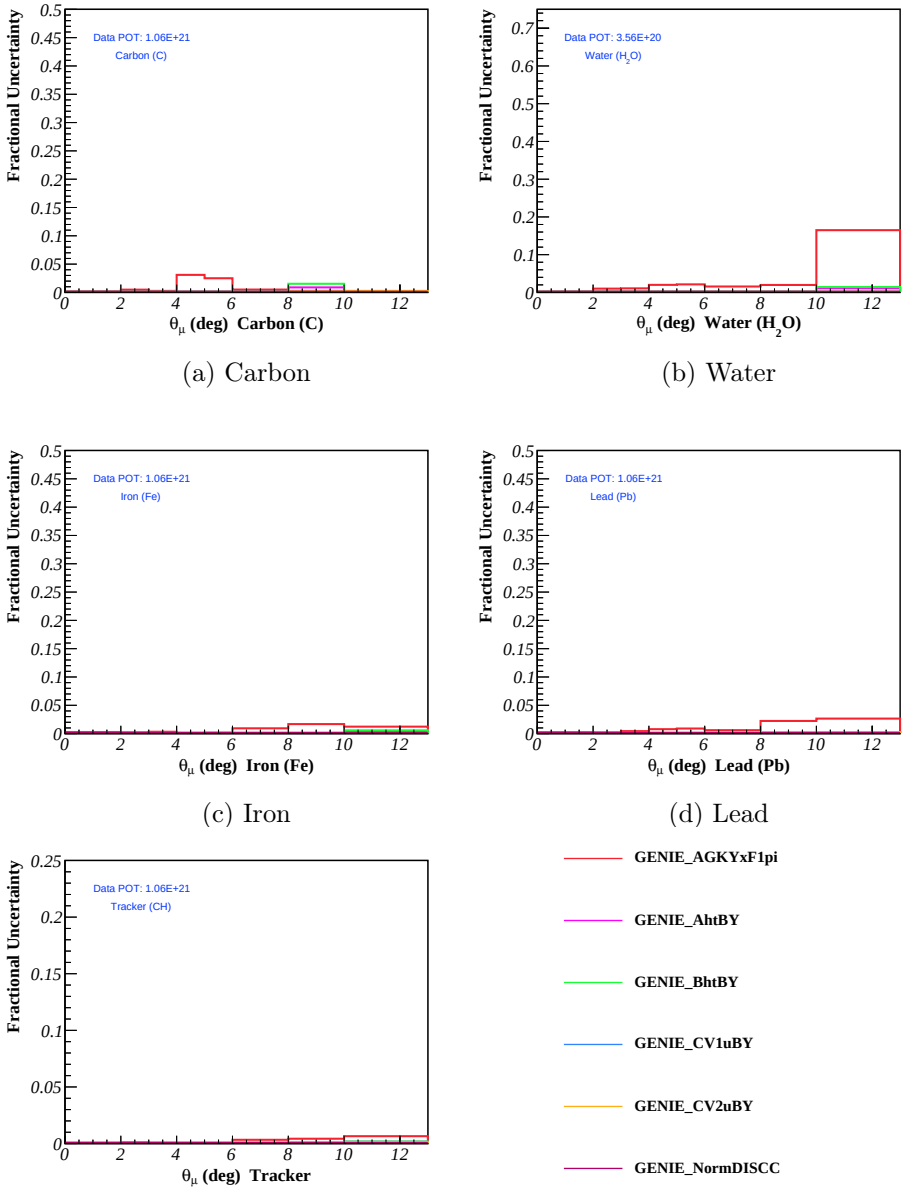
(d) Lead





(e) Scintillator

Figure E-35: $p_{\mu,T}$ DIS/Hadronization Model Errors



(a) Carbon

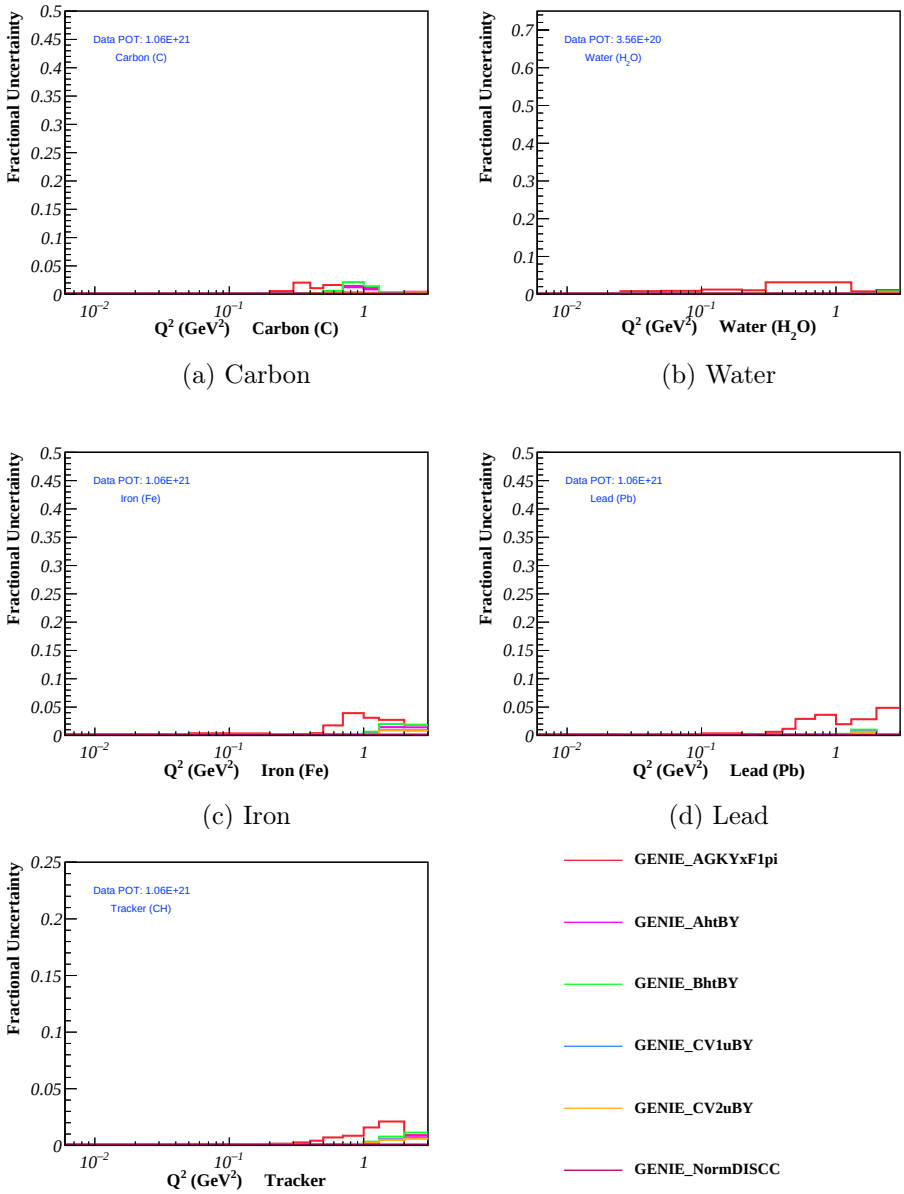
(b) Water

(c) Iron

(d) Lead

(e) Scintillator

Figure E-36: θ_μ DIS/Hadronization Model Errors



(a) Carbon

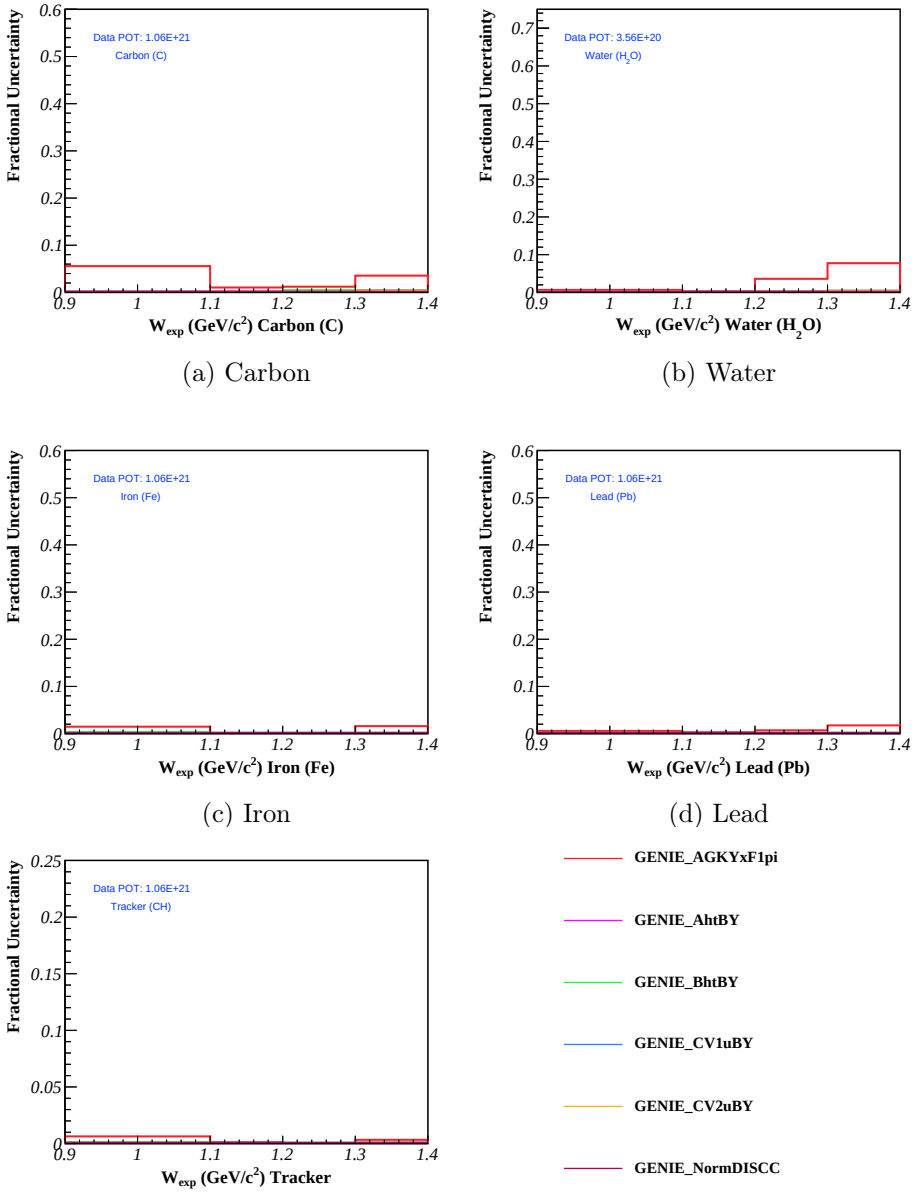
(b) Water

(c) Iron

(d) Lead

(e) Scintillator

Figure E-37: Q^2 DIS/Hadronization Model Errors



(a) Carbon

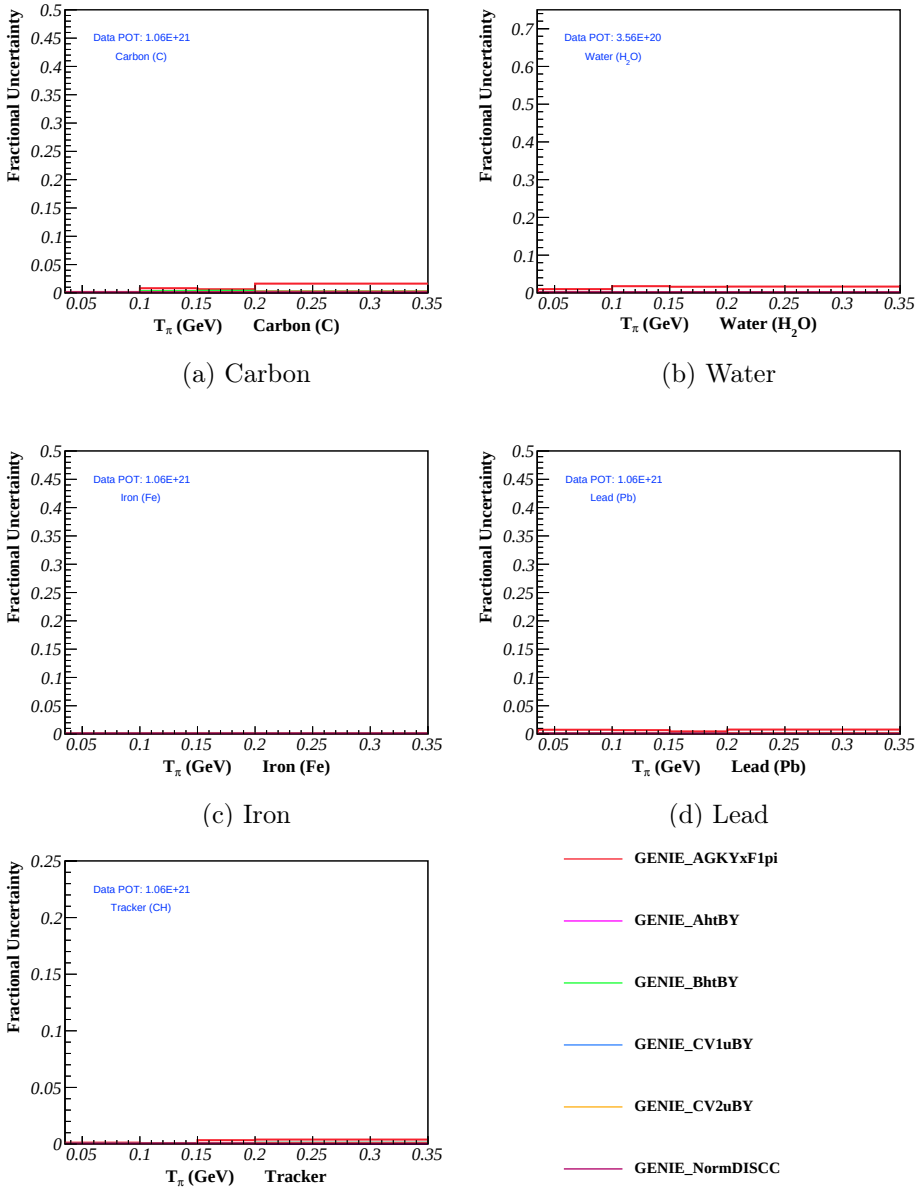
(b) Water

(c) Iron

(d) Lead

(e) Scintillator

Figure E-38: W_{exp} DIS/Hadronization Model Errors



(a) Carbon

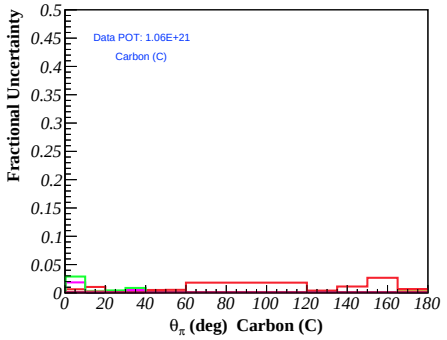
(b) Water

(c) Iron

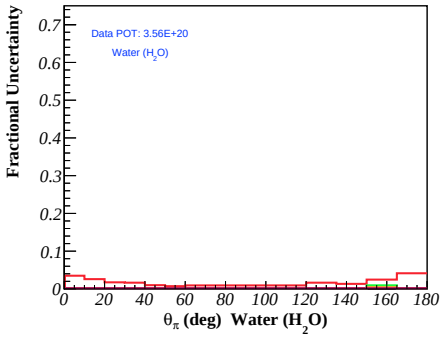
(d) Lead

(e) Scintillator

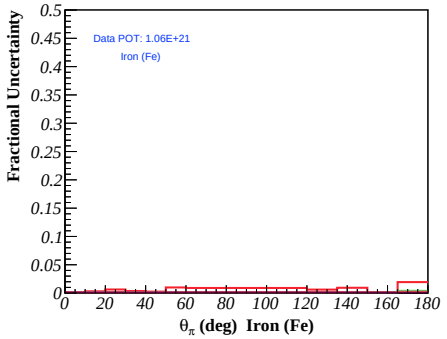
Figure E-39: T_π DIS/Hadronization Model Errors



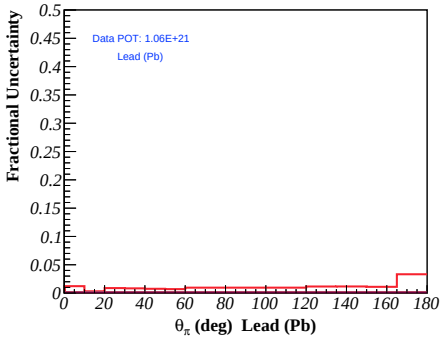
(a) Carbon



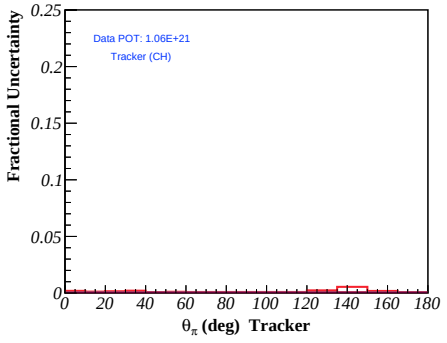
(b) Water

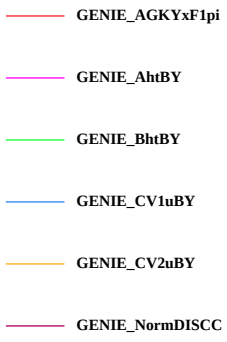


(c) Iron



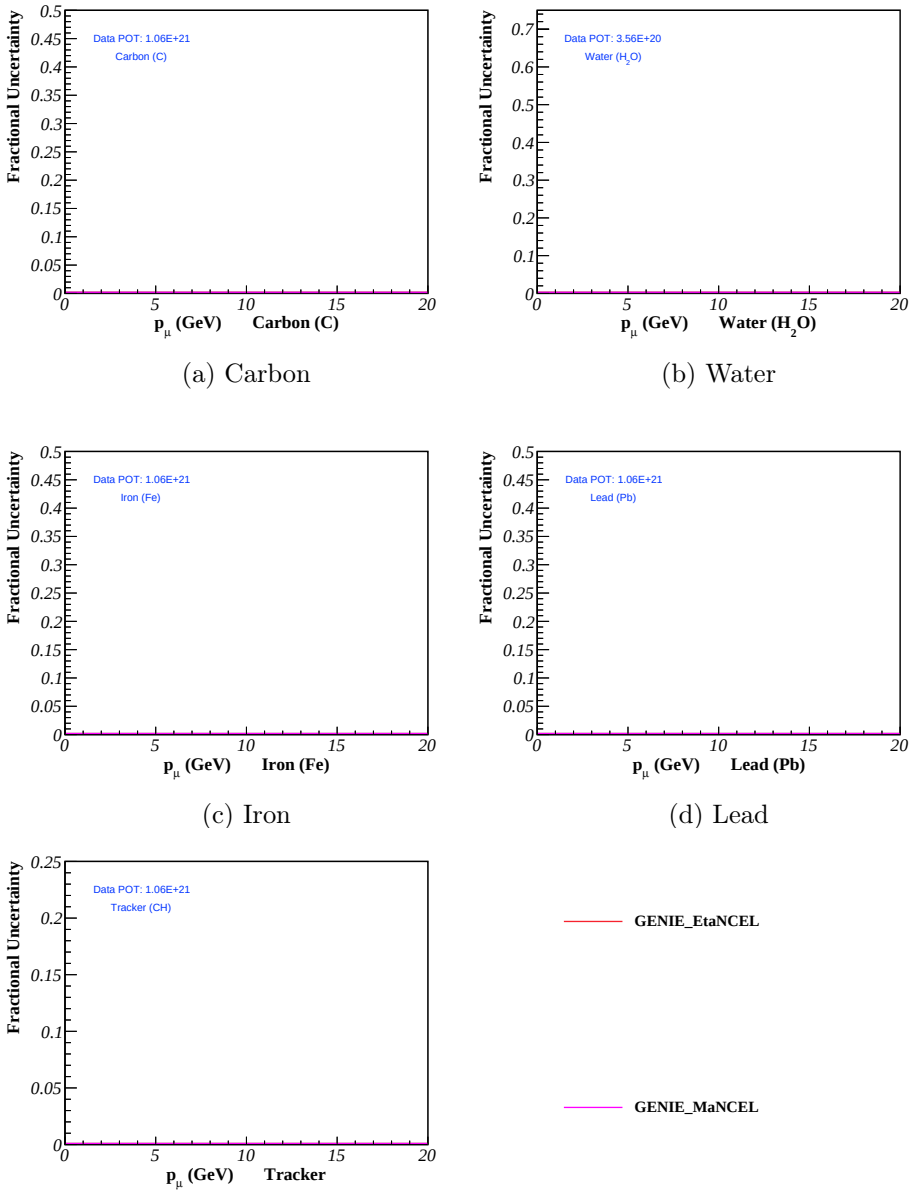
(d) Lead





(e) Scintillator

Figure E-40: θ_π DIS/Hadronization Model Errors



(a) Carbon

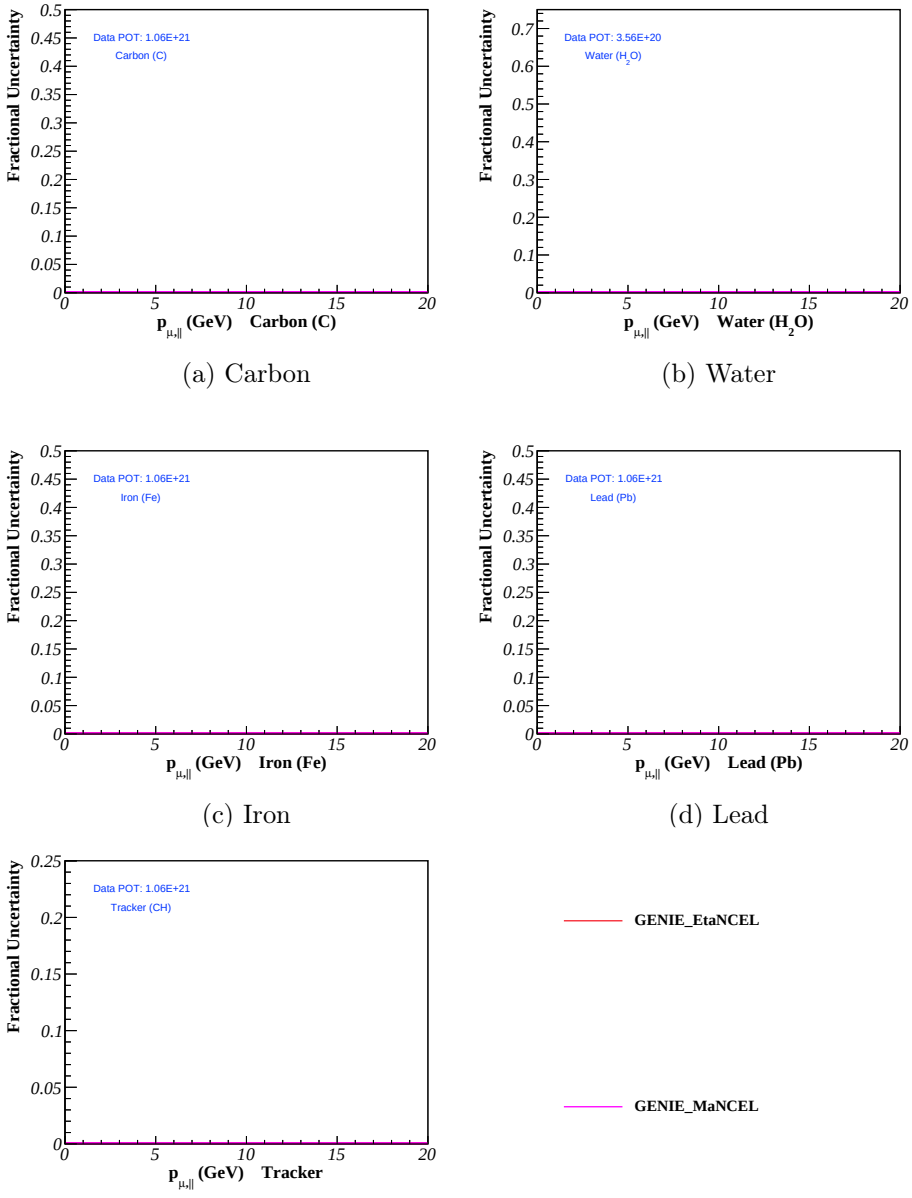
(b) Water

(c) Iron

(d) Lead

(e) Scintillator

Figure E-41: p_μ Elastic Scattering Model Errors



(a) Carbon

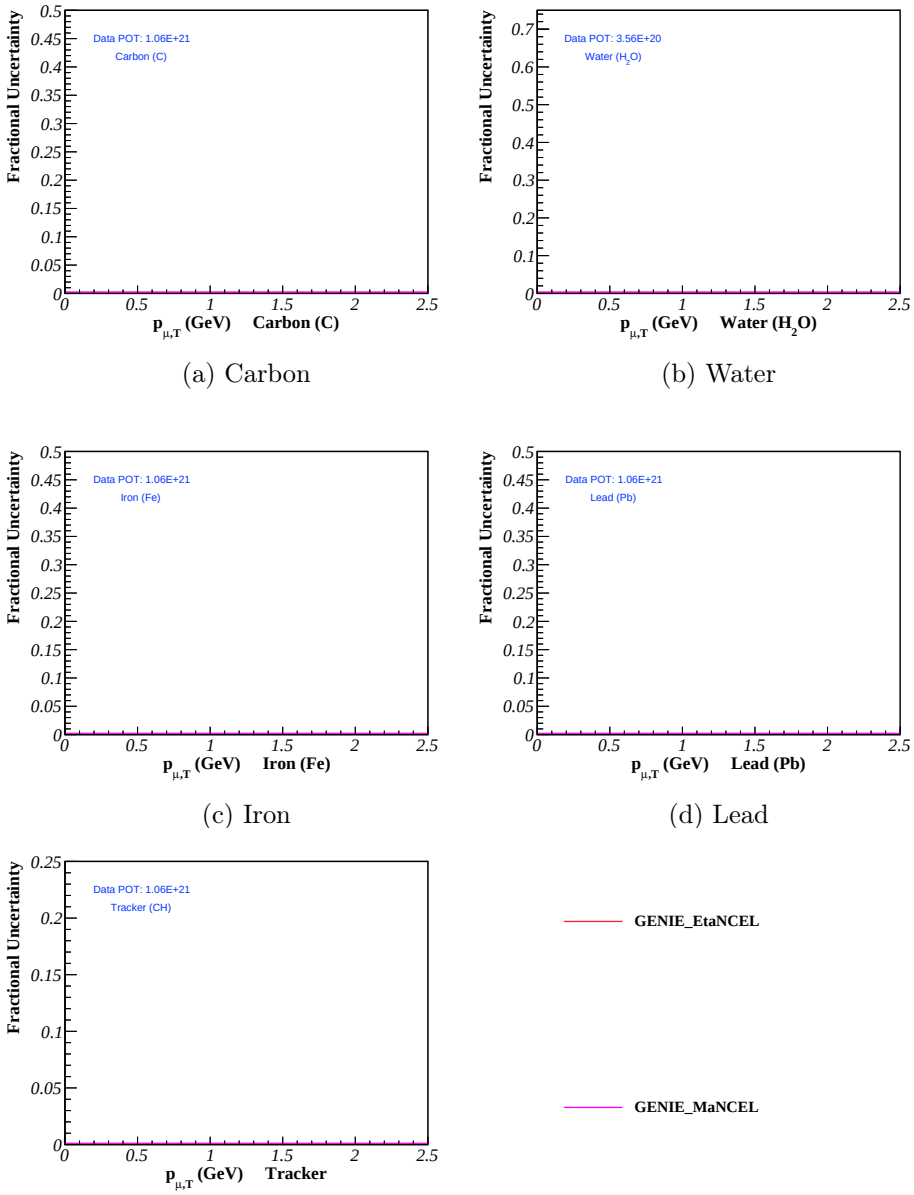
(b) Water

(c) Iron

(d) Lead

(e) Scintillator

Figure E-42: $p_{\mu,||}$ Elastic Scattering Model Errors



(a) Carbon

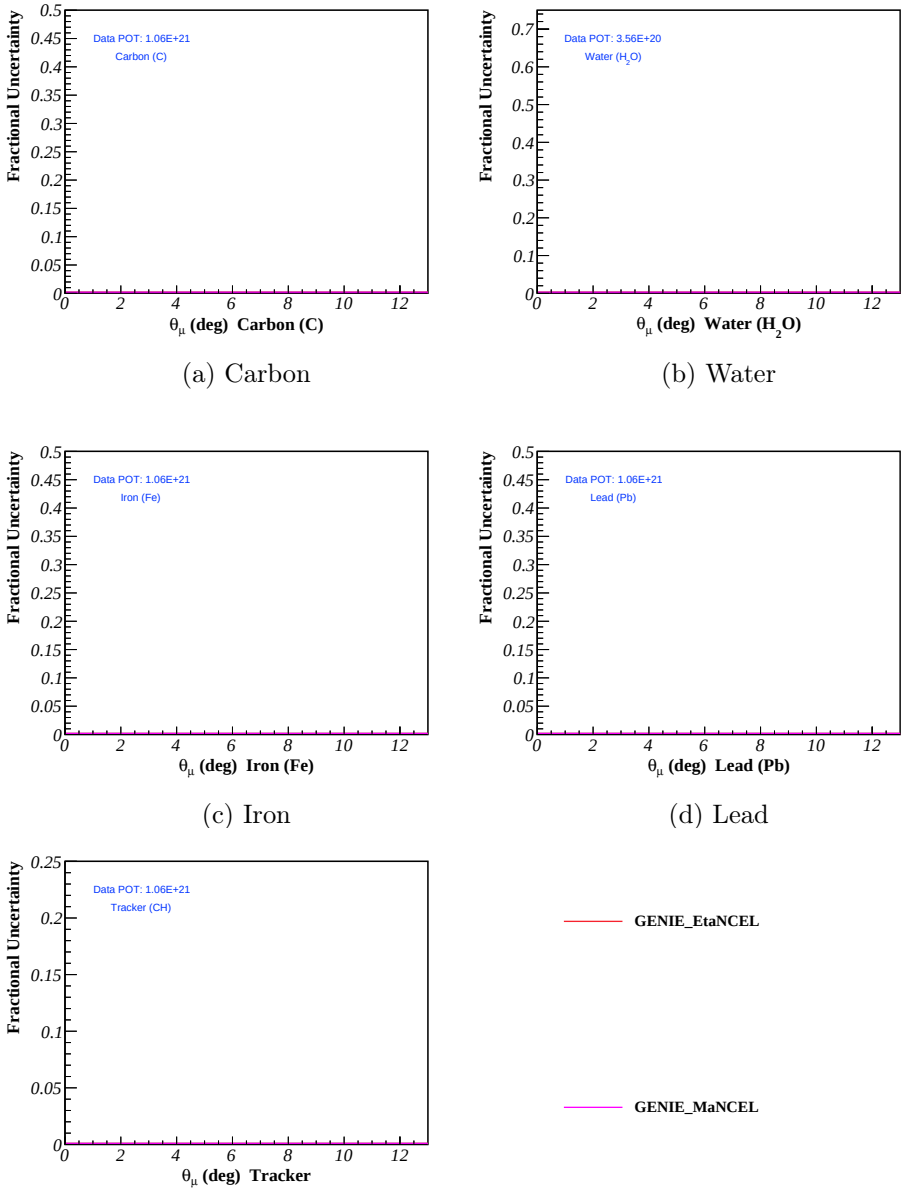
(b) Water

(c) Iron

(d) Lead

(e) Scintillator

Figure E-43: $p_{\mu,T}$ Elastic Scattering Model Errors



(a) Carbon

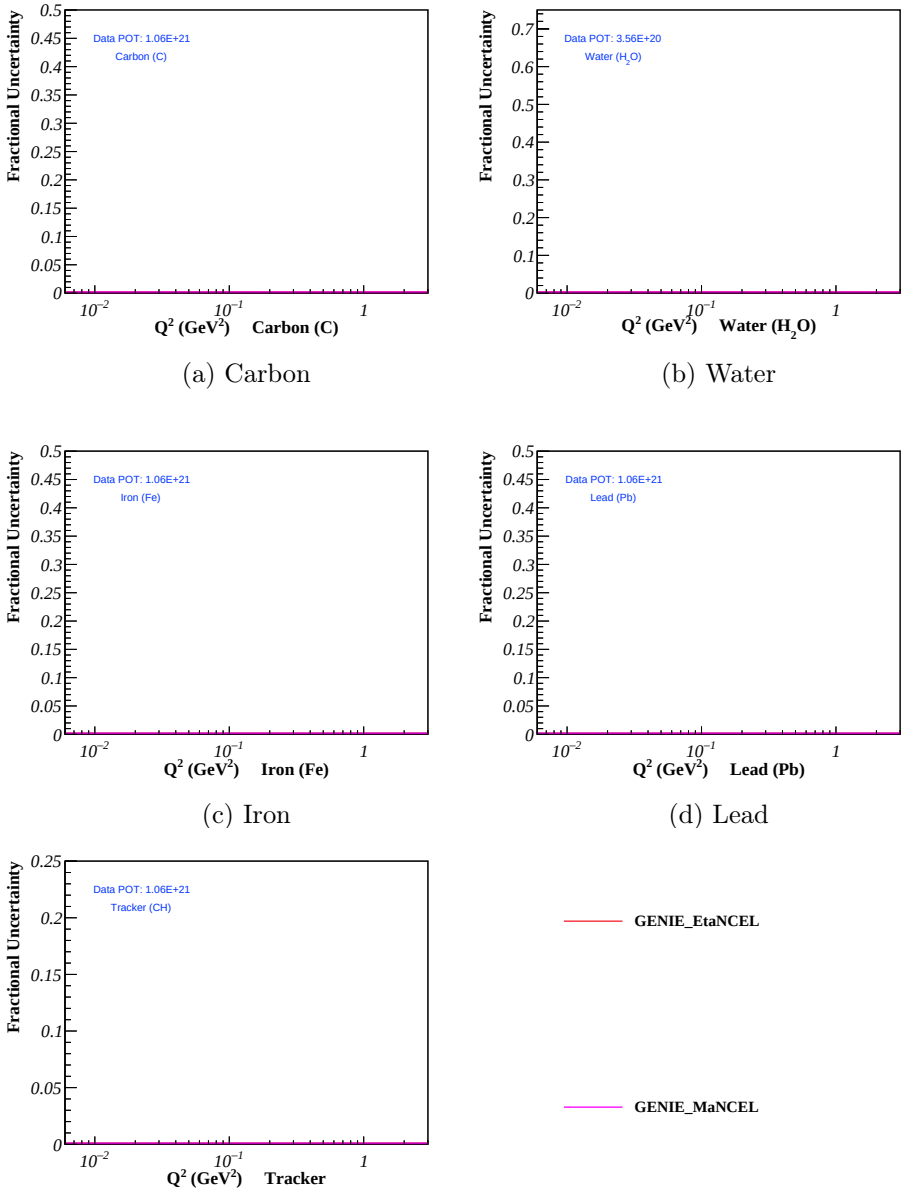
(b) Water

(c) Iron

(d) Lead

(e) Scintillator

Figure E-44: θ_μ Elastic Scattering Model Errors



(a) Carbon

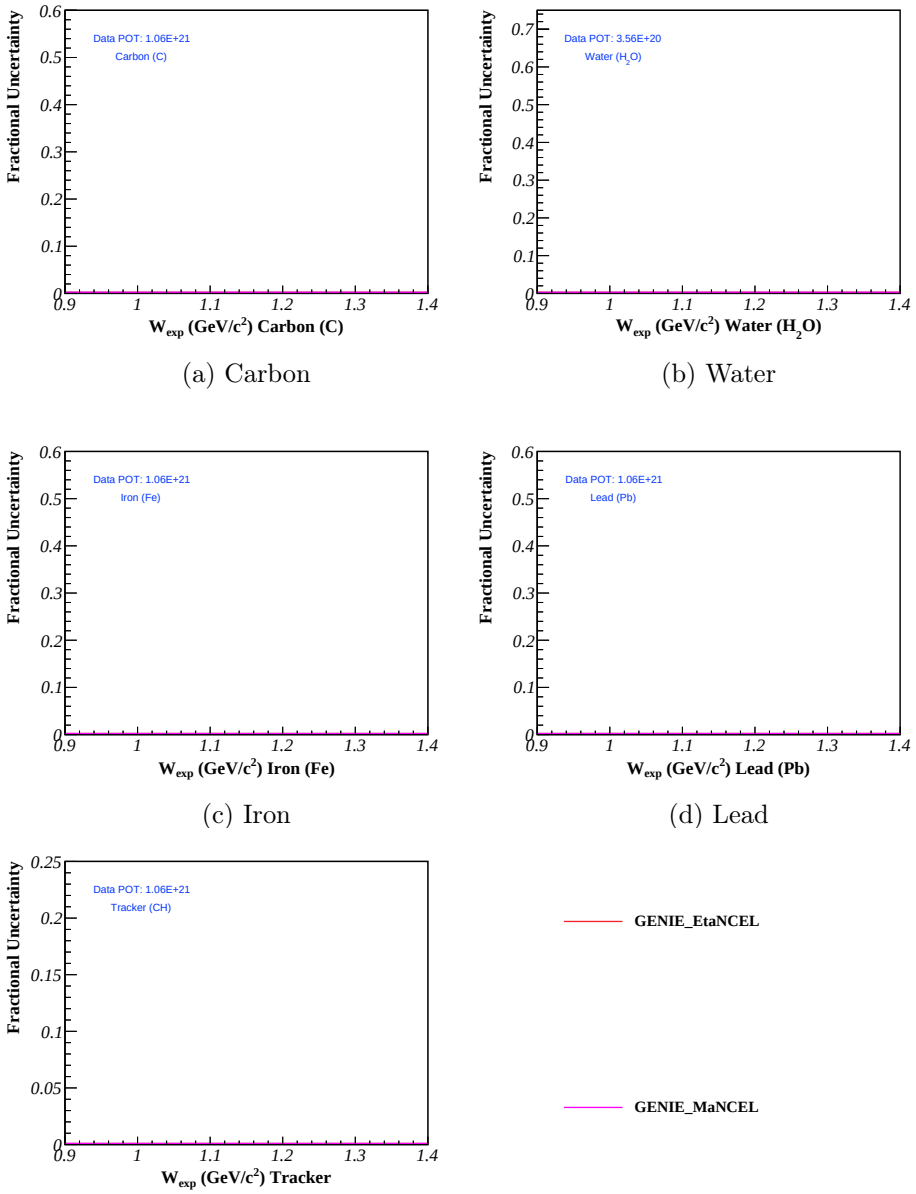
(b) Water

(c) Iron

(d) Lead

(e) Scintillator

Figure E-45: Q^2 Elastic Scattering Model Errors



(a) Carbon

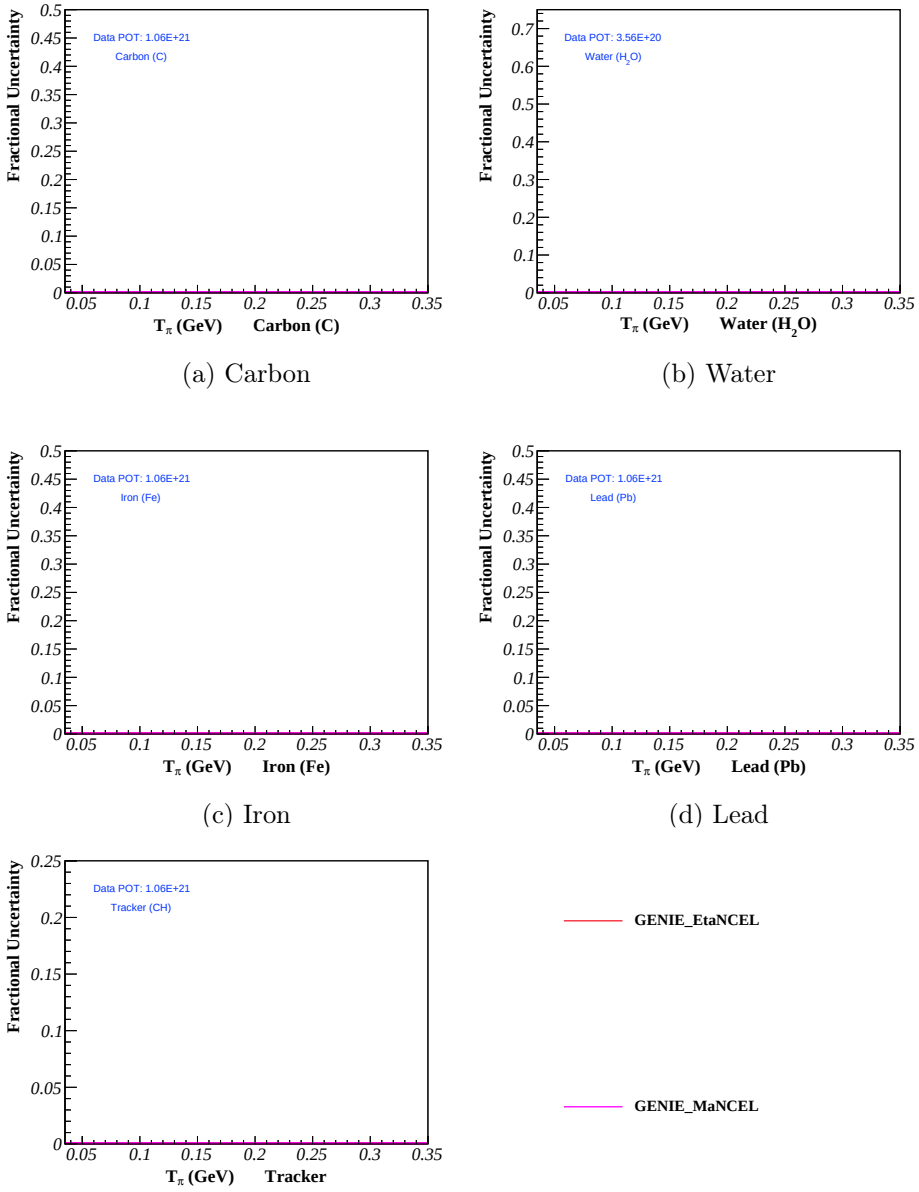
(b) Water

(c) Iron

(d) Lead

(e) Scintillator

Figure E-46: W_{exp} Elastic Scattering Model Errors



(a) Carbon

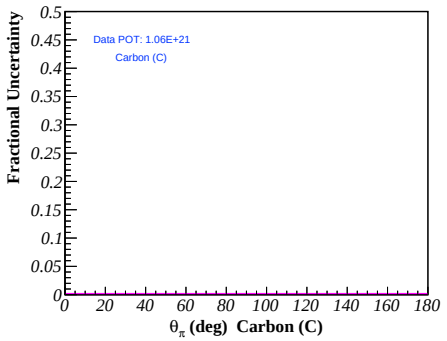
(b) Water

(c) Iron

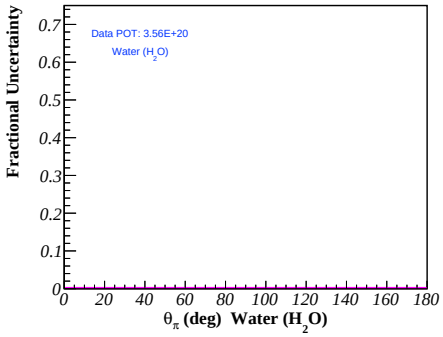
(d) Lead

(e) Scintillator

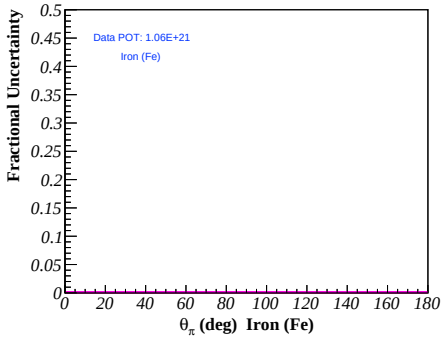
Figure E-47: T_π Elastic Scattering Model Errors



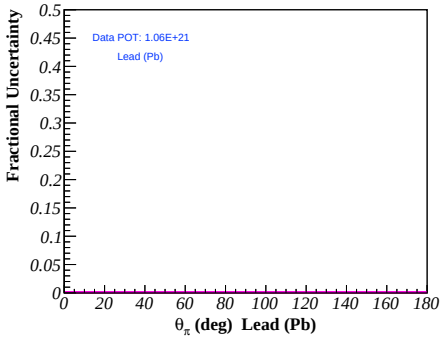
(a) Carbon



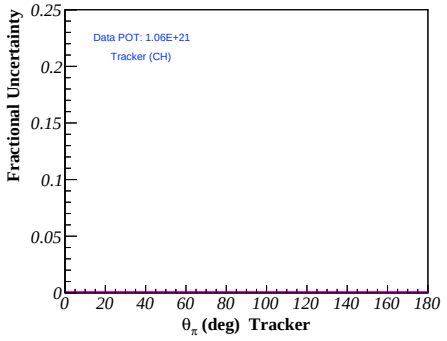
(b) Water



(c) Iron

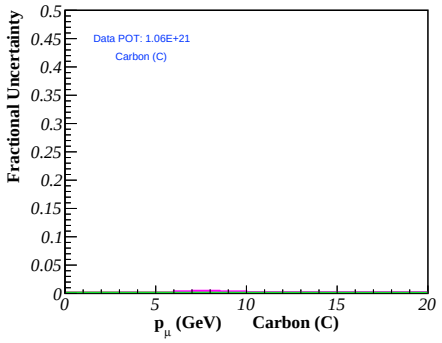


(d) Lead

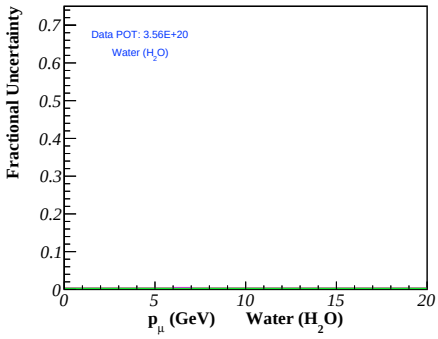


(e) Scintillator

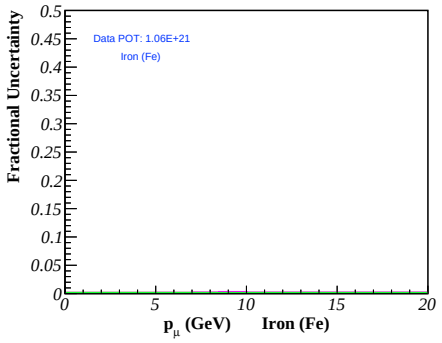
Figure E-48: θ_π Elastic Scattering Model Errors



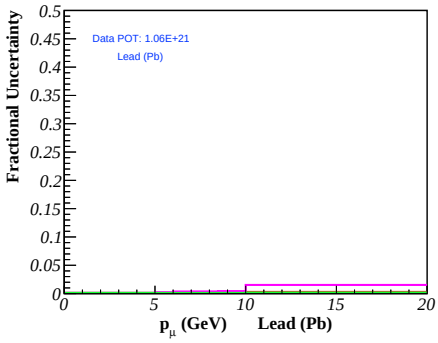
(a) Carbon



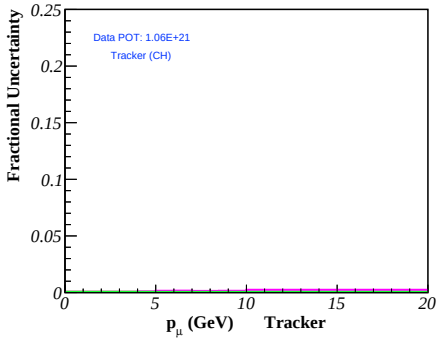
(b) Water

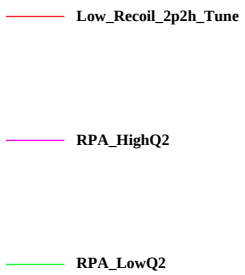


(c) Iron



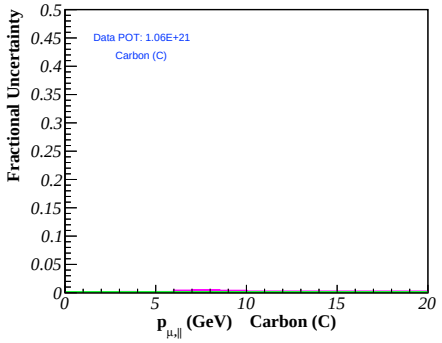
(d) Lead



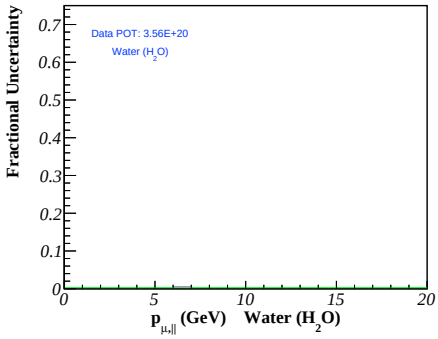


(e) Scintillator

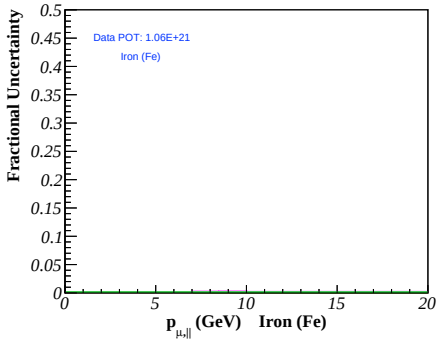
Figure E-49: p_μ MnvTune Model Errors



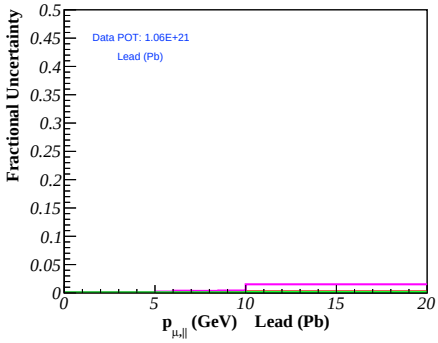
(a) Carbon



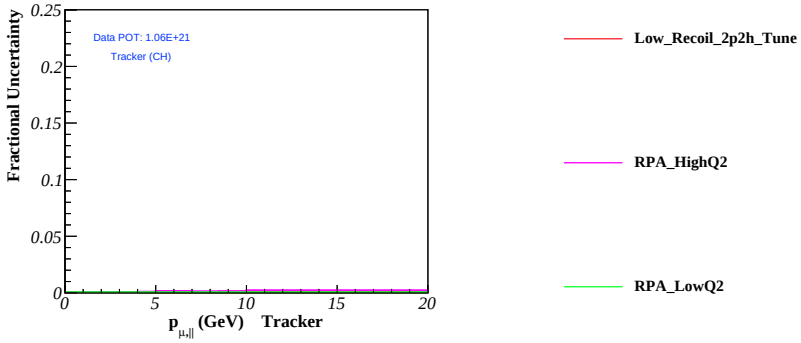
(b) Water



(c) Iron

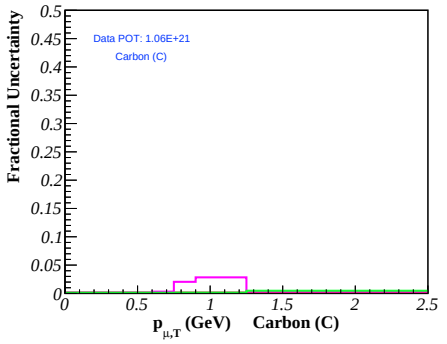


(d) Lead

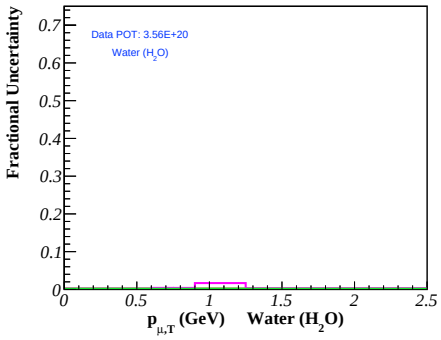


(e) Scintillator

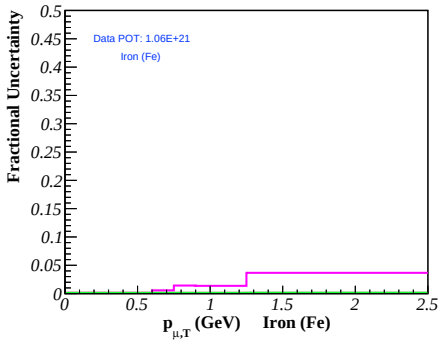
Figure E-50: $p_{\mu,||}$ MnvTune Model Errors



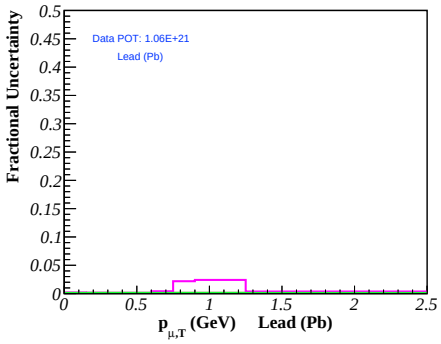
(a) Carbon



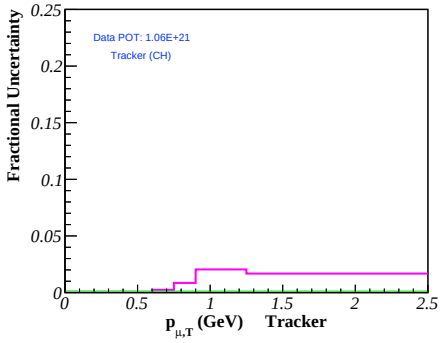
(b) Water

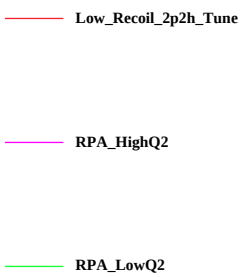


(c) Iron



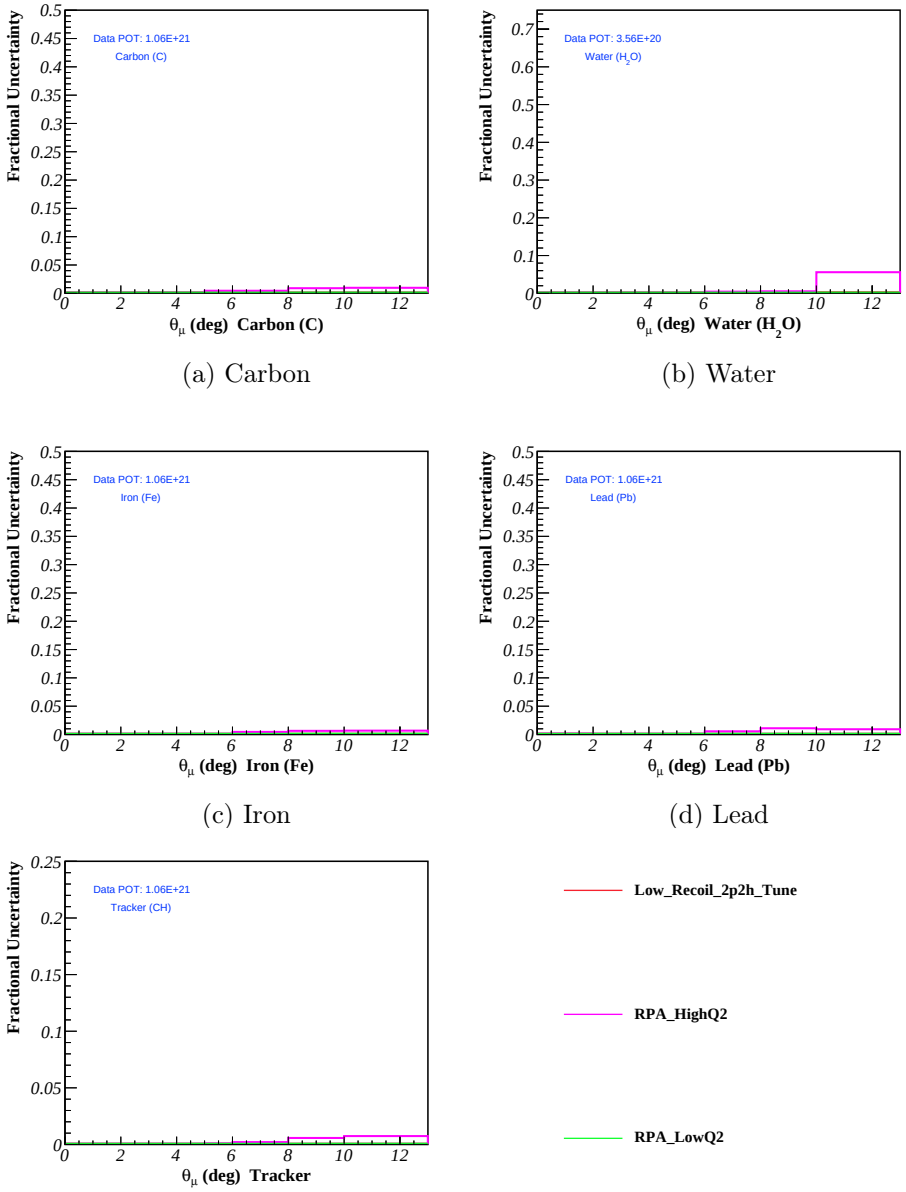
(d) Lead





(e) Scintillator

Figure E-51: $p_{\mu,T}$ MnvTune Model Errors



(a) Carbon

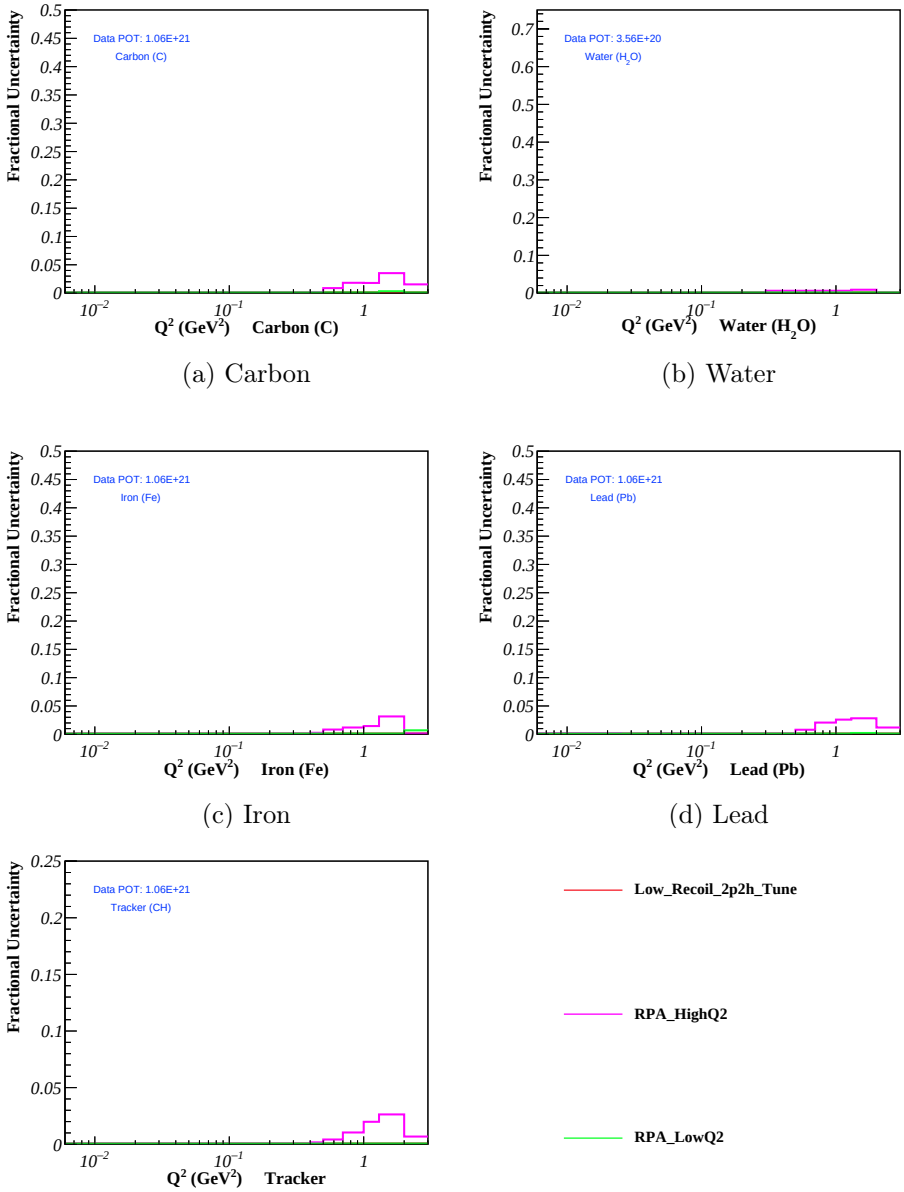
(b) Water

(c) Iron

(d) Lead

(e) Scintillator

Figure E-52: θ_μ MnvTune Model Errors



(a) Carbon

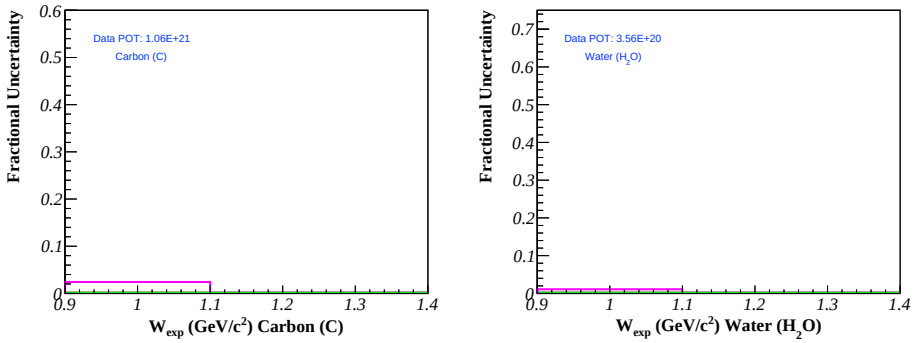
(b) Water

(c) Iron

(d) Lead

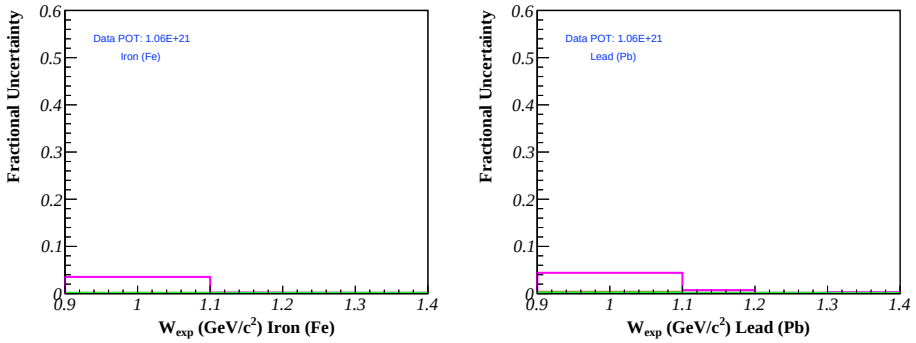
(e) Scintillator

Figure E-53: Q^2 MnvTune Model Errors



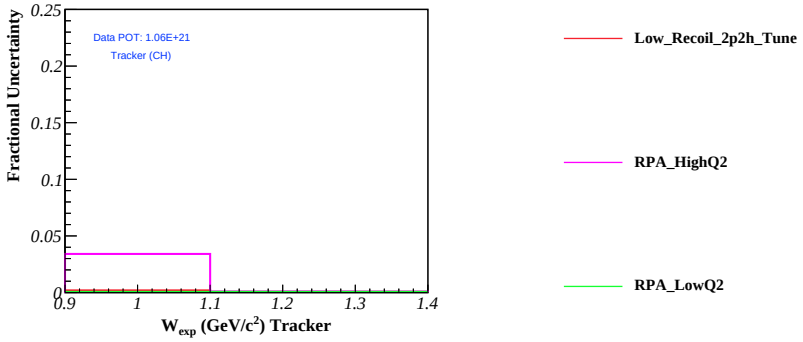
(a) Carbon

(b) Water



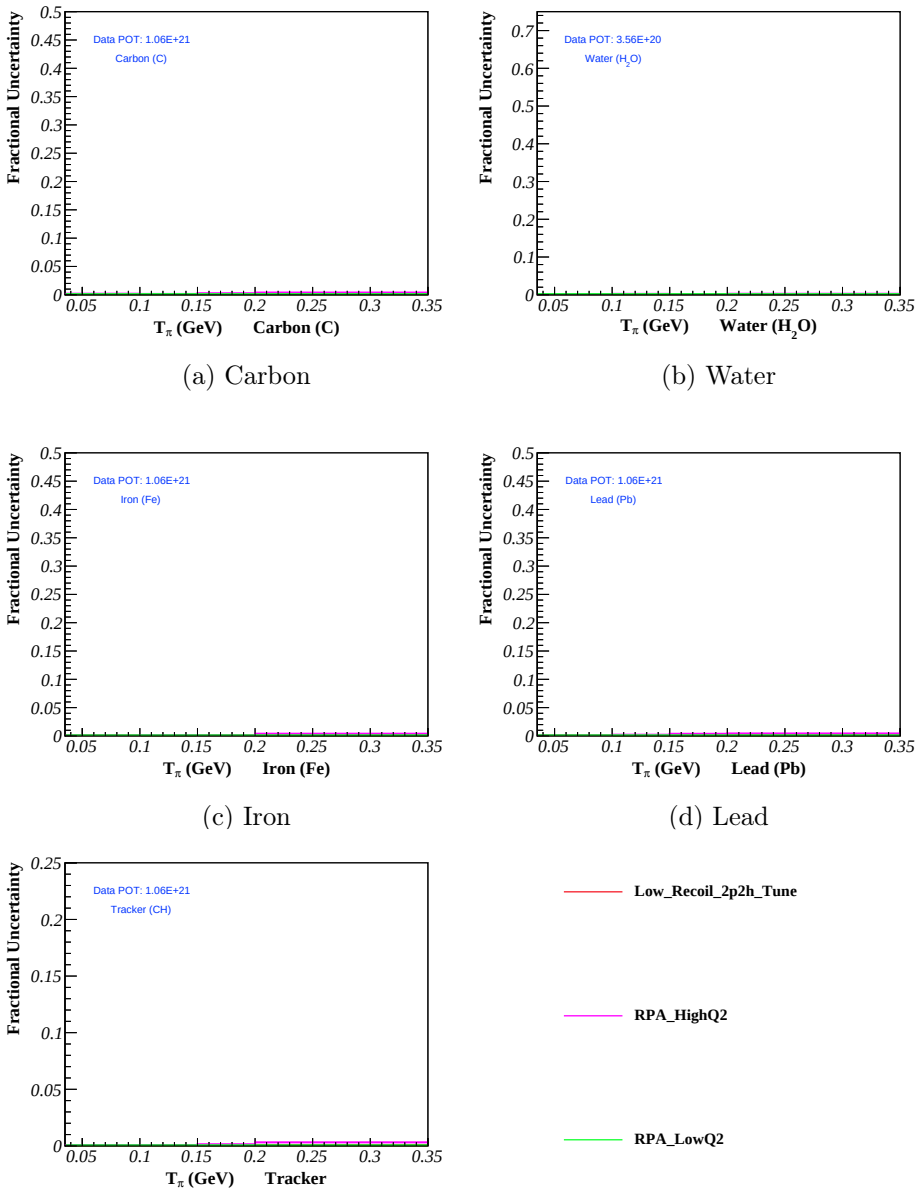
(c) Iron

(d) Lead



(e) Scintillator

Figure E-54: W_{exp} MnvTune Model Errors



(a) Carbon

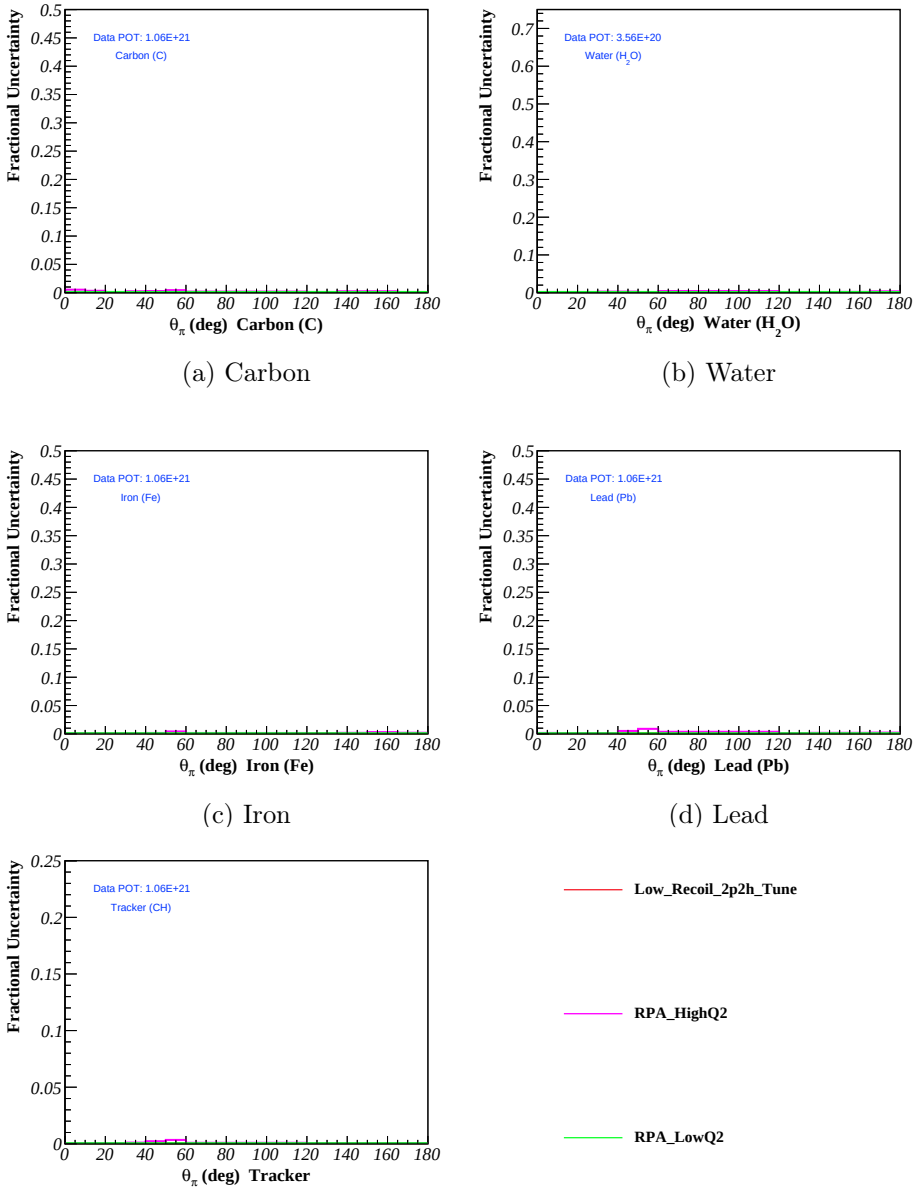
(b) Water

(c) Iron

(d) Lead

(e) Scintillator

Figure E-55: T_π MnvTune Model Errors



(a) Carbon

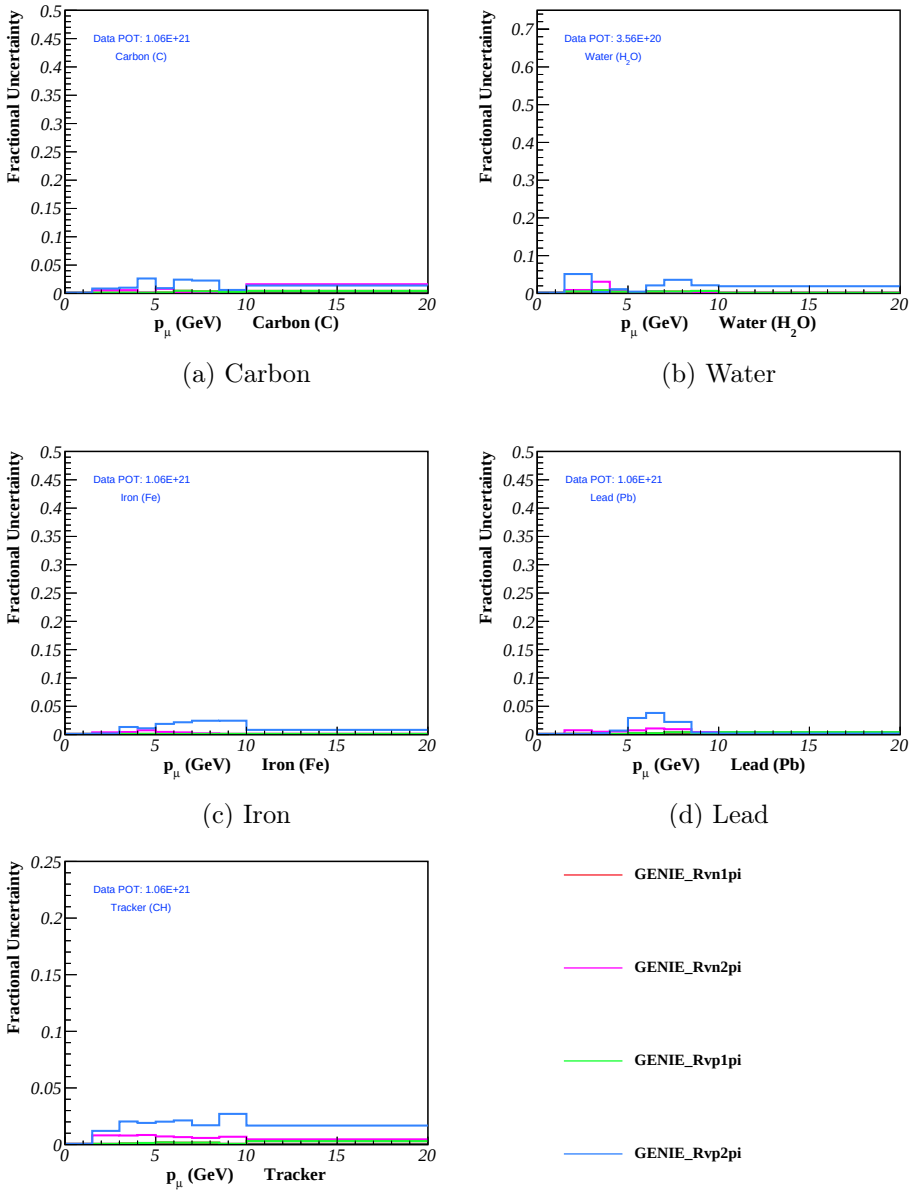
(b) Water

(c) Iron

(d) Lead

(e) Scintillator

Figure E-56: θ_π MnvTune Model Errors



(a) Carbon

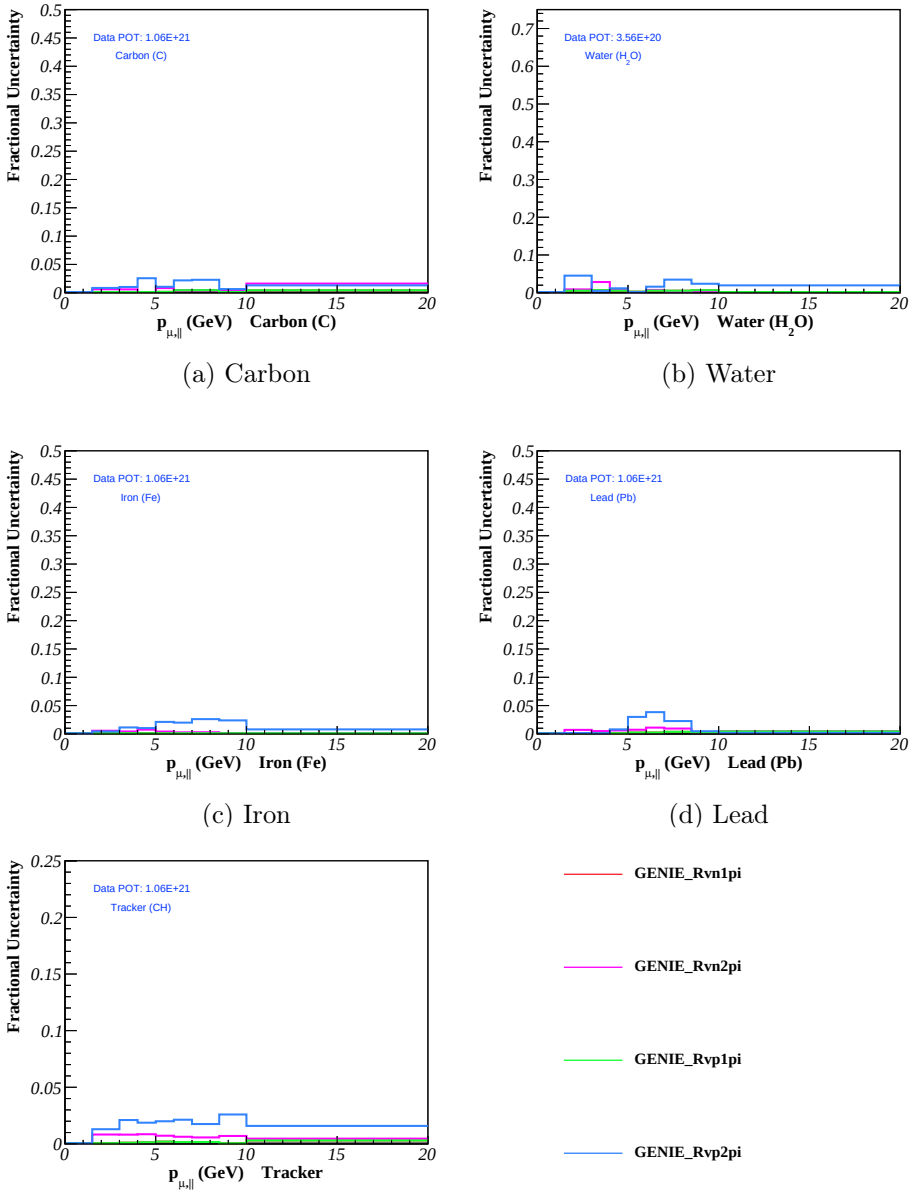
(b) Water

(c) Iron

(d) Lead

(e) Scintillator

Figure E-57: p_μ Nonresonant π Model Errors



(a) Carbon

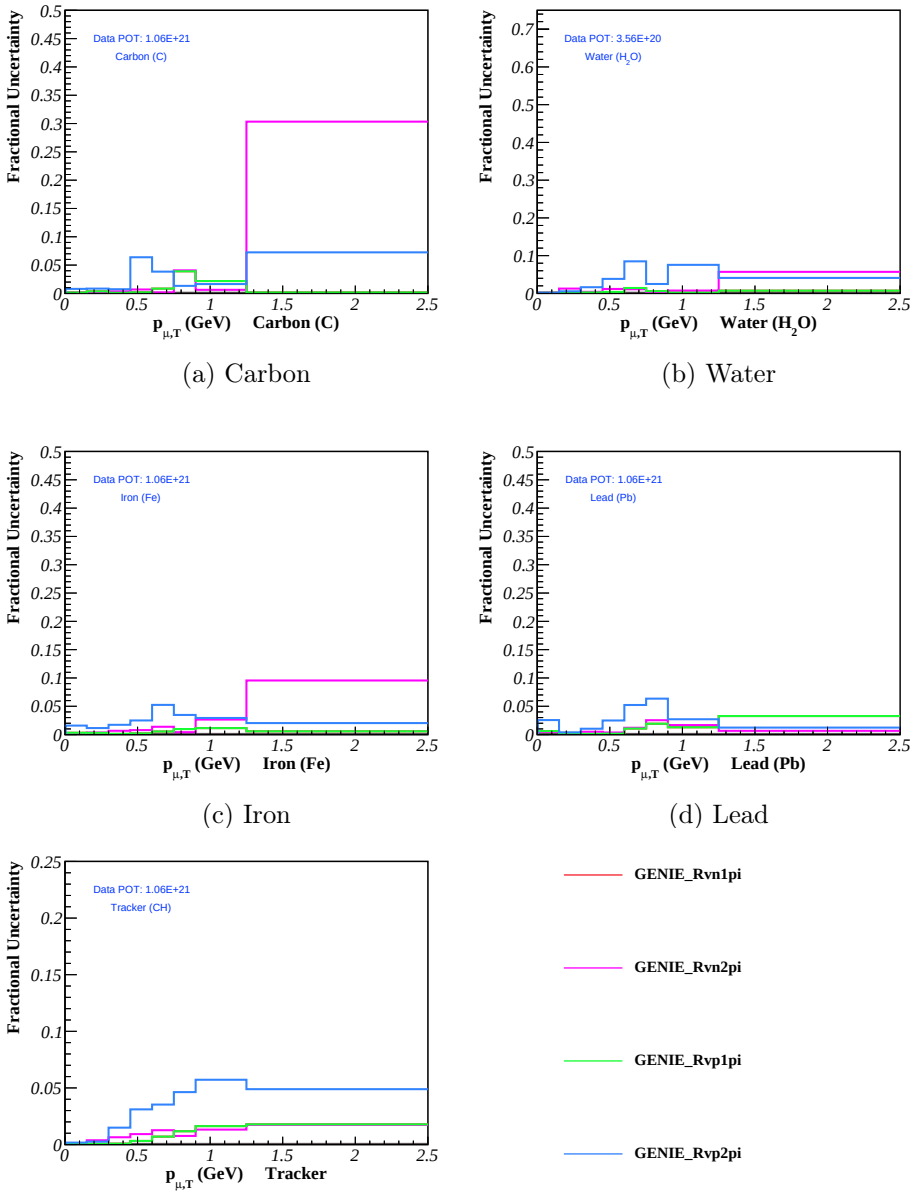
(b) Water

(c) Iron

(d) Lead

(e) Scintillator

Figure E-58: $p_{\mu,||}$ Nonresonant π Model Errors



(a) Carbon

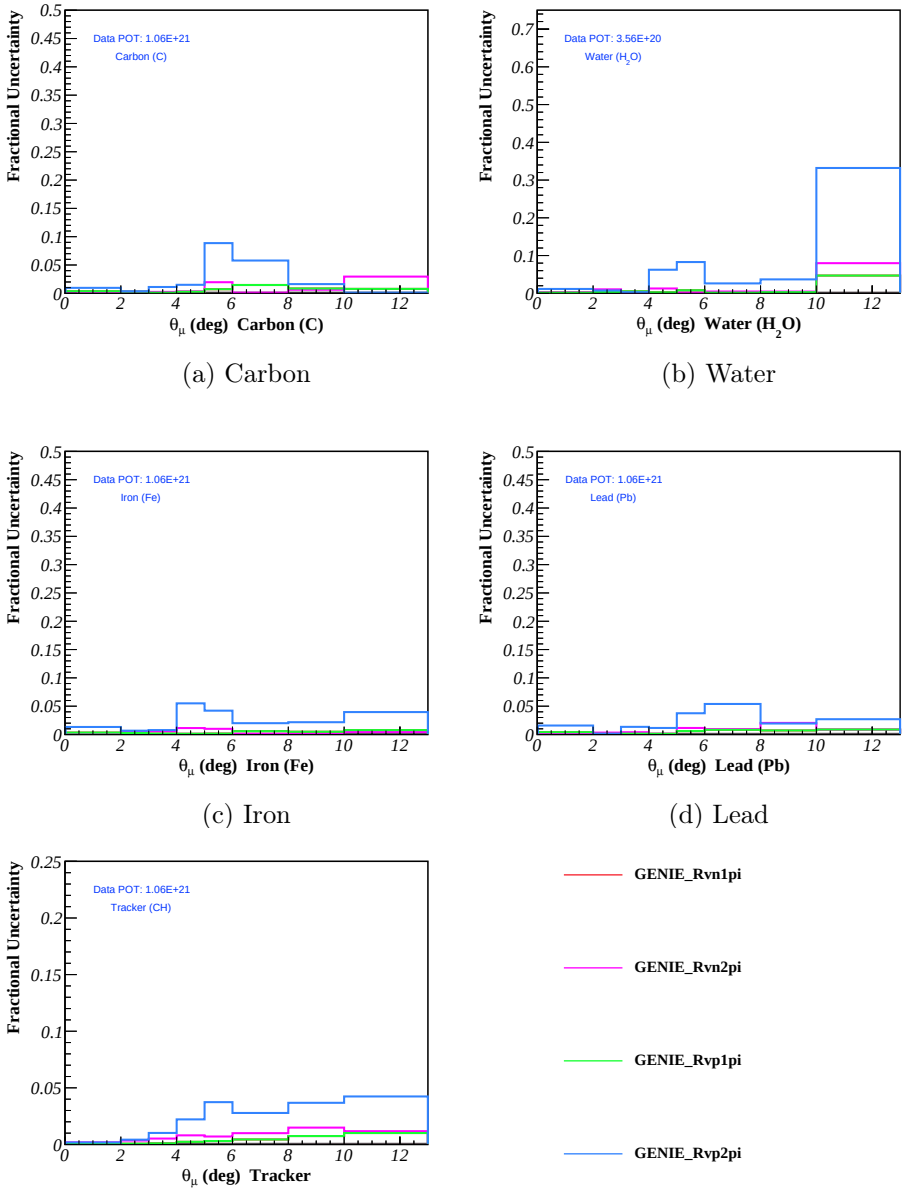
(b) Water

(c) Iron

(d) Lead

(e) Scintillator

Figure E-59: $p_{\mu,T}$ Nonresonant π Model Errors



(a) Carbon

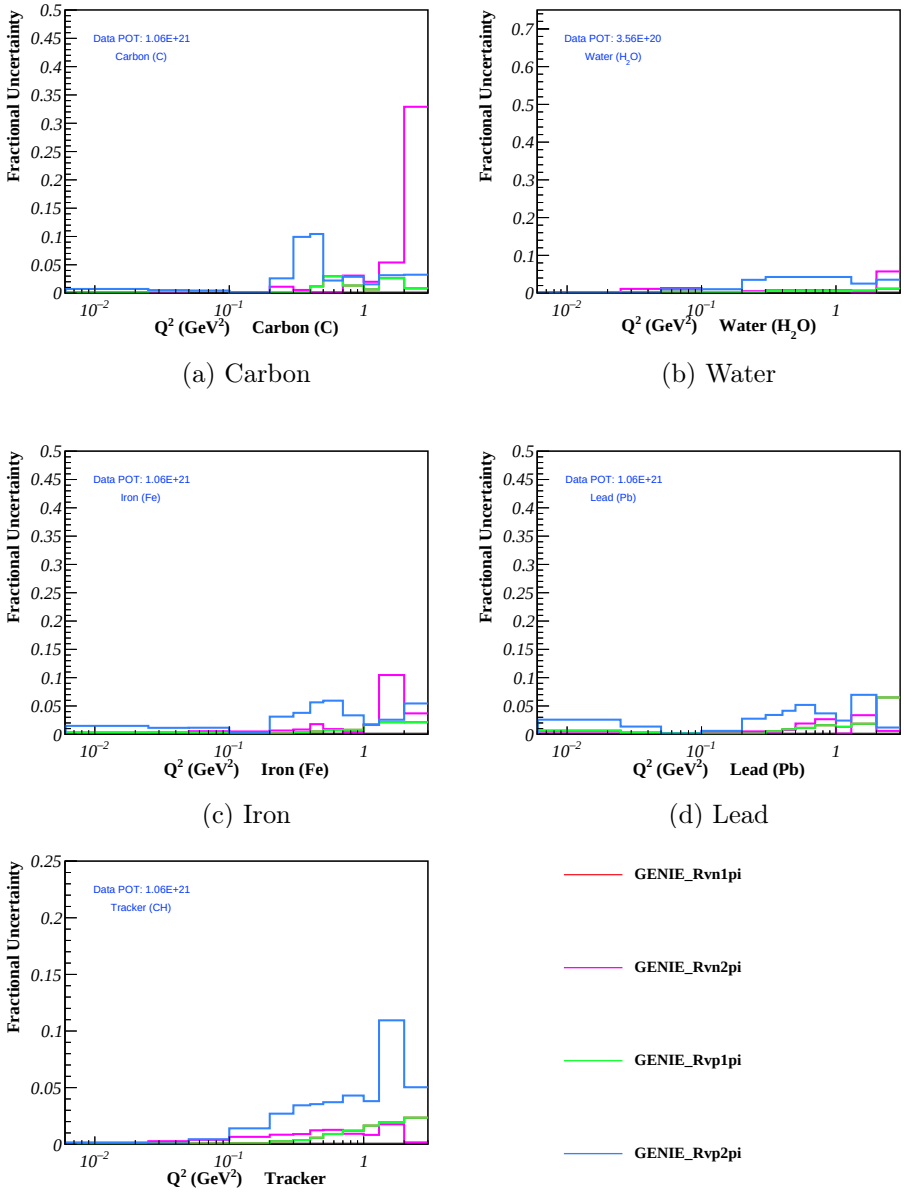
(b) Water

(c) Iron

(d) Lead

(e) Scintillator

Figure E-60: θ_μ Nonresonant π Model Errors



(a) Carbon

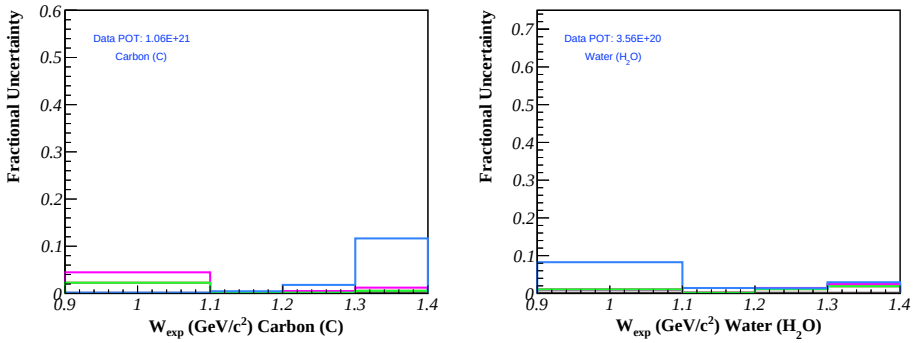
(b) Water

(c) Iron

(d) Lead

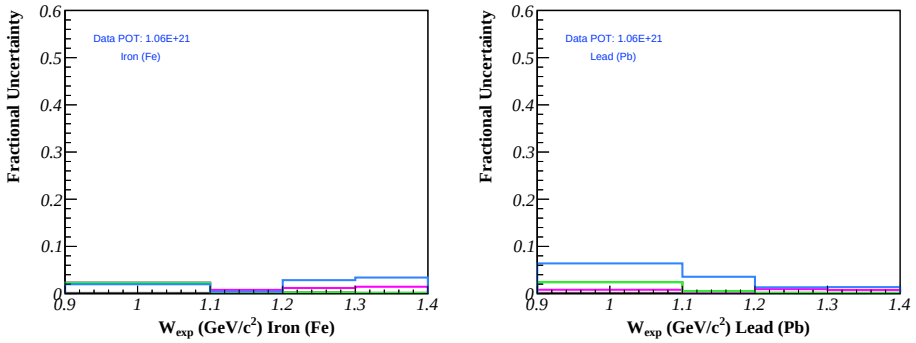
(e) Scintillator

Figure E-61: Q^2 Nonresonant π Model Errors



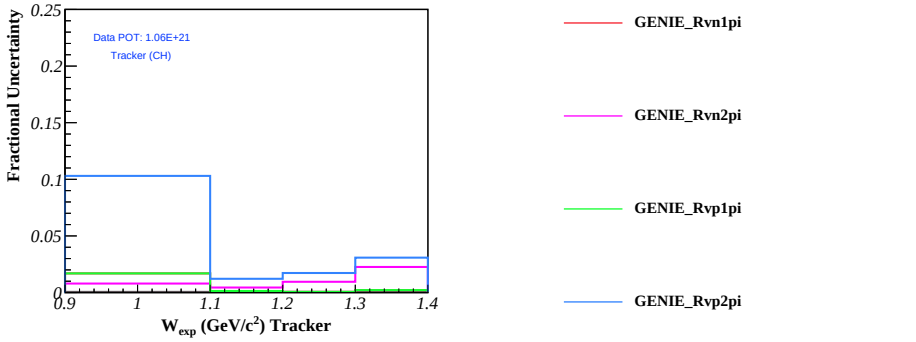
(a) Carbon

(b) Water



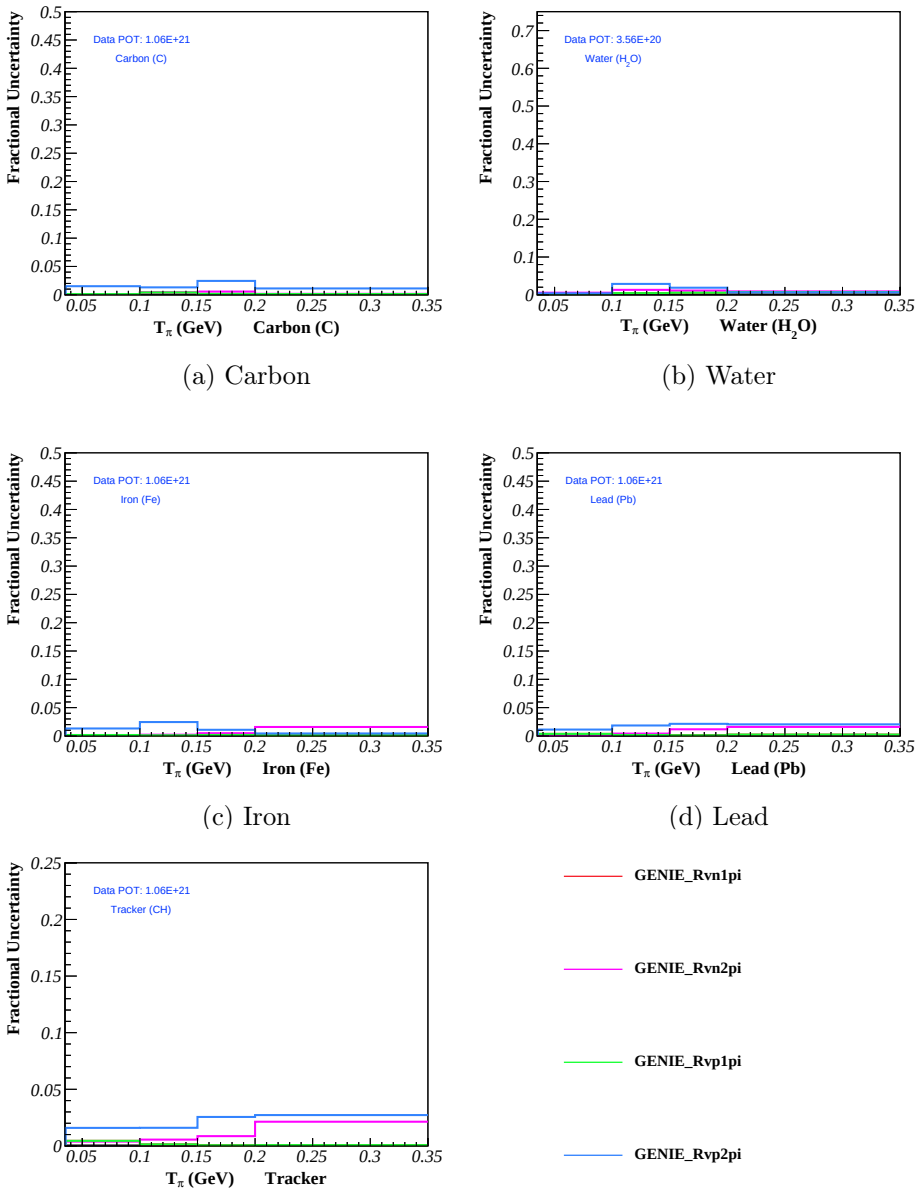
(c) Iron

(d) Lead



(e) Scintillator

Figure E-62: W_{exp} Nonresonant π Model Errors



(a) Carbon

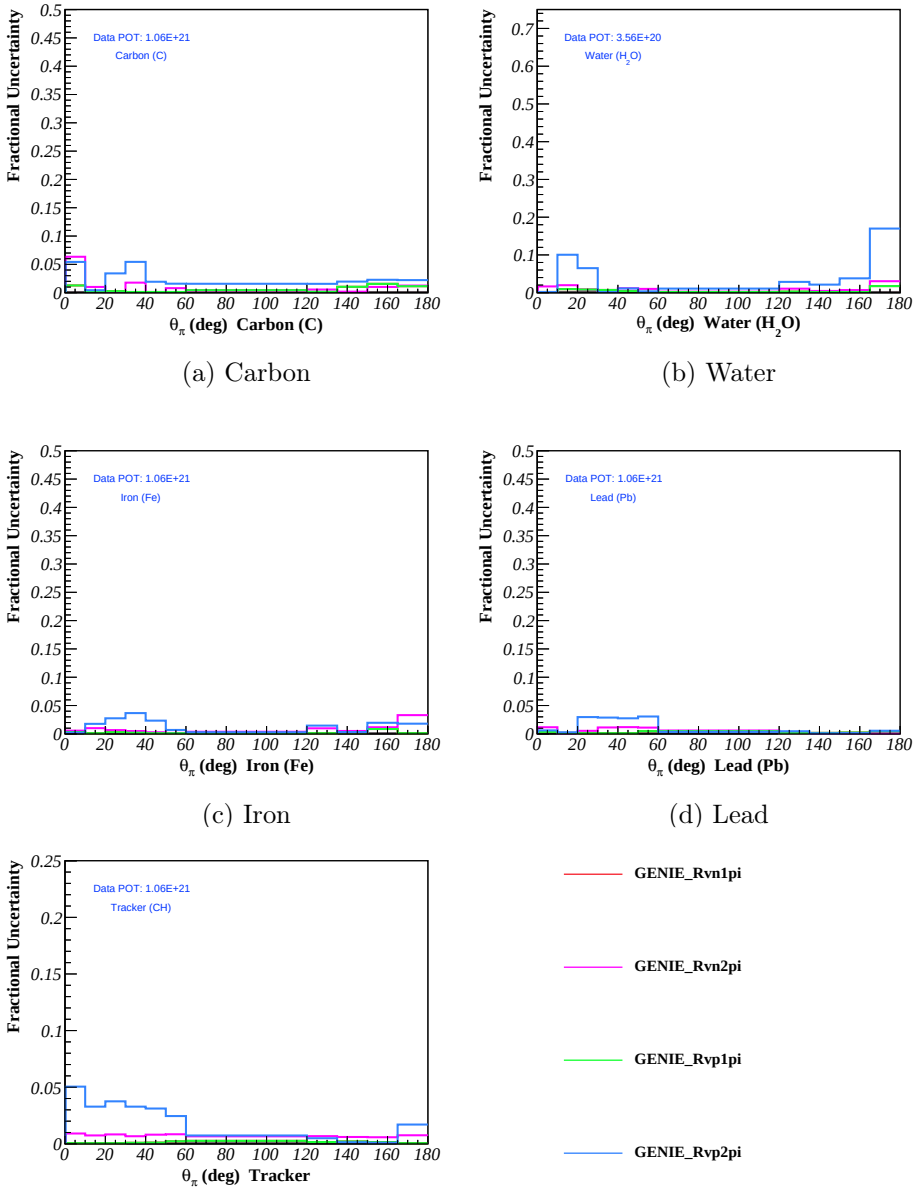
(b) Water

(c) Iron

(d) Lead

(e) Scintillator

Figure E-63: T_π Nonresonant π Model Errors



(a) Carbon

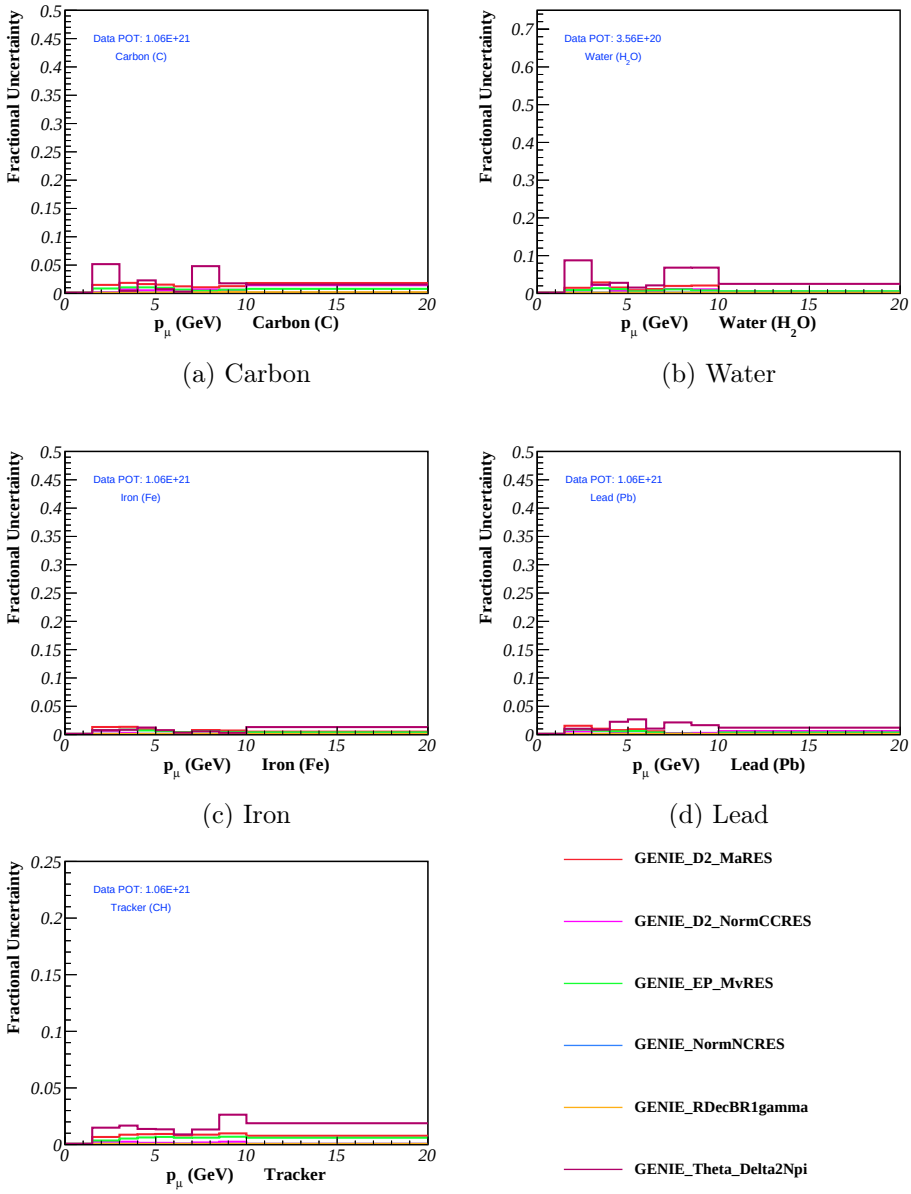
(b) Water

(c) Iron

(d) Lead

(e) Scintillator

Figure E-64: θ_π Nonresonant π Model Errors



(a) Carbon

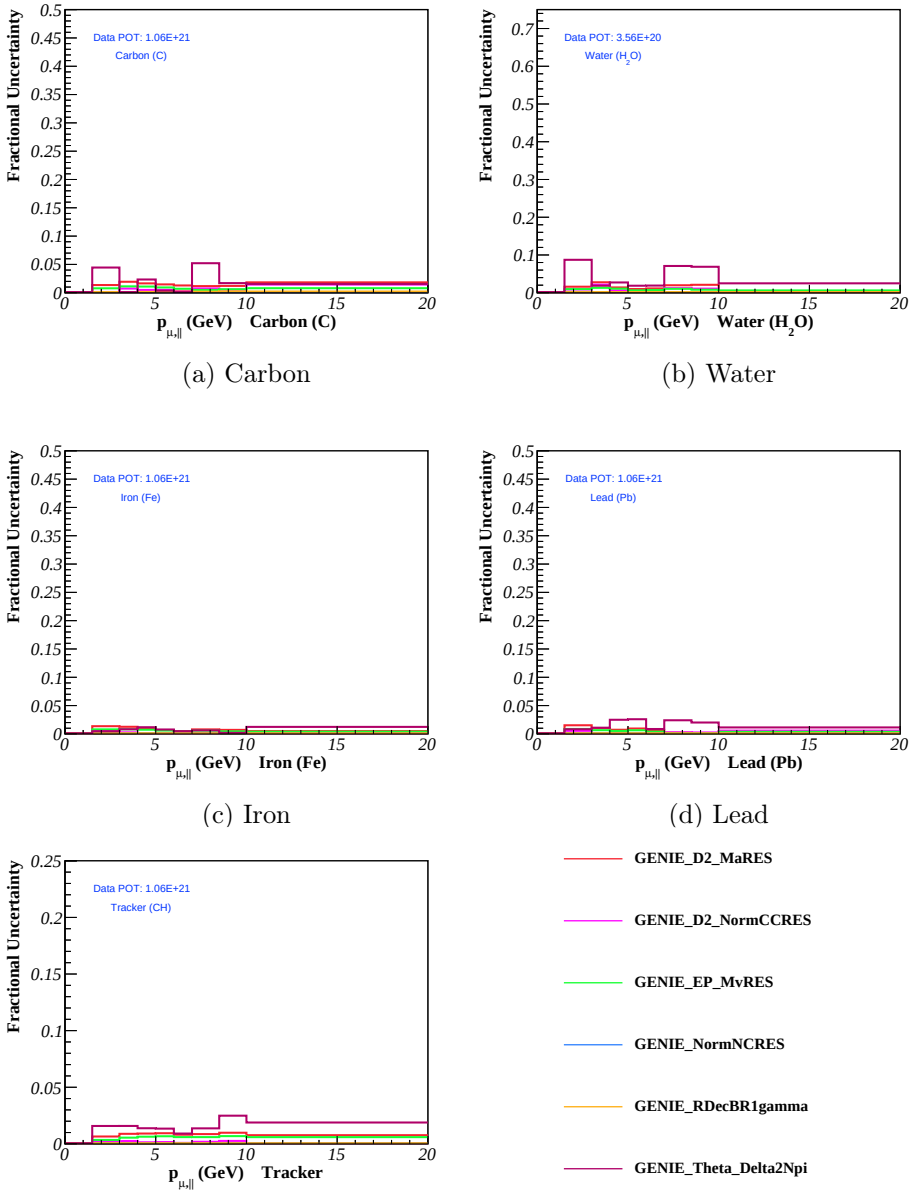
(b) Water

(c) Iron

(d) Lead

(e) Scintillator

Figure E-65: p_μ Resonant π Model Errors



(a) Carbon

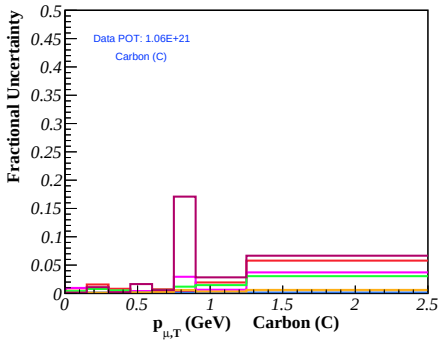
(b) Water

(c) Iron

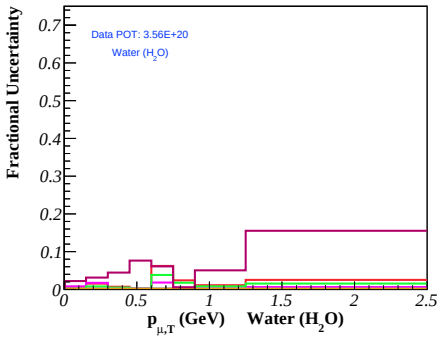
(d) Lead

(e) Scintillator

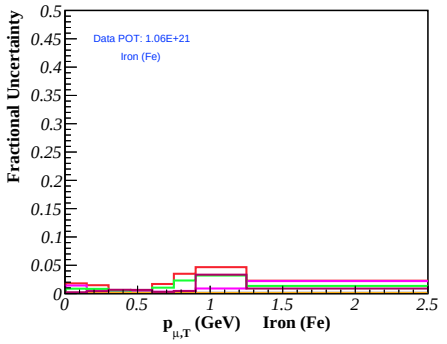
Figure E-66: $p_{\mu,||}$ Resonant π Model Errors



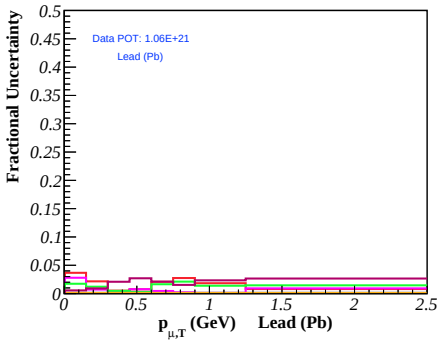
(a) Carbon



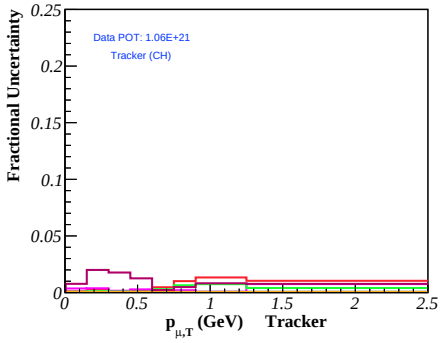
(b) Water



(c) Iron



(d) Lead



(e) Scintillator

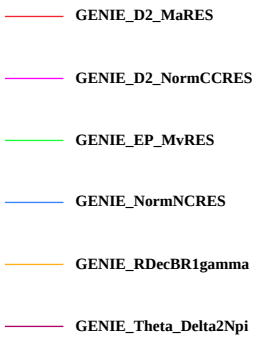
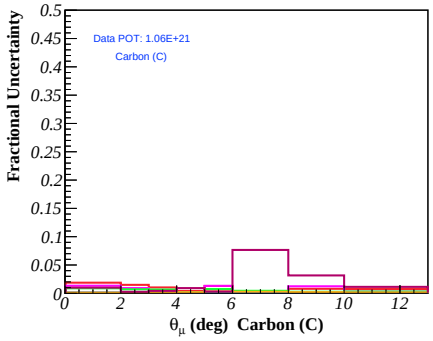
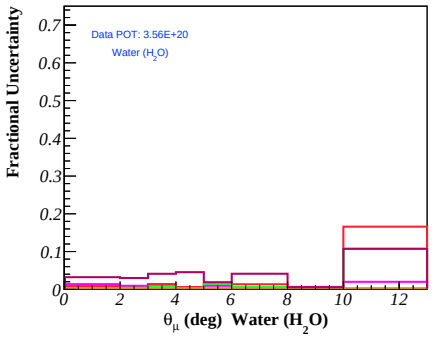


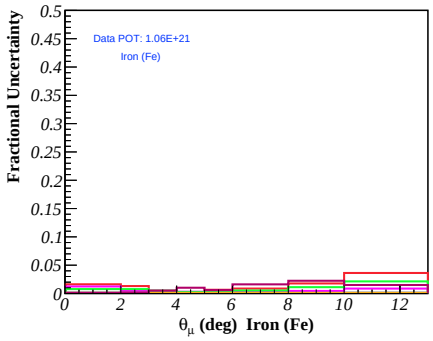
Figure E-67: $p_{\mu,T}$ Resonant π Model Errors



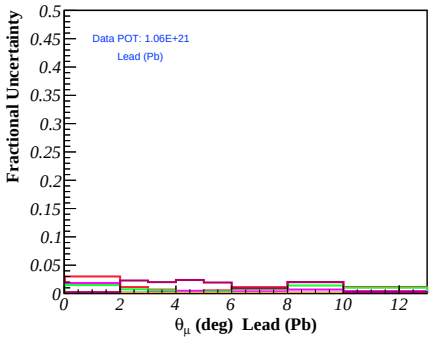
(a) Carbon



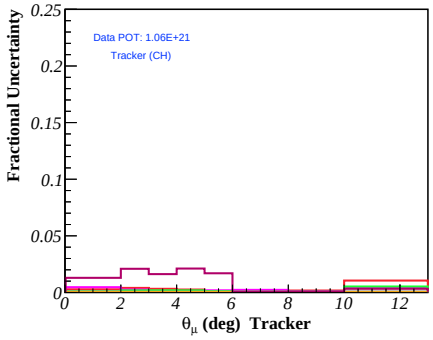
(b) Water

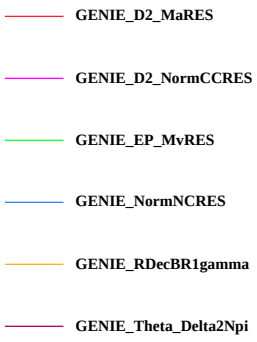


(c) Iron



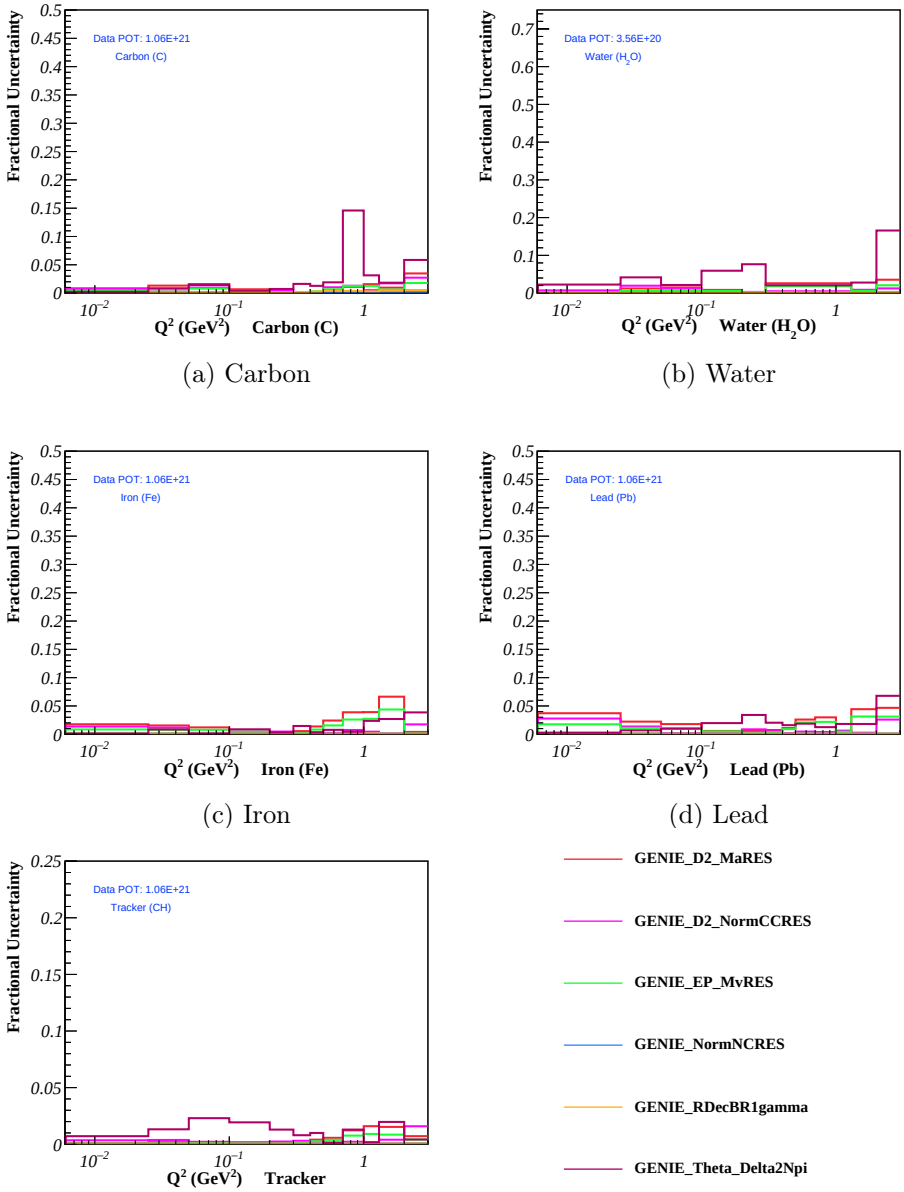
(d) Lead





(e) Scintillator

Figure E-68: θ_μ Resonant π Model Errors



(a) Carbon

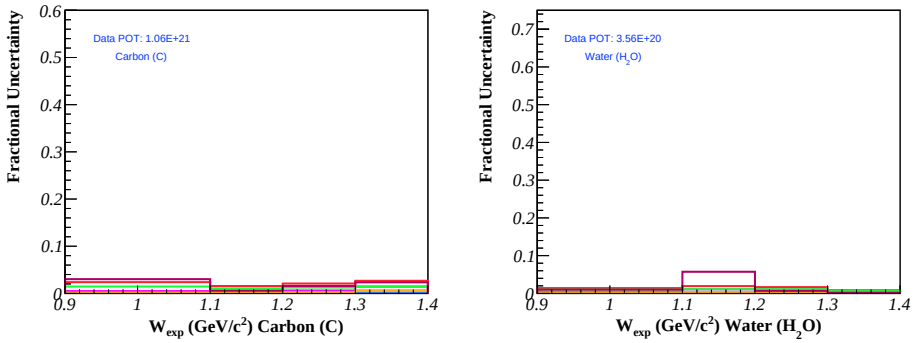
(b) Water

(c) Iron

(d) Lead

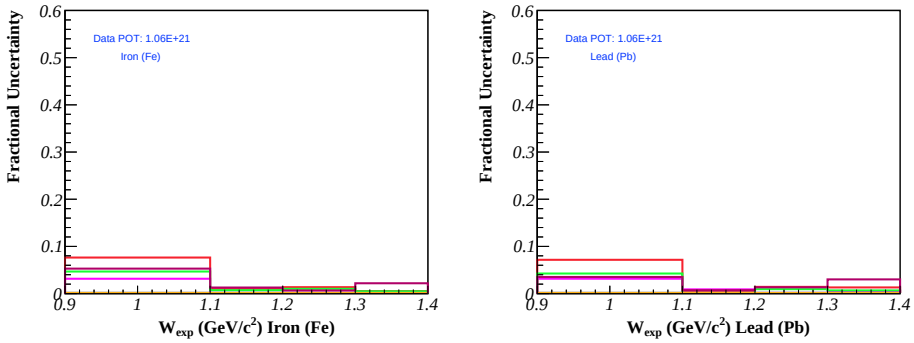
(e) Scintillator

Figure E-69: Q^2 Resonant π Model Errors



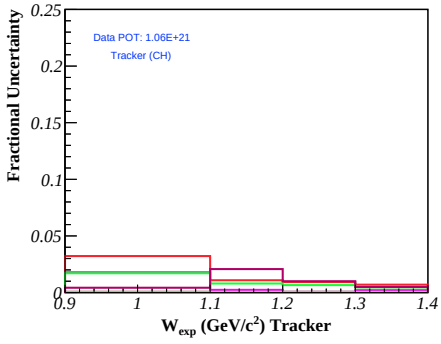
(a) Carbon

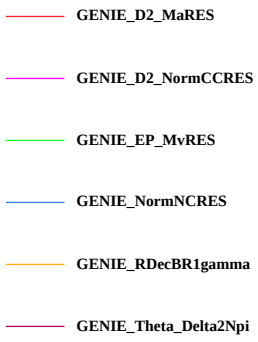
(b) Water



(c) Iron

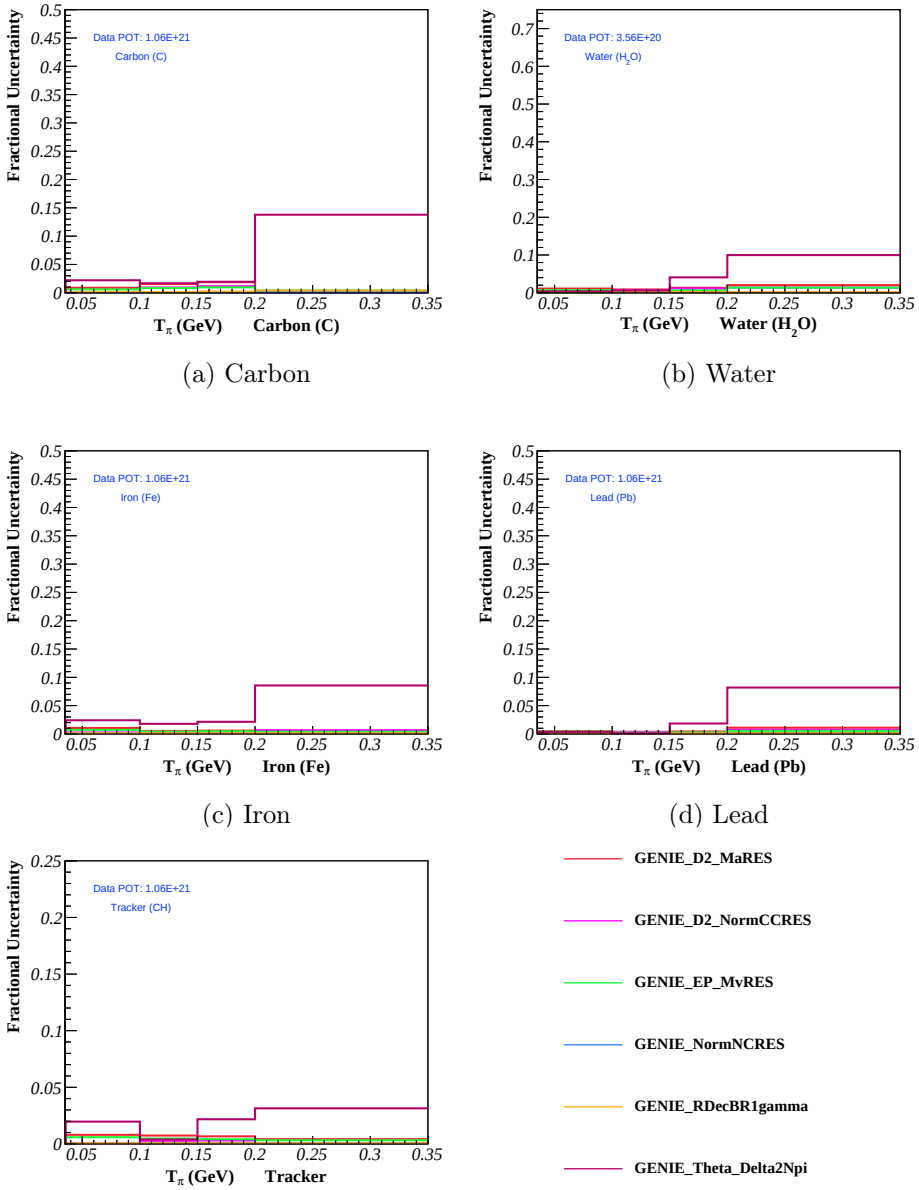
(d) Lead





(e) Scintillator

Figure E-70: W_{exp} Resonant π Model Errors



(a) Carbon

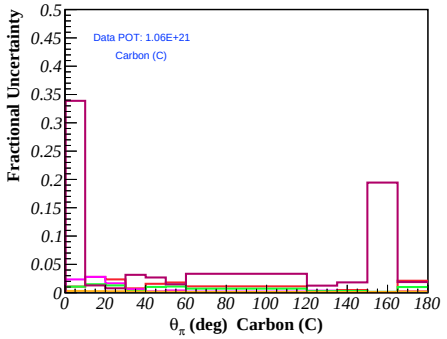
(b) Water

(c) Iron

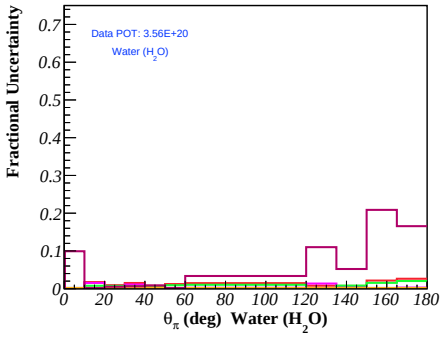
(d) Lead

(e) Scintillator

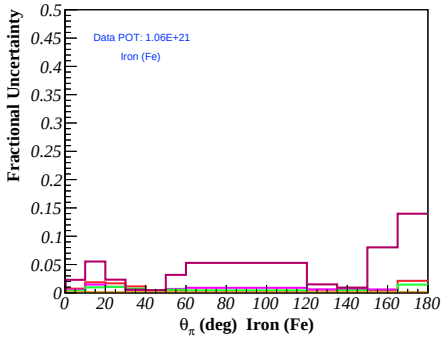
Figure E-71: T_π Resonant π Model Errors



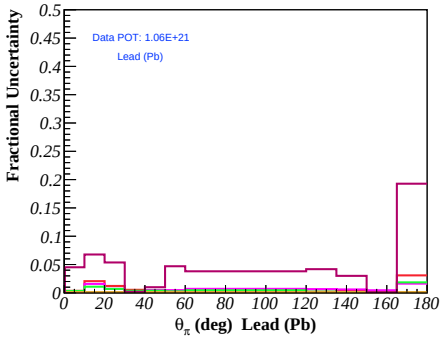
(a) Carbon



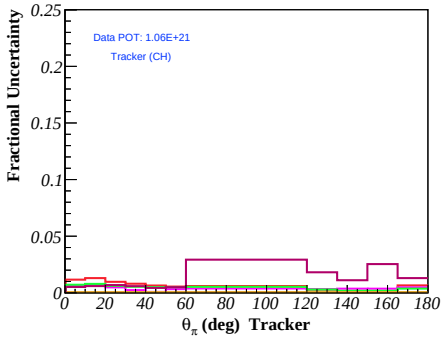
(b) Water

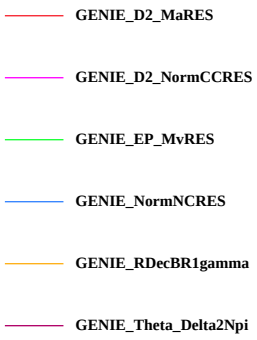


(c) Iron



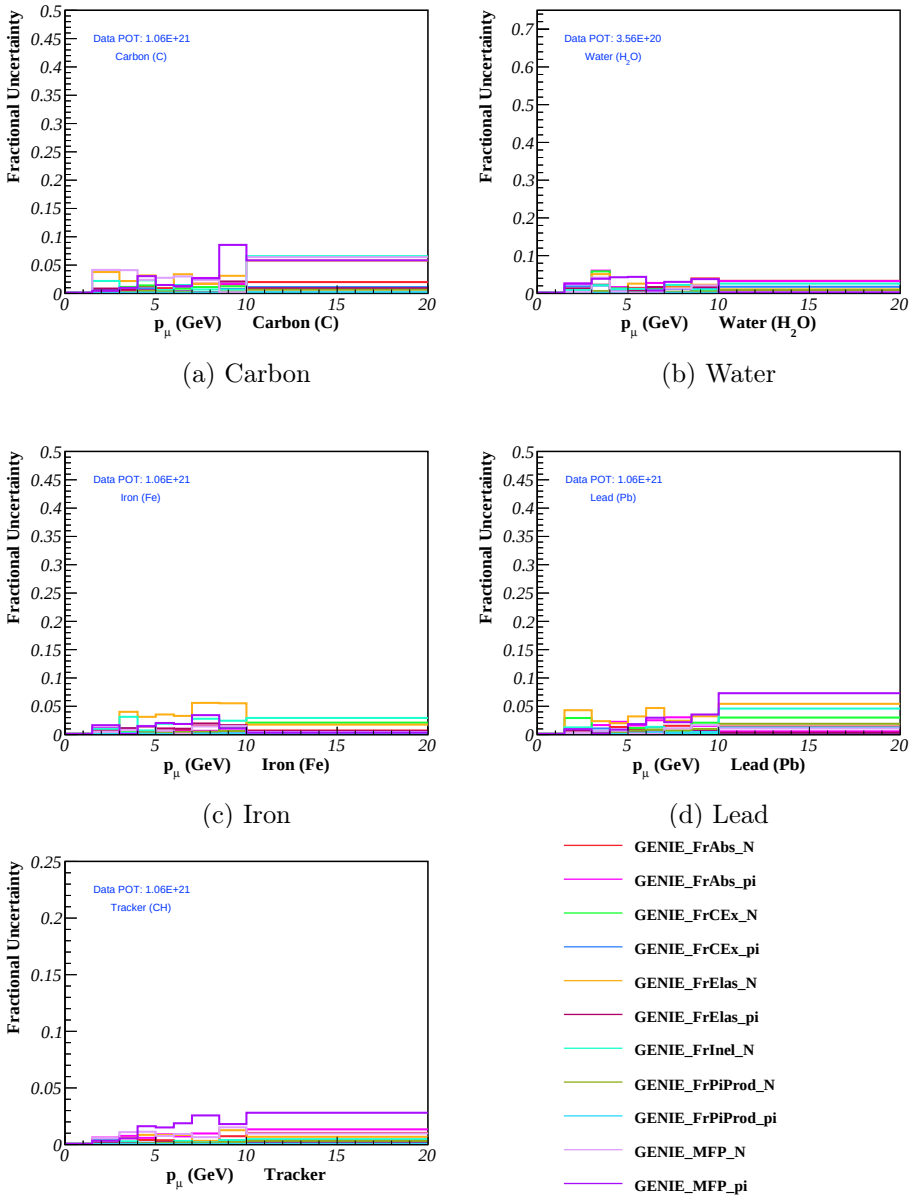
(d) Lead





(e) Scintillator

Figure E-72: θ_π Resonant π Model Errors



(a) Carbon

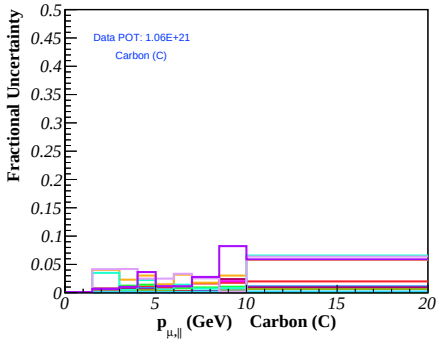
(b) Water

(c) Iron

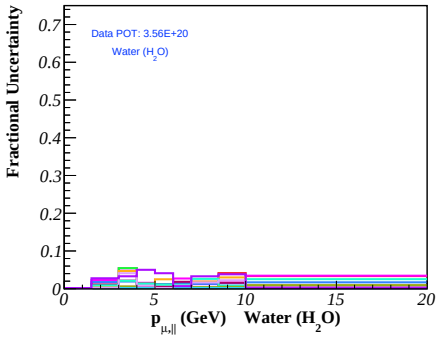
(d) Lead

(e) Scintillator

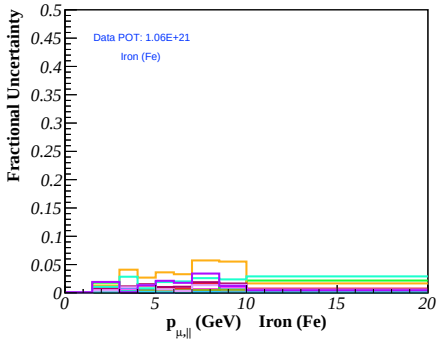
Figure E-73: p_μ FSI Errors



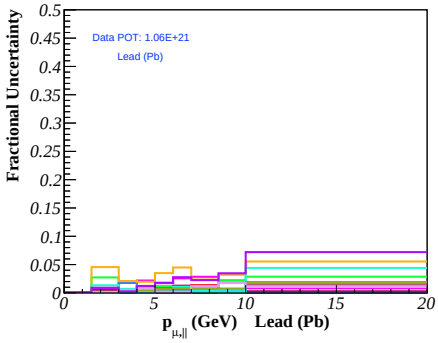
(a) Carbon



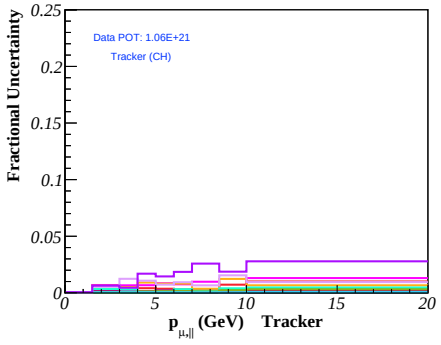
(b) Water



(c) Iron



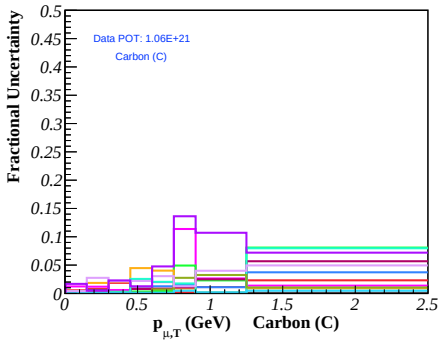
(d) Lead



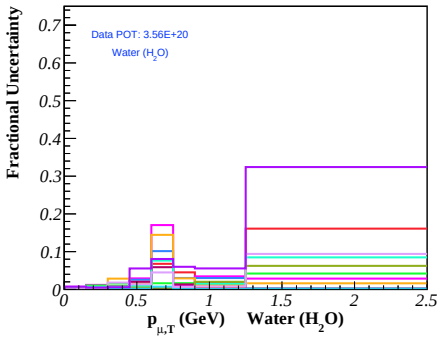
(e) Scintillator



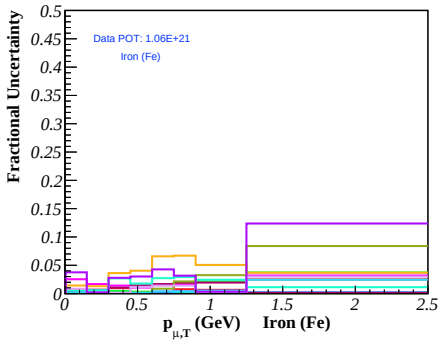
Figure E-74: $p_{\mu,||}$ FSI Errors



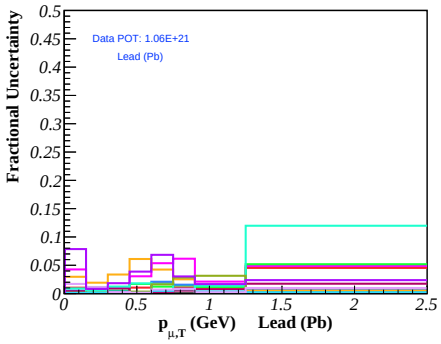
(a) Carbon



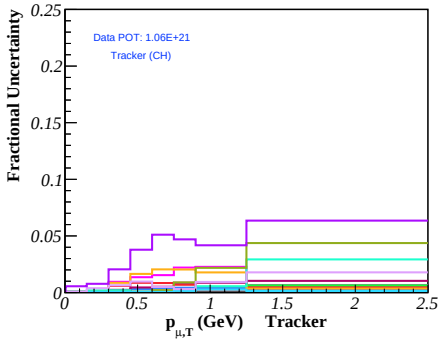
(b) Water



(c) Iron



(d) Lead



(e) Scintillator

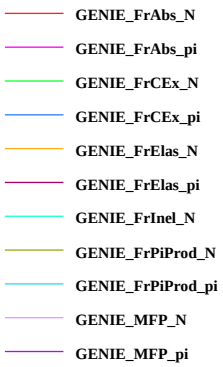
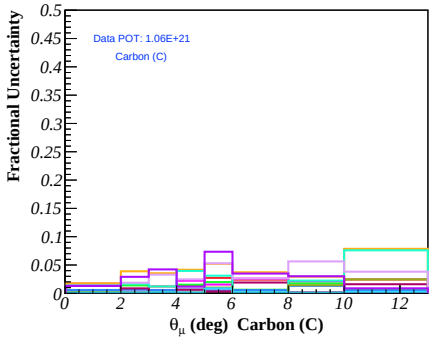
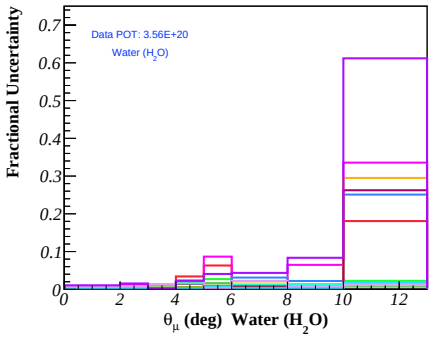


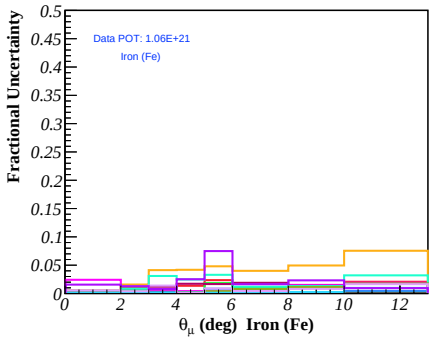
Figure E-75: $p_{\mu,T}$ FSI Errors



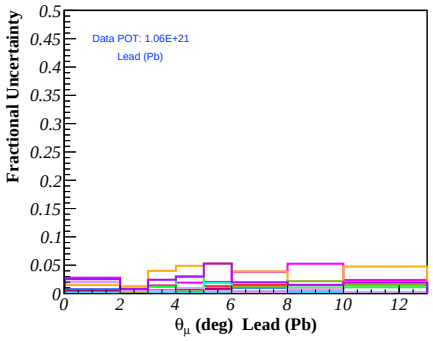
(a) Carbon



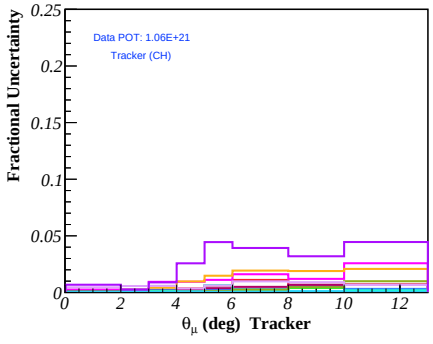
(b) Water



(c) Iron



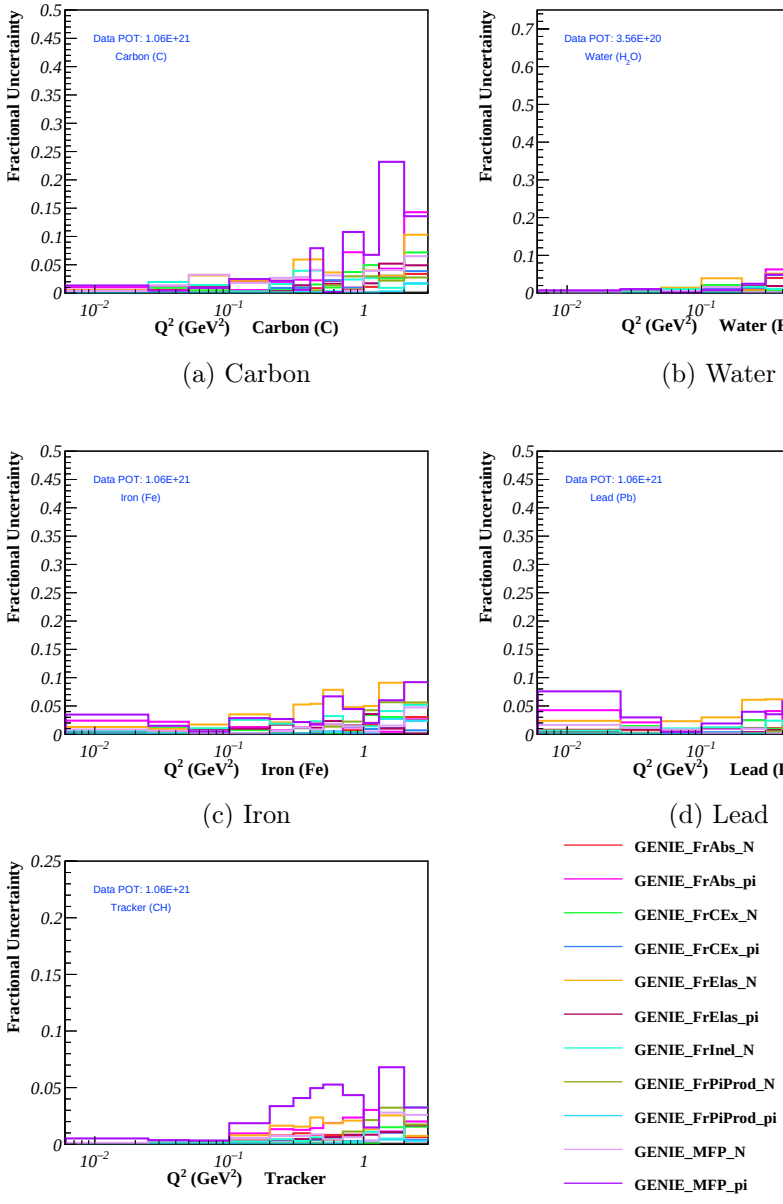
(d) Lead



(e) Scintillator



Figure E-76: θ_μ FSI Errors



(a) Carbon

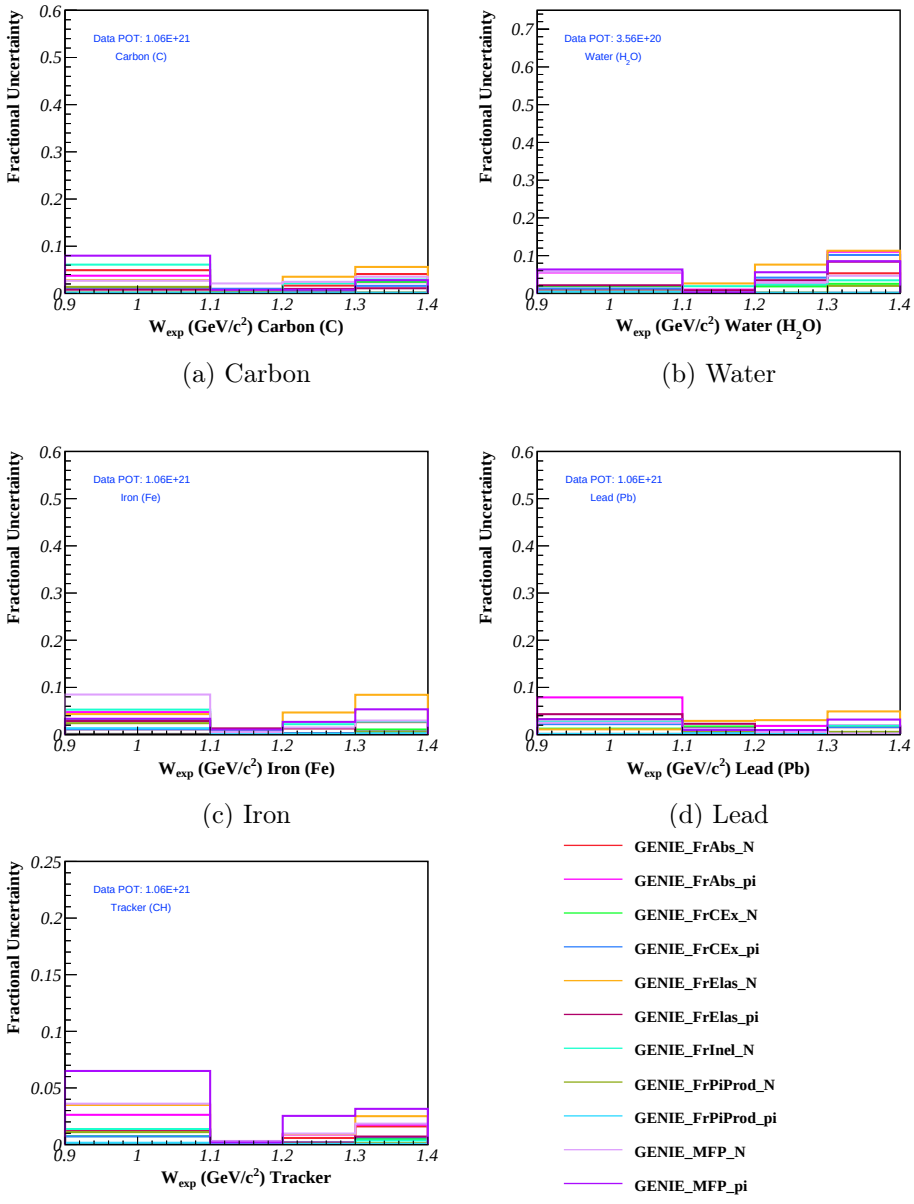
(b) Water

(c) Iron

(d) Lead

(e) Scintillator

Figure E-77: Q^2 FSI Errors



(a) Carbon

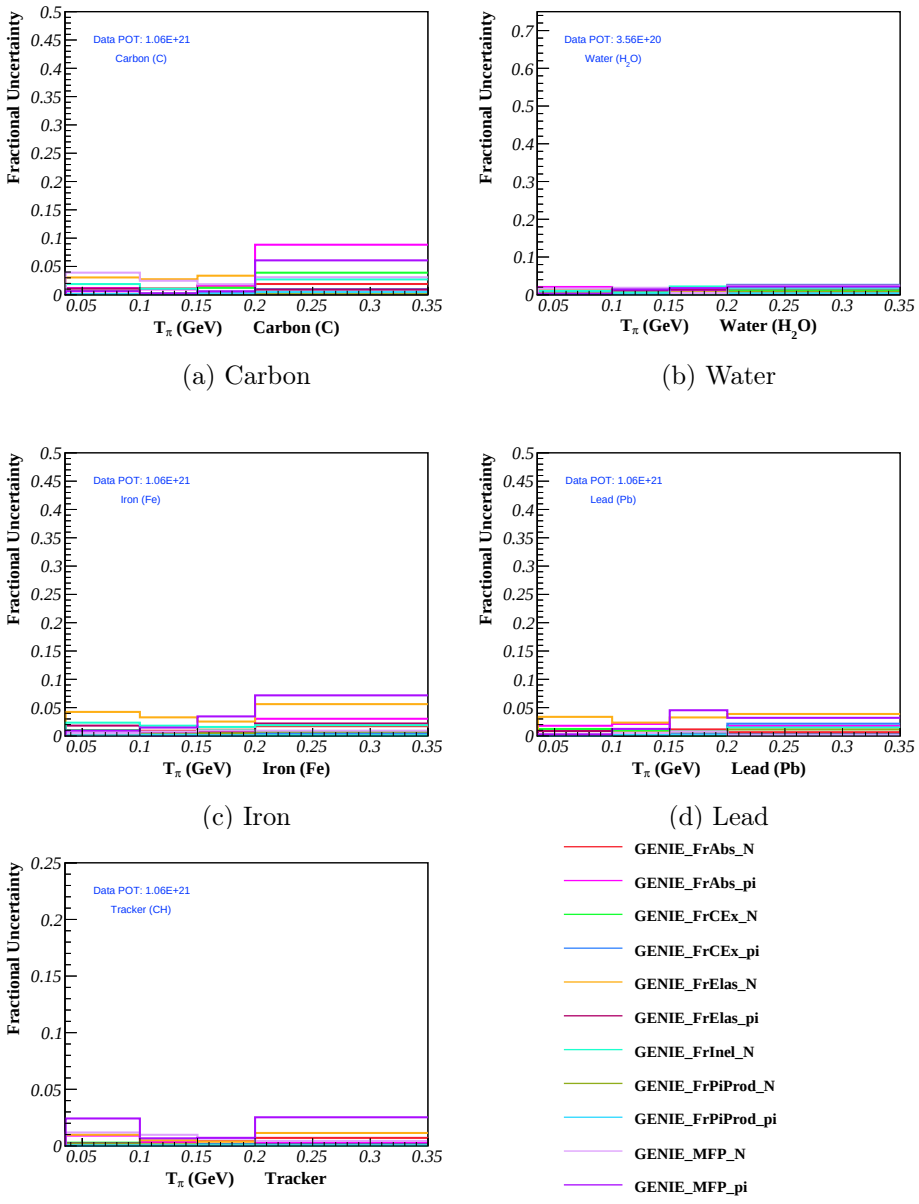
(b) Water

(c) Iron

(d) Lead

(e) Scintillator

Figure E-78: W_{exp} FSI Errors



(a) Carbon

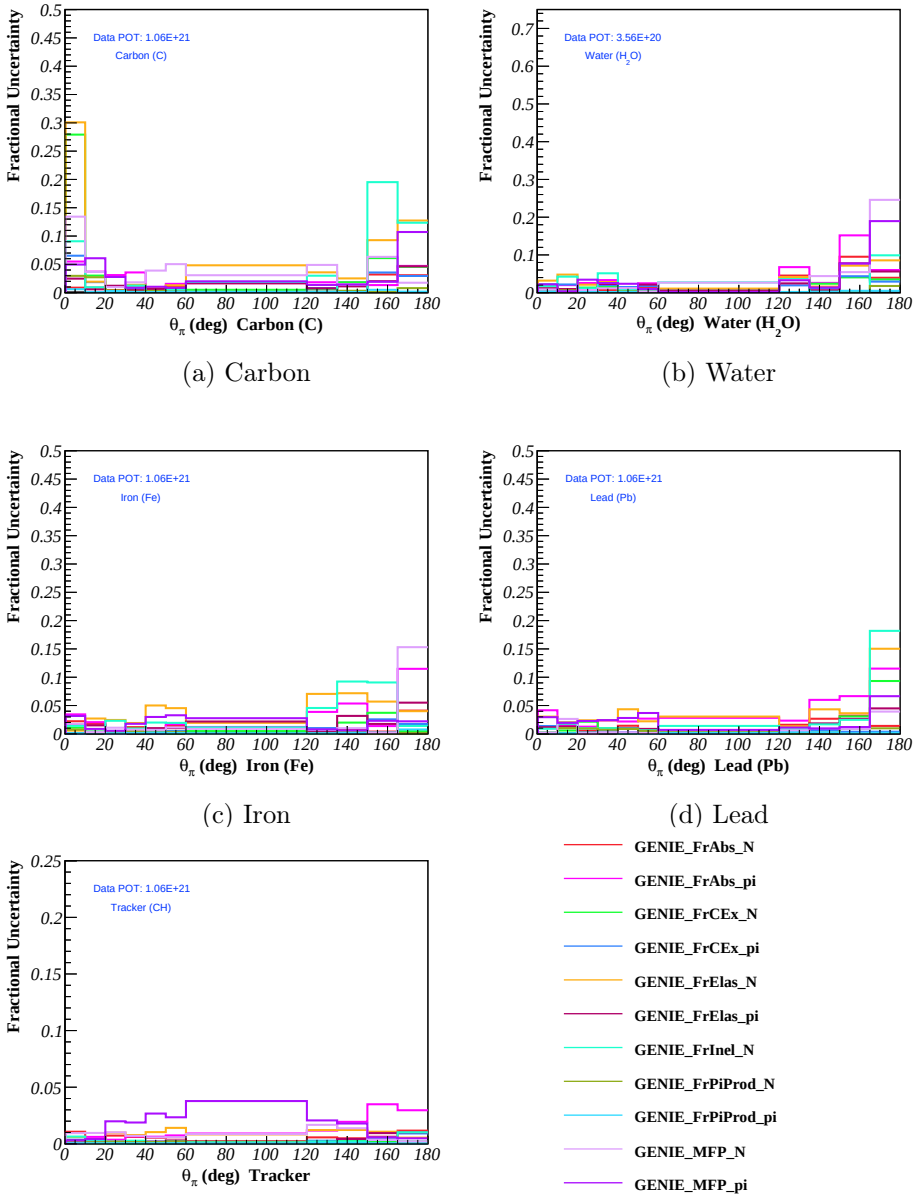
(b) Water

(c) Iron

(d) Lead

(e) Scintillator

Figure E-79: T_π FSI Errors



(a) Carbon

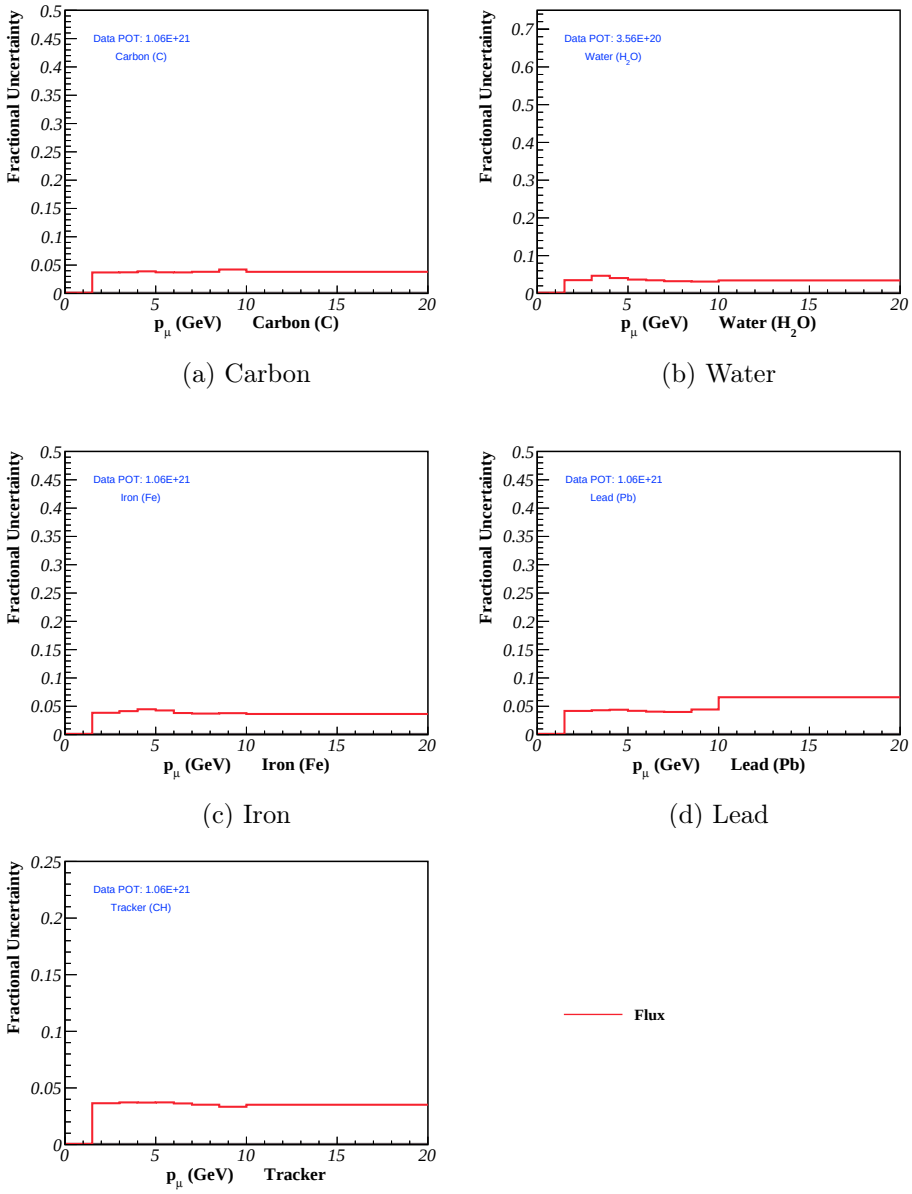
(b) Water

(c) Iron

(d) Lead

(e) Scintillator

Figure E-80: θ_π FSI Errors



(a) Carbon

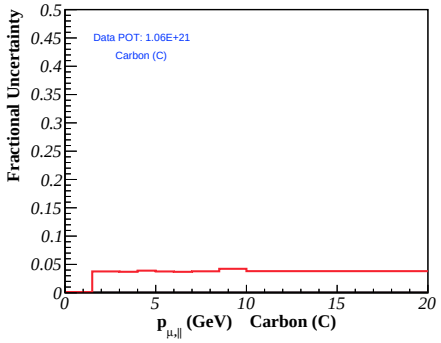
(b) Water

(c) Iron

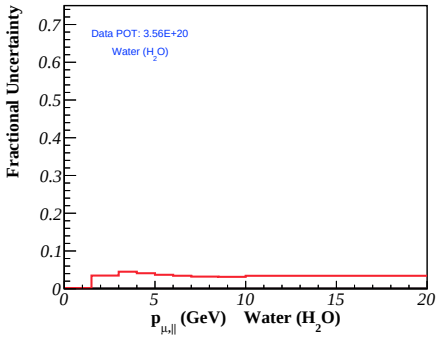
(d) Lead

(e) Scintillator

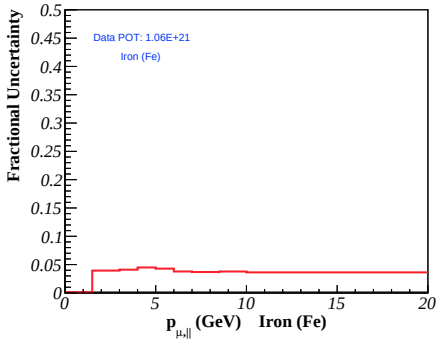
Figure E-81: p_μ Flux Error



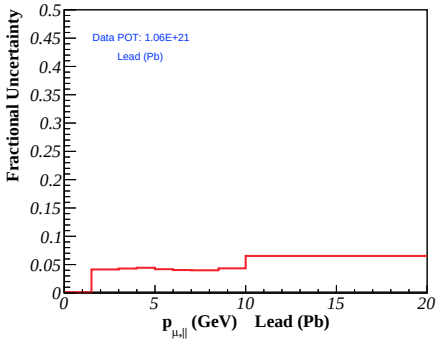
(a) Carbon



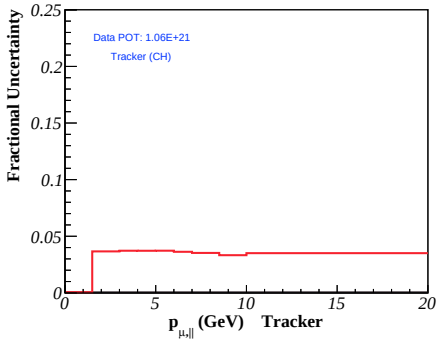
(b) Water



(c) Iron

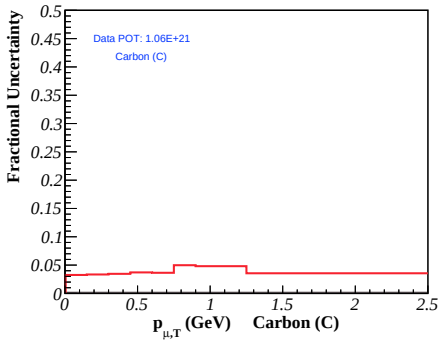


(d) Lead

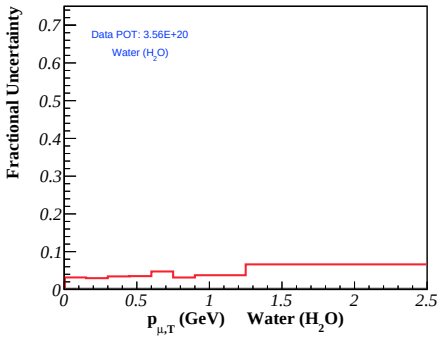


(e) Scintillator

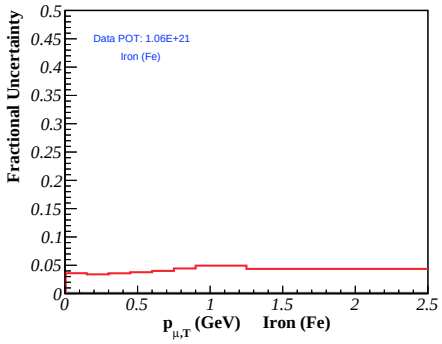
Figure E-82: $p_{\mu,||}$ Flux Error



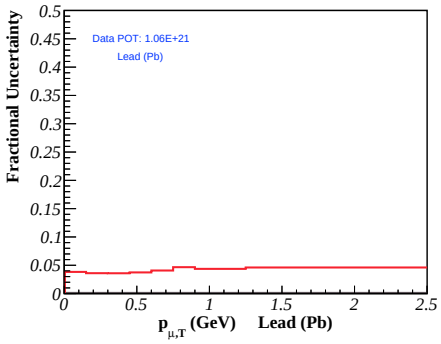
(a) Carbon



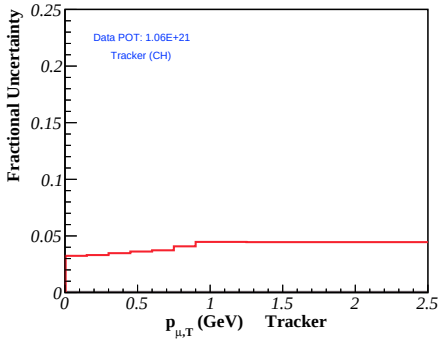
(b) Water



(c) Iron

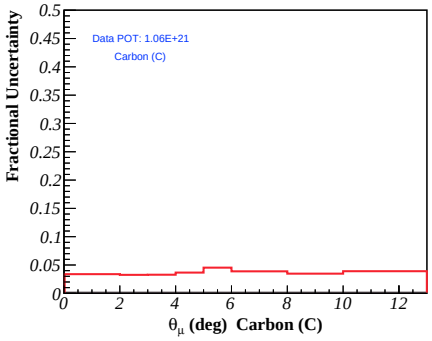


(d) Lead

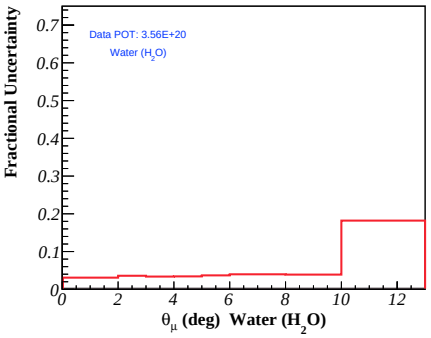


(e) Scintillator

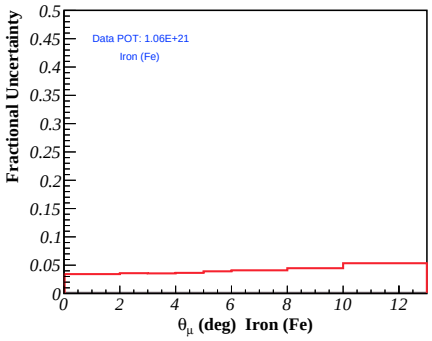
Figure E-83: $p_{\mu,T}$ Flux Error



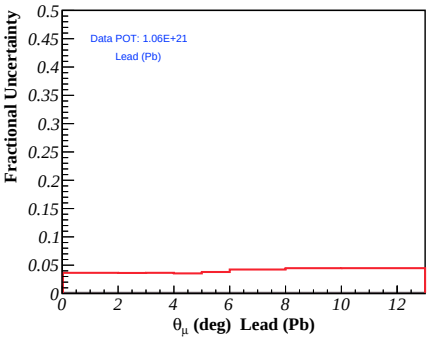
(a) Carbon



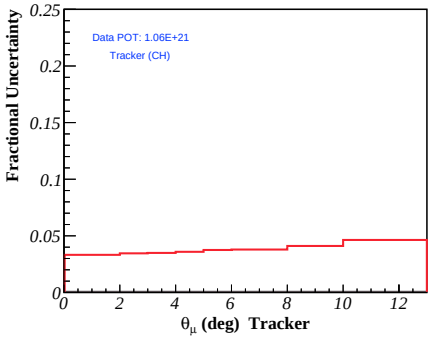
(b) Water



(c) Iron

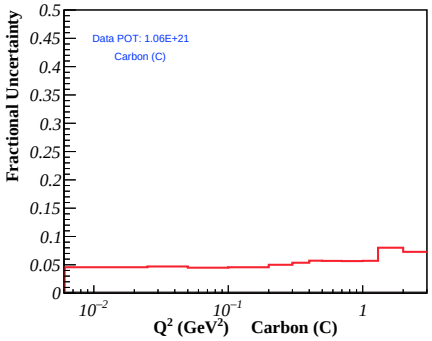


(d) Lead

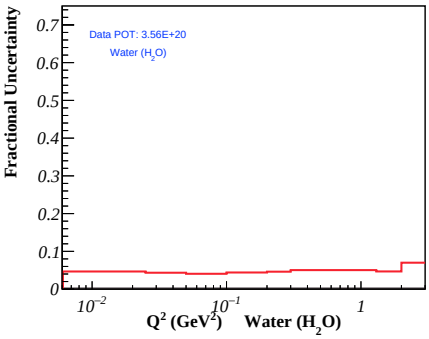


(e) Scintillator

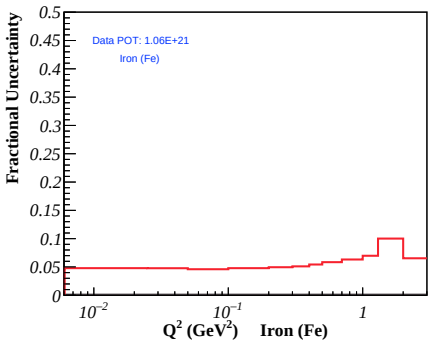
Figure E-84: θ_μ Flux Error



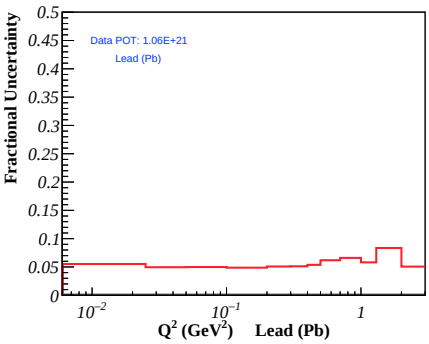
(a) Carbon



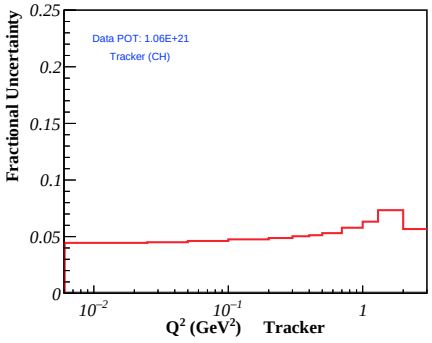
(b) Water



(c) Iron

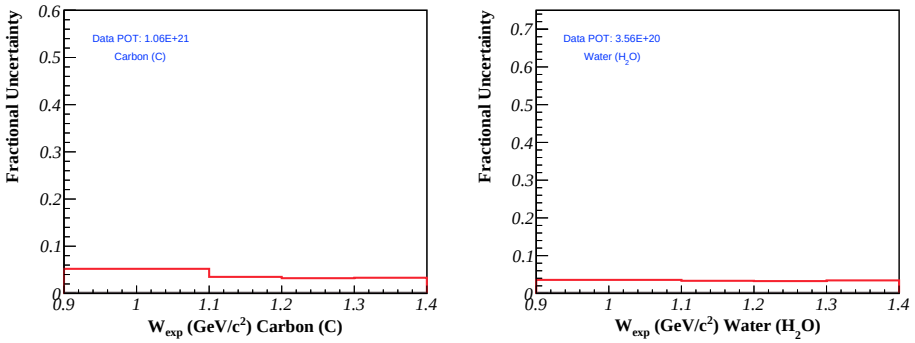


(d) Lead



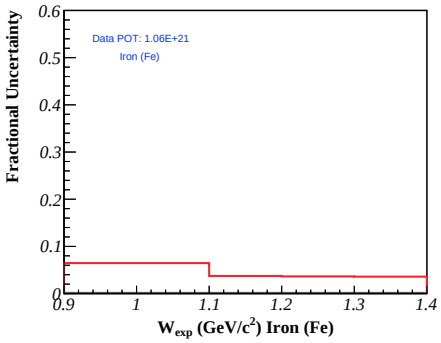
(e) Scintillator

Figure E-85: Q^2 Flux Error

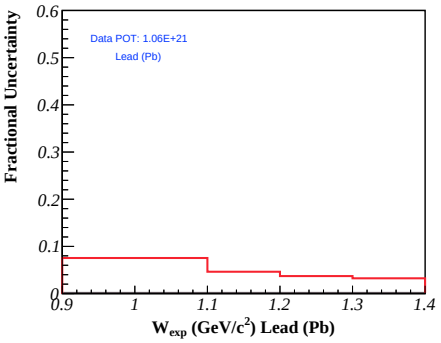


(a) Carbon

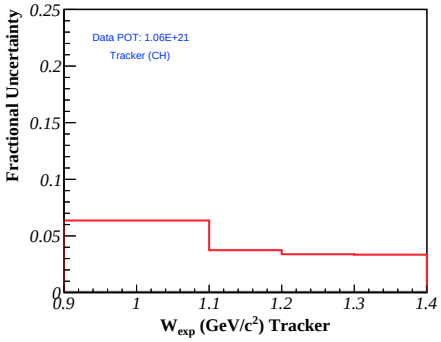
(b) Water



(c) Iron

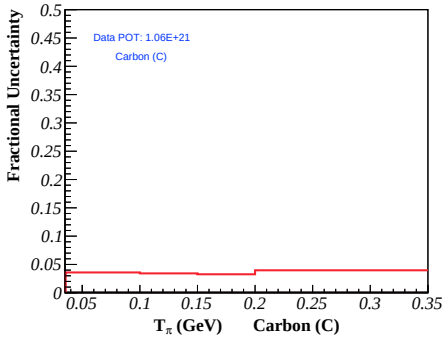


(d) Lead

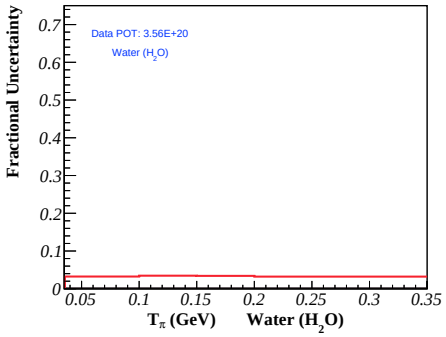


(e) Scintillator

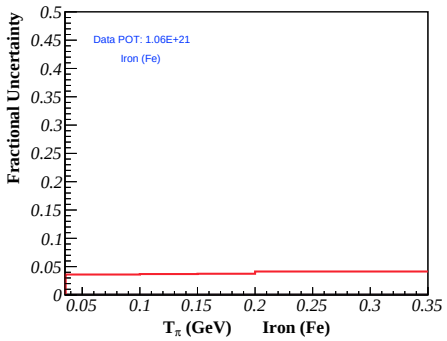
Figure E-86: W_{exp} Flux Error



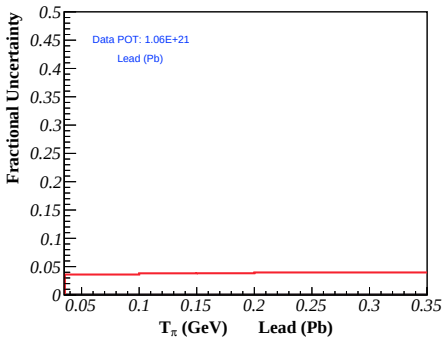
(a) Carbon



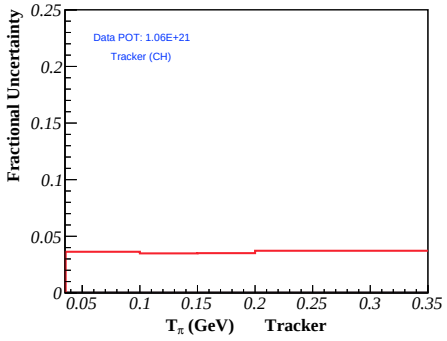
(b) Water



(c) Iron

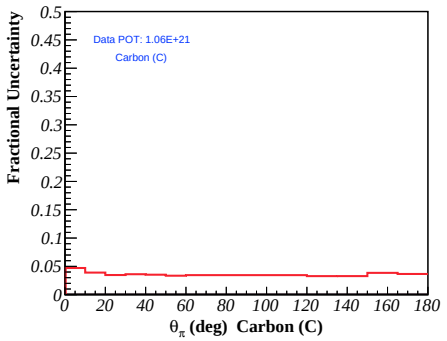


(d) Lead

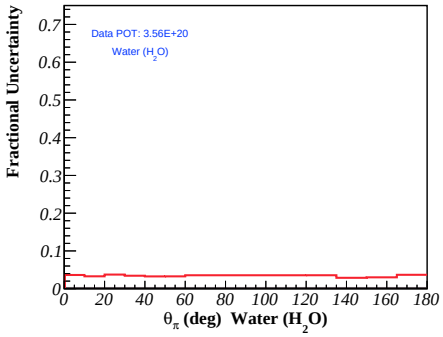


(e) Scintillator

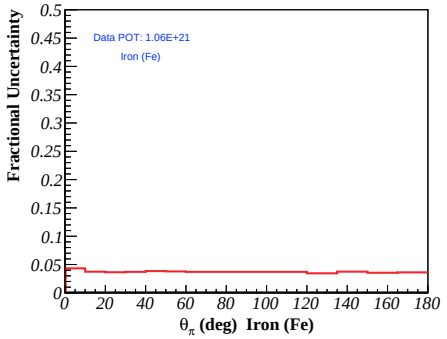
Figure E-87: T_π Flux Error



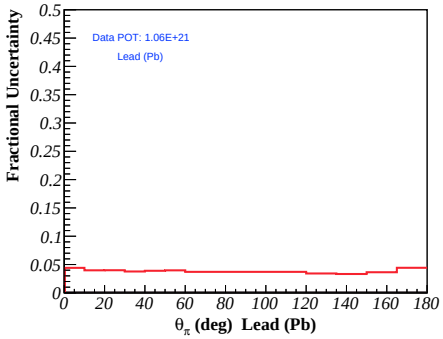
(a) Carbon



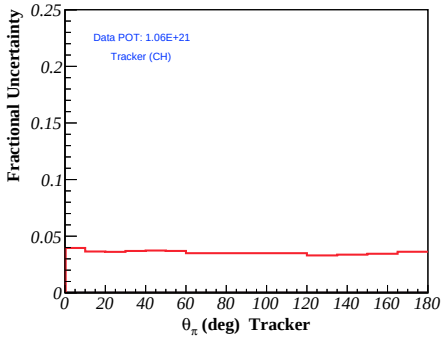
(b) Water



(c) Iron

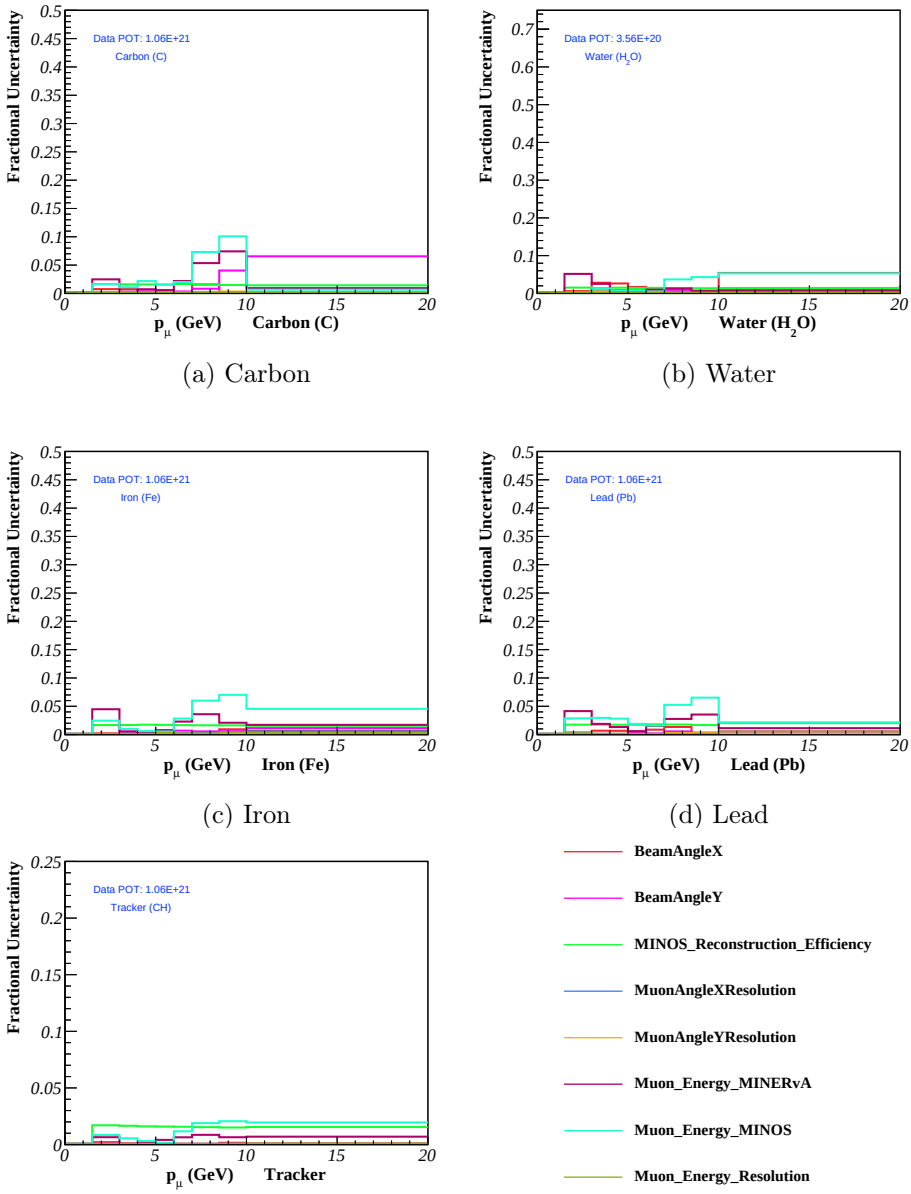


(d) Lead



(e) Scintillator

Figure E-88: θ_π Flux Error



(a) Carbon

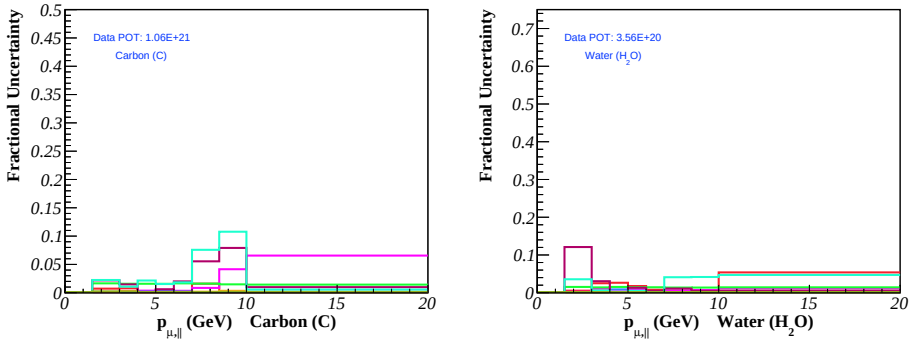
(b) Water

(c) Iron

(d) Lead

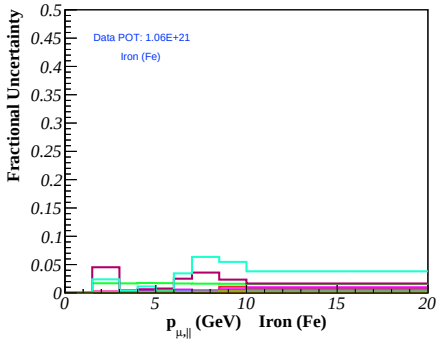
(e) Scintillator

Figure E-89: p_μ Muon Reconstruction Errors

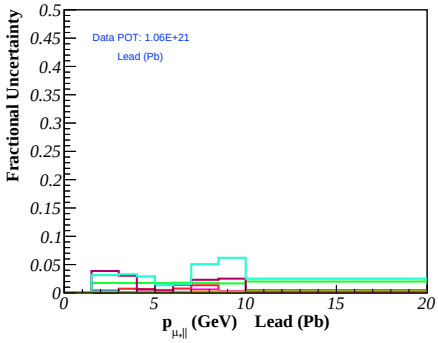


(a) Carbon

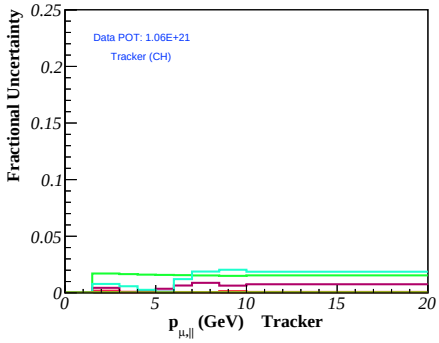
(b) Water



(c) Iron



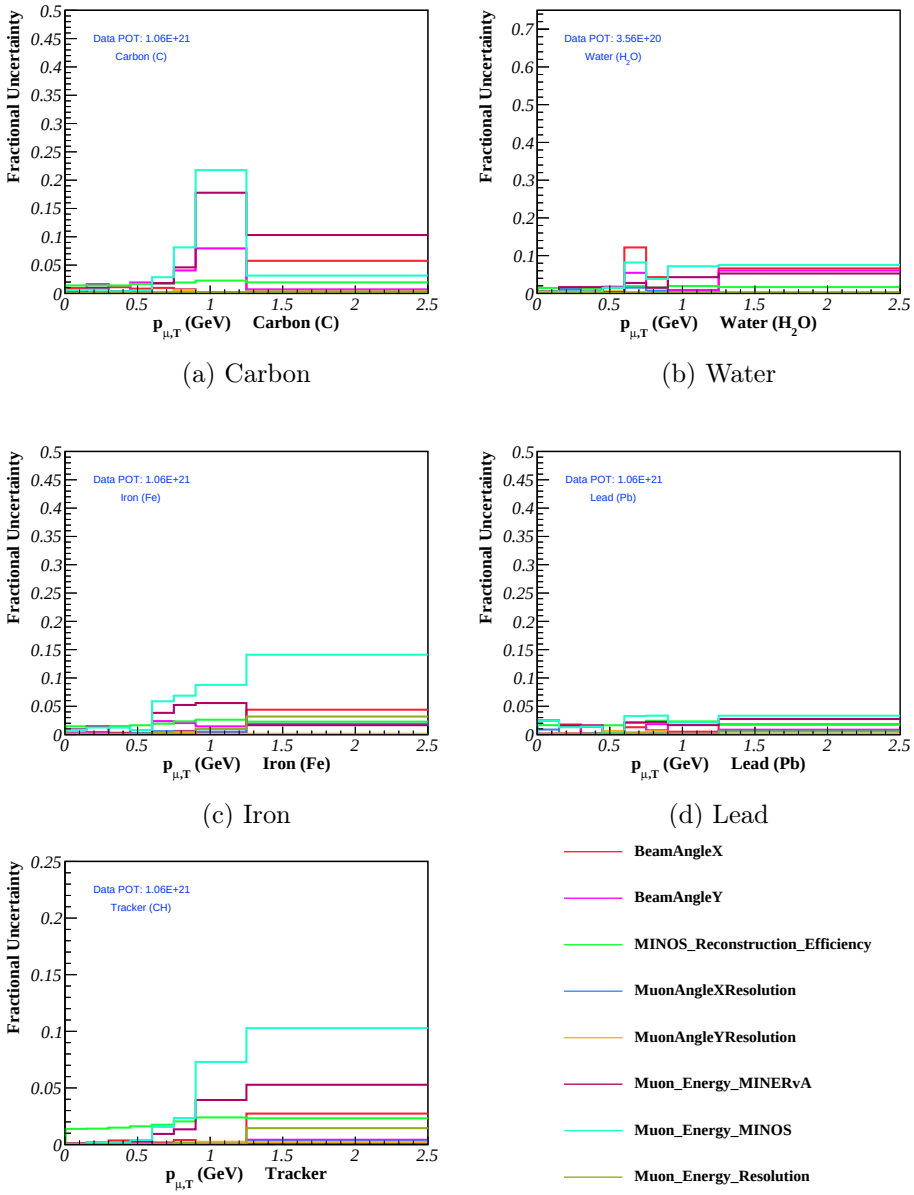
(d) Lead





(e) Scintillator

Figure E-90: $p_{\mu,||}$ Muon Reconstruction Errors



(a) Carbon

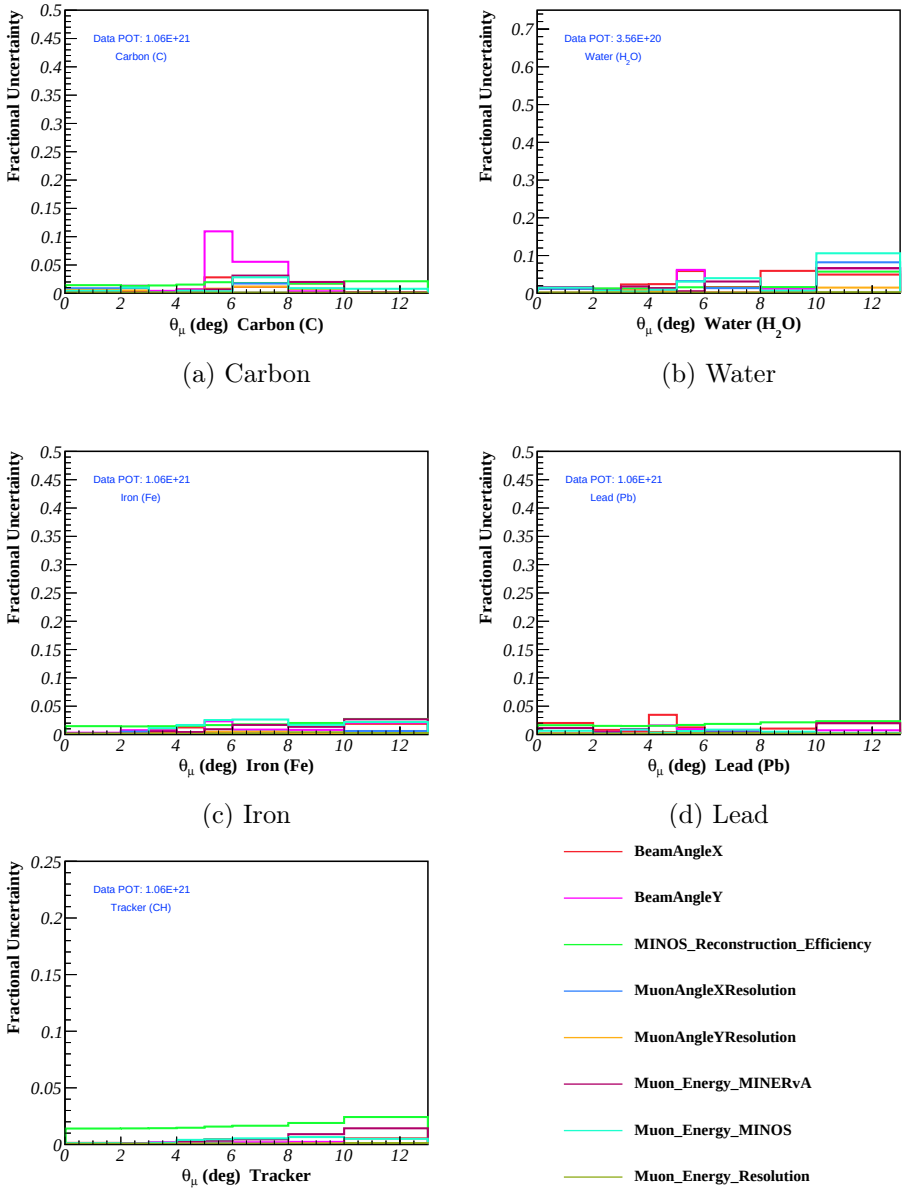
(b) Water

(c) Iron

(d) Lead

(e) Scintillator

Figure E-91: $p_{\mu,T}$ Muon Reconstruction Errors



(a) Carbon

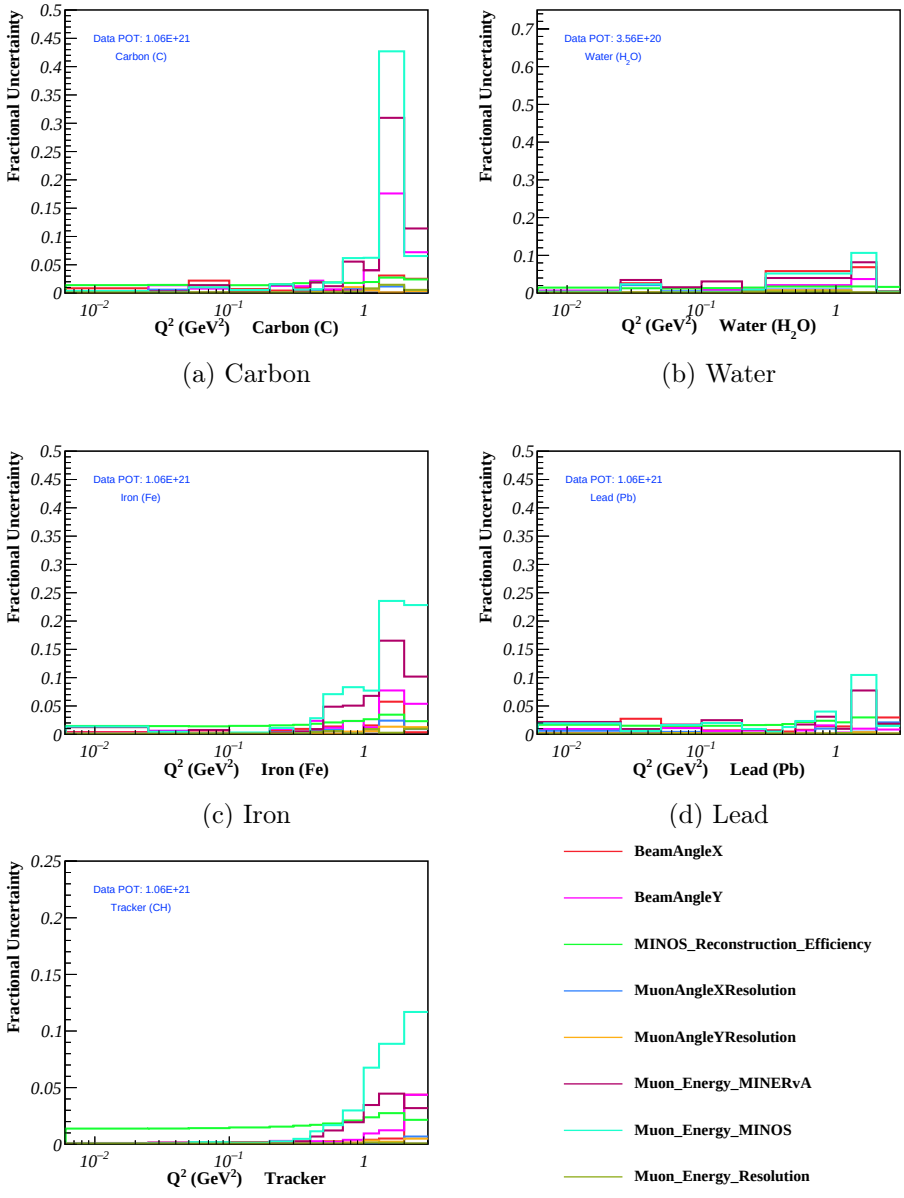
(b) Water

(c) Iron

(d) Lead

(e) Scintillator

Figure E-92: θ_μ Muon Reconstruction Errors



(a) Carbon

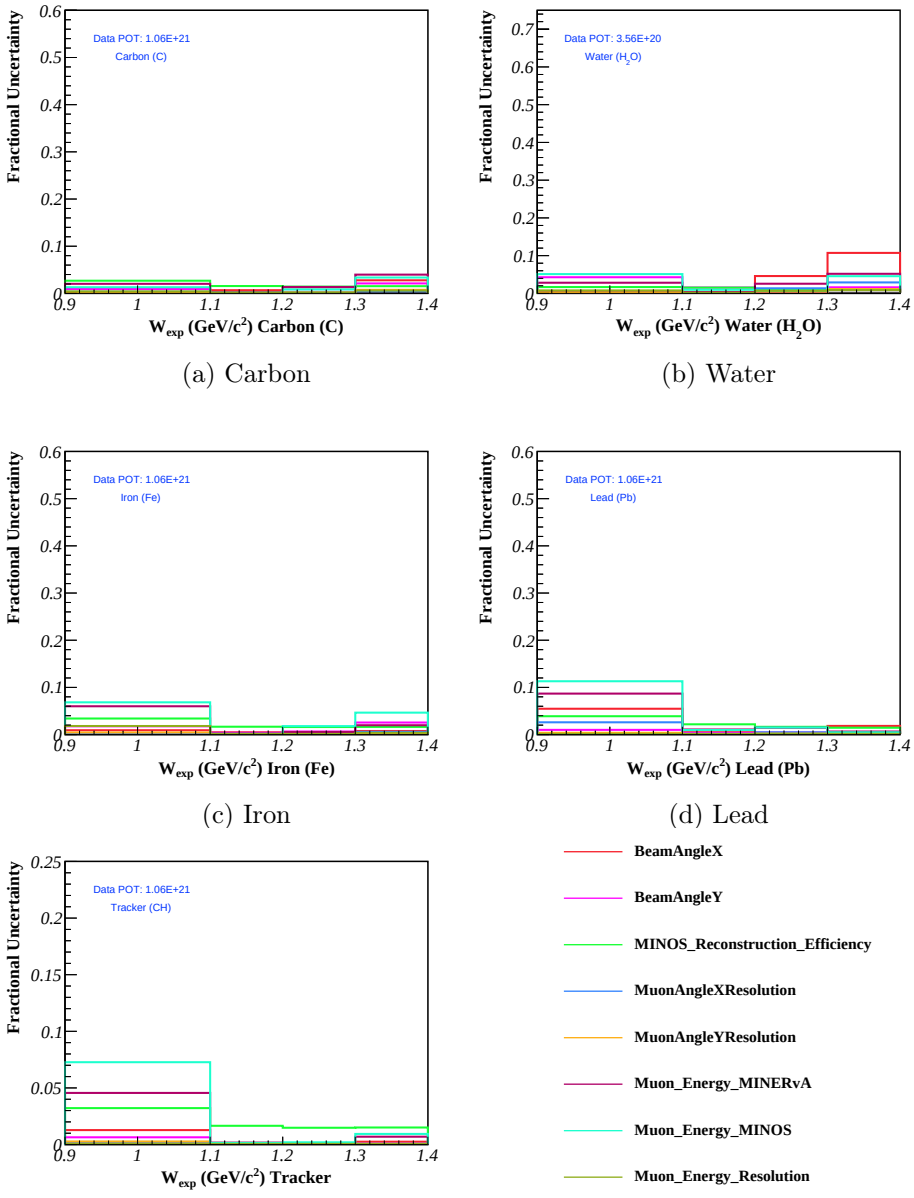
(b) Water

(c) Iron

(d) Lead

(e) Scintillator

Figure E-93: Q^2 Muon Reconstruction Errors



(a) Carbon

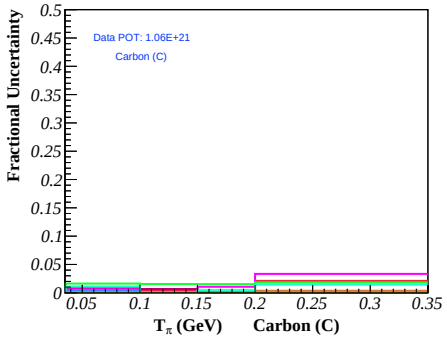
(b) Water

(c) Iron

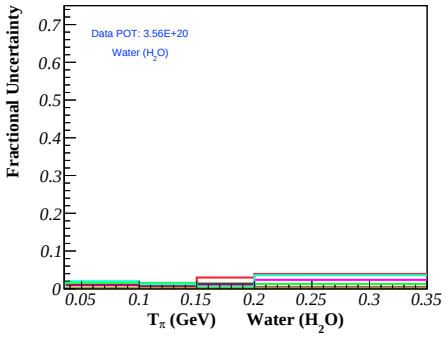
(d) Lead

(e) Scintillator

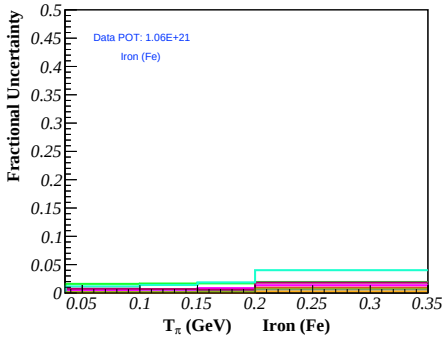
Figure E-94: W_{exp} Muon Reconstruction Errors



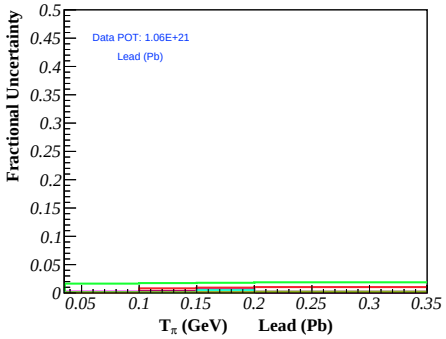
(a) Carbon



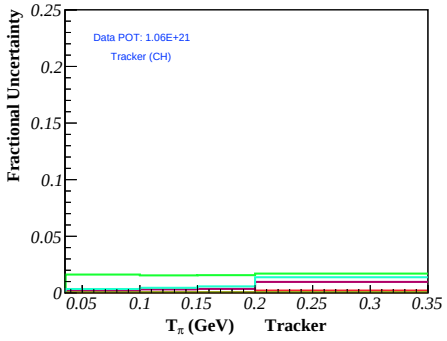
(b) Water



(c) Iron



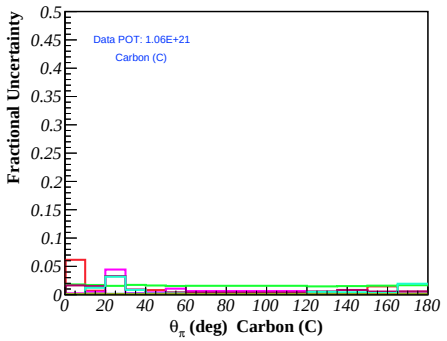
(d) Lead



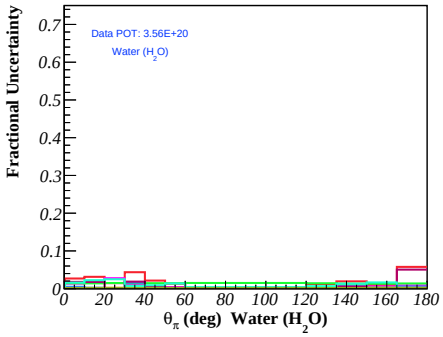


(e) Scintillator

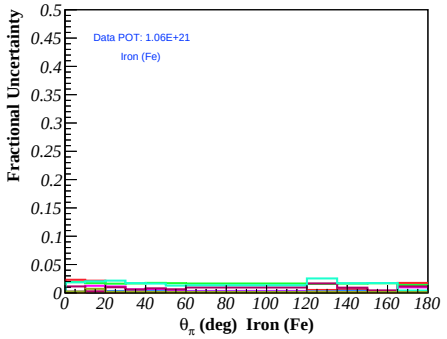
Figure E-95: T_π Muon Reconstruction Errors



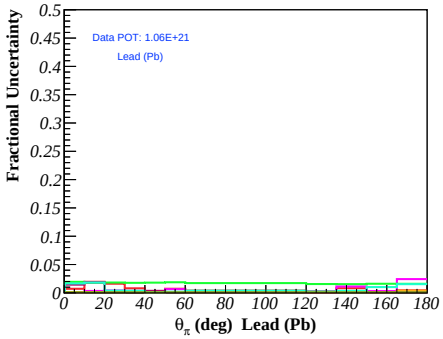
(a) Carbon



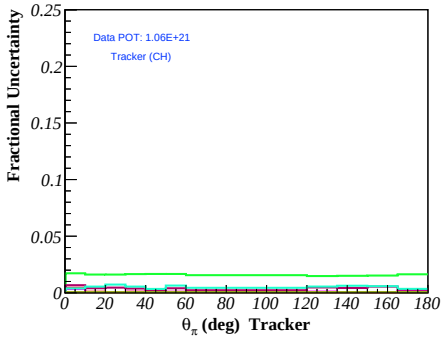
(b) Water

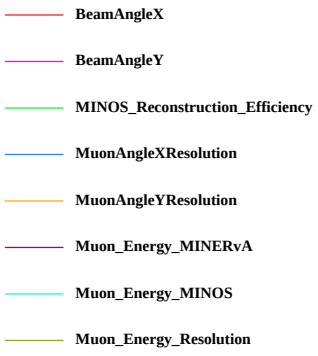


(c) Iron



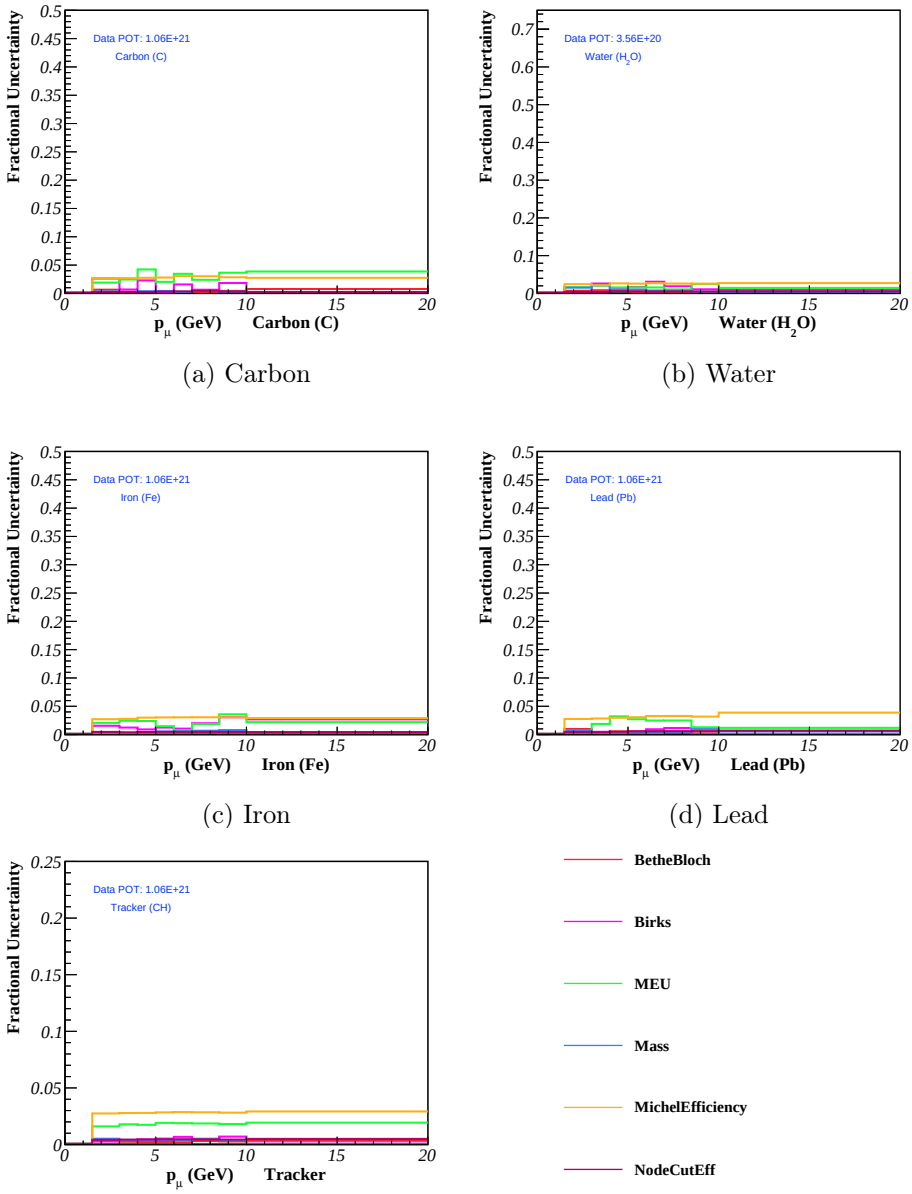
(d) Lead





(e) Scintillator

Figure E-96: θ_π Muon Reconstruction Errors



(a) Carbon

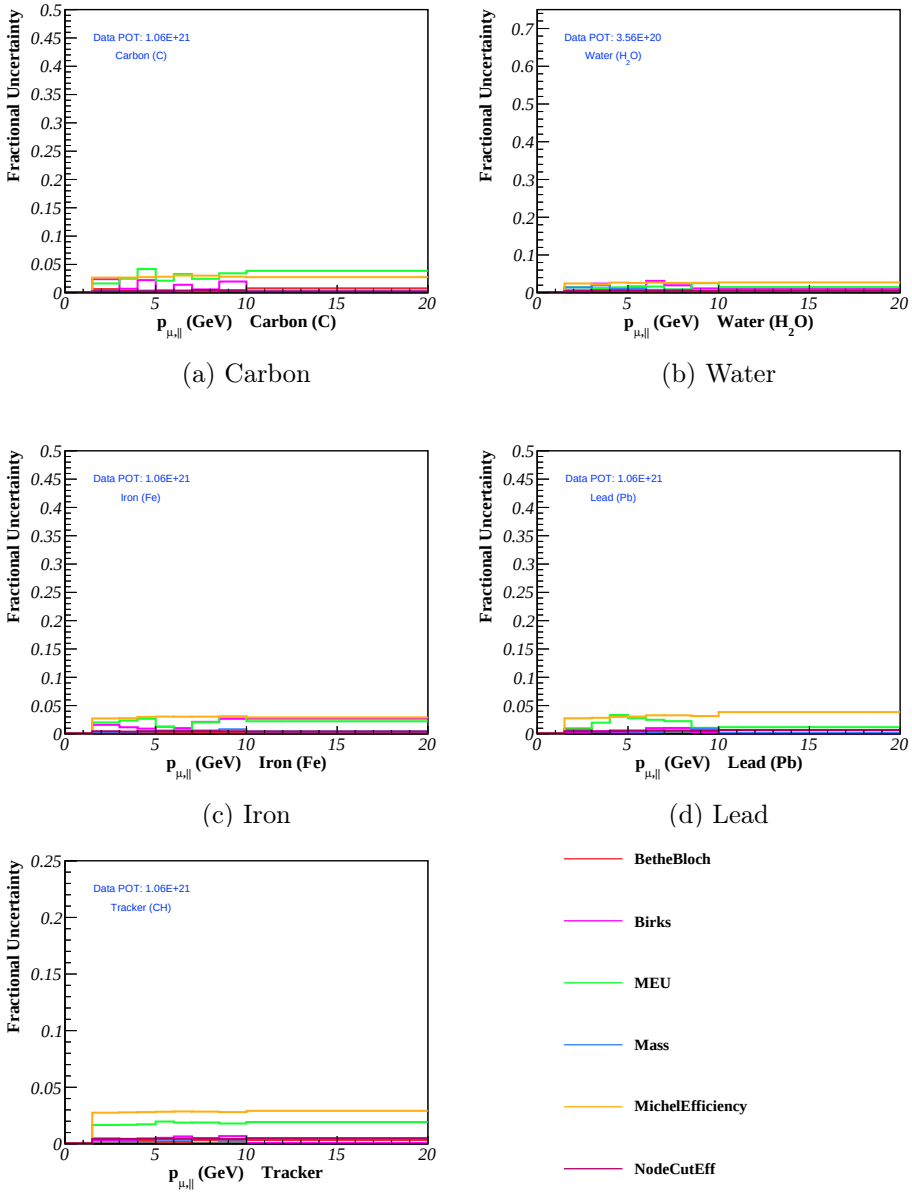
(b) Water

(c) Iron

(d) Lead

(e) Scintillator

Figure E-97: p_μ Pion Reconstruction Errors



(a) Carbon

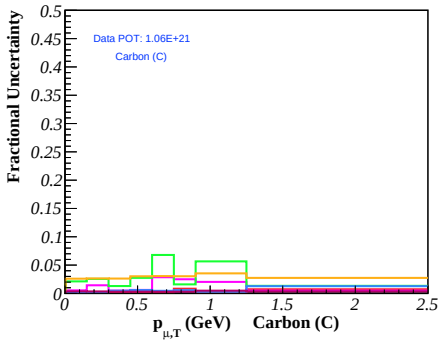
(b) Water

(c) Iron

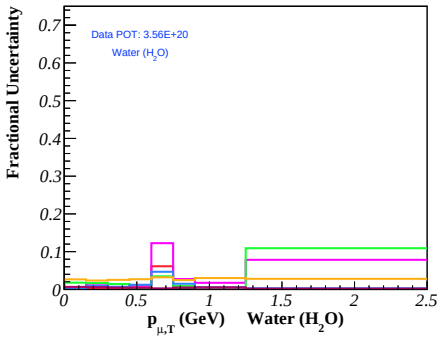
(d) Lead

(e) Scintillator

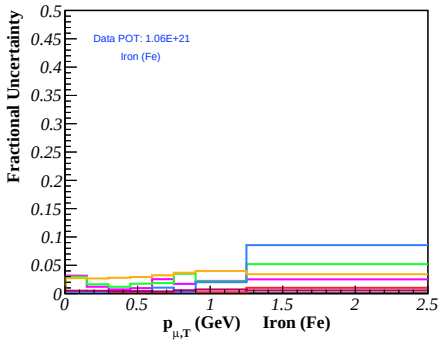
Figure E-98: $p_{\mu,||}$ Pion Reconstruction Errors



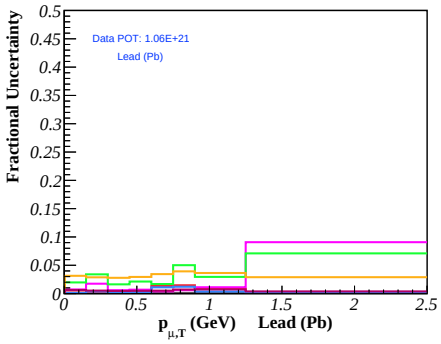
(a) Carbon



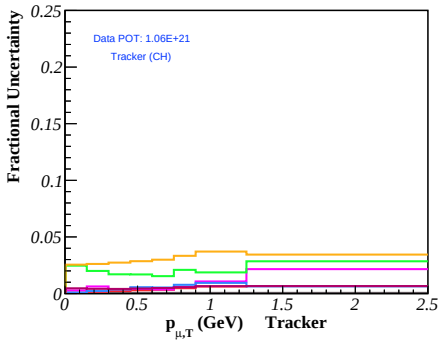
(b) Water

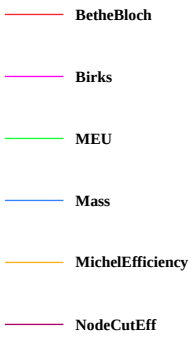


(c) Iron



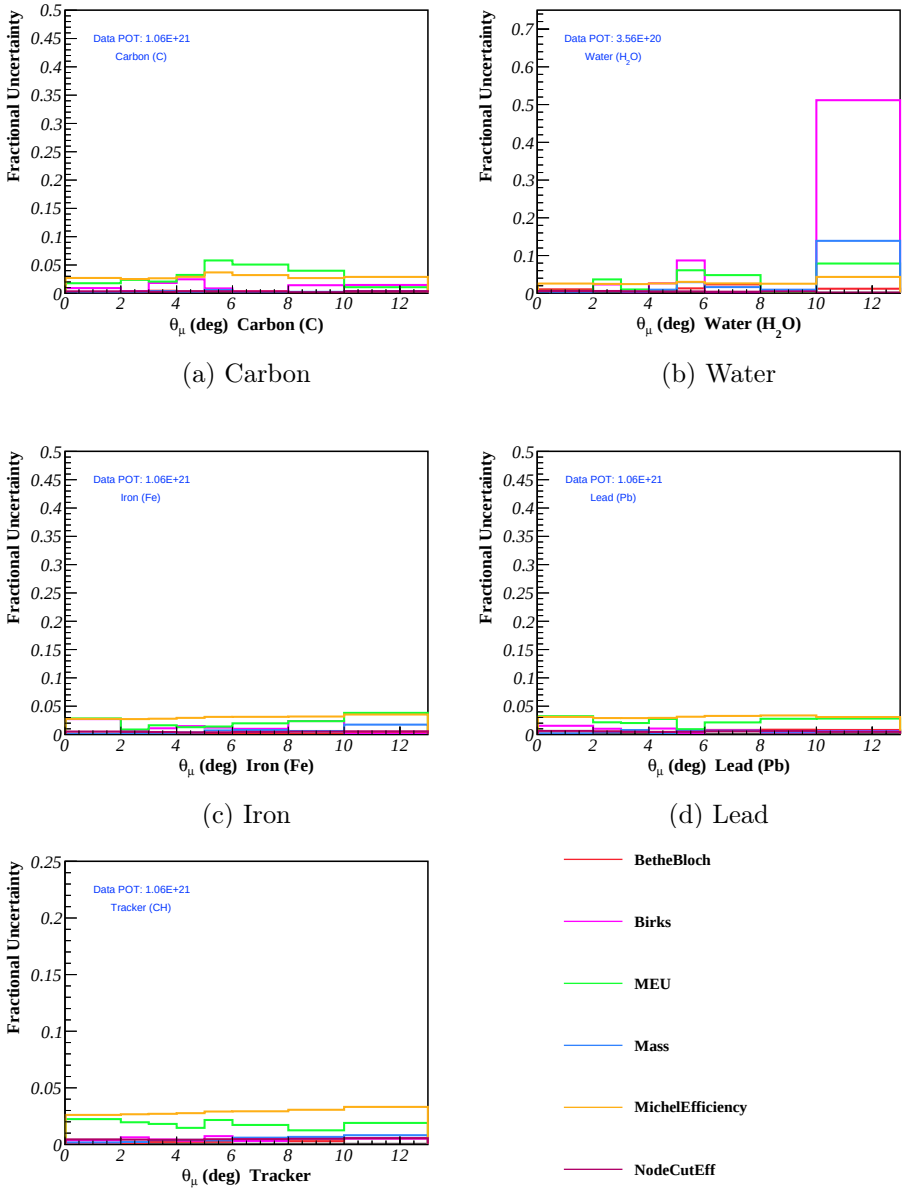
(d) Lead





(e) Scintillator

Figure E-99: $p_{\mu,T}$ Pion Reconstruction Errors



(a) Carbon

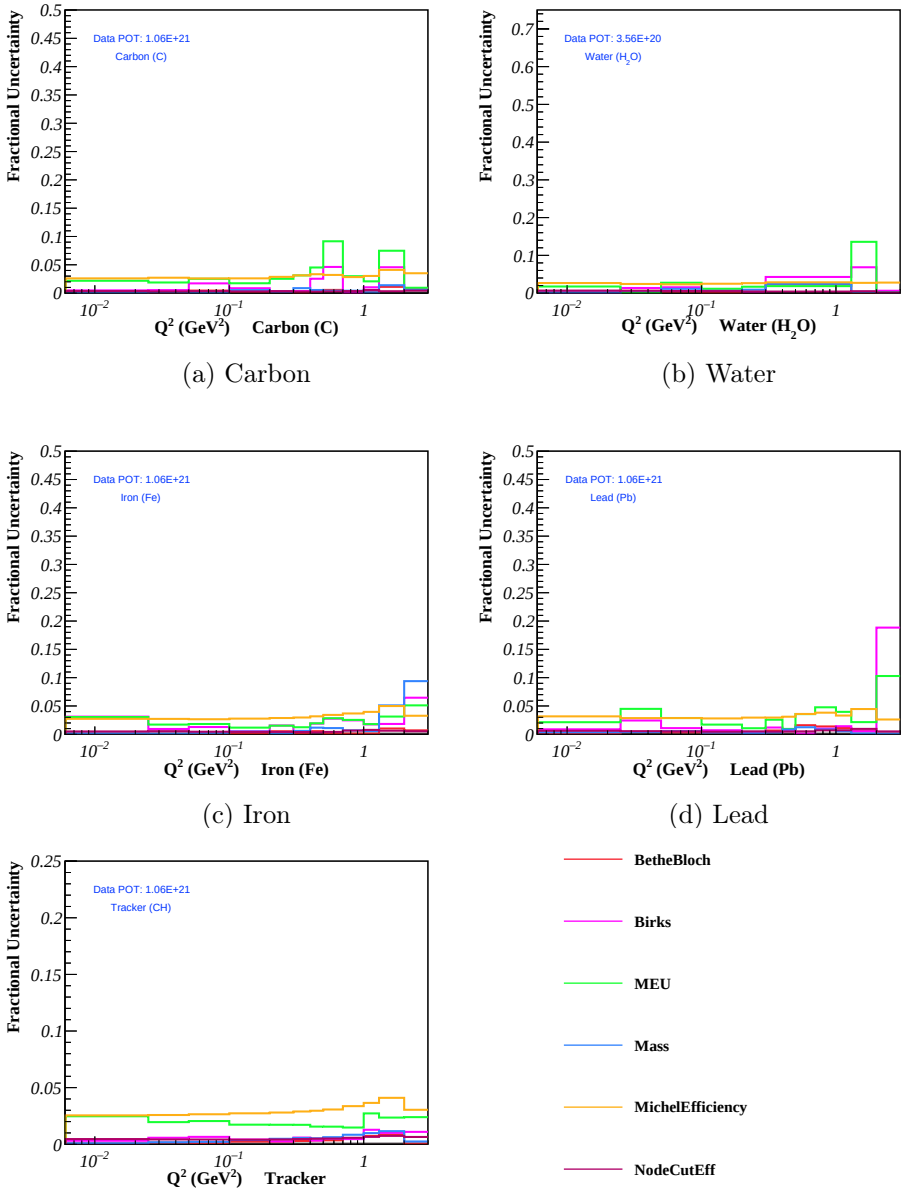
(b) Water

(c) Iron

(d) Lead

(e) Scintillator

Figure E-100: θ_μ Pion Reconstruction Errors



(a) Carbon

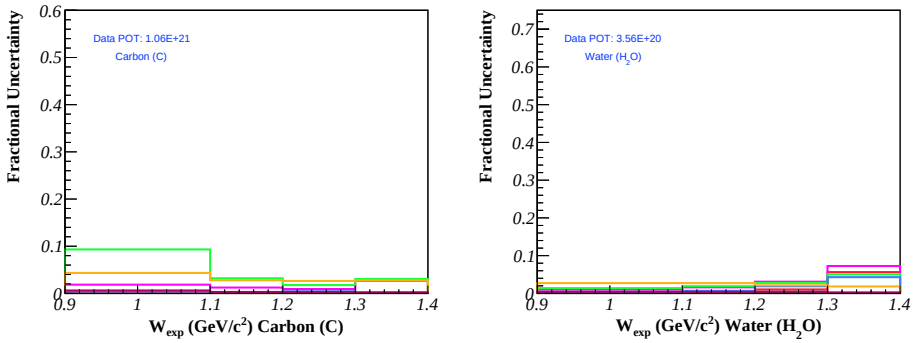
(b) Water

(c) Iron

(d) Lead

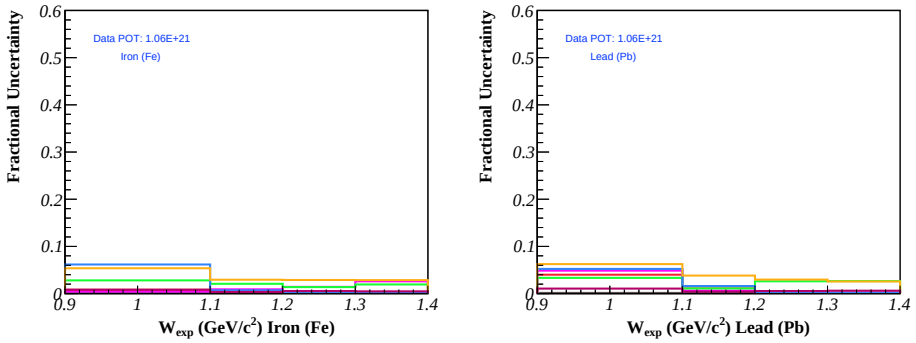
(e) Scintillator

Figure E-101: Q^2 Pion Reconstruction Errors



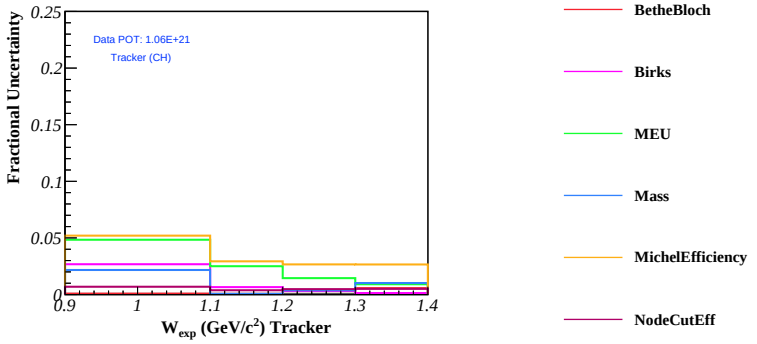
(a) Carbon

(b) Water



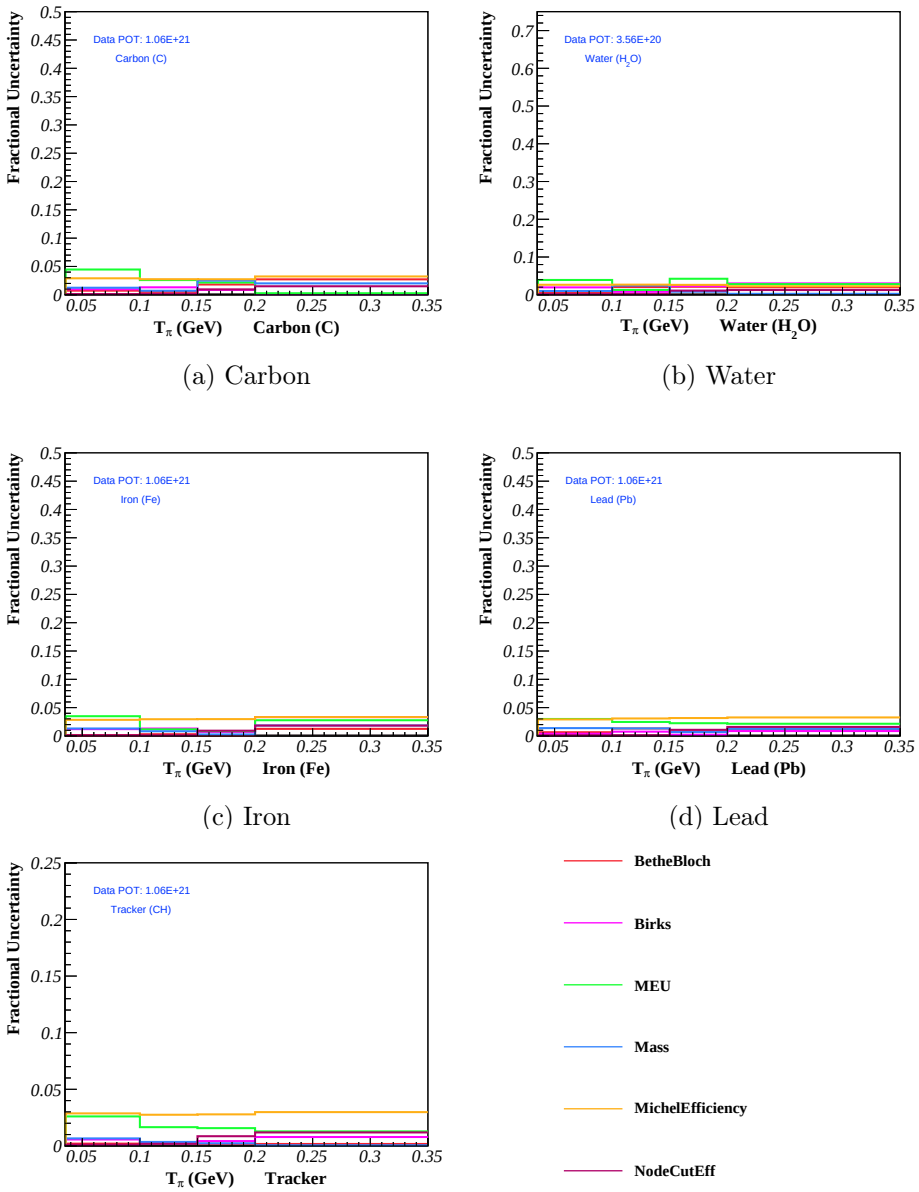
(c) Iron

(d) Lead



(e) Scintillator

Figure E-102: W_{exp} Pion Reconstruction Errors



(a) Carbon

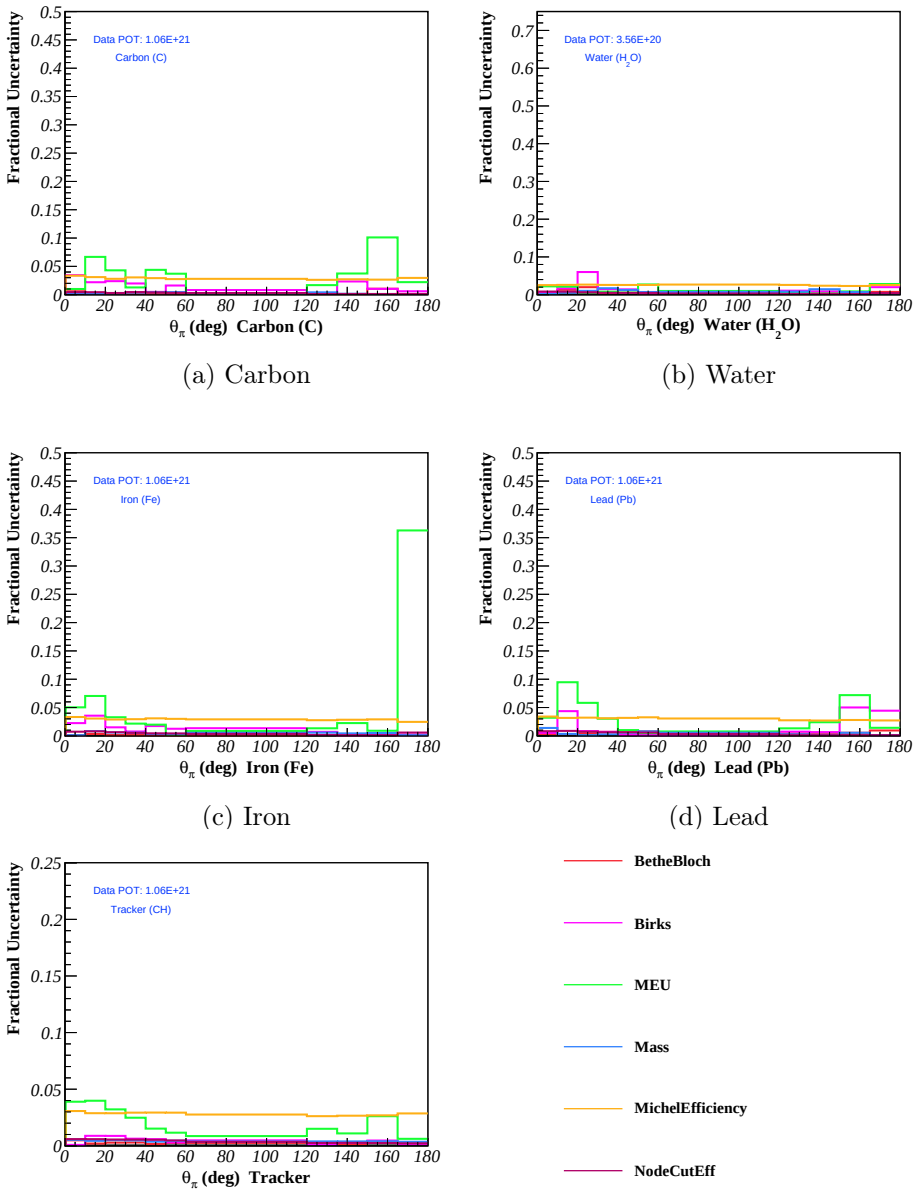
(b) Water

(c) Iron

(d) Lead

(e) Scintillator

Figure E-103: T_π Pion Reconstruction Errors



(a) Carbon

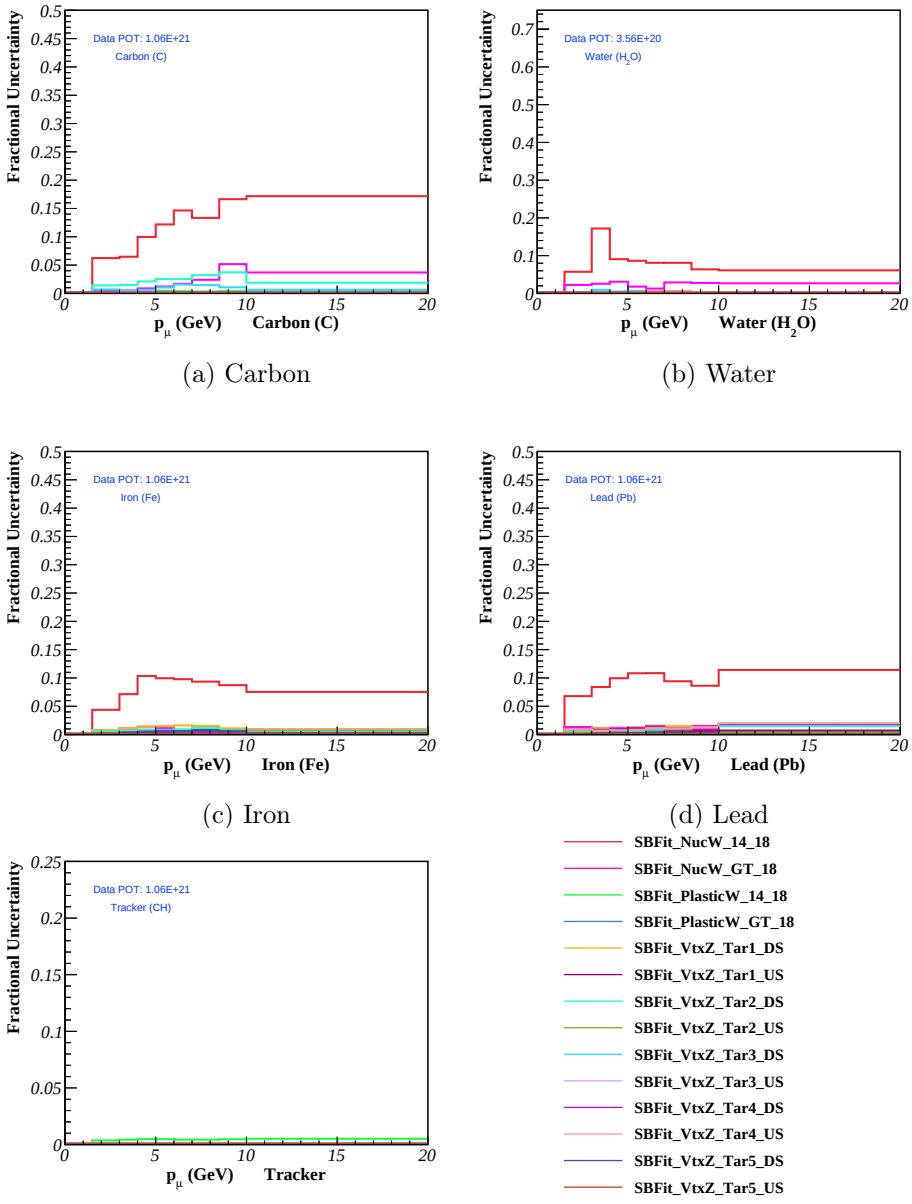
(b) Water

(c) Iron

(d) Lead

(e) Scintillator

Figure E-104: θ_π Pion Reconstruction Errors



(a) Carbon

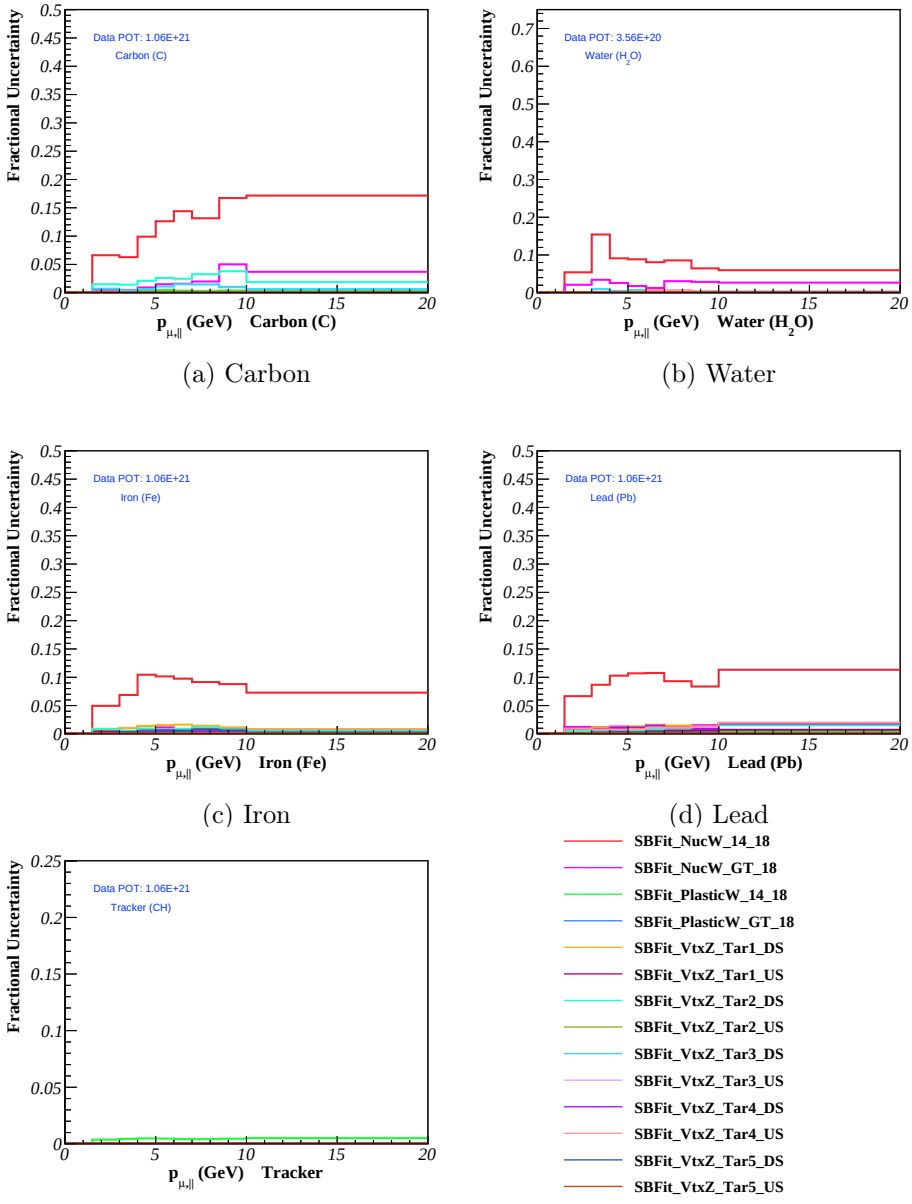
(b) Water

(c) Iron

(d) Lead

(e) Scintillator

Figure E-105: p_μ Sideband Fit Errors



(a) Carbon

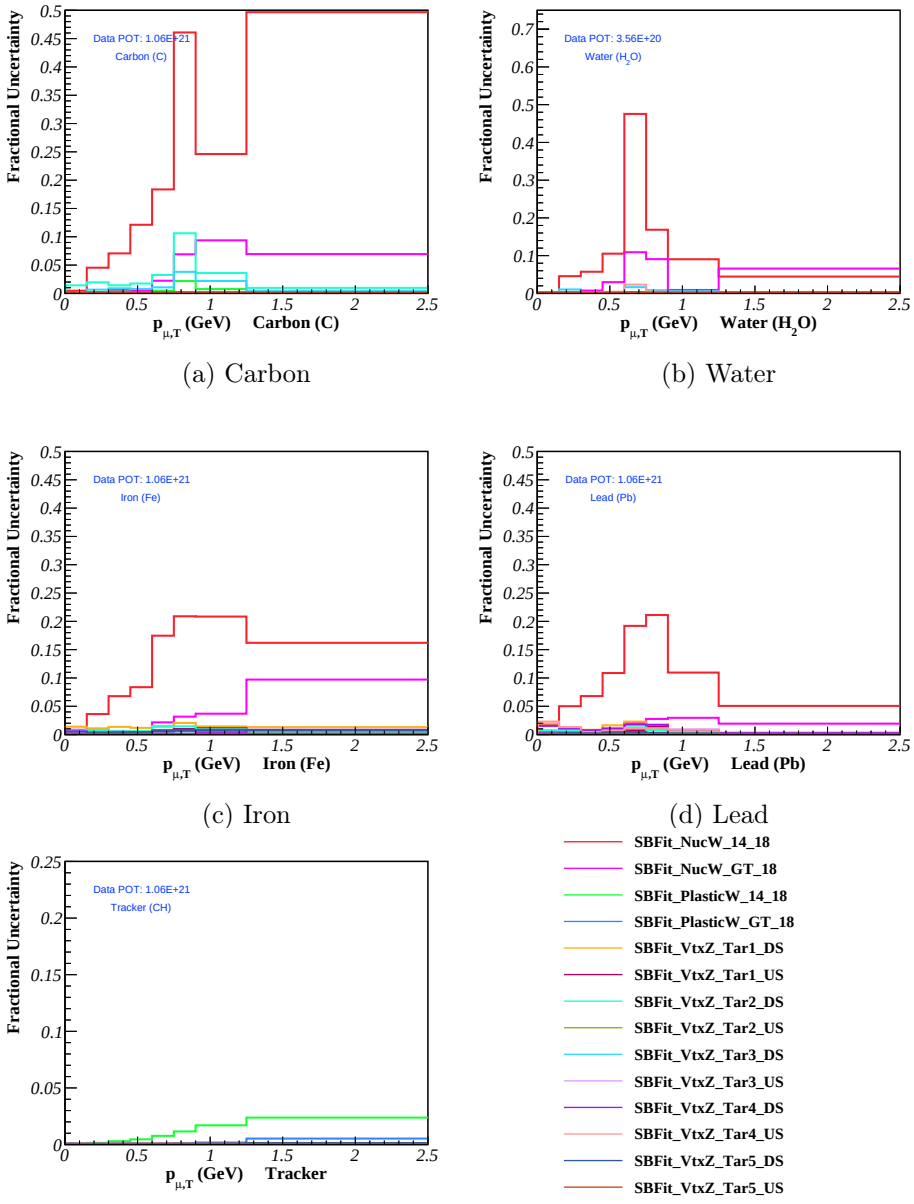
(b) Water

(c) Iron

(d) Lead

(e) Scintillator

Figure E-106: $p_{\mu,||}$ Sideband Fit Errors



(a) Carbon

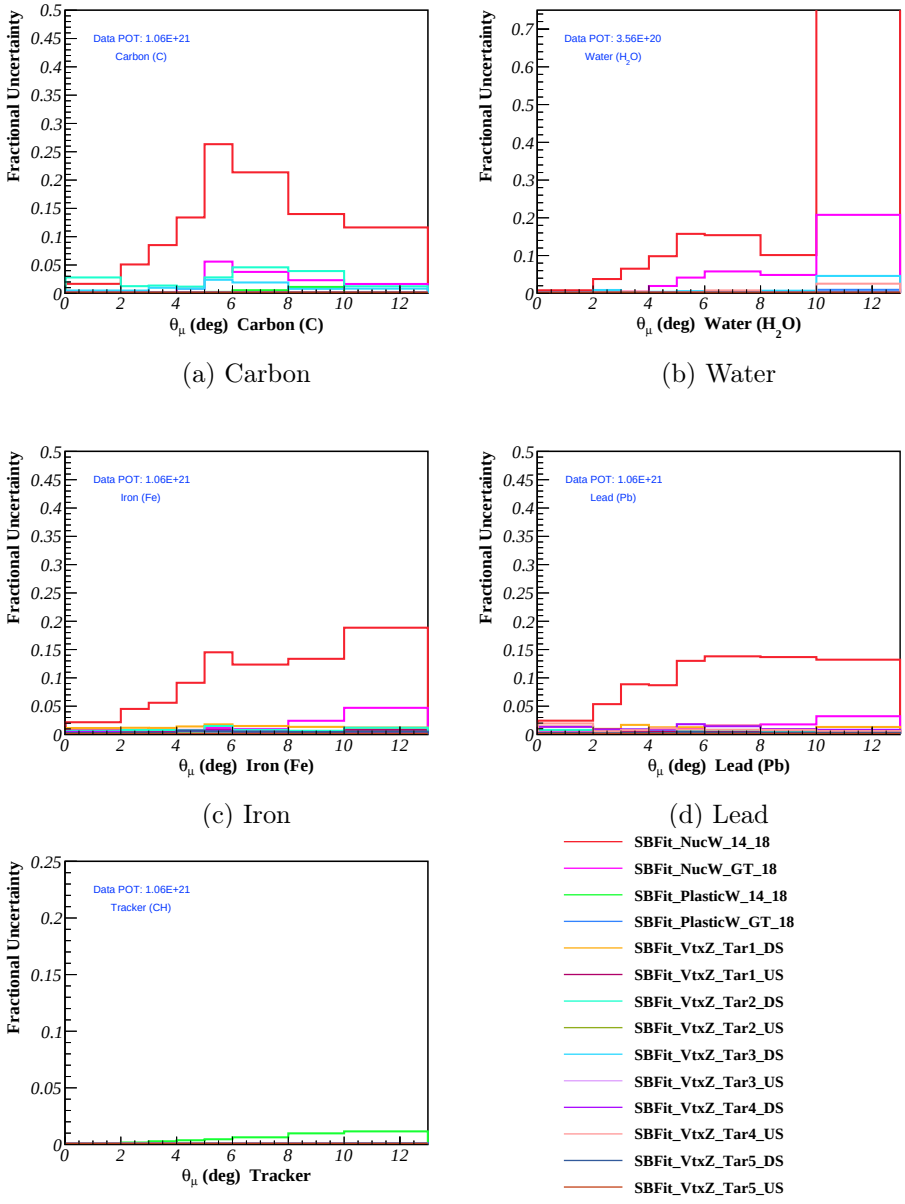
(b) Water

(c) Iron

(d) Lead

(e) Scintillator

Figure E-107: $p_{\mu,T}$ Sideband Fit Errors



(a) Carbon

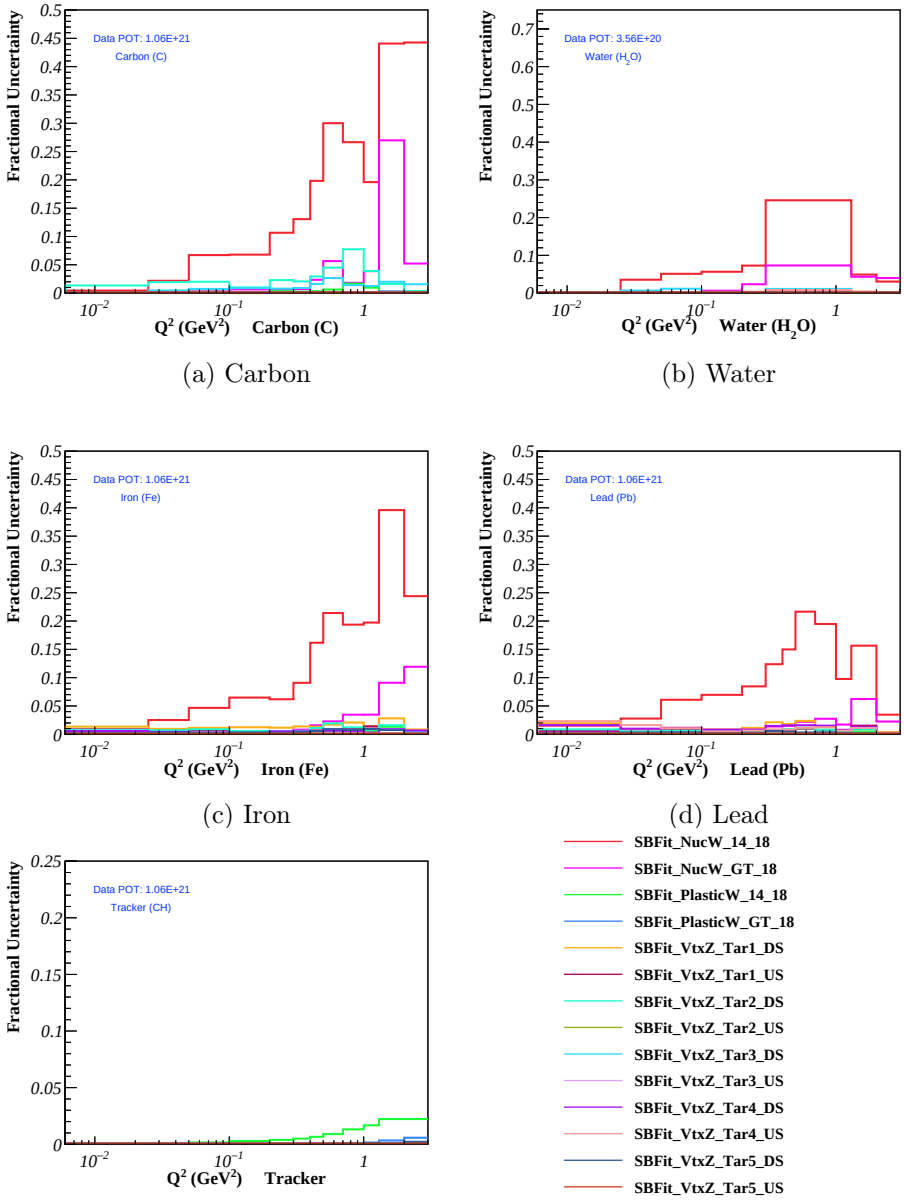
(b) Water

(c) Iron

(d) Lead

(e) Scintillator

Figure E-108: θ_μ Sideband Fit Errors



(a) Carbon

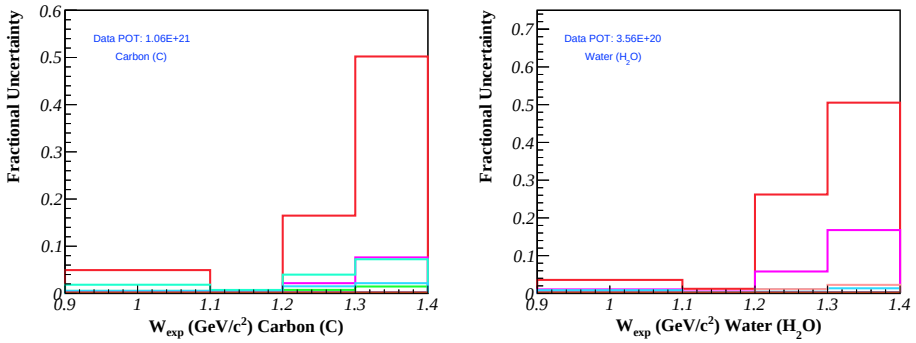
(b) Water

(c) Iron

(d) Lead

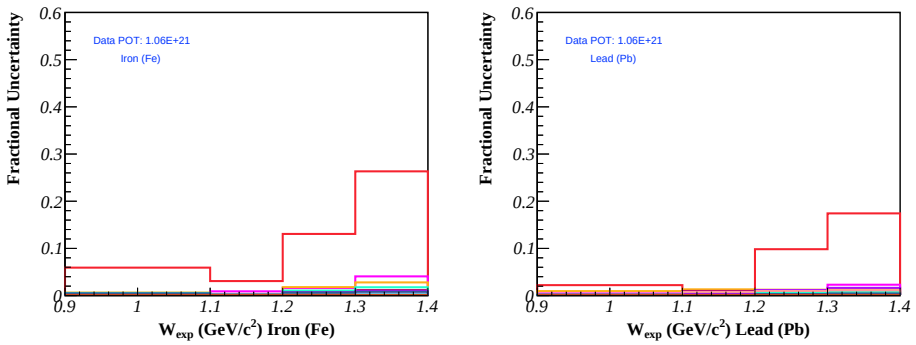
(e) Scintillator

Figure E-109: Q^2 Sideband Fit Errors



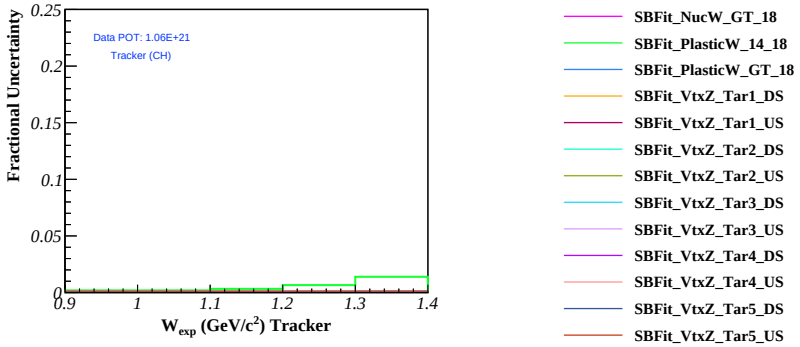
(a) Carbon

(b) Water



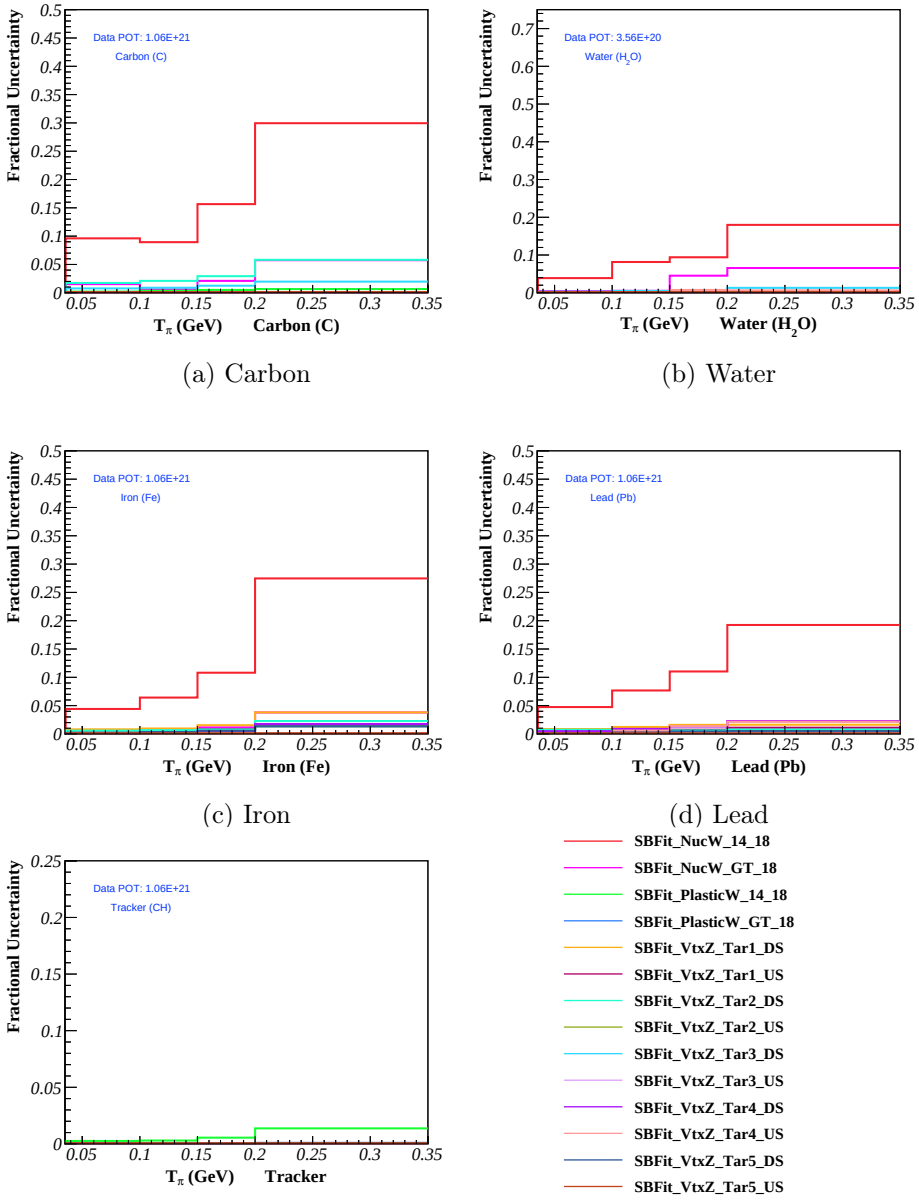
(c) Iron

(d) Lead



(e) Scintillator

Figure E-110: W_{exp} Sideband Fit Errors



(a) Carbon

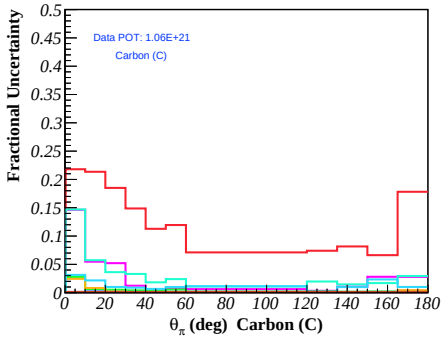
(b) Water

(c) Iron

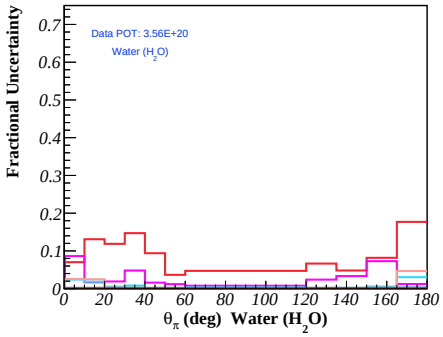
(d) Lead

(e) Scintillator

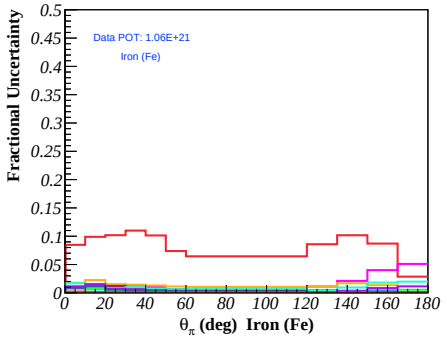
Figure E-111: T_π Sideband Fit Errors



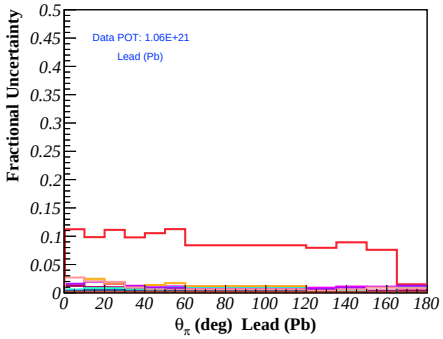
(a) Carbon



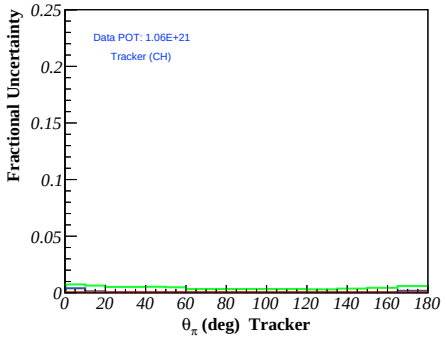
(b) Water



(c) Iron



(d) Lead



(e) Scintillator

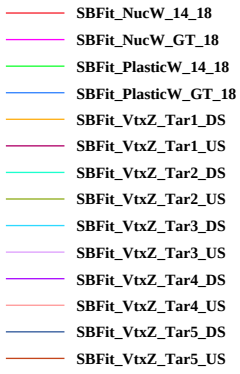
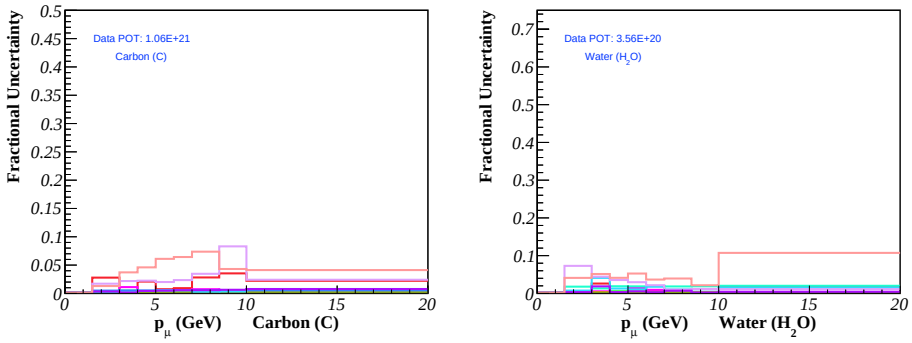
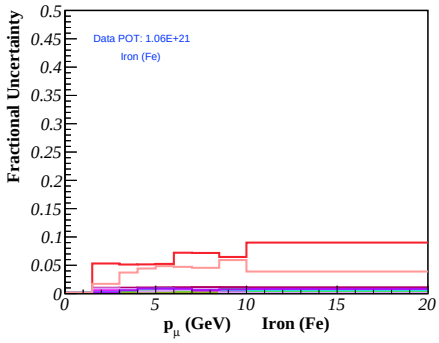


Figure E-112: θ_π Sideband Fit Errors

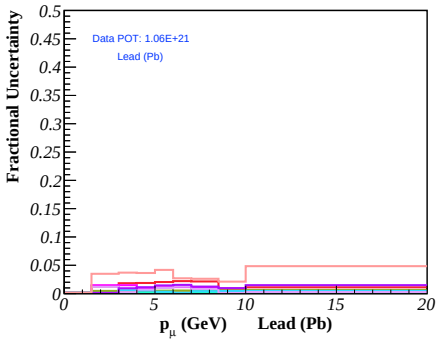


(a) Carbon

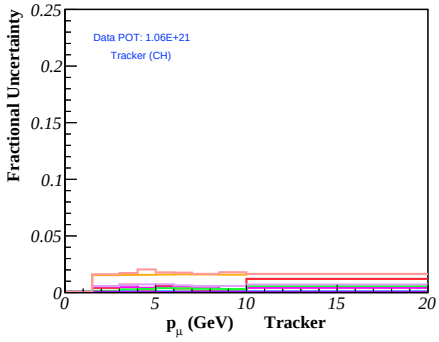
(b) Water



(c) Iron



(d) Lead



(e) Scintillator

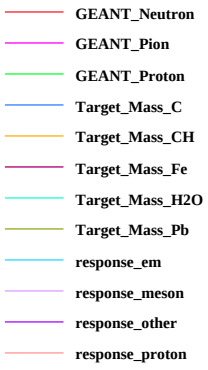
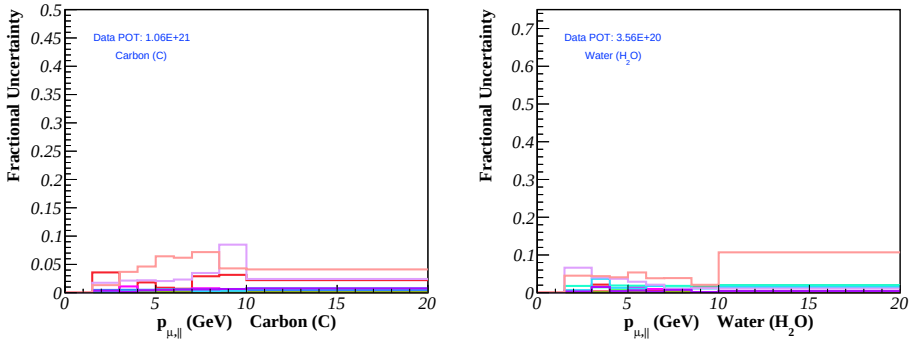
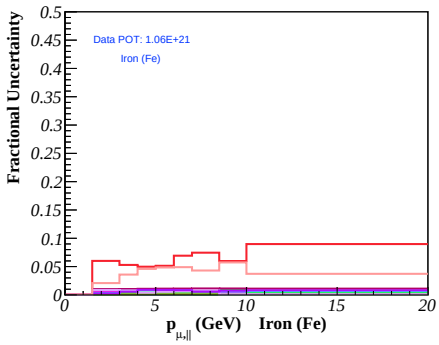


Figure E-113: p_μ Other Systematic Errors

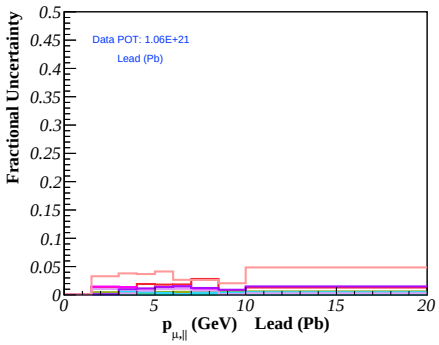


(a) Carbon

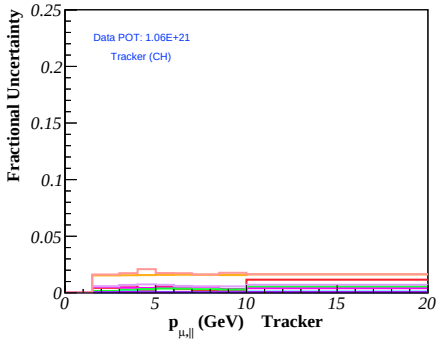
(b) Water



(c) Iron



(d) Lead



(e) Scintillator

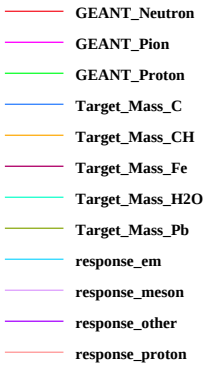
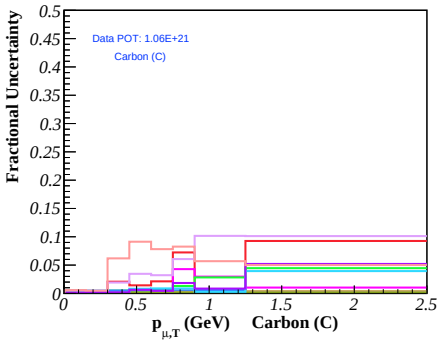
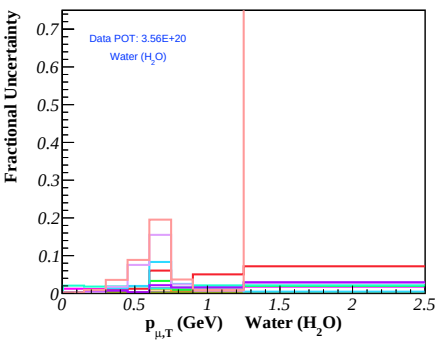


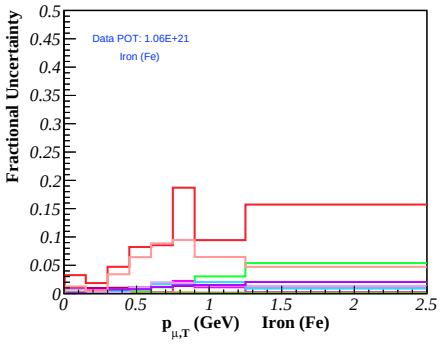
Figure E-114: $p_{\mu,||}$ Other Systematic Errors



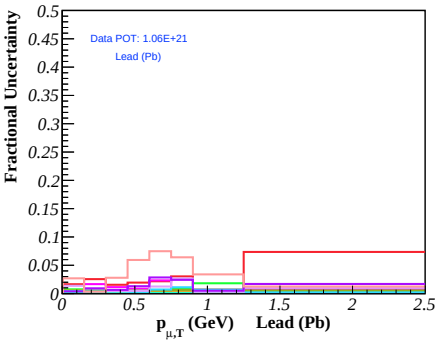
(a) Carbon



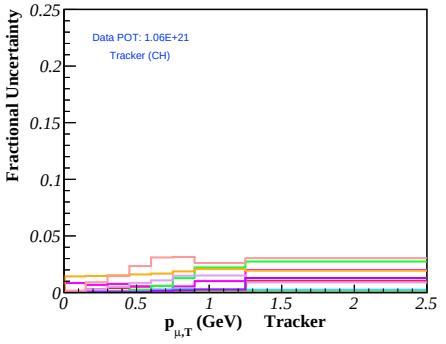
(b) Water



(c) Iron



(d) Lead



(e) Scintillator

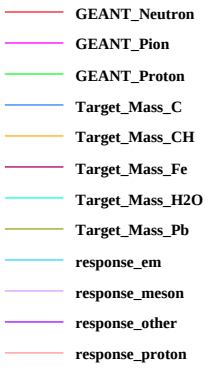
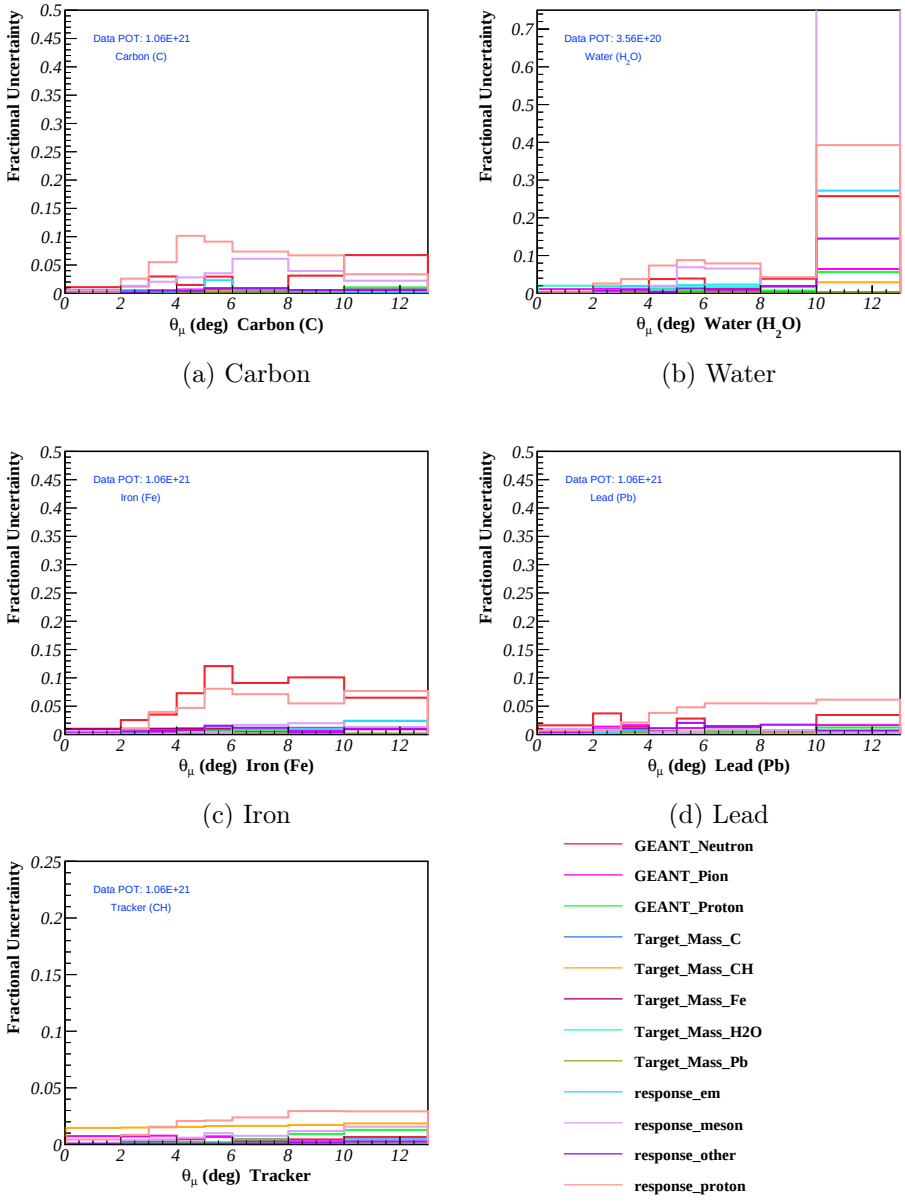


Figure E-115: $p_{\mu,T}$ Other Systematic Errors



(a) Carbon

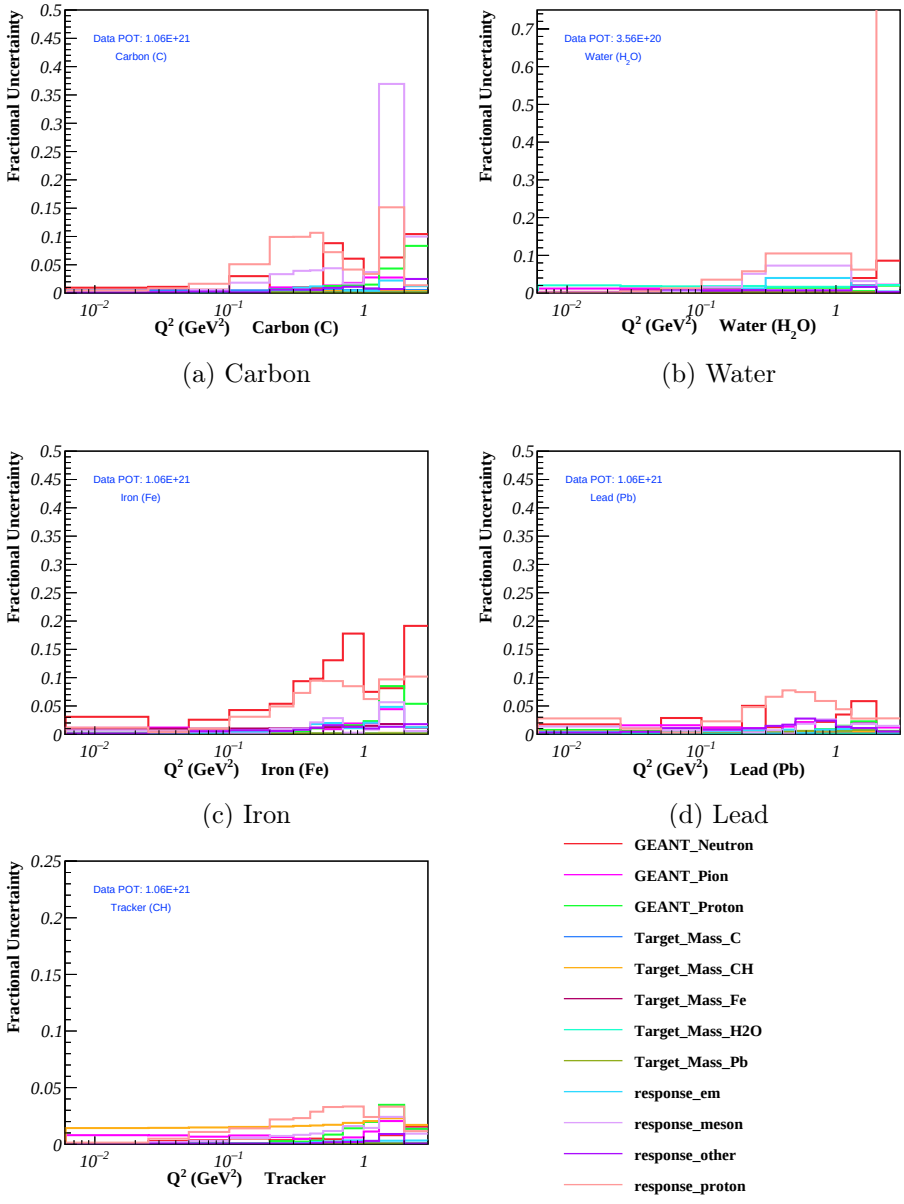
(b) Water

(c) Iron

(d) Lead

(e) Scintillator

Figure E-116: θ_μ Other Systematic Errors



(a) Carbon

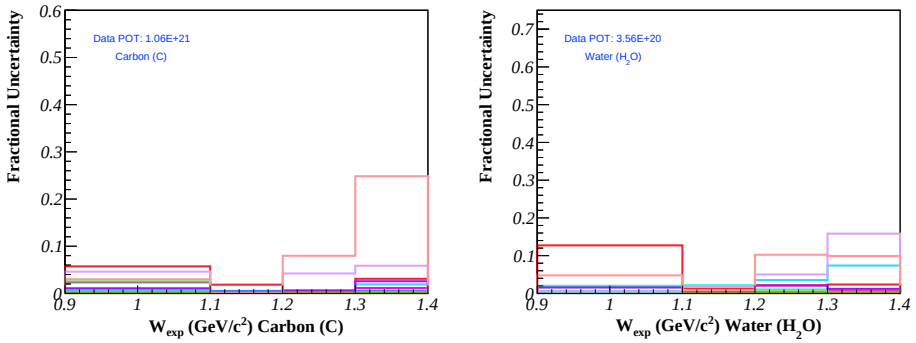
(b) Water

(c) Iron

(d) Lead

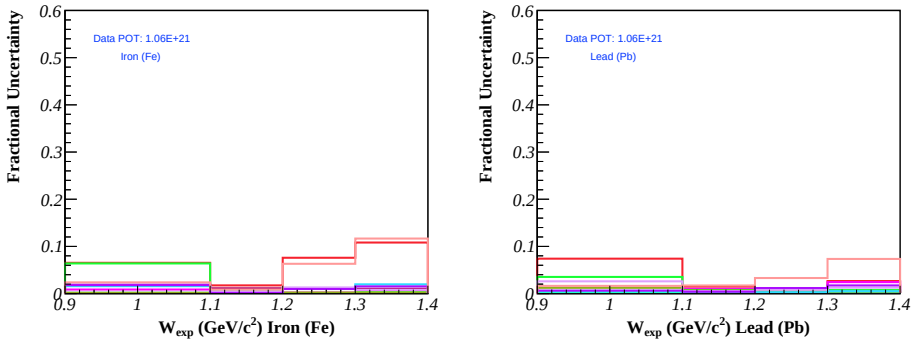
(e) Scintillator

Figure E-117: Q^2 Other Systematic Errors



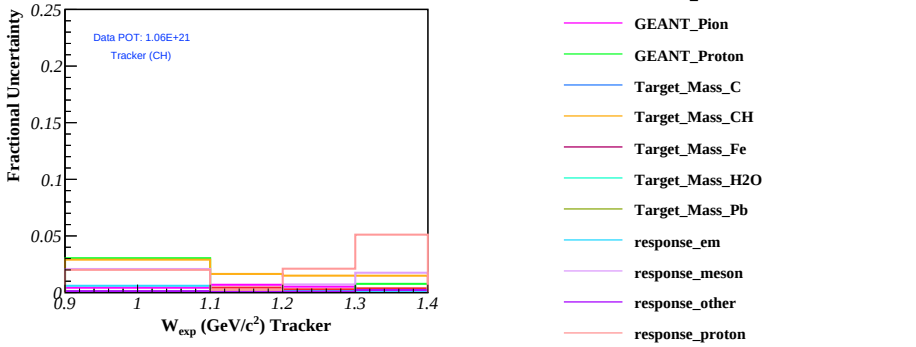
(a) Carbon

(b) Water



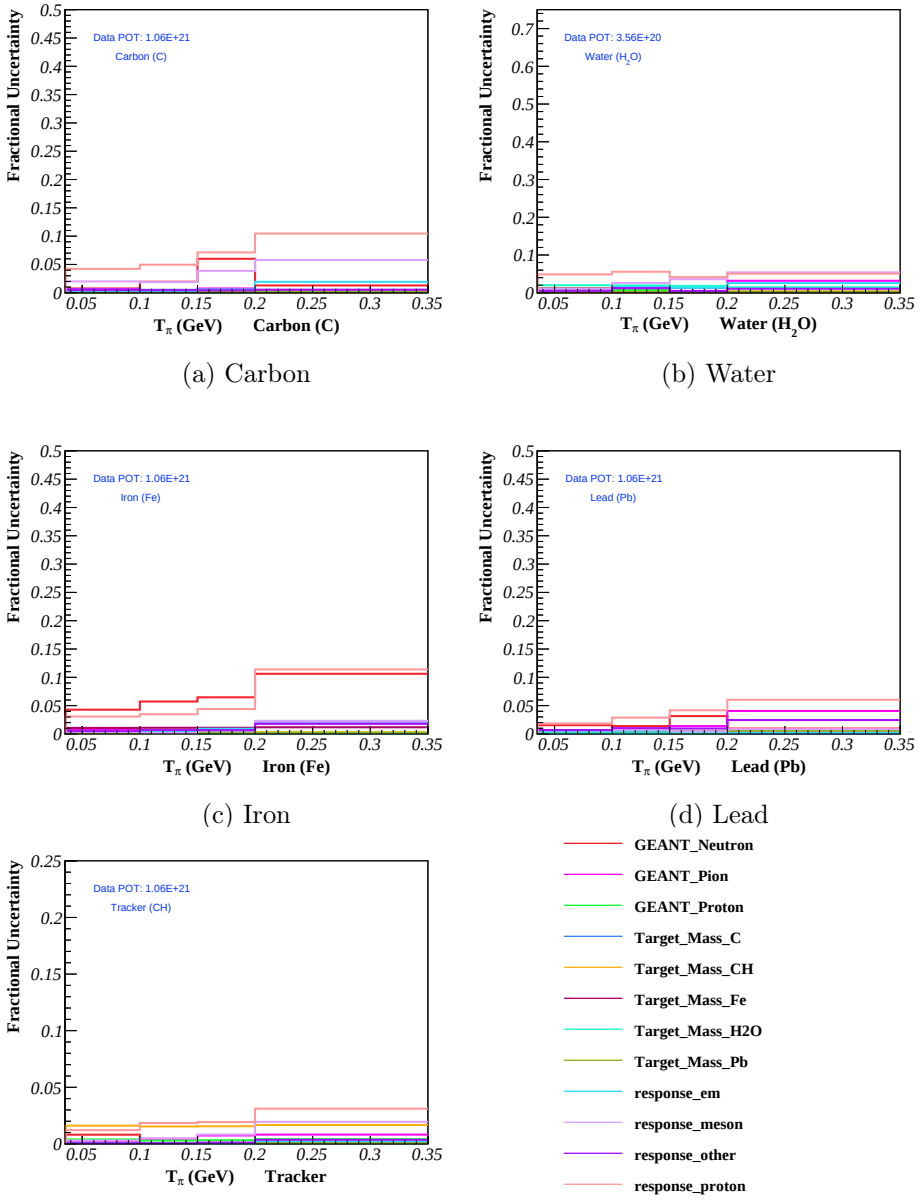
(c) Iron

(d) Lead



(e) Scintillator

Figure E-118: W_{exp} Other Systematic Errors



(a) Carbon

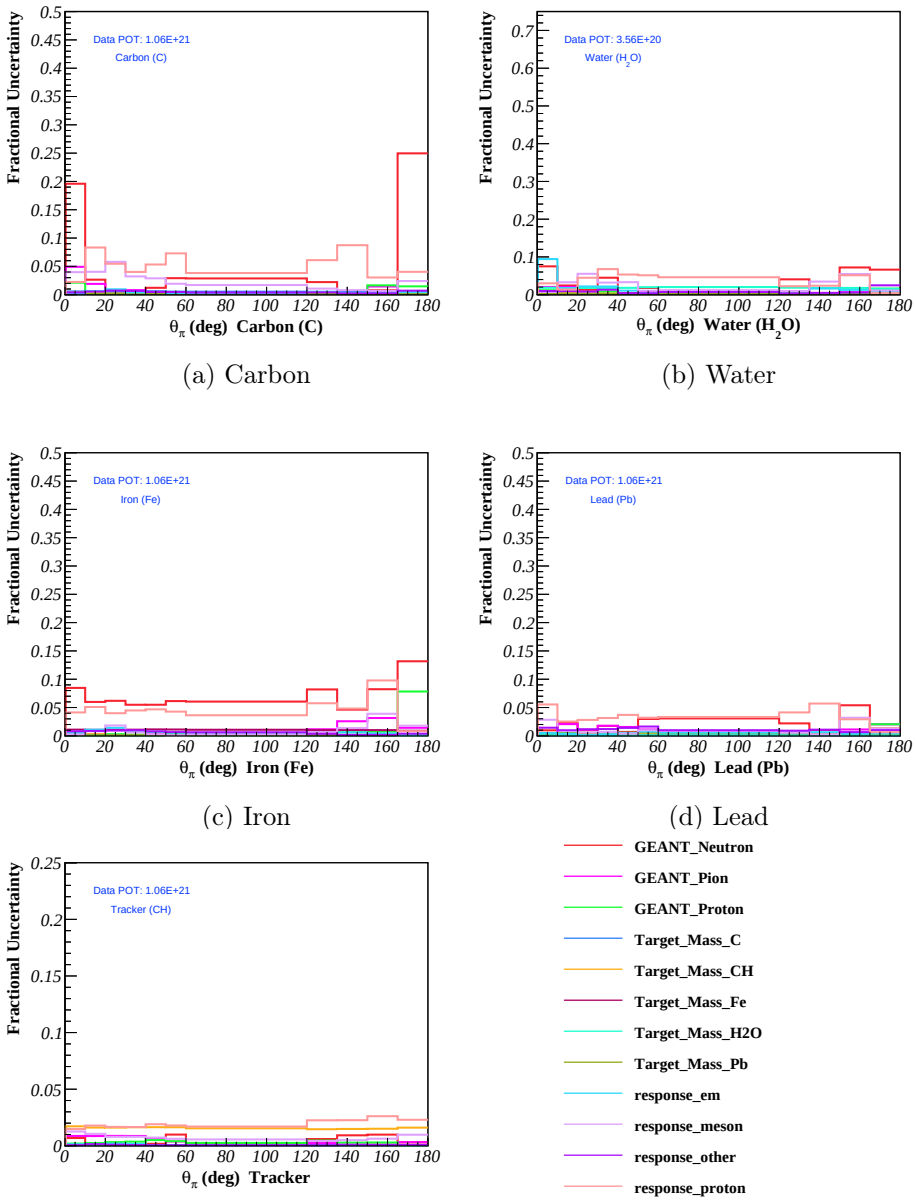
(b) Water

(c) Iron

(d) Lead

(e) Scintillator

Figure E-119: T_π Other Systematic Errors



(a) Carbon

(b) Water

(c) Iron

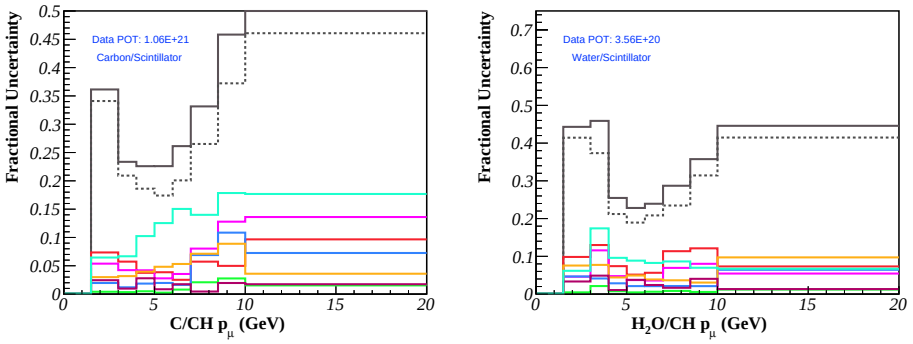
(d) Lead

(e) Scintillator

Figure E-120: θ_π Other Systematic Errors

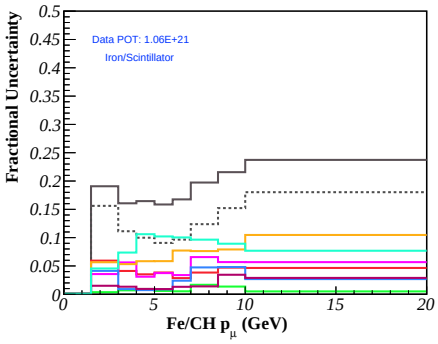
Appendix F

Cross Section Ratio Error Plots

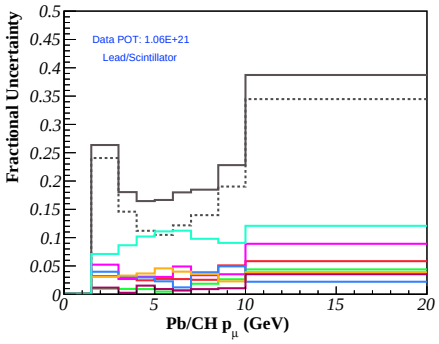


(a) Carbon/Scintillator

(b) Water/Scintillator



(c) Iron/Scintillator



(d) Lead/Scintillator

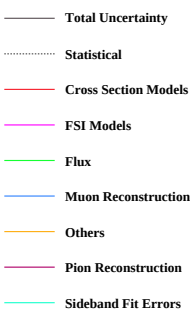
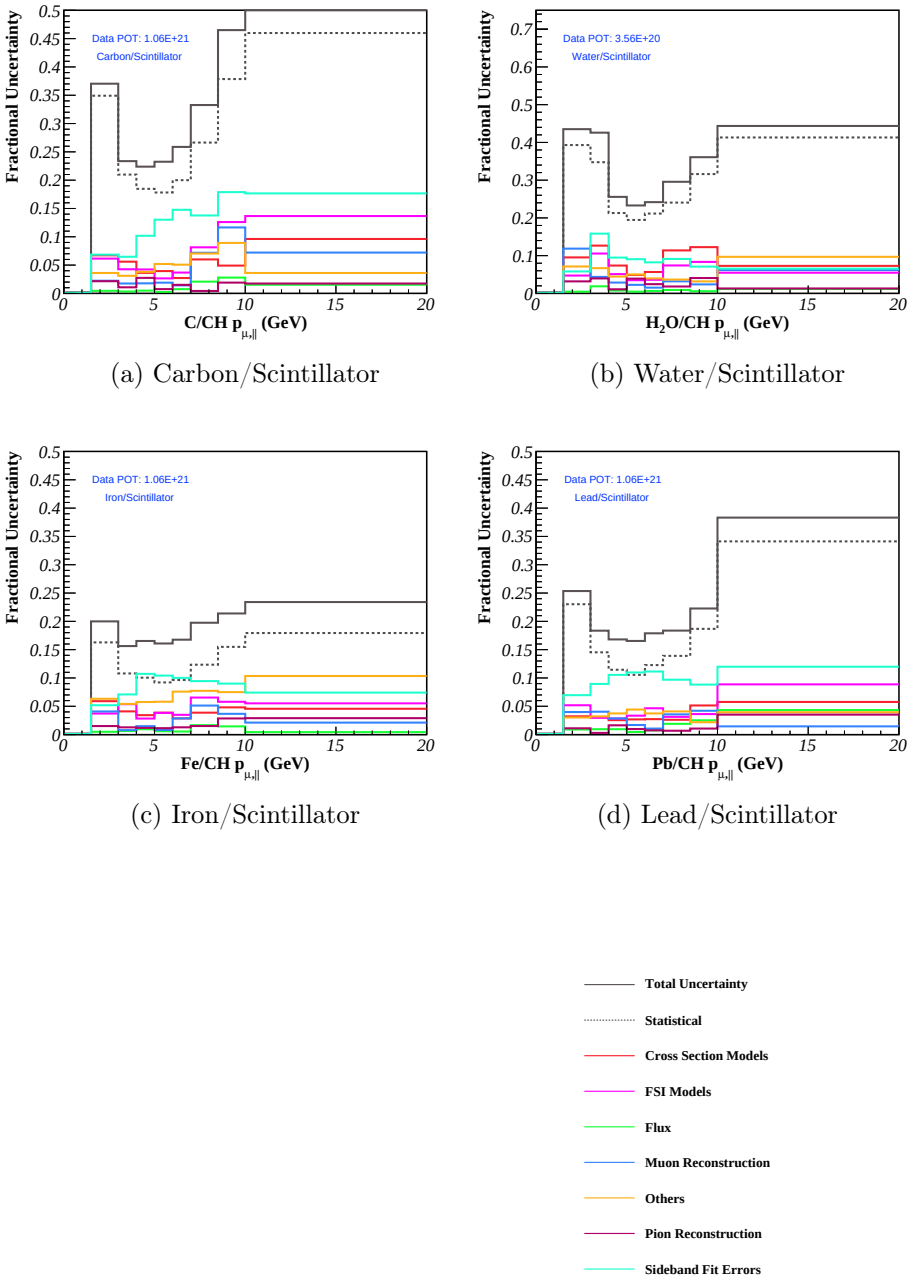


Figure F-1: p_μ Error Summary

1



(a) Carbon/Scintillator

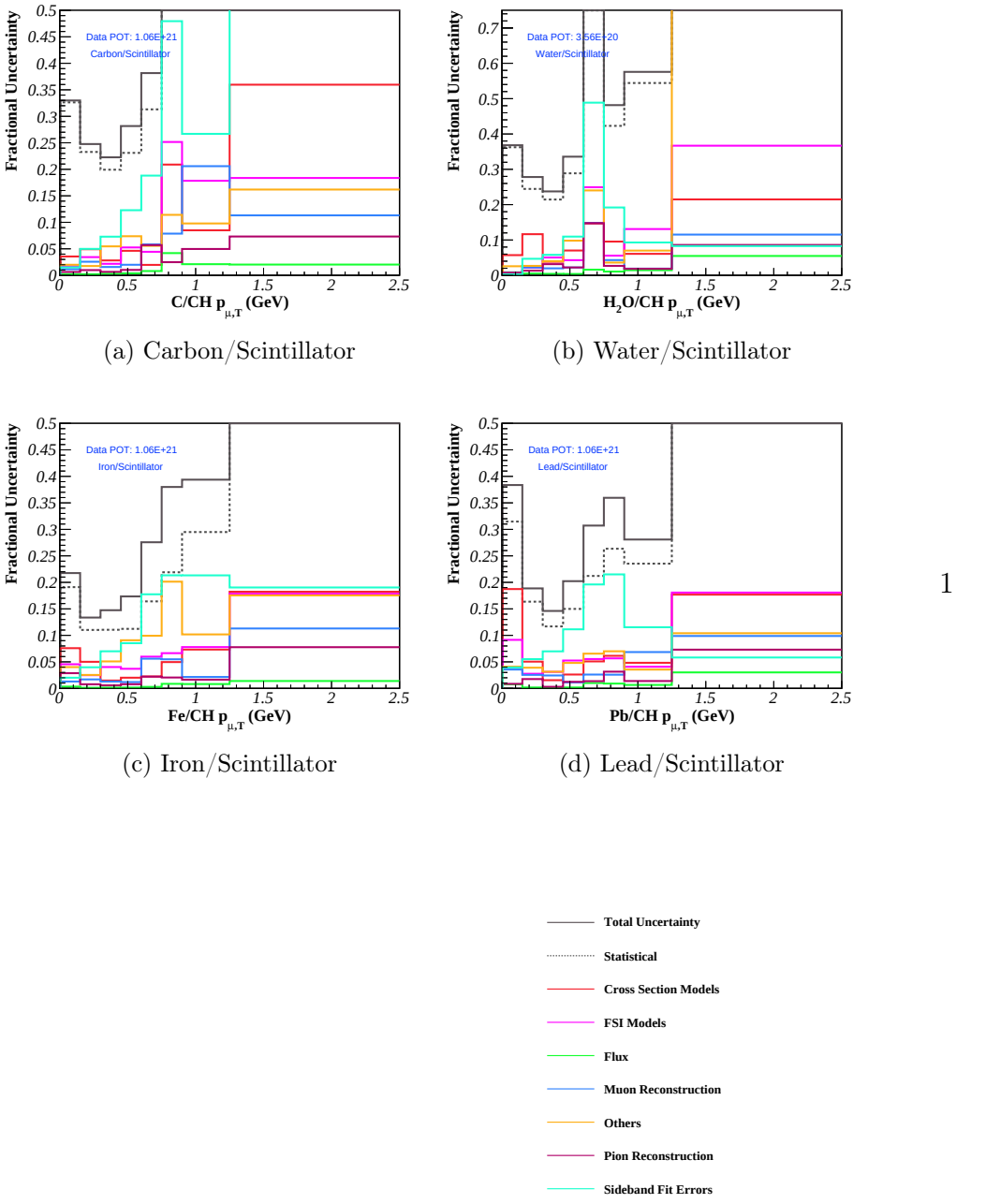
(b) Water/Scintillator

(c) Iron/Scintillator

(d) Lead/Scintillator

1

Figure F-2: $p_{\mu,||}$ Error Summary



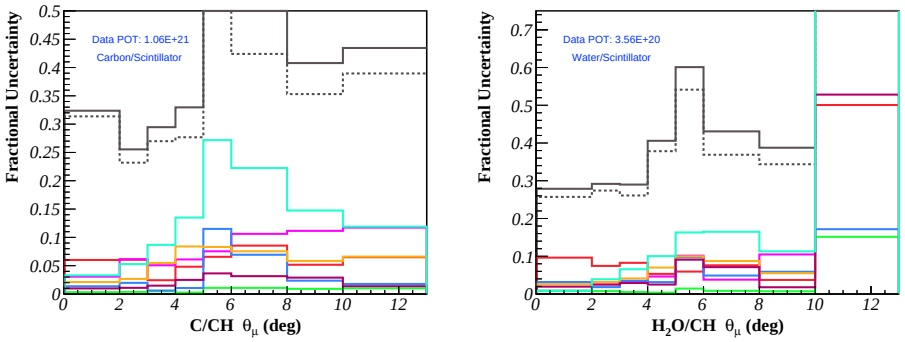
(a) Carbon/Scintillator

(b) Water/Scintillator

(c) Iron/Scintillator

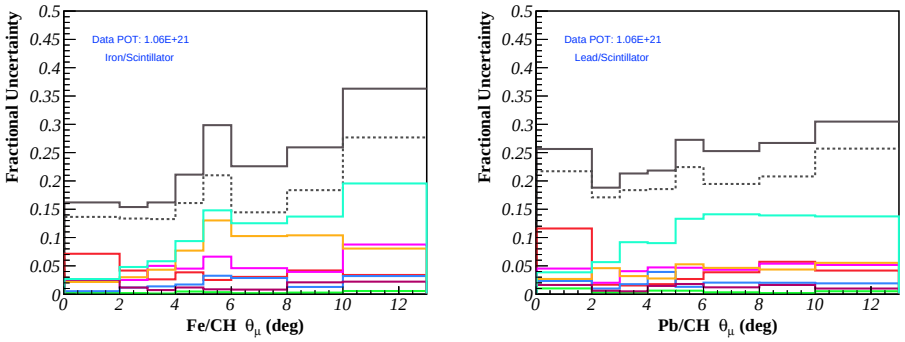
(d) Lead/Scintillator

Figure F-3: $p_{\mu,T}$ Error Summary



(a) Carbon/Scintillator

(b) Water/Scintillator



(c) Iron/Scintillator

(d) Lead/Scintillator

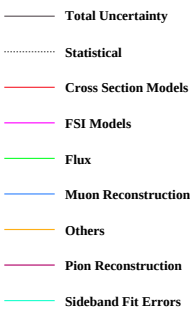
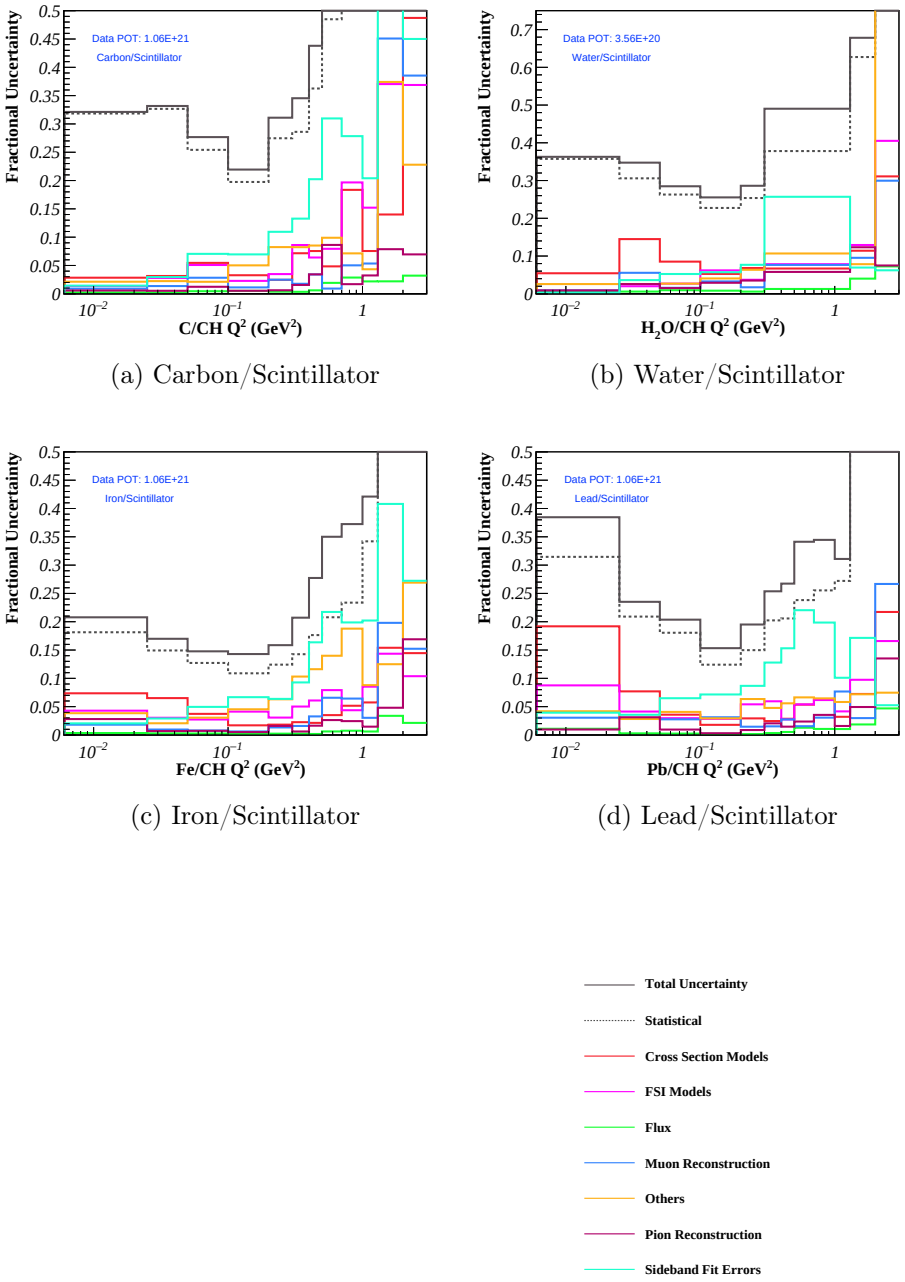


Figure F-4: θ_μ Error Summary

1



(a) Carbon/Scintillator

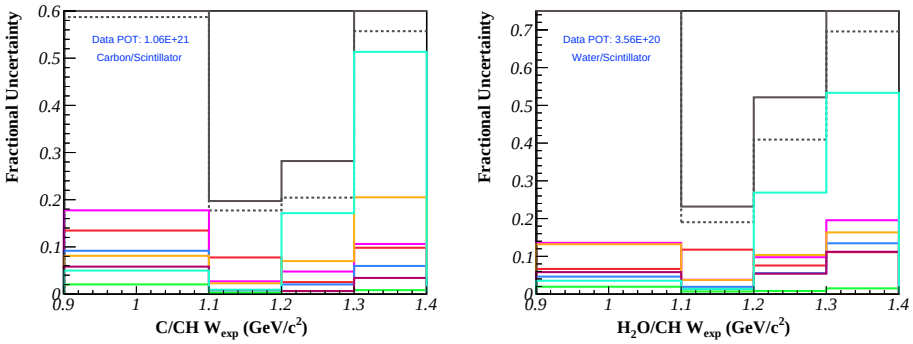
(b) Water/Scintillator

(c) Iron/Scintillator

(d) Lead/Scintillator

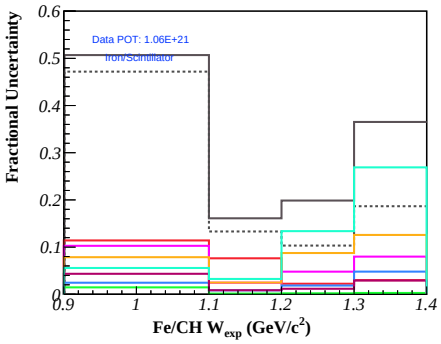
1

Figure F-5: Q^2 Error Summary

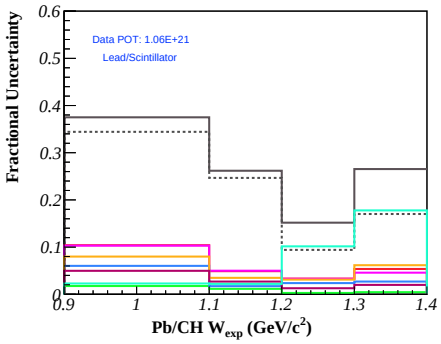


(a) Carbon/Scintillator

(b) Water/Scintillator



(c) Iron/Scintillator



(d) Lead/Scintillator

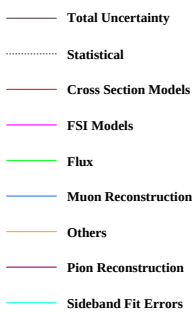
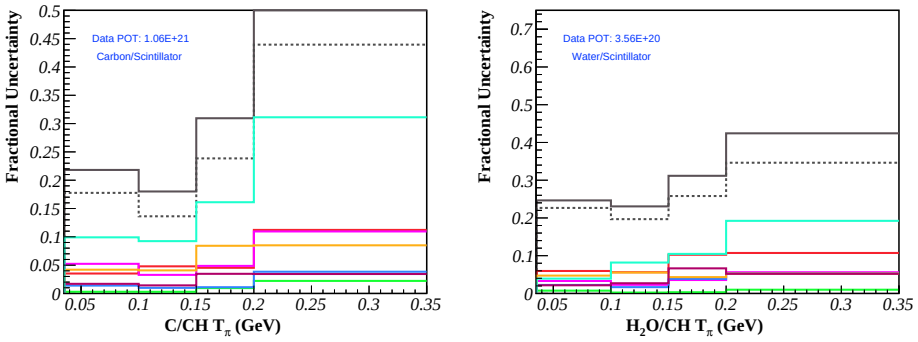


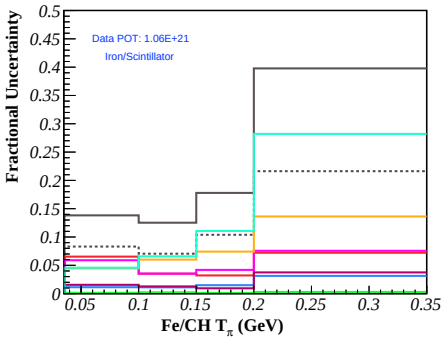
Figure F-6: W_{exp} Error Summary

1

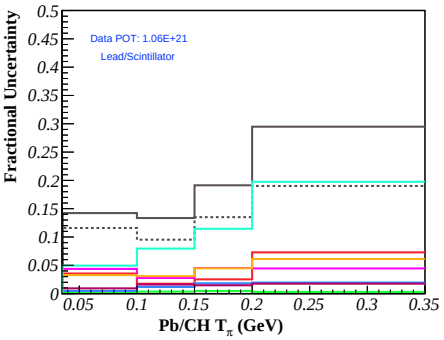


(a) Carbon/Scintillator

(b) Water/Scintillator



(c) Iron/Scintillator



(d) Lead/Scintillator

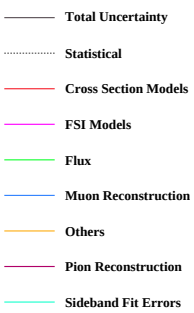
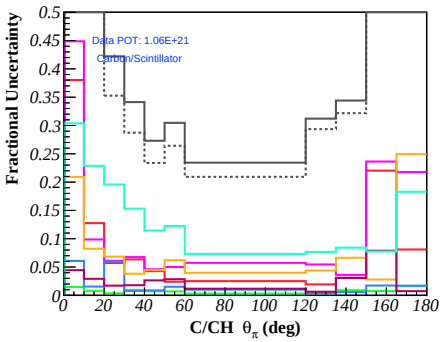
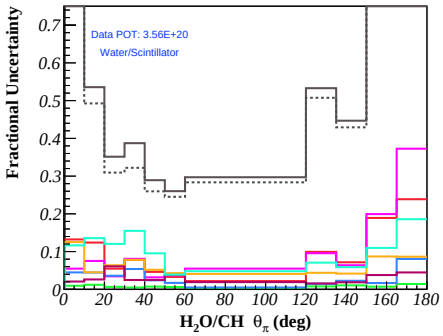


Figure F-7: T_π Error Summary

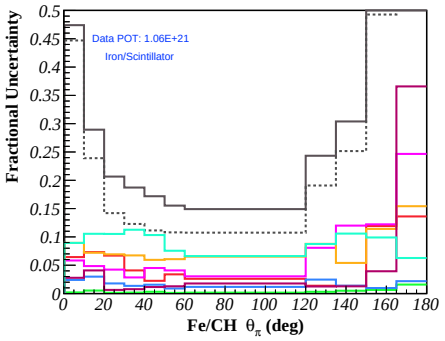
1



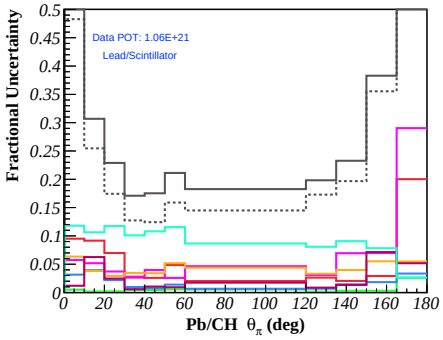
(a) Carbon/Scintillator



(b) Water/Scintillator



(c) Iron/Scintillator



(d) Lead/Scintillator

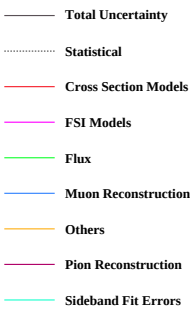
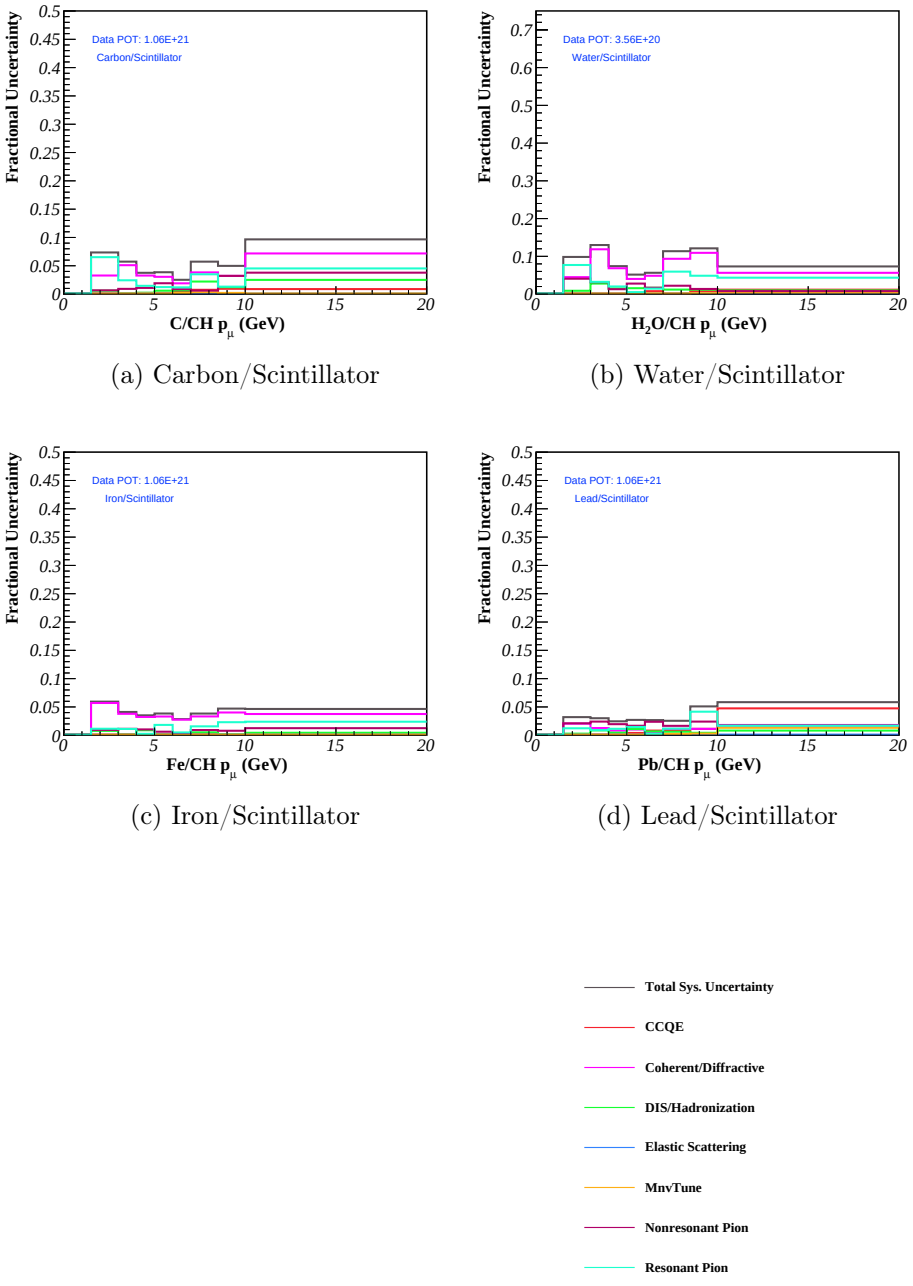


Figure F-8: θ_π Error Summary

1



(a) Carbon/Scintillator

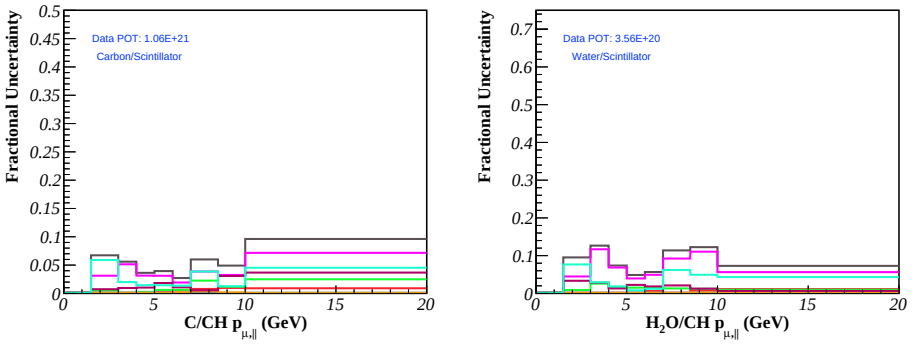
(b) Water/Scintillator

(c) Iron/Scintillator

(d) Lead/Scintillator

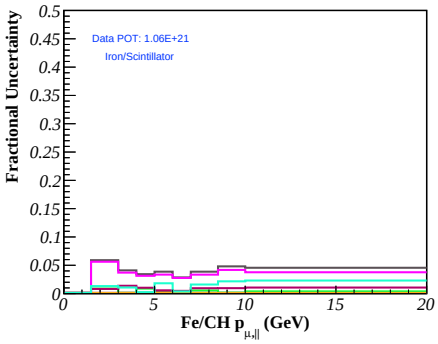
1

Figure F-9: p_μ All Cross Section Model Errors

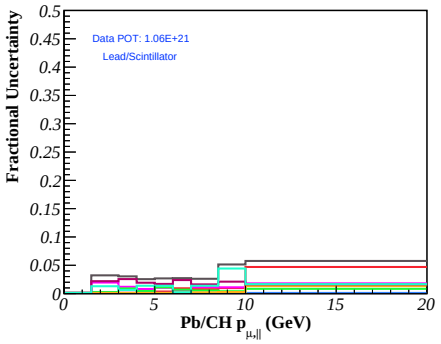


(a) Carbon/Scintillator

(b) Water/Scintillator



(c) Iron/Scintillator

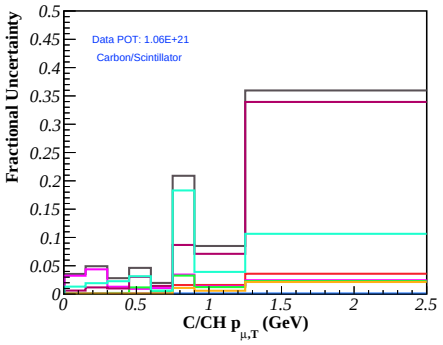


(d) Lead/Scintillator

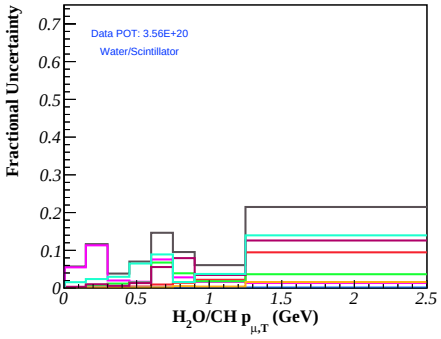
1



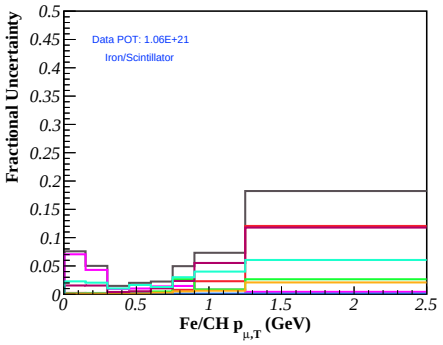
Figure F-10: $p_{\mu,||}$ All Cross Section Model Errors



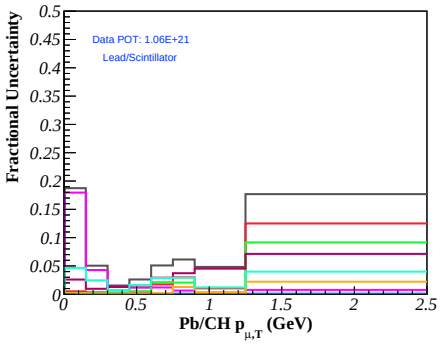
(a) Carbon/Scintillator



(b) Water/Scintillator



(c) Iron/Scintillator



(d) Lead/Scintillator

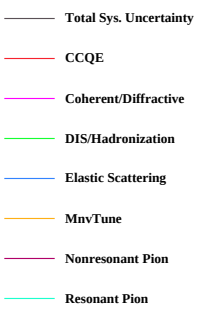
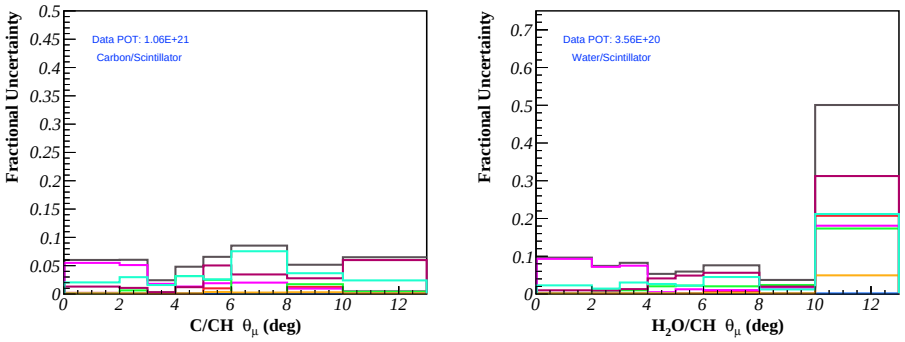


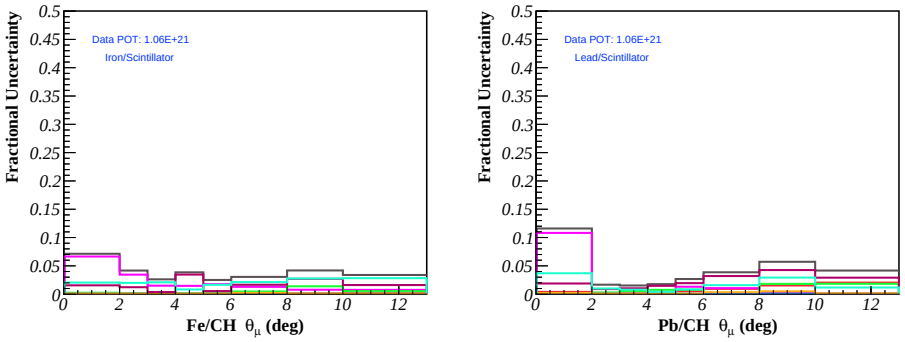
Figure F-11: $p_{\mu,T}$ All Cross Section Model Errors

1



(a) Carbon/Scintillator

(b) Water/Scintillator



(c) Iron/Scintillator

(d) Lead/Scintillator

1

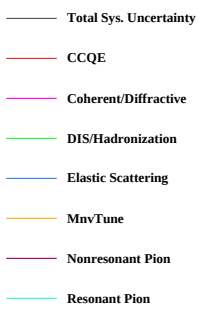
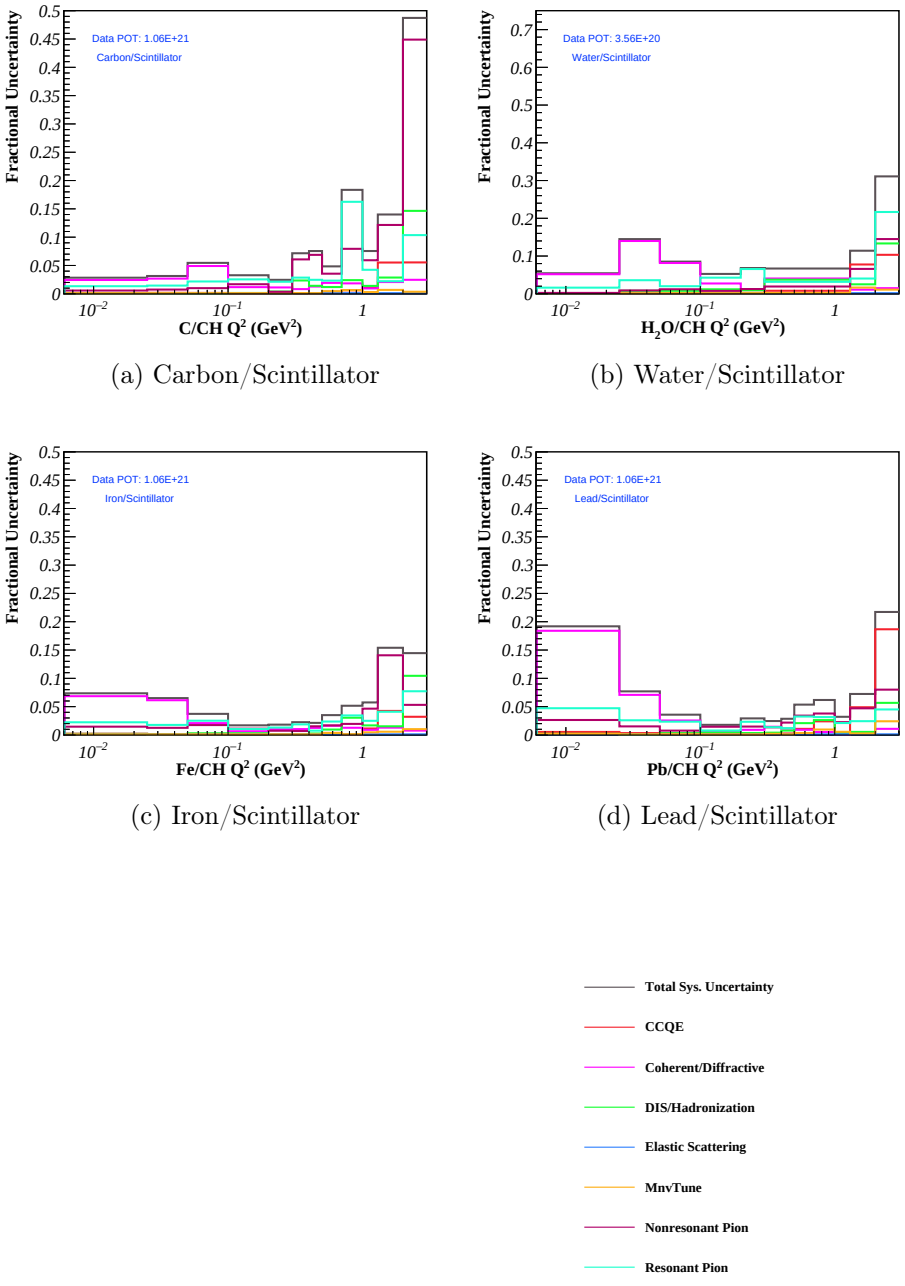


Figure F-12: θ_μ All Cross Section Model Errors



(a) Carbon/Scintillator

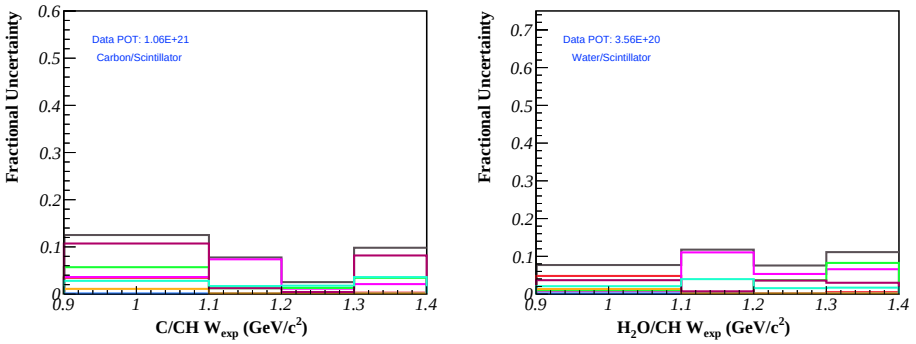
(b) Water/Scintillator

(c) Iron/Scintillator

(d) Lead/Scintillator

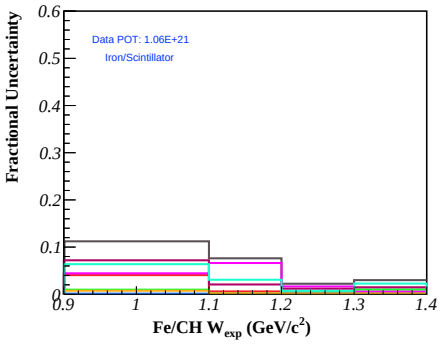
1

Figure F-13: Q^2 All Cross Section Model Errors

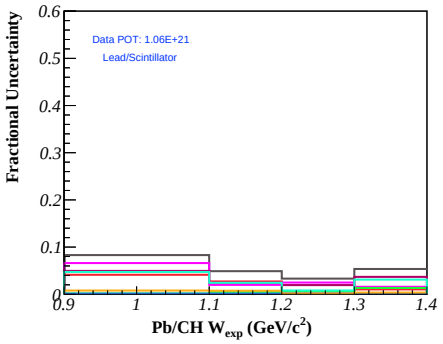


(a) Carbon/Scintillator

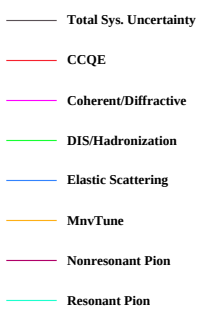
(b) Water/Scintillator



(c) Iron/Scintillator

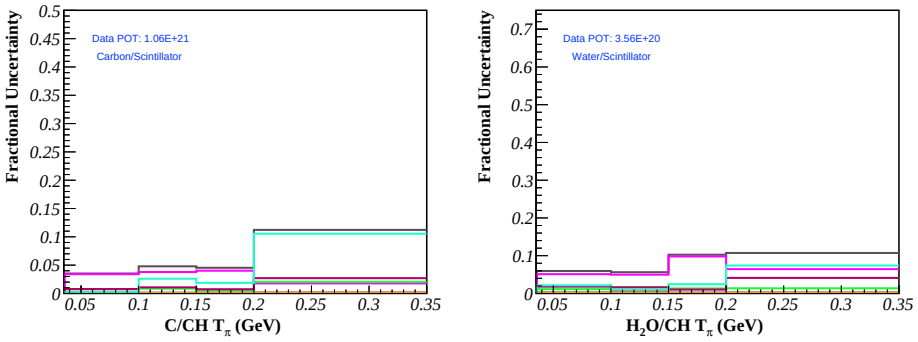


(d) Lead/Scintillator



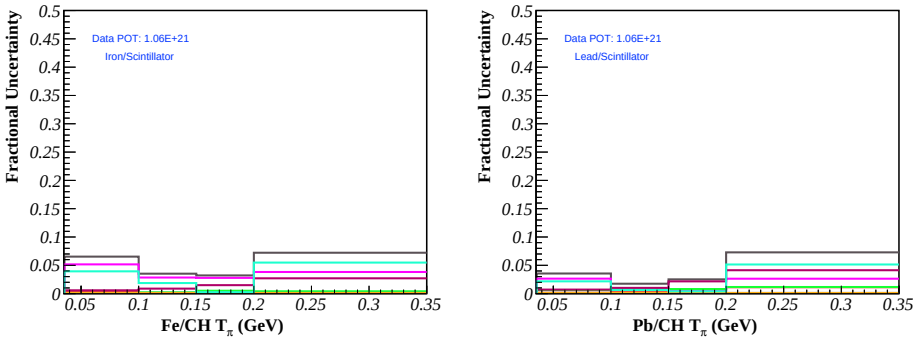
1

Figure F-14: W_{exp} All Cross Section Model Errors



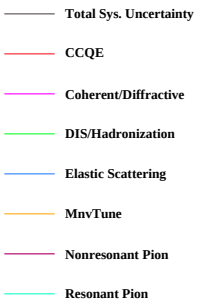
(a) Carbon/Scintillator

(b) Water/Scintillator



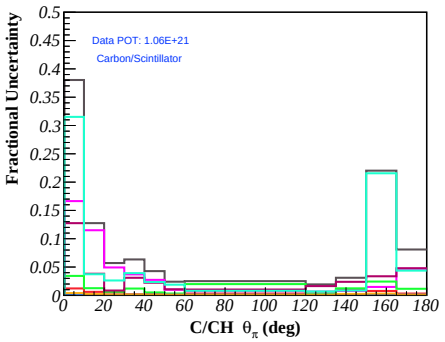
(c) Iron/Scintillator

(d) Lead/Scintillator

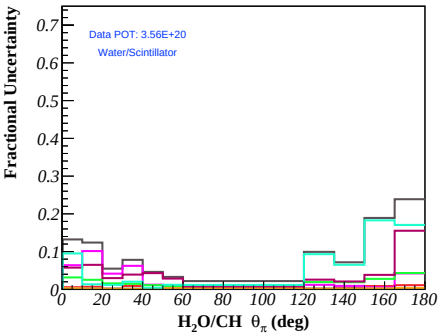


1

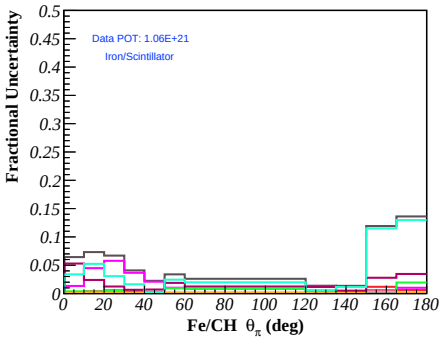
Figure F-15: T_π All Cross Section Model Errors



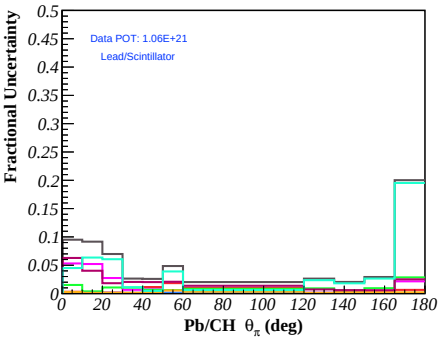
(a) Carbon/Scintillator



(b) Water/Scintillator



(c) Iron/Scintillator

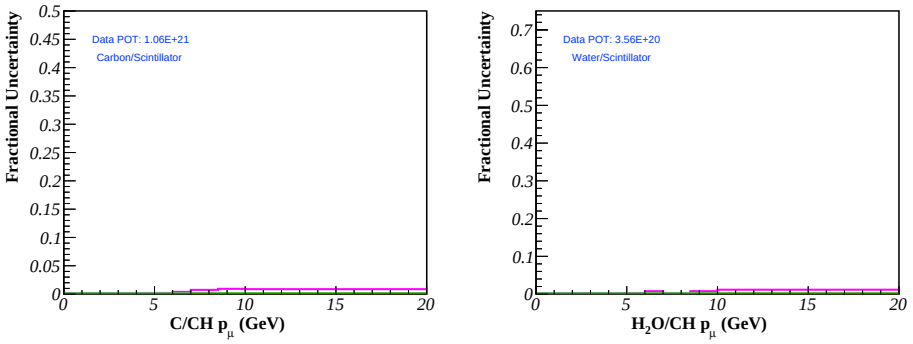


(d) Lead/Scintillator



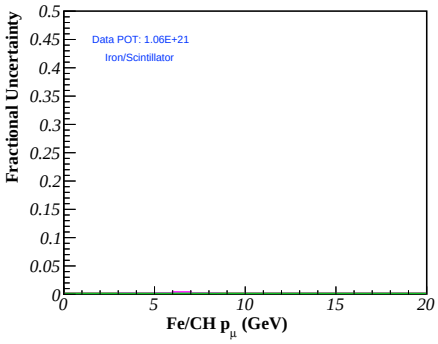
Figure F-16: θ_π All Cross Section Model Errors

1

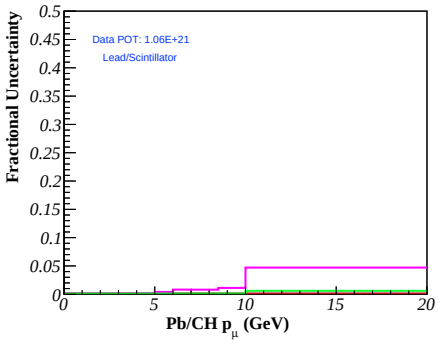


(a) Carbon/Scintillator

(b) Water/Scintillator



(c) Iron/Scintillator



(d) Lead/Scintillator

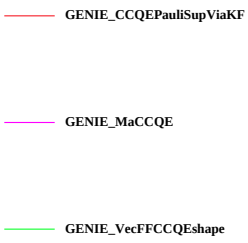
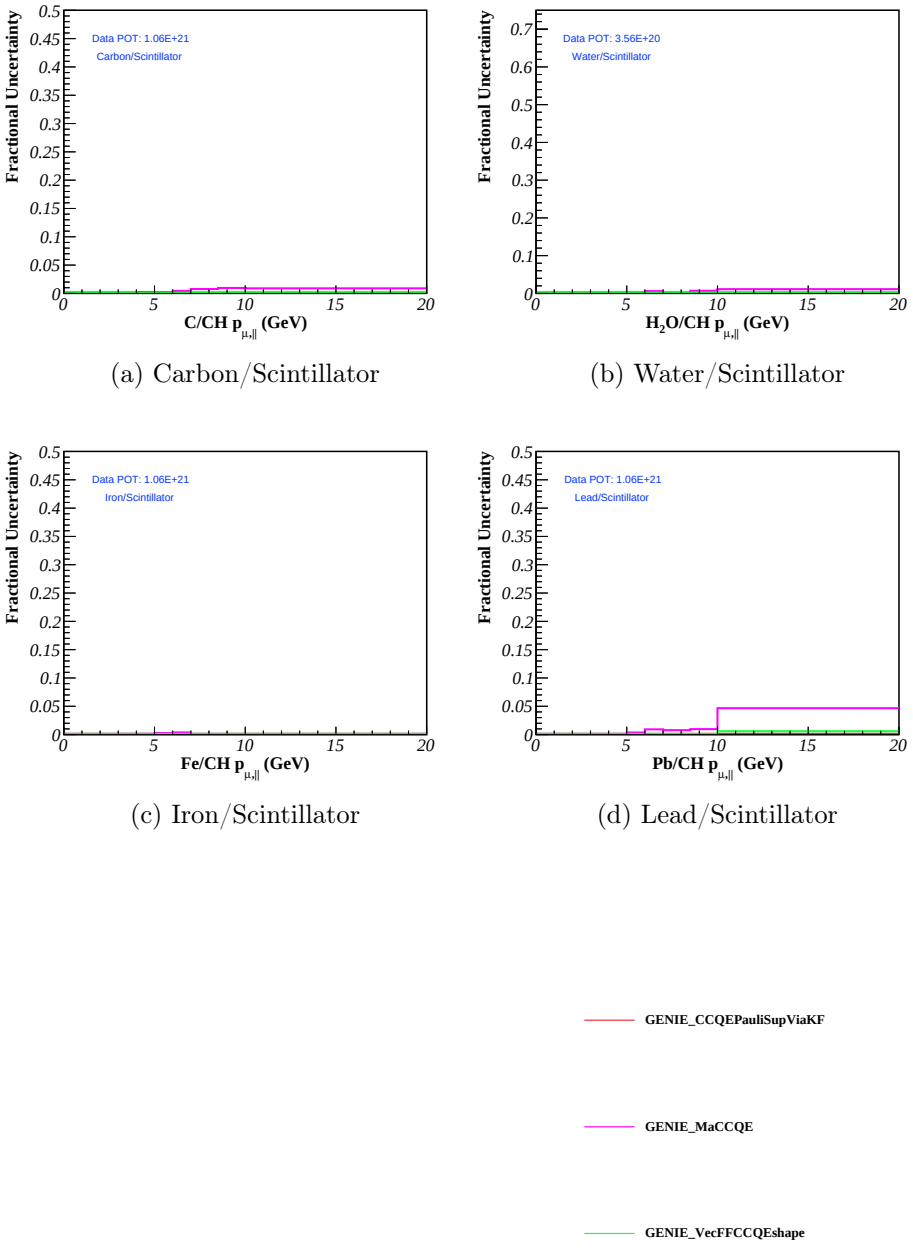


Figure F-17: p_μ CCQE Model Errors

3



(a) Carbon/Scintillator

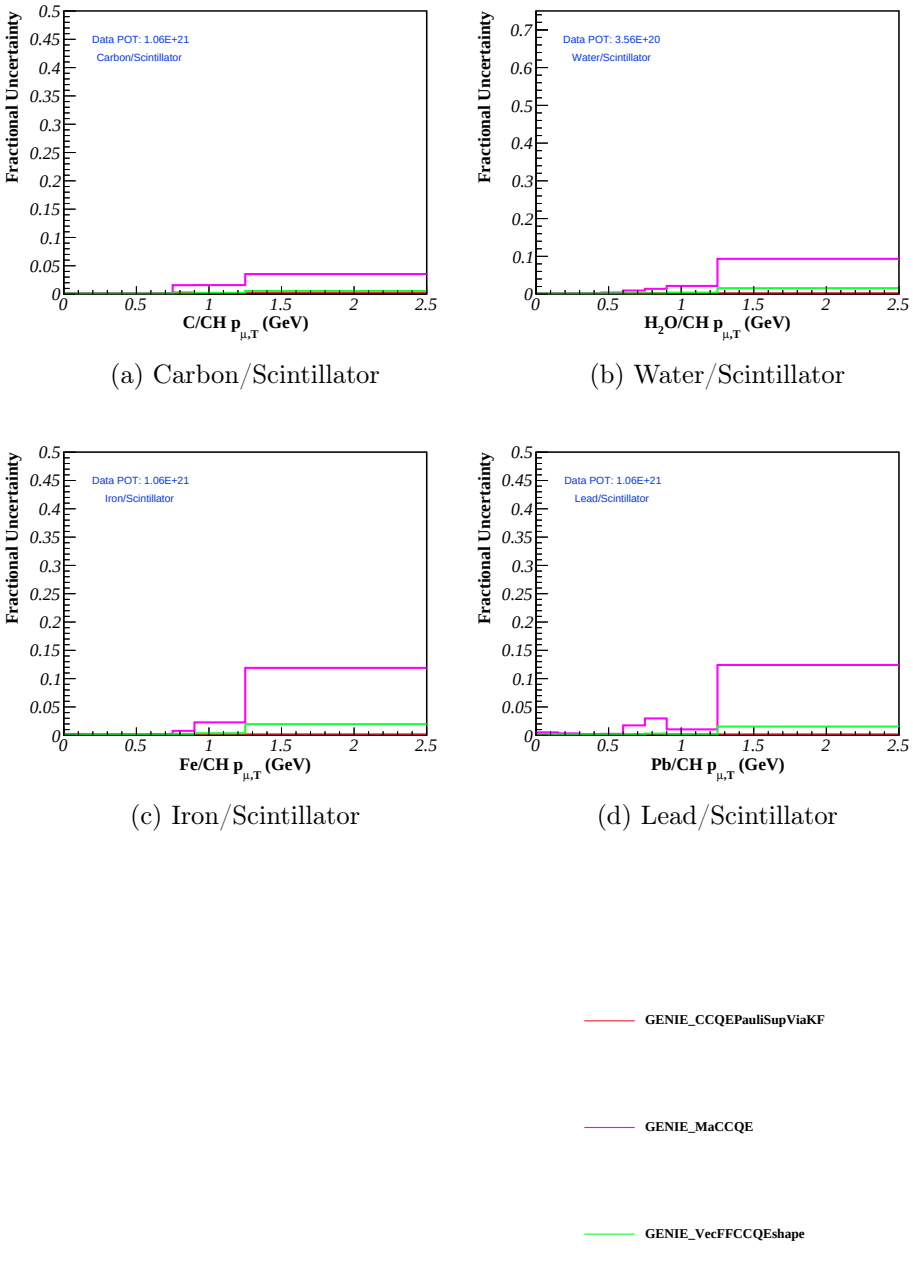
(b) Water/Scintillator

(c) Iron/Scintillator

(d) Lead/Scintillator

3

Figure F-18: $p_{\mu,||}$ CCQE Model Errors



(a) Carbon/Scintillator

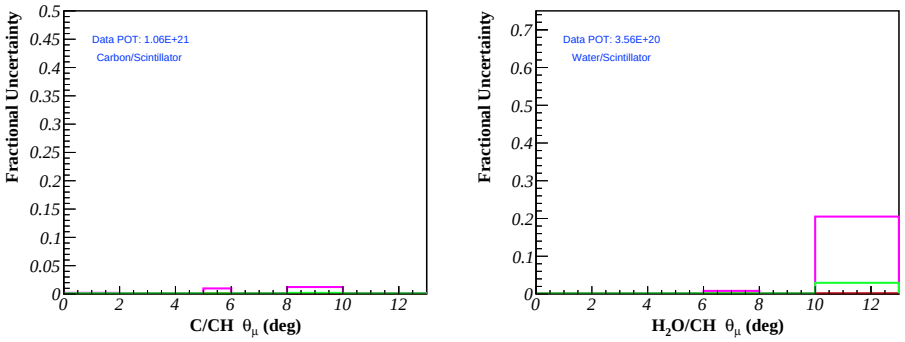
(b) Water/Scintillator

(c) Iron/Scintillator

(d) Lead/Scintillator

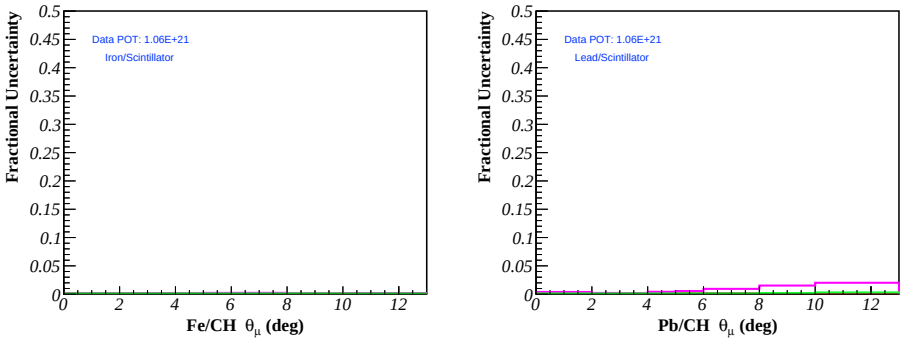
3

Figure F-19: $p_{\mu,T}$ CCQE Model Errors



(a) Carbon/Scintillator

(b) Water/Scintillator



(c) Iron/Scintillator

(d) Lead/Scintillator

3

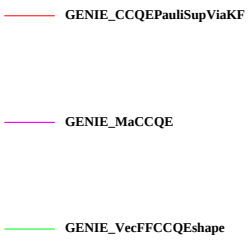
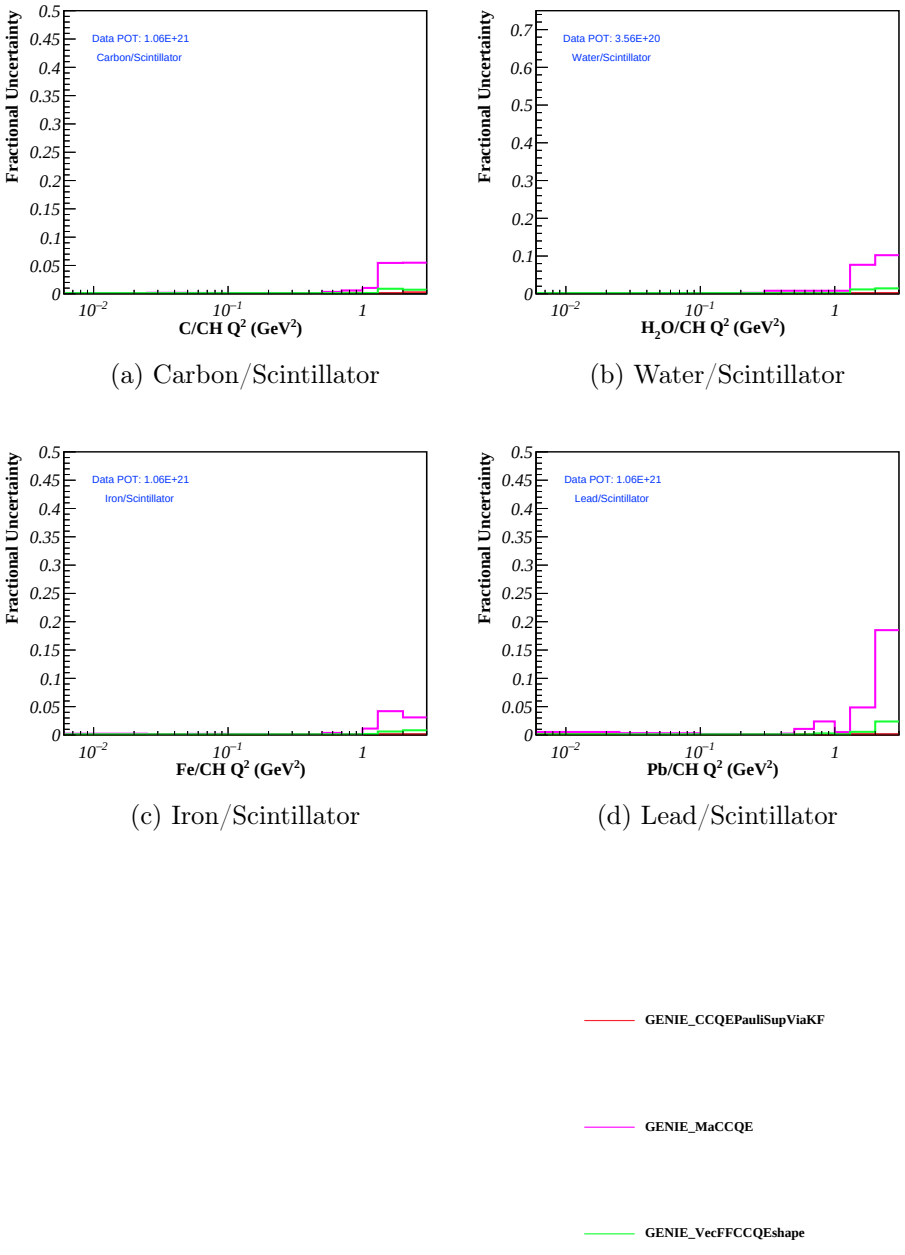


Figure F-20: θ_μ CCQE Model Errors



(a) Carbon/Scintillator

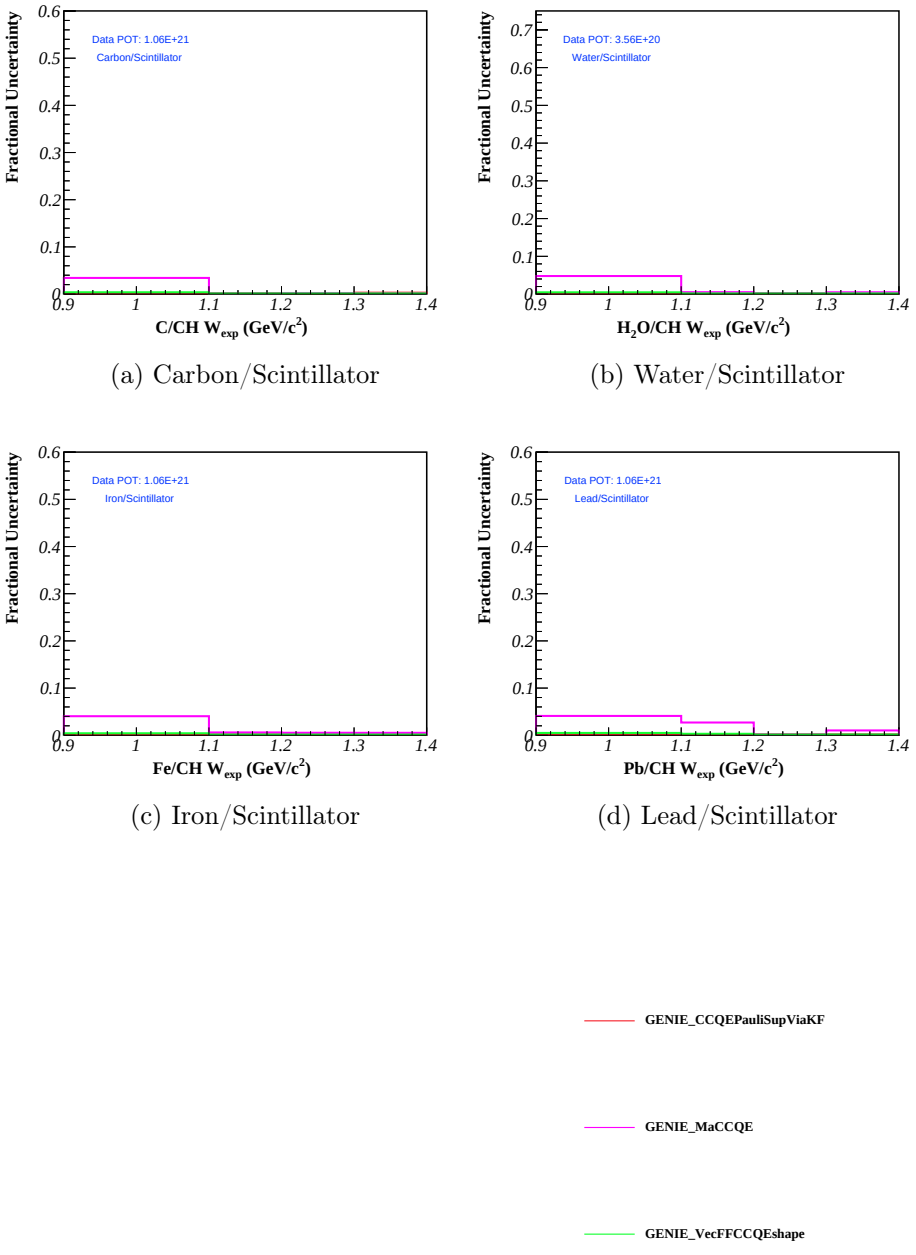
(b) Water/Scintillator

(c) Iron/Scintillator

(d) Lead/Scintillator

3

Figure F-21: Q^2 CCQE Model Errors



(a) Carbon/Scintillator

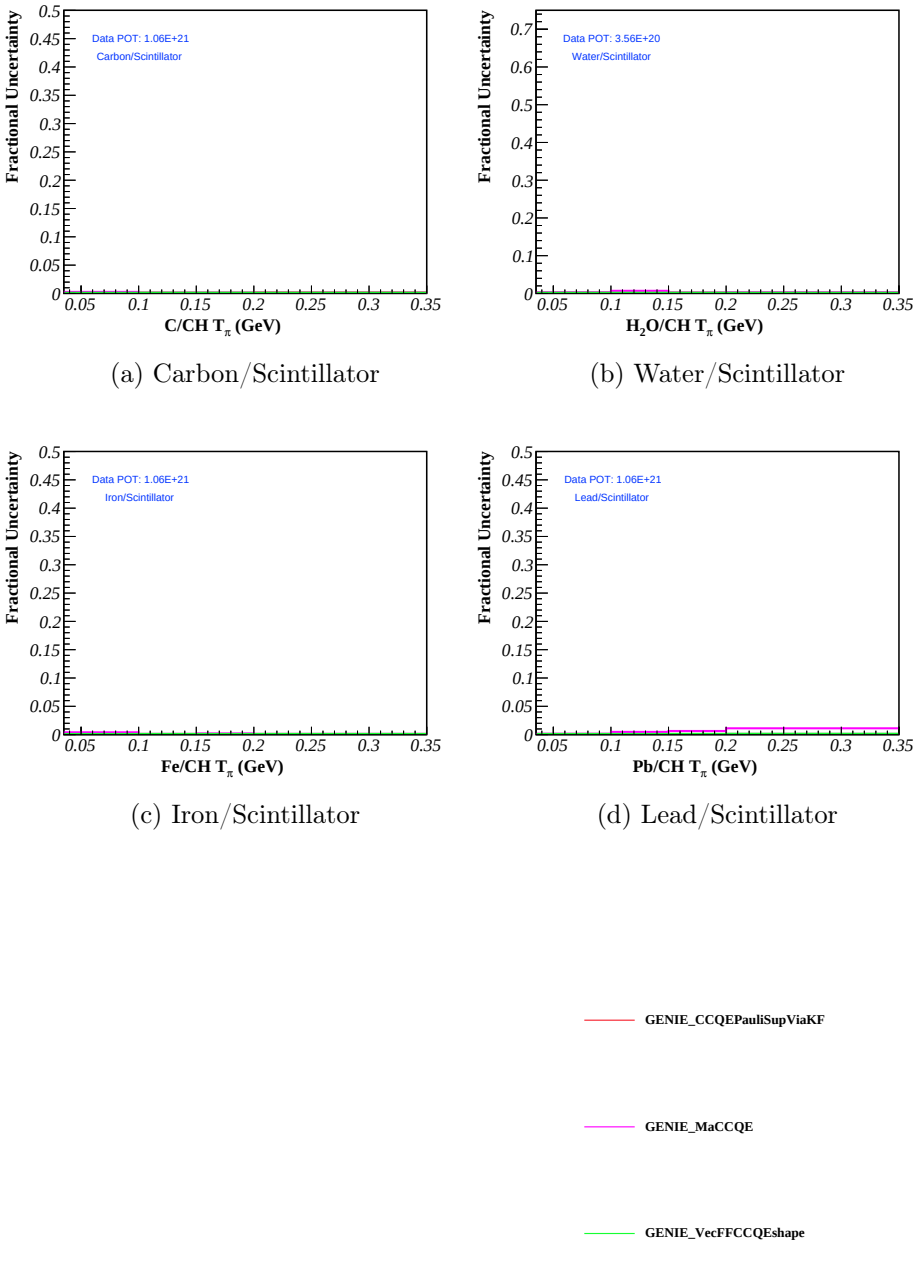
(b) Water/Scintillator

(c) Iron/Scintillator

(d) Lead/Scintillator

3

Figure F-22: W_{exp} CCQE Model Errors



(a) Carbon/Scintillator

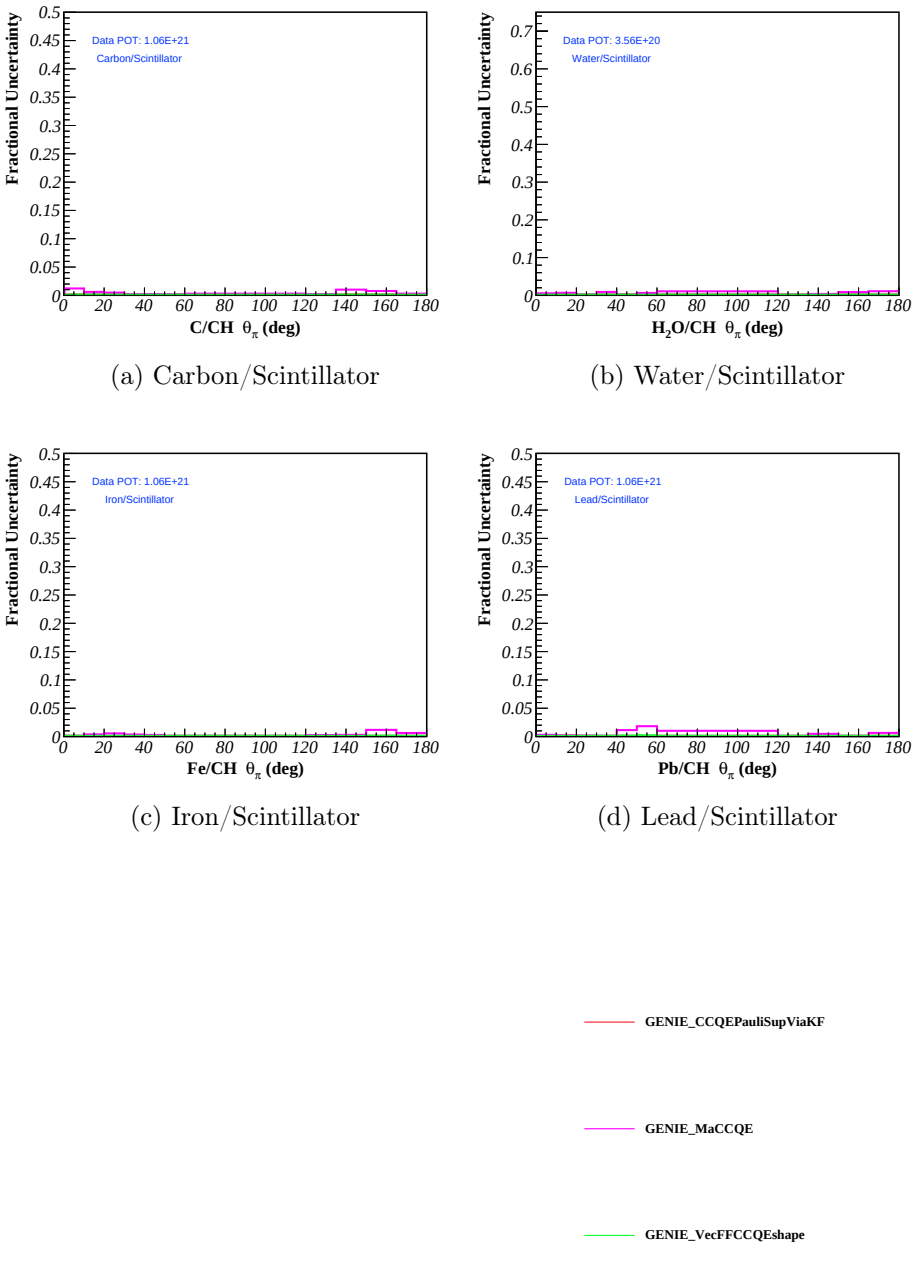
(b) Water/Scintillator

(c) Iron/Scintillator

(d) Lead/Scintillator

3

Figure F-23: T_π CCQE Model Errors



(a) Carbon/Scintillator

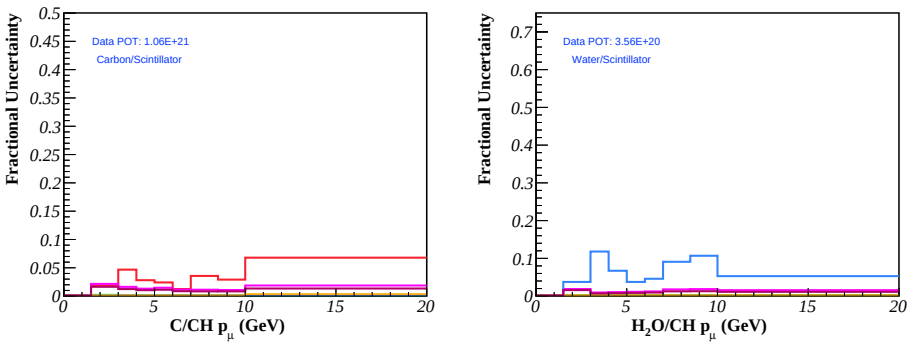
(b) Water/Scintillator

(c) Iron/Scintillator

(d) Lead/Scintillator

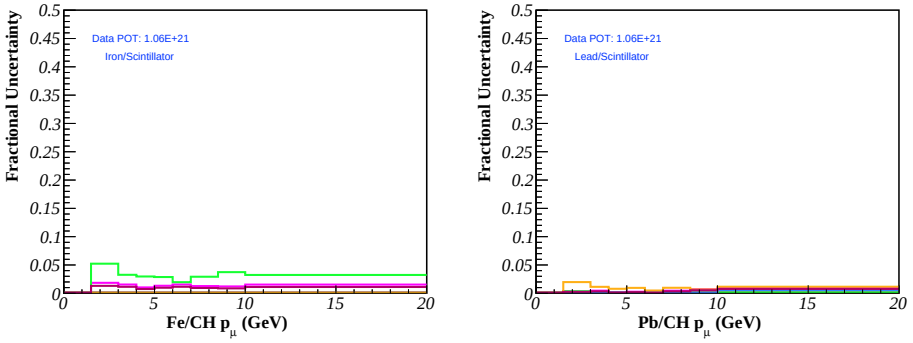
3

Figure F-24: θ_π CCQE Model Errors



(a) Carbon/Scintillator

(b) Water/Scintillator



(c) Iron/Scintillator

(d) Lead/Scintillator

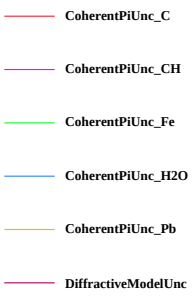
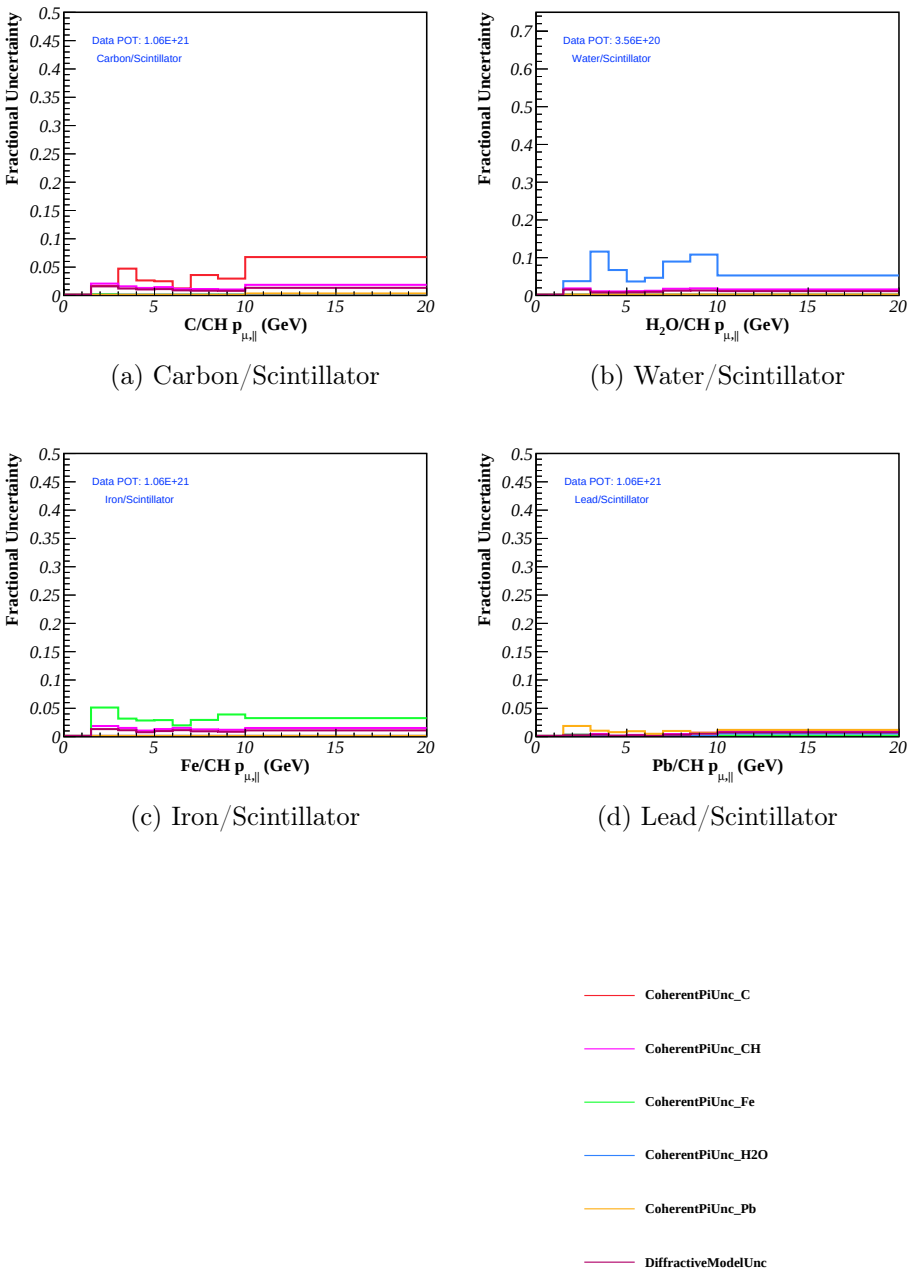


Figure F-25: p_μ Coherent/Diffractive π Model Errors



(a) Carbon/Scintillator

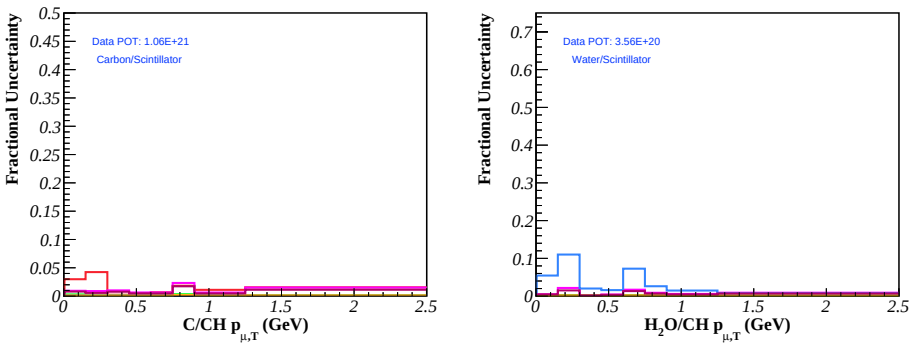
(b) Water/Scintillator

(c) Iron/Scintillator

(d) Lead/Scintillator

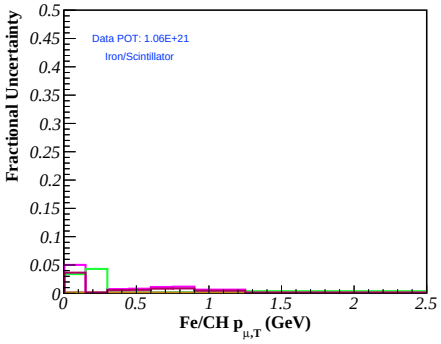
8

Figure F-26: $p_{\mu,||}$ Coherent/Diffractive π Model Errors

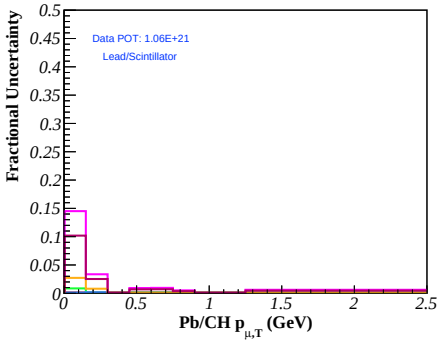


(a) Carbon/Scintillator

(b) Water/Scintillator



(c) Iron/Scintillator



(d) Lead/Scintillator

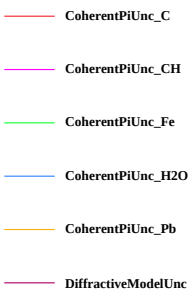
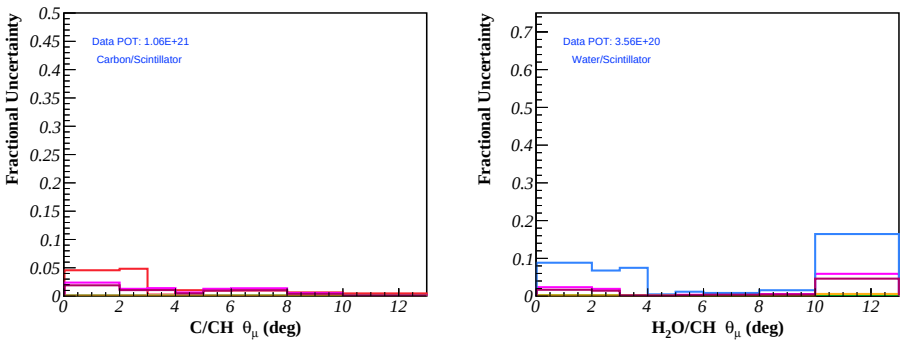
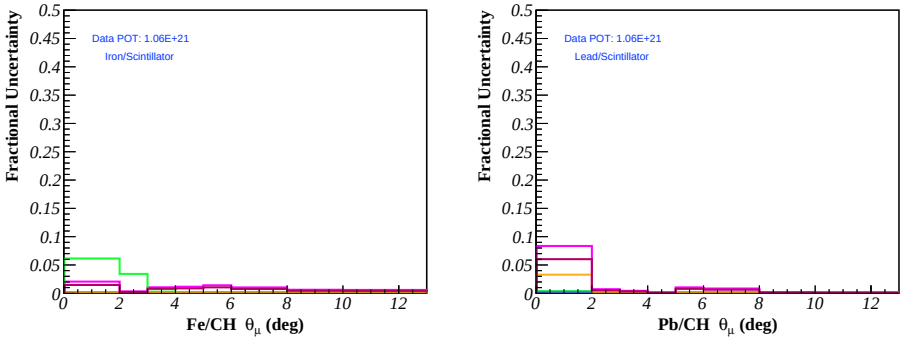


Figure F-27: $p_{\mu,T}$ Coherent/Diffractive π Model Errors



(a) Carbon/Scintillator

(b) Water/Scintillator



(c) Iron/Scintillator

(d) Lead/Scintillator

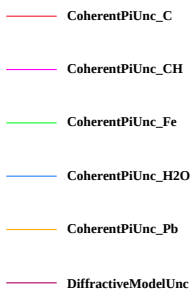
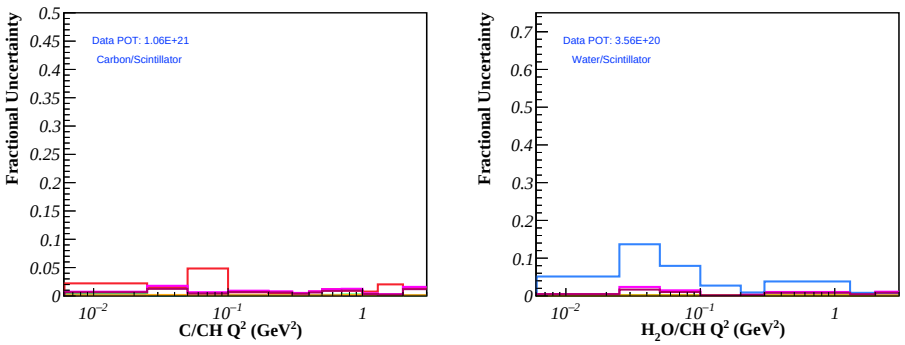
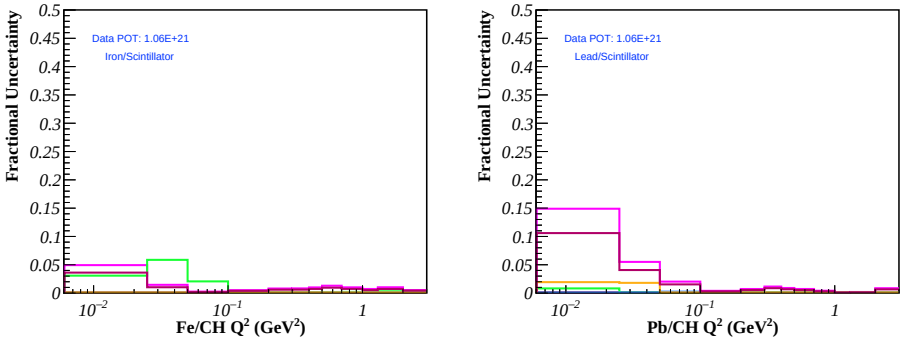


Figure F-28: θ_μ Coherent/Diffractive π Model Errors



(a) Carbon/Scintillator

(b) Water/Scintillator



(c) Iron/Scintillator

(d) Lead/Scintillator

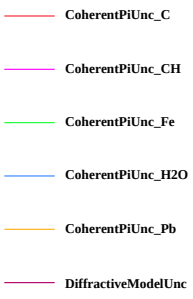
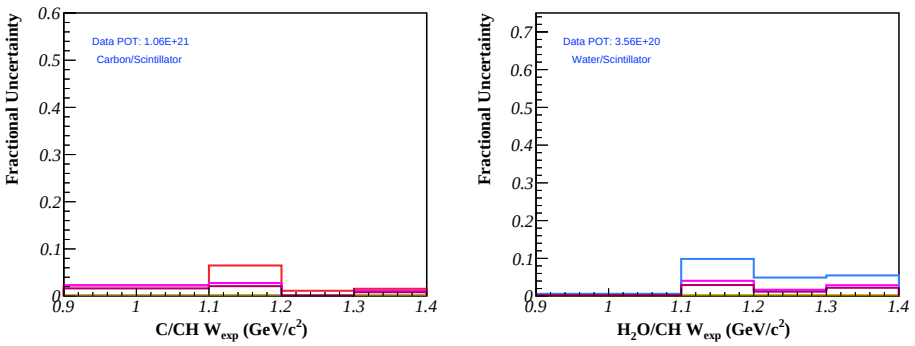
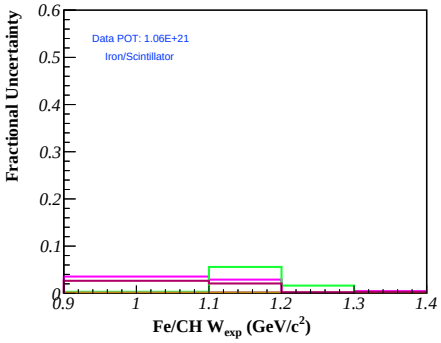


Figure F-29: Q^2 Coherent/Diffractive π Model Errors

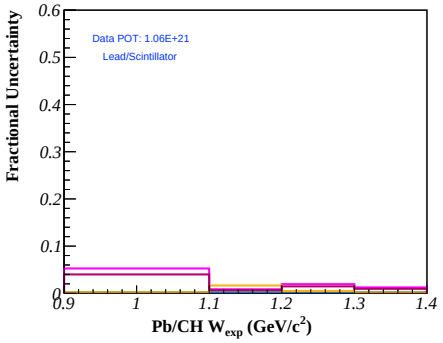


(a) Carbon/Scintillator

(b) Water/Scintillator



(c) Iron/Scintillator



(d) Lead/Scintillator

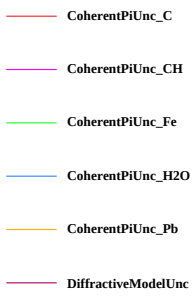
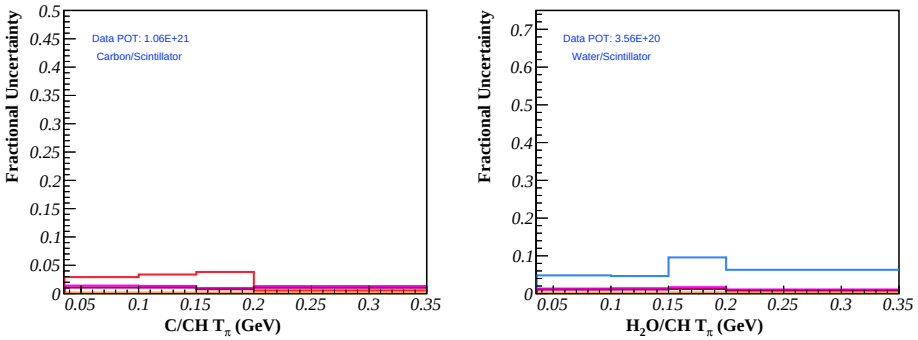


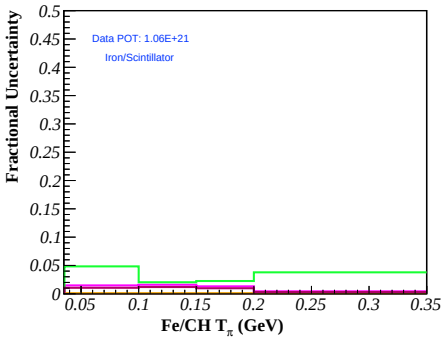
Figure F-30: W_{exp} Coherent/Diffractive π Model Errors

8

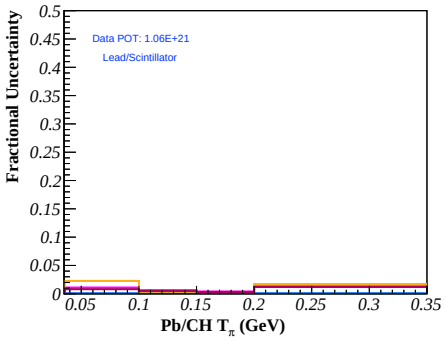


(a) Carbon/Scintillator

(b) Water/Scintillator



(c) Iron/Scintillator



(d) Lead/Scintillator

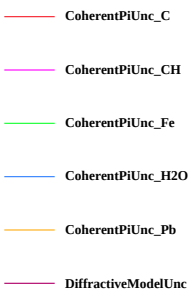
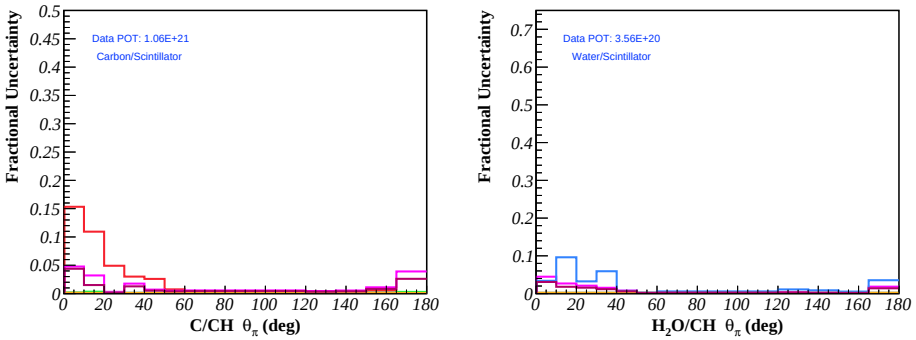


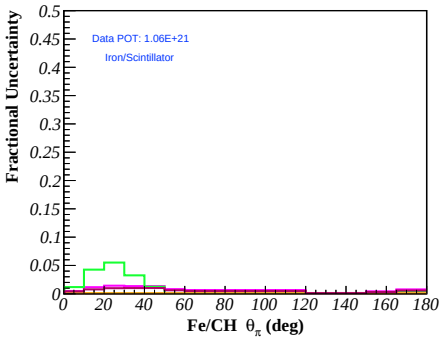
Figure F-31: T_π Coherent/Diffractive π Model Errors

8

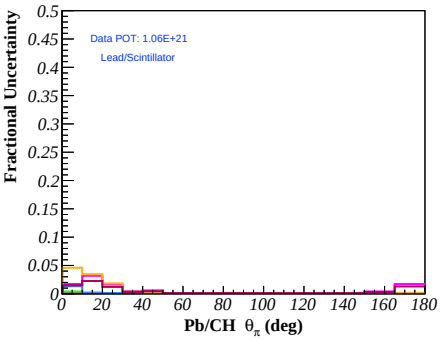


(a) Carbon/Scintillator

(b) Water/Scintillator



(c) Iron/Scintillator



(d) Lead/Scintillator

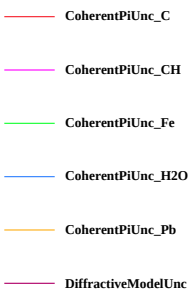
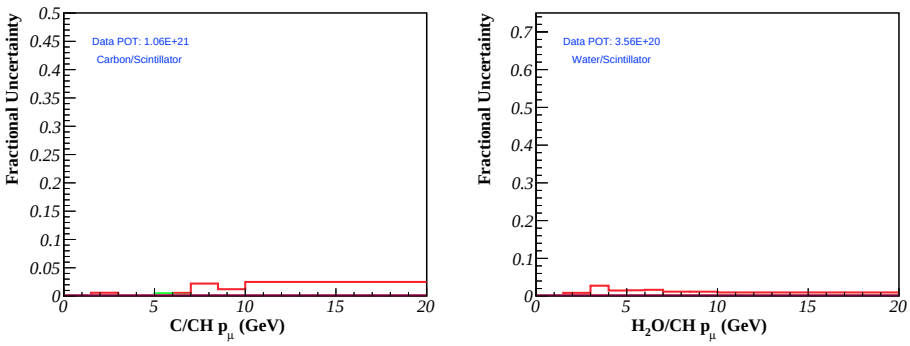
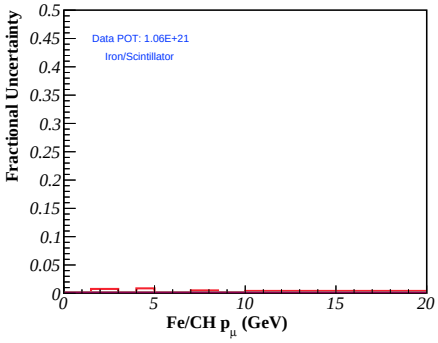


Figure F-32: θ_π Coherent/Diffractive π Model Errors

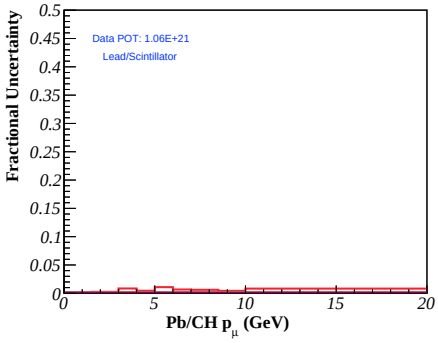


(a) Carbon/Scintillator

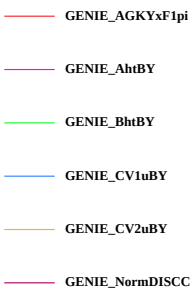
(b) Water/Scintillator



(c) Iron/Scintillator

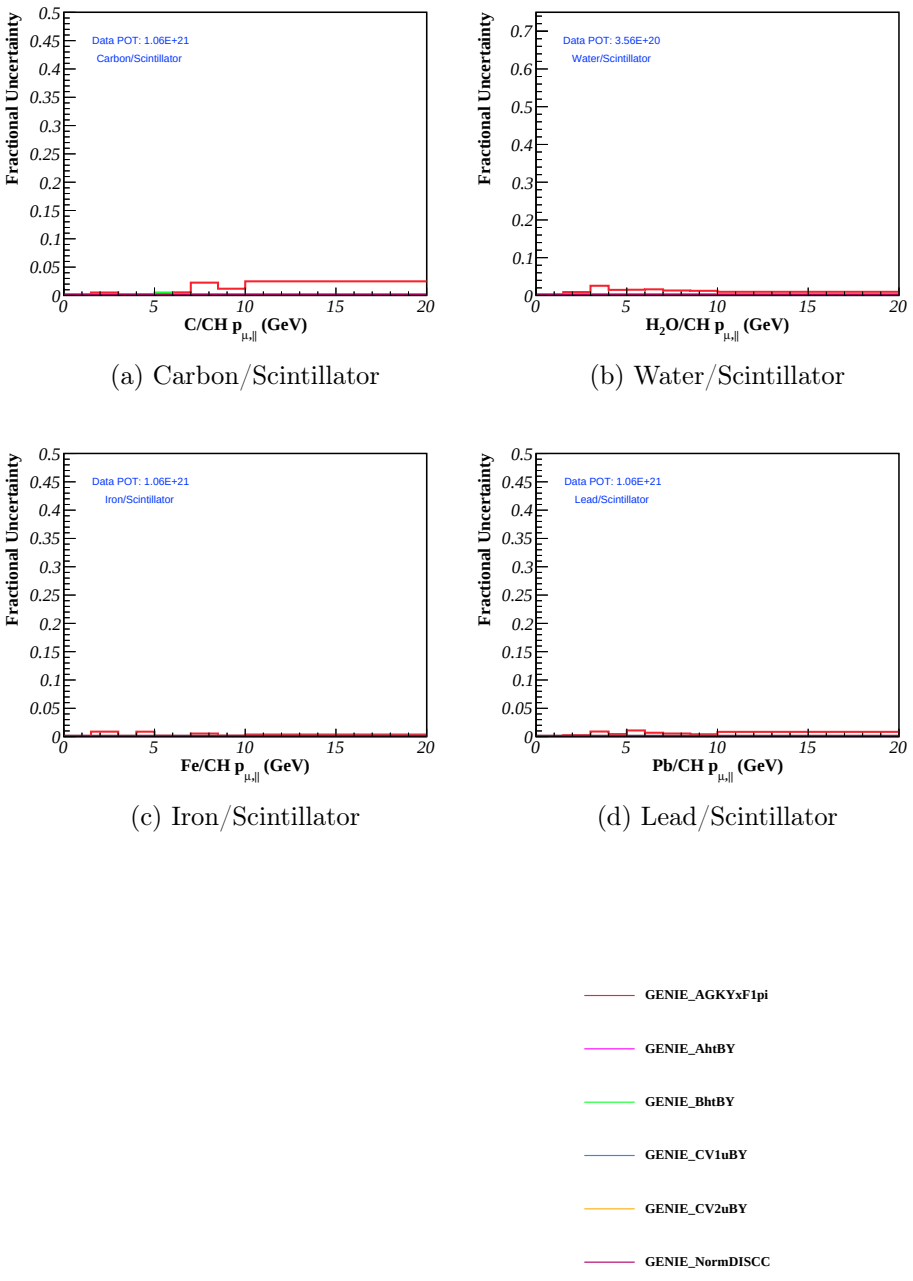


(d) Lead/Scintillator



2

Figure F-33: p_μ DIS/Hadronization Model Errors



(a) Carbon/Scintillator

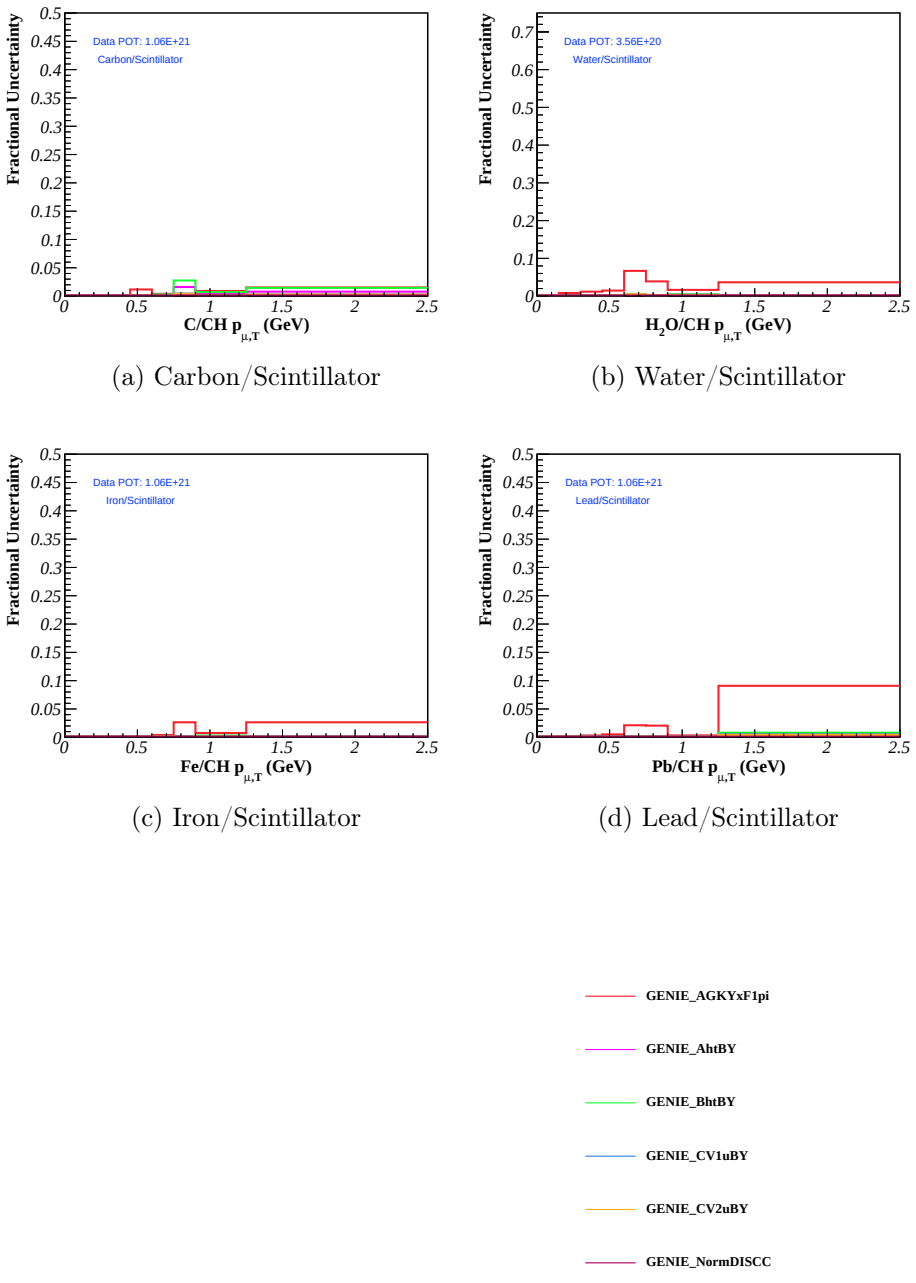
(b) Water/Scintillator

(c) Iron/Scintillator

(d) Lead/Scintillator

2

Figure F-34: $p_{\mu,||}$ DIS/Hadronization Model Errors



(a) Carbon/Scintillator

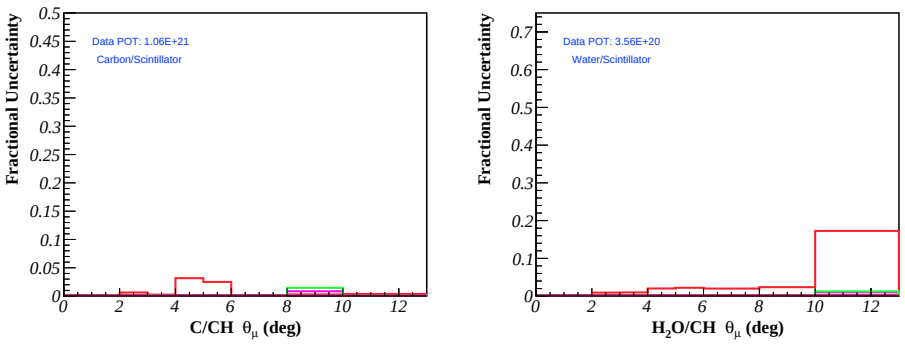
(b) Water/Scintillator

(c) Iron/Scintillator

(d) Lead/Scintillator

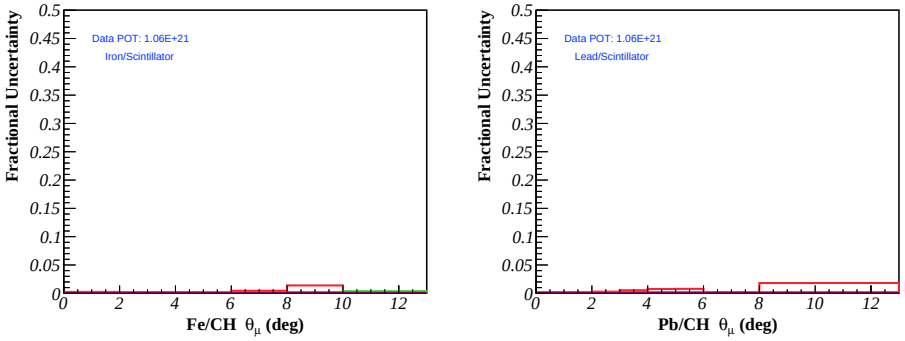
2

Figure F-35: $p_{\mu,T}$ DIS/Hadronization Model Errors



(a) Carbon/Scintillator

(b) Water/Scintillator



(c) Iron/Scintillator

(d) Lead/Scintillator

2

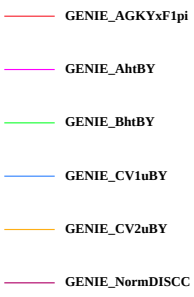
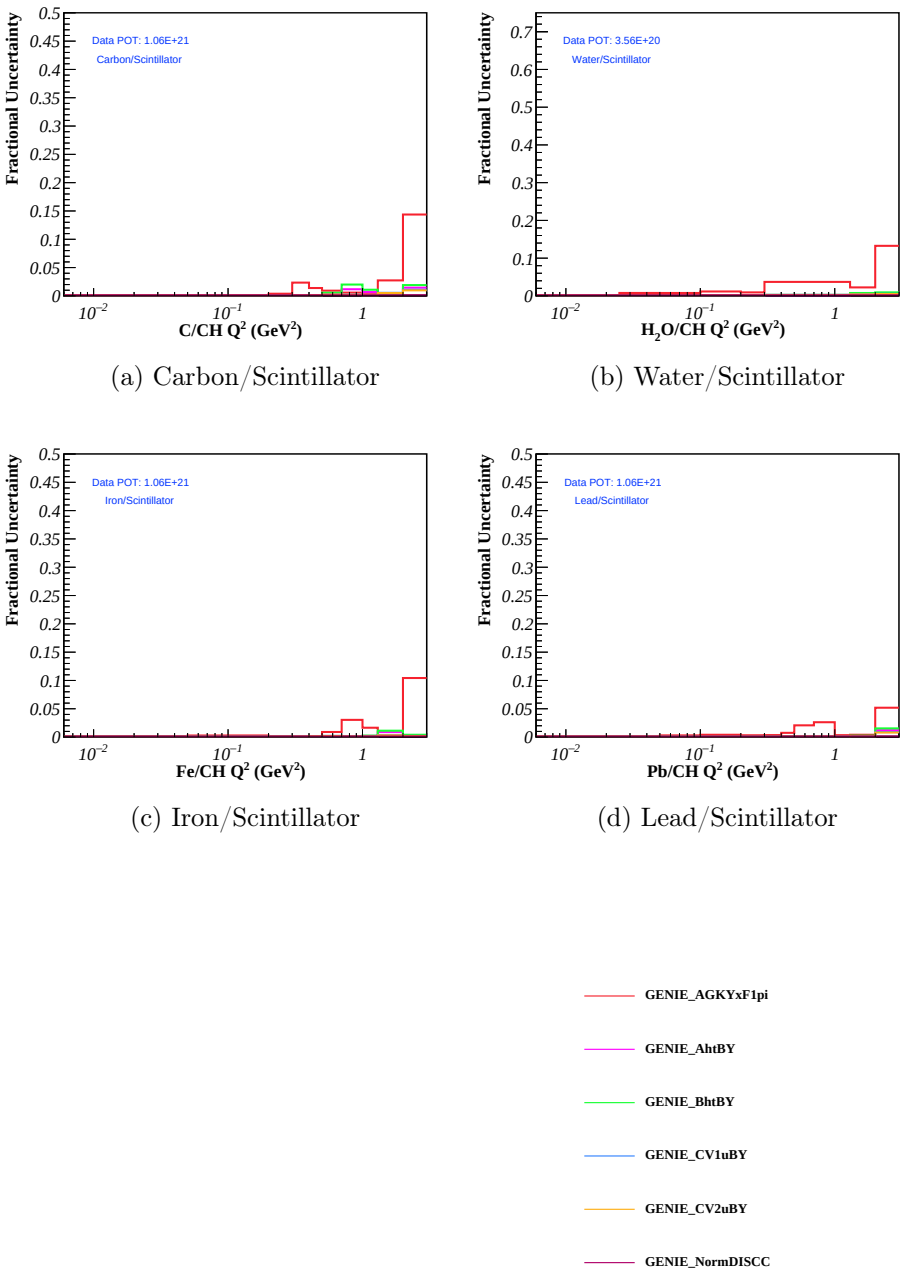


Figure F-36: θ_μ DIS/Hadronization Model Errors



(a) Carbon/Scintillator

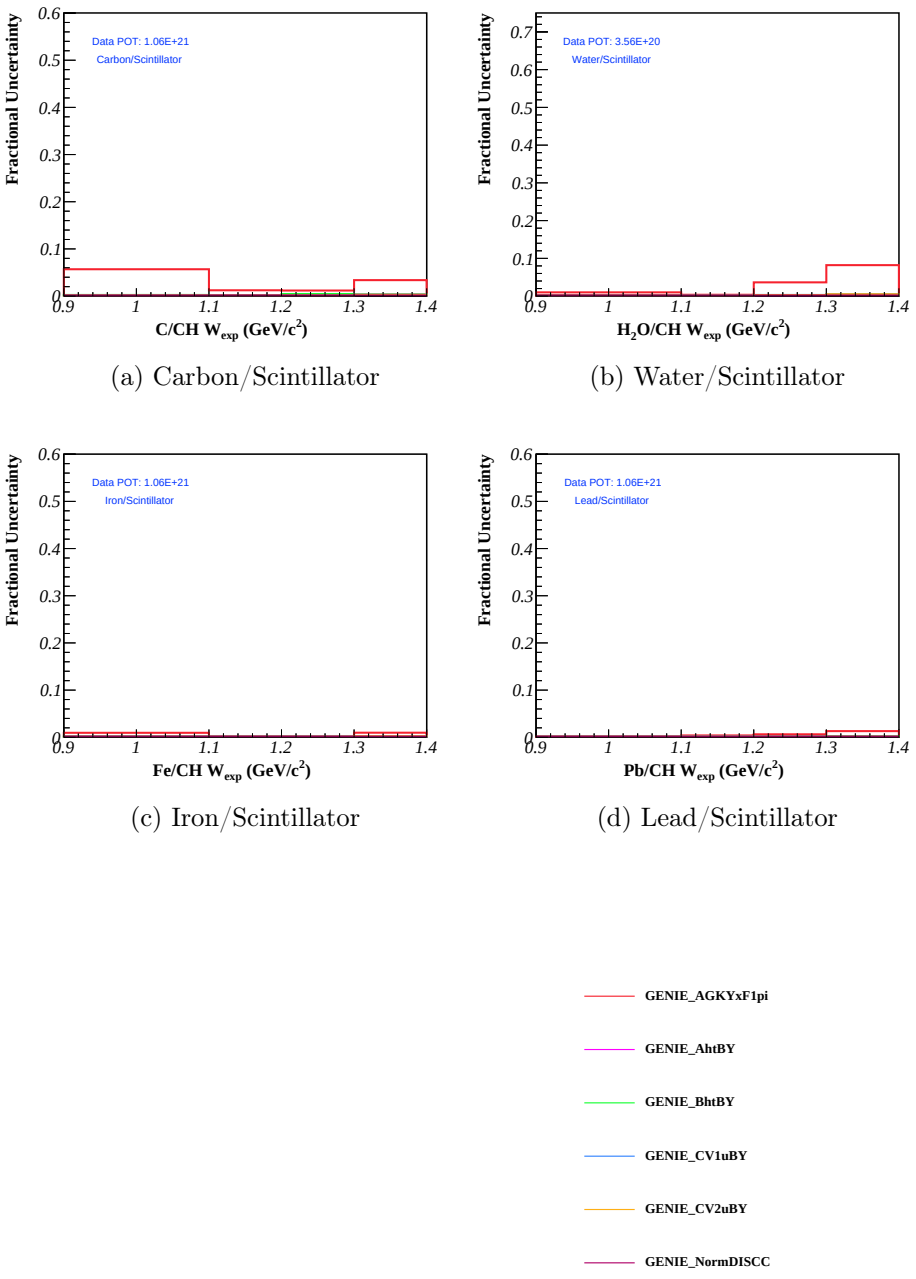
(b) Water/Scintillator

(c) Iron/Scintillator

(d) Lead/Scintillator

2

Figure F-37: Q^2 DIS/Hadronization Model Errors



(a) Carbon/Scintillator

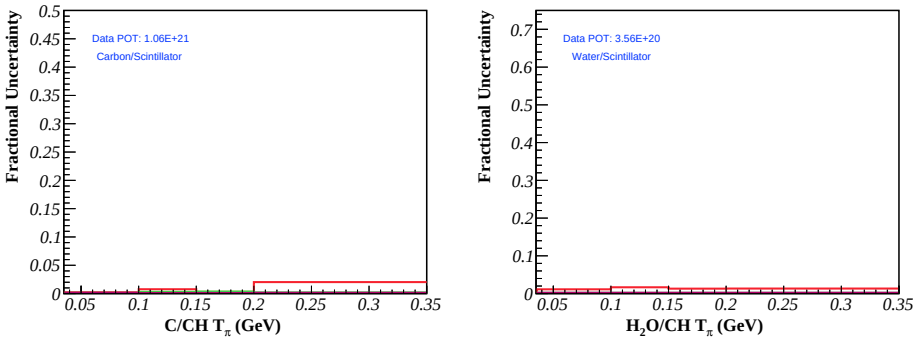
(b) Water/Scintillator

(c) Iron/Scintillator

(d) Lead/Scintillator

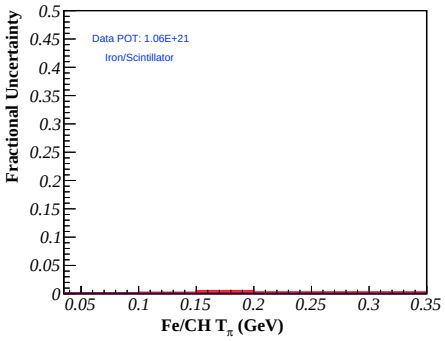
2

Figure F-38: W_{exp} DIS/Hadronization Model Errors

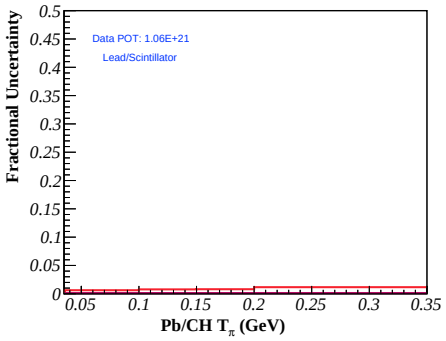


(a) Carbon/Scintillator

(b) Water/Scintillator



(c) Iron/Scintillator



(d) Lead/Scintillator

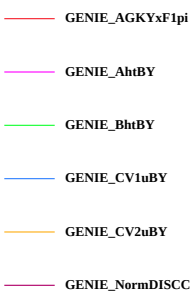
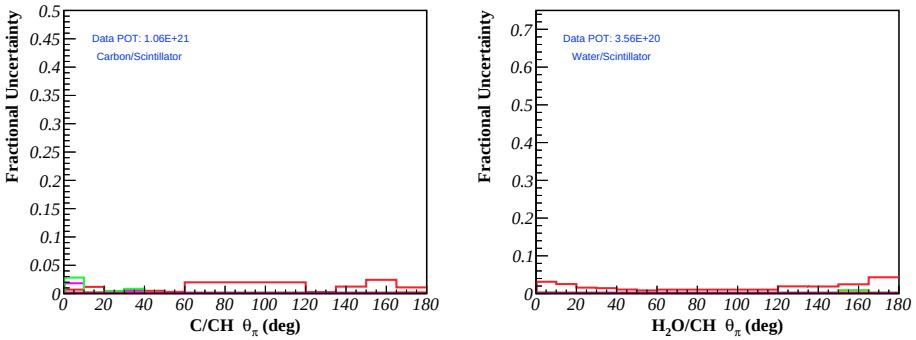


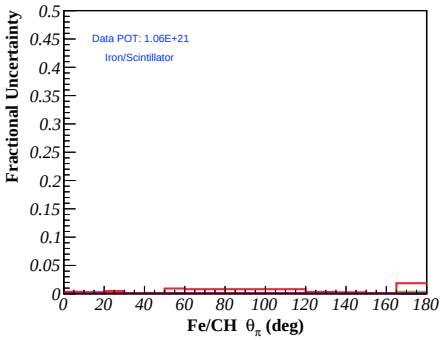
Figure F-39: T_π DIS/Hadronization Model Errors

2

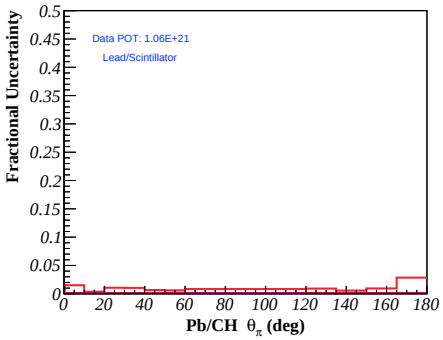


(a) Carbon/Scintillator

(b) Water/Scintillator



(c) Iron/Scintillator



(d) Lead/Scintillator

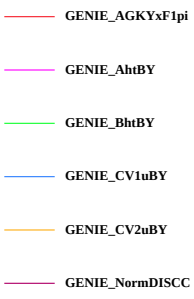
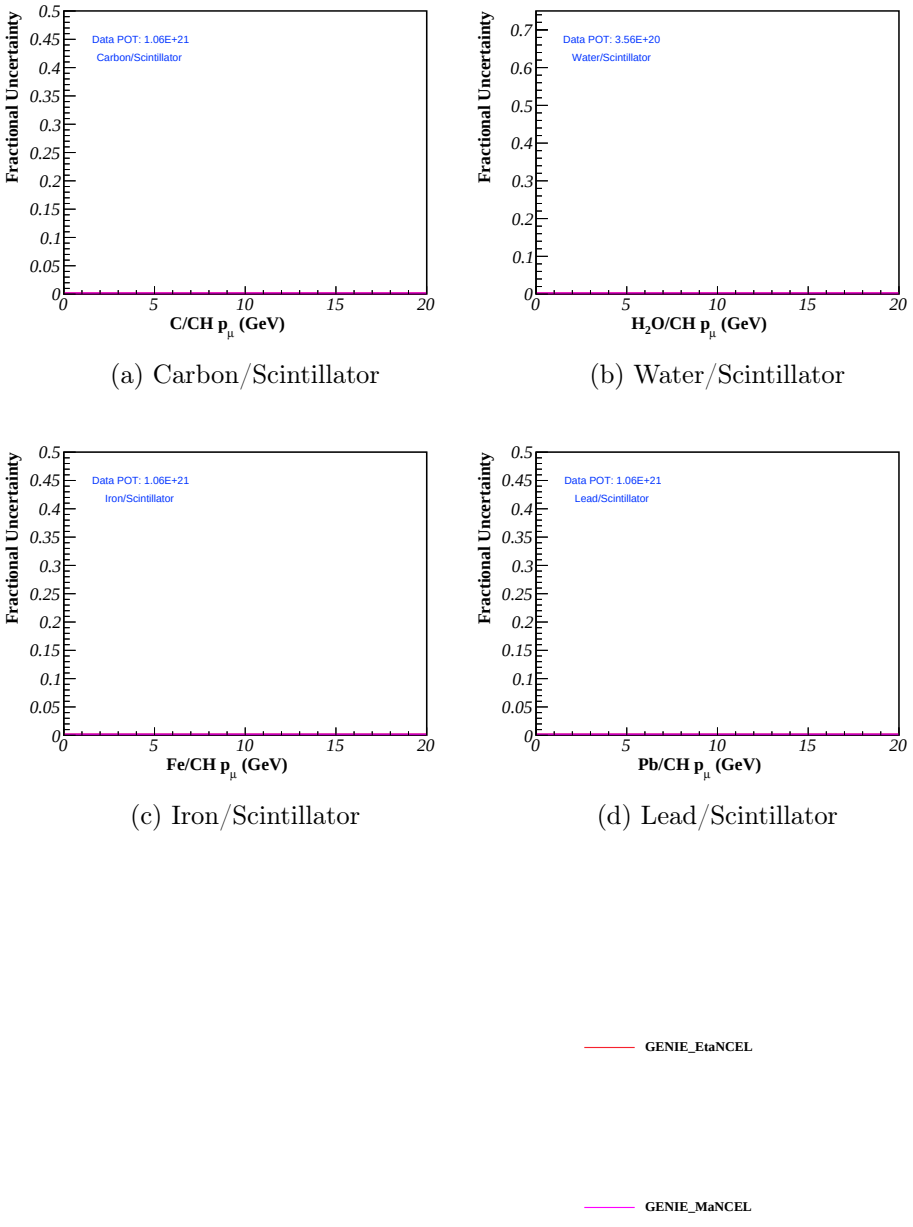


Figure F-40: θ_π DIS/Hadronization Model Errors

2



(a) Carbon/Scintillator

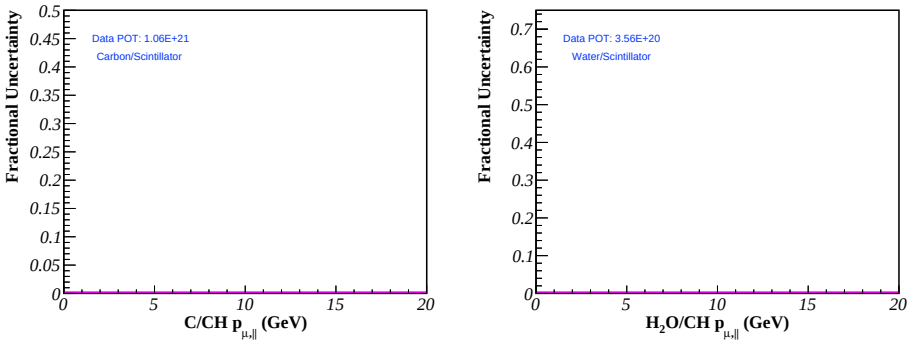
(b) Water/Scintillator

(c) Iron/Scintillator

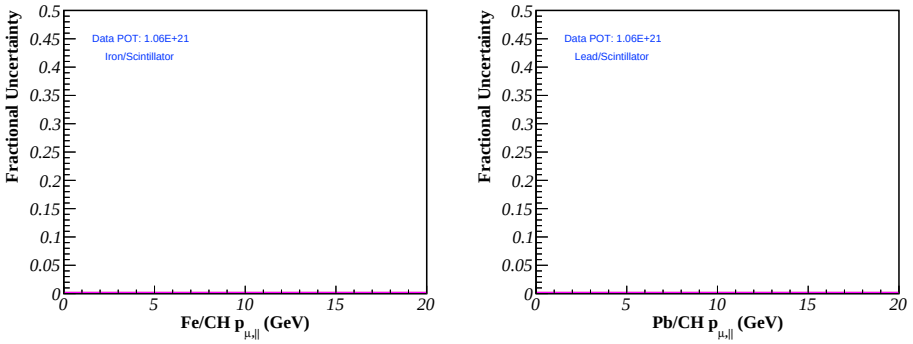
(d) Lead/Scintillator

4

Figure F-41: p_μ Elastic Scattering Model Errors



(a) Carbon/Scintillator (b) Water/Scintillator

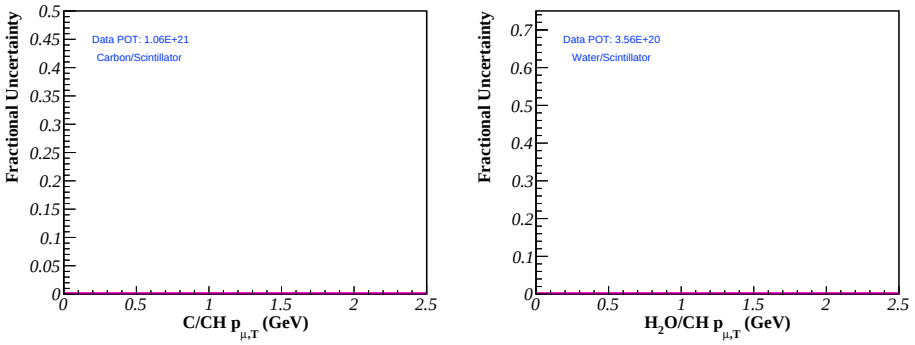


(c) Iron/Scintillator (d) Lead/Scintillator

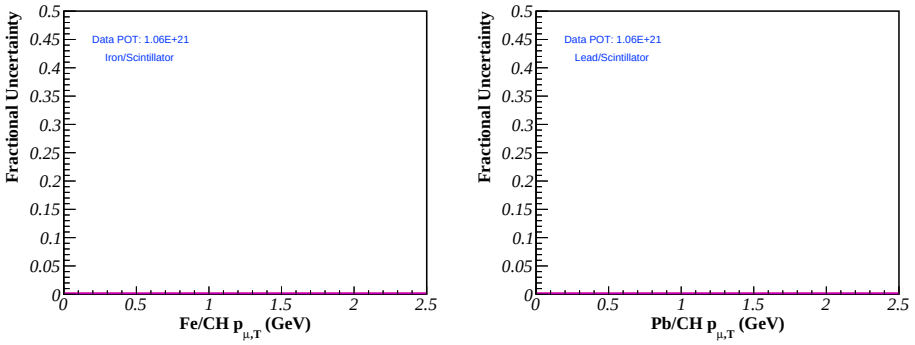
4



Figure F-42: $p_{\mu,||}$ Elastic Scattering Model Errors



(a) Carbon/Scintillator (b) Water/Scintillator

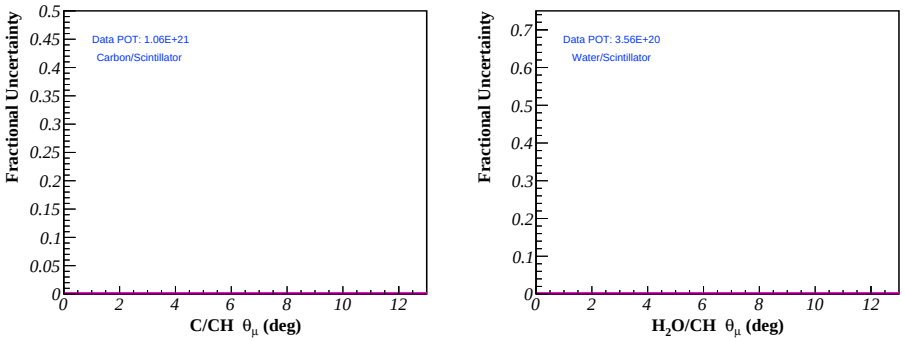


(c) Iron/Scintillator (d) Lead/Scintillator

4

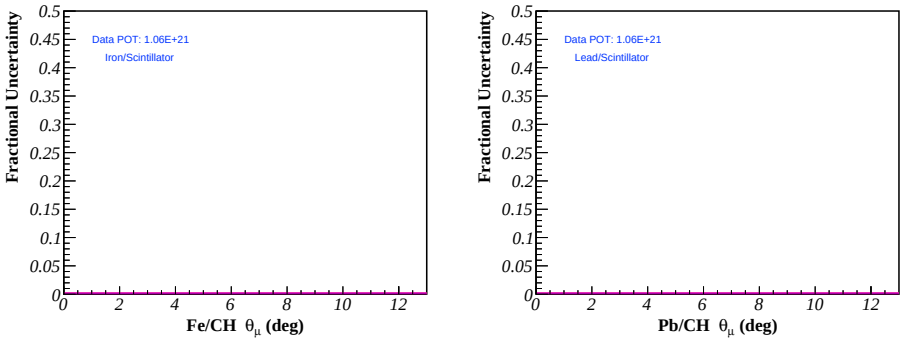


Figure F-43: $p_{\mu,T}$ Elastic Scattering Model Errors



(a) Carbon/Scintillator

(b) Water/Scintillator



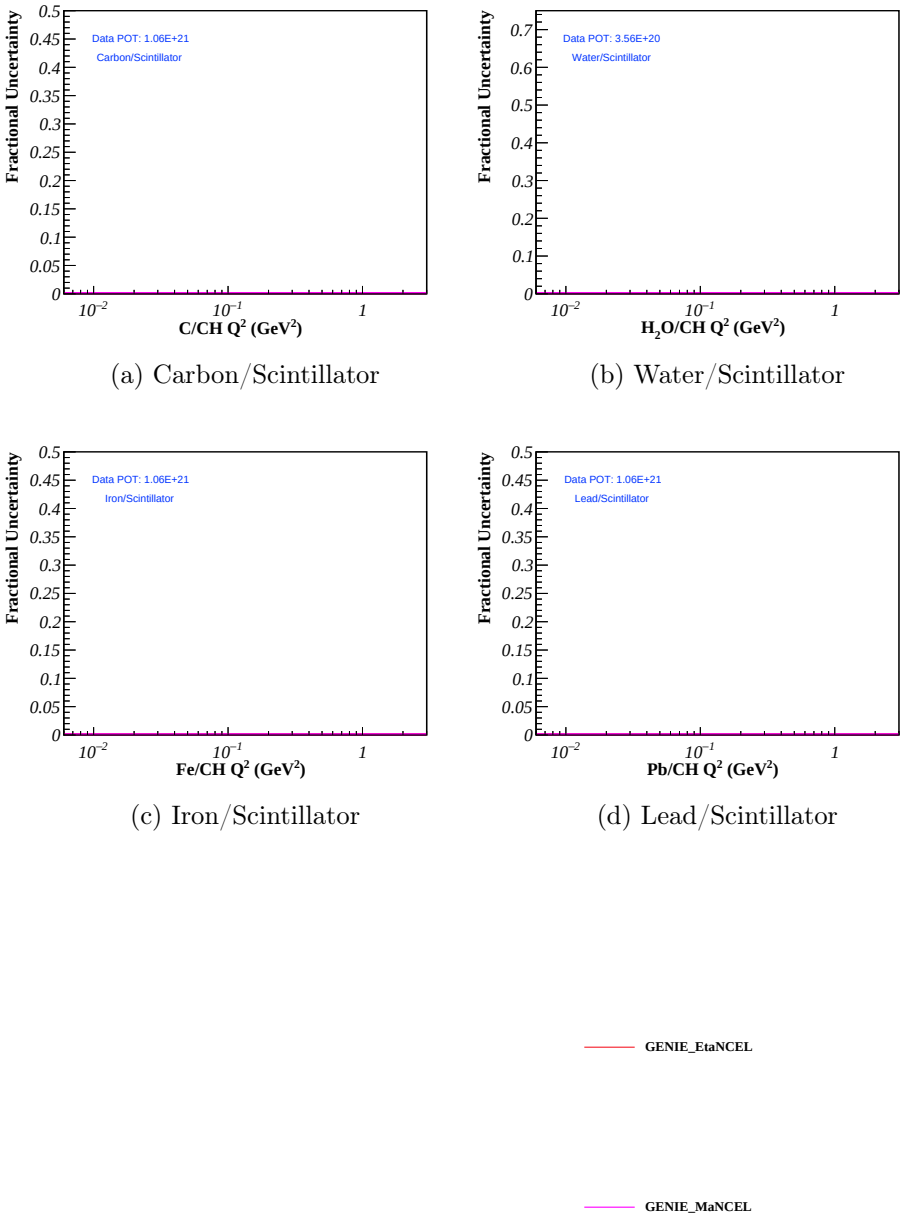
(c) Iron/Scintillator

(d) Lead/Scintillator

4



Figure F-44: θ_μ Elastic Scattering Model Errors



(a) Carbon/Scintillator

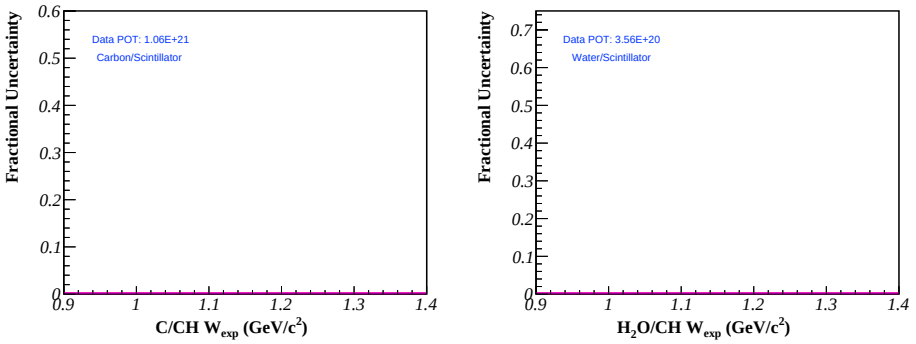
(b) Water/Scintillator

(c) Iron/Scintillator

(d) Lead/Scintillator

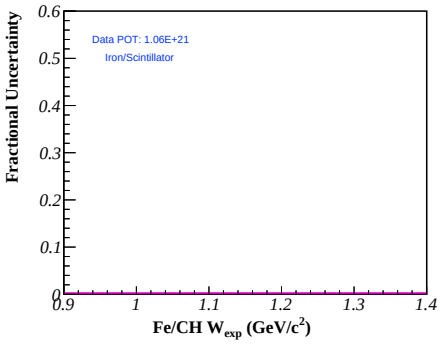
4

Figure F-45: Q^2 Elastic Scattering Model Errors

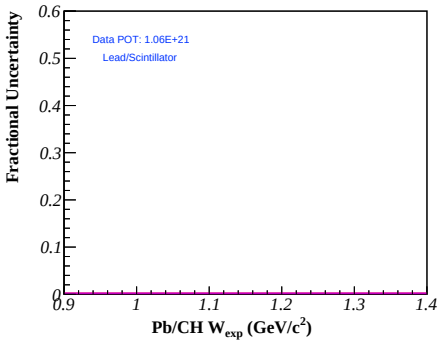


(a) Carbon/Scintillator

(b) Water/Scintillator



(c) Iron/Scintillator

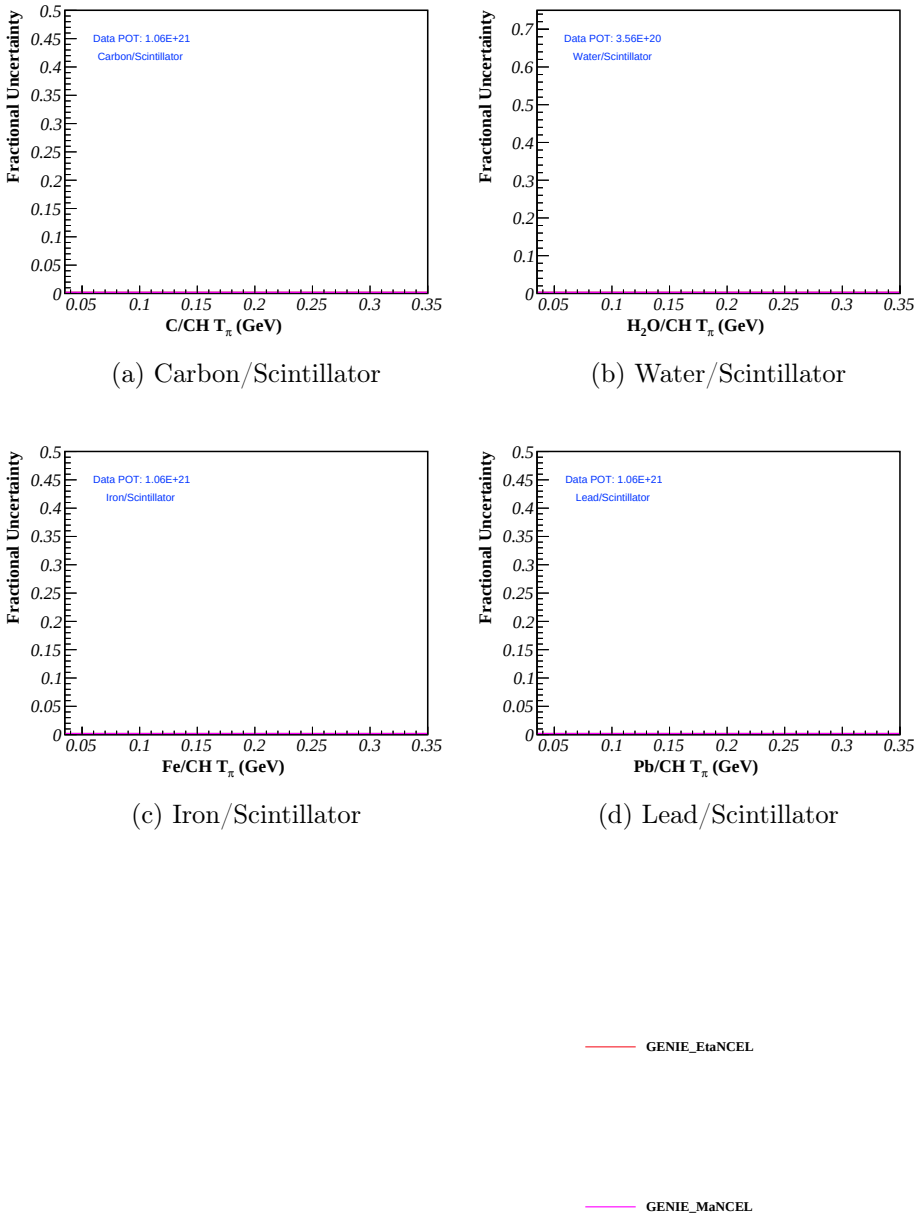


(d) Lead/Scintillator

4



Figure F-46: W_{exp} Elastic Scattering Model Errors



(a) Carbon/Scintillator

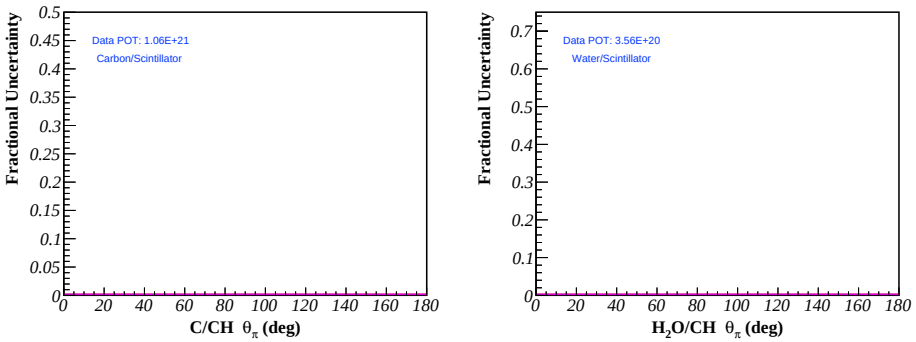
(b) Water/Scintillator

(c) Iron/Scintillator

(d) Lead/Scintillator

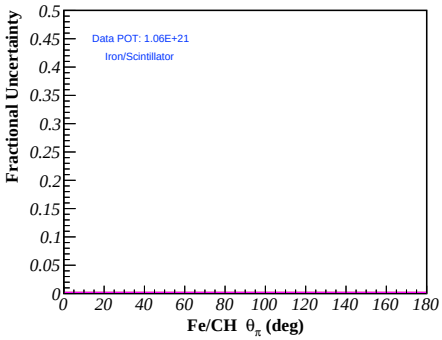
4

Figure F-47: T_π Elastic Scattering Model Errors

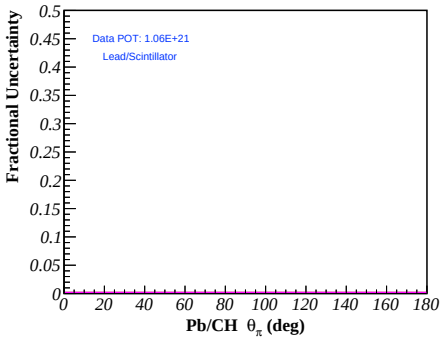


(a) Carbon/Scintillator

(b) Water/Scintillator



(c) Iron/Scintillator

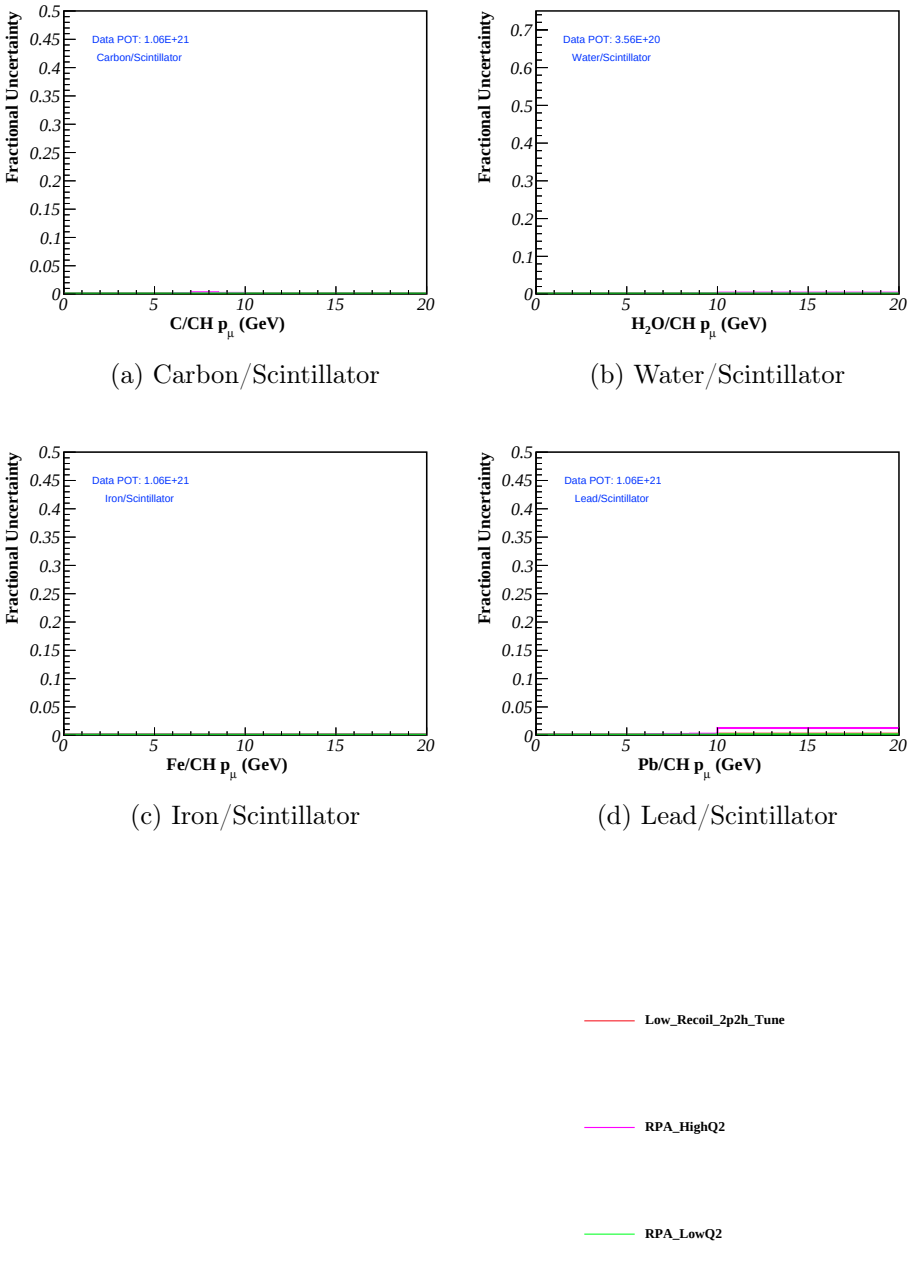


(d) Lead/Scintillator

4



Figure F-48: θ_π Elastic Scattering Model Errors



(a) Carbon/Scintillator

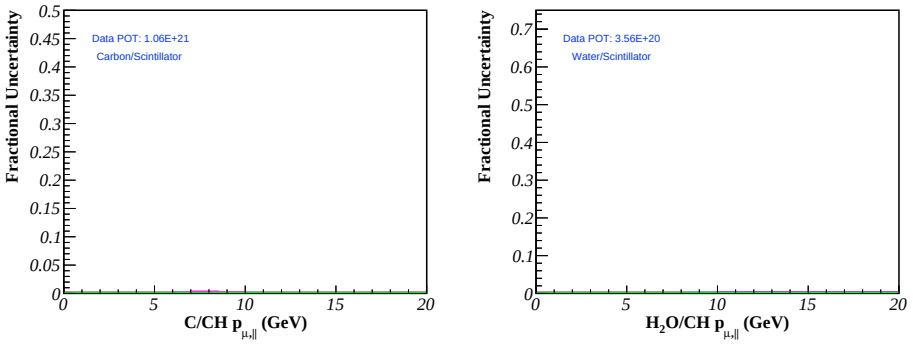
(b) Water/Scintillator

(c) Iron/Scintillator

(d) Lead/Scintillator

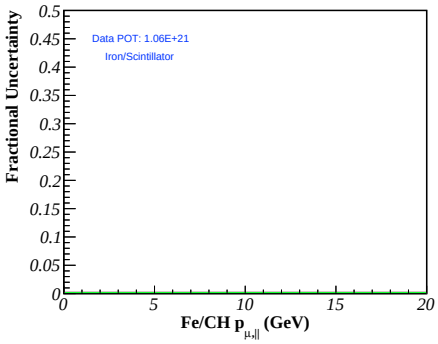
7

Figure F-49: p_μ MnvTune Model Errors

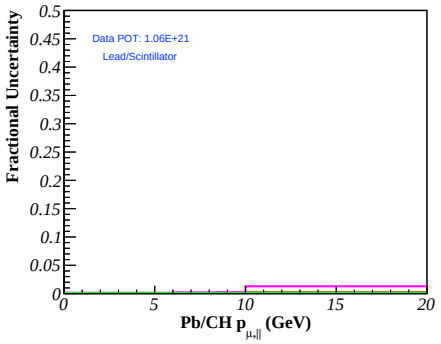


(a) Carbon/Scintillator

(b) Water/Scintillator



(c) Iron/Scintillator



(d) Lead/Scintillator

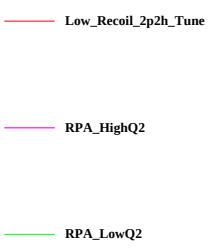
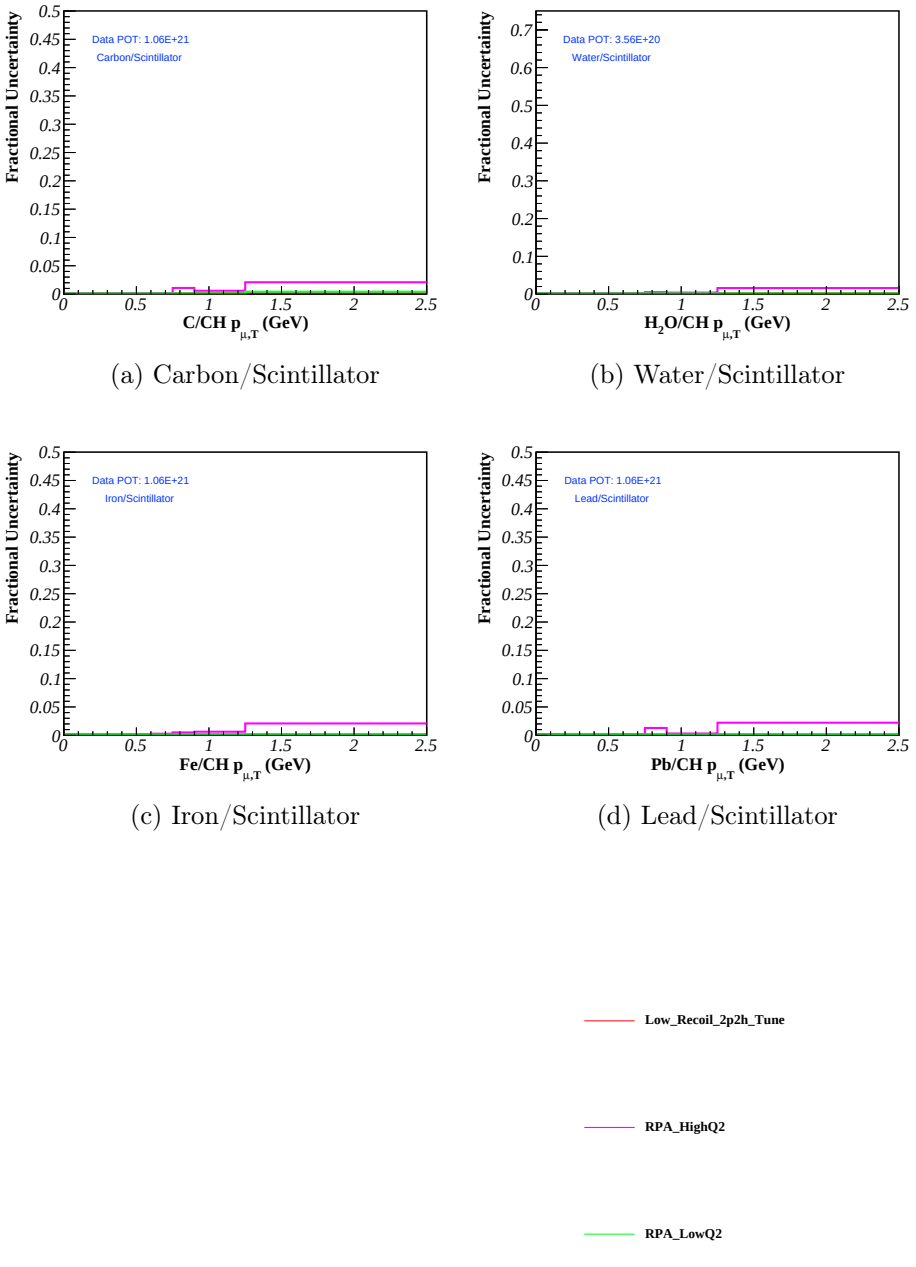


Figure F-50: $p_{\mu,||}$ MnvTune Model Errors



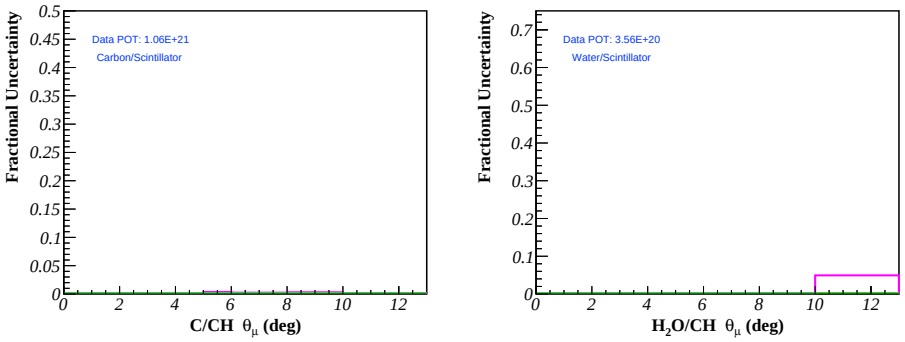
(a) Carbon/Scintillator

(b) Water/Scintillator

(c) Iron/Scintillator

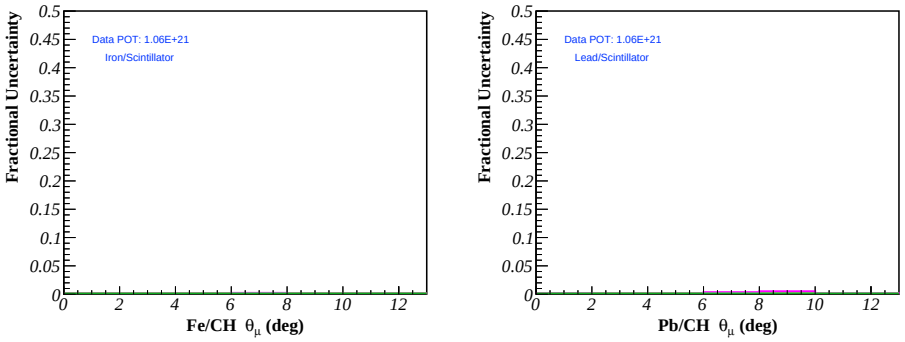
(d) Lead/Scintillator

Figure F-51: $p_{\mu,T}$ MnvTune Model Errors



(a) Carbon/Scintillator

(b) Water/Scintillator



(c) Iron/Scintillator

(d) Lead/Scintillator

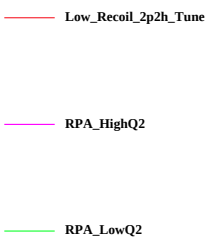


Figure F-52: θ_μ MnvTune Model Errors

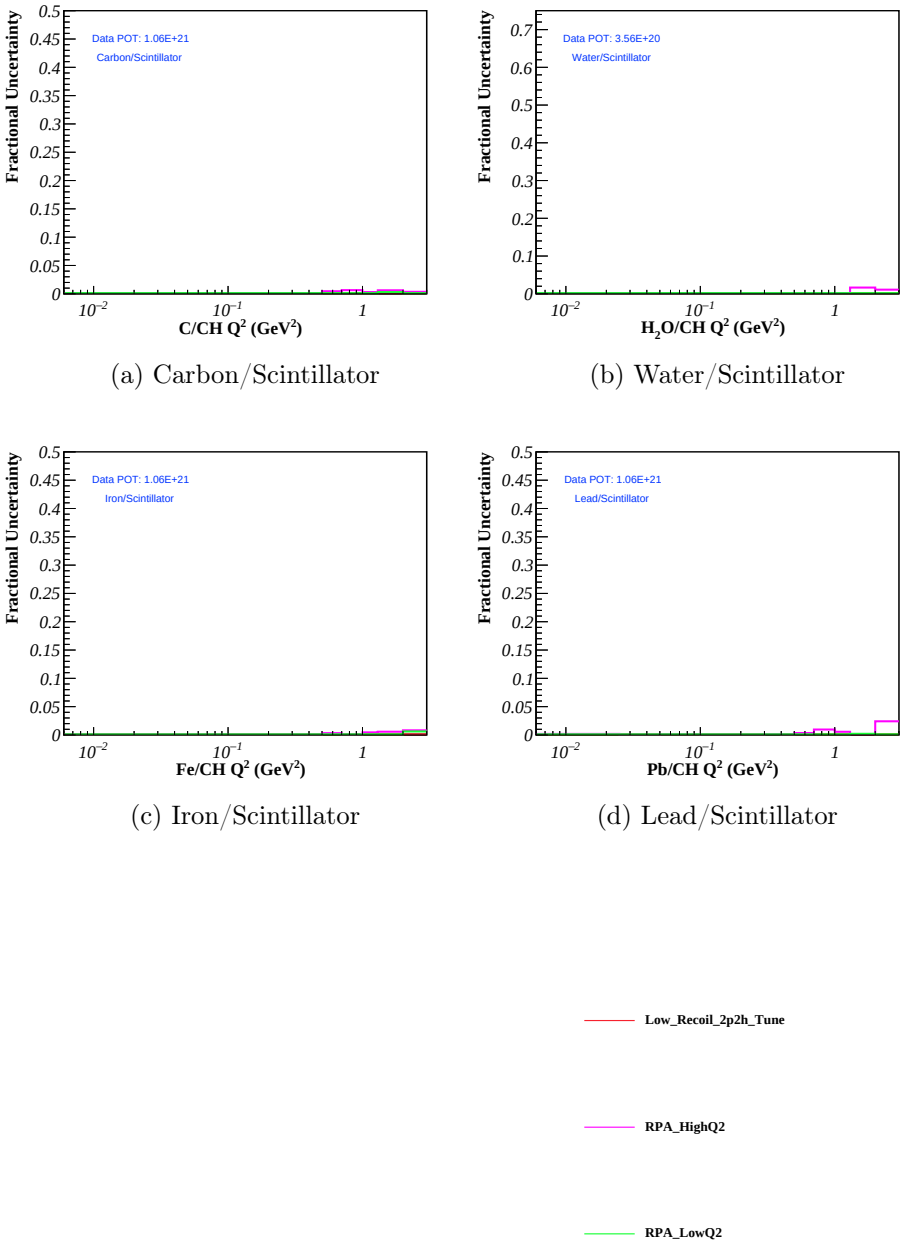
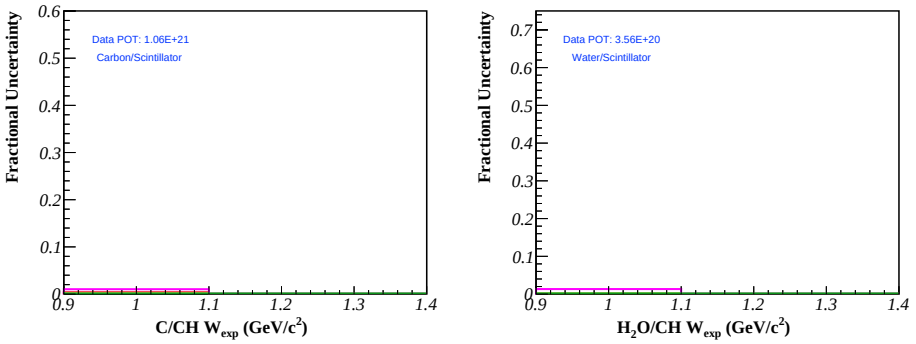
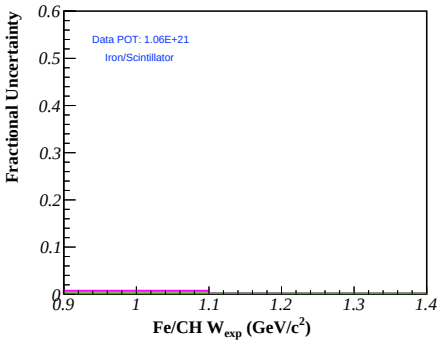


Figure F-53: Q^2 MnvTune Model Errors

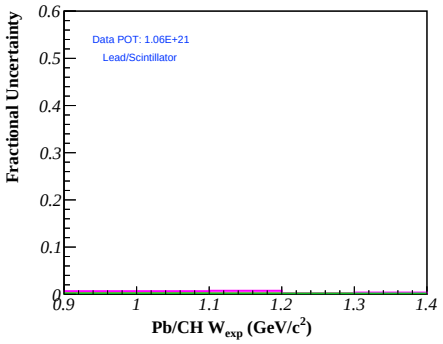


(a) Carbon/Scintillator

(b) Water/Scintillator



(c) Iron/Scintillator



(d) Lead/Scintillator

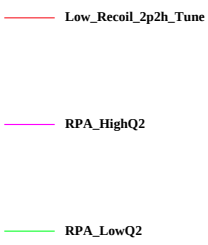
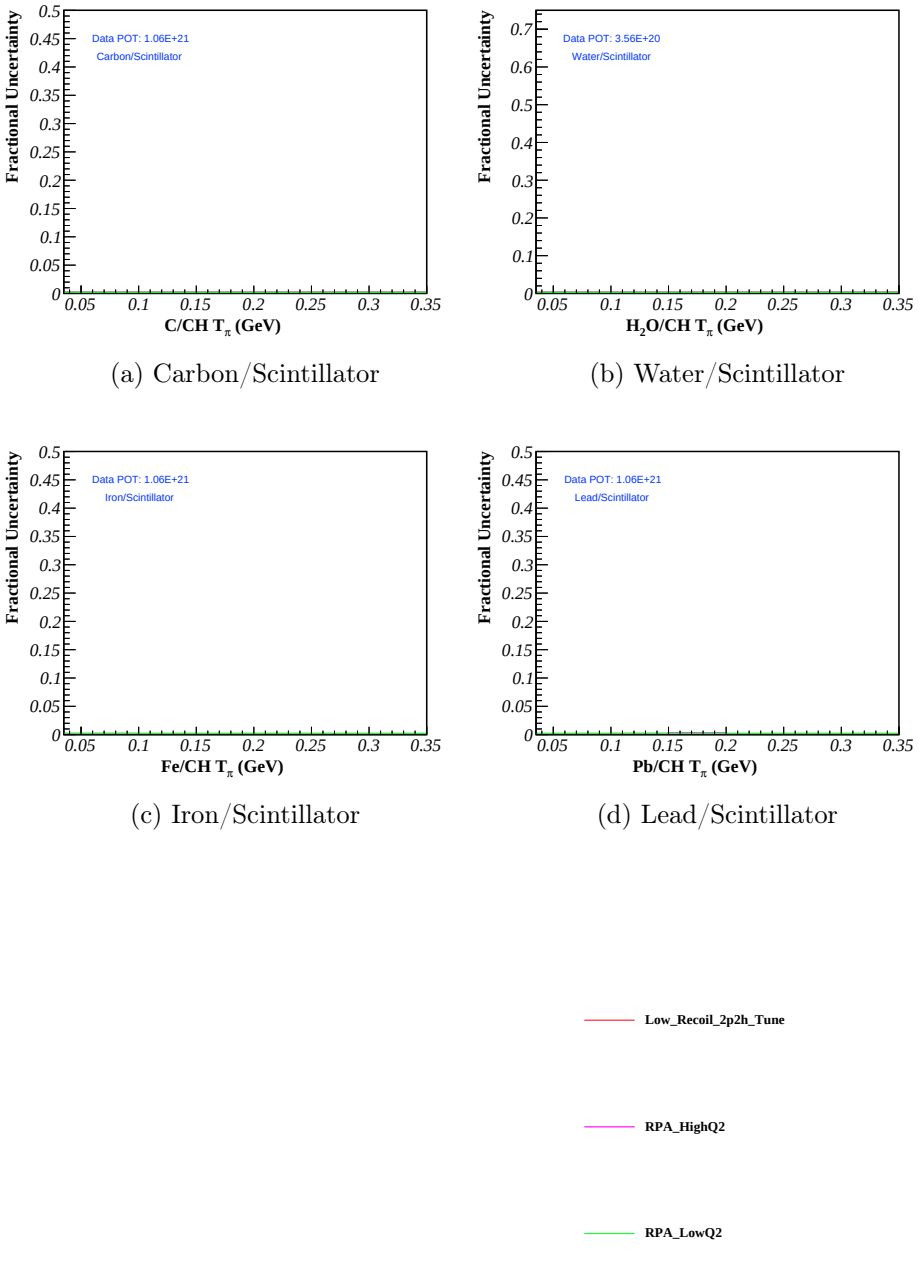


Figure F-54: W_{exp} MnvTune Model Errors



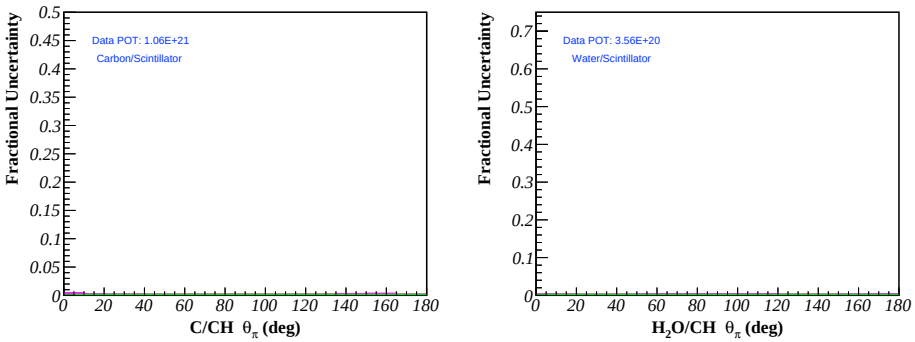
(a) Carbon/Scintillator

(b) Water/Scintillator

(c) Iron/Scintillator

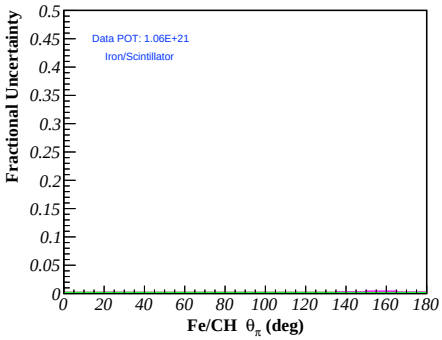
(d) Lead/Scintillator

Figure F-55: T_π MnvTune Model Errors

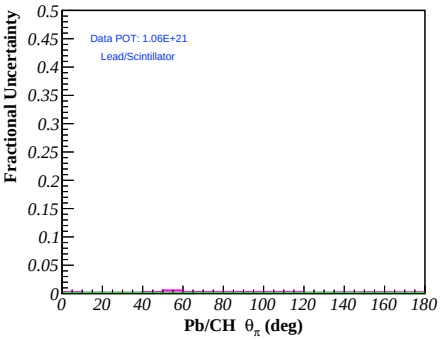


(a) Carbon/Scintillator

(b) Water/Scintillator



(c) Iron/Scintillator



(d) Lead/Scintillator

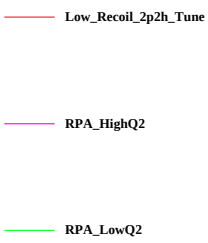
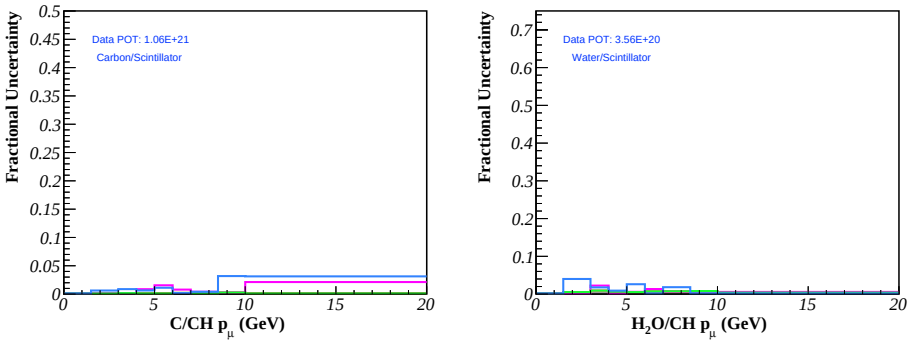
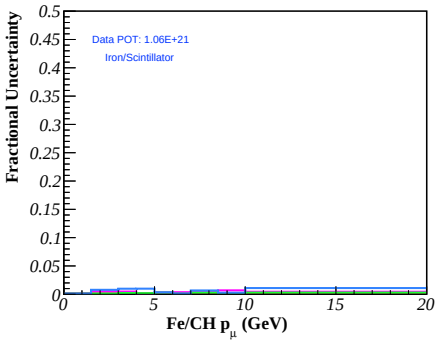


Figure F-56: θ_π MnvTune Model Errors

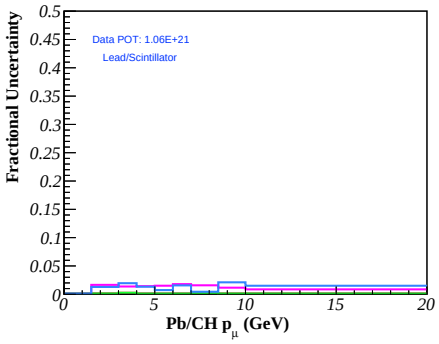


(a) Carbon/Scintillator

(b) Water/Scintillator



(c) Iron/Scintillator



(d) Lead/Scintillator

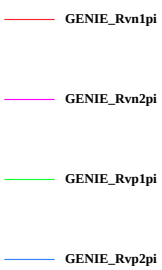
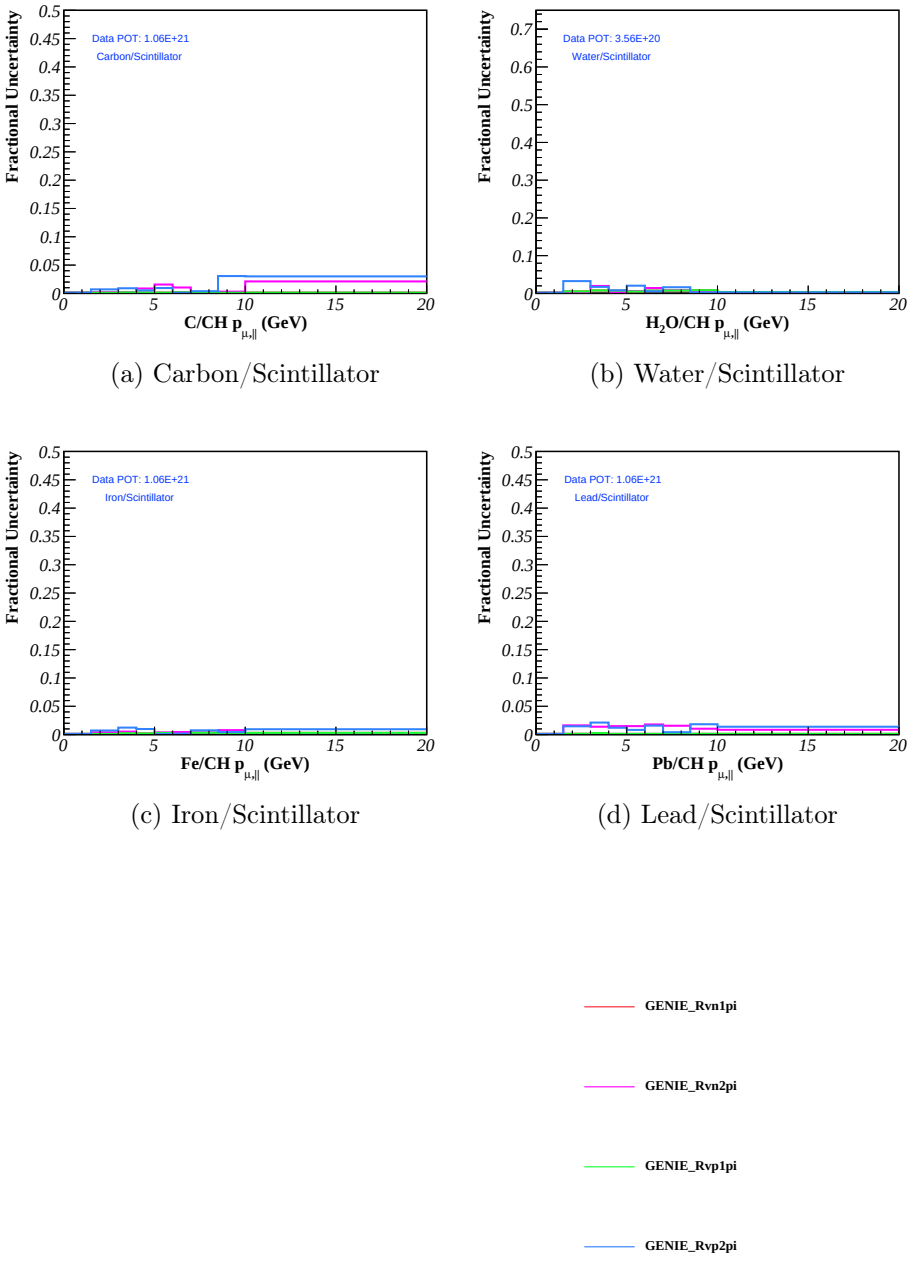


Figure F-57: p_μ Nonresonant π Model Errors

6



(a) Carbon/Scintillator

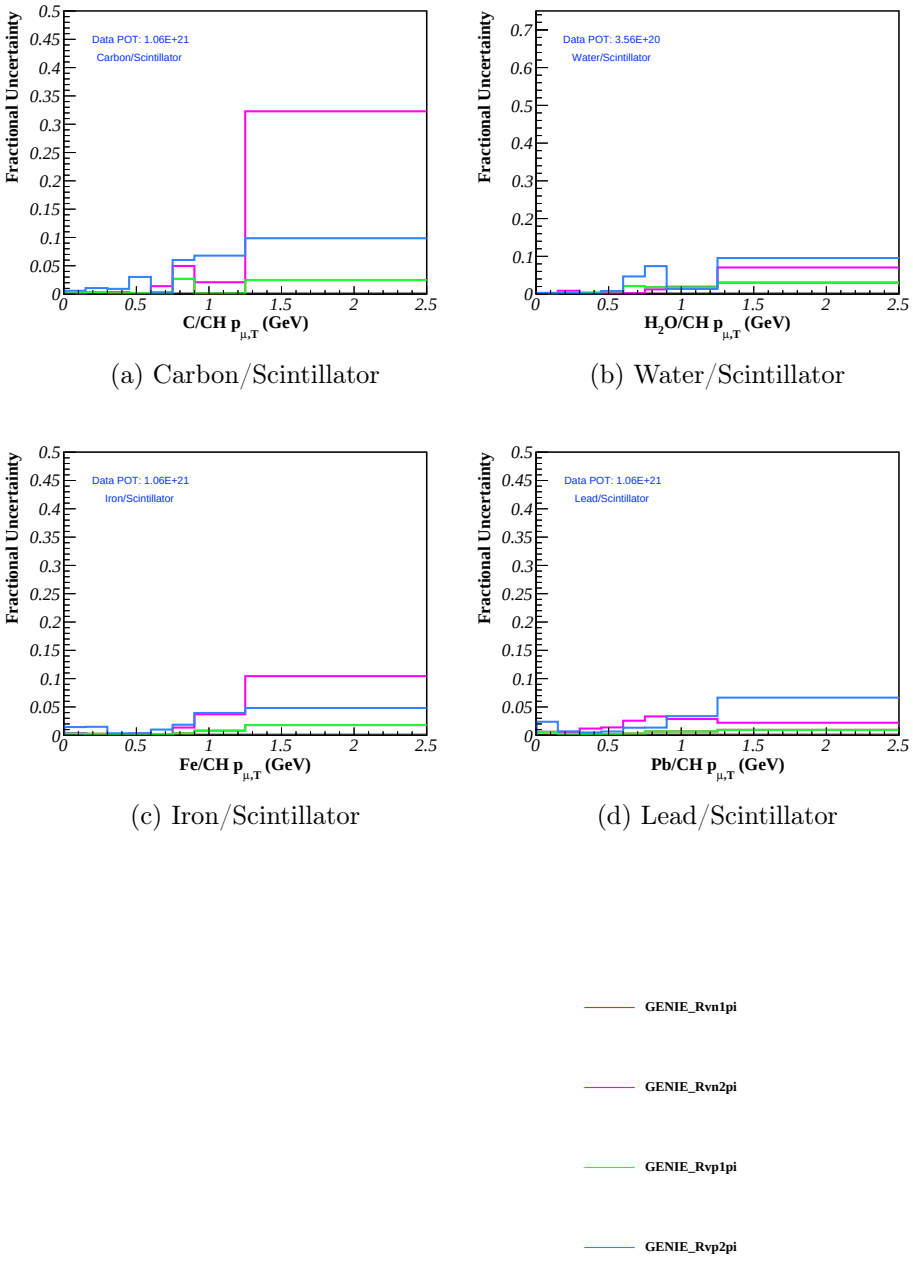
(b) Water/Scintillator

(c) Iron/Scintillator

(d) Lead/Scintillator

6

Figure F-58: $p_{\mu,||}$ Nonresonant π Model Errors



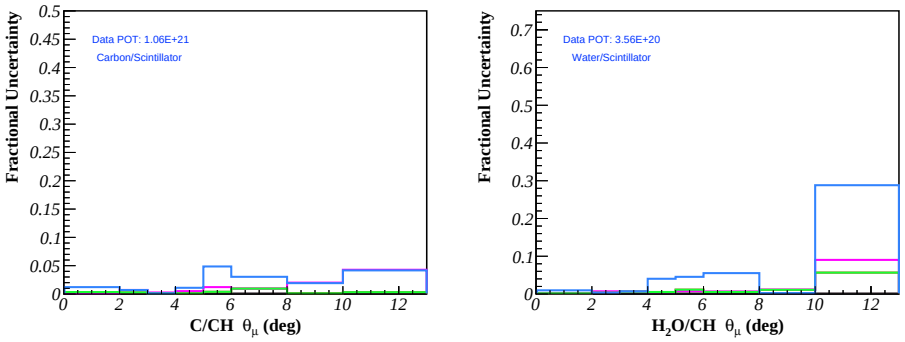
(a) Carbon/Scintillator

(b) Water/Scintillator

(c) Iron/Scintillator

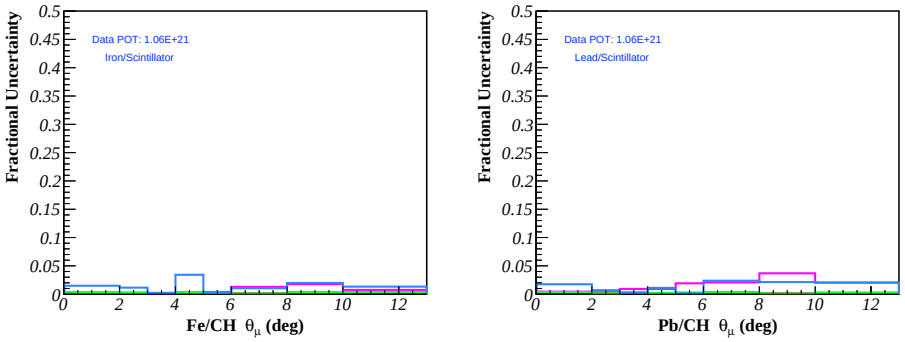
(d) Lead/Scintillator

Figure F-59: $p_{\mu,T}$ Nonresonant π Model Errors



(a) Carbon/Scintillator

(b) Water/Scintillator



(c) Iron/Scintillator

(d) Lead/Scintillator

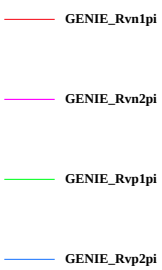
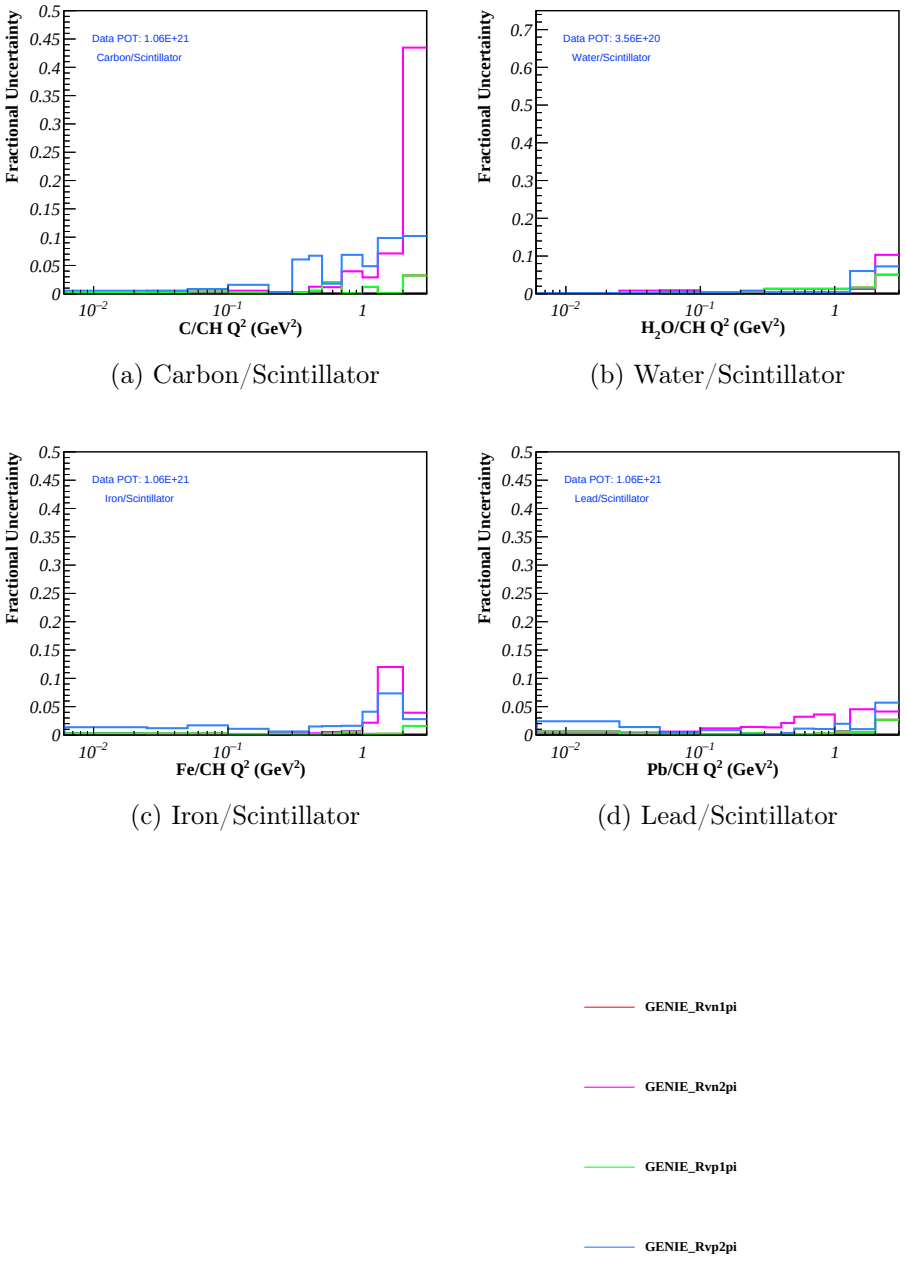


Figure F-60: θ_μ Nonresonant π Model Errors

6



(a) Carbon/Scintillator

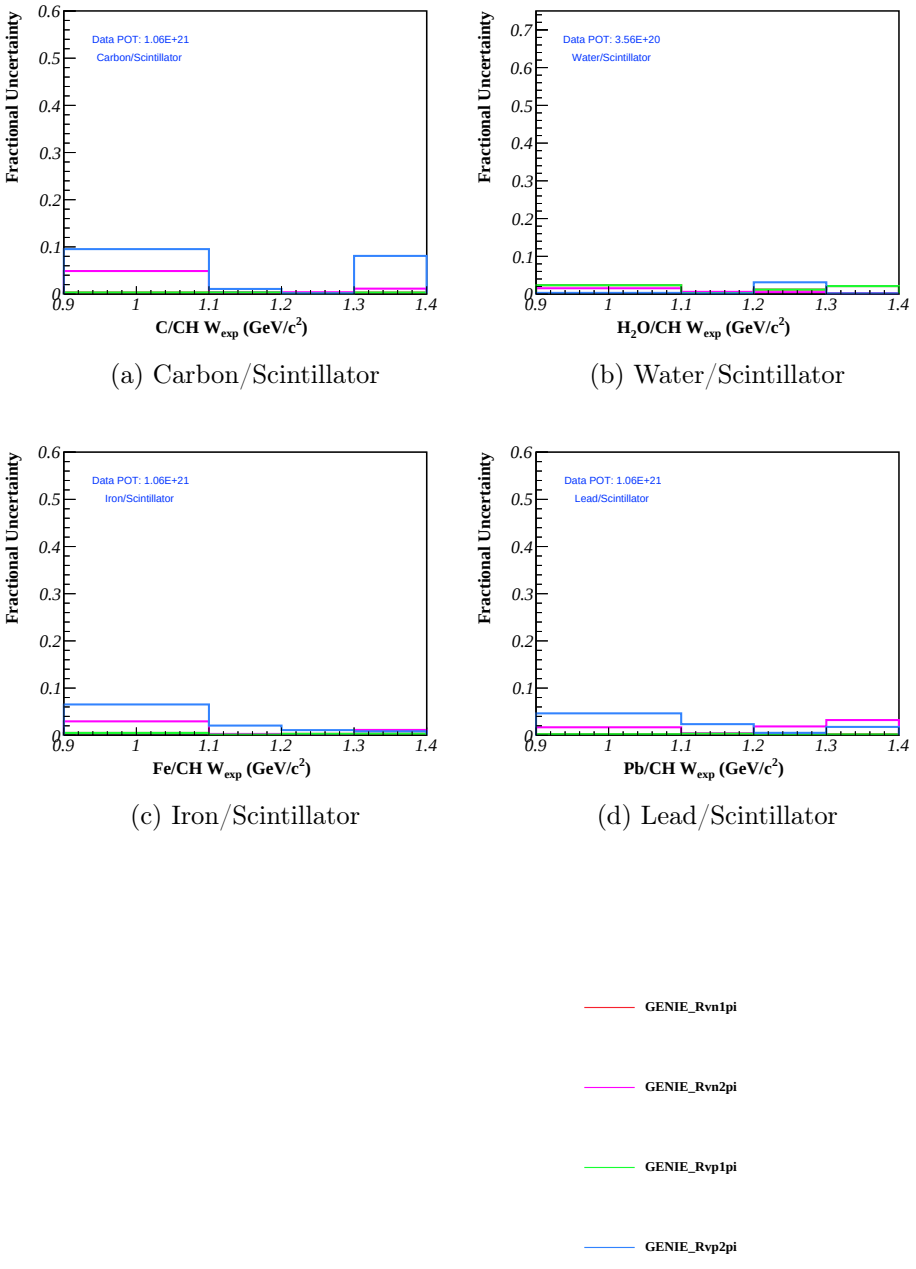
(b) Water/Scintillator

(c) Iron/Scintillator

(d) Lead/Scintillator

6

Figure F-61: Q^2 Nonresonant π Model Errors



(a) Carbon/Scintillator

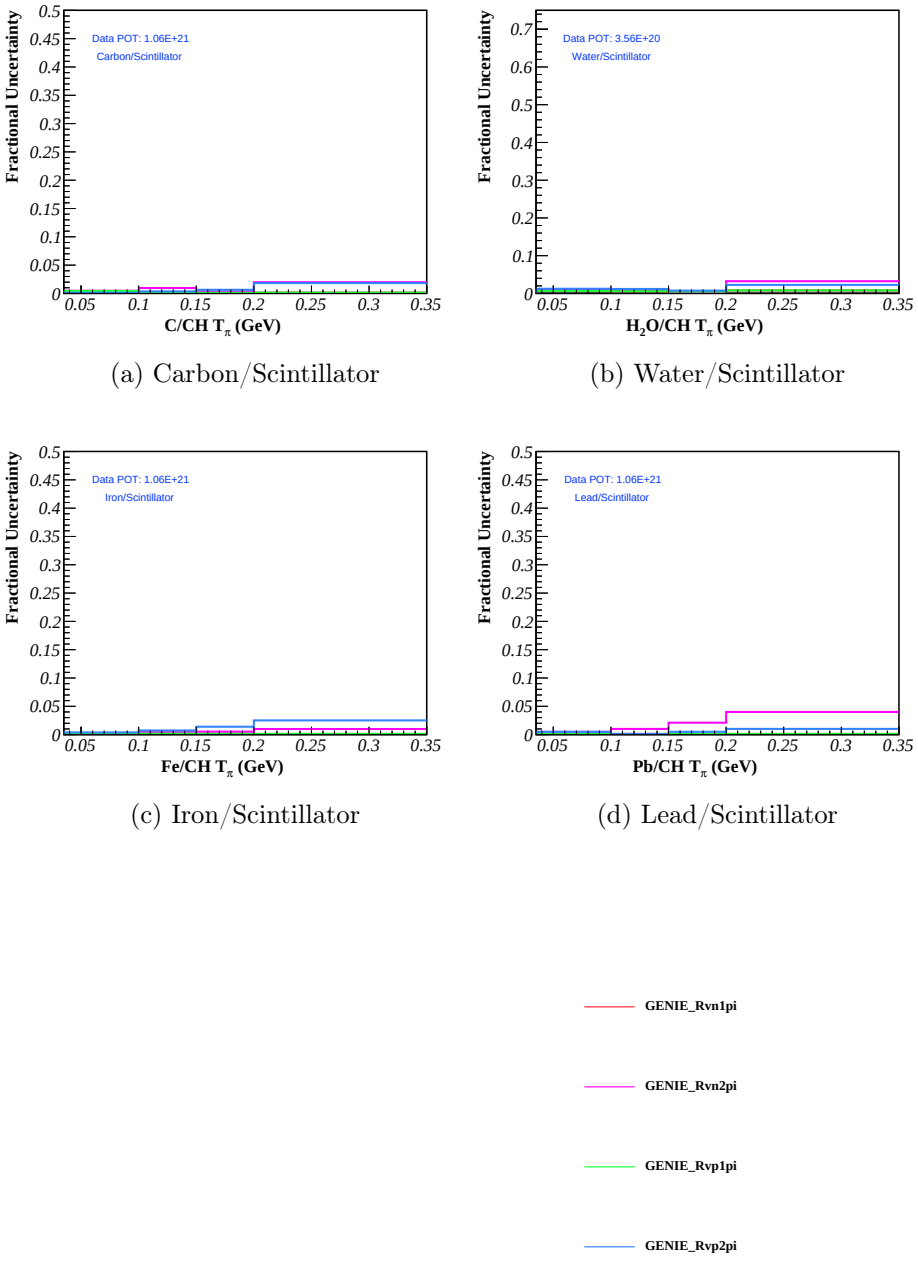
(b) Water/Scintillator

(c) Iron/Scintillator

(d) Lead/Scintillator

6

Figure F-62: W_{exp} Nonresonant π Model Errors



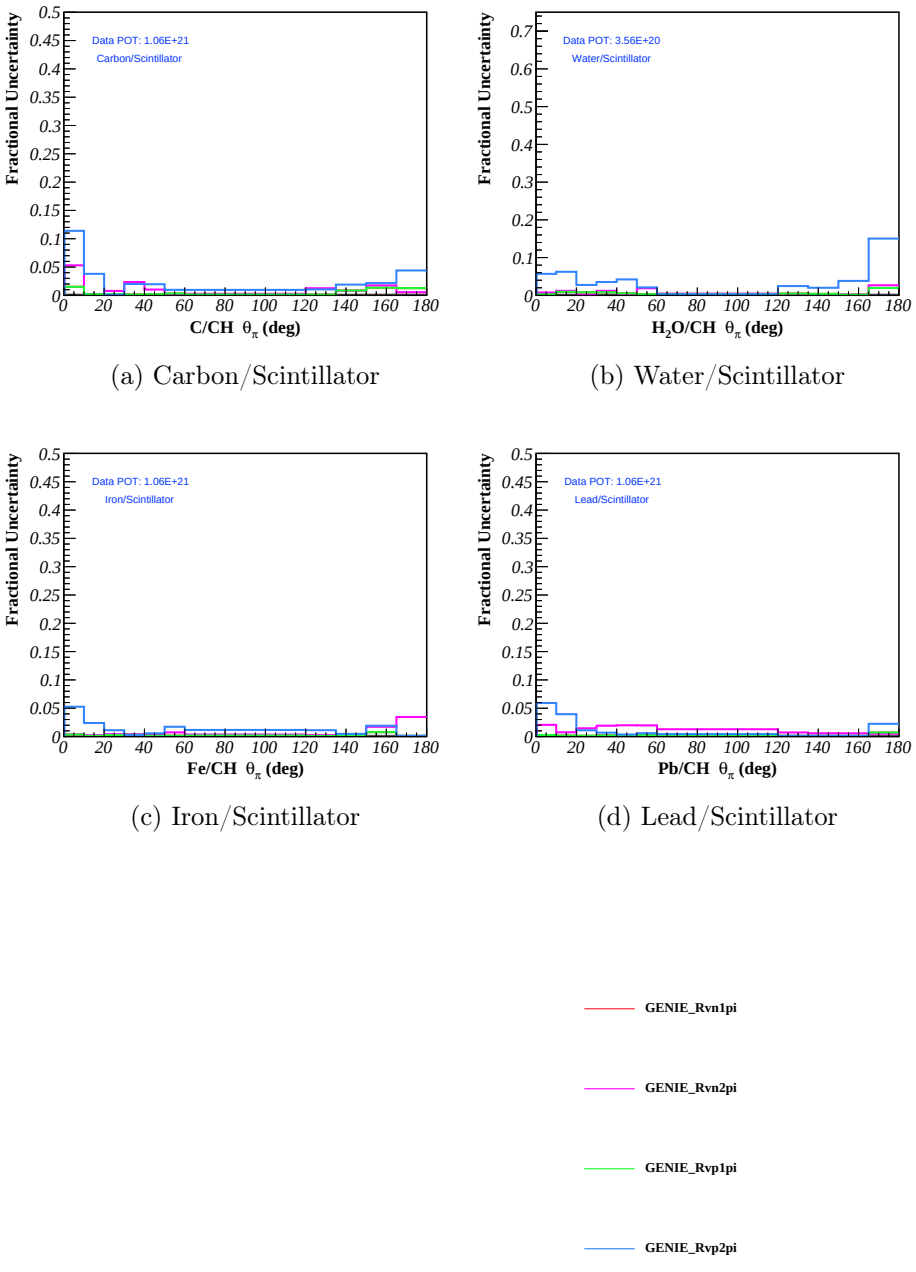
(a) Carbon/Scintillator

(b) Water/Scintillator

(c) Iron/Scintillator

(d) Lead/Scintillator

Figure F-63: T_π Nonresonant π Model Errors



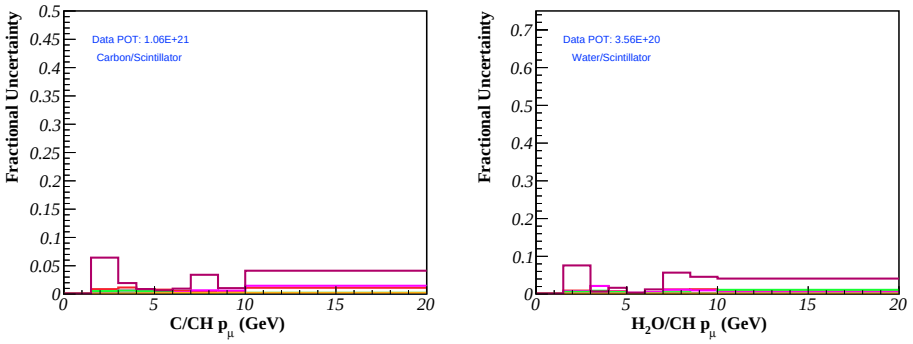
(a) Carbon/Scintillator

(b) Water/Scintillator

(c) Iron/Scintillator

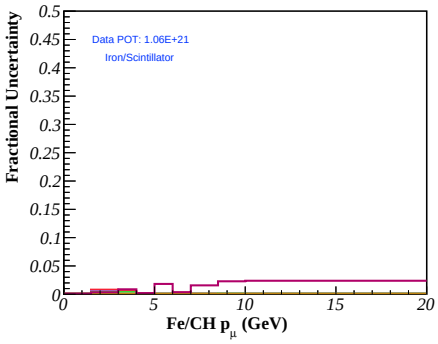
(d) Lead/Scintillator

Figure F-64: θ_π Nonresonant π Model Errors

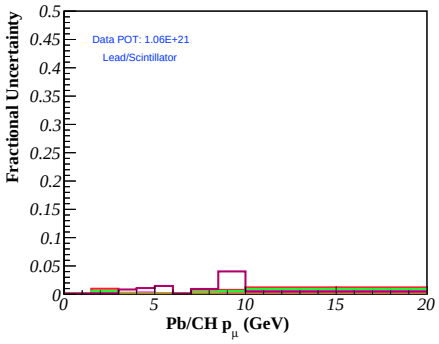


(a) Carbon/Scintillator

(b) Water/Scintillator



(c) Iron/Scintillator



(d) Lead/Scintillator

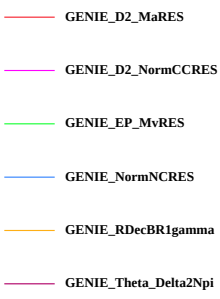
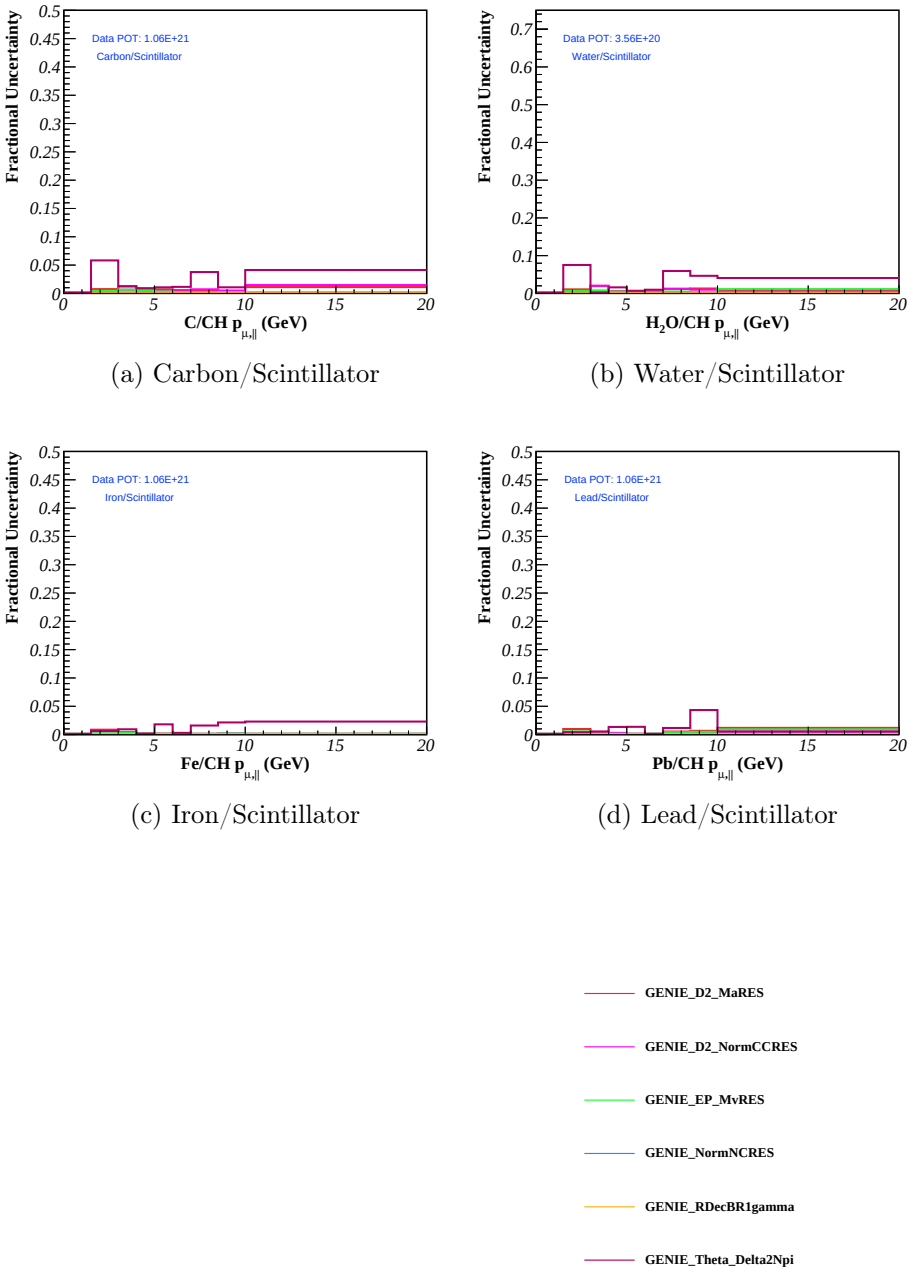


Figure F-65: p_μ Resonant π Model Errors



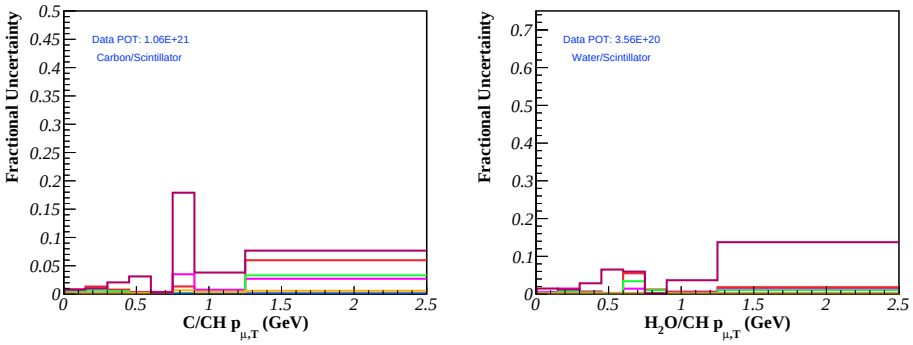
(a) Carbon/Scintillator

(b) Water/Scintillator

(c) Iron/Scintillator

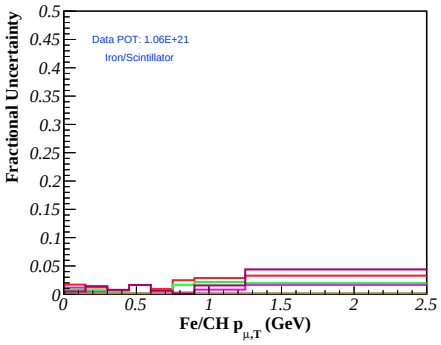
(d) Lead/Scintillator

Figure F-66: $p_{\mu,||}$ Resonant π Model Errors

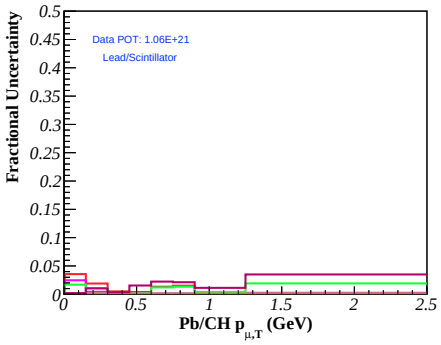


(a) Carbon/Scintillator

(b) Water/Scintillator



(c) Iron/Scintillator



(d) Lead/Scintillator

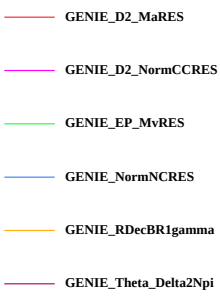
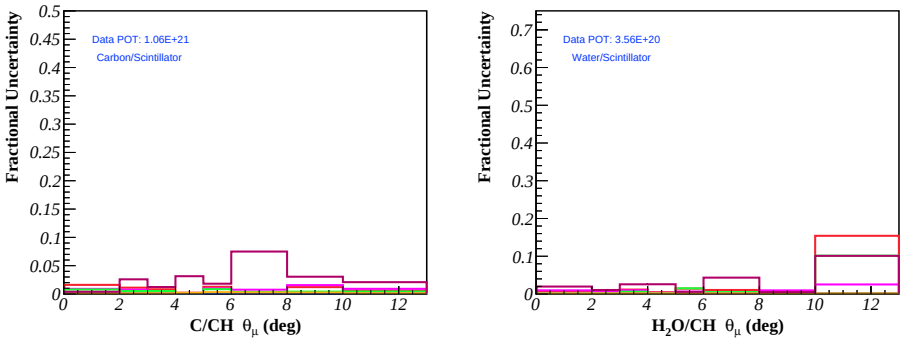
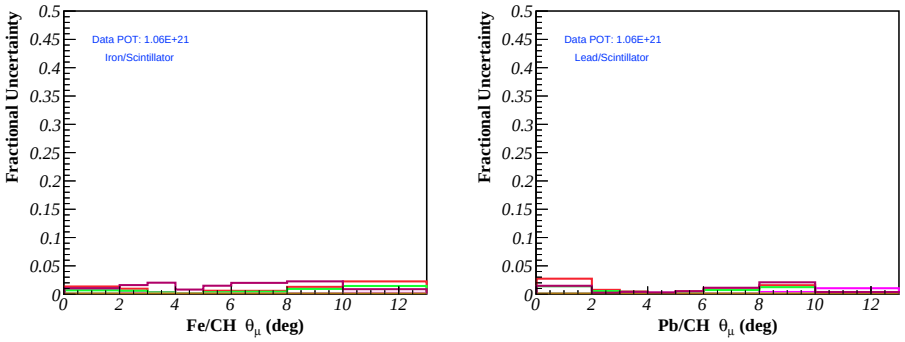


Figure F-67: $p_{\mu,T}$ Resonant π Model Errors



(a) Carbon/Scintillator

(b) Water/Scintillator



(c) Iron/Scintillator

(d) Lead/Scintillator

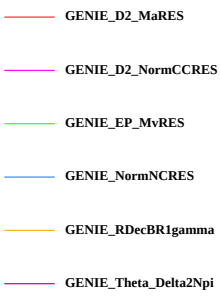
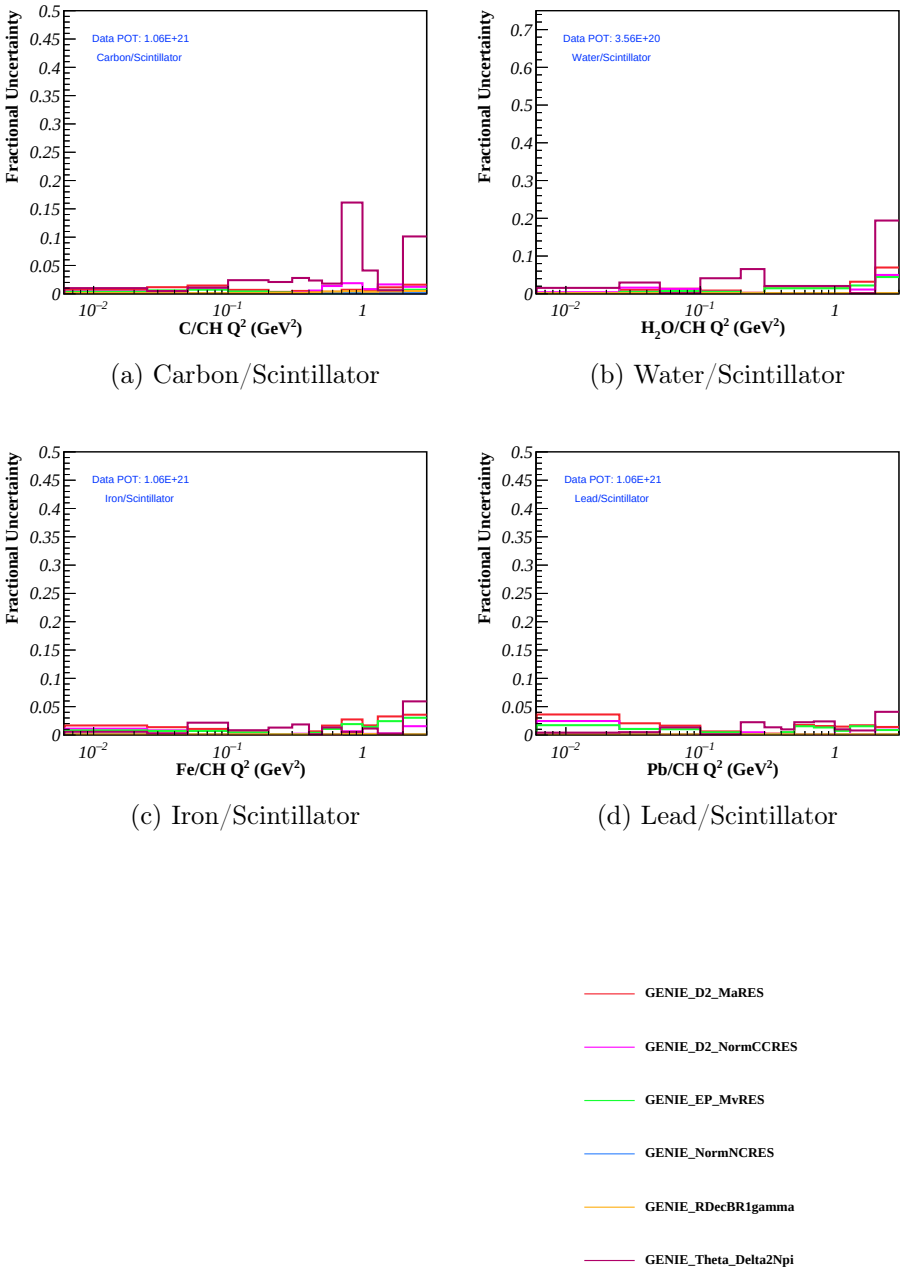


Figure F-68: θ_μ Resonant π Model Errors



(a) Carbon/Scintillator

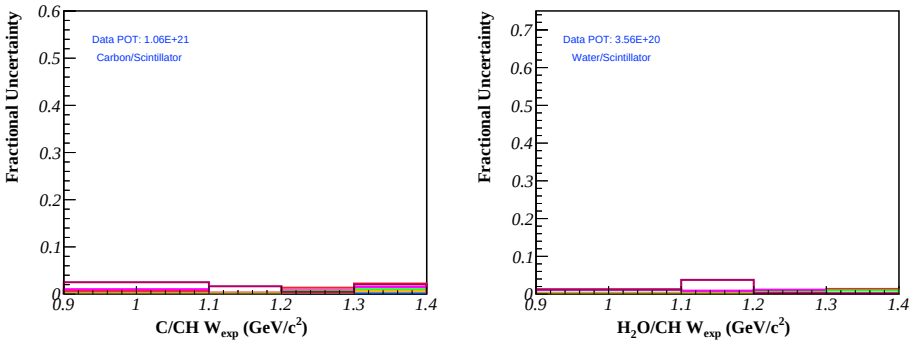
(b) Water/Scintillator

(c) Iron/Scintillator

(d) Lead/Scintillator

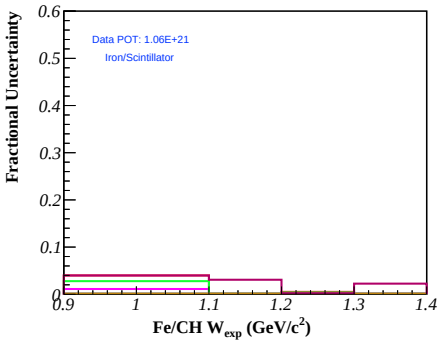
5

Figure F-69: Q^2 Resonant π Model Errors

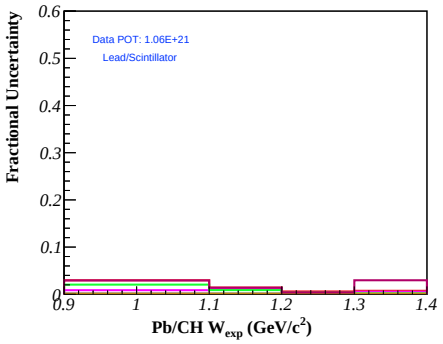


(a) Carbon/Scintillator

(b) Water/Scintillator



(c) Iron/Scintillator



(d) Lead/Scintillator

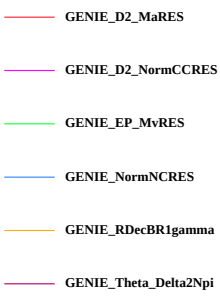
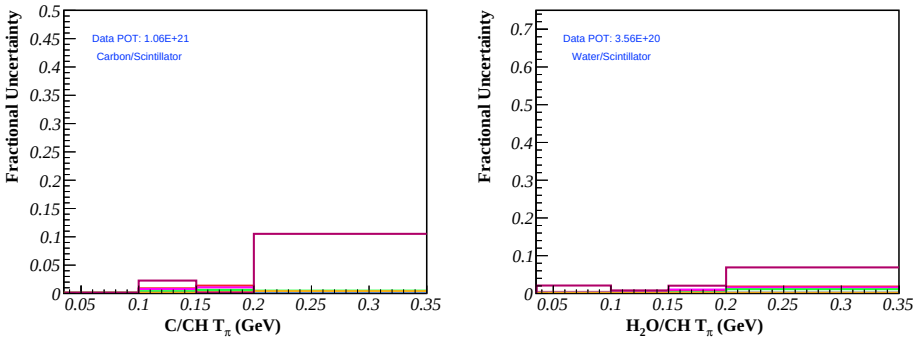
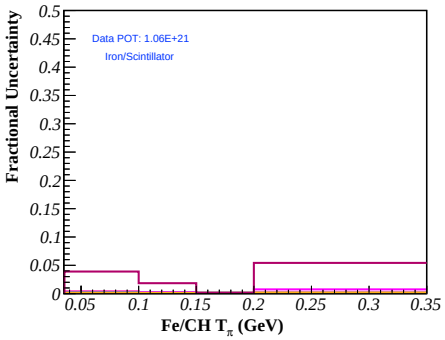


Figure F-70: W_{exp} Resonant π Model Errors

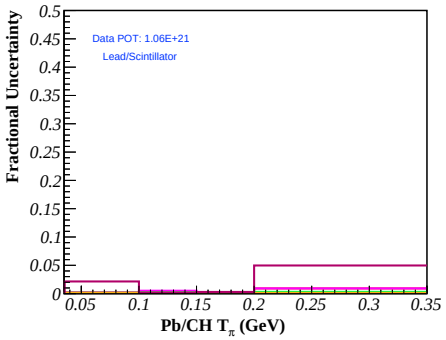


(a) Carbon/Scintillator

(b) Water/Scintillator



(c) Iron/Scintillator



(d) Lead/Scintillator

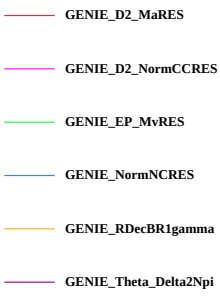
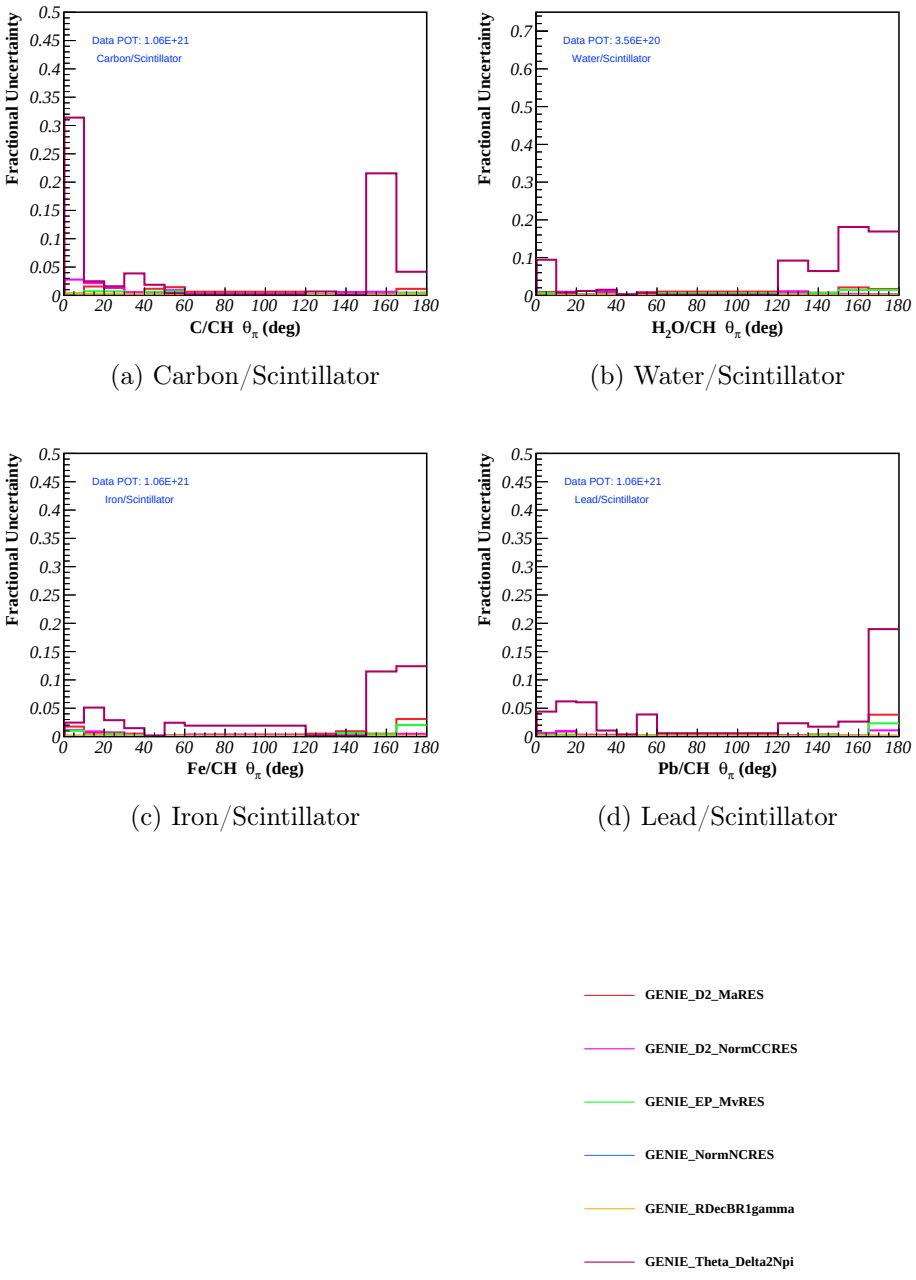


Figure F-71: T_π Resonant π Model Errors



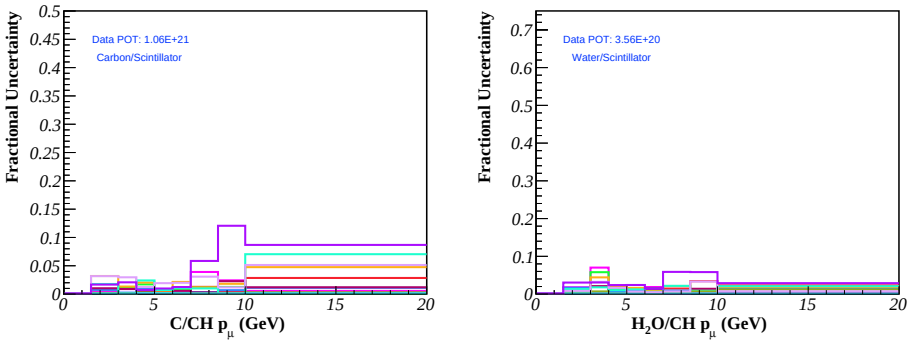
(a) Carbon/Scintillator

(b) Water/Scintillator

(c) Iron/Scintillator

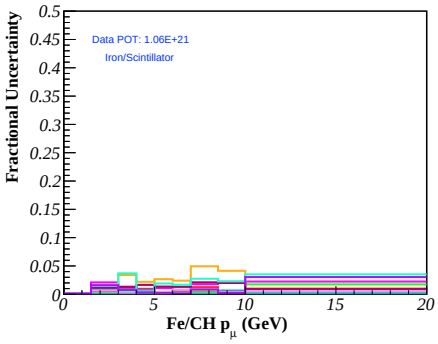
(d) Lead/Scintillator

Figure F-72: θ_π Resonant π Model Errors

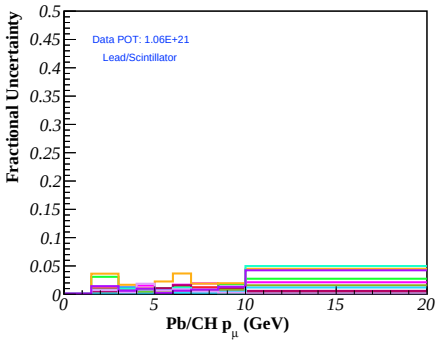


(a) Carbon/Scintillator

(b) Water/Scintillator



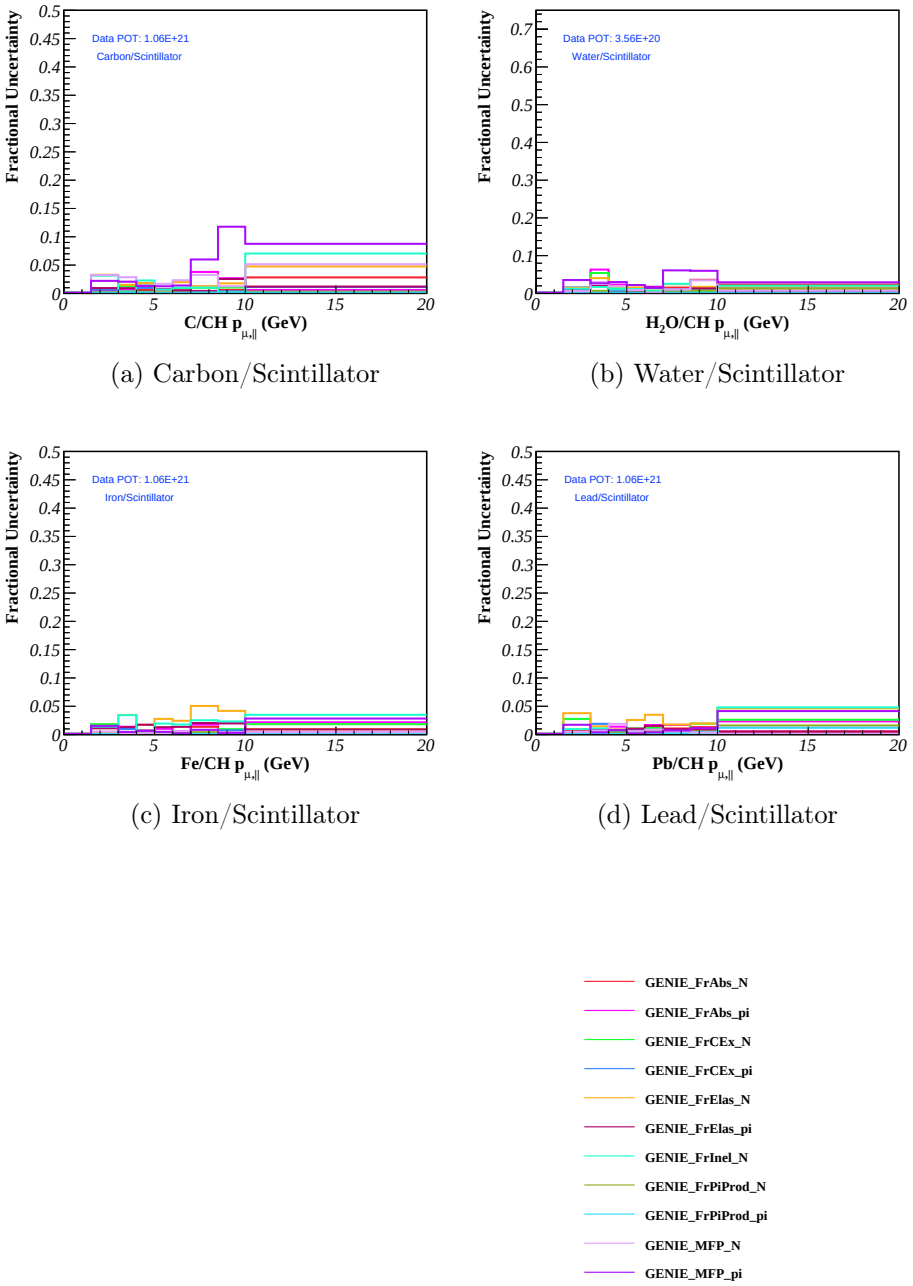
(c) Iron/Scintillator



(d) Lead/Scintillator



Figure F-73: p_μ FSI Errors



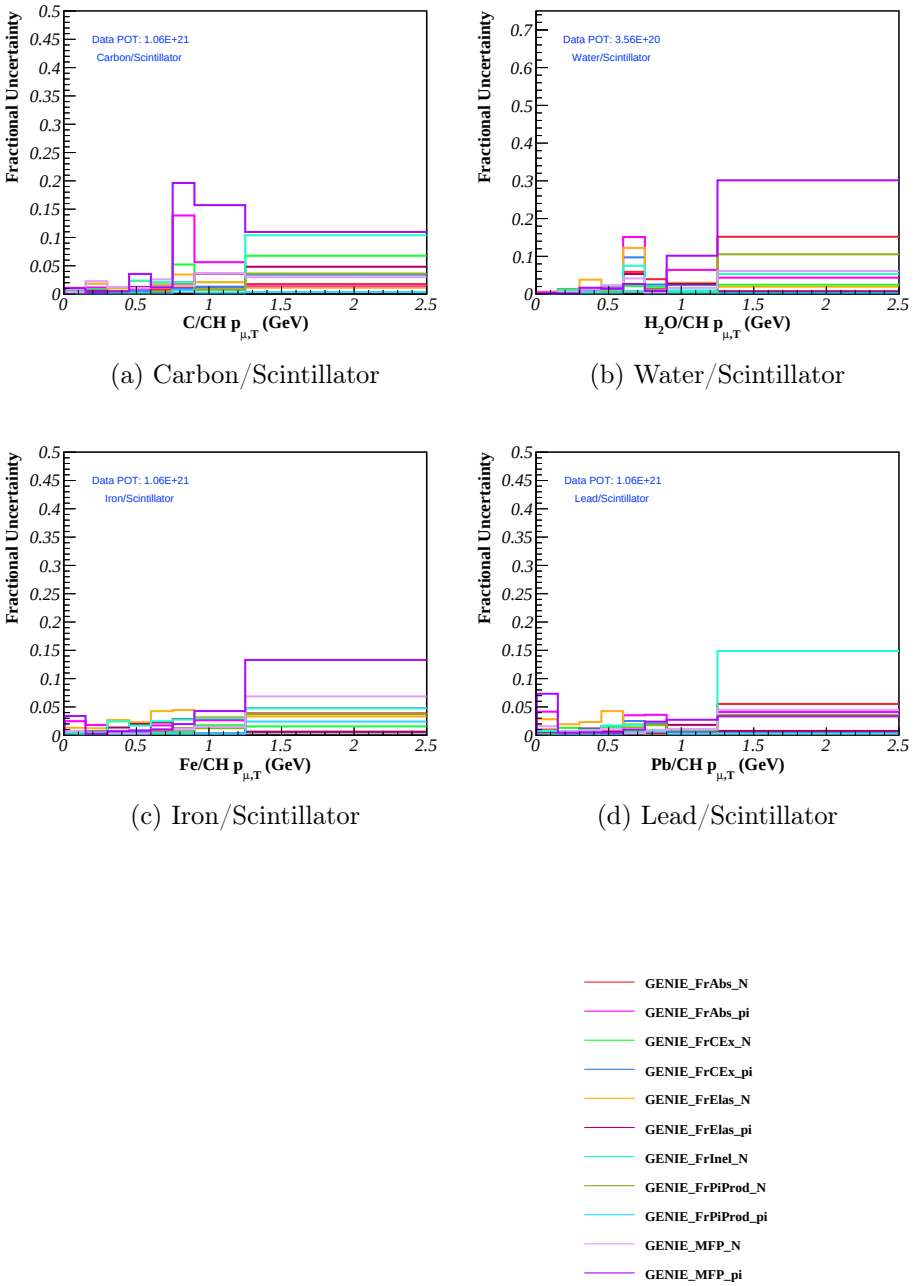
(a) Carbon/Scintillator

(b) Water/Scintillator

(c) Iron/Scintillator

(d) Lead/Scintillator

Figure F-74: $p_{\mu,||}$ FSI Errors



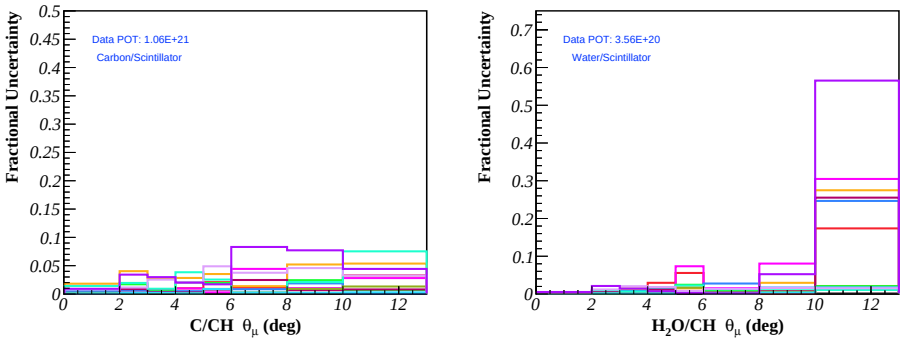
(a) Carbon/Scintillator

(b) Water/Scintillator

(c) Iron/Scintillator

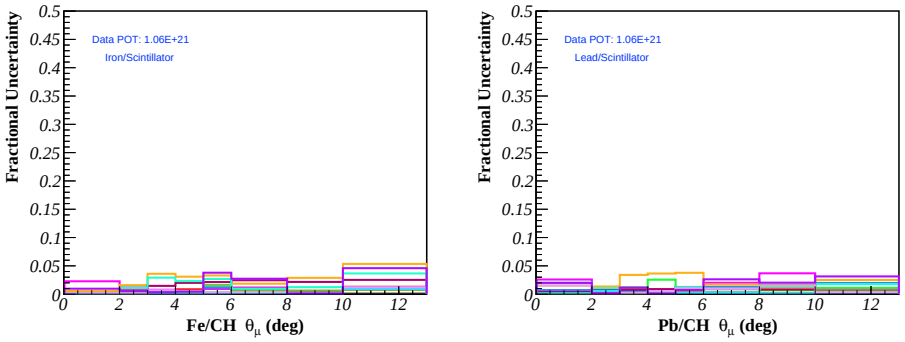
(d) Lead/Scintillator

Figure F-75: $p_{\mu,T}$ FSI Errors



(a) Carbon/Scintillator

(b) Water/Scintillator



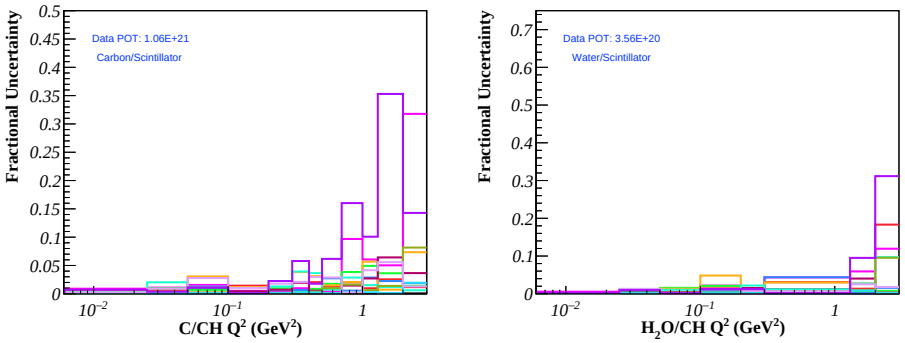
(c) Iron/Scintillator

(d) Lead/Scintillator



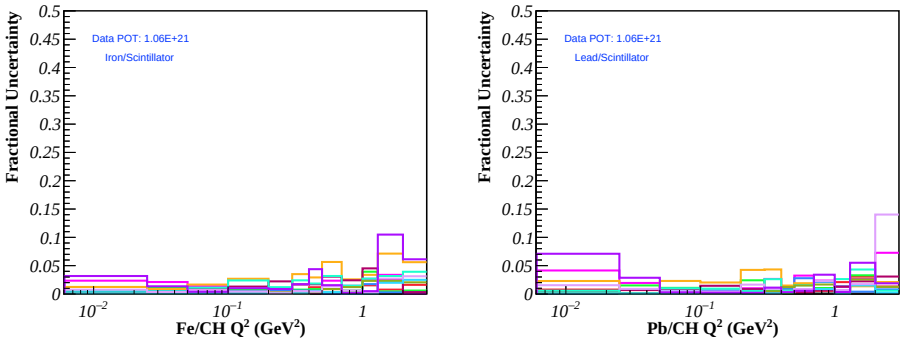
Figure F-76: θ_μ FSI Errors

7



(a) Carbon/Scintillator

(b) Water/Scintillator



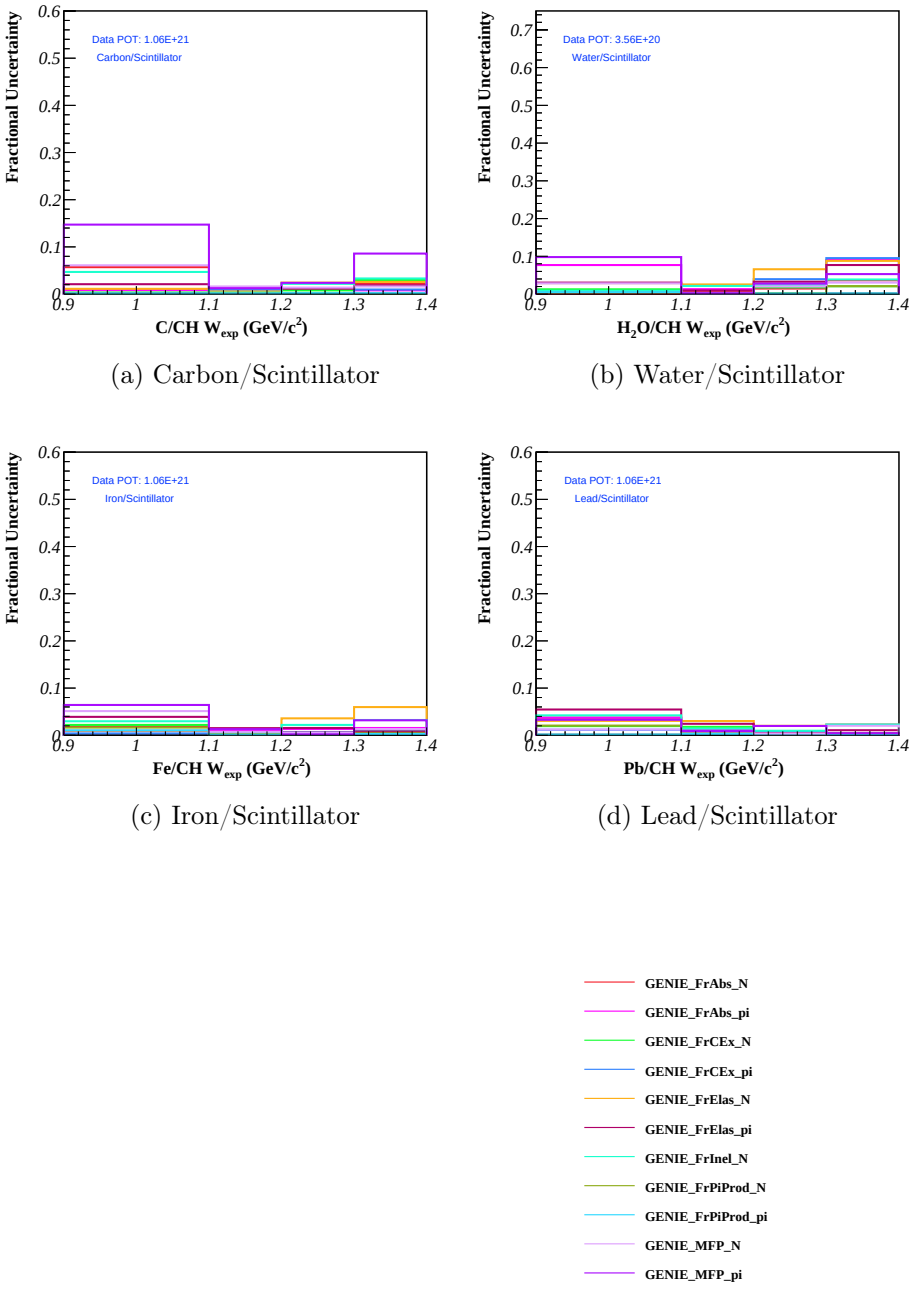
(c) Iron/Scintillator

(d) Lead/Scintillator



Figure F-77: Q^2 FSI Errors

7



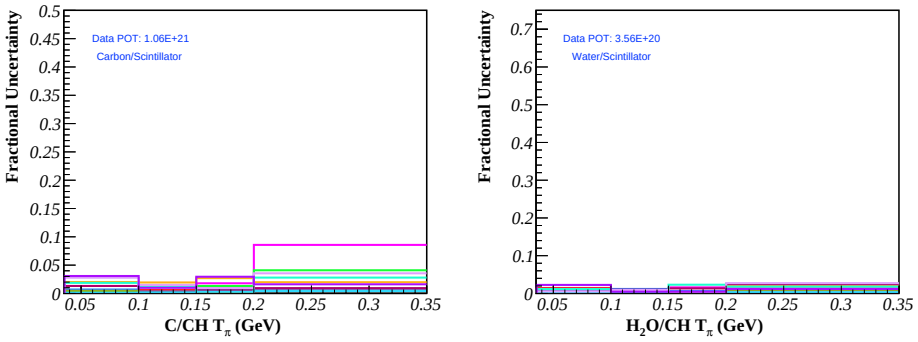
(a) Carbon/Scintillator

(b) Water/Scintillator

(c) Iron/Scintillator

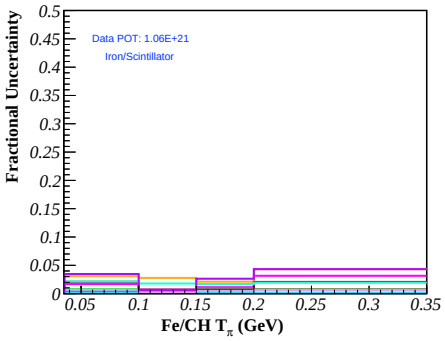
(d) Lead/Scintillator

Figure F-78: W_{exp} FSI Errors

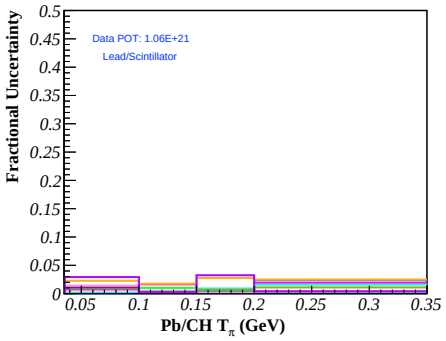


(a) Carbon/Scintillator

(b) Water/Scintillator



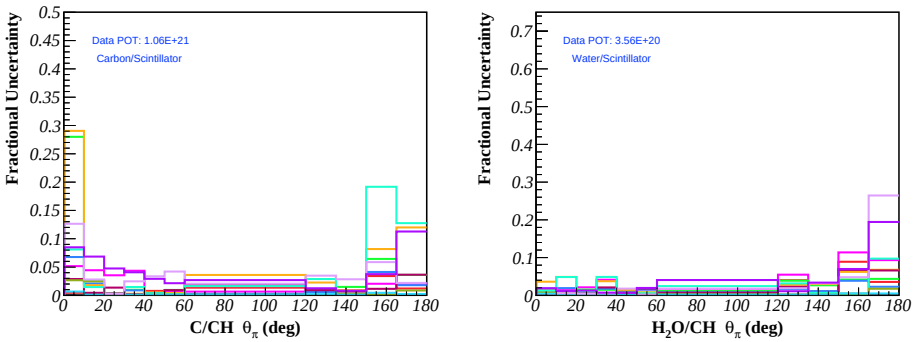
(c) Iron/Scintillator



(d) Lead/Scintillator

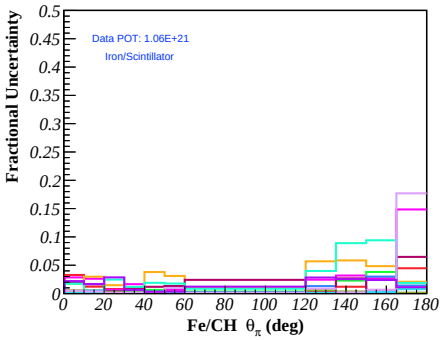


Figure F-79: T_π FSI Errors

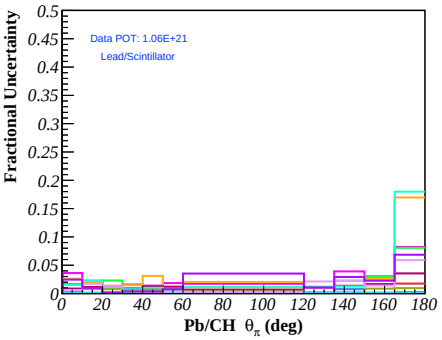


(a) Carbon/Scintillator

(b) Water/Scintillator



(c) Iron/Scintillator

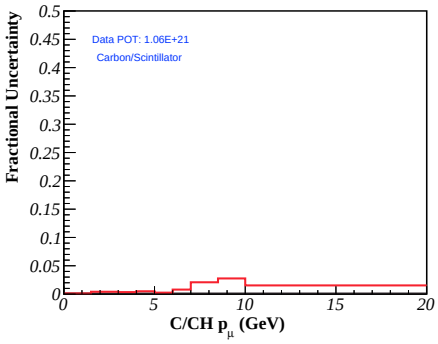


(d) Lead/Scintillator

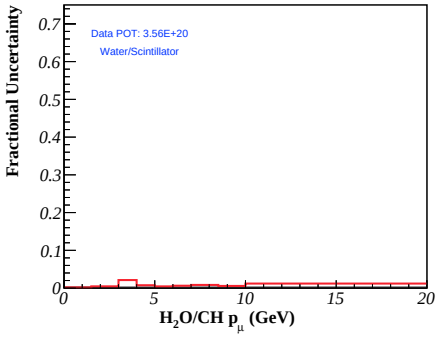


Figure F-80: θ_π FSI Errors

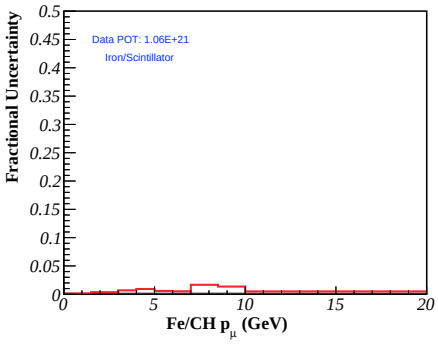
7



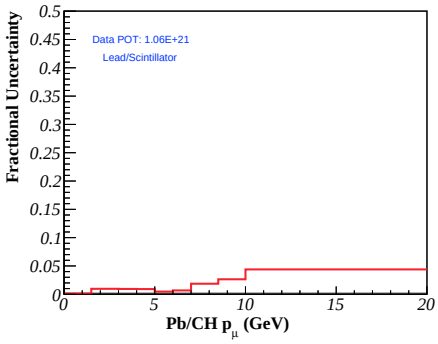
(a) Carbon/Scintillator



(b) Water/Scintillator



(c) Iron/Scintillator

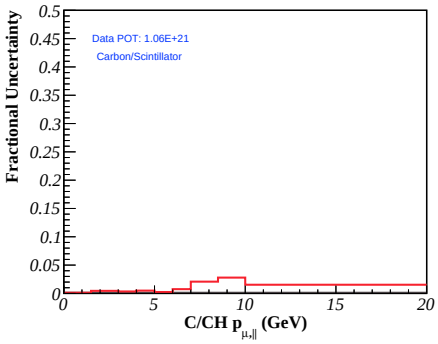


(d) Lead/Scintillator

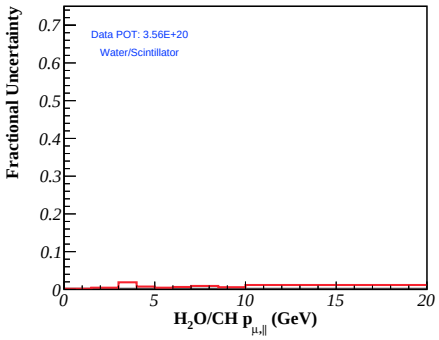
6

Flux

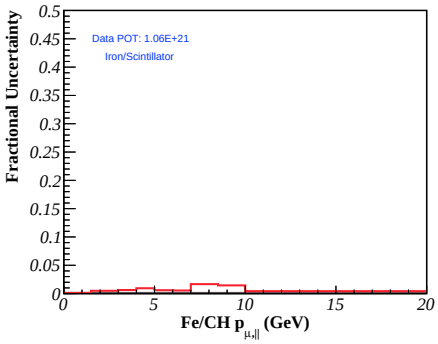
Figure F-81: p_μ Flux Error



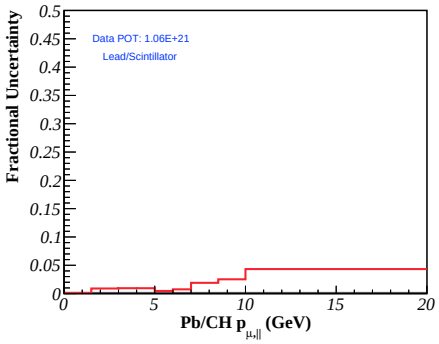
(a) Carbon/Scintillator



(b) Water/Scintillator



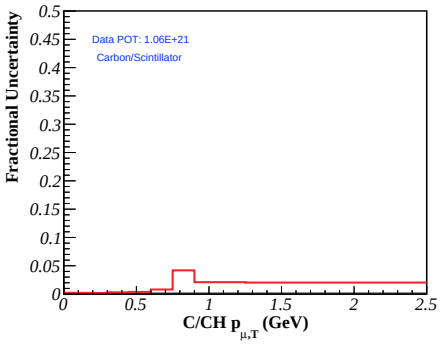
(c) Iron/Scintillator



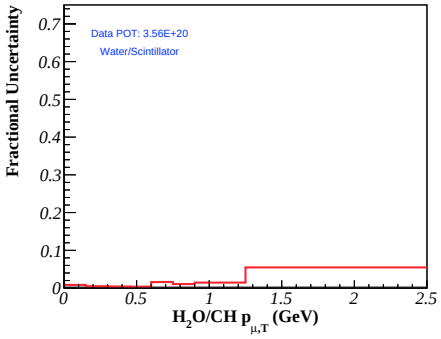
(d) Lead/Scintillator

6

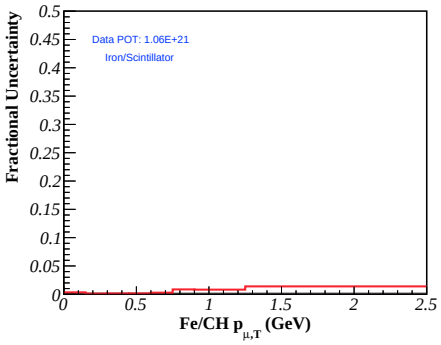
Figure F-82: $p_{\mu,||}$ Flux Error



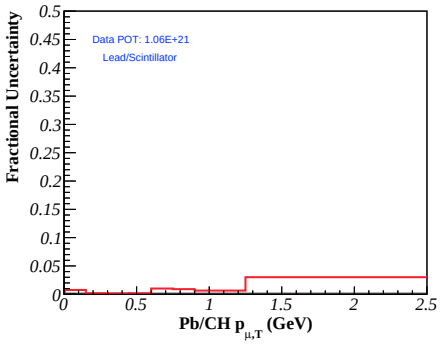
(a) Carbon/Scintillator



(b) Water/Scintillator



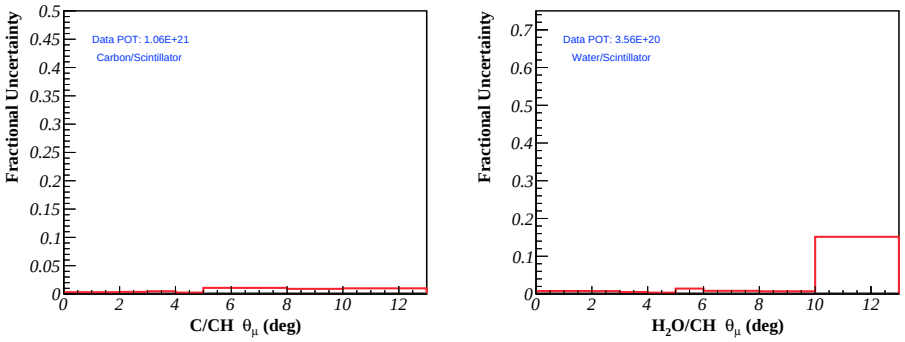
(c) Iron/Scintillator



(d) Lead/Scintillator

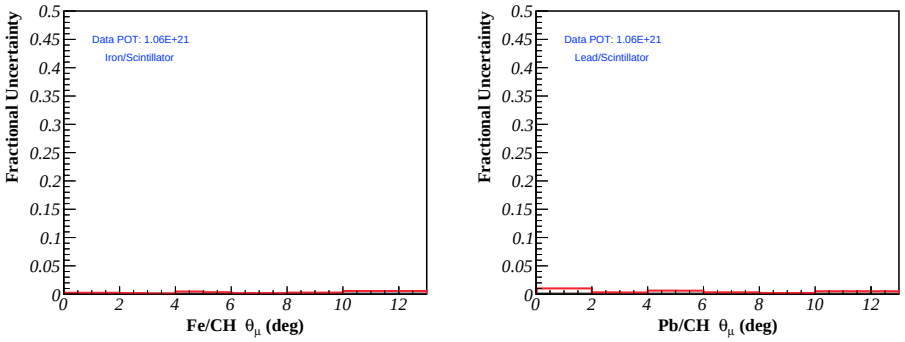
6

Figure F-83: $p_{\mu,T}$ Flux Error



(a) Carbon/Scintillator

(b) Water/Scintillator

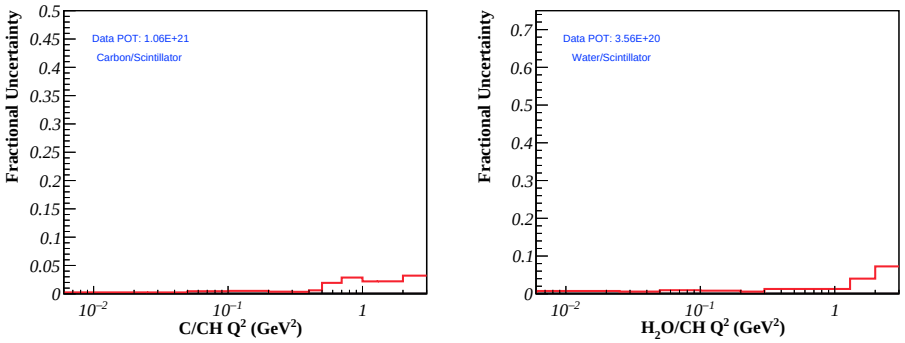


(c) Iron/Scintillator

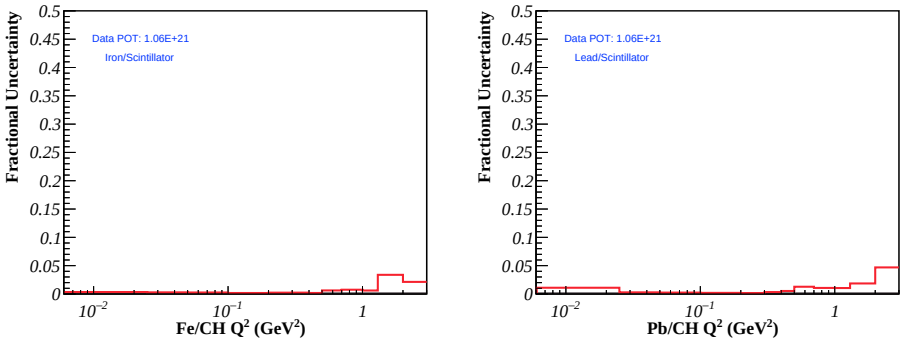
(d) Lead/Scintillator

6

Figure F-84: θ_μ Flux Error



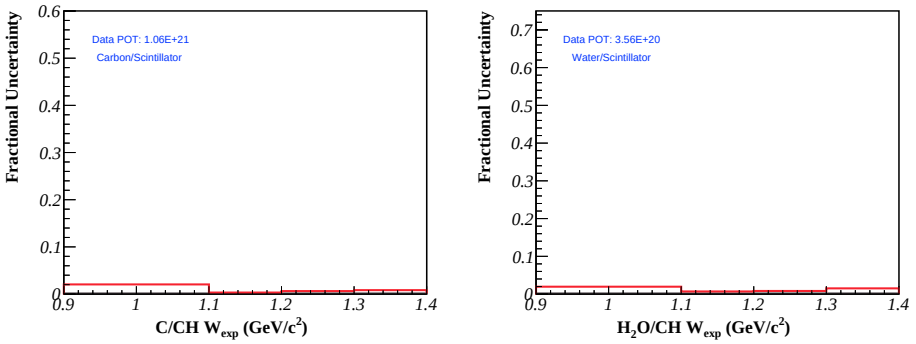
(a) Carbon/Scintillator (b) Water/Scintillator



(c) Iron/Scintillator (d) Lead/Scintillator

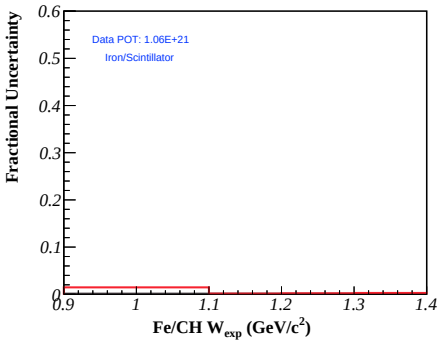
6

Figure F-85: Q^2 Flux Error

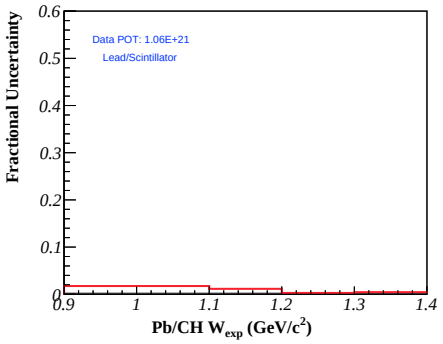


(a) Carbon/Scintillator

(b) Water/Scintillator



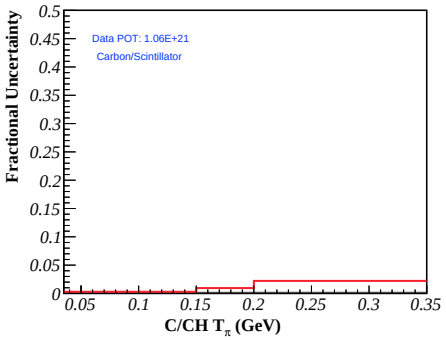
(c) Iron/Scintillator



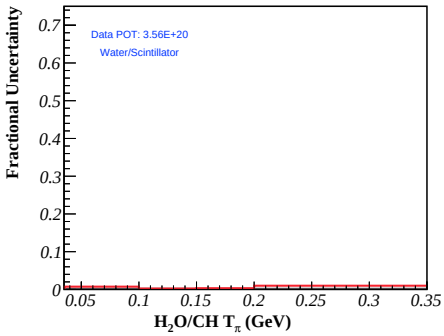
(d) Lead/Scintillator

6

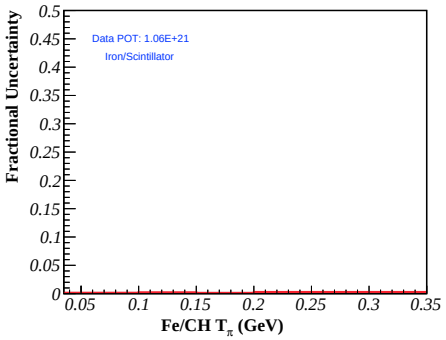
Figure F-86: W_{exp} Flux Error



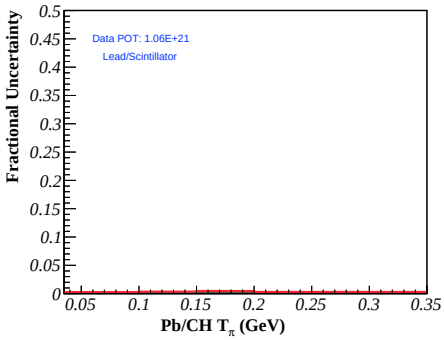
(a) Carbon/Scintillator



(b) Water/Scintillator



(c) Iron/Scintillator

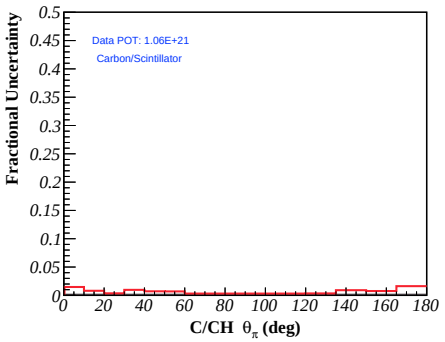


(d) Lead/Scintillator

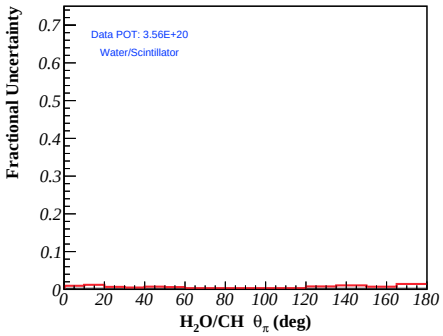
6

Flux

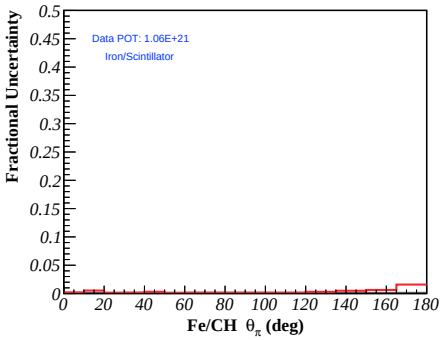
Figure F-87: T_π Flux Error



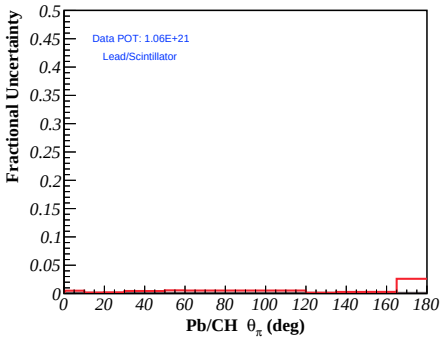
(a) Carbon/Scintillator



(b) Water/Scintillator



(c) Iron/Scintillator

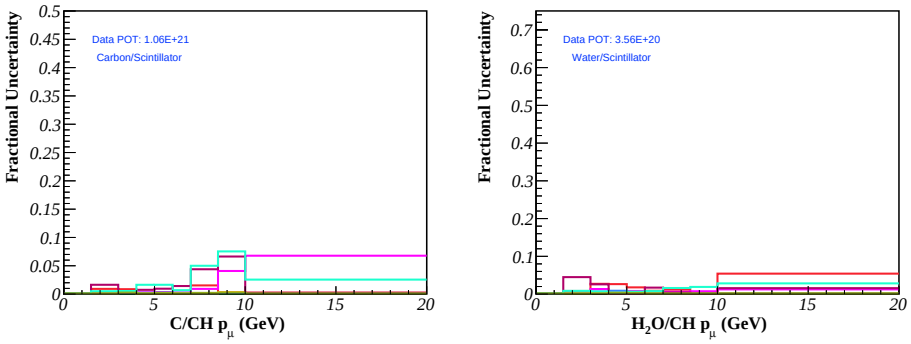


(d) Lead/Scintillator

6

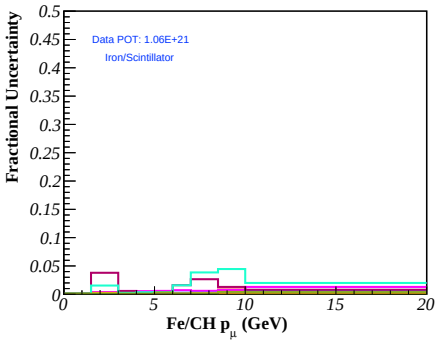
Flux

Figure F-88: θ_π Flux Error

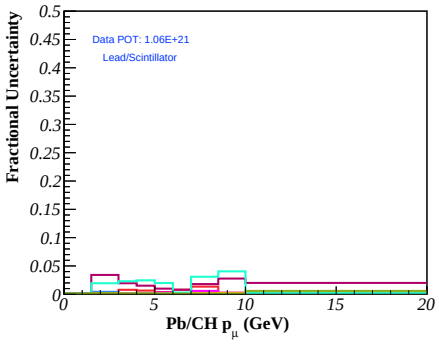


(a) Carbon/Scintillator

(b) Water/Scintillator



(c) Iron/Scintillator

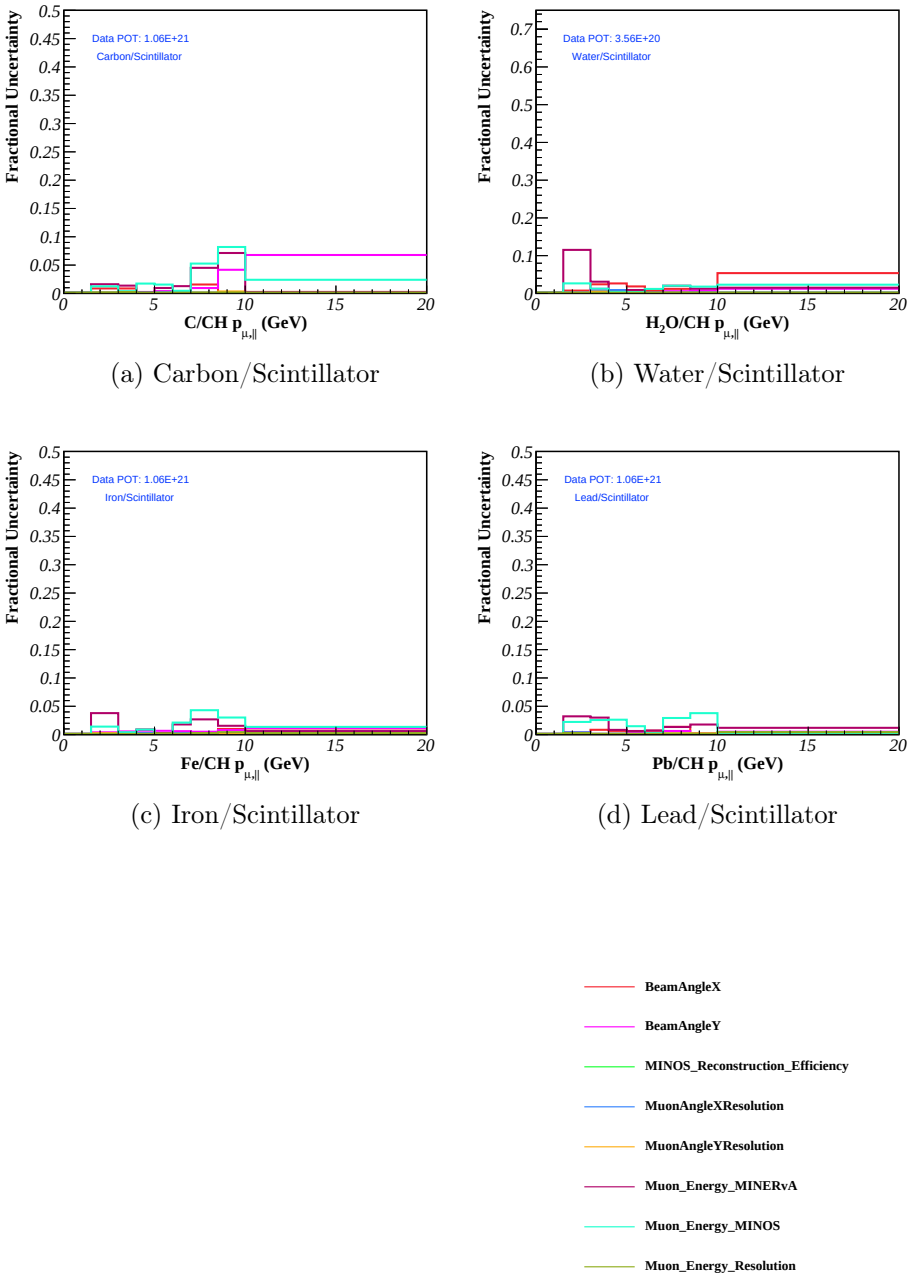


(d) Lead/Scintillator



Figure F-89: p_μ Muon Reconstruction Errors

2



(a) Carbon/Scintillator

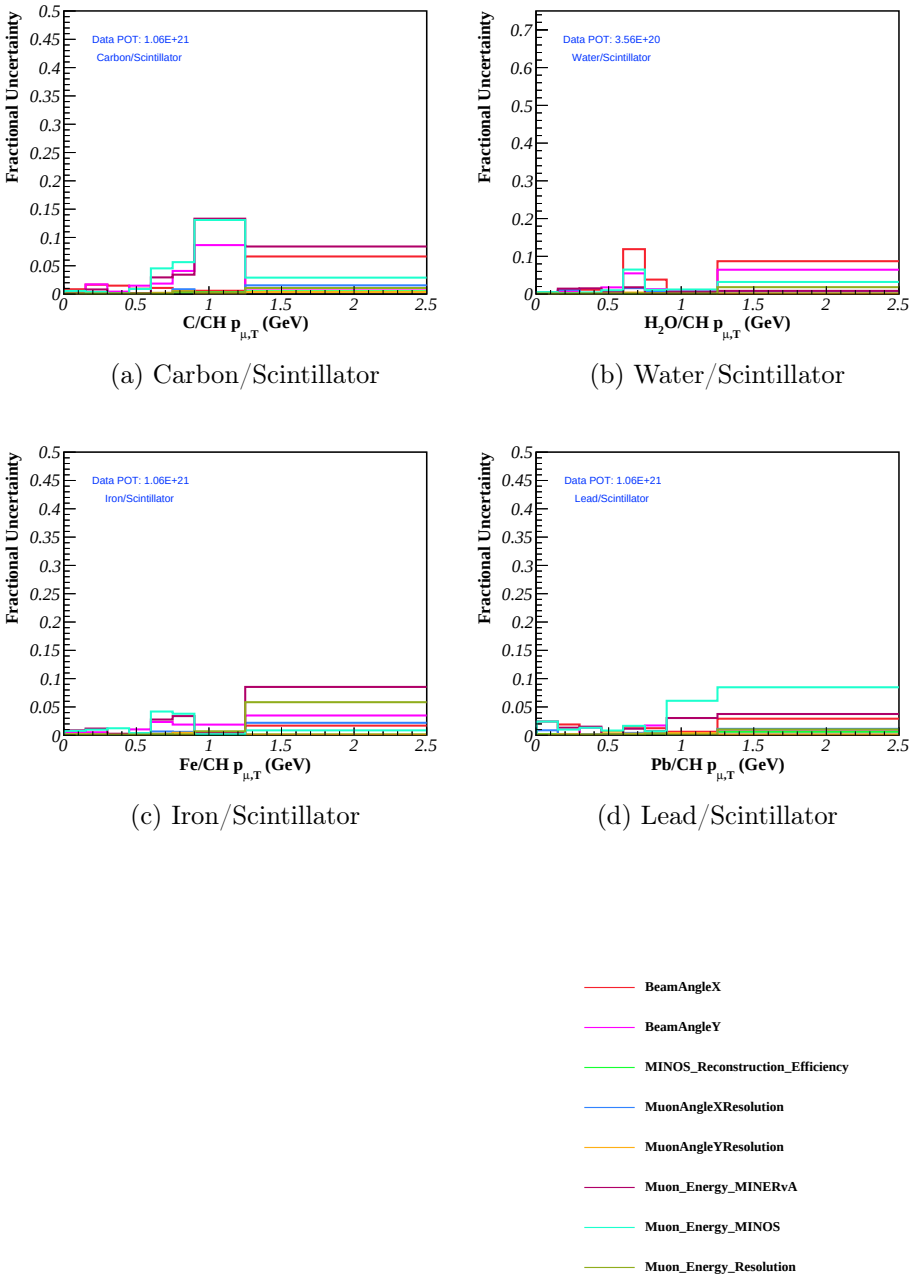
(b) Water/Scintillator

(c) Iron/Scintillator

(d) Lead/Scintillator

2

Figure F-90: $p_{\mu,||}$ Muon Reconstruction Errors



(a) Carbon/Scintillator

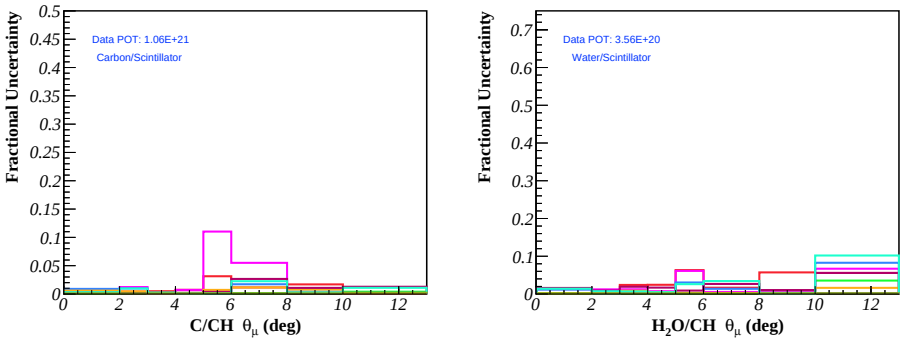
(b) Water/Scintillator

(c) Iron/Scintillator

(d) Lead/Scintillator

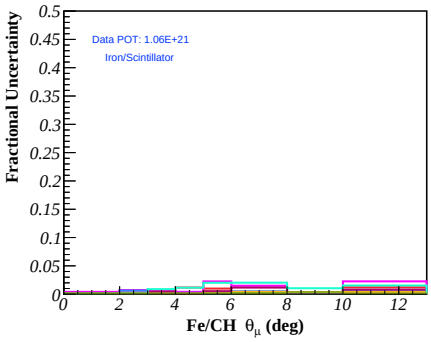
2

Figure F-91: $p_{\mu,T}$ Muon Reconstruction Errors

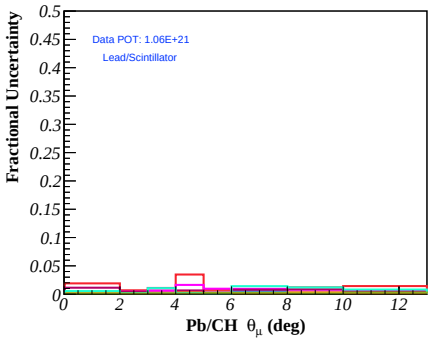


(a) Carbon/Scintillator

(b) Water/Scintillator



(c) Iron/Scintillator

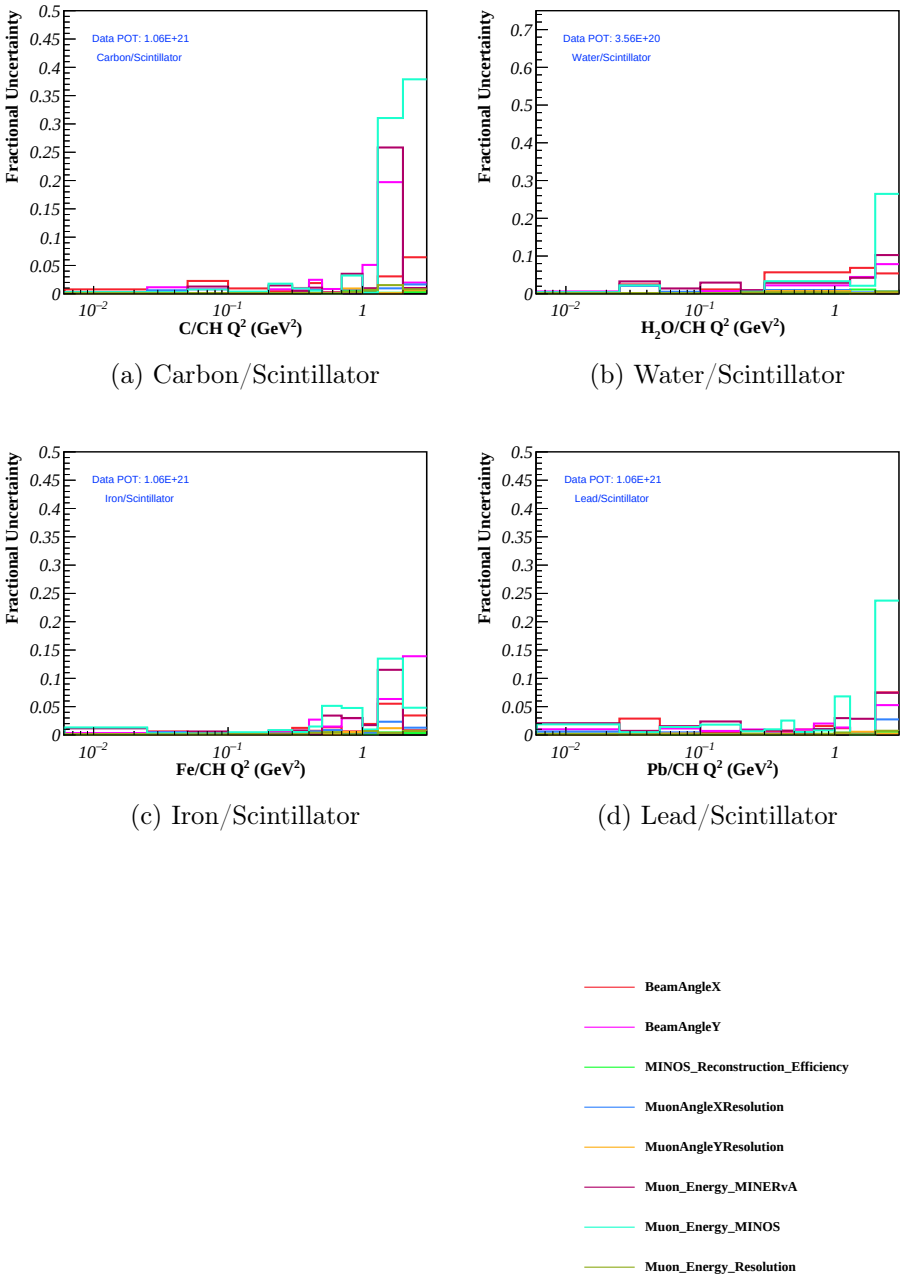


(d) Lead/Scintillator



Figure F-92: θ_μ Muon Reconstruction Errors

2



(a) Carbon/Scintillator

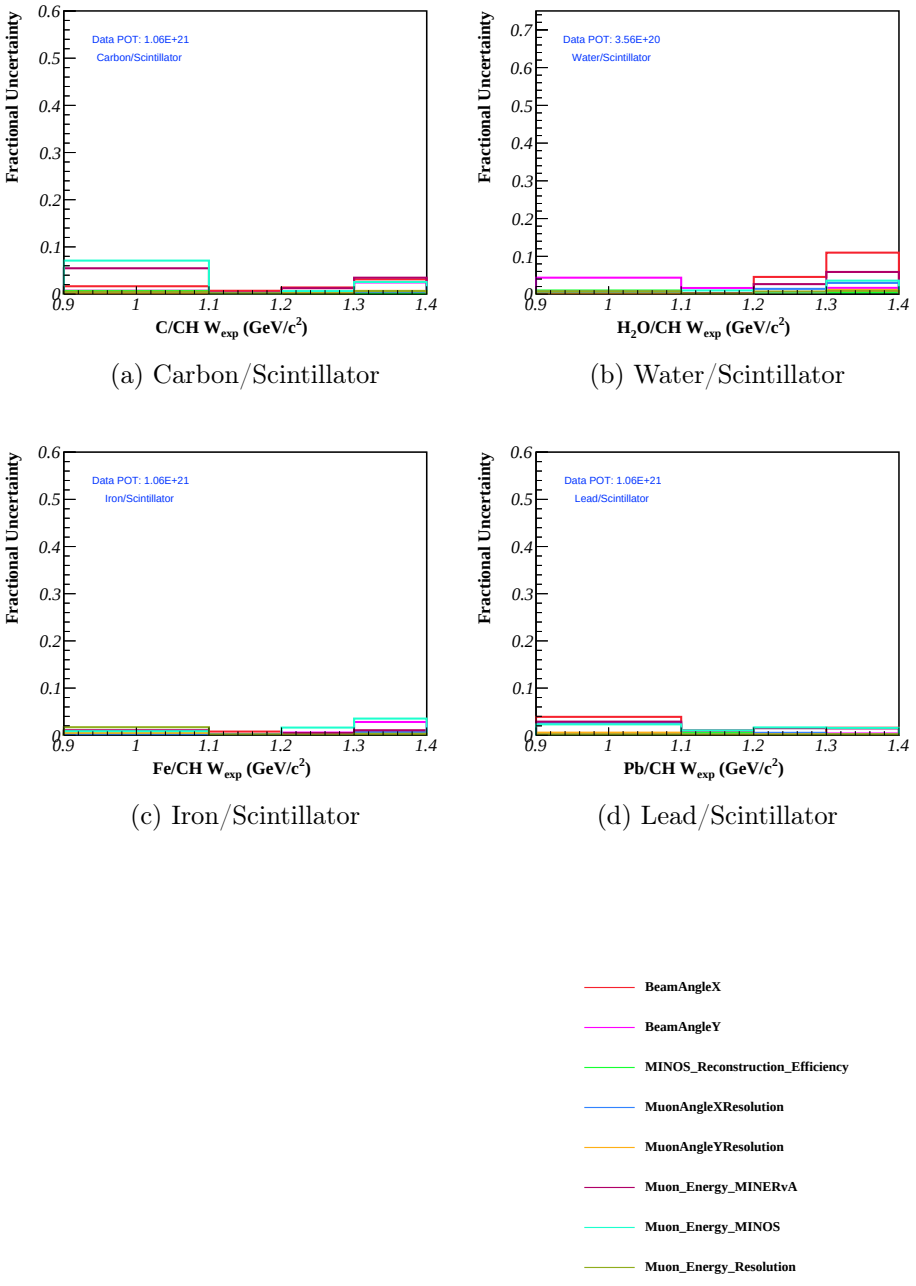
(b) Water/Scintillator

(c) Iron/Scintillator

(d) Lead/Scintillator

2

Figure F-93: Q^2 Muon Reconstruction Errors



(a) Carbon/Scintillator

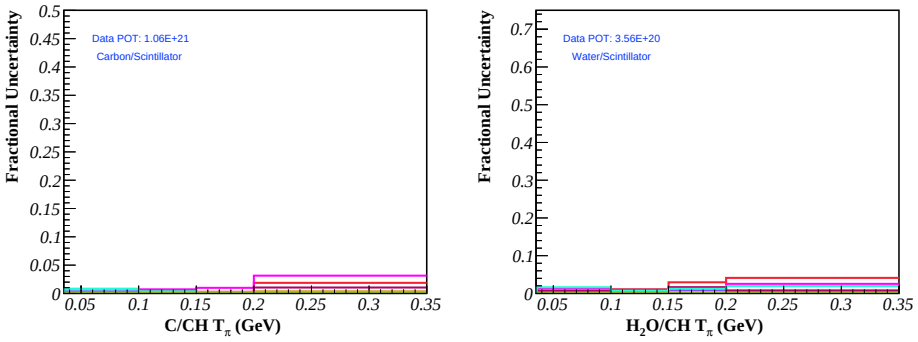
(b) Water/Scintillator

(c) Iron/Scintillator

(d) Lead/Scintillator

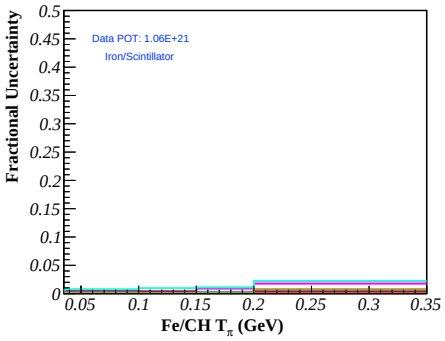
2

Figure F-94: W_{exp} Muon Reconstruction Errors

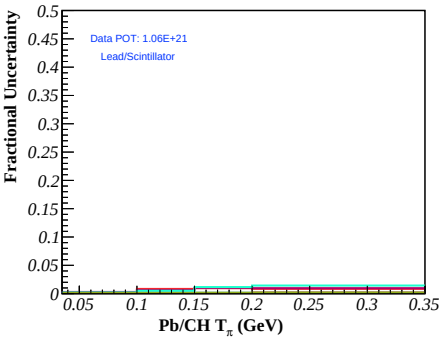


(a) Carbon/Scintillator

(b) Water/Scintillator



(c) Iron/Scintillator

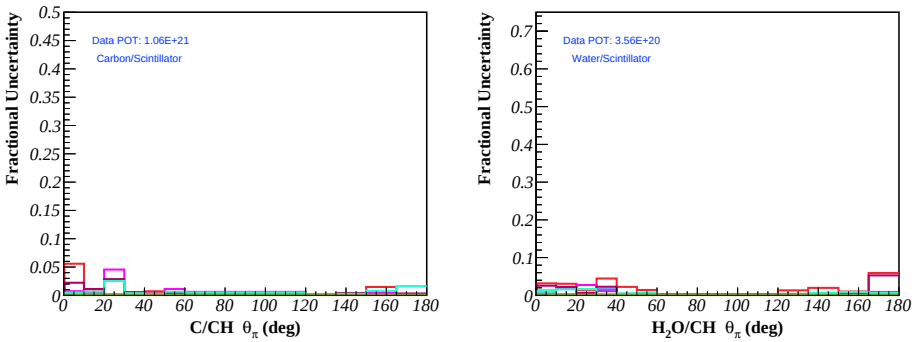


(d) Lead/Scintillator



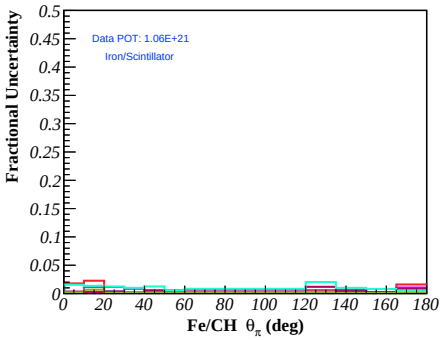
Figure F-95: T_π Muon Reconstruction Errors

2

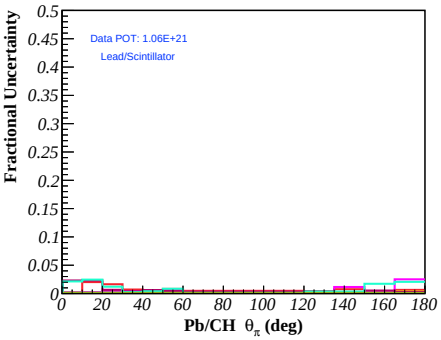


(a) Carbon/Scintillator

(b) Water/Scintillator



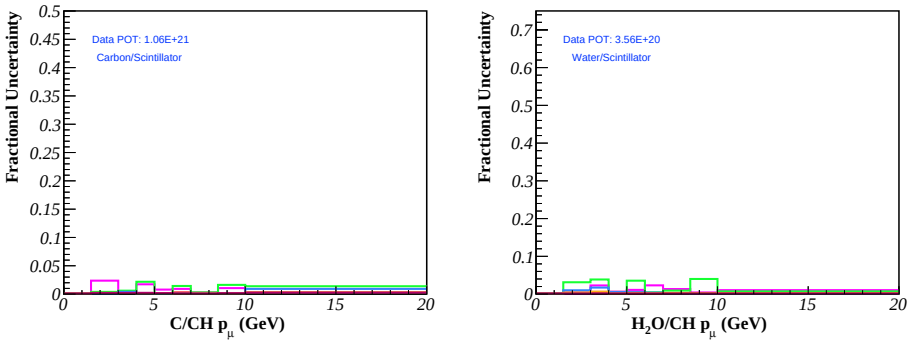
(c) Iron/Scintillator



(d) Lead/Scintillator

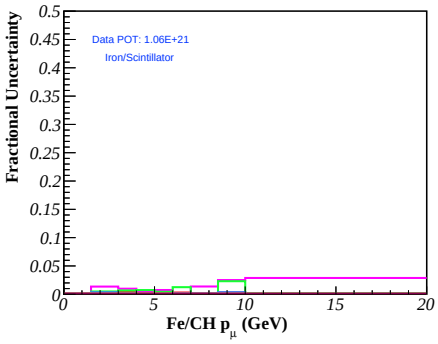


Figure F-96: θ_π Muon Reconstruction Errors

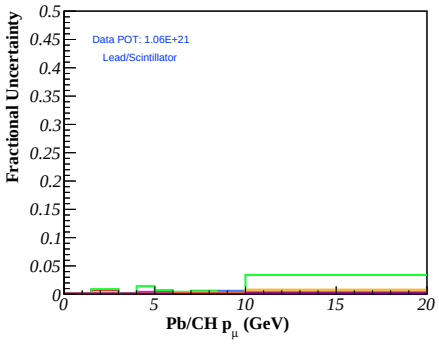


(a) Carbon/Scintillator

(b) Water/Scintillator



(c) Iron/Scintillator



(d) Lead/Scintillator

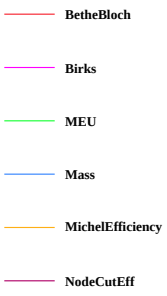
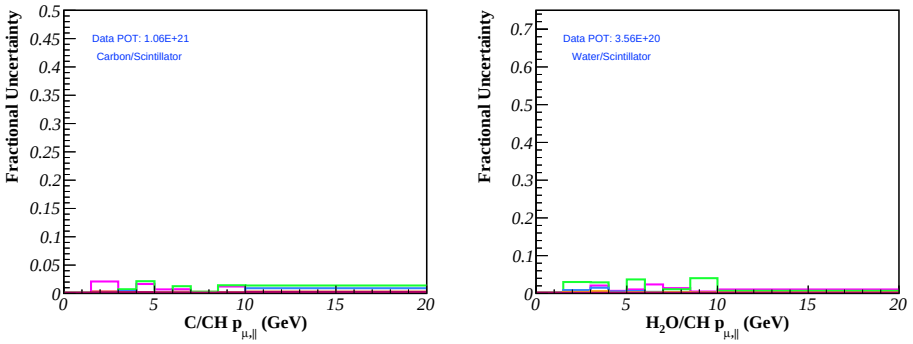


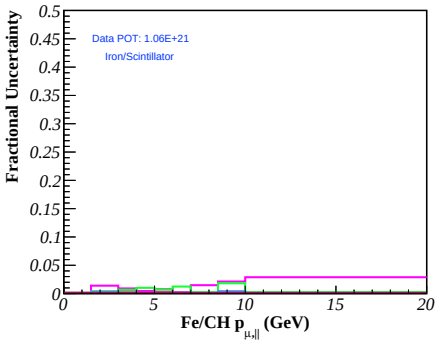
Figure F-97: p_μ Pion Reconstruction Errors

3

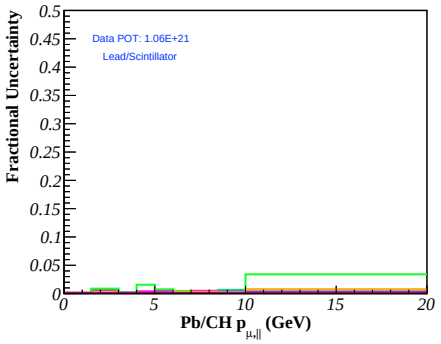


(a) Carbon/Scintillator

(b) Water/Scintillator



(c) Iron/Scintillator



(d) Lead/Scintillator

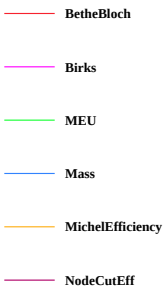
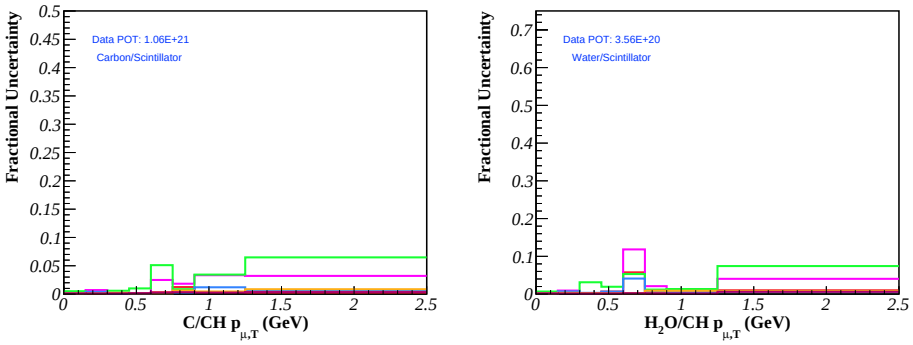


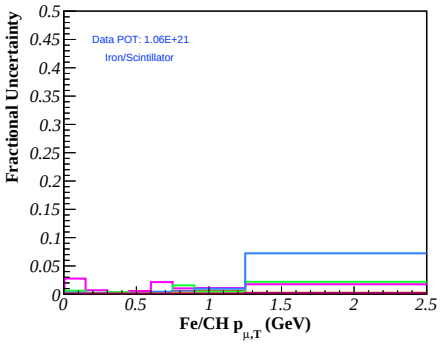
Figure F-98: $p_{\mu,||}$ Pion Reconstruction Errors

3

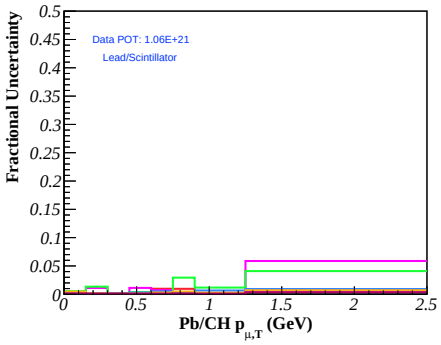


(a) Carbon/Scintillator

(b) Water/Scintillator



(c) Iron/Scintillator



(d) Lead/Scintillator

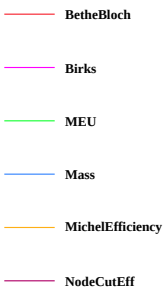
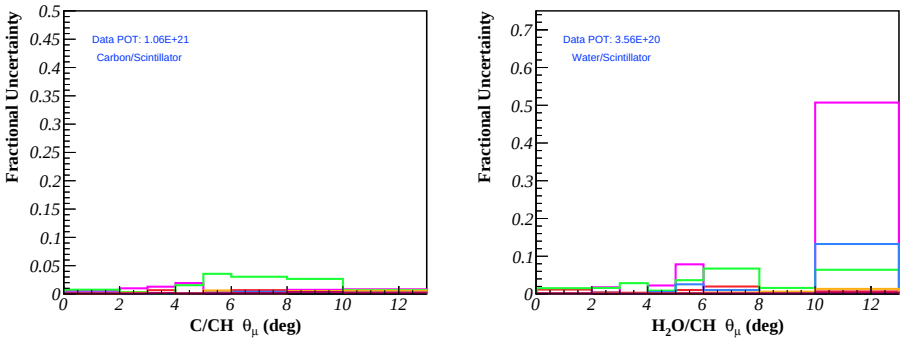
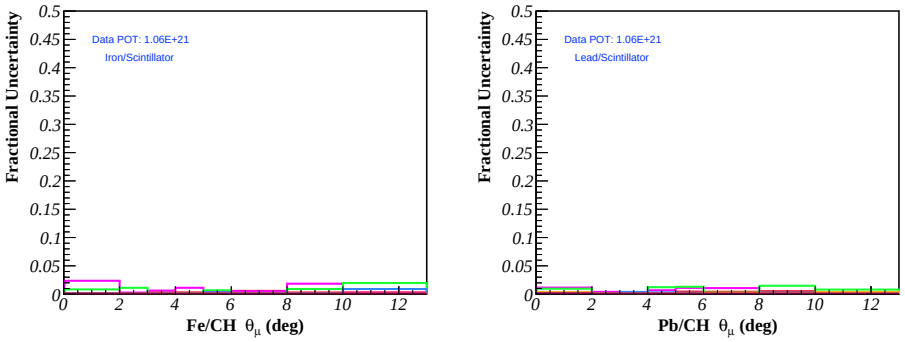


Figure F-99: $p_{\mu,T}$ Pion Reconstruction Errors



(a) Carbon/Scintillator

(b) Water/Scintillator



(c) Iron/Scintillator

(d) Lead/Scintillator

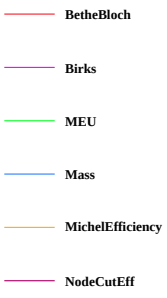
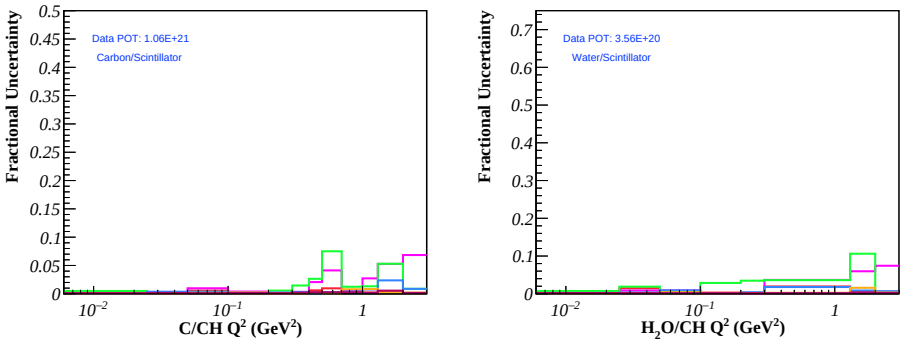


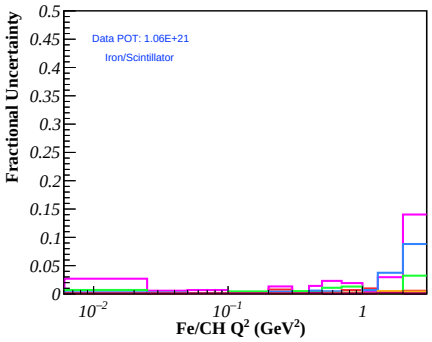
Figure F-100: θ_μ Pion Reconstruction Errors

3

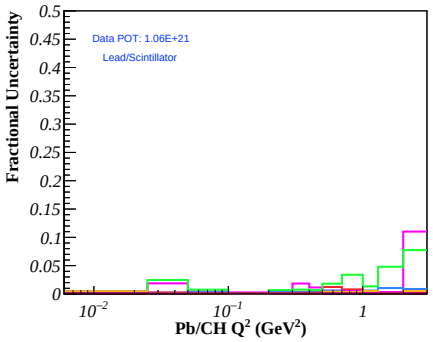


(a) Carbon/Scintillator

(b) Water/Scintillator



(c) Iron/Scintillator



(d) Lead/Scintillator

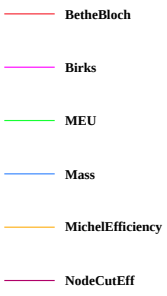
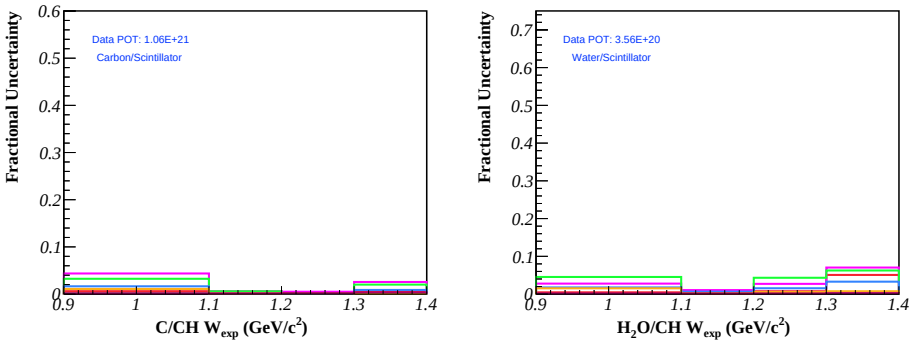


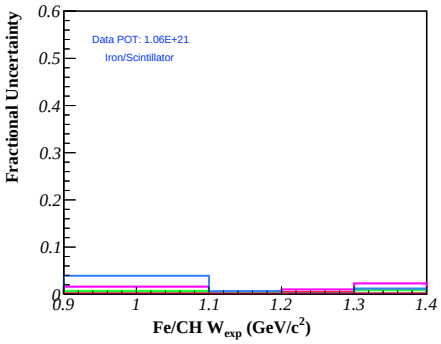
Figure F-101: Q^2 Pion Reconstruction Errors

3

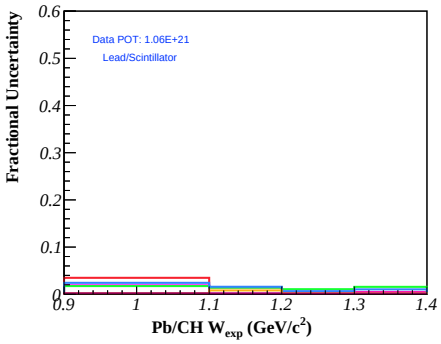


(a) Carbon/Scintillator

(b) Water/Scintillator



(c) Iron/Scintillator



(d) Lead/Scintillator

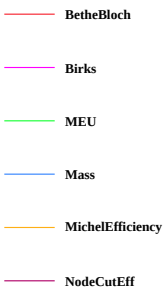
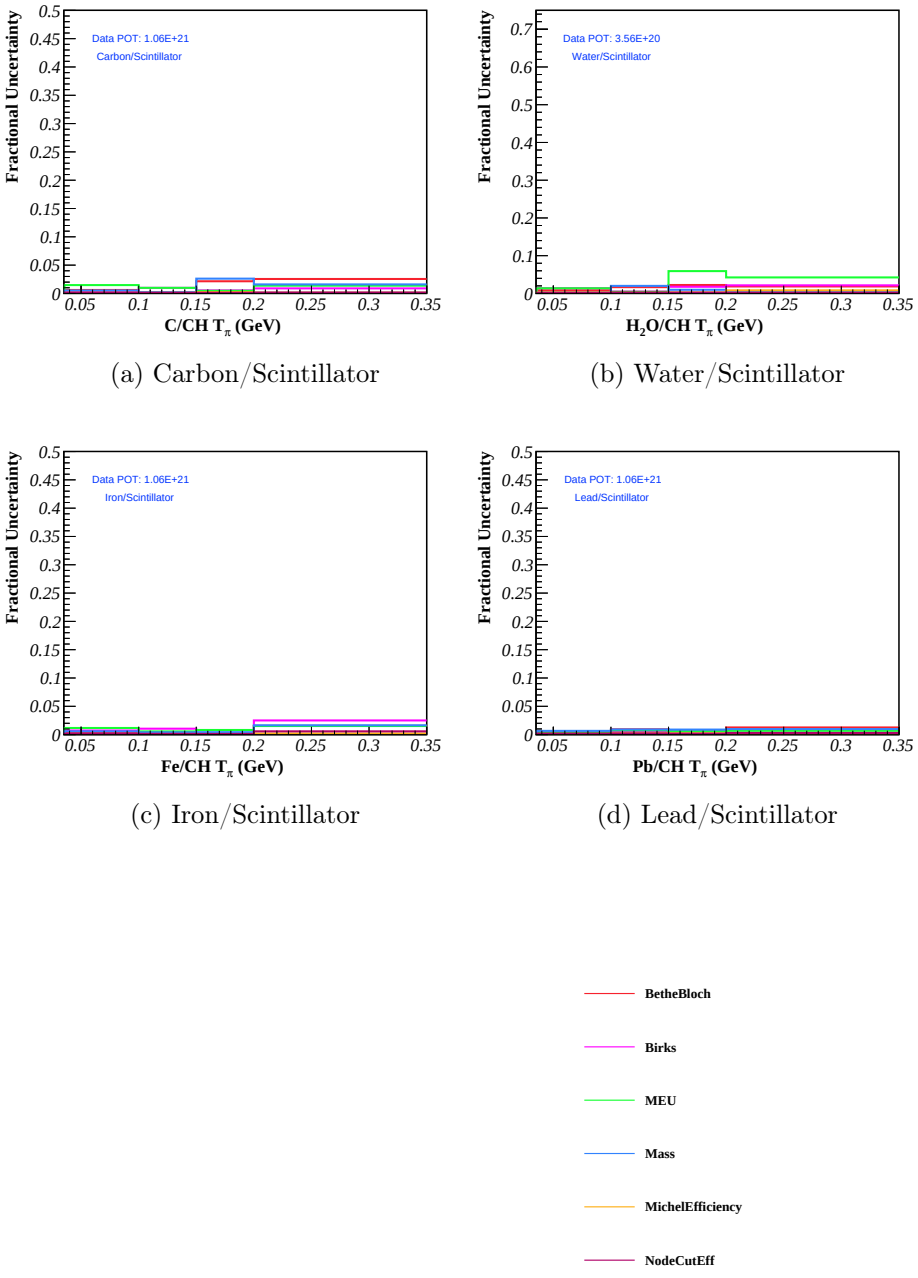


Figure F-102: W_{exp} Pion Reconstruction Errors

3



(a) Carbon/Scintillator

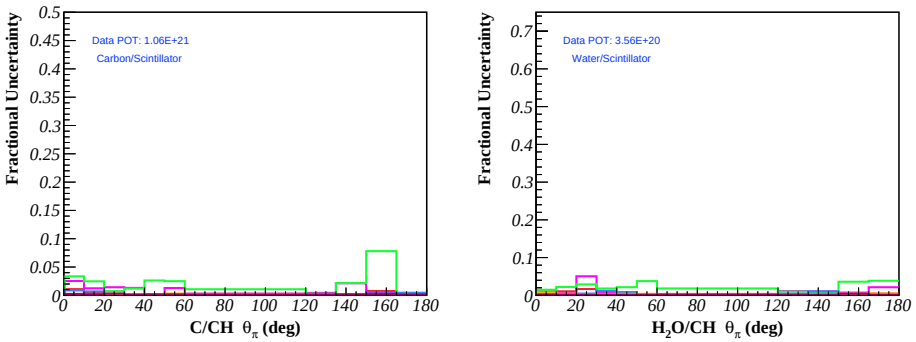
(b) Water/Scintillator

(c) Iron/Scintillator

(d) Lead/Scintillator

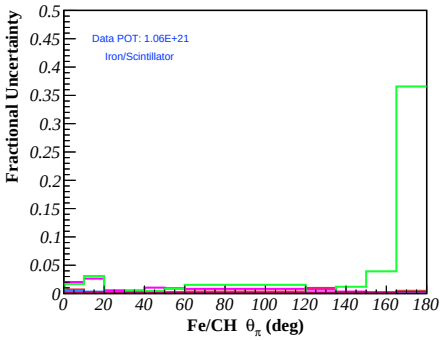
3

Figure F-103: T_π Pion Reconstruction Errors

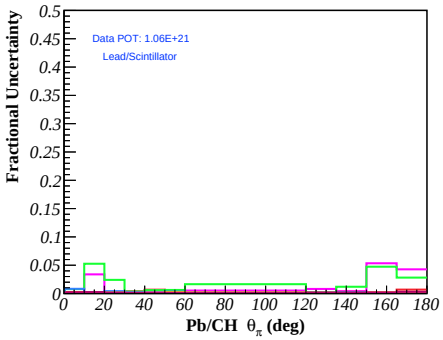


(a) Carbon/Scintillator

(b) Water/Scintillator



(c) Iron/Scintillator



(d) Lead/Scintillator

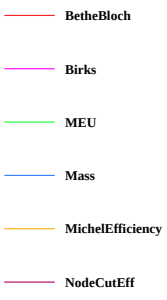
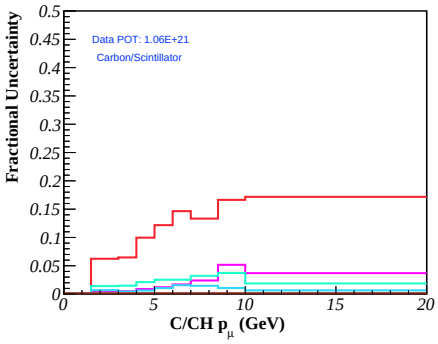
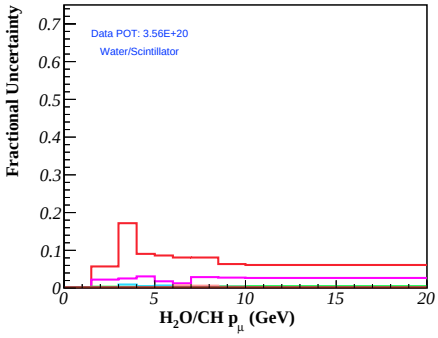


Figure F-104: θ_π Pion Reconstruction Errors

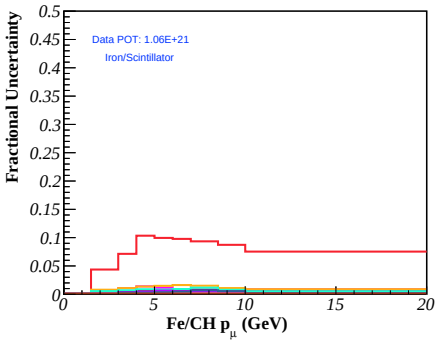
3



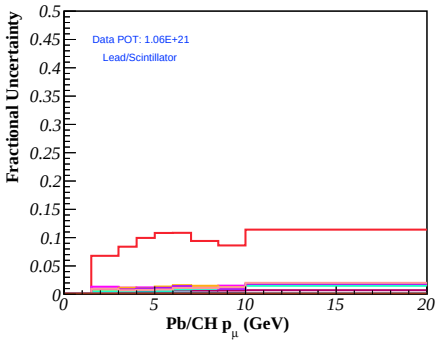
(a) Carbon/Scintillator



(b) Water/Scintillator



(c) Iron/Scintillator



(d) Lead/Scintillator

5

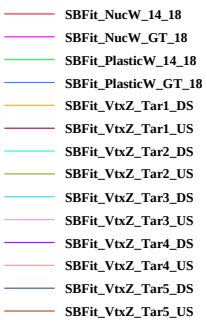
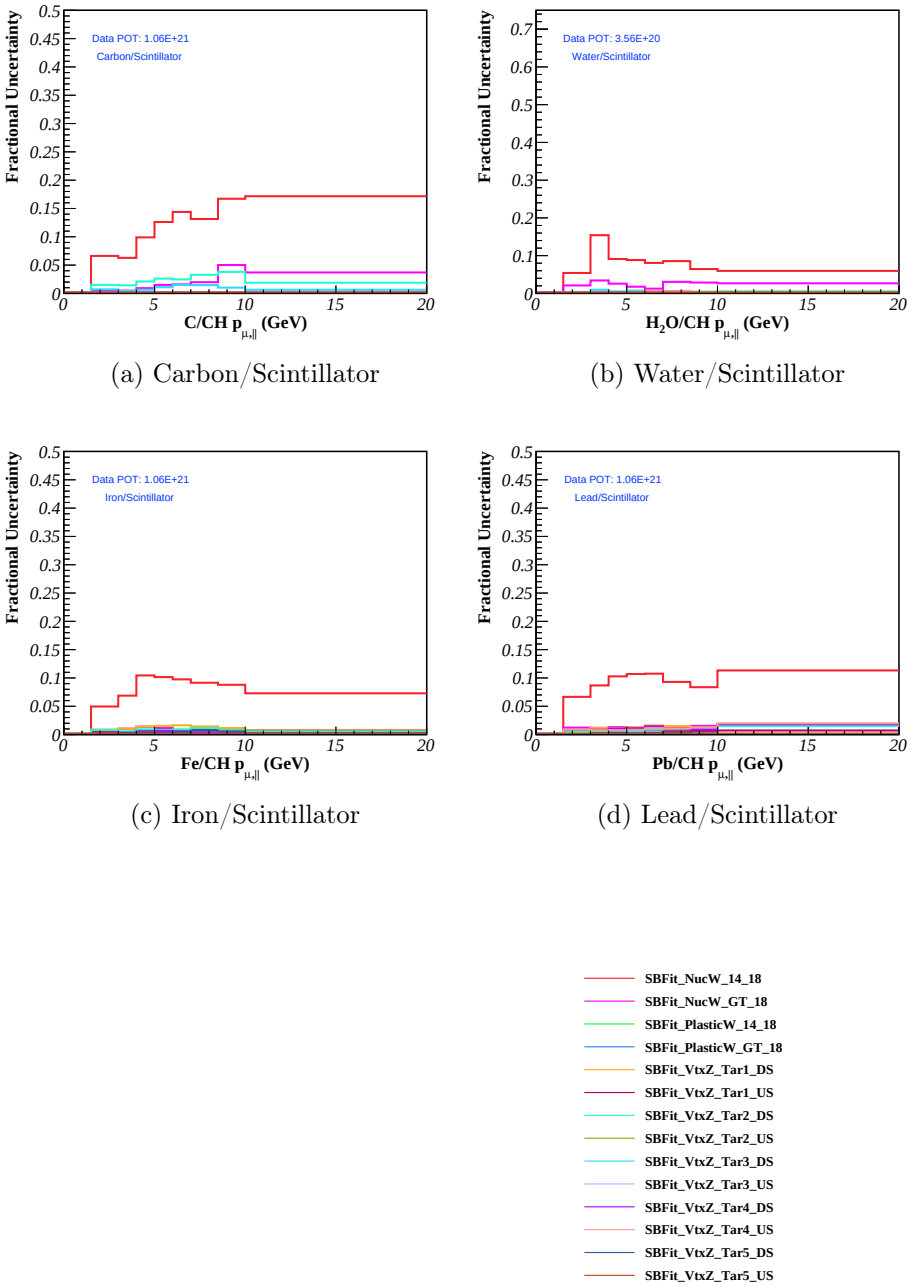


Figure F-105: p_μ Sideband Fit Errors



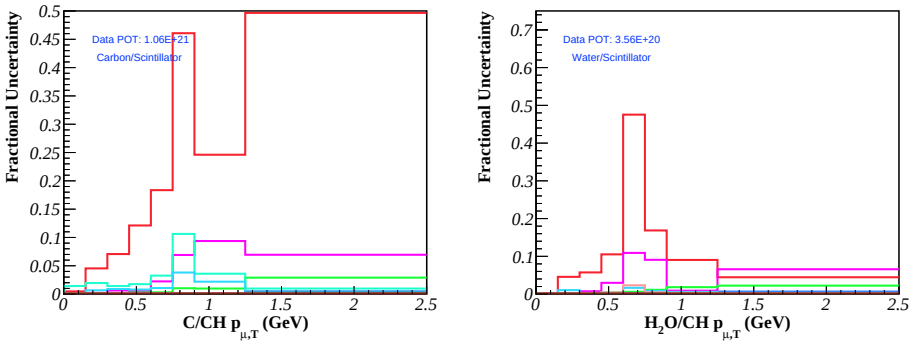
(a) Carbon/Scintillator

(b) Water/Scintillator

(c) Iron/Scintillator

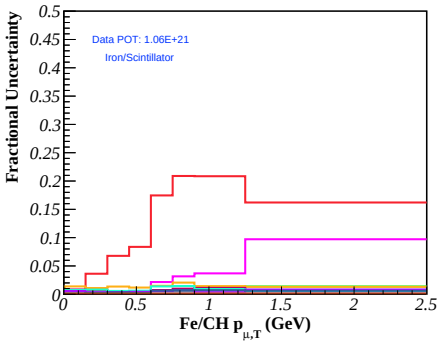
(d) Lead/Scintillator

Figure F-106: $p_{\mu,||}$ Sideband Fit Errors

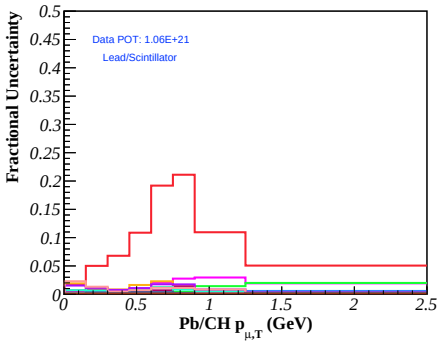


(a) Carbon/Scintillator

(b) Water/Scintillator



(c) Iron/Scintillator



(d) Lead/Scintillator

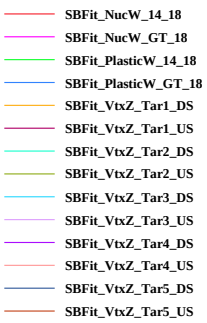
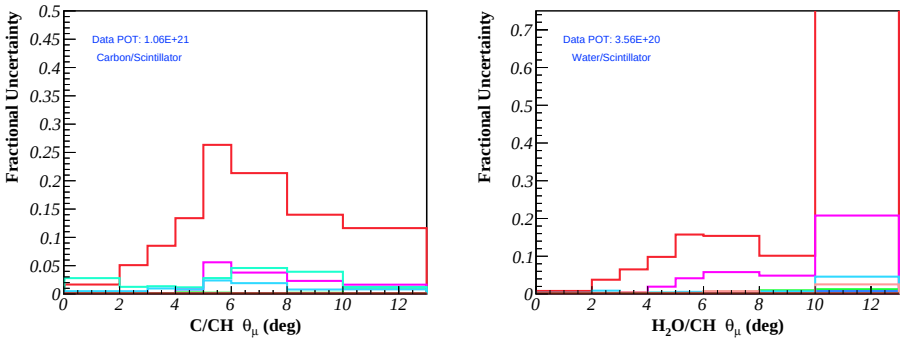
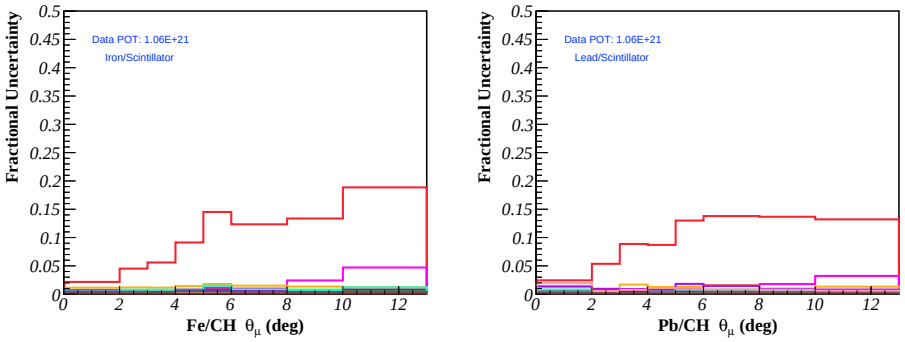


Figure F-107: $p_{\mu,T}$ Sideband Fit Errors



(a) Carbon/Scintillator

(b) Water/Scintillator



(c) Iron/Scintillator

(d) Lead/Scintillator

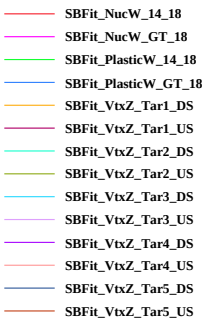
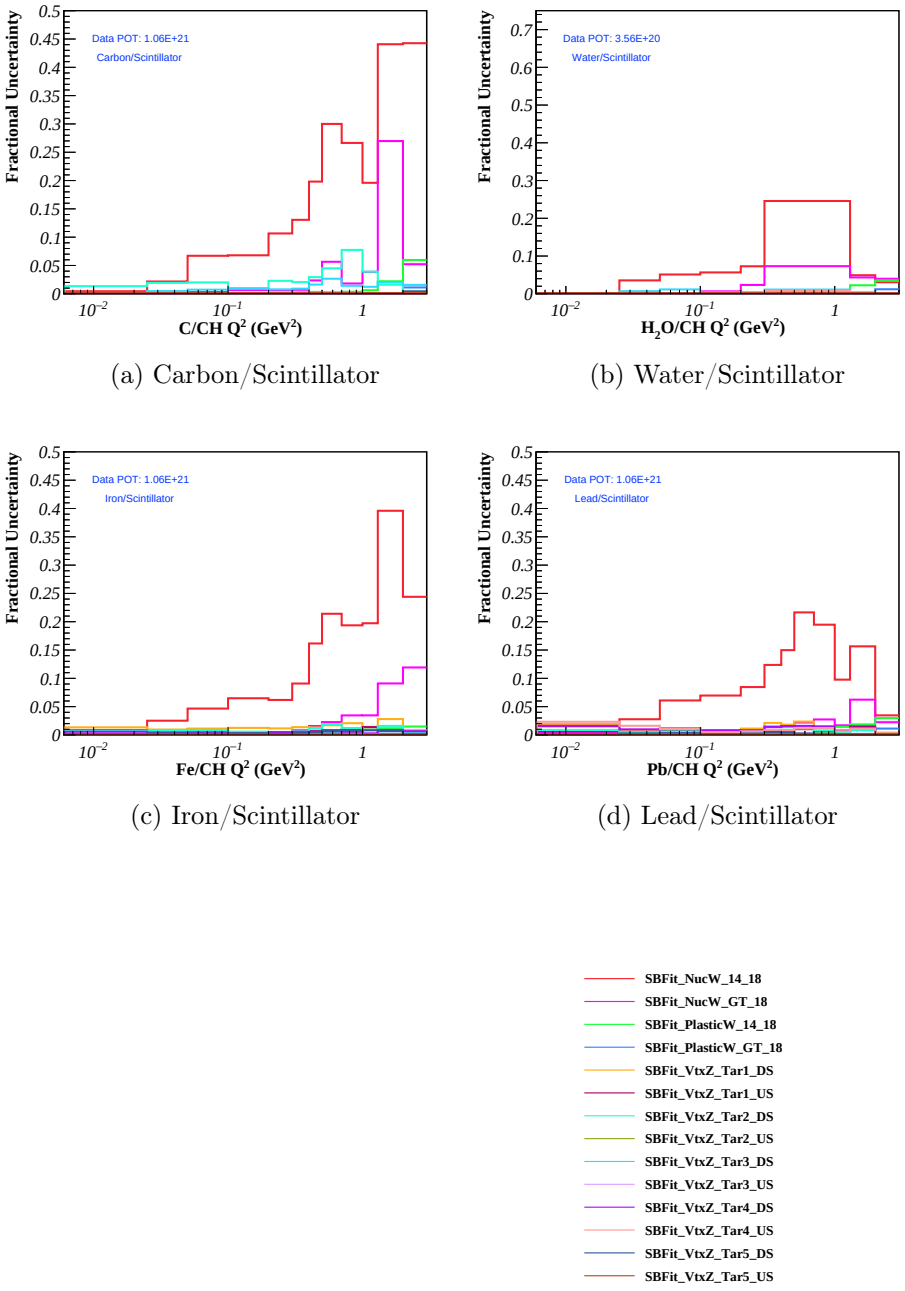


Figure F-108: θ_μ Sideband Fit Errors



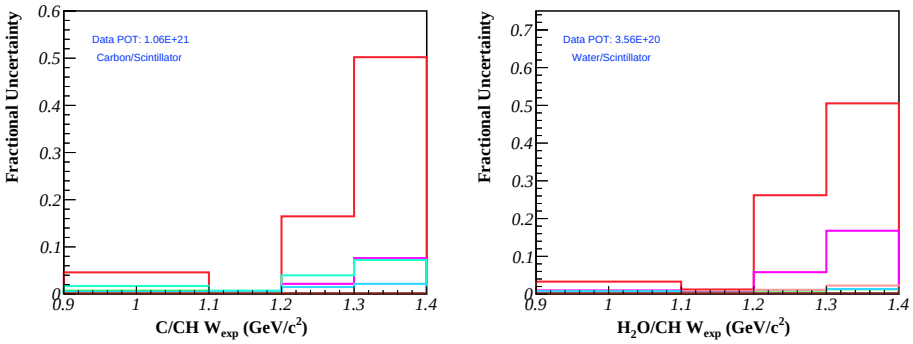
(a) Carbon/Scintillator

(b) Water/Scintillator

(c) Iron/Scintillator

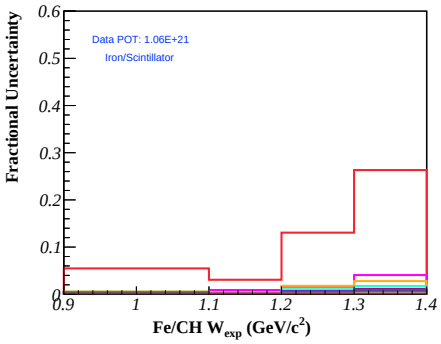
(d) Lead/Scintillator

Figure F-109: Q^2 Sideband Fit Errors

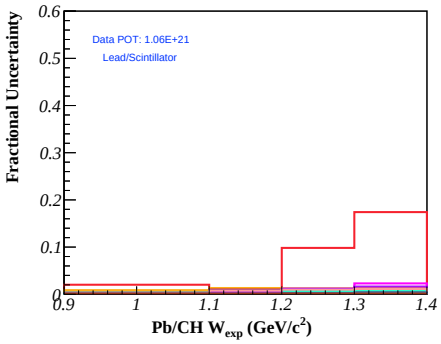


(a) Carbon/Scintillator

(b) Water/Scintillator



(c) Iron/Scintillator



(d) Lead/Scintillator

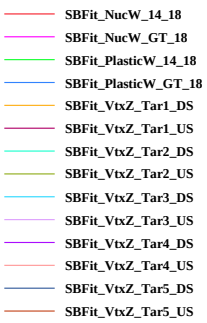
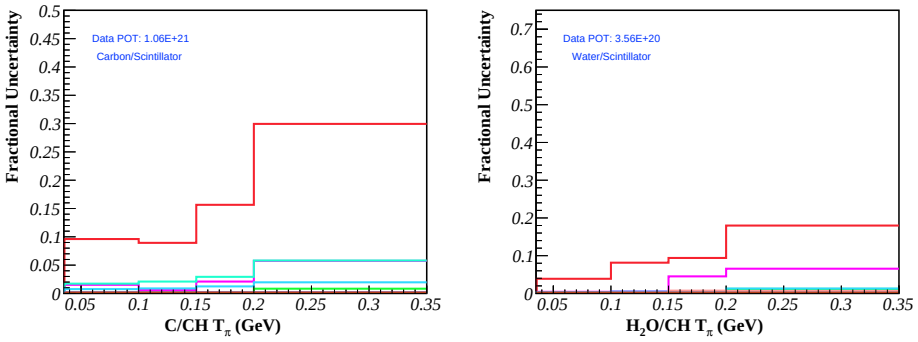


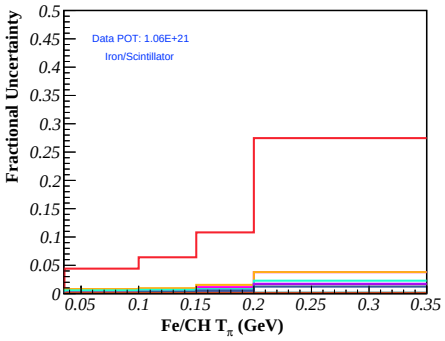
Figure F-110: W_{exp} Sideband Fit Errors

5

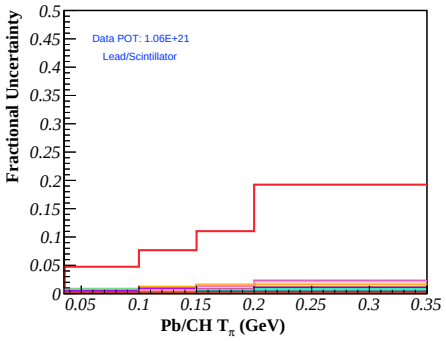


(a) Carbon/Scintillator

(b) Water/Scintillator



(c) Iron/Scintillator



(d) Lead/Scintillator

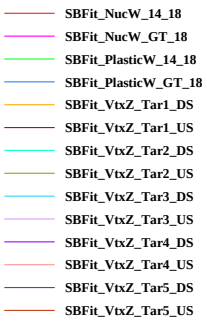
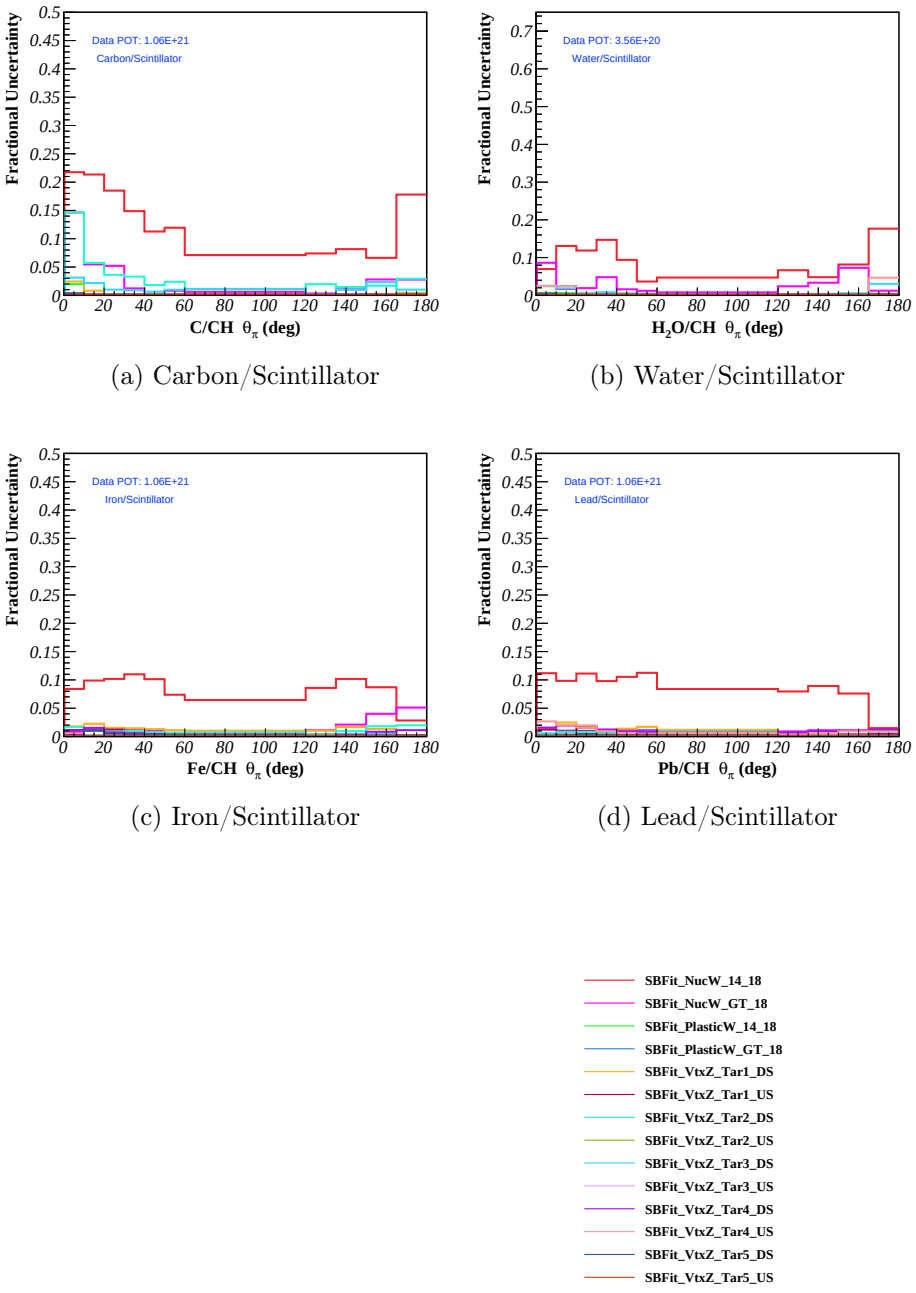


Figure F-111: T_π Sideband Fit Errors



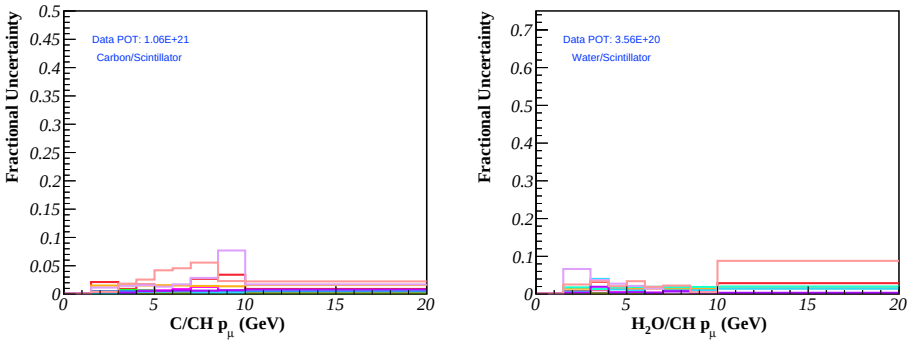
(a) Carbon/Scintillator

(b) Water/Scintillator

(c) Iron/Scintillator

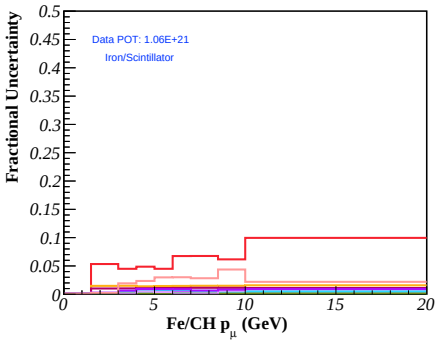
(d) Lead/Scintillator

Figure F-112: θ_π Sideband Fit Errors

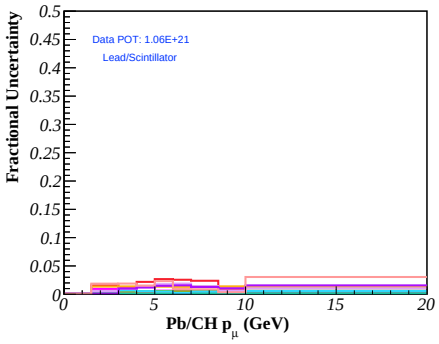


(a) Carbon/Scintillator

(b) Water/Scintillator



(c) Iron/Scintillator



(d) Lead/Scintillator

4

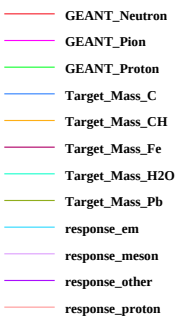
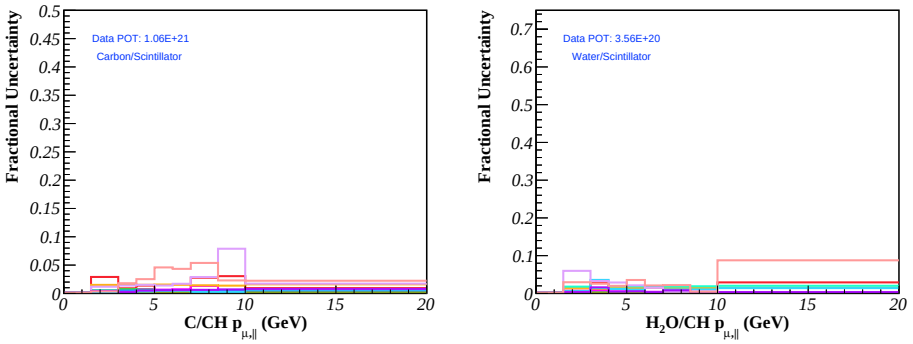
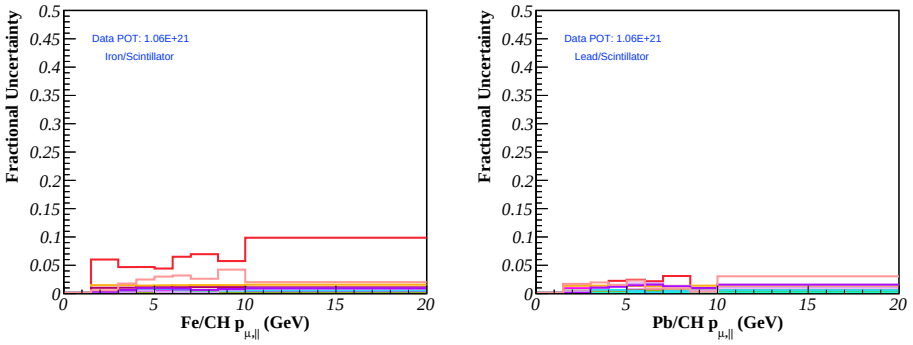


Figure F-113: p_μ Other Systematic Errors



(a) Carbon/Scintillator (b) Water/Scintillator



(c) Iron/Scintillator (d) Lead/Scintillator

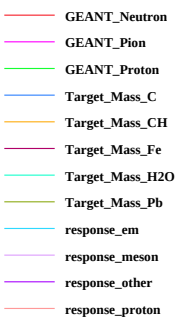
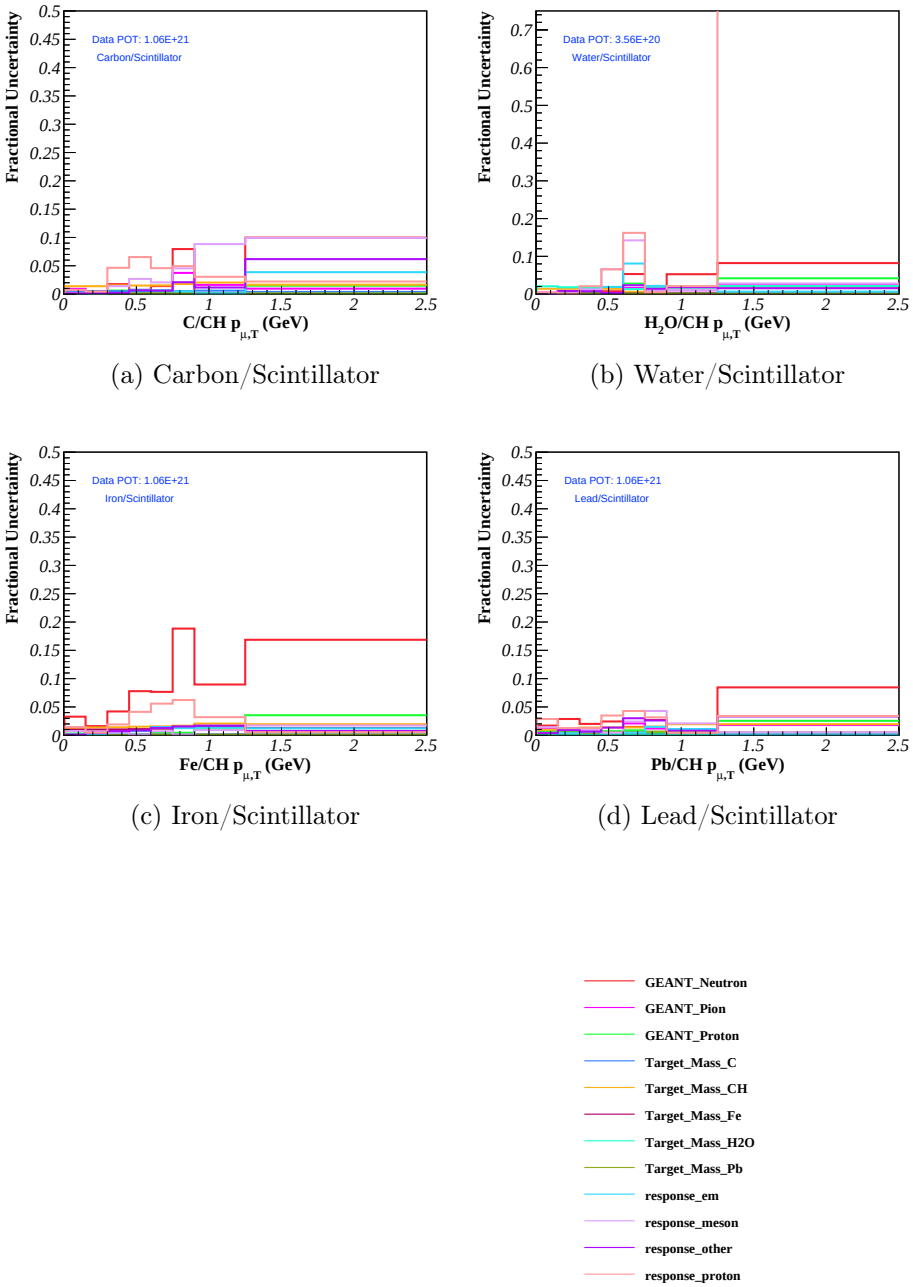


Figure F-114: $p_{\mu,||}$ Other Systematic Errors

4



(a) Carbon/Scintillator

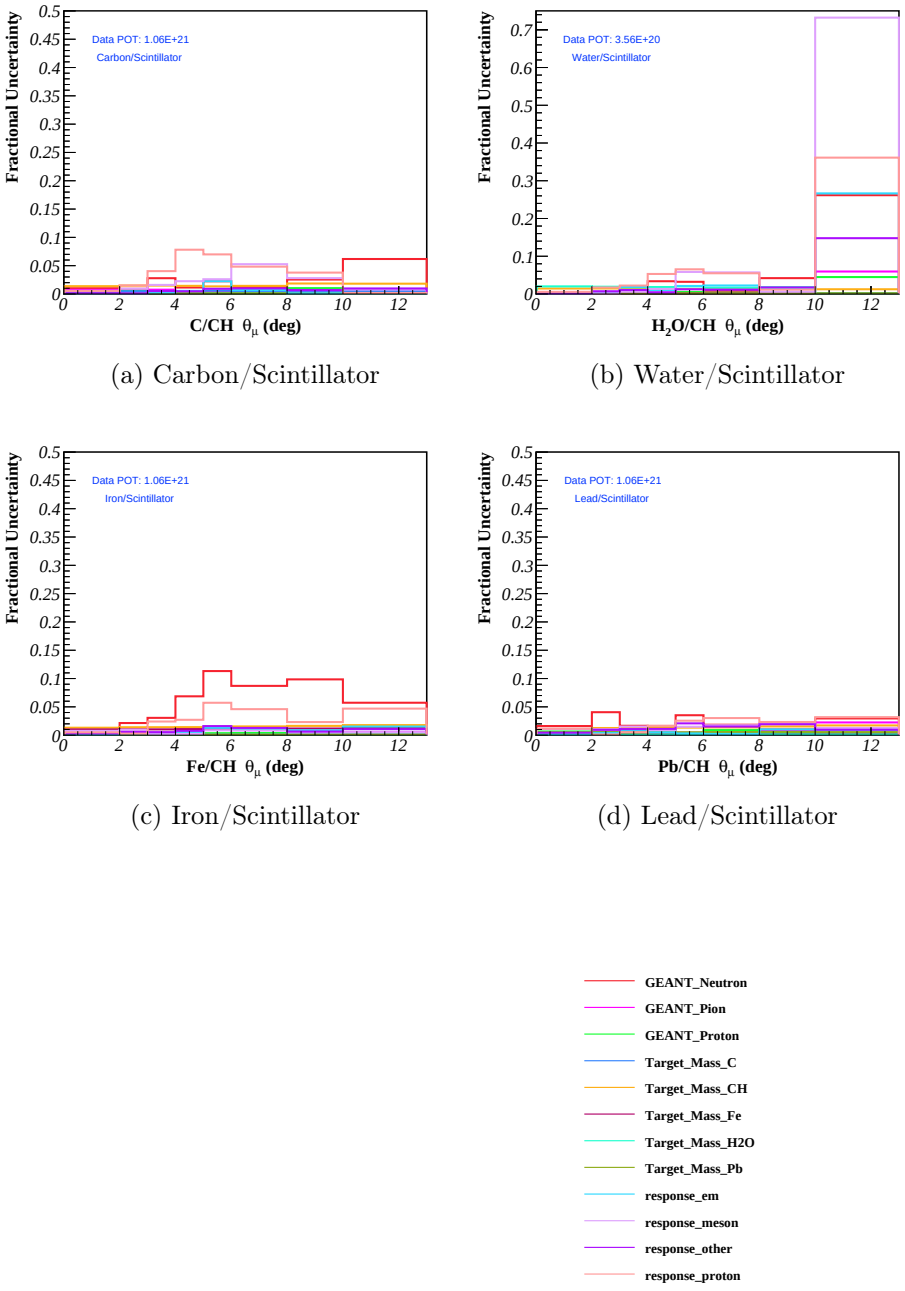
(b) Water/Scintillator

(c) Iron/Scintillator

(d) Lead/Scintillator

4

Figure F-115: $p_{\mu,T}$ Other Systematic Errors



(a) Carbon/Scintillator

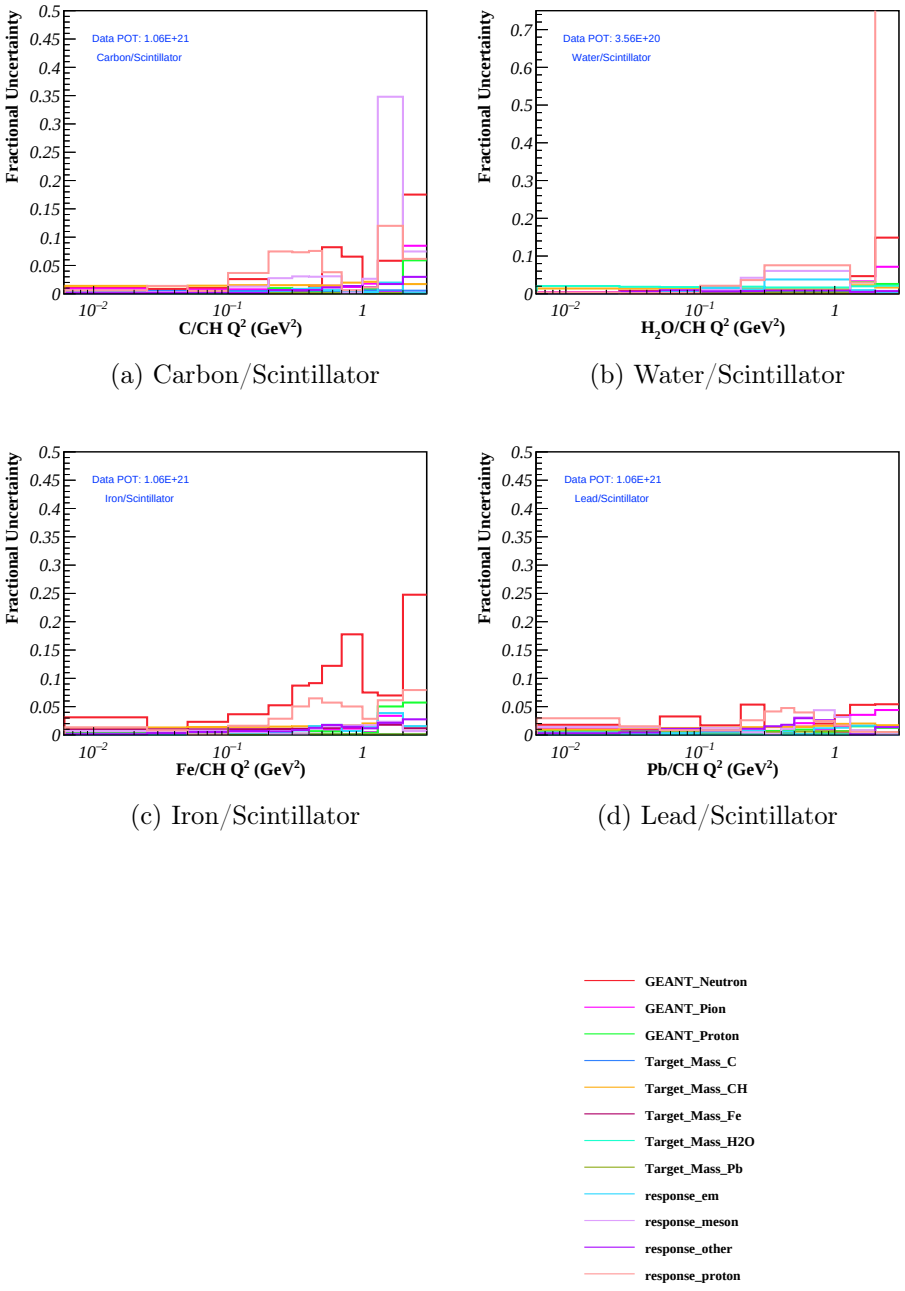
(b) Water/Scintillator

(c) Iron/Scintillator

(d) Lead/Scintillator

4

Figure F-116: θ_μ Other Systematic Errors



(a) Carbon/Scintillator

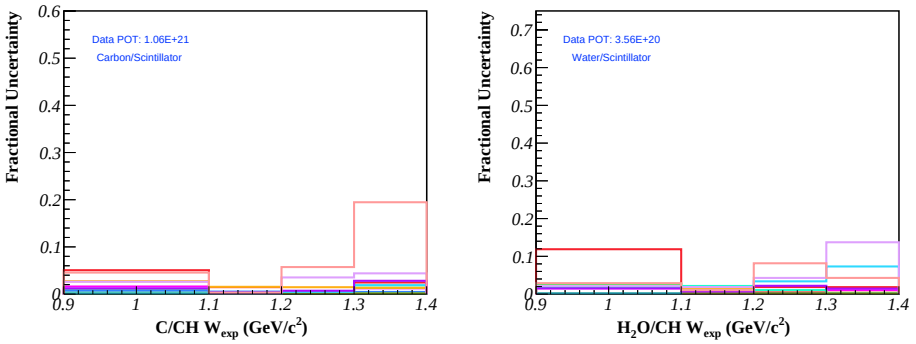
(b) Water/Scintillator

(c) Iron/Scintillator

(d) Lead/Scintillator

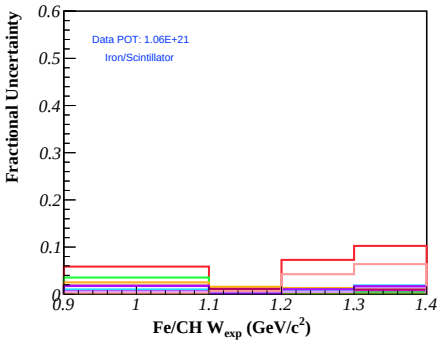
4

Figure F-117: Q^2 Other Systematic Errors

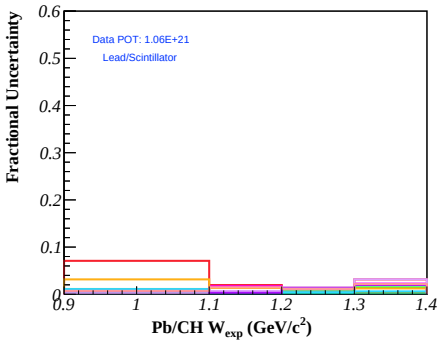


(a) Carbon/Scintillator

(b) Water/Scintillator



(c) Iron/Scintillator



(d) Lead/Scintillator

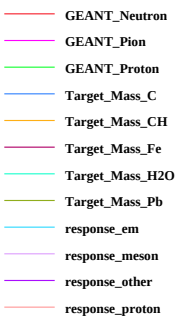
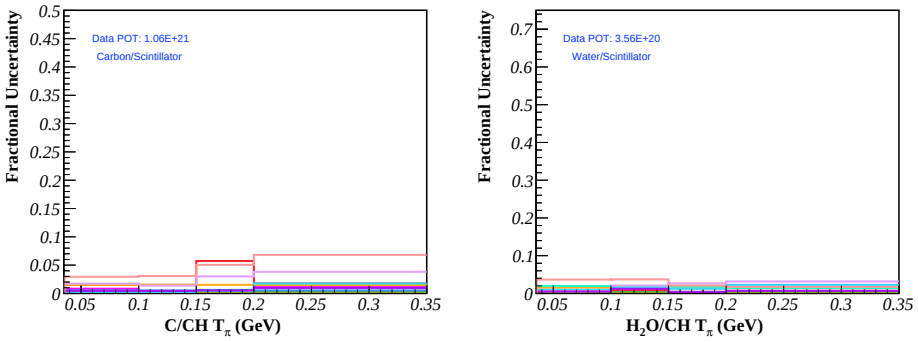


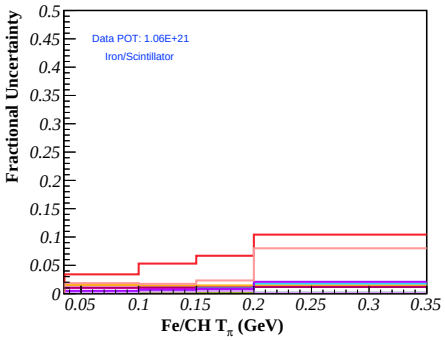
Figure F-118: W_{exp} Other Systematic Errors

4

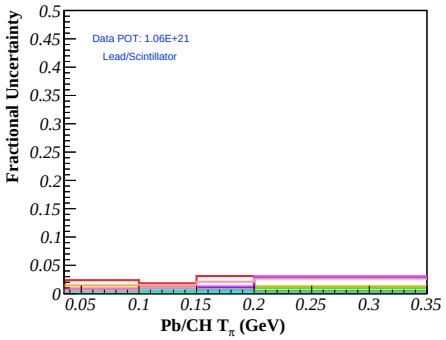


(a) Carbon/Scintillator

(b) Water/Scintillator



(c) Iron/Scintillator



(d) Lead/Scintillator

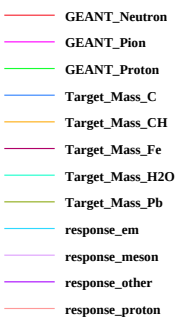
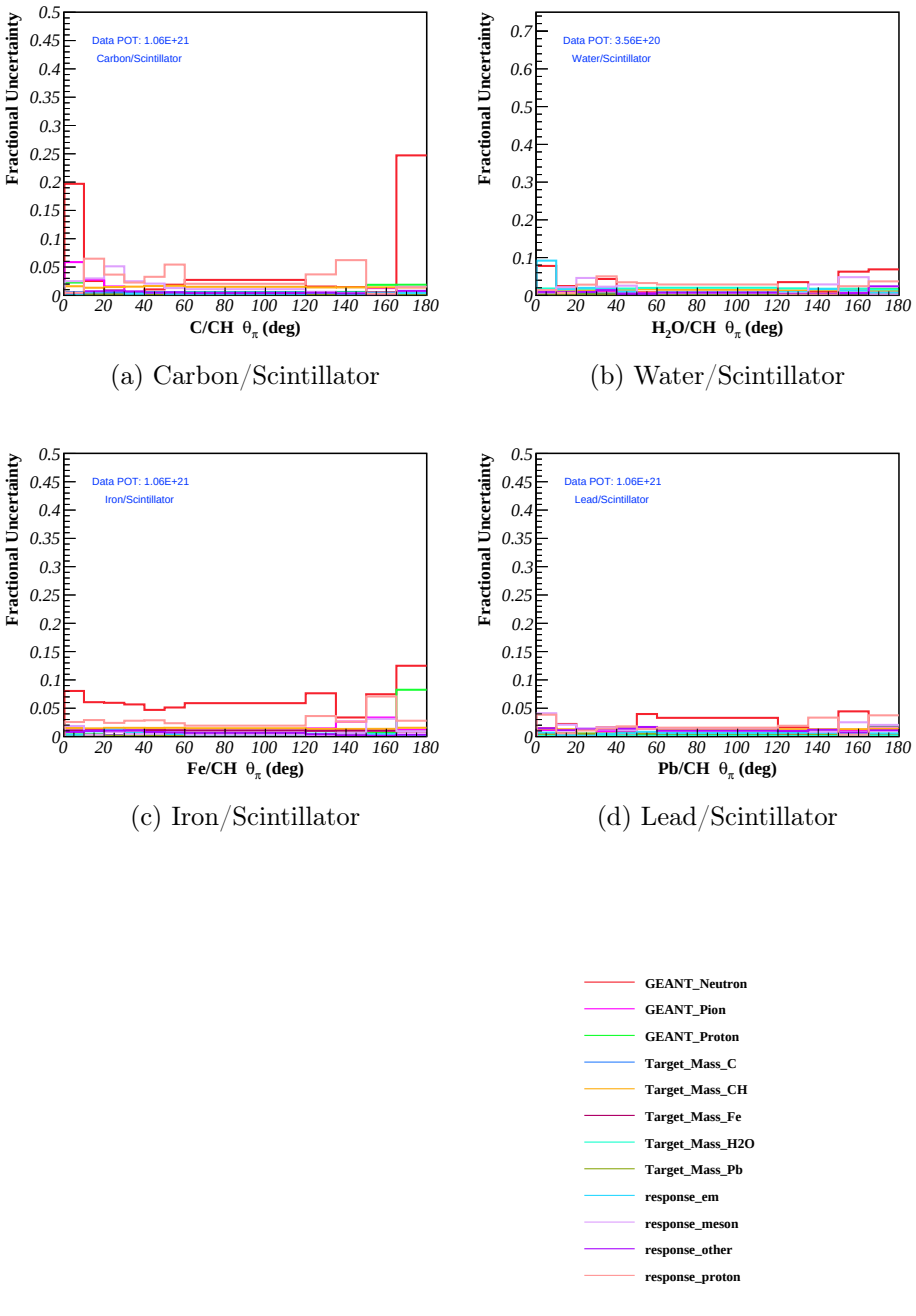


Figure F-119: T_π Other Systematic Errors

4



(a) Carbon/Scintillator

(b) Water/Scintillator

(c) Iron/Scintillator

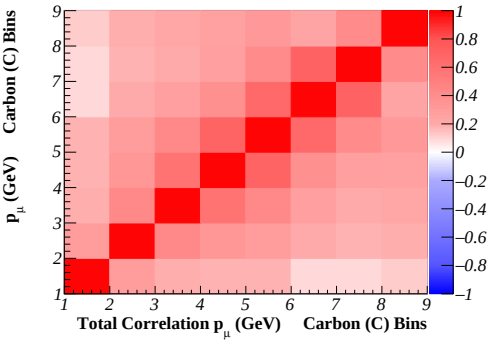
(d) Lead/Scintillator

4

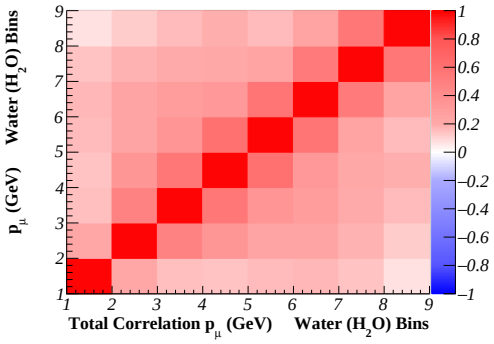
Figure F-120: θ_π Other Systematic Errors

Appendix G

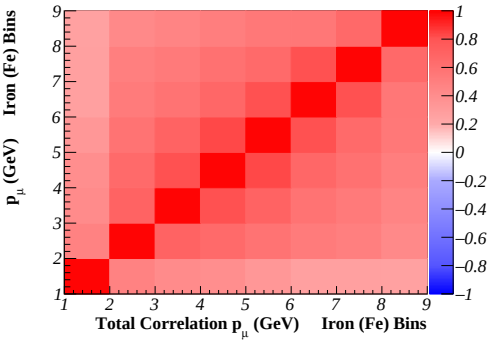
Cross Section Correlation Matrices



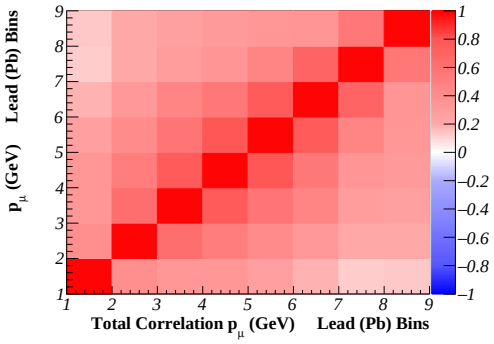
(a) Carbon



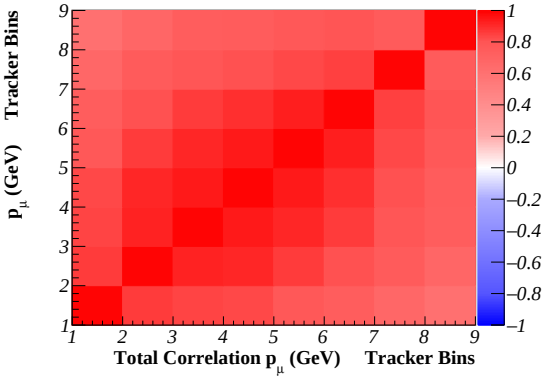
(b) Water



(c) Iron

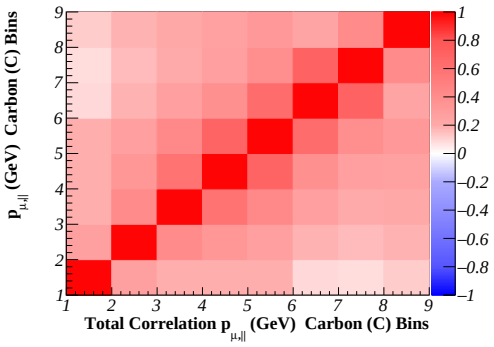


(d) Lead

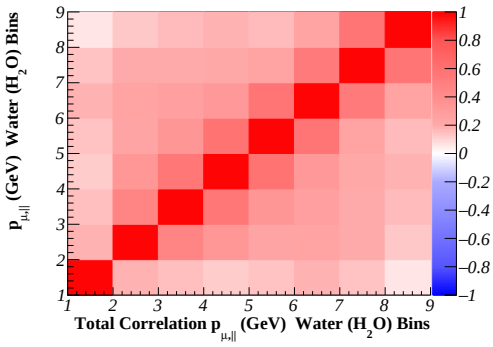


(e) Scintillator

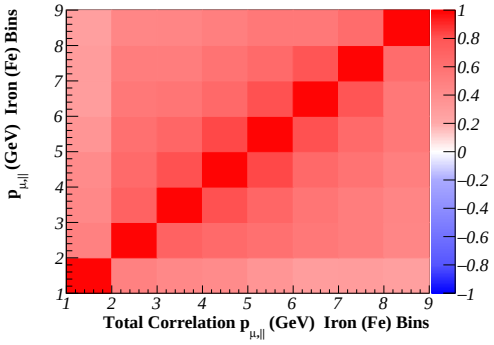
Figure G-1: p_μ Total Cross Section Correlation Matrix



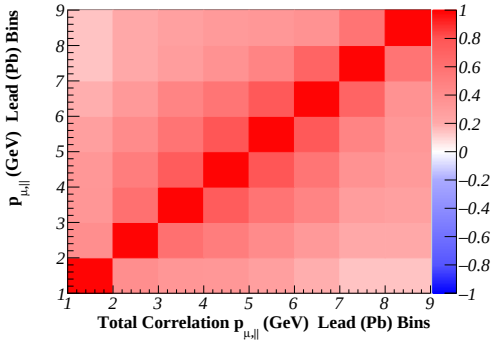
(a) Carbon



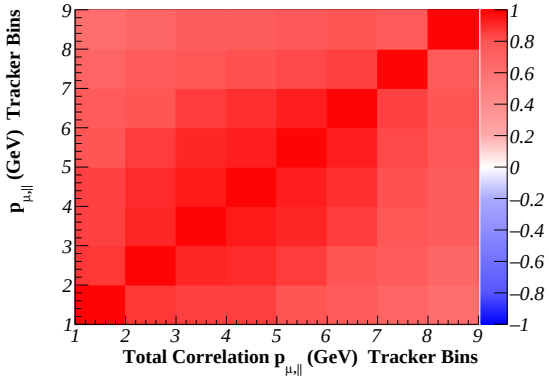
(b) Water



(c) Iron

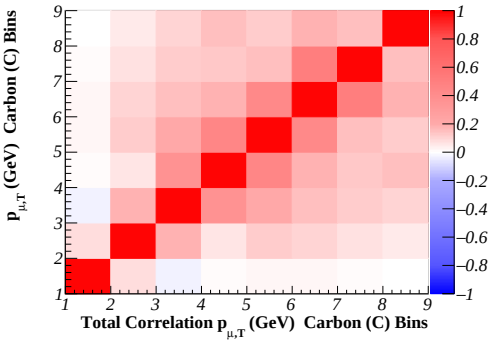


(d) Lead

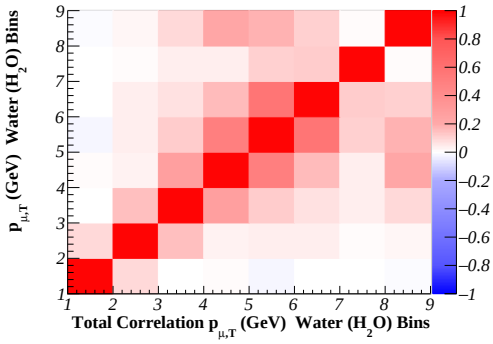


(e) Scintillator

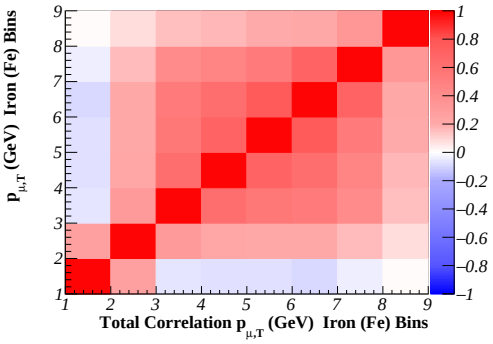
Figure G-2: $p_{\mu,||}$ Total Cross Section Correlation Matrix



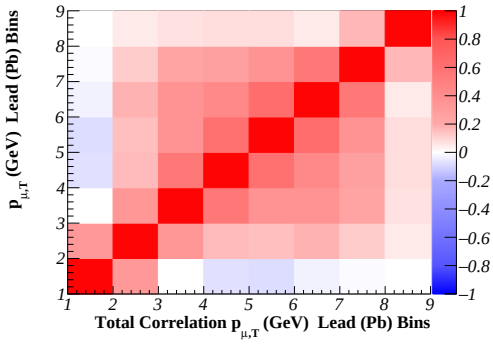
(a) Carbon



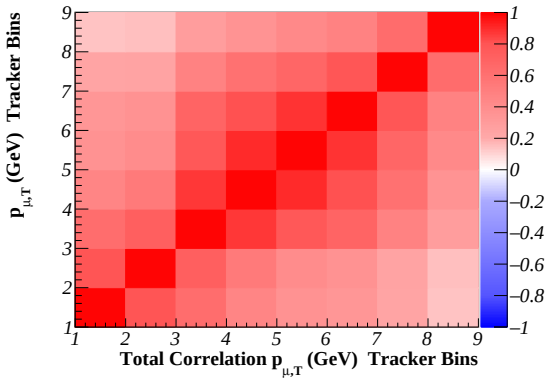
(b) Water



(c) Iron

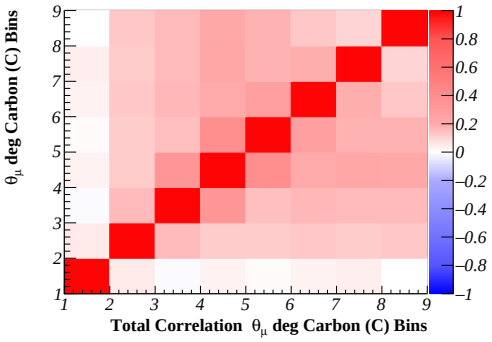


(d) Lead

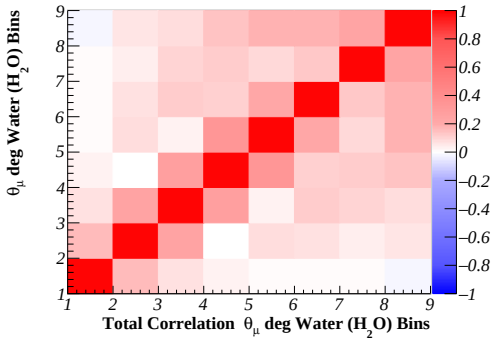


(e) Scintillator

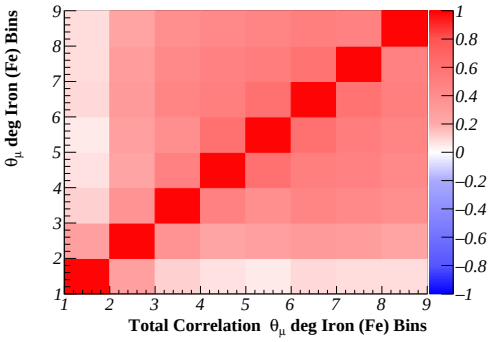
Figure G-3: $p_{\mu,T}$ Total Cross Section Correlation Matrix



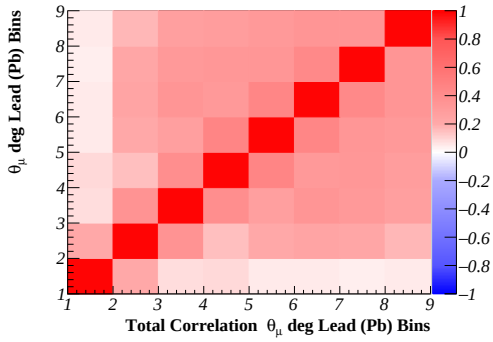
(a) Carbon



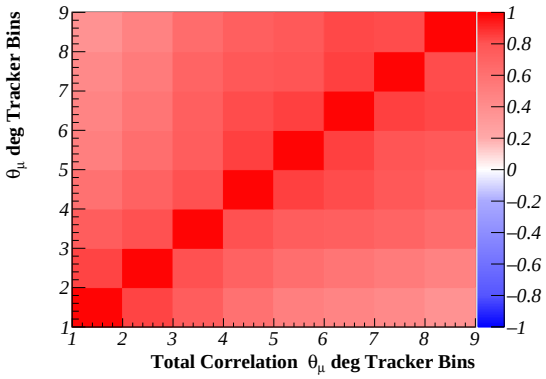
(b) Water



(c) Iron

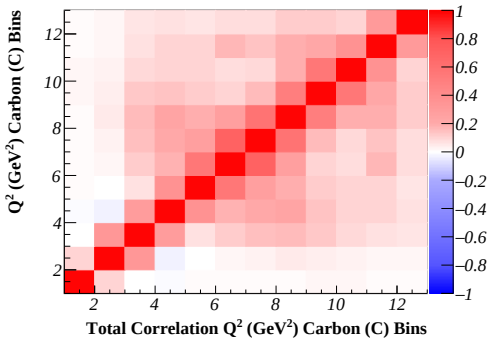


(d) Lead

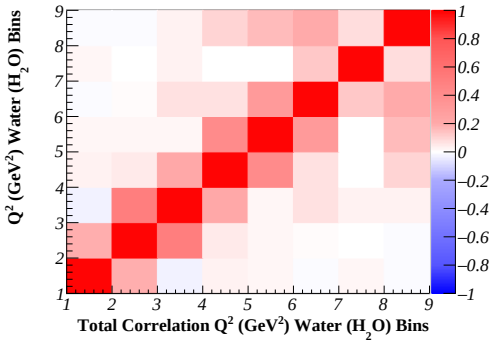


(e) Scintillator

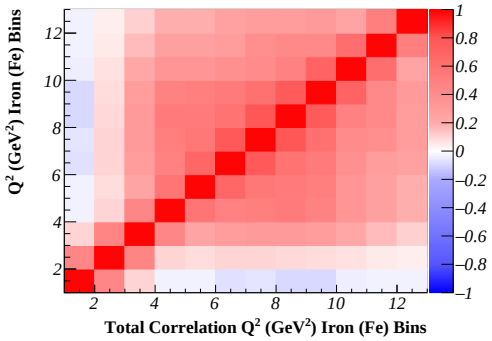
Figure G-4: θ_μ Total Cross Section Correlation Matrix



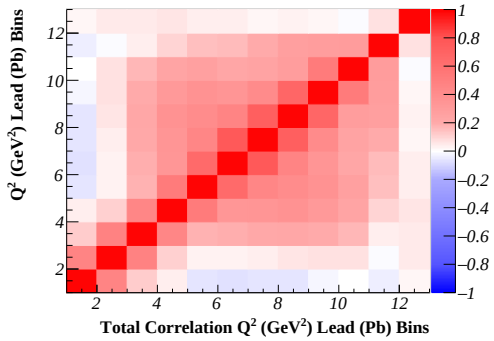
(a) Carbon



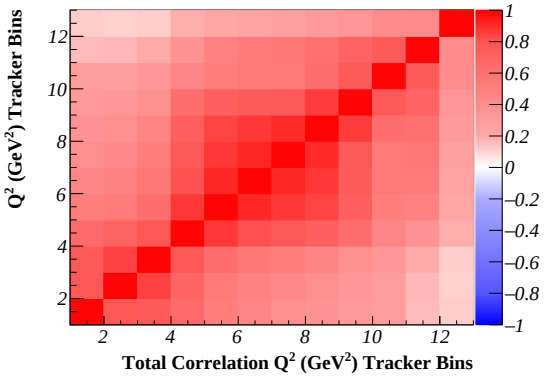
(b) Water



(c) Iron

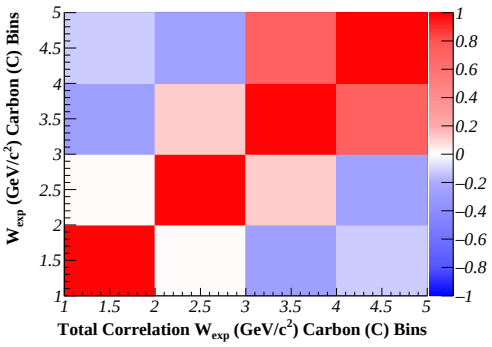


(d) Lead

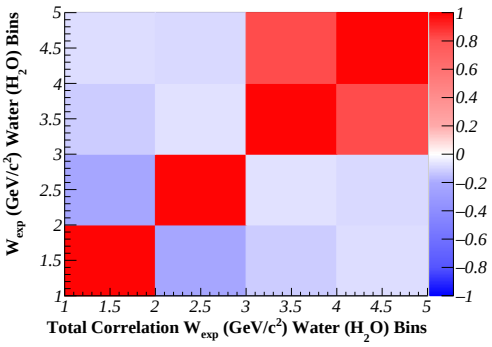


(e) Scintillator

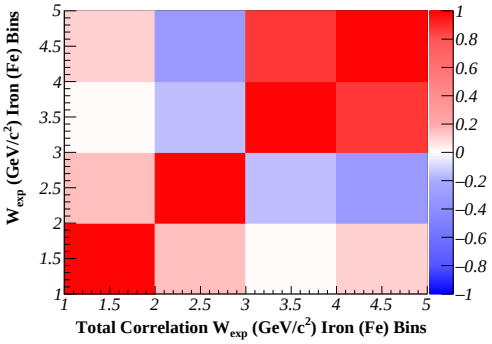
Figure G-5: Q^2 Total Cross Section Correlation Matrix



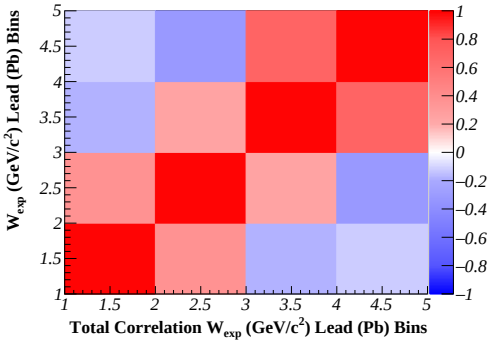
(a) Carbon



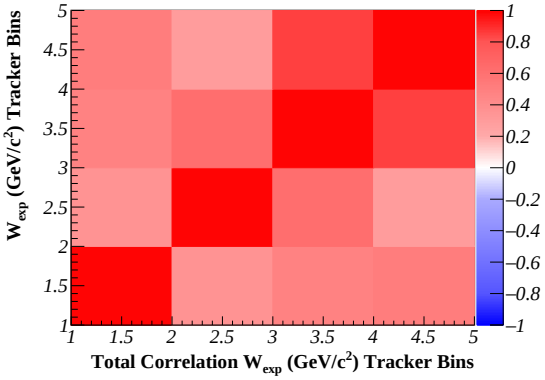
(b) Water



(c) Iron

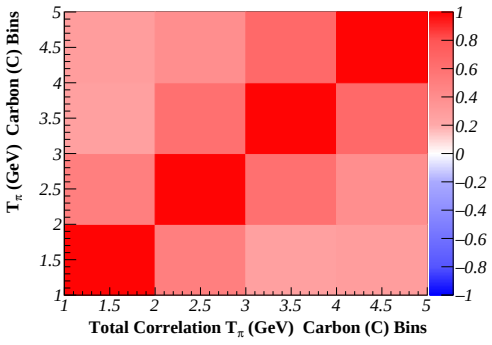


(d) Lead

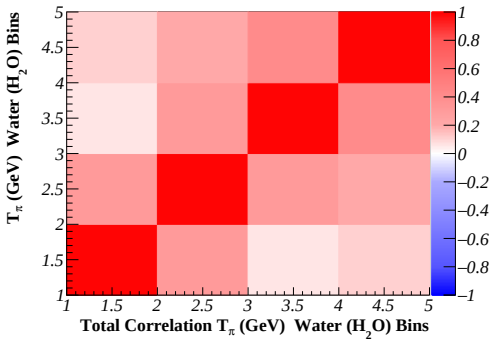


(e) Scintillator

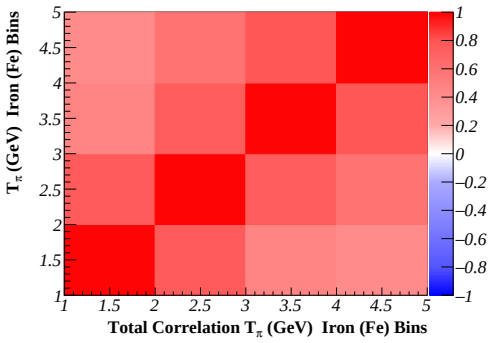
Figure G-6: W_{exp} Total Cross Section Correlation Matrix



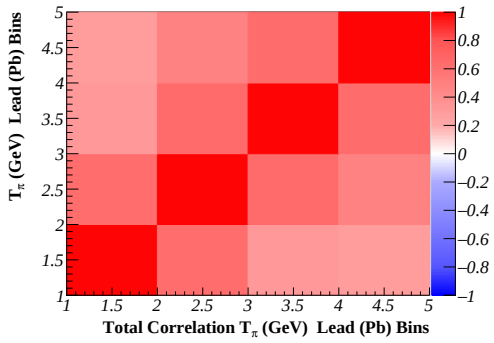
(a) Carbon



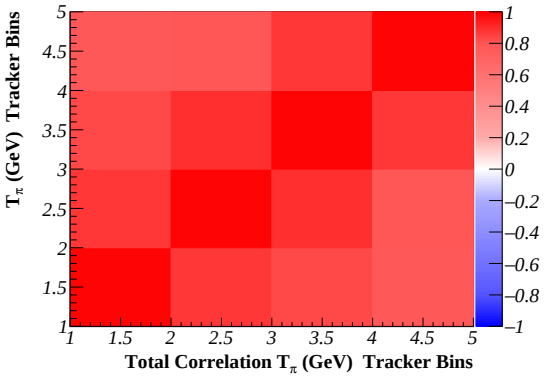
(b) Water



(c) Iron

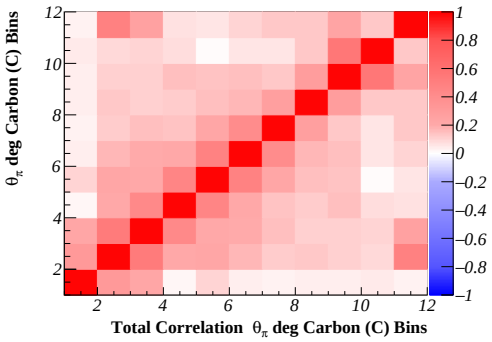


(d) Lead

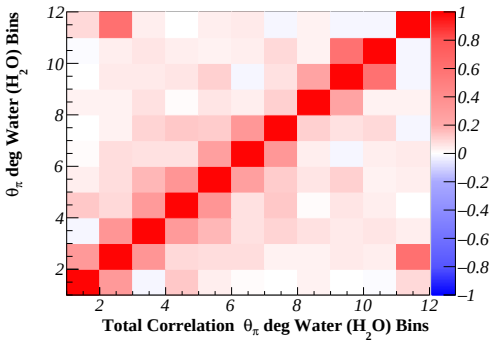


(e) Scintillator

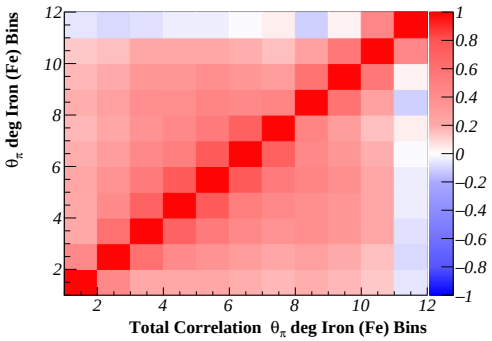
Figure G-7: T_π Total Cross Section Correlation Matrix



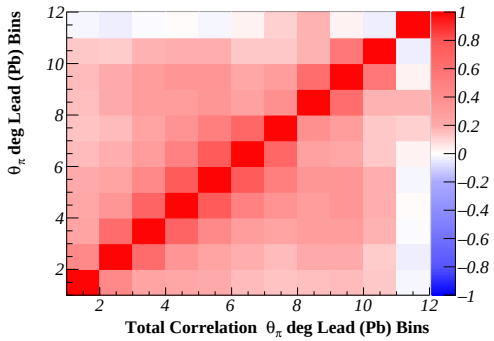
(a) Carbon



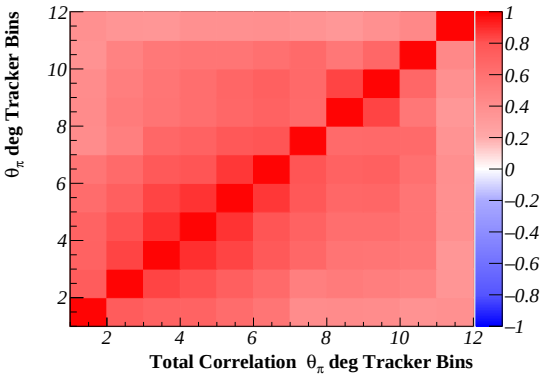
(b) Water



(c) Iron

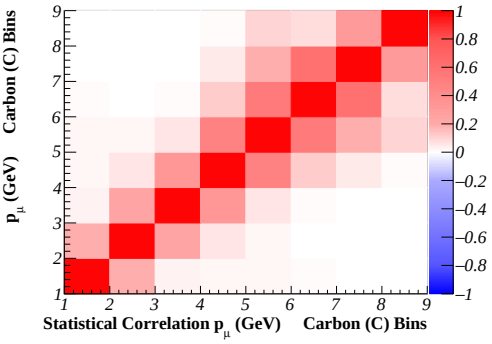


(d) Lead

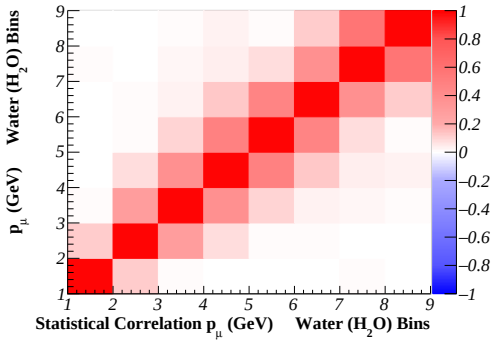


(e) Scintillator

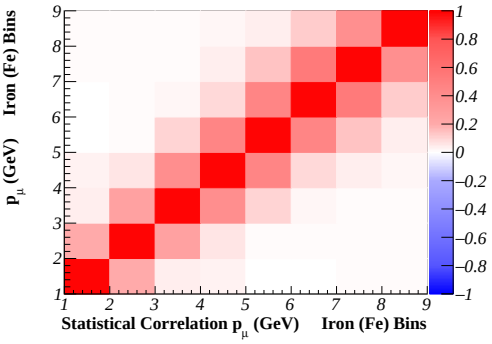
Figure G-8: θ_π Total Cross Section Correlation Matrix



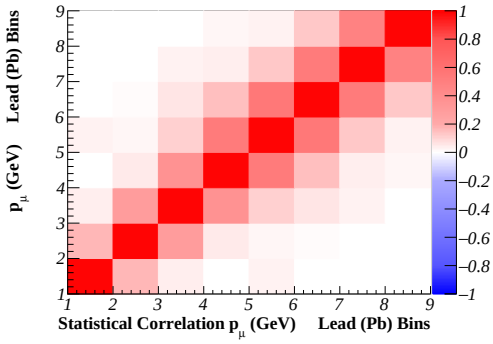
(a) Carbon



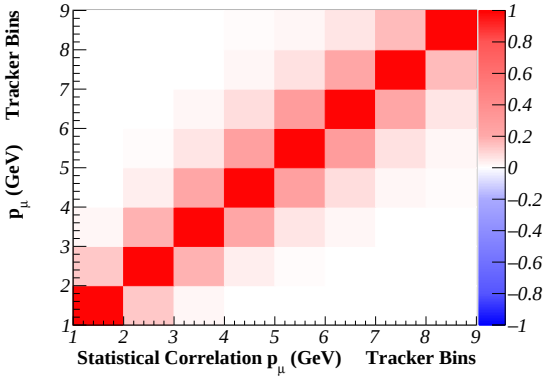
(b) Water



(c) Iron

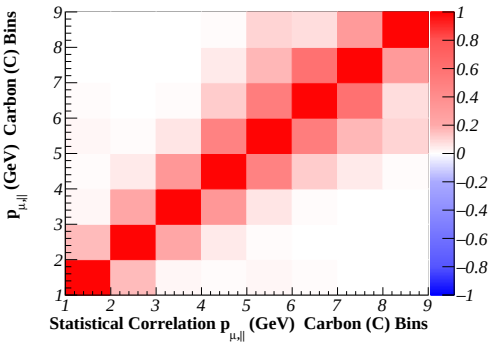


(d) Lead

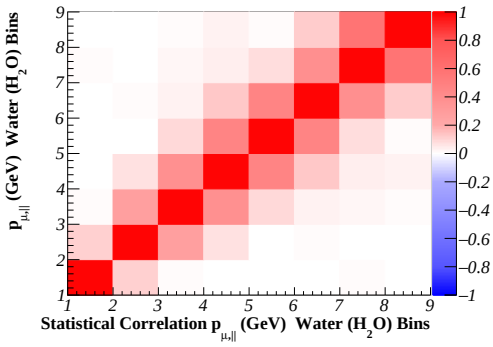


(e) Scintillator

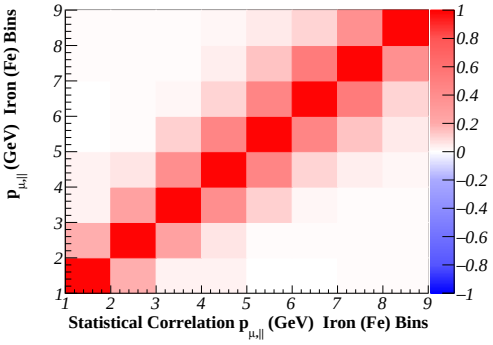
Figure G-9: p_μ Statistical Cross Section Uncertainty Correlation Matrix



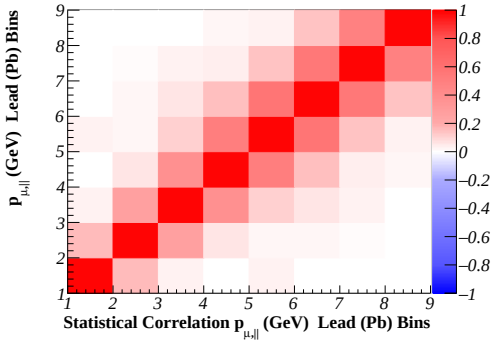
(a) Carbon



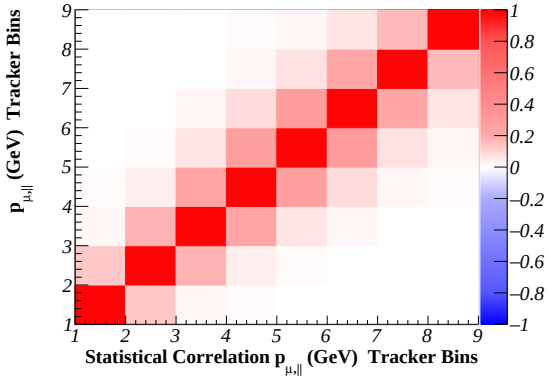
(b) Water



(c) Iron

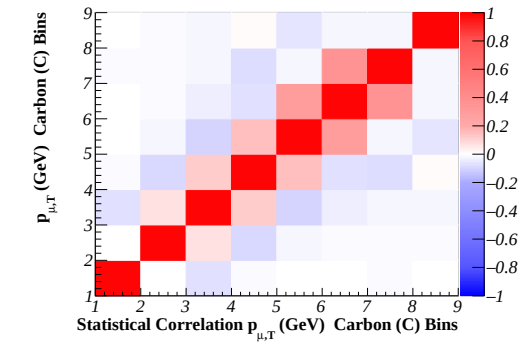


(d) Lead

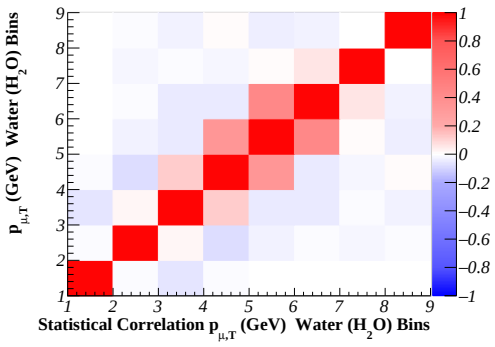


(e) Scintillator

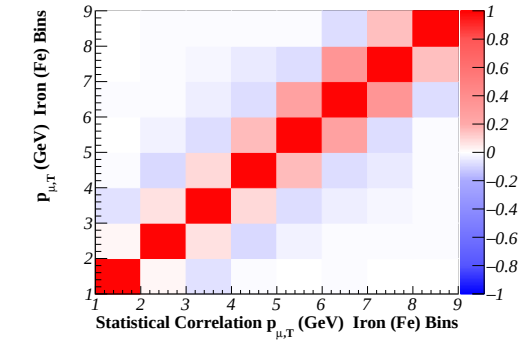
Figure G-10: $p_{\mu,||}$ Statistical Cross Section Uncertainty Correlation Matrix



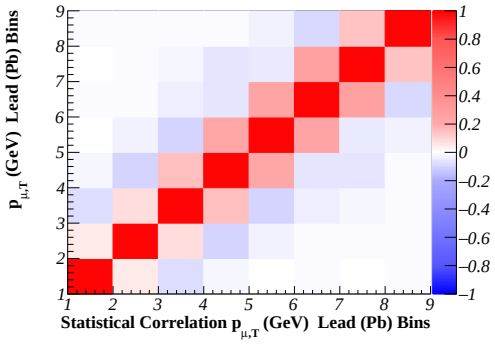
(a) Carbon



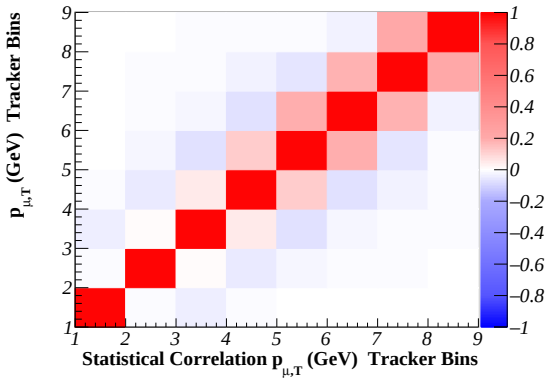
(b) Water



(c) Iron

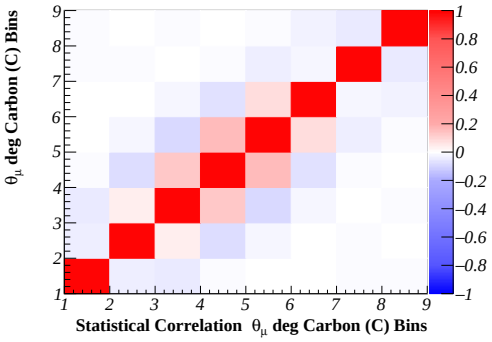


(d) Lead

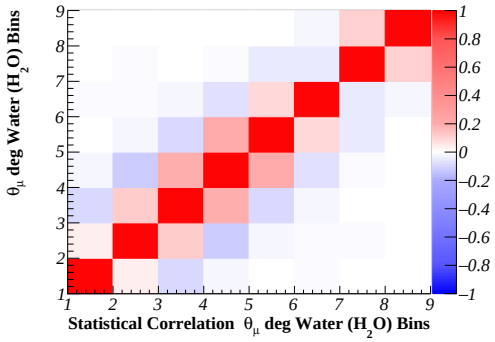


(e) Scintillator

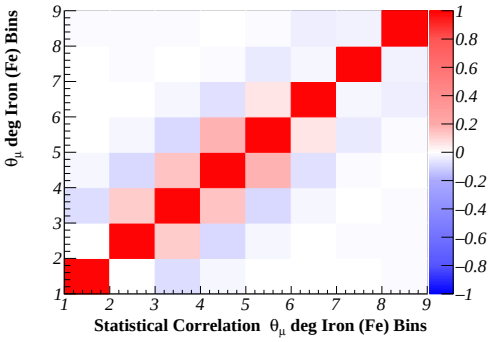
Figure G-11: $p_{\mu,T}$ Statistical Cross Section Uncertainty Correlation Matrix



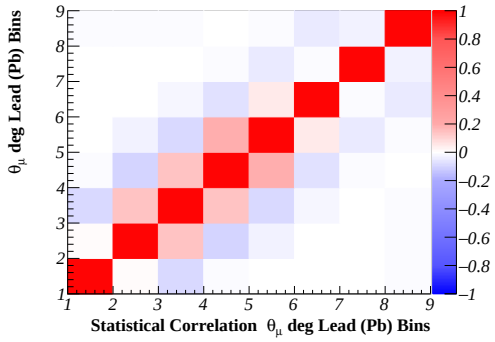
(a) Carbon



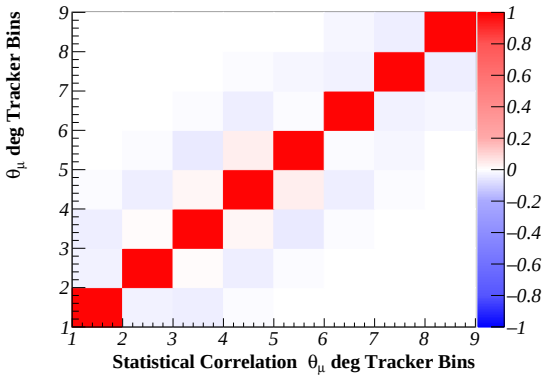
(b) Water



(c) Iron

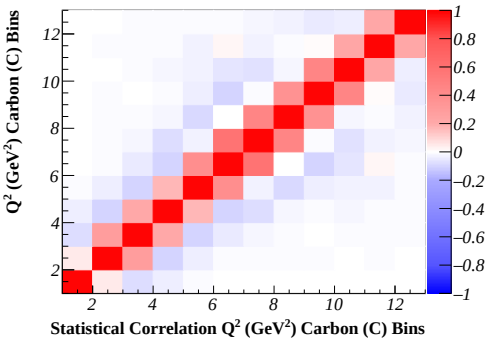


(d) Lead

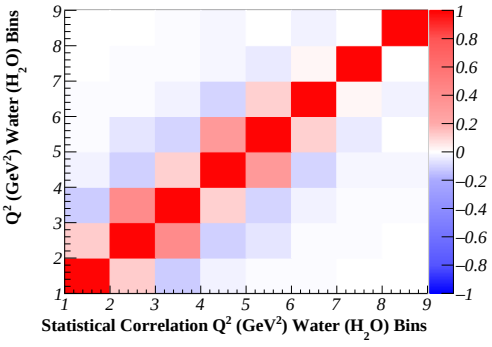


(e) Scintillator

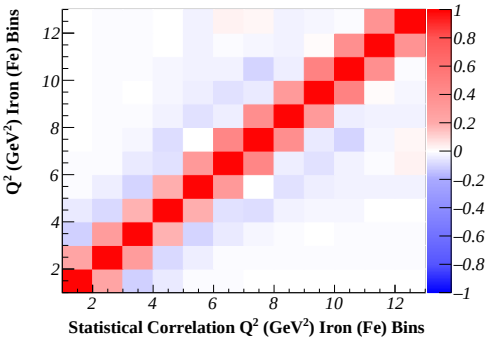
Figure G-12: θ_μ Statistical Cross Section Uncertainty Correlation Matrix



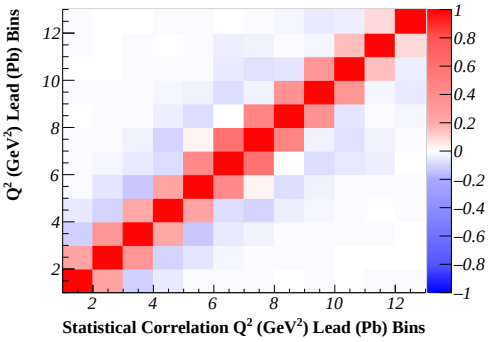
(a) Carbon



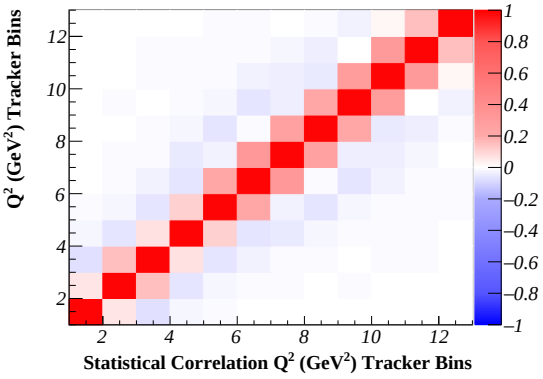
(b) Water



(c) Iron

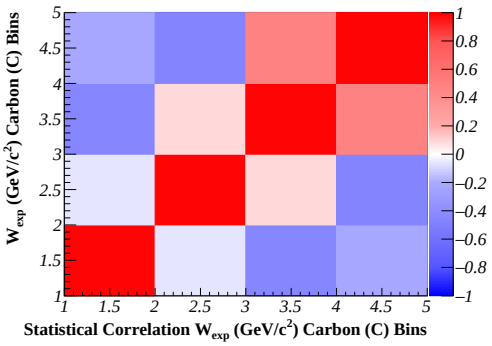


(d) Lead

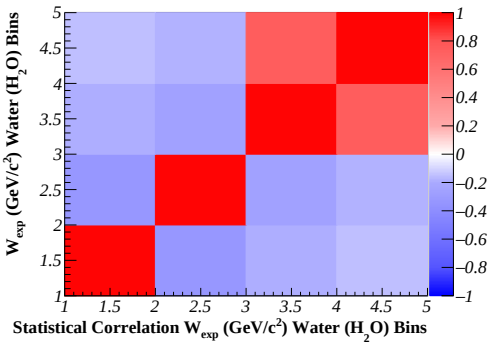


(e) Scintillator

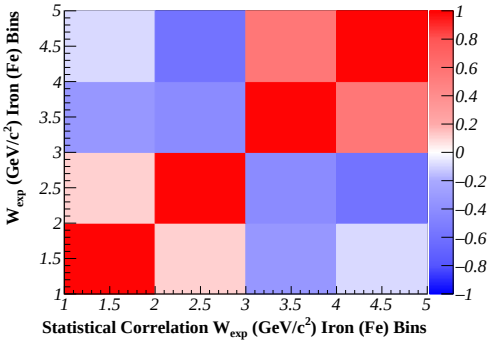
Figure G-13: Q^2 Statistical Cross Section Uncertainty Correlation Matrix



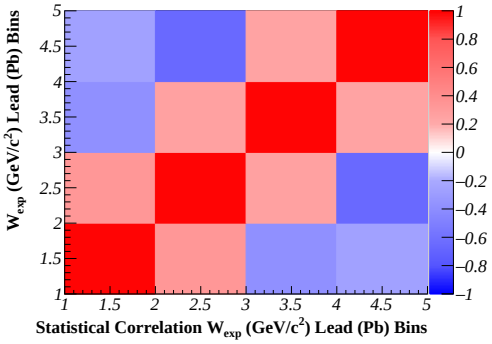
(a) Carbon



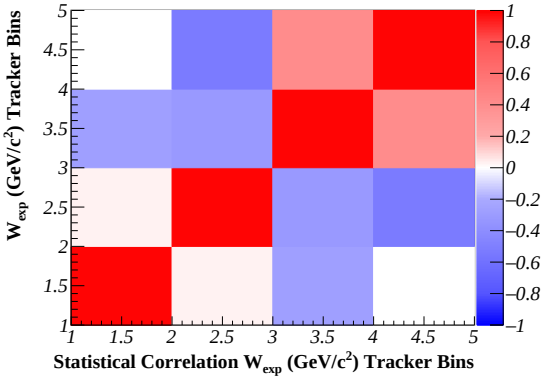
(b) Water



(c) Iron

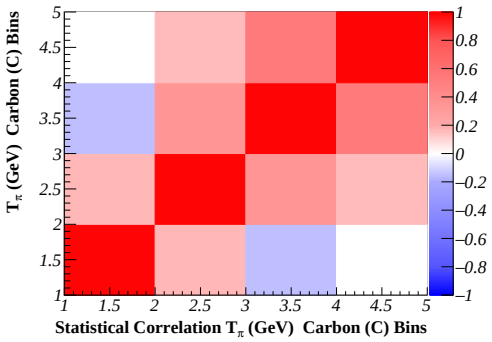


(d) Lead

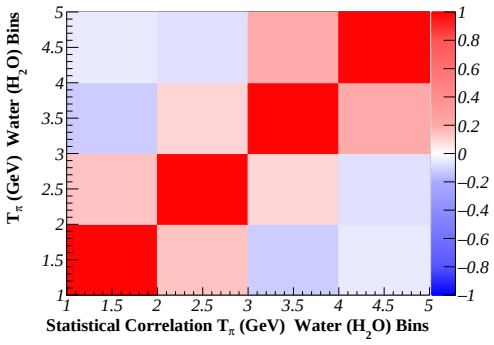


(e) Scintillator

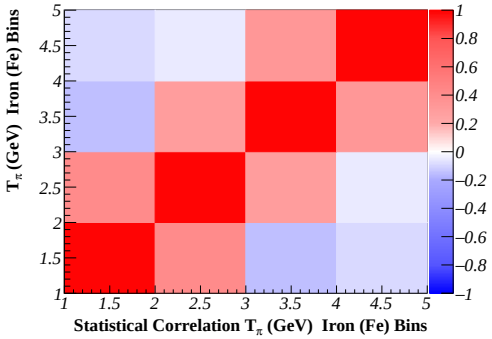
Figure G-14: W_{exp} Statistical Cross Section Uncertainty Correlation Matrix



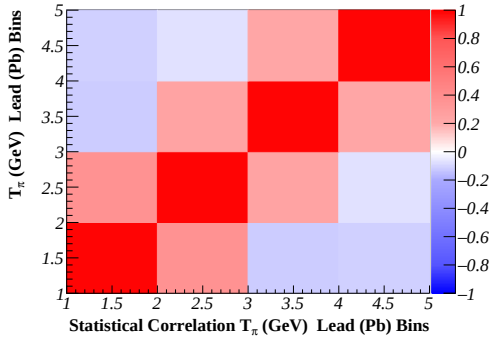
(a) Carbon



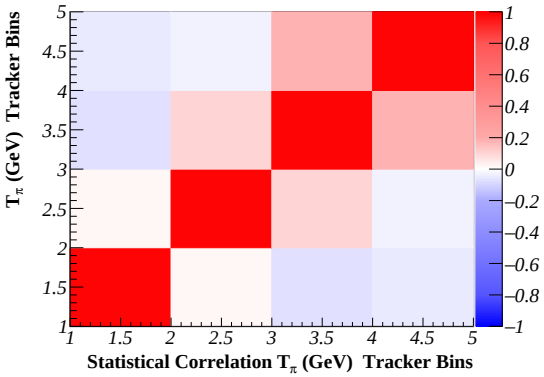
(b) Water



(c) Iron

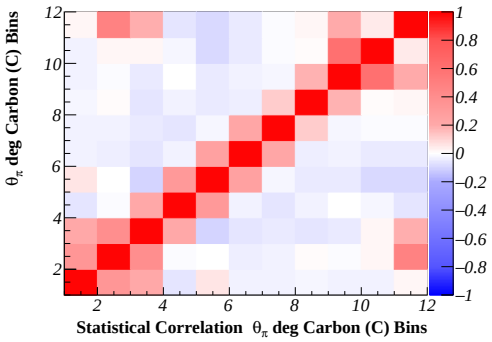


(d) Lead

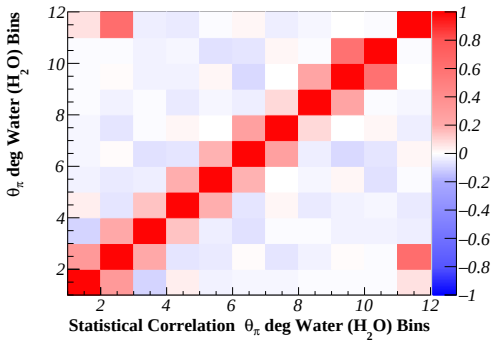


(e) Scintillator

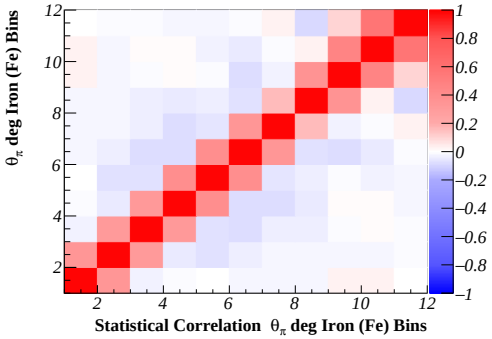
Figure G-15: T_π Statistical Cross Section Uncertainty Correlation Matrix



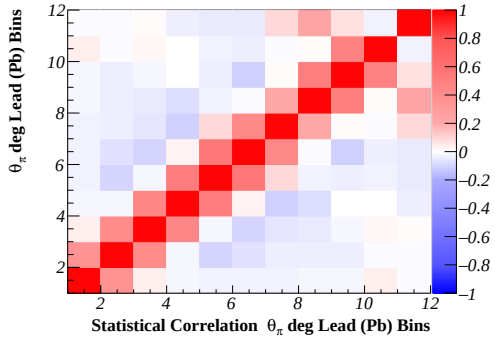
(a) Carbon



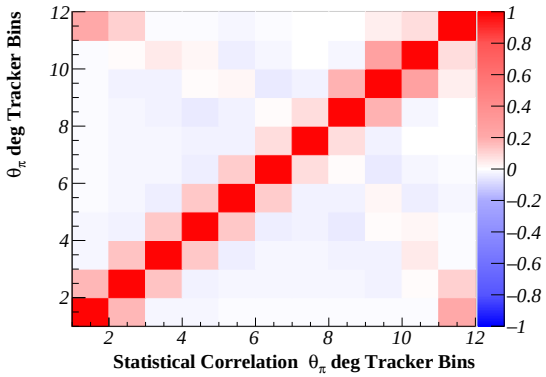
(b) Water



(c) Iron

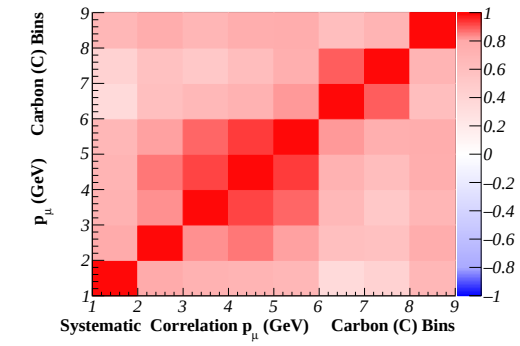


(d) Lead

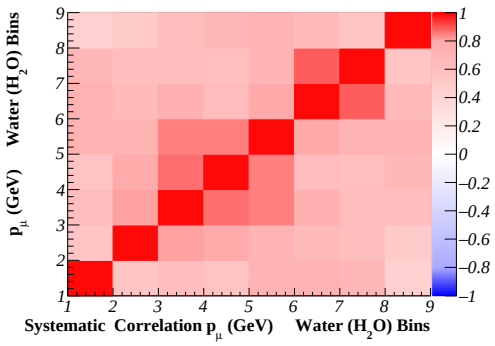


(e) Scintillator

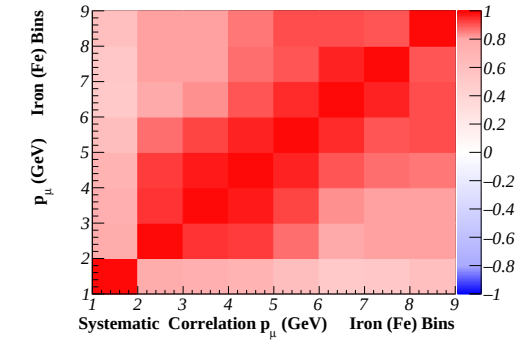
Figure G-16: θ_π Statistical Cross Section Uncertainty Correlation Matrix



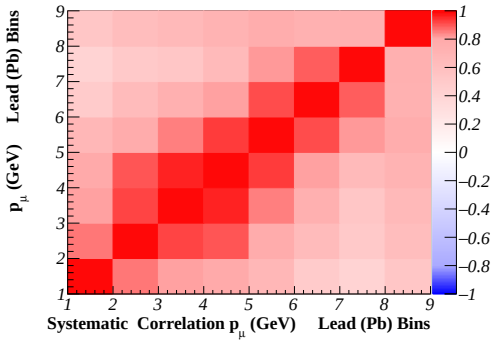
(a) Carbon



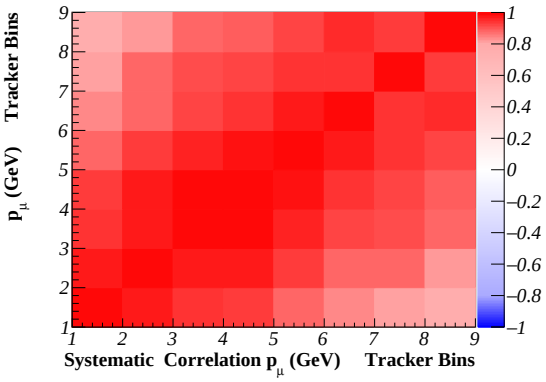
(b) Water



(c) Iron

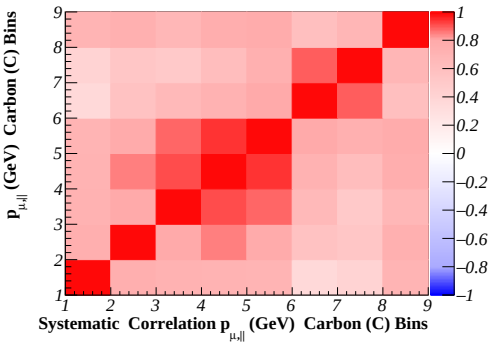


(d) Lead

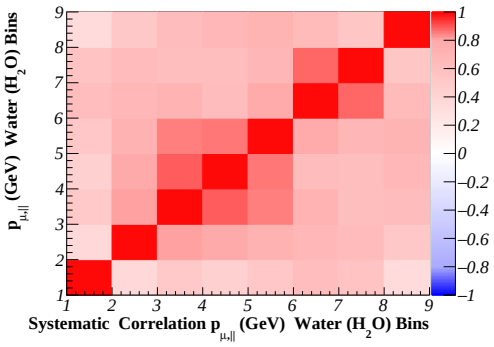


(e) Scintillator

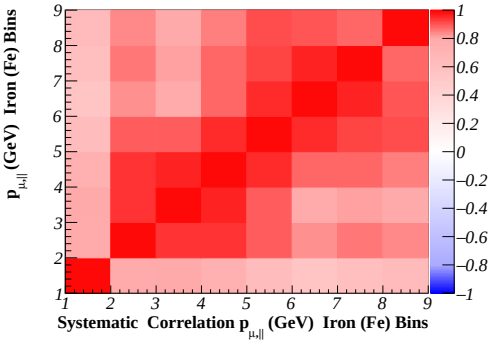
Figure G-17: p_μ Systematic Cross Section Uncertainty Correlation Matrix



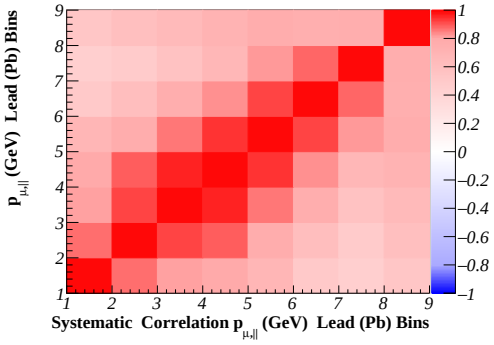
(a) Carbon



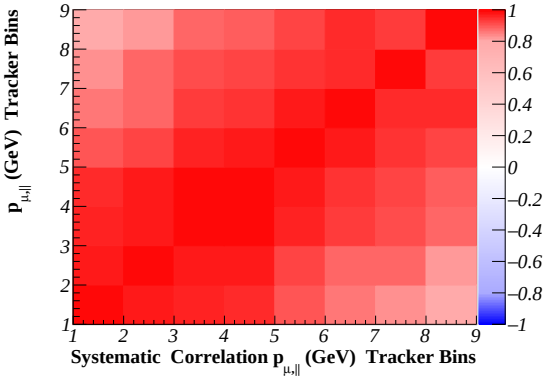
(b) Water



(c) Iron

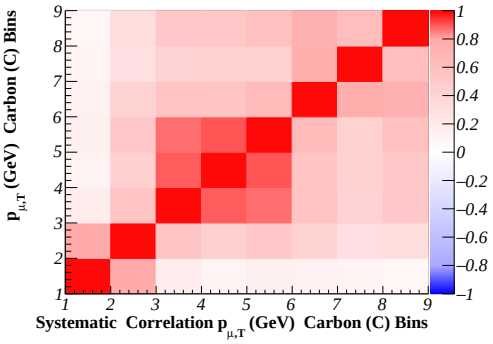


(d) Lead

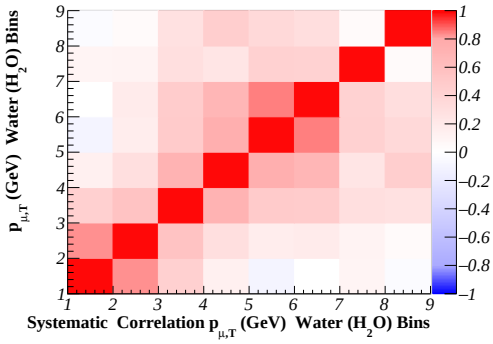


(e) Scintillator

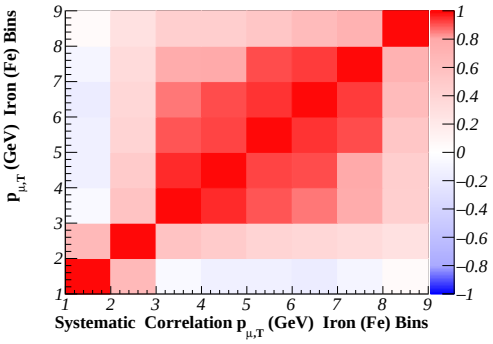
Figure G-18: $p_{\mu,||}$ Systematic Cross Section Uncertainty Correlation Matrix



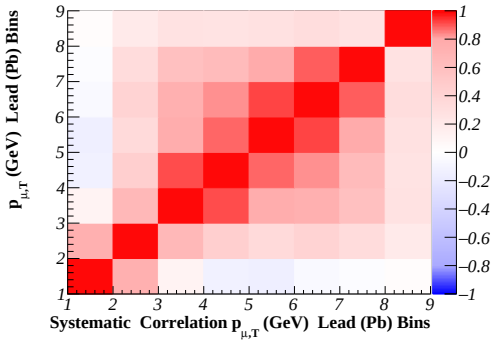
(a) Carbon



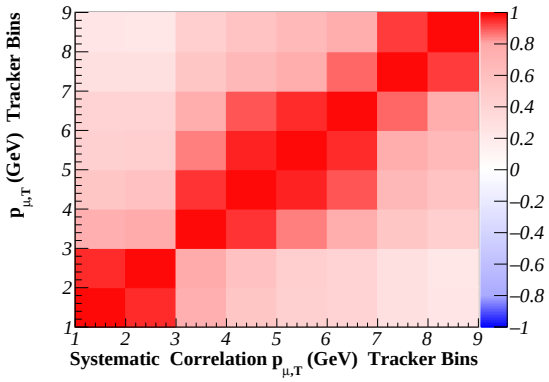
(b) Water



(c) Iron

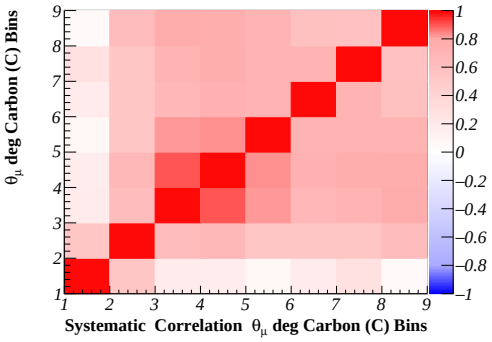


(d) Lead

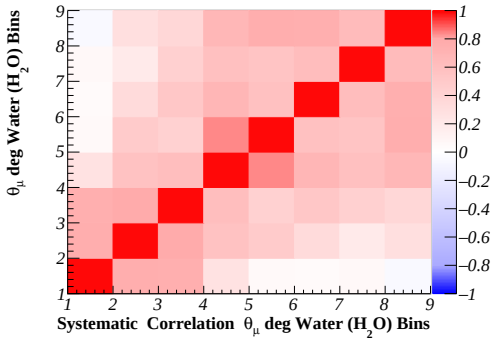


(e) Scintillator

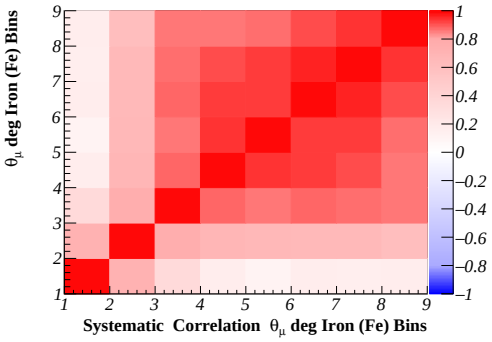
Figure G-19: $p_{\mu,T}$ Systematic Cross Section Uncertainty Correlation Matrix



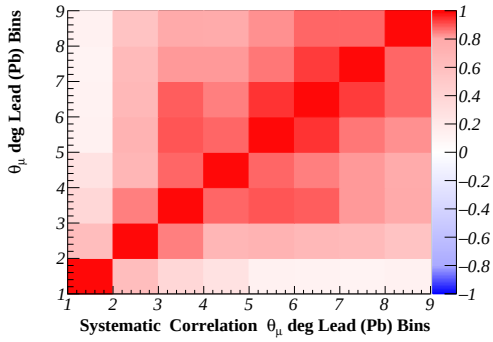
(a) Carbon



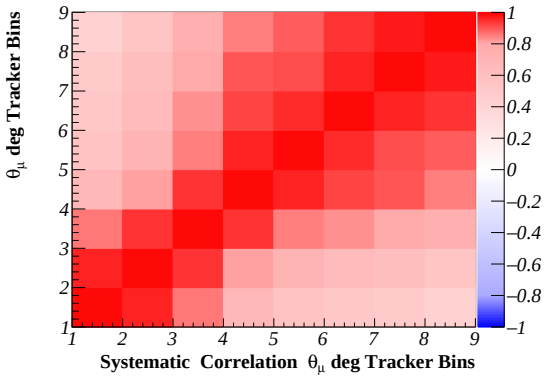
(b) Water



(c) Iron

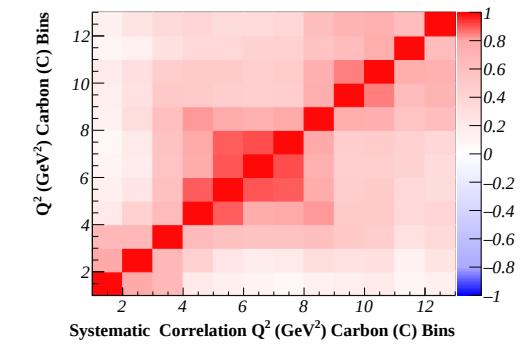


(d) Lead

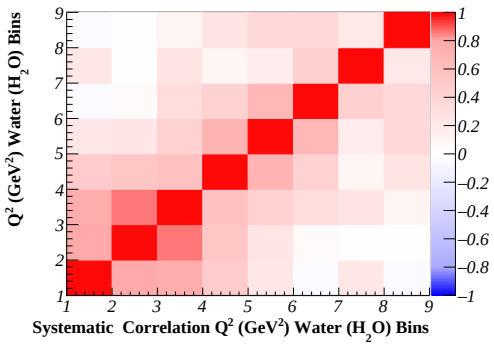


(e) Scintillator

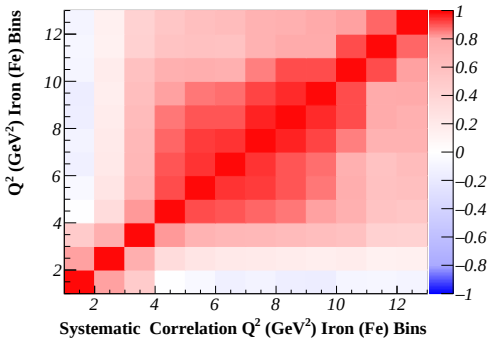
Figure G-20: θ_μ Systematic Cross Section Uncertainty Correlation Matrix



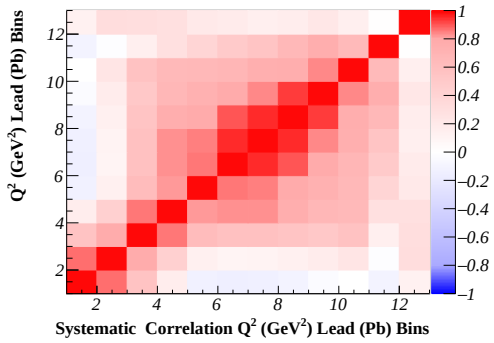
(a) Carbon



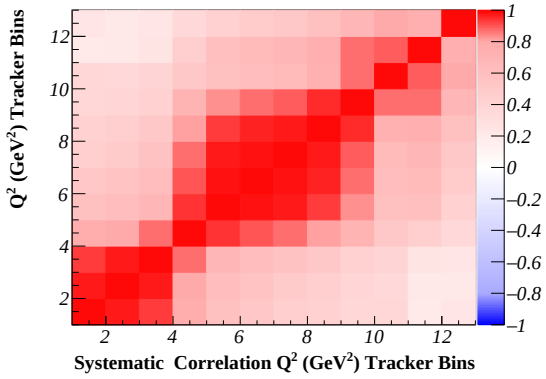
(b) Water



(c) Iron

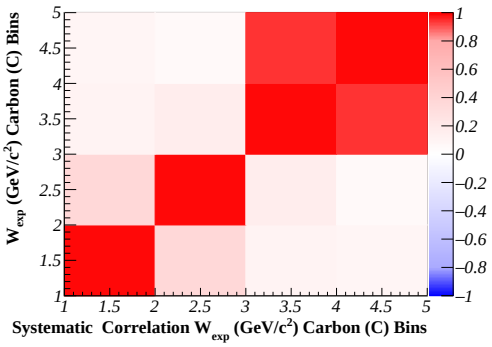


(d) Lead

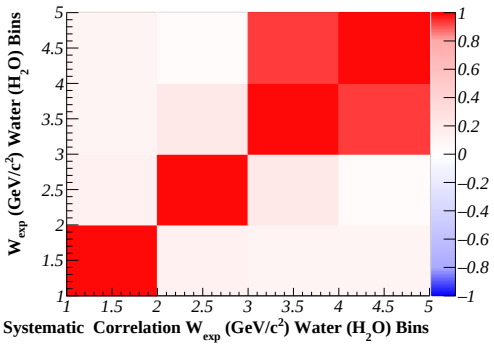


(e) Scintillator

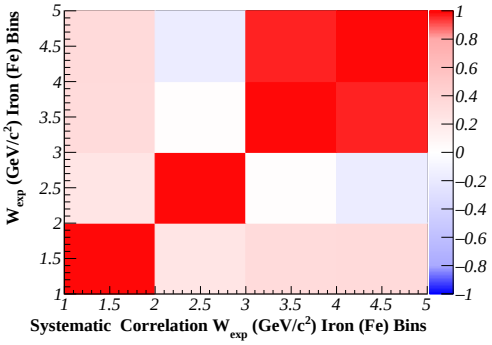
Figure G-21: Q^2 Systematic Cross Section Uncertainty Correlation Matrix



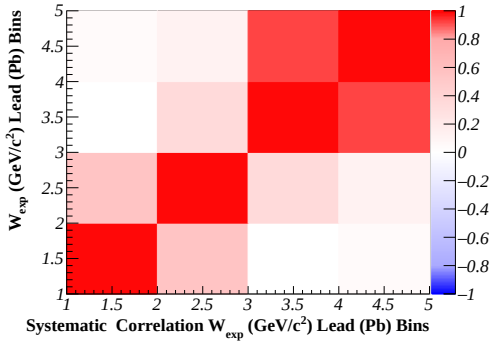
(a) Carbon



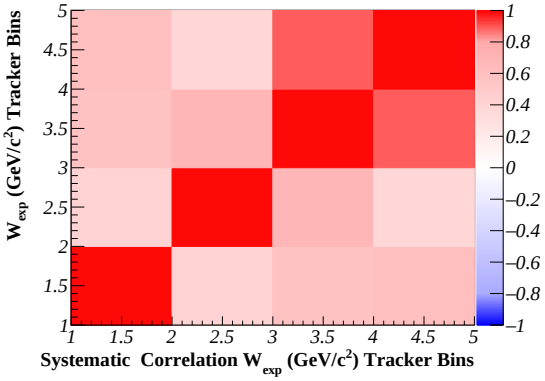
(b) Water



(c) Iron

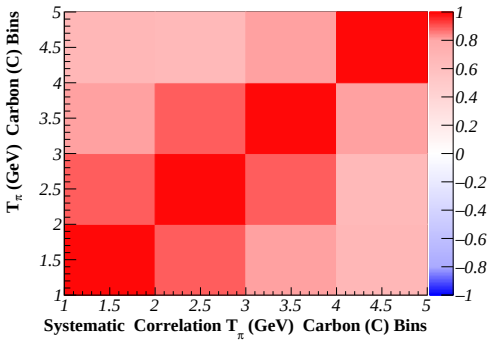


(d) Lead

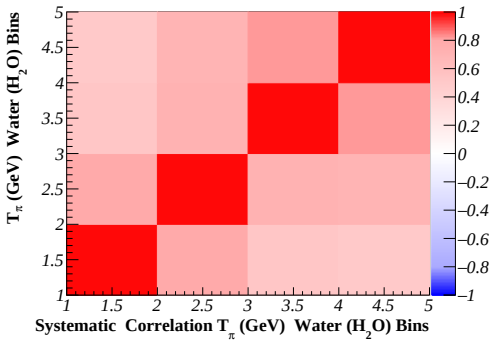


(e) Scintillator

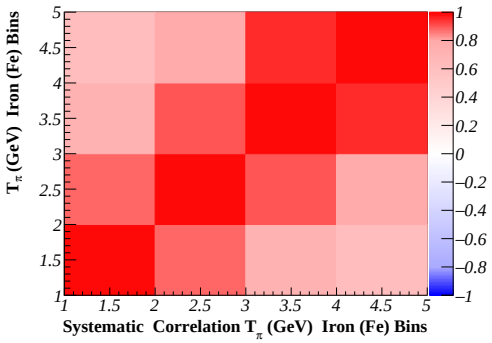
Figure G-22: W_{exp} Systematic Cross Section Uncertainty Correlation Matrix



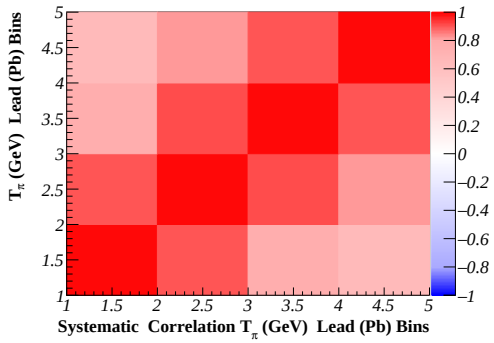
(a) Carbon



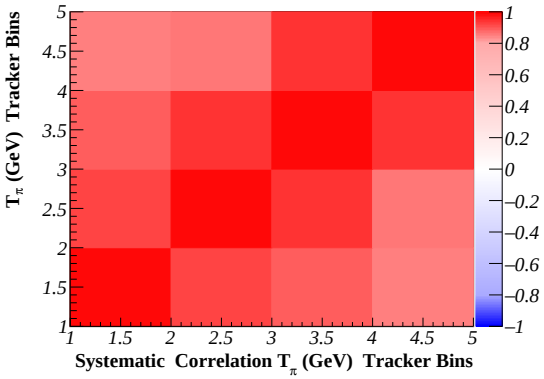
(b) Water



(c) Iron

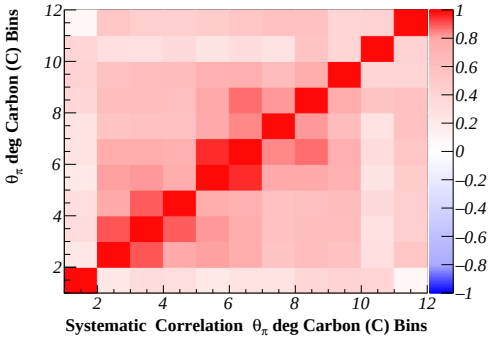


(d) Lead

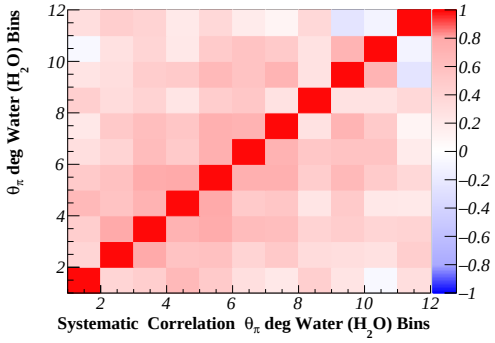


(e) Scintillator

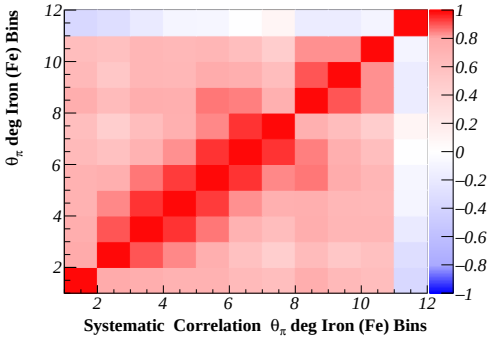
Figure G-23: T_π Systematic Cross Section Uncertainty Correlation Matrix



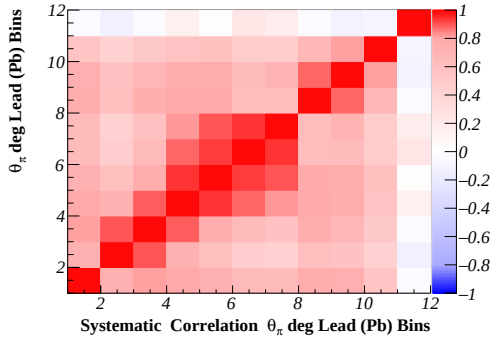
(a) Carbon



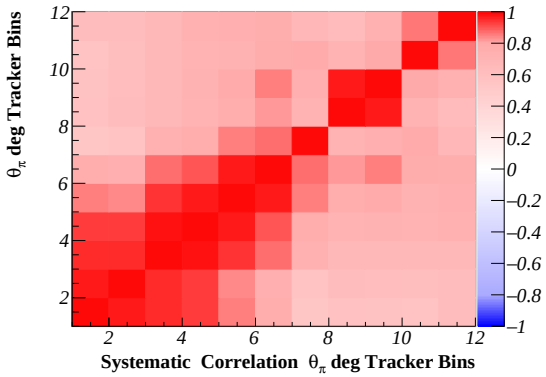
(b) Water



(c) Iron



(d) Lead

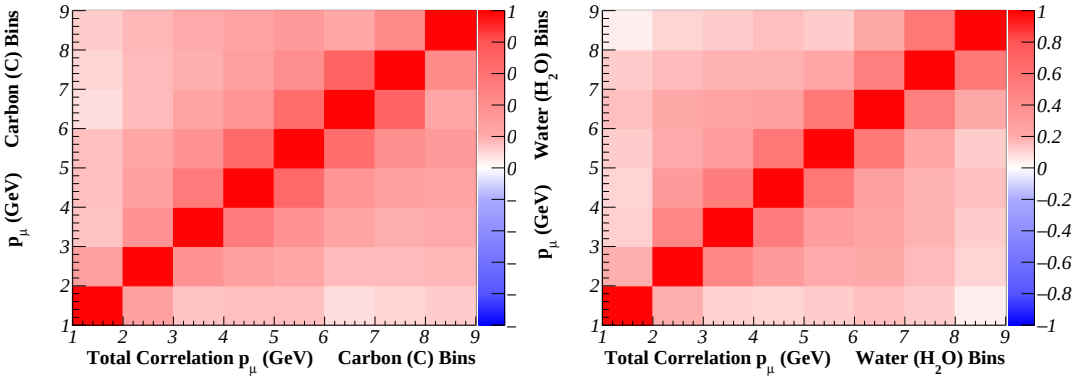


(e) Scintillator

Figure G-24: θ_π Systematic Cross Section Uncertainty Correlation Matrix

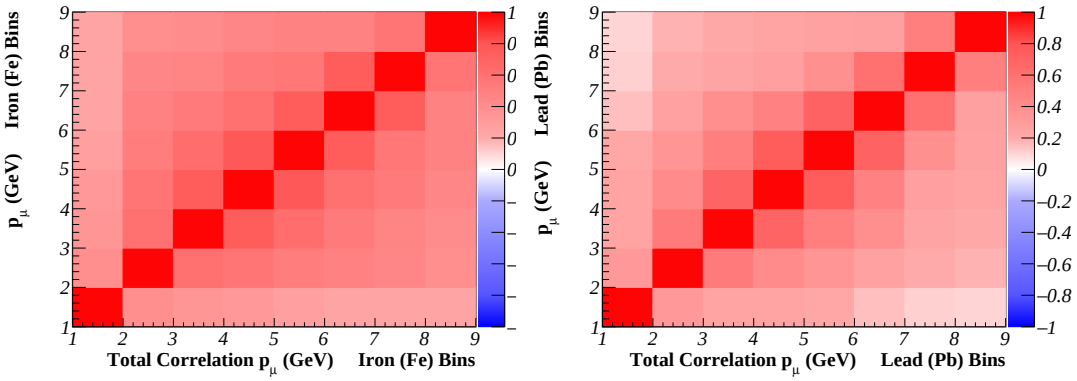
Appendix H

Cross Section Ratio Correlation Matrices



(a) Carbon

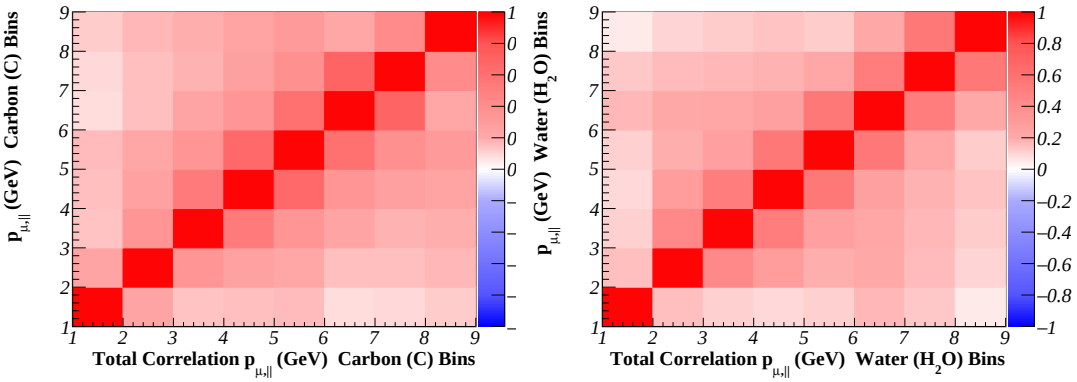
(b) Water



(c) Iron

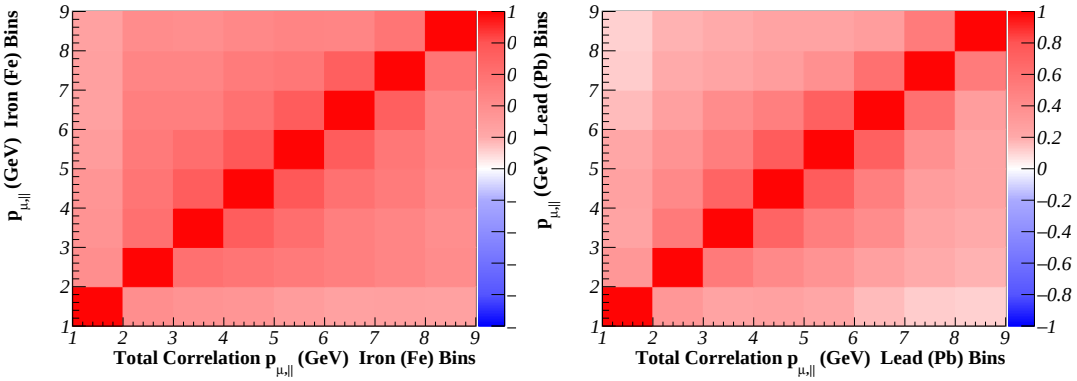
(d) Lead

Figure H-1: p_μ Total Cross Section Ratio Correlation Matrix



(a) Carbon

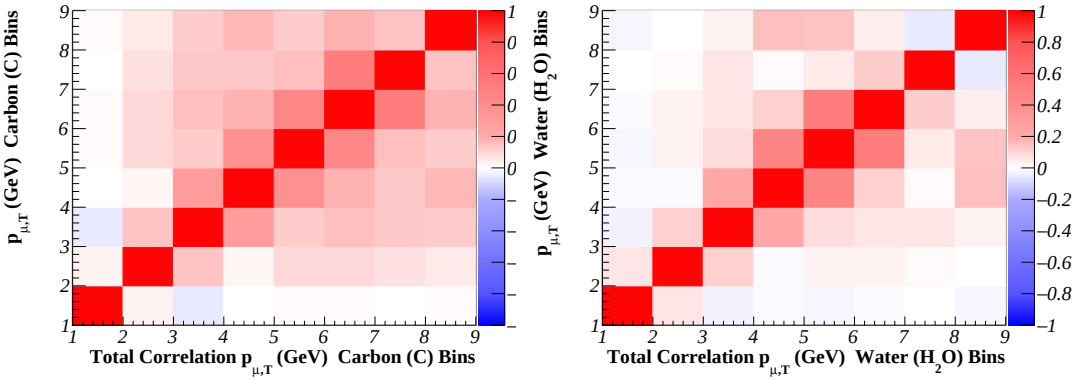
(b) Water



(c) Iron

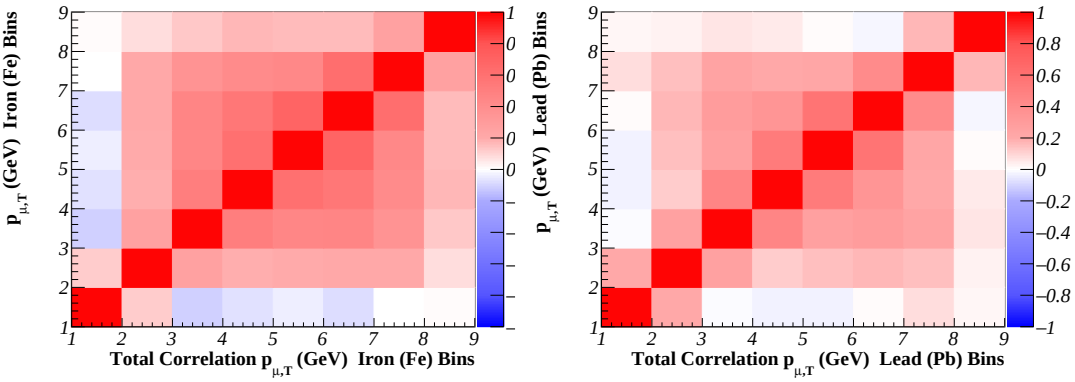
(d) Lead

Figure H-2: $p_{\mu,||}$ Total Cross Section Ratio Correlation Matrix



(a) Carbon

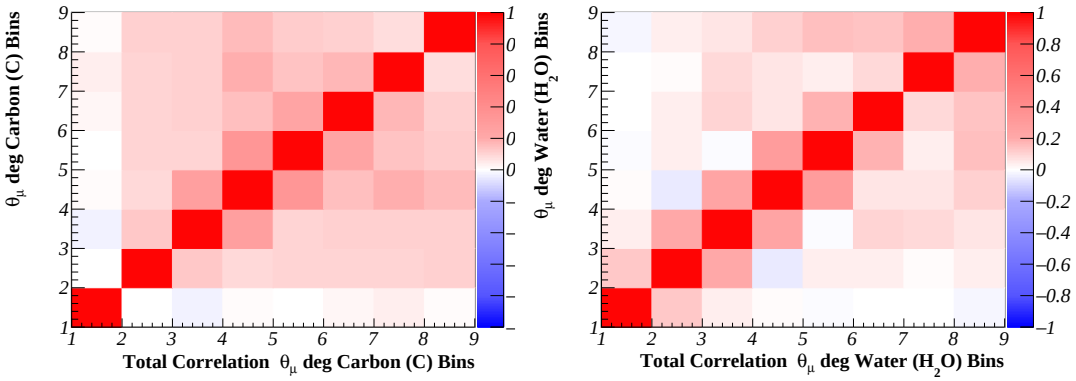
(b) Water



(c) Iron

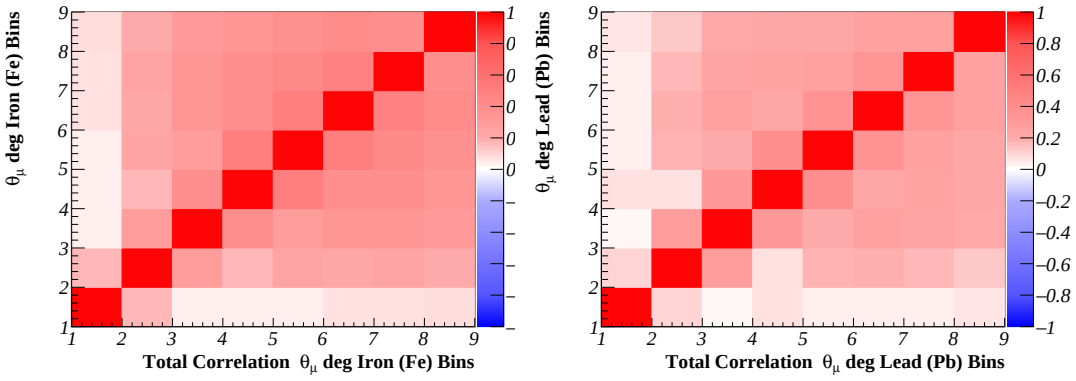
(d) Lead

Figure H-3: $p_{\mu,T}$ Total Cross Section Ratio Correlation Matrix



(a) Carbon

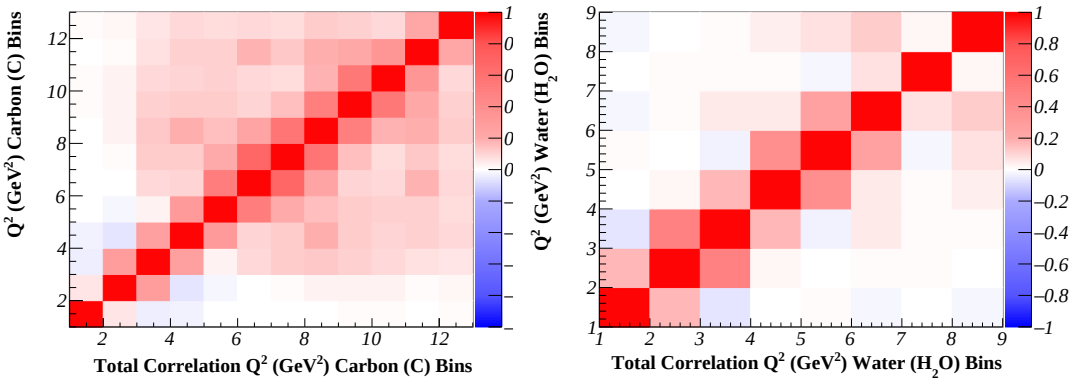
(b) Water



(c) Iron

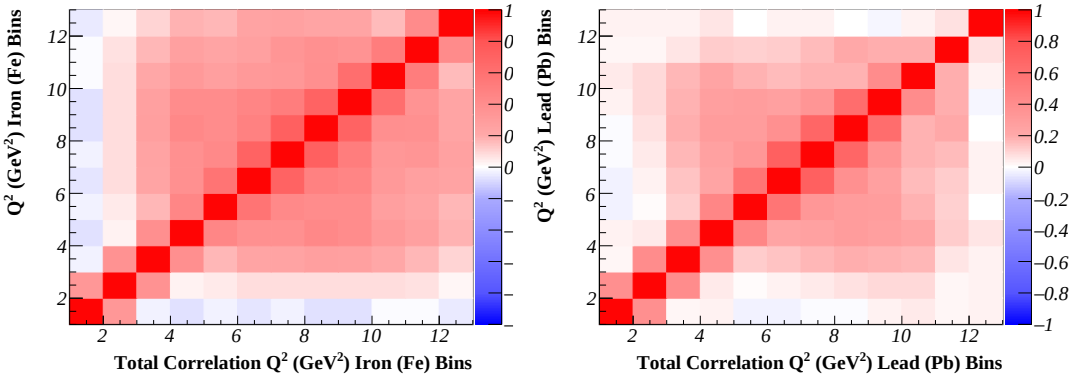
(d) Lead

Figure H-4: θ_μ Total Cross Section Ratio Correlation Matrix



(a) Carbon

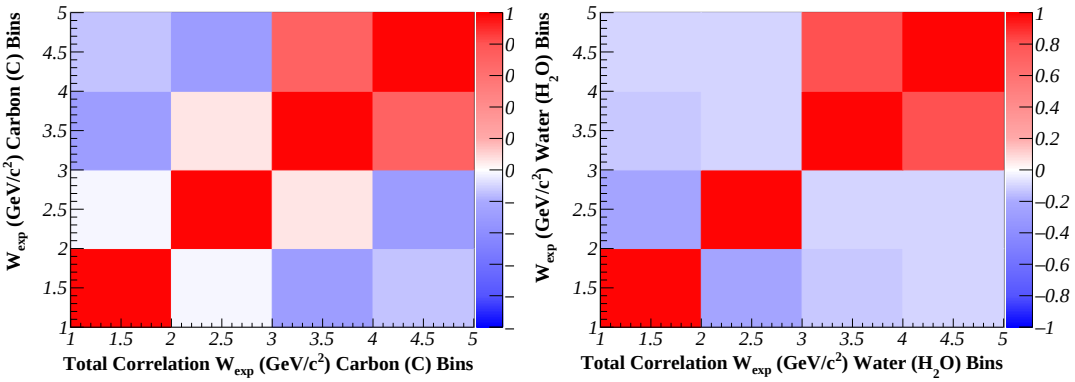
(b) Water



(c) Iron

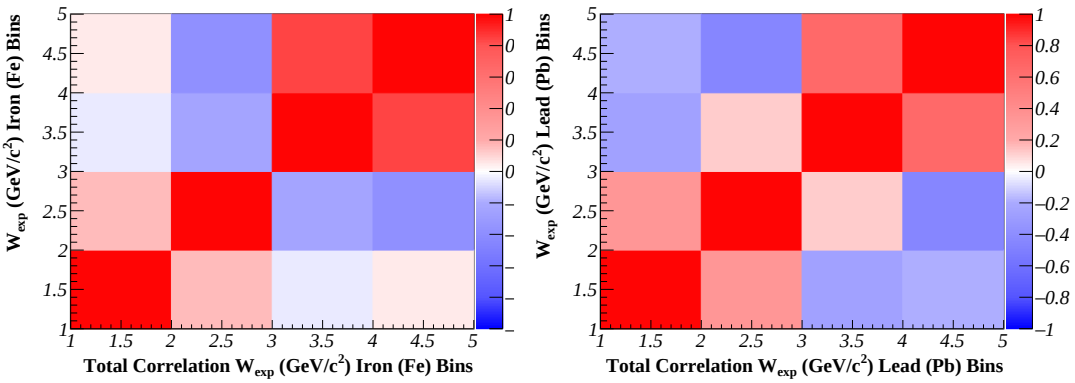
(d) Lead

Figure H-5: Q^2 Total Cross Section Ratio Correlation Matrix



(a) Carbon

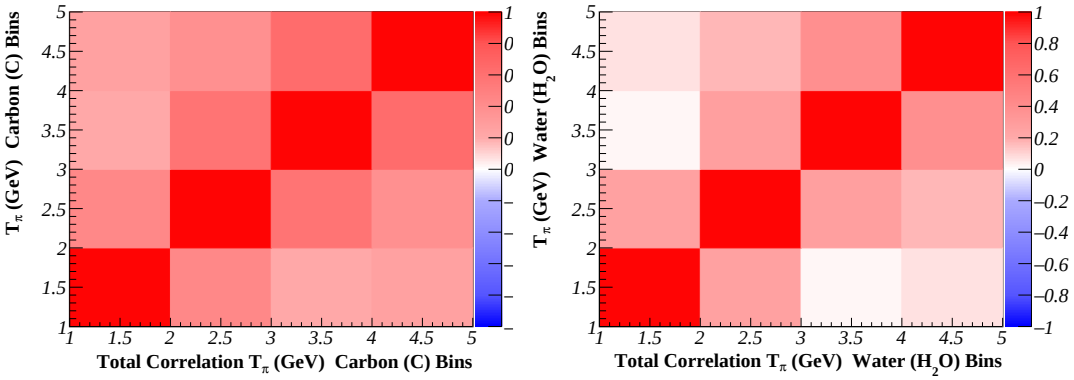
(b) Water



(c) Iron

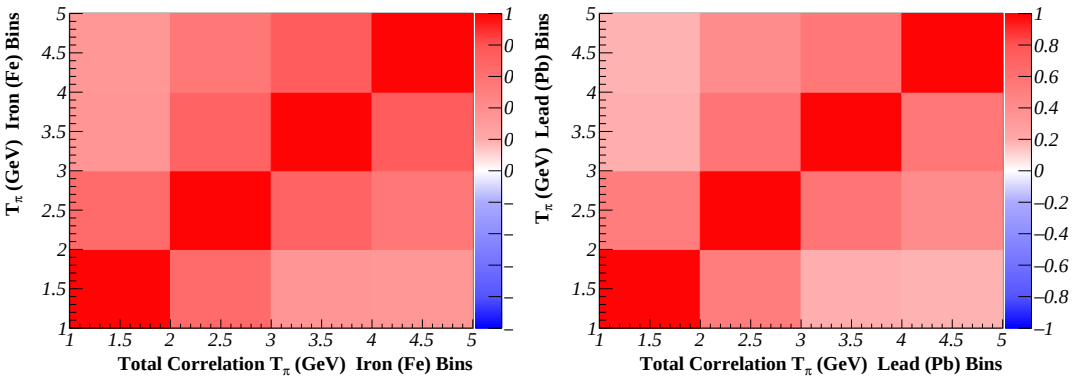
(d) Lead

Figure H-6: W_{exp} Total Cross Section Ratio Correlation Matrix



(a) Carbon

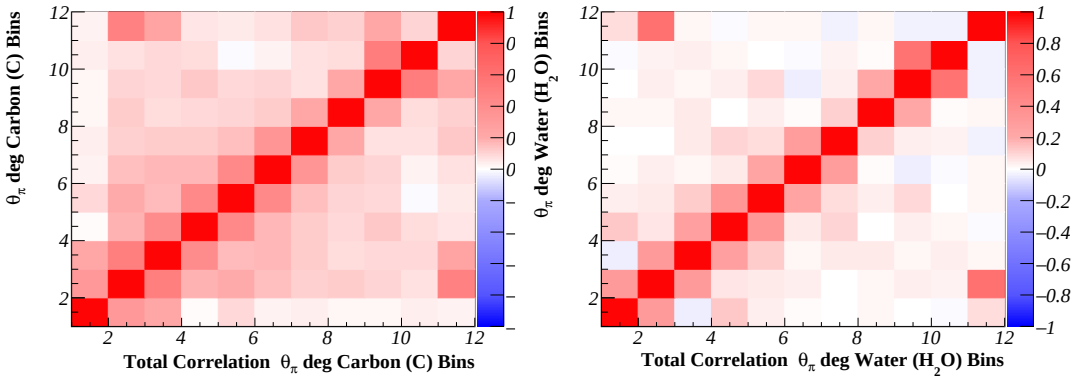
(b) Water



(c) Iron

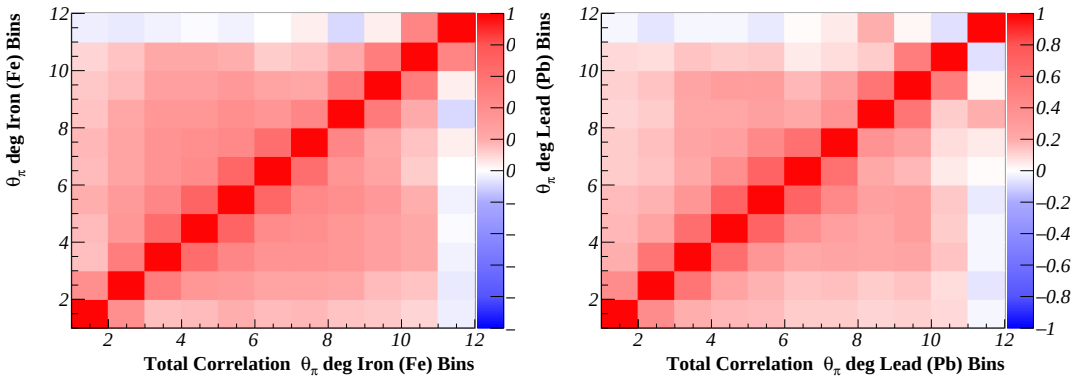
(d) Lead

Figure H-7: T_π Total Cross Section Ratio Correlation Matrix



(a) Carbon

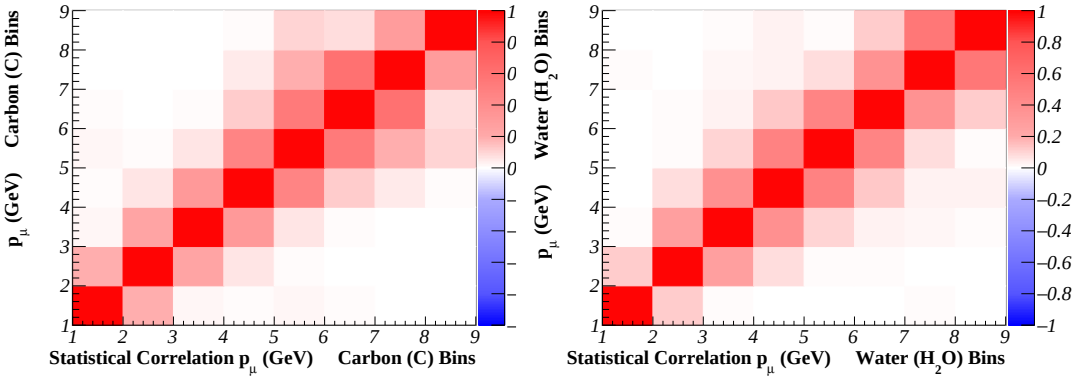
(b) Water



(c) Iron

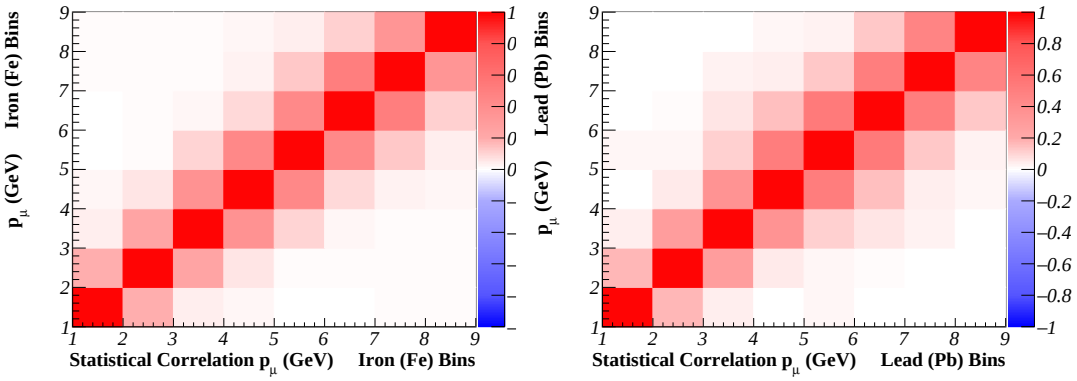
(d) Lead

Figure H-8: θ_π Total Cross Section Ratio Correlation Matrix



(a) Carbon

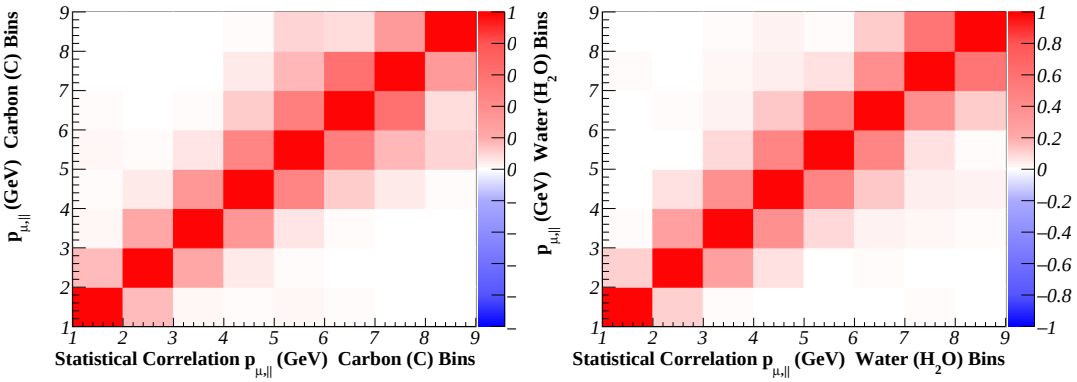
(b) Water



(c) Iron

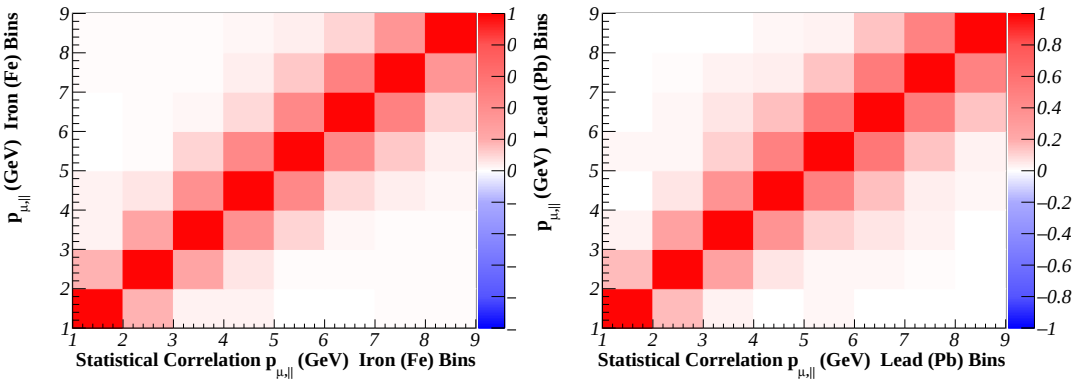
(d) Lead

Figure H-9: p_μ Statistical Cross Section Ratio Uncertainty Correlation Matrix



(a) Carbon

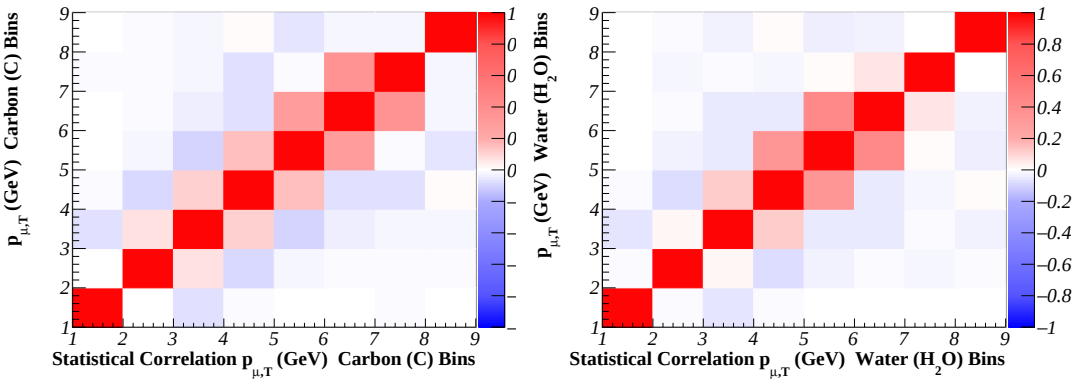
(b) Water



(c) Iron

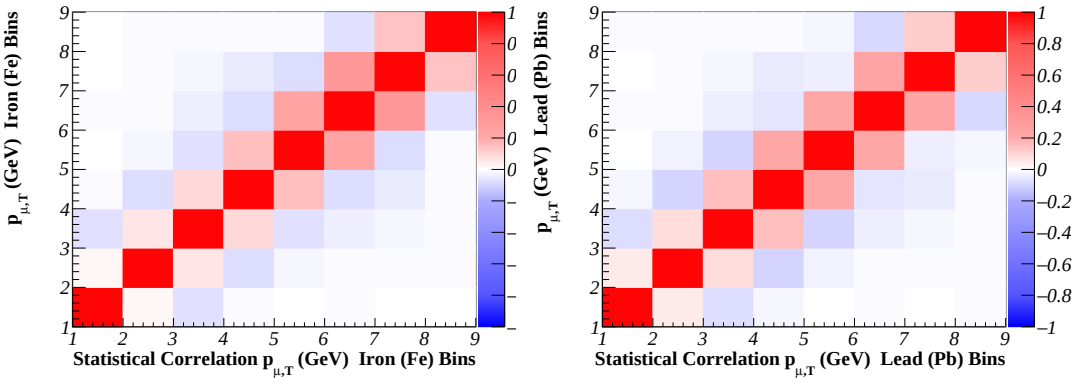
(d) Lead

Figure H-10: $p_{\mu,||}$ Statistical Cross Section Ratio Uncertainty Correlation Matrix



(a) Carbon

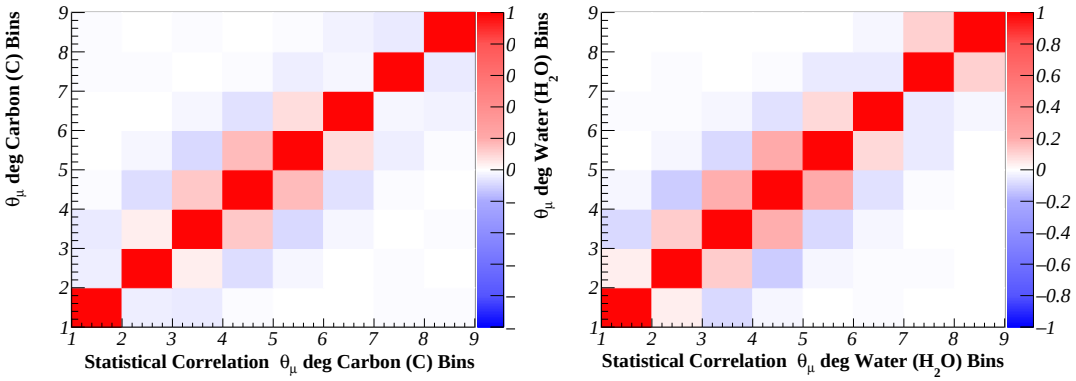
(b) Water



(c) Iron

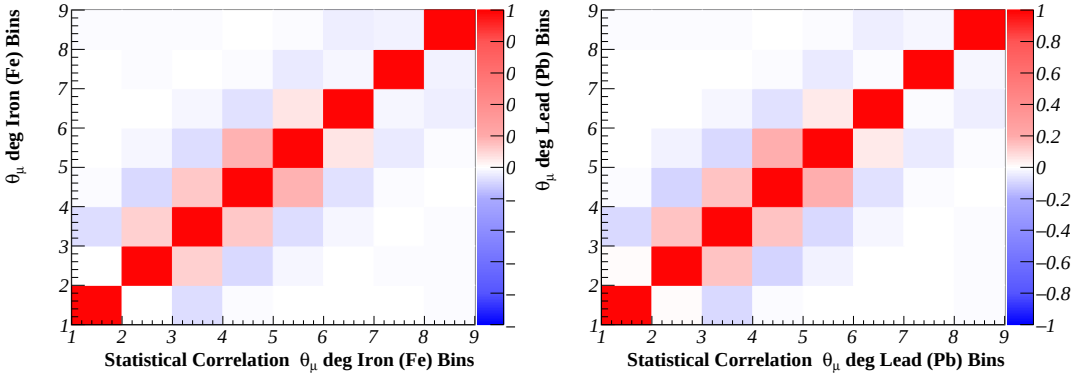
(d) Lead

Figure H-11: $p_{\mu,T}$ Statistical Cross Section Ratio Uncertainty Correlation Matrix



(a) Carbon

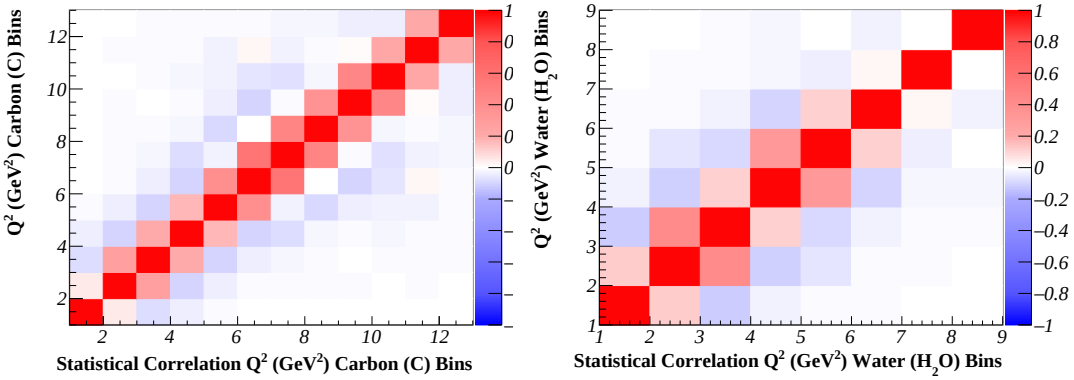
(b) Water



(c) Iron

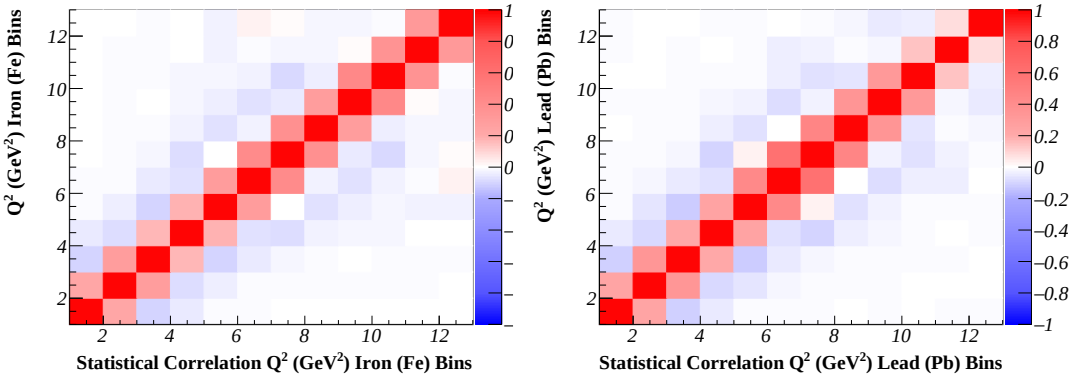
(d) Lead

Figure H-12: θ_μ Statistical Cross Section Ratio Uncertainty Correlation Matrix



(a) Carbon

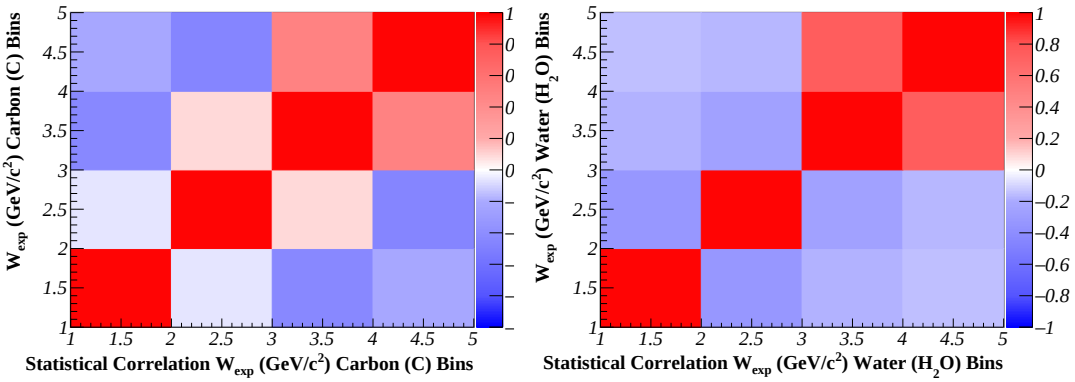
(b) Water



(c) Iron

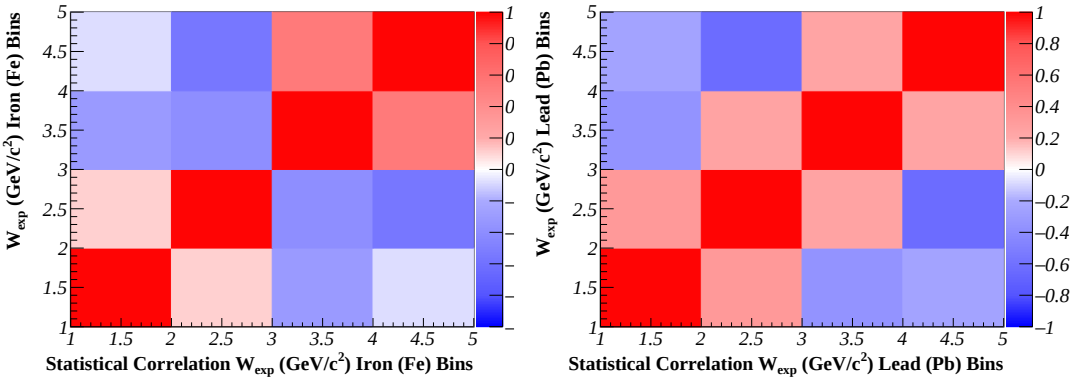
(d) Lead

Figure H-13: Q^2 Statistical Cross Section Ratio Uncertainty Correlation Matrix



(a) Carbon

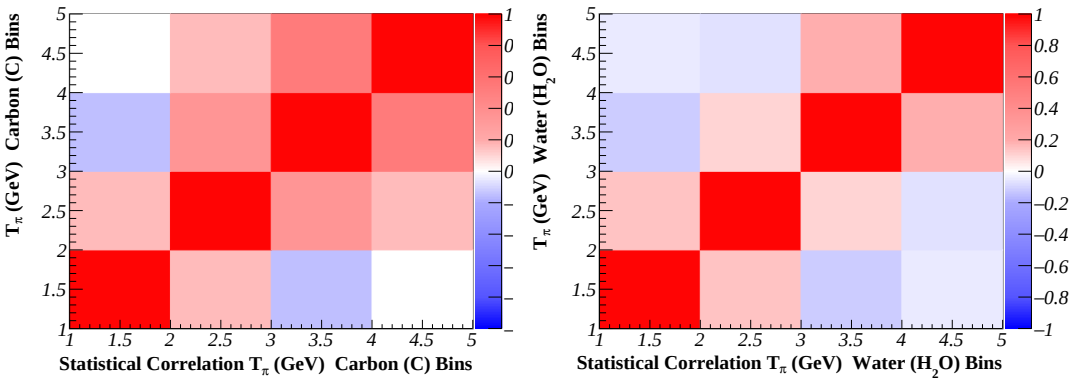
(b) Water



(c) Iron

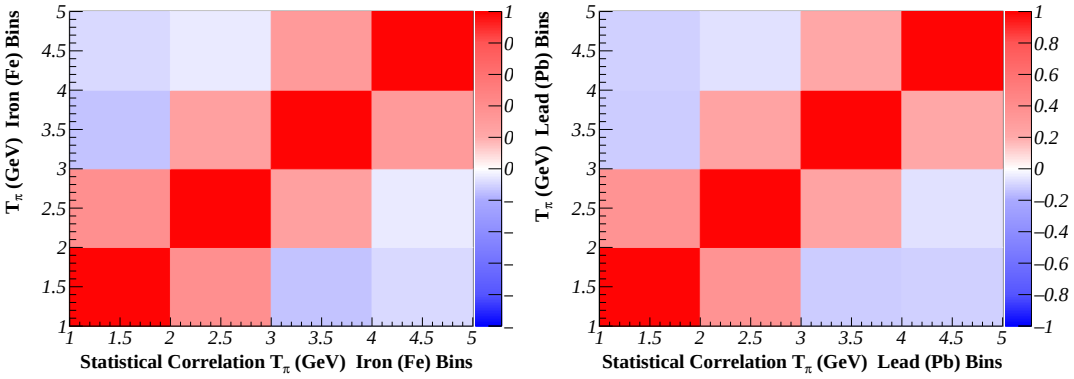
(d) Lead

Figure H-14: W_{exp} Statistical Cross Section Ratio Uncertainty Correlation Matrix



(a) Carbon

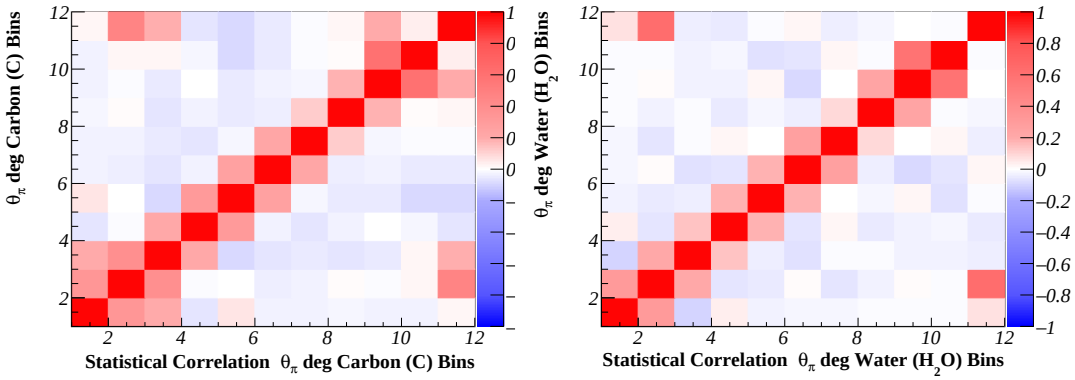
(b) Water



(c) Iron

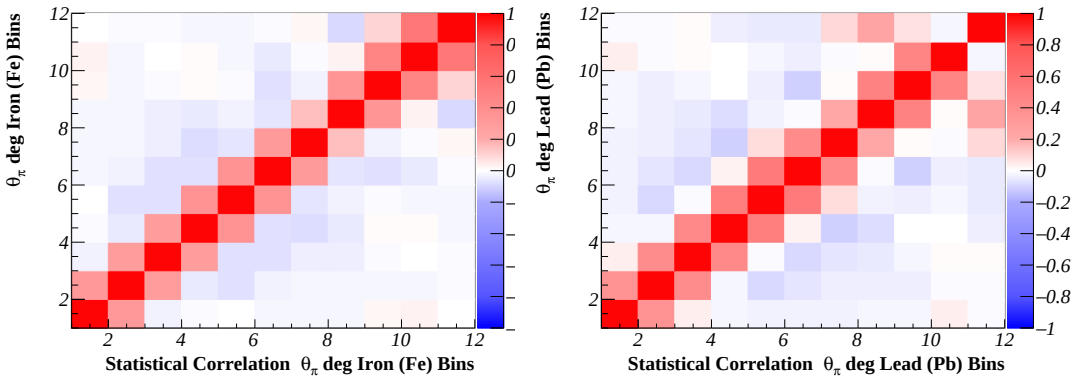
(d) Lead

Figure H-15: T_π Statistical Cross Section Ratio Uncertainty Correlation Matrix



(a) Carbon

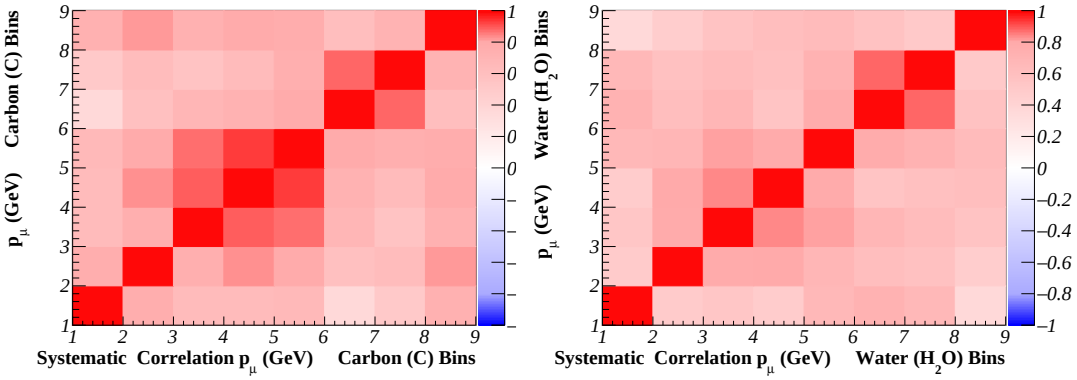
(b) Water



(c) Iron

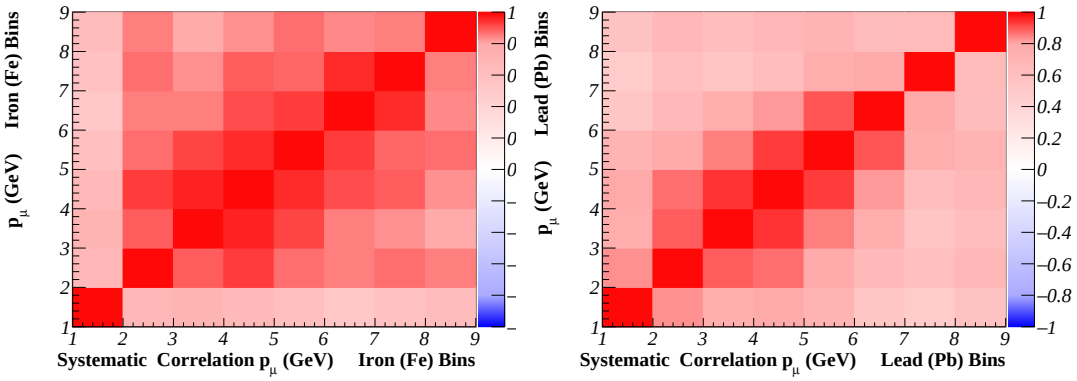
(d) Lead

Figure H-16: θ_π Statistical Cross Section Ratio Uncertainty Correlation Matrix



(a) Carbon

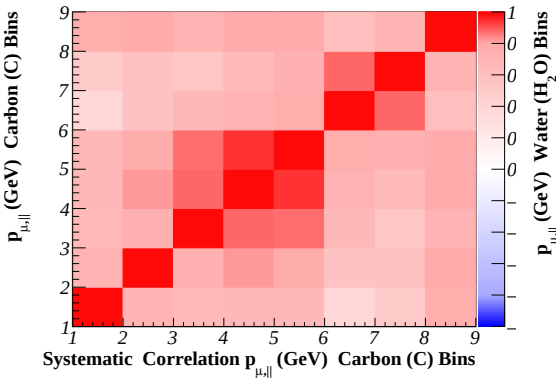
(b) Water



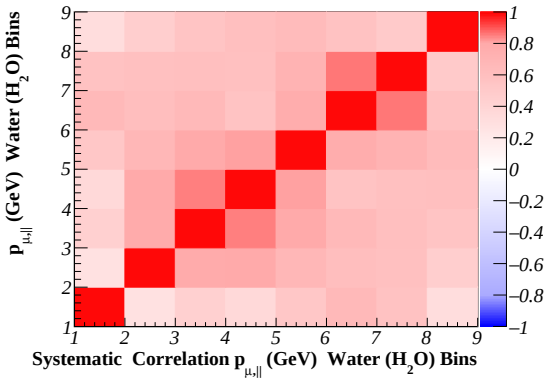
(c) Iron

(d) Lead

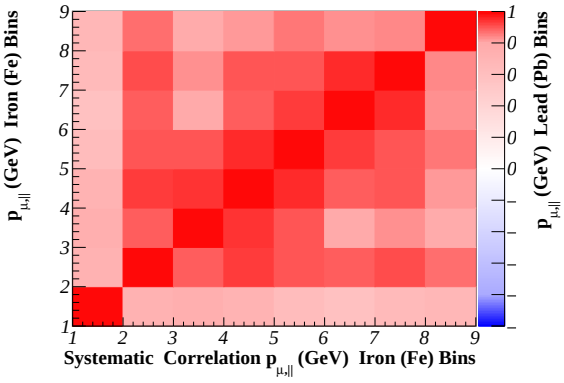
Figure H-17: p_μ Systematic Cross Section Ratio Uncertainty Correlation Matrix



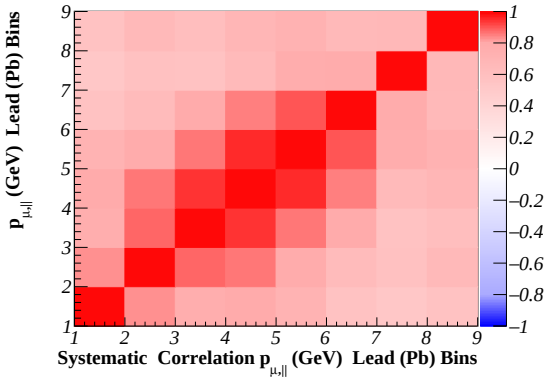
(a) Carbon



(b) Water

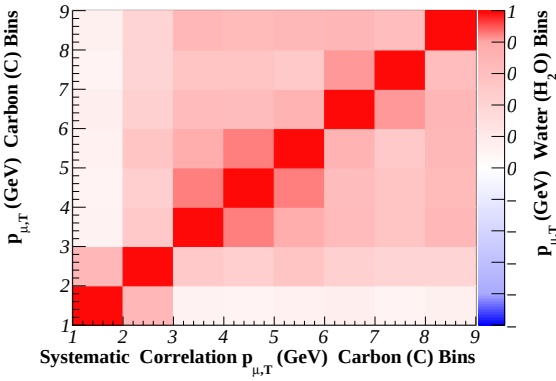


(c) Iron

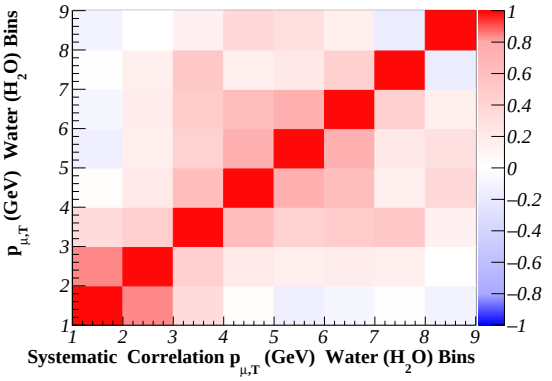


(d) Lead

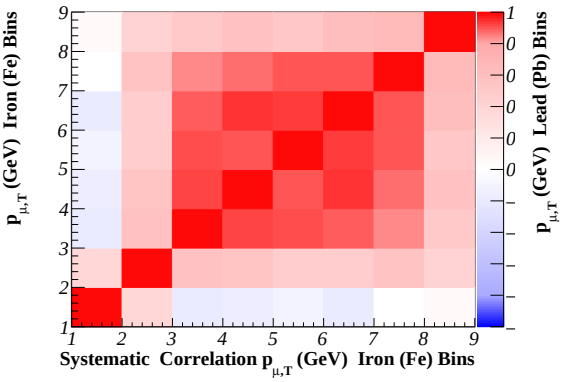
Figure H-18: $p_{\mu,||}$ Systematic Cross Section Ratio Uncertainty Correlation Matrix



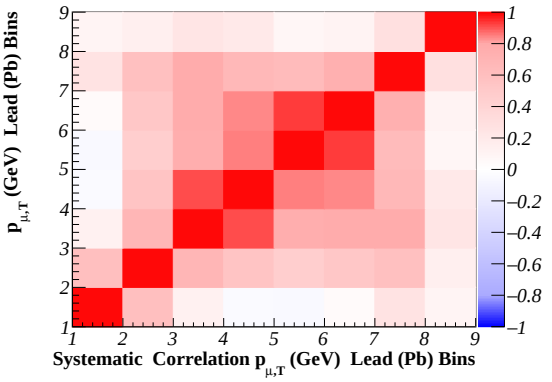
(a) Carbon



(b) Water

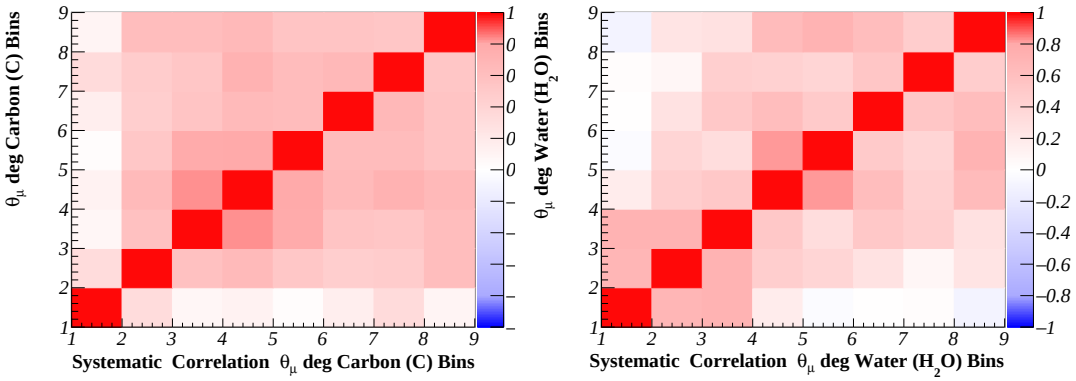


(c) Iron



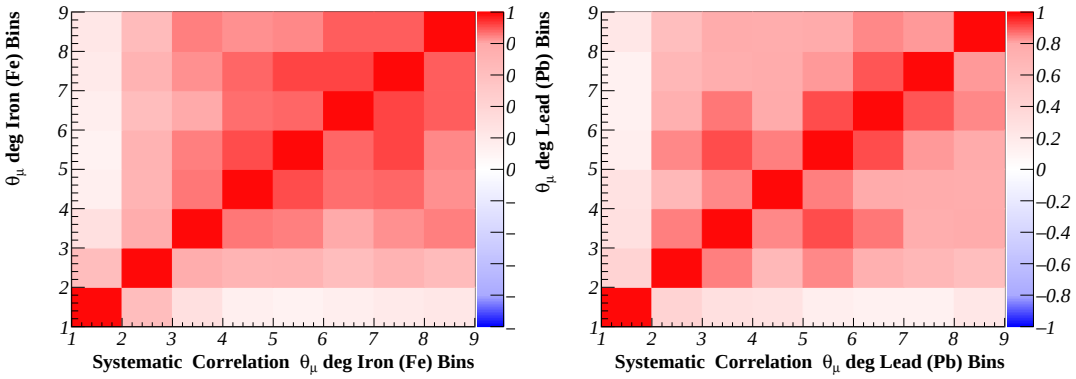
(d) Lead

Figure H-19: $p_{\mu,T}$ Systematic Cross Section Ratio Uncertainty Correlation Matrix



(a) Carbon

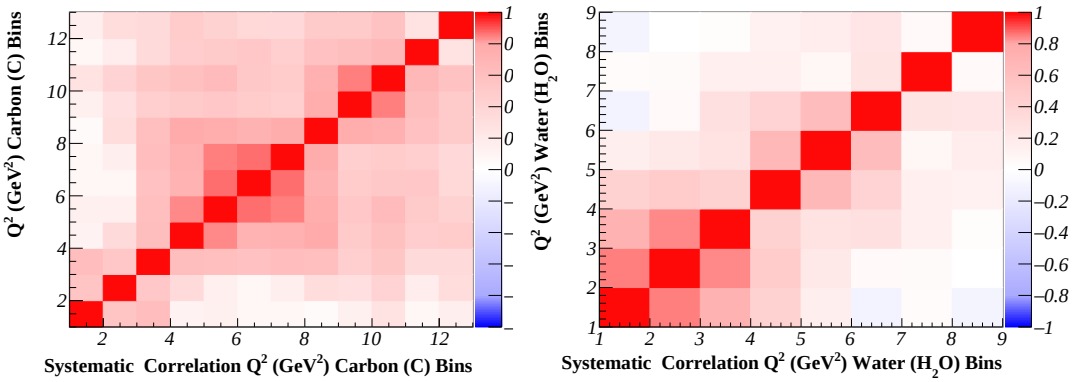
(b) Water



(c) Iron

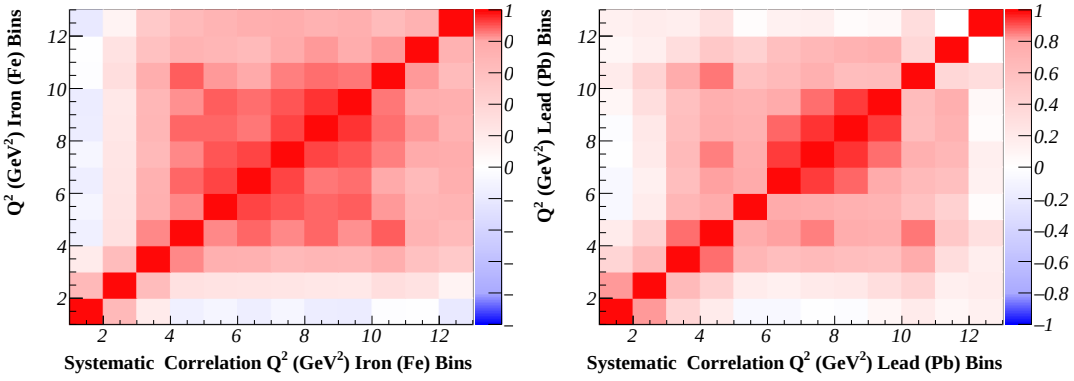
(d) Lead

Figure H-20: θ_μ Systematic Cross Section Ratio Uncertainty Correlation Matrix



(a) Carbon

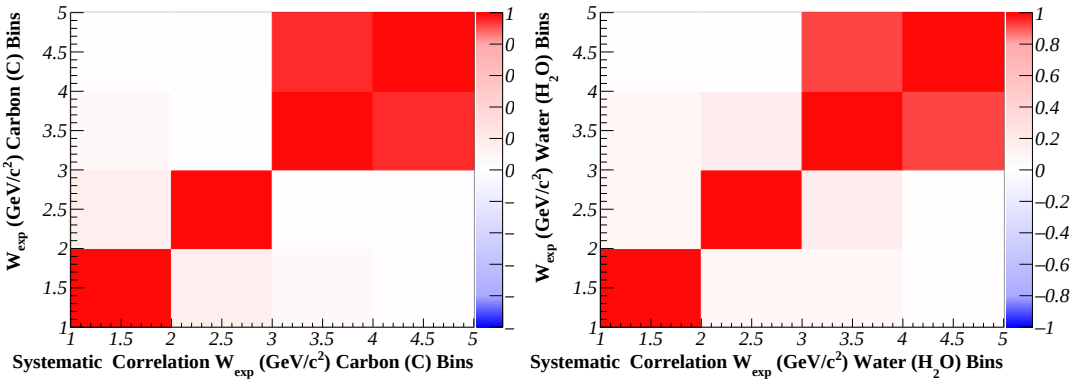
(b) Water



(c) Iron

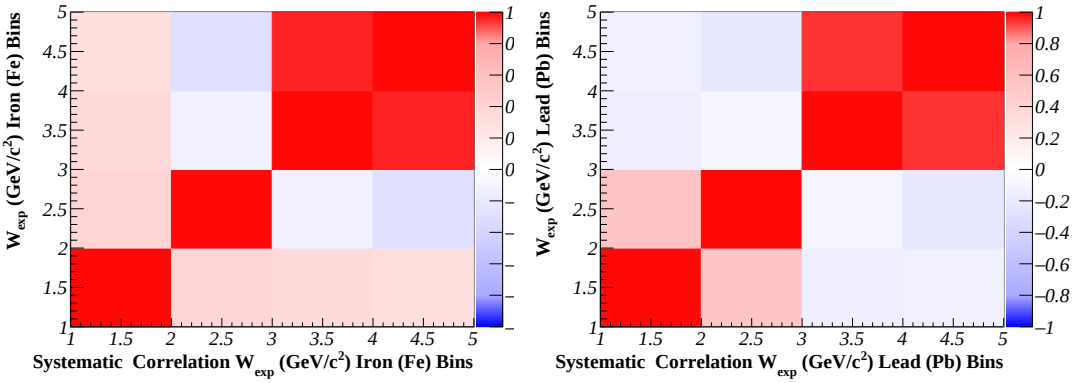
(d) Lead

Figure H-21: Q^2 Systematic Cross Section Ratio Uncertainty Correlation Matrix



(a) Carbon

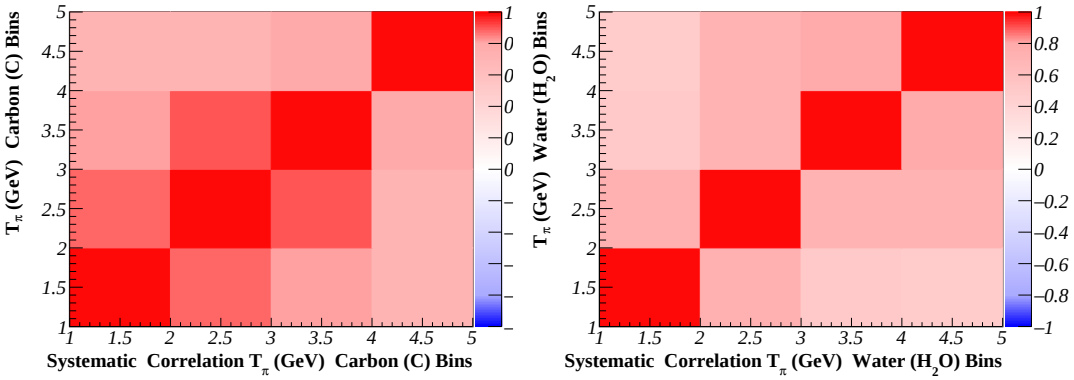
(b) Water



(c) Iron

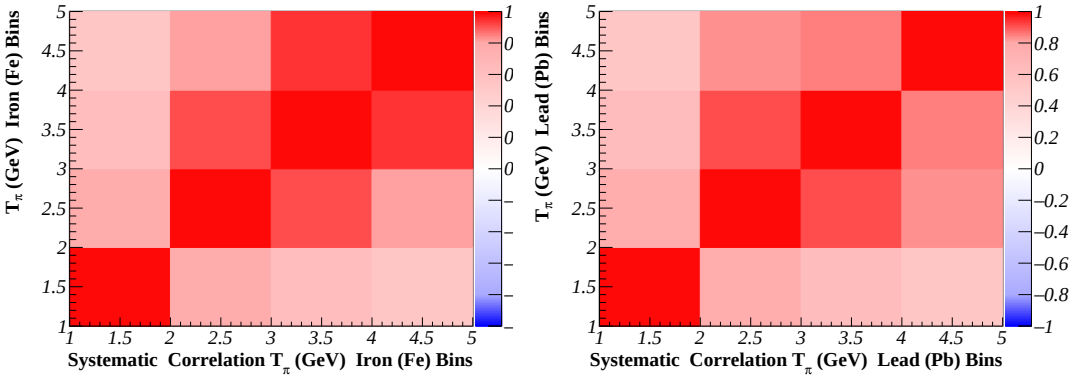
(d) Lead

Figure H-22: W_{exp} Systematic Cross Section Ratio Uncertainty Correlation Matrix



(a) Carbon

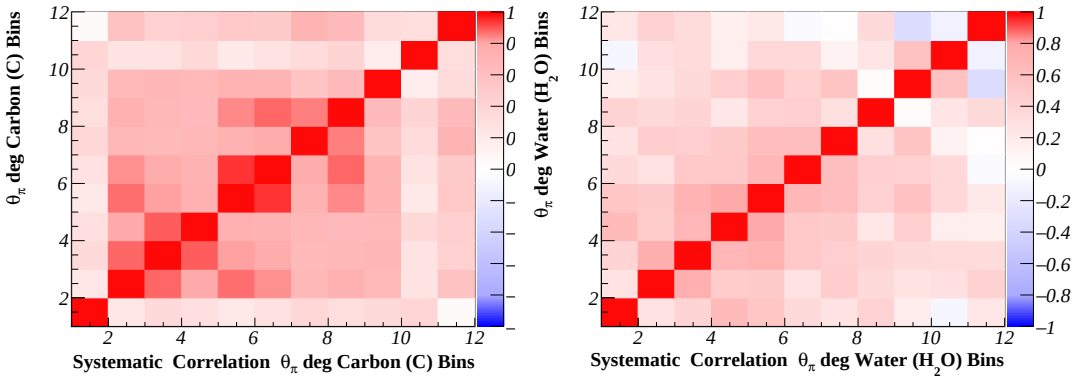
(b) Water



(c) Iron

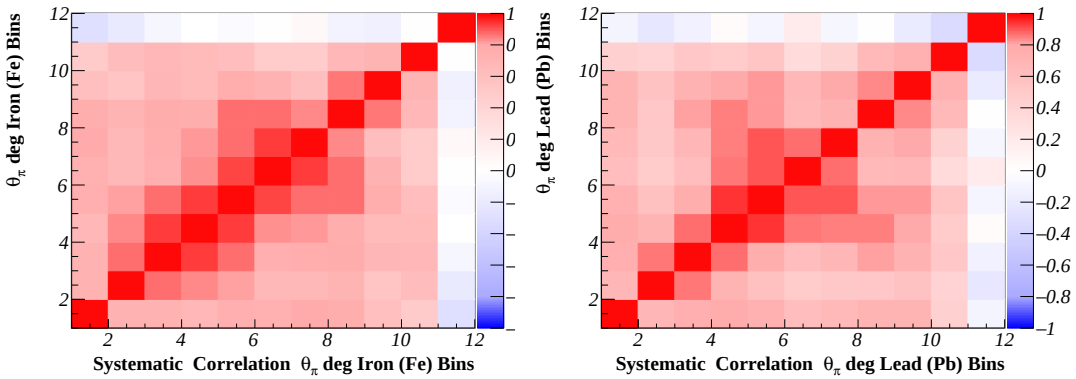
(d) Lead

Figure H-23: T_π Systematic Cross Section Ratio Uncertainty Correlation Matrix



(a) Carbon

(b) Water



(c) Iron

(d) Lead

Figure H-24: θ_π Systematic Cross Section Ratio Uncertainty Correlation Matrix